ISBN 978-89-950027-8-0[95550]



Proceedings of the

Joint 18th International Heat Pipe Conference and 12th International Heat Pipe Symposium

(Joint 18th IHPC and 12th IHPS)

June 12 – 16, 2016

Ramada Plaza Jeju Hotel, Jeju, Korea



Edited By

Heat Pipe Committee
Korean Society of Mechanical Engineers

Copyright © 2018, Heat Pipe Committee, Korean Society of Mechanical Engineers (KSME)

All rights reserved

No part of this ebook may be reproduced in any form, by photostat, microfilm, xerography, or any other means, or incorporated into any information retrieval system, electronic or mechanical, without the written permission of the publisher.

All inquiries should be emailed to ksmepco@ksme.or.kr

Korean Society of Mechanical Engineers (KSME), Heat Pipe Committee
Room 702, KSTC New Bldg., 7 gil 22 Teheran-ro, Gangnam-gu, Seoul 06130, Korea
Tel:(02) 501-3646, 3648 FAX:(02) 501-3649
Visit us at **www.ksme.or.kr**
ISBN : 978-89-950027-8-0[95550]

Proceedings

Proceedings are the final collection of papers from the Joint of 18th IHPC and 12th IHPS. They are typically produced after the conference such that "no-show" papers are deleted.

Proceedings are published by *Heat Pipe Committee, Korean Society of Mechanical Engineers (KSME)*, they will be citable via an ISBN and a unique industry-standard identifier assigned to every paper.

Copyright conditions

"All publication material submitted for presentation at **the Joint of 18th IHPC and 12th IHPS** must be original and hence cannot be already published, nor can it be under review elsewhere. The authors take responsibility for the material that has been submitted. The conferences will abide by the highest standard of ethical behavior in the review process and the authors will abide by the publication ethics guidelines.

The author(s) must confer the copyright to KSME when they submit the final version of the paper through the paper submission process. The author(s) retain the right to use a copy of the paper for personal use, internal institutional use at the author(s)' institution, or scholarly posting at an open web site operated by the author(s) or their institution, limited to noncommercial use. Any other use of the paper requires approval by Heat Pipe Committee, Korean Society of Mechanical Engineers.

Table of Contents

Joint 18th International Heat Pipe Conference and 12th International Heat Pipe Symposium

Foreword v

Organizing Committee vii

International Committee

Local Organizing Committee

Program Information ix

Conference Topic

List of Keynote Lectures x

List of Papers xi

Keynote Lectures 1

Abstracts and Full Papers 25

Author Index 453



Organizedby

Heat Pipe Committee
KSME Korean Society of Mechanical Engineers

Supported by

JAPAN ASSOCIATION for HEAT PIPE

Jeju CVB
Jeju Convention & Visitors Bureau
|사|제주컨벤션뷰로

KOREA TOURISM ORGANIZATION
www.visitkorea.or.kr

Sponsored by

DAEHONG ENTERPRISE CO., LTD.

SAMJINTECH Thermal Solution

KIER 한국에너지기술연구원
KOREA INSTITUTE OF ENERGY RESEARCH

UJ UNIWEL

APACK, INC.

JNM MECA Tech

Auras

Foreword



Professor
Joon Hong Boo
Conference Chair

It is our great pleasure to present the Proceedings of the Joint 18th International Heat Pipe Conference and the 12th International Heat Pipe Symposium (Joint 18th IHPC and 12th IHPS), which was held in Jeju, Korea, during June 12-16, 2016.

On the heels of the success of the IHPC and the IHPS series, this conference was organized as a joint event for the first time ever in the history of heat pipe societies. The conference encompassed the broad spectrum of topics related to heat pipe and thermosyphon developments, and provided a forum to enable scientist and engineers to exchange state-of-the-art technology and information. The conference was organized by the Heat Pipe Committee of the Korean Society of Mechanical Engineers (KSME) under the coordination of the Committee on the Joint International Heat Pipe Conferences and Symposia. This volume of proceedings was edited by the Local Organizing Committee.

More than 240 professionals and specialists from industry and academia from 23 countries participated in the conference to share their knowledge and experiences. Altogether 144 technical papers and four keynote lectures were presented in 16 technical sessions organized based on the following topics.

- General Aspects of Heat Pipes/Conventional Heat Pipes
- Loop Heat Pipes/Capillary Pumped Loops
- Pulsating Heat Pipes/Oscillating Heat Pipes
- Vapor chambers/Flat Heat Pipes
- Micro Heat Pipes
- Two-phase Thermosyphons/Loop Thermosyphons
- Special Heat Pipes/Novel Design of Heat Pipes

Among the presented papers during the conference, 61 papers have been published as the special issues in five renowned journals after rigorous peer review processes. The journal names and number of papers (in the parentheses) were as follows.

- Applied Thermal Engineering (26)
- Heat and Mass Transfer (17)
- Heat Transfer Engineering (6)
- Journal of Mechanical Science and Technology (6)
- Heat Pipe Science and Technology (6)

For those papers which have been published in the above journals, only the abstracts are included in the present volume of the proceedings to avoid copyright issues. However, the details for the access to the full papers are provided at the end of each abstract.

We hope that this publication will provide the readers with useful knowledge and information on up-to-date heat pipe science and technology, of which the application included energy conversion systems, heat transfer apparatuses, electronics cooling systems, and space as well as terrestrial thermal control devices. It is expected that the heat pipes will continue to expand their application in various emerging fields including mobile devices, electric vehicles, new and renewable energy systems, and bio-medical instruments.

Sincere thanks are due to the participants, especially the authors and presenters of the papers. Our thanks are extended to session chairs, sponsors and supporters of the conference. Especial appreciation is expressed to four distinguished Keynote Lecturers; Professors Massoud Kaviany, Sang Yong Lee, Jian Yin Miao, and Hosei Nagano for sharing their profound knowledge and valuable experience.

I would like to express gratitude to the International as well as Local Organizing Committee Members for their advice, guide, suggestions, and efforts for organizing and managing the conference. Finally, heartily thanks are expressed to Co-chairs, Dr. Young Soo Lee and Dr. Kwang Soo Kim, and Secretary General, Prof. Seok Ho Rhi, without whose passion and devotion the conference could have never been successful.

On behalf of the Local Organizing Committee of the Joint 18th IHPC and 12th IHPS, I wish that the next conference in Pisa, Italy in June, 2018 to be even more successful one.

Joon Hong Boo

Conference Chair

Organizing Committee

International Committee
(Committee on Joint International Heat Pipe Conferences and Symposia)

Honorary Chairman

Prof. **M. Groll** (Stuttgart, Germany)

Chairman

Prof. **J. Bonjour** (Lyon, France)

Past Chairman

Prof. **Yu. F. Maydanik** (Ekaterinburg, Russia)

Members

- Prof. A. Akbarzadeh (Melbourne, Australia)
- Prof. J. H. Boo (Seoul, Korea)
- Prof. C. A. Busse (Leggiuno, Italy)
- Prof. S. W. Kang (Taipei, Taiwan)
- Prof. M. Katsuta (Tokyo, Japan)
- Prof. S. Khandekar (Kanpur, India)
- Prof. M. Mantelli (Florianopolis, Brazil)
- Prof. J. M. Ochterbeck (Clemson, USA)
- Prof. K. S. Ong (Kuala Lumpur, Malaysia)
- Prof. W. Qu (Beijing, China)
- Prof. P. Stephan (Darmstadt, Germany)
- Mr. W. Supper (Noordwijk, Netherlands)
- Prof. P. Terdtoon (Chiang Mai, Thailand)
- Prof. L. L. Vasiliev (Minsk, Belarus)
- Prof. M. Marengo (Brighton, United Kingdom)



Local Organizing Committee

Chair

Prof. **J. H. Boo** (Korea Aerospace University)

Co-chair for Industry

Dr. **K. S. Kim** (Apack, Inc.)

Dr. **Y. S. Lee** (KIER)

Secretary General

Prof. **S. H. Rhi** (Chungbuk National University)

Members

- Prof. W. G. Chun (Jeju National University)
- Dr. W. Joung (KRISS)
- Prof. J. S. Kim (Pukyung National University)
- Prof. J. S. Seo (GyeongSang National University)
- Mr. S. S. Kim(Daehong Enterprise Co.,Ltd.)
- Prof. S. J. Kim (KAIST)
- Dr. K. W. Lee (KIER)
- Dr. W. H. Lee (KIER)
- Dr. S. H. Moon (ETRI)
- Prof. D. H. Cho (Daejin University)
- Prof. C. Byon (UNIST)
- Mr. C. Y. Choi (Samjin Tech Co., Ltd.)
- Dr. Y. P. Lee (KIST)
- Prof. M. S. Kim (Chung-Ang University)
- Dr. W. B. Chung (Daehong Enterprise Co., Ltd.)
- Prof. Y. C. Park (Jeju National University)



<History of IHPC and IHPS>

History of the International Heat Pipe Conference (IHPC) :

	LOCATION	YEAR
1st IHPC	Stuttgart, Germany	1973
2nd IHPC	Bologna, Italy	1976
3rd IHPC	Palo Alto, USA	1978
4th IHPC	London, UK	1981
5th IHPC	Tsukuba, Japan	1984
6th IHPC	Grenoble, France	1987
7th IHPC	Minsk, Belarus	1990
8th IHPC	Beijing, China	1992
9th IHPC	Albuquerque, USA	1995
10th IHPC	Stuttgart, Germany	1997
11th IHPC	Tokyo, Japan	1999
12th IHPC	Moscow, Russia	2002
13th IHPC	Shangai, China	2004
14th IHPC	Florianopolis, Brazil	2007
15th IHPC	Clemson, USA	2010
16th IHPC	Lyon, France	2012
17th IHPC	Kanpur, India	2013
18th IHPC and 12th IHPS	Jeju, Korea	2016

History of the International Heat Pipe Symposium (IHPS) :

	LOCATION	YEAR
1st IHPS	Tokyo, Japan	1985
2nd IHPS	Osaka, Japan	1987
3rd IHPS	Tsukuba, Japan	1988
4th IHPS	Tsukuba, Japan	1994
5th IHPS	Melbourne, Australia	1996
6th IHPS	Chiangmai, Thailand	2000
7th IHPS	Jeju, Korea	2003
8th IHPS	Kumamoto, Japan	2006
9th IHPS	Kuala Lumpur, Malaysia	2008
10th IHPS	Taipei, Taiwan	2011
11th IHPS	Beijing, China	2013
12th IHPS and 18th IHPC	Jeju, Korea	2016

Keynote Lectures



"Multi scale, Distributed Wicks"

Professor **Kaviany, Massoud**
Department of Mechanical Engineering, University of Michigan, USA _ ***3***



"Two-phase Flow Research in Mini/Micro Channels Relevant to Heat Pipe Applications"

Professor **Lee, Sang Yong**
Department of Mechanical Engineering, KAIST Korea _ ***4***



"Application of Phase Change Technology in China's Lunar Probe"

Professor **Miao, Jian Yin**
Beijing Key Laboratory of Space Thermal Control Technology,
China Academy of Space Technology, China _ ***16***



"Challenges in Expanding the Range of Application of Loop Heat Pipe to both Smaller Scale and Larger Scale"

Professor **Nagano, Hosei**
Department of Aerospace Engineering, Nagoya University Japan _ ***17***

List of Papers (Abstracts and Full Papers)

1. General Aspects of Heat Pipes / Conventional Heat Pipes 29

Effect of Meniscus on the Permeability of Sintered Particle Wicks/Sora Jeon, Chan.....29

Experimental Performance and Parametric Analysis of Heat Pipe Heat Exchanger for Air Conditioning Application Integrated with Evaporative Cooling / Tushar S. Jadhav 29

Preparation and Testing of Nickel-based Superalloy/Sodium Heat Pipes/Longfei Hu, Qin Lu, Haitao Han, Siyuan Chen, Bangcheng Ai, Zhihu Xue 30

Experimental Study and Analysis of Applying Thermoelectric Cooler to Improve LHP Operation with Non-condensable Gas / Rui Yang, Guiping Lin, Jiang He, Lizhan Bai, Jianyin Miao 30

Experimental Investigation for the Optimization of Heat Pipe Performance In Latent Heat Thermal Storage / Chandrakishor L. Ladekar, S. K. Chaudhary, S. S. Khandare 31

Modeling and Performance of Heat Pipes With Long Evaporator Sections / Wessel W. Wits, Gert Jan TeRiele 31

Permeability Model of Sintered Porous Media: Analysis and Experimental / Juan Pablo Flórez M., Maria E. Chiamulera, Marcia B.H. Mantelli 32

A Study on the Performance Characteristics of Heat Pipes with Multiple Heat Sources / Joon Hong Boo, Hyun Gon Kim 32

Heat Pipe System Development for Railway Application Working with Speed Motion Convection / Thomas Albertin, Jérôme Coulloux 33

Examination of the Thermoelectric Inhomogeneity of Thermocouples in an Electric Furnace with Heat Pipe Liner / Yonggyoo Kim, Wukchul Joung, Suyong Kwon 33

Modeling of Heat Transfer in the Evaporation and Condenser of the Working Fluid in the Heat Pipe / Richard Lenhard, Milan Malcho, Jozef Jandacka 34

Thermoelectric System to Increase the Cooling Power of Natural Convection Heat Pipes / Álvaro Martínez, David Astrain, Antonio Rodríguez, Patricia Aranguren, Miguel Araiz 34

Design and Startup of TZM High-temperature Heat Pipe / Qin. Lu, Longfei Hu, Siyuan Chen, Wei. Li.....35

Heat Dissipation for High Power Semiconductor Lasers by Heat Pipe Cooling System / Shu Shili, HouGuanyu, Wu Hao, Wang Lijie, Tian Sicong, Leonid L. Vassiliev, Tong Cunzhu 35

Experimental Analysis of Thermal Performance According to Heat Pipe Working Fluids for Evacuated Tube Solar Collector / Hongjin Joo, Heeyoul Kwak 36

Nanofluid Performance as a Working Fluid in the Heat Pipe / Joohyun Lee, KwonsuYong , Wukchul Joung 36

A Single Unit Cooling Fins Aluminum Heat Pipe for 100w Socket Type COB LED Lamp / S. H. Moon, Y. W. Park, H.M Yang 37

Development of Advanced High Porosity Wicks for the High Temperature Heat Pipes of Concentrating Solar Power / Sergii Khairnasov, Charles E. Andraka, Volodymyr Baturkin, Vladlen Zaripov, Oleksandr Nishchyk 37

High Power Heat Removal by Heat Pipes &Two Phase Heat Transfer for Electric Vehicle / Masataka Mochizuki, Yuji Saito, Koichi Mashiko, Thang Nguyen, Randeep Singh, Thomas van Raay ikura 38

Cooling of LED Headlamp in Automotive by Heat Pipes / Randeep Singh, Masataka Mochizuki,Yuji Saito, Tadao Yamada,Tien Nguyen,Thang Nguyen 46

Transport Phenomena of Liquid Film in Wick of Heat Pipes / A. Nouri-Borujerdi 54

An Evaluation of Hybrid Wick Design on High Performance Copper-Ethanol Heat Pipes / Guanghan Huang, Ahmed Abdulshaheed, Wei Chang, Chen Li.....59

Operational Characteristics and Thermal Performance of a Rectangular Heat Pipe Fabricated on a Plastic Board / Yasushi Koito, Hiroyuki Maehara, Daisuke Shimada, Toshio Tomimura.....67

Modelling of a Single Rotating Heat Pipe for Heat Pipe Assisted Annealing Concept/Metin Celik, Geert Paulussen, Pepijn Pronk, Laurent Sturnack, Wiebren de Jong and Bendiks Jan Boersma.....72

Comparison between CFD Simulation, Simple Calculation and Experiment Data for Heat Pipe Maximum Heat Transfer, Equivalent Thermal Conductivity and Thermal Resistance/ Chayatis Kirdnaimongkol, Masataka Mochizuki, Thang Nguyen, Yuji Saito, Yoji Kawahara, Tien Nguyen, and Mohammad Shahed Ahamed 79

Heat Pipe Heat Exchanger for Heat Recovery: How Much Working Fluid should We Charge / L.C. Ding, Y.H. Yau, M.F. Remeli, B. G. Orr, B. Singh, A. Date, A. Akbarzadeh 85

Hybrid Cooling System for High-Power Laser Diodes/Leonid L. Vassiliev, Leonid P. Grakovich, Shu Shili, Hou Guanyu,Wu Hao, Wang lijie, Tian Sicong and Tong Cunzhu 90

Self-Venting Arterial Heat Pipes for Spacecraft Applications/William G. Anderson, Derek Beard and Calin Tarau.....96

2. Loop Heat Pipes / Capillary Pumped Loops 101

Development and On-orbit Operation of Loop Heat Pipes System on Chinese Circumlunar Return and Reentry Spacecraft / Zhang Hongxing, Mi Min, Miao Jianyin, Wang Lu, Chen Yang, Ding Ting, Ning Xianwen, HuoYuhua 105

Design and Experimental Investigation of a Neon Cryogenic Loop Heat Pipe / He Jiang, GuoYuandong, Zhang Hongxing, Miao Jianyin, Wang Lu, Lin Guiping 105

A Numerical Study on Heat Transfer Characteristics of a Loop Heat Pipe Evaporator Using Three-Dimensional Pore Network Model / Masahito Nishikawara, Hosei Nagano, Marc Prat 106

Loop Heat Pipe-based Hydraulic Temperature Control Technique / Wukchul Joung, Yong Gyoo Kim, KeeSool Gam 106

Fabrication and Characterization of Efficient Wicks for Loop HeatPipes / R. Giraudon, S. Lips, D. Fabrègue, L. Gremillardb, E. Maire, V. Sartre 107

Microscale Infrared Observation of Liquid-vapor Interface Behavior on the Surface of Porous Media for Loop Heat Pipe, Kimihide Odagiri, Masahito Nishikawara, Hosei Nagano *107*

Analytical Model for the Dynamics of a Capillary Pumped Loop Subjected to High Amplitude Heat Load Steps: Estimation of the Liquid Flow Rate Overshoot / Sebastien Dutour, Ahmed Kaled *108*

Direct Numerical Simulation of Evaporation in a Biporous Media / Bharat. B. Sharma, Sudip. K. Samanta, Himadri Chattopadhyay, Gautam Biswas *108*

Development of a LHP for Power Avionics Application / Thomas Albertin, JérômeCoulloux *109*

Low-cost Manufacturing of Loop Heat Pipe for Commercial Applications / Bin-Juine Huang, Y. H. Chuan, P. E. Yang *109*

Startup Characteristics of Pump-assisted Capillary Phase Change Loop / Jiang Chi, Liu Wei, Liu Zhichun, Yang Jinguo, Duan Bin, Luo Xiaobing *110*

Analysis of Chaotic Flow in a 2D Multi-turn Closed-loop Pulsating HeatPipe / Sam M. Pouryoussefi, Yuwen Zhang *110*

A Novel "Multi-Stages" Loop Heat Pipe for Cooling Multiple Heat Sources / C. Figus, L. Dandaleix, J. Hill and L.Barremaecker *111*

The Operation Mode Study of an Integrated System with Double Pulse Tube Coolers and Double Cryogenic Loop Heat Pipes / Wang Lu, Miao Jianyin, Zhang Hongxing, Mo Qing, He Jing and Guo Yuandong *117*

Two Phase Loop Spray Impingement Cooling System/Thanh-Long Phan, Randeep Singh, Yuji Saito, Masataka Mochizuki *124*

Effect of Different Charge Ratio on Startup Performance of the Bifacial Evaporator Loop Heat Pipe/ZhiChun Liu, Song He, Wei Liu and JinGuo Yang *131*

Development of 100W-class Loop Heat Pipes for Space Use and On-orbit Experiment Test Plan / Atsushi Okamoto, Ryuta Hatakenaka, Takeshi Miyakita and Hiroyuki Sugita *138*

Capillary Thermosiphon Loop for High Power Electronic Cooling by Natural Convection / Vincent Dupont, Thomas Nicolle and Cyrille Billet *143*

Advanced Control Capillary Loop (ACL) Thermal Architecture with Multiple Evaporators and Condensers/D. Mishkinis, A. Kulakov, P. Prado, A. Torres and S. Lapensee *151*

Operational Characteristics of 10 m-Class Long-Distance Loop Heat Pipe under Anti-Gravity Condition/Kazuya Nakamura, Kimihide Odagiri and Hosei Nagano *159*

Vapor Modulated Variable Conductance Loop Heat Pipes for Space Applications / Paula Prado-Montes, Donatas Mishkinis and Alejandro Torres *167*

Cryogenic Loop Heat Pipe Characteristics Analysis coupling Satellite Infrared Detector and Cryogenic Radiator / Hyokjin Cho, Lingxue Jin, Guee-Won Moon and Sangkwon Jeong *178*

Designing and Research of Precise Thermal Control System with Loop Heat Pipe / V. Antonov, M. Balykin, A.Golikov, K. Goncharov, K. Korzhov and V.Buz *182*

A Study of Root-Zone Heating System using Bubble Jet Loop Heat pipe for Horticulture / Jongsoo Kim, Sangjin Park, Junha Kim, Jaeyoung Bae, Eonhwa Hwang, Dobin Kim, Sungbok Kim and Intaek Oh *187*

Development of Loop Heat Pipes with Sintered Nickel Wick Using Cold Isostatic Press Method / Won Bok Chung, Seon Hong Hwang, Cheol Min Park, Yoon Sung Kim and Sang Sik Kim *190*

Ground Test of Dual Loop Heat Pipe System/Yasuko Shibano, Naoko Iwata, Hiroyuki Ogawa *198*

Prototype of Thin Loop Heat Pipe with Glass Fiber Wick for Compact Electronics Cooling / Alexander A. Yakomaskin 203

Experimental Study on the Driven Mechanism of a Vapor-liquid Separated Flat Loop Heat Pipe Evaporator/Shuo Zhao, Kai Zhu, Mingzhu Zheng, Yabo Wang, Yang Yang and Jie Wei 209

Development and Mass Production of Loop Heat Pipes/Yury F. Maydanik, Arkadiy V. Ivanov and Mikhail Yu. Maidanik..... 217

3. Pulsating Heat Pipes/Oscillating Heat Pipes 219

Modeling and Experimental Investigation of a Thermally Driven Self-oscillating Pump / Marijn P. Zwier, Wessel W. Wits, Henk Jan van Gerner 221

Oscillation of an Isolated Liquid Plug Inside a Dry Capillary / Vyas Srinivasan, Siddhartha Kumar, Md. Asfer, Sameer Khandekar 221

A Pulsating Heat Pipe Cooler for Integrated High Power LEDs / LucangLv, Ji Li, Guohui Zhou 222

Experimental Study on a Hydrogen Pulsating Heat Pipe with Different Adiabatic Lengths / Haoren Deng, Xiao Sun, Dongyang Han, Shunhao Wang, Bo Jiao, J.M. Pfotenhauer, Zhihua Gan 222

In Situ Investigation of Liquid Films in PHP / Laura Fourgeaud, Vadim Nikolayev, Eric Ercolani, JérômeDuplat, Philippe Gully 223

Experimental Studies of Surface Modified Oscillating Heat Pipes / Tzong-ShyngLeu, Cheng-Han Wu 223

Innovative Thermal Design Satellite with Networked Variable Conductance Oscillating Heat Pipes / Naoko Iwata, Hiyoruki Ogawa, Yoshiro Miyazaki, Hiroki Kawai, Seisuke Fukuda 224

Visualizations of the Flow Patterns in a Closed Loop Flat Plate PHP with Channel Diameter above the Critical One and Tested under Microgravity / Vincent Ayel, Lucio Araneo, Pietro Marzorati, Cyril Romestant, Yves Bertin, Marco Marengo 224

Motion of Liquid Plugs between Vapor Bubbles in Capillary Tubes:A Comparison between Fluids / Rémi Bertossi, Vincent Ayel, Balkrishna Mehta, Cyril Romestant, Yves Bertin, Sameer Kandhekar 225

Hybrid Pulsating Heat Pipe for Space Applications with Non Uniform Heating Patterns: Ground and Microgravity Experiments / D. Mangini, M. Mameli, D. Fioriti, S. Filippeschi, L. Araneo, M. Marengo 225

An Experimental Investigation of Operating Limit in an Oscillating Heat Pipe / YulongJi, Qingzhen Zhang, Chao Chang, Hongbin Ma 226

Double Condenser Pulsating Heat Pipe Cooler / Daniele Torresin, Francesco Agostini, Bruno Agostini, Mathieu Habert..... 226

Visualization and Thermal Resistance of Magnetic Nanofluid Pulsating Heat Pipe /Ying-Chang Lu, Yao-Chun Wang, Hung Wang, Shung-Wen Kang 227

Ammonia Pulsating Heat Pipe: A New Full Visualization Experiment and the Operating Mechanism Study / Z. H. Xue, L. Chen, M. H. Xie, W. Qu, W. Li 227

Experimental Research on Start-up Characteristics and Heat Transfer Performance of Pulsating Heat Pipe with Rectangular Cross-section / Wang Xuehui, Hua Chao, Gao Xu, Zheng Haoce, Han Xiaohong, Chen Guangming 228

Thermal Performance Comparison of Closed-loop Tube Oscillating Heat Pipes with and without Internal Microgrooves / Jian Qu, Xiao Jun Li, Qian Wang, Qin Sun 228

Experimental Investigation on Silicon-based Pulsating Heat Pipes with Different Channel Geometries / Jungseok Lee, Sung Jin Kim 229

A Study on Thermal Performance of Parallel Connected Oscillating Heat Pipe / Byeong-Chan Kim, Daejoong Kim, Longnan Li, Ji Hoon Kim 229

Volume and Saturation Temperature Variation of an Expanding Taylor Bubble in a Heated Capillary / Antoine Voirand, Adel M. Benselama, Yves Bertin 230

Experimental Study on the Effect of the Ratio of Adiabatic Section Length to Condenser Length on the Thermal Performance of Pulsating Heat Pipes / Juno Kim, Sung Jin Kim 230

Experimental Investigation of a Novel Solar Collector with Pulsating Heat Pipe / H. Kavoosi Balotaki, M.H. Saidi 231

Effect of Tube Heat Conduction on the PHP Start-up /Vadim Nikolayev, Iaroslav Nekrashevych 231

Condenser Temperature Effect on the Transient Behavior of a Pulsating Heat Pipe / A.Betancur, D.Mangini, L. Mameli, S. Filippeschi, L. K. Slongo, K. Paiva, M. Marengo, M. Mantelli 232

Experimental Investigation of Oscillating Heat Pipes under Direct Current and Pulse Width Modulation Heating Input Conditions / Brent S. Taft, Matthew Rhodes 232

Experimental Investigation on the Thermal Performance of Pulsating Heat Pipes with Asymmetric Channels / Dong Soo Jang, Dongwoo Kim, Dowon Cha, Hanseok Mun, Yongchan Kim 233

Study on Thermal Cycle in Oscillating Heat Pipes by Numerical Analysis/Takurou Daimaru, Shuhei Yoshida and Hiroki Nagai....234

Performances and Limits of a Multi-Source Pulsating Heat Pipe Tested under High Heat Flux Density / David Dufraisse, Vincent Ayel, Yves Bertin and Cyril Romestant....242

Thermo-Hydrodynamics of Phase-Change Induced Oscillating Taylor Bubble Flows / Vyas Srinivasan, Manoj Rao, Sameer Khandekar, Frédéric Lefèvre and Jocelyn Bonjour....250

An Improved Correlation to Evaluate the Thermal Resistance of Pulsating Heat Pipes/Jean-antoine Gruss, Damien Gloriod, Nadia Caney, Geneviève Geffraye and Alain Memponteil....258

A study on circulation flow of Oscillating Heat Pipe with check valves by visualization / Shuhei Yoshida, Takurou Daimaru and Hiroki Nagai....264

Heat Transfer Characteristics of Flat Plate Pulsating Heat Pipe Using Self-Rewetting Fluids / Koki Yamagami, Koji Fumoto, Raffaele Savino, Tsuyoshi Kawanami and Takao Inamura 271

4. Two-phase Thermosyphon / Loop Thermosyphon/ Separate type Heat Pipe / Wickless Heat Pipes 277

Experimental Study on Different Control Modes of CSHP / Jingyu Cao, Gang Pei, Jiao Dongsheng, Zhao Pinghui, li Jing, Wang Yunyun 279

Long Horizontal Vapor Dynamic Thermosyphons for Renewable Energy Sources / Leonard. Vasiliev, A. S. Zhuravlyov, M. I. Rabetsky, L. P. Gracovich, Leonid L.Vassiliev Jr., Alexander Shapovalov, Alexei Rodin 279

Effect of Heat Source Size on Cooling Performance of a JEST-Type Loop Thermosyphon / Ayaka Suzuki, Kaoru Sato, Yasushi Koito, Toshio Tomimura 280

Simulation and Experimental Validation of a 400m Vertical CO_2 Heat Pipe for Geothermal Application / J.-Chr. Ebeling, S. Kabelac, S. Luckmann, H. Kruse 280

An Exhaust Heat Recovery System Utilizing Thermoelectric Generators and Heat Pipes / Bradley G. Orr, Aliakbar Akbarzadeh, Petros Lappas 281

Study of Thermal Characteristics in a Reverse Thermosyphon Loop / Meng-Chang Tsai, Hung Wang, Fong-Hao Wu, How-Ming Lee, Heng-Yi Li, Shung- Wen Kang 281

Thermal Behavior of Heat Pipe Assisted Alkali-metal Thermoelectric Converter / Jisu Lee, Wookhyun Lee, Riguang Chi, Wonsik Chung, Seokho Rhi, Kyebock Lee, Seonyong Jeong, Jongchan Park, Youngsoo Lee 282

Heat Transfer Capacity of a Closed Loop Two-phase Ammonia-stainless Steel Thermosyphon in Lunar Gravity / Ke Wu, Jian-Fu Zhao, Zhen-Dong Li, Hong-Xing Zhang,Jiang He, Jian-Yin Miao 282

Study on Heat Pipe Assisted Thermoelectric Power Generation System from Exhaust Gas / Riguang Chi, Jongchan Park, Wonsik Chung, Seokho Rhi, Kyebock Lee 283

Length Effect on the Entrainment Limitation of a Wickless Heat Pipe / Joseph Seo, Jae Young Lee 283

Numerical Investigation of a CO_2 Loop Themosyphon for Free Cooling of Data Centers / Hainan Zhang, Shuangquan Shao, Changqing Tian 284

Energy Saving Potentials from the Application of Heat Pipes on Geothermal Heat Pump Systems / Hyungjeong Lim, Minsung Kim 284

The Design of a Split Loop Thermosyphon Heat Exchanger for Use in HVAC Applications/Daniel Reist, Michael Ellis, Mark C. Stevens, and Pete M. Dussinger 285

Transient Detailed and Reduced Models of a Two-Phase Loop Thermosyphon/Serge H. Bodjona, Etienne Videcoq, Manuel Girault and Yves Bertin 289

Loop Thermosyphon Model for Condensers with Non-Condensable Gas Applied to Distillation Units/ Luis H.R. Cisterna, Estevan G. Tavares, Kênia W. Milanez, Tiago W. Uhlmann, Fernando H. Milanez and Marcia B.H. Mantelli 297

Theoretical and Experimental Analysis of an Herbs Dryer Assisted by Two-Phase Thermosyphons/ Luis H.R. Cisterna, Diogo M.M. Caldas, Fernando H. Milanez and Marcia B.H. Mantelli 305

How a Wall Thermosyphon can Enhance the Energy Savings in a Prefabricated House in Italy / F.Fantozzi, S. Filippeschi, M. Mameli, Marcia B. H. Mantelli and Fernando H. Milanez 313

Mechanism and Technology of High and Super High Temperature Heat Pipes/Wei Qu, Zhihu Xue and Jijun Yu 322

Experimental Investigate on Heat Transfer Performance of Flat Heat Pipe Receiver in Solar Power Tower Plant/Lin Yang, Rui W. Zhou, Xiang Ling and Hao Peng 329

Influence of Charging Ratio, Annular Clearance and Enhanced Boiling Surface on the Thermal Performance of Bubble Jet Loop Thermosyphon/Jongsoo Kim, Sungbok Kim, Sangjin Park, Junha Kim, Jaeyoung Bae, Eonhwa Hwang, Dobin Kim and Intaek Oh 334

A New Modified Model for Simulation of a Two-Phase Closed Thermosyphon/Houfa Shen, Yucan Fu and Jiajia Chen 338

A Study on the Boiling Heat Transfer Performance of Evaporators with Metal Foam of Loop Type Two-Phase Thermosyphon/Dong-Hyun Cho, Chan-Yong Gweon and Sang-Hun Yun 344

Experimental and Numerical Study on the Heat Transfer Performance of a Single Thermosyphon / S.H. Oh, S.I. Kim, J.W. Choi, K.J.Lee and W.P. Chun 350

Boiling Heat Transfer Mechanism Inside The Narrow Space of Double-Tube Heat Pipe/ Risa Suenaga, Masafumi Katsuta and Taro Kato1 353

Modeling of Processes in the Waste Heat Boiler with Thermosyphon/Savchenkova Natalia and Kravtsov Dmitry 360

Experimental Tests on Sodium Thermosyphons/Tiago W. Uhlmann, Marcia B. H. Mantelli, Miriam Manzoni, Marco Marengo and Per Eskilson 364

Numerical Modeling of Heat Transfer Performance of Two-phase Closed Thermosyphon with R245fa Based on Sinda/Fluint/Limin Ma, Xiaoying Yin, Linlin Shang and Zhongli Ji 370

Reverse Thermosyphon in Conjunction with a Ground Source Heat Pump/Heng-Yi Li, Meng-Chang Tsai, Wei-Chi Su, Fong-Hao Wu and Wei-Chun Liao 379

Transient Numerical Model for Thermal Performance Analysis of a Two-Phase Closed Thermosyphon/Zhongchao Zhao, Hao Hu, Xiao Zhang and Pengpeng Jiang 386

Turbulent Film Condensation in Thermosyphons/A. Nouri-Borujerdi 394

5. Special Heat Pipes/Novel Design of Heat Pipes 399

Hybrid Variable and Constant Conductance Heat Pipes for Lunar and Martian Environments and High Heat Flux Space Applications / Mohammed T. Ababneh, CalinTarau, William G. Anderson 401

Thermo-Mechanical Characterization of Flexible Heat Pipes / Tanmay Jaipurkar, Sameer Khandekar, Pushpit Kant, Bishakh Bhattacharya, Siddharth Paralikar 401

Heat Pipes with Variable Thermal Conductance Property Developed for Space Applications / V. Kravets, Ye. Alekseik, O. Alekseik, S. Khairnasov,V. Baturkin, T. Ho, L. Celotti 402

Modeling of a Revolving Heat Pipe for Cooling of Grinding Wheels / Jiajia Chen, Yucan Fu, Houfa Shen, Dan Ewing, Chan Y. Ching 402

Design of a Thermosyphon-based Thermal Valve for Controlled High Temperature Heat Extraction / Christopher Oshman, Corey Hardin, Jonathan Rea, Michele L. Olsen, Nathan Siegel, Phil Parilla, David Ginley, Eric S. Toberer 403

Preliminary Investigation on Operation Characteristics of a High temperature special-shaped Heat Pipe Used in a Solar Thermo chemical Reactor / Tingtinga Ma, Xiaoyuan Wang, Yuezhao Zhu, Jinling Zeng 403

Characterization of a High Performance Ultra-Thin Heat Pipe Cooling Module for Mobile Hand Held Electronic Devices / Mohammad Shahed Ahamed, Yuji Saito, Koichi Mashiko, Masataka Mochizuki 404

The Two-phase Spreading of High Heat Fluxes Density Dissipative Components for Space and Non-space Applications / Mikaël Mohaupt, Stéphane Van Oost, Laurent Barremaecker 404

Hot Reservoir Stainless-Methanol Variable Conductance Heat Pipes for Constant Evaporator Temperature in Varying Ambient Conditions/Jens Weyant, Darren Campo and Calin Tarau 405

Gas-controlled Heat Pipes for Thermal Control System of Small Spacecraft / Konstantin A. Goncharov, Yuriy V. Panin, Kirill N. Korzhov and Adik R. Gutkin 412

Design and Numerical Simulation of a Flexible Heat Pipe for Human Cooling Application / Luis M. Tapia and Gerardo Carbajal 418

A Two-phase loop Cooling System with Capillary Evaporator Employing Bi-layer Copper Wick / Y. An, H. Kang, B. Sung, K. Yim, D.-A. Borca-Tasciuc, J. Choi 425

6. Vapor Chambers/Flat Heat Pipes 431

Some Important Factors Affect the Qmax Measurement of the Vapor Chamber / Wei-Keng Lin, J. K. Chen 433

DevelopmentofVaporChamberHeatSpreaderforSupercomputerProcessorPackaging Cooled by Liquid Cold Plate / Yuichi Yokoyama, Thanh-Long Phan, Yuji Saito, Koichi Mashiko, Masataka Mochizuki 433

Fundamental Experiments of a Polymer-based Vapor Chamber (Effect of Inclination Angle) / Fumihiko Hideyama, Shuto Nonoshita, Yasushi Koito, Toshio Tomimura 434

7. Micro Heat Pipes 441

An Interfacial Transport Analysis of Micro Heat Pipe / EuiGuk Jung, Joon Hong Boo 443

Discussion on the Solar Concentrating Thermoelectric Generation Using Micro-Channel Heat Pipe Array (STEG-MCHP) / Guiqiang Li, Wei Feng, Song Lv, Yi Jin, Xiao Chen, Jie Ji 443

Electric Motor Thermal Management System Using L-Shaped Flat Heat Pipes / Nandy Putra, Bambang Ariantara 444

Development of an Aluminum Flat Heat Pipe with Carbon Wire Wick / Y. W. Park, S. H. Moon, S. H. Rhi, K. S. Choi, J. H. Lee 444

A New Encapsulation Method Using Low-melting-point Alloy to Seal Micro Heat Pipe / Congming Li, Xiaodong Wang, Chuanpeng Zhou, Yi Luo, Zhixin Li, Sidi Li 445

Combination of Thermal Storage and Heat Spreading for High Power Portable Electronics Cooling / Zhiwei Li, LvcangLv, Ji Li 445

Development of Thin Heat Pipe for Thin and High Performance Note-book PC / Yoji Kawahara, Yuji Saito, Mohammad Shahed Ahamed, Yuichi Yokoyama 446

Keynote Lectures

Keynote Lecture

Multi scale, Distributed Wicks

M. Kaviany

Department of Mechanical Engineering, University of Michigan, Ann Arbor, Michigan 48109 U.S.A.

Abstract

Capillary artery evaporators allow for separate passages for the liquid and vapor and for targeting the passive liquid delivery to hot spots. Their dryout (critical heat flux) is governed by the capillary-viscous, hydrodynamics-instability, or other limits. We review examples of nonuniform, multi scale liquid arteries (hetero-micorpore capillaries) and their performance, starting with the instability limit (modulated wicks in pool boiling) and then the capillary-viscous limit (modulated-wick pipes and distributed-artery vapor chambers). For the latter, we discuss optimization of the liquid artery and evaporator wicks, achieving dryout limit of 500 W/cm^2 and evaporator resistance of 0.05 $K/(W/cm^2)$.

Keywords: heat pipe; vapor chamber; heat spreader; wick, capillary artery; multi scale wick

Keynote Lecture

Two-phase Flow Research in Mini/micro Channels Relevant to Heat Pipe Applications

Sang Yong Lee*

Department of Mechanical Engineering, KAIST, 291, Daehak-ro, Yuseong-gu, Daejeon 34141, Korea

Abstract

In this lecture, fundamentals on the pressure drop and heat transfer of the two-phase flow in mini/micro-scale channels relevant to the heat pipe systems are discussed. The lecture consists of three parts; the basics on the hydrodynamics of two-phase flow and phase-change heat transfer, and as an example, application of the models to predict the thermal performance of a pulsating heat pipe system. The most probable flow patterns expected to occur in heat pipes with the mini/micro-scale cross sections are the plug and the annular flows, and typical analytical models to estimate the pressure drop are introduced. Especially, for the plug flow pattern, adoption of the numerical method (VOF method) is briefly discussed. The heat transfer phenomena are strongly coupled with the hydrodynamic behavior of the two-phase mixture and the heat transfer correlations pertinent to each case are introduced. Finally, in the application part, considered are the mass, momentum and energy conservations for the plug flow that includes the liquid slugs, vapor bubbles and the liquid films (surrounding the bubbles), along with the appropriate interface conditions. Here, the compressibility of the vapor phase was taken into account and the results were compared to the measured data. Finally, the presentation is concluded with the future research issues.

Keywords: Two-phase flow pattern; Pressure drop; Heat transfer coefficient; PHP application

1. INTRODUCTION

Heat pipes are widely used for efficient transport of the thermal energy from the hot side to the cold side. Fig. 1 shows typical examples of heat pipes commonly found in heat exchanging devices. The two-phase (liquid and vapor) mixture of a working fluid is flowing inside a tube (or a bundle of tubes) while in operation. Fig. 1(a) is a heat pipe with the internal porous (wick) structure constructed along the internal surface of the tube. In this case, vapor is generated at the hot side by evaporation and flowing through the center portion of the pipe to the cold side. Once the vapor reaches the cold side, it is condensed and the liquid returns back to the hot side through the wick structure. Thus a counter-current annular flow is formed and the fluid keeps circulating between the evaporator and condenser sections. On the other hand, Figs. 1(b) and (c) are the heat pipes without any internal wick structure, named as thermo-syphon and pulsating heat pipe, respectively. The thermo-syphon is basically operated by the gravitational force; the vapor is rising up from the evaporator section (at the bottom) to the condenser section (at the top) through the adiabatic section. Once condensation occurs, the liquid falls down along the wall in a film shape to the evaporator section and the flow cycle repeats. The main difference between the wick heat pipe and the thermo-syphon is that the returning mechanism of the liquid phase from the condenser side to the evaporator side; the former is by the capillary force while the latter is by the gravitational force.

That is, the thermo-syphon does not work when

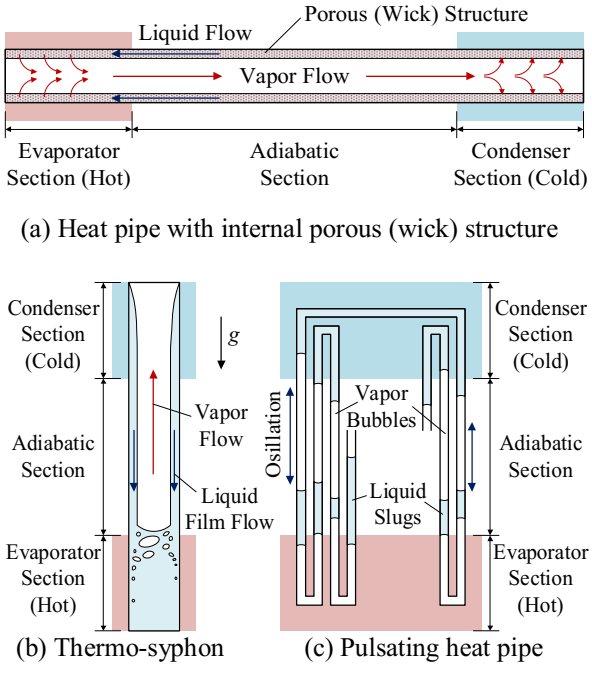


Fig. 1. Various configurations of heat pipes

*Corresponding author: sangyonglee@kaist.ac.kr, Phone: +82-42-350-3026, Fax: +82-42-350-8207

the heat source is located at the higher elevation compared to the heat sink. The pulsating heat pipe is operated by self-induced oscillation of the two-phase mixture inside a long, meandering tube between the hot and the cold sides. The liquid slugs (columns) are shaken by expansion and contraction of the neighboring vapor bubbles and the thermal energy is transported along with such an oscillation motion.

Hence, the hydrodynamic and heat transfer behavior of the two-phase mixture should be thoroughly understood for estimation of the thermal performance of the heat pipes, especially for the channels with the small cross-sectional area. The hydraulic-diameter range of the current interest is from 0.5mm to 5mm, which covers the size range of the channels in compact heat exchangers as well. Thus, in this lecture, some basic informations for prediction of the pressure drop and heat transfer rates of the two-phase flow in mini- and micro-scale channels are going to be introduced.

2. BASIC FLOW PATTERNS

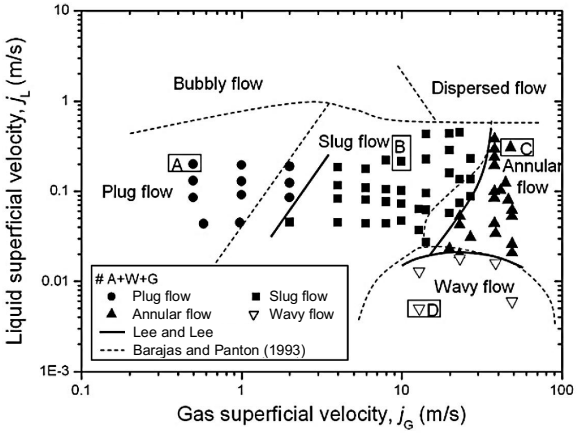
The first step to understand the two-phase flow behavior in the heat pipe system is to identify the flow pattern, such as bubbly, slug, plug, and annular flows. Once the flow pattern is identified, then the pressure drop and the heat transfer rate pertinent to each flow pattern could be estimated. The flow pattern depends not only on the flow rates and the fluid properties (such as density, viscosity) of the liquid and the gas (vapor) phases but also on the interfacial (surface) tension, wettability of the channel wall, method of heating (or cooling), and the channel configuration. Usually, the diameter of most of the heat pipes are less than 5 mm, which approximately corresponds to the range of the Eotvos number, N_{Eo}, below the unity (one) as follows:

$$N_{Eo} = \frac{gD_h^2(\rho_L - \rho_G)}{\sigma} < 1 \qquad (1)$$

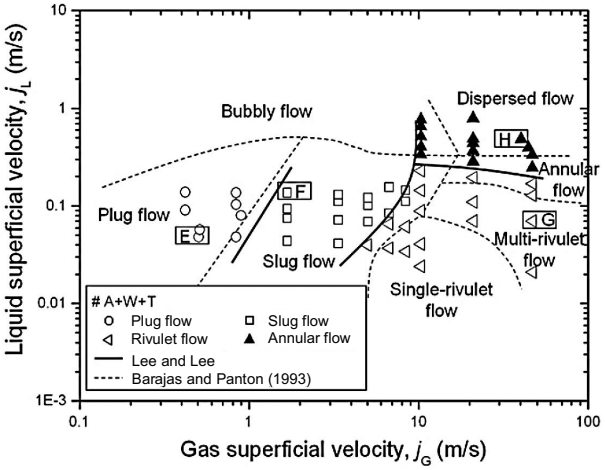
In this size range, the gravitational force is almost negligible whereas the interfacial tension (surface tension) plays a major role. There are extensive works reported on the two-phase flow patterns in mini/micro channels [1] – [21]. The two-phase flow behavior in micro-scale channels is very similar to that under the micro-gravity condition [8, 11, 13, 14, 17], which is extensively reviewed by Ohta [22].Thus the flow orientation (either vertical or horizontal) is not an important factor to be considered; thus the flow pattern maps in the plane of j_G and j_L, mostly adopted for the horizontal flows, are often employed to represent the two-phase flow regimes in mini/micro channels.

Fig. 2 is a typical flow pattern map of Barajas and Panton [6], later confirmed by Lee and Lee [21]. The ranges of j_G and j_L cover 0.2-100m/s and 0.003-2m/s, respectively, which encompass most of the flow rate ranges inside the heat pipes. As shown in Fig. 2(a), the plug flow occurs when both j_G and j_L are small. When j_L is increased while j_G is maintained low, the flow regime becomes bubbly. However, as the channel cross section becomes smaller, the bubbles have more chances to collide and merge with each other to form the elongated bubbles and the flow pattern changes to the plug flow. If j_G is raised while j_L remains fixed, the flow pattern is converted from the plug flow to the slug flow and then finally to the annular flow.

When j_G is kept high and if j_L is increased, the flow pattern changes from the annular flow to the dispersed flow because the drop entrainment from the liquid film to the core-air flow becomes more active. Also the wavy flow pattern is observed at



(a) Air-water flow in glass tube, A+W+G
(D = 1.46, 1.8mm; θ = 30°)



(b) Air-water flow in teflon tube, A+W+T
(D = 1.59mm; θ = 110°)

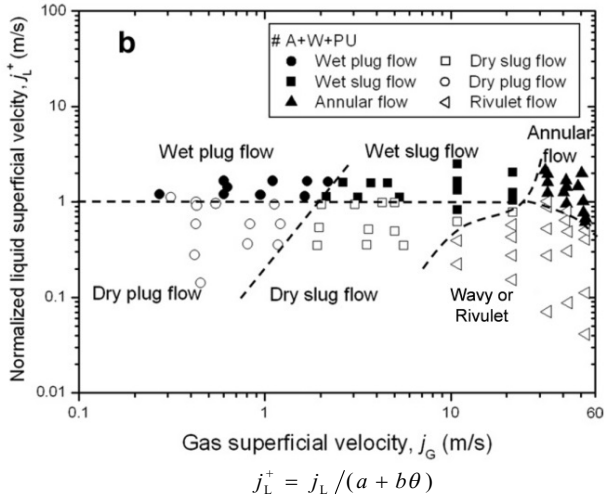
Fig. 2. Example of two-phase flow pattern map for small-scale tubes [6, 21])

the high-j_G condition if j_L is extremely small. The flow pattern map such as Fig. 2(a) is generally acceptable when the tube material is hydrophilic, for example, the air-water flow in glass tubes.

However, when the tube wall is hydrophobic (such as air-water flow in Teflon tubes, Fig. 2(b)), the flow pattern appears somewhat different. In this case, the wall surrounding the gas portion (of the plug- or slug-flow regime) tends to be dry, and the wavy flow in the high-j_G, low-j_L region is converted to the rivulet flow regime. This implies that, in mini- and micro-scale channels, the tube wettability should be taken into account additionally as an important factor. The effect of the tube materials was reported by Barajas and Panton [6], Iguchi and Terauchi [23-25], Nakamura et al. [26], Lee and Lee [20, 21], Rapolu and Son [27], etc. and the readers should refer to them. In Lee and Lee [21], to take account of the wettability effect, the modified liquid superficial velocity, $j_L^+(=j_L/(a+b\theta))$, was introduced, in which θ is the contact angle in radians and constants a and b are determined based on the degree of the surface wettability, i.e., highly wetting, marginally wetting and poorly wetting cases. For example, Fig. 3 is the modified flow pattern map for the marginally wetting case with its axes being j_G and j_L^+ (instead of j_G and j_L in Fig. 2), respectively, in which the dividing line between the "wet" and the "dry" regions is successfully represented by $j_L^+ = 1$. The criterion of $j_L^+ = 1$ is applicable to the highly wetting and poorly wetting cases as well.

At this stage, it is meaningful to check the flow pattern in the heat pipe systems. The bubbly and dispersed flows are practically unseen because the superficial velocity of the liquid phase is not large enough to form such flow patterns. In other words, the flow motion is induced only by heating (evaporation) and cooling (condensation) and the mass flow rate is rather low; hence the most probable flow patterns expected are the plug, slug and the annular flows.

It should be emphasized that the flow pattern maps as shown in Figs. 2 and 3 are simply the two-dimensional plots and the transition criteria cannot be expressed properly only with two parameters. That is, the flow pattern depends on the fluid properties as well as the superficial velocities of the gas and the liquid phases, and care should be taken in identifying the flow pattern.



$j_L^+ = j_L/(a+b\theta)$

Fig. 3. Generalized flow pattern map for mini-channels (Air-water flow in polyurethane tube, A+W+PU, D = 1.6mm, Lee and Lee [21])

3. TWO-PHASE FLOW PRESSURE DROP

Fig. 4 exemplifies typical measured results on the two-phase pressure drop in a rectangular channel with small gap by Lee and Lee [28]. As expected, the pressure drop gradient increases with increasing of the liquid and/or gas superficial velocities. The measured values depend on the mass flow rate, quality, fluid properties and channel configurations, and the ultimate goal of the two-phase modeling is to predict the pressure drop successfully in terms of those parameters. The details are discussed in the following sections.

3.1 Separated Flow Model

In principle, it is desirable to develop the models pertinent to each flow pattern to predict the pressure drop and the heat transfer. However, in many cases, the exact flow patterns are not known *a priori* and there should be other ways to handle those situations. Basically the pressure drop

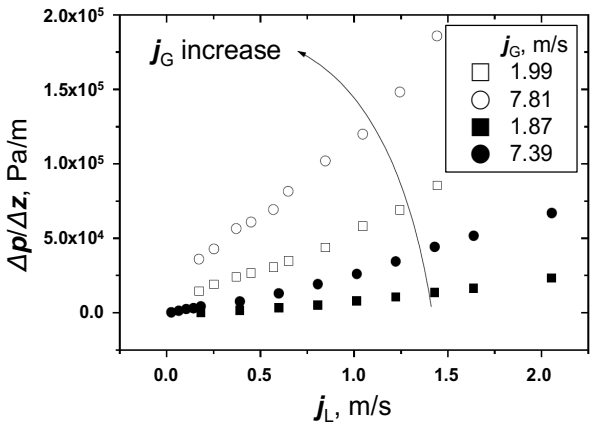


Fig. 4. Typical variation of pressure gradient with liquid and gas superficial velocities (Open symbols; 0.4×20mm^2; Solid symbols: 4×20mm^2, Lee and Lee [28])

gradient consists of the frictional, accelerational and the gravitational components. However, the gravitational component is negligibly small in mini/micro-scale channel flows. Also, the accelerational component is easily estimated with the proper information on the void fraction. Thus, the main focus is placed on the frictional component. One of the most popular ways to predict the friction pressure drop is using of the Lockhart-Martinelli model [29]. The Lockhart-Martinelli model is a type of the separated flow models in which the velocity difference between the gas and the liquid phases is considered, and is widely used in conventional two-phase flow analysis. In this model, the roles of the liquid- and gas-phases and the interaction between them are considered in determining the pressure-drop gradient by friction as shown in the equation below.

$$\left(-\frac{\mathrm{d}p}{\mathrm{d}z}F\right)=\left(-\frac{\mathrm{d}p}{\mathrm{d}z}F\right)_{\mathrm{L}}+C\left[\left(-\frac{\mathrm{d}p}{\mathrm{d}z}F\right)_{\mathrm{L}}\left(-\frac{\mathrm{d}p}{\mathrm{d}z}F\right)_{\mathrm{G}}\right]^{1/2}+\left(-\frac{\mathrm{d}p}{\mathrm{d}z}F\right)_{G} \quad (2)$$

Here, the first term in the right-hand side stands for the pressure-drop gradient for the liquid-only flow while the last term for the gas-only flow and they can be expressed as, respectively:

$$\left(-\frac{\mathrm{d}p}{\mathrm{d}z}F\right)_{\mathrm{L}}=\frac{2G^2(1-x)^2v_{\mathrm{L}}f_{\mathrm{L}}}{\mathrm{D}} \quad (3)$$

$$\left(-\frac{\mathrm{d}p}{\mathrm{d}z}F\right)_{G}=\frac{2G^2x^2v_{\mathrm{G}}f_{\mathrm{G}}}{\mathrm{D}} \quad (4)$$

Also, parameter C represents the measure of the interaction between the gas and the liquid phases, and is known to depend on the flow regime of each phase. By introducing the two-phase frictional multiplier based on the liquid-only flow, ϕ_{L}^2 , defined as

$$\phi_{\mathrm{L}}^2=\left(-\frac{\mathrm{d}p}{\mathrm{d}z}F\right)\Big/\left(-\frac{\mathrm{d}p}{\mathrm{d}z}F\right)_{\mathrm{L}} \quad (5)$$

and the Martinelli parameter as

$$X=\left[\left(\frac{\mathrm{d}p}{\mathrm{d}z}F\right)_{\mathrm{L}}\Big/\left(\frac{\mathrm{d}p}{\mathrm{d}z}F\right)_{\mathrm{G}}\right]^{1/2}, \quad (6)$$

Eq. (2) can be re-written as follows:

$$\phi_{\mathrm{L}}^2=1+\frac{C}{X}+\frac{1}{X^2} \quad (7)$$

For tubes of conventional size, constant values are given for C, specific to the flow regimes of the liquid and the gas phases whether they are laminar or turbulent, respectively. In other words, there are four combinations of the liquid-gas flow regimes, namely, laminar-laminar, laminar-turbulent, turbulent-laminar and turbulent-turbulent regimes, and the values are 5, 10, 12 and 20, respectively. [30] However, Mishima and Hibiki [12] have reported that C depends on the channel diameter as well; the value is smaller with the smaller channel diameter, and the following correlation was proposed:

$$C=21\left[1-\exp(-0.319D_{\mathrm{h}})\right] \quad (8)$$

According to Wambsganss et al. [31], C is also a function of the flow rate as:

$$C=mX^{w} \quad (9)$$

where m and w are expressed in terms of $\mathrm{Re}_{\mathrm{Lo}}$, the all-liquid Reynolds number. The above equation is recommended for use in the ranges of the mass quality greater than 0.05 and the mass velocity less than 350kg/m^{2}s, which corresponds to X<1 and $\mathrm{Re}_{\mathrm{Lo}}$<2200, respectively. For the mass velocity greater than about 400kg/m^{2}s ($\mathrm{Re}_{\mathrm{Lo}}$>2200), C = 21 was recommended.

Later on, Lee and Lee [28] proposed a correlation for C which takes account of the flow rates and the channel size simultaneously as:

$$C=A\lambda^{q}\psi^{r}\,\mathrm{Re}_{\mathrm{Lo}}^{s} \quad (10)$$

Here,

$$\psi=\frac{j\mu_L}{\sigma} \quad \text{(Capillary number)} \quad (11)$$

$$\lambda=\frac{\mu_{\mathrm{L}}^2}{\rho_{\mathrm{L}}\sigma D_{\mathrm{h}}} \quad \left(=\frac{\psi}{\mathrm{Re}_{\mathrm{j}}}\right) \quad (12)$$

$$\mathrm{Re}_{\mathrm{j}}=\frac{\rho_{\mathrm{L}}jD_{\mathrm{h}}}{\mu_{\mathrm{L}}} \quad (13)$$

with the values of A, q, r and s depending on the flow regimes as listed in Table 1. Here, applicable ranges of X and $\mathrm{Re}_{\mathrm{LO}}$ are given in the article by Lee and Lee [28]. Many more pressure drop

correlations are available from the review article by Kim et al. [32] and also from the text book by Ghiaasiaan [33].

Table 1. Coefficient and exponents for Eq. (10) (Lee and Lee [28])

Flow Regime		A	q	r	s
Liquid	Gas				
lam	lam	6.833×10^{-8}	-1.317	0.719	0.557
lam	turb	6.185×10^{-2}	0	0	0.726
turb	lam	3.627	0	0	0.174
turb	turb	0.408	0	0	0.451

lam: Laminar (Re_L, Re_G < 2000); turb: Turbulent (Re_L, Re_G > 2000)

3.2 Flow-pattern Model

Since the motion of the working fluid inside the heat pipes is induced inherently by external heating and cooling, the total mass flux cannot be large. Thus the most probable flow patterns are the plug and annular flows at the low- and the high-quality conditions, respectively, and the slug flow pattern appears in the middle-quality range. In this section, therefore, the basic approach to estimate the pressure drop for the annular and the plug flows will be discussed.

3.2.1 Annular Flow

As shown in Fig. 5, the annular flow shows a well-defined interface between the liquid film (along the inner wall of the channels) and the gas (in the core portion), and an analytical approach is possible with a reasonable accuracy. As shown in the figure, the pressure drop can be estimated from the wall shear stress, τ, which depends on the liquid film thickness, δ. The liquid film thickness is determined by the film flow rate, W_{LF}, which is related to τ in turn. Hence, the pressure drop can be obtained from the triangular relationship among τ, δ and W_{LF}.

Another simple (and straightforward) method to analyze the annular flow is using of the concept of the two-phase frictional multipliers, ϕ_L^2 and ϕ_G^2, based the mass fluxes of the liquid and the gas flows. The definition of ϕ_L^2 is given in Eq. (5) and ϕ_G^2 is defined similarly as follows:

$$\phi_G^2 = \left(\frac{dp}{dz}F\right)\Big/\left(\frac{dp}{dz}F\right)_G \tag{14}$$

Usually, the liquid film is very thin and its velocity is much smaller (creeping along the tube wall) compared to the gas velocity in the core portion. Hence the frictional pressure drop is determined primarily by the core-gas flow. Physically, the frictional pressure drop of the core-gas flow is proportional to the square of the relative velocity between the gas and the liquid film, u_G–u_L, and the interfacial friction factor, and these depend on the liquid film thickness (or void fraction). More specifically, from the following relationships [34],

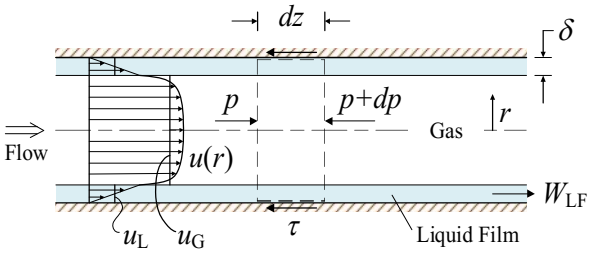


Fig. 5. Annular flow model

$$\phi_L^2 = \frac{1}{(1-\alpha)^2} \tag{15}$$

$$\phi_G^2 = \frac{1+75(1-\alpha)}{\alpha^{5/2}} \tag{16}$$

$$\left(\frac{dp}{dz}F\right) = \left(\frac{dp}{dz}F\right)_L \phi_L^2 = \left(\frac{dp}{dz}F\right)_G \phi_G^2 \tag{17}$$

the void fraction and the frictional pressure drop can be obtained simultaneously.

3.2.2 Plug Flow

As shown in the Fig. 6, the horizontal plug flow consists of elongated bubbles with liquid slugs between them. Thus, the total pressure drop can be estimated by adding the pressure drops in the liquid slug portions and those in the bubble portions along with the interfacial portions taken into account appropriately. For the horizontal wet-plug case (Fig. 6(a)), as noted in the classical paper by Suo and Griffith [1], the liquid film remains almost stationary, and the elongated bubbles are gliding over the liquid film. Thus contribution to the pressure drop is mostly predominated by the liquid slug portion. That is, contribution to the pressure drop by the elongated bubble portions is almost negligible, and the frictional pressure drop is primarily governed by the liquid slugs which are moving with the total superficial velocity j. Since the liquid slugs behave the same as the single-

phase liquid flow of velocity j, the pressure drop gradient in this portion can be obtained easily. In horizontal plug flows, the bubble velocity, u_b, is higher than the liquid-slug velocity, j, because of the stationary liquid film. The ratio between the bubble velocity and the liquid slug velocity, u_b/j, depends on the capillary number ψ and parameter λ, defined as Eqs. (11) and (12), respectively. From the bubble velocity information, both the film thickness and the void fraction can be estimated. Then the length of the liquid slug can be calculated to get the frictional pressure drop eventually. In addition, for mini- and micro-scale channels, the pressure jumps across the curved interfaces at the front and the rear parts of the bubbles seriously affect the pressure drop along the flow direction. The interface curvature depends on the flow rates and the fluid properties, and further studies are needed to get the information. Once the pressure drops in the liquid-slug and at the interface portions are obtained, we simply have to sum them up (to get the total pressure drop).

Another thing to consider is the surface wettability. As shown in the Fig. 6(b), when the tube-wall surface is hydrophobic, the liquid films in the bubble portions are tend to be depleted and the gas phase is directly in contact with the tube wall. In such a case, the contact lines appear between the liquid slugs, bubbles and the tube wall and the contact-line resistance should be considered in addition to the curvature effect at the liquid-gas interface. The detailed physics of the contact-line resistance are still to be unveiled but known to depend on the surface wettability and the velocity of the contact lines. The surface wettability is basically expressed in terms of the static contact angle and the velocity effect is represented by the advancing and receding contact angles. According to Lee and Lee [35, 36], the pressure drop increases as the number of the interfaces is increased. That is, for a given length of the tube, l, the frictional pressure drop of a dry-plug flow, Δp, is written as:

$$\Delta p = \Delta p_G + \Delta p_{MCL} + \Delta p_L \tag{18}$$

$$\Delta p_G = \frac{2 f_G \rho_G j^2 l \alpha}{D} \tag{19}$$

$$\Delta p_L = \frac{2 f_L \rho_L j^2 l (1-\alpha)}{D} \tag{20}$$

$$\Delta p_{MCL} = -\frac{4\sigma_{LG}}{D} \sum_{i=1}^{n_{LS}} \left[\cos\theta_A + \cos(180^o - \theta_R) \right] \tag{21}$$

$$\theta_A = \cos^{-1}\left[\cos\theta_s - c\psi^d (\cos\theta_s + 1) \right] \tag{22}$$

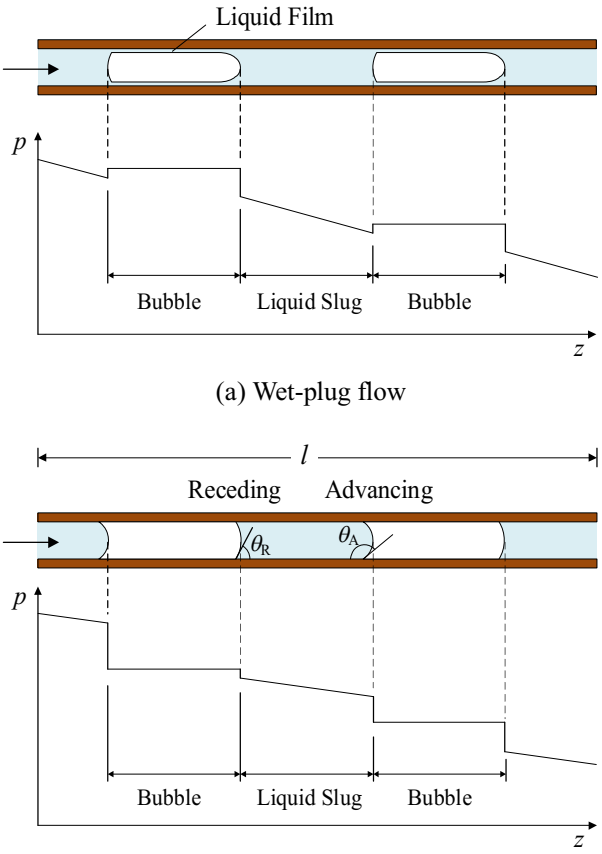


Fig. 6. Pressure drop in plug flows

$$\theta_s - \theta_R = \theta_A - \theta_s \tag{23}$$

where, θ_s, θ_R and θ_A are the static, receding and the advancing contact angles, respectively, and n_{LS} stands for the number of the liquid slugs over the tube length l. Also, in Eq. (22), ψ is the Capillary number and c and d are the values that are specific to the liquid-wall combination. The important implication of the above equations is that although the void fraction, α, remains the same, the pressure drop depends directly on n_{LS} which is determined by the bubble formation process.

3.3 Numerical Approach

Recently, the volume of fluid (VOF) method is widely adopted for simulation of two-phase flow behavior because the interface between the liquid and the gas phases can be traced with a reasonable accuracy [37-40]. Considering that the most probable flow pattern appearing in PHP systems is the plug flow as shown in Fig. 6(a), and adoption of this method is quite viable. Moreover, an open-source CFD code named OpenFOAM is easily available. The continuity and the momentum

equations pertinent to the plug-flow regime can be written as follows:

$$\frac{\partial \rho}{\partial t} + \nabla \cdot \left(\rho \vec{u} \right) = 0 \tag{24}$$

$$\frac{\partial (\rho \vec{u})}{\partial t} + \nabla \cdot \left(\rho \vec{u} \vec{u} \right) = -\nabla p + \nabla \cdot \mu \left(\nabla \vec{u} + \nabla \vec{u}^{\mathrm{T}} \right) + \rho \vec{g} + \sigma \kappa \nabla \varepsilon \tag{25}$$

Here, ε is the phase indicator; ε =1 in the liquid phase while ε =0 in the gas phase, and 0< ε <1 in the interface region. Often, the location of the interface is set to be at ε = 0.5. Distribution of the phase indicator can be obtained from the velocity-field information and the following equation:

$$\frac{\partial \varepsilon}{\partial t} + \nabla \left(\varepsilon \vec{u} \right) - \nabla \left[\varepsilon \left(1 - \varepsilon \right) \vec{u}_{\mathrm{r}} \right] = 0 \tag{26}$$

The last term in the left-hand side of the above equation is the artificial compression term to control the sharpness of the interface and $\vec{u}_{\mathrm{r}}$ is the artificial compression velocity for numerical calculation. [41] Also, ρ and μ are the density and the viscosity of the two-phase mixture, given as

$$\rho = \varepsilon \rho_{\mathrm{L}} + \left(1 - \varepsilon \right) \rho_{\mathrm{G}} \tag{27}$$

$$\mu = \varepsilon \mu_{\mathrm{L}} + \left(1 - \varepsilon \right) \mu_{\mathrm{G}} \tag{28}$$

and κ is the interface curvature which can be expressed as follows:

$$\kappa = \nabla \left(\nabla \varepsilon / \left| \nabla \varepsilon \right| \right) \tag{29}$$

Then, by introducing a train of elongated bubbles of arbitrary shapes at the far upstream along with the liquid slugs between them, and with no-slip, no-penetration boundary condition at the tube wall, the shape of the interfaces as well as the velocity distributions inside the bubbles and the liquid slugs are approaching the fully-developed profiles as flowing downstream. Such a practice is available not only with the round tubes but also with rectangular channels, and even more complicated cases such as branching of the plug flow at T-junctions have been solved. [38, 39] Even though the model for the film dryout at the tube wall (such as in Fig. 6(b)) is still to be developed, the VOF method is considered to be a promising tool for prediction of the two-phase flow behavior.

4. PHASE-CHANGE HEAT TRANSFER

Another important aspect to be considered in mini/micro-scale channels is the heat transfer behavior. Fig. 7 shows typical experimental results on the heat transfer coefficient for an evaporating flow in a rectangular channel by Lee and Lee [42], and the similar results are observed for the circular tubes. It can be readily realized that the heat transfer coefficient varies with the change of the mass velocity and the quality but not significantly with the heat flux. In other words, the heat transfer characteristics of two-phase flows are strongly coupled with the hydrodynamic behavior including the flow pattern.

Various correlations on the heat transfer coefficient for boiling and condensation have been reported. [42-53] Basic heat transfer modes are the nucleate boiling and the two-phase forced convection. The nucleate boiling mode is associated with high heat flux and low quality, and the most probable flow pattern will be either the bubbly or the plug flow. In this case, the heat transfer coefficient increases with the increase of the heat flux which enhances the bubble motion (formation, growth and detachment from the heated wall). On the other hand, in the annular flow regime, the two-phase convective heat transfer is the prevailing mode which occurs at high quality, high mass velocity conditions. In this mode, heat is transferred by conduction and convection through the liquid film and evaporation occurs continuously at the vapor-film interface.

In the nucleate boiling mode, Nusselt number (Nu) is expressed in terms of the Boiling number (Bo), all-liquid Reynolds number ($\mathrm{Re_{Lo}}$), liquid Prandtl number ($\mathrm{Pr_L}$), and Confinement number ($\mathrm{N_{CONF}}$) defined as:

$$\mathrm{Nu} = \frac{hD_{\mathrm{h}}}{k_{\mathrm{L}}}, \quad \mathrm{Bo} = \frac{q''}{Gi_{\mathrm{fg}}}, \quad \mathrm{Re_{Lo}} = \frac{GD_{\mathrm{h}}}{\mu_{\mathrm{L}}},$$

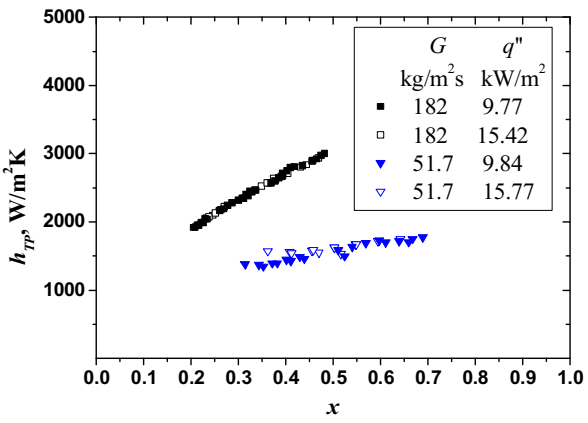


Fig. 7. Typical heat transfer coefficients in rectangular boiling channels (2×20mm^2, R-113, based on Lee and Lee [42])

$$\mathrm{Pr_L} = \frac{\mu_L c_{p,L}}{k_L}, \quad \mathrm{N_{CONF}} = \left[\frac{\sigma}{g(\rho_L - \rho_G) D_h^2}\right]^{1/2} = \mathrm{N_{Eo}^{-1/2}} \quad (30)$$

For example, Tran [51] proposed a correlation for the heat transfer coefficient in the nucleate-boiling-dominant region as:

$$\mathrm{Nu} = 770(\mathrm{Re_{Lo}\, N_{CONF} Bo})^{0.62}\left(\frac{\rho_G}{\rho_L}\right)^{0.297} \quad (31)$$

On the other hand, in the two-phase forced convection mode, the heat transfer coefficient is successfully expressed by the enhancement factor, F, which is in turn a function of the Martinelli parameter, X. For example, one of the useful correlations for the forced convection mode (with annular flow) in rectangular horizontal channels with the aspect ratio of AR has been proposed by Lee and Lee [42] as

$$h = h_L \cdot F \quad (32)$$

$$F = 10.3\mathrm{AR}^{0.398}\phi_L^{0.598} \quad (33)$$

for $\mathrm{Re_{LF}} < 200$ with $C = (6.185 \times 10^{-2})\mathrm{Re_{Lo}}^{0.726}$ that corresponds to the laminar(liquid)-turbulent(gas) regime which may found in the heat pipe systems. For the higher values of $\mathrm{Re_{LF}}$ (>200) which correspond to the higher mass velocity cases, the Kandlikar's flow boiling correlation [43] cover the experimental data with a reasonable accuracy.

The most probable flow pattern in the pulsating heat pipes is the plug flow and the heat transfer to the two-phase mixture can be divided into two parts: convective heat transfer to the liquid-slug portion and the heat transfer to the vapor bubble through the liquid film, for which the heat transfer correlations are available. Consequently, correct information on the liquid film thickness is essential in estimating the heat transfer rate.

All the methods discussed up to this point are applicable only when the mass flow rate is given. However, in heat pipe systems, the flow is self-induced by the external heating and cooling and the flow rate should be estimated somehow. In this respect, the loop-wise flow behavior should be examined. In the next section, some of the attempts to predict the flow rate and thermal performance are discussed with the focus placed on the pulsating heat pipes.

5. APPLICATION TO PHP SYSTEM

Most of the researches on the heat pipes are being performed by experiments, and the overall thermal performance is estimated based on the heat transfer rate and the temperature difference between the evaporator and the condenser. However, the modeling works are also useful to understand the details on the two-phase flow behavior and thereby the preliminary design will be possible. There have been a number of works related to the modeling of the pulsating heat pipes. [54-62] Fig. 8 shows the schematic of a two-turn, vertical PHP as an example. Often, the plug flow inside the pulsating heat pipe is simply simulated as a spring-mass system to find the frequency and amplitude of oscillations. However, sizes of the liquid slugs and vapor bubbles are keep changing due to evaporation and condensation, and the balance equations along with appropriate constitutive relations and boundary conditions should be solved for exact simulation. [62] Hence, for the analysis, the axial coordinate is defined along the loop in the arrow direction from the origin (point A in Fig. 8). Then, for simplicity, one dimensional flow was assumed; that is, the velocity and temperature profiles are averaged over the cross section of the channel for the liquid slugs, vapor bubbles and the liquid films. The mass, momentum and energy conservation equations are constructed for the liquid slugs ①, vapor bubbles ② and the liquid films ③, and also the non-steady conduction heat transfer in the tube-wall region ④ is considered. Here, a special care is needed in handling the computational cells in the vicinity of the menisci of the vapor bubbles (⑤~⑩) because of the volume change of the liquid slugs and vapor bubbles. Since the model is one dimensional, appropriate correlations for the friction factors, heat transfer coefficients and the film thickness are needed. Also, to take account of the bubble formation, a nucleation model was adopted. Similar approach has been performed by Mamelli et al. [58] and Senjaya and Inoue [59, 60].

Fig. 9 shows the change of the temperature difference between the evaporator and the condenser for various heat inputs and the predicted results show good agreement with the measured results by Mamelli [58], from which the effective thermal conductivity can be deduced.

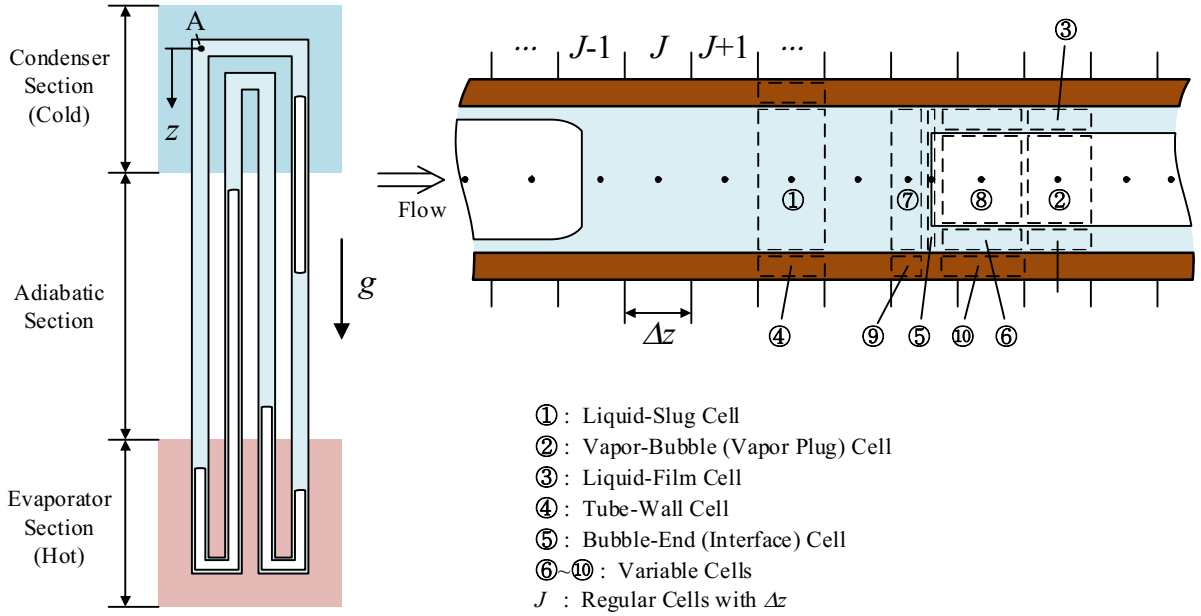


Fig. 8. Schematics of PHP and control volumes for one-dimensional analysis

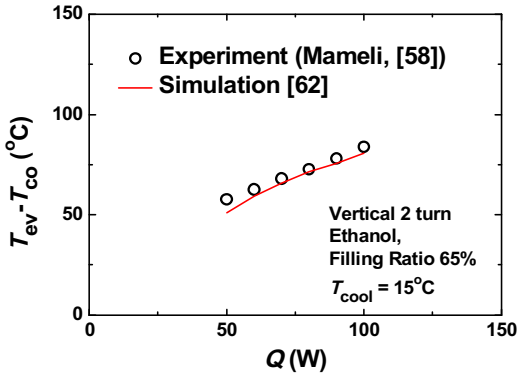


Fig. 9. Variation of temperature difference between evaporator and condenser with heat input (Mameli [58], Bae et al. [62])

Again, a good part of this numerical simulation is that it provides more detailed information that cannot be obtained easily through experiments, such as the local velocities, temperatures, pressures and the overall motions of the liquid slugs and the vapor bubbles. Basically, the oscillatory motion is the predominant mode, but due to the local bubble nucleation, some portions of the liquid slugs are separated out to the neighboring liquid slugs and the loop-wise circulation exists. Also, the volumes of the vapor bubbles are keep changing with time due to the compressibility of the gas phase, and the major frequency of the liquid-slug oscillations can be estimated.

6. CONCLUSION AND SUGGESTION

In this presentation, the state-of-the-art of the researches on the two-phase flow with phase-change heat transfer relevant to the heat pipe application is briefly discussed. Basic flow patterns are identified first and then the widely accepted techniques to estimate the pressure drop and heat transfer rates were introduced. Also, as an advanced numerical technique, the VOF method is being attempted; however it is still away from the viewpoint of practical design of the heat pipe systems because the computation takes long time even for very simple geometrical configurations and flow conditions. Thus, the one-dimensional numerical approach with appropriate constitutive relations on the friction factors, heat transfer coefficients and the bubble nucleation seems to be more viable. Finally, as an example, prediction of the hydrodynamic and heat transfer behavior of the two-phase flow in a two-turn PHP system was demonstrated with a success. The same numerical approach is also applicable to the PHP systems with many more turns. As a future work, some more sophisticated models are needed to reflect the wetting and de-wetting phenomena at the internal-wall surface and the thermodynamic non-equilibrium associated with the heat transfer behavior. In the long run, the non-steady, three-dimensional full computational model may have to be constructed along with the development of the higher performance computers.

ACKNOWLEDGEMENT

This work was supported by Global Surveillance Research Center (GSRC) program funded by the Defense Acquisition Program Administration (DAPA) and Agency for Defense Development (ADD).

NOMENCLATURE

A : Coefficient (-)
AR : Aspect ratio (-)
a : Constant (-)
Bo : Boiling number (-)
b : Constant (-)
C : Parameter (-)
c : Coefficient (-)
c_p : Specific heat (J/kg·K)
D : Diameter (m)
d : Exponent (-)
F : Enhancement factor (-)
f : Friction factor (-)
G : Mass flux (kg/m^2)
g : Gravity (m/s^2)
h : Heat transfer coefficient (W/m^2·K)
i : Enthalpy (J/kg)
j : Superficial velocity (m/s)
k : Thermal conductivity (W/m·K)
l : Tube length (m)
m : Coefficient (-)
n : Number (-)
N_{CONF}: Confinement number (-)
N_{Eo} : Eotvos number (-)
Nu : Nusselt number (-)
p : Pressure (N/m^2)
Pr : Prandtl number (-)
q : Exponent (-)
Re : Reynolds number (-)
r : Exponent (-)
s : Exponent (-)
t : Time (s)
u : Velocity (m/s)
v : Specific volume (m^3/kg)
W : Flow rate (kg/s)
w : Exponent (-)
X : Martinelli parameter (-)
x : Quality (-)
z : Axial coordinate

Greeks

α : Void fraction (-)
δ : Liquid film thickness (m)
ε : Phase indicator (-)
$\square^2$: Two-phase frictional multiplier (-)
κ : Interface curvature (m^{-1})
λ : Dimensionless parameter (-)
μ : Viscosity (N·s/m^2)
ψ : Capillary number (-)
ρ : Density (kg/m^3)
σ : Surface tension (N/m)
τ : Wall shear stress (N/m^2)
θ : Contact angle (radian, degree)

Subscripts

A : Advancing
b : Bubble
CL : Three-phase contact line
G : Gas/vapor
fg : Quantity between vapor and liquid
h : Hydraulic
j : Based on total superficial velocity
L : Liquid
LF : Liquid film
LG : Liquid-gas
Lo : All liquid
LS : Liquid slug
MCL: Moving contact line
R : Receding
s : Static

REFERENCES

[1] Suo, M. and Griffith, P., Two-phase flow in capillary tubes, *J. Basic Eng.*, 86 (1964) 576-582.
[2] Troniewski, L. and Ulbrich, R., Two-phase gas-liquid flow in rectangular channels, *Chem. Eng. Sci.*, 39 (1984) 751-765.
[3] Damianides, C. A. and Westwater, J. W., Two-phase flow patterns in a compact heat exchanger and in small tubes, *Proc. 2nd UK National Conf. on Heat Transfer*, (1988) 1257-1268.
[4] Lowry, B. and Kawaji, M., Adiabatic vertical two-phase flow in narrow flow channels, *AIChE Symposium Series*, 84 (1988) 133-139.
[5] Wambsganss, M. W., Jendrzejczyk, J. A. and France, D. M., Two-phase flow patterns and transitions in a small, horizontal, rectangular channel, *Int. J. Multiphase Flow*, 17 (1991) 327-342.
[6] Barajas, A. M. and Panton, R. L., The effect of contact angle on two-phase flow in capillary tubes, *Int. J. Multiphase Flow*, 19 (1993) 337-346.
[7] Mishima, K., Hibiki, T. and Nishihara, H., Some characteristics of gas-liquid flow in narrow rectangular ducts, *Int. J. Multiphase Flow*, 19 (1993) 115-124.
[8] Zhao, L. and Rezkallah, K. S., Gas-liquid flow patterns at microgravity conditions, *Int. J. Multiphase Flow*, 19 (1993) 751-763.
[9] Fukano, T. and Kariyasaki, A., Characteristics of gas-liquid two-phase flow in a capillary tube, *Nuclear Engineering and Design*, 141 (1993) 59-68.
[10] Wilmarth, T. and Ishii, M, Two-phase flow regimes in narrow rectangular vertical and horizontal channels, *Int. J. Heat Mass Transfer*, 37 (1994) 1749-1758.
[11] Galbiati, L. and Andrein, P., Flow pattern transition for horizontal air water flow in capillary tubes. A microgravity "equivalent system" simulation, *Int. Comm. Heat Mass Transfer*, 21 (1994) 461-468.

[12] Mishima, K. and Hibiki, T., Some characteristics of air-water two-phase flow in small diameter vertical tubes, *Int. Journal of Multiphase Flow*, 22 (1996) 703-712.

[13] Rezkhallah, K. S., Weber number based flow-pattern maps for liquid-gas flows at microgravity, *Int. J. Multiphase Flow*, 22 (1996) 1265-1270.

[14] Bousman, W. S., McQuillen, J. B. and Witte, L. C., Gas-liquid flow patterns in micro-gravity: Effects of tube diameter, velocity and surface tension, *Int. J. Multiphase Flow*, 22 (1996) 1035 – 1053.

[15] Xu, J. L., Cheng, P. and Zhao, T. S., Gas-liquid two-phase flow regimes in rectangular channels with mini/micro gaps, *Int. J. Multiphase Flow*, 25 (1999) 411-432.

[16] Triplett, K. A., Ghiaasiaan, S. M., Abdel-Khalik, S. I. and Sadowski, D. L., Gas-liquid two-phase flow in microchannels. Part I: Two-phase flow patterns, *Int. J. Multiphase Flow*, 25 (1999) 377-394.

[17] Lowe, D. C. and Rezkallah, K. S., Flow regime identification in microgravity two-phase flows using void fraction signals, *Int. J. Multiphase Flow,* 25 (1999) 433-457.

[18] Ghiaasiaan, S. M. and Abdel-Khalik, S. I., Two-phase flow in microchannels, *Advances in Heat Transfer*, 34 (2001) 145-254.

[19] Hibiki, T. and Mishima, K., Flow regime transition criteria for upward two-phase flow in vertical narrow rectangular channels, *Nuclear Engineering and Design*, 203 (2001) 117-131.

[20] Lee, C. Y. and Lee, S. Y., Effect of interfacial tensions on behavior of two-phase plug flow in round mini-channels, *Proc. 18th International Symposium on Transport Phenomena*, (2007) 1474-1479.

[21] Lee, C. Y. and Lee, S. Y., Influence of surface wettability on transition of two-phase flow pattern in round mini-channels, *International Journal of Multiphase Flow*, 34 (2008) 706-711.

[22] Ohta, H., Microgravity heat transfer in flow boiling, *Advances in Heat Transfer*, 37 (2003) 1-76.

[23] Iguchi, M. and Terauchi, Y., Rising behavior of air-water two-phase flows in vertical pipe of poor wettability, *ISIJ Int. (Iron Steel Inst. Jpn.)*, 40 (2000) 567-571.

[24] Iguchi, M. and Terauchi, Y., Boundaries among bubbly and slug flow regimes in air-water two-phase flows in vertical pipe of poor wettability, *Int. J. Multiphase Flow*, 27 (2001) 729-735.

[25] Iguchi, M. and Terauchi, Y., Microgravity effects on rising velocity of bubbles and slugs in vertical pipes of good and poor wettability, *Int. J. Multiphase Flow*, 27 (2001) 2189-2198.

[26] Nakamura, D., Tamura, N., Hazuku, T., Takamasa, T. and Hibiki, T., Effect of surface wettability on flow patterns in a vertical gas-liquid two-phase flow, *Proc. 13th International Conference on Nuclear Engineering*, (2005) ICONE13-50508.

[27] Rapolu, P. and Son, S. Y., Capillary effect on two-phase flow resistance in microchannels, *Proc. 18th International Symposium on Transport Phenomena*, (2007) 1431-1436.

[28] Lee, H. J. and Lee, S. Y., Pressure drop correlations for two-phase flow within horizontal rectangular channels with small heights, *International Journal of Multiphase Flow*, 27 (5) (2001) 783-796.

[29] Lockhart, R. W. and Martinelli, R. C., Proposed correlation of data for isothermal two-phase flow two-component flow in pipes, *Chem. Eng. Prog.*, 45 (1949) 39-48.

[30] Chisholm, D., A theoretical basis for the Lockhart-Martinelli correlation for two-phase flow, *Int. J. Heat Mass Transfer*, 10 (1967) 1767-1778.

[31] Wambsganss, M. W., Jendrzejczyk, J. A., France, D. M. and Obot, N. T., Frictional pressure gradients in two-phase flow in a small horizontal rectangular channel, *Exp. Thermal Fluid Sci.*, 5 (1992) 40-56.

[32] Kim, M.-H., Lee, S. Y., Mehendale, S. S. and Webb, R. L, Microchannel heat exchanger design for evaporator and condenser applications, *Advances in Heat Transfer*, 37 (2003) 297-429.

[33] Ghiaasiaan, S. M., *Two-phase flow, boiling, and condensation*, Cambridge (2008).

[34] Wallis, G. B., *One dimensional two phase flow*, McGraw-Hill (1969).

[35] Lee, C. Y. and Lee, S. Y., Pressure Drop of two-phase plug flow in round mini-channels: Influence of surface wettability, *Experimental Thermal and Fluid Science*, 32 (2008) 1716-1722.

[36] Lee, C. Y. and Lee, S. Y., Pressure drop of two-phase dry-plug flow in round mini-channels: Effect of moving contact line, *Experimental Thermal and Fluid Science*, 34 (2010) 1-9.

[37] Ghaini, A., Mescher, A. and Agar, D. W., Hydrodynamic studies of liquid-liquid slug flows in circular microchannels, *Chem. Eng. Sci.*, 66 (2011) 1168-1178.

[38] Hoang, D. A., van Steijn, V., Portela, L. M., Kreutzer, M. T. and Kleijn, C. R., Modeling of low-capillary number segmented flows in microchannels using OpenFOAM, *AIP Conf. Proc.*, 1479 (2012) 86-89.

[39] Kim, S., *Split of Two-phase plug flow at micro-scale branching T-junction*, Ph.D. Dissertation, KAIST, (2015).

[40] Kim, S. and Lee, S. Y., Split of two-phase flow with elongated bubbles at a micro-scale branching T-junction, *Chemical Engineering Science*, 134 (2015) 119-128.

[41] Berberovic, E., van Hinsberg, N. P., Jakirlic, S., Roisman, I. V. and Tropea, C., Drop impact onto a liquid layer of finite thickness: dynamics of the cavity evolution, *Phys. Rev. E: Stat. Nonlinear Soft Matter Phys.*, 79 (2009) 036306.

[42] Lee, H. J. and Lee, S. Y., Heat transfer correlation for boiling flows in small rectangular horizontal channels with low aspect ratios, *International Journal of Multiphase Flow*, 27 (2001) 2943-2062.

[43] Kandlikar, S. G, A general correlation for saturated two-phase flow boiling heat transfer inside

horizontal and vertical tubes, *Trans. ASME, Journal of Heat Transfer*, 112 (1990) 219-228.

[44] Cornwell, K. and Kew, P. A., Boiling in small parallel channels, in Plivachi, P. A. (Ed.), *Energy Efficiency in Process Technology*, Elsevier, New York, (1993) 624- 638.

[45] Kew, P. A. and Cornwell, K., Confined bubble flow and boiling in narrow spaces, *Proc. 10th Int. Heat Transfer Conference*, (1995) 473-478.

[46] Lazarek, G. M. and Black, H. S., Evaporative heat transfer, pressure drop and critical heat flux in a small vertical tube with R-113, *Int. J. Heat Mass Transfer*, 25 (1982) 945-960.

[47] Wambsganss, M. W., France, D. M., Jendrzejczyk, F. A. and Tran, T. N., Boiling heat transfer in a horizontal small-diameter tube, Trans. ASME, J. Heat Transfer, 115 (1993) 963-972.

[48] Oh, H. K., Katsuta, M. and Shibata, K., Heat transfer characteristics of R-134a in a capillary tube heat exchanger, *Proc. 11th Int. Heat Transfer Conference*, 6 (1998) 473-478.

[49] Yan, Y.-Y. and Lin, T.-F., Evaporation heat transfer and pressure drop to refrigerant R-134a in a small pipe, *Int. J. Heat Mass Transfer*, 41 (1998) 4183-4194.

[50] Kureta, M., Kobayashi, T., Mishima, K. and Nishihara, H., Pressure drop and heat transfer for flow-boiling of water in small-diameter tubes, *JSME International Journal, Series B*, 41 (1998) 871-879.

[51] Tran, T. N., *Pressure drop and heat transfer study of two-phase flow in small channels*, Ph.D. dissertation, Texas Tech Univ. (1998).

[52] Kuznetsov, V. V. and Shamirzaev, A. S., Two-phase flow pattern and flow boiling heat transfer in non-circular with a small gap, *Proc. Two-Phase Flow Modelling and Experimentation*, (1999) 249-253.

[53] Yan, Y. Y. and Lin, T. F., Condensation heat transfer and pressure drop of refrigerant R134a in a small pipe. *Int. J. Heat Mass Transfer*, 42 (1999) 697-708.

[54] Holley, B. and Faghri, A., Analysis of pulsating heat pipe with capillary wick and varying channel diameter, *Int. J. Heat Mass Transfer*, 48 (2005), 2635-2651.

[55] Ma, H. B., Hanlon, M. A. and Chen, C. L., An investigation of oscillating motions in a miniature pulsating heat pipe, *Microfluid Nanofluid*, 2 (2006) 171-179.

[56] Nikolayev V. S., A dynamic film model of the pulsating heat pipe, *J. Heat Transfer*, 133 (2011) 081504.

[57] Mameli, M., Marengo, M. and Zinna S., Numerical investigation of the effects of orientation and gravity in a closed loop pulsating heat pipe, *Microgravity Sci. Technol.*, 24 (2012) 79~92.

[58] Mameli M., *Pulsating heat pipes: Numerical modeling and experimental assessment*, Ph.D. Thesis, Universita' Degli Studi di Bergamo, (2012).

[59] Senjaya, R. and Inoue, T., Oscillating heat pipe simulation considering bubble generation Part I: Presentation of the model and effects of a bubble generation, *Int. J. Heat Mass Transfer*, 60 (2013) 816-824.

[60] Senjaya, R. and Inoue, T., Oscillating heat pipe simulation considering dryout phenomena, *Heat Mass Transfer*, 50 (2014) 1429-1441.

[61] Peng, H., Pai, P. F., and Ma, H. B., Nonlinear thermomechanical finite-element modeling, analysis and characterization of multi-turn oscillating heat pipes, *Int. J. Heat Mass Transfer*, 69 (2014) 424-437.

[62] Bae, J., Lee, S. Y. and Kim, S. J., Numerical platform for performance prediction of pulsating heat pipes, in preparation, (2016).

Keynote Lecture

Application of Phase Change Technology in China's Lunar Probe

Miao Jianyin, Wang Lu, He Jiang, Lv Wei, Zhang Hongxing and Zhang Bingqiang

Beijing Key Laboratory of Space Thermal Control Technology,
Beijing Institute of Spacecraft System Engineering, China Academy of Space Technology, Beijing 100094, China

Abstract

The Chang'E-3 was a key part of China's Lunar Exploration Program. The temperature difference of nearly 300℃ between lunar day and night asked for a thermal control system with strong self-regulating capability. A variable cooling capacity radiator had been developed based on variable conductance heat pipe (VCHP), whose heat rejection ability was changeable. A kind of C_4F_8 heat pipe had been developed for an independent payload's thermal control system, which could stop working at -41.4℃ of C_4F_8's freezing point. A lunar-gravity-driven closed two-phase thermosyphon (LGDT) with ammonia as the working fluid had been successfully developed. The function of LGDT is to remove heat from radioisotope heater unit (RHU) installed outside the lunar probe (Rover and Lander) and transport heat to components sensitive to temperature during the lunar night. Until March 1, 2016, the Lunar Lander had been working on the Moon for more than two years. All the phase change thermal equipment including VCHP, C_4F_8 heat pipe and LGDT had been working at normal status and will consequently serve the tasks followed-up.

Keywords: Lunar Probe; Variable Conductance Heat Pipe; C4F8 Heat Pipe; Closed Two-Phase Thermosyphon

Keynote Lecture

Challenges in Expanding the Range of Application of Loop Heat Pipes to both Smaller Scale and Larger Scale

Hosei Nagano[1]

[1]*Department of Mechanical Science and Engineering, Nagoya University, Aichi 464-8603, Japan.*

Abstract

A two-phase heat transfer device with capillary action in a microscale porous structure such as a loop heat pipe (LHP) is a promising heat transport technology. It is capable of higher heat transfer power and longer heat transport distances with no electrical power compared to conventional heat pipes. The LHP has been widely studied in both aerospace and terrestrial fields for more than 40 years. There are many challenges in expanding the range of applications for the LHPs to include much smaller and larger scales, much higher heat-flux, and much lower thermal-resistances.
In this paper, technological challenges for smaller-scale and larger-scale LHPs in our research is introduced. For smaller-scale LHPs, a new evaporator with a 3 mm thickness has been proposed for thermal management of small electric devices. The LHP with the thin evaporator has been designed based on a three-dimensional analytical model, and has been fabricated and tested. For larger-scale LHPs, an LHP with a 10 m heat transport distance from the evaporator to the condenser has been developed for energy utilization. The thermal performance of the 10 m LHP is presented.

Keywords: Loop heat pipes; Long distance LHP; Small scale LHP; Two-phase heat flow

1. INTRODUCTION

A loop heat pipe (LHP) is a two-phase heat-transfer device that utilizes the evaporation and condensation of a working fluid to transfer heat and the capillary forces developed in fine porous wicks to circulate the fluid. The LHP can transport heat over a long distance with no electrical power. LHPs have recently gained increasing acceptance for spacecraft thermal control because of their robustness, self-starting function, and versatility [1-3]. Recently, they have been investigated not only for heat transport in cooling devices but also for effective energy utilization.

As next-generation heat pipes, the oscillating heat pipe and loop-type thermosiphon have been examined in addition to the LHP [4-7]. The features of the LHP compared with these two heat pipes are as follows. Similarly to the conventional heat pipe, capillary force is used as the operating principle in the LHP, whereas the operating principles of the oscillating heat pipe and loop-type thermosiphon are self-oscillation and gravitational force, respectively. The LHP can be operated in a horizontal orientation and even in the top heat mode if the capillary force is larger than the pressure loss and gravity head. That is, when the LHP is designed with the effect of gravity, it can be operated regardless of the heat-source position. Thus, the range of applications of the LHP to terrestrial instruments is very wide. It is important to confirm the range of the applications of the LHP from the viewpoints of maximum and minimum heat-transfer power, distances, size, heat flux, thermal resistance, etc.

In this paper, the technological challenges for small- and large-scale LHPs in our research are introduced. Regarding small-scale LHPs, a new evaporator with a 3-mm thickness was proposed for the thermal management of small electric devices. The LHP with the thin evaporator was designed according to a three-dimensional (3D) analytical model and was fabricated and tested. Regarding larger-scale LHPs, an LHP with a 10-m heat-transport distance from the evaporator to the condenser was developed for energy utilization. The thermal performance of the 10-m LHP is presented.

2. OPERATING PRINCIPLE OF LHP

Because many good papers explain the operating principle of the LHP in detail [1, 2] it is briefly summarized here. The LHP consists of an evaporator, a wick, a vapor line, a condenser, a liquid line, and a compensation chamber (CC). The operating principle of the LHP is the capillary force generated in the wick, which is made of fine porous media. The LHP can be operated as long as the maximum capillary force is larger than the pressure loss that the working fluid undergoes in the LHP system. To estimate the maximum heat-transport capability and operating temperature accurately, it is necessary to estimate the pressure loss in each component accurately. Additionally, the thermofluid properties of the working fluid

*Corresponding author: nagano@mech.nagoya-u.ac.jp, Phone: +81-52-789-4470

needed to estimate the pressure losses and energy balance—such as the surface tension, viscosity, density, latent heat, heat capacity, and thermal conductivity—are strongly dependent on its temperature and phase state. In particular, the uncertainty of the vapor-liquid state in the wick and the condenser strongly affect the accuracy of the performance estimation. It is very important to evaluate the energy conservation of the LHP accurately.

3. TREND OF LHP DEVELOPMENT

LHPs have been mainly developed and applied in the field of space development. However, they has recently been investigated and reported actively for terrestrial applications. The main feature of the LHP is that it can transport a larger amount of heat for longer distance than the conventional heat pipe. The LHP can be used not only as a cooling device but also for effective heat utilization. For use as a cooling device, the following targets are considered and reported: light-emitting diode lamps [8], inverters of trains [9], dashboards of automobiles [10], central processing units of personal computers (PC) [11], electric boxes on the seats of airplanes [12], and micro electric devices [13]. For effective heat utilization, the following targets are considered and reported: anti-icing systems of UAVs [14], the heat utilization of fuel cells [15], and solar water heating [16].

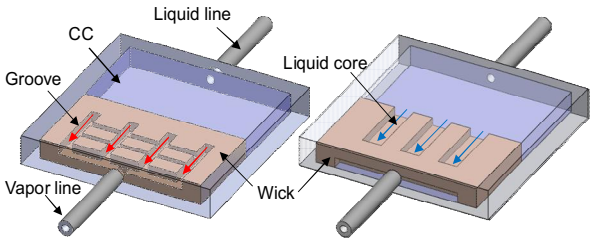
Generally, the LHP can transport heat of several tens of Watts to several hundred Watts for several tens of centimeters to several meters. The thickness of the evaporator system is on the order of several centimeters. To extend the potential of the LHP, studies on far smaller- and larger-scale LHPs are conducted. Herein, the technological challenges for smaller- and larger-scale LHPs in our research are introduced.

4. THIN-LHP

The targets of the ultra-thin LHP include mobile devices such as laptop PCs, tablets, and mobile phones. There are several reports on small-scale LHPs [13, 17-21]. The thinnest evaporator known to the author is 0.6 mm thick and was developed by Shioga et al [22]. This LHP can be operated up to 15 W and can transfer heat for about 10 cm. In our laboratory, a thin LHP with a 3-mm evaporator, which can transfer heat for about 20 cm, is under development. Figure 1 shows the newly proposed thin evaporator.

4.1 3-mm Evaporator

The proposed structure of the miniature loop heat pipe (MLHP) requires an evaporator thickness of 3 mm and an evaporator size of 20 mm × 10 mm for adaptation to small electronic devices. If the LHP is smaller and thinner, the pressure drop occurring when the working fluid passes through the wick increases. Moreover, the size of the evaporator is limited and the volume of the CC is reduced because this volume depends directly on the length and inner diameter of the condenser and vapor line. To increase the heat-transport distance, it is necessary to reduce the inner diameter of the transport lines or increase the CC volume. The pressure drop in the transport pipe is proportional to the square of the inner diameter. Therefore, if the inner diameters of the transport lines decrease, the maximum heat-transport amount decreases. Thus, the evaporator must be fabricated such that the pressure loss in the wick is reduced and a sufficient CC volume is ensured. If the flat evaporator is adapted to the target size, it is very difficult to achieve the two aforementioned conditions in design and production surfaces. Accordingly, herein, we propose that grooves corresponding to liquid cores be provided on the CC side (Fig. 1).



(a) Heating side (b) Rear side

Fig. 1 Schematic of 3-mm new evaporator structure for thin LHP.

Because these grooves increase the flow passage area through the inside of the wick and decrease the average distance from the CC to the grooves, it is possible to reduce the pressure drop in the wick. In addition, because the CC volume increases depending on the volume of the liquid cores, it is possible to increase the internal diameter of the transport lines and the transport distance. The pressure drop across the wick can be expressed as,

$$\Delta P_{wi} = \frac{\dot{m}\mu}{K\rho_l}\int \frac{L_{wi}}{S_{wi}} dL \qquad (1)$$

Here, μ is the viscosity coefficient of the liquid, and ρ_l is the liquid density. When liquid cores are installed, the area through which the working fluid flows increases, and the average distance from the CC to the grooves decreases; hence, in this case, the pressure drop in the wick reduces by 1/5 compared with the case where no liquid cores are installed.

Figure 2 compares the pressure drops in the presence and absence of liquid cores in the wick. The pressure drop through the wick with liquid cores is about 1/5 smaller than that of the wick without liquid cores.

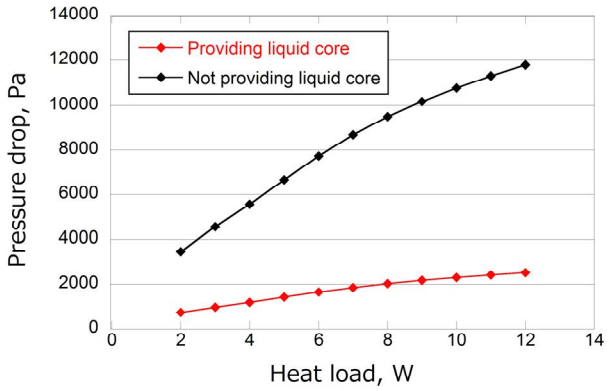


Fig. 2 Effect of the heat load on the pressure loss for the new evaporator structure.

However, it is considered that the heat leakage on the CC side and the operating temperature increase if liquid cores are provided. Therefore, the heat leakage is reduced by using a low-thermal-conductivity polytetrafluoroethylene (PTFE) wick [23]. In addition, because evaporation occurs at the groove surface, transverse grooves are installed in addition to the vertical grooves, to increase the evaporation area. The geometric characteristics of the PTFE wick are presented in Table 1.

Table 1 Characteristics of the PTFE wick used for the MLHP

Pore radius	2.2 μm
Porosity	50%
Permeability	6.48×10^{-14} m^2
Thermal conductivity	0.25/mK

4.2 Experimental Setup

The geometric characteristics of the experimental MLHP are shown in Table 2. Figures 3 and 4 ((a) and (b)) show photographs of the MLHP system, evaporator-CC section, and wick, respectively. Ethanol is used as the working fluid because its operating temperature is low and it is non-toxic. The vapor line, liquid line, and condenser are made using 1/16-in tubes. The condenser is made using an Al5052 aluminum plate (70 mm × 74 mm × 3 mm). A 1.7-mm-wide, 1.7-mm-deep groove is installed in the plate, and a tube is buried in the groove.

Table 2 Geometric characteristics of the MLHP

Evaporator	Size, mm	20 × 10 ×3
	Thickness, mm	0.5
Wick (PTFE)	Size, mm	17 × 9 × 2
CC	Size, mm	17 × 9 ×2
Heater	Size, mm	10 × 10
Vapor line (SUS304)	Length, mm	200
	O.D., mm	1.56
Liquid line (SUS304)	Length, mm	200
	O.D., mm	1.56
Condenser (SUS304)	Length, mm	120
	O.D., mm	1.56
	Area, mm^2	120 × 70
Working fluid	Volume of ethanol, mL	0.3

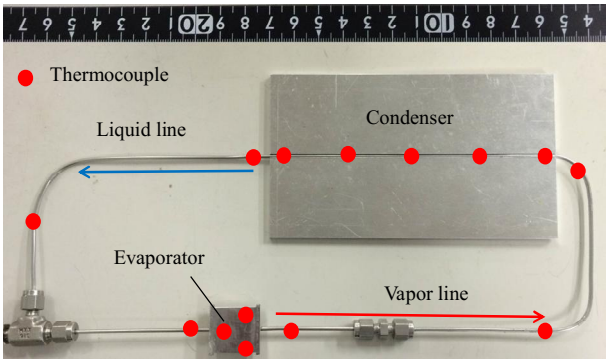
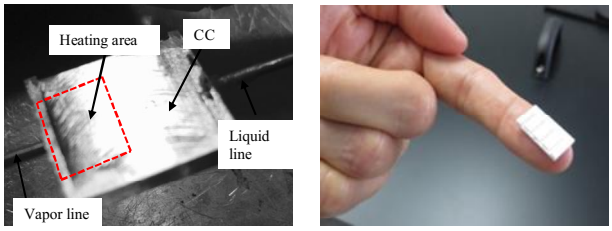


Fig. 3 Photograph of the MLHP with thermocouples location.



(a) Evaporator-CC (b) Wick

Fig. 4 Photographs of (a) the evaporator-CC section and (b) the core side of the PTFE wick.

To measure the temperature, the LHP is mounted with T-type thermocouples at the positions shown in Fig. 3. Signals from the thermocouples are collected using a data-acquisition system through a GPIB cable and sent to a PC. A ceramic heater (10 mm × 10 mm) is used to heat the evaporator, and the heating of the devices is simulated by using direct-current (DC) power. The heat provided by the ceramic heater is controlled by the voltage applied by a power supply, which receives a specified value from the PC. The applied voltage and flow current values are sent to the PC through a GPIB cable. The specified and measured calorific values and the temperatures measured using the thermocouples are collectively managed by a measurement program. The experimental conditions under which the LHP performance is evaluated are listed in Table 3.

Table 3 Experimental conditions for MLHP

Heat-load history	1-W steps
Cooling condition	Air natural convection (22 ± 2 °C)
Time interval	1,200 s
LHP attitude	Horizontal
Heating condition	Heating using ceramic heater

4.3 Experimental Results

The experimental results representing the temperature history are shown in Fig. 5. The temperature of the vapor line inlet (VL1) rapidly increases about 20 second after the starting point when a heat load of 2 W is applied; if the vapor flows into the vapor-line side, it is considered that the LHP is operating correctly. The evaporator temperature does not change substantially until the heat load is 7 W, and it starts rising as the heat load increases beyond 8 W. The CC temperature decreases gently at a heat load of 7 W and starts rising as the heat load increases beyond 8 W. This trend is due to the cooling of the supercooled return fluid in the condenser. The mass flow rate increases with the heat load, and the liquid-line temperature is lower than the evaporator temperature by 30 °C or more until the heat load reaches 7 W, which indicates that the cooling effect is substantial. As the heat load increases further, the mass flow rate also increases, but because the temperature of the return liquid also increases, the operating temperature increases. The MLHP developed in this study is capable of transporting heat loads up to 11 W, and the temperature reaches the wick heatproof temperature at 12 W. Figure 10 shows the variations in the evaporator temperature, CC temperature, and thermal resistance. The thermal resistance is calculated as,

$$R_{LHP} = \frac{T_{ev} - T_{con}}{Q_{load}} \tag{2}$$

Here, T_{ev} is the average temperature of the evaporator, T_{con} is the average temperature of the condenser, and Q_{load} is the heat load. T_{ev} is 80.5 °C for a target heat load of 10 W, and the heat resistance is minimized at 1.21 °C/W.

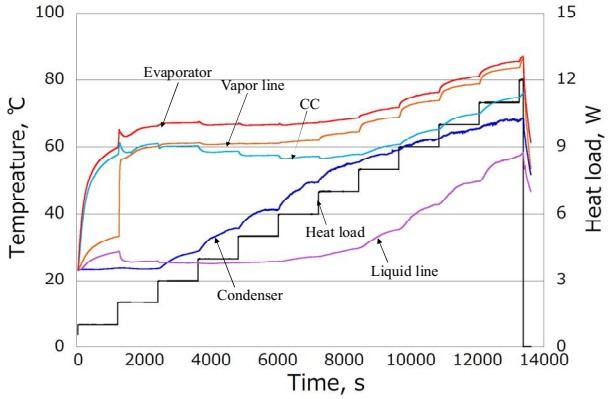


Fig. 5 Temperature profile of the MLHP from 1W to 12W power application.

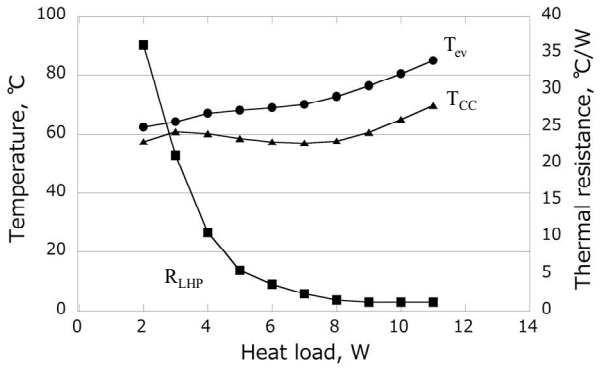


Fig. 6 Effects of the heat load on the evaporator temperature (T_{ev}), CC temperature (T_{cc}), and thermal resistance (R_{LHP}) of MLHP.

As mentioned above, the operation of the MLHP with 3-mm evaporator was demonstrated. The orientation dependence of the thermal performance for the MLHP against the gravity was also evaluated. Additionally, now the MLHP with 1-mm thick evaporator is under development. Detail of the thinner MLHP will be reported in a separate paper.

5. LONG-DISTNCE LHP

The application targets of the long-distance LHP (LLHP) include the energy systems of smart houses, the energy utilization of fuel cells, and the thermal management of automobiles.

To the knowledge of the author, the longest LHP is the 21-m LHP developed by Maydanik [24]. The working fluid of the LHP is ammonia, and the LHP can transfer 1.7 kW.

At Nagoya University, to evaluate the feasibility of the LLHP, LHPs with one-way transport lengths of 2, 4, and 10 m were fabricated and tested in the horizontal condition. The 10-m LHP could transport up to 160 W with a thermal resistance of 0.12 K/W [25].

In this study, to accomplish an LHP with a far higher power and low thermal resistance, the analytical model was reconsidered, and a 300-W-class LLHP with the same evaporator was redesigned, fabricated, and tested.

5.1 Re-Design of LLHP

Table 4 shows a previously reported 10-m LHP [25]. The wick material and working fluid are PTFE porous media and ethanol, respectively. The LHP can transport up to 160 W with a thermal resistance of 0.12 K/W. The analytical model of the LLHP was modified according to experimental results, and the pressure losses and energy balance in each component of the LHP were estimated in detail. By using the modified LLHP model, a 300-W-class LLHP was designed. Figure 7(a) shows the calculated results for the pressure losses in each component with respect to the applied power. These results indicate that the pressure loss in the liquid line is dominant.

Generally, for an LHP of typical size, the pressure losses in the wick or in the vapor line are the largest in each component. However, because the liquid line of the aforementioned LLHP had an inner diameter of 1.8 mm, the pressure loss of the liquid line was extremely large in the case of a 10-m LHP. The pressure losses in the wick and the vapor line were large next to that of the liquid line. On the basis of this result, the inner diameters of the liquid line, vapor line, and wick were significantly widened in order to reduce the pressure losses.

Next, the energy balance of the LLHP between the heat leakage, condensation, and heat loss from the vapor and liquid transport lines and applied power were estimated. The heat leakage from the evaporator to the CC was approximately 11%, the heat loss from the vapor and liquid transport lines was approximately 58%, and the condensed heat was only 31% of the applied heat. To reduce the heat loss from the vapor and liquid transport lines and increase the condensed heat in the condenser, it is necessary to increase the insulation performance of the transport lines.

Table 4 Geometric characteristics of the old model of the LLHP

Evaporator (SUS304)	O.D.	21 mm
	Length	150 mm
CC (SUS304)	O.D.	75 mm
	Length	50 mm
Wick (PTFE)	O.D.	19 mm
	Inner diameter (I.D.)	13 mm
	Length	140 mm
	Pore radius	1.2 μm
	Porosity	34%
	Permeability	2×10^{-14} m^2
	Groove no.	12
Vapor Line (SUS304)	O.D.	6.4 mm
	I.D.	4.6 mm
	Length	10 m
Liquid Line (SUS304)	O.D.	3.2 mm
	I.D.	1.8 mm
	Length	10 m
Condenser (SUS304)	O.D.	6.4 mm
	I.D.	4.6 mm
	Length	3 m
Working fluid	Material	Ethanol
	Volume	283ml

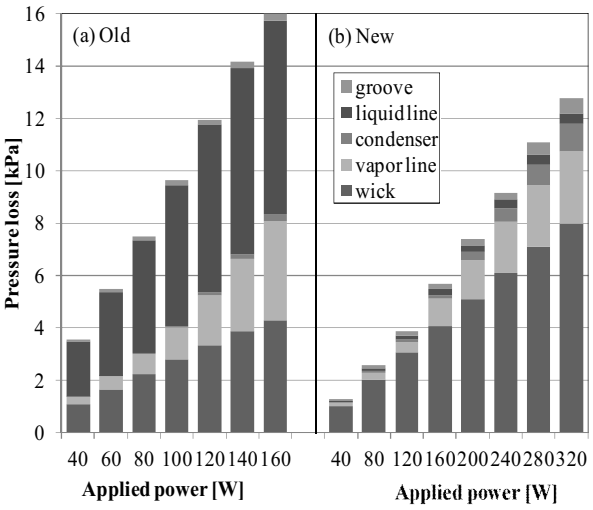


Fig. 7 Calculated pressure losses over the parts of (a) the old LLHP and (b) the new LLHP.

According to the above evaluations, the specifications of the LLHP that accomplishes 300 W of heat transport were determined. Table 5

compares the specifications before and after the redesign of the LLHP. The wick inner diameter increased by a factor of 1.1, the inner diameters of the vapor line and the condenser increased by a factor of 1.7, and the inner diameter of the liquid line increased by a factor of 2.6. According to the increasing insulation performance, the length of the condenser was redesigned as 8 m, that is, 2.7 times larger than that of the original LLHP. The total length of the LLHP became 28 m. While the pressure losses were reduced by increasing the inner diameter of the loop, the amount of working fluid required increased by a factor of 4.

Figure 7(b) shows the calculated results for the pressure losses in each component as a function of the applied power for the new LLHP. Compared with the pressure loss of the original LLHP, which is shown in Fig. 7(a), the pressure loss in the liquid line was reduced drastically. The pressure losses in the vapor line and wick were also reduced.

Table 5 Comparison of the component sizes between old and new LLHP

Element	Old	New	Change ratio
Wick I.D.	13 mm	14 mm	1.1
Vapor line I.D.	4.6 mm	8 mm	1.7
Liquid line I.D.	1.8 mm	4.6 mm	2.6
Condenser length	3 m	8 m	2.7
Volume	283 ml	1,160 ml	4.1



Fig. 8 Photo of the new LLHP in horizontal position.

5.2 Experimental Apparatus

Figure 8 shows the redesigned LLHP. A heat source made of an aluminum alloy (Al 5052) with eight cartridge heaters is attached to the evaporator. The heaters are heated by a DC power supply. The area of the condenser is 500 × 810 mm, and fins with a height of 30 mm and pitch of 10 mm are attached to one side. The condenser is cooled by natural convection. Fifty-two T-type thermocouples are used to measure the temperature distribution of the LHP. Four, six, 24, six, eight, and two thermocouples are attached to the evaporator, vapor line, condenser, liquid line, CC, and heater block, respectively, and two thermocouples are used for ambient-temperature measurement. Insulators made of ethylene propylene rubber are attached to the LLHP, except for the evaporator and condenser.

5.3 Experimental Results

Figure 9 shows the temperatures of the evaporator and the CC, as well as the thermal resistance, with respect to the applied power. It was demonstrated that the new LLHP can transport up to 290 W with a thermal resistance of 0.08 K/W, whereas the original LLHP can transport 160 W with a thermal resistance of 0.12 K/W. The condensed heat in the condenser was estimated to be 67% of the applied power of 290 W, whereas that of the original LHP was 33%. To enhance the performance, additional improvement of the insulation is required. Now the effect of the gravity is evaluated and the test under 1-m top-heat mode is conducted. A new LHP which can be operated under 10-m top-heat mode is under development. Detail of these results will be reported in a separate paper.

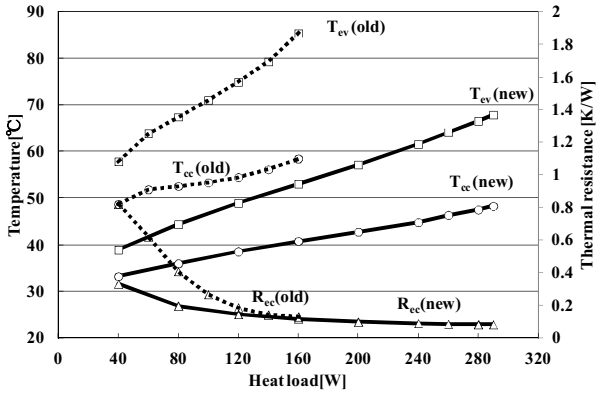


Fig. 9 Temperature of the evaporator and CC, and thermal resistance for old LLHP and new LLHP as a function of the heat load.

6. CONCLUSION

The technological challenges for small- and large-scale LHPs in our research were introduced. Regarding small-scale LHPs, a new evaporator with a 3-mm thickness was proposed for the thermal management of small electric devices. The LHP with the thin evaporator was designed and was fabricated and tested. The MLHP can be operated up to 11 W and can transfer heat for 20cm. Regarding large-scale LHPs, an LHP with a 10-m heat-transport distance from the evaporator to the condenser was developed for energy utilization. The thermal performance of the 10-m LHP was presented. The

LLHP can be operated up to 290 W with a thermal resistance of 0.08 K/W.

The range of applications of the LHP can be extended significantly. There have been several field studies on LHPs and the development of LHPs by electric companies. Thus, practical applications of the LHP will arise in the near future.

ACKNOWLEDGEMENT

This research was conducted as part of the Strategic Research Program PRESTO of the JST in the research area "Phase Interfaces for Highly Efficient Energy Utilization." And wrote to express their gratitude to. The author also would like to thank to Mr. Kazuki Fukushima, and Mr. Masataka Mitomi for their assistance.

NOMENCLATURE

L_{wi} : Thickness of wick (m)
$\dot{m}$: Mass flow rate (g/s)
Q_{load} : Applied power (W)
R_{LHP} : Thermal resistance (K/W)
S_{wi} : Cross-section area of wick (m^2)
T_{ev} : Average temperature of evaporator (^oC)
T_{con} : Average temperature of condenser (^oC)
ΔP_{wi} : Pressure loss through wick (Pa)
K : Permeability (m^2)
μ : Liquid viscosity of working fluid (Pa·s)
ρ_l : Liquid density of working fluid (g/cm^3)

REFERENCES

[1] Y. F. Maydanik, Loop heat pipe, *Applied Thermal Engineering*, 25, (2005) 635-657.

[2] J. Ku, Operating characteristics of loop heat pipes, *Proc. of 29th International Conference on Environmental System*, SAE Paper No. 1999-01-2007.

[3] S. Launay, V. Sartre, and J. Bonjour, Parametric analysis of loop heat pipe operation: a literature review, *International Journal of Thermal Sciences,* 46 (2007) 621-636.

[4] Y. Zhang, and A. Faghri, Advances and unsolved issues in pulsating heat pipes, *Journal of Heat Transfer Engineering,* 29 (1) (2008), 20–44.

[5] N. Iwata, H. Ogawa, and Y. Miyazaki, Temperature-controllable oscillating heat pipe, *Journal of Thermophysics and Heat Transfer*, 25 (3) (2011) 386-392.

[6] Koito, Y., Ahamed, M. S., Harada, S. and Imura, H., Operational characteristics of a top-heat-type long heat transport loop through a heat exchanger, *Applied Thermal Engineering*, 29 (2-3) (2009) 259-264.

[7] W. Qu, Hydrodynamics of two-phase loop thermosyphon," *Frontiers in Heat Pipes (FHP)*, 1, 023004 (2010).

[8] B. J. Huang, H. H. Huang, C. W. Chen, and M. S. Wu, Development of high-power LED lighting luminaires using loop heat pipe, *Journal of Light and Visual Environment* 32 (2) (2008) 148-155.

[9] V. Ayel, L. Lachassagne, Y. Bertin, C. Romestant, and D. Lossouarn, Experimental analysis of a capillary pumped loop for terrestrial application, *Journal of Thermophysics and Heat Transfer*, 25 (4) (2011) 561-571.

[10] R. Singh, A. Akbarzadeh and M. Mochizuki, *Experimental Heat Transfer*, 21 (4) (2008) 296-313.

[11] V. G. Pastukhov, and Y. F. Maydanik, Active coolers based on copper-water LHPs for desktop PC, *Applied Thermal Engineering*, 29 (14-15) (2009) 3140-3143.

[12] Yu. F. Maydanik, S.V. Vershinin, V.G. Pastukhov, M.A. Chernysheva, C. Sarno, and C. Tantolin, Passive cooling system for electronic box of in-flight entertainment, International Conference "Heat Pipe for Space Application", 15-18 September, 2009, Moscow, Russia.

[13] C. T. Wang, T. S. Leu, and T. M. Lai, Micro capillary pumped loop system for a cooling high power device, *Experimental Thermal and Fluid Science,* 32 (2008) 1090-1095.

[14] Gregori, C., Mishkinis, D., Prado, P., Torres, A., and Pérez R., Loop heat pipe technology for aircraft anti-icing applications, *Proc. of 2007 SAE Aircraft and Engine Icing International Conference*, SAE Technical Paper 2007-01-3312, (2007).

[15] R. Singh, M. Mochizuki, Y. Saito, T. Nguyen, Z. Guo, M. Ohashi, T. Nguyen, E. Haghighi, and V. Wuttijumnong, Fuel cell co-generation system with loop heat pipe based thermal control, *Proc. of International Heat Transfer Conference,* IHTC15-9120/TMG-K-514 (2014).

[16] Z. Wang, W. Yang, A review on loop heat pipe for use in solar water heating, *Energy and Buildings*, 79 (2014), 143–154.

[17] V. G. Pastukhov, Y. F. Maidanik, C. V. Vershinin, and M. A. Korukov, Miniature loop heat pipes for electronics cooling, *Applied Thermal Engineering*, 23 (9) (2003) 1125-1135.

[18] Y. Chen, M. Groll, R. Mertz, Y.F. Maydanik, and S.V. Vershinin, Steady-state and transient performance of a miniature loop heat pipe, *International Journal of Thermal Sciences,* 45 (11) (2006) 1084-1090.

[19] R. Singh, A. Akbarzadeh, and M. Mochizuki, Operational characteristics of a miniature loop heat pipe with flat evaporator, *International Journal of Thermal Sciences,* 47 (11) (2008) 1504-1515.

[20] Y. Maydanik, S. Vershinin, M. Chernysheva, and S. Yushakova, Investigation of a compact copperewater loop heap pipe with a flat evaporator, *Applied Thermal Engineering,* 31 (16)

(2011) 3533-3541.

[21] R. Singh, A. Akbarzadeh, C. Dixon, and M. Mochizuki, Theoretical modelling of miniature loop heat pipe, *Heat and Mass Transfer,* 46 (2) (2009) 209-224.

[22] T. Shioga, and Y. Mizuno, Micro loop heat pipe for mobile electronics applications, *Proc. of 31st Thermal Measurement, Modeling & Management Symposium (SEMI-THERM)*, (2015).

[23] H. Nagano, F. Fukuyoshi, and H. Ogawa, Development of an experimental small loop heat pipe with polytetrafluoroethylene wicks. *Journal of Thermophys and Heat Transfer* 25 (4) (2011) 547-552.

[24] Yu. F. Maydanik, V. G. Pastukhov, Development and investigation of a long loop heat pipe, *Proc. of International Workshop on Two-Phase Thermal Control Technology*, (2000).

[25] M. Mitomi, H. Nagano, Long-distance loop heat pipe for effective utilization of energy, International Journal of Heat and Mass Transfer, 77 (2014) 777-784.

Abstracts/ Full Papers

1. General Aspects of Heat Pipes/ Conventional Heat Pipes

Effect of Meniscus on the Permeability of Sintered Particle Wicks

Sora Jeon and Chan Byon

School of Mechanical Engineering, Yeungnam University, Gyeongsan 38541, Korea

Abstract

In the heat pipe, the wick structure provides the capillary pressure for driving the working fluid, as well as the flow passage and heat flow path. Therefore, the thermal performance of heat pipe is strongly dependent on the wick structure. The sintered particle wick is generally regarded as the most state-of-art type of heat pipe wick due to its high capillary pressure and moderate-high thermal conductivity. In this study, a semi-analytic model for predicting the permeability of sintered particle wick is proposed based on an extensive numerical study, with taking into account the effect of surface meniscus. The meniscus shape around the sintered particle is estimated based on the well-defined surface energy minimization algorithm. The estimated meniscus shape is then imported into a CFD study for predicting the permeability of the structure. The numerical study is conducted for a wide range of geometrical parameters for developing a correlation. The results show that the meniscus affects the permeability of sintered particle wick significantly, suggesting that the meniscus shape should be carefully considered in predicting the permeability.

Keywords: Meniscus; Permeability; Sintered particle wick.

Experimental Performance and Parametric Analysis of Heat Pipe Heat Exchanger for Air Conditioning Application Integrated with Evaporative Cooling

Tushar S. Jadhav[1] and Mandar M. Lele[2]

[1] *Research scholar, Research centre, Sinhgad COE, Pune and SOPRIM, National Institute of Construction, Management and Research, Pune 411045, Maharashtra, India*

[2] *Department of Mechanical Engineering, MAEER's MIT College of Engineering, Pune 411038, Maharashtra, India*

Abstract

The experimental performance of different heat pipe heat exchanger (HPHX) configurations using distilled water as the working fluid is reported in the present study. The three HPHX configurations in the present investigation include HPHX with single wick structure (HPHX 1), HPHX with composite wick structure (HPHX 2) and hybrid HPHX (HPHX 3) which is the combination of HPHX 1 and HPHX 2. The investigations are studied for air conditioning application involving sensible heat recovery between fresh outdoor air and conditioned return air. The parameters considered for the parametric analysis of HPHX in all the three configurations are outdoor air dry bulb temperature entering the evaporator section of HPHX (OA_{DBT}), return air dry bulb temperature entering the condenser section of HPHX (RA_{DBT}), outdoor air velocity (Ve) and return air velocity (Vc). The OA_{DBT} is varied between 40 °C to 24 °C and the OA and RA velocities between 0.6 to 2.4 m/s. In the present study, the integration of HPHX with evaporative cooling indicates the provision of lowering RA_{DBT} by evaporative cooling technique. The parametric analysis of HPHX without evaporative cooling is studied for RA_{DBT} = 24 °C whereas RA_{DBT} is maintained at 20 °C for the parametric analysis of HPHX integrated with evaporative cooling. In comparison with HPHX without evaporative cooling, the performance of HPHX with evaporative cooling is enhanced by 17 % for single wick structure (HPHX 1), 47 % for composite wick structure (HPHX 2) and 59 % for hybrid HPHX (HPHX 3) for OA_{DBT} = 40 °C and at Ve = Vc of 0.6 m/s. The results of the experimental analysis highlight the benefits of HPHX integrated with evaporative cooling for achieving significant energy savings in air conditioning application.

Keywords: Heat pipe heat exchanger; Water; Parametric analysis; Evaporative cooling.

■ *Published in Heat and Mass Transfer (2017) 53: 3287. https://doi.org/10.1007/s00231-017-2039-y*

Preparation and Testing of Nickel-Based Superalloy/Sodium Heat Pipes

Longfei Hu, Qin Lu, Haitao Han, Zhihu Xue, Siyuan Chen and Bangcheng Ai

China Academy of Aerospace Aerodynamics, Beijing 100074, P.R. China

Abstract

In this work, a kind of uni-piece nickel-based superalloy/sodium heat pipes is proposed. Five models of high temperature heat pipes are prepared using GH3044 and GH4099 alloys. And their startup performance and ablation resistance are investigated by a quartz lamp calorifier and wind tunnel test, respectively. It is found that the amount of charging sodium affects the startup performance of heat pipes apparently. No startup phenomenon is found for insufficient sodium charged model. The models charged with sufficient sodium experience a shorter startup time in wind tunnel test than that during quartz lamp heating. Moreover, the GH4099/sodium heat pipe shows better ablation resistance than of the GH3044/sodium heat pipe in wind tunnel test, resulting endurable deformation or ablation. Therefore, it is proposed that this kind of heat pipes has a potential application in thermal protection system of hypersonic cruise vehicles.

Keywords: Heat pipes; Superalloy; Sodium; Startup;Thermal protection.

Experimental study and analysis of applying thermoelectric cooler to improve LHP operation with non-condensable gas

Rui Yang[1*], Guiping Lin[1], Jiang He[2], Lizhan Bai[3] and Jianyin Miao[2]

[1] *School of Aeronautic Science and Engineering, Beihang University, Beijing 100191, China*
[2] *Beijing Key Laboratory of Space Thermal Control Technology, Beijing Institute of Spacecraft System Engineering, Beijing 100094, China*
[3] *School of Chemical and Process Engineering, University of Leeds, LS2 9JU, U.K*

Abstract

Non-condensable gas (NCG) is one of the main causes affecting the thermal performance and lifespan of the two-phase heat transfer devices. In this work, the effect of NCG on the operating performance of two types of loop heat pipes (LHPs) with different configuration of thermal straps was experimentally investigated. Nitrogen was selected as NCG, and the effects of TEC on the steady-state operation temperature, startup process, heat transfer limit and temperature oscillation of LHP with NCG were studied. The experimental results reveal that by employing the TEC, the steady state operating temperature and the maximum temperature of the evaporator during the start-up reduce notably, and the heat transfer limit increases so that the normal working range of the LHP is expanded. In addition, the application of TEC can effectively inhibit or eliminate the temperature oscillation in LHP operation with NCG. Furthermore, the defects of assembly design for the TEC are analyzed and discussed according to a series of unexpected results obtained from the experiments.

Keywords: Loop heat pipe; Non-condensable gas; Thermoelectric cooler; Start-up; Experiment

Experimental Investigation for the Optimization of Heat Pipe Performance in Latent Heat Thermal Storage

Chandrakishor L. Ladekar[1], Dr. S. K. Chaudhary[2] and Dr. S. S. Khandare[3]

[1*] *Research Scholar, RTMNU, BDCOE, Wardha & Asst. Professor at SPPU, PCCOE, Pune 411 102, India*
[2] *Professor, RTM Nagpur University, K. D. K. College of Engineering, Nandanwan, Nagpur, India*
[3] *Professor & Principal, RTM Nagpur University, V. M. Institute of Engineering and Technology. Butibori, Nagpur, India*

Abstract

The work has been undertaken to investigate optimum performance of Heat Pipe in latent heat thermal energy storage (LHTES). Classical plan of experimentation was used to optimize the parameters of heat pipe. Heat pipe fill ratio, Evaporator to condenser length ratio and heat pipe diameter was the parameter used for optimization, as result of parametric analysis. Experiment with flow rate of 10 lit/min was conducted for different fill ratio, heat pipe length ratio and different diameter. Fill ratio of 80%, heat pipe length ratio of 0.9 and heat pipe with diameter of 18 mm show better trend in charging and discharging. Comparison between the storage tank with heat pie and copper pipe shows almost 200% improvement in charging and 250% improvement in discharging time; however the storage density of storage tank reduces. Heat transfer between HTF and PCM increases with increase in area of heat transferring media, but storage density of storage tank decreases. Storage tank with heat pipe embedded in place of copper pipe is better option in terms of charging and discharging time as well heat storage capacity due to less heat lost. This justified the better efficiency and effectiveness of storage tank with embedded optimized heat pipe.

Keywords: TES; PCM; HTF; LHTES; Heat Pipe; Optimization of heat pipe; Fill ratio.

■ *Published in J Mech Sci Technol (2017) 31: 2627. https://doi.org/10.1007/s12206-017-0505-6*

Modeling and Performance of Heat Pipes with Long Evaporator Sections

Wessel W. Wits[1] and Gert Jan te Riele[2]

[1] *Faculty of Engineering Technology, University of Twente, P.O. Box 217, 7500 AE Enschede, Netherlands*
[2] *Thales Nederland B.V., P.O. Box 42, 7550 GD Hengelo, Netherlands*

Abstract

This paper presents a planar cooling strategy for advanced electronic applications using heat pipe technology. The principle idea is to use an array of relatively long heat pipes, whereby heat is disposed to a long section of the pipes. The proposed design uses 1 m long heat pipes and top cooling through a fan-based heat sink. Successful heat pipe operation and experimental performances are determined for seven heating configurations, considering active bottom, middle and top sections, and four orientation angles (0°, 30°, 60° and 90°). For all heating sections active, the heat pipe oriented vertically in an evaporator-down mode and a power input of 150 W, the overall thermal resistance was 0.014 K/W at a thermal gradient of 2.1 K and an average operating temperature of 50.7°C. Vertical operation showed best results, as can be expected; horizontally the heat pipe could not be tested up to the power limit and dry-out occurred between 20-80 W depending on the heating configuration. Heating configurations without the bottom section active demonstrated a dynamic start-up effect, caused by heat conduction towards the liquid pool and thereafter batch-wise introducing the working fluid into a two-phase cycle. By analyzing the heat pipe limitations for the intended operating conditions a suitable heat pipe geometry was chosen. To predict the thermal performance a thermal model using a resistance network was created. The model compares well with the measurement data especially for higher input powers. The deviation at lower power inputs is explained by the incorrect modeling of the effective condenser length. Finally, the thermal model is used for the design of a 1 kW planar cooling infrastructure featuring six 1 m heat pipes in parallel having a long (~75%) evaporator section.

Keywords: Dynamic start-up response; Evaporator-down mode; Heat pipes; Long evaporator section; Planar cooling.

■ *Published in Heat and Mass Transfer (2017) 53: 3341. https://doi.org/10.1007/s00231-017-2040-5*

Permeability Model of Sintered Porous Media: Analysis and Experiments

Juan Pablo Flórez M., Maria E. Chiamulera and Marcia B. H. Mantelli

Heat Pipe Laboratory – LABTUCAL, Mechanical Engineering Department, Federal University of Santa Catarina
Campus Universitário Trindade, 88040-900 - Florianópolis/SC – Brazil

Abstract

In this paper, the permeability of porous media fabricated from copper powder sintering process were modeled and measured, aiming the use of the porosity as input parameter for the prediction of the permeability of sintering porous media. An expression relating the powder particle mean diameter with the permeability was obtained, based on an elementary porous media cell, which is physically represented by a duct formed by the arrangement of spherical particles forming a simple or orthorhombic packing. A circular duct with variable section was used to model the fluid flow within the porous media, where the concept the hydraulic diameter was applied. Thus, the porous is modeled as a converging- diverging duct. The electrical circuit analogy was employed to determine two hydraulic resistances of the cell, based on the Navier-Stokes equation and on the Darcy's law. The hydraulic resistances are compared between themselves and an expression to determine the permeability as function of average particle diameter is obtained. The atomized copper powder was sifted to reduce the size dispersion of the particles. The porosities and permeability of sintered media fabricated from powders with particle mean diameters ranging from 20 to 200 microns were measured, by means of the image analysis method and using an experimental apparatus. The permeability data of a porous media, made of copper powder and saturated with distilled water, was used to compare with the permeability model. Permeability literature models, which considers that powder particles have the same diameter and include porosity data as input parameter, were compared with the present model and experimental data. This comparison showed to be quite good.

Keywords: Hydraulic resistance; Loop heat pipes; Permeability; Sintered porous media.

■ *Published in Heat and Mass Transfer (2017) 53: 3277. https://doi.org/10.1007/s00231-017-2028-1*

A Study on the Performance Characteristics of Heat Pipes with Multiple Heat Sources

Joon Hong Boo[1] and Hyun Gon Kim[2]

[1]*School of Aerospace and Mechanical Engineering, Korea Aerospace University, Goyang, Gyeonggi, 412-791 Korea*
[2]*Graduate School, Korea Aerospace University, Korea*

Abstract

In a simple model to predict heat pipe performance, uniform thermal loads are assumed over the heat transfer surfaces. The validity of the simple model is limited in many practices such as electronics cooling and space thermal control, where a heat pipe is often subject to multiple, unequal thermal loads. This study is aimed to identify experimentally the performance of a heat pipe under various multiple heat source configurations and thus to estimate quantitatively the deviation from the one under uniform condition. The model heat pipe was 9.53 mm in diameter and 0.6 m in length, with 0.4-m evaporator. The working fluid and the container wall were water and copper, respectively, and a wire mesh screen was inserted as capillary structure. The fluid charge ratios tested were 100% and 120% based on the wick void volume. The heat pipe was in gravity-assisted mode with inclination angle of 45° to extend the range of thermal input and to compare the performance with that of a thermosiphon in the future. Five small heaters were installed in the evaporator with 50-mm spacing of which the power inputs were controlled individually. Three different thermal load configurations were imposed: equal, increasing and decreasing distributions toward the condenser. The results were compared with each other from the viewpoint of the thermal resistance and the effective thermal conductance. While the thermal resistance of the heat pipe with a 100% fluid charge exhibited excellent values from 0.075 K/W (at 50 W) to 0.03 K/W (at 300 W) for a uniform heat load, those for the multiple thermal loads resulted in almost 100% increase for lower thermal load, and up to 40% increase for higher thermal loads, depending on the configuration. The behavior of the heat pipe with a fluid charge of 120% exhibited a little difference. The results herein can be employed to estimate the performance deviation of a heat pipe due to thermal load distribution.

Keywords: Multiple heat sources; Heat pipe; Thermal load distribution; Thermal resistance; Effective thermal conductance; Experimental

■ *Published in Applied Thermal Engineering, Volume 126, 5 November 2017, Pages 1209-1215, https://doi.org/10.1016/j.applthermaleng.2017.02.097*

Heat Pipe System Development FOR Railway Application Working with Speed Motion Convection

Jérôme Coulloux, Thomas Albertin

ATHERM, 1 rue Charles Morel – 38420 DOMENE, FRANCE

Abstract

Railway manufacturers look for saving space, weight and energy consumption in order to face economic and environmental issues. In this optic they are greatly interested in passive systems such as Heat Pipes, and especially those avoiding any fan use then any additional electrical apparatus and reducing maintenance needs. Their systems have also to face all weather conditions including very low temperatures.
In this context, an innovative concept of cooling system was developed recently. It is named as "cold wall" and it is a speed motion cooling system based on a Heat Pipes assembly, aiming at extracting more than 6kW from assembled IGBTs and able to work from -40°C, both in forced and natural convection.
For this development, numerical simulation and prototypes testing were combined to reach the performances. The objective of the present communication is to summarize and exemplify the development demarche and results of this new system.

Keywords: Heat-pipe; Thermosyphon; Railway; Speed-motion; Cold-temperatures.

Examination of the Thermoelectric Inhomogeneity of Thermocouples in an Electric Furnace with Heat Pipe Liner

Yong-Gyoo Kim, Wukchul Joung and Su Yong Kwon

Center for Thermometry, Korea Research Institute of Standards and Science (KRISS), Daejeon, Korea

Abstract

The temperature dependence of the thermoelectric inhomogeneity of the noble metal thermocouples such as type S, R and B was investigated up to 1000 °C using an electric furnace with sodium heat pipe liner inside. Without heat pipe liner, temperature gradient of larger than 10 °C was observed within ± 10 cm from the center of furnace, so it was not possible to examine the thermoelectric inhomogeneity of thermocouple. By applying sodium heat pipe liner in a same furnace, uniform temperature gradient inside the liner about ± 0.5 °C was observed within range of (30 ~ 40) cm, and thus precise thermoelectric voltage change due to inhomogeneity could be measured. From the measured variation of the thermoelectric voltage with the immersion depth, thermoelectric inhomogeneity can be calculated and thus calibration uncertainty of thermocouples can be estimated more accurately at the elevated temperature.

Keywords: Calibration uncertainty; Heat pipe liner; Noble metal thermocouple; Temperature gradient; Thermoelectric inhomogeneity.

Modeling of Heat Transfer in the Evaporator and Condenser of the Working Fluid in the Heat Pipe

Richard Lenhard[1], Milan Malcho[2] and Jozef Jandačka[3]

[1]*Researcher, Department of Power Engineering, Faculty of Mechanical Engineering, University of Zilina, Zilina, Slovakia*
[2]*Professor, head of department, Department of Power Engineering, Faculty of Mechanical Engineering, University of Zilina, Zilina, Slovakia*
[3]*Professor, Vice-Rector for Development, Department of Power Engineering, Faculty of Mechanical Engineering, University of Zilina, Zilina, Slovakia*

Abstract

The aim of this paper is to point out possible solutions to the further development of heat pipes by numerical modeling of phase-change heat transfer. Numerical modeling has now become a standard method that helps to reduce the economic costs of research and development of new and innovative devices. The article describes the procedures for using numerical simulation in phase-change heat transfer that occurs due to evaporation and condensation of the working fluid. The suggested procedure enables modeling of gravitational heat pipe under different changes in its geometry or under changes in the working fluid. From the simulation results we can find out how the heat pipe behaves under different geometric changes and how much heat output it transfers. The paper presents results obtained from modeling of heat pipes, such as classical gravitational heat pipe, heat pipe with capillary geometry and closed loop pulsating heat pipe (CLPHP). The results gathered from numerical simulation of heat pipes were compared with measurement results.

Keywords: Heat pipe; Heat transfer; Numerical simulation.

■ *Published in Heat Transfer Engineering, Vol. 40, Issue 3, 2019.*

Thermoelectric System to Increase the Cooling Power of Natural Convection Heat Pipes

Alvaro Martinez, David Astrain, Antonio Rodriguez, Patricia Aranguren and Miguel Araiz

Mechanical, Energy and Materials Engineering Department, Public University of Navarra, Pamplona 31006, Spain Institute of Smart Cities, Public University of Navarra, Pamplona 31006, Spain

Abstract

Thermoelectric self-cooling relates to the application of thermoelectrics to increase the cooling power of passive cooling systems. Up to now, finned heat sinks and fluidic systems have been addressed; one step further, this paper studies the application to heat pipe exchangers. In general, given a heat source attached to a passive cooling system, several thermoelectric modules are installed between them. These modules transform by Seebeck effect- part of the heat into electricity, which is directly used to operate a fan installed over the passive system. As a consequence, the cooling system becomes active, thus increasing the cooling power without external electricity. A prototype is constructed and tested, comprising a heat-generating device and a heat pipe exchanger, sandwiching six thermoelectric modules. A fan is installed over the fins to provide force convection, power-supplied directly by the thermoelectric modules. Source-to-ambient thermal resistance reduces by around 30 %, compared to that obtained with the heat pipe exchanger under natural convection. The minimal thermal resistance occurs for 80 ºC of source-to-ambient temperature difference, reaching 0.346 K/W, while the cooling power reaches 231 W (24.1 kW/m^2). For this temperature difference, the heat pipe exchanger under natural convection reaches only 149 W (15.5 kW/m^2), with 0.537 of thermal resistance. For the latter to reach 24.10 kW/m^2, a 55 % of additional convective surface area would be required, which shows the gain in compactness that entails the use of this technology. Furthermore, the system adapts to the cooling demand, reducing the global resistance for increasing heat. Additionally, simulation tests have also been conducted to assess potential improvements. Replacement of a thermoelectric module with a thermal bridge leads to 33.54 kW/m^2 of top cooling power. Likewise, thermoelectric modules with shorter legs and higher number of pairs lead to a top cooling power of 44.17 kW/m^2.

Keywords: Thermoelectric self-cooling; Seebeck effect; Heat pipe exchanger; Passive cooling.

Design and Start-Up of TZM High-Temperature Heat Pipe

Qin. Lu, Longfei Hu and Siyuan Chen, Wei Li

China Academy of Aerospace Aerodynamics, 17 West Yungang Street, Fengtai District, Bejing, 100074 China

Abstract

Thermal protection system (TPS) ,whichare correlated to the safety of hypersonic vehicles, will encounter severe challenges when exposed to the extreme heating during long-time hypersonic flight in the atmosphere. Stagnation regions, such as wing and tailing leading edges and nose caps, are critical design areas of hypersonic vehicles due to heat flux distribution varying sharply from leading edge to the big acreage. Refractory metal - TZM (Titanium-Zirconium-Molybdenum Alloy) high-temperature heat pipe is being considered for use on hypersonic vehicles due to good high temperature performance of TZM. A hemisphere- cylinder TZM with lithium working fluid was fabricated and tested to verify feasibility of heat pipe design. Start- up and steady state data are presented for TZM heat pipe test article.

Keywords: Heat pipe; TZM; Lithium working fluid; Hypersonic vehicles.

Heat Dissipation for High Power Semiconductor Lasers by Heat Pipe Cooling System

Shu Shili[1], Hou Guanyu[1], Wu Hao[1], Wang Lijie[1], Tian Sicong[1],
Leonid L. Vassiliev[2] and Tong Cunzhu[1]

[1] *State Key Lab of Luminescence and Applications, Changchun Institute of Optics, Fine Mechanics and Physics, Chinese Academy of Sciences, Changchun 130033, China*
[2] *Luikov Heat and Mass Transfer Institute, National Academy of Sciences of Belarus, Minsk 220072, Belarus*

Abstract

High power semiconductor lasers cooled by heat pipe cooling system were designed. The “n” shaped heat pipe cooling system could effectively dissipate the heat of about 73.4 W, and the output power of the single laser module could reach to 67.3 W at the driving current of 70A. Moreover, a high power semiconductor laser with five laser modules cooled by a “U” shaped heat pipe cooling system was designed and the “U” shaped heat pipe cooling system was simulated and fabricated. The heat dissipation capacity of the “U” shaped heat pipe cooling system was 300 W. Simultaneously, the optical power of the high power semiconductor laser cooled by the “U” shaped heat pipe cooling system was respected to be 285W.

Keywords: Heat dissipation; Heat pipe; High power; Semiconductor lasers; Heat transfer.

■ *Published in J Mech Sci Technol (2017) 31: 2607. https://doi.org/10.1007/s12206-017-0502-9*

Experimental Analysis of Thermal Performance According to Heat Pipe Working Fluids for Evacuated Tube Solar Collector

Hong-Jin Joo and Hee-Youl Kwak

Solar Thermal Division, Korea Institute of Energy Research (KIER), 152 Gajeong-ro, Yuseong-Gu, Daejeon

Abstract

The purpose of this study was experimentally to investigate thermal performance and operating characteristics of evacuated tube solar collector with various heat pipe working fluids. Heat pipe efficiency was evaluated by calculating the solar collector efficiency value according to four types of working fluids. The working fluids used Water, Ethanol, Flutec-pp9 and Methyl Acetate under the same operating condition for indoor experiment equipment. The experimental conditions are as follows, the incidence angle of evacuated tubular solar collector were 20o, 40o and 60o from the horizontal basis. The mass flow rate into the manifold of evacuated tubular solar collector was 0.3 kg/min. The heat flux on the collector surface was 870 W/m^2. As a result, the $F_R(\tau\alpha)$ value with Mathyl Acetate as working fluid in incidence angle 40^o was 0.6572, $F_R U_L$ value was -2.0086, the $F_R(\tau\alpha)$value with Water was 0.6636, $F_R U_L$ value was -1.8457, the $F_R(\tau\alpha)$ value with Ethanol was 0.6147, $F_R U_L$ value was -0.6353, the $F_R U_L$ value with Flutec pp-9 was 0.525, $F_R U_L$ value was -3.2313.

Keywords: Evacuated tube solar collector; Solar collector efficiency; Heat pipe; Working fluid.

■ *Published in Heat Mass Transfer (2017) 53: 3267. https://doi.org/10.1007/s00231-017-2029-0*

Nanofluid Performance as a Working Fluid in the Heat Pipe

Joohyun Lee[1], Su Yong Kwon[2] and Wukchul Joung[3]

[1] *Senior research scientist, Center for Thermometry, Korea Research Institute of Standards and Science (KRISS) 267 Gajeong-Ro, Yuseong-Gu, Daejeon 34113, Korea*

[2]Principal research scientist, Center for Thermometry, Korea Research Institute of Standards and Science (KRISS)

[3] *Senior research scientist, Center for Thermometry, Korea Research Institute of Standards and Science (KRISS)*

Abstract

Nanofluids, which consist of traditional heat transfer fluids and dispersed nanoparticles have shown remarkable thermal properties. Most of nanofluid research was focused on the thermal conductivity measurement using the transient hot wire method, and the reported thermal conductivity enhancement reaches up to 60 % with small volume concentration less than 5 %. However, there are only few studies on the nanofluid application to the heat pipes as working fluids. In this study, nanofluid performance as the working fluid of the heat pipe was evaluated. Nanofluids containing Al_2O_3 nanoparticles in DI water and graphene oxide in DI water were used as the working fluids. Volume concentration of the nanoparticles was changed from 0.01 % to 0.05 %, and the effect of the sonication time on the thermal performance of the heat pipe was also investigated. The nanoparticles were characterized with SEM images, and their thermophysical properties including thermal conductivity and heat capacity were measured by the transient hot wire method and Calvet calorimeter, respectively. The experimental apparatus was designed to be consisted of a heating part and a cooling part, which employed a film heater and a circulation chiller, respectively. Type T thermocouples were attached on the surface of the heat pipe, and temperatures were recorded by a DAQ system. The thermal performance of the heat pipe including the operating temperatures and the thermal resistances were evaluated, and comparison was carried out between the base fluid and the nanofluids.

Keywords: Heat pipe; Al_2O_3 nanofluid; Graphene oxide nanofluid; Nanofluid application.

A Single Unit Cooling Fins Aluminum Heat Pipe for 100W Socket Type COB LED Lamp

Seok Hwan Moon[1], Yoon Woo Park[1], Hong MoYang[2]

[1]3 Dimensional New Devices Research Section, ETRI, Daejeon 34129, Korea
[2]Redix co., Daejeon 34302, Korea

Abstract

Although the LED light has higher energy conversion efficiency compared with the conventional metal halide lamp, it is well known that there is a thermal burden due to the poor photoelectric conversion efficiency of the semiconductor diode. SMD (Surface Mount Device) LED lamp which has been mainly used has induced a problem of poor optical efficiency though it has relatively large heat dissipation area. Much effort has been put to improve the optical efficiency through COB(Chip on Board) LED lamp, but the thermal problem particularly in the over 100 W application is still exist. As the studies for applying the heat pipe to the high power LED, an embedding technology the heat pipe in the MCPCB(Metal Core Printed Circuit Boards), loop heat pipe, and a columnar heat pipe for 90 W et al were developed and may apply to COB LED lamp. In this paper, a single unit cooling fins aluminum flat heat pipe(AFHP) with U shape is developed for the 100 W COB LED lamp with 120*120*170 mm^3 of small volume and socket type electric connection. The U shape AFHP module has less than 900 g, low price by extrusion method and socket type lamp, therefore replacement and maintenance of the lamp for factory-light or street-light could be easily conducted. Through the study, a single unit cooling fins AFHP is designed and fabricated. And the heat transfer characteristics of the AFHP with two condensers have been investigated, and the junction temperature of the COB LED module was also evaluated within 85 °C at 100 W of input power.

Keywords: Aluminum heat pipe; LED; COB; Fin.

■ *Published in Applied Thermal Engineering, Volume 126, 5 November 2017, Pages 1164-1169, https://doi.org/10.1016/j.applthermaleng.2016.11.077*

Development of Advanced High Porosity Wicks for the High Temperature Heat Pipes of Concentrating Solar Power

Sergii Khairnasov[1], Charles E. Andraka[2], Volodymyr Baturkin[1, 3], Vladlen Zaripov and Oleksandr Nishchyk[1]

[1] Heat Pipes Laboratory of National Technical University of Ukraine "Kyiv Polytechnic Institute", Peremogy Pr.37, Kyiv, 03056, Kyiv, Ukraine,
[2]Concentrating Solar Power Department 06123, Sandia National Laboratories, PO 5800 MS 1127, Albuquerque NM, USA NM 87185,
[3] Institute of Space Systems, Robert-Hooke-Straße 7, 28359 Bremen, Germany

Abstract

Sandia National Laboratories and Heat Pipes Laboratory of National Technical University of Ukraine «KPI» developed several methods of improving robustness of the high-temperature heat pipe wick for their application to concentrating solar power (CSP) systems with stirling engine. In this case the wick structures must retain high heat pipe performance with robustness for long term operation. Recent modeling indicates that wicks based on various fiber combinations could provide the robustness combined with sufficientperformance. Results of the development, characterization, modeling, and testing of an advanced felt metal wicks that addresses durability issues while maintaining sufficient performance are showed in the paper.

He project resulted in an ongoing durability bench-scale heat pipe that simulates wick load conditions required for an 80kWth throughput solar receiver, including periodic non-destructive evaluation of the wick durability. Two mock-ups of high-temperature heat pipes were made for long life and performance tests: the first sample with wick based on 12 μm felt; and second with hybrid wick based on 30 μm felt and 6.5 μm felt. Second heat pipe operation has continued unattended at 775°C vapor temperature for nearly 11,700 hours, with no observable loss of performance or change in startup characteristics.

Keywords: Felt metal wick; High-temperature heat pipe; Stirling engine; Concentrating solar power.

■ *Published in Applied Thermal Engineering, Volume 126, 5 November 2017, Pages 1170-1176, https://doi.org/10.1016/j.applthermaleng.2017.02.109*

High Power Heat Removal by Heat Pipes & Two Phase Heat Transfer for Electric Vehicle

Masataka Mochizuki*, Yuji Saito, Koichi Mashiko, Thang Nguyen, Thomas van Raay, and Randeep Singh

Fujikura Ltd. 1-5-1 Kiba, Koto-Ku, Tokyo 135-8512, Japan

Abstract

Recently, there is an increase in heat pipe application for modern vehicles, however, most of these applications are for cooling of low power consumption electronics devices such as LED head lamps, LED backlights, Electronic Control Unit (ECU), and the like. The power consumption system is quite different for gasolines engine vehicle and electric vehicle (EV). The EV has 3 main power sources and they are Electric Motor, Battery, and Insulated Gate Bipolar Transistor (IGBT), all of which generate considerably high heat. For example, a motor of 100 kW output would generates 0.4 kW of magnetic heat loss, the IGBT 1-2 kW switching heat loss, and battery 1 kW discharging heat loss. Similarly to semiconductor, for reliability concerns, these devices has limitation on maximum allowable junction operating temperatures (Tj-max) and ambient temperature (Ta). The temperature difference (Tj-max to Ta), and the heat flux are the critical functions to determine the maximum heat transfer capability. The weight and space also are limited factors in the vehicle, therefore, method of cooling needs to be considered of light weight, robust and compact. This paper discusses about optimization of high power devices cooling of vehicle based on consideration of thermal performance, weight, space and cost.

Keywords: Electric motor, Electric vehicle, Heat pipe, IGBT, Li ion battery

1. INTRODUCTION

Fig. 1 shows the schematic concept comparison between water cooling and air cooling systems in the electric vehicle (EV). There are three main power devices under consideration for cooling are battery, the motor and the IGBT. In the following sections contain design analysis of method of cooling for each of these devices. A cold plate with water is applied to cool battery and IGBT but motor is cooled by rotational heat pipe with water cooling in water cooling system. In air cooling system, battery and IGBT are cooled by air cooled heat pipes and a motor is cooled by a rotaional heat pipe with air cooling.

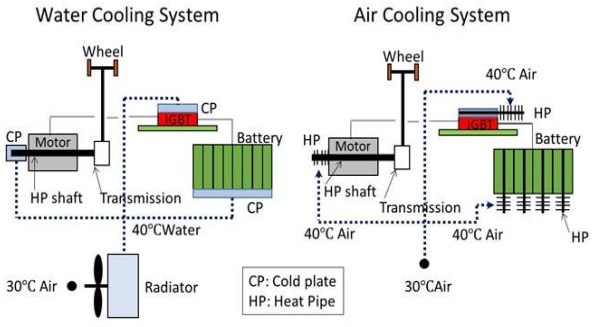


Fig. 1 Concept of water cooling and air cooling systems in the EV

Fig. 2 shows a standard calculation results for heat transfer capability for various tube sizes and various methods of cooling such as air, water or two phase heat transfer. The general condition of parameters used for calculation are as follows.

dT: Temperature difference of cooling medium between inlet and outlet is 10 °C.

V: Velocity of cooling medium for air = 3 m/s, for water = 1 m/s, and for two phase = 0.5 m/s.

Cooling medium: Air or water.

If the allowable tube size is limited to 20 mm, the electronic devices in vehicle with heat generation less than 200 W such as LED headlamps can be air cooled. For higher heat dissipation devices less than 10 kW such battery and IGBT would required liquid cooling as forced air cooling is not suitable. The two phase heat transfer has the highest heat transfer capability of 70 kW, thus it is applicable for cooling of the engine.

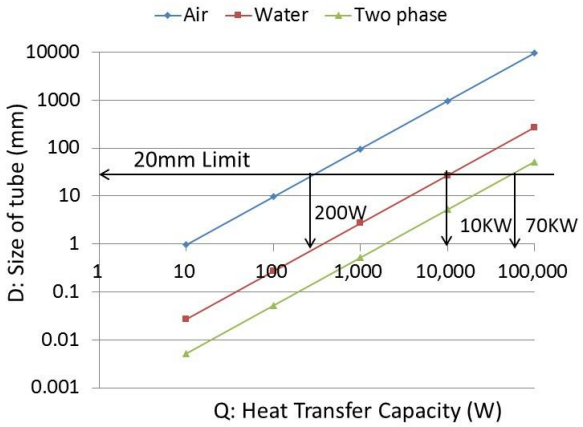


Fig. 2 Heat transfer capacity for various tube sizes and various methods of cooling

*Corresponding author: mmotizuk@fujikura.co.jp
Phone: +81-3-5606-1174, Fax: +81-3-5606-1514

2. BATTERY COOLING

2.1 Traditional Air Cooling

Fig. 3 shows an example case study of the battery pack in EV. The battery cells stacks up and electronic control unit (ECU) are cool by the fan forced air flow through it. The battery stacks layout configuration, the air flow distribution, and the dimensions are shown on detail in Fig. 4. The overall size of the enclosed unit is approximately width 520 mm x length 360 mm x height 120 mm. There are 72 battery cells divided into 4 blocks formation. Each block has 18 cells which are divided into 6 cells per module. The heat dissipation for each cell is about 7 W, thus a total of about 504 W needed to be removed from the system.

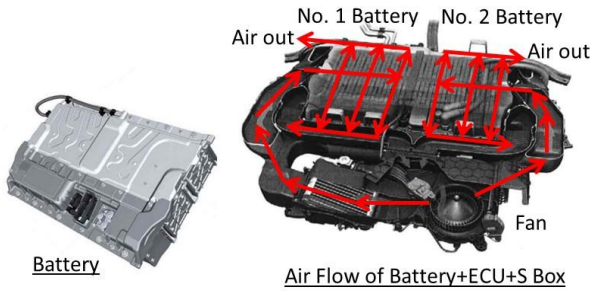


Fig. 3 Example of the air cooling for battery packs in electric vehicle

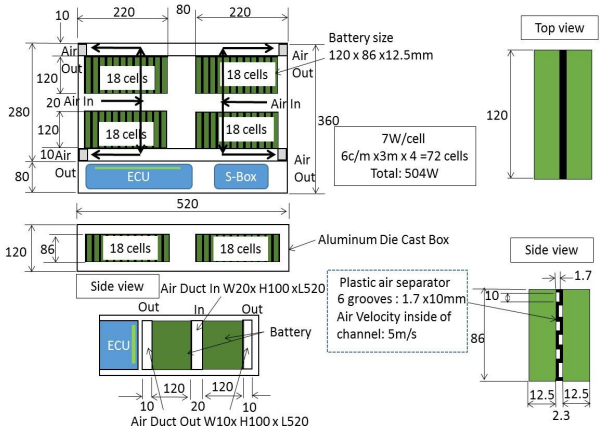


Fig. 4 A case study of battery layout configuration

Fig. 5 shows calculation model for a module of 6 cells. The air inlet temperature is assumed at 25 °C, and volume air flow 10 m^3/hr enter a common header channel for air distribution between cells. The air flow is assumed evenly distribution in the channels of the air separator plate which is sandwiched between the battery cells. The thermal network is shown on detail in Fig. 6. The calculated sum of this thermal network is approximately 0.485 K/W.

Fig. 7 shows calculation results for the temperature of the battery vs. heat dissipation. If assuming that the temperature of the battery set at the limit of 60 °C, then the maximum heat dissipation are 12 W and 7 W at inlet air temperature of 25 °C and 40 °C respectively. The latter represent more realistic case.

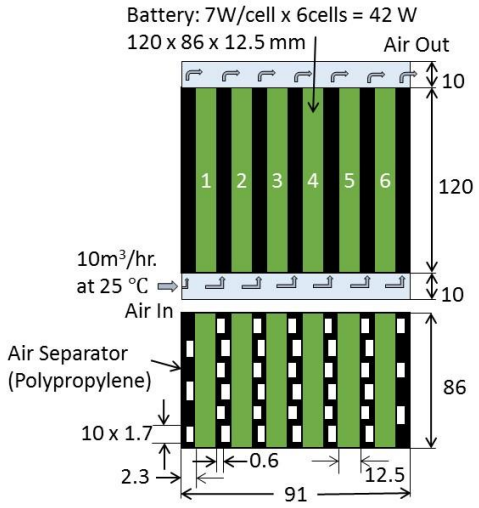


Fig. 5 Battery module 6 cells Layout

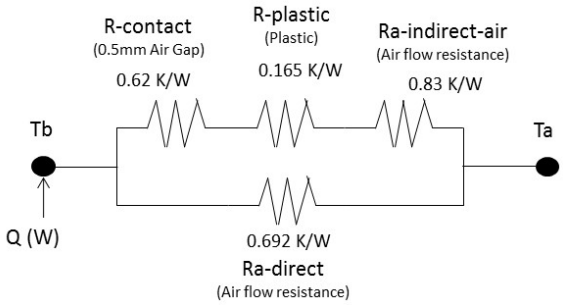
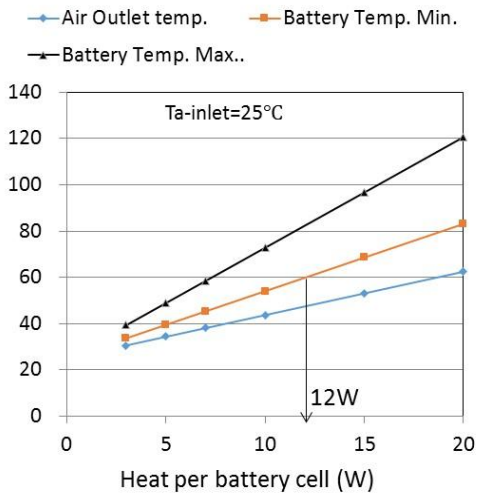
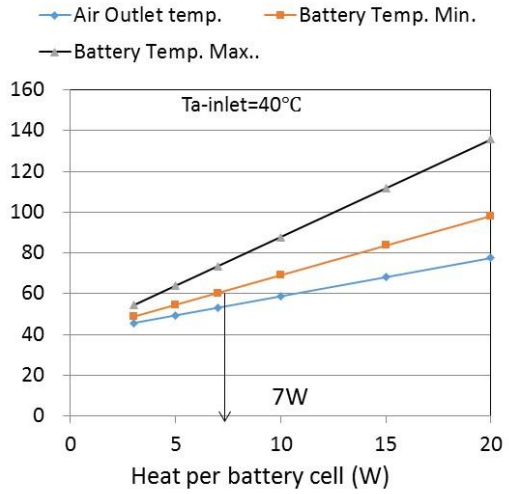


Fig. 6 Battery module 6 cells thermal network



(a)



(b)

Fig. 7 Battery temperature against heat dissipation

2.2 Air Cooling With Heat Pipe and Fins Heat Exchanger[4]

Fig. 8 shows the same case study as in section 2.1 traditional air cooling, but with heat pipes and fins heat exchanger incorporated. Heat pipe is of original diameter 6 mm and length 140 mm, which is flattened to width 8.3 mm and thickness 2 mm, and it is sandwiched between 2 battery cells, therefore there are 3 heat pipes per 6 cells battery module. The heating and cooling lengths of each heat pipe are 120 mm, and 20 mm respectively. For each heat exchanger consisted of 10 pieces Aluminum plate fins of sizes approximately width 85mm, length 27 mm, thickness 0.5 mm and fin pitch 1.7 mm.

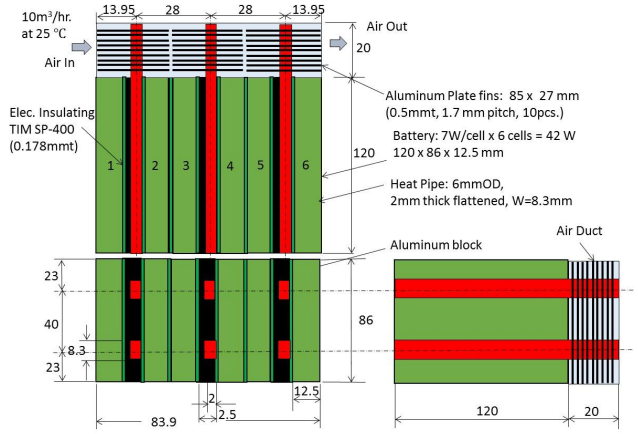


Fig. 8 Battery module 6 cells with heat pipes and fins heat exchanger

Fig. 9 shows the calculation results for battery cell temperature distribution comparison between forced air cooling with and without heat pipe. The results shows same performance for both cases.

The battery has a large thermal mass, so it is necessary to carry out the transient thermal analysis to check the steady state design calculation. Fig. 10 shows the transient thermal analysis for forced air cooling without heat pipe, and Fig. 11 for the case with heat pipe. Results clearly showed that the saturated temperature for the transient analysis is same as steady state design temperature for both cases air cooling with and without heat pipe.

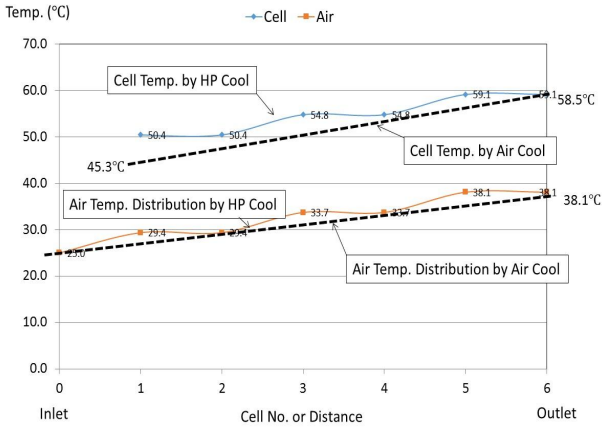


Fig. 9 Battery cell temperatures comparison between forced air cooling with and without heat pipe.

Conventional Air Cooling	
Power/cell	7W/cell
Cell NO.	6 cells
Power(W)	42
Ta(°C)	25
Thermal capacity/cell(J/K)	330
Thermal Resistance(K/W)	0.485

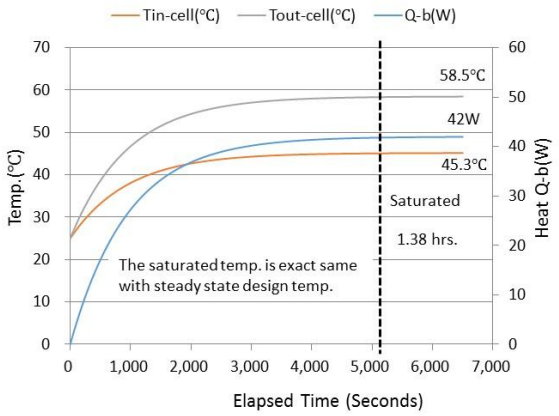


Fig. 10 Battery cell transient temperature analysis for forced air cooling without heat pipe

Heat Pipe Air Cooling	
Power/cell	7W/cell
Cell NO.	6 cells
Power(W)	42
Ta(°C)	25
Thermal capacity/cell(J/K)	330
Thermal Resistance(K/W)	2.88/6=0.48

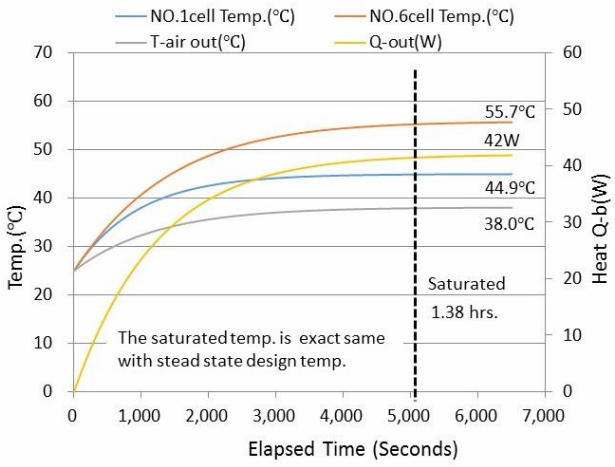


Fig. 11 Battery cell transient temperature analysis for forced air cooling with heat pipe

Based on the case study calculation it seems that it is no thermal performance gain for using heat pipes with fins heat exchanger for forced air cooling. Even if the design can be optimized to improve the thermal performance, authors believe the performance improvement will not be significant to justify the cost, size and weight increased due to the additional parts heat pipes fins heat exchanger.

An alternative feasible option is use of heat pipes with liquid cool cold plate. In this concept of cooling, heat pipe is used to transfer the heat from the battery cells to an existing external liquid cold plates.

Another option is use a different type of heat pipe called loop heat pipe which has higher heat transport over a much longer distance.[1][2][3] The concept is schematically shown in Fig. 12 and 13. The loop heat pipe transports the heat from the battery stacks which are normally located towards the rear end of the vehicle, to the front where liquid cold plates can be positioned close to the existing vehicle radiator for heat removal.

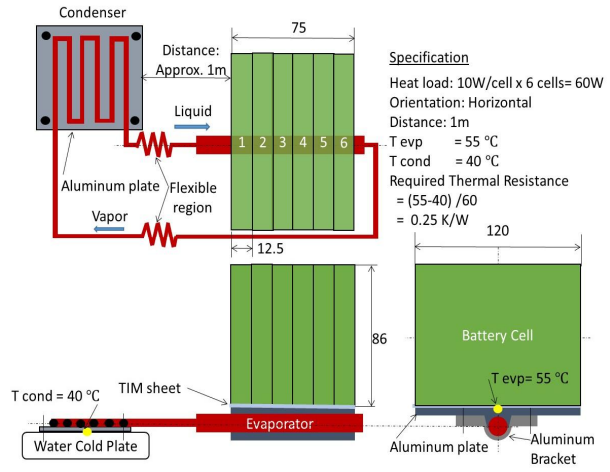


Fig. 12 Battery cell concept of cooling with loop heat pipe

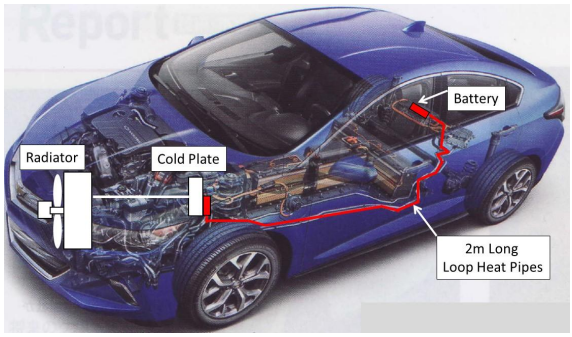


Fig. 13 Battery cell concept of cooling with loop heat pipe application in electric vehicle

3. MOTOR COOLING

3.1 Rotational Heat Pipe for Cooling Motor

Fig. 14 shows a conceptual design of cooling of motor shaft using rotational heat pipe. This is a case study in reference to a request study from a car manufacturer. The basic idea is to replace the existing motor shaft with the rotational heat pipe. Heat pipe is required to transfer about 350 W heat dissipation from mainly the motor and the rotor, to external of the motor housing for cooling. The expected maximum rotational speed of the motor is about 12,000 RPM. In this case study two cooling methods are considered, air and water. Design and calculation approximation will be presented in this section.

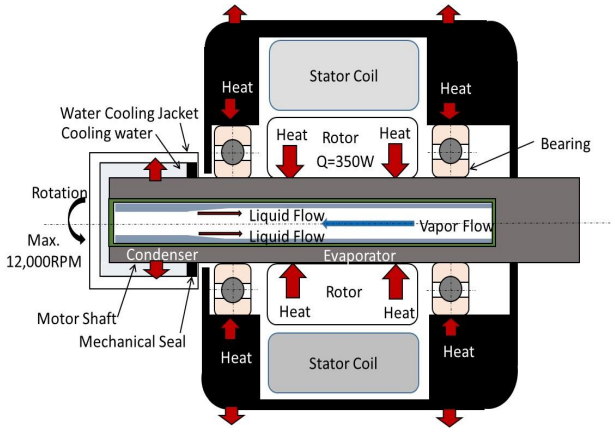


Fig. 14 Conceptual design of cooling motor shaft in electric vehicle using rotational heat pipe

There are various design of rotational heat pipe having variety of internal structures, but mainly there are three types as shown in Fig. 15.[5][6] They are straight, taper and screw types. For the straight heat pipe, the liquid returns to the evaporator from the condenser by the axial centrifugal force generation from the liquid layers thickness difference between the evaporator and the condenser, and the condenser has thicker liquid film. As for the taper heat pipe, the axial centrifugal force generation from the difference radii from larger in the evaporator to smaller in the condenser. Lastly, for the screw type the generation force is from the angle of the thread. From the literatures and author's experiences, the taper type rotational heat pipe has the most stable operation, and therefore the design and calculation hereafter will be only for taper type at condenser.

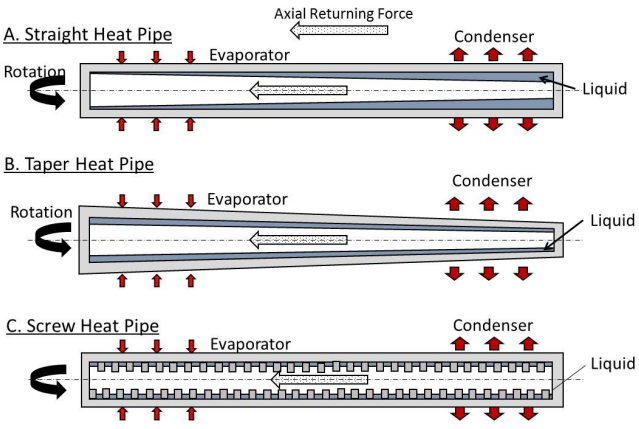


Fig. 15 Various types of rotational heat pipe

3.2 Liquid Cool Rotational Heat Pipe

The design concept and the thermal resistance network are shown in Fig. 16 & 17. Heat pipe dimensions are approximately – Outer diameter 15.9 mm and wall thickness 1.5 mm, Total length 300 mm, Evaporator length 140 mm, Condenser length 10-50 mm, and tapered 3 degrees. Heat pipe is designed to transfer minimum of 350 W. Detail calculation analysis will not be given in this paper, only the calculation results and discussion are presented.

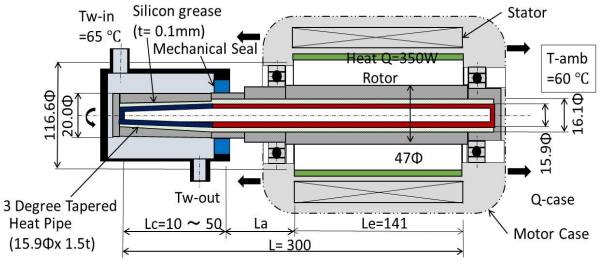


Fig. 16 Design concept for liquid cooling rotational heat pipe

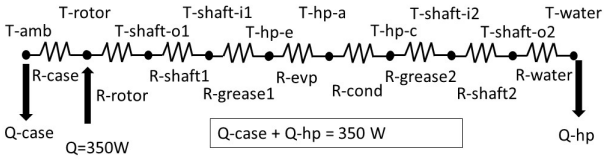


Fig. 17 Thermal resistance network for liquid cooling rotational heat pipe

The nomenclature for the thermal resistance network shown in Fig. 17 are shown as follows:

Q-case: Heat dissipation from case (W)
Q-hp: Heat dissipation from heat pipe (W)
R-case: Thermal resistance from rotor to ambient (K/W)
R-rotor: Thermal resistance from rotor to shaft outer diameter (K/W)
R-shaft1: Thermal resistance from shaft outer to inner diameter (K/W)
R-grease1: Thermal resistance of grease from shaft to heat pipe evaporator (K/W)
R-evp: Thermal resistance of heat pipe evaporator (K/W)
R-cond: Thermal resistance of heat pipe condenser (K/W)
R-grease2: Thermal resistance of grease from heat pipe to shaft (K/W)
R-shaft2: Thermal resistance from shaft inner to outer diameter (K/W)
R-water: Thermal resistance from shaft outer diameter to water (K/W)
T-amb: Ambient temperature (^{o}C)
T-rotor: Rotor temperature (^{o}C)
T-shaft-o1: Shaft outer diameter temperature at heating section (^{o}C)
T-shaft-i1: Shaft inner diameter temperature at heating section (^{o}C)

T-hp-e: Heat pipe evaporator temperature (°C)
T-hp-a: Heat pipe adiabatic temperature (°C)
T-hp-c: Heat pipe condenser temperature (°C)
T-shaft-i2: Shaft inner diameter temperature at cooling section (°C)
T-shaft-o2: Shaft outer diameter temperature at cooling section (°C)
T-water: Cooling water temperature (°C)

Fig. 18 shows the rotor temperature and heat dissipation by heat pipe and the motor case against the length of the heat pipe condenser. In case of no heat pipe cooling, the rotor temperature reaches about 173.5 °C, and when heat pipe is use to remove heat from the rotor, its temperature can be reduced to 110.3 °C. The ratio of the heat dissipation from the motor case and from the heat pipe varies with condenser length. The longer the length of the condenser, the more heat remove by the heat pipe, and less heat remove by the motor case.

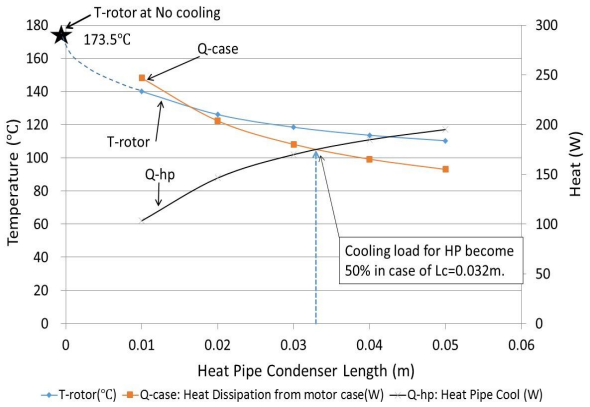


Fig. 18 Rotor temperature and heat dissipation from heat pipe and motor case against heat pipe condenser length

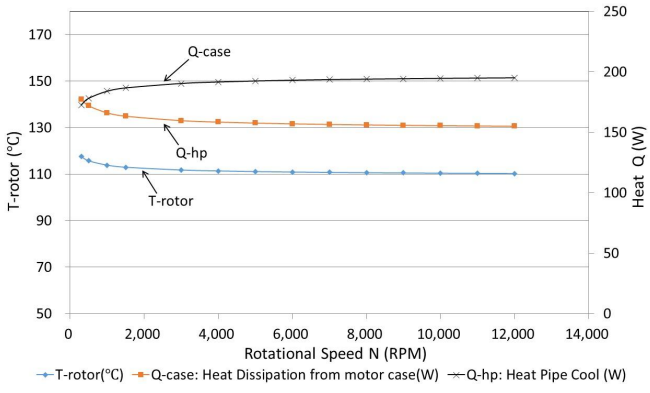


Fig. 19 Rotor temperature and heat dissipation from heat pipe and motor case against heat pipe rotational speed

Fig. 19 shows the rotor temperature, heat dissipation by heat pipe and the motor case against heat pipe rotational speed. The calculation results show that there is no significant impact on the rotor temperature when speed changes from about 1,500 through to 12,000 RPM. Fig. 20 shows the heat transfer coefficient comparison for various cooling liquid medium of water, LLC(Long Life Coolant) 30%, and oil. The heat transfer coefficient increases with rotational speed and water shows the best. Although water has the highest heat transfer coefficient, but when considering overall thermal resistance, all three cases have no significant differences in thermal performance as indicate in Table 1.

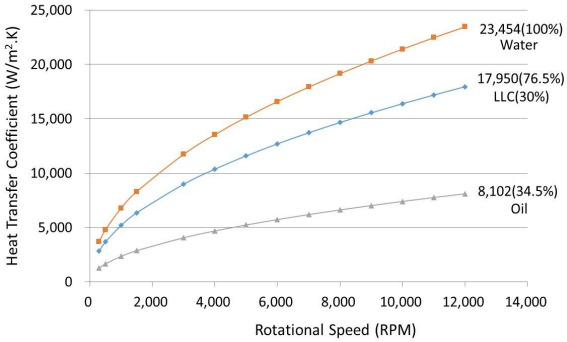


Fig. 20 Heat transfer coefficient for various cooling liquids against rotational speed

Table 1 Summary of thermal performance for liquid cooling

	Water	LLC	Oil
T-rotor (°C)	110.3	110.7	113.1
Q-case (W)	155	156	164
Q-hp (W)	195	194	187
Rtotal (K/W)	0.232	0.236	0.258

3.3 Air Cool Rotational Heat Pipe

Fig. 21 shows the design concept for cooling rotational heat pipe by air. This is exact same design as described in section 3.2, but replaced the liquid cooling with air cooling. The thermal network is same with air replaced liquid as shown in Fig. 22. There are 15 pieces fins, which are Aluminum of outer diameter 60 mm, inner diameter 20 mm, 0.5 mm thick and fin pitch 3 mm. The inlet air temperature assumed 40 °C and air velocity 2.5 m/s. A summary of the thermal performance comparison between liquid and air cooling is shown in Table 2. For the same size and configuration, the total thermal resistance of the air cooling is almost three times worse than the liquid cooling, and the rotor temperature for air cooling is about 20 °C higher. It is therefore concluded that air cooling is not suitable design option for cooling of the motor shaft of the electric vehicle.

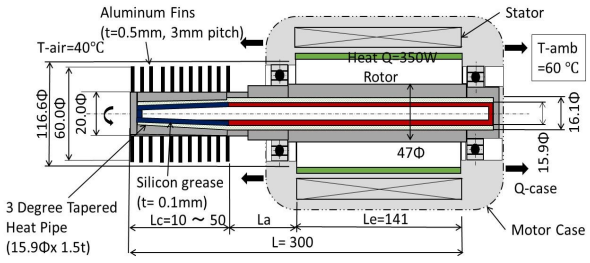


Fig. 21 Design concept for air cooling rotational heat pipe

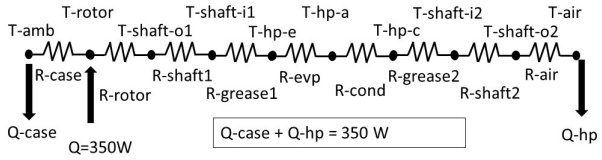


Fig. 22 Thermal network for air cooling rotational heat pipe

Table 2 Summary of thermal performance for liquid and air cooling

	Water	LLC	Oil	Air
T-rotor (°C)	110.3	110.7	113.1	131
Q-case (W)	155	156	164	219
Q-hp (W)	195	194	187	131
Rtotal (K/W)	0.232	0.236	0.258	0.695

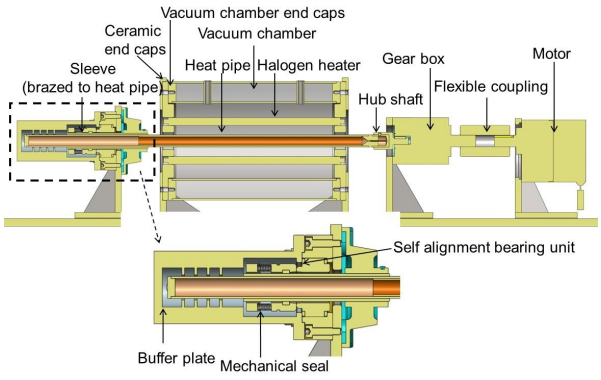


Fig. 23 Design of rotational heat pipe liquid cooling prototype for experimental evaluation

To validate the design concept, a prototype will be built as shown in Fig. 23. The rotational heat pipe is about 500 mm long, and outer diameter of 15.9 mm, made of Copper and working fluid is water. The heat pipe is driven by a motor coupling with a gear box for controlling and varying the rotational speed. An alternative is use a belt pulley system to provide a more stable torque to the system. The heat input to the heat pipe is simulated by means of Halogen heaters enclosed in a vacuum chamber at the evaporator section of the heat pipe. The condenser of the heat pipe is cool by an enclosed water jacket. Fig. 24 shows the test set up for the rotational heat pipe. Experimental work for this prototype will be conducted in year 2016.

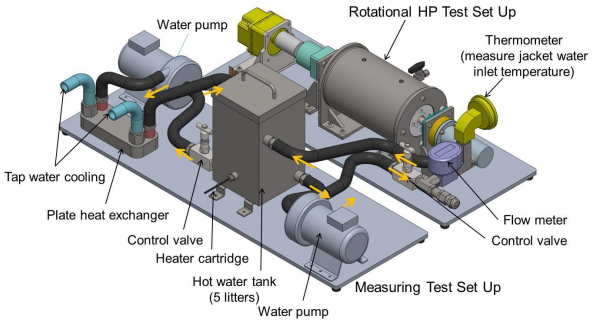


Fig. 24 Design of rotational heat pipe cooling prototype for experimental testing

4. IGBT COOLING

The last section for this paper is the cooling of IGBT inverter for the power control unit in electric vehicle. The existing cooling method of IGBT is liquid cooling. If air cooling can be used, the power consumption of running fan for air cooling would be much smaller compare to the liquid pump. The proposal is to use heat pipe heat exchanger air cooling as show in Fig. 25.[4] The design consists of 6 identical heat pipe modules (left image shows total assembly and the right image shows a single heat pipe module). The thermal specification is the total thermal resistance is about 0.18 K/W at an air flow of 0.4 m^3/min and the heat dissipation of 1.4 kW. There are 18 heat pipes of diameter 8 mm. The volume of the stacked fin heat exchanger is approximately 180 mm x 180 mm x 80 mm. The fin is a special design which is called Louver Fin. The principle of the Louver Fin is reducing the fin surface air boundary layer thickness, promoting mix flow and thus enhancing the air heat transfer coefficient. As the result of the heat transfer enhancement, the fin length could be reduced from 300 mm to 180 mm for the same cooling capacity.

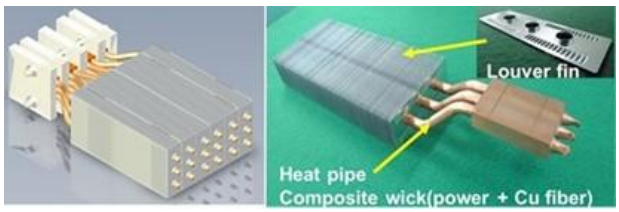


Fig. 25 An example of IGBT cooling using heat pipes fins heat exchanger

For the current IGBT, the material is Si (Silicon) and the chip maximum junction temperature (Tj-max) is about 150 °C, but for the future IGBT, the Tj-max can be increased to 300 °C due the material changed from Si to SiC (Silicon Carbide). Fig. 26 shows an estimation of the thermal resistance, Tj-max and cost comparison between Si IGBT and SiC IGBT. Based on this study, it seems that with the increased of Tj-max it is feasible to use forced air cooling with heat pipe fins heat exchanger.[7]

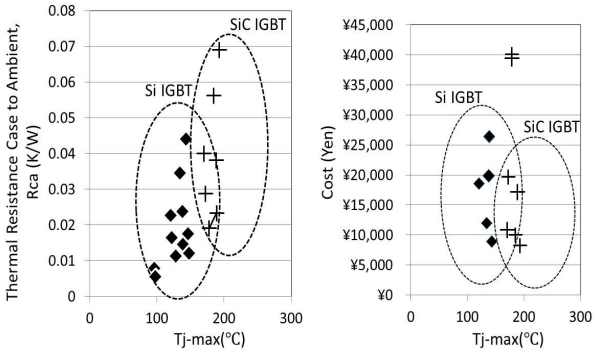


Fig. 26 Thermal resistance, junction temperature and cost comparison for Si IGBT and SiC IGBT

It depends on case by case of the design of the IGBT assembly structure and its application, the heat pipe heat exchanger air cooling may not be applicable. An example is shown in Fig. 27 for the application of cooling IGBT in Hybrid vehicle. There are multiples IGBT modules densely packed together, therefore it is not practical to use heat pipe fins exchanger for air cooling because of the space constraints and air cooling required larger volumetric heat exchanger compared to liquid cooling. In this example it is best to use stacked liquid cooling plates as shown in Fig.27.

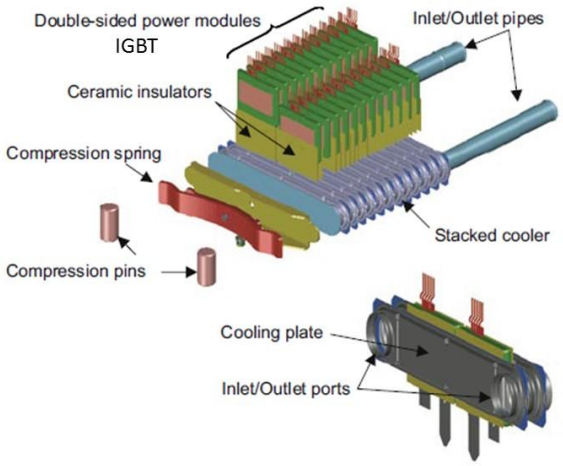


Fig. 27 An example of IGBT cooling using liquid cooling plates

5. CONCLUSIONS

The trend of the power electronics devices required compact in size, multi-tasks capability, and increase in computing performance, and that associates with higher heat flux and heat dissipation. This would continue creating new challenges in thermal management. Air cooling becoming more difficult to satisfy the thermal performance requirement due to air is a low capacity heat transfer medium, and therefore required a large volumetric heat exchanger, and this is unfavourable due to size constraint priority. As a result, liquid cooling inevitably becoming necessary for cooling of high power devices. Regardless of whatever method of cooling air or liquid, heat pipes still a feasible device for use in the heat transfer to enhance the thermal performance.

Cases study above are only few examples presented here for ideas and practical application of heat pipes. Heat pipe is the best known passive device for effectively transfer heat from one end to another. Whatever the application that is needed for heat transfer from one point to another place, one can find ideas for the use of heat pipe.

REFERENCES

[1] Maydanik, Y., and Vershinin, S., Development and investigation of coper water loop heat pipes with high operating characteristics, *International Heat Pipe Science and Technology*, Vol. 1, No. 2 (2010) 151-162.

[2] Maydanik, Y., and Pastukhov, V., Copper water loop heat pipe – issues and achievement, *9th Minsk International Seminars "Heat Pipes, Heat Pumps, Refrigerator, Power Sources"*, Minsk, Belarus, 7-10 September (2015).

[3] Maydanik, Y., and Vershinin, S., Development and investigation of coper water loop heat pipes with high operating characteristics, *International Heat Pipe Science and Technology*, Vol. 1, No. 2 (2010) 151-162.

[4] Mochizuki, M., Nguyen, Thang, Mashiko, K., Saito, Y., Ahamed, S., Singh, R., Nguyen, Tien, and Wuttijumnong, V., Latest trends in heat pipe application, *9th Minsk International Seminars "Heat Pipes, Heat Pumps, Refrigerator, Power Sources"*, Minsk, Belarus, 7-10 September (2015).

[5] Otsuka, Y., Doctorate Dissertation, Kyoto University, 23 May (1986), Japan, http*://hdl.handle.net/2433/138400*.

[6] Ritsuo, H., Keiji, M., Hikotaro, I., Kenji, K., and Yasuro, T., Heat transport performance of rotating heat piped installed in high speed spindle, *Technical Review Mitsubishi Heavy Industries Ltd*, Vol. 33, No. 2 (1996).

[7] Takahashi, K., Ryuichi, S., Kenji, K., Kinja, N., Hideaki, I., and Kaname, S., High power density inverter technology for hybrid and electric vehicle applications, *Hitachi Review*, Vol. 63, No. 2 (2014).

Cooling of LED Headlamp in Automotive by Heat Pipes

Randeep Singh[1*], Masataka Mochizuki[2], Yuji Saito[2], Tadao Yamada[2], Tien Nguyen[2], Thang Nguyen[2]

[1]*Fujikura Automotive Europe GmbH, Albin-Koebis Strasse 6, D-51147 Koeln, Germany*
[2]*Fujikura Ltd., 1-5-1, Kiba, Koto-Ku, Tokyo 135-8512, Japan*

Abstract

Trends in automotive headlamps are changing from halogen/xeon towards light emitting diode (LED) type light functions. LEDs have 2 times higher light efficiency, longer illumination distance, 10-15 times longer lifetime and better styling features than halogen lamps. Unlike halogens, LEDs need temperature control to maintain their monochromaticity, light intensity and longevity. A typical LED headlamp can dissipate 25 to 70 W heat load depending on light functions and styling features. Traditionally, aluminum die cast heat sinks is used as cooling solution for LEDs, which are thermally low efficient and structurally heavy and space intensive. In the present investigation, heat pipe based cooling systems for different designs and styles of LED headlamps and thermal capability of up to 20 W/per-module have been proposed, designed and characterized. Heat pipe configurations include 6-8 mm diameter, 200-400 mm length, copper wick/container and water as working fluid. In combination with different heat sink designs and cooling options, heat pipes can provide 2 to 3 times higher heat capability and up to 50% lighter cooling module, as compared to die cast heat sinks. Based on requirements from headlamp manufacturers, different innovative designs of heat pipes, including high-performance cylindrical/flattened copper-water heat pipe for low/high beam cooling, hinge heat pipe for adaptive headlamp with swivel function cooling and flexible heat pipe for remotely mounted heat sink, has been developed. Heat pipes due to their ultra-high thermal conductivity (~ 5000 W/m.K or higher) can drastically improve heat dissipation capability of heat sink (natural or fan cooled) and allow different heat sink design options (chassis/frame type, die cast type, stacked-thin-fin type). This allows for better space utilizations inside headlamps, possibility of fully passively cooled headlamps and shared heat sinks between different light functions. LED headlamp with heat pipe thermal modules will tend to be cooler, lightweight and compact.

Keywords: Passive cooling, Flexible heat pipe, Hinge heat pipe, Piezo, Lighting, Automotive thermal management

1. INTRODUCTION

Headlamps in automotive have lighting functions for occupants and outsiders, and provide specific styling signature to the vehicle. Lights in Automotive provide two main functions: 'seeing function' (e.g. low beam, high beam, front fog light) and 'to be seen function' (e.g. direction indicators, Daytime Running Light (DRL), position/parking light).

As per definition, headlamp refers to low and high beams, however the trend is moving towards incorporating most light functions into headlamps, which provide modular, space-conservative and cheaper design. Headlamps, like wheels and body, provide opportunity to makers to display unique styles and brand signatures. Today, it is easy to identify vehicle maker and even model from its headlamp design and shape.

Headlamps can be classified into four main categories, based on light source (or lamp) type: Halogen, Xeon, Light Emitting Diode (LED) and Laser. Halogen lamp constitute glass housing with tungsten filament in nitrogen/argon gas, Xeon lamp has quartz housing with tungsten electrode with metal halide mix and Xeon gas, LED lamp has glass window with Gallium Nitride (GaN) semiconductor and laser light is emitted by phosphorous gas heated by laser source. Halogen and Xeon are cheaper but with shorter lifetime and low efficiency. LED [1] has longer lifetime (10-15 times), higher efficiency, longer illumination length (300 m) but expensive than halogen/xeon. Laser lamps have been recently applied in headlamp and provide most superior lighting characteristics, however their high cost have limited them to specific carlines and makers. LED lamps provide best combination of performance, technology, design options and cost. Fig. 1 compares heat load output by different lamp types, which provides direct indication of lamp light efficiency.

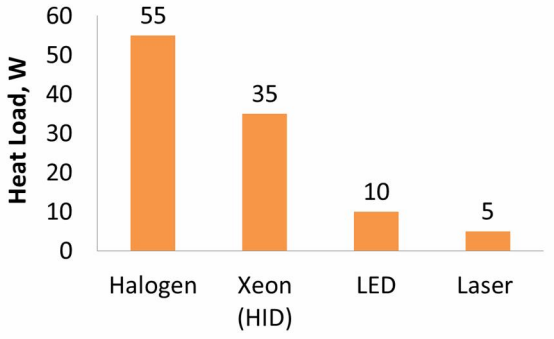


Fig. 1. Heat load output by different lamp types

Headlamps are often provided by mix of lamps types e.g. Xeon combined with LED. This helps to provide mix of performance and cost to overall headlamp.

Halogen and Xeon headlamp uses tungsten as light source which can withstand high operating temperature without need of any cooling. However, LEDs and laser uses semiconductor, for light generation, that need temperature control, to maintain their reliability, monochromaticity (light colour) and light intensity. An LED headlamp can dissipate anywhere between 25 to 70 W of total heat load depending on light functions and styling features (carline grade). Fig. 2 compares the heat dissipation versus device size for different electronic and electrical systems in automotive.

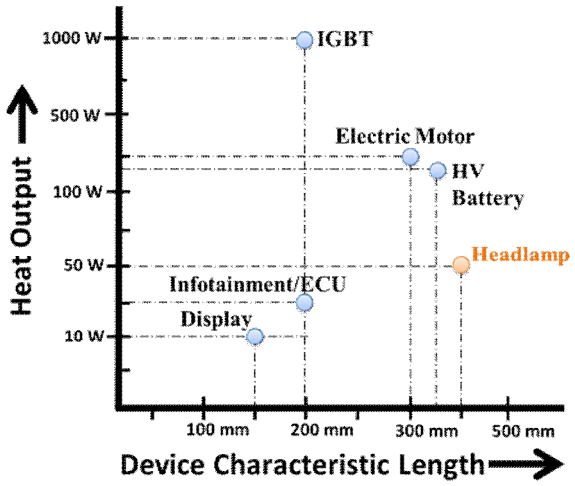


Fig. 2. Heat output versus device length for different automotive electronic/electric systems

Heat output by LED headlamp is higher than other LED and processing devices but lower than high power electronic/electrical equipment. Here, device characteristic length represents dimension of device which can provide estimate on its size scale. From cooling solution point of view, characteristics length also represents maximum distance for heat transfer for dissipation inside device enclosure or minimum distance up to which heat have to be transported for remote dissipation outside device enclosure. As evident from Fig. 2, headlamp is classified as one of the bulky electronic system in automotive.

Headlamps have close enclosure (not air tight) therefore output heat is required to be dissipated inside the casing. Thermal management of LED headlamp is challenging owing to its inherent location (in front of hot engine room and side of radiator), covered frontal area (no possibility of enclosure air exchange for cooling of internal electronic) and trends towards headlamp size compaction (to conserve space for other frontal features).

LEDs have high power efficiency and provide diverse lighting systems in automotive that includes low/high beams, turn indicators, daytime running lights, cornering lights, weather/fog lights, front display panel, head-up display (HUD), back or rear lights and other interior lights. LED based lighting system for automotive is gaining significant attention due to their technical competency and design freedom. Due to its compact size and high heat output, thermal management of the LED systems is one of the main issues.

Fig. 3 shows the 5 LED chip package for headlamp application [2]. LED chips are made from thin GaN which are soldered to the substrate provided with the backside aluminum heat spreader.

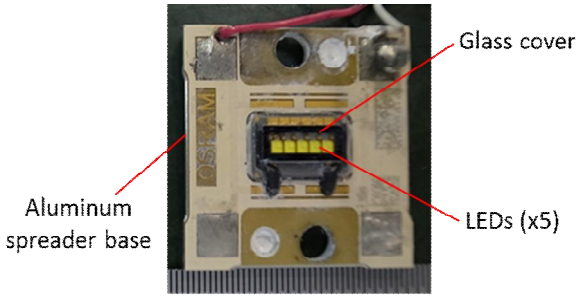


Fig. 3. LED package for automotive headlamp

Each chip measures 1 x 1 mm^2 and can produce 2.45 W of heat load which accounts to very high heat flux of 245 W/cm^2. LEDs need efficient cooling system which should be able to maintain their junction temperature below 125°C. Depending on the intended function, LED package can have single chip (low beam, DRL) or multiple chips (high beam, weather light, cornering light). Accordingly, heat output from the package will vary depending on number of chips. Number of LED packages is combined to provide low beam, high beam and other light functions. Placement of these LEDs in headlamp helps to attribute specific styling to headlamps. Typical thermal resistance from junction to package base for such module is 2.65 K/W. Light emitted by the chips is magnified by the reflector for lighting purpose. The top of the chips need access to the optical system therefore cooling is only possible from the backside. Most common cooling system involves die cast aluminum heat sink which is attached to the back side of the LED module and dissipate heat by natural convection or forced cooling using fan. Die cast heat sink are heavy due to their metallic body, and need to be large size due to their high spreading resistance from LEDs to heat sink body.

In this paper, thermal design, technical requirements, advantages and system options for heat pipe based cooling system [3-6] for LED headlamp has been investigated in detail. Current

cooling systems for LED headlamp has been outlined and compared to heat pipe based system. Different components of thermal module (namely heat pipe element, heat sink, heat dissipation mechanism) and their possible design options have been discussed. Overall, the paper will provide niche of heat pipe system in headlamps, in particular, and automotive electronics, in general.

2. LED HEADLAMP

Cooling of LED is a necessity owing to their temperature specific performance and reliability.

2.1 Cooling Requirements

For an LED, optimum operating temperature range is -40 to 125 °C with maximum allowable junction temperature of 150 °C [7]. In short time applications (100 hr), junction temperature can be maximum 175 °C. At elevated temperature, there are both performance degradation (light color change, flickering light, dimming of light) and structural degradations (package discoloration, wiring melt, chip damage).

2.2 Headlamp Thermal Control

Headlamp is provided with two type of thermal control: hardware based (heat sink module) and software based (current de-rating). Mostly, LED packages in headlamp have dedicated heat sinks owing to spatial placement of LEDs, distance between lights, package functionalities or light type and package mobility needs (swivel or spin function). Heat sink module is designed to maintain LED package temperature below 125 °C for high ambient temperatures of 40 °C (due to proximity of engine room).

At adverse operating conditions, including high ambient temperatures and full-functions on, the heat sink cooling capacity could be insufficient. In such circumstances, current de-rating is activated to keep LED temperature within permissible range. Current de-rating refers to software based reduction in input current to LEDs to control their temperature. Software takes its feedback from a thermistor installed on the LED package. Extent and rate of de-rating depends on rate of change of temperatures of LED package. Typical, LED operating at 3.15 V with 1 A max current will start de-rating current as package temperature approaches 125 °C. Current de-rating is limited to 15 to 20% of max value, due to safety aspect related to reduction in visibility with LED current reduction. Headlamp manufacturer try to avoid or minimize current de-rating as much as possible by oversizing heat sink. Here, oversize heat sink will have additional weight penalty. Therefore efficient heat sink is a requirement in headlamps.

2.3 Headlamp Cooling Module

Fig. 4 shows typical thermal module for LED package cooling. LED package constitutes of LED mounted on ceramic substrate that is attached to aluminum base, which behaves as local heat spreader for LED source. This LED package is installed on one side of metal base with natural or forced convection cooled fins on other side of metal base. It should be noted that package is not shown installed directly on top of heat sink because in most cases there is not enough space available in the vicinity of package to mount heat sink directly on top of it. Heat spreader and sink is generally made from aluminum die cast due to its acceptable thermal conductivity, lightweight and cheaper cost.

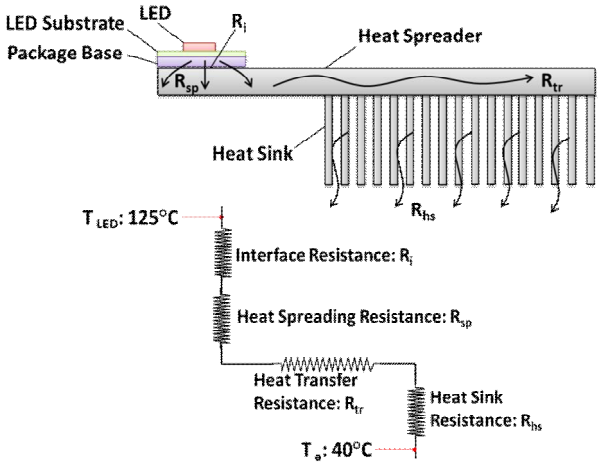


Fig. 4. Schematic of LED package with thermal module (top), and system thermal resistance network (bottom)

Waste heat release by LED package is first spread on heat spreader base, then transferred to heat sink base, followed by dissipation from sink fins to ambient via natural convection, in most cases, or forced convection, in very specific high-end headlamps. Total thermal resistance (R_t) for heat flow from LED package to ambient, as shown by thermal resistance diagram at the bottom of Fig. 4, can be expressed by:

$$R_t = R_i + R_{sp} + R_{tr} + R_{hs} \quad (1)$$

Where, R_i is interface resistance between LED package and metal sink base, R_{sp} is conduction spreading resistance inside metal base, R_{tr} is heat transfer resistance due to conduction along heat spreader base and R_{hs} is heat sink resistance for heat dissipation from metal sink base to ambient. For temperature limits of 125 °C on LED package side, and 40 °C on ambient side, a single LED package with heat load of 2.45 W will have total

available thermal resistance of 34.7 °C/W.

Interface resistance (R_i) depends on the quality of contact and thermal conductivity of thermal gap filler (normally limited to 1 W/m.K). Heat spreading (R_{sp}) and heat transfer resistance (R_{ts}) depends on the thermal conductivity of the thermal module (90 W/m.K for typical aluminum die cast: ADC12). In case of heat sink resistance (R_{hs}), mechanical properties (thermal conductivity), geometrical properties (fin thickness, fin gap, fin height) and heat removal conditions from heat sink (natural or forced convection) are important. Aluminum die cast material has limited thermal conductivity and casting process allows limited control over geometrical properties of heat sink (e.g. fin thickness and fin gap cannot be easily reduce below 5 mm). As a result of these limitations, die cast heat sink have to be made thick (to reduce their spreading/transfer resistance) and need fan to improve heat dissipation from heat sink. Die cast fins have limited natural convection heat removal due to lower surface area to volume ratio. In this regard, heat pipe heat sink, with ultra-high thermal conductivity of heat pipes (> 5000 W/m.K), and superior conductivity (~ 210 W/m.K) and geometrical properties of stacked fins, can offer to reduce heat transfer and heat spreading resistances dramatically thereby improving performance to weight ratio of heat sink.

Heat sink dissipates heat from LED packages to the inside ambient of the headlamp enclosure from where heat is transferred to outside ambient via enclosure wall. This is possible due to larger surface area of headlamp casing. Locating heat sink outside headlamp is generally difficult due to assembling issues and severe engine room ambient.

3. HEAT PIPE BASED COOLING FOR HEADLAMP

Thermal module for headlamp should be thermally efficient (high performance to weight ratio) and structurally lighter and robust (to withstand severe vibrations and shock in automotive operating environment).

3.1. Benefits

Heat pipe module provides number of advantages related to design and performance. Thermal conductivity of heat pipes is significantly higher (50 to 100 times) than die cast material, as a result they can provide highly efficient thermal transfer link between LEDs and heat sink. In addition to this, heat pipe help to spread heat over heat sink fins, thereby improving fin-stack efficiency.

In electronics, mostly, it is not possible (due to space issues) or recommended (to control ambient temperatures) to dissipate heat around the area where it is produced. Similarly, in headlamps, space is available towards the back of enclosure rather than near LED where wiring and holding mechanism is installed. In this case, heat pipes offer an efficient heat transfer device and help to use available space inside headlamp for heat sink installation. Positively, the space utilization character of heat pipe helps to provide fully passive cooling solutions for headlamp. Die cast heat sink are more of local coolers and needs fan for heat dissipation, if LED package heat load is high (e.g. high beams). Reliability of fan in headlamp is serious issue due to rigorous working environment. Generally, headlamp is sealed plastic enclosure. Fan cooled headlamps should be easy to dismantling to replace damaged/faulty fan which increases headlamp assembly cost significantly. In this context, heat pipe heat sink provides reliable and passive thermal solution for headlamps.

With die cast solution, each LED package need to have dedicated heat sink which increases the number of parts and thus cost of the headlamp. Heat pipes provide an innovative design approach for headlamp by combining heat sink for certain light functions. For example, there can be a common heat sink for high beam and weather light as either one of them would be used at a time. This will help to reduce heat sink quantity as well as material, which will compliment weight reduction attribute of heat pipe heat sink. With die cast heat sink, this is not possible due to distance between different lights.

With heat pipes, it is possible to use die cast heat sink or stacked fins. Stacked fins can be made from high conductive aluminum sheet (~ 210 W/m.K) that helps to further improve heat sink performance. Also, stacked fins have more design flexibility than die cast stack, thus providing customized high performance heat sinks.

Stacked fins provide heat transfer area 2 to 3 times higher than die cast heat sink. As for efficiency, stamped fins can be 3 to 5% better than die cast fins. There is limited increase in efficiency with stacked fins as die cast fins are very thick (~ 5 to 7 mm) therefore their efficiency is good. Combined effect of fin area and efficiency increase provides efficient heat dissipation characteristics to stacked fins. Thermal module using heat pipe and stacked fins can be 40 to 50% lighter than die cast heat sink for similar cooling requirements. Weight advantage of heat pipe solution comes from low material quantity in hollow heat pipes and thin stacked fins.

Heat pipe heat sinks are generally more expensive than die cast heat sink, however, at system level, the combined effect of reduction in parts, less material quantity, no fan assembly and efficient heat sink (that provide LED lifetime longevity) tend to offset the added cost.

3.2. Design Options

Heat pipe based thermal module consists of heat pipe, heat sink and optional fan, depending on thermal requirements. There are different design options for heat pipe and heat sink, depending on thermal and structural requirements.

3.2.1 Heat Pipe Design

Capillary heat pipe is the most viable heat pipe type which can be used in cylindrical and/or flattened form for heat transfer and heat spreading function inside headlamp. The characteristic length scale, as outlined in Fig. 2, provides an important indication on maximum possible lengths of heat pipe required in each device. For headlamp thermal control, length of heat pipe between 200 to 400 mm can be required, depending on headlamp size and available space. Fig. 5 shows heat pipe heat sink for cooling high beam inside headlamp. Heat pipe is made from copper with copper powder wick and water as working fluid. Two capillary heat pipes, 6 mm outer diameter, transfer approximately 20 W of heat from two LED packages to finned heat sink from where heat is dissipated inside headlamp ambient, with 40 °C air, using natural convection [8]. Total thermal resistance of heat pipe heat sink was 3.5 °C/W.

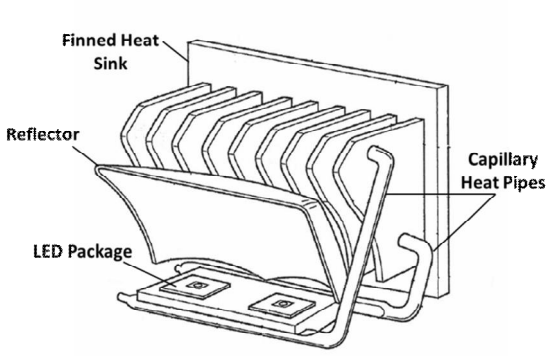


Fig. 5. Heat pipe heat sink for cooling high beam LED package inside headlamp

In Fig. 6, heat pipe heat sink is shown installed inside the headlamp. Two LED packages were mounted on the spreader plate with two embedded heat pipes (Fig. 5)

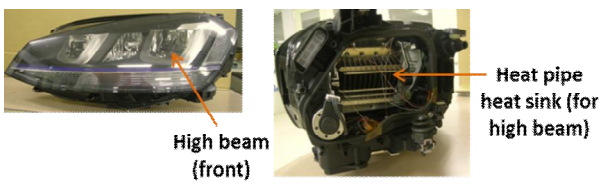


Fig. 6. Heat pipe heat sink for headlamp high beam cooling

Fig. 7 shows test results on actual headlamp using heat pipe cooling. It is evident that heat pipe system is able to maintain LED package temperature below 80 C for 25 °C ambient.

For adverse operating conditions (40 °C ambient, all light functions ON), heat pipe thermal module was able to maintain LEDs temperature below 110 °C which is well below maximum permissible limit of 125 °C. Heat pipe heat sink was 40% lighter than die cast heat sink for similar thermal capacity.

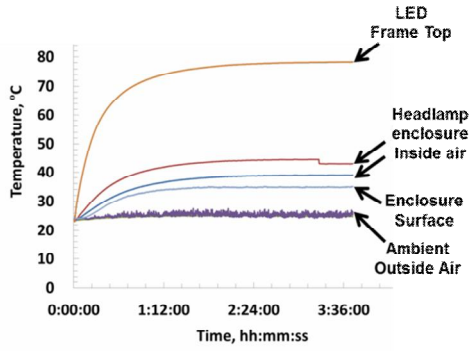


Fig. 7. Thermal test on LED headlamp with heat pipe based cooling of high beam

In adaptive headlamps, low and high beams have swivel or rotate function that require either direct back mounting of heat sinks or flexible link between LED package and heat sink. For high power LED packages, back mounting is not possible due to weight issues. In order to address this problem, hinge heat pipe assembly, as shown in Fig. 8, was developed.

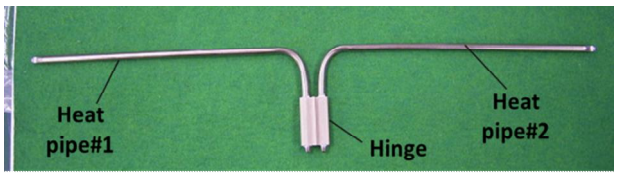


Fig. 8. Hinge heat pipe assembly

Hinge heat pipe consists of two heat pipe which are connected by copper hinge. Here, hinge provided the thermal link between two heat pipes and single degree of freedom to move/rotate. To increase degree of freedom further, additional hinge with heat pipe can be added. Based on experiments, it was determined that hinge resistance was approximately 1 °C/W, which was acceptable based on available thermal resistance from LED package to ambient air inside headlamp.

Fig. 9 presents heat pipe heat sink with thermal hinge for cooling LED with swivel function.

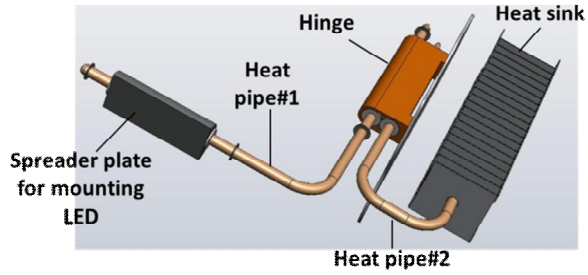


Fig. 9. Hinge heat pipe assembly for cooling LED package with swivel function

In compact headlamps, there is limited space inside the headlamp to install heat sink for all light functions. In that case, heat sink can be mounted externally on the wall of the headlamp. Due to assembling tolerances and light beam setting requirements, thermal link (i.e. heat pipe) between the LED package and wall mounted heat sink need to have certain level of flexibility. Such requirements can also exist for larger headlamp where space is not available near LED package for installing heat sink. Fig. 10 shows flexible heat pipe which was developed to thermally connect LED with remotely mounted heat sink. Flexible heat pipe consists of bendable corrugated metal link connected by normal heat pipe on both sides. The corrugated link can be made from copper or steel depending on compatibility with heat pipe working fluid.

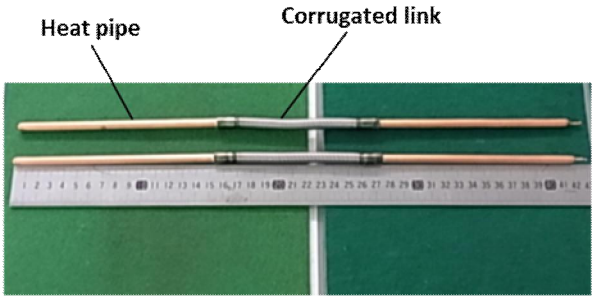


Fig. 10. Flexible heat pipe

3.2.2 Heat Sink Design

Heat pipe heat sink for headlamp can have different types of sink designs and cooling options. Design possibility for heat sink includes headlamp body/chassis as heat sink, die cast or extrusion heat sink, and stacked/stamped fins as heat sink. Cooling options include natural convection cooled or fan cooled heat sink. It should be noted that such design options are only possible with heat pipes.

Fig. 11 shows heat pipe assembly using headlamp frame as heat sink. There are two heat sink arrangements including extrusion heat sink which is mounted at backside of LED and frame heat sink with heat pipe as thermal link from LED to frame.

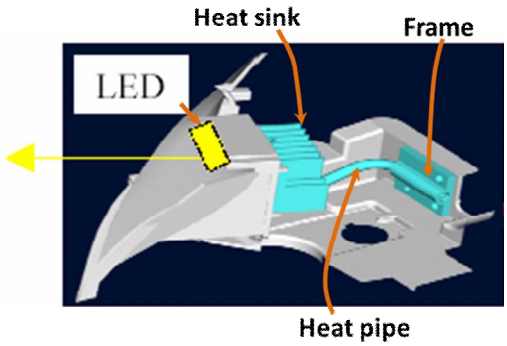


Fig. 11. Heat pipe assembly with frame as heat sink

In Fig. 12, actual sample is presented that consists of aluminum heat sink and copper-water heat pipe as remote heat transfer device. Here, heat was dissipated from heat sinks to 40 °C ambient using natural convection. The assembly was able to dissipated 15 W heat output by LED package and maintained LED temperature below 90 °C.

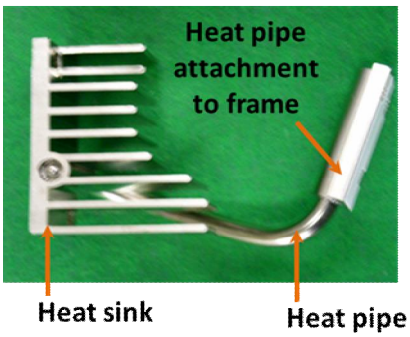


Fig. 12. Heat pipe assembly for cooling fog light LED package in headlamp

Fig. 13 shows an example of heat pipe module with high conductive stacked thin-fin heat sink for low beam LED cooling in headlamp. Heat pipe heat sink, with 6 mm diameter copper-water heat pipe, was able to dissipate 10 W heat from LED package using natural convection to 40 °C ambient. Thermal module was able to maintain LED package temperature below 80 °C.

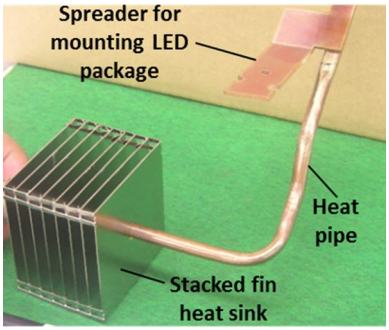


Fig. 13. Heat pipe heat sink for low beam LED package cooling.

In high-end headlamps like matrix LED headlamp, natural convection is not sufficient to dissipate output heat from the heat sink. In such cases, forced cooling using electric fan is inevitable. For forced convection cooling, centrifugal or axial fan similar to electronics cooling can be used. Fig. 14 shows the axial fan installed inside the headlamp for cooling heat sink by forced convection. Such a fan can enhance heat transfer coefficient inside headlamp to as high as 35 W/m^2.K which is almost 7 times higher than heat transfer coefficient for natural convection (5 W/m^2.K). However, as discussed before, there are long term reliability issues with fan and lack of available space for the installation of fan inside headlamp.

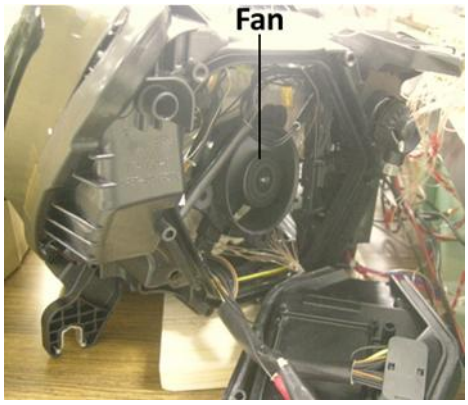


Fig. 14. Axial fan installed inside headlamp for forced convection cooling.

Forced convection using piezo fan with very thin form factor can address integration issues incurred by normal large size fans. Fig. 15 shows the impingement type round piezo fan [9] with 26 mm blade (or disk) diameter, 19.7 mm piezo disk diameter, fan thickness of 2 mm and flow aperture of 3 mm.

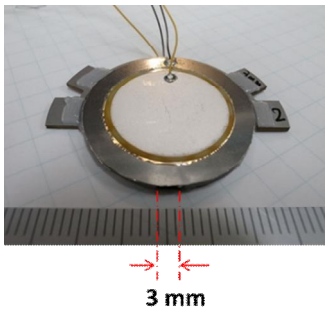


Fig 15. Round type Piezo fan

Fig. 16 presents the outlet air velocity plot of piezo fan as function of distance from flow aperture. It is noted from graph that at 10 mm distance from aperture, flow velocity as high as 7.5 m/s is possible. As the distance from aperture increase to 80 mm, flow velocity trails off to 1.5 m/s.

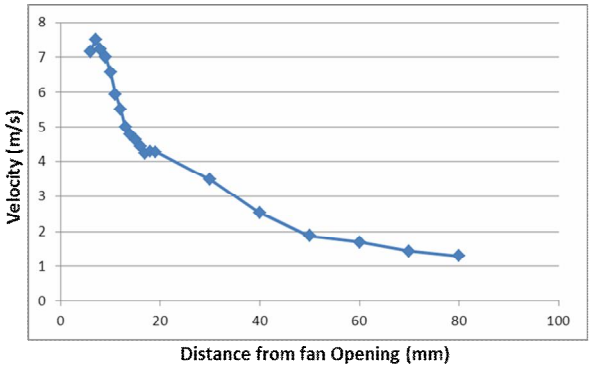


Fig 16. Velocity profile of round piezo fan

Two round piezo fans were installed inside LED headlamp with heat pipe heat sink for high beam cooling, as shown in Fig. 6. High beam with two LED packages have total heat load of 20 W. Piezo fan provided two functions: directly impinging high velocity air over the LED package and move the air inside the headlamp thereby increase heat transfer coefficient from heat pipe heat sink.

Fig. 17 presents the real time temperature profile obtained during the test. It is evident from the temperature graph that piezo fan manifest thermal improvements in two different ways 1) direct impingement of the LED package that reduces the source temperature by 7.6 °C (31% improvement as compared to natural convection case) and 2) increase in the heat transfer coefficient inside the headlamp enclosure that increase the inside air temperature by 3.7 °C (48% improvement in heat removal from heat sink due to enhancement in the internal air heat transfer coefficient).

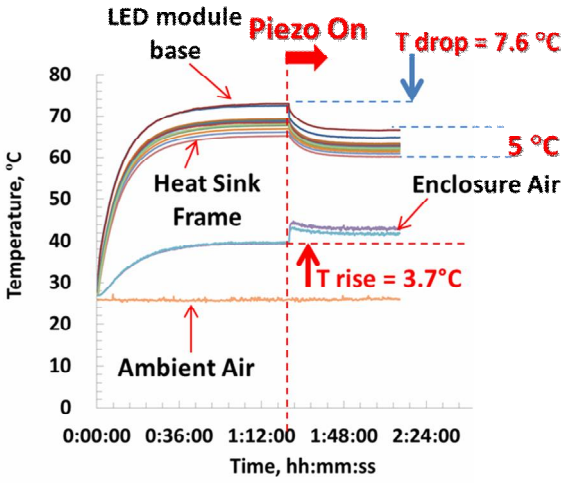


Fig 17. Cooling enhancement for LED headlamp using piezo fan

Using piezo fan, heat transfer coefficient inside headlamp enclosure increases from 5 W/m^2.K (natural convection) to 15 W/m^2.K (3 times

improvement). Here, increase in the enclosure air heat transfer coefficient will facilitate heat removal from heat sink inside headlamp as well as heat dissipation from enclosure air to the outside ambient air. These enhancements by piezo fan helped to increase the heat dissipation capacity of heat sink. Alternatively, this can reduce the mass of the heat sink for the same cooling rate, which is very contributing for the automotive applications.

It should be noted that heat sink design and cooling options, as discussed above, is better realized with heat pipes, due to their high thermal conductivity that improve the heat spreading and heat removal from heat sink stack, and their remote heat transfer feature which is not possible with traditional heat sinks. It is evident from the assortment of design options possible with heat pipes and heat sink arrangements that heat pipe heat sink system can provide innovative and high performance cooling systems for LED headlamp cooling.

4. CONCLUSIONS

Heat pipe based cooling solutions for LED headlamp has been proposed, designed and characterized. As compared to die cast heat sink, heat pipe thermal modules are 40-50% lighter and have 2-3 times higher heat removal capability. High thermal conductivity, design flexibility and technological development in heat pipes will qualify them as most potential candidate for cooling of new headlamp types like adaptive and matrix headlamps. Heat pipes can be made ultra-thin and flat, flexible with required degrees of freedom and with higher design tolerances. This allows efficient combinations of heat pipes with different types of heat sink designs and cooling arrangements. With these design attributes, heat pipes will be able to provide highly efficient, fully passive and compact cooling modules for high-end headlamps with complicated styling features.

NOMENCLATURE

R : thermal resistance (°C/W)

Subscripts

t : total
i : interface
sp : spreading
tr : transfer
hs : heat sink

REFERENCES

[1] US Department of Energy, Energy Efficiency of LEDs, PNNL-SA-94206, March 2013, Available: http://energy.gov/eere/ssl/downloads/energy-efficiency-leds

[2] OSRAM GmBH, Viewed: 27 March 2016, Available: http://www.osram-os.com/osram_os/en/index.jsp

[3] Singh, R., Mochizuki, M., Saito, Y., Yamada, T., Nguyen, T., Nguyen, Ti., Heat pipe applications in automotive electronics cooling, *Proc. 9th Minsk International Seminar on Heat Pipes, Heat Pumps, Refrigerators, Power Sources,* Minsk, Belarus, 07-10 September, 2015

[4] Singh, R., Mochizuki, M., Saito, Y., Yamada, T., Nguyen, T., Nguyen, Ti., Akbarzadeh, A., Loop heat pipe applications in automotive thermal control, *Proc.17th International Heat Pipe Conference*, Kanpur, India, 13-17 October, 2013

[5] Singh, R., Ahamed, M.S., Mochizuki, M., Saito, Y., Mashiko, K., Thin heat-management solutions for advanced packaging, *Proc. International Conference on Electronic Packaging*, Osaka, Japan, 10 – 12, April, 2013

[6] Singh, R., Mochizuki, M., Ahamed, M.S., Saito, Y., Jalilvand, A., Matsuda, M., Kawahara, Y., Goto, K., Low profile cooling solutions for advanced packaging based on ultra-thin heat pipe and piezo fan, *Proc. IEEE CPMT Symposium Japan 2013*, Kyoto, Japan, 11-13 November, 2013

[7] OSRAM OSTAR Headlamp, Datasheet version 1.2, LE UW D1W1 01, May 2013

[8] Singh, R., Mochizuki, M., Cooling device for vehicle headlights, US Patent: 9188305, Granted: 17, Nov. 2015

[9] Singh, R., Jalilvand, A., Goto, K., Mashiko, K., Saito, Y., Mochizuki, M., Direct impingement cooling of LED by piezo fan, *Proc. International Conference on Electronic Packaging,* Toyama, Japan, 23 – 25 April, 2014

Transport Phenomena of Liquid Film in Wick of Heat Pipes

A. Nouri-Borujerdi

School of Mechanical Engineering, Sharif University of Technology, Tehran, Iran.

Abstract

This paper developed a new mathematical model to investigate the heat transfer as well as the necessary requirement of the wick thickness. The model was set up by conservative equations of continuity, momentum and energy in the thermal boundary layer. Using the similarity variable, the governing equations were changed to a set of ordinary differential equations and they were solved numerically by the forth order Runge-Kutta method. The flow variables such as velocity components, wick thickness, local heat transfer and Nusselt number were obtained. The results show that the Nusselt number is proportional to the root square of the Darcy-modified Rayleigh number and that inversely square root of the distance from the edge of the condenser surface. Furthermore, the thickness of the wick material depends on the Jakob number .

Keywords: Counter current two-phase flow; Annular condensation flow; Porous media; Heat transfer

1. INTRODUCTION

A closed two-phase heat pipe is made of a thin metal tube with high thermal conductivity. There exists an annular wick on the inside surface of the tube. The container of the heat pipe can be constructed from metals, ceramics, composite materials, or glass. Heat can be transferred in circulation loops in two ways: one with vapor as the latent heat of evaporation and the other one with liquid as the sensible heat of the liquid. The heat pipe has numerous industrial applications in a wide range of temperatures. These applications include temperature and humidity control in HVAC related to the energy development, cooling large diesel pistons, Wang [1], the removal of heat from laser diodes and the removal of heat dissipation from the leading edge of hypersonic aircraft.

Gaugler [2] utilized a wicking material as part of a passive two-phase heat transfer device capable of transferring large quantities of heat with a minimal temperature drop. Trefethen [3] reexamined this concept in connection with the space program and in the form of a patent application (Brennan and Kroliczek [4]). In their experimental study of a concentric annular heat pipe, Faghri and Thomas [5] found that not all of the working fluid that condenses onto the inner pipe wall in the condenser section reaches the inner evaporator section. This phenomenon should be prevented by proper wick and end cap design, which would increase the amount of heat that can be transferred by the inner pipe. Many other investigators who have analyzed the conventional heat pipes using a variety of numerical and experimental techniques include Chi [6], Dunn and Reay [7], Terpstra and Van Veen [8], Peterson [9] and Faghri [10]. They have published several of these techniques, theories, and applications of different heat pipe structures. Nouri-Borujerdi and Layeghi [11] simulated the vapor flow and pressure drop along a concentric annular heat pipe for various symmetric and asymmetric heat addition and rejection circumstances. They showed that under asymmetric heat addition and rejection circumstances, a number of recirculation zones may be created at both of the evaporator and condenser sections. They discussed qualitatively that these recirculation zones can be very effective zones for increasing heat transfer between objects of different diameters even at high radial Reynolds numbers.

In this paper, an overview of theoretical results for the analysis of low-temperature conventional heat pipes is presented. The mathematical modeling of the fluid flow and heat transfer in the vapor space and liquid film region are also described.

2. PHYSICAL MODEL

Heat pipe is a closed pipe in which a fluid heat transfer agent circulates naturally between the heating zone or evaporator and the cooling zone or condenser, consists of a sealed container lined with a wicking material (as a porous medium). In this device, the vapor is produced in the evaporator section at the bottom of the pipe and moves upward spontaneously. The vapor is condensed in

*Corresponding author: anouri@sharif.edu,
Phone: +98-21-6616-5547, Fax: +98-21-6600-0021

the condenser section at the top of the pipe and then penetrates through the wicking material, (see Fig. 1).

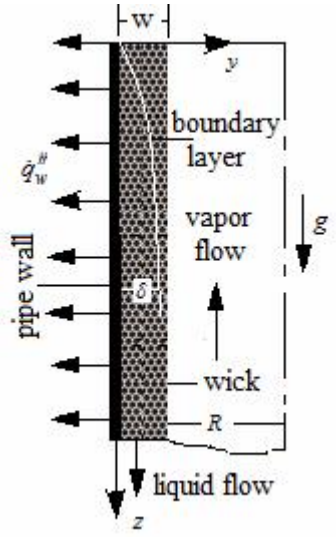


Fig. 1 Vapor flow in core and liquid flow in wick lined on the surface of condenser section of a heat pipe

we assume this material will be saturated with water, i.e., the space between the fiber of wicking material is entirely filled with water and this water will flow as a result of the gravity and surface tension forces simultaneously imposed on the material. In other words, there will be free convection flow in the wick.

Usually the saturated flow in the porous media is described by the Darcy model (without viscous term) or by the Brinkman model [12] used in order to account for the high porosity of porous media or to impose no-slip conditions on solid walls). In order to decide which model is adequate there exists a rule of thumb: the Darcy model is used if the Reynolds number of the corresponding free flow is less than $\mathrm{Re} < 10$. For this case, the Darcy model through the wick in the absence of the inertial force may be obtained as follows.

$$-\frac{\mu_f}{K}u_f - \frac{\partial p_f}{\partial z} + \rho_f g = 0 \tag{1}$$

$$-\frac{\mu_f}{K}v_f - \frac{\partial p_f}{\partial y} = 0 \tag{2}$$

In which, the viscous term is the usual Darcy term. K denotes the permeability tensor of the wick, u_f and v_f are the volumetric average of the velocities or the Darcy velocities in the z- and y-directions respectively. P_f is the intrinsic fluid pressure. Integrating of Eqs. (1) and (2) with respect to y and z respectively and subtraction them from each other, the final result after combining with volume expansion coefficient, $\rho_f \beta = -\partial \rho_f / \partial T$, will be:

$$\frac{\partial u_f}{\partial y} - \frac{\partial v_f}{\partial z} = -\frac{g\beta K}{\nu_f}\frac{\partial T_f}{\partial y} \tag{3}$$

It is assumed that the thickness of thermal boundary layer is small so that the temperature differences across the boundary layer will be significant. As a result, the diffusion in the y-direction is much greater than that in the x-direction and the energy equation can be approximated by:

$$u_f \frac{\partial T_f}{\partial z} + v_f \frac{\partial T_f}{\partial z} = \alpha_{eff} \frac{\partial^2 T_f}{\partial y^2} \tag{4}$$

Defining a stream function, ψ, where satisfies the continuity equation.

$$u_f = \frac{\partial \psi}{\partial y}, \qquad v_f = -\frac{\partial \psi}{\partial z} \tag{5}$$

Eqs. (3) and (4) change to the following respectively.

$$\frac{\partial^2 \psi}{\partial y^2} + \frac{\partial^2 \psi}{\partial z^2} = -\frac{g\beta K \Delta T}{\nu_f}\frac{\partial T_f}{\partial y} \tag{6}$$

$$\frac{\partial \psi}{\partial y}\frac{\partial T_f}{\partial z} - \frac{\partial \psi}{\partial z}\frac{\partial T_f}{\partial y} = \alpha_{eff}\frac{\partial^2 T_f}{\partial y^2} \tag{7}$$

where, $\Delta T = T_{fsat} - T_w$ and T_{fsat} is outside saturation temperature of the liquid boundary layer.
In order to solve the above equation, we assume

$$\psi = \Gamma(z) f(\eta), \quad \theta(\eta) = \frac{T_{fsat} - T_f}{T_{fsat} - T_w}, \quad \eta = \frac{y}{\delta(z)} \tag{8}$$

where δ is the boundary layer thickness.
After neglecting $\partial^2 \psi / \partial z^2$ in comparison with $\partial^2 \psi / \partial y^2$ and introducing the unknown variables from Eq. (8) into Eqs. (6) and (7), the final results read respectively.

$$f'' - \frac{g\beta K \Delta T_f}{\nu_f}\frac{\delta}{\Gamma}\theta' = 0 \tag{9}$$

$$\theta'' + \frac{\delta \Gamma'}{\alpha_{eff}} f\theta' = 0 \tag{10}$$

In order to the above two equations being only function of η, it is required

$$\delta = \frac{z}{\sqrt{Ra_z}}, \qquad \Gamma(z) = \alpha_{eff}\sqrt{Ra_z} \tag{11}$$

where, $Ra_z = g\beta Kz\Delta T / \nu_f \alpha_{eff}$ is defined as the Darcy-modified Rayleigh number, $\Delta T = T_{fsat} - T_w$ and $\alpha_{eff} = [\phi k_f + (1-\phi)k_s]/\rho_f C_{pf}$ denotes the effective thermal diffusivity. $\phi = \forall_f / (\forall_f + \forall_s)$ in which $\forall$ is volume of an element of solid and fluid mixture.
Inserting expressions δ, Γ and $\Gamma' = d\Gamma/dz$ from Eq. (11) into Eq. (9) and (10), the final results are respectively.

$$f'' - \theta' = 0 \tag{12}$$

$$\theta'' + \frac{1}{2} f\theta' = 0 \tag{13}$$

With the help of Eq. (5), the velocity components in direction of parallel and normal to the wall are.

$$u_f = \frac{\alpha_{eff} Ra_z}{z} f' \tag{14}$$

$$v_f = \frac{\alpha_{eff}\sqrt{Ra_z}}{2z}[\eta f' - f] \tag{15}$$

The boundary conditions of Eqs. (12) and (13)are

$$\theta(0) = 1, \qquad \theta(\eta \to \delta) = 0 \tag{16}$$

$$f(0) = 0, \qquad f'(0) = 0, \tag{17}$$

The local Nusselt number is

$$Nu_D = \frac{\dot{q}''_w D}{k_{eff}\Delta T} = -\frac{D}{\delta(z)}\left.\frac{\partial\theta}{\partial\eta}\right|_{\eta=0} = -\sqrt{\frac{DRa_D}{z}}\left.\frac{\partial\theta}{\partial\eta}\right|_{\eta=0} \tag{18}$$

$Ra_D = g\beta KD\Delta T/\nu_f\alpha_{eff}$ and $k_{eff} = \phi k_f + (1-\phi)k_s$.
The mean Nusselt number along the condenser length is then given as:

$$\overline{Nu}_D = \frac{1}{L_c}\int_0^{L_c} Nu_z dz = -2\sqrt{\frac{DRa_D}{L_c}}\left.\frac{\partial\theta}{\partial\eta}\right|_{\eta=0} \tag{19}$$

In order to obtain the thickness of the wick, it is necessary, the energy balance between the rate of latent heat release by the condensing vapor and heat transfer rate through the film to the wall to be identical, or:

$$\pi DL_c \bar{h}\Delta T = \rho_f \pi D h_{fg}\int_0^w u_f dy \tag{20}$$

where, D is the tube diameter and L_c is the condenser length.
Introducing Eqs. (5), (11) and (19) into Eq. (20), the wick thickness will be:

$$f[\frac{w}{L_c}\sqrt{Ra_{Lc}}] = -2Ja\sqrt{L_c/D}\left.\frac{\partial\theta}{\partial\eta}\right|_{\eta=0} \tag{21}$$

where, $Ja = C_{pf}\Delta T / h_{fg}$ is the Jakob number and w is the thickness of the wick. After calculation of the right hand side of Eq. (21), the wick thickness will be calculated from the function f.

3. SOLUTION METHOD

Eqs. (12) and (13) which are a pair of simultaneous ordinary differential equations are integrated numerically by the fourth order Runge-Kutta method simultaneously along with the boundary conditions (16) and (17) to give the variations of the stream function as well as the temperature. Once the distribution of f and θ. has been determined, the flow variables such as velocity components, local Nusselt number, the rate of heat transfer and the wick thickness are obtained from Eqs. (14,15, 18) and Eq.(21).

4. RESULTS AND DISCUSSION

A closed two-phase water-vapor heat pipe made of a thin copper tube with length of adiabatic, $L_a = 0.4\,m$ and those of condense and evaporator of $L_c = L_e = 0.3\,m$ has been considered. The wick material of the heat pipe is made of wire crimps with thickness of w and porosity of $\phi = 0.7$.

Fig. 2 illustrates the variation of stream function versus Raleigh number for different similarity parameters, η. In this figure, $\psi(z,\eta)$ changes monotonically and approaches 4 and 16 for $\eta. = 0.05$ and 0.1 respectively.

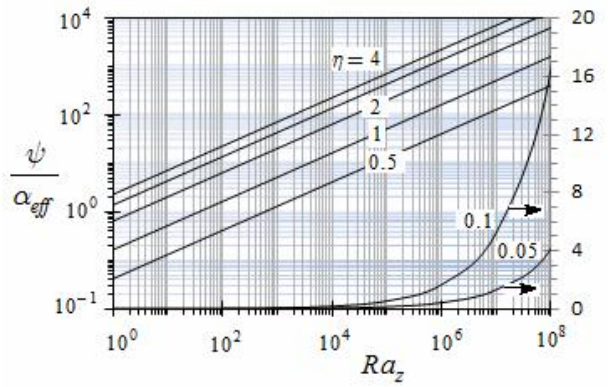


Fig. 2 Variation of stream function along the condenser

Fig. 3 depicts the function $f(\eta)$ and its derivatives versus similarity function. The value of $f(\eta)$ approaches 0.33206 when $\eta \to 6$. It should be mentioned that the similarity parameter is inversely proportional to the dimensionless of liquid film thickness, $\eta = y/\delta$. Fig. 4 exhibits the variation of the velocity components of u_f and v_f in the parallel and normal to the wall. As we can see, the velocity component of v_f is insignificant in comparison with velocity of u_f and reached a maximum value of $0.8604\,\alpha_{eff}\sqrt{Ra_z}/z$.

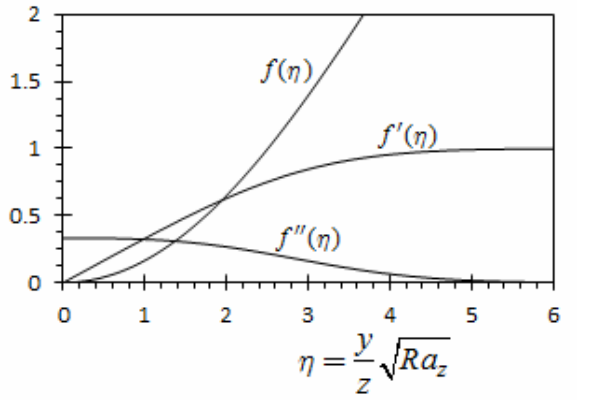


Fig. 3 Thermal boundary layer thickness

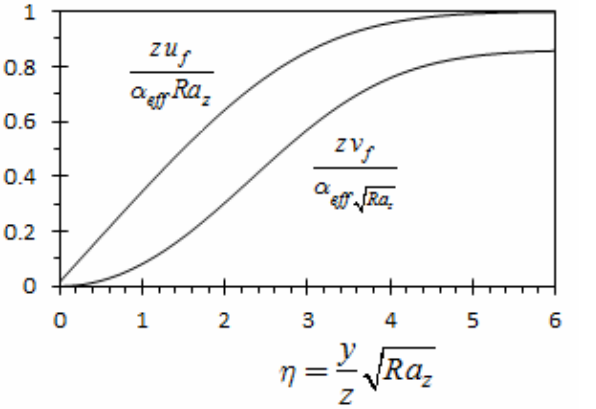


Fig. 4 Variation of u_f and v_f versus similarity variable

Fig. 5 shows the local temperature distribution against the similarity parameter, η. The figure indicate that the film temperature approaches the saturation temperature when the thermal boundary layer approaches the film thickness.

Fig. 6 illustrates the Nusselt number in z-direction along the condenser. This gives the variation of the local heat transfer rate with z. The total heat flux rate to the condenser section is then given by $\dot{q}_w = 1.043\,k_{eff}\,\Delta T\sqrt{DRa_D / L_c}$.

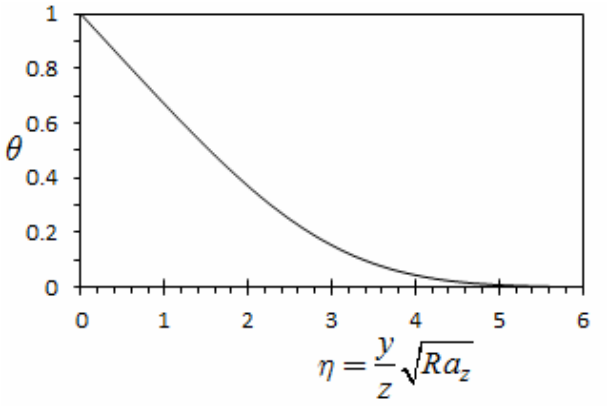


Fig. 5 Local Nusselt number along the condenser

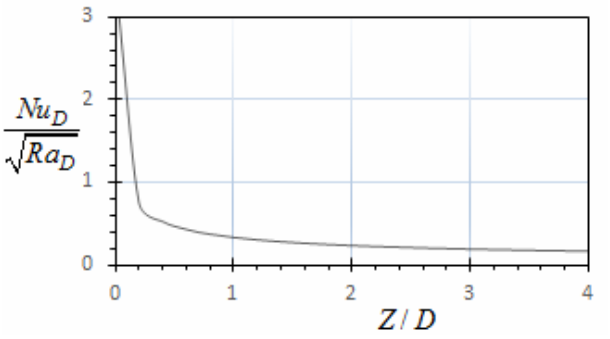


Fig. 6 Local Nusselt number along the condenser

5. CONCLUSIONS

This paper developed a mathematical model to investigate the heat transfer as well as the necessary requirement of the wick thickness. The model was set up by the continuity, momentum and energy equations in the thermal boundary layer. Using the similarity variable, the governing equations were changed to a set of ordinary differential equations and they were solved numerically by the forth order Runge-Kutta method. The results show that the Nusselt number is proportional to the root square of the Darcy-modified Rayleigh number and that inversely square root of the distance from the edge of the condenser surface.

Furthermore, the thickness of the wick material depends on the Jakob number .

NOMENCLATURE

C_P : Costant pressure specific heat, (kJ/kg.K)
D : Pipe diameter (m)
f : Stream function
g : Gravity acceleration (m/s^2)
h_{fg} : Latent heat (kJ/kg)
Ja : Jakob number, $C_P(T_{sat}-T_w)/h_{fg}$
k : Thermal conductivity (W/m.K)
K : Permeability (m2)
L : Length (m)
Nu : Nusselt number, $\dot{q}''_w z/k_{eff}\Delta T$
$\dot{m}$: Mass flow rate (kg/m^2.s)
P : Pressure (N/m^2)
$\dot{q}''_w$: Heat flux (W/ m^2)
Q_w : Total heat transfer rate (W)
Ra : Darcy-modified Rayleigh number
T : Temperature (K)
u : Velocity in z-direction (m/s)
v : Velocity in y-direction (m/s)
w : Wick material thickness, (m)
y : Distance from wall (m)
z : z-direction

Greek Letters

α : Molecular thermal diffusivity (m^2/s)
β : Expansion coefficient, (1/K)
δ : Fil thickness (m)
η : Similarity variable, y/δ
Δ : Difference
ϕ : Porosity
μ : Viscosity (kg/m.s)
ν : Kinetic viscosity (m^2/s)
θ : Temperature, $((T_{sat}-T)/(T_{sat}-T_w)$
ψ : Stream function (1/m), $g(z)f(\eta)$
ρ : Density (kg/m^3)
$\forall$: Volume

Subscripts

c : Condenser
f : Liquid
eff : Effective
sat : Saturation
TP : Two-phase
w : Wall

Superscripts

— : Mean
t' : Derivative

REFERENCES

[1] Wang, Q., Cao, Y., Wang, R., Mignano, F., and G. Chen, Studies of a Heat Pipe Cooled Piston Crown, *ASME Journal of Engineering for Turbines and Power*, 122: (2000) 99−105.
[2] Gaugler, R. S., Heat transfer devices, *U.S. Patent* 2, (1944) 350, 348.
[3] Trefethen, L., On the surface tension pumping of liquids or a possible role of the candlewick in space exploration, *G. E. Tech. Info*., serial no. 615 D114, Detroit, MI, (1962).
[4] Brennan, P.J., E.J. Kroliczek, Heat pipe design handbook, B&K Engineering, Towson, MD, (1979).
[5] Faghri, A., and S. Thomas, Performance characteristics of a concentric annular heat pipe, Part I: Experimental prediction and analysis of the capillary limit, *Journal of Heat Transfer*, 111: (1989) 851−857.
[6] Chi, S. W., Heat Pipe Theory and Practice, *Hemisphere*, Washington, DC, (1976).
[7] Dunn, P. D., and D. A. Reay, Heat Pipes, *Pergamon*, Oxford, (1982).
[8] Terpstra, M., and J. G. Van Veen, Heat Pipes: Construction and Application, *Elsevier Applied Science*, New York, (1987).
[9] Peterson, G. P., An Introduction to heat pipes: Modeling, Testing, and Applications, *John Wiley*, New York, (1994).
[10] Faghri, A., Heat pipe science and technology. *Taylor & Francis*, Washington, DC, (1995).
[11] Nouri-Borujerdi, A., and M. Layeghi, A numerical analysis of vapor flow in concentric annular heat pipes, *ASME Journal of Fluids Engineering*, 126: (2004) 442−448.
[12] Brinkman H.C., A calculation of the viscous force exerted by a flowing fluid on a dense swarm of particles. *Applied Science Research*. A1: (1948) 27-34.

An Evaluation of Hybrid Wick Design on High Performance Copper-Ethanol Heat Pipes

Guanghan Huang[1], Ahmed Abdulshaheed[1], Wei Chang [1], Chen Li[2]

1 Graduate student, Department of Mechanical Engineering, University of South Carolina,
2 Professor, Department of Mechanical Engineering, University of South Carolina,
300 Main Street, Columbia, SC 29208, USA, Phone: +1 803-777-7155, e-mail: li01@mailbox.sc.edu

Abstract

Hybrid wicks have been extensively investigated for their promise in enhancing heat pipe performance. In this study, Novel groove-mesh hybrid wicks have been developed and fabricated to achieve high performance heat pipes. Two layer of 5709m^{-1} (145$in.^{-1}$) copper woven meshes were sintered on the inner wall of a 12.7mm-O.D. and 370mm-long copper pipe with 75±2 grooves at ~1010°C in H_2 atmosphere. The height of grooves is 0.28±0.05 mm. Three heat pipes with different copper mesh coverage length, i.e., zero (groove), 370mm (full hybrid wick) and 110mm (partial hybrid wick), were fabricated to evaluate the effect of the hybrid wick design on heat pipe performances. ~6.5ml ethanol is charged in all heat pipes in this study. A test setup was built and calibrated to test heat pipes. The effective thermal conductivity is calculated using Fourier's law. Experimental results show that the heat pipe performance is not always enhanced using hybrid wicks. Careful attention should be taken to design wick structures. In this study, the heat pipe with partial hybrid wick only in the evaporation region can achieve an effective thermal conductivity of 30.9 kW/m·K at 150W and significantly outperforms the other two heat pipes. The underlying enhancement mechanism is the uniform temperature distribution and highly efficient evaporation enabled by the capillary evaporation on the copper mesh-groove hybrid wick. However, this type of enhancement cannot be applied in the condensation region as we demonstrated in the full hybrid wick heat pipe, which shows the lowest performance, due to the additional thermal resistance resulting from the liquid film confined by the hybrid wick in condensation region. This study well demonstrates that optimizing evaporation and condensation regions separately should be more effective to maximize heat pipe performance.

Keywords: Copper-ethanol; Groove-mesh; High performance; Heat pipe; Hybrid wick

1. INTRODUCTION

Nowadays, heat pipes are known to be efficient two-phase heat transfer devices and widely used in applications of thermal management and thermal energy harvest or conversion. These applications include, but not limited to, integrated circuits (ICs) cooling, solar energy collectors, thermal power plants, etc. Taking the advantages of highly efficient evaporation and condensation heat transfer mechanisms, heat pipes can achieve excellent temperature uniformity with a fast response and high reliability [1, 2].

The heat pipe performance is primarily governed by wick structures, which determine the liquid renewal efficiency by prompting capillary flow as well as the evaporation and condensation heat transfer rate. There are several typical wick structures such as grooves, sintered mesh or powders and fibers [3]. The grooved wicks [4-6] and mesh wicks have been extensively studied. The effect of number of meshes layer on heat pipe performance was studied by R. Kempers et al. [7] and the authors also characterized the evaporation and condensation thermal resistance of heat pipes with mesh wicks [8].

The permeability of grooved wicks is high but with limited capability in generating large capillary pressure. While the mesh wicks can generate high capillary pressure, but suffering from high flow resistance. Hybrid wick structures that can combine the strengths of these two types of wick structures are highly desirable to achieve high performance heat pipes in terms of effective thermal conductivity as well as working load. Powder-groove wick [9, 10] and mesh-groove wick are two types of hybrid wicks developed to enhance heat pipe performance. The mesh-groove wick with relatively higher permeability is favorable to reduce the flow resistance, particularly, with the assistance of gravity. Frédéric Lefèvre et al. [11] designed and fabricated a flat plate heat pipe with screen mesh covered grooves as wick. A nucleate boiling limitation was observed at a low heat flux working conditions; while this type of hybrid wick structures work not well in a tilted position. J.C. Hsieh et al. [12] developed a novel coronary-stent-like model, instead of sintering, to compact the micro-rectangular groove and copper mesh to form the hybrid wick. The maximum heat transport rate was enhanced in a single mesh

*Corresponding author: *li01@mailbox.sc.edu*,
Phone: *+1 803-777-7155*,

hybrid wick compared to a groove wick structure. The results showed that the heat transfer coefficient in the evaporation section was reduced with increasing the number of screen mesh layers. Most recently, Dai et al. [13] fabricated a superhydrophilic groove-mesh hybrid wick with atomic layer deposited (ALD) silica (SiO_2) coatings. The evaporation rate of a hybrid wick can be enhanced by up to 56% under the capillary thin film evaporating using the hydrophilic SiO_2 coatings. Groove-mesh hybrid wick structures have been developed to enhance microscale flexible flat heat pipe performance as well [14].

Due the fabrication convenience, groove-mesh hybrid wick structures have been normally adopted in flat heat pipes. The challenge to well bond mesh to inner-grooved round pipes has hindered the implementation of such type of hybrid wick structures in the widely used round copper heat pipes.

In this study, round copper heat pipes with novel groove-mesh hybrid wick structures are designed, fabricated, characterized, and evaluated. A module has been developed to assure great contact conditions between the mesh and grooves during sintering processes. In addition, the effect of hybrid wick structures on condensation and evaporation and hence, on the overall heat pipe performance is experimentally evaluated.

2. FABRICATION

2.1 Major dimensions

The outer diameter of the grooved copper pipe is 12.7 mm, with material statue of TP2 copper (Fig.1). The wall thickness of the grooved pipe is 0.8±0.05mm and the height of triangle grooves is 0.28±0.05 mm. There are 75±2 grooves in each pipe with a length of 370mm. The mesh number of copper mesh is 5709 m^{-1} (145 $inch^{-1}$) with a wire diameter of 56μm. Two layers of meshes are sintered in the grooved copper pipe to form the hybrid wick.

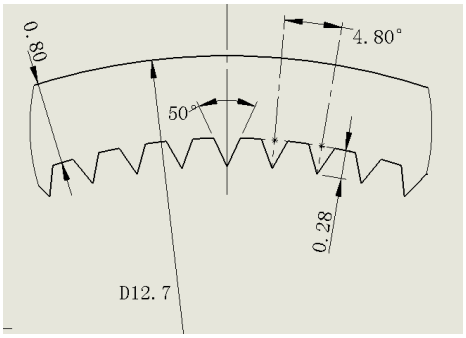


Fig.1 Major dimensions of the grooved copper pipe sample (mm)

2.2 Cleaning Process

The grooved pipe is first immersed in DI water and cleaned by ultrasonic wave for 5 minutes to remove small particles and dusts. Then, the pipe is placed into ethanol solution to remove the lubricating oil. Sulphuric acid (H_2SO_4) with a mass concentration of 10% is later used to further clean the pipe for 10 minutes. The pipe is then immersed in an acetone bath for 5 minutes to clean the acid and organic materials. In the last step, DI water is used to rinse the pipe for 5 minutes.

2.3 Bonding Mesh and Grooved Pipe

In order to assure an excellent contact between the mesh and the grooves, a 1010 °C sintering process is utilized in a H_2 atmosphere to achieve great mechanical strength and minimize the thermal resistance. A novel sliding-opening device (Fig. 2) is developed to tightly attach the mesh on the inner grooved pipe wall during the whole sintering process.

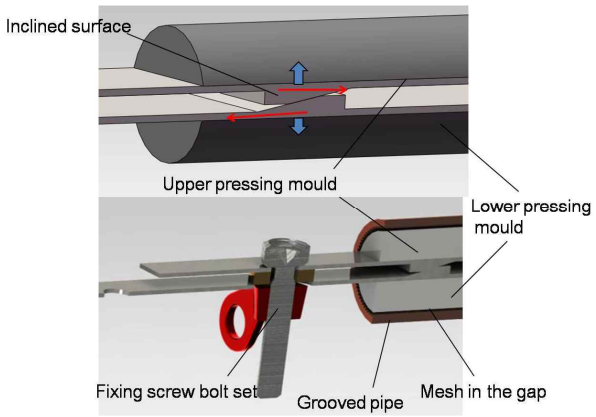


Fig.2 The sliding-opening module to tightly attach mesh on the inner-grooved pipe wall during sintering process.

The device consists of an upper mold, a lower mold, and a pair of fixing screw bolts on the ends. In each mold, there are several inclined surfaces, which can transfer horizontal movements into vertical movements. While the two molds move relatively in horizontal direction, the molds also expand in the radial direction. Thus, the mesh can be well attached to the inner wall of a grooved copper pipe. After sintering, two layers of meshes are bonded on the tip of grooves using the diffusion bonding technique.

2.4 Sintering Process

MTI OTF-1200X furnace equipped with a Vacuum pump is used to sinter samples in this study. The furnace is heated up to 1010°C and kept for 20 minutes in a hydrogen atmosphere. After the hybrid wick is formed, power will be turned off and let the

furnace slowly cool down to room temperature in approximately 2 hours. Fig.3 shows the overview of fabrication processes of the groove-mesh hybrid wick.

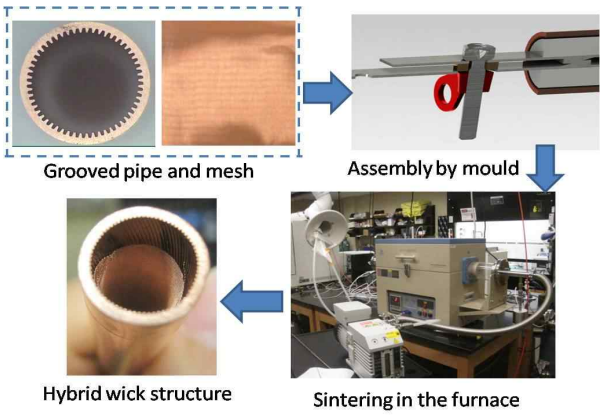


Fig.3 Typical fabrication processes of groove-mesh hybrid wick

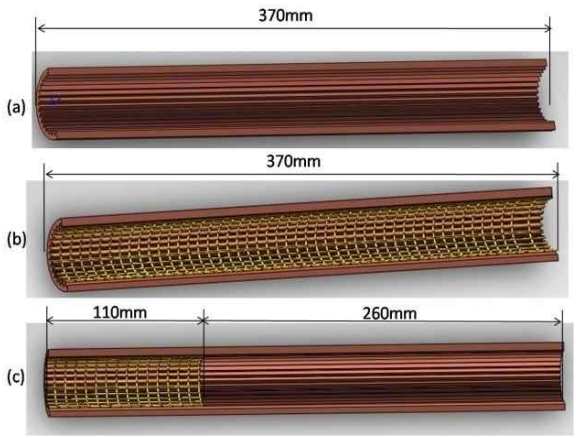


Fig. 4 Schematic of wick structures: (a) grooves, (b) full hybrid wick, and (c) partial hybrid wick in the evaporation region.

Three different wick structures corresponding to three coverage lengths (Fig.4), i.e., zero (groove), 370mm (full hybrid wick) and 110mm (partial hybrid wick) are prepared and tested in this study.

2.5 Charging process

During the vacuum process, the heat pipe is connected to a vacuum system. The vacuum degree can reach 6.667 Pa (0.05 Torr) in five hours. An auxiliary heater is used to heat up vacuum system in order to evacuate residue gases. In addition, non-condensable gases can be further removed using a mixture of dry ice and acetone.

When the pipe is vacuumed to 0.15 Torr, degassed 6.5 ml ethanol is charged into the pipe from a syringe. To further reduce the non-condense gas, a second vacuum process is utilized [15]. First, the vertically placed heat pipe is heated to ~ 95 °C, the non-condense gas is compressed and accumulated at the top of the heat pipe. After 1 minute, the top charging pipe will be sealed below the line of non-condense gases to assure minimizing the residual non-condensable gases in the pipe.

3. Experimental study

3.1 Test Setup

The test setup is shown in Fig.5. The 370 mm long heat pipe sample is positioned at a 55° inclined angle. The length of evaporation section, adiabatic section, and condensation section are 110mm, 100mm and 160mm, respectively. Experiment is operated at an ambient temperature (21±0.3 °C) and 1 ATM in a lab environment.

The experimental system consists of three parts: (1) Heating system: a constant voltage power source is provided by a VSP12010 automatic DC voltage stabilizer. Evaporator section is insulated by a blanket to isolate the heat pipe from ambient and reduce the heat loss. The major heat is assumed to transfer from heater to heat pipe. The heat loss of the test system is experimentally calibrated prior to tests.

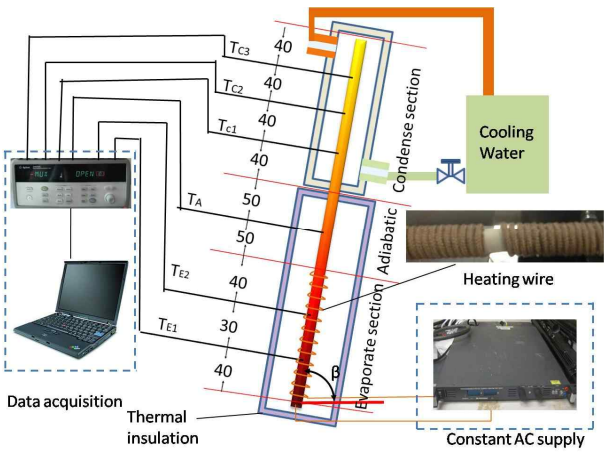


Fig.5 The heat pipe test setup

(2) Cooling system: a thermostatic water source provided a constant-temperature water to cool down the condenser section. The flow rate of cooling water is carefully controlled to keep the condenser section temperature stable.

(3) Data acquisition system: allocations of the thermocouples are shown in Fig.5. Six K-type thermocouples are utilized to measure heat pipe temperature distribution. All temperature data are automatically monitored and collected by an

Agilent 34970A data acquisition through a LabVIEW Program.

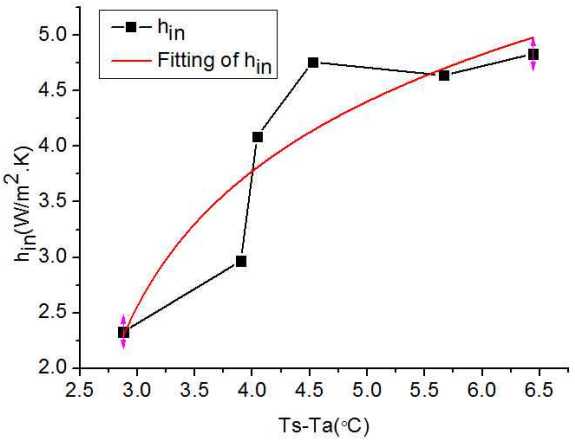


Fig.6 Heat loss in terms of heat transfer coefficient as a function of the temperature difference between the insulation surface and ambient temperatures

3.2 Calibration of Heat Loss

In order to accurately assess the heat loss during the operation of a heat pipe in evaporate section, two thermal couples (T_{s1},T_{s2}) are mounted on the surface of thermal insulation outer surfaces and one thermal couple is used to measure the air(T_a) temperature. The heat loss primarily comes from air convection. Thus, the heat loss can correlated using the temperature difference (T_s-T_a), area of surface and heat transfer coefficient (h_{in}). The heat transfer coefficient (h_{in}) is a function of (T_s-T_a). A preliminary experiment has been conducted to relate h_{in} and (T_s-T_a) as shown in Fig.6. By a nonlinear fitting method, the relation can be expressed as:

$$h_{in} = 3.226\ln(T_s - T_a) - 0.86 \quad (1)$$

3.3 Data Reduction

The average temperature of evaporator section is calculated as:

$$T_E = \frac{(T_{E1} + T_{E2})}{2} \quad (2)$$

The average temperature of condenser section is calculated as:

$$T_C = \frac{(T_{C1} + T_{C2} + T_{C3})}{2} \quad (3)$$

The temperature difference of heat pipe is calculated as:

$$\Delta T = T_E - T_C \quad (4)$$

The heat loss by the thermal insulation is calculated as following:

$$Q_{loss} = h_e A_{in}(\frac{T_{s1} - T_{s2}}{2} - T_a) \quad (5)$$

The real heat transferred by heat pipe is then estimated from:

$$Q_{real} = Q_{inp} - Q_{loss} \quad (6)$$

The thermal resistance of heat pipe is defined as:

$$R = \frac{T_E - T_C}{Q_{real}} \quad (7)$$

The effective thermal conductivity of heat pipe is defined as:

$$k_{eff} = \frac{L_{eff}}{A_p R} \quad (8)$$

Where T_{E1} and T_{E2} are temperature measuring points of evaporator section,℃; T_{C1} ,T_{C2} and T_{C3} are three temperature measuring points of condenser section, ℃; T_{s1} and T_{s2} are two temperature measuring points of insulation surface, ℃; T_a is the temperature of ambient air, ℃; Q_{loss} is the heat loss by thermal insulation, W; Q_{inp} is the heat input by heat wire, W; Q_{real} is the real heat transferred by heat pipe, W ; A_{in} is the area of insulation surface,m^2; R is the thermal resistance, ℃/W; L_{eff} is the distance between the center point of evaporator section and condenser section, m; A_p is the cross-section area of heat pipe,m^2; k_{eff} is the effective thermal conductivity, W/(m·k).

3.4 Uncertainty Analysis

The accuracy of 34970A data acquisition system is 0.01%. The resolution of K-type thermocouple is ±0.5℃. The accuracy of thermocouple location along heat pipe axial direction is within 0.5mm. From a standard error analysis method [16], the uncertainty of the actual power (Q_{real}) is calculated to be within 2.0%. The uncertainties of thermal resistance and effective thermal conductivity are within 3.5% with the input power larger than 60W, but it is up to 6.3% at 30W. The detailed uncertainties are presented in Fig. 7.

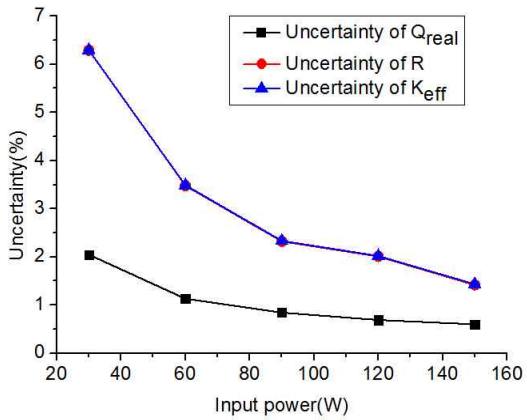


Fig.7 Uncertainties of actual power, thermal resistance and effective thermal conductivity

4. RESULTS AND DISCUSSION

4.1 Effect of Wick Structure On Temperature Distribution

From Fig.8 to Fig.10, the systematical results of steady-state wall temperature distributions for three heat pipes with various coverage of hybrid wick are presented. Temperature distributions are measured in the tilted angle of 55°on the surface of mesh-groove hybrid wick heat pipe, with various coverage lengths of 0mm, 110mm and 370mm.

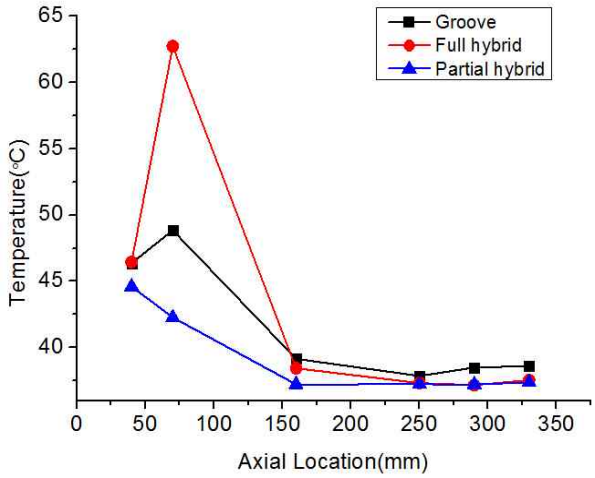


Fig.8 Steady-state wall temperature distributions of heat pipes with various coverage of hybrid wicks at the heat load of 90W

Fig.8-Fig.10 all show that the temperature distribution on the partial hybrid wicked heat pipe is more uniform than the other two heat pipes with groove wick or full hybrid wick structures, respectively. The second point of evaporation section (T_{E2}) is lower than the first point (T_{E1}) in partial hybrid wicked heat pipe while it is opposite in both groove wick and full hybrid wick heat pipe. Moreover, the second point of evaporation section (T_{E2}) of the full hybrid wick heat pipe is extremely high, which indicate a bad thermal performance.

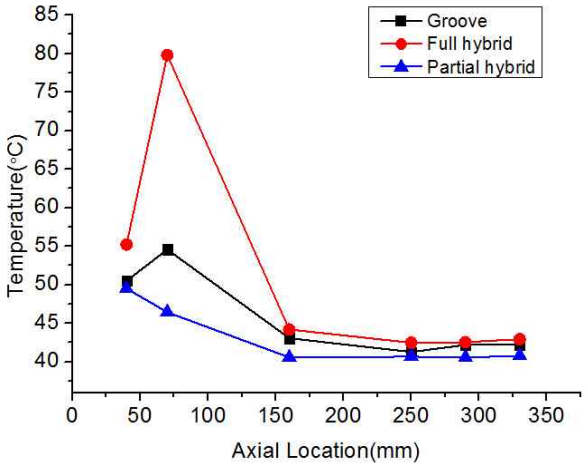


Fig.9 Steady-state wall temperature distributions of heat pipes with various coverage of hybrid wicks at the heat load of 120W

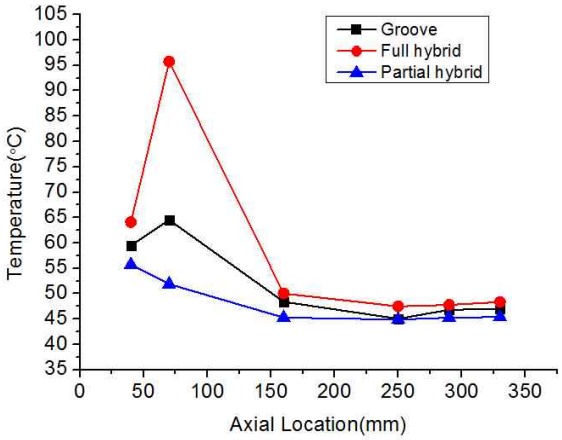
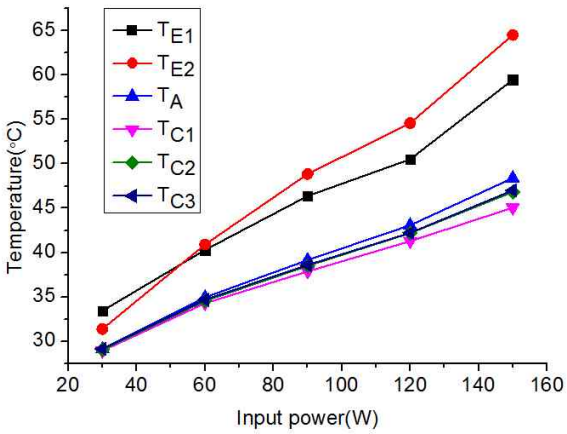


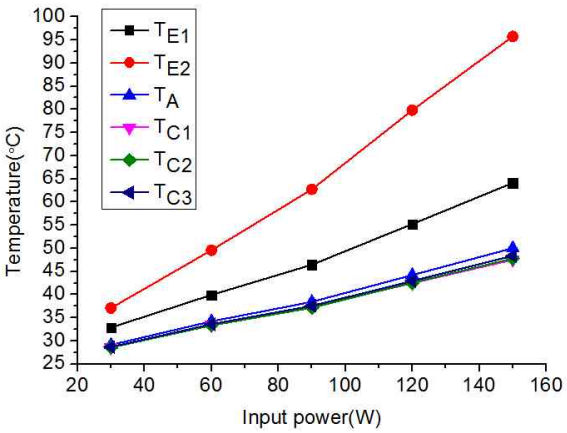
Fig.10 Steady-state wall temperature distributions of heat pipes with various coverage of hybrid wicks at the heat load of 150W

Fig.11 shows stead-state temperature trends of heat pipes with a various coverage of hybrid wick at different measuring points versus the heat load. Fig.12 presents comparisons of the evaporator-condenser temperature difference between heat pipes with a various coverage of hybrid wick structures. For partial hybrid wicked heat pipe (Fig.11(c)), T_E and T_C increase equally with the heat load. Thus, the temperature difference between the evaporation and condensation sections is nearly flat or stable. It ranges from 5.6 ℃ at 30W to 8.6℃ at 150W, as illustrated in Fig.12. However, for the full hybrid wicked heat pipe (Fig.11(c)), T_{E2} increases with the slope significantly larger than that of T_{C1}, T_{C2} and T_{C3}. Consequently, the temperature difference between

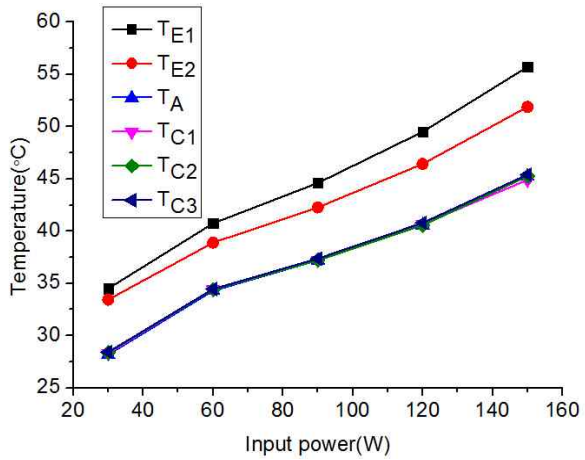
the evaporation and condensation sections increases quickly as the heat load increases. At a heat load of 150W, the temperature difference reaches 32 ℃, which indicates worse isothermal performance of full hybrid wicked heat pipe.



(a) Groove



(b) Full hybrid



(c)Partial hybrid

Fig.11 Stead-state temperature trends of heat pipes with various coverage of hybrid wick at different points versus the heat load; (a) groove;(b) full hybrid;(c) partial hybrid.

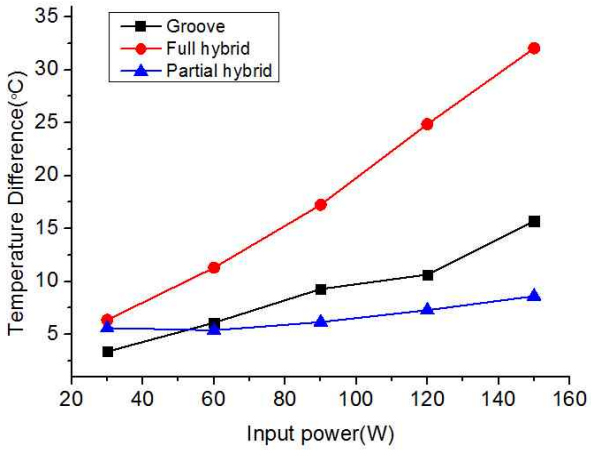


Fig.11 Comparisons of the temperature difference between the evaporation and condensation sections for three types of hybrid wick structures

4.2 Effect of Wick Structure On Effective Thermal Conductivity

Fig. 13 and Fig.14 present the comparisons between heat pipes with various coverage of hybrid wick in terms of thermal resistance and effective thermal conductivity (k_{eff}), respectively. As the input power increasing from 30W to 150W, the thermal resistance of groove wick and full hybrid wick heat pipe almost keep constant at about 0.10℃/W and 0.20℃/W, respectively. However, the thermal resistance of the partial hybrid wicked heat pipe decreases significantly as the heat load increasing with a larger slope at input power smaller than 90W. After heat load exceeding 90 W, the thermal resistance decreases slightly until the input power reaches 150W. The minimum thermal resistance of the partial hybrid wicked heat pipe is 0.06 ℃/W at the input power of 150W, which is significantly lower than the other two heat pipes at the same heat load.

The small thermal resistance indicates large effective thermal conductivity. The k_{eff} of groove heat pipe is higher than that of the partial hybrid wicked heat pipe at the input power of 30W. But the k_{eff} of the partial hybrid wick heat pipe increases significantly as the input power increases and substantially outperforms the groove heat pipe when the heat load exceeds 60W. Due to existence of the non-condense gas in the cold condenser side, the thermal performance of a heat pipe is affected by working load, especially at a low input power. However, as the input power increasing, the non-condense gas is compressed, leading to higher heat transfer rate on the condenser [17]. Thus, the k_{eff} of heat pipe increases as the input power increasing

with the slopes varying from heat pipes with different wick structures.

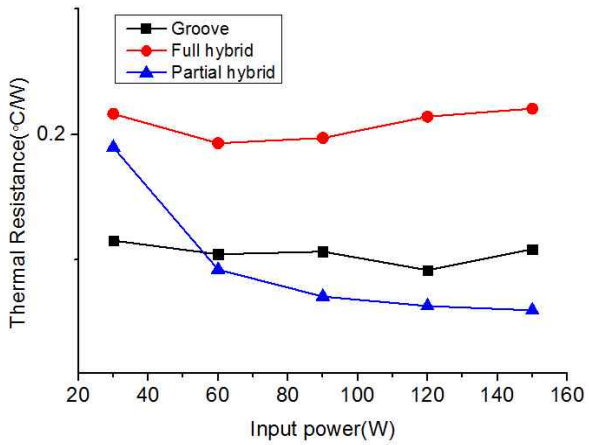


Fig.13 Comparisons of thermal resistance between heat pipes with various coverage of hybrid wick

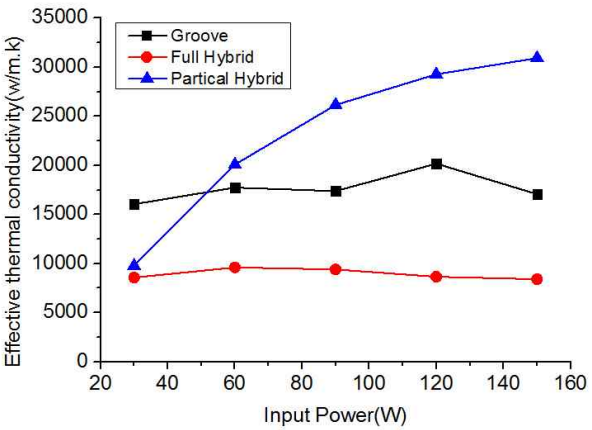


Fig.14 Comparisons of effective thermal conductivity between heat pipes with various coverage of hybrid wick

As illustrated in Fig.14, the k_{eff} of the partial hybrid wicked heat pipe increases rapidly with the slope significantly larger than the other two heat pipes. The heat pipe with partial hybrid wick in the evaporation region can achieve an effective thermal conductivity of 30.9 kW/m·K at 150W and significantly outperforms the other two heat pipes. The partial hybrid wick enhances the heat pipe by about 80% of groove wick and 267% of full hybrid wick.

The underlying enhancement mechanism is the uniform temperature distribution and highly efficient evaporation enabled by the highly efficient capillary evaporation on the copper mesh-groove hybrid wick. However, this type of enhancement cannot be applied in the condensation region as we demonstrated in the full hybrid wick heat pipe with the lowest performance, owing to the additional thermal resistance resulting from the liquid film confined by the hybrid wick in condensation region. This also reaches an agreement with the results reported by J.C. Hsieh[12] in a micro-rectangular groove structure covered with mesh layers. The full coverage of mesh-groove hybrid wick performs even worse than the groove wick. It can be concluded that optimizing evaporation and condensation regions separately is an effective way to maximize heat pipe performance.

5. CONCLUSION

In this study, novel groove-mesh hybrid wicks are developed and fabricated to achieve high performance heat pipes. Three coverage lengths (described as groove, full hybrid wick and partial wick), are fabricated to evaluate the effect of the hybrid wick design on heat pipe performances. Experimental results show that the partial hybrid wick greatly enhances the heat pipe by ~80% compared to the heat pipe with groove wick. High efficient evaporation enabled by the capillary evaporation on the mesh-groove hybrid wick appears to be the primary enhancement mechanism. However, the heat pipe performance is not always enhanced by hybrid wicks. Additional thermal resistance resulting from the liquid film formed by hybrid wick in condensation region would result in lower heat pipe performance. The technique to enhance evaporation and condensation sections should be separated in order to maximize heat pipe performance.

ACKNOWLEDGEMENTS

This research is financially supported by NSF under the grant 1357920 and the Chinese Scholarship Council.

NOMENCLATURE

A : Area (m^2)
h : Heat transfer coefficient ($W/(m^2 \cdot K)$)
k : Effective thermal conductivity ($W/(m \cdot K)$)
L : Length (m)
Q : Heat load(W)
R : Thermal resistance (°C/W)
T : Temperature (°C)

Subscripts

A : Adibatic

a : Air
C : Condense
E : Evaporate
eff : effective
in : Insulation
inp : Input power
p : Pipe
real : Real power
s : Surface of insulation

REFERENCES

[1] S. Chi, Heat pipe theory and practice: a sourcebook, (1976).
[2] G.P. Peterson, An introduction to heat pipes. Modeling, testing, and applications, Wiley Series in Thermal Management of Micro-electronic and Electronic Systems, New York, Chichester: Wiley, c1994, 1 (1994).
[3] A. Faghri, Heat pipe science and technology, Global Digital Press, 1995.
[4] Y. Tang, Z. Hu, J. Qing, Z. Xie, T. Fu, W. Chen, Experimental investigation on isothermal performance of the micro-grooved heat pipe, Experimental Thermal and Fluid Science, 47 (2013) 143-149.
[5] Z.-H. Liu, Y.-Y. Li, R. Bao, Thermal performance of inclined grooved heat pipes using nanofluids, International Journal of Thermal Sciences, 49(9) (2010) 1680-1687.
[6] T. Yong, C. Ping, W. Xiaowu, Experimental investigation into the performance of heat pipe with micro grooves fabricated by Extrusion–ploughing process, Energy Conversion and Management, 51(10) (2010) 1849-1854.
[7] R. Kempers, D. Ewing, C.Y. Ching, Effect of number of mesh layers and fluid loading on the performance of screen mesh wicked heat pipes, Applied Thermal Engineering, 26(5–6) (2006) 589-595.
[8] R. Kempers, A.J. Robinson, D. Ewing, C.Y. Ching, Characterization of evaporator and condenser thermal resistances of a screen mesh wicked heat pipe, International Journal of Heat and Mass Transfer, 51(25–26) (2008) 6039-6046.
[9] L. Jiang, J. Ling, L. Jiang, Y. Tang, Y. Li, W. Zhou, J. Gao, Thermal performance of a novel porous crack composite wick heat pipe, Energy Conversion and Management, 81 (2014) 10-18.
[10] J. Wang, I. Catton, Enhanced evaporation heat transfer in triangular grooves covered with a thin fine porous layer, Applied Thermal Engineering, 21(17) (2001) 1721-1737.
[11] F. Lefèvre, J.-B. Conrardy, M. Raynaud, J. Bonjour, Experimental investigations of flat plate heat pipes with screen meshes or grooves covered with screen meshes as capillary structure, Applied Thermal Engineering, 37 (2012) 95-102.
[12] J. C. Hsieh, H.J. Huang, S.C. Shen, Experimental study of microrectangular groove structure covered with multi mesh layers on performance of flat plate heat pipe for LED lighting module, Microelectronics Reliability, 52(6) (2012) 1071-1079.
[13] X. Dai, M. Famouri, A.I. Abdulagatov, R. Yang, Y.-C. Lee, S.M. George, C. Li, Capillary evaporation on micromembrane-enhanced microchannel wicks with atomic layer deposited silica, Applied Physics Letters, 103(15) (2013) 151602.
[14] C. Oshman, S. Bo, L. Chen, Y. Ronggui, Y.C. Lee, G.P. Peterson, V.M. Bright, The Development of Polymer-Based Flat Heat Pipes, Microelectro-mechanical Systems, Journal of, 20(2) (2011) 410-417.
[15] Y. Li, S. Chen, B. He, Y. Yan, B. Li, Effects of vacuuming process parameters on the thermal performance of composite heat pipes, Applied Thermal Engineering, 99 (2016) 32-41.
[16] J. R. Taylor, An Introduction to Error Analysis, second ed, University Science Books, (1997).
[17] Y. Tang, R. Zhou, L. Lu, Z. Xie, Anti-Gravity Loop-shaped heat pipe with graded pore-size wick, Applied Thermal Engineering, 36 (2012) 78-86.

Operational Characteristics and Thermal Performance of a Rectangular Heat Pipe Fabricated on a Plastic Board

Yasushi Koito*, Hiroyuki Maehara, Daisuke Shimada and Toshio Tomimura

Department of Advanced Mechanical Systems, Kumamoto University, Kumamoto 860-8555, Japan

Abstract

Experimental study is conducted on a rectangular heat pipe fabricated in a polycarbonate board. The heat pipe is 5.0 mm × 5.0 mm × 100 mm (length), and water is used as a working fluid. In the present study, a simplified wick structure is placed in the heat pipe to make a comparison with the authors' previous study. The wick structure is flat in shape and made of sintered copper powders. In the experiment, the heat pipe was heated by a heater and cooled by water through a cooling jacket. The transient temperature variations of the heat pipe were measured by using K-type thermocouples. A heat input and a liquid volume inside the heat pipe were changed as 2.0 W – 6.0 W and 0 mL – 3.0 mL, respectively; the cooling water temperature at the inlet of the cooling jacket was maintained at 20 °C. The experimental results on the start-up characteristics of the heat pipe are shown. From the experimental results, the heat transfer coefficients at the heat and the cooled section of the heat pipe are calculated. It is found that the heat transfer coefficient at the heated section is entirely higher than that at the cooled section. Moreover, by using a thermal circuit model, the effective thermal conductivity of the heat pipe is also evaluated. Although the simplified wick structure is used in the present study, the operation of the heat pipe in the plastic board is confirmed.

Keywords: Effective thermal conductivity; Heat transfer coefficient; Heat transfer enhancement; Polymer heat pipe; Simple wick structure

1. INTRODUCTION

A heat pipe is a widely-used thermal device to transport heat from one position to another. A relatively large amount of heat is transported with a small temperature drop because the latent heat of evaporation and condensation of a working fluid is utilized inside the heat pipe. Moreover, the use of capillary force of a wick structure enables to circulate a working fluid naturally and therefore the heat pipe operates without consuming any external power. The heat pipe is one of the promising options and many types of heat pipes have been developed for heat transfer enhancement, thermal management and thermal energy utilization etc.

The authors have made the attempt to fabricate a heat pipe directly in a plastic board [1, 2]. This proposal aims at the enhancement of heat transfer to overcome the drawback of low thermal conductivity of a plastic board. It is noted here that this type of heat pipe is categorized as a polymer heat pipe.

Jones *et al*. [3] and Wits *et al*. [4] conducted the experimental studies to make a heat pipe in a printed circuit board. The heat transfer enhancement is required because the printed circuit board is basically made of polymer materials such as epoxy resin. Oshman *et al*. [5] fabricated a polymer heat pipe by using a liquid-crystal polymer as a case material. Thermal vias were also employed to reduce the thermal resistances at a heated and a cooled section of the polymer heat pipe. According to the study by Oshman *et al*. [5], Shi *et al*. [6] also fabricated a polymer heat pipe and showed its heat transfer characteristics. Moreover, Yang *et al*. [7] made a polymer heat pipe by using FR4. FR4 is commonly used for a printed circuit board as a substrate. Thermal vias were also employed to reduce the thermal resistances. More recently, Chen *et al*. [8] presented a review article including the studies of polymer heat pipes.

This paper describes an experimental study of a heat pipe fabricated in a plastic board. In this study, a simplified wick structure is used to make a comparison with the authors' previous study [2]. The experimental results are presented and the discussion is made concerning the heat transfer characteristics and the thermal performance of the heat pipe.

2. EXPERIMENTAL METHOD

Except for a shape of a wick structure, the experimental apparatus and procedure in the present study is essentially the same as described in the authors' previous paper [2]. Hence, only the main points of the experimental method are described in this section.

As shown in Fig. 1, a heat pipe was fabricated in a polycarbonate board of 8.0 mm thickness. A copper plate of 1.0 mm thickness was also used to close the heat pipe. This is a rectangular heat pipe having a

*Corresponding author: koito@gpo.kumamoto-u.ac.jp,
Phone: +81-96-342-3760, Fax: +81-96-342-3760

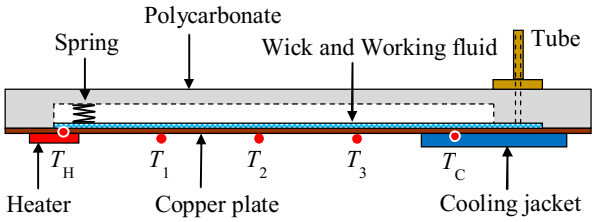


Fig. 1. Schematic diagram of the heat pipe.



(a) Photograph of the wick structure



(b-1) Previous study [2] (b-2) Present study

(b) Cross section of the wick structure

Fig. 2. Wick structure.

cross-sectional area of 5.0 mm × 5.0 mm and a length of 100 mm. The wick structure is shown in Fig. 2. In the present study, the heat pipe was placed horizontally and a flat-plate type wick structure was used on the bottom of the heat pipe. This is a simplified wick structure compared with the authors' previous one [2]. A sintered copper powder and water were used as the wick structure and the working fluid, respectively. To reduce heat loss, the heat pipe was covered with a thermal insulator except for a heated and a cooled section.

In the experiment, the heat pipe was heated by a heater and cooled by water through a cooling jacket. The transient variation of the temperatures was measured by using K-type thermocouples. The measuring points of the temperatures (T_H, T_1 ~ T_3, T_C) are also shown in Fig. 1. The heated area, A_H, and the cooled area, A_C, of the heat pipe were 1.0 cm^2 and 4.0 cm^2, respectively. The experiment was conducted by changing the liquid volume of the working fluid, V, and the amount of the heat input Q, as V = 0 mL – 3.0 mL and Q = 2.0 W – 6.0 W, respectively. It is noted that V = 0 mL implies the case when the working fluid is not charged inside the

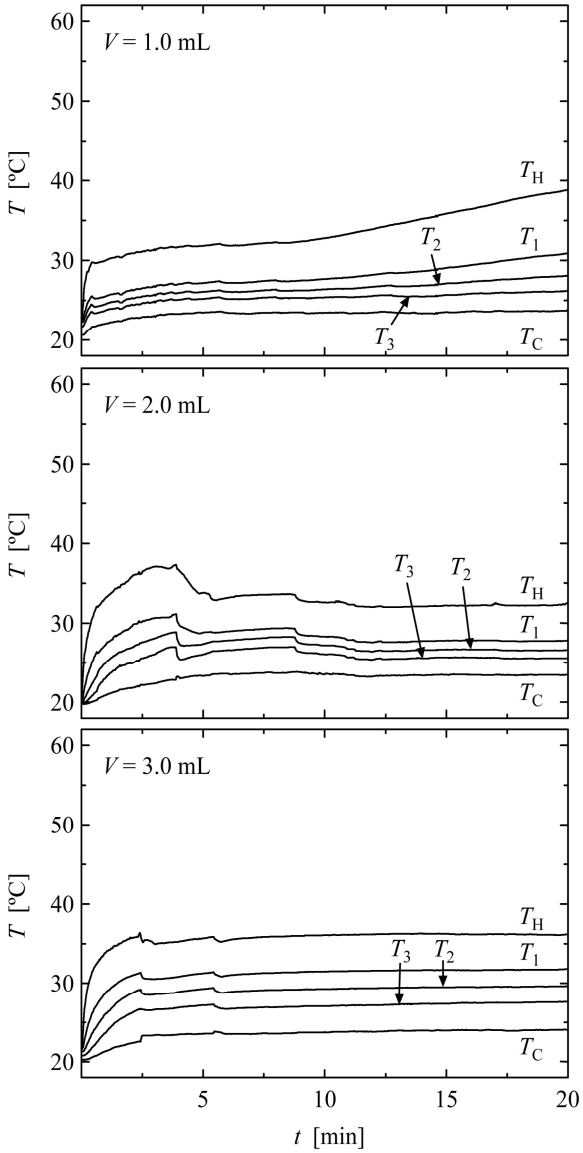


Fig. 3. Start-up characteristics of the heat pipe (Q = 4.0 W).

heat pipe. The cooling water temperature at the inlet of the cooling jacket was maintained at 20 °C.

When V = 0 mL, the numerical calculation was also performed to obtain the relation between the temperature distribution of the heat pipe and the heat input. Then, the heat loss from the heat pipe was estimated by comparing the experimental results at V = 0 mL with the numerical ones. It was found that the heat loss was less than 6.0 % in the present experimental range.

3. RESULTS ANS DISCUSSION

Fig. 3 shows the transient variations of the temperatures of the heat pipe. The temperatures at the heated section, T_H, the adiabatic section, T_1 ~ T_3, and the cooled section, T_C, of the heat pipe are shown with time, t. The heating of the heat pipe was

Table 1 Conditions for steady-state operation.

Q [W]	V [mL]				
	1.0	1.5	2.0	2.5	3.0
2.0	○	○	○	○	○
4.0	×	○	○	○	○
6.0	×	×	×	×	×

started at t = 0 min. The comparison is made at Q = 4.0 W between the experimental results of V = 1.0 mL, 2.0 mL and 3.0 mL. In the case of V = 2.0 mL and V = 3.0 mL, although the temperature changes were unstable for a few minutes after the heating was stated, it was found that the temperature changes reached a steady state thereafter. Moreover, it was also revealed that the temperature difference between the heated and the cooled section, $T_H - T_C$, for V = 2.0 mL was slightly smaller than that for V = 3.0 mL. In the case of V = 1.0 mL, on the other hand, a steady-state temperature distribution of the heat pipe was not obtained. Due to the shortage of the working fluid inside the heat pipe, the dry-out phenomena were occurred in this case. Table 1 shows the experimental conditions when the steady-state operation of the heat pipe was obtained in the present experimental range. As expected, the increase in the heat input, Q, also causes the dry-out phenomena inside the heat pipe.

The average temperature, T_A, at the adiabatic section of the heat pipe is calculated by

$$T_A = \frac{T_1 + T_2 + T_3}{3} \tag{1}$$

and the heat transfer coefficient at the heated section, α_H, and the cooled section, α_C, of the heat pipe are defined respectively by,

$$\alpha_H = \frac{Q}{A_H(T_H - T_A)} \tag{2}$$

$$\alpha_C = \frac{Q}{A_C(T_A - T_C)} \tag{3}$$

where A_H and A_C are the surface area of the heated section and the cooled section. A_H = 1.0 cm^2 and A_C = 4.0 cm^2 as mentioned above.

Fig. 4 and Fig. 5 show the heat transfer coefficient at the heated section, α_H, and the cooled section, α_C, of the heat pipe, respectively. These heat transfer coefficients were obtained from the temperature distribution at steady state. It was found that α_H was entirely higher than α_C. Moreover, α_H and α_C became smaller with the increase in the liquid volume, V. Because both α_H and α_C were affected by V as shown in the figure, further investigations are required to optimize the liquid volume inside the heat pipe.

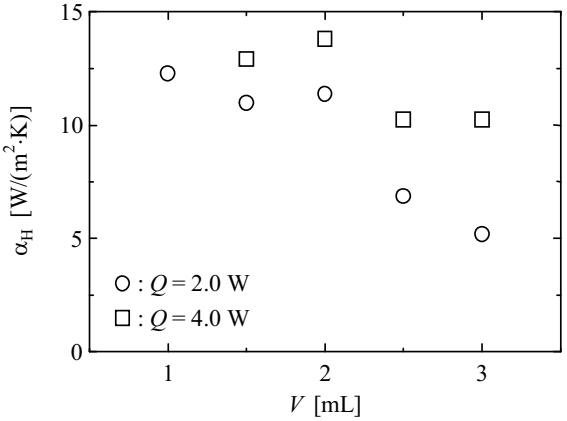


Fig. 4. Heat transfer coefficient at the heated section of the heat pipe.

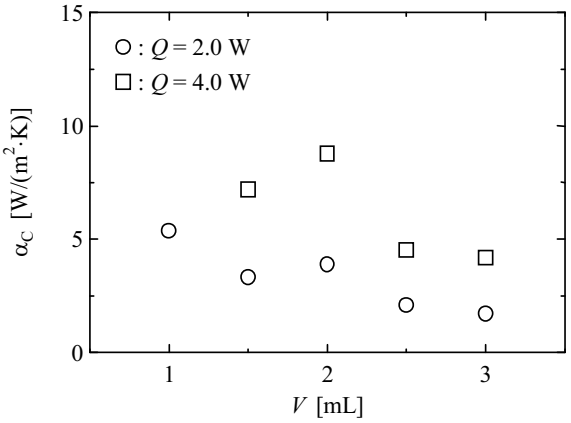


Fig. 5. Heat transfer coefficient at the cooled section of the heat pipe.

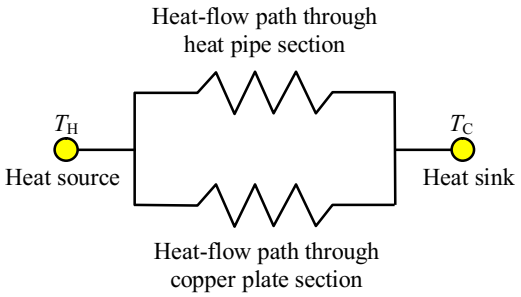


Fig. 6. Thermal circuit of the heat pipe.

The effective thermal conductivity, λ_{eff}, of the heat pipe is evaluated by

$$\lambda_{eff} = \frac{L}{A_{HP}}\left(\frac{Q_{net}}{T_H - T_C} - \frac{\lambda_{CU}A_{CU}}{L}\right) \tag{4}$$

where L is the heat transport distance from the heated to the cooled section, A_{HP} the cross-sectional area of the heat pipe, A_{CU} the cross-sectional area of the copper plate, λ_{CU} the thermal conductivity of the copper plate. Eq. (4) was derived from the thermal circuit model shown in Fig. 6. This model considers the two heat-flow paths of the heat pipe section and the copper plate section. It is noted that the value of λ_{eff} reflects only the heat flow through the heat pipe section.

Fig. 7 shows the effective thermal conductivity, λ_{eff}, of the heat pipe when the steady-state temperature distribution was obtained. For comparison, the effective thermal conductivity of the heat pipe obtained by using the previous wick structure [2] (see Fig. 2) is also shown in this figure. It was found that the variation in λ_{eff} for the present wick structure was slightly larger than that for the previous one. Moreover, most of λ_{eff} in the present study was higher than the thermal conductivity of the copper plate (λ_{CU} = 398 W/(m·K)). Although the wick structure was simplified in the present study, the operation of the heat pipe in the plastic board was confirmed.

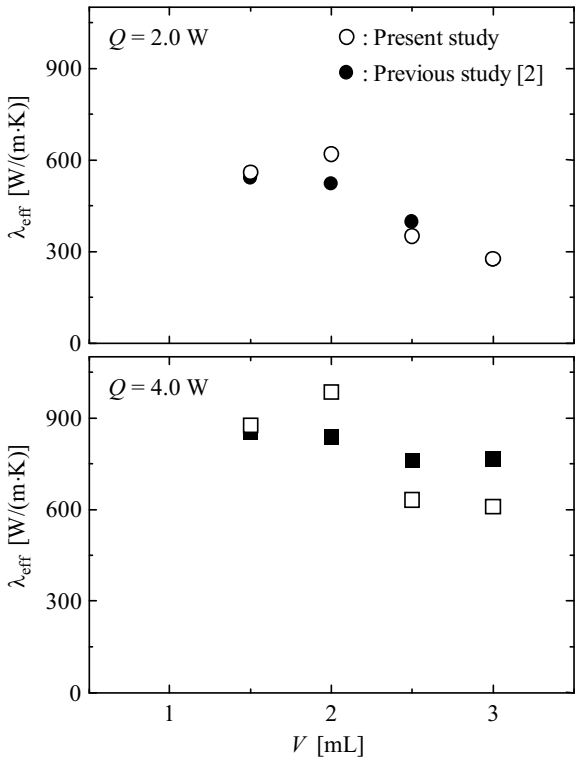


Fig. 7. Effective thermal conductivity of the heat pipe.

4. CONCLUSIONS

By using a simplified wick structure, the experimental study was conducted on the operational characteristics and the thermal performance of the heat pipe fabricated in the plastic board. The wick structure was flat in shape and made of sintered copper powders. Water was used as the working fluid. From the experimental results, the heat transfer coefficient at the heat and the cooled section of the heat pipe was calculated. It was found that the heat transfer coefficient at the heated section was entirely higher than that at the cooled section. Moreover, the effective thermal conductivity of the heat pipe was also evaluated. Although the simplified wick structure was used, the operation of the heat pipe in the plastic board was confirmed.

ACKNOWLEDGEMENT

This work was supported by JSPS KAKENHI Grant Number 26420150.

NOMENCLATURE

A : Area (m^2)
L : Length (m)
Q : Heat flow rate (W)
T : Temperature (°C)
t : Time (min)
V : Liquid volume (mL)
λ : Thermal conductivity (W/(m·K))

Subscripts

1-3 : Positions
C : Cooled section
CU : Copper plate
eff : Effective
H : Heated section
HP : Heat pipe

REFERENCES

[1] Koito, Y., Maehara, H. and Tomimura, T., Fabrication of heat pipes on an acrylic resin board, *Proc. of InterPACK2013*, San Francisco, USA (2013) InterPACK2013-73277.

[2] Koito, Y., Maehara, H., Shimada, D. and Tomimura, T., A capillary-wick heat pipe fabricated on a plastic board (fundamental experiments on heat transport characteristics), *Proc. of InterPACKICNMM2015*, San Francisco, USA (2015) InterPACKICNMM 2015-48308.

[3] Jones, K., Cao, Y. and Gao, M., Development of micro heat pipes embedded in laminate substrates for enhanced thermal management (tm) for printed wiring boards (PWBs), *Technical Report,AFRL-PR-WP-TR-2003-2011*, Florida International University (2002).

[4] Wits, W., Kok, J., Legtenberg, R., Mannak, J. and Zalk, B., Manufacturing and modeling of flat miniature heat pipes in multilayer printed circuit board technology, *Proc. of the 14th International Heat Pipe Conference*,

Florianópolis, Brazil (2007) 169-175.

[5] Oshman, C., Shi, B., Li, C., Yang, R., Lee, Y. C., Peterson, G. P. and Bright, V. M., The development of polymer-based flat heat pipes, *Journal of Microelectromechanical Systems*, 20 (2011) 410-417.

[6] Shi, B., Wang, Y. B. and Shan, Y. J., An experimental investigation of thermal performance of a polymer-based flat heat pipe, *Heat Transfer - Asian Research*, in press.

[7] Yang, K. S., Yang, T. Y., Tu, C. W., Yeh, C. T. and Lee, M. T., A novel flat polymer heat pipe with thermal via for cooling electronic devices, *Energy Conversion and Management*, 100 (2015) 37-44.

[8] Chen, X., Ye, H., Fan, X., Ren, T. and Zhang, G., A review of small heat pipes for electronics, *Applied Thermal Engineering*, 96 (2016) 1-17.

Modelling of a Single Rotating Heat Pipe for Heat Pipe Assisted Annealing Concept

Metin Celik[1], Geert Paulussen[2], Pepijn Pronk[2], Laurent Sturnack[3], Wiebren de Jong[1] and Bendiks Jan Boersma[1]

[1]*Process & Energy Department, Delft University of Technology, Delft, The Netherlands, email:m.celik@tudelft.nl.*
[2]*R&D Thermal Processes Group, Tata Steel, IJmuiden, The Netherlands.*
[3]*Project Development Drever International, Liège, Belgium.*

Abstract

Annealing is an essential heat treatment process for the production of cold rolled steel that aims at achieving desired properties like ductility and toughness of the steel. However, annealing of the steel in a conventional way is an energy intensive process, as it requires energy for both heating the strip up to around 700°C and then cooling it back to room temperature. Therefore, an alternative technology to achieve energy efficient annealing of the steel strip is investigated. The new technology involves the concept of rotating heat pipes that continuously extract heat from the steel strip on the evaporator side and re-use this heat to increase the temperature of the steel strip on the condenser side. The heat transfer from the hot strip to cold strip via several rotating heat pipes would enable the implementation of a full annealing processing line. As a part of this research, a 2D axisymmetric swirl model for a rotating heat pipe using water as working fluid is modelled using the commercial software of ANSYS Fluent 15.0. The Euler-Euler approach and the Volume of Fluid method are used, along with the Lee model for phase change. Due to the large diameter to length ratio of the heat pipe, the main vapor flow occurs close to the liquid/vapor interface and far away from the symmetry line. Below the main vapor flow, a reversed flow is observed. It is further seen that the heat pipe vapor region is nearly isothermal.

Keywords: Computational fluid dynamics; Continuous annealing; Energy efficiency; Multiphase flow; Rotating heat pipe

1. INTRODUCTION

The rotating heat pipe is a wickless hollow shaft rotating around its symmetric axis. It contains a fixed amount of working fluid and has a substantial heat transfer capability. Since first proposed by Gray [1], rotating heat pipes have been widely investigated to be used in various applications, such as in rotors of electrical machinery, rollers for presses or rotary cutting tools [2]. One such potential application is the use of multiple rotating heat pipes for the annealing of steel strip. Annealing is an essential heat treatment process in the steel industry that aims at achieving desired properties like ductility and toughness of the steel. The conventional annealing is a very energy intensive process. It requires energy for both heating the strip up to around 700 °C and then cooling it back to room temperature. Therefore, using multiple rotating heat pipes to continuously extract heat from the steel strip on the evaporator side and to re-use this heat to increase the temperature of the steel strip on the condenser side can be very efficient [3,4]. In order to implement this technology, the transport phenomena inside a single rotating heat pipe with relatively high diameter to length ratio have to be understood.

A number of theoretical investigations have previously been carried out to understand the heat and mass transfer inside rotating heat pipes. Early studies mostly focused on the condenser part of the rotating heat pipe. Chan et al. [5] used a classical Nusselt approach for film condensation for the case of a horizontal rotating heat pipe. Marto [6] also made a similar analysis for the condenser section of the heat pipe. Daniels et al. [7] investigated the performance of the heat pipe with a modified Nusselt type analysis which takes the drag effects of vapor flow into account. Because the previous models using Nusselt type analysis estimated the friction coefficient at the interface empirically or just simply neglected it, Faghri et al. [8] analyzed the vapor flow inside the rotating heat pipe to study the shear stress profiles.

More extensive models which treat the rotating heat pipe as a single domain (rather than focusing only on the condenser) were developed later on. Li et al. [9] modelled all of the sections of the heat pipe, with the assumption of negligible vapor core pressure drop. The evaporation is analyzed in a similar way to film condensation. Another complete rotating heat pipe model was made by Harley et al. [10], including the vapor pressure drop, the interfacial shear stress and heat conduction in the heat pipe wall. Another analysis has been made by Song et al. [11] for high-speed rotating heat pipes. The major difference of this model compared to the previous ones was that it included a mixed convection evaporator model, instead of a simple

Nusselt film evaporation approach.

In the current analysis, the rotating heat pipe with water as working fluid is modelled using the commercial software of ANSYS Fluent. The model is an axisymmetric 2D model taking into account the swirl velocity. The analyzed heat pipe has a diameter to length ratio of 0.4. This ratio is significantly higher compared to the previously modelled heat pipes in the literature [9-11]. This difference is expected to produce a different velocity profile at the vapor core of the heat pipe. The evaporation and condensation are modelled using the Lee model, as opposed to previous analyses in the literature.

2. BACKGROUND

2.1 Heat Pipe Assisted Annealing Concept

In a conventional continuous annealing line, steel strip is heated up to around 700 °C with natural gas and kept at this temperature for about 30 seconds. Afterwards, the strip is quickly cooled down to around 400 °C and kept at this temperature again for 30 seconds. Finally, the strip is cooled down to room temperature (see Fig. 1). Heat removed during the cooling process is not recovered.

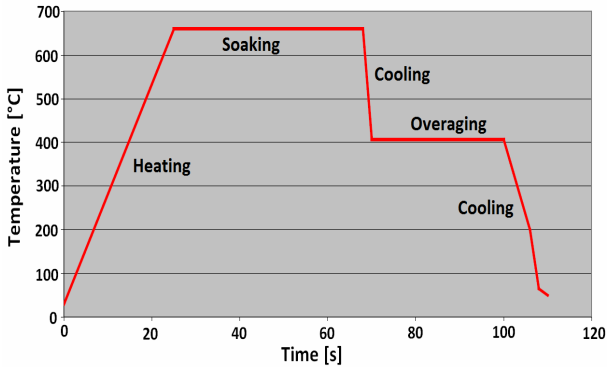


Fig.1. Conventional continuous annealing line cycle

Because of the excellent heat transfer properties of heat pipes, the same thermal cycle as conventional annealing of steel strip can be achieved through a series of rotating heat pipes (see Fig. 2). This concept would enable a substantial reduction in the energy consumption, as well as a decrease in the CO_2 emissions caused by natural gas consumption. The only conventional heating and cooling would be used at the beginning and the end of the process.

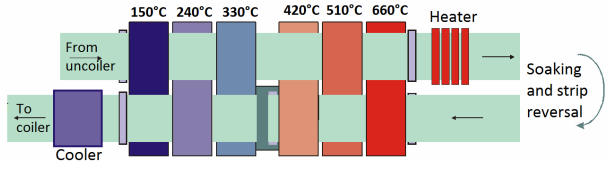


Fig. 2. Heat pipe assisted annealing concept.

In order to reduce the stress induced creep on the rotating heat pipes, the operating pressures inside the heat pipes should be limited. Therefore, different working fluids would be required throughout the process. However, the first step in the operational range can be covered with water, which is the working fluid used in the current analysis.

2.2 Thermal Resistances in the Single Rotating Heat Pipe

A typical heat pipe can be considered as a network consisting of several components with different thermal resistances [12]. The same idea can easily be applied to a rotating heat pipe. In this approach, the major difference for a rotating heat pipe is the absence of a wick structure. For the heat pipe assisted annealing concept, however, there is an additional thermal resistance: the contact resistance between the steel strip and the rotating heat pipe.

The thermal resistances in the single rotating heat pipe subject to this study can be seen in Fig. 3. Considering this network, it is crucial to understand whether the thermal resistances inside the rotating heat pipe will play an important role or not.

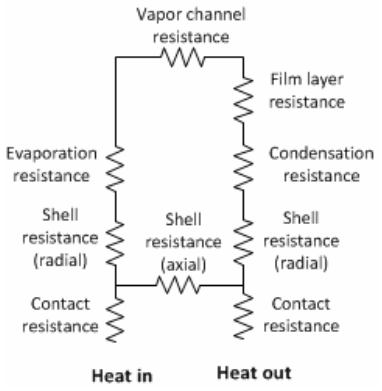


Fig. 3. Thermal resistances in the single heat pipe.

For this purpose, the contact resistances should be predicted for a relevant strip tension. There are various theories for calculating the contact resistance between two materials, but the most reliable results can be obtained through experiments [13]. Therefore, experiments have been conducted with a strip tension varying from 30 MPa to 50 MPa at the test rig built to investigate the current concept. Experiments resulted in a heat transfer coefficient of around 12000 $W/m^2/K$. This value shows that the contact heat transfer coefficient is relatively high. Therefore, contact resistance is not expected to be the dominant heat transfer resistance and the thermal resistances inside the heat pipe should be thoroughly investigated. This requires a detailed model of a single rotating heat pipe.

3. MODEL DEVELOPMENT

3.1 CFD Simulation and Governing Equations

In this study, the CFD simulation is carried out based on the finite volume method with the commercial software of ANSYS Fluent 15.0. A transient computation is performed. The geometry is 2D axisymmetric . The flow is laminar. The Euler-Euler approach is adopted, where different phases are treated as interpenetrating continua. The Volume of Fluid (VOF) method is used to determine the location of the interface between liquid and vapor.

The VOF model introduces a variable called 'volume fraction' to the equations. This variable gives an indication of the phase that occupies the computational cell. In case the volume fraction inside a cell is 0 or 1, one of the fluids occupies this cell. In case it is between 0 and 1, the interface between the two fluids lies in this cell. Based on the value of the volume fraction in each cell, appropriate material properties are assigned to this cell [14].

Since the geometry of the model is axisymmetric, the governing equations for both continuity and momentum are written in cylindrical coordinates and discarding the derivatives with respect to tangential coordinates.

The continuity equation for the volume fraction of the liquid phase (water) is solved as follows:

$$\frac{\partial}{\partial t}\left(\alpha_w \rho_w\right)+\frac{\partial}{\partial x}\left(\alpha_w \rho_w v_x\right) +\frac{1}{r}\frac{\partial}{\partial r}\left(r\alpha_w \rho_w v_r\right)=\dot{m}_{s-w}-\dot{m}_{w-s} \tag{1}$$

with the following constraint:

$$\alpha_w+\alpha_s=1 \tag{2}$$

The density and viscosity in the cells where interface lie are determined with the following formulas:

$$\rho=\alpha_w \rho_w+\left(1-\alpha_w\right)\rho_s \tag{3}$$

$$\mu=\alpha_w \mu_w+\left(1-\alpha_w\right)\mu_s \tag{4}$$

The velocity field is deduced from a single set of momentum equations solved throughout the domain for both phases. These momentum equations are dependent on the volume fractions and on material properties calculated with eqn. 3. It should also be noted that gravity is not included in the momentum equations.

Axial, radial and tangential momentum conservation equations, respectively, are:

$$\begin{aligned}&\frac{\partial}{\partial t}\left(\rho v_x\right)+\frac{\partial}{\partial x}\left(\rho v_x v_x\right)+\frac{1}{r}\frac{\partial}{\partial r}\left(r\rho v_r v_x\right)= \\ &\quad -\frac{\partial p}{\partial x}+\frac{\partial}{\partial x}\left[\mu\left(2\frac{\partial v_x}{\partial x}-\frac{2}{3}\left(\nabla\bullet\vec{v}\right)\right)\right]+ \\ &\quad \frac{1}{r}\frac{\partial}{\partial r}\left[r\mu\left(\frac{\partial v_x}{\partial r}+\frac{\partial v_r}{\partial x}\right)\right]+F_x\end{aligned} \tag{5}$$

$$\begin{aligned}&\frac{\partial}{\partial t}\left(\rho v_r\right)+\frac{\partial}{\partial x}\left(\rho v_x v_r\right)+\frac{1}{r}\frac{\partial}{\partial r}\left(r\rho v_r v_r\right)-\rho\frac{v_\theta^2}{r}= \\ &\quad -\frac{\partial p}{\partial r}+\frac{1}{r}\frac{\partial}{\partial r}\left[r\mu\left(2\frac{\partial v_r}{\partial r}-\frac{2}{3}\left(\nabla\bullet\vec{v}\right)\right)\right]+ \\ &\quad \frac{1}{r}\frac{\partial}{\partial x}\left[r\mu\left(\frac{\partial v_r}{\partial x}+\frac{\partial v_x}{\partial r}\right)\right] \\ &\quad -2\mu\frac{v_r}{r^2}+\frac{2}{3}\frac{\mu}{r}\left(\nabla\bullet\vec{v}\right)+F_r\end{aligned} \tag{6}$$

$$\begin{aligned}&\frac{\partial}{\partial t}\left(\rho v_\theta\right)+\frac{\partial}{\partial x}\left(\rho v_x v_\theta\right)+\frac{1}{r^2}\frac{\partial}{\partial r}\left(r^2\rho v_r v_\theta\right)= \\ &\quad \frac{\partial}{\partial x}\left[\mu\frac{\partial v_\theta}{\partial x}\right]+\frac{1}{r^2}\frac{\partial}{\partial r}\left[r^3\mu\frac{\partial}{\partial r}\left(\frac{v_\theta}{r}\right)\right]\end{aligned} \tag{7}$$

with

$$\nabla\bullet\vec{v}=\frac{\partial v_x}{\partial x}+\frac{1}{r}\frac{\partial r v_r}{\partial r} \tag{8}$$

The energy conservation equation, also solved throughout the computational domain for both phases, has the following form:

$$\begin{aligned}&\frac{\partial}{\partial t}\left(\rho E\right)+\nabla\bullet\left(\vec{v}\left(\rho E+p\right)\right)= \\ &\quad \nabla\bullet\left(k\nabla T\right)+\left(\dot{m}_{s-w}-\dot{m}_{w-s}\right)L\end{aligned} \tag{9}$$

with

$$E=U+\frac{v^2}{2} \tag{10}$$

The internal energy and the temperature are treated as mass-averaged variables, whereas thermal conductivity is interpolated according to the volume fraction (as other material properties).

For evaporation and condensation, the Lee model is used [14]. The mass transfer due to evaporation and condensation are based on the following temperature regimes:

If $T_w > T_{sat}$ (evaporation)

$$\dot{m}_{w-s}=coeff\left(\alpha_w \rho_w\right)\frac{\left(T_w-T_{sat}\right)}{T_{sat}} \tag{11}$$

with *coeff* chosen as 0.1.

If $T_s < T_{sat}$ (condensation)

$$\dot{m}_{s-w}=coeff\left(\alpha_s \rho_s\right)\frac{\left(T_{sat}-T_s\right)}{T_{sat}} \tag{12}$$

with *coeff* chosen as 10.

The coefficient *coeff* can be interpreted as relaxation time for the rate of the mass transfer. It is a coefficient that should be fine-tuned according to experiments. It does not necessarily have to be the same for evaporation and condensation [14]. In this study, the coefficients are selected such that they created comparable evaporation and condensation rates.

Finally, the conduction within the heat pipe wall is solved as 1D conduction. This implies that the wall is not included in the computational domain. It merely sets the boundary condition on the outside of the specified wall thickness. According to this formulation, the thermal resistance of the wall is simply taken as $\Delta r_{wall}/k_{wall}$.

3.2 Model Geometry and Mesh

The geometry of the model is a 2D axisymmetric representation of the single heat pipe that is part of the test rig built to investigate the concept of heat pipe assisted annealing (see Fig. 4).

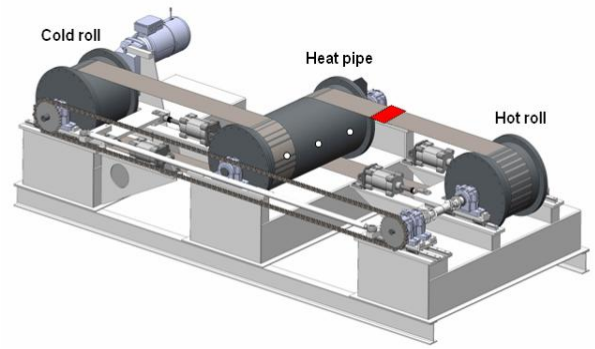


Fig. 4. Representation of the experimental test rig built for the investigation of the heat pipe assisted annealing concept.

The stainless steel heat pipe is divided into three sections, namely evaporator, condenser and the adiabatic section. In the actual test rig, the steel strips determine the locations of the evaporator and condenser. Since steel strips are 0.3 m wide each and they are not exactly aligned with the edge of the rotating heat pipe, the size of the condenser and the evaporator are each 0.3 m, located at a distance of 0.05 m away from the edges of the heat pipe. The total length of the heat pipe is 1.21 m. Therefore, the length of the adiabatic section is 0.51 m. The inner radius of the heat pipe is 0.2445 m, whereas the outer radius is 0.251 m. This implies that the wall thickness is 0.0065 m (see Fig.5). There is no taper at the inner wall of the heat pipe.

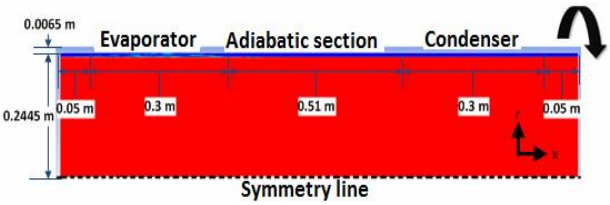


Fig. 5. Geometry of the model.

The mesh consists of 16696 quadratic cells. It is rather coarse for the vapor phase away from the interface with a sizing of 5 mm x 5 mm and more refined near the interface with a sizing of 0.6 mm x 5 mm. The interface is more finely meshed to capture the position of the interface, the thin liquid film and the evaporation and condensation phenomena in a more detailed way (see Fig. 6).

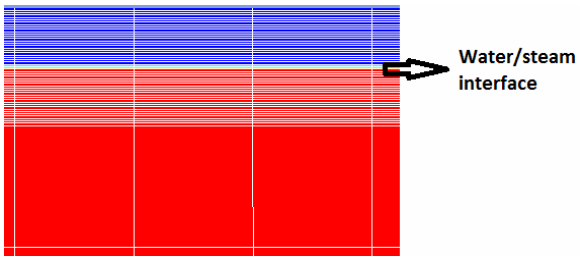


Fig. 6. Mesh sizing near the liquid/vapor interface.

3.3 Numerical Procedure

The time step used for the transient simulations is 0.01 s. The simulations are stopped at quasi-steady-state, at around 250 s.

The discretized governing equations are solved using the PISO scheme, which enables the pressure-velocity coupling. The discretization for the continuity, momentum and energy equations is performed using the QUICK method.

The convergence criteria require that the residuals decrease to 10-3 for all of the equations, except for the energy equation for which the residual should decrease to 10^{-6}.

4. RESULTS

The heat pipe simulation is performed for 2 different cases, both for the same geometry but with variations in the angular velocity. Constant heat flux is applied to both evaporator and condenser as boundary conditions. The heat input and output are kept constant and equal to each other throughout the simulations. The summary of the simulated cases can be found in Table 1. The initial condition for both cases is the same, with 5 mm of liquid layer at 350 K and vapor at 350 K and 42.5 kPa, representing a saturated initial condition.

Table 1. Simulated cases.

	Angular velocity (rpm)	Heat input / output (W/m^2)
Case 1	200	5000
Case 2	600	5000

Figure 7 shows the axial velocity profiles at various radial locations the two cases. The radial locations of r=0.01 m, r=0.21, r=0.22 m and r=0.24 m represent the vapor core, the vapor flow about 3 cm away from the interface, the vapor flow about 2 cm away from the interface and the vapor flow at the interface, respectively. For both cases, the absolute axial velocity at the core is around zero. This is mainly caused by rotation and by the large diameter to length ratio of the heat pipe. The vapor flow near the interface is from the evaporator to the condenser, as expected, due to the pressure difference. The vapor flow slightly away from the main vapor flow is from the condenser to the evaporator. This phenomenon is called reversed flow and it has been reported in other studies as well [8,10]. The flow reversal occurs because the vapor flowing to the condenser is not completely removed by condensation and because of the lower pressure region at lower radial positions (towards the core of the heat pipe) mainly formed due to rotation of the heat pipe. However in the previous studies [8,10], the reversed flow is observed at the central core. In this study, the flow reversal occurs at higher radial locations compared to other studies (closer to the interface) due to the larger diameter to length ratio of the heat pipe. It should be noted that the reversed flow occurs closer to the interface in the high rotational speed case (at r=0.21 in Case 1 and at r=0.22 in Case 2). This is caused by the higher centrifugal force shifting this flow in the outwards direction. It is further observed that the main vapor flow velocity slightly increases with rotational speed, due to higher evaporation rate.

Figure 8 shows the temperature profiles at various radial locations for both cases. The radial locations are r=0.01 m and r=0.22 m, representing the vapor core and the vapor slightly away from the interface. It is observed that the temperatures at the evaporator, the adiabatic section and the condenser are nearly the same throughout the vapor region. This shows that the heat pipe vapor region acts as a superconductor and the vapor channel resistance for these cases are negligible. This isothermal behavior is also observed in previous studies [7,10].

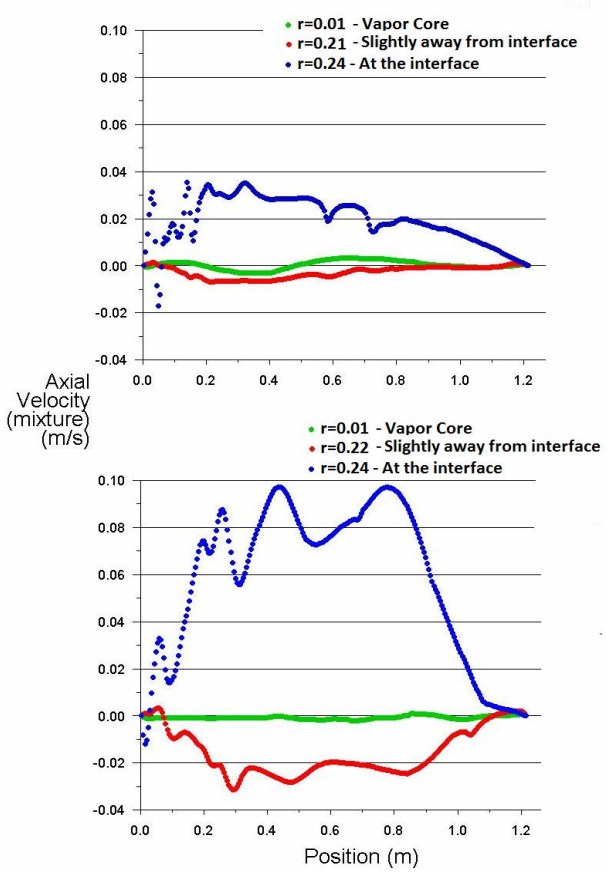


Fig. 7. Axial velocity profiles at different radial positions (Case 1 and Case 2, respectively).

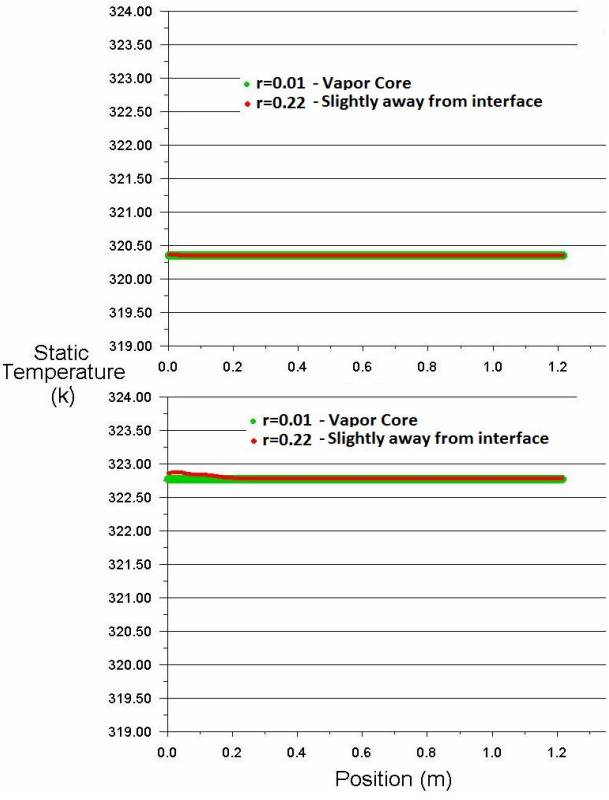


Fig. 8. Temperature profiles at different radial positions (Case 1 and Case 2, respectively).

Table 2 shows the overall heat transfer coefficients at the evaporator and condenser sides for the two cases. The heat transfer coefficients are calculated for the axial positions of x=0.25 m and x=0.96 m, representing the middle of the evaporator and the condenser respectively. With selected *coeff* values in Equations 11 and 12, the heat transfer coefficients at the evaporator side are found to be much higher than the heat transfer coefficients at the condenser side. It is also observed that a clear correlation between the rotational speed and heat transfer coefficient is not found.

Table 2. Heat transfer coefficients at the condenser and the evaporator for the selected *coeff* values in Equations 11 and 12.

	Condenser heat transfer coefficient ($W/(m^2.K)$)	Evaporator heat transfer coefficient ($W/(m^2.K)$)
Case 1	130	2300
Case 2	115	2220

5. CONCLUSIONS

A new 2D axisymmetric swirl model for a rotating heat pipe using water as working fluid is modelled in the commercial software of ANSYS Fluent 15.0. The model is made in the scope of the heat pipe assisted annealing concept. The Euler-Euler approach and the Volume of Fluid (VOF) method are used, along with the Lee model for phase change. The effect of rotational speed on the axial velocity profiles, the temperature profiles and the heat transfer coefficients were investigated with this model. The axial vapor flow from the evaporator to the condenser occurs near the interface. A reversed flow, on the other hand, is observed slightly away from the main vapor flow, significantly away the axis of symmetry. The temperature profiles point to an isothermal vapor region. The next step in this study will be the validation of the results with experimental measurements.

NOMENCLATURE

k : Thermal conductivity (W/(m.K))
 : Mass transfer rate ($kg/(m^3.s)$)
p : Pressure (Pa)
r : Radial coordinate (m)
t : Time (s)
v : Velocity (m/s)
x : Axial coordinate (m)
E : Specific energy (J/kg)
F : External force (N)
L : Specific latent heat (J/kg)
T : Absolute temperature (K)
U : Specific internal energy (J/kg)
α : Volume fraction
μ : Dynamic viscosity (Pa.s)
ρ : Density (kg/m^3)

Subscripts
r : Radial
s : Steam
w : Water
x : Axial
θ : Tangential
sat : Saturation
s-w : Steam to water
w-s : Water to steam

REFERENCES

[1] Gray, V. H., The rotating heat pipe-A wickless, hollow shaft for transferring high heat fluxes, *Proc. of ASME/AIChE Heat Transfer Conf.*, Minneapolis, USA (1969) 1-5.
[2] Reay, D. A., Kew, P. A. and McGlen, R. J., *Heat Pipes Theory, Design and Applications*, Sixth Ed., Butterworth-Heinemann, (2014), 165-167.
[3] Paulussen, G., Corus Technology B. V., Heat pipe assisted strip treatment, WO2011012257 A1 (2011).
[4] Pronk, P., Paulussen, G., Heat pipe assisted annealing to reduce fuel consumption up to 70%, *European Steel Environment & Energy Conf.*, Teesside, UK (2014).
[5] Chan, S. H., Kanai Z. and Yang W. T., Theory of a rotating heat pipe, *Journal of Nuclear Energy*, 25(10) (1971) 479-487.
[6] Marto, P. J., Laminar film condensation on the inside of slender, rotating truncated cones, *Journal of Heat Transfer*, 95(2) (1973) 270-272.
[7] Daniels, T. C. and Al-Jumaily F. K., Investigations of the factors affecting the performance of a rotating heat pipe, *International Journal of Heat and Mass Transfer*, 18(7) (1975) 961-973.
[8] Faghri, A., Gogineni, S. and Thomas, S., Vapor flow analysis of an axially rotating heat pipe, *International Journal of Heat and Mass Transfer*, 36(9) (1993) 2293-2303.
[9] Li, H. M., Liu, C. Y. and Damodaran, M., Analytical study of the flow and heat transfer in a rotating heat pipe, *Heat Recovery Systems and CHP*, 13(2) (1993) 115-122.
[10] Harley, C. and Faghri, A., Two dimensional heat pipe analysis, *Journal of Heat Transfer*, 117(1) (1995) 202-208.
[11] Song, F., Ewing, D. and Ching, C. Y., Fluid flow and heat transfer model for high-speed rotating heat pipes,

International Journal of Heat and Mass Transfer, 46(23) (2003) 4393-4401.

[12]Zuo, Z. J. and Faghri, A., A network thermo-dynamic analysis of the heat pipe, *International Journal of Heat and Mass Transfer*, 41(11) (1998) 1473-1484.

[13]Bergman, T. L., Lavine, A. S., Incropera, F. P. and Dewitt, D. P., *Fundamentals of Heat and Mass Transfer*, Seventh Ed., John Wiley & Sons, (2011), 117-119.

[14]ANSYS Fluent, *Theory Guide (Release 15.0)*, ANSYS Inc., (2013) 474-481.

Comparison between CFD Simulation, Simple Calculation and Experiment Data for Heat Pipe Maximum Heat Transfer, Equivalent Thermal Conductivity and Thermal Resistance

Chayatis Kirdnaimongkol, Masataka Mochizuki*, Thang Nguyen, Yuji Saito, Yoji Kawahara, Tien Nguyen, and Mohammad Shahed Ahamed

Fujikura Ltd. 1-5-1 Kiba, Koto-Ku, Tokyo 135-8512, Japan

Abstract

Commercial computer simulation software required input of thermal conductivity values for thermal simulation. Heat pipe involves a two phase heat transfer phenomenon, not a solid heat conduction device that has a unique thermal conductivity value. Heat pipe equivalent thermal conductivity varies depend on numerous parameters such as heat pipe dimensions, geometries, wick structures, heat transfer capability, and so on. The objective of this study is to develop a simple mathematical model to predict heat pipe performance such as - maximum heat transfer, equivalent thermal conductivity and thermal resistance. The thermal equivalent thermal conductivity then can be used in commercial computer simulation software. The maximum heat transfer calculation is based on the maximum capillary capacity of the wick against total pressure drop associated in the heat pipe. The capillary of the wick and pressure drop in heat pipe are calculated using fundamental fluid equations, while heat pipe thermal resistance and equivalent thermal conductivity are calculated using own modified equation of heat pipe standard thermal resistance. Results of the mathematical model are then compare to the CFD (Computational Fluid Dynamic) simulation and experimental data. The results of the simulation are reasonably well in agreement with the experimental data.

Keywords: Computer cooling; Heat Pipe, Thermal conductivity; 2-Phase heat transfer

1. INTRODUCTION

In the commercial computer thermal and flow simulation software, heat pipe is usually modelled as a solid metal with a fixed value of thermal conductivity. This is not a correct assumption because heat pipe is a two phase heat transfer device, not a solid heat conduction device which has a unique thermal conductivity value. Due to the two phase heat transfer, heat pipe equivalent thermal conductivity varies depend on numerous parameters such as heat pipe dimensions, geometries, wick structures, heat transfer capability, and so on. The objective of this study is to provide a simple mathematical correlation model to predict heat pipe maximum heat transfer, equivalent thermal conductivity and thermal resistance. The calculated equivalent thermal conductivity then can be used in the commercial computer simulation software.

2. FORMULATION

The pressure drop calculation in heat pipe is generally shown in equation 1. The notations dP_{cap} is the capillary pressure of the wick; dP_L is the pressure drop of the liquid; dP_v is the pressure drop of vapor; dP_g is the gravitational pressure loss; and dP_e and dP_c are pressure drop due to evaporation and condensation at liquid-vapor interface respectively. dP_e and dP_c are usually small and will be neglected in this analysis. In order for heat pipe to function properly, the dP_{cap} must be larger or at least equal to the sum of all the pressure losses mentioned above.

$$dP_{cap} \geq dP_L + dP_v + dP_g + dP_e + dP_c \quad (1)$$

The analysis in this paper is only for copper heat pipe with working fluid water, and wick is assumed a spherical copper powder. As shown in equation 2.1, to increase capillary pressure will require high liquid surface tension σ, low contact angle θ (ie. high liquid wettability) and small powder size for low effective pore size radius R_{eff} which is estimated in equation 2.2, and R is the radius of the copper powder.

$$dP_{cap} = 2\sigma\cos\theta / R_{eff} \quad (2.1)$$

$$R_{eff} = 0.41R \quad (2.2)$$

Formula for calculation of the liquid pressure drop is shown in equation 3.1. The notation L, m_L, ρ_L and μ_L are length of heat pipe, liquid mass flow rate, liquid density and liquid dynamic viscosity respectively. High permeability K and large cross sectional flow area A_w of the wick will give low liquid pressure drop. To achieve high permeability

*Corresponding author: mmotizuk@fujikura.co.jp,
Phone: +81-3-5606-1174, Fax: +81-3-5606-1514

required larger powder size, but this would effect on lower capillary pressure. Therefore, iteration is required to achieve the optimum condition. The permeability can be calculated using equation 3.2, where E is the porosity and R is the radius of the copper powder. The optimum condition achieved by experiment is copper powder radius approximately 50 um and porosity 50%.

$$dP_L = \mu_L m_L L / KA_w\rho_L" \quad (3.1)$$

$$K = (2R)^2E^3 / 150(1-E)^2 \quad (3.2)$$

Equation 4 is for the vapor pressure loss calculation. The notation d, f, L, V_v and ρ_v are hydraulic diameter of vapor flow cross sectional area, friction factor, length of heat pipe, vapor velocity and vapor density respectively. Usually, the vapor pressure loss is small in comparison to liquid pressure drop.

$$dP_v = fL\rho_v V^2_v / 2d \quad (4)$$

Pressure drop due to gravity effect is shown in equation 5, where g is gravitational acceleration, h is liquid height and p_L is liquid density. Heat pipe has lower capillary pressure when it operates against gravity (ie. heating section is above cooling section), and vice versa it has higher capillary pressure when it operates with gravity assist (ie. heating section is below cooling section).

$$dP_g = \rho_L gh \quad (5)$$

Formula for calculating the heat pipe thermal resistance is shown in equation 6. In the traditional formulation there was no parameter $f(L_{eff})$. This parameter was newly incorporated to account for the vapor and liquid flow pressure drop which are dependent on the heat pipe length. If without this addition parameter, the heat pipe thermal resistance would remained constant regardless of heat pipe length, and this assumption may be incorrect. The surface areas of evaporation and condensation of heat pipe are denoted as A_e and A_c respectively, and the corresponding heat transfer coefficient of evaporation and condensation are h_e and h_c. Based on our experimental test data from various products, the average evaporation and condensation heat transfer is approximately 15000 W/m^{2}K.

$$R_{hp} = 1/(h_eA_e) + 1/(h_cA_c) + f(L_{eff}) \quad (6)$$

Fig. 1 shows a schematic presentation of the heat pipe. L, L_c, and L_e represent length of heat pipe, condenser, and evaporator respectively. dX or L_{eff} is defined as an effective length. For comparison of thermal conductivity between a heat pipe and a solid metal, we defined the thermal resistance of solid metal as shown in equation 7. The notation A, k and R_{solid} are cross sectional area, thermal conductivity and conduction thermal resistance of solid metal respectively. When equating equations 6 & 7, ie. R_{hp}=R_{solid}, the equivalent thermal conductivity of heat pipe k can be calculated.

$$R_{solid} = dX / kA \quad (7)$$

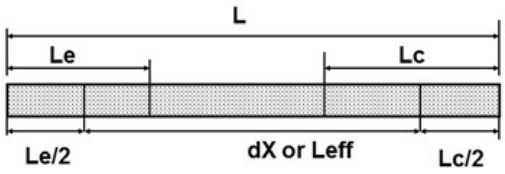


Fig. 1 Schematic of heat pipe model

3. CALCULATION RESULTS

Fig. 2 shows an example of calculation result for heat pipe maximum heat transfer (Q_{max}) and thermal conductance (G) against heat pipe effective length (L_{eff}) for horizontal operating condition. Heat pipe has diameter 6 mm, 300 mm length, and sintered powder wick of thickness 0.75 mm, and has average powder size of 100 um diameter, and porosity approximately 50%. As predicted, Q_{max} and G decreases when L_{eff} increases due to the liquid and vapor pressure drop along the length of heat pipe. Similarly, the heat pipe equivalent thermal conductivity (K_{eq}) and thermal resistance (R) increases with L_{eff} as shown in Fig. 3.

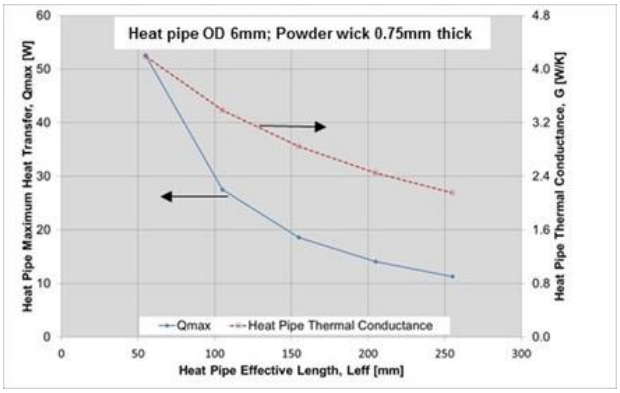


Fig. 2 Heat pipe maximum heat transfer and thermal conductance vs. heat pipe effective length for horizontal operating condition

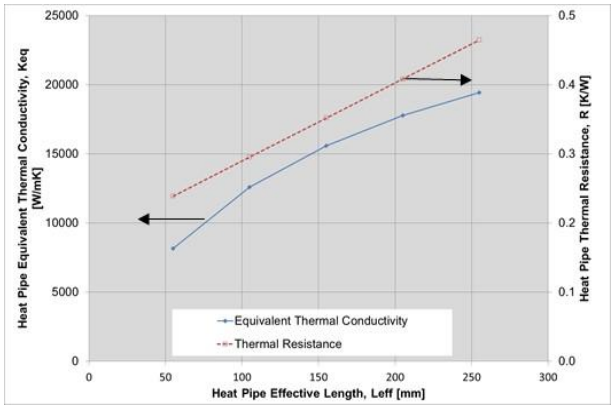


Fig. 3 Heat pipe equivalent thermal conductivity and thermal resistance vs. heat pipe effective length for horizontal operating condition

Fig. 4 shows a summary of heat pipe performance for various operating conditions and they area – horizontal heat mode (heating and cooling position on the same level); bottom heat mode (heating is below cooling position); and top heat mode (heating is above cooling position). It is evidently showed that Q_{max} and G is highest for bottom heat mode where gravity assisted the condensed liquid flow from the condenser to the evaporator. Similarly, Fig. 5 shows K_{eq} is highest for bottom heat mode. Note that the rate of K_{eq} increases lower for top heat mode compare to other modes, and at a certain point it decreases due to a large increases in heat pipe thermal resistance. Fig. 6 shows heat pipe performance for various heat pipe diameter. Calculation results showed that larger heat pipe diameter will give larger Q_{max}, but lower K_{eq}.

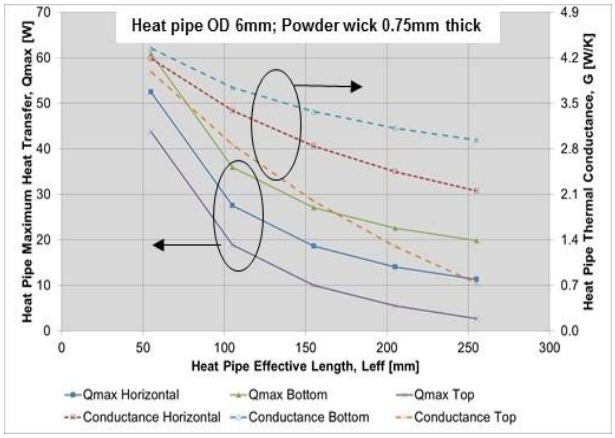


Fig. 4 Heat pipe maximum heat transfer and thermal conductance vs. heat pipe effective length for horizontal, bottom and top heat mode operating conditions

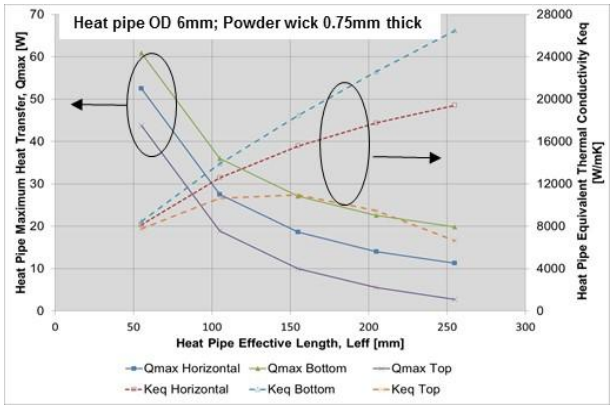


Fig. 5 Heat pipe maximum heat transfer and equivalent thermal conductivity vs. heat pipe effective length for horizontal, bottom and top heat mode operating conditions

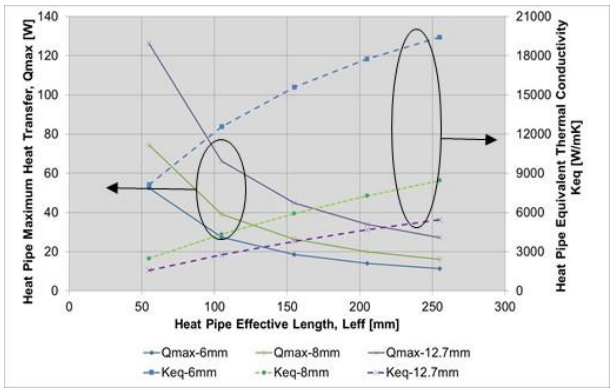


Fig. 6 Heat pipe maximum heat transfer and equivalent thermal conductivity vs. heat pipe effective length for various heat pipe diameter

4. EXPERIMENTAL RESULTS

Table 1 shows heat pipe samples configuration for testing. There are 4 types consist of 2 wick thicknesses 0.75 mm and 1.5 mm, and 2 heat pipe lengths of 200 mm and 300 mm. Fig. 7 shows a schematic diagram of the thermal test set up. T-type thermocouples are placed along and on the external surface of the heat pipe. Heat input to heat pipe is by means of electrical heating cartridges embedded in a copper block which sandwiched the heat pipe at one end. The other end of the heat pipe is cooled by water flows in and out of the liquid cooling jacket in which heat pipe is enclosed.

Table 1. Heat pipe configuration.

	Type A	Type B	Type C	Type D
Heat pipe OD (mm)	6	6	6	6
Heat pipe ID (mm)	5.5	5.5	5.5	5.5
Wick thickness (mm)	0.75	1.5	0.75	1.5
Heat pipe length (mm)	200	200	300	300
Evaporator length (mm)	40	40	40	40
Condenser length (mm)	80	80	80	80

Fig. 8 and 9 show heat pipe thermal resistance against heat input for wick thickness 0.75 mm and 1.5 mm respectively. Experimental results show it is comparable to the theoretical calculation. At the time of writing this paper, there is no conclusive on the results due to limited samples tested. More heat pipe samples of different diameter, length and wick thickness are being make for more extensive testing.

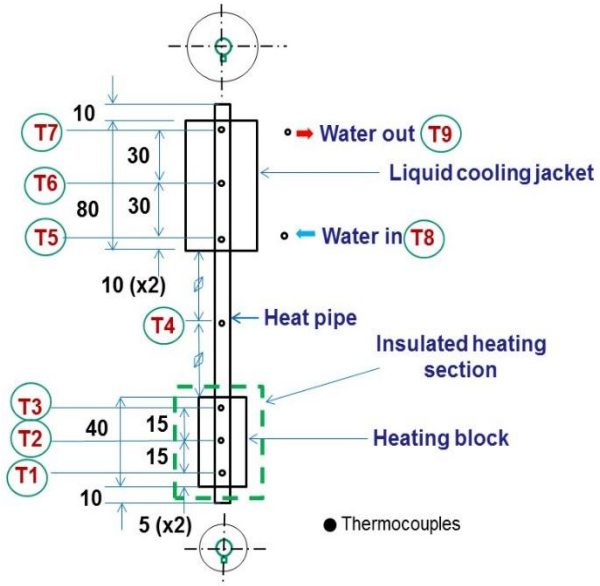


Fig. 7 Heat pipe maximum heat transfer and equivalent thermal conductivity vs. heat pipe effective length for various heat pipe diameter

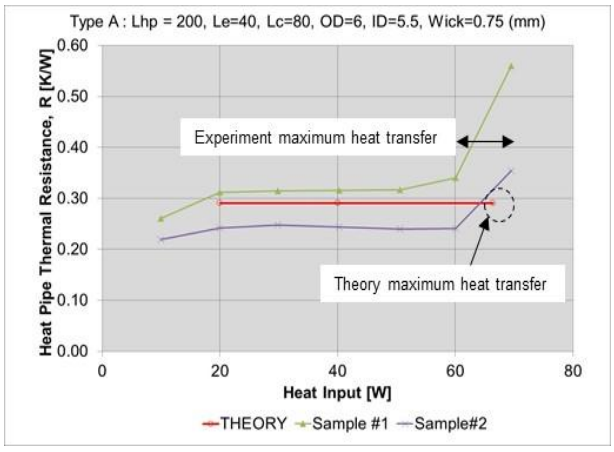


Fig. 8 Heat pipe thermal resistance vs. heat input for heat pipe wick thickness 0.75mm

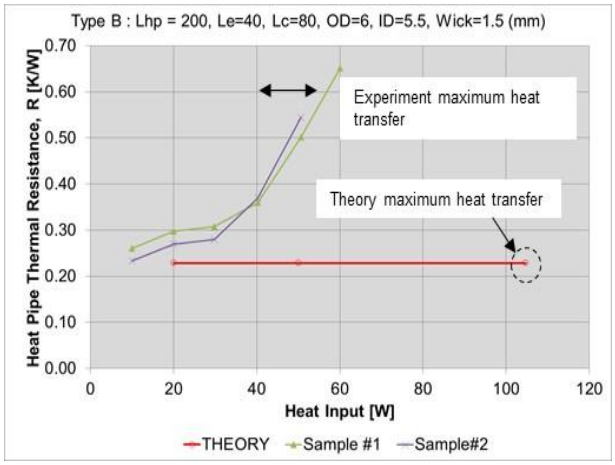


Fig. 9 Heat pipe thermal resistance vs. heat input for heat pipe wick thickness 1.5mm

In regarding to the maximum heat transfer, the calculation and the experiment results are well in agreement for the thin wick 0.75 mm as shown in Fig. 10. However, for thicker wick 1.5mm, data are very much difference between calculation and experiment. The hypothesis for the discrepancy is that for thicker wick, boiling occur inside the wick and generating vapor which block the liquid returning from the condenser to the evaporator, and that will cause "dry-out" of evaporator, and consequently increase heat pipe thermal resistance. Fig. 11 shows heat pipe equivalent thermal conductivity derive from the heat pipe thermal resistance experimental data.

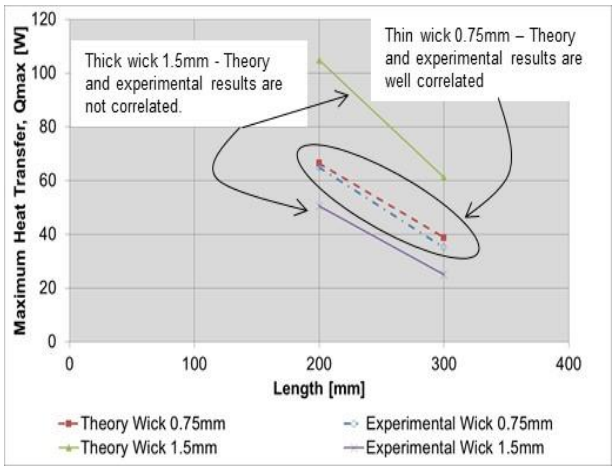


Fig. 10 Heat pipe maximum heat transfer vs. heat pipe length for wick thickness 0.75mm & 1.5mm

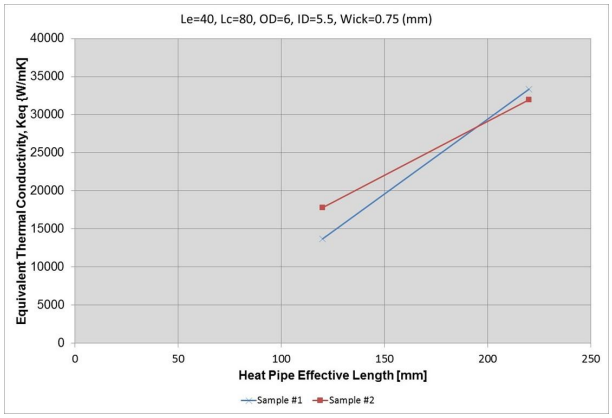


Fig. 11 Heat pipe thermal resistance vs. heat input for heat pipe wick thickness 0.75mm

For the CFD simulation, the input equivalent thermal conductivity is calculated from the proposed mathematical model. The result of heat pipe thermal resistance is shown in Fig. 12, which shows the theory and CFD simulation are in well agreement with experimental data.

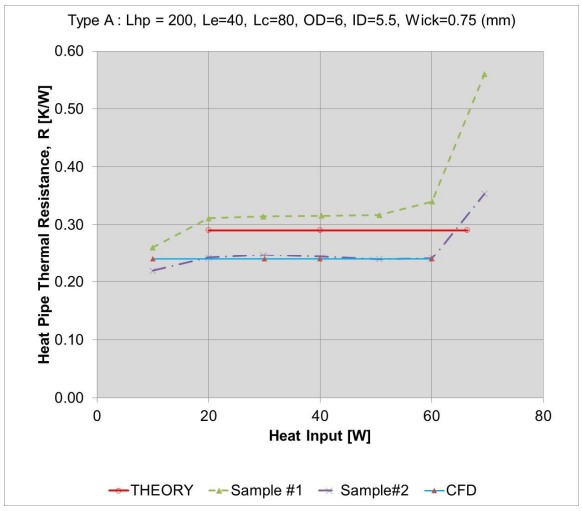


Fig. 12 Heat pipe thermal resistance comparison between theory, CFD simulation and experiment

Another example of CFD simulation is shown in Fig. 13. This is an actual product case which consists of an assembly of heat block, heat pipe and fins heat exchanger. Heat applies at the heat block, and heat pipe transfers the heat to the fins heat exchanger for cooling. Since the design is symmetrical, a half-model is used in the CFD simulation to reduce the calculation run time. The half-model is shown in Fig. 14. The equivalent or effective thermal conductivity calculated from the mathematical model is about 30,000 W/mK, and this value is used in the CFD simulation to calculate total thermal resistance of the product design shown in Fig. 13. Results of the CFD simulation and experimental data are shown in table 2. The heat pipe thermal resistance (R_{hp}) is well correlated, however, the total thermal resistance from heat block to inlet air (R_{ca}) showed large difference. The reasons for the difference values obtained for the R_{ca} are most probably due to the difference of the values assumed for the contact thermal resistance between the mating interfaces, and they are – interface between heat source to heat block; heat block to heat pipe; and heat pipe to fins heat exchanger.

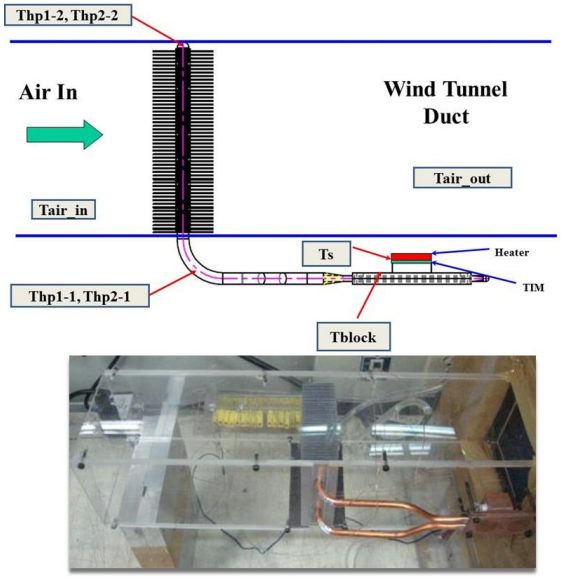


Fig. 13 Product case study for CFD simulation

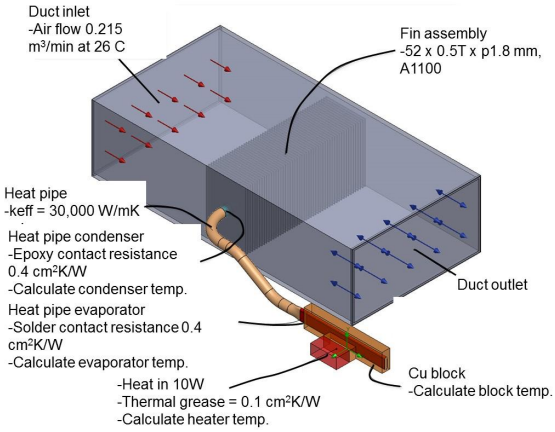


Fig. 14 Schematic of CFD simulation half model

Table 2. CFD and experimental results.

Cases	Heat pipe thermal resistance R_{hp} [K/W]	Total thermal resistance from heat block to inlet air R_{ca} [K/W]
CFD simulation	0.27	0.78
Experimental	0.26	0.51

5. CONCLUSIONS

Proposal of a new parameter f(L_{eff}) in the traditional formula of heat pipe thermal resistance calculation to take into account of the effect of the vapour and the liquid pressure drop which are dependent on the heat pipe length. Otherwise, without this additional parameter, heat pipe thermal resistance would remained constant regardless of heat pipe length, and this assumption may be incorrect.

The maximum heat transfer calculation is well correlated with experimental results for thin wick thickness 0.75 mm. However, it was not correlated for thicker wick thickness 1.5 mm. The hypothesis for the discrepancy is that for thicker wick, boiling occurs inside the wick and generating vapor which blocks the liquid returning from the condenser to the evaporator, and that will cause "dry-out" of the evaporator, and consequently increases the heat pipe thermal resistance.

The calculation and experiment result shows that the maximum heat transfer and the thermal conductance of heat pipe decrease when heat pipe length increase. Heat pipe equivalent thermal conductivity increase when heat pipe length increase up to the maximum heat transfer limit. One would expect that the equivalent thermal conductivity should be constant regardless of length just like a heat conduction in a solid metal. However, because heat pipe transfers heat mainly by a two-phase of evaporation and condensation heat transfer, the temperature differential with length is very small compared to the increases in heat transfer length. Therefore, heat pipe equivalent thermal conductivity always increases with length. But note that this is only applicable up to the maximum heat transfer limit of heat pipe. If the length is longer than the calculated maximum heat transfer limit, then heat pipe thermal resistance can degrades significantly, and causes significant reduction in heat pipe thermal conductivity.

The thermal resistance calculation from the mathematical model, and CFD simulation are well in agreement with the experimental results. Therefore, it is reasonable assumed that the proposed mathematical model works well. This simple mathematical model can be easily created in Excel Spreadsheet for quick but reasonable accurate for estimation of the heat pipe performance such as - maximum heat transfer, equivalent thermal conductivity, thermal conductance and thermal resistance of heat pipe. The model can be used to optimize heat pipe design parameters for a given design specification. The calculated equivalent thermal conductivity then can be used in the commercial computer simulation software.

REFERENCES

[1] Faghri, A. *Heat pipe science and technology*, Taylor & Francis, (1995).

[2] Incropera, F., and De Witt, D., Fundamental of heat and mass transfer, John Wiley & Sons, 3rd edition (1990).

[3] Mochizuki, M., and Nguyen, T., Heat Pipes: Evolution of endless application opportunities, *17th International Heat Pipe Conference (17th IHPC)*, Kanpur, India, 13 October, (2013).

[4] Nguyen, T., Mochizuki, M. et al., Advanced thermal solution using vapor chamber technology for cooling high performance desktop CPU in notebook computer, The 1st International Symposium on Micro & Nano Technology, Honolulu, Hawaii, USA, 4-7 March, (2004).

[5] Mochizuki, M., Nguyen, Thang., Saito, Nguyen, Tien, and Wuttijumnong, V., A simple mathematical model to predict heat pipe maximum heat transfer, equivalent thermal conductivity and thermal resistance, *9th Minsk International Seminar "Heat Pipes, Heat Pump, Refrigerators, Power Sources"*, Minsk, Belarus, 7-10 September, (2015).

[6] Nguyen, T., Mochizuki, M., et al., Advanced thermal solution using vapor chamber technology for cooling high performance desktop CPU in notebook computer, The 1st International Symposium on Micor & Nano Technology, Honolulu, Hawaii, USA, 4-7 March, (2004).

Heat Pipe Heat Exchanger for Heat Recovery: How Much Working Fluid Should we Charge?

L.C. Ding[1*], Y.H. Yau[2], M.F. Remeli[3], B. G. Orr[1], B. Singh[3], A. Date[4], A. Akbarzadeh[5]

[1] Graduate student, School of Aerospace, Mechanical and Manufacturing Engineering, RMIT University, Building 251, Level 1 Bundoora East Campus, Plenty Road Bundoora VIC 3083
[2] Professor, Department of Mechanical Engineering, University of Malaya, Kuala Lumpur, Malaysia
[3] Lecturer, Faculty of Mechanical Engineering, University Teknologi Mara, Shah Alam, Malaysia
[4] Lecturer, School of Aerospace, Mechanical and Manufacturing Engineering, RMIT University
[5] Professor, School of Aerospace, Mechanical and Manufacturing Engineering, RMIT University

Abstract

The countries in the tropics often possess hot and humid climates, which in turn has an impact on the cooling load on both cooling and dehumidification. This impact is even evident when the air conditioning system requires a full requirement of outdoor fresh air, such as hospital operating room (or clean room) where no recirculation allowed for contaminated air. Under such condition, the inclusion a heat recovery system is highly advisable. There are number of devices will able to achieve the purpose of heat recovery. Heat pipe heat exchanger (HPHX) is a static device that will able to perform such heat recovery. The heat pipe heat exchangers are available in vertical (also known as thermosyphon) and horizontal arrangement. When the HPHX is intended to be installed in the ducting system and there is a limit on the ceiling height, the use of horizontal HPHX is needed to accommodate the space allowance. Without the assistance of gravity, the operation of horizontal HPHX is purely rely on the wicking action from the wick in the heat pipe. Hence, adequate charging of working fluid is essential for the optimum efficiency of the HPHX. The optimisation study consists of 150 independent tests (charging ratio of 80% to 120% of wick volume by 20% increment, evaporator inlet temperature of 27°C – 35°C of 2°C increment, air velocity at 1.5 m/s –2.5 m/s with 0.2 m/s increment). Since there will be no moist air condensation for 2-row HPHX (which confirmed to be true in the experiment), the air humidity was excluded in this parametric study. It was found that, optimum filling ratio for a HPHX is 110% of the wick volume in a constant air volume (CAV) system. The HPHX efficiency under the determined optimum condition at 35°C evaporator inlet temperature is 28.3 % and 22.3% at lowest and highest air velocity, respectively. The outcome of this study, will serve as a direct reference for the designer in determining the optimum working fluid charging ratio for the mentioned operating condition.

Keywords: Heat pipe heat exchanger; Heat transfer; Working fluid optimization; Heat recovery

1. INTRODUCTION

Based on the thermal comfort requirement, 24°C is the most desired temperature where the occupant feels comfortable [1]. Hence, the return air temperature (i.e. the condenser inlet temperature of the HPHX) is assumed to have a constant temperature of 24°C in this study. The outdoor temperature in the tropics (near to the equator) flucatuate whithin a limited range, typically 20 °C – 35°C [2]. At this range of evaporator inlet temperature, several working fluids are suitable for the HPHX such as water, acetone, R134a [3]. An experimental study on the performance of HPHX in a fully insulated system (Fig. 1) by variable parameter to obtain optimum working fluid filling ratio was carried out. A test rig as shown in Fig. 1 was set in order to carry out the experiment study. The layout of the test rig is such way due to the limitation of the shape of individual duct and space constrain. The duct has a cross section dimension same as the evaporator or condenser, which is 0.42 x 0.35 m^2. A 2-row HPHX (as in Fig. 2) with dimension of 420mm (L) x 349.25mm (H) and adiabatic length of 180mm, consist of a total of 21 heat pipes with brass wire mesh as the wick are accomodated in the fins of 12 fins per inch (12 FPI). In reality, the number of row for the HPHX will be higher than 2 rows in order to pre-cool the air better. The result from 2-row HPHX will serve as the baseline for 4, 6, or 8-row HPHX.

In order to have a temperature control, a heater control box was designed base on calculated power which is needed for heating. The heater box is able to provide 5.5 kW of heating; it utilizes a 3 phase power supply and 3 wires RTD as feedback sensor. A variable speed fan was used as to provide different flow volume in the duct. In order to obtain the air velocity across the HPHX, a traverse study is done. As to obtain a better measurement of the air velocity, an extra duct and flow straightener was built to required length and dimension at the downstream of the fan. The function of a flow straightener is to effectively produce a virtually uniform velocity of

*Corresponding author: s3403093@student.rmit.edu.au,
Phone: +(61)399256183

flow across the air stream. It is also used to eliminate eddies and the rotation of the air stream produced by the change in direction due to the test product configuration and/or the fan. Information on the required dimension of flow straightener can be obtained is available [4]. The duct was fully insulated with Superloan insulation sheet with thickness of 1/2 inch.

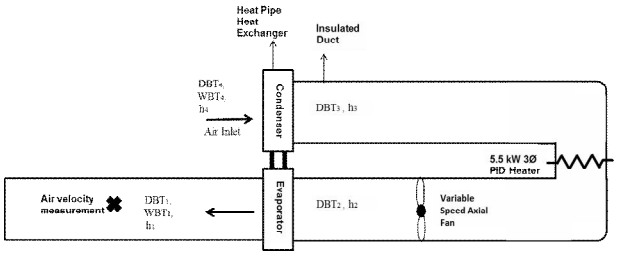


Fig. 1. Experimental setup.



Fig. 2. The insulated 2-row HPHX.

2. METHODOLOGY

In present work, a few independent variables are involved, which is, flow velocity, percentage of working fluid charging of wick volume, evaporator inlet temperature. Dependent variable of the experiment is temperature difference across evaporator and hence heat pipe's effectiveness. For flow velocity, a velocity range of 1.5-2.5 m/s is set with 0.2 m/s increment. This is the typical velocity range where air flows in a duct. Five different charging percentage of working fluid 80%, 90%, 100%, 110%, 120% of wick volume, are the second group of parameters in the experiment. As mentioned, the working fluid in this experiment is R134-a. The mass of R134-a corresponds to the different charging percentage are 15.5g, 17.4g, 19.4g, 21.3g, 23.3g respectively, by referring to the R134-a density and wick volume. The charging process was done by using a weighing scale of 0.5g accuracy, Dupont R134-a refrigerant, charging hose and charging manifold, as well as vacuum pump.

Third group of parameters in this experiment is the evaporator inlet temperature. The inlet temperature has to correspond to the outdoor dry bulb temperature range. Temperatures of 27°C, 29°C, 31°C, 33°C, and 35°C are chosen to represent the outdoor air temperature range. Evaporator inlet temperature lower than 27°C is not tested in this experiment, since the heat exchange will not be significantly occurs. The condenser inlet room temperature is fixed at a nominal value of 24°C. Thus, for this series of experiments, tests were performed as follows:

- Fluid charge values of 80%, 90%, 100%, 110%, and 120%.
- Face velocity values in the range of 1.5 m/s-2.5 m/s with 0.2 increments.
- Evaporator inlet DBT values, 27°C, 29°C, 31°C, 33°C, 35°C.

There are a total of (5 x 6 x 5) 150 tests in this experiment. For determining the sensible and total effectiveness, following conditions are assumed.

i. The testing rig has a steady flow and the air is well mixed at each measuring state so that all measured psychometric properties are representative of each air state.
ii. The HPHX is operating under steady state conditions for supply of fresh air and exhaust coil leaving air during each experiment.
iii. No external energy is supplied into or lost from the HPHX between its inlet and outlet states (i.e. the HPHX is fully insulated and the intervening heat transfer to environ can be neglected).
iv. For 2-row heat pipe, the HPHX operate sensibly, with no dehumidification.

Note that assumption (i), (ii) and (iii) made above are recommended in ANSI/ASHRAE [5]. Since the supply of condenser inlet air is from room air, thus, it is assumed that the air entering the condenser is well mixed. The air entering evaporator is assumed to be well mixed by the blowing action of axial fan before the coil. From the intervening heat transfer study, by letting the heat pipe being empty charged, it was found that the maximum temperature difference between the coil for both evaporator and condenser were 0.1°C.Thus, intervening heat transfer was neglected. From the room (wet bulb and dry bulb) temperature readings, it was found that the relative humidity in the laboratory is around 20-40 % RH. Thus, after undergoing heating process in the condenser, and heater, the air RH condition for

evaporator inlet should be lower, and the air state is far away from the saturation line in psychometric chart. By this reason, assumption (iv) was made. The instruments involved in this experiment were 6 Pt 100 Class A Resistance Temperature Detectors (RTD), Measurement Computing's USB TEMPT with 8 channels temperature measurement, which can support thermocouple, RTD, thermistor as well as semiconductor sensor which function as Analog Digital Converter. Dasylab software, which is compatible with the data logger, was used to acquire the data from the sensor. The RTDs were calibrated at the range of 10 to 50°C against a laboratory Fluke Dry-Well calibrator having an accuracy of +/-0.1°C and stability of 0.01°C. A VelociCalc Air Velocity Meter (TSI Model 8345) with the accuracy of +/-0.015 m/s was used to measure the face velocity by carrying out the velocity traverse through 25 point grid in the testing duct. 25 traverse measuring points using Log Tchebycheff Rule for rectangular duct was used in the velocity traverse study as require by ANSI/ASHRAE [6].The air velocity at certain point is measured when the reading is steady. A few set points were set in order to have a relation between the axial fan set frequency and air flow rate. The relationship between these two variables should be linear. Thus, required air flow (i.e. air velocity) was interpolated to required frequency setting. Every time before commencing the test, all RTDs were put into a water container to detect any drifting in the reading. The dry bulb temperatures at every measurement point were recorded at 1 second intervals. For each testing condition, the data were taken around 5 minutes after changing the parameter setting for each test, after the steady condition had been reached. In the Dasylab module, steady state condition was defined as the changing of temperature readings were less than 0.2°C within 30 seconds. The mean value for 60continuous data was calculated and the values were used in the calculations.

The effectiveness is judged to be the most relevant in determining the performance of an HPHX as a means of energy savings. The effectiveness for an HPHX, ε_{HPHX}, is defined as the ratio of the actual heat transfer rate to the maximum possible heat transfer rate:

$$\varepsilon_{HPHX} = \frac{\dot{q}_{actual}}{\dot{q}_{\max}} \tag{1}$$

where

$$\dot{q}_{actual} = \dot{m}_s (h_2 - h_1) \tag{2}$$

and

$$\dot{q}_{\max} = \dot{m}_{\min} (h_2 - h_4) \tag{3}$$

From equations (1) – (3), it follows that the total effectiveness can be determined by:

$$\varepsilon_t = \frac{\dot{m}_s (h_2 - h_1)}{\dot{m}_{\min} (h_2 - h_4)} \tag{4}$$

where h_1 is the fresh air specific enthalpy [in kJ/kg] (State 1), h_2 is the coil entering air specific enthalpy (State 2) and h_4 is the coil leaving air specific enthalpy (State 4); and where $\dot{m}_s$ is the air mass flow rate of the supply fresh air; $\dot{m}_e$ is the air mass flow rate of the exhaust coil leaving air; and $\dot{m}_{\min}$ is the smaller of $\dot{m}_s$ and $\dot{m}_e$. However, in the presence study, $\dot{m}_s = \dot{m}_e = \dot{m}_a = \dot{m}_{\min}$ in which law of mass conservation applies and therefore, equation (4) can be simplified to:

$$\varepsilon_t = \frac{(h_2 - h_1)}{(h_2 - h_4)} \tag{5}$$

Note that the mass flow rate for both inlets is same, thus, the effectiveness recorded were the lowest value of possible effectiveness of the HPHXs for constant air volume. Besides, equation (5) can also be used to determine the sensible energy effectiveness with the exception that the dry bulb temperature, T instead of specific enthalpy, h.

$$\varepsilon_{sen} = \frac{\dot{q}_{actual}}{\dot{q}_{\max}} = \varepsilon_t = \frac{(T_2 - T_1)}{(T_2 - T_4)} \tag{6}$$

Since there will be no error analysis done on the data, in order to make checking the data obtained, the ratio of temperature difference across evaporator to temperature difference across condenser was used to ensure the temperature difference including respective uncertainty range are at least overlap. Acceptable range for the ratio is range from 0.8 to 1.2, with ratio of equal to unity is very desirable.

3. RESULT AND DISCUSSION

Fig. 3. to Fig. 7 show the influence of face velocity on the temperature across evaporator, i.e. the heat transfer across evaporator, for different

working fluid charging percentage. For every types of working fluid charging volume, the heat transfer across evaporator decrease as the air velocity increase. It may be attributed to the fact that by increasing the face velocity or mass flow rate, the duration time to exchange heat is insufficient (a decreased in opportunity for contacting the fin) and consequently heat transfer between air and tubes decreases. Also, the maximum temperature difference (3.15°C) occur when evaporator inlet temperature is 35.3 °C at 110% working fluid charging of wick volume, air velocity of 1.5 m/s, whereas minimum temperature (0.49°C) when the evaporator inlet temperature is 27.2°C at 80% working fluid charging of wick volume, air velocity of 1.9 m/s.

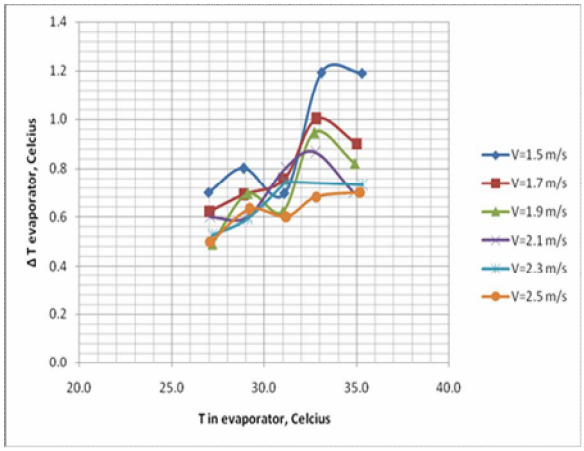


Fig. 3. Temperature difference across evaporator vs. inlet temperature for 80% charging.

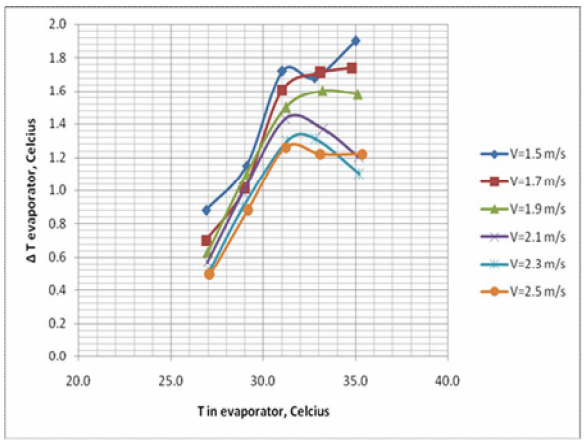


Fig. 4. Temperature difference across evaporator vs. inlet temperature for 90% charging.

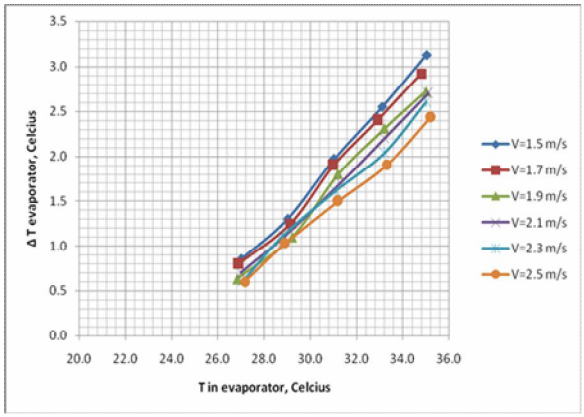


Fig. 5. Temperature difference across evaporator vs. inlet temperature for 100% charging.

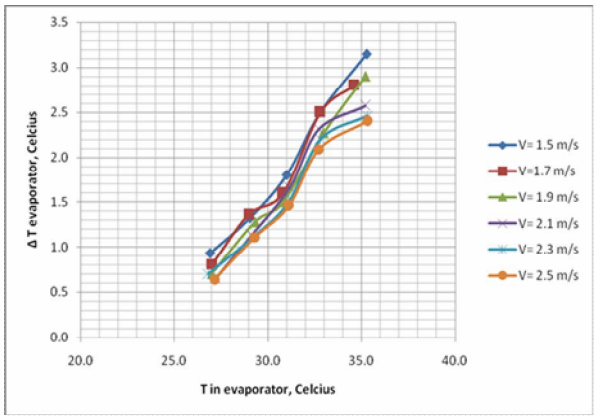


Fig. 6. Temperature difference across evaporator vs. inlet temperature for 110% charging.

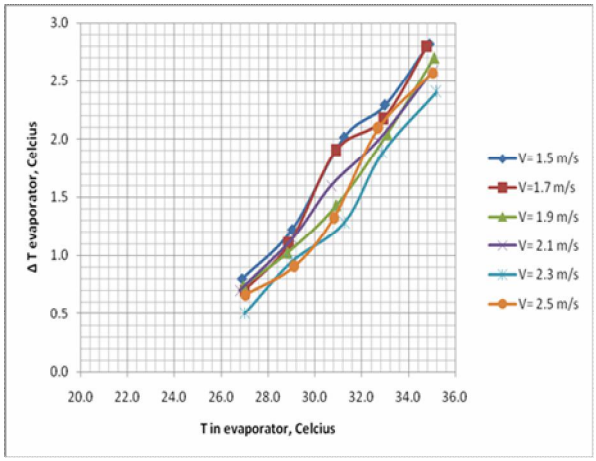


Fig. 7. Temperature difference across evaporator vs. inlet temperature for 120% charging.

Also, from Fig. 3 to Fig. 7, with a smaller-than-saturation charge, the temperature difference is reduced when inlet temperature increase, but

with larger-than-saturation charge, the temperature difference is increase as evaporator inlet temperature increases, since maximum possible heat transfer is increased. For convenience, contour plots are plotted using SigmaPlot as to give a clearer insight on the results. The contour plots are obtain from a surface plot which is smoothed via smoother LOESS (Locally Weighted Scatter plot Smoothing), sampling proportion of one with polynomial degree of 2. From the contour plots shown in Fig. 8, working fluid charging of 110% of wick volume is most optimize in order to give a best performance for inlet temperature of 27°C to 25°C. Therefore the present research support the idea that for optimum performance of heat pipes the fluid charge should be slightly more than the amount required to saturate the wick.

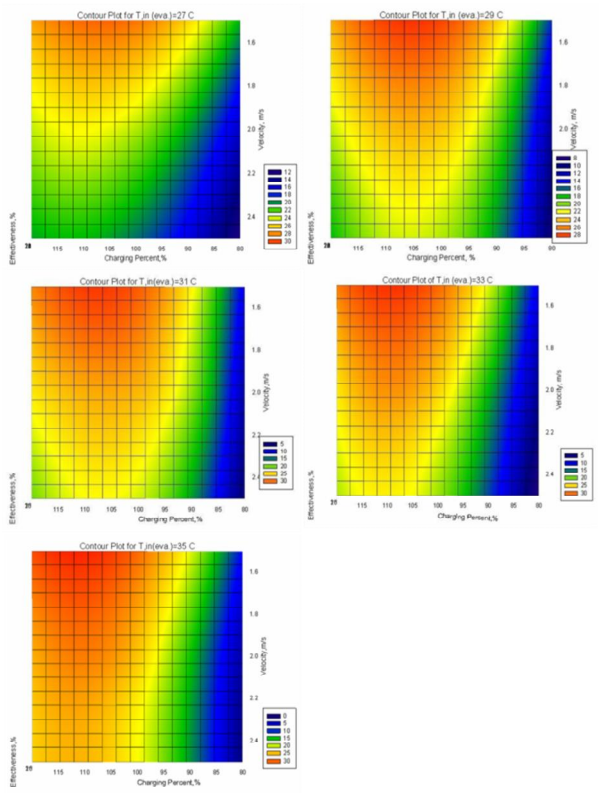


Fig. 8. Contour plot for the efficiency of HPHX with respect to optimisation parameters.

4. CONCLUSIONS

The optimum filling ratio for a HPHX is 110% of the wick volume in a constant air volume (CAV) system. The HPHX efficiency under the determined optimum condition at 35°C evaporator inlet temperature is 28.3 % and 22.3% at lowest and highest air velocity, respectively.

ACKNOWLEDGEMENT

The authors would like to acknowledge the full financial assistance from the Ministry of Science, Technology and Innovation (MOSTI), Malaysia, via e-Science Fund Project no. 13-02-03-3034 for research work to be conducted in the University of Malaya, Kuala Lumpur, Malaysia.

NOMENCLATURE

ε : Efficiency
$\dot{q}$: Heat transfer (W)
$\dot{m}$: Mass flow rate (kg/s)
h : Enthalpy (kJ/kg)
T : Temperature (°C)

REFERENCES

[1] Y.H. Yau, B.T. Chew, Adaptive Thermal Comfort Model For Air-Conditioned Hospitals In Malaysia, *Building Services Engineering Research & Technology*, CIBSE, Sage Publications, Vol. 35(2)，pp. 117-138, 2014.
[2] Malaysian Meteorological Department, http://www.met.gov.my/
[3] P. D. Dunn, D. Reay, Heat Pipes,3rd edition, Elsevier, pp. 90-91, 2012.
[4] ANSI/ASHRAE (1991a), Laboratory Methods of Testing Fans for Aerodynamic Performance Ratings, ASHRAE, Atlanta, Standard 51-1999.
[5] ANSI/ASHRAE (1991b), Method of Testing Air-to-air Heat Exchanger, ASHRAE, Atlanta, 1991, Standard 84-1991.
[6] ANSI/ASHRAE (1992), Standard Methods for Laboratory Airflow Measurement, ASHRAE, Atlanta, Standard 41.2-1987 (RA 1992).

Hybrid Cooling System for High-power Laser Diodes

Leonid L. Vassiliev[1], Leonid P. Grakovich[2],Shu Shili[3], Hou Guanyu[3],Wu Hao[3],Wang lijie[3], Tian Sicong[3], Tong Cunzhu[4]

[1]*Ph.D, Head of Porous media Lab, Luikov Heat and Mass Transfer Institute, National Academy of Sciences of Belarus ,15 Brovka Str., 220072 Minsk Belarus, Phone: +375445333275, e-mail: leonid.l.vasiliev.jr@gmail.com*
[2]*Ph.D, Porous Media Lab., Luikov Heat and Mass Transfer Institute,* National *Academy of Sciences of Belarus*
[3]*Ph.D, State Key Lab of Luminescence and Applications, Changchun Institute of Optics, Fine Mechanics and Physics, Chinese Academy of Sciences*
[4]*Professor, Deputy Director of State Key Lab of Luminescence and Applications, Changchun Institute of Optics, Fine Mechanics and Physics, Chinese Academy of Sciences (3888 Dongnanhu Road, Changchun 130033, China, Phone: 8643186176348, e-mail: tongcz@ciomp.ac.cn*

Abstract

This study is focused on the application of the heat pipes and thermoelectric cooler modules in thermal management system of the solid state laser (SSL) diodes. Such combination of cooling techniques is significant to make laser diode (LD) in compact size, light weight with low energy consumption, which is essential especially for the portable SSL units. Furthermore, this cooling system is able to cool the LDs down to the temperature below ambient. SSL radiator that consist of five 8 mm ID copper heat pipes with sintered powder inside it and can easily handle with up to 330 W heat loads comes from four TEC modules at the temperature below 45 degree C.

Keywords: Heat transfer, Heat pipe, Porous media, Solid laser

1. INTRODUCTION

The high-power LD is employed in a wide range of industrial applications as pumping of solid-state lasers (SSL). For example, in medical sector SSL are widely used as surgical instruments Aerospace and military applications for LDs include electro-optical systems for field uses such as LIDAR, target illuminators, target designators, or high-energy lasers. Also LDs are used to precisely cut the material in the production of sophisticated designed products. LDs efficiently convert electric energy into laser light. In particular, near infrared (IR) LDs operating between about 800 and 1000 nm typically have 50-60% electro-optical conversion efficiency, while LD operating around 1300-1600 nm have electro-optical efficiencies around 35-40%[1]. Electric power not converted into optical output is turned into waste heat, which must be efficiently removed to ensure normal operation. The typical issues in SSL associated with LD thermal management are the ultra-high peak power, super-high electro-optical conversion efficiency, low beam divergence, high brightness, narrow spectrum line width, high operation temperature, high reliability, wavelength stabilization and fundamental transverse mode operation etc. Therefore, thermal management and thermal stress diminishing are critical points for the compact sized lasers.

In many applications, the conventional liquid cooling system and associated controls add undesirable complexity, size, and weight. Therefore, there is a big room for two phase flow cooling in the future of thermal control of LD because of high heat transfer coefficients and low thermal resistance [2-3]. If there is a necessity to cool down LD below ambient temperature, two phase heat sink ought to be combine with active cooler such as thermo electrical (Thompson effect) or refrigerator unit.

Since more than 10 years a number of papers were devoted to the analyses of SSL improvement performance by applying the combination of heat pipes and TEC modules [4-6]. The aim of this study is the development of heat pipes based heat sink with the operating temperature limit below 45 degr. C.

2. SSL RADIATOR DESIGN

The entire experimental equipment is composed of the SSL radiator, support unit, data acquisition system and power supply unit. The SSL radiator (Fig. 1) that have been under investigation in this study consist of copper board with five embedded

*Corresponding author: leonid.l.vasiliev.jr@gmail.com, Phone: +375-44-5333275, Fax: +375-172-842133

evaporators of HPs, box with HPs finned condenser and two air fans. The heat load is supplied by five TEC modules (TEC1-12708), attached to the radiator copper board from its hot side. On the opposite cold side of the TEC elements there are LDs fixed through the thermal grease.

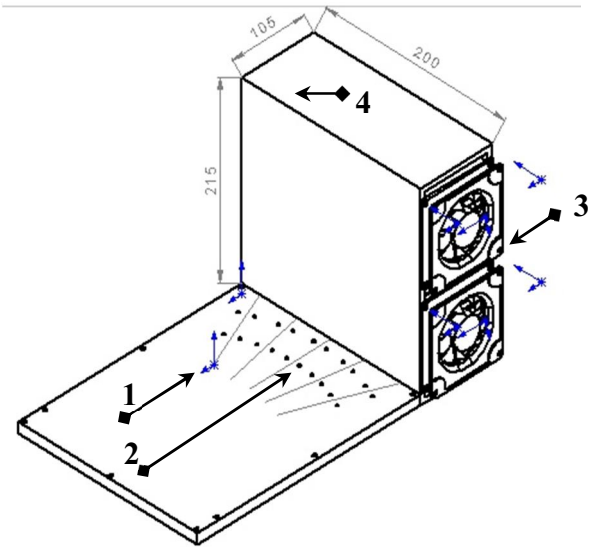


Fig.1. SSL radiator. 1- HP evaporator embedded in the copper board (CB); 2- holes to attach TEC elements to CB; 3- air fans; 4 – box with finned HP condensers.

Five 8 mm ID copper heat pipes with copper sintered powder inside it were embedded in 200x250 mm radiator copper board. As the HPs working fluid the refrigerant R 290 (propane) was selected. The R 290 has a relatively large surface tension and latent heat capacity under the operation temperature in the range of (-30) – 45 °C.

The cooling fins (215×200×105 mm^3), a fan (NF-A9 DC 12 V, 0.1 A), and a duct are attached at the HPs condenser to achieve the forced convection cooling. Thermal grease (MX-4, 0.9 W/m °C) is applied between the CB and TEC modules to minimize the thermal contact resistance.

The stabilized power supply unit Agilent 34410A has been used as the source of energy in order to tune the applied power with tolerance +/- 0,1 W for any TEC. The temperatures drop between the outer wall of the heat pipes and the atmosphere are measured using T-type thermocouples. The thermocouples are attached via soldering to two locations on the 120 mm long evaporator section, one location on the adiabatic zone and two locations on the condenser section of the heat pipe. The temperature distribution along heat pipes is measured using twenty six copper-constantan thermocouples (T–type). To monitor the temperatures evaluation of the copper board of radiator during the test, the set of thermo resistors Heraeus Sensor Technology (FRG) L-420 (and M-422) class A is used. All thermo sensors are connected with Data Acquisition Switch Unit Agilent 34970A. Therefore, the accuracy of the temperature measurement is not exceeded +/- 0,02 ^{0}C. The tested radiators reach the steady state conditions when temperature deviation is not exceeded 0,1 degree C for 5 minutes approximately after 30 minutes from the start. Then all experimental data were recorded each 5 seconds and store in the computer file.

2.1 Copper HPs thermal performance.

The copper heat pipe L-type with horizontal evaporator having copper sintered powder wick saturated with R290 as the working fluid and vertical finned condenser have been chosen in this study to achieve of high local heat removal rate at low temperature. Heat pipes require an effective wick design because they are made with 90 ^{0} bend between the evaporator and condenser to improve heat transfer from circuit boards to the air flow. Sintered powder wick because of the close particle to particle spacing, generate very high pumping capabilities as compared to more conventional grooves or mesh screen wicks. Moreover, they have relatively high thermal conductivity in turn means a higher heat flux performance capability, due to the enhanced fin effect which the sintered powders provides in the evaporator region of the heat pipe. But an efficient sintered powder wick needs to be optimized to ensure the high heat flux performance capability. The problem of the wick structure optimization is related with structural porous wick parameters: the particle size and its form, wick porosity, specific surface of porous wick, pore diameter. The heat pipe with sintered wick guarantees the uniform temperature distribution in radiator copper board.

For the successful operation of the heat pipe the HP wick has to provide capillary head, which is equal or exceeds all pressure losses in the system.

$$\Delta p_c \geq (\Delta p_{sum}) \geq \Delta p_l + \Delta p_v \pm \Delta p_{gr} + \Delta p_{phc} \qquad (1)$$

where Δp_c is the capillary pressure losses which are the function of liquid surface tension forces, pore radii r_{pr} and solid surface wettability:

$$\Delta p_c = \frac{2\sigma \cos\theta}{r_{pr}} \quad (2)$$

It is important to note that the pressure loss due to phase change Δp_{phc} is not significant for such kind of HP and could be not taking into account. Thus the pressure balance equation ought to be expressed as:

$$\Delta p_c \geq \Delta p_l + \Delta p_v + \Delta p_{\parallel} + \Delta p_{+} + \Delta p_{\delta} \quad (3)$$

where Δp_l and Δp_v frictional pressure losses along liquid and vapor paths, $\Delta p_{\parallel}$ and Δp_{+} pressure losses along and across of the heat pipe due to action of the gravity force and Δp_{δ} - pressure losses due to working fluid trapping by the wick in the HP condenser.

The pressure losses in the HP vapor path is evaluated by the Poiseuille equation :

$$\Delta p_v = \left(\frac{C(f_v \operatorname{Re}_v)\mu_v}{2(r_{h,v})^2 A_v \rho_v h_{fg}} \right) L_{eff} Q \quad (4)$$

where $L_{eff}=0.5L_e+L_a+0.5L_c$ and values C and f_v Re_v are depended on the vapor flow regimes.Following the Darcy equation the pressure losses in the HP $_{liquid}$ path could be found as:

$$\Delta p_l = \left(\frac{\mu_l}{K A_w h_{fg} \rho_l} \right) L_{eff} Q \quad (5)$$

where K represents the wick permeability. Hydrostatic pressure head across and along the HP could be accordantly expressed as:

$$\Delta p_{+}=\rho_l g d_v \cos\varphi,\ \Delta p_{\parallel}=\rho_l g L \sin\varphi \quad (6)$$

Capillary force by action of which the working fluid trapped in the wick on the HP evaporator zone could be determinate as:

$$\Delta p_{\delta}=2\sigma\cos\theta/r_{h,\delta}. \quad (7)$$

As it was mentioned above, the main strict limitation in the HP cooling capability is the capillary limit:

$$Q_c = \frac{\Delta p_c - \Delta p_{+} + \Delta p_{\parallel} - \Delta p_{\delta}}{\Delta p_v / Q + \Delta p_l / Q} \quad (8)$$

and, finally, by taking into account the equations (2-7), the equation (8) could be expressed in next form:

$$Q_c = \frac{\left(\frac{1}{r_c} - \frac{1}{r_{h,\delta}} \right) 2\sigma\cos\theta - \rho_l g d_v \cos\varphi + \rho_l g L \sin\varphi}{\left(\frac{C(f_v \operatorname{Re}_v)\mu_v}{2(r_{h,v})^2 A_v \rho_v h_{fg}} + \frac{\mu_l}{K A_w h_{fg} \rho_l} \right) L_{eff}} \quad (9)$$

Assuming that a vapor pressure loss in HP due to action of the gravity force is negligible and Re_v >2300, equation (9) could be simplified as:

$$Q_c = \frac{\frac{2\sigma\cos\vartheta}{r_m} - \rho g l \sin\varphi}{L_{ef}\left(\frac{\mu_l}{\rho_l \pi h_{fg} (D_{in}^2 - D_{ch}^2) K} + \frac{128\mu_v}{\pi h_{fg} D_{ch}^{\ 4} \rho_v} \right)} \quad (10)$$

2.2 Results of the experimental data

In this experimental set up 5 heat pipes evaporators were installed inside of CB of SSL radiator parallel to its flat surface (Fig.1). Propane (R290) was chosen as a beneficial working fluid for heat pipes due to its good thermodynamic properties, low cost, availability, compatibility with constructional materials, and environmental friendliness. Sintered powder capillary wick of HP enhances heat transfer not only in the regime of formation of a thin liquid film but also when there are the liquid pool and flooded surface. In this case wick plays the role of additional centers for stable vapor generation, which do not require high superheating of the surface.

The results of the experiments with HPs are shown on Fig.2-6. During experiments the temperature of the HP evaporator was maintained near 40 degree C. As one can see from the Fig.2-6, HP cooling capability is increased with rising of the operation temperature. Also it's important to note that the experimental data are in good correlation with calculated ones and a capillary limit is only one which should be taken into account for the simulation of the HP with sintered wick thermal performance.

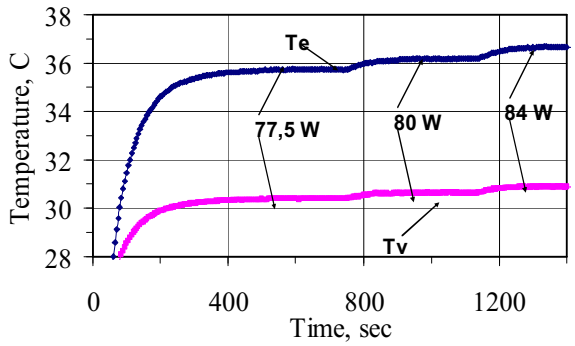


Fig. 2. Temperature evolution of the HP evaporator surface T_e and the saturated vapor in the vapor flow T_v as a function of time for different heat load Q.

The thermal resistance R_e of the HP evaporator, Fig.3, slightly decreases from 0.08 K/W to 0,075 K/W as a function of Q in the heat load interval 40-90 W.

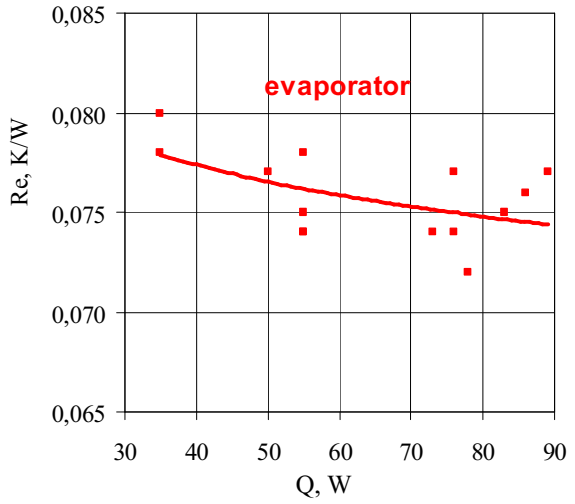


Fig.3. The HP evaporator thermal resistance R_e as a function of the heat load.

The mean thermal resistance R_c of the HP condenser was near two times less to compare with the R_e (evaporator thermal resistance) due to the long length of the condenser and the air convection cooling of the HPs condenser fins. The thermal resistance R_c of the HP condenser, Fig.4, is increasing from 0.04 K/W up to 0.053 K/W as a function of heat sink Q (heat load) in the interval 40-90 W.

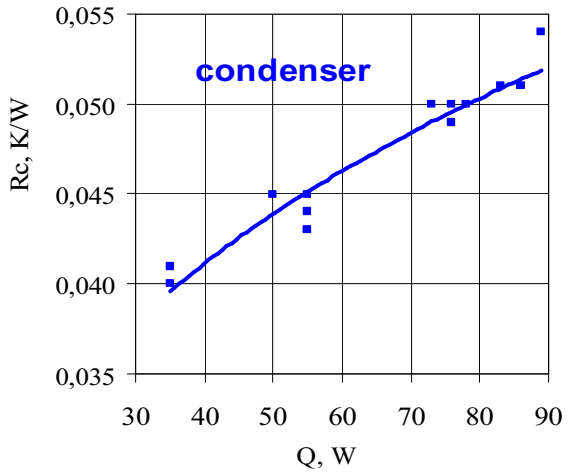


Fig.4. The HPcondenser thermal resistance R_c as a function of different heat loads Q.

Following the calculated data (validated by the experimental data) the mean heat transfer coefficient α_e in the HP evaporator is near constant (4800 W/m ^{0}K) for the heat load diapason Q from 35 W up to 90 W, Fig.5.

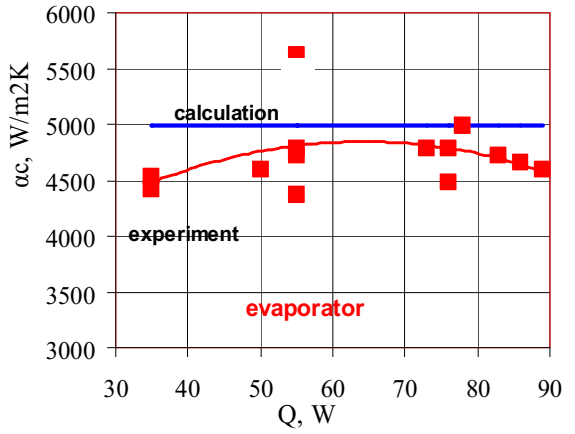


Fig.5. Heat transfer coefficient α_e in the HP evaporator as the function of heat load Q (W).

In the HP condenser the mean heat transfer coefficient (calculated and experimental data) is decreasing from 2500 W/m^{2}K down to 1900 W/m^{2}K) when the heat load of HP is increasing from 35 up to 90 W, Fig.6.

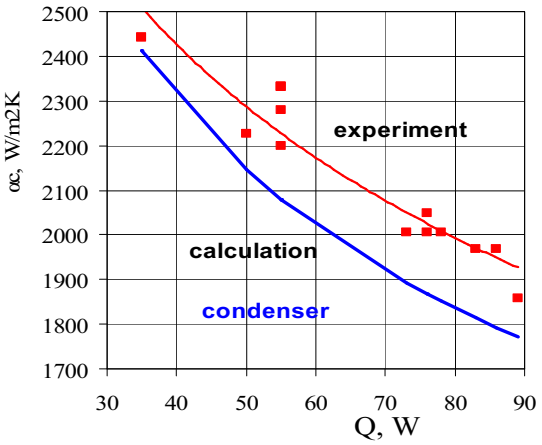


Fig.6. Heat transfer coefficient α_c in the HP condenser as the function of heat load Q (W).

3. SSL RADIATOR THERMAL PERFORMANCE

The set of experiments was performed to evaluate the SSL radiator cooling capability and maximum temperature level of CB for different heat loads and steady-state operation cycles. On the Fig. 7 is shown the position of the seven thermal sensors on the surface of SSL CB. The mean CB temperature level was used later for SSL analysis. For all tests, two air fans with blowing flow rate 2,3 m/s were used to remove heat from the HPs finned condenser. For fixed cooling conditions and space orientation, a step-by-step increasing and decreasing heat load was applied (five steps, each step is 50 W up to 330 W, starting from Q=100 W) in order to detect the maximum cooling capability of SSL radiator for the operation temperature limit.

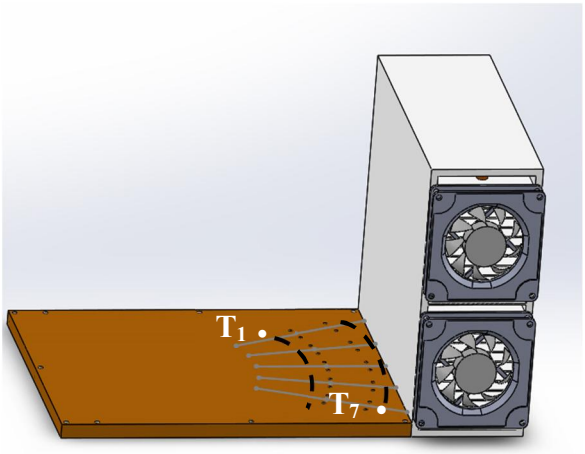


Fig. 7 SSL radiator sheme with thermal sensor positions (dash lines) .

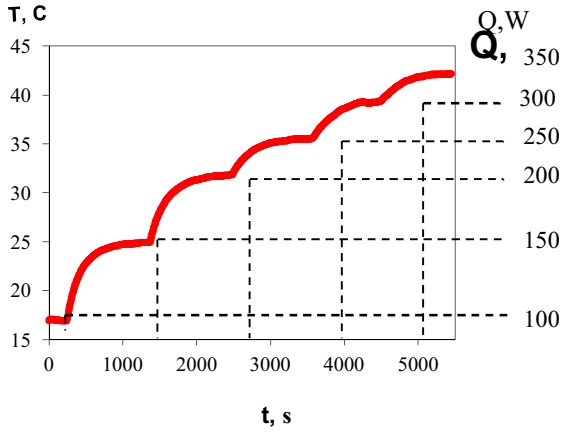


Fig.8. SSL mean temperature evolution in the time period 0-5.000 s for different heat load (100-330 W). The room temperature is 17 °C.

Figure 8 shows that the SSL radiator with 5 HPs and R 290 as a working fluid transports up to 330 W keeping the temperature of heat wall below 45°C. This latter is the maximum admissible temperature for the LDs that were under investigations in this study.

4. CONCLUSION

1. SSL radiator based on heat pipes application for the intense SL diode cooling was suggested, developed and tested in the temperature range 17-40 ^{0}C and heat load interval 100W-330W, using air force convection as a heat sink.
2. Due to a small thermal resistance of the SSL (HP) radiator the mean temperature of the SSL was less 40 ^{0}C for the heat load on the SSL radiator 300 W.
3. The HP used as the cooling component of the SSL has 8mm diameter, made from the copper, has a sintered copper wick saturated with R290 as a working fluid.
4. The thermal resistance of the HP evaporator (120 mm long) is near 0.075 K/W, while the thermal resistance of finned HP condenser is 0.04-0.05 K/W.

ACKNOWLEDGEMENT

This work is supported by International Science Technology Cooperation Program of China (No 2013DFR00730) and State Program of Scientific Researches of Belarus “Power systems, Processes and Technologies”, Task 2.19

NOMENCLATURE

A – heat transfer surface, m^2 ; D – diameter, m; f –coefficient of friction; g – gravity force, m/s^2; h_{fg} – latent heat, Jg/kg; K – permeability , m^2; L – HP length, м; Q – heat load, W; p – pressure, Pa; σ – surface tension, Н/м; ρ – density, kg/m^3. Subscripts : a- adiabatic; c- capillary, condenser ;	e – evaporator; eff- effective; h- hydraulique; l- liquide; pr – pore ; v- vapor ; w- wall ; ch-channel ; m- mean ;

REFERENCES

[1] John Vetrovec, "Quasi-Passive Heat Sink for High-Power Laser Diodes" *Paper N 7198-12 LASE 2009 Conference, San Jose, CA, January 26-30*2009.

[2] L. L. Vasiliev, "Heat Pipe in Modern Heat Exchangers", *Applied Thermal Engineering*, Elsevier, (01) (2005) 1-25.

[3] L.L. Vasiliev," Micro and Miniature Heat Pipes" *Chapter in the Book Title Microscale Heat Transfer Fundamentals and Applications,* (*Vol. 193*) *of series NATO Science Serie II, Physics and Chemistry (2004) 413-428.*

[4] Atul Bhardwaj*, Lalita Agrawal, and Anil Kumar Maini, "Design and Development of Intracavity Optical Parametric Oscillator-based Eye Safe Laser Operating at 20 Hz without Forced Air Cooling", *Defense Science Journal (63/3) (2013) 599-605.*

[5] Tsung-Han Tsai, Hsin-Tang Chien and Ping-Hei Chen, "Improvement on thermal performance of a diskshaped miniature heat pipe with nanofluid", *Nanoscale Research Letter (2011)*

[6] Rasheed Nema Abed, "The Thermal Management System of Laser Diode. A Review", *ARPN Journal of Engineering and Applied Sciences (10-12) (2015) 5250-5260*

Self-Venting Arterial Heat Pipes for Spacecraft Applications

William G. Anderson[1], Derek Beard[1], and Calin Tarau[1]

[1] *Advanced Cooling Technologies, Inc. 1046 New Holland Ave., Lancaster, PA 17601, U.S.A.*

Abstract

NASA is examining small fission reactors for future space transportation and surface power applications, with alkali metal heat pipes to supply energy to the Stirling convertors to produce electricity. Simultaneously, titanium/water heat pipes will be used to carry the waste heat from the convertors to a radiator, where the heat is rejected. The entire system must be tested on Earth before launch, and must be able to operate in micro-gravity, as well as on the Moon and Mars. Grooved and arterial wicks are the default design for heat pipes operating in micro-gravity; however, these heat pipes are not suitable for a nuclear power system. Unlike earlier spacecraft heat pipes, these heat pipes must be capable of operating in the following orientations: operation in space, with zero gravity; operation on earth, with a slight adverse orientation, to estimate performance in space; ground testing, with the heat pipes operating gravity aided; and launch, with the evaporator elevated above the condenser. During vertical ground testing, the heat pipe wick will de-prime, and will need to re-prime for operation in space after launch. Hybrid grooved and arterial self-venting heat pipes offer potential benefits over the standard arterial heat pipes: 1. The grooves cannot be de-primed, and 2. The self-venting pipes are less susceptible to de-priming, as well as having a lower mass. The self-venting arterial wick design was chosen for these heat pipes, since this design is known to automatically re-prime after de-priming, and could carry the required power for the alkali metal pipes with a smaller diameter. A series of sodium/Haynes 230 heat pipes with a self-venting wick were fabricated and tested. These heat pipes will be tested in a complete, electrically heated reactor system next year.

Keywords: Heat pipe, Kilopower, Self-venting arterial wick, Spacecraft thermal control, Thermosyphon, Spacecraft fission power

1. INTRODUCTION

NASA is examining small fission reactors for future space transportation and surface power applications [1, 2]. The Fission Surface Power System (FSPS) is designed to operate from 10 to 100 kWe while current Radioisotope Power Systems (RPSs) operate below 500 We. The Kilopower system would address the power gap between current RPS and FSPS, with power generation from 1 to 10 kWe.

The Kilopower system uses sodium heat pipes to carry the power from the nuclear reactor to the Stirling convertors to produce electricity; see Figure 1. Simultaneously, titanium/water heat pipes will be used to carry the waste heat from the Stirling to a radiator, where the heat is rejected. The Kilopower system will be designed to operate in space, as well as on Earth, the Moon, and Mars.

Previous spacecraft heat pipe designs have neglected ground testability, and assumed a grooved wick. The Kilopower heat pipes must accommodate four different operating conditions:

1. Operation in space, with zero gravity. Liquid is returned from the condenser to the evaporator by capillary forces in the wick.
2. Operation on earth, with a slight adverse orientation, to estimate performance in space. The heat pipe is operated with the evaporator slightly oriented above the condenser. The adverse orientations are typically 0.1, 0.2, and 0.3 inches.
3. Ground testing, with the heat pipes gravity aided. The heat pipes will deprime in this orientation.
4. Launch, with the evaporator elevated above the condenser

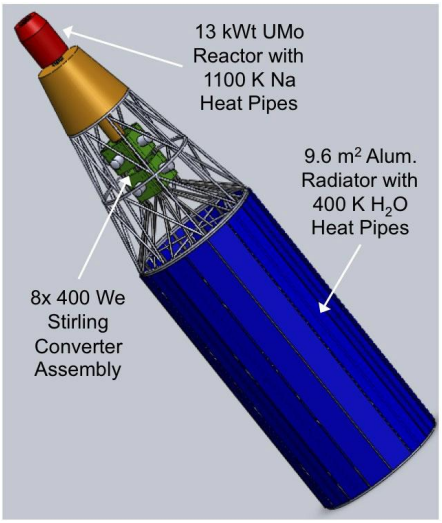


Figure 1. Nominal Kilopower system [1].

*Corresponding author: Bill.Anderson@1-act.com
Phone: +1-717-295-6104, Fax: +1-727-295-6064

2. HEAT PIPE WICKS

The length of the Kilopower titanium/water heat pipes can be up to several meters. There are four types of wicks that carry significant power over these long distances in space:

1. Arterial heat pipes with sintered powder (or screen) wicks
2. Grooved heat pipe wicks
3. Hybrid grooved screen wicks
4. Russian self-venting arterial heat pipes.

Arterial and grooved heat pipes are not suitable for this application. The arterial pipes will de-prime during testing and during launch and it is not possible to reliably re-prime arterial pipes. Grooved heat pipe designs that will work in space have also been developed but the grooved wick is unable to prime the evaporator in a vertical orientation, which is necessary for ground testing of Kilopower.

The two wicks that can be used for the Kilopower system are the hybrid grooved/screen wick, and the self-venting arterial heat pipe. The hybrid wick has a porous wick in the evaporator, and grooves in the adiabatic and condenser sections.

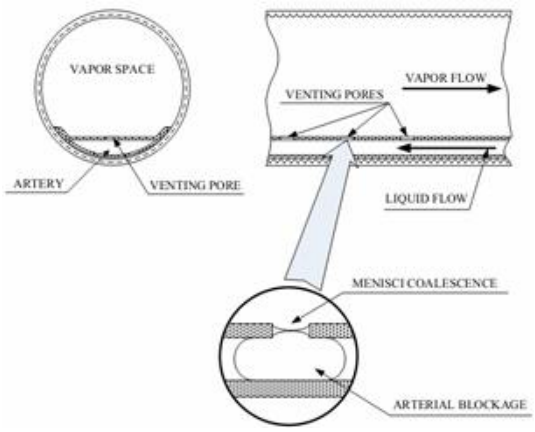


Figure 2. Russian developed self-venting arterial heat pipe with a screen wick. [3]

The wick design chosen for the Kilopower hot end heat pipes is a self-venting arterial heat pipe developed by Goncharov et al. at Lavochkin in Russia [4]; see Figure 2. Standard arterial heat pipes utilize a single artery as well as a screen or sintered wick for liquid return. The combination of a single artery with a screen wick gives the heat pipe the benefit of a wick with high effective liquid permeability as well as a small pore size and thus a high capillary limit. When the artery is primed (full of liquid), arterial heat pipes can transfer high heat loads over long distances. On the other hand, the heat pipe fails if the artery is de-primed by non-condensable gas generation or vapor generation in the artery. These standard arterial heat pipes are not suitable for Kilopower, as discussed below, since the arteries will deprime during ground testing. To allow the arteries to reprime, self-venting arterial heat pipes use small venting pores that are located in the evaporator section of the heat pipe.

2.1 Wick De-priming

During ground testing the Kilopower system will be oriented so that the proposed heat pipes will be operating vertically as thermosyphons. In this orientation the arteries in the heat pipe will deprime due to the variation in liquid pressure along the length of the heat pipe due to gravity; see Figure 3. Assume that the heat pipe is in a vertical orientation and not operating. In this case, the vapor pressure and liquid pressure at the bottom of the heat pipe are identical. As the height increases, the liquid pressure drop decreases, due to the hydrostatic head. Figure 3 shows the location along the length of the heat pipe where the pressure ΔP between the liquid and vapor is equal:

$$\Delta P = \frac{2\sigma}{r_c}$$

At higher elevations, vapor will be sucked into the artery, depriming it. Since these heat pipes are more than 1 m high, they are always deprimed when operating vertically.

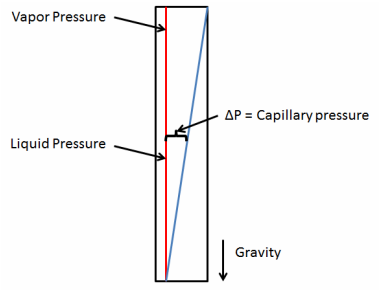


Figure 3. Vapor pressure vs. liquid pressure comparison in a long, vertical heat pipe.

3. DESIGN AND FABRICATION

3.1 Design Requirements

The heat pipe developed on the current program will be used in a 1 kWe Kilopower reactor that is

being developed by NASA Glenn and the Department of Energy. Table 1 gives the heat pipe design requirements. The minimum power that each heat pipe must carry is 380W, but higher powers are desirable to demonstrate operation if one of the heat pipes fail.

Table 1. Kilopower heat pipe design requirements.

Total Thermal Power, kW	3
Number of Heat Pipes	8
Heat Pipe Power, W	380
Operating Temperature, °C	720 - 800
Working Fluid	Sodium
Envelope Material	Haynes 230
Wick Material	Stainless 316
Heat Pipe O.D., in. (cm)	0.5 (1.27)
Wall Thickness, in. (cm)	0.035 (0.089)
Evaporator Length, in. (cm)	14 (35.6)
Adiabatic Length, in. (cm)	34 (86.4)
Condenser length, in. (cm)	3.5 (8.89)

The heat pipes must operate both as gravity aided thermosyphons, and in space. Operating is space is simulated by testing the heat pipes almost level, with a slight adverse elevation (0.1 inch, 0.254 cm).

When tested in a horizontal orientation, the artery spontaneously reprimes. When tested in a vertical orientation, the artery deprimes. Roughly 3 in. (7.62 cm) of the heat pipe extends below the reactor, to provide a small sump to accommodate some of the fluid.

3.2 Working Fluid and Envelope Selection

Table 2. Sodium/superalloy heat pipe life tests

Material	Hours	Operating Temperature	Ref.
316L SS	115,000	650 to 700°C	[4]
Hastalloy B	14,400	1020°C	[5]
Hastalloy X	29,600	1000°C	[5]
Haynes 188	22,500	900°C	[5]
Haynes 230	20,000	~ 700°C	[4]
Haynes 230 (NaK)	7500	750°C	[6]
Inconel 601	83,000	600 to 650°C	[4]
Inconel 617	>25,000	680°C	[7]
Inconel 625 (NaK)	800	700°C	[8]
Inconel 718	41,000	~ 700°C	[4]

The potential working fluids in the temperature range of interest are sodium and potassium. Potassium was eliminated from consideration, since it reacts strongly with fast neutrons.

A list of stainless and superalloy materials compatible with sodium is shown in Table 2. The 316 stainless steel is suitable for the wick, but not for the envelope, since it has very little structural strength at the operating temperature. Haynes 230 was chosen because it has the best creep strength at elevated temperatures.

3.3 Kilopower Heat Pipe Design

The design considered both self-venting arterial wicks, as well as hybrid screen/groove wicks. Both wick designs can easily carry the required power in a 0.75 in. (1.91 cm) O.D. heat pipe in a slight adverse orientation. From a reactor design consideration, 0.5 in. (1.27 cm) O.D. pipes gave a better design. The hybrid wicks could not carry the required power, so a self-venting arterial design was selected.

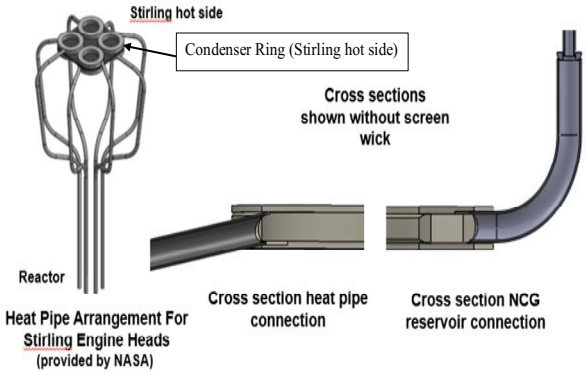


Figure 4. Kilopower sodium heat pipes.

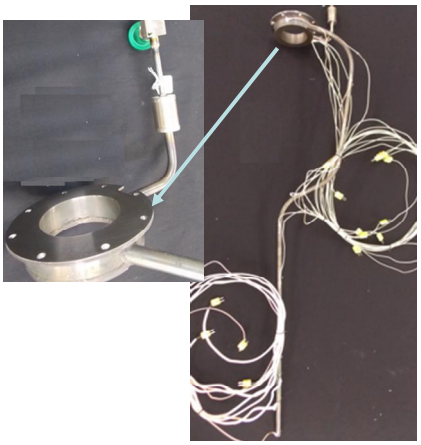


Figure 5. Kilopower heat pipe with thermocouples attached. The insert shows the annular condenser, which for this heat pipe mounts to the underside of the mounting plate.

A schematic of the Kilopower sodium heat pipes is shown in

Figure 4, and a picture is shown in Figure 5. The evaporator is located next to the reactor core, fitting into a semi-circular groove. The adiabatic section jogs out and then back in, around the reactor shielding. The annular heat pipe condensers are attached to a mounting plate. Heat is conducted from the condenser to the Stirling convertors through the mounting plate. This design is not thermally efficient; it was chosen so that the Stirling convertors will be easy to remove after testing.

The heat pipes have a Non-Condensable Gas (NCG) reservoir to aid in start-up. Two of the heat pipes have a larger reservoir that can be electrically heated to shut the heat pipe down, simulating a heat pipe failure. Thermocouple locations are shown in Figure 6.

Given the number (8) of heat pipes required by the Kilopower system and the cost and risks associated with the self-venting arterial wick development, it was decided that both thermosyphons and self-venting arterial heat pipes will be developed. Note that the geometry of both types of heat pipes is the same, the only difference being the wick inside the heat pipe envelope.

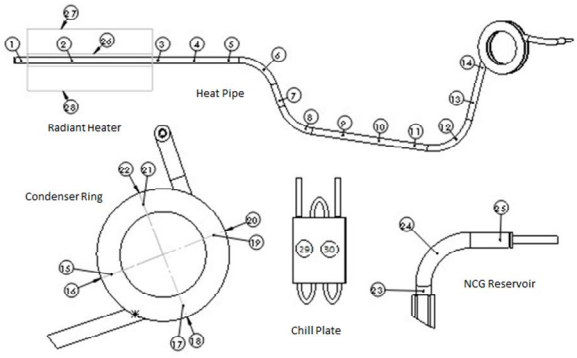


Figure 6. Thermocouple locations and numbering.

4. RESULTS

Repriming of alkali metal heat pipes with self-venting arteries has been demonstrated in a previous paper [10]. This paper reports on vacuum testing of two self-venting arterial heat pipes with 0.4 inches unfavorable elevation and also on ambient testing of the thermosyphons in vertical position.

4.1 Self-Venting Arterial Heat Pipes for Space

The arterial wick developed for the two Kilopower heat pipes was made of stainless steel screen with square shaped artery with holes for NCG or vapor venting in the evaporator. The artery went from the bottom of the liquid reservoir below the evaporator all the way up to the entrance of the annular condenser. The condenser wick did not have an artery. A thick layer of screen wick was attached to the internal adiabatic surfaces of the condenser to decrease the hydraulic resistance for the liquid return in compensation for the lack of artery.

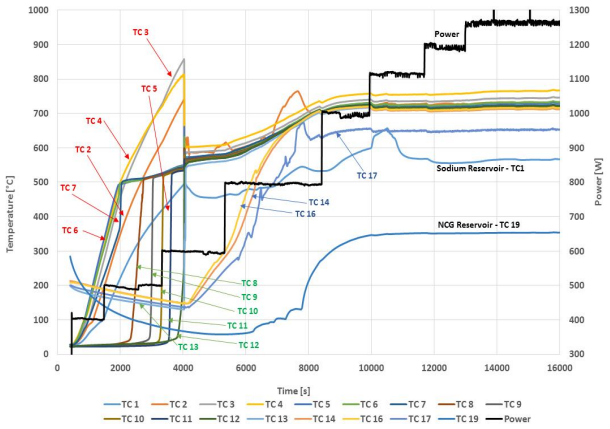


Figure 7. During rapid start-ups, there is a large temperature spike in the heat pipe evaporator temperature, required to initiate boiling.

As mentioned before, the two arterial heat pipes were tested in vacuum at a 0.4 in (1 cm) adverse elevation. Since the fabrication procedure required the bending of the pipes with primed sodium arteries, two tests were performed for each pipe. The first test was performed on straight pipes before bending, to assure the presence of sodium in the artery and the second test was performed after bending, on the final geometry of the heat pipe. The performance of each of the two heat pipes is shown in Table 3 for both straight and bent geometries.

Table 3. Performance of self-venting arterial heat pipes with 0.4 inches of adverse elevation

Pipe #	Performance (W)	
	Straight	Bent
1	370	210
2	405	290

As seen Table 3, the heat pipe performance decreased after bending for both pipes. Since the final performance for each pipe was below the requirements (380W), the wick is being redesigned. The results of this development will be published in more detail in a future paper.

4.2 Ground Tests of the Thermosyphons

As mentioned above, the second category of heat pipes developed for the Kilopower program was thermosyphons and they were tested in ambient in vertical position.

When testing vertically, sodium drips down along the walls in the adiabatic section. When the heat pipe is turned off, all of this sodium drains into the evaporator.

The sodium charge was determined experimentally, by adjusting the sodium charge to maximize the power. With our initial heat pipe and heat collector, the charge was much larger than what would be calculated from a falling film analysis. This occurred due to fluid pooling in the flat condenser, and in the "horizontal" portions of the adiabatic section. When the heat pipe was shut down, the sodium occupied 13 inches of the evaporator.

Nine heat pipes (thermosyphons) were developed and delivered for the Kilopower program. The pipes were intensively tested before delivery. The performance for each of the nine thermosyphons is shown in Table 4. The measurements were performed in ambient and the heat losses were 570W. As seen in the table, since the requirements were met, dry out was not reached for any of the heat pipes.

Table 4. Heat pipe performance

Pipe No	Electric Power	Net Power	Dry Out
1	1250	680	No
2	1250	680	No
3	1200	630	No
4	1050	480	No
5	1150	580	No
6	1250	680	No
7	1200	630	No
8	1250	680	No
9	1200	630	No

Alkali metal heat pipes are known for having difficulties at startup because of several reasons: the necessary superheat to initiate boiling, the low sonic limitation that chokes the pipe during its temperature increase towards the operating point and finally because of potential freezing of the working fluid in the condenser. Adding NCG inside the heat pipe is a typical method in addressing the start-up difficulties. One of the effects is that it gives a shorter effective heat pipe length during start-up, since the NCG blocks most of the adiabatic section. However, in the heat pipes under discussion, the presence of NCG did not mitigate entirely the start-up related temperature spikes. An example is shown in Figure 7. The heat pipe started up successfully, but still required a very large superheat in the evaporator before starting up. As discussed below, this is very common with a deep alkali metal pool.

4.3 Thermosyphon Modifications

The start-up related difficulties occurred because the evaporator was partly filled with liquid sodium. Two changes were made to the system to reduce the required sodium inventory. First, the slopes of the two roughly horizontal sections of the heat pipes were increased, improving drainage.

Second, the liquid hold-up in the annular condenser was reduced. As shown in

Figure 8, the heat collector plate that is the actual heat sink for the condensers was modified so that each condenser sloped towards the adiabatic section of the heat pipe. As discussed below, these changes improved the start-up behavior.

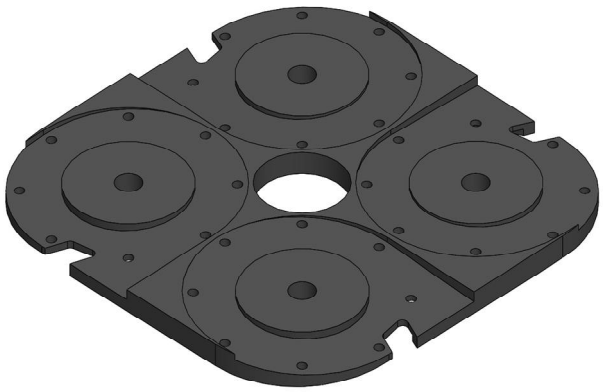


Figure 8. The heat collector plate was modified to add slopes under each condenser, allowing them to drain more easily.

4.4 Alkali Metal Pool Boilers

Besides reducing the sodium inventory, an additional change was made to improve start-up. As shown in Figure 7, the evaporator wall temperatures can exceed 800°C before the heat pipe starts, with superheats of several hundred degrees. This occurred because most of the evaporator was full of liquid sodium during start-up. High superheat is a known problem with alkali metal pool boilers [9]. For the heat pipe to start operating, boiling in the liquid pool must occur. In alkali metal systems, the alkali metal cleans off the oxides on the surface, suppressing

the nucleation sites. The wick helps to suppress the superheat, but further modifications are required.

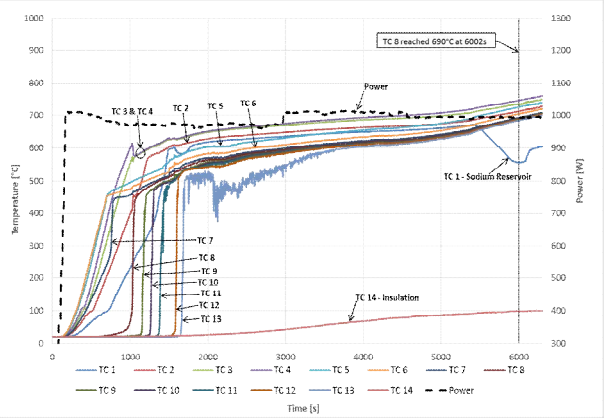


Figure 9. Start-up was improved by modifying the evaporator wick to lower the sodium pool. This start-up at 1000 W has a much lower temperature spike, with improved start-up time.

The easiest solution would be to add a larger sump to hold the liquid sodium during start-up. Unfortunately, the reactor design considerations allowed only a short stub below the reactor. As discussed above, the angled heat transfer interface between the condenser and the heat collector plate increased the slope of the roughly horizontal sections of the heat pipe, both of which lowered the total sodium charge.

In addition, the evaporator wick was modified by adding screen in the evaporator, filling the inner diameter almost entirely except a 0.125 in. (3.2 cm) diameter hole in the center for vapor venting. The additional portion of the screen has a larger pore size allowing the primary wick to retain the liquid during normal operation. Since start-up improvement was a major requirement for the Kilopower program, intensive testing was carried for the new evaporator wick configuration. The new evaporator wick was inserted in a 0.5 inch outer diameter stainless steel tube with 0.35 inch wall thickness and 48 inch length. Four individual tests were carried for four constantly applied powers: 800, 900, 1000 and 1100W.

Figure 9, shows as an example the case where a power of 1000W was constantly applied during start-up. As seen in the figure, despite the high power applied constantly, the temperature spikes did not exceed 600°C. Moreover, all of the four tests showed significant start-up improvement in terms of both temperature spikes and start-up time necessary for the pipe to reach nominal temperature.

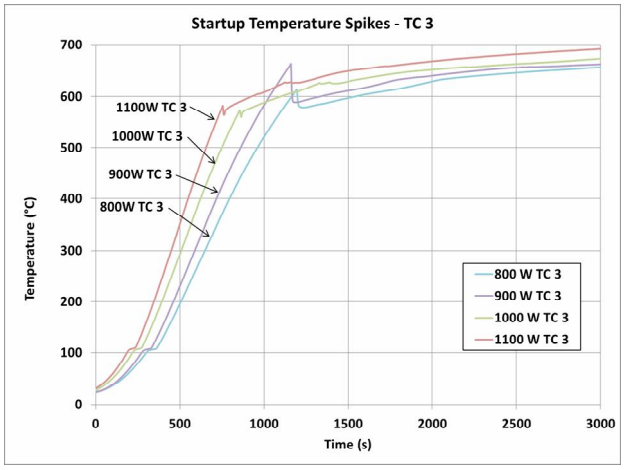


Figure 10. Temperature evolution of TC 3 during start-up for all four powers

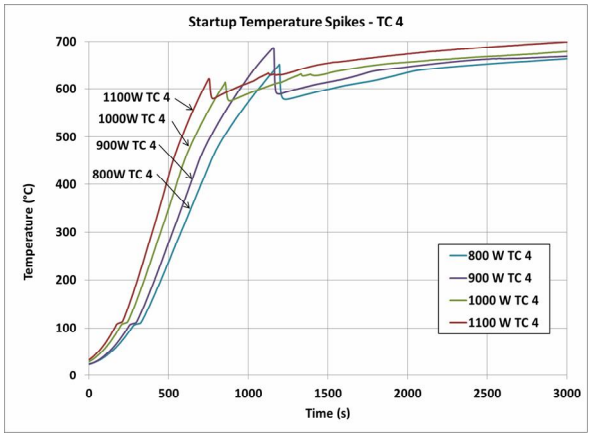


Figure 11. Temperature evolution of TC 4 during start-up for all four powers

Figure 10 and Figure 11 show the temperatures recorded by TC 3 and TC 4 during start-up for all the four start-up power mentioned above. These thermocouples are attached to the lowest portion of the evaporator and their exact locations are shown above in Figure 6. As seen in Figure 10 and Figure 11, the value of the highest temperature spike is 692°C and is recorded at the location of TC 4 when a power of 900W is applied. Taking into consideration that this value is already lower than the nominal operating temperature (720-810°C) in the actual system while the applied power is significantly higher than in the actual system (400 – 500W per pipe) it can be concluded that the start-up improvement was a success. Moreover, the start-up time was also significantly reduced from several hours to values around two hours depending of the total power applied and the operating point as shown in Figure 12

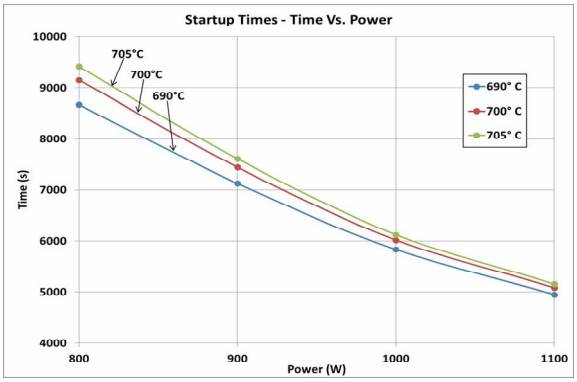


Figure 12. Summary of start-up duration after thermosiphon wick improvement.

5. CONCLUSIONS

A series of sodium heat pipes and thermos-syphons were developed for the Kilopower nuclear reactor test. The sodium heat pipes had a self-venting arterial wick, while the thermosyphons had a wick in the evaporator to assist in start-up.

The thermosyphons delivered the required power; however, the self-venting arterial heat pipes did not carry the required power when tested in a slightly adverse elevation. ACT is currently modifying the heat pipe wicks to increase the power.

The evaporator wick in the thermosyphons was successfully modified to mitigate start-up related temperature spikes and also to reduce the duration of the start-up in future pipes.

NASA Glenn Research Center is currently working on a thermal vacuum test of the Kilopower fission power system, including:

1. Electrically heated, depleted uranium core
2. Sodium heat pipes and thermosyphons developed on the current program
3. 8 Stirling Convertors
4. Due to limitations in the vacuum chamber size, the titanium/water heat pipes will be replaced with pumped liquid cooling.

The depleted uranium system will be tested in 2017. In 2018, a second unit will be tested with a live reactor core. ACT is currently developing the heat pipes for the 2018 nuclear test.

ACKNOWLEDGEMENT

This research was sponsored by NASA Glenn Research Center under Contract No. NNX12CE07P. Any opinions, findings, and conclusions or recommendations expressed in this article are those of the authors and do not necessarily reflect the views of the National Aeronautics and Space Administration. Mr. Marc Gibson was the NASA GRC contract technical monitor. Tim Wagner, Larry Waltman and Corey Wagner were the laboratory technicians responsible for the development of the self-venting arterial heat pipe.

NOMENCLATURE

ΔP : Pressure difference (Pa)
σ : Surface Tension (N/m)
r_c : wick pore size (m)

REFERENCES

[1] L. Mason, M. Gibson, and D. Poston, "Kilowatt-class Fission Power Systems for Science and Human Precursor Missions," Nuclear and Emerging Technologies for Space (NETS-2013), Albuquerque, NM, February 25-28, 2013.

[2] D. Palac, "Nuclear Systems Kilopower Overview," Nuclear and Emerging Technologies for Space (NETS-2015), Huntsville, AL, February 22-25, 2016.

[3] T. Kaya and K. Goncharov, "Analysis of a Gas-Tolerant High-Capacity Single-Artery Heat Pipe," 15th International Heat Pipe Conference (15th IHPC), Clemson, SC, April 25-30, 2010

[4] J. Zuo et al., 'An Overview of Long Duration Sodium Heat Pipe Tests," NASA Technical Memorandum NASA/TM-20040212959, March 2004.

[5] W. B. Kaufman and L. K. Tower, "Compatibility of Sodium and Lithium in Superalloy Heat Pipes," Air Force Final Report, AFWAL-TR-85-2006, April, 1985.

[6] C. E. Andraka et al., "NaK Pool-Boiler Bench-Scale Receiver Durability Test: Test Results and Materials Analysis," Proceeding of the 29th Annual IECEC, Vol. 4, pp. 1942-1949, AIAA, Washington, D.C., 1994.

[7] R. Ponnappan, "Thermal Energy Storage and Heat Transfer Support Program Vol III: Task 5. Heat Pipe Life Test Study; Facilities Upgrading and Maintenance," Air Force Report wRDC-TR-90-2121 Vol. III, March 1991.

[8] W.G. Anderson et al., "Alkali Metal Pool Boiler Life Tests for a 25 kWe Advanced Stirling Conversion System," Proceeding of the 26th Annual IECEC, Vol 5, pp. 343-348, American Nuclear Society, LaGrange Park, IL, 1991.

[9] W. G. Anderson et al., "Design of a Pool Boiler Heat Transport System for a 25 kWe Advanced Stirling Conversion System," Proceeding of the 26th Annual IECEC, Vol 5, pp. 376-381, American Nuclear Society, LaGrange Park, IL, 1991.

[10] K.L. Walker, C. Tarau, and W. G. Anderson, "Grooved and Self-Venting Arterial Heat Pipes for Space Fission Power Systems,: 17th International Heat Pipe Conference, Kanpur, India, October 13-17, 2013.

2. Loop Heat Pipes/ Capillary Pumped Loops

Development and On-orbit Operation of Loop Heat Pipes on Chinese Circumlunar Return and Reentry Spacecraft

Zhang Hongxing, Mi Min, Miao Jianyin, Wang Lu, Chen Yang, Ding Ting, Ning Xianwen and Huo Yuhua

Beijing Key Lab of Space Thermal Control Technology, China Academy of Space Technology, Beijing 100094, P.R.China

Abstract

This paper describes the development, ground experiment results and on-orbit operation of the loop heat pipes for the Chinese Circumlunar Return and Reentry Spacecraft (CRRS). A novel loop heat pipe (LHP) was developed to satisfy thermal control requirements of the inertial measurement units (IMU) in the CRRS. Specifically, the LHP consists of an integrated evaporator subassembly, a cambered condenser and an electric explosion valve to discharge the working fluid. The ground experiments were conducted to investigate start-up characteristics, heat transfer and heat insulation performances of the LHPs in horizontal and vertical orientations. Moreover, during the flight mission, the LHPs worked as a thermal switch by performing the functions of heat transfer and heat insulation respectively. Before the reentry capsule separated from the CRRS to return to the earth's atmosphere, the valves were opened to discharge the working fluid in order to prevent the heat transfer from the heated capsule wall to the devices. In the fight mission, the loop heat pipes performed all the required functions, thus the IMUs' temperatures were maintained within the allowable range.

Keywords: Chinese circumlunar return and reentry spacecraft; Loop heat pipe; On-orbit operation; Thermal switch.

■ *Published inJ Mech Sci Technol (2017) 31: 2597. https://doi.org/10.1007/s12206-017-0501-x*

Design and Experimental Investigation of a Neon Cryogenic Loop Heat Pipe

He Jiang[1], Guo Yuandong[1,2], Zhang Hongxing[1], Miao Jianyin[1], Wang Lu[1] and Lin Guiping[2]

[1]*Beijing Key Laboratory of Space Thermal Control Technology, Beijing Institute of Spacecraft System Engineering, China Academy of Space Technology, Beijing 100094, China*
[2]*Aeronautic Science and Engineering, Beihang University, Beijing 100191, China*

Abstract

Next generation space infrared sensor and detector have pressing requirement for cryogenic heat transport technology in the temperature range of 30-40K. Cryogenic loop heat pipe (CLHP) has excellent thermal performance and particular characteristics such as high flexibility transport lines and no moving parts, thus it is regarded as an ideal thermal control solution. Under some engineered limitations, a cryogenic loop heat pipe (CLHP) with neon as working fluid was designed. Then, series of tests were conducted to experimentally investigate the operating characteristics of the neon CLHP. Based on the experimental results, important conclusions can be drawn as follows: (1) the supercritical startup were realized successfully at cases of 1.5W secondary evaporator power, but the startup was failed when 0.5W and 1W heat load applied to secondary evaporator; (2) the maximum heat transport capability is between 4.5W to 5 W; (3) before startup, even the heat sink temperature decreased to 35K, the primary evaporator can still maintain at almost 290K; and the primary evaporator temperature increased at once when the powers were cut off, which indicated the CLHP has a perfect function of thermal switch; (4) the CLHP could adapt to sudden changes of the primary evaporator power, and reach a new steady-state quickly. Besides, some failure phenomena were observed during the test, which indicated that proper secondary evaporator power and heat sink temperature play important roles on the normal operation.

Keywords: Cryogenic loop heat pipe; Neon; Operating characteristics; Experiment.

■ *Published in Heat and Mass Transfer, Vol. 53, issue 11 (DOI: https://doi.org/10.1007/s00231-017-2005-8)*

A Numerical Study on Heat Transfer Characteristics of a Loop Heat Pipe Evaporator Using Three-Dimensional Pore Network Model

Masahito Nishikawara[1], Hosei Nagano[2] and Marc Prat[3]

[1]*Department of Mechanical Engineering, Toyohashi University of Technology, 1-1, Hibarigaoka, Tenpaku-cho, Toyohashi, Aichi, 441-8580, Japan*
[2]*Department of Aerospace Engineering, Nagoya University, Japan*
[3] *Université de Toulouse, INPT, UPS, IMFT, Toulouse, France*

Abstract

This paper investigates the heat transfer characteristics of a loop heat pipe (LHP) evaporator by a three dimensional pore network model. The simulation considered a saturated wick with liquid at a low heat flux and an unsaturated state at a high heat flux. Transition from the saturated state to the unsaturated state is calculated with boiling critical superheat at the contact surface between the case and the wick. In unsaturated state, the liquid-vapor interface is calculated based on pore radius distribution. The simulation results show the transition heat flux on stainless steel-ammonia LHP, PTFE-ammonia LHP and copper-water LHP. Copper-water LHP had the highest transition heat flux due to high boiling critical superheat. On copper-water LHP, the heat flux at the capillary limit can be comparable with the transition heat flux to the unsaturated state. Therefore, when optimum evaporator shape of the copper – water LHP is designed, it is reasonable that the phase state is assumed to be the saturated wick with liquid. On the other hand, on ammonia LHP design, the phase state is assumed to be the unsaturated wick with vapor and liquid. Simulation results explained the heat transfer structure in the wick formed axial grooves and applied heat flux concentrated at the three-phase contact line among the case, the wick and the grooves. It is proposed that the evaporator heat-transfer coefficient can be enhanced by making three-phase contact line longer. Then, the evaporator configuration with circumferential and axial grooves was simulated to investigate effect of length of the three-phase contact line. The evaporator heat-transfer coefficient of stainless steel-ammonia LHP increased. It is indicated that optimum shape of the evaporator can be designed by length of the three-phase contact line.

Keywords: Capillary evaporator; Loop heat pipe; Nucleation superheating; Pore network model; Unsaturated wick.

■*Published in Applied Thermal Engineering, Volume 126, 5 November 2017, Pages 1098-1106, https://doi.org/10.1016/j.applthermaleng.2017.02.050*

Loop Heat Pipe-Based Hydraulic Temperature Control Technique

Wukchul Joung[1, 2], Yong-Gyoo Kim[1, 2] and Kee Sool Gam[1]

[1]*Center for Thermometry, Division of Physical Metrology, Korea Research Institute of Standards and Science, Daejeon 34113, Korea*
[2]*Scince of Measurement, University of Science and Technology, Daejeon 34113, Korea*

Abstract

In this work, a hydraulic operating temperature control of loop heat pipes (LHPs) was proposed to achieve a precise, stable, and theoretically predictable operating temperature control. To this end, a pressure controlled LHP was devised to control the saturated vapor temperature at the evaporator by applying hydraulic action on the compensation chamber with an immiscible control gas. In particular, by forming an isothermal region in the vapor transport line, it was attempted to control the temperature of the isothermal region, and the resulting operating temperature controllability was investigated in terms of stability, precision, and predictability. Theoretical basis and limitations of the proposed method were established based on the thermo-hydraulic operating principles of the LHPs, and experimental validation was performed using Dowtherm A as a working fluid and helium as the control gas. Test results showed that the devised pressure controlled LHP was able to control the isothermal region temperature within the stability of 25 mK, and the resolution of the temperature control was around 60 mK at 100 Pa change in the control gas pressure. Large scale operating temperature changes were also possible without any temperature overshoots or undershoots, and a various method to achieve a stable operating temperature control was suggested. Details on the design and fabrication of the devised pressure controlled LHP and the experiment are alsoprovided.

Keywords: Loop heat pipe; Hydraulic temperature control; Pressure controlled loop heat pipe.

Fabrication and Characterization of Efficient Wicks for Loop Heat Pipes

R. Giraudon[1], S. Lips[1], D. Fabrègue[2], L. Gremillard[2], E. Maire[2] and V. Sartre[1]

[1] CETHIL UMR5008, Université de Lyon, CNRS, INSA-Lyon, F-69621, Villeurbanne, France
[2] MATEIS UMR 5510, Université de Lyon, CNRS, INSA-Lyon, F-69621, Villeurbanne, France

Abstract

Mono and bi-layer capillary structures are designed by means of a thermo-hydraulic model of a loop heat pipe in order to improve the performance of the system. The model tends to show that bi-layer wicks with a conductive bottom layer and an insulating top layer are the most efficient in loop heat pipes. Eight samples made of copper powder have been manufactured following a two-level fractional factorial design. The experimental characterization of the samples, enables to determine the influence of each sintering parameter as well as the interaction between them. These samples are manufactured in order to get as close as possible to the ideal bottom layer determined with the model. The sintering parameters are adjusted to provide porous samples with sufficient mechanical resistance. The characteristics of the porous samples are found to be mainly affected by the sintering time and the pressure. High values of these parameters decrease the permeability and the porosity but increase the maximum capillary pressure due to a smaller effective pore radius. The porous structure permeability and its capacity to provide a sufficient capillary pressure are evaluated using a specific test bench dedicated to this study, as well as with microstructural observations (tomography, microscopy). Some of the samples obtained have characteristics close to the optimum. However, their permeability is not as high as expected.

Keywords: Loop heat pipe; Capillary structure; Sintering; porosity; Permeability.

■ *Published in Heat Pipe Science and Technology, An International Journal*

Microscale Infrared Observation of Liquid-Vapor Interface Behavior on The Surface of Porous Media for Loop Heat Pipe

Kimihide Odagiri[1*], Masahito Nishikawara[2] and Hosei Nagano[1]

[1] Graduate school of Aerospace Engineering, Nagoya University, Furo-cho, Chikusa-ku, Nagoya, Aichi, 464-8603, Japan [2] Department of Mechanical Engineering, Toyohashi University of Technology, 1-1 Hibarigaoka, Tempaku-cho, Toyohashi, Aichi, 441-8580, Japan

Abstract

Loop Heat Pipe (LHP) performance strongly depends on the performance of a wick that is porous media inserted in an evaporator. In this paper, the visualization results of thermo-fluid behavior on the surface of the wick with microscopic infrared thermography were reported. In this study, 9 different samples that simulate a part of wick in the evaporator were used. The wicks were made by different two materials; polytetrafluoroethylene (PTFE) and stainless steel (SUS). Their pore radius are 1.2μm and 1.0μm. Other properties; thermal conductivity, permeability and porosity are different. Firstly, the difference of thermo-fluid behavior between PTFE wick and SUS wick was discussed. The heat transfer coefficient, wick's operating mode change and the difference of heat leak through the wick were discussed. Secondarily, the effect of vapor groove width on the maximum heat flux and the depth of vapor pocket in the wick was discussed based on the observation results of 5 PTFE wicks and 4 SUS wicks that has different vapor groove width. As results, there is a trend the wick that has smaller groove width has higher heat transfer capacity except sample that has the smallest groove width. In addition, the wick that has smaller fin width is greater at the point of preventing vapor pocket formation in the wick.

Keywords: Loop Heat Pipe; Evaporator; Porous media; Liquid-vapor phase change; Microscale infrared observation.

■ *Published in Applied Thermal Engineering, Volume 126, 5 November 2017, Pages 1083-1090, https://doi.org/10.1016/j.applthermaleng.2017.03.113*

Analytical Model for the Dynamics of A Capillary Pumped Loop Subjected to High Amplitude Heat Load Steps: Estimation of the Liquid Flow Rate Overshoot

Sébastien Dutour and Ahmed Kaled

University of Toulouse;UPS, INPT, CNRS; LAPLACE(Laboratoire Plasmaet Conversiond' Energie); 118routede Narbonne, F-31062 Toulouse cedex 9, France

Abstract

A linear transient model was developed and used to provide some analytical results on the dynamics of a Capillary Pumped Loop subjected to high amplitude heat load steps. This study actually focused on the estimation of the liquid flow rate overshoot, as this peak value can be so large that it leads to the loop failure. A comparison with data and with a set of simulations investigating different CPL configuration showed that the maximal deviation (over estimation) is about 40%. As they provided essential quantitative information and explicit parameter dependency on the loop transient, these results are precious for engineers allowing them to design loops that are suitable for demanding power cycles.

Keywords: CPL; Liquid flow rate overshoot; Theoretical model; Transient.

■ *Published in Applied Thermal Engineering, Volume 126, 5 November 2017, Pages 1107-1114, https://doi.org/10.1016/j.applthermaleng.2017.02.065*

Direct Numerical Simulation of Evaporation in a Biporous Media

Bharat. B. Sharma [1], Sudip. K. Samanta [1], Himadri Chattopadhyay [2] and Gautam Biswas [3]

[1]*CSIR-Central Mechanical Engineering Research Institute, Durgapur, India*
[2]*Center of Excellence-Phase Transformation and Product characterization & Dept of Mechanical Engg., , Jadavpur University, Kolkata, India*
[3]*Indian Institute of Technology Guwahati, India*

Abstract

Biporous Media having clusters of size range 300 – 425 µm, 425 – 600 µm , > 600 µm have been sintered at 950 °C, 180 min using gas atomized spherical particles (D50 of 90 microns) of pure copper in reducing atmosphere of pure Hydrogen gas. MicroCT scan of biporous samples have been performed to and then images have been reconstructed to 3D CAD models, which further have been discretized into tetrahedral mesh using image processing and reconstruction software Avizo Fire 8.0. Direct Numerical Simulations have been performed to obtain evaporative heat transfer coefficient (EHTC) over the surface of these biporous clusters. The transient evaporation phenomena and effect of cluster size on evaporation has been investigated in this paper. These results have been compared with the experimental results available in literature for evaporative heat transfer coefficient for biporous media.

Keywords: Loop Heat Pipe; Direct Numerical Simulation; Evaporative Heat Transfer Coefficient; microCT scan; Biporous.

■ *Published in J Mech Sci Technol (2017) 31: 2635. https://doi.org/10.1007/s12206-017-0506-5*

Development of a LHP for Power Avionics Application

Jérôme Coulloux and Thomas Albertin

ATHERM, 1 rue Charles Morel – 38420 DOMENE, FRANCE

Abstract

Civil and Military aeronautic French manufacturers needs in the field of diphasic systems (and mainly Loop Heat Pipes) are expected to increase during next years to face the increasing of power flux of electronic components, following the Moore's law. This approach is applicable for low power electronics as well as power components such as diodes or IGBTs.
In order to expand his scope of competences, since 2010, Atherm has been developing sintered heat pipes and sintered porous media to explore LHP technology markets.
Involved in a large European project named TOICA, and in collaboration with a final customer leader in the field of aeronautics, helped by a laboratory, Atherm has developed a "power LHP".
This 1.5meter LHP has been developed, aiming at replacing a liquid cold plate used to thermalize diodes dissipating up to 400W each, main objectives being gains on maintenance operations and gains on weights.

Keywords: Loop Heat-Pipe; Avionics; Power electronic; Weight reduction

Low-Cost Manufacturing of Loop Heat Pipe for Commercial Applications

Bin-Juine Huang[1], Y.H. Chuan [2] and P.E. Yang [2]

[1] *Professor, Department of Mechanical Engineering, National Taiwan University, Taipei, Taiwan 106*
[2] *Graduate students, Department of Mechanical Engineering, National Taiwan University, Taipei, Taiwan 106*

Abstract

In this paper, we reported a patented novel LHP design associated with simple manufacturing process to bring the cost down dramatically for commercial applications. The cost of 100W LHP is reduced to less than 20 USD in mass production. The yield rate in mass production is higher than 90%. The LHP was successfully used in LED luminaire, solar water heater, and thermoelectric power generator to transfer or dissipateheat.

Keywords: Cooling device; Heat pipe; Heat transfer device; Loop heat pipe.

■ *Published in Applied Thermal Engineering, Volume 126, 5 November 2017, Pages 1091-1097, https://doi.org/10.1016/j.applthermaleng.2016.12.062*

Startup Characteristics of Pump-Assisted Capillary Phase Change Loop

Jiang Chi, Liu Wei, Liu Zhichun, Yang Jinguo, Duan Bin and Luo Xiaobing

School of Energy and Power Engineering, Huazhong University of Science and Technology, Wuhan, China

Abstract

In this work, startup characteristics of pump-assisted capillary phase change loop under different operational conditions were experimentally investigated. For the loop design, the impeller pump, which was designed and fabricated autonomously to reduce the weight of the loop, was selected for the mechanical pumping force. Methanol was chosen as the working fluid. Test results indicated that the pre-conditions in the evaporator had a great impact on the startup characteristics. When the vapor chamber partially or completely occupied with liquid before startup, a notable temperature overshoot would appear on the heater wall temperature profile. As a higher heat load added to the evaporator, vapor bubble would generate in the compensation chamber. Under such circumstances, the loop could still operate steadily and the heat transfer capability of the evaporator improved to some extent. To avoid the boiling conditions appeared in the compensation chamber, either lowering the heat sink temperature or increasing the pumping power was the effective manners.

Keywords: Heat leak; Impeller pump; Pre-conditions; Startup; Temperature overshoot.

■ *Published in Applied Thermal Engineering, Volume 126, 5 November 2017, Pages 1115-1125, https://doi.org/10.1016/j.applthermaleng.2017.02.043*

Analysis of Chaotic Flow in a 2D Multi-turn Closed-loop Pulsating Heat Pipe

S. M. Pouryoussefi and Yuwen Zhang

Department of Mechanical and Aerospace Engineering, University of Missouri, Columbia, MO, 65211, USA

Abstract

Numerical study has been conducted for the chaotic flow in a multi-turn closed-loop pulsating heat pipe (PHP). Heat flux and constant temperature boundary conditions have been applied for heating and cooling sections respectively. Water was used as working fluid. Volume of Fluid (VOF) method has been employed for two-phase flow simulation. Volume fraction results showed formation of perfect vapor and liquid plugs in the fluid flow of PHP. Non-linear time series analysis, power spectrum density, correlation dimension and autocorrelation function were used to investigate the chaos. Absence of dominating peaks in the power spectrum density was a signature of chaos in the pulsating heat pipe. It was found that by increasing the filling ratio and evaporator heating power the correlation dimension increases. Decreasing of the autocorrelation function with respect to time showed the prediction ability is finite as a result of chaotic state. An optimal filling ratio of 60% and minimum thermal resistance of 1.62˚C/W were found for better thermal performance of the pulsating heat pipe.

Keywords: Chaotic flow; Numerical simulation; Pulsating heat pipe; Thermal performance.

■ *Published in Applied Thermal Engineering, Volume 126, 5 November 2017, Pages 1069-10275, https://doi.org/10.1016/j.applthermaleng.2017.01.097*

A Novel "Multi-stages" Loop Heat Pipe for Cooling Multiple Heat Sources

C. Figus[1], L. Dandaleix[1], J. Hill[1], L. Barremaecker[2]

[1]*Airbus Defence and Space, 31 Av. des Cosmonautes, 31402 Toulouse Cedex, France*
[2]*Euro Heat Pipe, Rue de l'Industrie, 24 B-1400 Nivelles, Belgium*

Abstract

Heat pipe and Loop Heat pipe are well known heat transfer devices, with benefits and drawbacks. Heat pipe are easy to use, thermally efficient and cost effective but affected by gravity and limited in heat transport capacity and size. They can be used as heat spreader, heat collector or heat transport device. Loop Heat pipe have more heat transfer capacity at a higher cost and more complex operation. They can be used as heat transport device in a one-way or reversible way between a dissipative unit and a cold source (radiator or equipment). Based on the pumping head generated by the Loop Heat pipe evaporator, a novel architecture has been developed and tested in order to combine the benefits of Loop heat pipe (heat transport capacity) with the one of Heat pipe (simple and efficient). The "Loop Heat pipe evaporator" called evaporator is used to generate the fluid flow (vapour at the outlet of the evaporator). This flow is condensed (partially or totally) at an intermediate cold source (radiator or other), and then is vaporized (totally or partially) in heat exchangers along the return line. Before flowing to the evaporator, the fluid routs through a final cold source in order to have a liquid saturated flow (liquid at the inlet of evaporator). The intermediate cycle (between evaporator and final condenser) can be performed several times as soon as the pressure drops are not exceeding the pumping head capacity of the evaporator. With such architecture, it is then possible to cool down several units (equipment, components …) with a single Loop heat pipe. Moreover with reduced pipe section it is possible to provide very efficient small heat transport capacity. An example of application in an electronic box is presented with associated test results. Benefits and further applications are discussed.

Keywords: Loop heat pipe, Multi-stages, Heat transfer

1. INTRODUCTION

Since more than 30 years extensive work and developments have been performed on Loop heat pipe. However this heat transfer device is not widely used has Heat pipe technology. The LHP technology offer good thermal performances (heat transfer and heat transport capacity) but the operation and cost limit the benefits (see RD[1]).

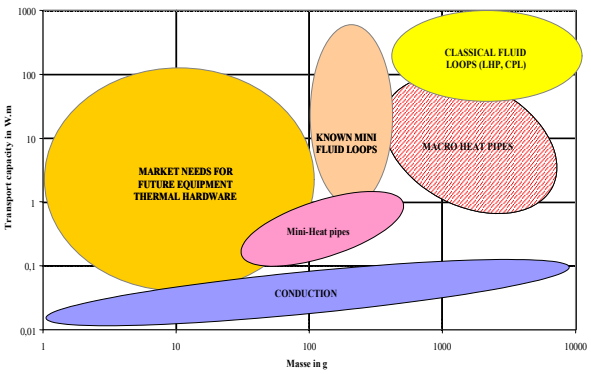


Figure 1: Heat transport technology comparative(RD[1])

One of the major limitations of the LHP (compare to Heat pipe) is its limitation to drain heat from several dissipative heat sources. In Space systems, the heat collection has to be performed through Heat pipes.

Another one, remains in the operation constraints, with start-up power and or potential oscillating behavior (see RD[2]).

In order to improve these drawbacks, in 2009, Airbus Defence and Space has investigated a new way to operate Loop heat pipe with the "multi-stages" concept (see RD[3]).

The aim of this concept is to use the flow generated by the LHP evaporator in order to cool down several other dissipative units. Such concept would allow combining the good pumping capacity of capillary evaporator, the integration simplicity with tubing, and the efficient thermal transfer of heat exchangers.

2. THE "MULTI-STAGES" CONCEPT

The "multi-stages" concept is based on the use of a single loop heat pipe with one capillary evaporator. The flow is generated by the heat applied in front of the capillary evaporator. The vapour flow is condensed at condenser level. The

partially or fully (see after) condensed fluid is then flowing through the tubing over other dissipative units in order to cool them down. The various areas in front of dissipative components are called heat exchangers in order to differentiate from the capillary evaporator. Thus after total or partial vaporization of the fluid (see after) it is condensed a new time at condenser level with an additional condenser part. This routing can be performed several times as soon as the pressure drops through the Loop are lower than the maximal capillary pressure of the porous wick, and the surface area of the condenser is large enough for the heat transfer.

$$\Delta P_{\max\ LHP\ \ pumping\ \ head} \geq \sum \Delta P \qquad (1)$$

Thus owing to the flow generated by the capillary evaporator it is possible to cool down several components. The system operates only when heat is applied on capillary evaporator

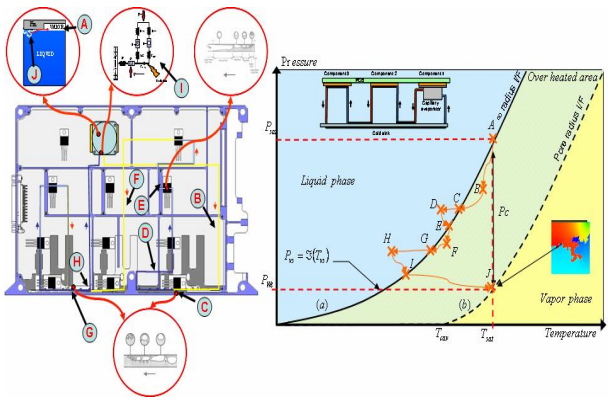


Figure 2: "Multi-stages" LHP principle

3. APPLICATION TO A PCB COOLING

One potential application of such concept is the electronic cooling. Thus, with the general trend of power and dissipation increase of electronics, benefit of miniaturized and efficient cooling system becomes a major objective.

Component direct cooling is beneficial when a single component dissipates a very large amount of heat, such as an ASIC, FPGA, ADC, DAC or POL dissipating several watts. In these situations the thermal resistance of the component case to PCB and PCB itself can make it impossible to maintain the derated junction temperature of the component by conduction through the PCB.

In addition many flight components are adapted from commercial applications intended to have a heatsink on the top surface of the package, these have a high internal thermal resistance to the PCB surface. They also have reliability requirements for lower temperatures to get a better fit rate on components, which override the derated limit requirement. Use of conductive devices (Aluminum frame, Copper or Pyrolytic graphite strap, diamond vias,…) can improve locally the heat dissipation, but become very limited in ratio thermal performance/mass when distance between component and cold sink is more than few centimeters. Thus most of the time dissipative components are located close to the cold sink interface, and limitation occur as soon as several dissipative components are required on the board.

In 2007 (RD[4]) Airbus Defence and Space did present the test results of a miniaturized Loop Heat pipe integrated on an electronic board demonstrator.

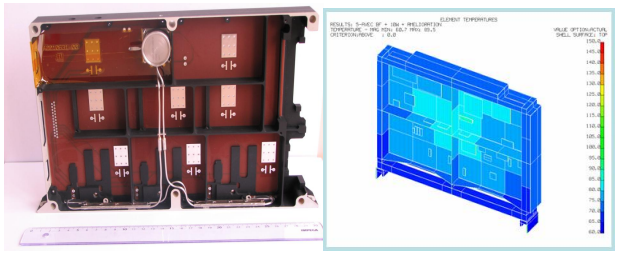


Figure 3: Mini-LHP PCB cooling demonstrator (2007)

The demonstrator was able to be tested in all directions on ground and test results demonstrated some local improvements of the cooled component temperature (100% of component power transferred by LHP). However, due to the poor thermal conductivity of the board, less than 1% of board power was collected and transferred by LHP. The total heat rejected through the LHP was low and not enough in order to demonstrate a large benefit (average PCB temperature decrease of about 10°C). Use of a several heat collectors would have significantly improved the board temperature.

In order to illustrate the interest, it was decided to test on a real PCB configuration the "multi-stages application".

4. PCB COOLING DEMONSTRATOR

The demonstrator is based on a board with at least two main dissipative heat sources. A digital processor (the main source) with a dissipated power of 15 W (can be increased by soft). The component is closed (less than 40 mm) to the cold source interface. A secondary heat source is generated by power converter (5W) on the top of the board (about 140 mm far from cold source interface).

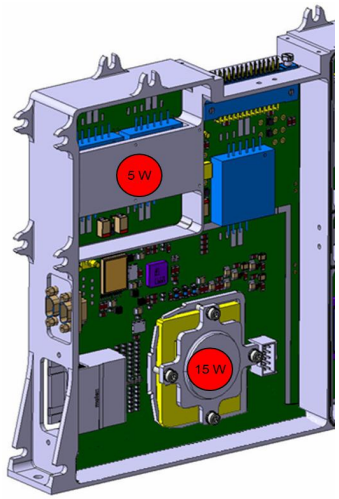


Figure 4: Tested electronic board (2014)

In order to cool down the board, a simple "dual stages" Loop Heat pipe has been designed. The capillary evaporator of the LHP is based on a Nickel wick mini-LHP evaporator. Such flat evaporator (OD < 30 mm; Height < 20 mm, mass < 50 g) is limited in volume and mass and offer a large pumping head capacity (>20 000Pa). The evaporator is fixed on the processor with 4 bolts (and no thermal filler). Two thirds of the cold interface plate is used for the primary condenser (175 mm long) done by simple tube (ID 1.6 mm) brazed on an aluminum saddle. Then a 230 mm long tubing is fixed on the board stiffener up to the heat exchanger fixed on the secondary heat source. The heat exchanger is fixed with 6 bolts to the aluminum board frame in front of the components. Then another 250 mm pipe long routes the fluid to the second condenser of 75 mm long.

The total mass of the LHP (with heat exchanger and fixation) is less than 100g.

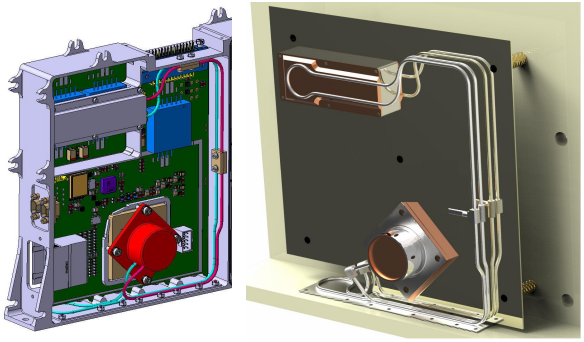


Figure 5: Multi-stages LHP routing on demonstrator

The LHP was integrated on the board and instrumented. The complete model was tested in vacuum conditions.

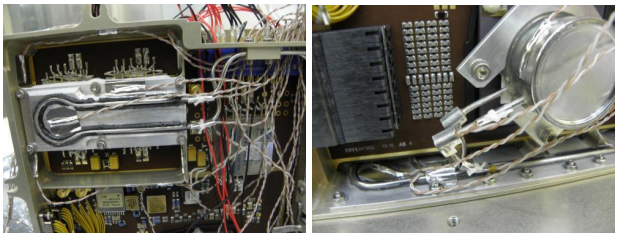


Figure 6: LHP integrated on the board

Several conditions were tested in hot and cold environment, with the LHP operating vertically against gravity. Tests were performed with large and small dissipation of the processor (heat source 1) and of the power converter (heat source 2). As indicated on the curve below the power converter (heat source 2) was operating at the vapor temperature of the LHP (driven by the capillary evaporator operation conditions)

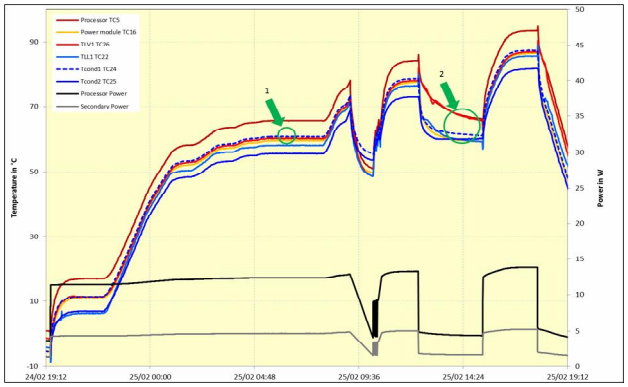


Figure 7: Test results in hot environment

Thus, as indicated on the plot:

- In circle 1, when large (versus evaporator) heat (5W) is applied on power converter, the heat exchanger is two-phase flow.
- In circle 2, with too few (less than 2) watts are applied on the power converter, the heat exchanger is liquid flow.

Moreover, it can be observed at large heat load the LHP "system" adapt the vapor pressure (and temperature) such to have enough liquid title in heat exchanger in order to dissipate the power. This phenomenon is illustrated on the two plots hereafter. At 15 W (on processor) + 5 W (on power converter), LHP vapor temperature is about 66°C and the vapor title (amount of vapor) is 40% at the outlet of the heat exchanger.

At 15 W (on processor) + 10 W (on power converter), the LHP vapor temperature increases at 69°C, with a vapor title of 75% at the outlet of the heat exchanger.

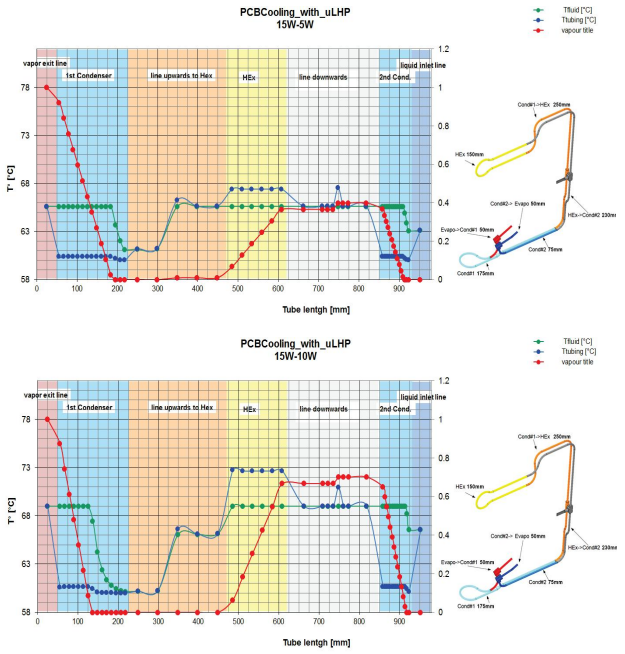


Figure 8: Temperature and vapor title evolution LHP

The tested system was very robust. No start-up or oscillating issue was observed. It was possible to test the secondary source with large variation of power load, the fluid flow regime moving from Churn flow (at low heat load) to slug flow a larger one.

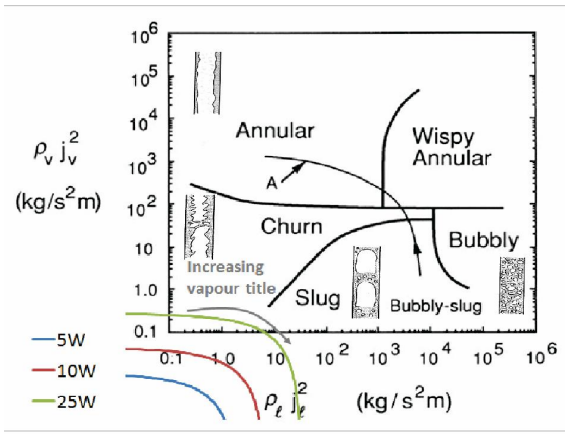


Figure 9: Flow regime in heat exchanger (RD[5])

Thus at PCB level, the results have shown the benefit of the "multi-stages" concept. With a single LHP it was possible to cool down several dissipative units and thus decrease the average PCB temperature by more than 15°C. Moreover the concept allows reducing the size of the heat exchanger to small tubing easier to route and attach through the board. Of course the model was not optimized (no thermal filler at interface, only one heat exchanger…) but the concept was proved to be efficient and further development are on-going.

5. EXTENSION TO MULTI HEAT EXCHANGERS

Based on correlated model, the concept has been extended to multiple condensers and heat exchangers. A reference board without any LHP was tested in vacuum and the following temperature distribution and thermal dissipations were obtained (see figure 10).

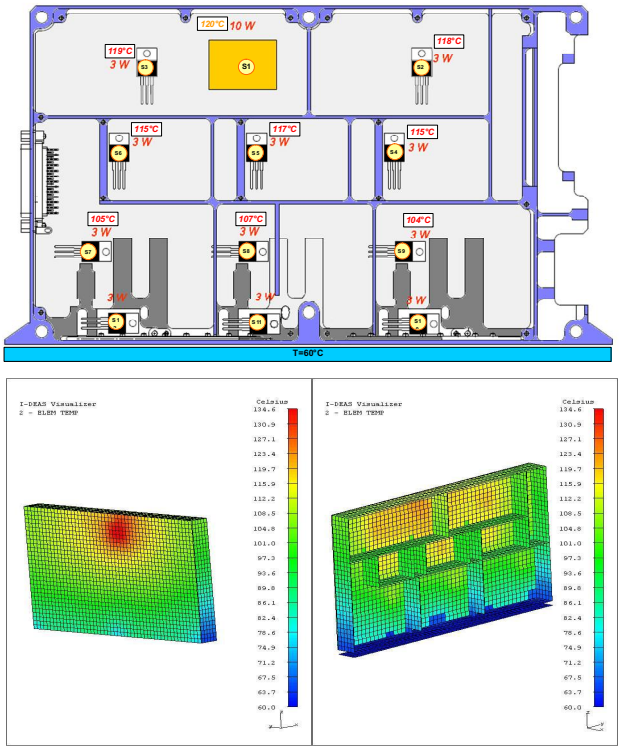


Figure 10: Heat distribution and temperature mapping of PCB reference case (Test & model)

A double stages LHP was simulated (based on a correlated model). With 9.9W transported by the capillary evaporator, most of the heat dissipated in front of the LHP evaporator is drained. Such a heat allows a fluid flow of typically 0.01 g/s.

With 80 mm of condenser length in contact with the sink at 60°C, it is possible to condensate 70% of the vapour. The fluid is then still at a saturation temperature of 69°C (the same as the one at capillary evaporator level). Thus, the two-phase fluid flows through the tubing to heat exchangers in contact with heat source 9 (S9), heat source 4 (S4) and heat source 2 (S2).

Along the two first heat sources, the temperature is kept constant as the fluid is two-phases (vapour title is between 0.3 and 0.75). The heat exchangers drain respectively 1.9 W and 2.5 W from the sources. At heat source 3 the vapour title achieves 1 (full vapour), thus the heat transfer is finalized

with some superheated vapour. Vapour temperature increases of few degrees up to 71°C. However, even with superheated vapour the heat exchanger absorbs 2.6W from heat source 3 (S3).

A second stage is performed with a second 80 mm condenser length (in contact with sink temperature at 60°C), with two additional heat sources (S7 and S8). As the vapour is superheated (when leaving heat source 3), the vapour title at the outlet of the second condenser is only 0.55.

In the same way, as the first stage, heat transfers are performed at constant vapour temperature. When vapour title reaches 100%, heat transfer is done with superheated vapour. After this second stage, a longer condenser branch condensates the vapour and sub-cool the liquid in order to achieve 67.5°C.

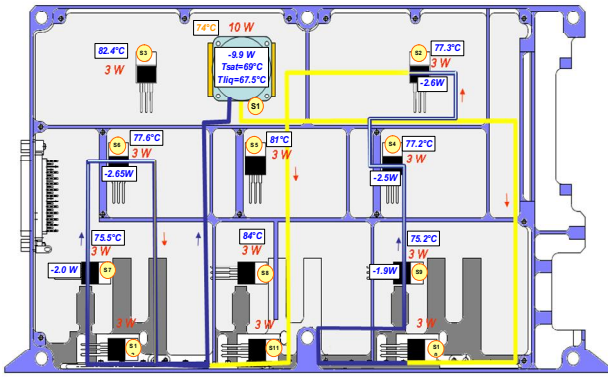


Figure 11: Heat distribution and temperature mapping of PCB with dual-stages LHP (model)

When we look to the thermodynamic cycles of the LHP it appears that the two intermediate condensation stages (point D and H on figure 13) are not affecting the behavior of the Loop operation. The vapor title will be more or less important at heat exchanger level but the flow rate and vapor temperature (T_A see figure 13) will not be affected. The global operation of the Loop will be driven by the last condenser (J point on figure 13). This condenser will need to deliver to the LHP evaporator the required subcooling in order to maintain the cavity temperature at the required balanced temperature. Thus it will have to follow the following rule (see RD[2]):

$$T_A - T_J = \frac{\alpha * Q^2 + \beta * Q + \delta}{\xi * Q + \varepsilon} \qquad (2)$$

Where α, β, δ, ξ, ε are explicit parameters of the LHP and operating conditions (fluid, pressure drops,…)

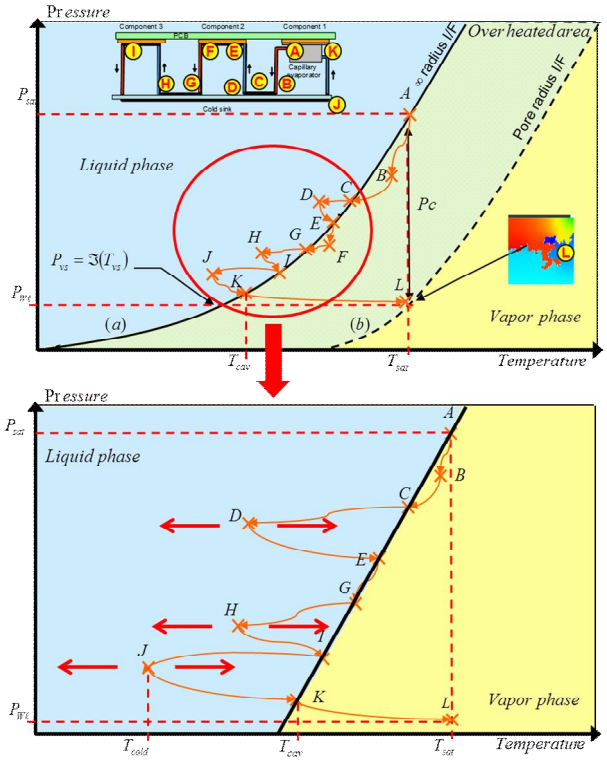


Figure 12: Thermodynamic cycle of the dual stages LHP

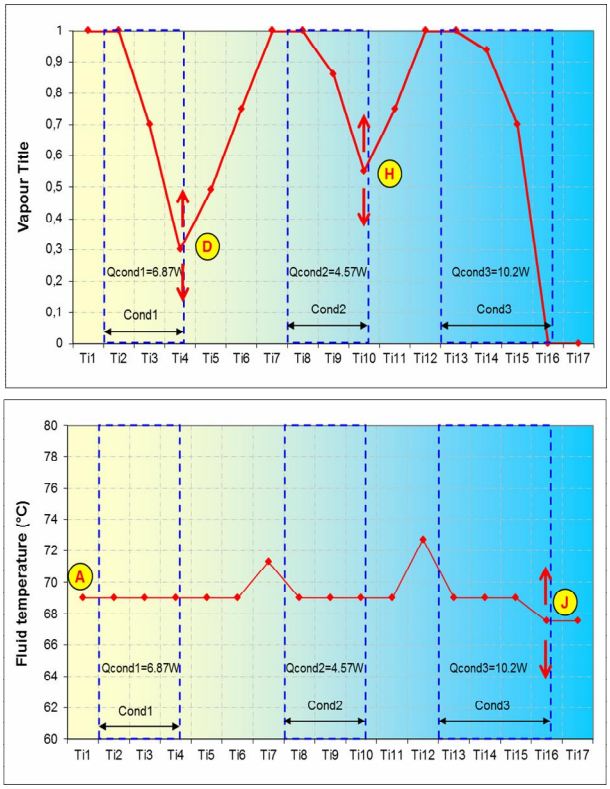


Figure 13: Vapour Title and temperature of the dual stages LHP

Parameters of relation (2) are dependent of the loop pressure drops. As the total flow rate is fixed by the capillary evaporator, loop pressure drops are increasing more or less with the vapor title in

heat exchangers. Introducing this evolution effect on relation (2), it is possible to calculate a thermal efficiency C_η of the system based on the ratio between the total heat transported by the loop (Heat on capillary evaporator + heat on heat exchangers) and the required temperature difference T_A-T_J.

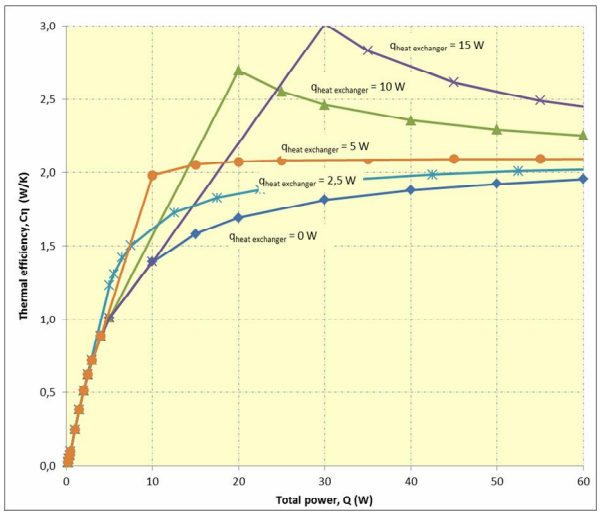


Figure 14: Thermal efficiency of multi-stages LHP

As indicated on figure 14, the effect of adding heat exchangers on the LHP improves the global thermal efficiency of the system. The pump (the capillary evaporator) is slightly affected by the additional pressure drops (several Pascal of additional pressure drops generate very few thousandths of degree of variation of vapor temperature).

5. OTHER APPLICATIONS AND CONCLUSION

Of course, there are many potential applications of such concept. The principle can be extended to large dissipation at system level. Owing to the existing pumping capacity of Loop heat pipe (>30 000 Pa), a single evaporator could provide the cooling capacity for a 10 kW spacecraft.

For aeronautics it could bring enough cooling capacity for engine or electronic cooling, with the possibility to reduce the power consumption (the heat dissipated by equipment like engine, could cool passively other equipment like wing actuators).

For data-center, with evaporator fixed on the power supply it could cool down the complete bay, and thus reduce the energy print of the system.

Based on this innovative architecture, benefits of Loop Heat pipe application become very important. Thus, many other applications are foreseen and are investigated by Airbus Defence and Space owing to the multi-stages arrangement.

In this time where energy saving becomes of prime importance; it is very pleasant to think that parasitic heat dissipation could become the cooling energy for tomorrow.

ACKNOWLEDGEMENT

This work was co-funded by Airbus Defence and Space and ESA (European Space Agency) and has been performed in closed collaboration with Euro Heat Pipe.

NOMENCLATURE

ADC :	Analogue to Digital converter
ASIC :	Application Specific for Integrated Circuit
DAC :	Digital to Analogue converter
C_η :	Thermal efficiency (W/°C)
FPGA :	Field Programmable Gate Arrays
ID :	Inner Diameter
LHP :	Loop heat pipe
OD :	Outer Diameter
P :	Pressure
PCB :	Printed Circuit Board
POL :	Point-Of-Load (DC/DC converter)
Q :	Power
T :	Temperature
	UNITS
°C :	Degree Celcius
g :	Grams
Mm :	Millimeters
Pa :	Pascal
W :	Watts
kW :	Kilo-Watts

REFERENCES

[1] C. Figus and al. Capillary Fluid Loop Developments in Astrium (12th IHPC), Moscow, May 19-24, 2002.
[2] C. Figus and al. Loop heat pipe thermal model (16th IHPC), Lyon, France, May 20-24, 2012.
[3] C. Figus, Cooling device; patent WO2013092386 A1.
[4] C. Figus and al. Long term life test & in orbit test of miniaturized loop heat pipe (14th IHPC), Florianópolis, Brazil, April 22-27, 2007.
[5] Carey V P. Liquid-vapor phase change phenomena, Taylor & Francis, 1992.

The Operation Mode Study of an Integrated System with Double Pulse Tube Coolers and Double Cryogenic Loop Heat Pipes

Wang Lu[1], Miao Jianyin[1 *], Zhang Hongxing[1], Mo Qing[1], He Jing[1]and Guo Yuandong[1,2]

[1]*Beijing Key Laboratory of Space Thermal Control Technology, Beijing Institute of Spacecraft System Engineering, China Academy of Space Technology, Beijing 100094,China*
[2]*Aeronautic Science and Engineering, Beihang University, Beijing 100191, China*

Abstract

In the paper, we develop an integrated system which consists of double pulse tube coolers and double cryogenic loop heat pipes. The supercritical startup, heat transfer characteristic of the CLHPs and the operation modes of the integrated system have been investigated. Experimental results reveal that when the pulse tube cooler operates as the heat sink and the heat load applied to the secondary evaporator is 0.5W, the heat transport capacity of the primary evaporator can achieve 4W. The integrated system with double pulse tube coolers and double cryogenic loop heat pipes can meet the requirement of the infrared optical sensor which should operate at low temperature(below 120K) and heat load of the infrared optical sensor does not exceed 3W. The flexible fine long pipes of the cryogenic loop heat pipe can isolate the vibration and electromagnetic interference induced by the pulse tube cooler from the infrared optical sensor effectively. The integrated system can realize normal operation mode, normal switch operation mode, failover switch operation mode and cooperation mode. This can improve the life and reliability of the infrared optical sensor effectively.

Keywords: Integrated system; Operation mode; Cryogenic loop heat pipe; Pulse tube cooler

1. INTRODUCTION

Infrared optical sensors must rely on low temperature conditions in order to obtain better imaging quality. Pulse tube coolers can provide deep low temperature working conditions for infrared optical sensors. If the pulse tube cooler and the infrared optical sensor couple directly, it will cause such problems difficult to solve: 1) it is difficult to design the interface because of their structure; 2) the mechanical vibration from the pulse tube cooler will affect the imaging quality of the infrared optical sensor; 3) it is difficult to take measures to isolate the electromagnetic interference induced by the pulse tube cooler from the infrared optical sensor; 4) heat leaks from the pulse tube cooler to the infrared optical sensor when it does not run; 5) it is difficult to arrange backup of the pulse tube cooler to improve the life and reliability of the infrared optical sensor. To overcome those problems, we can establish a bridge between the pulse tube cooler and the infrared optical sensor which should collect and transfer heat effectively, isolate the mechanical vibration and electromagnetic interference induced by the pulse tube cooler from the infrared optical sensor, arrange the backup of the pulse tube cooler conveniently. This bridge can effectively improve the life and reliability of the infrared optical sensor. On the current level of technology, the most simple and reliable technique of the bridge is cryogenic loop heat pipe (CLHP).

The primary evaporator and condenser of CLHP are respectively coupled with the infrared optical sensor and pulse tube cooler. So it is easy to design their interface. The characteristic of internal two-phase flow ensures efficient heat collecting and transmission between the infrared optical sensor and the pulse tube cooler. The flexible fine long pipes of CLHP can weaken the influence of mechanical vibration from the pulse tube cooler on the imaging quality of the infrared optical sensor and block heat leakage from the pulse tube cooler to the infrared optical sensor when it does not run. The pulse tube cooler and the infrared optical sensor are separated, so it is convenient to arrange backup of the pulse tube cooler and take measures to isolate the electromagnetic interference induced by the pulse tube cooler from the infrared optical sensor. In view of the unique advantages of integrated system of cryogenic loop heat pipes and pulse tube coolers, it will become the core technology in the field of spatial cryogenics heat collection and transmission.

In recent years, based on the demands for spacecraft cryogenic thermal control, many researchers have investigated the cryogenic loop heat pipes deeply. In order to solve the cooling problem of an optical system, Dave Glaister[1] put forward the concept of a two-axis cross gimbal cryogenic loop heat pipe. From then on, various types of cryogenic

*Corresponding author: miaojianyin@hotmail.com,
Phone: +86-010-6874-6029, Fax: +86-010-6874-5883

loop heat pipes have been rapidly developed and the suitable temperature has been expanded to liquid nitrogen, liquid neon and liquid hydrogen gradually. Aiming at the low temperature thermal control of the infrared optical sensor, James Yun[2] designed a cryogenic loop heat pipe which working fluid was ethane. The low temperature radiator worked as the heat sink. It would start up from the supercritical temperature of ethane (335K) successfully. When the heat load applied to the secondary evaporator was 5W, the heat transport capacity of the primary evaporator achieved 50W at the temperature of 215K. D.Bugby[3] developed a cross gimbal CLHP, a short distance transmission CLHP and a long distance transmission CLHP. Nitrogen was chosen as the working fluid of the cross gimbal CLHP. Its operation temperature was from 80K to 100K. It could achieve a two-dimensional direction rotation at the azimuth angle of ±180°and the pitching angle of ±45°. The design heat transport capacity was 20W and the temperature stability was ±2K. The short distance transmission CLHP operated at about 35K. Neon was used as working fluid. The design heat transport capacity was 2.5W and the heat transmission distance was greater than 10cm. The thermal resistance was greater than 1000K/W when it didn't operate, while thermal resistance was less than 1K/W when it was operating. The long distance transmission CLHP operated in the range of 30K-35K. Neon was also used as working fluid. The design heat transport capacity was 1W and the heat transmission distance was greater than 250cm. Triem T.Hoang[4,5] designed a cryogenic loop heat pipe. Hydrogen was chosen as working fluid. When the secondary evaporator was applied 2.5W, 25 minutes later, the temperature of the primary evaporator and primary CC was below the supercritical temperature of 32K. It would operate steadily when the primary evaporator was applied 5W. Mo Qing[6] designed a cryogenic loop heat pipe with only one loop which completed supercritical startup relying on gravity. Its working fluid was nitrogen and heat transport capacity was 11W. Zhou Shuntao[7] designed a cryogenic loop heat pipe with heat transmission distance of 1m, its working fluid was nitrogen. When the secondary evaporator was applied 5W, the heat transport capacity would achieve 30W. This CLHP had the ability of anti-gravity.

From the above introduction we can see that many researchers have investigated the heat transport capacity and heat transmission distance of CLHPs deeply. But little work has been carried out on the thermal characteristic of the integrated system of coolers and CLHPs. However, in the space application the CLHP must rely on the cold source provided by coolers to operate normally. So it is necessary to study the thermal characteristic of the integrated system.

2. EXPERIMENTAL SETUP

Fig.1 shows the schematic of the integrated system of double pulse tube coolers and double cryogenic loop heat pipes. It has two Loops. That is Loop 1# and Loop 2#. Each Loop has a pulse tube cooler and a cryogenic loop heat pipe. The cryogenic loop heat pipe couples with the cold finger of pulse tube cooler through its thin cylindrical cold block. Two primary evaporators connect with each other through a copper saddle, as shown in Fig.2. Nitrogen is chosen as the working fluid. The maximum cold quantity of every pulse tube cooler is 5W when it operates at 80K. By reducing the working voltage the cold quantity of pulse tube cooler can be reduced. Two thin film heaters are installed on the two secondary evaporators to help CLHP to realize the supercritical startup while another thin film heater is installed on the copper saddle to simulate the heat load of the infrared optical sensor. A DC supply with three outputs supplies current to thin film heaters. 12 platinum resistance temperature sensors are used to measure the temperature of the integrated system. TC1~TC6 are respectively installed on the thin cylindrical cold block(heat sink), the secondary CC, the secondary evaporator, the primary CC, the primary evaporator and the copper saddle(heat source) of Loop 1#. While TC7~TC12 which correspond to TC1~TC6 one by one are installed on the same position of Loop 2#. The position of TC6 and TC12 are shown as Fig. 2. Four 34970A Agilent Data Acquisitions are used to collect and display the temperature real-timely.

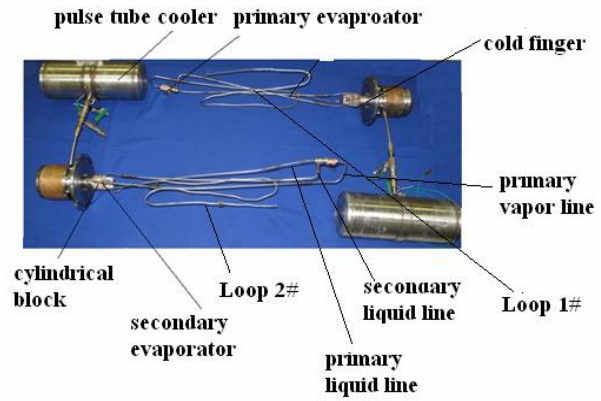


Fig. 1 Schematic of the integrated system

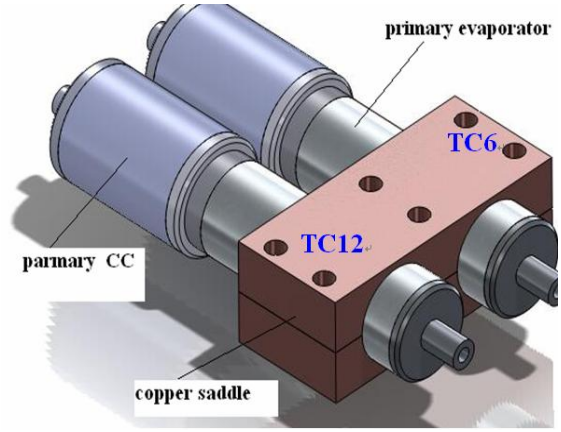


Fig. 2 Three-dimensional model of the copper saddle

3. EXPERIMENTAL RESULTS AND ANALYSIS

3.1 Supercritical startup of the integrated system

The supercritical startup of the integrated system of the Loop 1# and the pulse tube cooler is shown as in Fig.3. At 0th minute the pulse tube cooler begins to run and the temperature of the thin cylindrical cold block, the secondary CC and the secondary evaporator begins to decrease. While the temperature of the primary CC, the primary evaporator and the copper saddle (TC6) almost remains the same. At 30th minute the temperature of the secondary CC and the secondary evaporator falls below the supercritical temperature of nitrogen and the liquid nitrogen begins to generate in them. At 58th minute the secondary CC and the secondary evaporator are filled with liquid nitrogen. Then the secondary evaporator is applied 1.5W, the secondary loop starts up and the cold liquid nitrogen flows from the primary condenser to the primary evaporator for cooling the primary evaporator. So the temperature of the primary CC, the primary evaporator and the copper saddle (TC6) decreases rapidly. At about 208th minute the primary CC and the primary evaporator are full of liquid nitrogen. Then heat load applied to the secondary evaporator reduces to 0.5W and the primary evaporator is applied 2W, we can see that the primary loop runs stably. The supercritical startup of Loop 1# succeeds. However we see that at about 160th minute the temperature of all the temperature sensors begins to rise unexpectedly. Then heat load applied to the secondary evaporator is turned off. That is because the pulse tube cooler breaks down and about 5 minutes later it operates normally again. When the temperature of the secondary evaporator decreases below 100K, 1.5W is applied to the secondary evaporator and the temperature of the primary evaporator begins to decrease.

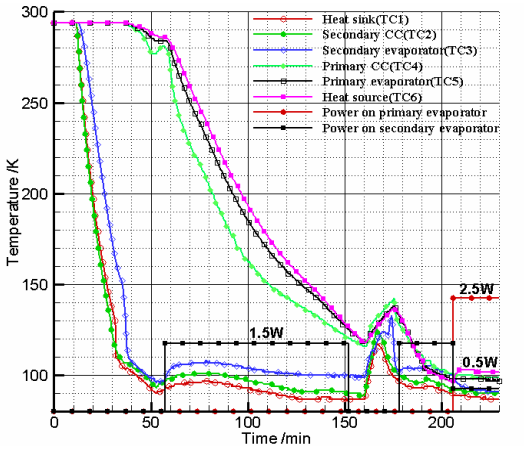


Fig. 3 Supercritical startup of the integrated system of Loop 1#

3.2 Heat transport capacity of the integrated system

The heat transport capacity of the Loop 1# and Loop 2# is shown as Fig. 4 and Fig. 5 respectively. When the heat transport capacity of one Loop is being tested, the other one does not operate. As shown in Fig. 4, when 0.5W is applied to the secondary evaporator of the Loop 1# and heat load applied to the primary evaporator (the copper saddle) gradually increases from 1W to 4W, the temperature of the Loop 1# can remain stable. This indicates that the Loop 1# can operate normally. However, when heat load applied to the primary evaporator increases to 5W, the temperature of the primary evaporator and heat source rapidly rises. So the Loop 1# fails to operate and the heat transport capacity of Loop 1# is 4W. As shown in Fig. 5, when 0.5W is applied to the secondary evaporator of Loop 2# and heat load applied to the primary evaporator (copper saddle) gradually increases from 1W to 3W, the temperature of Loop 2# can remain stable. This indicates that Loop 2# can operate normally. However, when heat load applied to the primary evaporator increases to 4W, the temperature of the primary evaporator and heat source rapidly rises. So Loop 2# fails to operate and the heat transport capacity of Loop 1# is 3W. Although the structure of Loop 2# is the same as Loop 1#, the heat transport capacity of Loop 2# is less than that of Loop 1#. The main reason for the difference may lie in the manufacturing process.

For Loop 1#, when heat load applied to the primary evaporator is 4W, the temperature of TC6 and TC12 is 85.6K and 89.6K and the temperature of TC1 is 82.1K. So the thermal resistance of Loop

1# is 1.38K/W. For Loop 2#, when heat load applied to the primary evaporator is 3W, the temperature of TC6 and TC12 is 92.3K and 87.9K and the temperature of TC7 is 85.6K. So the thermal resistance of Loop 2# is 1.5K/W. when Loop 1# is running and Loop 2# is cold backup, the temperature of heat sink (TC7) of Loop 2# is 298K. Because the temperature of heat source is less than 95K, heat that leaks from pulse tube cooler when it stop working is less than 0.05W which is calculated according to Fourier's law of heat conduction. So the flexible fine long pipe of CLHP can block heat leakage from the pulse tube cooler to the infrared optical sensor when the pulse tube cooler stops running.

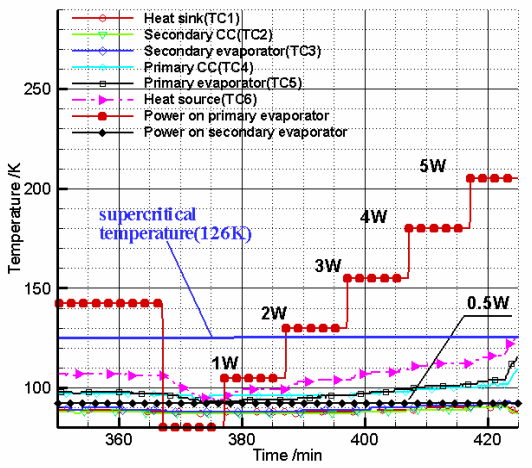


Fig. 4 Heat transport capacity of Loop 1#

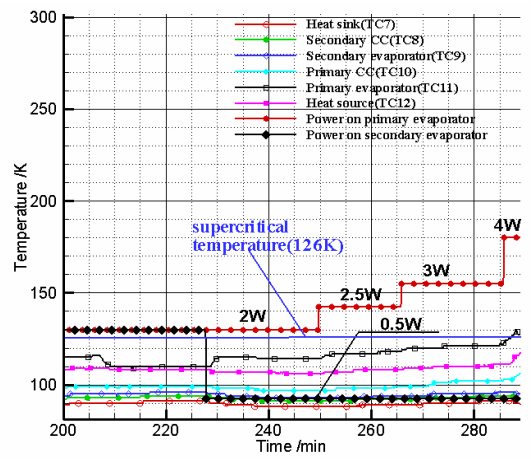


Fig. 5 Heat transport capacity of Loop 2#

3.3 Vibration-isolating test

In order to test the characteristic of the vibration-isolating of the CLHP, we choose another integrated system with a pulse tube cooler and a cryogenic loop heat pipe. This integrated system is placed on the vibration test bench, as shown in Fig. 6. Three sensors are installed on the integrated system. The first sensor locates at the pulse tube cooler where vibration happens. The second sensor locates at the cold finger. The third sensor locates at the primary evaporator which will connect with the infrared optical sensor. The test result is shown in Fig. 7. It reveals that no matter in which direction the vibration is isolated by the fine long pipe of CLHP.

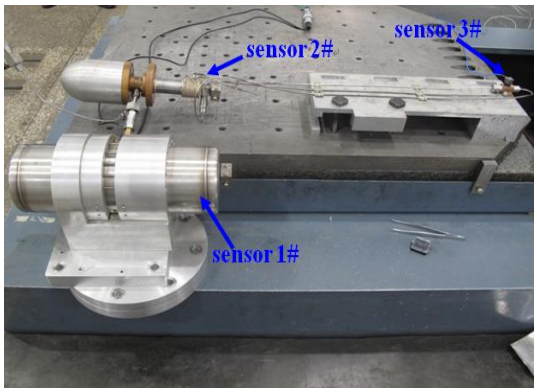


Fig. 6 Vibration-isolating test

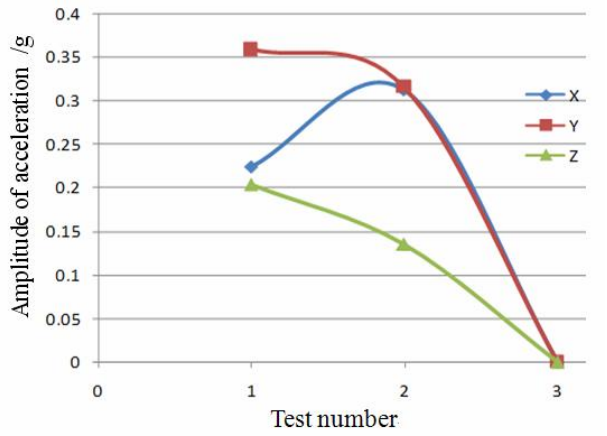


Fig. 7 The result of vibration test

3.4 Operation modes of the integrated system

The operation modes of the integrated system are also investigated in the paper. There are four operation modes, as follows:

1) Normal operation mode. One loop is operating while the other one does not operate;

2) Normal switch operation mode. One loop is operating stably while the other one begins to start up. When the second loop is running stably, the first loop stops running;

3) Failover switch operation mode. One loop is running. Suddenly it breaks down. A few minutes later, the other one begins to start up and run.

4) Cooperation mode. The two loops start up and run together.

The normal operation mode of the integrated system is shown in Fig.4 and Fig.5. Both of the two loops can succeed to start up and run stably. The normal switch operation mode is shown in Fig.8 and Fig.9. In Fig.8, when heat load applied to the secondary evaporator is maintained at 0.5W and heat load applied to the copper saddle is maintained at 2.5W, Loop 1# can run stably. At 317th minute the pulse tube cooler of Loop 2# begins to operate and the temperature of the secondary CC and the secondary evaporator decreases gradually. At 342th minute the secondary CC and the secondary evaporator are filled with liquid nitrogen and 0.5W is applied to the secondary evaporator of Loop 2#. The secondary loop of Loop 2# can succeed to run. At 352th minute the pulse tube cooler of Loop 1# stops running and the heat load applied to the secondary evaporator of Loop 1# is turned off. From Fig.9 we can see that Loop 2# can keep stable operation. The integrated system can realize the normal switch operation mode.

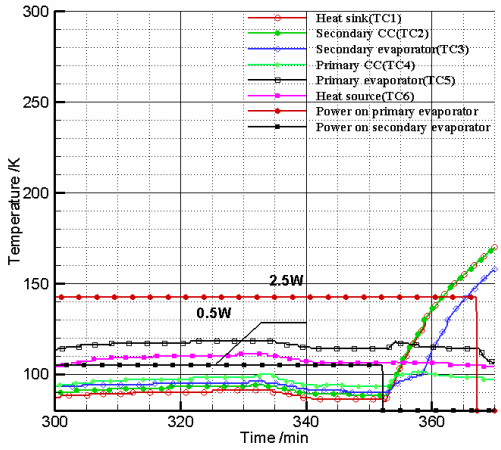


Fig. 8 Normal switch operation mode of Loop 1#

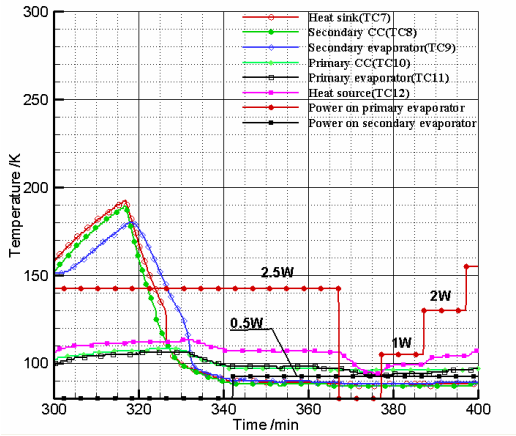


Fig. 9 Normal switch operation mode of Loop 2#

The failover switch operation mode is shown in Fig.10 and Fig.11. At 252th minute the pulse tube cooler of Loop 1# stops working and the heat load applied to the secondary evaporator and the primary evaporator of Loop 1# is turned off. The temperature of the integrated system begins to rise rapidly. This process simulates the failure of Loop 1#. At 275th minute the pulse tube cooler of Loop 2# starts up and the temperature of the secondary CC and the secondary evaporator of Loop 2# decreases rapidly. At 320th minute the secondary CC and the secondary evaporator of the Loop 2# is full of liquid nitrogen. Then 1.5W is applied to the secondary evaporator of Loop 2#, the secondary loop of the Loop 2# begins to run and the super-cooled liquid nitrogen flows from the primary condenser of Loop 2# to the primary evaporator and the copper saddle. So the temperature of the copper saddle decreases gradually. At 377th minute heat load applied to the secondary evaporator is reduced to 1W and 2W is applied to the primary evaporator. From Fig.11 we can see that Loop 2# can succeed to run stably. The integrated system can realize the failover switch operation mode.

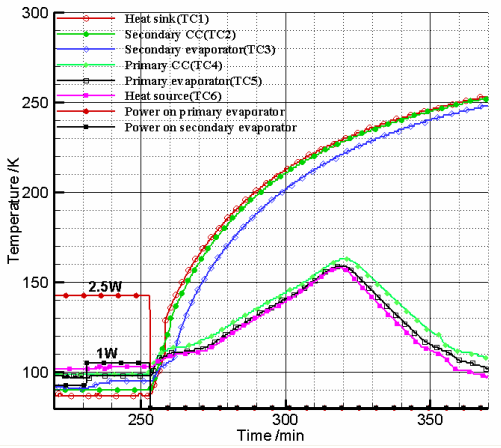


Fig. 10 Failover switch operation mode of Loop 1#

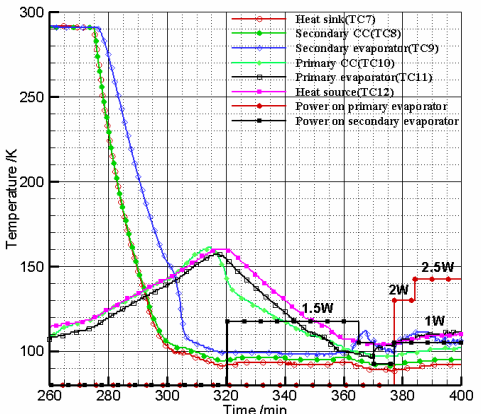


Fig. 11 Failover switch operation mode of Loop 2#

The cooperation mode of the integrated system is shown as Fig.12 and Fig. 13. At 0 minute the two pulse tube coolers both start up and the temperature of the secondary evaporators and the secondary CCs decreases rapidly. At 56th minute the secondary evaporators and the secondary CCs are filled with liquid nitrogen. 1.5W is applied to the two secondary evaporators individually at the same time. The two secondary loops of Loop 1# and Loop 2# begin to run. The temperature of the primary evaporators and the primary CCs decrease gradually. At 106th minute heat load applied to the two secondary evaporators is reduced to 1W. At 118th minute the primary evaporators and the primary CCs are full of liquid nitrogen and 2.5W is applied to the copper saddle(heat source). From Fig.12 and Fig. 13 we can see that each of the two Loops can run stably. The integrated system can realize the cooperation mode.

In Fig. 3 it can be seen that in the process of supercritical startup of one Loop(Loop 1#) , the cooling time of the secondary evaporator takes about 58 minutes from room temperature to the temperature at which the secondary evaporator is filled with liquid nitrogen. In Fig.12 and Fig. 13, the cooling time of the secondary evaporators takes about 56 minutes from room temperature to the temperature at which the secondary evaporators are filled with liquid nitrogen. The time is almost equal. In Fig. 3 when the secondary evaporator is applied 1.5W, the cooling time of the primary evaporator of Loop 1# takes about 125 minutes which does not include failover time of 25 minutes from room temperature to the temperature at which the primary evaporator is filled with liquid nitrogen. In Fig.12 and Fig. 13, when the secondary evaporators are both applied 1.5W, the cooling time of the both primary evaporators takes about 62 minutes from room temperature to the primary evaporators filled with liquid nitrogen, which is about half of that of a single Loop.

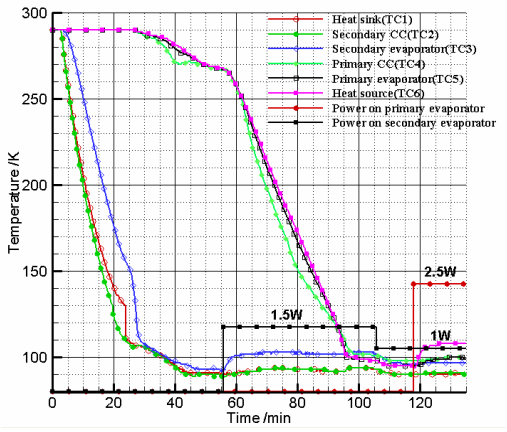


Fig. 12 Cooperation mode of Loop 1#

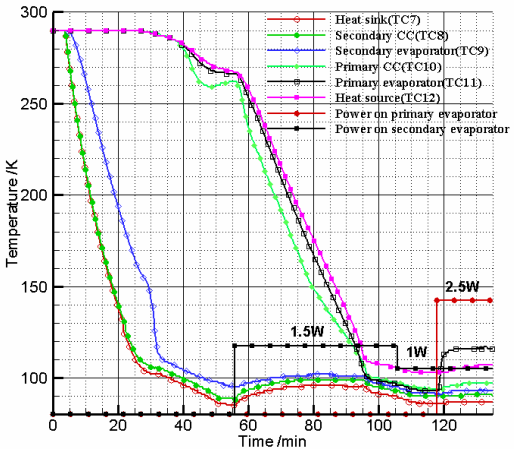


Fig. 13 Cooperation mode of Loop2#

4. CONCLUSIONS

An integrated system with double pulse tube coolers and double cryogenic loop heat pipes is developed in the paper. The supercritical startup，heat transport capacity of CLHPs and the operation modes of the integrated system are experimentally investigated. The results of the experimental study can be summarized as follows:

1) When the pulse tube cooler works as the heat sink, CLHP can succeed to startup and the heat transport capacity of Loop 1# can achieve 4W below 110K. It can meet the requirement of the infrared optical sensors which must operate below 120K and heat load of the infrared optical sensors does not exceed 3W.

2) The flexible long pipes of CLHP can isolate the vibration induced by the pulse tube cooler from the infrared optical sensor and block heat leakage from the pulse tube cooler to the infrared optical sensor when it does not work.

3) The integrated system can realize normal operation mode，normal switch operation mode，failover switch operation mode and cooperation mode. This can improve the life and reliability of the infrared optical sensors effectively.

ACKNOWLEDGEMENT

Financial grants from the National Natural Science Foundation of China (NSFC Grant No. 51406009) are gratefully acknowledged.

NOMENCLATURE

CLHP : Cryogenic Loop Heat Pipe
CC : Compensation Chamber
TC : Thermocouple

REFERENCES

[1] Dave Glaister. Potential solutions for a cryogenic thermal link across a two Axis gimbal for optics cooling. AIAA-98-5205,1998

[2] James Yun, Ed Kroliczek, Larry Crawford. Development of a cryogenic loop heat pipe (CLHP) for passive optical bench cooling applications. SAE TECHICAL PAPER SERIES, 2002-01-2507,2002

[3] D. Bugby, B. Marland, C. Stouffer, et.al. Across-gimbal and miniaturized cryogenic loop heat pipes. STAIF, America Institute of Physics, 2003

[4] Triem T. Hoang, Tamara A. O'Connell, et.al. Development of a flexible advanced loop heat pipe for across-gimbal cryocooling. Proceedings of SPIE, Cryogenic Optical Systems and Instruments, 2003

[5] Triem T. Hoang, Tamara A.O'Connell, et.al. Design optimization of a hydrogen advanced loop heat pipe for space-based IR sensor and detector cryocooling. Proceedings of SPIE, Cryogenic Optical Systems and Instruments, 2003

[6] Mo Qing, Cai Jinghui, Liang Jingtao. Experimental Study of a cryogenic loop heat pipe at the temperature of liquid nitrogen. Vacuum and Cryogenics. 2005, 11(3) : 162-169

[7] Zhou Shuntao. The study to the characteristic of the supercritical startup and stable operation of a cryogenic loop heat pipe [D]. Beijing: Institute of spacecraft system engineering, CAST, 2010

Two Phase Loop Spray Impingement Cooling System

Thanh-Long Phan[1*], Randeep Singh[1], Yuji Saito[1], Masataka Mochizuki[1]

[1]*Thermal Technology Division, Electronics Business Company Fujikura Ltd*
1-5-1, Kiba, Koto-Ku, Tokyo 135-8512, Japan

Abstract

Semiconductor chip packaging machine utilizes cyclic heating and cooling of the bonder head to attach chip to the substrate using solder bumps. In common existing bonding machines, the bonder head is cooled by compressed air based active cooling system which involves long cooling time and releases unhygienic hot air into the room. In order to improve the productivity of the bonding machine by shorten cooling time of chip bonder head, an innovative two-phase loop impingement cooling system with high cooling efficiency and very short cooling time have been proposed, designed and tested. The component of two phase loop impingement cooling system includes a passive loop heat pipe for heat removal and transfer to the remote heat sink and, an active pressurization system to get high pressure liquid impingement flow on the heated surface. Impingement system includes orifice plate in the evaporator with multiple divergent nozzles through which high velocity liquid is injected by means of metallic bellow externally pressurized by compressed nitrogen gas. High pressure liquid spray impingement provide high evaporation heat transfer coefficient in the loop heat pipe evaporator. Fluid removal and heat removal from the evaporator was through total passive evaporation-condensation process in loop heat pipe. In this case, the passive loop heat pipe and active impingement system were separated from each other through a pressure valve. Based on the experimental results of current proposed cooling solution, it was established that more than 80% reduction in the cooling time. It was also established that superior rate of heat removal, h=150,000 W/m^{2}K, were archived during transient cooling of 400^{o}C bonder head with current proposed two phase loop impingement cooling. It was found that the single phase heat removal by nozzle spray is quite small while evaporation heat transfer of spray liquid on sintered powder wick was main contributed. Proposed system will provide high response system for semiconductor bonder with advantages of both active and passive heat transfer systems.

Keywords: bonder head, Loop heat pipe, Spray impingement system, Evaporation, Transient heat removal

1. INTRODUCTION

In production of semiconductor chip packaging, in order to assembly chip to substrate using solder bump , which serves as the interconnection points between chip and circuit substrate, the bonder head utilizes cyclic heating and cooling of the bonder head to melting and solidity of solder bump. Fig. 1 (a) shows bonder head components in assembly chip to substrate process. The heater has vacuum mounting suction for holding semiconductor chip

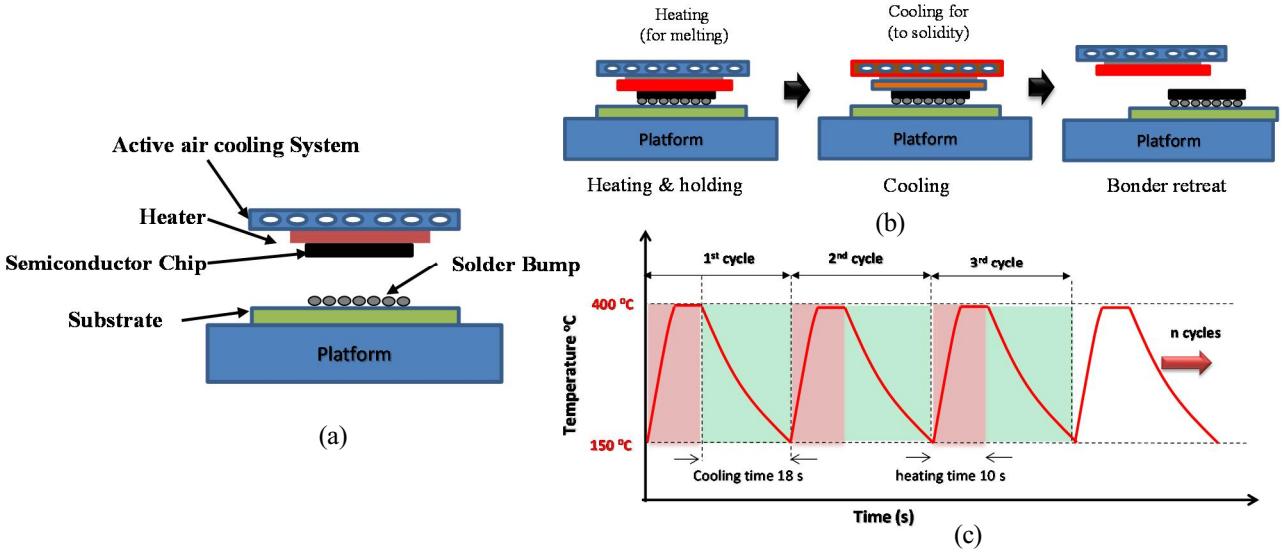


Fig. 1 Bonder head ; (a) components , (b) fabrication process (c) heater temperature profile with heating and cooling with processing time

*Corresponding author: thanhlong.phan@.jp.fujikura.com.
Phone: +81-3-5606-1174, Fax: +81-3-5606-1514

and active air cooling system for cooling process. Fig.1 (b) shows fabrication process flow for the typical heating and cooling cycle of solder bump for joining chip to substrate that can be described as follow. Semiconductor chip is held by vacuum to bonder head and substrate is placed on a platform. After the alignment of the chip and substrate are performed, the bonder head is moved down and the chip is placed on the substrate, and then bonder head temp will be heated for melting solder bump (heating & holding process). Following, the cooling process is for solidity of solder bump. Once the bonding is completed, the bonder head releases the packaged chip and ready for repeating next cycle.

Fig. 1(c) show an example of current existing bonder head temperature profile in multiple cycles with processing time scale. As seen, this is cyclic heating and cooling processes. First bonder head will be heating up to 400°C then hold at that temperature for liquids of solder ball, then cooling down to 150oC for solidity of solder, then bonder header heating/cooling will repeat in next cycle. In existing bonding machines, the bonder head is cooled by compressed air which involves long cooling time of poor performance air cooling. As seen in Fig.1 (c) the cooling time (18s) is about double total heating and holding time (10s) of bonder head, it means over 50% production time of bonder head is just for cooling.

In order to improve the productivity of the bonding machine by shorten cooling time of chip bonder head, an innovative two-phase loop impingement cooling system with high cooling efficiency and very short cooling time have been proposed [1], designed and experimentally conducted.

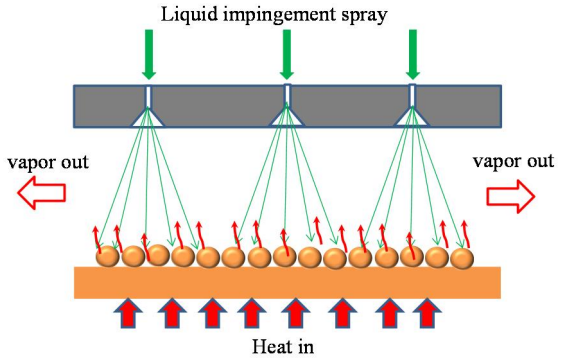


Figure 2. Fundamental concept of heat removal

The objectives of this work are as follows;

(1) Increasing productivity of existing bonder head by shorten 70% cooling time (18s) of existing air cooling solution, which target cooling time is about 5 seconds.

(2) Demonstrate the heat removal capacity of proposed cooling concept for practical design of next version of head bonder.

2. TWO PHASE LOOP SPRAY IMPINGEMENT

Fig 2. shows the selected fundamental concept of heat removal for current two-phase loop spray impingement. The liquid will be sprayed on the hot surface of capillary wick, then heat is mainly removed by latent heat of evaporation. The spray will be activated when bonder need to be cooled right after heating and holding process of bonder head. The purpose of using active liquid impingement spray is for fast cooling purpose with precise amount of liquid needed to be spray. It is

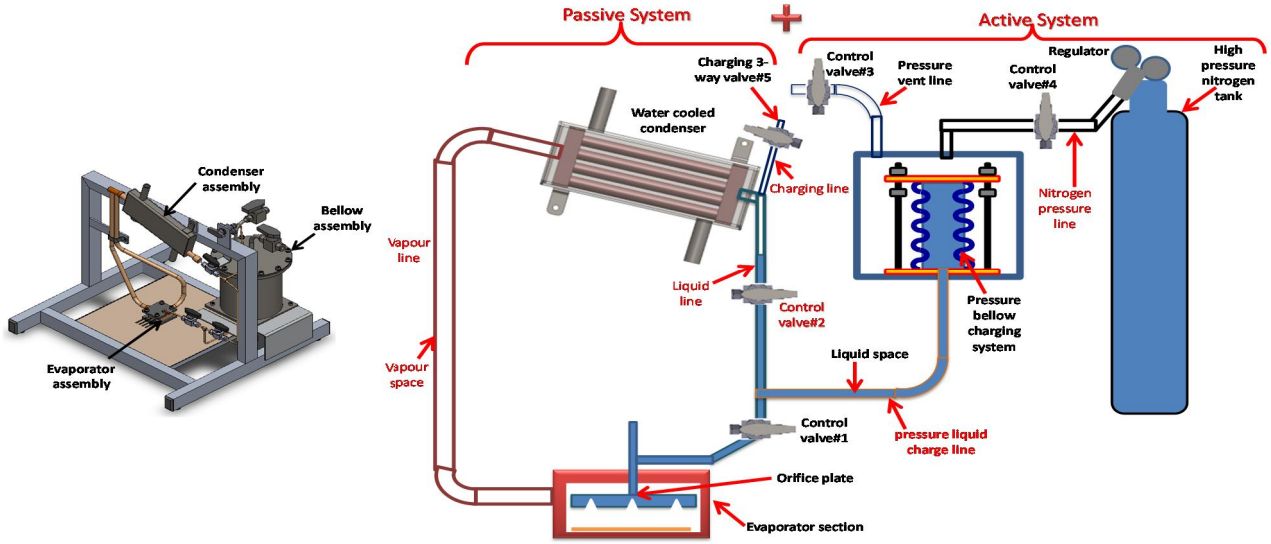


Figure 3. Component level (a) and schematics of two phase loop impingement cooling system (b)

worth to note that in this application, cycles of heating and cooling processes is accurate in timing and repeating, therefore excess liquid spray is not allow, since it will cause longer heating of bonder head. This is main reason high pressure spray impingement was used with closed loop heat pipe. The two-phase loop spray impingement can archive superior high heat removal rate (h=10,000~50,000 W/m2K) utilizing evaporation of thin film liquid on porous media surface structures compared to conventional force air convection (10~1000 W/m2K) or water liquid cooling (1000~10,000 W/m2K). Based on the needed high heat removal rate for fast cooling purpose, the two phase loop spray impingement cooling system was initial design.

Figure 3. (a) shows concept component level of two phase loop impingement cooling system. Basically, it is a hybrid system consist a complete passive closed loop heat pipe and additional active high pressure spray impingement. Fig. 3 (b) depicts schematic of current two-phase loop spray impingement, that includes a passive loop heat pipe for heat removal and transfer to the remote heatsink and, an active pressurization system to get high pressure liquid impingement flow on the heated surface. Impingement system includes orifice plate in the evaporator with multiple divergent nozzles through which high velocity liquid is injected by means of metallic bellow externally pressurized by compressed nitrogen gas. High pressure liquid spray impingement provide high evaporative heat transfer coefficient in the loop heat pipe evaporator. Fluid removal and heat transfer from the evaporator was through total passive evaporation-condensation process in loop heat pipe. In this case, the passive loop heat pipe and active impingement system were separated from each other through a pressure valve.

3. DESIGN OF TWO PHASE LOOP SPRAY IMPINGEMENT

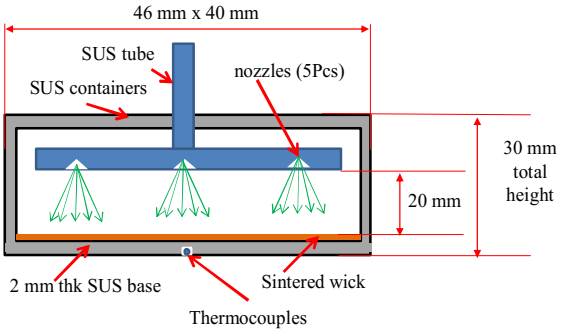


Fig. 4 Evaporator chamber

Table 1 Estimated liquid spray volume for nozzle calculation

Bonder head & Evaporation	Unit	value
Max temp.of system	°C	400
Min temp. of system	°C	150
Total thermal mass of system	J/K	22.8
Total heat need to extract	J	5700
Liquid spray estimation		
letent heat of evaporation	J/kg	2264000
Needed spray volume	cc	5.0

3.1 Evaporator

The heat removal of current system can be contributed by single phase spray impingement and evaporation of sprayed liquid. Since heat removal capacity of evaporation is much higher than that in single phase of sprayed liquid, so it expected that heat removal by evaporation process will be dominated in the system. Fig. 4 shows the schematic of evaporator chamber and main parameters that includes evaporator base which have thin powder copper layer, five nozzles spray and containers. The sinter wick will enhance evaporation heat as well as uniformly distribute the spray water by capillary action to all evaporation area. Since the purpose of current application is fast cooling a head bonder, therefore, the low thermal mass material was selected that is stainless steel SUS 304.

3.2 Spray nozzles

The nozzle spray calculation was based on energy balance of needed heat removal and latent heat of equivalent liquid spray.

$$m = \frac{Q}{h_{fg}} \tag{1}$$

Table 1. shows needed liquid spray volume of current system with current existing temperature condition of bonder head., total mass of bonder head

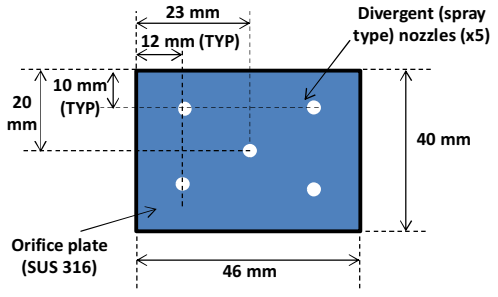


Fig.5 Nozzle layout

Table 2 Nozzle calculation

Nozzle calculation	Unit	value
Number of nozzles		5
Flow rate of nozzle	m/s	43
Nozzle inlet diameter	mm	0.12

and evaporator base was estimated. Speed of liquid injected by bellow is calculated as below;
Bernoulli equation

$$P_1 + \frac{1}{2}\rho v_1^2 + \rho g h_1 = P_2 + \frac{1}{2}\rho v_2^2 + \rho g h_2 \quad (2)$$

Where $v_2 = \sqrt{\frac{2(P_2 - P_1)}{\rho}} = \sqrt{2g(H_2 - H_1)}$

Nozzles diameter was calculated using continuity equation

$$V = A_1 v_1 = A_2 v_2 \quad (3)$$

Nozzle diameter $D_1 = \sqrt{\frac{4A_1}{\pi}}$ (4)

Table 2. show the calculation results for nozzles design. The five micro divergent nozzles with 120µm diameter were fabricated on stainless steel orifice.

3.3 Active high pressure bellows system

The bellows was design for inject high pressure liquid to nozzles. The deflation of bellow was calculated based on needed liquid charged amount. The high velocity liquid is injected by means of metallic bellow externally pressurized by compressed nitrogen gas as seen at Fig. 3 (bellows parts). The bellows have two processes, injection liquid to orifice nozzle plate, and suction condensate liquid back to bellow. At injection stage, high pressure nitrogen gas supplied by gas tank will be fully filled external bellows which located inside vessel chamber. At suction stage, nitrogen gas will be fully released by control valve to lower pressure external of bellow, then let it sucks condensate liquid from condenser back into bellow, then by controlling valves, high pressure nitrogen gas is again filled into chamber external of bellow which it is ready for next cycles.

4. EXPERIMENTAL METHODS

4.1 Operating procedure

Fig. 6 shows the test station, which includes fabricated two phase loop impingement cooling system, heater controller and data logger. The pure water was selected as spray liquid in this work, because its high latent heat of evaporation (2438 kJ/kg) and simplicity in operation. The complete cycle of the system is described as follow. As seen in Fig. 3, firstly water is initially charged in the

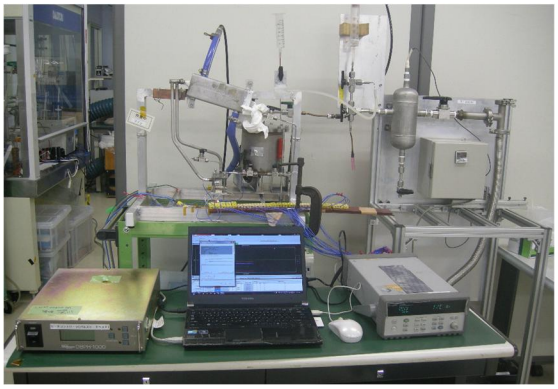
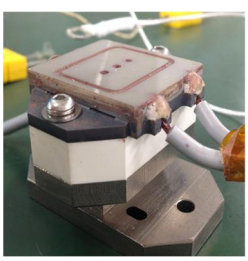
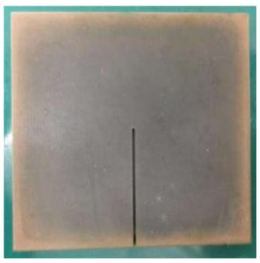


Fig. 6 Test station with heater controller and data logger



(a) Ceramic heater



(b) Evaporator base

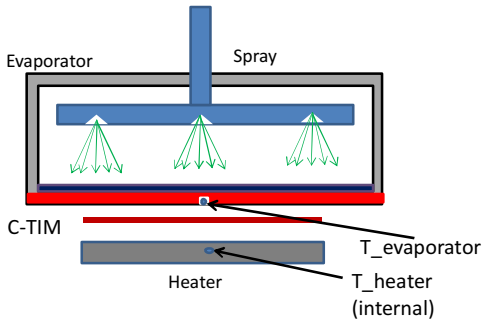


Figure 7. Test-setup for cooling heater

bellow, then high pressure nitrogen gas will be supplied to vessel chamber by opening valve#4. Water inside bellow is ready for injection to evaporator for active cooling. When the heater, which is located under evaporator, reaches the setting temperature (400°C), the control valve #1 will open for active spray through nozzles. The volumetric flow rate of spray water is controlled by opening time of valve#1 located just upstream of orifice plate. In evaporation liquid water is sprayed over the surface of wick structures and then evaporates into the vapor line connecting to condenser tube banks, where its turns to condensate liquid. By releasing high pressure nitrogen gas using valve#3, valve#2 will open to let , the bellow sucking the condensate water back into bellow for finishing one cycle of phase loop impingement cooling system.

4.2 Ceramic heater

The actual existing stand-alone ceramic heater used in chip solder bump bonder head with controller was used in this work. The heater consists of electrical heater part, and ceramic base equipped with active compressed air cooling parts on heater. The heater can be set power input power embed with multi–steps temperature controlling. In this work, 490W maximum heating rate of heater was set. Ceramic heater place on thick insulation plate. The heater has size of 32x25mm which is smaller than current surface area of evaporation in 46 x 40 mm. The maximum working temperature of heater currently is set at 400°C, and the minimum working temperature (solid point) is set at 150°C. In the center of heater have two thermocouples which are for temperature controller and data recorder.

4.2 Data acquisition

The data acquisition system looped through a routine that update all temperature measurement approximately every one second. Temperatures are measured by K-type thermocouples and temperature measurement points are the heater surface temperature (T_heater), temperature of evaporator base (T_evaporator) as seen in Fig. 7(a)

5. EXPERIMENTAL RESULTS AND DISCUSSIONS

5.1 Single phase modelling

The heat removal by spray impingement heat of a single nozzle in this work adopted Martin [2] empirical equation for 2000<Re<30000 as follow;

$$Nu = Pr^{0.42}\frac{D}{r}\frac{1-1.1D/r}{1+0.1\left(\frac{H}{D}-6\right)D/r}F \quad (5)$$

The calculation parameter and results are shown in Table 3. The nozzle exit average velocity of water spray 43m/s. The jet impingement has Reynold number of 6363 which indicate that current spray impingement is still laminar flow, that deliver an average Nu of 13.5 over a circular target spanning 125 time of nozzle diameter (15x15mm2). Finally, the estimated heat removal rate of single-phase spray impingement is 1630W/m^{2}K.

5.2 Heating mode by heater

The lumped capacitate method is used for estimate transient temperature of heater during heating process. In assumption that heater, thermal grease and evaporator are one single solid component with

Table 3 Calculation of heat removal by single phase spray impingement

Pressure of gas (1 Mpa)		Pa	900000
Pressure of spring P=F/A		Pa	4.1233
Hook F=k.x		KN/m	700000
Inflation rate x		m	0.003
Area of bellow	A	m2	0.001963495
dP-Pressure different		Pa	899995.8767
Water density		kg/m3	1000
Velocity of water nozzle-v=sqrt(2* P/ρ)		m/s	42.43
Nozzle diameter	D	m	0.00012
Water Kinetic viscosity ν(m2/s)		m2/s	0.0000008
Reynolds number of spray Re=U*D/ν		Re	6363.96
High of nozzle		H	0.015
Radial position		Ra	0.0025
Prandtl number			7
Martin average Nusselt number, Nu_avg	Nu		13.59161716
$Nu = Pr^{0.42}\frac{D}{r}\frac{1-1.1D/r}{1+0.1\left(\frac{H}{D}-6\right)D/r}F$			
F=1.36*Re^0.574 (For 2000<Re <30,000)	F		207.4333113
Nu=hd/k			
Water thermal conductivity	k	W/m.K	0.6
Heat removal rate h=Nu*k/d	h	W/m2K	1630.99

no temperature gradient inside the system. The heat losses due to stainless steel wall of evaporator within wick structures is negligible in the model, as follow;

$$\begin{bmatrix}\text{Rate of heat}\\ \text{in system}\end{bmatrix} = \begin{bmatrix}\text{Rate of increase}\\ \text{internal energy}\end{bmatrix}$$

$$\frac{dE_{in}}{dt} = \rho VCp\frac{dT}{dt} \quad (6)$$

Thermal mass of system consists heater, thermal grease and evaporator base is defined by as below;

$$\rho VCp_{system} = \rho VCp_{heater} + \rho VCp_{TIM} + \rho VCp_{evaporator} \quad (7)$$

Table 4 shows the parameter and estimated result of total thermal mass of system, which is 22.8 J/K.

The transient temperature of heater during heating process is defined by bellow equation;

$$dT = \frac{dE_{in}}{\rho VCp_{system}} \quad (8)$$

Fig. 8 shows compression transient temperature profile of heater in heating mode between experiment results and calculation result. As seen, estimation temperature profile of heater has reached 400°C earlier than that in experimental results , this due to in modelling, the heat losses of system due to container wall and surrounding environment was neglected. Overall experimental results slightly longer than predicted, but trends relative between estimation and data appear to be correctly captured. These findings indicate that current modeling using lumped capacitate method can evaluate cooling performance of current system.

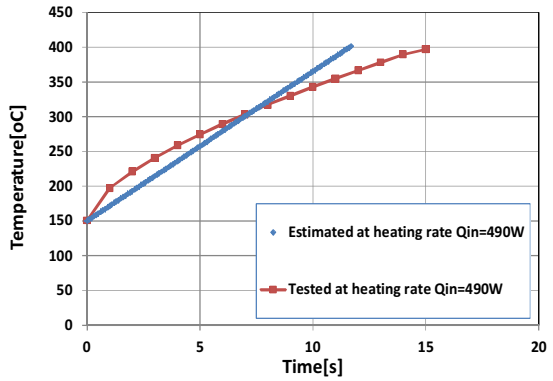


Fig. 8 heater transient temperature profile: experimental results vs. calculation results

5.2 Cooling performance of two phase loop spray impingement.

For cooling process, the he lumped capacitate method is used for estimate the rate of heat removal by the proposed cooling system. The heater need to be cooling down from its maximum temperature, 400°C, to its minimum setting temperature of 150°C. It is assuming that;

+ the rate of heat removal h (W/m^{2}K) is constant during transient cooling process.

Table 4 Thermal mass estimation of modelling system consists heater, thermal grease, and evaporator

Heater part	Symbol	Unit	value
ALN Density	ρ	kg/m3	**3330**
Specific heat Cp	Cp	J/Kg K	**749**
Thermal conductivity	k	W/m.K	**160**
Weight	m	kg	**0.006**
Thermal mass	ρVCp	J/Kg	**4.490**
ALN Base (air cooling)			
Weight (ALN)	m	kg	**0.005**
Thermal mass	ρVCp	J/Kg	**3.99**
Thermal grease C-TIM			
TIM density	ρ	kg/m3	**2900**
Specific heat Cp	Cp	J/Kg K	**1**
Thermal conductivity	k	W/m.K	**6**
Thickness (50µm)	T	m	**0.00005**
Thermal mass	ρVCp	J/K	**0.77**
Evaporator SUS base			
SUS density	ρ	kg/m3	**8000**
Specific heat Cp	Cp	J/Kg K	**460**
Thermal conductivity	k	W/m.K	**9**
Weight	m	kg	**0.02944**
Thermal mass	ρVCp	J/K	**13.54**
TOTAL THERMAL MASS OF SYSTEM		**J/K**	**22.80**

+ Active evaporation surface area is same as foot-print surface of heater (20x30mm)

+ Heat losses are negligible

$$-\begin{bmatrix}\text{Rate of heat}\\ \text{removal}\end{bmatrix}=\begin{bmatrix}\text{Rate of decrease}\\ \text{internal energy}\end{bmatrix}$$

$$-\frac{dE_{out}}{dt}=\rho VCp\frac{dT}{dt} \quad (9)$$

$$-hA_e(T_i-T_\infty)=\rho VCp\frac{dT}{dt} \quad (10)$$

where T_∞ is constant =150°C.

Fig. 9 present experimental result of evaporator base temperature profile and heater temperature profiles. As seen, there is a certain temperature different between heat and evaporator. The evaporator base temperature has fallen from 400C to 150C in just 2.5 second, while the heater needs 12 second to reach 150°C. This is due to the thermal contact resistance between evaporator base and heater surface.

Fig. 10 presents the comparison between estimated evaporator temperature profiles in three level rate of heat removal (h=150,0000, 100,000 and 50,000 W/m^{2}K) with experimental data. As seen, the estimated evaporator base temperature profile having rate of heat removal at h=150,000W/m^{2}K is very well matching with experimental data. It means that current heat removal rate which is mainly contributed by evaporation heat transfer of sprayed liquid on wick structure is over level of 150,000W/m^{2}K. With this very high heat removal, it

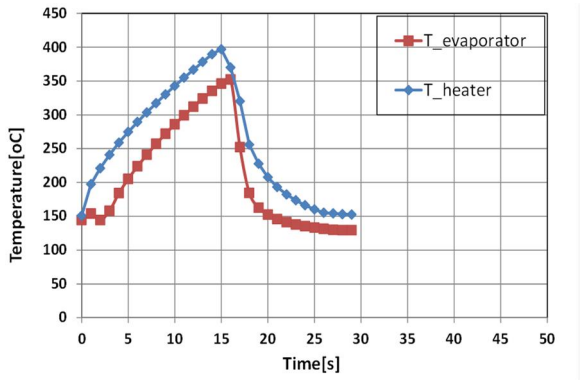


Fig.9 Experimental transient temperature profiles

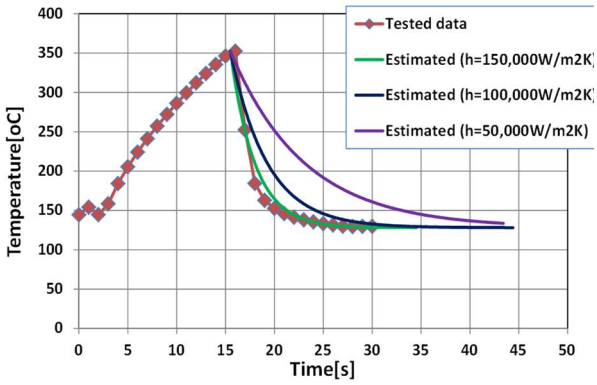


Fig.10 Estimated rate of heat removal with experimental data

is expected the cooling time bonder head having current proposal cooling solution can be within 3 seconds that is 80% shorten cooling time of current existing cooling by air.

6. CONCLUSIONS

Liquid spray impingement on capillary sintered wick structure cooling is an appropriate technique for super high rate of heat removal requirement application, especially for fast cooling system with sensitive processing devices. By taking advantage of high latent heat of evaporation om sintered powder wick. Two phase loop spray impingement cooling, liquid impingement spray cooling has demonstrated to be an superior way of removing heat from a hot from surfaces, requiring only small amount of liquid.

In this work, a two phase loop spray impingement cooling system has proposed for semiconductor bonder head cooling applications. The following are concluding remarks;

1) It has demonstrates that the rate of heat removal of current system is over 150,000W/m^{2}K, which is potential for super-fast cooling method. The heat removal was mainly contributed by evaporation process since the calculated singe phase by nozzle spray impingement is very small.
2) It was established that more than 80% reduction in the cooling time, which is within 3 seconds.
3) For particular semiconductor chip bonder application, more work is required to integrate proposed cooling solution into actual semi-conductor chip bonder head.

REFERENCES

[1] Patent JP 5638049, *High pressure liquid injection system for heat pipe* Sigh R, Phan TL., Mochizuki M., (2012)

[2] Martin, H. *Heat and mass transfer between impinging gas jets and solid surfaces*. Adv. Heat Transfer, (1977).13, 1–60.

[3] Frank P. Incropera, David P. DeWitt, Theodore L. Bergman, Adrienne S. Lavine, *Fundamentals of heat and mass transfer*, Six Ed., Wiley &Son, (2007) 225-300.

[4] Lin, L.C., Leland Q., Multi-nozzle spray cooling in a closed loop, *Proc. of ASME/JSME Thermal Engineering Joint Conference*, Honolulu, Hawaii, USA (2011).

Effect of Different Charge Ratio on Startup Performance of the Bifacial Evaporator Loop Heat Pipe

ZhiChun Liu[1*], Song He[1], Wei Liu[1], JinGuo Yang[1]

[1] School of Energy and Power Engineering, HuaZhong University of Science and Technology, 1037 LuoYu road, Wu Han, Bei, China

Abstract

Loop Heat Pipe (LHP) is an efficient two-phase heat transfer device that has been widely studied in recent years, its applications have been expanded from spacecrafts to terrestrial electronic device cooling. In this paper, the LHP with the bifacial evaporator is put forward to cool the compact electronics. For the bifacial evaporator, heat load can be applied to both sides of the evaporator, breaking through only a surface of the existing flat LHPs for heat dissipation. Two nickel wicks and a secondary wick encircle an annular cavity, working as the compensation chamber that is integrated inside the evaporator, both a secondary wick and the assisted-gravity elevation make sure that two nickel wicks were flooded with the liquid. With the evaporator temperature below 90±2°C, startup performance was investigated at different charge ratio of 60% and 75%. The experimental results showed that the system could start up successfully with one-heated-side and two-heated-side of the evaporator at the given heat load range. When charge ratio was 60% in the horizontal orientation, startup with two-heated-side simultaneously applied 20W-20W manifested reverse flow, and for operation with 10^0 of the tilt angle, startup with one-heated-side could entered into steady state when heat load ranged from 10W to 140W, corresponding to the maximum heat flux for 14.55W/cm^2. However, under the conditions of 75% of the charge ratio and 10°of the tilt angle, the operating performance with two-heated-side was improved greatly, and the total maximum heat load transferred by two-heated-side was up to 240W, similar behavior of two sides was observed. Especially at low heat load ranges, startup time was shorter than that with one-heated-side, and operating temperature showed more stable. Otherwise, continuous operation with two-heated-side was conducted, and the overall thermal resistance of the LHP was analyzed.

Keywords: Bifacial evaporator; Charge ratio; Operating performance; Startup process

1. INTRODUCTION

The rapid advance in thermal packaging of electronic equipment leads to large amount of waste heat from electronic devices [1], various cooling technologies have been developed to address these thermal problems. Loop heat pipes (LHPs) are highly efficient two-phase heat-transfer device with a considerable potential for development and application in various fields [2]. In past decades, LHPs have been successfully tested and employed in aerospace engineering [3], and its applications gradually extend from spacecraft to terrestrial electronics [4]. The key component of the LHP is the evaporator structure mainly affecting the heat transfer performance and the maximum transferred heat load. With the development of the LHP technology, the shape of LHP evaporators have been evolved into two types : the cylindrical and the flat, based on the purpose, the shape and dimensions of heat source, and also working fluid used [5]. Flat evaporators benefit from its flat surface without additional cylinder-plane reducer for thermal contact with flat heat source, but still suffering from higher deformative nature of the flat surface, high heat leak from the active zone and temperature oscillations [6].

In order to implement LHPs inside limited space, numerous experiments and theoretical analysis have been carried out to improve the structure of the flat evaporator and investigate the operating characteristics of the flat evaporator LHP. More efforts have been made to the design of the miniature loop heat pipes (m-LHP), which can be easily integrated inside the compact enclosure of electronic equipment [7-9]. Depending on the relative direction of the main liquid flow in the wick and heat flow to the evaporator wall, a clearly defined development of two main types of the flat

*Corresponding author: zcliu@hust.edu.cn,
Phone: +86-27- 8754-2618, Fax: +86- 27-8754-0724

evaporators are evaporators with opposite replenishment (EOR) and evaporators with longitudinal replenishment (ELR) [5], respectively. Wang et al. have done lots of experiments to study the effect of various factors, including porous wicks, orientations, different working fluids and charge ratio, on the heat transfer performance of the flat evaporators with EOR [10-13], making much contribution to developments of flat evaporator LHPs. For the evaporators with ELR, Randeep al et. presented results about the compensation chamber positioned on the side of the wick structure [14], and Wukchul al et. investigated a flat bifacial evaporator with ELR, transient response and steady state were discussed in detail [15-16]. However, concerning the bifacial evaporator with EOR is rarely published, the lack of data about this structure necessitates further investigation of the flat evaporators with ELR.

In this work, the structure of the bifacial evaporator with EOR was proposed. The LHP with red-copper as the evaporator wall and with methanol as the working fluid was conducted, and its transient response and startup process were discussed at different charge ratio.

2. TEST SETUP

The test system was a miniature methanol-copper flat LHP which consisted of an evaporator with the integrated compensation chamber (CC), two nickel wicks, a secondary wick, liquid/vapor line transport lines, and a condenser, Tab1. gave the geometry parameters of the loop, where O.D. and I.D. represented the outer and inner diameter, respectively. Main features of the miniature LHP were that two sides of the bifacial evaporator could be applied heat load, breaking through only a side of the existing flat LHP for heat dissipation. Fig. 1 presents the details of the internal evaporator structure. Two nickel wicks and a secondary wick were inserted into the evaporator, and they encircled an annular cavity, working as the compensation chamber. The space between the top heating side and the bottom formed the vapor chamber for collecting vapor from the vapor grooves. The evaporator and the condenser are joined together by vapor and liquid transport lines, developing a closed loop. The tube-in-tube condenser was used to cool the working fluid, whose temperature was controlled by a chiller. Heat source simulator was made of copper block with three embedded cartridge heaters and had an active area with outer diameter of 35mm. the applied heat load was regulated by the wattmeter with relative accuracy of 0.5%. For reducing the effect of the ambient temperature on the system, the loop and heat source simulator were wrapped by 10mm thickness nano-adiabatic material with conductivity of 0.012 W/m K. Before charging the working fluid, the system was evaluated to pressure of 4.0×10^{-4} Pa and 4.1×10^{-4} Pa at two different charge ratio of 60% and 75%. 24 T-type thermocouples were attached to the LHP system to monitor the temperature of characteristic points, and the data was acquired by Keithley-2700 data acquisition system.

3. RESULTS AND DISCUSSIONS

A successful startup is the most important

Table 1. Summary of design parameters

Components	Dimensions	value
The evaporator	O.D./height	43.30/16.65 (mm)
The nickel wick 1	Thickness/groove width/groove depth	4.26/2/1.59 (mm)
	porosity	75%
The nickel wick 2	Thickness/groove width/groove depth	4.21/2/1.59 (mm)
	porosity	78%
Circular stainless steel wire mesh	O.D./I.D./thickness	37.6/27/6 (mm)
Vapor line	O.D. /I.D. /length	4/3/330 (mm)
Liquid line	O.D. /I.D. /length	4/3/490 (mm)
Condenser	O.D. for the working fluid	4 (mm)
	O.D. for the coolant	12 (mm)
	Length	802 (mm)

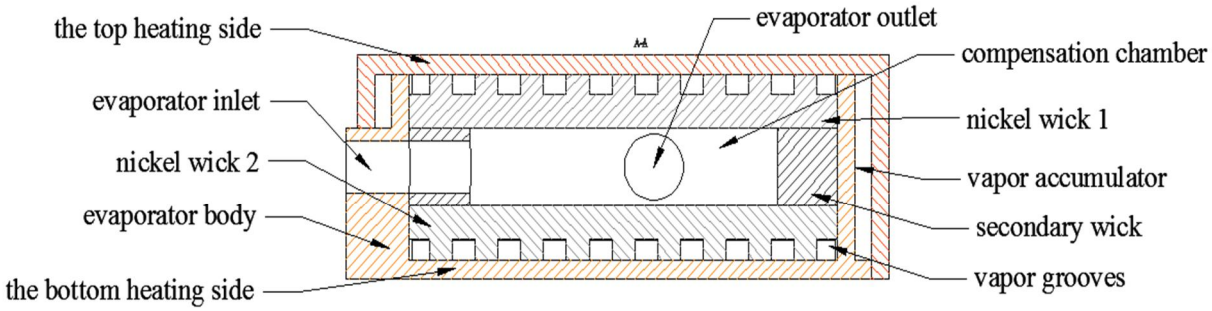


Figure 1. The internal structure of the evaporator

performance for the LHP, and is defined as that the operating process of the LHP reaches a quasi-steady-state or steady state. However, startup behavior is closely related with many factors, including heat load, charge ratio, tilt angle, working fluid used, heat sink temperature and system structure and materials. In the present paper, the operating performance of a LHP with the bifacial evaporator was investigated at different charge ratio of 60% and 75%.

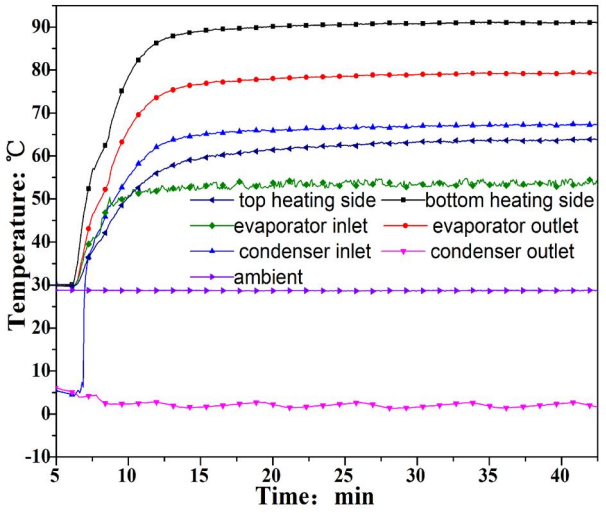


Fig 2. Startup at 140W-10^0-60%

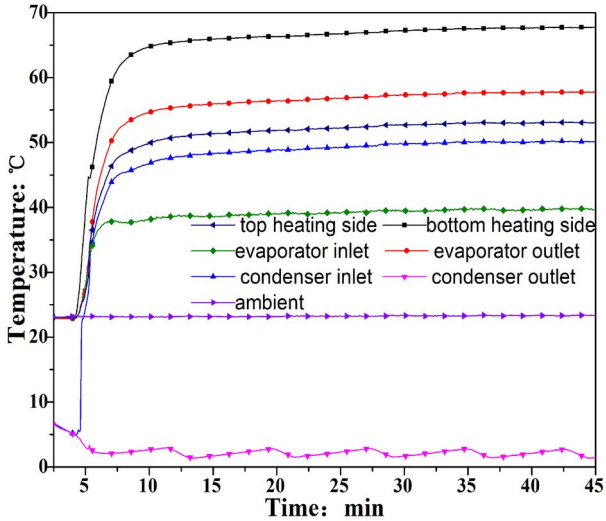


Fig 3. Startup at 140W-10^0-75%

3.1 performance of startup process

Under the same conditions except for charge ratio, startup with one-heated side was made a comparison. Heat load was only applied to the bottom heating side, Fig 2-3 depicted two startup processes of 140W. With the evaporator temperature below 90± 2 ^{0}C，the maximum transferred heat load was 140 W at 60% while 210W at 75%. With charge ratio increasing from 60% to 75%, share of liquid phase in the CC also became lagre, which made two nickel wicks fully saturated. Heat transfer limit of the nickel wick was improved, so the maximum heat load was up to 210W at 75%.

At the same heat load of 140W, similar behavior of two startup processes was observed, and the lower operating temperature was achieved at 75%. The temperature difference between top heating side and bottom one, closely related with the driving force of the working fluid circulation, was 24.3 ^{0}C and 14.5 ^{0}C at 60% and 75%, respectively. At higher charge ratio, the loop achieved smaller temperature difference, implying that greater pressure drop across the wick was established. With charge ratio increased, there was less space reserved for phase change in the internal loop [17]. Although keeping the stable operation at 60% required lower pressure drop, the wicks might dry out because of liquid insufficient when heat load increased larger than 140W.

Fig. 4 gave the startup process of 20W-20W in the horizontal orientation and at charge ratio of 60%. Similar to the startup process of conventional

LHPs, the temperature of top heating side, bottom heating side, evaporator inlet and outlet rose together as two heating sides of the evaporator was applied heat load simultaneously. However, the temperature of the condenser inlet suddenly jumped above the ambient temperature, and subsequently decreased below the temperature of the condenser outlet. After this procedure, the working fluid circulation seemed to be established and the loop started to enter into the steady state, startup appeared to be completed.

Unfortunately, the flow direction of the working fluid in the loop was entirely different from the normal fluid circulation occurred in the internal loop, which the vapor first reached the condenser inlet and condensed into liquid, then returned to the CC through the liquid line. Startup process of 20W-20W at charge ratio of 60%, the working fluid circulation showed reverse direction, moving from the CC to the evaporating surface through the external loop, the temperature of evaporator outlet and condenser inlet was lower than that of evaporator inlet and condenser outlet. There were two reasons that accounted for this phenomenon. Firstly, two nickel wicks participated in vaporization at the same time and more liquid was needed, one of two nickel wicks might dry out because of insufficient liquid supply at small charge ratio. Second, heat leak from the heating surface to the CC was very serious because of the copper possessing high thermal conductivity coefficient, leading to liquid vaporization in the CC and formed the opposite pressure difference. Although successful startup and steady state operation of the loop were achieved at charge ratio of 60%, there still exists some difficulties for applying the bifacial evaporator LHP to electronic device cooling for high operating temperature of 92℃ and bad heat transfer performance.

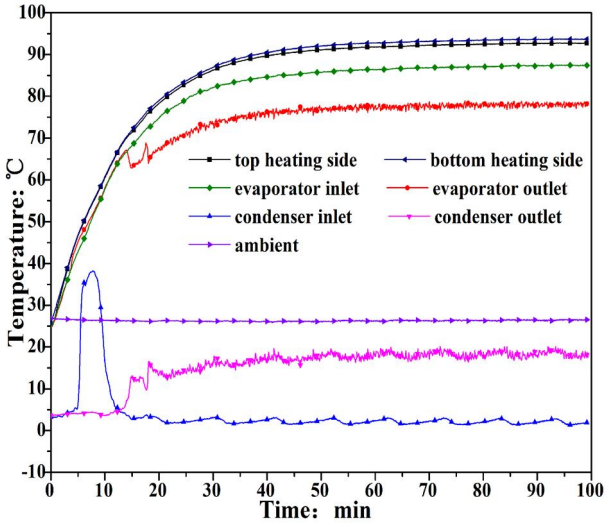


Fig.4 Startup at 20W-20W-0^0-60%

Fig. 5 showed startup process of 20W-20W under the conditions of 10° of tilt angle (the condenser above the evaporator) and 75% of charge ratio. Both high charge ratio and gravity-assisted elevation made sure that two nickel wicks were saturated with liquid, avoiding the occurrence of wicks' dry-out. Under this circumstance, the working fluid circulation became normal, and startup behavior of two heating sides was almost identical. The loop quickly entered into the steady state and operated at temperature of 28℃, similar to startup processes of the existing LHPs with flat disk-shaped evaporator [8].

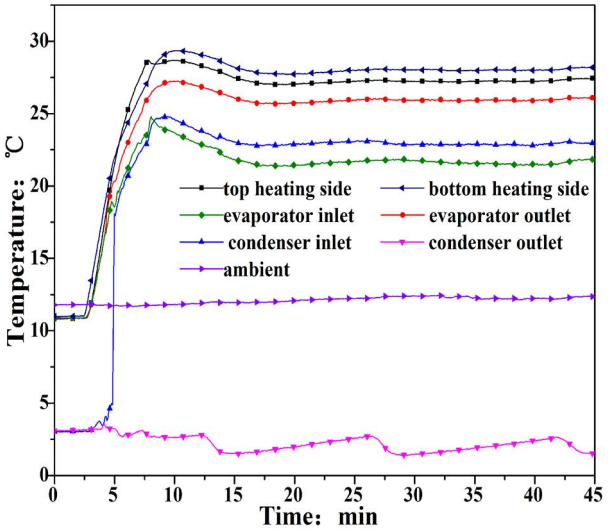


Fig. 5 Startup at 20W-20W-10^0-75%

Increasing charge ratio from 60% to 75%, operating performance of two sides heated simultaneously was greatly improved. Higher charge ratio could saturated two nickel wicks inside the evaporator, inhibiting insufficient liquid supply. In addition, promoting charge ratio could extend the heat transfer capacity of the evaporator for this structure.

3.2 Response to continuous heat load

Two heat source simulators worked as thermal equipment, and were separately attached to two sides of the evaporator. Two different ways of heat

load arrangement were conducted, and the tested results indicated the bifacial evaporator could utilize its two sides to dissipate heat, breaking through only one side of the existing flat LHPs for heat dissipation.

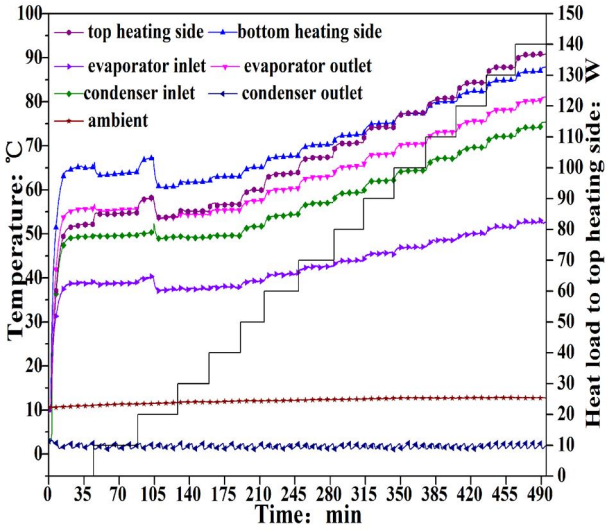


Fig. 6 continuous operation of top heating side fixed at 100W and bottom heating side with the increment of 10W

Fig. 6 described operation process with continuous heat load. Bottom heating side fixed at 100W started up successfully, and then heat load with the increment of 10W was applied to top heating side. When 10W was loaded to top heating side, the established equilibrium state was abruptly broken, triggering liquid evaporation on the nickel wick 1 near the top heating side. The bottom heating surface temperature decreased slightly and the top one increased accordingly. Heat conduction from the evaporator sidewall laid a foundation for the top heating side startup process, operation with 10W quickly entered into steady state. Meanwhile, amount of generated vapor enlarged, the co-evaporation of two nickel wicks reduce the bottom heating side temperature. With heat load increasing to 20W, temperature overshoot was noticed and a small rise of the evaporator inlet and outlet temperature was gained. Thus, the liquid exiting the condenser might achieve insufficient subcooling, leading to the temperature increase in the CC. However, the CC temperature dominated the loop operating temperature, and temperature overshoot was a response to it. Heat load ranging from 30W to 140W, the bottom heating side temperature and the top one varied with heat load increasing. Based on temperature difference between two heating side, the whole operation process could be divided into three parts: a) smaller than 100W, the bottom temperature was higher; b) the temperature of two heating sides was equal when 100W was loaded to the top; c) higher than 100W, the top temperature was higher.

3.3 Analysis of thermal property

Thermal resistance is always used to evaluate the operating performance of the LHP. For the conventional LHPs, thermal resistance is defined as the ratio of the difference between heating side temperature and the average temperature of the condenser inlet and outlet to the applied heat load, but unsuitable for the bifacial evaporator. From the view of heat transfer, the bifacial evaporator amounts to two parallel evaporators, only sharing the external loop. Similar to electrical resistance, the overall thermal resistance for the bifacial evaporator may be calculated as follows:

$$R = \frac{T_e - T_{cond}}{Q_{app}} \tag{1}$$

$$R_{total} = \frac{R_t \cdot R_b}{R_t + R_b} \tag{2}$$

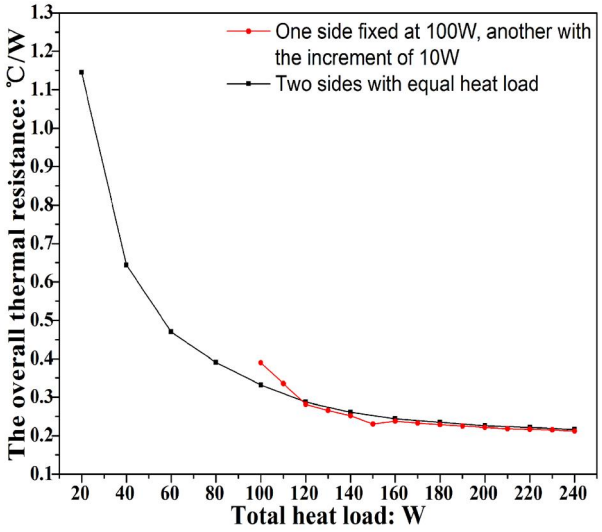


Figure 7. Analysis of thermal resistance for two sides heated simultaneously

Where T_e was the heating side temperature, T_{cond} is the average of the condenser inlet and outlet, Q_{app}

was the applied heat load, R_t and R_b were thermal resistance of the top heating side and the bottom one, respectively. Based on the equations (1) and (2), the overall thermal resistance for two sides heated simultaneously were analyzed when continuous equal heat load or top heating side fixed at 100W and bottom heating side with the increment of 10W were applied to the evaporator, Fig 7. gave thermal resistance dependence of total heat load. From the calculation results, thermal resistance for continuous equal heat load varied from 1.145 ℃/W to 0.216 ℃/W while ranging from 0.390 ℃/W to 0.212 ℃/W for another case. Total heat load higher than 110W, thermal resistance for two different heat load cycles showed almost the same performance.

4. CONCLUSIONS

Aiming at solving thermal management issues with narrow space, the novel evaporator structure was introduced into the LHP. In the present paper, the LHP with a bifacial evaporator structure was investigated at different charge ratio of 60% and 75%. It could be concluded from the experimental results:

(1) At charge ratio of 60%, the circulation direction of the working fluid showed abnormal for two sides heated simultaneously. the new loop could start up from 10W to 140W at 10^0 of tilt angle while from 10W to 210W at 75%.

(2) Increasing charge ratio from 60% to 75%, startup process with two-heated-side quickly entered into steady state, and similar behavior of two heating sides was observed.

(3) The system demonstrated a good response to variable heat load under the condition of the bottom heating side fixed at 100W and the top one with increment of 10W.

(4) Thermal resistance for the bifacial evaporator were analyzed at different heat load cycles, and their values were almost equal when heat load higher than 110W.

ACKNOWLEDGEMENT

The current work was supported by the National Natural Science Foundation of China (Grant Nos. 51276071 and 51376069).

REFERENCE

[1] A. Bar-Cohen, State-of-the-art and trends in the thermal packaging of electronic equipment, *J. Electron. Packaging*, 114 (1992) 257-270.

[2] Pastukhov V.G., Maidanik Yu.F., Vershinin C.V., Korukov M.A., Miniature loop heat pipes for electronics cooling, *Appl. Therm. Eng.*, 23 (2003) 1125-1135.

[3] Goncharov K., Golovin O., Orlov A., Lavochkin and TAIS experience in field of loop heat pipes development and application in spacecraft, *International Workshop on Two-Phase Thermal Control Technology*, 6-7 July 2000, Noordwijk, The Netherlands.

[4] Lin G. P., Li N., Bai L. Z., Wen D. S., Experimental investigation of a dual compensation chamber loop heat pipe, *Int. J. Heat and Mass Transfer*, 53 (2010) 3231-3240.

[5] Maydanik Y. F., Chernysheva M. A., Pastukhov V.G., Review: Loop heat pipes with flat evaporators, *Appl. Therm. Eng.*, 67 (2014) 294-307.

[6] Wang D. D., Liu Z. C., Shen J., Jiang C., Chen B. B., Yang J. G, Tu Z. K., Liu W., Experimental study of the loop heat pipe with a flat disk-shaped evaporator, *Exp. Thermal Fluid Sci.*, 57 (2014) 157-164.

[7] Celata G. P., Cumo M., Furrer M., Experimental tests of a stainless steel loop heat pipe with flat evaporator, *Exp. Thermal Fluid Sci.*, 34 (2010) 866-878.

[8] Singh R., Akbarzadeh A., Mochizuki M., Operational characteristics of a miniature loop heat pipe with flat evaporator, *Int. J. Therm. Sci.*, 47 (2008) 1504–1515.

[9] Pastukhov V. G., Maidanik Y. F., Vershinin C. V., Korukov M. A., Miniature loop heat pipes for electronics cooling, *Appl. Therm. Eng.*, 23 (2003) 1125-1135.

[10] Liu Z. C., Gai D. X., Li H., Liu W., Yang J. G., Liu M. M., Investigation of impact of different working fluids on the operational characteristics of miniature LHP with flat evaporator, *Appl. Therm. Eng.*, 31 (2011) 3387-3392.

[11] Liu Z. C., Li H., Chen B. B., Yang J. G., Liu W., Operational characteristics of flat type loop heat pipe with biporous wick, *Int. J. Therm. Sci.*, 58 (2012) 180-185.

[12] Chen B. B., Liu Z. C., Liu W., Yang J. G., Li H., Wang D. D., Operational characteristics of two biporous wicks used in loop heat pipe with flat evaporator, *Int. J. Heat Mass Transfer*, 55 (2012) 2204-2207.

[13] Chen B. B., Liu W., Liu Z. C., Li H., Yang J. G., Experimental investigation of loop heat pipe with flat evaporator using biporous wick, *Appl. Therm. Eng.*, 42 (2012) 34-40.

[14] Singh R., Akbarzadeh A., Dixon C., Mochizuki M., Novel design of a miniature loop heat pipe evaporator for electronic cooling, *Journal of Heat Transfer,* 129(2007)1445-1452.

[15] Joung W., Yu T., Lee J., Experimental study on the operating characteristics of a flat bifacial evaporator loop heat pipe, *Int. J. Heat Mass Transfer*, 53 (2010) 276-285.

[16] Joung W., Yu T., Lee J., Experimental study on the loop heat pipe with a planar bifacial wick structure, *Int. J. Heat Mass Transfer*, 51 (2008) 1573-1581.
[17] Chen B. B., Liu W., Liu Z. C., Yang J. G, Li H., Experimental Study on Miniature Loop Heat Pipe with Flat-Plate Evaporator, *Journal of Astronautics*, 4(32)953-957.

Development of 100W-class Loop Heat Pipes for Space Use and On-orbit Experiment Test Plan

Atsushi Okamoto[1], Ryuta Hatakenaka[1], Takeshi Miyakita[1] and Hiroyuki Sugita[1]

[1]*Research and Development Directorate, Japan Aerospace Exploration Agency, Tsukuba 305-8505, Japan*

Abstract

It has recently become difficult to meet the increasing thermal control requirement of spacecraft with only existing thermal control devices. A loop heat pipe (LHP) is an effective method to satisfy such a requirement. The LHP is a two phase heat transfer device that utilizes the evaporation and condensation of a working fluid to transfer heat and capillary force to circulate the fluid. The LHP can transport much heat for a long distance against gravity and has many other excellent characteristics, such as high controllability of operating temperature and a shutdown function. In this study, 100W-class LHP for space application has been developing. As a part of the study, bread board model (BBM) of LHP was designed and fabricated. As a result of on-ground test of BBM, it is confirmed that BBM can satisfy all requirement (e.g. maximum transport rate, minimum required heat load for start-up, operating temperature control and shutdown function). In order to apply the LHP to the thermal control system of spacecraft, the thermal characteristic under the micro-gravity condition should be examined in advance. On-orbit experiment of a LHP radiator system is planned. This paper describes the result of the on-ground test of LHP (BBM) and the test plan of on-orbit experiment of a LHP radiator system.

Keywords: loop heat pipe, heat transfer, space, on-orbit experiment

1. INTRODUCTION

It has recently become difficult to meet the increasing thermal control requirement of spacecraft with existing thermal control devices. A loop heat pipe (LHP) is an effective method to satisfy the requirement. An LHP is a two phase heat transfer device that utilizes the evaporation and condensation of a working fluid to transfer heat and capillary force to circulate the fluid [1-4]. Figure 1 shows a schematic of an LHP. It consists of an evaporator, a vapor transport line, a condenser, a liquid transport line, and a reservoir (also called a compensation chamber or a hydro-accumulator). The evaporator contains a porous wick that develops a capillary force to circulate the fluid. The operating principle of the LHP is as follows: As heat load is applied to the evaporator, the working fluid is vaporized and a meniscus is formed at the vapor/liquid interface in the evaporator wick. The meniscus develops capillary force and the capillary force circulates the working fluid. The vapor enters the condenser through the vapor line and condenses in the condenser by dissipating the heat to the heat sink. The liquid is subcooled and goes back to the evaporator through the liquid line and bayonet tube. The excess liquid is stored in the reservoir. The LHP can transport much heat for a long distance against gravity and has many other excellent characteristics, such as high controllability of operating temperature and a shutdown function. Due to its excellent characteristics, the LHP has gained great acceptance as an essential thermal control device among spacecraft thermal engineers and is being applied to many U.S., Russian, and European satellites [5-8]. A double-condenser-type LHP was used on the Monitor of All-sky X-ray Image (MAXI) in the Japanese Experiment Module (JEM) on the International Space Station (ISS), but it was not manufactured in Japan [9]. Although research and development of an LHP has been conducted for a long time in Japan, a Japanese LHP has not yet been employed in a practical mission. Two types of LHP are under development: One is a normal LHP and the other is a Reservoir Embedded LHP (RELHP). In the RELHP, a reservoir is not connected to the evaporator, and the evaporator core is used as the reservoir. The RELHP is in the space demonstration phase and an on-orbit experiment of an RELHP-based deployable radiator is being conducted [10-15].

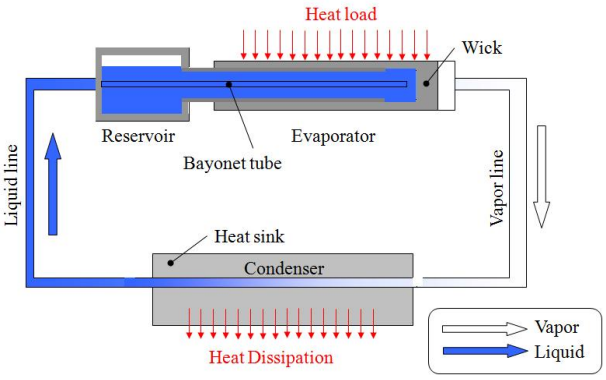


Fig. 1. Schematic of an LHP.

Meanwhile, the normal LHP, in which the reservoir is connected to the evaporator, is in the BBM development phase. So far, development of hardware (primary wick, secondary wick and laboratory model) was performed and the simulation model for the prediction of the behavior of LHP was also built. As a part of the development, visualization of the working fluid inside LHP using neutron radiography technology was conducted for the better understanding of LHP [16]. Since the technology is matured, design and fabrication of BBM was performed. This paper describes the on-ground testing of BBM and the test plan of on-orbit experiment of a LHP radiator system.

2. DEVELOPMENT OF BBM

Figure 2 and Fig.3 show a picture of the LHP BBM and a close-up picture around evaporator are respectively. The major design parameters of LHP BBM are summarized in Table 1. LHP BBM consists of an evaporator, a vapor line, a condenser, a liquid line, and a reservoir. The evaporator casing is made of stainless steel and houses a stainless steel wick with a pore radius of 1.2 μm. Aluminum evaporator saddle is attached to the evaporator to be able to obtain good thermal conductance between heat source and the evaporator. Ceramic heaters capable of delivering 400W are attached to the evaporator saddle to provide heat load to the evaporator. The vapor line and liquid line, each 3000 mm long, are made of stainless tubes with an I. D. of 4.57mm and 2mm respectively. The condenser is made of stainless steel tube of 4.57 mm in I. D. x 1800 mm in length. A cold plate is attached to the condenser pipe by soldering. This cold plate play a role of radiator panel in thermal vacuum testing. For the purpose of the thermal vacuum testing, cold plate is black painted whose infrared emissivity is relatively high. Ammonia was employed as a working fluid. The reservoir is 23.0 mm in I. D. x 190 mm in length. Pressure of the vapor inside reservoir is measured using pressure sensor and the temperature of the working fluid inside reservoir is also measured using type-T thermo-couple. By comparing the measured pressure and the saturated vapor pressure at measured temperature, non-condensable gas (NCG) can be detected because the pressure inside reservoir will increase by a partial pressure of NCG if NCG generates in the loop. The LHP have a secondary wick for the purpose of supplying enough amount of working fluid from reservoir to the evaporator core under any conditions. The piping layout is arranged so that the entire LHP matches the space chamber for small satellite to be able to conduct the thermal vacuum testing using the chamber. In ambient testing, the LHP is wrapped with the insulation material.

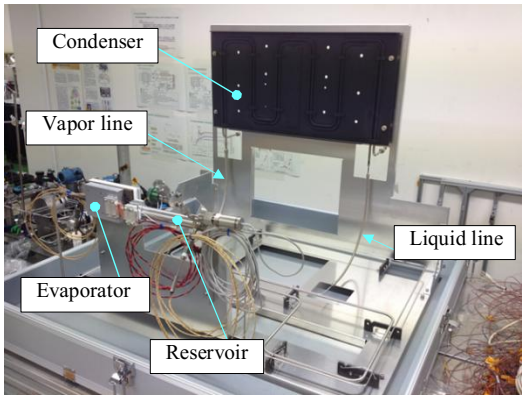


Fig. 2. Picture of LHP BBM.

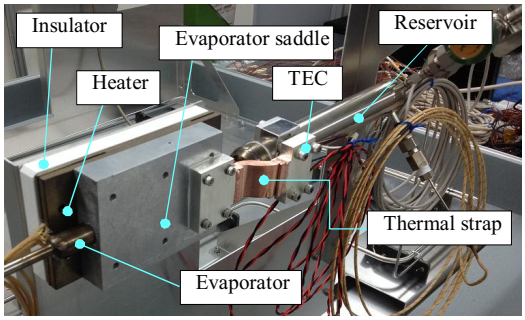


Fig. 3. Close-up picture around evaporator of BBM.

Table 1. Major specifications of LHP BBM.

Evaporator	O.D.:12.7mm, Length:10cm
Primary Wick	Sintered stainless steel
Vapor line	I.D.:4.57mm, Length:3m
Condenser line	I.D.4.57mm, Length:1.8m
Liquid line	I.D.2mm, Length:3m
Working Fluid	Ammonia

3. ON-GROUND TESTING OF BBM IN AMBIENT

3.1 Overview of on-ground testing

A comprehensive series of on-ground testing was performed to characterize thermal performance under 1-g and ambient conditions. During the test, all components of LHP are insulated with insulating material to prevent the heat exchange with the ambient. Heat is applied to the evaporator saddle by electrical heater and the temperature of a cold plate is controlled by circulating the coolant in the pipe attached to the cold plate. Temperature of each component of LHP are measured with T-type thermo-couples.

3.2 Start-up and step-wise power test

In this test, heat load to the evaporator saddle was increased stepwise from 5 W to 125 W. The temperature of cold plate was set at 10degC. The LHP successfully started up at 5 W and operated stably at every heat load up to 125W as shown in Fig. 4. Operating temperature under different heat load is shown in Fig.5. The operating temperature curve shows typical shape of operating temperature of LHP. The heat leak from the evaporator to reservoir is one of the major parameter which affect the LHP performance, especially operating temperature of LHP, is shown in Fig.6. The heat leak ratio is calculated by Eq. (1);

$$Q_{leak}/Q_{eva} = {}^{C_{pl} \times \Delta T_{sub}}/_{H_{fg}} \quad (1)$$

As shown in Fig. 6, heat leak ratio at each heat load to the evaporator saddle are less than 5%.

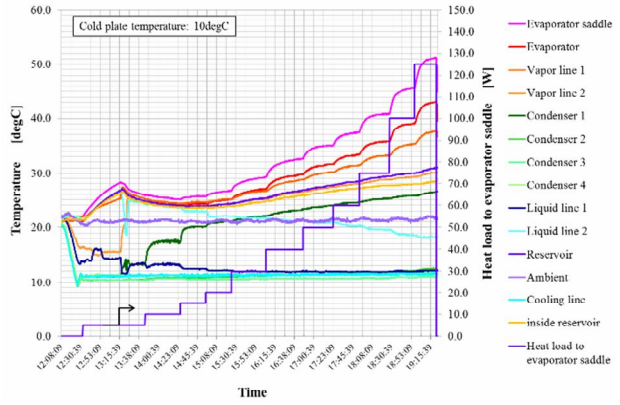


Fig. 4. Result of step-wise power test (cold plate temperature: 10degC).

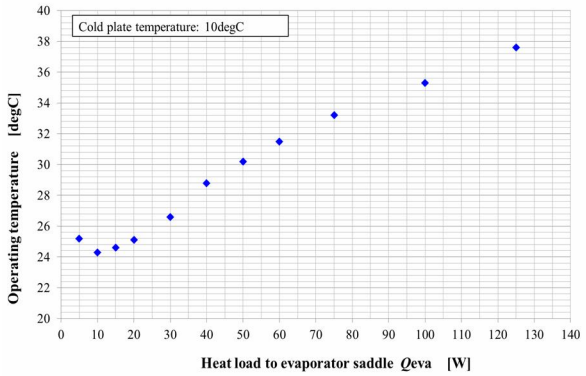


Fig. 5. Operating temperature vs heat load to evaporator saddle (cold plate temperature: 10degC).

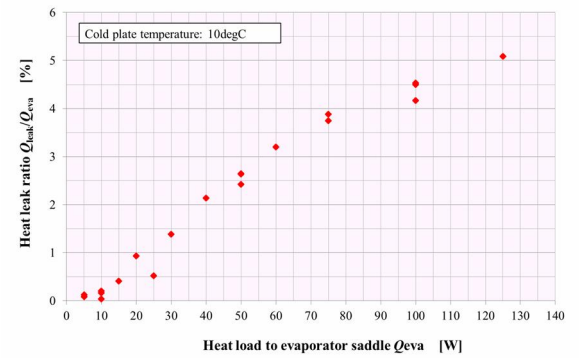


Fig. 6. Heat leak ratio vs heat load to evaporator saddle (cold plate temperature: 10degC).

3.3 Power cycle test

In this test, heat load to the evaporator saddle was suddenly changed to confirm the tolerance against the rapid change in heat load considering the on-orbit operation in practical mission. The temperature of cold plate was set at 10degC.

The LHP successfully started up at 100 W without any failure. After reaching the equilibrium state, heat load to the evaporator was suddenly decreased to 5W and cycled between 5W and 100W. When heat load rapidly changed from 100W to 5W, there was a possibility that LHP lost its heat transfer function due to the rapid change in the amount of liquid in the reservoir and the evaporator core which could lead to the lack of working fluid required for the stable operation of LHP. However, the LHP did not lose its heat transfer function and reached new steady state following the rapid change in the heat load to the evaporator saddle.

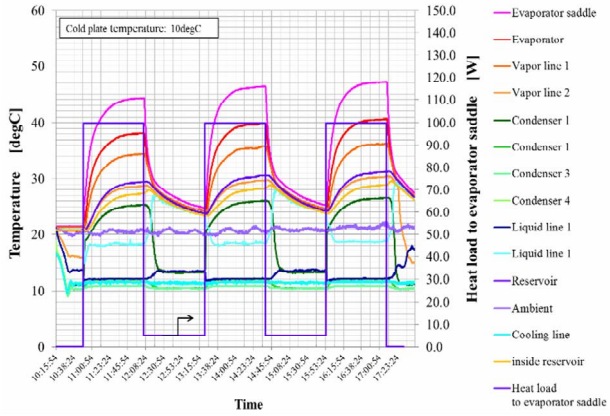


Fig. 7. Result of power cycle test (cold plate temperature: 10degC).

3.4 Condenser sink temperature change test

In this test, condenser sink temperature was suddenly changed from 10degC to 35degC to

confirm the tolerance against the rapid change in thermal condition of LHP radiator. The heat load to the evaporator saddle was constant (100W).

As shown in Fig. 8, LHP started-up successfully right after 100W was applied to the evaporator saddle. After reaching the equilibrium state, condenser sink temperature was rapidly changed from 10degC to 35degC. LHP did not lose its heat transfer function and gradually reached a new steady state following a condense sink temperature change. From this result, it is confirmed that LHP can show stable behavior if the thermal condition (e.g. heat input by solar irradiation, radiation sink temperature) rapidly changes on orbit.

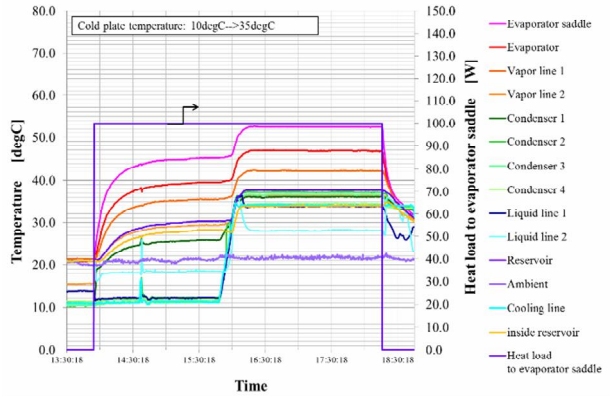


Fig. 8. Result of condenser sink temperature change test (heat load to the evaporator saddle: 100W).

4. ON-ORBIT EXPERIMENT TEST PLAN

As described in previous chapter, the thermal performance of LHP BBM under 1-g condition was successfully evaluated. And the effect of the gravity on the thermal performance of LHP was also experimentally investigated by changing the orientation of the test article relative to the gravity direction. However, in order to apply the LHP to the thermal control system of spacecraft, the thermal characteristic under the micro-gravity condition should be examined in advance to confirm that LHP can operate as expected also in u-g condition. On-orbit experiment of a LHP radiator system is planned. On-orbit experiment will be carried out on ISS/JEM. Experimental apparatus mainly consists of LHP radiator ("LHP" in Fig.10) and the electric component ("ELE" in Fig.10) LHP radiator will be installed on MPEP which is grabbed by JEM/RMS. Piping layout of LHP will be designed so that all components of LHP are able to be fit into the box as shown in Fig.11 and upper panel of the LHP box is used as a radiator panel. In orbit experiment, heat is applied to the evaporator saddle via heater block and heat is transferred by LHP to the radiator and is radiated from the surface of radiator to space. Behavior of LHP will be evaluated based on the temperature data. And pressure inside reservoir will be also measured for the NCG evaluation. Major test parameter are heat load to the evaporator and a radiator sink condition which can be controlled by changing the orientation of radiator panel using RMS. Operating temperature control test and the shut-down test will be also performed. Hardware development is going on toward the launch in winter of 2016.

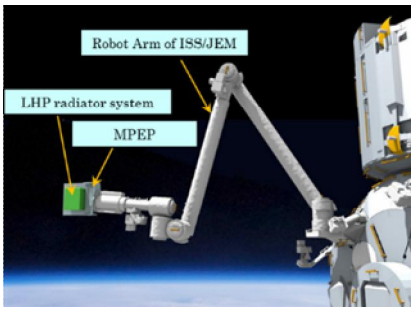


Fig. 9. Image of LHP radiator on-orbit experiment on ISS/JEM.

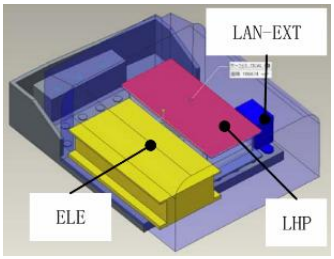


Fig. 10. Installation configuration of LHP radiator on MPEP.

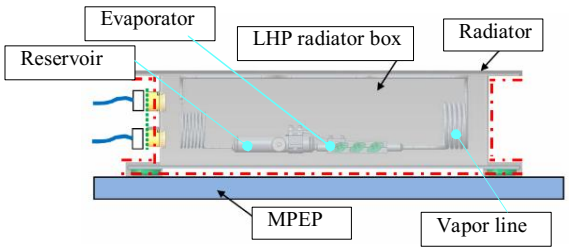


Fig. 11. Preliminary design of LHP radiator for on-orbit experiment.

5. CONCLUTION

The development of 100W-class LHP (BBM) was introduced. BBM showed good thermal performance in 1-g condition. Before applying this LHP to space applications, on-orbit experiment of LHP radiator is planned in order to confirm the thermal performance under u-g condition. Preliminary plan of on-orbit experiment was also

introduced. The LHP radiator will be launched in winter of 2016 and the development of hardware for on-orbit experiment is going on.

NOMENCLATURE

LHP : Loop Heat Pipe
ISS : International Space Station
JEM : Japanese Experimental Module
MPEP : Multi-Purpose Experiment Platform
RMS : Remote Manipulator System
Q_{eva} : Heat load to evaporator (W)
Q_{leak} : Heat leak to reservoir (W)
C_{pl} : Specific heat (liquid) (J/(kgK))
ΔT_{sub} : Subcool temperature (K)
H_{fg} : Latent heat (J/kg)

REFERENCES

[1] J. Ku: Operating Characteristics of Loop Heat Pipes, SAE Paper No.1999-01-2007, 1999.
[2] Y.F. Maidanik and Y.G. Fershtater: Theoretical Basis and Classification of Loop Heat Pipes and Capillary Pumped Loops, Proc. 10th International Heat Pipe Conference, X-7, pp.1-15, 1997.
[3] T. Kaya and T.T. Hoang: Mathematical Modeling of Loop Heat Pipes and Experimental Validation, Journal of Thermophysics and Heat Transfer, Vol.13, No.3, July-September, 1999.
[4] T.T. Hoang and J. Ku: Heat and Mass Transfer in Loop Heat Pipes, Proceedings of 2003 ASME Summer Heat Transfer Conference, July 21–23, 2003, Las Vegas, Nevada, USA
[5] S. Oost, M. Dubois, G. Bedaert, B. Moschetti and M. Amidies: High Performance Capillary Loop, Operation Mapping and Applications on STENTOR, SAE Paper No.961565, 1996.
[6] F. Bodendieck, R. Schllit, O. Romberg, K. Goncharov, V. Buz, and U. Hildebrand: Precision Temperature Control with a Loop Heat Pipe, SAE Paper No.2005-01-2938, 2005.
[7] D. Douglas, J. Ku and T. Kaya: Testing of the Geoscience Laser Altimeter System (GLAS) Prototype Loop Heat Pipe, AIAA Paper No.98-1587, 1998.
[8] E.W. Grob: System Accommodation of Propylene Loop Heat Pipes for the Geoscience Laser Altimeter System (GLAS) Instrument, SAE Paper No.2001-01-2263, 2001.
[9] H. Nagai and S. Ueno: Performance Evaluation of Double-condenser Loop Heat Pipe onboard Monitor of All-sky X-ray Image (MAXI) in Thermal Vacuum Testing, SAE Paper No.2005-01-2939, 2005.
[10] T. Ogushi, M. Murakami, A. Yao, T. Okamoto, and H. Masumoto: Heat Transfer Performance of Flexible Looped Heat Pipe, Proc. of 10th IHPC, pp.1-6, 1997.
[11] T. Ogushi, A. Yao, J. Xu, H. Masumoto, and M. Kawaji: Heat Transfer Characteristic of Flexible Looped Heat Pipe under Micro-gravity Condition, Proc. of 11th IHPC, pp.1-6, 1999.
[12] T. Ogushi, S. Haga, H. Ishikawa, A. Yao, A. Miyasaka, and H. Noda: Mathematical Modeling for Predicting Steady State and Transient Characteristics of Reservoir Embedded Looped Heat Pipe (RELHP), SAE Paper No.2001-01-2239, 2001.
[13] H. Ishikawa, A. Yao, T. Ogushi, S. Haga, A. Miyasaka, and H. Noda: Development of Loop Heat Pipe Deployable Radiator for Use on Engineering Test Satellite VIII (ETS-VIII), SAE Paper No.2001-01-2341, 2001.
[14] H. Kawasaki, T. Yabe, A. Okamoto, H. Ishikawa, T. Nomura, and Y. Saito: Characteristics of Reservoir Embedded Loop Heat Pipe in an Orbital Environment in the First Year, SAE Paper No.2009-01-2518, 2009.
[15] H. Kawasaki, H. Noda, T. Yabe, H. Ishikawa, T. Nomura, and Y. Saito: Characteristics of Reservoir Embedded Loop Heat Pipe in Deployable Radiator on ETS-VIII at Beginning of the Experiment under Orbital Environment, AIAA Paper No.08-3926, 2008.
[16] A. Okamoto, R. Hatakenaka and M. Murakami: Visualization of a Loop Heat Pipe Using Neutron Radiography, Heat Pipe Science and Technology 21-4) : pp. 161-172, 2011.

Capillary Thermosiphon Loop for High Power Electronic Cooling by Natural Convection

Vincent Dupont[1*], Thomas Nicolle[1] and Cyrille Billet[1]

[1]*CALYOS S.A., rue de l'Industrie, 24, B-1400 Nivelles, BELGIUM.*

Abstract

The present paper describes an innovative coupling between a capillary loop system and a two-phase loop thermosiphon. The main benefit of this innovative configuration are to suppress the reservoir of the capillary side and allow to place the heat load anywhere on the complete height of the thermosiphon without significate change in the overall performances. The "double loop" concept has been validated by test with two demonstrators, one with liquid cooling (water) and the other with natural convection (air), with a total system power up to 3.2 kW (heat flux ranging from 5 to 35 W/cm²) and a fluid saturation temperature ranging between 36°C to 103°C. Full power startup capabilities has also be checked.

Keywords: capillary Loop, thermosyphon, power electronics cooling, high heat flux, natural convection

1. INTRODUCTION

1.1 Two-Phase Loop Thermosiphons (TPLT)

Two-Phase Loop Thermosiphon TPLT are low cost and efficient heat transfer devices [1-3]. For example, Insulated Gate Bipolar Transistor module (IGBT) has been successful cooled with such a device thank to microchannel technology [2]. The working principle is simple, the liquid flows back from the condenser to the evaporator zone thanks to gravity forces inside a dedicated liquid line to avoid sheer stress issue between vapor and liquid phases (counter flow). The main constraint is the location of the condenser area that must be above the evaporator in order to create enough hydrostatic pressure.

Fig. 1 shows an overview of the TPLT thermal performances based on recent reviews [1-2]. In order to compare different heat source sizes and different kind of cooling systems (forced, free convection, water, air, etc.), the thermal transmittance is plotted versus the average heat flux at evaporator wall level:

$$Tr = \frac{T_{wall\ evap} - T_{coolant\ INLET}}{Q_{heat\ load}} S_{heat\ load} \quad (1)$$

Only two sets of Fig. 1 data are related to free convection (green points) and one can notice that, if the size of the air exchanger is large enough, the thermal performances can be better than forced liquid cooling system. For the IGBT study [2] the local heat flux is probably higher than the average value plotted on the graph and, as a rule of thumb, a factor two might be applied [4]. The maximum heat flux on this non exhaustive database is nearly 25W/cm².

Another issue of TPLT is the critical heat flux (CHF) at evaporator wall level. Especially at low temperature, the vaporization flow tends to prevent the liquid to wet efficiently the heating wall off the evaporator. The evaporator thermal resistance increases dramatically when this dry-out event occurs.

The disturbance between vapor and liquid counter flow at evaporator level can interact with the pulsations generated at condenser level (for instable flow regimes) and creates an overall pressure pulsations inside the device [1][3]. The resulting saturation temperature pulsations can be a concern in term of IGBT module life time if their amplitude is too large.

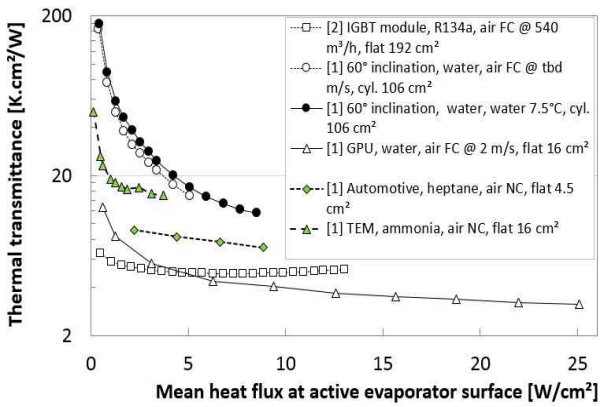


Fig. 1. Thermal performances of TPLT from the literature as the function of the average heat flux at evaporator. Legend: ref. / heater type / working fluid / cooling source / shape and active surface of the evaporator.

1.2 Capillary Loops (CaL)

In the present article, the term Capillary Loops is a reference to Loop Heat Pipes (LHP) and Capillary Pumped Loops (CPL) that are using a porous wick at evaporator level. The hydraulic connections, between evaporator and condenser, are simple tubes that can be equipped with flexibles lengths. The capillary pressure created at the wick interface is able to generate a large pressure head that allows to pump against gravity forces and a location of the condenser below the evaporator. Thus, the integration of the system is easier than for a TPLT.

Natural cooling i.e. a combination of natural convection and forced convection created by the motion of a vehicle has been successful combined with a CPL for IGBT modules cooling - for example a 1.3 kW module inboard train [5]. Such a standard IGBT module are also widely used in industry (motor drive, wind turbine, etc.)

By design, the porous wick inside the evaporator separates the vapor departure flow from the liquid arrival, this function improve the CHF of the system beyond the values reached in pool boiling and convective boiling [6]. For example, a CPL system with four evaporators was able to transfer up to 27 kW with heat flux higher than 100 W/cm² [7]. A constraint of the CaL is the size and the location of the reservoir. This element plays a role in the thermal expansion and fluid inventory management. The passive pressurization of this reservoir allows full startup at low temperature, down to -50°C, and improves CHF capabilities of CPLs [8].

Despite of all these performances advantages, the addition of an evaporator wick and a reservoir make the CaL system more expensive than the TPLT one. The hybrid capillary system proposed in this paper is a way to combine the benefits of the two solutions at lower cost by removing the reservoir component.

2. CAPILLARY TPLT Principle (CaTPLT[1])

2.1 Thermodynamic cycle

As explained above, the limitations of the TPLT thermal performances and transport capabilities are mainly due to the influence of the heat transport function (massflow) on the evaporation function (flow boiling). The CaTPLT uses a capillary evaporator in order to create and inject the vapor inside the TPLT with two main benefits. First, the porous media separates the vaporization area from the TPLT flow and improve the evaporator dry-out capability. Second, the vapor injection can be located far below the heat source in order to maximize the heat sink height and enable natural convection exchanger. According to the TPLT classification based on the Capillary length, Weber and Bond numbers analysis the system is designed to works in flow boiling mode dominated by gravity [3].

The Fig. 2 describes the vaporization cycle of the CaTPLT. The location of each point on the pressure-temperature graph (a) refers to the physical location on the system (b) and is susceptible to change from a design to another.

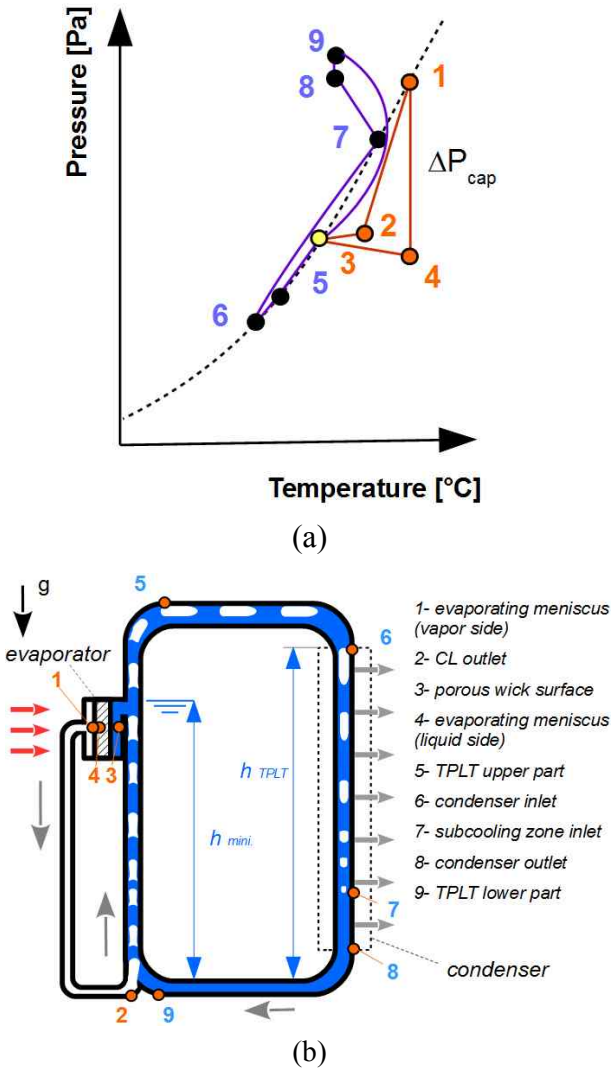


Fig. 2. Scheme of a CaTPLT thermodynamic cycle (a) and corresponding point locations on the physical system (b).

The working fluid vaporizes inside the porous wick (1), at meniscus level, creating the capillary pressure head P4-1 given by the Laplace law [9]. The vapor flows through the porous wick experimenting a significant pressure drop associated with a superheating and arrives to the

[1] the acronym CLTPT has already been used [3]. Thus, CaTPLT is proposed to avoid confusion

tee-junction (2) with the TPLT side through a network of grooves and pipes that increases the pressure drops. On the vertical branch the pressure decreases due to both two-phase pressure drops and hydrostatic effect and remains on the saturation curve i.e. the dotted line. If the liquid at the outlet of the condenser is in subcooled condition, a part of the vapor flow condensates into the vertical section. Then, the liquid is pumped through the porous wick thickness (3-4) to arrive at vaporization meniscus level in a superheated state thanks to the liquid-vapor curvature effect. The local heat flux i.e. the hot spots of the heat load is driving the pressure drops $\Delta P_{3\text{-}4}$. [6] inside the wick.

For a CaL, the total pressure drops (1-2-3-4) are balanced by the capillary pressure. The merit figures are mainly driven by the latent heat of vaporization, the surface tension and the vapor density [9]. Thus, ammonia, methanol and water are privileged. But, in CaTPLT and for a compact design of the evaporator side, it is possible to use poor ranking working fluids, such as dielectric fluids or refrigerants, which have a larger liquid density i.e. a larger hydrostatic pressure head for TPLT side. Neglecting the sensible heat due to superheating at meniscus level, the CaL vapor massflow is directly imposed by the input power:

$$Q_{total} = \dot{m}_{vap}\, \Delta h_{LV} \quad (2)$$

The hydrostatic pressure head i.e. the density difference, on the h_{TPLT} height (cf. Fig. 2), for the upward and downward vertical channels balances the pressure drops of the complete TPLT (9-3-5-6-7-8-9). Thus, for the TPLT, the massflow is not imposed by the heat load but by the pressure drops:

$$\dot{m}_{TPLT} = \gamma \dot{m}_{vap} \quad (3)$$

where, γ is an amplification factor.

In nominal mode, $\gamma > 1$, there is an extra massflow circulating inside the TPLT. For a pure CaL system, without subcooling, $\gamma = 1$. If $\gamma < 1$, the TPLT is not able to transfer the heat from the CaL to the condenser and the pressure i.e. T_{sat} increases until a stable regime is achieved (startup or power step) or the system reach its mechanical limit (no enough cooling and/or too much pressure drops).

If the system power is below $Q_{max,}$ T_{sat} passively adapt itself in order to reach the cooling exchanger temperature that permit to evacuate the heat to the cold source. The evaporator heat transfer coefficient can be affected by the T_{sat} variation and the condenser HTC can be change by both γ and T_{sat} evolutions. Moreover, the initial filling ratio plays a significant role on the TPLT performances on the condenser flow regimes and on the subcooling length (7-8). For natural cooling the minimization of the subcooler volume is an important target because the parasitic heat flux at evaporator is not an issue for CaTPLT (with respect to LHP).

Numerical model and design of a CaTPLT is complex and tests campaign are needed in order to proof and to better understand the system behavior.

2.2 Startup issues

At startup, the TPLT side can be considered as an LHP reservoir for the CaL side. Thus, boiling incipience, T_{sat} drift, etc. must be considered in the system design like for any LHP. Moreover, a capillary system requires a minimum liquid level h_{mini} (cf. Fig. 2) to operate at startup. If a part of the wick is located above the liquid level, the porous material must be able to pump it against gravity. After, when the vapor is generated, the wick must be also able to push the liquid column (1-2) in order to deliver the vapor to the TPLT side.

At startup, typically, the system is at the cold source temperature. As explained in §2.1, $\gamma << 1$ and T_{sat} increases and the whole LTPT, including the liquid, plays the role of a condenser thanks to the thermal inertia. Finally the TPLT starts and transfers the heat from the capillary evaporators to the cold source.

3. TEST APPARATUS

The evaporator performances are evaluated from the temperatures measured, inside the 5 mm thickness wall, in front of the 3 heating zones per evaporator side. These 6 thermocouples (TC1 to TC6) are sealed inside a 1.2 mm diameter groove. The typical precision on the temperature measurement is +/- 0.3°C. The other thermocouples are located on the inlet and outlet parts of the system. The system pressure is measured at distributor level on the top of the TPLT part with an absolute pressure transducer Keller PAA-33X, 0-10 bars pressure transducer with an accuracy of 0.10% EM i.e. +/-10 mbar, on the measurement range. P_{TPLT} is used to determine the saturation temperature T_{sat} (P_{TPLT}) inside the loop.

Two specific heating tools are used to apply high heat flux on the two faces of the evaporator [6]. The heating elements consist of two ceramic glow igniters made of silicon nitride (active part: 90 x 20 X 5.0 mm^3) with a maximum contact temperature of 580°C. The heater is clamped on a copper

blocks and the active contact surface per evaporator side is 57 cm² (cf. Fig 4 and 5). The 6 heaters are electrically connected to 2 Agilent 600V-8.5A power supplies. The resulting heat flux is above the today 140 x 190 mm² IGBT module standard values.

The data acquisition device is an Agilent 34980A connected to a PC via an Ethernet connection and a LabVIEW interface.

4. CaTPLT POC-3.1, FORCED LIQUID (WATER)

A first proof-of-concept of a CaTPLT has been tested in CALYOS with an active liquid cooling.

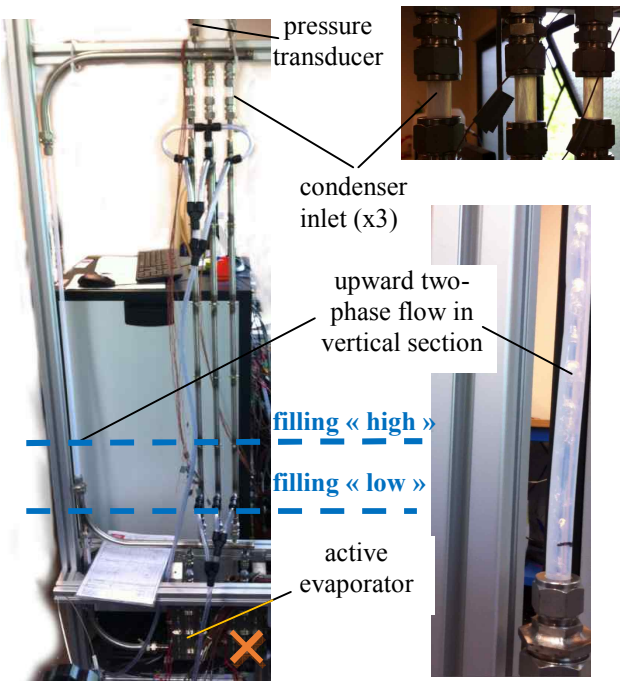


Fig. 3. POC 3.1 test bench overview (left), the three condenser inlets (top) and the vertical part of the TPLT (downstream the capillary vapor junction) with slug flow at 1.6 kW (right).

This POC-3.1 design has not been optimized and built from existing part. The cold source was the water from the domestic network with an inlet temperature of 14°C and a massflow, evaluated from an enthalpy balance, of 0.433 m³/h. The main parameters of the POC-3.1 are summarized between brackets in Table 1 and Fig. 3 shows an overview of the test apparatus with a close up of the condenser inlet and of the vertical tube located after the vapor inlet (3) from the CaL. In this first development step, the evaporators have been located below the LTPT to insure the liquid feeding of the wick. Just one evaporator has been used during the tests. The cold source is compact with respect to the free convection target. Two methanol filling have been tested, one below the tee-junction level and the second 65 mm above.

The active length and characteristics of the condenser copper tube was representative of the natural cooling POC-3.2 demonstrator described in §5. The system has startup and worked very satisfactorily. The visual observation at the inlet of the condenser and the temperatures analysis have validated the distributor design and the good two-phase phase sharing among the tubes. For reference, the global performances of the demonstrator are plotted in Fig. 10 and T_{sat} versus Q_{system} in Fig. 7. At maximum power tested (4kW, 35W/cm²) the global thermal resistance for a single module (2kW) is 0.04 K/W.

5. CaTPLT POC-3.2, FREE CONVECTION (AIR)

5.1 System presentation

The POC 3.2 demonstrator, described in Table 1 and Fig. 4, is based on a single capillary evaporator developed for railways applications that use methanol as a working fluid with a nickel wick [4].

Table 1. Demonstrator parameters, POC3.2 (*POC 3.1*).

Component	Material	Value
Evaporators body	Cu	size: 243 x 140 (*300*) x 28 mm³
Wick type	Ni	Sintered powder Pore dia.: 6.1 microns Permeability: $3.0.10^{-13}$ m²
Evaporator outlet	SS	i.d. 18 mm, length 285 mm
Evaporator inlet	SS / PTFE	i.d. 10 mm, length 702 mm
Upward tube	SS / PTFE	i.d. 10 mm, length 638 mm
Distributor	SS	i.d. 18 mm, length 998 mm
Condenser IGT	Cu	o.d. 5 mm, length 1250 mm, with 50 mm inactive number: 15 (3) in parallel
Collector	SS	i.d. 18 mm, length 781 mm
Heat sink	Al	Width: 550 mm Depth: 260 mm Height: 1'200 mm Fin pitch: 13.7 mm Fin height: 119 mm Mass: 95 kg
Working fluid	Methanol	0.8 kg

The TPLT rejects the heat to the air by natural convection thanks to fifteen enhanced copper tubes embedded inside aluminum heat sinks for a total mass of 95 kg. This large thermal inertia value is used to smooth power overload in a specific duty cycle.

The system was not insulated during the tests and the thermal losses have been measured to 100W with an evaporator at 100°C in vacuum condition inside the system.

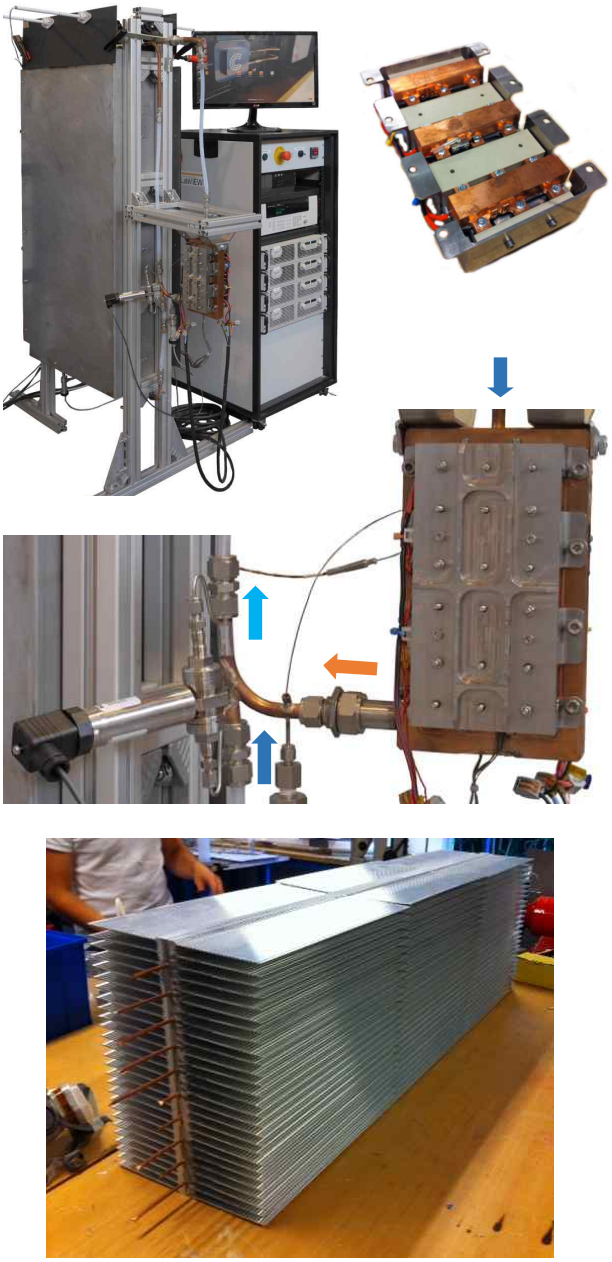


Fig. 4. POC 3.2 test bench overview (top left), the three 20 x 95 mm² heated zones of the heating tool (right) and the detail of the tee-junction between the capillary evaporator and the TPLT (middle) and a part of the heat exchanger with IGTs (below).

5.2 Behavior and parameters evolutions

5.2.1 Continuous power steps

Fig. 5 gives the typical evolution of the temperatures of the system for a continuous step power increase. The duration of each step is one hour. The plotted evaporator temperatures are the hotter thermocouple of the each side. The power has been stopped because the evaporator wall temperature reaches 110°C. No system depriming has been observed.

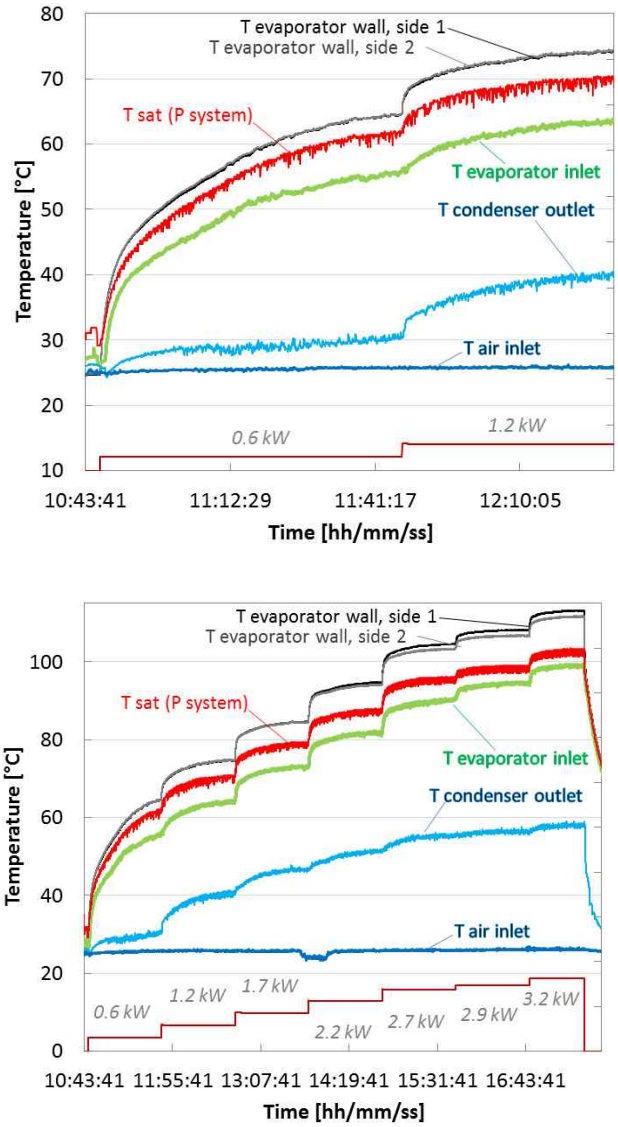


Fig. 5. POC 3.2, evolutions of the temperature and total power of the system for a continuous power increase with a close-up of the startup phase (top).

The saturation temperature exhibits small variations, but without impact on the temperature of the evaporator walls thanks to the filter effect of the evaporator copper wall thermal inertia and the

six evaporator temperatures remains at +/-1.8 K at 3.2kW i.e. 28 W/cm². Based on the last power step and the value of T_{sat}, the thermal resistance of the evaporator is only 6% of the total. Clearly the air exchanger in natural convection is the component where the improvement margins are the more promising.

5.2.1 Startup power steps

The capability of the system to start at the maximum heat flux encountered on standard IGBT module (24 W/cm²) has been checked. Fig. 6 describes "oscillations-free" behavior of the CaTPLT. The startups have been repeated 6 times with one hour at full power and 30 minutes without power.

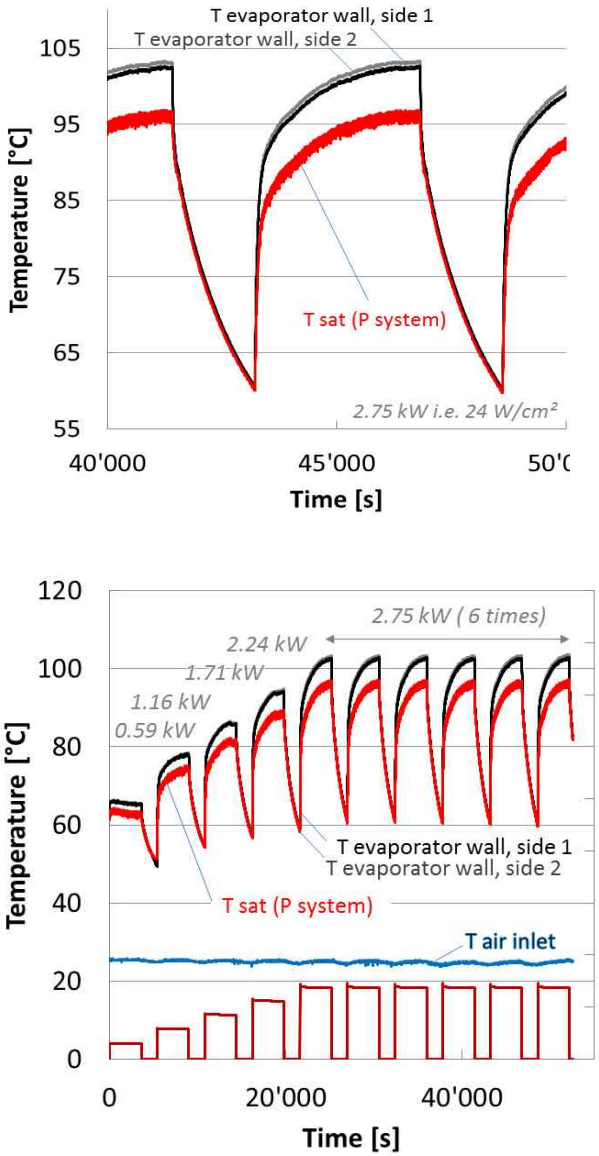


Fig. 6. POC 3.2, evolution of the temperature and total power of the system for startup at full power with a close-up of the 24 W/cm² step (top).

5.3 Overall system performances

5.3.1 Saturation temperature evolution

The saturation temperature is calculated from the pressure measurement thanks to the saturation law for methanol (software NIST REFPROP 9.0). Fig. 7 shows the typical variation for the two filling ratios tested (the liquid cooled demonstrator is presented for reference). For these tests conditions the fluid temperature is a quasi-linear function of the power.

Two filling ratios have been tested ("low" and "high"). Increasing the filling ratio increases T_{sat} at low power but decreases the slope of the curve i.e. below 3kW the performances at condenser side are better with the lower filling ratio. This phenomenon seems due to the extension of the subcooled height inside the condenser tubes that reduces the heatsink active volume available for the air exchange. A numerical model will help to better understand these results.

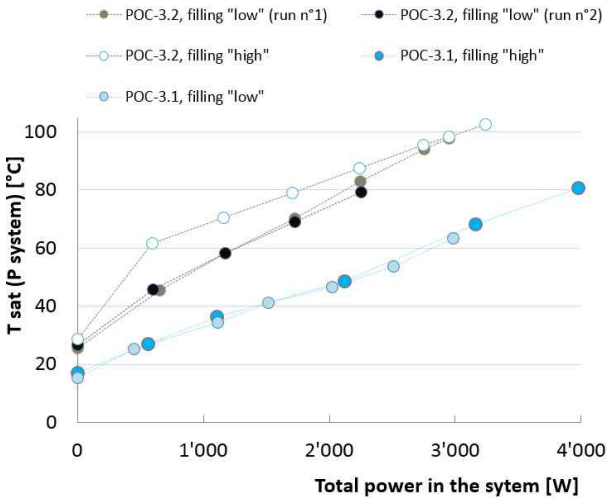


Fig. 7. Saturation temperature versus total power for continuous power steps tests.

5.3.2 Total thermal resistance for continuous increments

The total evaporator-to-air thermal resistance at heating tool level, Rth_{module} is calculated with the average evaporator wall temperatures of the two sides (6 thermocouples), the air inlet temperature and the power of a single heating tool (half system power) with the following definition:

$$Rth_{module} = \frac{\overline{T_{evap\ wall}} - T_{cooling\ inlet}}{Q_{heater}} \quad (4)$$

On Fig. 8, Rth $_{module}$ is plotted as a function of the heat flux at contact heating tool level for continuous power steps tests. The lower filling ratio gives the better result and the values are nearly the same for the two runs. Over 20W/cm² the filling has no impact on the thermal resistance. More tests with different filling are needed to confirm this behavior.

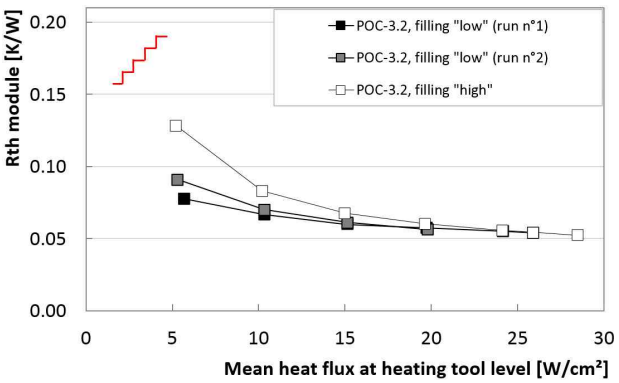


Fig. 8. POC 3.2, total thermal resistance versus the evaporator heat flux for two filling ratios for continuous power increments tests.

5.3.3 Total thermal resistance for startup steps

According to Fig. 6 evolutions, the temperature stabilization duration for the startup tests are lower than for the continuous power increments tests but sufficient to calculate the Rth $_{module}$ at the end of each step. Fig. 9 shows the resulting thermal resistance as a function of the average evaporator heat flux and no significant differences with continuous increment step was observed. Thus, like CPL, CaTPLT is well adapted to fast transient duty cycle.

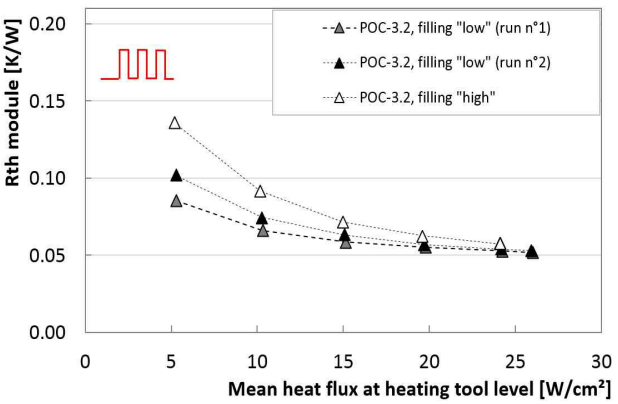


Fig. 9. POC 3.2, total thermal resistance versus the evaporator heat flux for two filling ratios for startup power steps tests.

5.3.4 Thermal transmittance

As defined in § 1.1, the transmittance is the overall performance seen by the heat load at hot spot level, regardless the system size.

The Fig. 10 summarizes the performances of the two demonstrators with the best filling i.e. the "low filling" ratio for the continuous increment power steps. Data from the literature from Fig. 1 are presented in grey. The demonstrators, despite their lack of optimization, are already as performing as the best forced convection systems. In other word, if enough room is available, for example a cabinet inside a building, CaTPLT is able to remove the heat from the standard IGBT power modules hot spots without any active elements. Of course it is possible to over perform the 95 kg heat exchanger in natural cooling with only 3 copper tubes with water cooling.

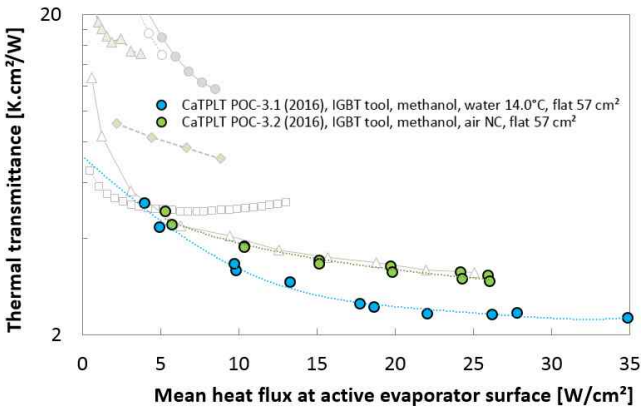


Fig. 10. Thermal performances of POC-3.1 and 3.2 demonstrators as the function of the average heat flux at evaporator. Legend: ref. / heater type / working fluid / cooling source / shape and active surface of the evaporator. The legend of the grey points are in Fig. 1.

6. CONCLUSIONS AND PERSPECTIVES

The hybrid capillary system proposed in this paper is a way to combine the benefits of the capillary loop to extend the performances of the TPLT solutions at lower cost by removing the reservoir and injecting the vapor at the lowest point of the thermosiphon. The solution is particularly well adapted to IGBT modules cooling for motionless applications in cabinets, where the constraints are considerably lower in terms of pumping capabilities and integration than for moving systems.

The CaTPLT has reached a TR-4 level:

- thanks to a fully passive cooling (natural convection). The global thermal resistance for a single module was 0.05 K/W at maximum

power tested (1.6kW, 28.5W/cm²),

- thanks to an active cooling (water exchanger). The global thermal resistance for a single module was 0.04 K/W at maximum power tested (2kW, 35W/cm²).

For in-door applications (or hot countries), water will be available has a working fluid thanks to the CALYOS development of a new copper wick technology able to reach the hydraulic performances (pore radius and permeability) of the state-of-the-art nickel wick. TRL-3 characterization already shows a considerable improvement of the evaporator thermal performances.

A new evaporator configuration with a single active face will be available in the middle of 2016 with nickel or copper wick. This design will decrease the cost of the system when double side active evaporator are not mandatory,

TRL-5/6 will be reached at the end of 2016 thanks to a compact product-oriented design where the connection between the evaporator and the thermosiphon is implemented directly inside the evaporator.

Filling optimization must be done in the coming months and a numerical model is also under development in order to optimize the design of the future CaTPLTs. Today, the natural convection thermal resistance is dominant and give us promising way to improve the global performances.

ACKNOWLEDGEMENT

The authors would like to thanks the Euro Heat Pipes S.A expert team for their helpful and constructive discussions related with this project.

NOMENCLATURE

CaL : Capillary Loop i.e. LHP or CPL ( )
FC : Forced Convection
H : height (m)
HTC : Heat transfer coefficient (W/m²K)
i.d. : Tube inside diameter (m)
IGT : Inner grooved tube
o.d. : Tube outside diameter (m)
$\dot{m}_{vap}$: Massflow from evaporator (kg/s)
NC : Natural cooling or free convection ( )
P : Absolute pressure (Pa)
Q : Input power (W)
r_p : pore radius of the evaporator wick (m)
S : Heating tool contact active surface (m²)
T : Absolute temperature (°C)
TPLT : Two-Phase Loop Thermosiphon ( )
Δh_{LV} : Latent heat of vaporization (kJ/kg)
ΔP_{cap} : Capillary pressure i.e. $2\ \sigma / r_p$ (Pa)
γ : massflow amplification factor at TPLT level
σ : Surface tension (N/m)

REFERENCES

[1] Maydanik, Y.F., Two-Phase Loop Thermosyphons, Proc. of VIII Minsk International Seminar Heat pipes, Heat Pumps, Refrigerators, Power Sources, Minsk, Belarus, Sept. 12-15 (2011) 144-154.

[2] Agostini, B. and Habert, M., Compact Thermosiphon Heat Exchanger for Power Electronics Cooling, *Proc. of the 16th IHPC*, May 20-24, Lyon, France (2012) no printed version.

[3] Filippeschi, S. and Franco, A., Experimental analysis of the instabilities effect on the Thermal performances of a closed loop two-phase thermosyphon, *Proc. of the 17th IHPC*, Kanpur, India (2013) pp. no printed version.

[4] Dupont, V., Billet, C., and Nicolle, T., High Performances Passive Two-Phase Loops for Power Electronics Cooling, *Proc. PCIM*, May 10-12, Nuremberg, Germany, (2016) pp. not yet available.

[5] Dupont, V., Van Oost, S., Barremaecker, L. and Nicolau, S. Railways qualification tests of Capillary Pumped Loop on a train, *Proc. of the 17th IHPC*, Kanpur, India, (2013) pp. no printed version.

[6] Dupont, V., Thermal Performances of a fully passive capillary pumped loop with heat flux up to 90 W/cm² at evaporator", *10th European Advanced Technology Workshop on Micropackaging and Thermal management*, February 4 & 5, La Rochelle, France (2015), no printed version.

[7] Dupont, V., Van Oost, S., Barremaecker, L., Nicolau, S., Experimental investigations on a methanol capillary evaporator equipped with four flat evaporators, *Proc. of 15th Int. Heat Pipe Conf.*, Clemson, USA, (2010) pp. no printed version.

[8] Dupont V., J.C. Legros Van Oost S., Barremaecker L., Experimental investigations of a CPL pressurized with NCG inside a centrifuge up to 10g, *Proc. of 15th Int. Heat Pipe Conf.*, Clemson, USA, (2010) pp. no printed version.

[9] Faghri, A., *Heat Pipe Science And Technology*, Taylor & Francis, (1995).

Advanced Control Capillary Loop (ACL) Thermal Architecture with Multiple Evaporators and Condensers

D. Mishkinis[1], A. Kulakov[1], P. Prado[1], A. Torres[1], S. Lapensee[2]
[1] *IberEspacio Tecnologia Aeroespacial, C/Magallanes 3, 28010 Madrid, Spain.*
[2] *European Space and Technology Centre (ESTEC) ESA, Keplerlaan 1, 2201 AZ Noordwijk, Netherlands*

Abstract

Advanced Control Capillary Loop (ACL) heat transfer system with 4 different evaporators and 2 condensers was developed and tested on the second stage of ESA Technology Research Program "Multiple-Evaporator Multiple-Reservoir Loop Heat Pipe". First stage of the project (2 evaporators and 2 condensers system) was presented earlier in [1]. An extensive thermal test campaign was performed to validate the novel thermal architecture concept, to investigate the system performance in very harsh environmental and operational conditions and to look for the system limits. The campaign included a number of various tests: thermal performance, minimum and maximum power, start up, heat sharing, multiple input power and heat sink temperature sharp alteration, etc. Innovative method of ACL thermal control was successfully verified.

Keywords: Advanced control loop, Two phase capillary heat transfer loop, Loop heat pipe, Capillary pumped loop, Spacecraft thermal control

1. INTRODUCTION

Capillary driven loop technology has found a wide application for thermal control systems in many spacecraft applications, which usually use loops with a single evaporator [1]. However, nowadays more and more applications require thermal control of multiple remotely located heat sources or large thermal contact surface payloads.

Developers of multiple evaporators and multiple condenser designs of capillary driven loops (known as LHPs, CPLs, hybrid two-phase heat loops, etc.) intend to create thermal control systems having the following characteristics: optimized functional layout, scalability, expandability, effective heat loads sharing, flexibility in components locations, thermal coupling between separate radiators and minimized mass and volume. It is a challenging technical problem. To resolve that Advanced Control Loop (ACL) with Remote Compensation Chamber (RCC) was proposed [2].

Experimental investigation described in [1] testifies that it is a promising and advantageous solution which overcomes the problem of a limited number of evaporators (classical LHP design) and the problem of instability of operation in transient modes with increased parasitic heat leak through the capillary wick wall (classical CPL design).

The first step in the ACL development was the design, and testing of a one-evaporator one-condenser ACL. On the second stage of the project (in the frame of ESA program "Multiple-Evaporator Multiple-Reservoir Loop Heat Pipe") the second evaporator and the second condenser have been added to the design.

Unlike ordinary LHP systems, the proposed ACL is controlled by a RCC, in which two-phases always co-exist. In contrast to ordinary CPL systems, the stabilization-compensation chamber (SCC) is provided in the ACL for each evaporator. SCC is connected and attached to the evaporator and together with an advanced control scheme serves to reliably supply the primary capillary pump with a sufficient amount of subcooled liquid in any operational conditions, even in very unfavorable transient ones.

As a part of the novel design an advanced algorithm of ACL control was proposed [1, 2]. The RCC temperature T_{RCC} is regulated according to the following law:

$T_{RCC\text{-}LHP} = (MAX\{T_{SCC1}..T_{SCCn}\}+\Delta T_C)$ – for multiple n-evaporators design ACL with LHP-type control mode.

For CPL-type control mode it can be defined as:

$T_{RCC\text{-}CPL} = (\{T_{set}$ if $T_{RCC} > T_{RCC\text{-}LHP}\}$ OR $\{T_{RCC\text{-}LHP}$ if $T_{RCC} \le T_{RCC\text{-}LHP}\})$

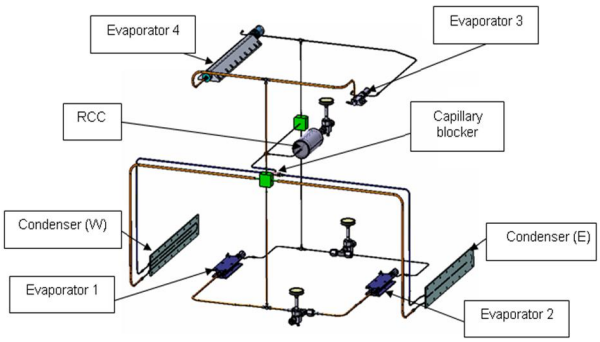
Where ΔT_c is the specified control temperature difference, usually in the range from 1 to 10°C and T_{set} is ACL temperature setpoint in CPL mode which govern the temperature levels of all evaporators and operational temperatures of the cooled equipment (for instance, 40°C).

For one-evaporator design ACL the LHP-type control low is as simple as $T_{RCC} = T_{SCC} + \Delta T_c$

2. ACL DESIGN

ACL engineering model consist of:

- 4 evaporators of different sizes, from 40 mm to 400 mm length to assess the operability of the system with different power inputs to each evaporator;
- Every evaporator comprises the primary capillary pump with external vapour removing channels outside the primary wick, secondary capillary pump-wick and an individual stabilization-compensation chamber;
- One remote compensation chamber to manage working fluid volume changes during ACL start-up and functioning and serving as system operational temperature reference for the entire ACL;
- Common vapor and liquid lines to transport heat load from dissipating units to the radiators;
- Two condensers to verify the ACL operation with two thermally unbalanced radiators (for instance, to model the East and West radiators environmental conditions for geostationary telecom satellites), with different environmental conditions.



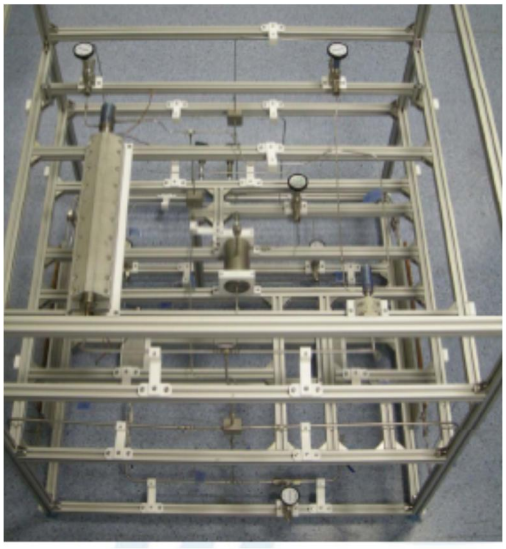


Fig. 1. ACL setup schematic and photo

The ACL includes a capillary blocker at the condensers outlet to prevent the vapour flow from one condenser to the other one and to the liquid line.

Particularities of design are described in [1] and operating principle of ACL is explained also in [2].

The ACL includes four evaporators to assess the operability of the system with different power inputs to each evaporator. The evaporators are:

- Evaporator 1: medium size (the same evaporator tested in Phase 1 [1])
- Evaporator 2: medium size (the same evaporator tested in Phase 1)
- Evaporator 3: small size
- Evaporator 4: large size

Main design characteristics of the ACL evaporators are summarized in Table 1.

One of main novelties of the proposed design is that the evaporator includes a SCC, consisting of a SCC hydro-accumulator and a two-phase reservoir, which collects any bubbles (vapour, NCG) generated in the evaporator. The bubbles generated in the evaporator are collected in the two-phase reservoir, which is in contact to the subcooled hydro-accumulator.

The heat exchange between both reservoirs make the bubbles condense. The main characteristics of the evaporators SCCs are summarized in Table 2.

Main characteristics of the ACL transport lines are shown in the Table 3.

Main characteristics of the condenser lines and plates are summarized in Table 4.

Table 1. Evaporators characteristics.

Evaporator	Small (No3)	Medium (No 1&2)	Large (No4)
envelope material	SS 316		
saddle material	Al 6082 – T6		
saddle footprint	45x45 mm	152x51 mm	400x75 mm
length	57mm	165mm	432mm
Primary wick OD	11 mm	14 mm	22 mm
Pore size	2.5 µm	1 µm	1 µm
Porosity	65 %	65 %	47 %
Permeability	$3 \cdot 10^{-13}$	$8 \cdot 10^{-14}$	$3 \cdot 10^{-14}$
Wick material	SS316 (fiber)	Nickel	SS316 (powder)

Table 2. SCC characteristics.

SCC	Small (No. 3)	Medium (No.1&2)	Large (No. 4)
material	SS 316		
volume	14 cm^3	15cm^3	58 cm^3
length	57mm	51mm	67mm
ID	20 mm	20 mm	30 mm

Table 3. Transport lines characteristics.

Line	Value
Material	SS 316
Vapour ODxID	6x4 mm
Vapour total length	4140 mm
Liquid ODxID	3x2 mm
Liquid total length	4800 mm

Table 4. Condenser characteristics.

Condenser	Value
Material	SS 316
ODxID	3x2 mm
Length,	1020 mm
Plate size Width x Length	70x450 mm

Remote Compensation Chamber has volume 280cm^3. It vas calculated taking into account all components of the ACL and its temperature range.

3. TEST SET UP

The ACL was installed to testing jig (Fig. 2).

Cold plates were cooled by chiller attached to the condenser plates.



Fig. 2. Test set up.

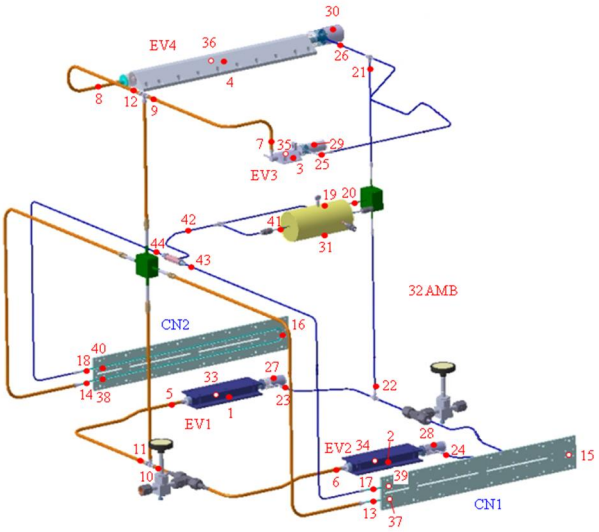


Fig. 3. Measurement plan.

Cartridge heater blocks were attached to every evaporator saddle. Dedicated flexible Kapton type heater was installed on the RCC for ACL control.

The test specimen was instrumented in accordance with the measurement plan (Fig. 3), and thermally insulated by Armaflex material.

In total 44 thermocouples type T have been installed to analyze operation of the system. The most representative thermocouples were selected for given paper (Table 5) to demonstrate ACL performance.

Table 5. List of measurement thermocouples.

TC ID	Position
1 EV1	Evaporator 1
2 EV2	Evaporator 2
3 EV3	Evaporator 3
4 EV4	Evaporator 4
15 C_1	Condenser line, middle 1
16 C_2	Condenser line, middle 2
19 RCC	RCC top, at the middle
27 SCC1	Evaporator 1 SCC
28 SCC2	Evaporator 2 SCC
29 SCC3	Evaporator 3 SCC
30 SCC4	Evaporator 4 SCC
39 C1OUT	Condenser 1 line outlet
40 C2OUT	Condenser 2 line outlet

4. TEST CAMPAIGN DESCRIPTION

The performed test campaign covered the following objectives:

- Verification of the system performance in horizontal configuration for the power range from 20 W to the system maximum.

- Measurement of the system maximum and minimum powers
- Measurement of the system thermal conductance in each operational mode
- Assessment of the start-up reliability
- Verification of the response of the system to transient regimes, which is linked to the sizing of the SCC
- Assessment of the system performance with different sink conditions, related to the use of East/West radiators for power dissipation

The experimental campaign of the ACL included the following test blocks:

- Test #1 is maximum heat load verification. Behaviour of novel components such as the RCC, the SCCs was analyzed in 4-evaporators configuration. Test was carried out with every evaporator to verify individual maximum heat transfer capability and with all evaporators in operation to verify total maximum heat load capability of the entire ACL.
- Test #2 is a functional thermal performance test including verification start up ability and operation in RCC-LHP control mode. Behaviour of ACL was characterized for hot and cold cases.
- Test #3 is a functional thermal performance in RCC-CPL control mode with fixed operational temperature.
- Test #4 was carried out to evaluate the system response to large and sharp heat load variations at every evaporator level.
- Test #5. The sink conditions of each condenser were varied to simulate radiators environmental conditions changes in GEO orbit (East-West radiators).
- Test #6 is performed to assess the sensitivity of the system performance to different positions and orientation of condensers and RCC.

5. TEST RESULTS

Following results of maximum power Test 1 for evaporators operating individually were obtained:

Medium size evaporators 1 and 2 could transfer 600W without dry out. These evaporators could transfer at least 800W. Power higher than 600W was not applied due to power supplies limitations. The smallest evaporator sustained 200W, and the biggest one was operable at 1200W. Results of Test 1 of evaporator 4 are shown in Fig. 4. In all tests dry-out was not reached. The test was stopped because of limitations of power supplies or maximum temperature limit.

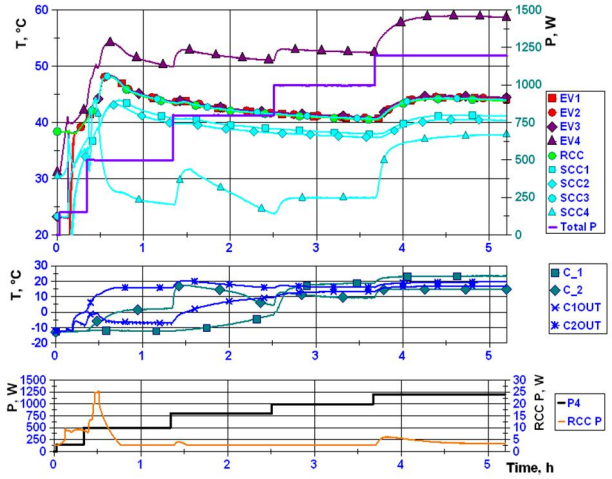


Fig. 4. Maximum power of evaporator 4

Verification of maximum power of ACL with all evaporators active was performed according to power sequence at Table 6. The ACL could sustain at least 1207W (Fig. 5).

Table 6. Power sequence (W).

EV1	150	200	300	360	350
EV2	100	140	140	180	150
EV3	50	60	60	67	67
EV4	200	400	500	393	640
ACL	500	800	1000	1000	1207
ΔT_c, ºC	10				

In the following graphs power distribution of evaporators is shown by 4 numbers P1-P2-P3-P4 corresponding to EV1-EV2-EV3-EV4.

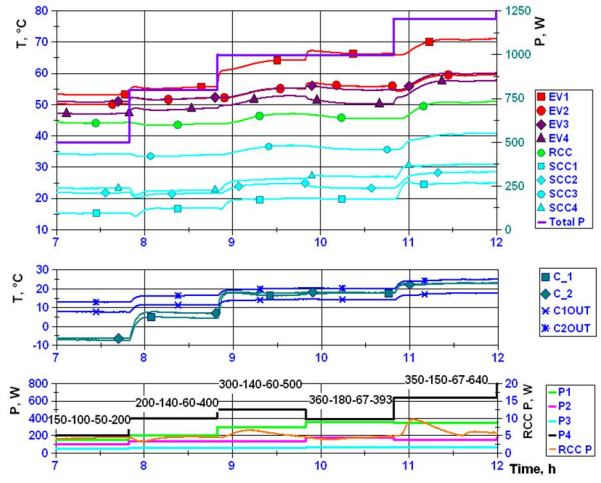


Fig. 5. Performance + maximum power at T_{CN} = -15 ºC with all evaporators active.

ACL can steadily and reliably operate only if a certain temperature difference between RCC and

SCC is assured. The next Fig. 6 demonstrates RCC control principle. Maintained temperature difference set point was 10ºC during the test. That set point value was applied to the minimum temperature difference between RCC and SCCs: related to evaporator 3.

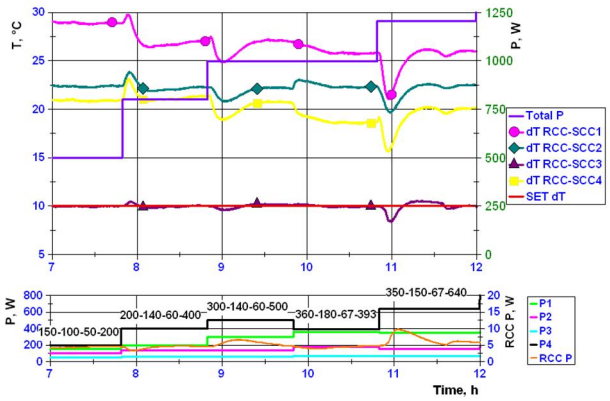


Fig. 6. Temperature difference between RCC and SCCs evolution Tc=10°C

Verification of ability of start-up of evaporators individually with power applied to other evaporators and restart simultaneously was conducted with power steps applied according to Table 7.

Table 7. Power sequence (W).

EV1	0	50	80	80	0	50
EV2	50	80	80	130	0	50
EV3	0	0	0	50	0	50
EV4	0	0	50	100	0	50
ACL	50	130	210	360	0	50
ΔT_c, ºC	5					

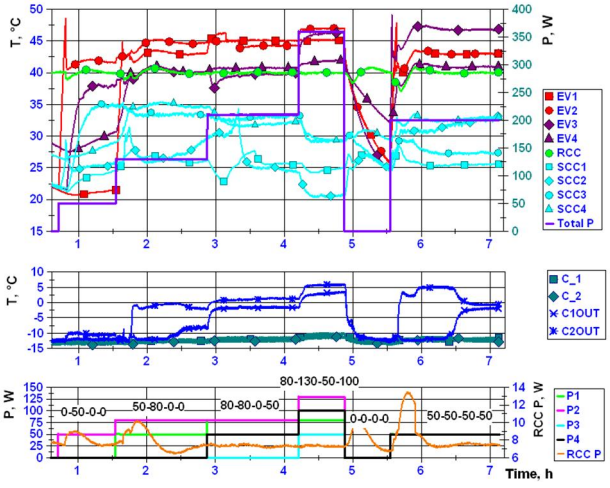


Fig. 7. Start-up test at T_{CN} = -15ºC. RCC-CPL mode of control T_{set}=40 ºC ΔT_c=5°C.

ACL had easy startups in tested configurations.

During performance tests ACL has demonstrated stable operation for both modes of ACL control: LHP-mode, Fig. 8, 9 and CPL-mode, Fig. 10. ACL was tested at different sink temperatures: -15ºC and +10ºC.

An example of ACL operation at sink temperature -15ºC is presented in the next Fig. 8.

Table 8. Power sequence (W).

EV1	50	0	150	360
EV2	50	180	180	180
EV3	0	0	0	0
EV4	50	0	150	360
ACL	200	247	547	967

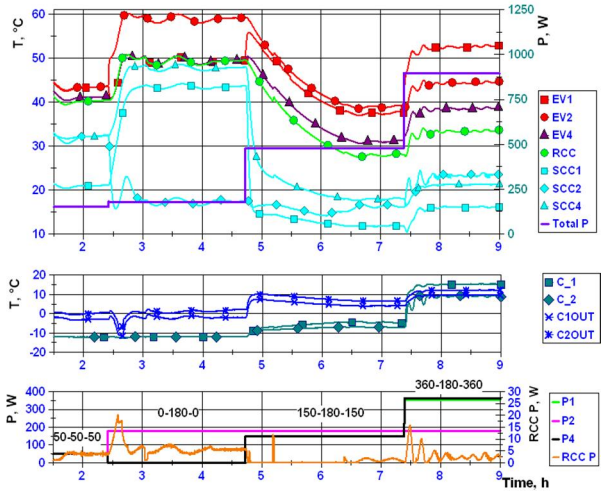


Fig. 8. Performance test at T_{CN} = -15ºC, ΔT_c =10°C.

Next performance test, conducted at sink temperature TCN = 10ºC, demonstrated also ability of start-up of evaporators individually.

Table 9. Power sequence (W).

EV1	50	50	0	150	360	360	0	150	0	50
EV2	0	50	180	180	180	0	0	180	180	50
EV3	0	0	0	0	0	0	0	0	0	0
EV4	50	50	0	150	360	640	800	150	0	50
ACL	100	150	180	480	900	1000	800	480	180	150

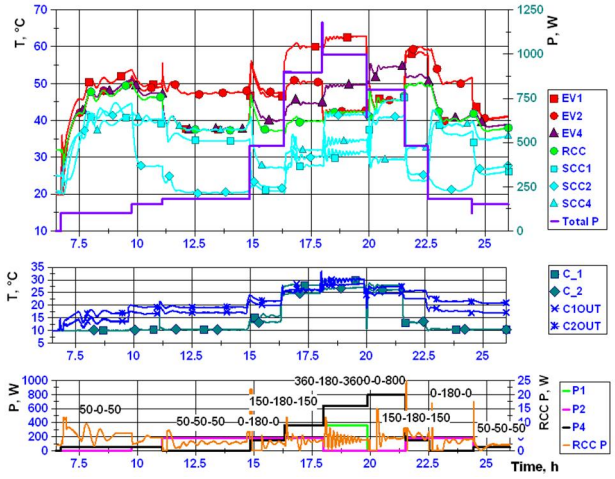


Fig. 9. Start-up + hot case performance at T_{CN} = 10 ºC including ability of start-up of evaporators individually. Only 3 evaporators are working P1-P2-P4. ΔT_c is varied from 3 to 10ºC.

Some instability existed on the first step. Acceptable performance in general was obtained, but PID control parameter should be adjusted to reduce oscillatory behavior during certain steps.

Ability of ACL to operate at constant operational temperature (CPL control mode) was demonstrated (Fig 10). RCC temperature maintained at 40 ºC while power applied to the evaporators alternated according to table 10.

Table 10. Power sequence (W).

EV1	50	0	150	360	360	0	150	0	50
EV2	50	180	180	180	0	0	180	180	50
EV3	50	67	67	67	0	0	67	67	50
EV4	50	0	150	360	640	800	150	0	50
ACL	200	247	547	967	1000	800	547	247	200
T_{set},ºC	40 ºC								

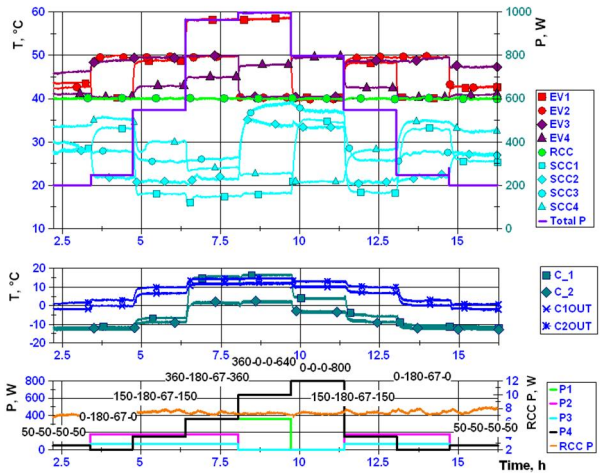


Fig. 10. Hot case regulation with RCC control at T_{CN} = 10 ºC; T_{set} = 40 ºC, Tc=5 ºC.

Two types of dynamic tests were performed. The first test verified ACL performance at high heat load variations (Fig. 11). Power was changed in wide variation range according to Table

Table 11. Power sequence (W).

EV1	0	0	0	0	374	50	374	50
EV2	212	50	212	50	0	0	0	0
EV3	100	43	100	43	0	0	0	0
EV4	0	0	0	0	690	100	690	100
ACL	312	93	312	93	1064	150	1064	150
ΔT_c,ºC	5							

Second dynamic test (Fig. 12) verifies performance at high condenser temperature variations. It is a thermal performance tests with different sink conditions: condensers temperatures varied from -10 to 30°C.

Table 12. Power sequence (W).

EV1	200	200	200	200	200	200	200	200
EV2	100	100	100	100	100	100	100	100
EV3	50	50	50	50	50	50	50	50
EV4	300	300	300	300	300	300	300	300
ACL	650	650	650	650	650	650	650	650
TCN_1	10	-15	10	-15	30	30	30	30
TCN_2	30	30	30	30	10	-15	10	-15
ΔTc,ºC	8							

Operative condenser is colored in green.

The ACL sustained all rapid changes of power and sink conditions.

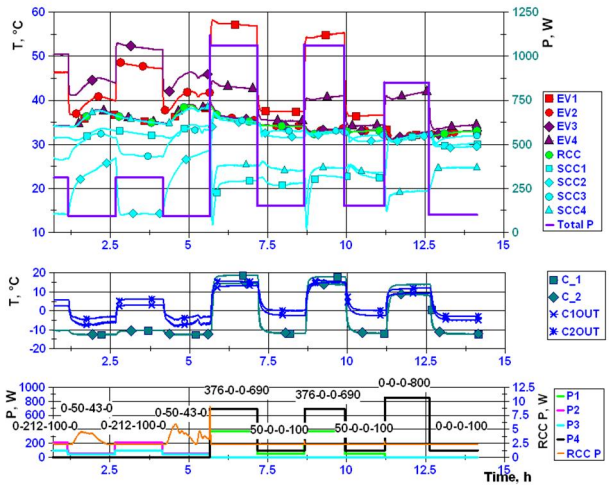


Fig. 11. Dynamic test/ Power cycling at T_{CN} = -15 ºC.

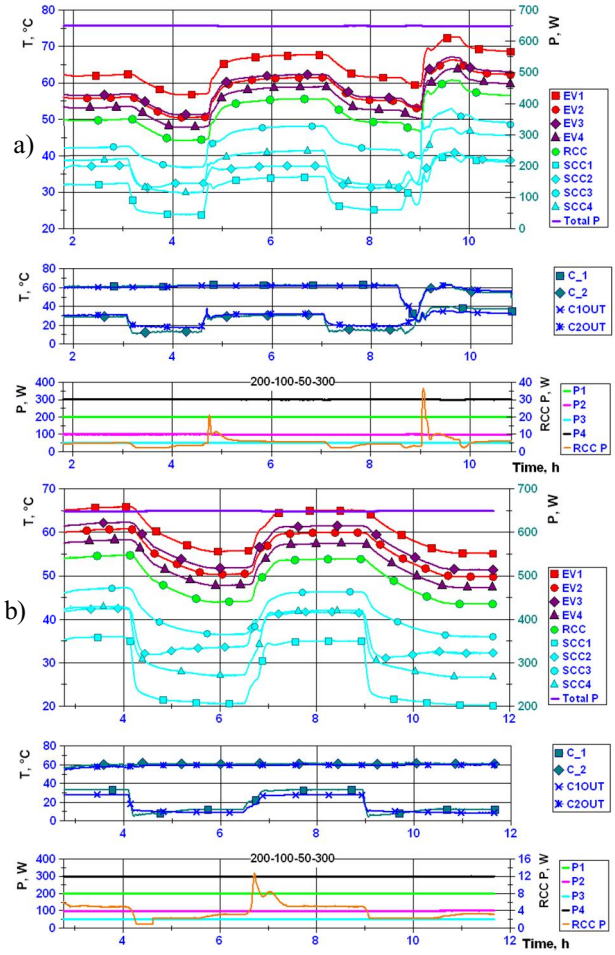


Fig. 12. Dynamic test/ Condenser cycling and switching. a) Part 1. b) Part 2.

The ACL sustained all power steps with one condenser not operating and condenser switching.

The ability of ACL to operate at different spatial configurations has been demonstrated. ACL could steadily operate at different relative positions between evaporators and RCC in gravity field.

Table 13. Power sequence (W).

EV1	100	150	200	300
EV2	50	100	140	140
EV3	50	50	60	60
EV4	150	200	400	500
ACL	350	500	800	1060
ΔT_c, °C	10			

Performance with change of condensers position was verified (Fig. 13). Turning of condenser 90° was done: condenser plates are in horizontal, one plate is on the top and second is on the bottom of testing jig. Evaporators 1 and 4 are in the top position and 2 and 3 are in the bottom.

The second test (Fig. 14) was performed with change of RCC position by 0.5 m (decreasing RCC level).

The ACL sustained all power steps. No any significant difference between various ACL positions was observed.

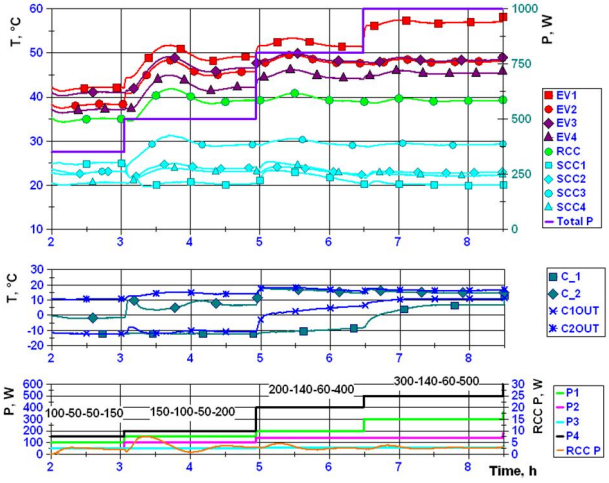


Fig. 13. Performance with change of condensers position.

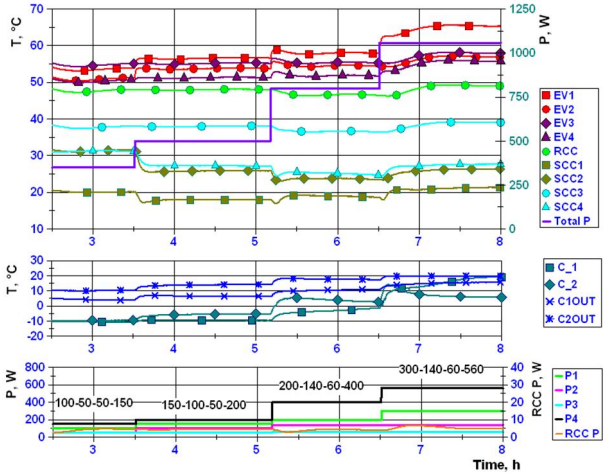


Fig. 14. Performance with change of RCC position (negative horizontal elevation 0.5 m).

6. CONCLUSIONS

New Advanced Control Loop concept has been developed and experimentally validated. ACL with Remote Compensation Chamber is a promising and advantageous solution which overcomes the problem of a limited number of evaporators of classical LHP and the problem of instability of operation in transient modes of classical CPL. A development model of ACL with 4 evaporators which have small standardized stabilization compensation chambers were successfully developed, manufactured and tested.

Innovative algorithm of ACL temperature control was applied to guarantee stable and robust operation of the system: LHP-type mode of control.

Traditional CPL-type algorithm of control was improved and combined with LHP-type mode of control to enhance performance of the system.

Control of ΔT_c parameter is very important. Different approaches can be implemented to optimize the ACL conductance or to improve system robustness for transient regimes. If the conductance is considered as a driving factor, ΔT_c has to be minimized. Medium values of ΔT_c could be valid for all operational regimes (including steady-state and transients). But conservative, relatively high, values should be necessary for the systems with very large and rapid variations in input power and condenser conditions. Also, two (or several) different ΔT_c could be defined (programmed): high ΔT_c for startups and transients and a low ΔT_c for stationary operational regimes.

Despite the ACL being tested in unfavorable conditions (different spatial positions of ACL components, variety of heat load redistributions, dynamic regimes, negative elevations) its reliable performance was clearly demonstrated.

The proposed thermal architecture implies an autonomous, self-regulated, lightweight and very efficient centralized two-phase heat transport system (thermal bus concept), to be potentially used for the thermal control in space and terrestrial applications. One of the main advantages of ACL is the absence of any mechanical pumped means and, as consequence, high reliability and life time.

ACKNOWLEDGEMENT

Financial grant from ESA are gratefully acknowledged.

NOMENCLATURE

c : *Control*
P : Power (W)
T : Temperature (K)

REFERENCES

[1] D. Mishkinis, A. Kulakov, P. Prado, A. Torres, S. Lapensee. Experimental Investigation of Advanced Control Heat Transfer Loop with Remote Compensation Chamber. *Heat Pipe Science and Technology, An International Journal.* Volume 4, 2013 Issue 4, pages 307-332. DOI: 10.1615/ HeatPipeScieTech.2014012164

[2] Torres, A., Mishkinis (2016) Advanced Control Two Phase Heat Transfer Loop, *Patent Application* US2016 / 0047605A1

Operational Characteristics of 10m-class Long-distance Loop Heat Pipe under Anti-gravity Condition

Kazuya Nakamura[1*], Kimihide Odagiri[1] and Hosei Nagano[1]

[1]*Graduate school of Aerospace Engineering, Nagoya University, Furo-cho,Chikusa-ku, Nagoya, Aichi, 464-8603, Japan*

Abstract

This paper reports test results and evaluation of a gravity effects on long-distance loop heat pipe (LLHP) with 10 m distances for heat transport. First, the one-dimensional steady-state model was developed to design and fabricate the LLHP. Test results showed that the LLHP could transport heat up to 340 W for 10 m and the thermal resistance between evaporator and condenser was 0.11 K/W under horizontal condition. By contrast, the maximum heat transports were 310, 270, 220 W and the thermal resistances were 0.13, 0.29, 0.31 K/W under 30, 60, 100 cm anti-gravity condition respectively. The heat transfer efficiency of the LLHP was discussed in detail. The evaluation results showed that 71.4 % of the 340 W heat load was dissipated at the condenser line under the horizontal condition. On the other hand, 62.8, 61.8, 57.1 % of the maximum heat load was dissipated at the condenser under anti-gravitational conditions respectively. The calculated results of numerical model was good agreement with the experimental results by considering the vapor pocket between the evaporator case and the wick and indicated that the vapor blanket generates easily when the gravity effect increases.

Keywords: heat transfer, long-distance loop heat pipe, PTFE, two phase flow

1. INTRODUCTION

Loop heat pipe (LHP) is an efficient two-phase heat transfer device that utilizes the evaporation and condensation of a working fluid, and capillary force developed in a fine porous wick to circulate the working fluid [1-3]. It has been developed and applied in the field of space engineering, however, it is being investigated for use in the terrestrial field. This is because of the current trend of energy saving and the advantages of LHP such as no utility power requirement, capability of transferring heat over long distance and anti-gravity orientation. Electronics and computers are quite a promising sphere of LHP application [1,4]. In the future, LHP could be applied in the field of smart houses, automobiles, snow melting [5]. Applying for LHP for these fields, transferring heat over long distance and anti-gravity direction could be required. Considering that LHP utilizes one of the devices for energy management of smart house, LHP could be applied to use the heat gained from the sun during daylight for floor heating, water heating, and heat storage tank.

In author's previous study, a long-distance loop heat pipe that has one-way heat transport distances of 10 m has been designed and fabricated based on a one-dimensional steady-state flow [5]. The experimental results showed that the fabricated long-distance loop heat pipe could transport heat up to 160 W and the thermal resistance between the heat absorbing portion and the heat radiating portion was 0.13 K/W. The performance of the LHP was not enough for the practical realization and the efficiency of the heat transfer needs to be evaluated.

This paper reports the development of the long-distance loop heat pipe (LLHP) that has 10 m one-way heat transport distances based on the one-dimensional steady-state model. The tests were conducted under horizontal and anti-gravity conditions. In the anti-gravity conditions, evaporator was located 30, 60, 100 cm higher than the condenser respectively. The anti-gravity effects on the operating temperature and the efficiency of the heat transport was evaluated based on the temperature data of the tests results. Heat leak from the evaporator to the CC and the total pressure drop were evaluated from the computational results of the one-dimensional model that was adjusted to the test results.

2. NUMERICAL MODELING OF LOOP HEAT PIPE

One-dimensional steady-state numerical model was constructed to design the LLHP and evaluate the performance.

Fig. 1 shows the configuration of LHP that this model assumed. LHP consists of cylindrical evaporator, vapor line, condenser, liquid line and compensation chamber (CC). A cylindrical wick is

*Corresponding author: nakamura@prop2.nuae.nagoya-u.ac.jp, Phone: +82-052-789-4405, Fax: +82-052-789-4405

enclosed in the evaporator and a core and grooves are machined in the wick. Working fluid absorbs heat by evaporation in the evaporator and then is transported to the condenser through the vapor line. The absorbed heat is dissipated in the condenser by condensation and working fluid is returned to the evaporator through the liquid line, and bayonet tube.

In this model, some assumptions are introduced: (1) there is no vapor zone in the wick i.e. wick is totally wetted. (2) There is axisymmetric flow to the evaporator's axis. (3) The temperature of the case of CC is identical with working fluid in it. (4) Heat leak from the evaporator case to the vapor line is not considered.

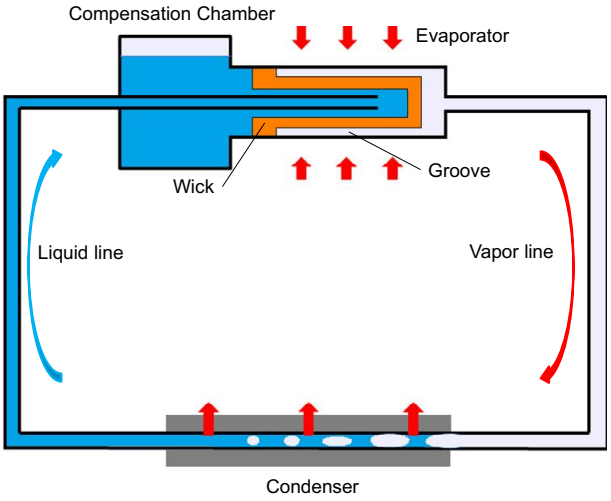


Fig.1. LHP configuration.

2.1 Evaporator and wick model

The energy balance in the evaporator can be expressed by eq. (1).

$$Q_{load} = Q_{ev} + Q_{gr} + Q_{hl} + Q_{amb} \quad (1)$$

Where, Q_{load} is the heat load, Q_{ev} is evaporation heat, Q_{gr} is overheat of groove, Q_{wi} is the heat leak from the evaporator to the CC and Q_{amb} is heat loss. Q_{ev} is written by eq. (2) and (3).

$$Q_{ev} = h_{ev} A_{ev} \left(T_{ec} - T_{ev}\right) \quad (2)$$

$$Q_{ev} = \dot{m}\lambda \quad (3)$$

Where, h_{ev} is estimated experimentally, because the number strongly depends on the degree of contact between the evaporator and the wick and the position of the vapor-liquid interface also effects on the number. Q_{gr} is computed by the heat transfer coefficient of the forced convection of the vapor through the groove. Q_{hl} consists of two elements, i.e. the heat leak through the wick (Q_{hl_wi}) and the heat leak from the evaporator case to the CC case (Q_{hl_ca}). Q_{hl} is expressed by eq. (4).

$$Q_{hl} = Q_{hl_wi} + Q_{hl_ca} \quad (4)$$

Q_{hl_wi} and Q_{hl_ca} are calculated by eq. (5) and (6) respectively.

$$Q_{hl_wi} = \frac{2\pi L_{wi} k_{eff}}{\log\left(D_o / D_i\right)} \left(T_{ev} - T_{cc}\right) \quad (5)$$

$$Q_{hl_ca} = k_{ca} A_{ca} \left(T_{ec} - T_{cc}\right) \quad (6)$$

Where, k_{eff} is the effective thermal conductivity and is calculated by eq. (7) with eq. (8) and (9).

$$k_{eff} = \left(k_{\max}\right)^{n} \times \left(k_{\min}\right)^{1-n} \quad (7)$$

$$k_{\max} = \varphi k_f + (1-\varphi) k_s \quad (8)$$

$$k_{\min} = \frac{k_f k_s}{\varphi k_f + (1-\varphi) k_s} \quad (9)$$

Q_{amb} is calculated by the heat transfer coefficient of the natural convection of the ambient air. The pressure loss in the wick is calculated by eq. (10).

$$\Delta P_{wi} = \frac{\dot{m}\mu \ln\left(D_o / D_i\right)}{2\pi\rho K L_{wi}} \quad (10)$$

2.2 Transport lines and condenser

The condition of working fluid in the transport lines and condenser is classified into three, i.e. single-phase vapor/liquid, and two-phase vapor-liquid. Different formulas are used between the single and two phase flow. The single-phase flow is calculated based on the Darcy's law. The temperature at two-phase flow is determined by the vapor pressure curve and the pressure drop and determined by eq. (11).

$$T_{i+1} = T_i - \left(\frac{dT}{dP}\right)_{sat} \Delta P_i \quad (11)$$

The pressure drop of the two-phase flow is computed by the Lockhart-Martinelli method [11,12]. The heat transfer coefficient for the two-phase flow was predicted by the laminar filmwise condensation of the flowing vapor on a horizontal cylinder [9].

2.3 Compensation chamber

Working fluid in the CC is two-phase state, therefore, the temperature of the CC is determined

by the summation of the pressure drop from the evaporator to the bayonet tube and the vapor pressure curve of working fluid.

$$T_{cc}' = T_{sat}\left(P_{ev} - \Delta P_{ev_bay}\right) \quad (12)$$

The heat leak from the evaporator that is calculated by eq. (4) is also expressed by eq. (13).

$$Q_{hl}' = Q_{cc_ll} + Q_{cc_amb} \quad (13)$$

Where, Q_{cc_ll} is the amount of subcooling in the returning liquid, and Q_{cc_amb} is the heat loss from the CC to ambient air.

2.4 Solution algorithm

The solution flowchart for the LHP model presented above is shown in Fig.2. Simulations are conducted using the numerical analysis software MATLAB. The models of groove, vapor/liquid lines and condenser are divided into 10, 200, 200, and 200 nodes respectively and calculations are conducted on every node. The physical properties of working fluid are obtained from REFPROP version 9.1 [10]. The saturation temperature of the evaporator (T_{ev}), CC (T_{cc}), and the temperature of evaporator case are determined by iteratively solving eq. (4) and (13), eq. (12) and assumption, and eq. (1) respectively. The convergence condition was set to 3% of difference respectively. Calculation was stopped when the total pressure loss reached the capillary limit that is written by eq. (14).

$$P_{cap} = \frac{2\sigma\cos\theta}{r_{pore}} \quad (14)$$

Contact angle θ was measured using the drop-shape method, and the average pore radius was measured using mercury porosimetry [7].

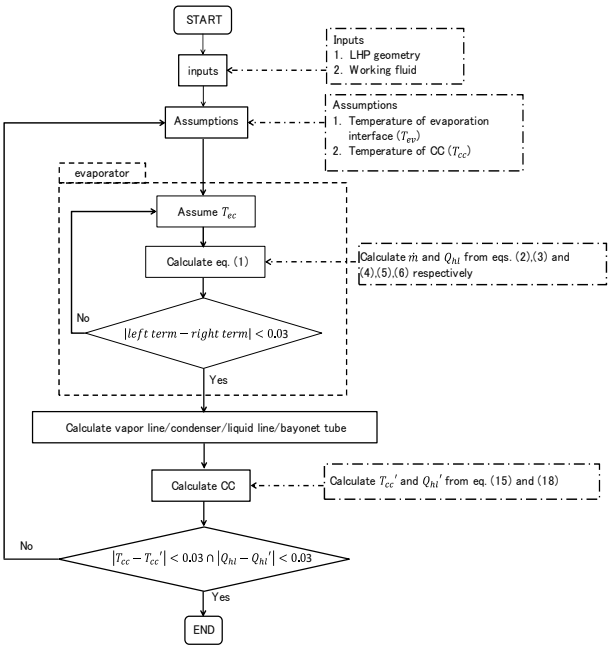


Fig. 2. Solution flowchart for the LHP model

3. EXPERIMENT

3.1 Configuration of the constructed LLHP

10m-class long-distance loop heat pipe was designed and fabricated based on the computation model. Fig. 3 shows the overview figure of the LLHP that has 10 m one-way heat transport distances. Table 1 lists the main characteristics of the LLHP.

Two aluminum heater blocks were attached to the

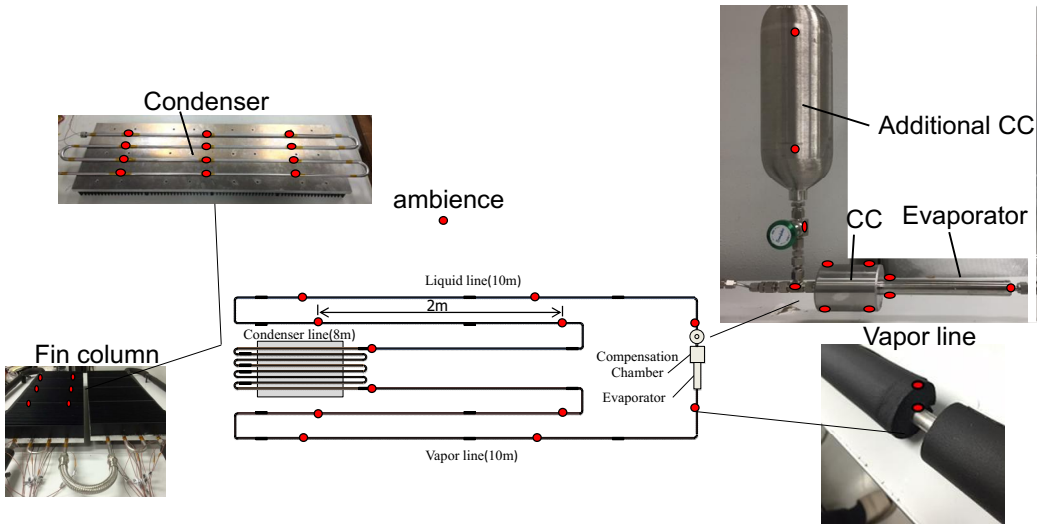


Fig. 3. Overview figure of the LLHP

evaporator to simulate instrument mass and eight cartridge heaters were inserted into them to provide heat loads to the evaporator. Polytetrafluoroethylene (PTFE) porous material was used for the wick which was inserted to the evaporator. The cooling method of the condenser was natural convection. AL5052 aluminum plate (250 × 810 × 15 mm) was attached to the condenser line on one side. On the other side, the four vertical fins were attached to enhance the natural air cooling; each fin was 30 mm in height with a 10 mm pitch and each array contained 20 fins. During the test, the entire LLHP was covered with ethylene propylene synthetic rubber as the thermal insulators. Temperatures in the LLHP were measured by 59 T-type thermocouples. Red points in Fig. 3 denote the measurement locations. Four thermocouples were attached to the evaporator, four to the Compensation Chamber (CC), twenty four to the condenser, six to the fin, and two to the heater blocks. The temperatures of the vapor and liquid lines were measured at six points each at intervals of two meters on the pipes, and six points on the insulator of the vapor line were also measured, and the temperature of ambient air was also measured with one thermocouples. During the test, the ambient temperature in the laboratory was maintained at 24±1 ℃.

Table 1. LLHP characteristics.

Evaporator (SUS304)	O.D	21mm	Vapor Line (SUS304)	O.D	10mm
	Length	160mm		I.D	8mm
CC (SUS304)	O.D	60mm		Length	10m
	Length	70mm	Liquid Line (SUS304)	O.D	6.4mm
Wick (PTFE)	O.D	19mm		I.D	4.6mm
	I.D	13mm		Length	10m
	Length	140mm	Condenser (SUS304)	O.D	10mm
	Pore radius	1.2μm		I.D	8mm
	Porosity	34%		Length	8m
	Permeability	$2\times10^{-14}m^2$	Working fluid	Material	Ethanol
	Groove No.	8		Volume	1250cc

3.2 Experimental results

Experiments were conducted at the heat load increments of 40 W starting from 40 W. Four experimental conditions were conducted, one was horizontal and the others were anti-gravity conditions. In the anti-gravity conditions, three conditions were further experimented i.e. evaporator was 30, 60, 100 cm higher than condenser respectively. Experiments were stopped when the average evaporator case

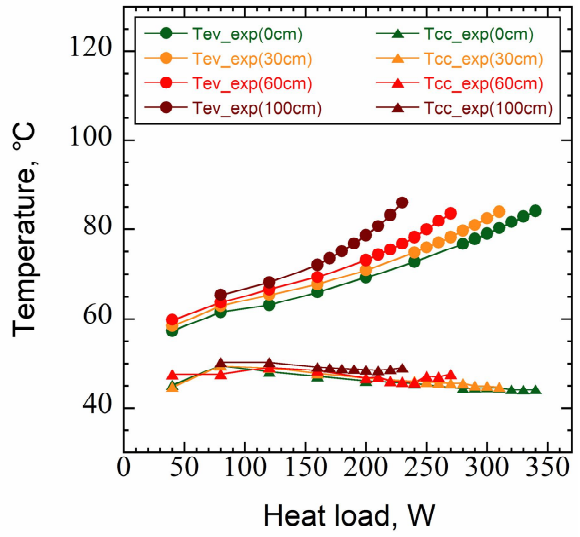


Fig. 4. Effect of heat load on evaporator case and CC temperatures.

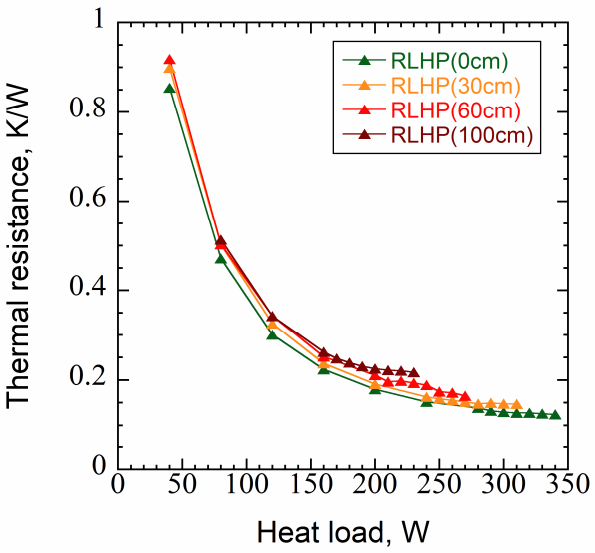


Fig. 5. Effect of heat load on thermal resistance.

temperature reached at 100 ℃ or the PTFE wick reached capillary limit. The steady-state temperatures at the evaporator and CC, and the thermal resistance between the evaporator and the condenser were shown in Fig. 4, and 5. Thermal resistance offered by R_{LHP} is used to access the heat transfer performance of the device which is defined by the equation (20).

$$R_{LHP} = \frac{T_{ev} - T_{con}}{Q_{load}} \tag{20}$$

Where, Q_{load} is the heat load, and T_{ev} and T_{con} are the average temperatures of the evaporator case and condenser respectively. The maximum heat load was 340 W at the horizontal condition and the thermal

resistance was 0.11 K/W at the maximum heat load. On the other hand, the maximum heat loads were 310, 270, 220 W and the thermal resistances were 0.13, 0.29, 0.31 K/W at the 30, 60, 100 cm anti-gravity condition respectively. The evaporator temperature became higher as the evaporator was raised. This trend is mentioned in the paper [2]. It was expected that the heat transfer efficiency of the anti-gravity condition became lower than the horizontal condition because the temperature of the evaporator and the thermal resistance became higher.

3.3 Discussions

3.3.1 Estimation of the heat transfer coefficient

The amount of heat loss from the vapor and liquid lines and the heat dissipation from the condenser were calculated by equation (21).

$$Q_i = h_i A_i \sum_l \left(\left(\frac{T_i(l) + T_i(l+1)}{2} \right) - T_{amb} \right) \quad (21)$$

Where, the subscript i means the each part of the LLHP i.e. vapor line, liquid line, condenser line. h_i, A_i, T_i, T_{amb} are heat transfer coefficient, radiation surface area, and temperature of l-th T-type thermocouples and ambient. The heat loss from the evaporator and CC was estimated by equation (22) which was derived from the energy equation of entire part of the LLHP.

$$Q_{ev} = Q_{load} - Q_{vl} - Q_{ll} - Q_{con} \quad (22)$$

Where, Q_{ev}, Q_{vl}, Q_{ll} are the heat loss from the evaporator and CC, vapor line, liquid line respectively, and Q_{con} is the heat dissipation from the condenser. The heat transfer coefficients of vapor line and condenser were estimated by the equation (22) and (23) respectively.

$$\frac{1}{h_i A_i} = R_i + \frac{\log(D_{ins_out} / D_{ins_in})}{2\pi k_{ins}} + \frac{1}{\pi D_{ins_out} h_{air}} \quad (22)$$

$$\frac{1}{h_{con} A_{con}} = R_{con} + \frac{1}{(A_0 + \eta A_{fin}) h_{fin}} \quad (23)$$

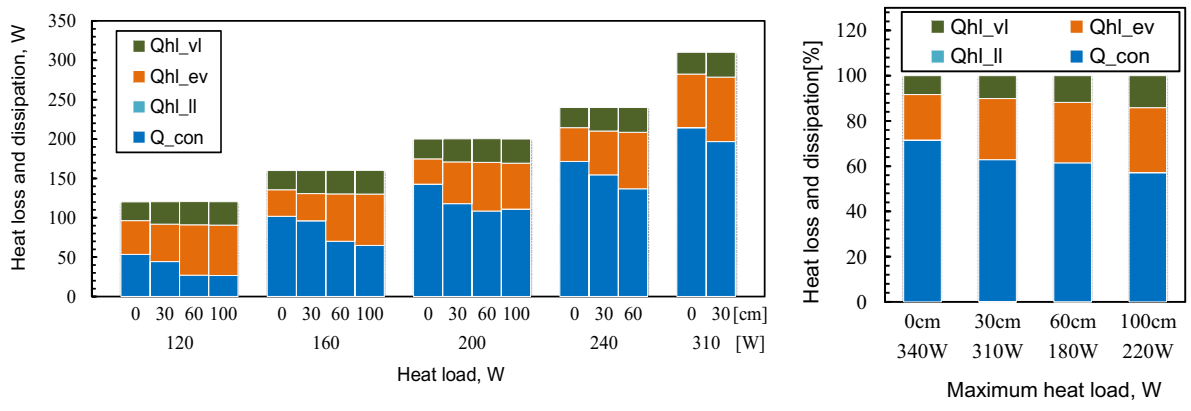
Where, R_i is thermal contact resistance between the pipe and the insulator, D_{ins_out} and D_{ins_in} are the outer diameter and the inner diameter of the insulator respectively, k_{ins} and h_{air} are heat conduction coefficient of the insulator and heat transfer coefficient from the outer wall of insulator to the ambient respectively. Equation (22) assumes that the temperatures of inner and outer walls of the pipe are same. R_{con} is thermal resistance between the pipe and the fin. A_0 and A_{fin} are heat dissipation areas of no fin part and fin part respectively. η is fin efficiency and h_{fin} is heat transfer coefficient from the fin to the ambient. Table 2 shows the estimation results of coefficient of heat transfer. Where, the same value with the coefficient of heat transfer at the vapor line was used for the liquid line because the adiabatic condition is same.

Table 2 Coefficient of heat transfer

	[W/m^{2}K]
Vapor(Liquid) line	1.79
Condenser line	26.21

3.3.2 Estimation result of the amount of heat loss and dissipation

Fig. 6 shows the calculation results of the amount of heat loss and dissipation as the function of the applied heat load for LLHP. It is not shown in Fig. 6, however, heat was absorbed at the liquid line in some experimental conditions. Especially, the maximum value of heat absorption was 0.32 W



(a) Amount in each heat load (b) Ratio in each maximum heat load

Fig. 6. Effects of heat load and gravity on heat loss and dissipation of each experimental condition

Table 3 Coefficient of heat transfer between the evaporator case and wick

	40[W]	...	180[W]	200[W]	220[W]	240[W]	260[W]	280[W]	300[W]	320[W]	340[W]	360[W]
0[cm]	1800	...	1800	1800	1800	1800	1800	1800	1800	1800	1800	1800
30[cm]	1800	...	1800	1800	1800	1800	1800	1750	1680	-	-	-
60[cm]	1800	...	1800	1800	1750	1680	1580	-	-	-	-	-
100[cm]	1800	...	1700	1600	1500	-	-	-	-	-	-	-

when evaporator was 100 cm higher than condenser and applied heat load was 80 W. As the heat load was increased, the heat dissipation rate from the condenser line was improved in each experimental condition. The possible reason is that the mass flow rate became increased as the heat load was increased. As a result, the ratio of latent heat of vaporization in heat load and the amount of heat that was carried to the condenser became larger. As shown in Fig. 6(b), 71.4 % of the heat loads of horizontal condition. On the other hand, 62.8, 61.8, 57.1 % of the maximum heat load was dissipated at the condenser under anti-gravitational conditions respectively. Comparison between the horizontal and anti-gravitational conditions showed that the performance of heat dissipation at the condenser under anti-gravity condition was lower than the horizontal condition and the amount of the heat loss from the vapor line and the evaporator were increased. There are two possible reasons for this. As shown in Fig. 4, the evaporator temperature under anti-gravity conditions became higher than the horizontal condition. Consequently, heat leak from the evaporator to the CC was increased and the amount of the heat that was carried to the condenser was decreased. Second possible reason is that temperature dependence of the latent heat. The value of latent heat of ethanol becomes lower as the temperature increases and result, the latent heat of vaporization in the evaporator decreased under anti-gravity condition.

To improve the performance of the heat dissipation at the condenser, the adiabatic performance of the evaporator and the CC is necessary in addition to that of the vapor line.

4. ANALYSIS FROM THE POINT OF MODEL

4.1 Comparison between the computational results and experimental results

Fig. 7 shows the calculation results of the evaporator case and CC with the one-dimensional steady-state model. Comparing with the Fig. 4 and Fig. 7, there is a same trend that the temperature of the evaporator case became higher as the evaporator case is located higher place, however, there are essential difference between them. Based on the results of calculation, the temperature of the evaporator case increased almost linearly as the heat load increased in all experimental conditions. On the other hand, experimental results showed that the temperature of the evaporator case increased quadratically and the slope of the curve increased as the heat load increased. This is because of the generation of the vapor between the evaporator case and the wick as the heat load increased. This is called vapor blanket in [15,16]. When the vapor blanket appeared, the coefficient of heat transfer between the evaporator case and wick becomes smaller. In this study, this parameter is chosen comparing with the experimental results. Table 3 shows the results of the parameters of the coefficient of heat transfer and Fig. 8 shows the comparisons of calculation and experimental results of the evaporator case and CC. The numerical result was good agreement with the experimental results and this result indicates that the vapor pocket tends to appear easier when the gravity effect became increased.

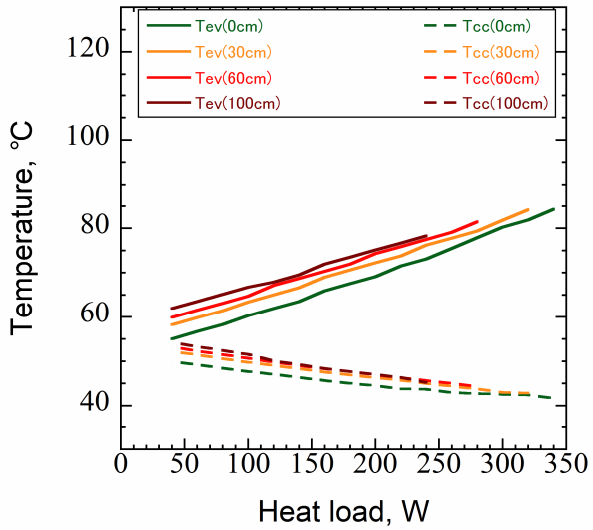


Fig. 7. Calculation results of the effect of heat load on evaporator case and CC temperatures

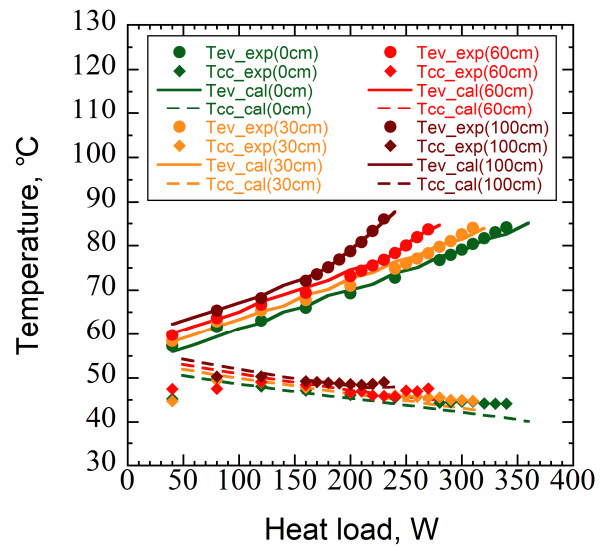


Fig. 8. Comparisons of experimental and computational temperature distributions

4.2 Calculation results of heat leak

Fig. 9 shows the calculation results of the heat leak from the evaporator to CC of each experimental condition. The heat leak increased as the gravitational effect became increased. This result agreed with some results that were discussed above, i.e. (i) the temperature of the evaporator case became higher as the gravitational effect became increased, (ii) the efficiency of the heat dissipation decreased as the gravitational effect became increased. The heat leak decreased as the heat load increased in each experimental condition, and this tendency also consists with the experimental result that the efficiency of the heat dissipation from the condenser increased as the heat load is increased.

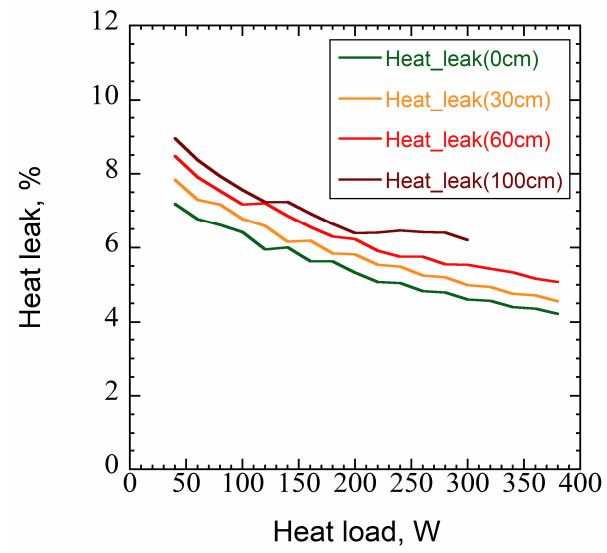


Fig. 9. Effect of heat load and gravity on the heat leak from the evaporator case to CC

4.3 Calculation results of pressure losses over LLHP

Fig. 10 shows the calculated distributions of the pressure losses for the LLHP. This result showed that the pressure losses from the vapor line and the wick are the dominant part of the LLHP. The effect of the gravity on the gravity is also critical for the total pressure losses. To improve the performance of the LLHP, high-performance wick, which has high capillary pressure and high permeability is needed, because the bubble point pressure of this wick is 18200 Pa.

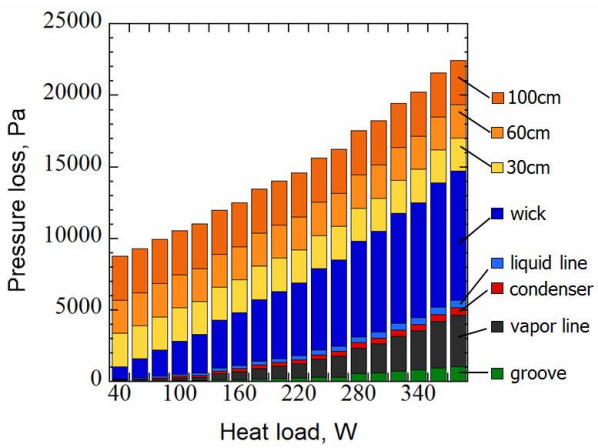


Fig. 10. Calculation results of the pressure loss over the parts of the LLHP

5. CONCLUSIONS

One-dimensional steady-state model was developed to design and fabricate the 10m-class LLHP. Test results showed that the LLHP could transport 340W under horizontal condition, on the other hand, the maximum heat transports were 310, 270, 220 W under 30, 60, 100 cm anti-gravity conditions respectively. Evaluation of the amount of heat loss and dissipation of the LLHP was conducted from the temperature data of test results for applying LLHP to the terrestrial field. The calculation results showed that heat dissipation performance at the condenser was improved as the heat load becomes increased. It was also showed that the effect of gravity degrades the heat dissipation performance. Numerical model showed the good agreement with the experimental results by considering the vapor pocket between the evaporator case and wick and showed the effects of the gravity on the occurrence of vapor pocket. The numerical model indicated that the high-performance wick would be necessary for applying the LLHP under more severe anti-gravity conditions.

ACKNOWLEDGMENT

This research was partly supported by JST, PRESTO.

REFERENCES

[1] Maydanik, Y. F., Loop heat pipe, *Int. J. Applied Thermal Engineering*, 25, pp. 635-657, (2005).
[2] Ku, J., Operating Characteristics of Loop Heat Pipes, *Proc. of 29th Int. Conf. on Environmental System,* SAE Paper No. 1999-01-2007
[3] S. Launay, V. Sartre, J. Bonjour, Parametric analysis of loop heat pipe operation: a literature review, *Int. J. Thermal Sciences*, 46 (2007) 621-636
[4] L. Vasiliev, D. Lossouarn, C. Romestant, A. Alexandre, et al., Loop heat pipes for cooling of high-power electronic components, *Int. J. Heat and Mass Transfer*, 53 (2009) 301-308
[5] Mitomi, M., Nagano, H., Long-distance loop heat pipe for effective utilization of energy, *Int. J. Heat and Mass Transf.*, 77, pp. 777-784, (2014).
[6] J. I. Rodriguez, M. Pauken, Performance characterization and model verification of a loop heat pipe, *International Conference On Environmental Systems*, Toulouse, July 2000 (SAE paper 2000-01-2317), 7 pp
[7] H. Nagano, F. Fukuyoshi, H. Ogawa, Development of an experimental small loop heat pipe with polytetrafluoroethylene wicks, *J. Thermophys. Heat Transfer* 25 (4) (2011) 547-552.
[8] D. Chisholm, A theoretical basis for the Lockhart-Martinelli correlation for two-phase flow, *Int. J. Heat and Mass Transf.*, 10 (12) (1967) 1767-1778.
[9] T. Fujii, H. Uehara, C. Kurata, Laminar filmwise condensation of flowing vapor on a horizontal cylinder, *Int. J. Heat and Mass Transf.*, 15 (1972) 235-246.
[10] NIST Reference Fluid Thermodynamic and Transport Properties Database (REFPROP): Version 9.1 NIST Standard Reference Database 23, 2013. <http://www.nist.gov/srd/nist23.cfm>
[11] Zhao, T.S., Liao, Q. "On capillary-driven flow and phase-change heat transfer in a porous structure heated bu a finned surface: measurement and modeling". International Journal of Heat and Mass Transfer, 43, 2000, pp. 1141-1155.
[12] D, Khrustalev, A, Faghri. Heat transfer in the inverted meniscus type evaporator at high heat fluxes, International Journal of Heat Mass Transfer, 38 (16) (1996) pp. 3091-3101.

Vapor Modulated Variable Conductance Loop Heat Pipes for Space Applications

Paula Prado-Montes[1*], Donatas Mishkinis[1], Alejandro Torres[1]

[1] *IberEspacio Tecnología Aeroespacial, C/ Magallanes 3, 28015 Madrid, Spain*

Abstract

A Vapor Modulated Loop Heat Pipe (VMLHP) is a Loop Heat Pipe (LHP) incorporating a Pressure Regulating Valve (PRV) at its evaporator outlet. The PRV provides variable conductance function to the LHP and it is able to thermally disconnect the evaporator from the condenser when the temperatures go below a certain set point. This function, which can be called as Thermal Switch function, is particularly interesting for equipment facing harsh environments with extreme low temperatures. Different thermal switches have been studied and developed for different space missions, including low temperature, propylene-filled VMLHPs for a Lunar Lander, the instrument ASIM-MXGS to be integrated on the International Space Station (ISS) and LHPs for ExoMars 2018 Rover Module, and a medium temperature, ammonia-filled VMLHP to be launched onboard satellite UPMSAT2, for educational purposes. Analysis and experimental results show that the VMLHP concept allows achieving very high on/off thermal conductance ratio values, in the range 1000:1, in addition to other advantages such as efficient temperature control function ~± 1°C, high flexibility in set point, from -40 ºC to +80 ºC, wide power operational range, from ~0.1 W to kilo Watts, fully passive operation, mass and volume minimization, scalability, flexibility, easy integration, functional gravity field independence and very small response time.

Keywords: Heat transfer; Pressure regulating valve; Space applications; Thermal switch; Vapor modulated loop heat pipe

1. INTRODUCTION

Loop Heat Pipes (LHPs) are currently used as efficient thermal control devices in different space applications. Their advantages in terms of heat transport capability, high thermal conductance, flexibility and testability on ground have been demonstrated. Nevertheless, the performance of constant conductance LHPs can be limited for equipment operating in harsh environmental conditions, such as deep space, solar system planets, planet satellites and asteroids. Such applications are demanding the development of a variable conductance LHP or thermal switch with high ON/OFF thermal conductance ratio, able to keep the evaporator, and therefore the equipment, at a certain temperature even if the condenser is facing a sink at extreme low temperatures.

Vapor Modulated LHP (VMLHP) technology is a good candidate to solve this thermal challenge. The VMLHP consists of a LHP incorporating a Pressure Regulating Valve (PRV) at the evaporator outlet. The PRV provides the variable conductance function and it is able to thermally disconnect the evaporator from the condenser when the temperatures go below a certain set point. Deep analyses of LHPs with PRVs have been conducted, as reported in [1], [2], [3] and [4]. The Thermal Switch function is particularly interesting for instruments undergoing extreme low temperatures, such as planetary landers and rovers. In these cases, the use of propylene based thermal switches shows its good performance allowing the LHPs operation at temperatures below -160ºC at condenser side, keeping the onboard electronics in safe temperature limits.

*Corresponding author: ppn@iberespacio.es, Phone: +34-91-444-1500, Fax: +34-91-445-1764

1.1 VMLHP operating principles

VMLHPs operation as a variable conductance device is based on the implementation of a PRV in the LHP. The PRV operation is driven by the movement of a piston which depends on the pressure balance between the working fluid in the LHP and in the PRV reservoir, filled by an activating fluid. For applications with a constant set point argon is usually chosen for the PRV reservoir charging. A schematic of the PRV components and operation modes is depicted in Fig. 1.

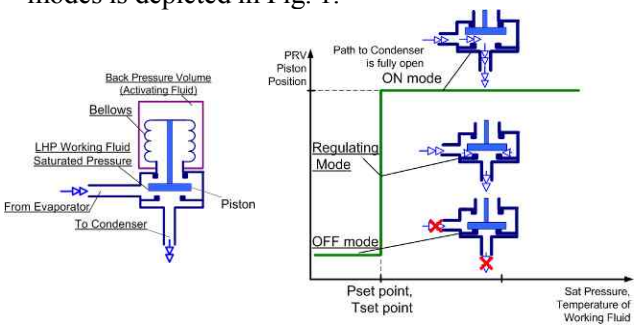


Fig. 1. PRV components and operation modes schematic.

Mainly, three operational modes can be identified in a VMLHP operation. The first mode is called "ON mode" and in this case the pressure of the working fluid in the LHP is higher than the pressure of the argon plus the piston load. The PRV is totally open and the LHP works as a constant conductance

device, in the same way as an LHP without PRV. The second mode is called "regulation mode". In the regulation mode the piston PRV moves close to the closed position. There is still fluid circulation in the LHP, but the PRV piston position implies an additional pressure drop, which is translated in a decrease of the thermal conductance of the LHP. The heat leak to LHP compensation chamber is increased. The operating temperature, usually measured at the compensation chamber, is maintained at the specified set point. This effect is shown in the P-T diagram in Fig. 2.

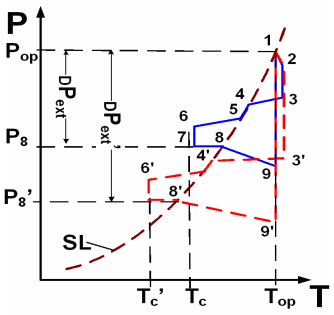


Fig. 2. P-T diagram for a LHP in ON mode (blue line) and in regulation mode (red line).

For high power and/or low sink conditions, the required ΔPext may come close to wick pumping capability ΔPcap. In this condition, the wick provides the maximum pumping and the evaporation front in the wick recedes toward the evaporator core (EV outlet vapor overheating). This produces a higher heat leak through the wick. It is important that the design of the interface between primary and secondary wicks provides the necessary heat leak to the compensation chamber in the regulating mode, without drastically degrading the LHP conductance in the ON mode.

The third operational mode corresponds to the "OFF mode", in which the PRV is totally closed and the fluid circulation is interrupted. The thermal conductance in this case corresponds only to the conduction through the LHP transport lines.

2. MEDIUM TEMPERATURE VMLHP FOR MICRO-SATELLITES

The VMLHP concept is the baseline used for the Micro Heat Switch (MHS) experiment to be launched onboard satellite UPMSat-2. The UPMSat-2 project aims at building a micro-satellite that can be used as an in-orbit technology demonstration platform. The main part of the project is being carried out at the "Ignacio da Riva" Institute which is part of Universidad Politécnica de Madrid, with the collaboration of some other University groups and Spanish space companies, for educational purposes. With the aim of achieving a complete in-flight characterization of a miniature size VMLHP, IberEspacio developed the MHS as one of the experiments on-board.

The MHS was designed to have a set point at +26 ± 1.5 ºC. Ammonia was selected as the working fluid. Thermal analysis of the MHS was performed using the software EcosimPro [5]. The simulation showed the ability of the MHS to keep its evaporator at a temperature higher than 26 ºC, with an ON conductance of 1.8 W/K with the PRV totally open (operation out of regulation) region and 0.06 W/K in the regulation region. The OFF conductance, when there is no fluid circulation, corresponds to the conduction through the LHP lines and it was estimated of 0.005 W/K. The LHP thermal conductance was calculated as:

$$C_{MHS} = \frac{Q}{T_{EV_ave} - T_{CN_out}} \quad (1)$$

The Thermo-Mathematical-Model (TMM) schematic and simulation results can be seen in Fig. 3 and Fig. 4.

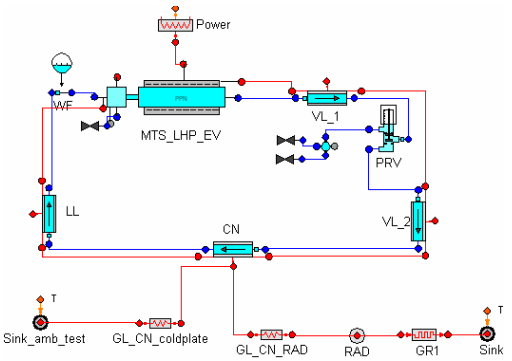


Fig. 3. MHS TMM schematic.

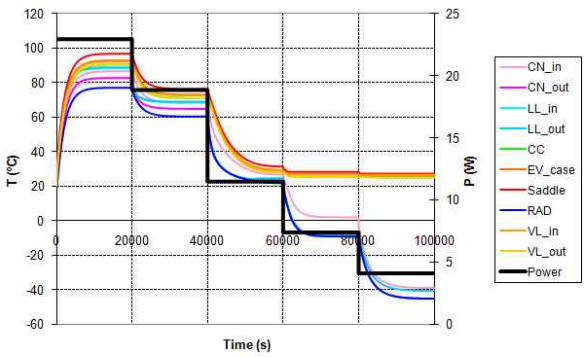


Fig. 4. MHS simulation results.

Two MHS models were designed, manufactured and tested. The first prototype of MHS was tested in ambient and promising results were obtained [6]. The experimental data revealed that MHS ON/OFF conductance ratio was significantly higher than 100:1, typical for paraffin-based thermal switches,

with an operating ON conductance of 2.4 W/K and an OFF conductance of 0.018 W/K (ambient). In addition, MHS showed a precise (26 ± 1.5 ºC) and robust temperature control together with a functional gravity field independence and low mass (160g).

The second MHS was even lighter than the first one, with a mass of less than 150 g. the set point was set in this case at +20 ± 1 ºC Its main features are summarized in Table 1.

Table 1. MHS main features.

EV	OD = 12 mm; L = 40 mm
EV Saddle	W x L = 32 x 32 mm^2
CC	Double; OD = 17 mm; L = 8 mm
CN line	ID = 1 mm
CN saddle	h = 1.5 mm; OD = 60 mm
RAD	A = 28 cm^2
VL	OD = 3 mm; L = 30 mm
LL	OD = 2 mm; L = 60 mm
PRV	OD = 17 mm; L = 48 mm

It was tested in vacuum and the results revealed outstanding thermal performance with an ON conductance of 3.5 W/K and an OFF conductance of 0.006 W/K, what means an ON/OFF conductance ratio of 580, more than 5 times higher than that of the current state-of-the-arts paraffin heat switches [6]. Moreover, the MHS demonstrated precise, robust and totally passive temperature control in regulation mode with precision ± 1.5 °C. Its configuration with two compensation chambers allowed operation at any orientation, being insensitive to gravity field.

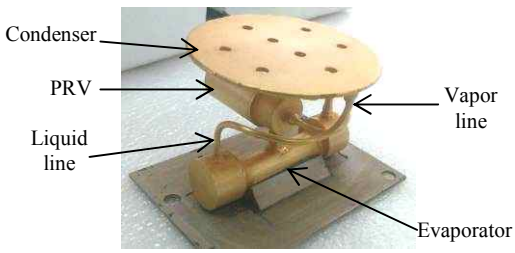


Fig. 5. MHS overview. Gold coating was implemented to reduce the heat leak to the environment.

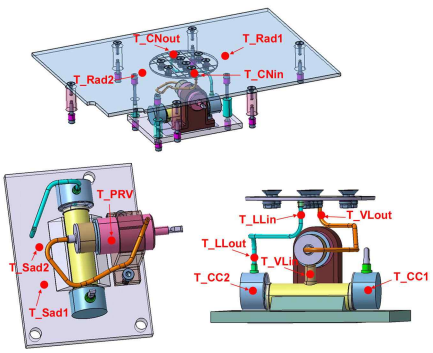


Fig. 6. MHS measurement plan.

The second MHS prototype is shown in Fig. 5. Its measurement plan and performance test results in horizontal can be seen in Fig. 6 and Fig. 7, respectively. In the graph in Fig. 7, OFF mode corresponds to 0.2 W and 0.4 W power inputs.

For the input power of 1.2 W, quick and smooth start up event without temperature overshooting takes place. Note that the temperature of vapor line increases as the 1.2 W is applied, indicating that the working fluid starts circulating. The PRV opens partially the path to the condenser and regulates the LHP temperature at 20 ºC on CC. Regulation mode is kept until 8.2 W. Finally, for 11.2 W the PRV opens totally the path to the condenser and the LHP works as a regular LHP without PRV. The MHS operates under ON mode and a thermal conductance of 3.5 W/K is achieved.

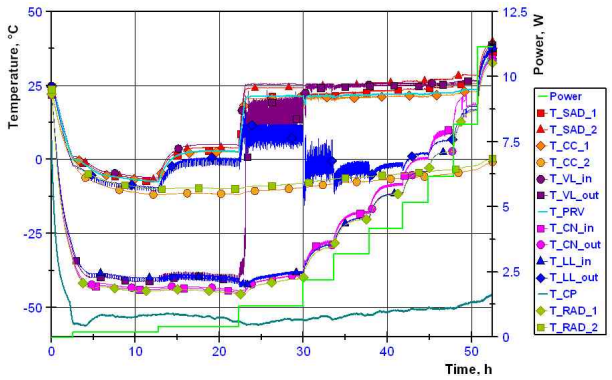


Fig. 7. MHS performance test.

The MHS also sustained operation at different orientations and under sharp power variations. Detailed information of the experimental test results of the MHS can be found in [8].

Currently, a third model of the MHS is under testing. This model is considered as a proto-flight model and will be also tested in flight, on-board UPMSat-2.

3. LOW TEMPERATURE VMLHP FOR ASIM-MXGS, ON ISS

MXGS stands for Monitor X-ray and Gamma-ray Sensor and it is the high energy sensor in the Atmospheric-Space Interaction Monitor (ASIM). ASIM was proposed for the International Space Station external facilities on the Columbus module, with the scientific goal of studying high-altitude optical emissions from the stratosphere and mesosphere, the so-called red sprites, blue jets, and elves (or Transient Luminous Events) and to provide evidence on the possible link between these optical emissions and Terrestrial Gamma Ray Flashes.

VMLHPs were selected as part of the thermal control system of the MXGS thanks to their thermal switch function. Due to the characteristics of the

interface, the system was designed to include two VMLHPs, each of them connected to two small-size Axial Grooved Heat Pipes (AGHPs), with an outer diameter of 6 mm, attached to their saddle to collect the heat from the edges of the instrument base-plate. Both the LHPs and the AGHPs were attached to the MXGS upper housing. The LHP condensers were attached to the system RAM radiator. The main MXGS LHPs' features are summarized in Table 2.

Table 2. MXGS VMLHPs main features.

EV	OD = 15 mm; L = 215 mm
EV Saddle	W x L = 76 x 200 mm^2
CC	OD = 27 mm; L = 49 mm
CN line	OD = 2 mm; L = 1 m
CN saddle	A = 200 cm^2
VL	OD = 3 mm; L_{LHP1} = 1.2 m; L_{LHP2} = 0.8 m
LL	OD = 2 mm; L_{LHP1} = 0.6 m; L_{LHP2} = 1 m
PRV	OD = 17 mm; L = 60 mm

An overview of the system composed by the two VMLHPs and the four AGHPs is shown in Fig. 8.

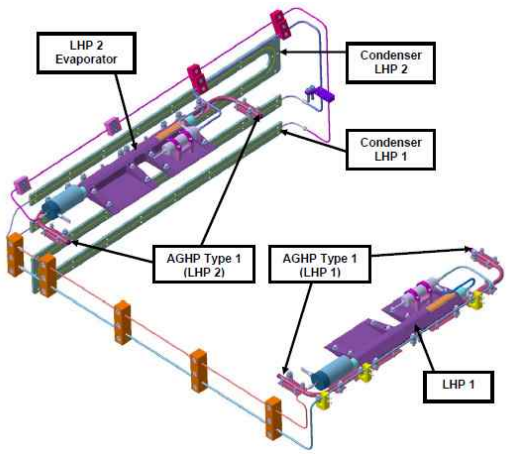


Fig. 8. MXGS LHPs overview.

The MXGS VMLHPs were designed to have a set point at +2.5 ± 1.5 ºC. Due to safety reasons as requested by the mission, propylene was selected as the working fluid. Thermal analysis of the MXGS LHPs, AGHPs and base-plate system was performed in EcosimPro. The TMM schematic with details of the two LHPs, the AGHPs, the common base-plate and radiator can be seen in Fig. 9. The simulation showed was used to predict the system behavior and to verify its ability to keep the base-plate at a temperature higher than the defined set point, even for the coldest sink conditions. The graph in Fig. 10 shows the simulated operation for a transient from hot to cold conditions for one of the LHPs, with the radiator temperature at +30 ºC and -41 ºC, respectively. The power level on the evaporator was 40 W.

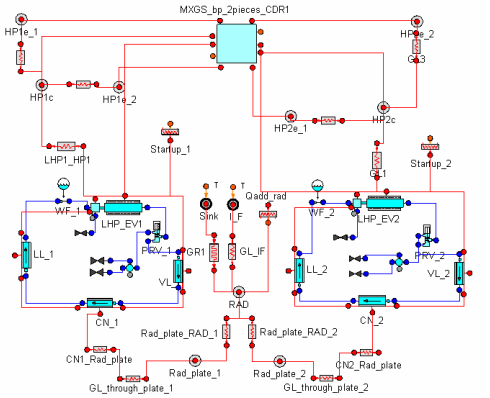


Fig. 9. MXGS VMLHPs TMM.

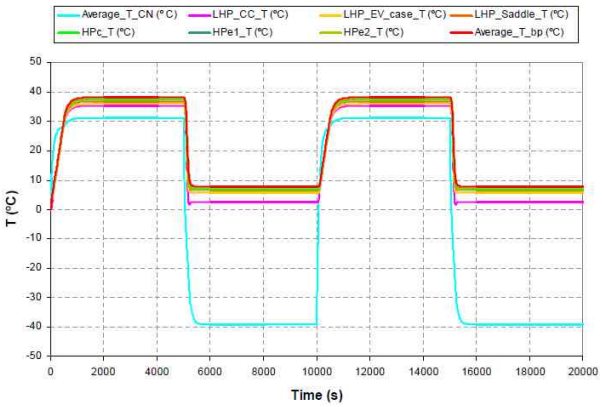


Fig. 10. MXGS LHPs overview.

It can be seen that the LHP works with variable conductance, keeping the evaporators and AGHPs at temperatures higher than 2.5 ºC. The LHP thermal conductance was calculated as:

$$C_{MXGS_LHP} = \frac{Q}{T_{EV_ave} - T_{CN_ave}} \qquad (2)$$

At hot conditions the PRV was totally open, working the LHPs as constant conductance devices. In this case, the thermal conductance according to the simulation was higher than 7 W/K. At cold conditions, the LHPs worked in regulation mode, being the PRVs partially closing the fluid path to the condensers. In this case the simulation showed a thermal conductance of 0.87 W/K.

Two MXGS thermal control system models were designed, manufactured and tested. The models consisted of a Structural Thermal Model (STM) and a Flight Model (FM). Both models underwent a full thermal characterization test campaign at IberEspacio. Their thermal switch function was verified experimentally.

The test set up including two LHPs is shown in Fig. 11. The test campaign was conducted in ambient and it included cold and hot performance tests, plus maximum power, start and shut-down

tests. All tests were performed successfully. The most representative test results of the VMLHP function for the FM are presented in Fig. 13-15. The test results of one of the LHPs, called LHP1, and its corresponding AGHPs is presented, while the results of the other LHP can be considered similar, due to the system symmetry. The measurement plan of LHP 1 assembly is shown in Fig. 12.

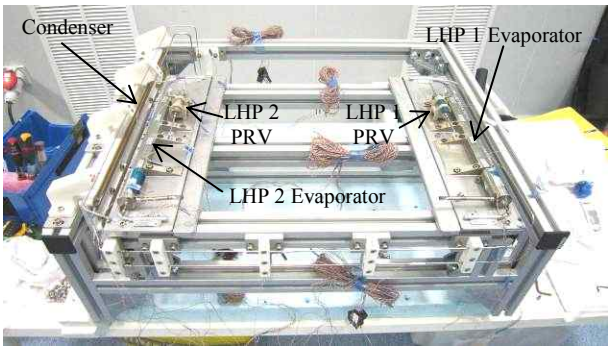


Fig. 11. MXGS LHPs & AGHPs test set up overview.

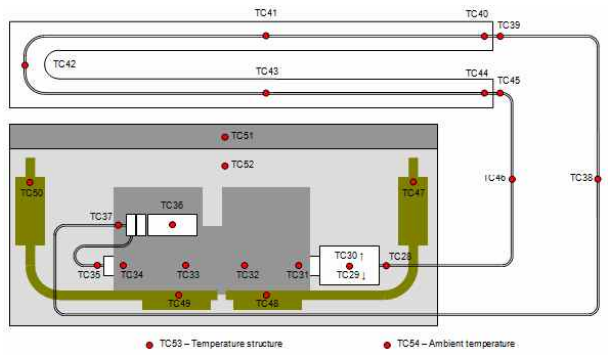


Fig. 12. MXGS LHP 1 measurement plan.

The test shown in Fig. 13 corresponds to the cold case operation of LHP 1. In this case the sink was kept at -50 ºC, which correspond to a condenser temperature around -30 ºC. In such conditions the PRV was in regulation mode and the VMLHP operated as a variable conductance device. As shown in the graph, the LHP evaporator temperature was maintained around +2 ºC for any power level, from 10 W to 50 W. The thermal conductance varied from 0.3 W/K to 1.7 W/K.

On the contrary, as shown in Fig. 14, the LHP achieves its maximum thermal conductance in the hot case. In such conditions the condenser temperature is around 50 ºC and the PRV is totally open, working the LHP as a constant conductance device, and achieving conductance values around 6 W/K, a little bit lower, but still in line with the results in the predictions.

A thermal balance test was not conducted for the MXGS LHPs due to the important influence of heat leaks in ambient conditions on the result. Nevertheless, considering the results other thermal switches, analytical results can be considered as a good approximation. OFF conductance mode verification will be performed during the instrument level test campaign in vacuum.

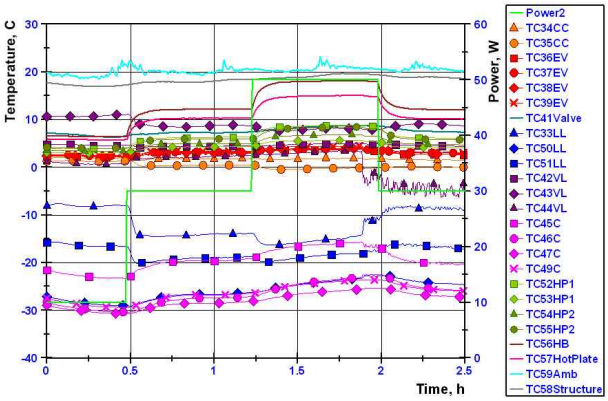


Fig. 13. MXGS LHP 1 performance at -50 ºC.

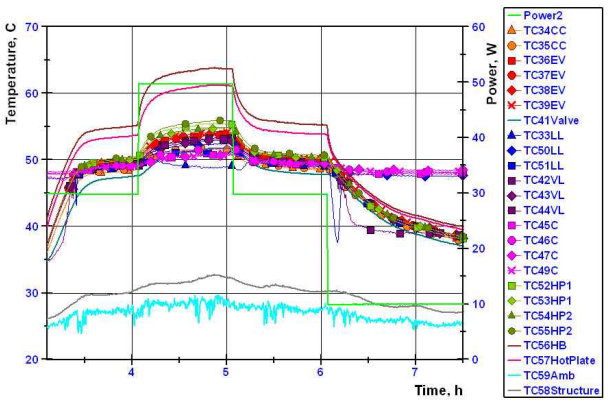


Fig. 14. MXGS LHP 1 performance at +50 ºC.

4. LOW TEMPERATURE VMLHP FOR A LUNAR LANDER

One of the most interesting applications of VMLHPs used as thermal switches is in planetary, satellite or asteroid missions, due to the harsh environment suffered by the equipment in the surface of such celestial bodies. On the Moon surface, night temperatures can be very low and it is necessary to prevent the electronics from overcooling. Specifically for rover and lander missions, passive control techniques are preferable since during the night only batteries power is available.

In this line, the VMLHP concept was selected as a promising option for a Lunar Lander. All electrical units of the Lander which have to survive the complete mission are embarked in a compartment called Central Thermal Box. All units inside the Central Thermal Box are cooled by LHPs coupled to the units' base-plates and to dedicated radiators. For redundancy and for heat transfer capability reasons, there are several LHPs needed to keep the Central

Thermal Box mounted units within their temperature limits. Because of the wide range of environmental conditions for the mission, these LHPs need the thermal switching function to decouple the radiators from the dissipating units during cold phases and in such way saving heater power.

A thermal control system breadboard based on the VMLHP concept was defined and proposed. The heat transport function was conducted by two LHPs connected to each radiator for redundancy purposes. The system included four radiators facing different environmental conditions. Propylene was selected as the working because of the very low temperatures involved in the mission. The main features of the LHPs are summarized in Table 3 and an overview of one of them is shown in Fig. 15.

Table 3. Lunar Lander VMLHPs main features.

EV	$OD_{LHP1\&2}$ = 12 mm; $OD_{LHP3\&4}$ = 15 mm; L = 130 mm
EV Saddle	W x L = 50 x 115 mm^2
CC	OD = 21 mm; L = m
CN line	$OD_{LHP1\&2}$ = 2 mm; $L_{LHP1\&2}$ = 2.0 m $OD_{LHP3\&4}$ = 4 mm; $L_{LHP3\&4}$ = 4.0 m
VL	$OD_{LHP1\&2}$ = 3 mm; $L_{LHP1\&2}$ = 1.0 m $OD_{LHP3\&4}$ = 4 mm; $L_{LHP3\&4}$ = 1.3 m
LL	$OD_{LHP1\&2}$ = 2 mm; $L_{LHP1\&2}$ = 0.7 m $OD_{LHP3\&4}$ = 3 mm; $L_{LHP3\&4}$ = 1.5 m
PRV	OD = 17 mm; L = 60 mm

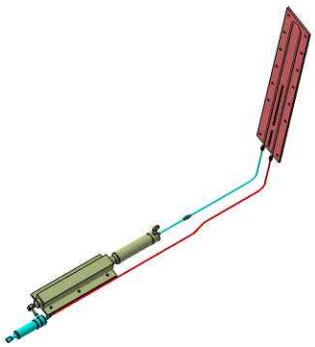


Fig. 15. Lunar Lander VMLHP overview.

Table 4. Lunar Lander Radiators main features and requirements.

RAD	Set point (ºC)	T_{CN} (ºC)	T_{EV} (ºC)	Power (W)	CN I/F area (mm^2)
1	25	-160 to 35°C	10 to 35°C	0 to 5	400 x 400
2	30	-160 to 50°C	-10 to 65°C	10 to 25	200 x 200
3	30	-160 to 35°C	-20 to 55°C	20 to 100	860 x 860
4	30	-160 to 50°C	-20 to 55°C	60 to 120	500 x 500

The main features and requirements corresponding to each radiator are shown in Table 4. A thermal analysis for the complete system was performed using EcosimPro for the four radiators. The LHP thermal conductance was calculated as:

$$C_{LuL_LHP} = \frac{Q}{T_{EV_ave} - T_{CN_ave}} \quad (3)$$

As a representative case, the analytical results of the LHPs attached to Radiator 1 are shown in Table 5. The LHP operates in regulation mode. The evaporator temperature is closer to the set point of 25ºC in Lunar Orbit Hot 1 and Lunar Eclipse cases. As for the thermal conductance, the maximum value is obtained for the Low Lunar Orbit Hot 2 case of the Radiator 4, with more than 13 W/K.

Table 5. TMM results for Lunar Lander VMLHP connected to Radiator 1.

Case	Q (W)	T_{RAD} (ºC)	T_{EV} (ºC)	C_{LuL_LHP} (W/K)
Low Lunar Orbit Hot 1	5	-30	25.3	0.09
Low Lunar Orbit Hot 2	5	35	37.0	2.61
Low Lunar Orbit Lunar Eclipse	5	-80	25.3	0.05
Lunar Surface Day	5	20	25.5	0.93

Even if the breadboard was not manufactured and experimental results of the LHPs operation are not available, the analyses verified the ability of the proposed VMLHPs to control the equipment temperature even during the extreme cold night conditions and, once again, the advantages of VMLHPs for lander applications, as efficient, passive thermal switches.

5. LOW TEMPERATURE VMLHP FOR EXOMARS 2018 ROVER MODULE

In a similar way as for the Lunar Lander, the design of the ExoMars 2018 Rover Module (RM) required the application of innovating thermal control technologies to sustain the extreme temperatures of the Mars surface. The use of VMLHPs concept is the cornerstone of the RM thermal control system, being used for heat transport during peaks of dissipations and as thermal switches to insulate the Rover internal payloads during the cold Martian night. Two LHPs are dedicated to the control of the RM Service Module (SVM) and two LHPs to control the Analytical Laboratory Drawer (ALD). Propylene was selected as the working fluid to prevent freezing at the coldest conditions, without

the need of active heater thermal control. The set points were defined as 0 ± 1.5 ºC for the SVM and -40 ± 1.5 ºC for ALD, being the latter a challenging condition due to the extreme low operating temperature, linked to very low argon pressures in the PRV argon reservoir.

The ExoMars 2018 RM LHPs project involves the complete design of the LHPs, the manufacturing of an ALD STM, SVM and ALD Qualification Models (QMs) and the corresponding ALD and SVM FMs. Currently, the full qualification of SVM and ALD LHPs is almost completed and the most relevant analysis and test results show outstanding performance, compatible with the stringent ExoMars 2018 mission requirements.

5.1 RM LHPs description

Each VMLHP consists of an evaporator, a compensation chamber, a PRV, vapor and liquid lines and a condenser. The condenser line is embedded into aluminum, white-coated radiator panel. All four evaporators are identical, as well as all compensation chambers. Design of each evaporator's saddle has slight variations from one to another LHP, keeping the same footprint. The main features of the LHPs are summarized in Table 6.

Table 6. ExoMars 2018 RM VMLHPs main features.

EV	OD = 12 mm; L = 130 mm
EV Saddle	W x L = 46 x 115 mm^2
CC	OD = 22 mm; L = 80 mm
CN line	$OD_{LHP1\&2}$ = 2 mm; L_{ALD_LOW} = 1.2 m; L_{ALD_UP} = 2.2 m; L_{SVM} = 0.8 m
CN saddle (RAD)	$(W \times L)_{ALD_LOW}$ = 245 x 525 mm^2 $(W \times L)_{ALD_UP}$ = 475 x 525 mm^2 $(W \times L)_{SVM}$ = 160 x 400 mm^2
VL	$OD_{LHP1\&2}$ = 3 mm; L_{ALD_LOW} = 1.8 m; L_{ALD_UP} = 0.9 m; L_{SVM} = 1.4 m
LL	$OD_{LHP1\&2}$ = 2 mm; L_{ALD_LOW} = 1.3 m; L_{ALD_UP} = 0.5 m; L_{SVM} = 1.2 m
PRV	OD = 17 mm; L = 60 mm

5.2 RM LHPs thermal analysis

In the design stage of the RM LHPs a complete thermal analysis was performed with EcosimPro and ESATAN-TMS. Due to the complexity of the models, the schematics are not presented in the paper. The model was used to predict the LHPs performance during launch & Entry, Descend and Landing, cruise and on Mars phases. Both steady states and transient regimes were analysed. According to the model, the conductance values shown in Table 7 were achieved by the LHPs, depending on the operational mode. In Fig. 16 an example of a transient on Mars is presented. In this case the ALD upper panel LHP is working in regulation mode, achieving a maximum thermal conductance of 12 W/K and a minimum thermal conductance of 4 W/K. The LHP thermal conductance was calculated as:

$$C_{RM_LHP} = \frac{Q}{T_{EV_ave} - T_{CN_out}} \quad (4)$$

Table 7. RM VMLHPs analytical thermal conductance values.

LHP	ON mode (50 W on the evaporator)	OFF mode
ALD LOW LHP	10 W/K	< 0.001 W/K
ALD UP LHP	12 W/K	
SVM LHP	7 W/K	

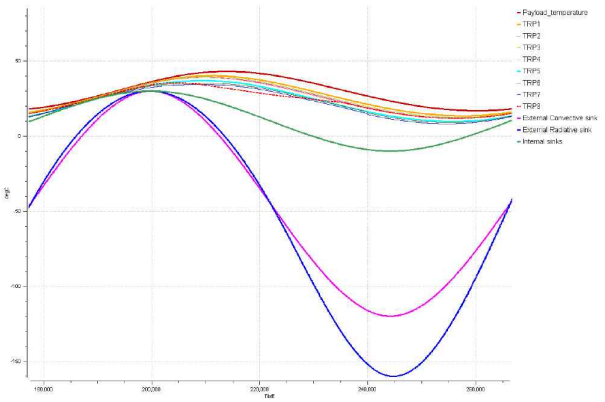


Fig. 16. ALD upper panel LHP transient case representing 1 sol on Mars. Heat load is constant (25W).

5.3 RM LHPs test campaign

The RM LHPs test campaign is conceived, including acceptance for STMs and FMs and qualification campaign for the QMs, aimed to assess the LHPs thermal performances in hot and cold conditions in terms of heat transport, and to demonstrate reliable start-up and shut down. The qualification campaign follows ESA standard ECSS-E-ST-31-02C, whose thermal tests include:

- Performance test at different power levels, in three different orientations, corresponding to transport, launch and on-Mars operation;
- Three start-up tests, each one representative of a flight scenario;
- Shut down test, to assess if fluid circulation can be stopped using the CC heater, occurrence of dry-out and its recovery.
- Maximum power tests, plus recovery after dry-out
- Thermal cycling, to prove that LHPs withstand the Martian wide range of temperatures (-120 °C to +55°C) without any degradation.

Start-up, performance and maximum power in the

orientation corresponding to on-Mars operation are verified both in climatic chamber and in vacuum. Dedicated testing jigs are used to support the LHPs during the campaign. The jigs include aluminum blocks with embedded cartridge heaters to be attached to each evaporator to simulate the SVM and ALD equipment thermal inertia. ChoTherm interfiller is used between each evaporator and aluminum block. To minimize the heat leaks to the environment, the LHPs are insulated with Armaflex during tests in climatic chamber and with single and multi-layer insulation during the tests in vacuum. T-type thermocouples are used for temperature monitoring. The measurement points are set on the evaporators, the valves, the condenser and the transport lines, to obtain a full picture of the temperature evolution along the loop. As an example, a detail of the measurement plan for ALD upper panel LHP is depicted in Fig. 17. An overview of the ALD LHPs test set-up is shown in Fig. 18.

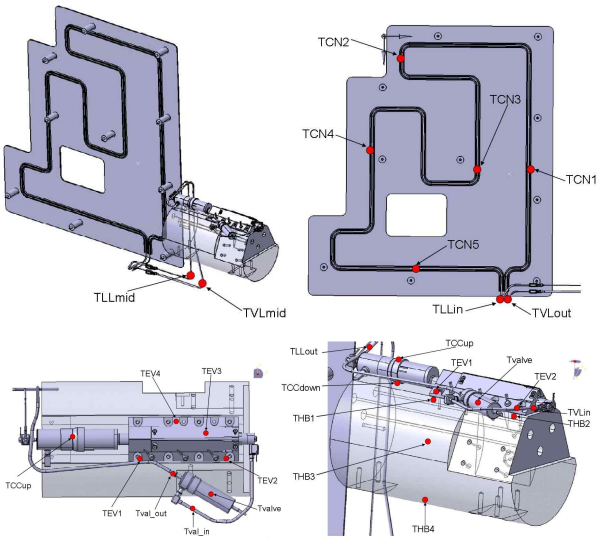


Fig. 17. ALD upper panel LHP measurement plan.

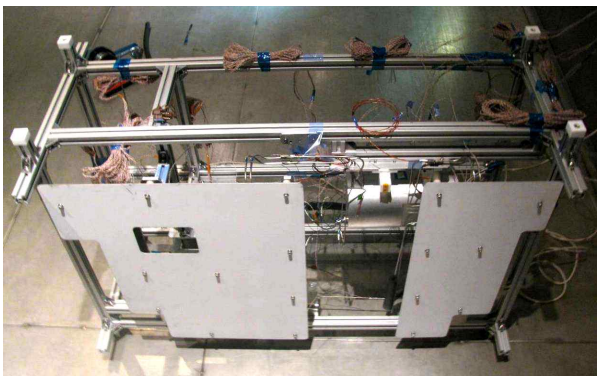


Fig. 18. ALD LHPs thermal test set-up overview.

Even if the overall test campaign is very extensive, the objective of this paper is to present the RM LHPs as the application of the VMLHP concept as a thermal switch. Therefore, the most representative tests of the switch function are shown hereafter.

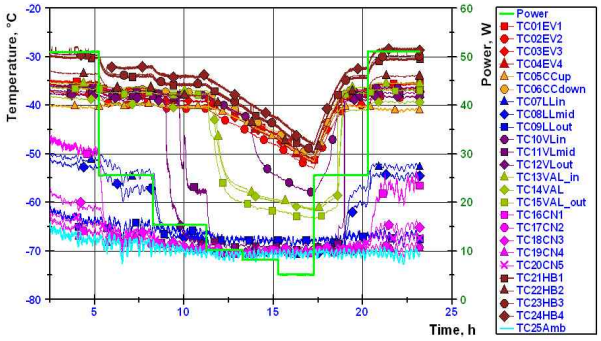


Fig. 19. ALD STM upper panel LHP cold performance test.

In Fig. 19 an example of a cold performance test is shown. This test is characteristic of the LHPs operation on Mars. At night, the environment temperature drops up to -120ºC, while the equipment shall be maintained at higher temperatures. The ALD and SVM valves set points are set at -40 ºC and 0 ºC respectively, on that purpose. This case corresponds to the ALD STM upper panel LHP cold performance in climatic chamber. It can be seen that the sink temperature is kept at -70 ºC. Thanks to the valve operation, the LHP evaporators are kept above -40 ºC independently of the injected power level, when the LHP is operating in variable conductance regime. For the lowest power levels, power ≤ 10 W, the LHP stops working due to the high heat leaks to the environment. In this case, the LHP conductance drops to values < 0.001 W/K, verified by analytical calculations.

In Fig. 20, a hot operational case corresponding to the same LHP is presented. The test is representative of the LHPs at the highest power rejection requirement. In such conditions, the power injected to the evaporators is maximum (50W) and the temperature reached by the evaporators is at the highest operating limit. Due to the restrictions implied by the PRV set point, the ALD maximum operating temperature is +57 ºC (±2 ºC), while the SVM can increase up to +65 ºC (±2 ºC), considering qualification margins. The presented test corresponds to the ALD STM upper panel LHP in climatic chamber. It can be seen that the sink temperature is kept at 45 ºC, after adjustment of the evaporator temperature at 55 ºC with 50W. The thermal conductance in this case reached 17.5 W/K (the PRV is totally open and the LHP is working in constant conductance regime). This value is even higher than the predicted one by TMM, as happens in general for all LHPs. Oscillations originated by the climatic chamber temperature control can be observed as variations of the ambient temperature in the graph. Even with such oscillations of the environmental conditions, the LHP operated stably.

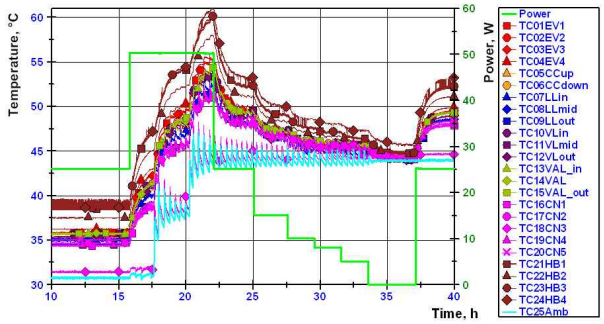


Fig. 20. ALD STM upper panel LHP hot performance test.

The last test, presented in Fig. 21, corresponds to a start-up case in cold conditions. The objective of the test is to verify the LHP start-up when the evaporator temperature rises above the set-point, starting from cold conditions, corresponding to the Martian night. The test starts with the environment 10 ºC below the set point of the LHP's valve. The initial conditions for the test include a non-working LHP, with the evaporator temperature below the corresponding PRV set point (OFF mode). Then, the cartridge heaters on the aluminium blocks are activated and heat is supplied from them, simulating the RM equipment heat dissipation.

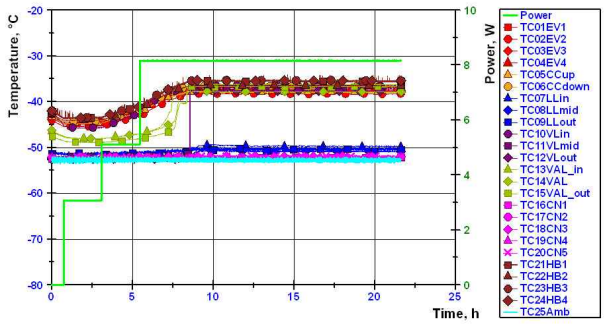


Fig. 21. ALD STM upper panel LHP start-up test in cold conditions (representative of start-up on Mars, from night).

The graph in Fig. 21 shows the start-up 1 of ALD STM upper panel LHP. In this case, the start-up is achieved around time = 8h, as indicated by the increase of the vapour line temperature increase until being close to the evaporator temperature. A power level of 3W, net to the evaporator, was needed by this LHP to start. The leaks to the environment are estimated in 5W. Thus, the total power injected by the cartridge heaters was 8W. Start-up is achieved smoothly, without overshoot, what is typically observed in LHPs starting from closed-PRV conditions.

7. VMLHP SUMMARY

In summary, VMLHPs have been identified as an efficient solution for the thermal control system of different missions. In Table 7 a summary of the achieved thermal performance for each of the studied switches is presented.

Table 7. VMLHPs performance features summary.

Mission	UPMSat-2	Exomars 2018 RM		Lunar Lander	ISS
No. of LHPs	1	4		4 (x2)	2
VMLHP model(s)	MHS FM	2 ALD	2 SVM	Breadboard	ASIM-MXGS
Working fluid	NH_3	C_3H_6			
Mass, g	146	1600	1100	450	700
OT Range, °C	-70 to +110	-120 to +55		-160 to +65	-50 to +50
Tset range, °C	-20 to +80	-40 to +80			
T set, °C	+20±1.5	-40 ± 1	0 ± 1	+25 ± 1 +30 ± 1	+2.5 ± 1.5
ON , W/K	>3.5	>15	>8	>12	>6
OFF , W/K	0.006	< 0.01		< 0.01	< 0.01
ON/OFF Ratio	>580	> 1500	>800	> 1200	>600
Power Range, W	0.7 to 70	3 to 50		5 to 120	10 to 50

8. CONCLUSIONS

This paper is focused on the presentation of the VMLHP as a thermal solution for applications where the equipment faces extremely harsh environments and no active thermal control is available to maintain its temperatures within safe limits. Thermal analysis and test results of thermal switches developed for different space missions are presented. The studied missions include low temperature, propylene-based VMLHPs (Lunar Lander, ASIM-MXGS and ExoMars 2018 Rover Module) and medium temperature, ammonia-based VMLHPs (MHS to be launched onboard satellite UPMSat2). Each thermal switch has different set points, according to the equipment requirements. For the propylene VMLHPs they are set as +25 ± 1 ºC and 30 ± 1 ºC for the Lunar Lander LHPs, 2.5 ± 1.5 ºC for the MXGS LHPs , 0 ± 1.5 ºC for the Exomars 2018 RM SVM and -40 ± 1.5 ºC for the RM ALD. As far as the ammonia VMLHP is concerned, its set point is defined at +20 ± 1.5 ºC.

The analyses and experimental data present the following advantages of the system:

- Very high ON/OFF thermal conductance ratio values, in the range 1000:1, a ratio impossible to reach for alternative heat switch technologies.
- Efficient temperature control function ~± 1°C
- High flexibility in set point (-40 ºC to 80 ºC)
- Wide power operational range (from ~0.1 W to kilo Watts),
- Fully passive operation
- Mass and volume minimization
- Scalability and design flexibility
- Easy integration
- Functional gravity field independence
- Very small response time (seconds)
- Lifetime is same as to standard LHPs and compatible with most space missions (> 15 years)

The obtained results confirm that the VMPLHP concept is an efficient thermal solution for different kind of missions. Miniaturized VMLHPs would be beneficial for small orbiting spacecrafts where the thermal mass is low and a relative long eclipse period could drive the heater power. Other possible applications are linked to the thermal control of spacecraft electronic boxes, power electronic components, batteries and high dissipative chips on PCB. Low temperature VMLHP such as the ones developed for the Lunar Lander or Exomars 2018 RM are good candidate for planetary, satellite and asteroid missions, where extreme low temperatures are experience and the power budget during night periods is very limited. In general, VMLHP technology maturity is proven and it is ready to be adapted to a wide range of mission requirements.

Further stages on VMLHP will include a deeper analysis on the technology limits, for instance in terms of maximum power in the regulation mode (linked to the primary and secondary wick I/F). In addition, detailed analysis of the flight data, which will be available very soon, will be the object of foreseen publications on the subject.

ACKNOWLEDGEMENT

All the work presented in this paper was conducted by IberEspacio personnel, which is gratefully acknowledged.

NOMENCLATURE

A : Area (mm^2; cm^2)
ALD : Analytical Laboratory Drawer
ASIM : Atmospheric Space Interaction Monitor
ave : Average
C : Thermal conductance (W/K)
CC : Compensation Chamber
CN : Condenser
EV : Evaporator
FM : Flight Model
h : thickness (mm)
ID : Inner Diameter (mm)
L : Length (m; mm)
LHP : Loop Heat Pipe
LL : Liquid Line
LuL : Lunar Lander
MHS : Micro Heat Switch
MXGS : Monitor X-ray and Gamma-ray Sensor
OD : Outer Diameter (mm)
out : Outlet
PRV : Pressure Regulating Valve
QM : Qualification Model
STM : Structural Thermal Model
RAD : Radiator
RM : Rover Module
STM : Structural Thermal Model
SVM : Service Module
T : Temperature (K)
TMM : Thermo Mathematical Model
VMLHP: Vapor Modulated Loop Heat Pipe
VL : Vapor Line
W : Width (mm)

REFERENCES

[1] Torres, A., Mishkinis D., Kulakov, A. Romera, F., Gregori, C. and Kaya, T., Thermal Control of Loop Heat Pipe with Pressure Regulating Valve, *Heat Pipe Science and Technology, An International Journal*, vol. 3, 2-4 (2012) 263-280.

[2] Torres, A., Mishkinis D., Romera, F., Corrochano, J. and Kaya, T., Set-point active control of Vapor Modulated Loop Heat Pipe, *Heat Pipe Science and Technology, An International Journal,* vol. 3 (2012) 263–280.

[3] Torres, A., Mishkinis D. and Kaya, T., Mathematical modeling of a new satellite thermal architecture system connecting the east and west radiator panels and flight performance prediction, *Applied Thermal Engineering*, vol. 65 (2014) 623-632.

[4] Torres, A., Mishkinis D. and Kaya, T., Mathematical model validation of a thermal architecture system connecting east/west radiators by flight data, *Applied Thermal Engineering,* vol. 66 (2014) 1-14.

[5] Kaya, T., Pérez, R., Gregori, C. and Torres, A., Numerical simulation of transient operation of loop heat pipes, *Applied Thermal Engineering*, vol. 28, Issues 8–9 (2008) 967-974.

[6] Gilmore, D. G. Chap. 10 *Spacecraft Thermal Control Handbook*, 2nd ed., The Aerospace Press, E1 Segundo, California (2002).

[7] Mishkinis D., Radkov, G., Corrochano, J. and

Torres, A., Miniature Vapor Modulated LHP Heat switch-Temperature Controller, *Proc. of the 2013 Spacecraft Thermal Control Workshop,* The Aerospace Corporation, El Segundo, California, USA (2013).

[8] Mishkinis, D., Corrochano, J. and Torres, A. Development of Miniature Heat Switch-Temperature Controller based on variable conductance LHP, *Proc. of Second International Conference, Heat Pipes for Space Application (2HPSA),* Moscow, Russia (2014).

Cryogenic Loop Heat Pipe Characteristics Analysis Coupling Satellite Infrared Detector and Cryogenic Radiator

Hyokjin Cho[1*], Lingxue Jin[2], Guee-Won Moon[1] and Sangkwon Jeong[2]

[1]*Space Test Division, Korea Aerospace Research Institute, Daejeon 34133, Korea*
[2]*Department of Mechanical Engineering, Korea Advanced Institute of Science and Technology, Daejeon 34141, Korea*

Abstract

A cryogenic loop heat pipe (CLHP) provides an efficient thermal conductive link between a satellite's infrared (IR) detector dissipating heat in cryogenic temperature and a cryogenic radiator facing extremely cold space. The characteristics of the nitrogen-charged CLHP model coupling the IR detector and the cryogenic radiator were analyzed using the thermal/flow analysis software, SINDA/FLUINT. Parametric studies were carried out to investigate the influence of each parameter on the CLHP circuit performance. The parameters include cryogenic radiator size, IR-detector heat load, and initial circuit pressure associated with fluid inventory. Based on the analysis results, the radiator size of 2.25 m^2 (1.5 m by 1.5 m) with the initial nitrogen-charging pressure of 2.5 MPa was proposed to dissipate 5 W heat from the IR-detector with maintaining the IR-detector temperature under 100 K. In comparison with a dimensionally equivalent copper rod circuit, the designed CLHP circuit achieved 50 times higher thermal conductance.

Keywords: Cryogenic loop heat pipe, Infrared detector, Cryogenic radiator, Satellite, Space

1. INTRODUCTION

Infrared (IR) detectors and sensitive magnetic sensors onboard satellites require being cooled down to cryogenic temperature commonly below 100 K. In order to sense radiation with a certain wavelength, incoming quantum energy (hc/λ) should be larger than inherent thermal phonon energy (kT) of detectors. In case of a HgCdTe detector, the detector shall be cooled down to 100 K to have a maximum detectable wavelength of 15 μm [1]. Therefore, many of satellites' IR-detectors are connected to a cryogenic radiator dissipating a heat into extremely cold space. However, a cryogenic radiator cannot be mounted on a detector directly due to spatial constraints inside a confined satellite volume. To solve this problem, a flexible conductive link is required between a cryogenic radiator and an IR detector with high heat transport capacity in cryogenic temperature.

A cryogenic loop heat pipe (CLHP) was proposed for these purposes. A CLHP has a secondary evaporator, a secondary compensation chamber (CC), a vapor flush line, and a hot gas reservoir in addition to the components of a room-temperature loop heat pipe (LHP). In comparison with a room-temperature LHPs, CLHPs have a relatively lower efficiency in performance because CLHPs use cryogenic fluids such as liquid nitrogen, oxygen, and methane that have lower surface tension, lower thermal conductivity, lower latent heat, and higher liquid viscosity than room-temperature fluids such as ammonia and water. Nevertheless, the CLHP is the most distinguished heat transport device in cryogenic temperature in that it utilizes the latent heat of a working fluid during phase changes and the capillary forces by the evaporator wick for the working fluid circulation without moving parts.

In the previous studies, B. F. Armaly verified that the CLHP using a nitrogen as working fluid has 10 times higher effective thermal conductivity than that of the equivalent copper rod in cryogenic temperature [1]. D. Khruslatev developed the oxygen CLHP to have 9 W heat transport at 75 K [2], and Ya'nan Zhao tested nitrogen CLHP to have 41 W heat transport at around 90 K [3]. The effect of the CLHP fluid inventory was investigated by Tao Yan et al. that the maximum heat transport capacity could be obtained with optimal fluid inventory [4]. Ya-nan Zhao et al. experimented the influence of the secondary evaporator on the CLHP performance, and verified that the CLHP should have minimum applied heat on the secondary evaporator for CLHP operation [5]. Ph. Gully et al. validated a CLHP prototype that has 19 W heat transport with 5 K difference over 0.5 m distance. The roles of cold reservoir shunted to the condenser with heaters were verified for optimal CLHP operation [6]. L. Bai et al. evaluated the thermal performances of the nitrogen-charged CLHP with various combinations of primary-evaporator heat loads and secondary-evaporator heat load [7].

This paper aims to perform parametric studies on the CLHP connecting the heat-dissipating IR-detector and the cryogenic radiator facing extremely cold space. The analyses are done by using the commercial thermal/flow analysis software, SINDA/FLUINT. First, the CLHP

*Corresponding author: wittycho@kari.re.kr, Phone: +82-42-860-2198, Fax: +82-42-860-2234

characteristics is depicted, and the CLHP operation process is described. The analytical model and the steady-state parametric-study results are summarized in the following sections. Based on the analysis results, the design for the optimal CLHP circuit is proposed and its performance is compared with that of the copper circuit at the conclusion.

2. CLHP OPERATION

Inherently, a CLHP requires ancillary components being different from a room-temperature LHP. The CLHP contains a secondary evaporator and a secondary CC for initial supercritical start-up by sending liquid nitrogen into the primary wick. It also functions the removal of undesirable heat ingress into the liquid line from the environment and heat by the back conduction into the primary CC during the operation. In addition, it needs a hot gas reservoir to moderate the entire circuit pressure down to an endurable level at a room temperature before operation.

The operation starts from the condenser-chilling by the cryogenic radiator facing cold space. The nitrogen in the condenser and the secondary CC experiences a phase change (liquefaction) and the circuit pressure decreases accordingly with a saturation temperature descent. In order to start the CLHP, the primary wick shall be wet before imposing the heat load on the primary evaporator from the IR detector. For the purpose of pushing the liquid in the condenser into the primary evaporator wick, the secondary evaporator is heated in proper amount by the patch heater on the secondary evaporator. The liquid nitrogen fills the primary evaporator wick, and then the capillary forces are realized by the evaporation at the wick menisci by the heat into the primary evaporator from the IR detector.

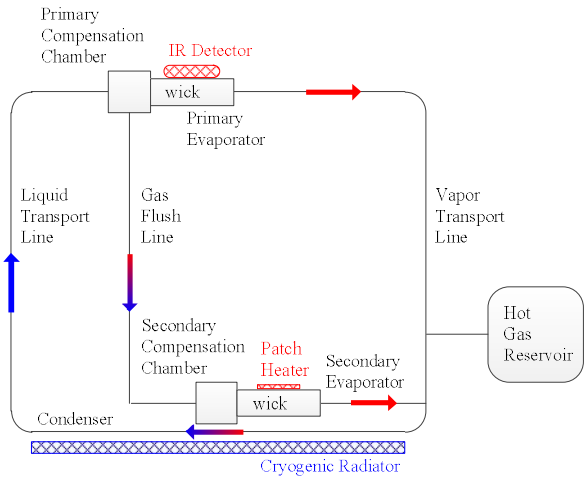


Fig. 1. CLHP configuration with the IR detector and the cryogenic radiator

The heat into the secondary evaporator is then optimally reduced but not a zero value to remove the vapor in the primary CC by the parasitic heat along the liquid line and the back-conduction from the evaporator to the primary CC.

3. ANALYTICAL MODEL

The analytical model specifications of the CLHP circuit are summarized in Table 1. Nitrogen is chosen as a working fluid to operate the CLHP in the target temperature lower than 100 K. The IR detector is modeled as a node to have 4,000 J/K thermal mass, and the heat dissipation of the IR detector is realized by imposing the heat on this node. The heat into the secondary evaporator is given directly by the patch heater and the value is fixed as 0.5 W. Appropriate thermal contact resistances are applied between the IR detector and the evaporator, the secondary CC and the condenser, and the condenser and the cryogenic radiator.

The materials of the primary and secondary evaporators, CCs, vapor transport line, liquid transport line, and condenser are set as stainless steel ANSI-304. The primary and secondary evaporators are both 15 mm in diameter and 30 mm long with 1 mm thickness. The diameter of the CCs is 22.5 mm and the length is 15 mm with 1 mm thickness. The CCs are thermally connected with the evaporators. The vapor, liquid transport lines and vapor flush line are all 600 mm long with 1 mm inner diameter and 1 mm thickness. The condenser is 450 mm long tube with 1 mm inner diameter and 0.5 mm thickness.

The primary and secondary wick properties are set identical to have same capillary forces in the same conditions. The exhaust gas transport line from the secondary evaporator is connected to the condenser entrance to push the liquid nitrogen inside the condenser. Hot gas reservoir has 500 ml volume and the line is coupled with the gas transport line.

Table 1. Analytical model specifications

Working fluid	Nitrogen
IR detector thermal mass	4,000 J/K
Secondary evaporator heat load	0.5 W
CLHP materials	Stainless Steel ANSI-304
Wick meniscus radius	1 μm
Wick porosity	55 %
Wick permeability	5×10^{-14} m^2
Primary/Secondary evaporator	Ø 15 mm × 30 mm
Primary/Secondary CC	Ø 22.5 mm × 15 mm
Condenser	Ø 1 mm × 450 mm
Vapor line	Ø 1 mm × 600 mm
Liquid line	Ø 1 mm × 600 mm
Hot gas reservoir	500 ml

Table 2. Variable parameters

PARAMETERS	RANGES
Cryogenic radiator area	1 m^2 – 25 m^2
IR-detector heat load	0 W – 10 W
Initial circuit pressure (fluid inventory)	1.0 MPa – 3.2 MPa

The cryogenic radiator connected with the condenser is assumed to face extremely cold space (2.73 K). The radiator is modeled as a 2-mm-thick aluminum-2024 T6 sheet, and the one side of the outer surfaces of the radiator is covered with optical solar reflectors that have the IR emissivity of 0.83. The other parts of the circuit are surrounded with the internal surfaces of the satellite which temperatures are 283 K.

The lines are wrapped with multi-layer insulation (MLI) that has effective IR-emissivity of 0.02. Monte-Carlo method is applied for the radiative heat transfer analysis in the software.

Cryogenic radiator area, IR-detector heat load, and circuit pressure convertible to fluid inventory are taken as variable parameters in the analytical studies (Table 2). Steady-state solutions were individually obtained by variation of these major parameters.

4. RESULTS

A series of analyses were carried out with various cryogenic radiator areas, IR-detector heat loads, and initial circuit pressures respectively. The obtained steady-state temperatures are presented in Figs. 2 to 4. The major interests are on the temperatures of the IR detector, cryogenic radiator, wick saturation, evaporators, CCs, condenser temperatures.

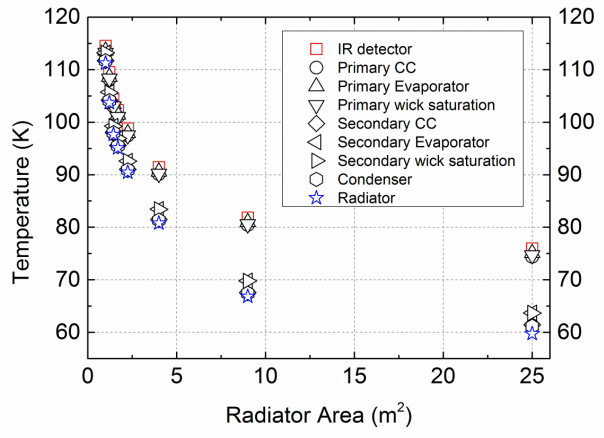


Fig. 2. Steady-state temperatures with the different cryogenic radiator sizes under the IR-detector heat load of 5 W and 1.2 MPa initial circuit pressure

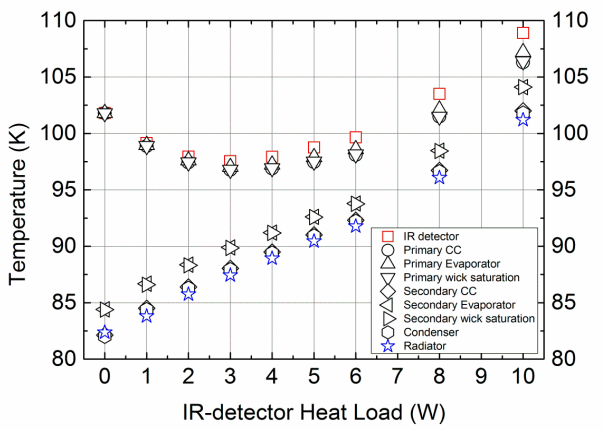


Fig. 3. Steady-state temperatures with different IR-detector heat loads in case of the 2.25 m^2 cryogenic radiator and 1.2 MPa initial circuit pressure

Fig. 2 is the analysis results with cryogenic radiator area variation under the IR-detector heat load of 5 W and 1.2 MPa initial circuit pressure. As the radiator area increases, the IR-detector temperatures decreases as expected. In consideration of the target temperature of maximum 100 K for the IR detector, the area larger than 2.25 m^2 is acceptable for space applications.

The contribution of the radiator size to the IR-detector temperature reduction becomes smaller as the radiator area increases. This trend results from the characteristics of a radiative heat transfer that is linearly proportional to a radiating area, but is inversely proportional to the 4th power of the radiator temperature that decreases.

Fig. 3 shows the steady-state temperatures of the major components with the IR-detector heat load variation from 0 W to 10 W. The IR-detector temperature has a minimum value of about 97.5 K with around 3 W heat load. On this analysis, the cryogenic radiator size of 2.25 m^2 and the initial circuit pressure of 1.2 MPa were applied. As shown in Fig. 3, the minimum amount of IR-detector heat load exists in order to have the minimum IR-detector temperature that is 3 W in this model. The CC is thermally connected with the evaporator and the wick, so the back-conduction heat loss from the wick to the CC is unavoidable. If the IR-detector heat load is not sufficient, then the capillary forces cannot be effectively generated because of the insufficient evaporation at the wick pores.

The fluid inventory can be estimated from the initial circuit pressure through the calculation of the nitrogen mass inside the entire circuit based on the information of the circuit inner-volume and the pressure at a certain temperature. In case of the initial circuit pressure of 1.2 MPa in 293 K, 6.96 g of nitrogen charges the circuit.

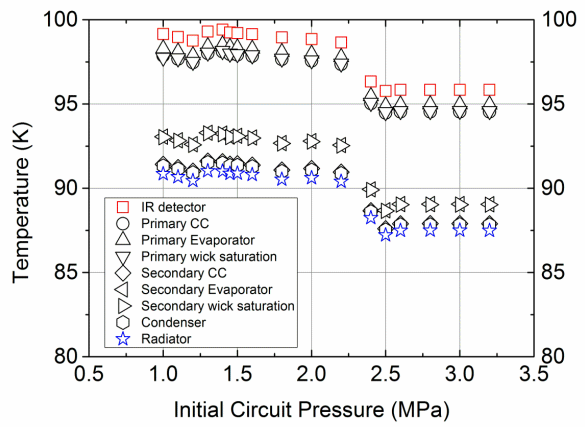


Fig. 4. Steady-state temperatures with different initial circuit pressures in conditions of the 5 W IR-detector heat load and 2.25 m^2 cryogenic radiator

The steady-state temperatures were obtained with various initial circuit pressures (Fig. 4). The insufficient pressure causes a lack of liquid inside the circuit to be evaporated at the wick. Meanwhile, higher pressure than the optimum obstructs CLHP operation by evaporation suppression at the wick pores induced by higher saturation temperature. The minimum IR-detector temperature of 95.8 K could be achievable with 2.5 MPa of the initial circuit pressure equivalent to 14.78 g of nitrogen. However, there was no improvement of the IR-detector temperature cooling capacity in the pressure higher than 2.5 MPa. The thermal and flow calculation was not possible in the pressure higher than 3.5 MPa assumed as an impossible physical condition.

The overall thermal-resistance of the CLHP circuit can be estimated by using Eq. (1). In order to evaluate the heat transport capacity of the circuit, the thermal resistance of the dimensionally equivalent copper rod circuit was obtained by thermal analysis. The comparison results are shown in Table 3.

$$R_{circuit} = \frac{T_{IR} - T_{Rad}}{Q_{IR}} \quad (1)$$

In Eq. (1) $R_{circuit}$ is a thermal resistance of the entire circuit; T_{IR} and T_{Rad} mean the temperatures of an IR-detector and a cryogenic radiator in steady state respectively. Q_{IR} is an IR-detector heat load. In the temperature ranges under 100 K, the thermal resistance of the CLHP circuit was 49.6 times smaller than that of the copper rod circuit.

Table 3. Thermal resistance comparison

CLHP circuit thermal resistance (a)	1.71 K/W
Copper rod circuit thermal resistance (b)	84.82 K/W
Heat transport capacity ratio (b/a)	49.6

5. CONCLUSIONS

The parametric studies were carried out on the proposed CLHP model by using thermal/flow analysis software, SINDA/FLUINT. The radiator size of 2.25 m^2, the IR-detector heat load of 5 W, and the initial circuit pressure of 2.5 MPa (14.78 g of nitrogen) was proposed to achieve the IR-detector temperature of 95.8 K in space. The overall thermal resistance of the designed CLHP circuit is estimated as 1.71 K/W that is 50 times higher thermal conductance than that of dimensionally equivalent copper rod circuit.

ACKNOWLEDGEMENT

This research is supported by a grant from Space Core Technology Development Program of National Research Foundation of Korea (NRF-2013-042033) funded by Ministry of Science, ICT & Future planning (MSIP).

NOMENCLATURE

h : Plank's constant
c : speed of light
λ : wavelength
k : Boltzmann's constant

REFERENCES

[1] B. F. Armaly, Effective thermal conductivity of a nitrogen heat pipe. *Cryogenics*, (1973), 304-306.

[2] D. Khruslatev, Cryogenic Loop Heat Pipes as Flexible Thermal Links for Cryocoolers, *Cryocoolers*, 12 (2003), 709-716.

[3] Ya'nan Zhao, Tao Yan, and Jingtao Liang, Experimental study on a cryogenic loop heat pipe with high heat capacity, *International Journal of Heat and Mass Transfer*, 54 (2011), 3304-3308.

[4] Ya-nan Zhao, Tao Yan, Jian-guo Li, Juan Wang, and Jingtao Liang, Experimental study on the secondary evaporator of a cryogenic loop heat pipe, *Advances in Cryogenic Engineering*, (2014), 20-27

[5] Tao Yan, Ya-nan Zhao, Jingtao Liang, and Fulong Liu, Investigation on optimal working fluid inventory of a cryogenic loop heat pipe, *International Journal of Heat and Mass Transfer*, 66 (2013), 334-337.

[6] Philippe Gully, Qing Mo, Tao Yan, Peter Seyfert, Laurent Guillemet, Pierre Thibault, and Jingtao Liang, Thermal behavior of a cryogenic loop heat pipe for space application, *Cryogenics*, 51 (2011), 420-428.

[7] Lizhan Bai, Guiping Lin, Hongxing Zhang, Jianyin Miao, and Dongsheng Wen, Experimental study of a nitrogen-charged cryogenic loop heat pipe, *Cryogenics*, 52 (2012), 557-563

Designing and Research of Precise Thermal Control System with Loop Heat Pipe

V. Antonov[1], M. Balykin[1], A.Golikov[1], K. Goncharov[1], K. Korzhov[1], V.Buz[2],

[1]*Heat Pipe Center of Lavochkin Association, Khimky 141400, Moscow region, Russia*
[2]*The Odessa National University, Odessa, Ukraine.*

Abstract

Controlled loop heat pipes (LHP) are being successfully used on board spacecrafts (SC) developed by Lavochkin association and other Russian space companies. For example, controlled LHP were integrated into thermal control systems (TCS) of the following SC: Mars-96, Phobos, Electro-L, Spectrum-R, Electro-L2, Yamal-200, ISS module Rassvet and other. LHP is an advantageous and very effective unit for TCS of SC. Up to date, not all performance capabilities of this rather new class of units are investigated and found their application. Application of LHP with high-precision thermal control performance is considered in this paper.

"Spectrum-R" SC that was developed by Lavochkin association was put into prolate elliptical orbit with apogee of 200000 km in July 2011. All SC systems are operating normally. Radio telescope with the TCS of so called "hydrogen frequency standard" developed on base of application of LHP with extra-high accuracy control is mounted on board the "Spectrum-R" SC (fig.1).

Key words: Loop heat pipe (LHP); thermal control system (TCS); pressure regulator (valve); LHP dynamic calculation.

1. INTRODUCTION

The scientific program was named as "Radio-Astron". Large radio telescope with aperture of more than 10 m (fig. 1) is integrated into the SC. Joint operation of space radio telescope and a system of ground-based radio telescopes makes it possible to build integrated radio telescope with aperture of several hundred thousand kilometers, observe radio wave sources in greatly long-wave spectrum and determine greatly remote sources with high accuracy.



Fig. 1. "Spectrum-R" SC.

Joint operation of a system of radio telescopes observing the same object simultaneously is possible only on condition that observing time marks are synchronized. Caesium and rubidium frequency standards are used to synchronize relativistic time on board usual SC. For "Spectrum-R" SC accuracy of usual time synchronizing systems is insufficient. Special Hydrogen frequency standard was developed for the SC. Application of Hydrogen frequency standard required to increase stabilization accuracy of its temperature conditions for increasing accuracy of the frequency keeping.

2. THERMAL CONTROL SYSTEM DESCRIPTION

Passive TCS designed on the base of controlled LHP application was used for H-maser thermostating. TCS of H-maser includes two hydrogen frequency standards combined into a single thermal module by a system of axial groove heat pipes (AGHP) (fig.2). LHP evaporator is mounted to AGHP condensers. Pressure regulator and bypass line are integrated into LHP design. Radiator with radiating surface of 0.3 m^2 is mounted to the center of the telescope bowl.

When changing ambient conditions on LHP evaporator and condenser, TCS shall assure the temperature of the equipment with accuracy of 0.1^{o}C from the average value of the H-maser temperature. Average temperature of the unit in the time interval of up to 2400 seconds shall not differ for more than 0.003 degrees in comparison with temperature in the adjacent time interval.

Heat generation of one H-maser is from 30 to 70 W when the second device is in cold redundancy mode. Changing of the SC orientation leads to variation of heat flow coming to Radiator. Direction of sun incident flux to radiator can vary from -90 to +30 degrees relative to radiator plane.

*K.Goncharov: heatpipe@laspace.ru,
Phone/Fax: +7- 495-573-63-74

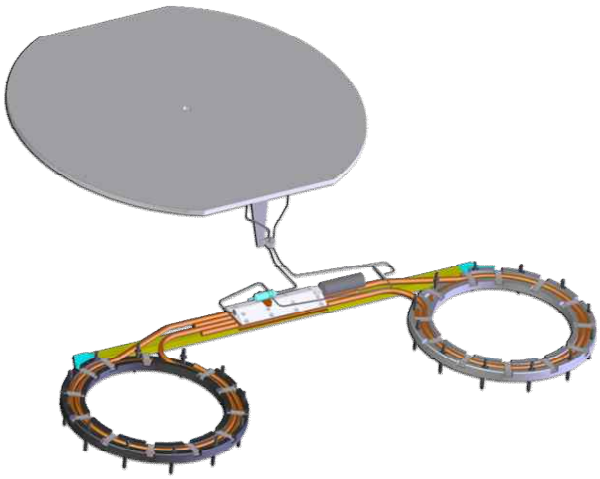


Fig. 2. TCS of H-maser layout

The following design solutions were applied for increasing thermostating accuracy:

1. Additional Aluminum heat storage capacity with the mass of 1 kg was mounted to compensation chamber (CC) of LHP evaporator.
2. Pressure regulator (valve) was mounted as close as possible to thermostaing object – onto evaporator saddle mounted to H-maser.
3. In this design we used the regulator with bellows shortened stroke.
4. Ammonia was used as LHP working fluid due to its high gradient of saturation line (dP/dT) in operation temperature range of H-maser. To prevent Ammonia from freezing when the unit was out of operation, guard heater mounted to radiator was switched on.

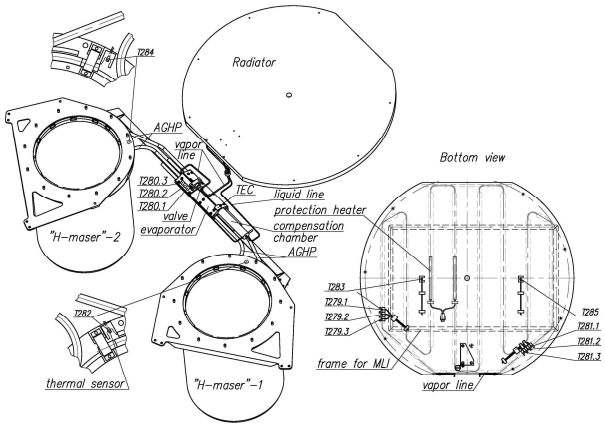


Figure 3. Layout of thermal sensors mounting.

3. LHP MODELLING

LHP dynamic calculation was made in two steps. Calculation of LHP without bypass line and pressure regulator (valve) was made at the first step. At the second step the model was updated: valve operation was taken into account.

Mathematical model developed at the first step is described in the papers [1,2,3,4].

The model includes energy equation for working fluid flow and for wall, momentum conservation equation for working fluid and combined heat and mass balance equation for reservoir (CC) (1)

$$r\left(\frac{dm''_{fR}}{d\tau} - G_4 x_4\right) = k_R(t_1 - t_R) + (\alpha_{ext})_R(t_R - t_{ext})S_R + \\ + (\alpha_{in})_R(t_R - t_4)S_4 - C_R\frac{dt_R}{d\tau} - G_4 c'_4(t_R - t_4) \quad (1)$$

The model is realized in EASY 2.0 program package.

At the first step the following main LHP parameters were determined without taking accounts LHP control: dimensions of evaporator, condenser and transport lines; transferred heat power at different temperatures; thermal resistance of all LHP components.

Dynamic model of LHP with bypass line and pressure regulator (valve) was developed at the second step. LHP layout is presented in the figure 4.

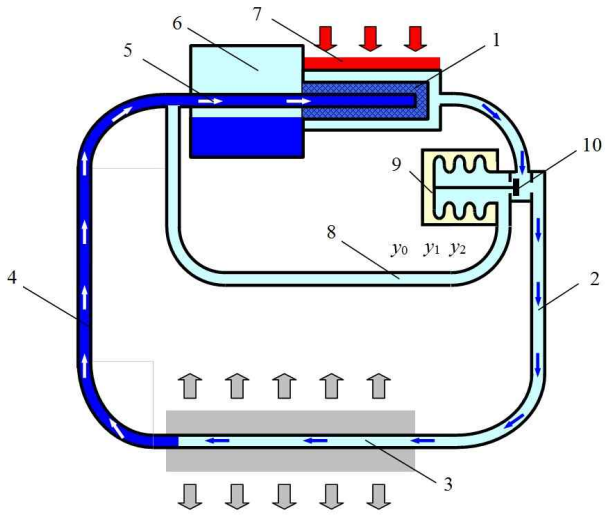


Figure 4. Layout of LHP with Pressure regulator.

1 – capillary wick of evaporator; 2 – vapor line; 3 – condenser; 4 – liquid line; 5 – a part of liquid line located inside CC; 6 – CC (reservoir); 7 – thermostatically controlled object; 8 – bypass line; 9 – bellows; 10 – valve

When model developing the following assumptions were made:

- there is no heat exchange in bypass line,
- hydraulic resistance of bypass line is negligible in comparison with valve hydraulic resistance,
- inertial constituent of vapor flow is negligible.

Flow of working fluid through bypass line G_8 can be determined from the equation

$$p_2 - p_6 = \left(\zeta_{V8} + \xi_8 \frac{l_8}{d_8}\right) \frac{G_8^2}{2\rho'' \omega_8^2} \quad (2)$$

For LHP with bypass line the calculation model will differ from the model developed at the step 1 by the following:

- Flow of working fluid through vapor line and then through condenser and liquid line shall be decreased by the value of G_8
- Pressure losses in vapor line will increased by the value of local losses in the valve and are approximately equal to

$$\Delta p = \zeta_{V2} \frac{G_2^2}{2\rho'' \omega_2^2} \quad (3)$$

In the equation of heat and mass balance for reservoir (CC) (1) it is necessary to take into account additional working fluid influx G_8. Then, the equation can be written in the following way:

$$r\left(\frac{dm''_{fR}}{d\tau} - G_4 x_4 - G_8\right) = k_R(t_1 - t_R) + (\alpha_{ext})_R (t_{ext} - t_R) S_R + \\ + (\alpha_{in})_R (t_4 - t_R) S_4 - C_R \frac{dt_R}{d\tau} - G_4 c'_4 (t_R - t_4) \quad (4)$$

Main difficulty of calculation is determination of hydraulic resistance coefficients ζ_{V2} and ζ_{V8} in the equations (2) and (3). Values of these coefficients change in dependence on the valve location.

Let's consider that coefficient of local losses in the valve is in inverse proportion to the rate of valve opening, i.e.

$$\zeta_8 = \frac{1}{A_1 (y - y_1)^2}, \quad (5)$$

Where A_1 is a numerical coefficient.

Then we will obtain the following equation from the equation (2) we have:

$$G_8 = \sqrt{\frac{(p_2 - p_6) 2\rho'' \omega_8^2}{\frac{1}{A_1 (y - y_1)^2} + \xi_8 \frac{l_8}{d_8}}} \quad (6)$$

Let's assume that coefficient of valve local resistance for vapor line is determined by the equation analogous to the equation (5):

$$\zeta_R = \frac{1}{A_R (y_1 + \delta_y - y)^2} \quad (7)$$

Solving the equations (2-7) together with combined equations described in the model developed at the first step of calculation, we can determine valve location, flow of working fluid through bypass line and all LHP dynamic parameters.

Additionally, operation of LHP with regulator is described by the following parameters:

constants A1 and A2;
bellows stiffness coefficient K;
bellows diameter d;
temperature of valve actuation t_{s1}
maximum valve stroke δy

Let's specify the following values of these parameters:

A1 = A2 =106 ; K = 2000; d = 15 mm; K = 300 °C; δy = 2 mm.

Calculation results allowed to specify and optimize LHP parameters and prove the possibility of meeting set requirements.

Calculation results for these parameters at $q_{r\max}$ = 130 W/m^2 and $q_{r\min}$ = 50 W/m^2 are presented in the figure 5. Results of calculations that were carried out in accordance with the developed model show that maximum deviation of the object thermostating temperature will not exceed 0,1 degree C (see fig. 5)

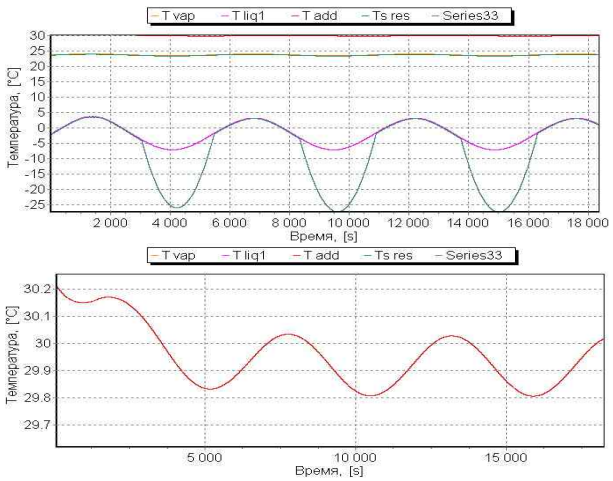


Figure 5. Results of LHP calculation

4. RESULTS OF GROUND TESTS

For carrying out ground tests, special bench was developed for high-accuracy measuring of numerous temperature parameters. Processing of large array of measured data makes it possible to cut off random error.

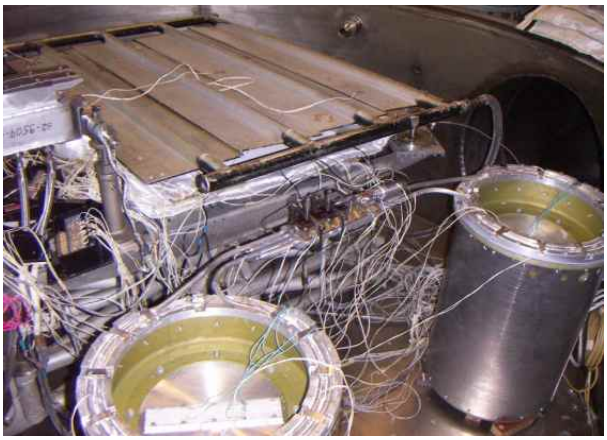


Figure 6. Thermal vacuum tests of H-maser TCS

Thermal vacuum test bench (before MLI mounting) is presented in fig. 6. Nitrogen screen is mounted over LHP radiator.

Predicted accuracy of H-maser control was proved experimentally. Test results obtained by Lavochkin Association when TCS thermal vacuum testing are presented in the pictures.

5. RESULTS OF FLIGHT OPERATION

Telemetric data obtained from "Spectrum-R" SC is presented in Figure 7. Orange line shows stability of operating unit foot temperature when changing environmental conditions (radiator temperature).

Resolution of telemetric system for evaporator and the unit is of 0.4 degrees. Telemetric data shows that accuracy of keeping the object temperature is not worse than resolution of telemetric system.

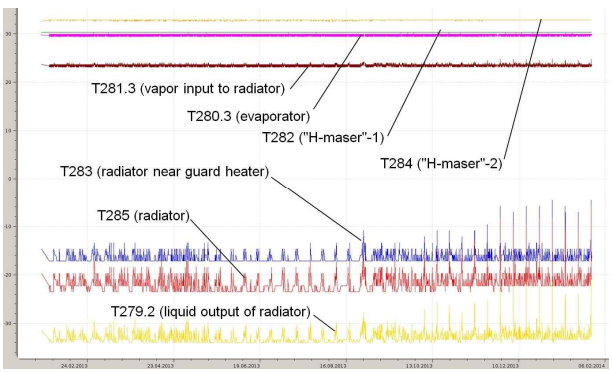


Fig. 7. Telemetric data obtained from "Spectrum-R" SC in the period 2013 – 2014.

Enormous amount of experiments and observations that were carried out for more than five tears of in-orbit SC operation proved quality and stability of H-maser operation which means that the system fulfils the requirements specified for stabilization of unit temperature.

6. CONCLUSIONS

LHP dynamic model that allows carrying out the calculation of LHP with pressure regulator and bypass line is developed.

TCS designed on the base of LHP application allows reaching extra-high accuracy of the equipment thermostating.

The TCS assured the temperature of the equipment with accuracy of 0.1°C from the average value. Average temperature of the unit in the time interval of up to 2400 seconds does not differ for more than 0.003 degrees in comparison with the unit temperature in the adjacent time interval.

Despite the fact that measuring accuracy of telemetry system is much worse than expected control accuracy we can conclude that thermostating accuracy meets expectations. It can be confirmed by implicit data – normal operation of H-maser.

REFERENCES

[1] Capillary pumped loop for the systems of thermal regulation of spacecraft, K. Goncharov, Yu. Maidanik, Yu. Fershtater, ICES 4th, October 21-24, 1991, Florence, Italy.

[2] Investigation of Temperature Fluctuations in Loop Heat Pipes", K. Goncharov, E. Kotlyarov, F. Smirnov, R. Schlitt, K. Beckmann, R. Meyer, R. Muller, ICES 24th Friedrichshafen, Germany, June 20-23, 1994.

[3] LHP and CPL mathematical model providing the description of some dynamic processes// Buz V.N., Smirnov H.F., Goncharov, K.A. CPL'98 International Two Phase Workshop. Los Angeles, USA, March 2-4, 1998.

[4] "Modeling of LHP Performances by Means of Specialized EASY Package Program", V. Buz, K. Goncharov, IHPC 12, 2002, Moscow, Russia

[5] Buz. V., Goncharov K. Modeling of LHP Performances by Means of Specialized EASY Package Program. // Heat Pipe Technology Application. Proceedings of the 12th Int. Heat Pipe Conference. Moscow, 2002, p. 182-187.

[6] K. Goncharov, V. Buz U. Hildebrand, O. Romberg, F. Bodendieck, R. Schlitt "Loop Heat Pipe for High-Precision Satellite Thermal Control" IAC-04-1.6.11, Vancouver, Canada, 2004.

[7] Development of Loop Heat Pipe with Pressure Regulator Goncharov K.A., Kochetkov A.Yu., Buz

V.N., International Two Phase Workshop, Los-Angeles March 7-9, 2005.

[8] Goncharov K.A., Kochetkov A.Yu., Buz V.N. Development of loop heat pipe with pressure regulator // Heat Pipe, Heat Pumps, Refrigerators. Proceedings of the VI Minsk Int. Seminar. Belarus, 2005, p. 167-172.

[9] V.N. Buz, Goncharov K.A., Antonov V.A. Modeling of Loop Heat Pipe with Pressure Regulator Dynamic Performance // Proceedings of the Fourth Russian National Conference on Heat Transfer. Ch.5. p 61– 64, Moscow Energy Institute, Moscow, 2006.

[10] K. Goncharov, O. Golovin «Working Fluid Defreesing in Radiator on Base of LHP» ICES 2007, Chicago, USA, 9-12 July 2007.

[11] K. Goncharov, Alexey Kochetkov, Vasili Buz, Reinhard Schlitt, First LHP in European satellite. International Two-Phase Thermal Control Workshop, September 19–21, 2008, Noordwijke, Netherlands.

[12] Goncharov K.A., Kochetkov A.Yu., Charging Fluid freezing Mode in the Loop Heat Pipes // Proceedings of Lavochkin Association #9, p.8. 2010.

[13] Goncharov K.A., Kochetkov A.Yu., Buz V.N., Travov V.Yu. Modeling of vapor generating in capillary structures of Loop Heat Pipe Evaporators. Proceedings of the Fifth Russian National Conference on Heat Transfer. p. 4, Moscow Energy Institute, Moscow, 2010.

[14] Modeling and experimental researches of condensation in LHP Buz V.N., Goncharov K.A., Kochetkov A.Yu., 15th International Heat Pipe Conference (15th IHPC) Clemson, USA, April 25-30, 2010.

[15] Modeling of vapor generating in small-porous capillary structures Buz V.N., Goncharov K.A., 15th International Heat Pipe Conference (15th IHPC) Clemson, USA, April 25-30, 2010.

[16] K. Goncharov, V. Buz. Modeling of condensation processes under the action of surface tension forces in microgravity conditions. VIII Minsk International Seminar “Heat Pipes, Heat Pumps, Refrigerators, Power Sources”, Minsk, Belarus, 12-15 September, 2011.

[17] Patent 130299 2013.07.20 Thermal control system of the spacecraft precision instrument.

A Study of Root-Zone Heating System using Bubble Jet Loop Heat Pipe for Horticulture

Jongsoo Kim[1], Sangjin Park[2], Junha Kim[2], Jaeyoung Bae[2], Eonhwa Hwang[2], Dobin Kim[2], Sungbok Kim[2] and Intaek Oh[2]

[1] *Professor, School of Engineering, Pukyoung National University,*
365 Sinseonro, Namgu, Busan, 608-739 Korea, Phone: +82-51-629-6176, e-mail: jskim@pknu.ac.kr
[2] *Graduate student, Graduate School of Pukyoung National University*

Abstract

We developed the high efficiency root-zone heating system using Bubble Jet Loop Heat Pipe(BJLHP) in order to reduce energy consumption in the greenhouse farm. We make BJLHP of 5m in length and use R-134a as a working fluid, and the charging ratio is 50%vol. Then we measure temperatures of the evaporating and condensing parts of BJLHP, soil, room air and outdoor air respectively. Also, we compare the daily energy consumption rate between the space heating system and the root-zone heating system . As a results of field tests during one month in the winter season, the BJLHP, when properly operated maintains the soil temperature at 19℃ which is the cucumber's proper growth temperature. When we apply the BJLHP root-zone heating system on the farm, the energy consumption has decreased by 17% compared with the space heating system. From the above results, we were able to confirm the energy efficiency of the BJLHP root-zone heating system.

Keywords: Bubble Jet Loop Heat Pipe; Energy Consumption; Horticulture; Root-Zone Heating

1. INTRODUCTION

Currently horticulture farmers in Korea have great difficulty in regards to heating during the winter due to the rise in price of heating fuel costs.

To solve this energy problem and improve the productivity, the development of the root-zone heating system for horticulture using a heat pipe has been studied.[1][2]

Also, by distributing this system to horticulture farmers at a cheap price, the famers can cut production costs, increase competitiveness in the market and improve the quality of agricultural products by root-zone heating.

The purpose of this study is the development of a high efficiency root-zone heating system using Bubble Jet Loop Heat Pipe(BJLHP) and we try to ascertain the applicability of BJLHP at actual horticulture farms through the field test by measuring energy consumption and crop production.

2. EXPERIMENTAL EQUIPMENT AND METHOD

Fig. 1. shows a schematic diagram of the experimental set up. Experimental equipment consists of BJLHP, temperature regulator, integrating electricity meter, data logger and PC for data acquisition. The specification of the BJLHP used in the field is shown in Table 1. We decided that the charging ratio is 50% of inner volume through the previous study.[3]

For the field test of BJLHP, a cucumber farm was rented. The 5 meters long BJLHP was buried in the ground and the surface temperature of the BJLHP was controlled by the temperature regulator. The integrating electricity meter was installed to measure the total power consumption of the BJLHP and an earth leakage circuit breaker was installed at each temperature regulator to prevent a short circuit.

Fig. 2. shows the schematic of the BJLHP used in the field and the temperature measuring point. The BJLHP was buried in the ground at a 20cm point and the welding connection of the heater was covered with a rubber insulation to prevent a short circuit.

In order to confirm the proper operation of the buried BJLHP, T-type thermocouples were attached to the surface of the heat pipe (one point of evaporating part, five points of condensing part).

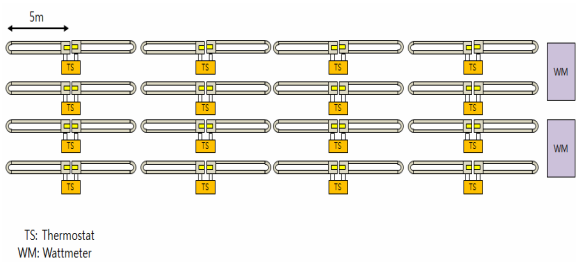


Fig. 1. Schematic diagram of experimental set up

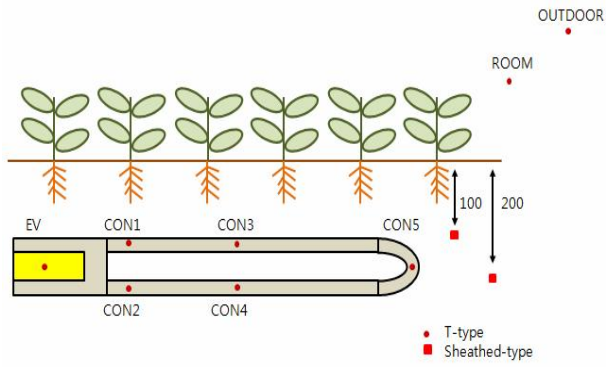


Fig. 2. Temperature measuring point

Table 1. Specification of BJLHP

Parameter		Specification	
Material		Copper	
Working fluid		R-134a	
Charging ratio		50% of inner volume	
Evaporating part	Outer tube	L (mm)	200
		D_O (mm)	28
	Heater	Capacity	220V 100W
		L (mm)	150
		D_O (mm)	22
Condensing part		L (mm)	10,000
		D_O (mm)	12.7
		U band width (mm)	55

To take measurements of the underground soil temperature, sheathed-type thermocouples were buried 10cm, and 20cm in the ground.

As a comparison group, the thermocouples were installed in the same location of soil where the BJLHP was not buried.

Temperature data was recorded using data loggers for 1 month, and the data was recorded from 1:00 pm to 1:00 pm the next day, for 24 hours.

In the case of the complex heating system, an oil heater was added where the BJLHP was installed. The complex heating was performed with minimum usage of the oil heater, within the range that does not interfere with the growth of cucumbers (cucumber injury growing temperature: 5 ℃).[4]

The fuel consumption and yield were recorded daily and these were used to average the data accumulated during one month.

3. EXPERIMENTAL RESULTS

In order to confirm the operating condition of BJLHP and the effect of the outdoor temperature on room temperature, we measured the room temperature, outdoor temperature, surface temperature of the BJLHP and soil temperature.

Fig. 3. shows temperature profiles of outdoor and room during space heating and complex heating.

The outdoor temperature was about -4℃ ~ 9℃ and it was confirmed that the room temperature has changed in accordance with outdoor temperature change. The average room temperature was 13.5℃ and 11.7℃ during space heating and complex heating respectively. Although the average temperature during complex heating was about 2℃ lower than space heating the lowest temperature did not decrease to the temperature that does interfere with growth of cucumbers.

Fig. 4. Shows the surface temperature profiles of the buried BJLHP. The temperature distribution of buried BJLHP was 19℃ ~ 23℃ under the influence of the temperature of the air and soil.

The BJLHP that is buried was operated properly and the temperature difference between the evaporating part and the condensing part was only 0.5℃.

The temperature profiles of soil were shown in Fig. 5. and the temperature of the soil where the BJLHP was buried was maintained appropriately at 19℃, which is moderate to the growth of cucumbers.

On the other hand, the temperature of the soil where the BJLHP was not buried shows a low temperature of 14℃ ~ 16℃ due to the influence of the outdoor temperature and there was a relatively large temperature fluctuation in comparison with the root-zone heating system.

Table 2. shows the comparison of the growth of cucumbers. The yield results were calculated as one day per cucumber tree based on the yield of 1 month.

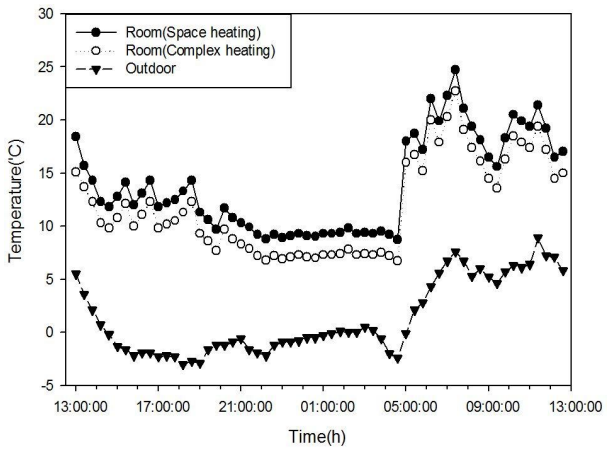


Fig. 3. Temperature profile of room and outdoor

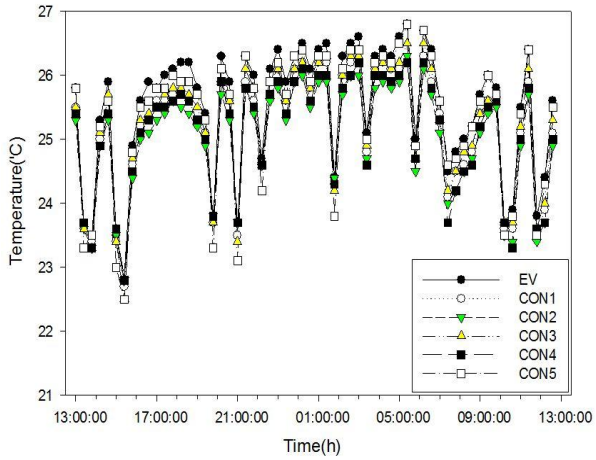


Fig. 4. Temperature profile of BJLHP

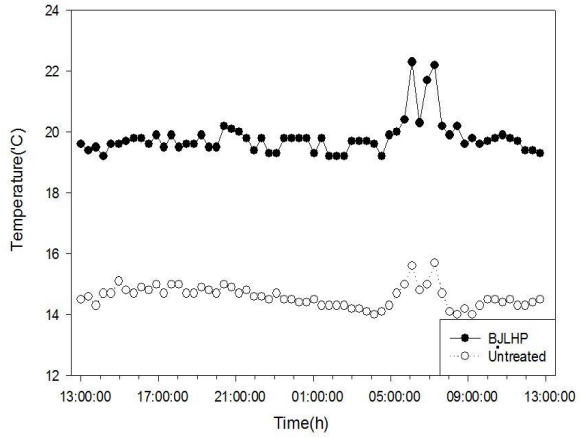


Fig. 5. Temperature profile of soil

Table 2. Comparison of growth

	Yield (unit/crop·day)	Length (m)
BJLHP	0.63	1.38
Untreated	0.53	1.34

Table 3. Comparison of fuel cost

	Electricity (kW/month)	Oil (L/month)	Total cost (won)
Space heating	-	4320.6	3,888,540
Complex heating	3792	3519.7	3,317,526

*Heating area: 1000m^2

*Electricity: 39.20won/kW

*Oil: 900won/L

The results show that trees of the root-zone heating system score higher in yield and growth than untreated trees, leaving a 19% and 2% gap respectively.

Although growth is not a big difference, it could be expected to increase in yield by applying the root-zone heating system.

Table 3. shows the results of converted fuel costs on the basis of monthly power consumption and the amount of used oil when space and complex heating system were applied. If the complex heating system was applied to the farm, it is possible to save approximately ₩ 570,000 per month, per 1000m^2.

That is, the use of a complex heating system could cut fuel costs by 17% compared with the space heating system.

3. CONCLUSIONS

The results are as follows.

(1) The BJLHP was operated properly and the temperature difference between the evaporating part and condensing part was only 0.5℃.

(2) The temperature of the soil where the BJLHP was buried was maintained appropriately at 19℃ which is moderate to the growth of cucumbers.

(3) The trees that are applied to the root-zone heating system produce 19% higher than those of untreated.

(4) If the complex heating system was applied to the farm, the fuel costs can be reduced by 17%.

(5) We confirmed the availability of the root-zone heating systems using BLJHP for horticulture.

REFERENCES

[1] S. W. Gong., Y. J. Gong and J. S. Kim., Loop Heat Pipe Using Bubble Jet, Korea, patent 10-1036685, (2011).

[2] J. S. Shin., Y. H. Kwon and J. S. Kim., Performance evaluation of high performance Bubble Jet Loop Heat Pipe using enhanced boiling surface in evaporating section, Proceedings of the KSME spring conference, (2013) pp. 236-239.

[3] D. K. Jeong., J. H. Woo and J. S. Kim., A Study on Heat Transfer and Flow Characteristics of Bubble Jet Loop Heat Pipe, Proceedings of the KSME spring conference, (2011) pp. 175-180.

[4] M. H. Seo., Research for Energy Saving Cultivation technology, Rural Development Administration Report LS-0208, (2000) pp. 169-179.

Development of Loop Heat Pipes with Sintered Nickel Wick Using Cold Isostatic Press Method

Won Bok Chung*, Seon Hong Hwang, Cheol Min Park, Yoon Sung Kim, Sang Sik Kim

Daehong Enterprise Co., LTD, Huimang-Kongwon-Ro 4, Siheung-city, Gyeonggi-do, 15101 Korea

Abstract

Porous structure is the key part effecting operation and performance of loop heat pipes (LHPs). This wick structure requires proper porosity, pore size, permeability and the machining. And the wick is made using monometallic, mixed metal materials with additional material for more porosity. In this study, the cold isostatic press method (CIP) was used to forming the nickel powder to make wick structure. The properties of the nickel sintered wick using CIP method were 60~70% of porosity, 1.0~1.5μm of pore radius. The heat transport ability at the various test condition with the U-shape type LHP applied this wick was in range of 0.5~1.8 kW.

Keywords: Cold isostatic press (CIP); heat transport capacity; loop heat pipe; sintered nickel wick

1. INTRODUCTION

The critical part effect to the operation and performance of LHP is porous structure. This wick structure is importantly proper that the porosity, pore size, permeability and machinability. Also it has properties that small pore size, high permeability, low thermal conductivity is advantage to improve heat transport ability, which is indicator of the LHP performance. The wick is made using monometallic and mixed metal materials to meet the corresponding attribute. Typically cooper, titanium, nickel, stainless steel and so on. The study of wick characteristics in manufacture the wick with various material (Albertin et al., 2012).[1] They have gained characteristics which are porosity and pore size in some manufacturing condition, especially in case of nickel has 870 °C sintering condition. The copper has 25~30% and 20~25 μm, the bronze has 45~50% and 12~14 μm, the nickel has 67~72% and 8~8.8 μm. The study of a manufactured wick with nickel material was conducted (Prasad, et al., 2013).[3] They have gained the nickel wick properties which are 4.8 μm in pore radius, 63.5% in porosity and 9.93 W/m-K in thermal conductivity at room temperature (nine times less than solid Ni). The nickel wick has a good characteristic to apply for LHP. Also, studied to porous characteristics of the nickel wick made by various type of nickel powder (Reimbrecht, et al., 1999).[4] They have gained characteristics with the nickel powder carbonyl 123 (NP-123, provided by INCO Co.), the atomized powder and the mixture powder. Each powder sintering results are 1~20 μm, 4~37 μm and 2~24 μm in pore size at sintering temperature range of 950~1050˚C. And another result was showed that increases pore size is decreasing machinability.

According to that studies found the advantage of property choice with nickel powder in wide range. For examples, results are 60~70% in porosity and the 1~24 μm in pore size. They were offered capability of the sintered nickel wick apply to LHPs.

In this study, confirming the manufacturing condition for to make a wick with the nickel material for satisfied characteristics to improve the LHP performance, which are the 65% mean porosity, low pore size, high permeability and high machinability. And establishing the procedure for made a certain product with the constant properties in above. Also, confirm the LHP performance applied to the manufactured wick as a test in various condition.

Possible to select two types of forming method for metallic form which is the cold isostatic press (CIP) and the die press. The die press method in advantage of made a certain size and a shape simply. The CIP method in advantage of made a cylindrical shape with the homogeneous density, because it has omnidirectional applied pressure mechanisms. In this study, using cylindrical shape wick with a hole which is located center of wick in axial direction. Prevent to irregular heat exchange at evaporator and condenser, using the CIP method to make a sintered wick which has advantage in foregoing.

According to the representation of the above, this study conducted to forming the nickel wick with CIP method and sintering to consider the various conditions, to object excellent properties for LHP performance.

*Corresponding author: wbchung@heatpipe.co,kr, Phone: +82-31-434-9300, Fax: +82-31-434-9307

2. MANUFACTURE OF WICK

2.1 Experimental Setup

2.1.1 Selection of metal materials

Using two types of nickel powder for wick manufacturing. Nickel powder named of T255 and T123 made by INCO Co. are carbonyl type. These powder has a little different characteristics. The T255 powder is filamentary shape, 2.5~2.8 μm in average particle size and 0.5~0.65 g/cm^3 in apparent density. The T123 powder is spherical shape, 3.0~7.0 μm in average particle size and 1.6~2.6 g/cm^3 in apparent density. Each powder SEM images are shown in Fig. 1.

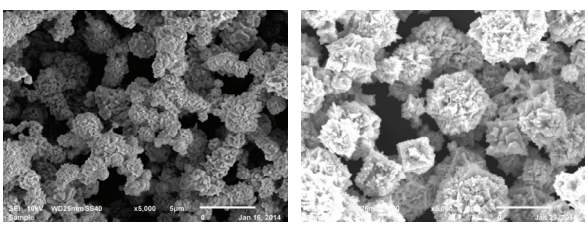
The nickel powder is improve the purity through sieving separation. That work is prevent to defect of the work process, especially sintering process, with removing impurities. Result of sieving separation for nickel powder showed that the nickel powder has 99.5% yield. That powder as known as exhibited good purity.

2.1.2 Forming mold

Forming with the CIP was using mold material of flexible and resistible to pressure, non-metallic, because that method is omnidirectional applied pressure system. Manufacturing the cylindrical shape mold with the urethane determined of the various non-metallic material. Additionally, manufacture the metallic rod for the inner hole of formed body. Dimensions of the forming mold were obtained through experiments in several times considered shrinkage on sintering process. The cap used for sealing on forming process is made by material of the MC nylon. But it is not used for that material, necessarily.

2.1.3 Sintering equipment

There were three types of furnace which are atmospheric, vacuum and gas atmosphere. The atmosphere must be choose possible to oxidation control, because the wick material is metallic. In this study, using the hydrogen reduction furnace.



a. T255 b. T123

Fig. 1. Nickel powder SEM image (x5000)

2.1.4 Measuring method

Various types of theory and equipment were used to measuring the characteristics of nickel wick to complete the forming and sintering. The porosity and pore size by the pore size analyzer (PSA), mercury porosimetry. It is measured the pore size by phenomenon of permeate to pore with the non-wetting fluid in pressure applied. Also it is measured the porosity by amount of permeate to pore with mercury. Measuring the permeability by liquid type method is using the porometer 3Gz. The visually measure equipment for the pore forming of sintered wick inner body and the shapes of surface is using the scanning electron microscope (SEM).

2.2 Characteristic comparison

2.2.1 Nickel type

Selection of the metallic material is compared to the carbonyl nickel powder T255 and T123. The manufacturing condition for the characteristic comparison were conducted to 3.7 MPa in forming pressure (minimum forming pressure of keep shape), 700˚C and 30 min sintering condition. That average value results of experiment are 62.6 and 43.4% in porosity, 3.1 and 2.5 μm in pore diameter, respectively.

The analyzing results, T123 powder is 30% less in porosity and 16% smaller in pore size than T255. The reason of it has a different filling density characteristics. To object, 60~70% in porosity and 2.0~3.0 μm in pore size, study conducted with T255 powder.

2.2.2 Forming condition

Establishing the forming condition based on experiment with the powder filling density and the forming pressure. In case of the filling density experiment in range of 1.0~1.44 g/cm^3, formed body was break regardless of the forming pressure. The results of it increasing step forming is showed that the filling density is need to more than 1.4 g/cm^3.

In next experiment for optimum forming pressure condition, conducted to applied pressure in range of 3.7 to 50.0 MPa. The sintering conditions were the 700˚C in temperature and 30 min dwell time (well-known value in previous study) condition. These experiment results are shown in Fig. 2. The permeability and porosity were increase according to applied pressure decreasing. The pore size was smaller according to applied pressure increasing. To meet the objective pore size range lower than 10.0 MPa in forming pressure but the porosity was to meet only in 3.7 MPa pressure condition

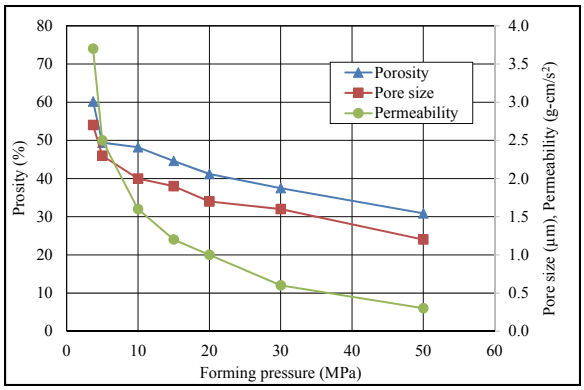


Fig. 2. Wick characteristics with forming pressure

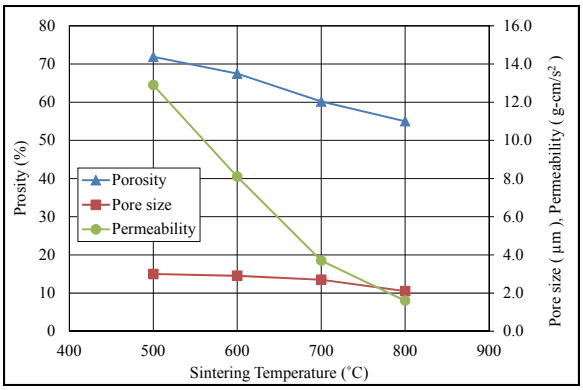


Fig. 3. Wick characteristics with sintering temperature

2.2.3 Sintering temperature

The porosity and machinability of the sintered metal wick are distinct features according to sintering temperature condition. The porosity was increase based on sintering temperature decreasing but machinability was decreasing. A scratching and break the sintered wick in process of the lathing and milling because of low temperature range at sintering process was generate week cohesion. In this experiments are conducted sintering temperature in range of 500 to 800˚C with 30 min dwell time. That results are shown in Fig. 3.

As a result, the porosity was increasing according to sintering temperature decreasing. But in case of 500˚C condition, the sintered wick was hard to machining because it was break easily. In case of 800 °C condition, machined surface of wick was smudged. The smudged wick was decreasing the porous property because hard to retain surface pore.

The sintered wick with 600, 700˚C temperature condition to meet the objective porosity and machinability was conducted strength test. Each test measuring the flexural strength and the compressive strength. Test results of 600˚C wick are 13±1 MPa in flexural strength and 8±2 MPa in compressive strength. And the results of 700˚C wick are 26±1 MPa and 12±2 MPa, respectively. In each test are conducted according to the test method of KS L 1591: 2013 and KS L 1601: 2011. The flexural strength was 44~55% higher in 700˚C condition than 600˚C. In case of the compressive strength was 57% higher in 700˚C condition than 600˚C.

2.2.4 Dwell time

The temperature dwell time on sintering was effected to porous characteristic. In this study, compared in case of 10, 30 and 120 min condition at 700˚C sintering temperature. The results are in Fig. 4. The porosity was decrease according to the dwell time was increase. The pore size was little change.

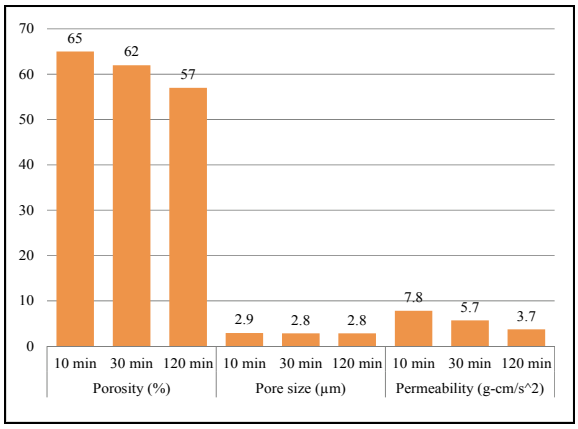


Fig. 4. Wick characteristics with sintering dwell time

2.3 Sintered nickel wick

The wick has a cylindrical shape with hole and its dimensions are 111±0.15 mm in length, 22.4±0.06 mm in outer diameter, 13.8 ±0.1 mm in inner diameter (diameter of hole), 1.0 ±0.05 or 2.0 ±0.05 mm in groove width. The wick shape in complete of manufacturing process (forming, sintering and machining) is shown in Fig. 5.

The optimum manufacturing condition and characteristics for sintered nickel wick are shown in Table 1. The wick characteristic values were confirmed with experimentally on ahead step in this study.

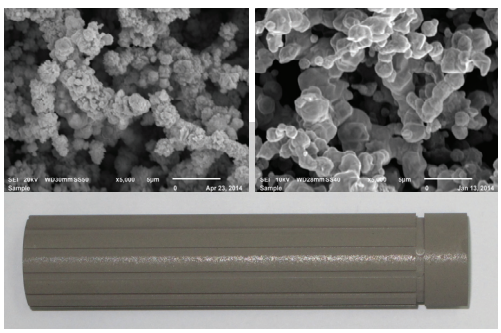


Fig. 5. Manufactured sintered nickel wick

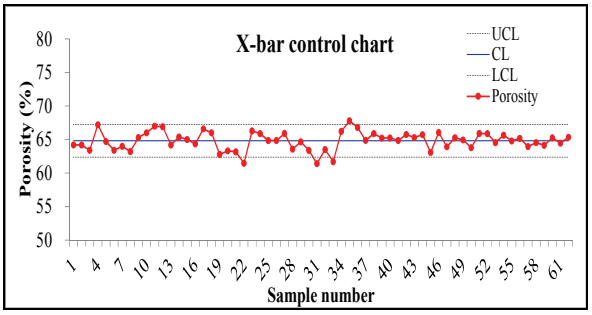
Table 1. The optimum manufacturing conditions and characteristics of sintered nickel wick

Manufacturing condition	Filling density	1.4 ~ 1.6 g/cm^3
	Forming pressure	3.7 MPa
	Sintering temperature	700 ˚C
	Sintering dwell time	10 min
Characteristic	Porosity	65 ±2 %
	Pore size	2.9 ±0.1 μm
	Permeability	5.9 ~ 8.1 g-cm/s^2

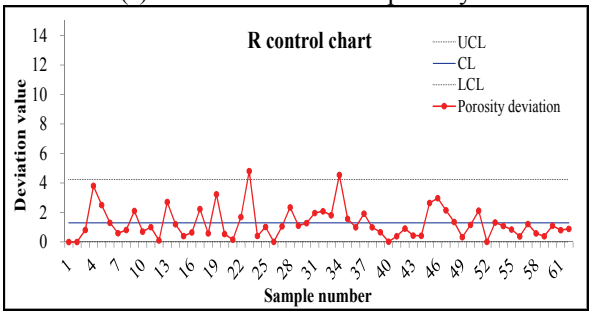
2.4 Wick production process management

The process management was conducted for regular characteristics of manufactured wick with statistical process control (SPC). Initially, produce 62 stations of the nickel wick with developed manufacturing condition. Measuring the porosity and pore size for checking that values are inside the range of objective, or not. Each values are distributed in Fig. 6, 7 for the x-bar and R control chart. The results of it, 3 stations product are off the range of objective porosity, and only 2 stations product are off the range of objective pore size.

The production process is has fine yield in range of 93~97%. And the results of R control, the process is stabilized in over time.

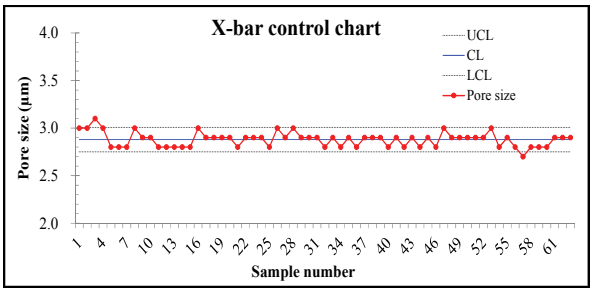


(a) x-bar control chart for porosity

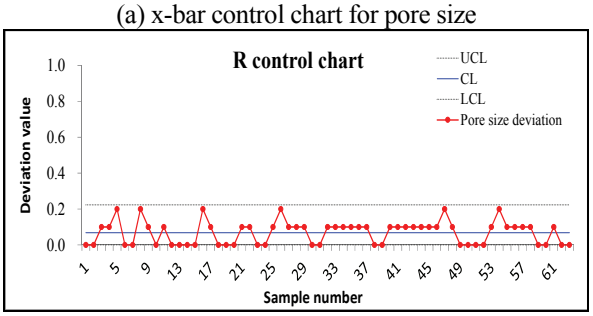


(b) R control chart for porosity

Fig. 6. The x-bar and R control chart for porosity



(a) x-bar control chart for pore size



(b) R control chart for pore size

Fig. 7. The x-bar and R control chart for pore size

Evaluation of the product quality and reliability with results, the developed manufacturing conditions and process in this study are has favorable reliability.

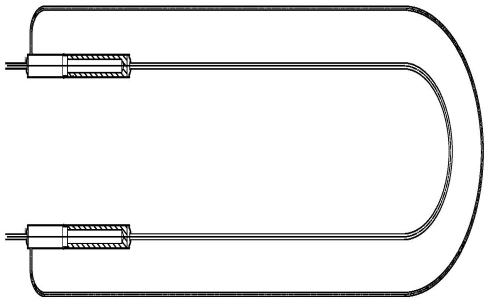
3. LHP PERFORMANCE TEST

3.1 Fabrication

The LHP was manufactured based on the dimension of the references [offered by Maidanik et. al][6-8]. It was shown in Table. 2. The test was conducted the U-shape LHP, the unfold type (connected between the evaporator and condenser with straight vapor line) straight LHP to be straight type and the 3 m long LHP had a one wick at evaporator and 3 m distance between evaporator and condenser. The 3-m type LHP characteristics are shown in table. 3. In this paper, the names of each types of LHP were the U-shape, the Straight-shape and the 3-m. Each LHP shapes were sowed at Fig. 8, schematically. In addition, manufactured the short distance LHP for heat flux test similar than 3-m LHP.

Table. 2. The U-shape type LHP main characteristics

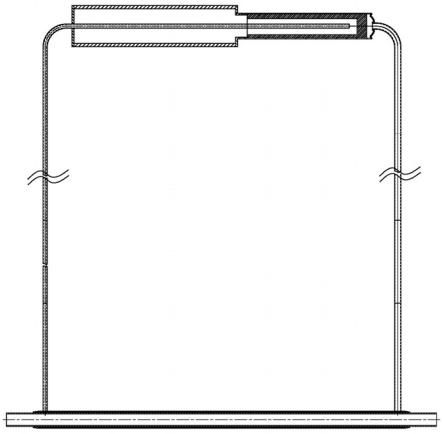
Specifications	Value
LHP container material	Stainless steel
Evaporator Length/Diameter	160/24 mm
Compensation Chamber Volume	26.8 cm^3
Vapor Line Length/Diameter	1307/5 mm
Liquid Line Length/Diameter	2048/4 mm
Wick material	Nickel
Wick Length/Diameter	155/22.4
Working fluid	Ammonia



(a) The U-shape type LHP



(b) The straight-shape type LHP



(c) The 3-m type LHP

Fig. 8. Drawing of each types LHP

Table. 3. The 3-m type LHP main characteristics

Specifications	Value
LHP container material	Stainless steel
Evaporator Length/Diameter	160/24 mm
Compensation Chamber Volume	170 cm^3
Vapor Line Length/Diameter	3048/5 mm
Liquid Line Length/Diameter	3048/4 mm
Wick material	Nickel
Wick Length/Diameter	155/22.4
Working fluid	Ammonia

3.2 Experimental setup

3.2.1 Test equipment

Heat input was using the heating block inserted the electrical resistance type heating element at the evaporator (maximum load was 2.1 kW). Input heat was controlled with power supply and was checked with power meter. Cooling was conducted the liquid convection with cooling block at condenser.

The coolant temperature was controlled with isothermal bath. The T-type thermocouples for measuring temperature were used at 12 points at the wall along the working fluid circulation path. All the experimental data, especially temperature, was measured and saved through the DAQ system at the same time. The experimental setup is shown schematically in Fig. 9.

3.2.2 Test conditions

Test conditions for each shapes performance are posture, coolant temperature and input heat load.

The postures were horizontal, anti-gravity and gravity. The horizontal posture is same gravitational height for evaporator and condenser. The anti-gravity posture is located the evaporator higher than the condenser, gravitationally. The gravity posture is reversed location of the anti-gravity posture.

The cooling conditions are the coolant temperature and flow rate. The temperature conditions are in case of -40, -20, 10 and 40˚C. The flow rate is more than 200 cm^3/sec (considering the condenser area and cooling path inner volume).

The input heat load is controlled in range of the operating start to the operating failure condition. The operating failure occurred by operating temperature (mean temperature for LHP).

The U-shape type LHP was tested to various condition, described above. Other types of LHP were tested typical condition.

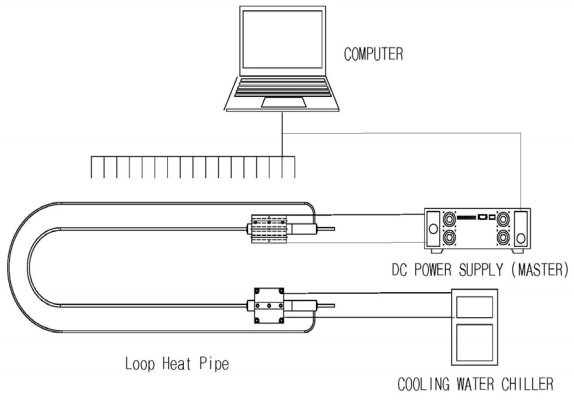


Fig. 9. Schematic of experimental setup

3.3 Test Results and Discussion

3.3.1 Comparison for LHP type

In this section, compare the LHP performance with LHP shape. The test results of each condition shown in Fig. 10. All types of LHP had reached 1.3 kW in maximum heat transport with the horizontal posture and the 10˚C coolant temperature condition. But the 3-m type LHP was showed the temperature variation differently and in case of 2 m height anti-gravity condition reached 500 W heat transportation ability.

The LHP startup feature is showed Fig. 11 in sample test of U-shape LHP with the horizontal posture and 10˚C coolant temperature condition. The results of each type LHP is shown in Fig. 12. The 3-m type LHP test results are distributed to large temperature difference between the evaporator and the condenser section than other type of LHP.

The shape feature of LHP was not effected to heat transport capacity but the temperature was effected. This result from the heat transportation length that was affected the area of exposed to ambient air.

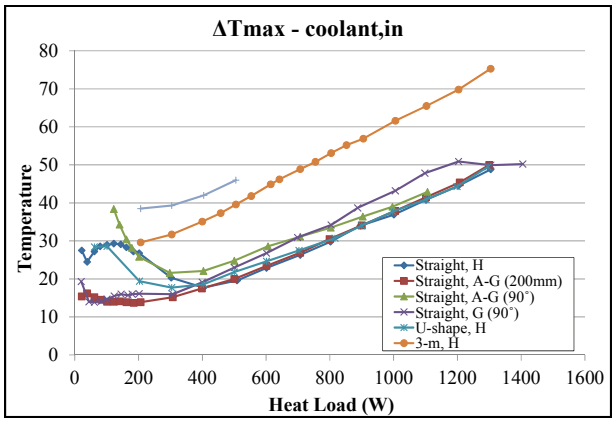


Fig. 10. Results summary of the LHP type test

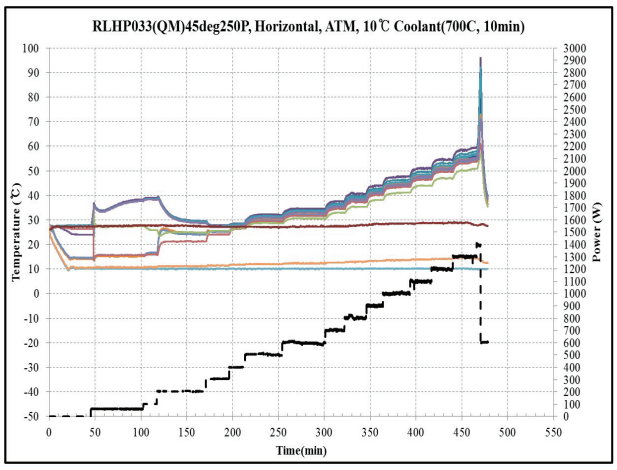
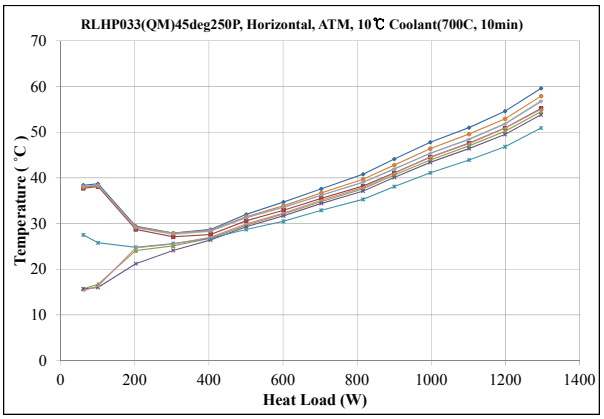
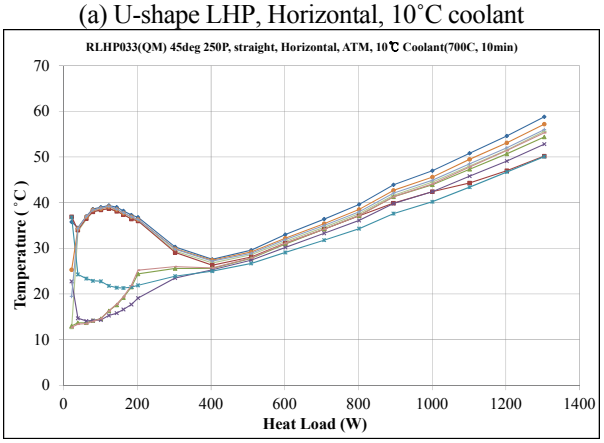


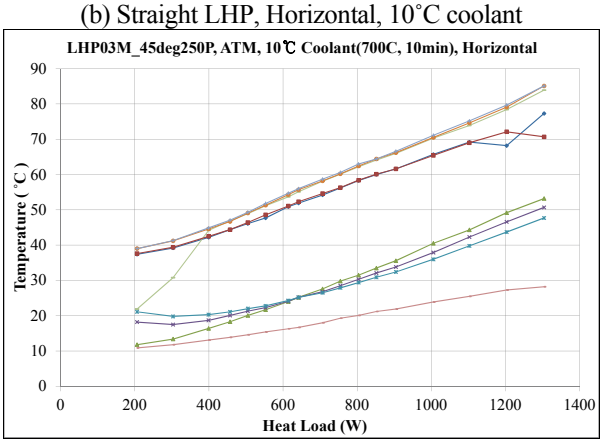
Fig. 11. Results summary of the LHP type test



(a) U-shape LHP, Horizontal, 10˚C coolant



(b) Straight LHP, Horizontal, 10˚C coolant



(c) 3-m long LHP, Horizontal, 10˚C coolant

Fig. 12. Test results of each type LHP

3.3.2 Comparison for test posture

In this section, compare the U-shape LHP performance with posture condition. The test results of each posture at 10˚C coolant temperature are shown Fig. 13. It is distributed the temperature differences between maximum and coolant inlet as a function of heat load. The maximum heat transport had reached at 1.0 kW in the horizontal and the anti-gravity posture and reached at 1.1 kW in the gravity posture. The performance in a different point, temperature difference, was showed that the gravity posture is best.

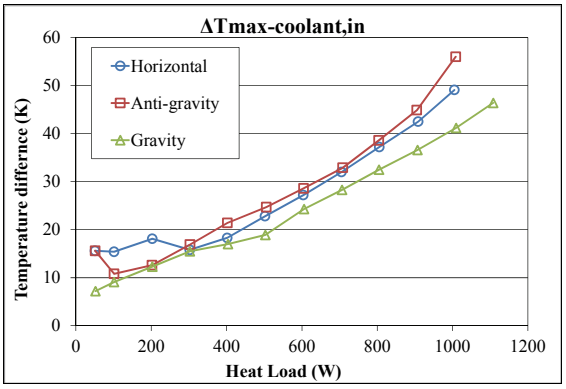


Fig. 13. Test results of U-shape LHP. 10˚C coolant

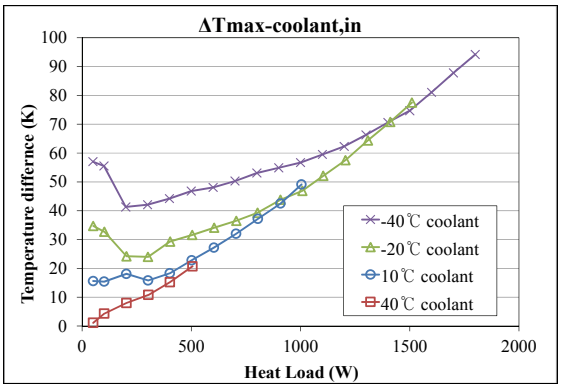


Fig. 14. Test results of U-shape LHP, Horizontal

Table 4. Temperature differences of posture test

Heat load (W)	ΔTmax-coolant,inlet (K)		
	Horizontal	Anti-gravity	Gravity
50	15.6	15.6	7.2
100	15.4	10.8	9.1
500	22.8	24.7	18.9
1,000	49.1	56.0	41.2
1,100	-	-	46.4

Table 5. Temperature differences of coolant temp. test

Heat load (W)	ΔTmax-coolant,inlet (K)			
	- 40˚C	- 20˚C	10˚C	40˚C
50	57.0	34.7	15.6	1.1
500	46.8	31.6	22.8	20.7
1,000	56.7	46.9	49.1	-
1,500	74.7	77.5	-	-
1,800	94.2	-	-	-

Except for some low heat input condition, the anti-gravity posture has the worst performance. Some representative results for detail value of temperature difference are shown Table 4. The temperature differences were showed less than 50˚C except for the anti-gravity posture.

These results showed that the gravity was affect to the heat transportation capacity and isothermal, but not big. The notable point is capable to 1.0 kW heat transportation in any posture.

3.3.3 Comparison for coolant temperature

Compare the U-shape LHP performance with the coolant temperature condition. The results of each coolant temperature at the horizontal posture are shown Fig. 14. That is distributed the temperature differences between maximum and coolant inlet temperature. The maximum heat transport had reached at 1.8 kW in the -40˚C coolant, 1.5 kW in the -20˚C coolant, 1.0 kW in the 10˚C coolant and 0.5 kW in the 40˚C coolant temperature condition.

Likewise, the temperature difference analyze in this results is meaningful. Except for maximum heat input point in each coolant temperature condition, higher coolant temperature condition result is shown best performance. The representative values are shown Table 5.

Inclusively, the heat transport ability and the temperature difference are decrease according to the coolant temperature rise.

3.3.4 Summary of U-shape LHP test

The U-shape LHP test results are shown in Fig. 15, respectively. These results are indicating the trend of performance through the test condition. Performance deviation according to the posture condition is smaller than according to the coolant temperature.

In conclusion, the LHP performance is improve according to the gravitational advantage. The heat transport capacity and the temperature differences in two aspects of performance are optional under the terms of coolant temperature.

3.3.5 Thermal load density test

Additionally, thermal load density test conducted for confirming the wick performance with the heat flux type LHP.

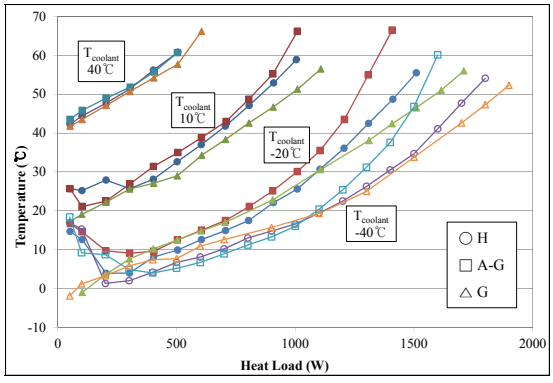


Fig. 15. Test results of U-shape LHP, T_{max}

The results were 750 W in maximum heat transport amount and 99.47 W/cm^2 in maximum thermal load density. The developed nickel wick has a good performance for the heat transportation, extremely high heat load density

4. CONCLUSIONS

Manufacturing process development of sintered nickel wick had been studied based on nickel powder using CIP method with various forming pressure, sintering temperature and dwell time. As the result, the sintered wick was the best performance under the condition, 1.4 ~ 1.6 g/cm^3 in filling density and 3.7 MPa in forming pressure of CIP, 700˚C in temperature and 10 min in dwell time of sintering at furnace. Manufactured wick has characteristics regularly in a narrow range. The porosity was 65.0 ±2%, pore radius was 1.5 ±0.1 μm and the permeability was 5.9 ~ 8.1 g-cm/s^2.

Experiment of LHP applied the developed wick in this study showed that the heat transport ability at various condition of the U-shape LHP was in range of 0.5~1.8 kW. In addition, this study showed that the LHP performances for various operating condition, respectively.

ACKNOWLEDGEMENT

This study was supported by a research project of the space critical technology development provided by the National Research Foundation of Korea.

NOMENCLATURE

UCL: The upper control limit
CL : The center line
LCL: The lower control limit
H : The horizontal posture
A-G : The anti-gravitational posture
G : The gravitational posture

REFERENCES

[1] Albertin, T. and Savard, J. F., Industrial Manufacturing of loop Heat Pipe Porous Media, *Proc. of 16th International Heat Pipe Conference,* Lyon, France (2012)

[2] Wu, S. C., Lin, F. C., Chen, S. H., Yeh, C. C., Wang, S. K., and Chen, Y. M., Manufacturing of the Complex Wick with Double-Layer Bi-Porous Structure and Applying to a Loop Heat Pipe, *Proc. of 10th International Heat Pipe Symposium,* New Taipei City, Taiwan (2011) 104-108.

[3] Prasad, A., Anand, A. R., Kumar, D. R., Ramkrishnan, V., Ambrirajan, A., Kumar D. and Dutta, P., Measurement of Thermal conductivity, Pour Size, Permeability and Coefficient of Thermal Expansion of Porous Nickel Wick for LHPs, *Proc. of 17th International Heat Pipe Conference*, Kanpur, India (2013)

[4] Reimbrecht, E. G., Fredel, M. C., Bazzo, E. and Pereira, F. M., Manufacturing and Microstructural Characterization of Sintered Nickel Wicks for Capillary Pumps, *Material Research,* 2 (3) (1999) 225-229.

[5] Reimbrecht, E. G. and Bazzo, E., Wick Manufacturing and Characterization, *Proc. of 14th International Heat Pipe Conference*, Florianopolis, Brazil (2007)

[6] Sudakov, R. G., Maidanik, Yu. F., Vershinin, S. V. and Pastukhov, V. G., Development and Tests of a Reversible Loop Heat Pipe, *IV Minsk International Seminar "Heat Pipes, Heat Pumps, Refrigerators"*, Minsk, Belarus (2000) 30-35.

[7] Sudakov, R. G., Maidanik, Yu. F., Ochterbeck J. M. and Choi, S. W., Development and Investigation of an Ammonia Reversible Loop Heat Pipe, *Proc. of 12th International Heat Pipe Conference,* Moscow, Russia (2002) 19-24.

[8] Delil, A. A. M., Maidanik, Yu. F. and Gerhart, C., Development of Different Novel Loop Heat Pipes within the ISTC-1360 Project, SAE-2003-01-2383.

[9] Weibel, J. A., Garimella, S. V. and North, M. T., Characterization of evaporation and boiling from sintered powder wicks fed by capillary action, *Int. J. of Heat and Mass Transfer*, 53 (2010) 4204-4215.

[10] Zan, K. J., Zan C. J., Chen, Y.M. and Wu, S. J., Analysis of the Parameters of the Sintered Loop Heat Pipe, *Heat Transfer-Asian Research*, 33 (8) (2004).

[11] Anderson, W. G., Dussinger, P. M., Garner, S. D., Hartenstine, J. R. and Sarraf, D. B., Loop Heat Pipe Design, Manufacturing, and Testing – An Industrial Perspective, *Proc. of the ASME 2009 Heat Transfer Summer Conference,* San Francisco, California, USA (2009)

[12] Samanta, S. K., Das, P. and Logar, A. K., Development of Tubular Ni Wick Used in LHP for Space Applications, *Proc. of 10th International Heat Pipe Symposium*, Taipei, Taiwan (2011) 109-114.

[13] German R. M., *Sintering Theory and Practice*, Wiley & Sons Inc., (1996)

[14] Semenic, T. and Catton, I., Experimental study of biporous wicks for high heat flux applications, *Int. J. of Heat and Mass Transfer*, 52 (2009) 5113-5121.

[15] Singh, R., Mochizuki, M., Goto, K., Nguyen, T., Nguyen, T., Mashiko, K., Saito, Y. and Wuttijumnong, V., High Heat Transport Capillary Evaporator Development for Loop Heat Pipes, *Proc. of 16th International Heat Pipe Conference,* Lyon, France (2012)

[16] North, M. T., Sarraf, D. B. and Rosenfeld, J. H., High Heat Flux Loop Heat Pipes, *Proc. of the 6th European Symposium on Space Environmental Control Systems,* Noordwijk, Netherlands (1997)

Ground Test of Dual Loop Heat Pipe System

Yasuko Shibano, Naoko Iwata, Hiroyuki Ogawa

Japan Aerospace Exploration Agency, 3-1-1, Yoshinodai, Sagamihara, Kanagawa, 252-5210 Japan,

Abstract

Loop Heat Pipes (LHPs) have been used in spacecrafts. Most of them were used as a single loop. "LHP network" composed of multiple LHPs enables a "thermal design free" system [1, 2], and a redundant heat transport system [3]. In the former concept LHPs are mounted on all panels to radiate heat from a heat source without considering sun incident direction making use of the LHP's diode characteristics. In the latter concept multiple LHPs connect a single heat source with (a) radiator(s) to give redundancy to the LHP heat transport system. In the present study, we used two ammonia LHPs manufactured by IberEspacio, whose wicks are made from Nickel (upper side LHP-A) and from Stainless Steel (bottom side LHP-B). Both LHPs have bypass valves whose set point were both 263K. The evaporators were both connected to a heat source. Each condenser temperature was controlled.

We studied the start-up characteristics and the heat transport behavior under the various conditions of the LHP network.

Keywords: At least four keywords; Loop Heat Pipe, network, low temperature

1. Introduction

A thermal design for a microsatellite is expected to develop with short-run development with low cost and sustained reliability. The thermal environment varies with every orbit, attitude, and various kinds of installed equipment, etc. The satellite had been designed to correspond with each requirement in order to maintain temperature by using thermal devices, likely some kinds of Heat Pipes to control with great efficiency. On the other hand, the design process for one-by-one satellite takes a long time and high cost to develop and verify for conforming high-reliability. To get results from this program, we proposed a thermal design concept in the past study; which is "free from restrictions in thermal design". This idea assumed that it had a center heat source (CHS) for transported heat from six radiator panels. Some LHPs are mounted between the CHS and each structure of the panel with a radiator. LHPs have suitable conditions; first, a waste heat pass is formed free relatively because the valor and liquid line have good flexibility. Second, a long-distance loop can be realized by selecting a wick. Third, LHPs have the ability of diode which means that the heat input (as solar input on orbit) from the condenser can be cut off. Finally, we can control the reserve pressure by heating. This concept shows the thermal control by using the LHPs network. The likely concept satellite had already launched onboard the Hispasat 1E satellite in 2010 as In-Orbit test phase of the CREW Experiment. This LHPs network can work these temperatures with corresponding variable environments in orbit. In this study, they used regulation valves set at room temperature. In our experiments, using two LHPs with regulation valves for working at low temperature (263K), we focus on the LHP network star-up and cc control and heat input change from radiator.

*Corresponding author: shibano.yausko@jaxa.jp,
Phone: +81-05-3362-4307, Fax: +81-42-759-8068

2. Experimental set up

2.1 LHP

We used two LHPs (ammonia as a working fluid) with pressure regulation valves (bypass valve) working at 263K. This valve is installed between the vapor line and liquid line, as shown in Fig.1. To open and close the valve by inert gas pressure with corresponding set point the flow can be controlled. It means when the valve temperature remains on under the set point; the valve open, working fluids only flow around the evaporator without condensing. It means that the amount of waste heat is decreased and the heat source equipment can maintain these temperatures. When the temperature increased and became over the set point, the valve is closed and fluid moves over the LHPs. The wick is made of sintered nickel powder (pore diameters are 3.5μm) and sintered stainless steel powder (pore diameters are 1.1μm), respectively. The thermal conductance and porosities are the same. The vapor and liquid length are 700 and 690mm including the coiling part for flexibility. The diameter of the former one is 3mm, and latter one is 2mm. The condenser (length 311mm x width 125mm x thickness 2mm)

is mounted on an aluminum plate (length 300mm × width 200mm × thickness 6mm). Two LHPs mounted on a heat block are installed with four cartridge heaters and four thermos-couples by bolts and laid horizontaly. Two LHPs evaporators were placed on the top and bottom side of the block (Fig.2). The aluminum plates are connected to a chiller which can cool fluid until 238K and also have a sheet heater to model heat input from the sun. Two LHPs set in a thermostatic chamber work at low temperature. Each LHPs has 11 thermo-couples as showed Fig.2

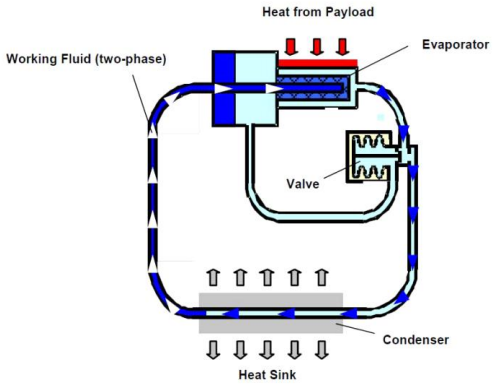


Fig. 1 LHP with bypass valve

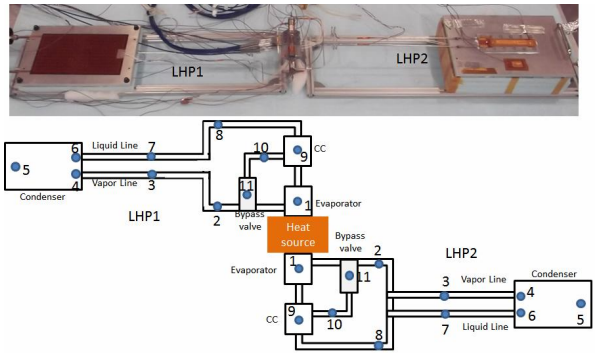


Fig. 2 Experimental set up Blue dots shows thermo-couples and orange box shows heat source.

2.2 Experimental conditions

Table 1 shows experimental conditions. The LHP of Nickel wick shows LHP1 and SUS wick shows LHP2. The LHP1 is placed on the top side of the heat block and LHP2 is placed on the bottom side in experiment No.1~3, and for No.4, the place of the LHP was reversed. Our study focused on the change of surrounding temperature, heat input and condenser control temperature. First, we confirmed thermal performance and start-up working with two LHPs networked at low temperature. Second, the condenser temperature was increased rapidly between 313K (modeled heat input from the sun) and 243K (modeled shadow). Note that 243K means a fluid temperature of the chiller because we cannot feedback control of the condenser. Third, two condensers control 273K and 253K, respectively, and each condenser set different temperatures. Finally, the cc with LHP2 was controlled by the heater.

Table 1 Experimental conditions

No.	Surround temperature (K)	Heat input (W)	Condenser control temperature (K)
1	253 233 213	20 – 80 20 - 100 20 - 200	LHP1: No control LHP2:No control
2	233	80 - 120	A: 313 - 243 B:No control A: 293 – 243 B:No control
3	273 253 233	40 - 140	A: 273 B: 253
4	273	20 - 140	A: 258 B: 258

3. Experimental results

3.1 Thermal performance at low temperature

Two LHPs were laid on a thermostatic chamber with setting at low temperature (253K, 233K and 213K, respectively). The LHP of Nickel wick (LHP1) was placed on the top side of the heat block and the SUS wick (LHP2) was placed on the bottom side. All parts were wrapped with insulator. These condenser plates were not controlled. The heat load was increased step-by-step, with waiting at each step until the thermal equilibrium was reached or over 20 minutes when it was not reached. Fig.3 shows the temperature history at the surrounding temperature of 233K, the up-side graph shows LHP1 and the bottom-side one shows LHP2. When each evaporator, CC and bypass valve temperatures reached 273K, the temperature gradient became slow. It may be showed that the bypass valves were closed and switched flowed far too long. Two LHPs started up at 40w heat input because each vapor line and condenser temperature increased. The LHP2's vapor line temperature changed more rapidly than LHP1, it may be showed that LHP2 got a larger amount of heat flow than LHP1 to depend on its wick capillary ability. This heat flow balance continued until 80W input because the LHP2 radiator temperature only increased. Over 80W, LHP2 cannot have enough waste heat, and LHP1 got more heat flux and its condenser temperature increased. It means that the start-up condition

effects not only starting but also steady working until the heat input becomes enough to work. The experiment at 213K showed the same features (Fig.4).

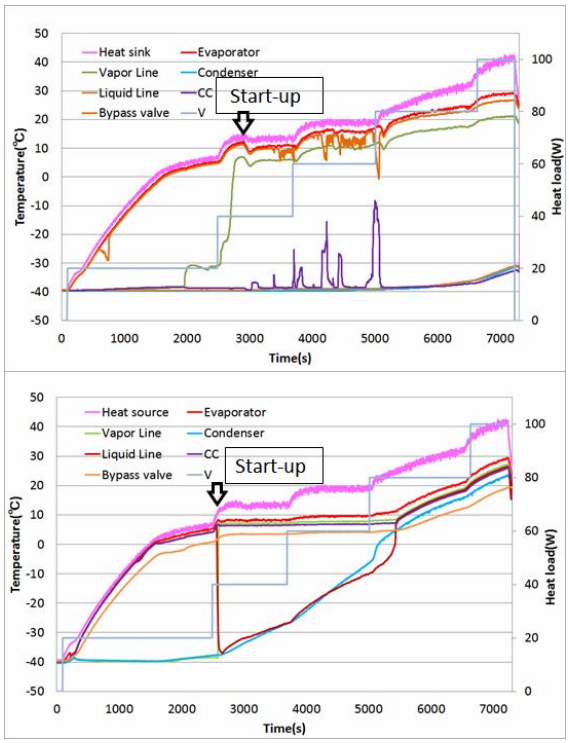


Fig. 3 The temperature history at the surroundings temperature of 233K (Upper-graph is LHP1, bottom one is LHP2)

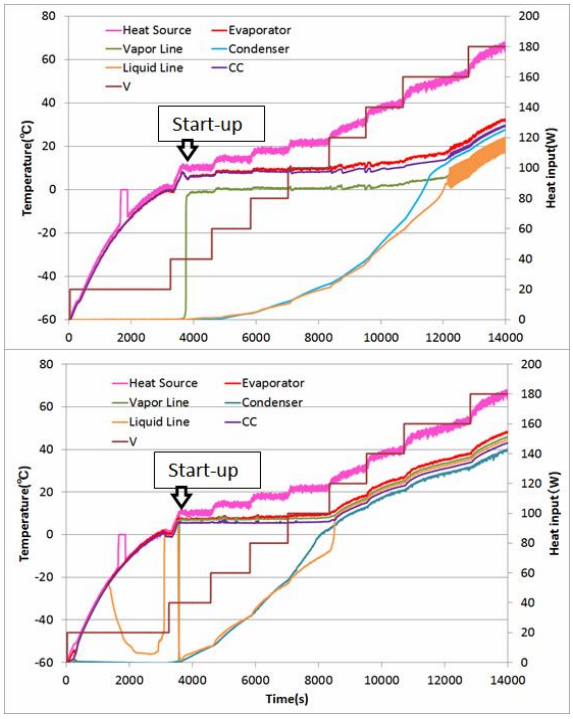


Fig.4 The temperature history at the surroundings temperature of 213K (Upper-graph is LHP1, bottom one is LHP2)

3.2 Rapidly changing of radiator temperature

In the next experiment, we changed the condenser temperature rapidly to model solar input or shadow on orbit. LHP1's radiator plate was cooled by using a chiller and heated to keep the temperature at 313K before start-up, but the LHP cannot work with characteristics of a diode. We added enough heat input for two LHPs start-up (80W), and waited until the thermal equilibrium was reached in the heat block. Just after radiator heater cut off, all temperatures of LHP1 decreased. On the other hand, the radiator of LHP2 temperature was influenced slightly. The condenser temperature decreased continually, the evaporator reached thermal equilibrium in both LHPs.

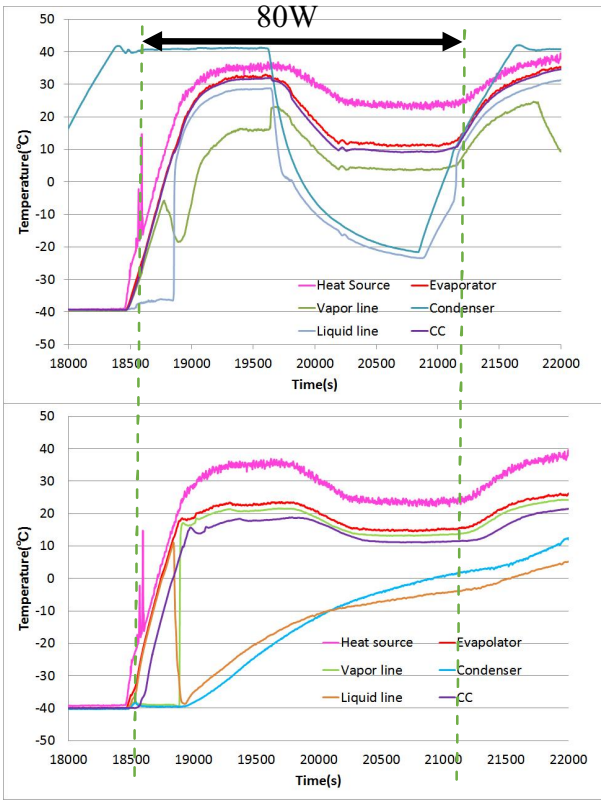


Fig.5 The temperature history at the surroundings temperature of 243K (Upper-graph is LHP1, bottom one is LHP2)

3.3 Condenser controlled

We assumed that the LHPs radiator on the satellite structure panels will be exposed to various temperature conditions one by one. The LHP1's radiator set at 273K was cooled by the chiller and the LHP2's one was heated to 293K by using a heater. We changed the surrounding temperature from 273K to 233K. At 273K, LHP2 started at 40W and LHP1 started at 60W and then

the evaporator, vapor line and CC were cooled without heat input (Fig.6). It is that amount of heat input from the block which becomes smaller than that of output at the condenser. In addition, it looks like each LHP works individually, not an LHPs network.

At 233K and 253K, when the liquid line reached over 273K, it may be just after the opened bypass valve, two LHPs start up respectively at 40 W. And then each LHP had been working with likely results of 273K. Note that LHPs get various heat input from these condensers depending on the surrounding temperature because the amount of heat increased to maintain the temperature setting as the surrounding temperature become low.

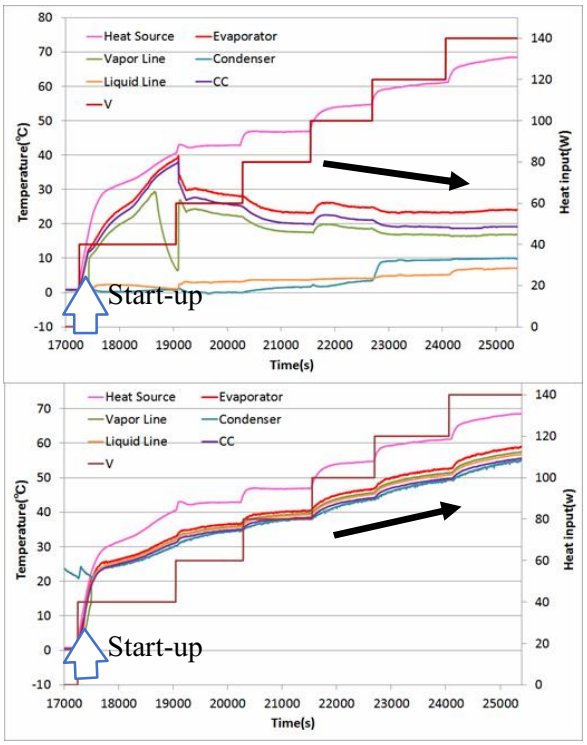


Fig.6 The temperature history at the surroundings temperature of 273K

3.4 CC control

In the above experiments, we found that LHPs network give uneven heat to LHP1 or LHP2 from the block when supplied with low heat input. In the case of not enough heat input, can we select start-up LHP. So, we mounted a heater on LHP2's CC and heat block to give 40W for LHP2 start-up at the surrounding temperature of 273K. After we confirmed that LHP2 was stable, the CC heater was turned on and we tried to exchange working LHP from LHP2 to LHP1. When the CC temperature become higher than the evaporator, LHP2 just stopped working (judging from the condenser temperature decreased). At the same time, we found that LHP1 started in place of LHP2. After 20 minutes, the CC heater was turned off and the CC temperature gradually became lower than the evaporator. LHP2 started again and returned to the initial temperature distribution. Continually, we tried to turn on the CC heater again, the heat transfer can be exchanged from LHP2 to LHP1, however, it cannot be returned from LHP1 to LHP2. After that, we increased the amount of heat input from the block, only LHP1 was working. Switching LHPs with CC control by using the heater had some problems and needs more research for the future.

We confirmed the heat flow when switching

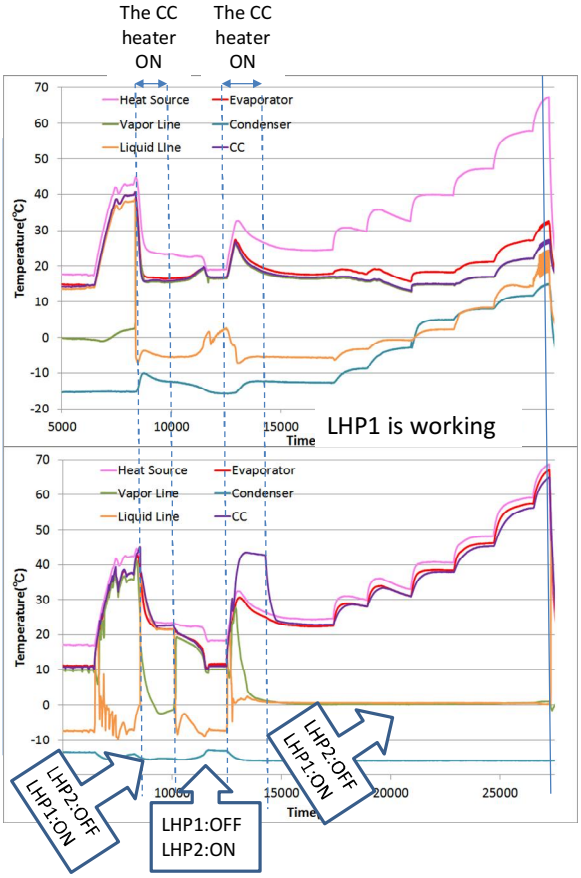


Fig.7 The switching working by the LHP2's CC controls.

carry on. In the heat block, there are two thermo-couples between the heater and the evaporator. The ΔT was measured to confirm the distance of heat flow. Fig.8 shows this result and it appears that the flow distance changes depending on the CC control. When the CC heater of LHP2 is turned on, heat flow starts to LHP1 rapidly and decreases the flow rate to LHP2. After it is turned off, heat flows to LHP2 again. This data also has supported switching control by the CC control. However, the second time, LHP1 continued

working after CC heater was turned off. It is questionable why heat flow returns or does not return after the CC heater is turned off. We need to confirm reliability of how to switch control.

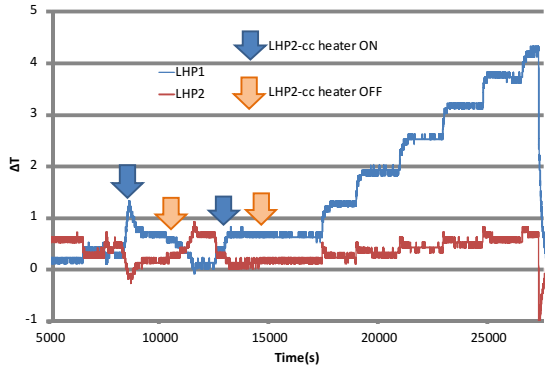


Fig.9 The heat flow exchange profile.

4. CONCLUSIONS

We studied the start-up characteristics and the heat transport behavior under low temperature by using two LHPs networks.

At low temperature, two LHPs with bypass valves work when there is enough heat input from the heat source. If the amount of heat input is not enough to start up two LHPs, one LHP only starts because the heat flow to LHP1 or to LHPs is uneven. In addition, as one LHPs work well, the other LHPs start-up becomes hard.

The heat input or cooling from the condenser affects the LHPs itself, however, the other LHPs slightly changes.

CC control by using a heater is switching heat flow and control working LHP. To get high-reliability, we need more experiments and verification for these phenomena

REFERENCES

[1] N. Iwata, and H. Ogawa, J.M. Molleda, “Thermal Control System of Microsatellite with Loop Heat Pipes,” AIAA 2012-3479, ICES 2012

[2] J.A. Ronera, J.L. Pastor, J.Alvarez, J.M.Boix, A.Torres, “Coupled radiator East-West Experiment Flight Data”, AIAA 2011 – 5164, ICES 2011

[3] C.D. Jones, A.B. Smith, and E.F. Roberts, *Book Title*, Publisher, Published year.

Prototype of Thin Loop Heat Pipe with Glass Fiber Wick for Compact Electronics Cooling

Alexander A. Yakomaskin*

Department of Thermophysics, Bauman Moscow State Technical University,
2nd Baumanskaya Street, 5, Moscow 105005, Russia

Abstract

For further implementation of loop heat pipes (LHP) to electronics cooling, it is necessary to pay attention to their dimensions, weight and manufacturing cost. Today almost every laptop is equipped at least with one heat pipe (HP). This heat transfer device is required to transfer and transform heat flux. Heat pipes are cheap and well developed. LHPs are less developed, cost much more but they have some advantages that can be significant when LHPs are applied to cooling of laptop computers. LHP are capable of transferring large heat fluxes, they can be easily bent to save space inside a laptop's cabinet, they provide more options to organize the condenser side of a heat removal system. This article describes a newly designed, manufactured and tested loop heat pipe prototype with a new type of evaporator, a thickness of 3 mm, and with a glass fiber wick. Distilled water was used as a heat transfer media. Charged volume was equal to 1.4 ml. Copper tubes were used to connect the evaporator and the condenser. Heat input was applied via a flat ceramic heater. During the experiments, power varied from 10 to 50 W in steps of 5 W. The lower heat conductivity of a wick applied the thinner design can be achieved. That is why the non-metal wick was applied. Technology for assembly of the evaporators having non-rigid wicks may increase tolerances for manufactured parts and the assembly itself, which may affect the manufacturing cost of LHP. The described prototype has the thickness of 3 mm. The thickness of the wick is 0.5 mm.

Keywords: Loop heat pipe; Evaporator; Non-metal wick; Compact electronics cooling

1. INTRODUCTION

Loop heat pipes are heat transfer devices which use evaporation and condensation of working fluid to transfer heat and use capillary forces to provide fluid circulation in a closed loop. One of the main applications of LHP is cooling of electronic components. At present, significant progress is achieved in the creation of miniature LHP for use in compact electronics cooling. Maydanik et al. developed a miniature LHP with a cylindrical evaporator with a thickness of 5 mm [1]. Lin et al. created a copper-water LHP prototype [2]. The device is ready to be installed inside a notebook computer instead of a regular heat pipe cooler. The prototype has a thickness of 3 mm. Singh et al. created LHP prototypes with flat thin evaporators with thicknesses of 5 mm and 10 mm and discussed the thermal potential of a flat evaporator miniature LHP for Notebook Cooling [3]. In recent years, the intensive work is conducted to create copper-water LHPs equipped with flat evaporators with a thickness between 3.2 and 8 mm [4]. The LHPs have a signifcant heat power of up to 900 W. Inspite of these successful examples, there are still unsolved problems, mainly technological, related to loop heat pipes. Ways to reduce LHPs' cost and dimensions were discussed in [5]. The following contains a brief description of the problems related to heat leaks in the evaporator and suggests solutions.

An LHP in its original concept combines a compensation chamber (CC) and an evaporator in a single enclosure. Such a design ensures a constant wetting of a wick structure by liquid and regulates fluid inventory change in the LHP under all heat loads. However, colocation of CC and the evaporator leads to high heat fluxes toward the CC across the wick which is saturated by liquid. This, in turn, increases the evaporator's temperature.

One of the ways to decrease the amount of heat leaks from the evaporator to the CC assumes the use of a wick made of material with low thermal conductivity, e.g. stainless steel, polypropelene, glassfiber etc. Not many studies have been devoted to LHP with non-metal wicks. In [6] the authors identified the following features of such wicks: low thermal conductivity, low manufacturing cost, low weight and easy assembly. Speaking of the low thermal conductivity of non-metallic wicks it is important to realize that only scheme with inverted meniscus is suitable for evaporators with non-metal wick. The wick in such LHP design performs the function of a heat barrier. The lower heat conductivity of a wick the thinner design can be achieved. On the other hand, the low thermal conductivity is a disadvantage, because the formation of even a thin vapor layer in the wick will create a significant

*Corresponding author: yak40@gmx.com,
Phone: +7 916 856 4719

temperature gradient. Therefore, for non-metallic wicks one should either apply low heat fluxes, or "unload" the menisci by providing more uniform heat input and vapor output. Paper [5] describes some ways to improve vapor removal channels configuration.

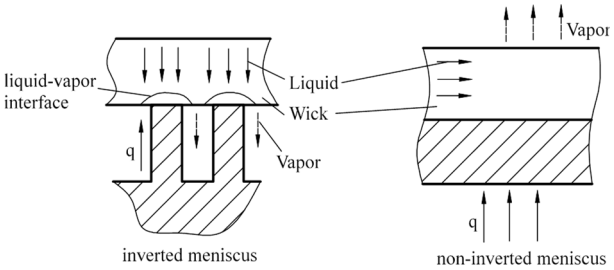


Figure 1. Evaporation process schematic.

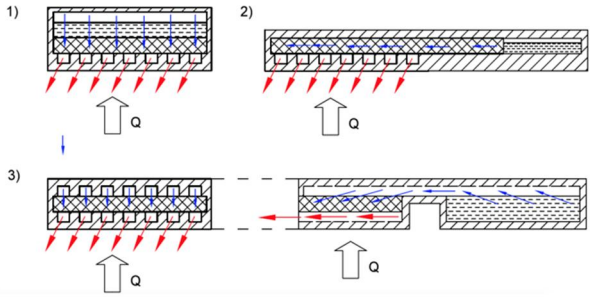


Figure 2. Evaporator types: 1 - EOR; 2 - ELR; 3 – new.

Another way to reduce heat leaks is choosing propper relative position of an Evaporator and CC. There are two main types of flat evaporators. One of them may be called “evaporators with opposite replenishment” (EOR) [7]. Their feature is that the liquid flow in the wick is directed towards the heat flow supplied to the evaporator (Fig. 2.1), and the compensation chamber is located on the side opposite to the heated surface. The amount of heat transferred to CC from the evaporator decreases with the increase of thickness of the wick. The overall thickness of such evaporators depends on the thickness of the wick and dimensions of the compensation chamber, which in turn, depends on the length and the diameter of the vapor line and the condenser. So this type of evaporators is not suitable for thin designs.

The second type is “evaporator with longitudinal replenishment” (ELR) (Fig. 2.2). Inside ELR liquid flow in the wick is directed along the evaporator’s heated wall, and the compensation chamber is located aside from the active zone. This allows increasing the distance between the evaporator and the CC as well as reduce contact area between them. Such colocation of the components gives the reduced overal thickness of the evaporator. On the other hand, the othe dimensions, the width and the length, increase.

In order to get the minimum evaporator thickness it is preferable to locate a compensation chamber aside of an evaporator. This article describes a new type of evaporator which combines features of EOR and ELR. To get LHP with better characteristics it is necessary to obtain an adequate thermal barrier, as already mentioned. That is for, in the new type of evaporator the CC and the evaporator core were put into separate enclosures, having hydraulic connection by a microchannel plate (Fig 2.3). The plate performs several tasks: 1) provides constant wetting of the wick; 2) it is the top cover of both evaporator and CC; 3) uniformely presses non-rigid wick material down to the evaporator’s heated surface. As can be noticed in the Fig. 2.3, liquid from the CC first is absorbed by the top microchannel plate then it moves to the to the other end of the plate where it is absorbed by the wick. So liquid most of the path flows inside relatevily large channels and only short part of the path it moves within the fine wick with high flow resistance. Such location of the CC makes possible to create thin configurations of evaporators. The thickness of the evaporator depends on the height of vapor removal channels, the height of liquid supplying microchannel plate and the thickness of the wick. Fig. 3. shows the cross-section of the compensation chamber.

2. PROTOTYPE DESCRIPTION AND EXPERIMENTAL SETUP

A miniature LHP prototype was designed and created to test the described type of the evaporator. (Fig. 4, 5). It consists of an evaporator, a condenser and connecting tubes. All connections were made by soldering and stage brazing.

The evaporator is flat and has a rectangular shape. It consists of the bottom finned copper plate, a vapor collector, a wick and the top microchannel plate.

The finned copper plate was used as a heat distribution element. Voids between the fins were used as vapor removal channels. The surfaces were produced by the patented deformational cutting method (DCM) [8]. The principle of this method is the following: The special form tool undercuts the plain surface layers of the workpiece and raises it to a certain angle by making plastic deformation.



Figure 3. Compensation chamber cross-section.



Figure 4. The LHP prototype.

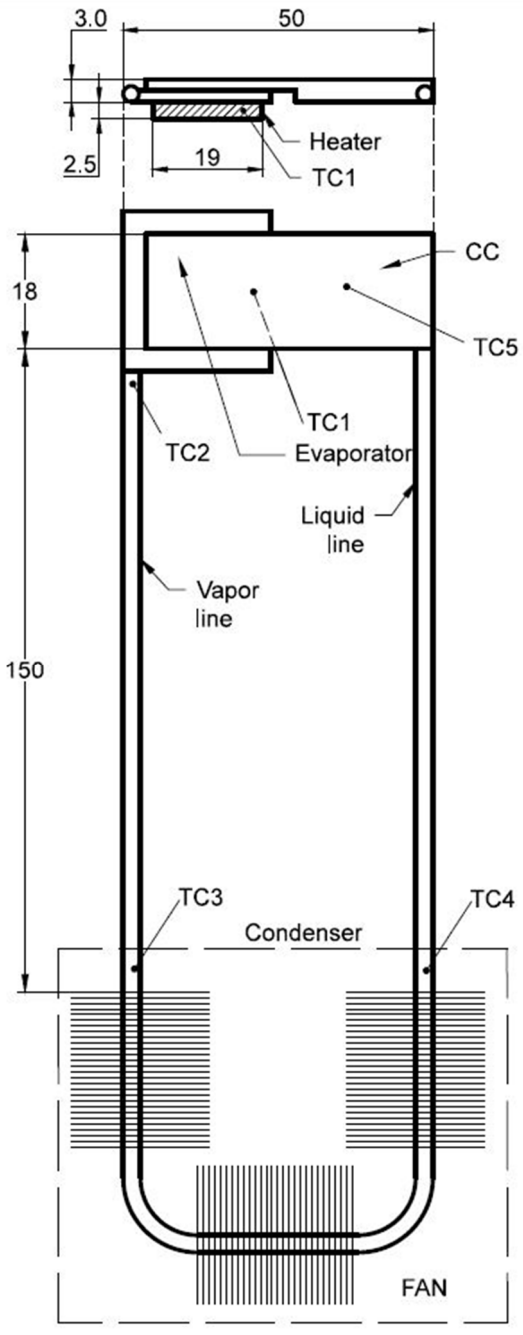


Figure 5. The LHP prototype and the heater.

Table 1. Wick properties.

Parameter	Value
Material	Glass Fiber Grade D Borosilicate
Thickness, mm	0.5
Pore size, um	2.6
Water flow, sec	5
Porosity, %	90 (undeformed)
Thermal conductivity, W/(m·K)	0.05

Layers of glass fiber filter were used as a wick in this experiment. Parameters of the material are given in Table 1.

Condenser is made of a copper tube of 2.4 mm outside diameter with copper plates soldered to it. The plates are of rectangular shape sizes 10 to 25 мм. The interval between the plates comprises 0.7 mm. The internal volume of the condenser has to be minimum to not get the requirement to create a CC of large volume. Especialy when there are strict limits on thickness of all elements, including the compensation chamber. The condenser has three zones as can bee noticed in Fig. 5.

Compensation chamber has flat design. It has smooth wall at the bottom and microchannels at the top cover (Fig. 3). The thickness of the CC does not exceed 3.0 mm. The width is 18 mm. The length is 25 mm. The internal volume of the CC must be greater or equal to the sum of volumes of the Evaporator core, the vapor line and the condenser. Flat design of CC gives greater surface area in comparison with cylindrical shape compensation chambers that improves natural convection cooling of the CC, that in turn improves the characteristics of the LHP. Parameters of the LHP are presented in Table 2.

Table 2. LHP parameters.

Parameter	Value
Evaporator shape	Flat, Rectangular
Evaporator thickness, mm	3.0
Evaporator area (length x Width), mm	25 x 50
Material	Copper/Stainless steel
Wick Material	Glass Fiber
Wick thickness, mm	0.5
Vapor removal channels (width/ depth), mm	0.1/0.7
Vapor/Liquid line Diameter (ID/OD), mm	1.8/2.4
Vapor line length, mm	150
Liquid line, length, mm	150
Condenser length, mm	130
Condenser type	Fin and tube
Working fluid	Water

3. EXPERIMENTAL PROCEDURES

Heat input was applied to the microchannel plate through a flat ceramic heater WATLOW measuring 19 mm by 19 mm, a thickness of 2.5 mm. Since the heater is made of ceramic with high thermal conductivity, the heat flow is evenly distributed thereon. The heater was linked via a power meter D5004 (accuracy ± 0.5 W) and a laboratory transformer Solby TDGC2-0.5-B. Because of the small thickness of the heater, and also considering that the heat flow from the heater to the microchannel plate is much higher than to the thermal insulation side, due to the evaporation process with a high heat transfer coefficient implemented on a plate, it is assumed that additional measures to clarify the magnitude of the heat flux are not required. Type-L thermocouples were used to measure the temperature. Data from the thermocouples were acquired using a data acquisition device L-card LTR 27. Thermocouples were mounted as shown in Fig. 5.

Before filling the internal surfaces of the loop heat pipe were cleaned with isopropanol. Then, the internal space of the LHP was dried by heating in an oven to 150 C. For the filling a copper vessel of cylindrical shape was used (Fig. 6).

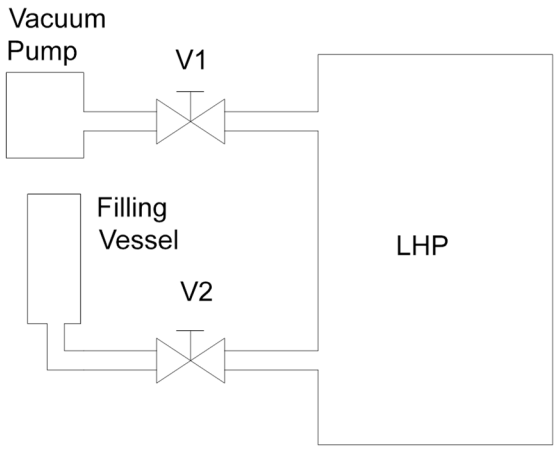


Figure 6. The filling procedure.

First, the filling vessel was filled with working fluid in an amount of from 1.2 to 1.6 ml. The working liquid was water. It was deionized and degassed by boiling. After the filling vessel was linked to the LHP, the valve 2 was shut off. Then, the liquid inside the filling vessel was freezed by applying low-boiling liquid spray FREEZER. After complete freezing the valve V2 was open and a vacuum pump produced vacuum inside the LHP and the filling vessel. After vacuumized the LHP was sealed by closing the valve V1. Then the valve V2 was open to let melted liquid flow from the filling vessel into the LHP. To ensure that all liquid escaped from the filling vessel it was turned upside down and its end was heated. Then the valve V2 was shut off and the filling procedure was completed. The filling volume was taken approximately equal to the volume of the CC. But then it was altered based on the experiments.

All connections were made by soldering and stage brazing. One has to overcome a set of challenging tasks during the loop heat pipe production and assembly processes. Here are some of them: implementation of all part and assembly tolerances; proper position of the internal components of the LHP; continuos contact between the wick and the heated surface; vacuum tightness; bypasses of vapor from the evaporator to the CC; brazing or soldering defects; cleanliness of internal surfaces of the LHP; chemical compatibility of materials and working fluid; non-condensable gases; oxidation of the wick.

Since the non-metal wick was used, oxidation was not the issue for the described evaporator, as well as chemical compatibility between the wick and structure materials/working fluid. The non-metal wick is soft material, that is why its properties, such as porosity, permeability depends on the degree of its compression. The positive effect is that the assembly of the evaporator with a non-rigid wick compensates errors accumulated during the production of component parts of an LHP, i.e. manufacturing tolerances of the parts can be given greater than in the case of rigid metal wicks. The soft wick, like a rubber gasket fills all gaps and ensures good wick/heated surface contact.

All tests were performed in horizontal position of the LHP in the gravity field. Tests were conducted under similar experimental conditions which included ambient temperature (23 ± 2 °C), fan type and flow characteristics (axial type with max 0.1 m^3/min at 5V, 0.1 A). The condenser zone was separated from the evaporator's zone by a wall to avoid any influence of the flow from the fan to the compensation chamber.

4. RESULTS

Tests performed for heat loads from 5 to 50 W. The results are shown for the filling volume 1.4 ml. Fig. 7 shows the temperature of the heater (thermocouple TC_1) of the LHP for all heat loads. Temperature did not exceed 90 °C for heat load Q=50 W, that result is comparable with the results in [2, 3]. The same can be said about values of the total thermal resistance R_t (Fig. 8), which was calculated as follows:

$$R_t = \frac{T_j - T_a}{Q} = \frac{TC_1 - T_a}{Q} \quad (1)$$

Here, the temperature T_j is the junction temperature that corresponds to the temperature of the thermocouple TC_1. T_a is the ambient temperature. The total thermal resistance R_t expresses the overall heat transfer performance of the cooling device. Another important characteristic of an LHP is its own thermal resistance R_{LHP} (Fig. 8):

$$R_{LHP} = \frac{T_{ev} - T_{cond}}{Q} \approx \frac{TC_1 - (TC_3 + TC_4)/2}{Q} \quad (2)$$

Here, T_{ev} is the temperature of the evaporator that is approximately equal to TC_1, T_{cond} is the temperature of the condenser. Since no thermocouple was mounted to the evaporator's bottom surface due to space limitations, the author used the heater's thermocouple TC_1 for the calculation of RLHP. So the contact resistance between the heater and the evaporator was also included into RLHP. The thermal resistance of the evaporator (Fig. 10) can be calculated as:

$$R_{evap} = \frac{T_{ev} - T_v}{Q} \approx \frac{TC_1 - TC_2}{Q} \quad (3)$$

This value also includes the contact resistance between the heater and the evaporator.

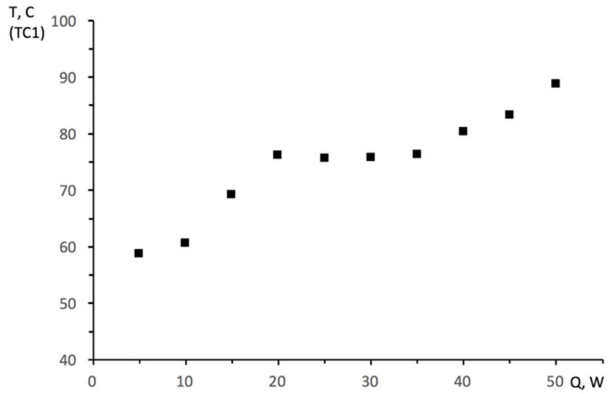


Figure 7. The heater's temperature (TC_1).

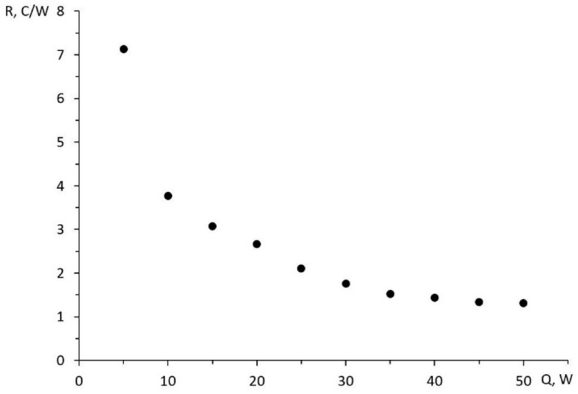


Figure 8. The total thermal resistance R_t.

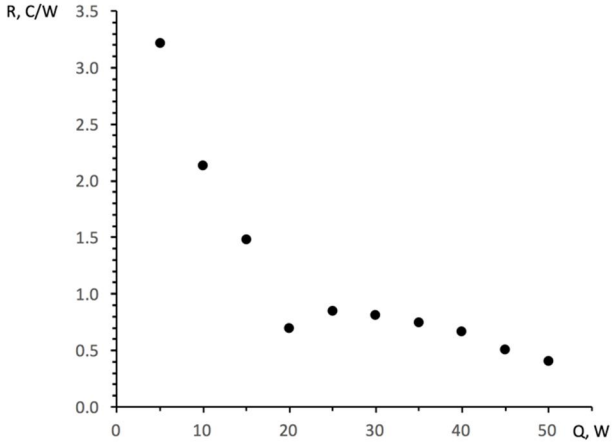


Figure 9. The thermal resistance of the LHP R_{LHP}.

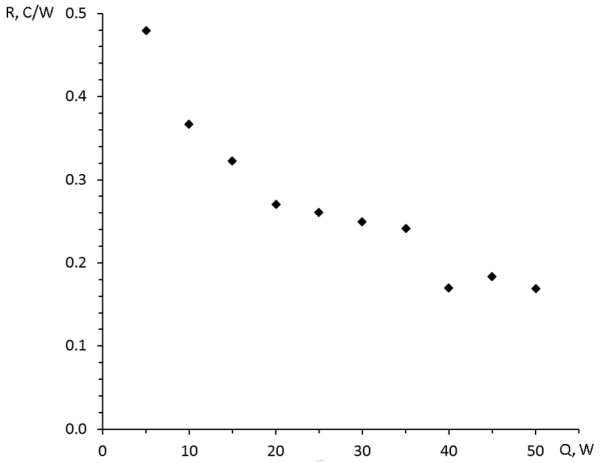


Figure 10. The thermal resistance of the evaporator R_{evap}.

5. CONCLUSIONS

This paper experimentally proves the thesises of the previous papers [5 and 9] and describes tests of the new type of evaporator with the non-metal wick.

The thickness of the evaporator described is equal to 3 mm. But this value is not the limit. By varying the heights of vapor removal channels and the height of the fins of the supplying microchannel plate, as well as the thickness of the wick, it is possible to create Evaporators thinner than 3 mm.

It was found that the LHP can transfer heat at low heat loads due to relatively distant location from each other of evaporator core and the compensation chamber. Such colocation makes possible to create greater temperature difference between these elements even at low heat loads.

Flat design of the compensation chamber gives additional means for using the natural convection mechanizm for cooling the compensation chamber's surfaces, and by this reduce temperature of the evaporator.

The described new type of evaporator showed

results comparable to the results of other researchers [2, 3]. Hovewer, this new design of the LHP leaves possibility for further reduction of the thickness of the evaporator.

ACKNOWLEDGEMENT

The author would like to thank Dr. Nikolay N. Zubkov (Bauman Moscow State Technical University) for his support in providing the experiments with microchannel surfaces produced by the DCM.

REFERENCES

[1] Maydanik Yu. F., Vershinin S. V., "Development and tests of ammonia Miniature Loop Heat Pipes with cylindrical evaporators," *Applied Thermal Engineering*, Vol. 29, Issues 11–12, August 2009, pp. 2297-2301.

[2] Lin, Z.R., Lin, W.Z., Zhang, L.W., Wang, S.F., "An experimental study on applying miniature loop heat pipes for laptop PC cooling," *Semiconductor Thermal Measurement and Management Symposium (SEMI-THERM)*, 2013 29th Annual IEEE, 17-21 March (2013), pp. 154-158.

[3] Singh, R., Akbarzadeh, A., and Mochizuki, M., "Thermal Potential of Flat Evaporator Miniature Loop Heat Pipes for Notebook Cooling," *IEEE Trans. Compon. Packag. Technol*., 33(1), (2010), pp. 32–45.

[4] Yu. Maydanik, S. Vershinin, M. Chernysheva, S. Yushakova, Investigation of a compact copper–water loop heat pipe with a flat evaporator, *Applied Thermal Engineering* 31 (16) (2011) 3533–3541.

[5] Yakomaskin A.A., Zubkov N.N., «Variants of vapor removal channels organization in inverted meniscus capillary evaporator», *Second International Conference "Heat Pipes for Space Application" (2HPSA)*, (2014).

[6] Nagano, H., Ogawa, H., Fukuyoshi, F., and Nagai, H., "Fabrication and Testing of a Small Loop Heat Pipe With a Plastic Wick," *proceedings of International Conference on Heat Pipes for Space Application*, Moscow, (2009).

[7] Maydanik Yu.F., Chernysheva M.A., Pastukhov V.G., Review: Loop heat pipes with flat evaporators, *Applied Thermal Engineering*, (2015).

[8] Zubkov N. N., and Ovchinnikov A. I., European patent for a "Method of Producing a Surface With Alternating Ridges and Depressions and a Tool for Carrying Out the Said Method," European Patent No. 0,727,269, pub. Date 21 august (1996).

[9] Yakomaskin A.A., Afanasiev V.N., Zubkov N.N., Morskoy D.N., "Investigation of Heat Transfer in Evaporator of Microchannel Loop Heat Pipe", *Journal of Heat Transfer*, vol. 135, (2013).

Experimental Study on the Driven Mechanism of a Vapor-liquid Separated Flat Loop Heat Pipe Evaporator

Shuo Zhao[1], Kai Zhu[2], Mingzhu Zheng[3], Yabo Wang[4], Yang Yang[3], Jie Wei[5]

[1] Ph.D. candidate, School of Environmental Science and Engineering, Tianjin University, 92 Weijin Road, Nankai District,Tianjin, P.R.China , 300072, Phone: +86-18920866516, zhaoshuo6@tju.edu.cn

[2] Professor, Tianjin Key Laboratory of Refrigeration Technology, Tianjin University of Commerce, Tianjin 300134, China

[3] Graduate student, Tianjin Key Laboratory of Refrigeration Technology, Tianjin University of Commerce, Tianjin 300134, China

[4] Lecture, Tianjin Key Laboratory of Refrigeration Technology, Tianjin University of Commerce, Tianjin 300134, China

[5] Dr. Fujitsu Advanced Technologies Limited, Japan

Abstract

The LHP with new driven mechanism is put forward, and the wick have no contact with the heated bottom in the evaporator. If a heat load is supplied to the evaporator, the liquid begins to evaporate from that clearance, as evaporating chamber, and the working fluid in the LHP circulate in one direction by the interaction between the evaporation interface and the condensation interface, of which the former works as a “heat source” and the later serves as a “heat sink”. The circulation of working fluid is driven by the force generated by liquid phase change in the evaporating chamber. Fig.1 shows the schematic diagram of the evaporator. An open cycle LHP with visual flat evaporator was developed to study the new driven mechanism, in which use water as working fluid. Fig.2 shows the schematic diagram of the experimental apparatus. A series of experiments for the characteristics of startup and operation under variable conditions with different heat load were carried out. The factors affecting the performance of the LHP were analyzed. The experimental results show that the operation is influenced by the heating power and the working fluid charge quantity, especially the height of the evaporating chamber. When the height is too low, the chamber is full of liquid making the LHP can’t be operated. However, if the chamber is too high, the hot vapor will penetrate in to the wick for the high pressure. Also the evaporating interface isolated from the wick help to improve the high back-conduction in the traditional LHP.

Keywords: Loop heat pipe, Phase-change driven mechanism, Visual study, evaporating chamber

1. INTRODUCTION

Traditional Loop Heat Pipe (LHP) is a passive cooling device mainly applied to the heat management process in specific space application and electronic device, simply by implementing closed circulation driven by capillary force. LHP concept was firstly put forward by Yu. F. Maydanik[1] based on the optimization of conventional heat pipe in 1972[2]. LHP evaporators, depending on the purpose, shape, heat source dimensions and also working fluid used, may be flat or cylindrical. Generally, flat evaporators have more advantages than cylindrical evaporators since most surfaces of the heat sources or devices needing to be cooled are flat type.

An excellent overall LHP performance is contributed by the good start-up and operational performance and lower thermal resistance. Start-up performance usually can be evaluated with the start-up time and the temperature overshoot during the start-up process[3]. Temperature overshoot reflected in the temperature results from the fact that the evaporation zone is not established yet, leading to a wall temperature rise and postponing the start-up time[3]. Overall, heat load, location of the vapor-liquid interface in the wick and the thermal conductivity of the wick have a vital influence on start-up process. Heat leak, an intrinsic phenomenon during operational process of LHP[4], has a big effect on LHP changeable heat load working situation. The heat leak heats the working fluid in the compensation chamber, resulting in a temperature rise in the evaporation zone and hence lowers the heat transfer capacity[5].

Many scholars attempt to reveal the mechanism of the loop heat pipe operation[6-9], optimizing the startup process, improve the loop heat pipe performance and reliability, and so on through a variety of research methods. By building loop heat pipe experimental device, using experimental methods LHP research and analysis it is always an effective research methods, especially in people not yet fully grasp LHP operation mechanism of the case [2]. With the finite element numerical algorithms, simulation technology and computer hardware and software technology has undergone rapid

development, finite element simulation and LHP aided research and design has become one of the scientists of the effective means to improve efficiency. In particular, played in the heat and mass transfer process of the wick in the working fluid, the temperature distribution in the wall like a role in promoting the development of LHP technology also played a very important role in[7]. But relying on the loop heat pipe is a porous wick capillary pressure head in the solid matrix and the working fluid due to surface tension and other factors driving the formation of the working fluid circulation of the closed loop two-phase heat transfer device. LHP systems are coupled to each other by a plurality of parts made in LHP startup and during operation, the interaction between the various parts, the operating mechanism is very complex[3]. Therefore, I want to first of all through the establishment of a complete LHP mathematical model, numerical calculation by the method of numerical simulation of the entire LHP be used to accurately describe its operation mechanism and features very difficult. So this paper by designing and building a set of open-loop heat pipe thermal evaporator experimental test system to working pair herein phase becomes the main driving force of the LHP during startup, operation, and stable process conditions change during operation the experimental phenomena and experimental data collation and analysis, and strive to truly reflect the loop heat pipe evaporator operating mechanism and performance features described herein.

Flatbed loop heat pipe After downsizing, whether the normal start and maintain stable operation, it is essential for high heat flux cooling devices to maintain continuous and efficient. Chapter 2 will be designed to work with the quality of this chapter becomes the main driving force of the loop heat pipe evaporator experimental study, and then get it up and running during the performance parameters and to determine the best technical solution, so as to further promote the optimization and development phase working fluid becomes the main driving force of LHP technology has laid a good experimental basis. This chapter Non capillary suction force of the drive loop heat pipe heat transfer mechanisms for the purpose of the flat heat pipe evaporator bottom surface of the wick entirely separate, constitute a phase change space-vapor chamber, the visualization system devices studied. In order to focus on the steam chamber vapor phase change characteristics of the loop heat pipe design for the open system. Research on the evaporation chamber operating parameters of the relationship between the height of the heat pipe start, through the steam chamber pre-boiling, boiling phase and the stabilization phase observation and experimental analysis of three processes, as well as through the evaporator loop heat pipe thermal resistance and total thermal resistance calculations to determine the ideal height of the evaporation chamber. And verification: the vapor phase change interface can not suck produce relatively large steam-driven pressure head within the liquid core, and if the bottom of the steam chamber of the heating surface, the phase interface, as well as the wick of the three operating parameters coupling, can effectively improve the LHP in the application process of the overall performance.

In this paper, a phase change space is placed between wick and the heating surface to help remove vapor-liquid interface from wick, and utilizing phase change force to drive working medium circulation at the same time. As liquid continually drop in the heating surface and vapor get away from evaporation chamber (EC), high efficiency heat transfer was obtained through relative separation of heat and mass transfer in the wick. Besides that, the visualization of evaporator is designed to observe the evaporation and flow in the evaporator, and start-up and power increasing experiment were conducted and thermal resistance was also analyzed. Three main experimental stages, pre-boiling, boiling and steady stage were experimentally observed during start-up process. Meanwhile, the experimental results showed that steam drive head resulted from vapor-liquid interface separated from the wick helped to improve its thermal performance when the wick, vapor-liquid interface and the bottom of the evaporator arrived at a reasonable situation.

2. EXPERIMENTAL

The visualization experimental setup of flat-loop heat pipe evaporator consist of the liquid supply system, visualization flat-loop heat pipe evaporator, steam cooling systems, simulation CPU heat source system, data acquisition and processing system, DC composed of power supply (100V, 10A), and some other high-speed CCD camera, shown in Figure 2.

A phase change space is placed between wick and the heating surface to help remove vapor-liquid interface from wick, and utilizing phase change force to drive working medium circulation at the same time. As liquid continually drop in the heating surface and vapor get away from evaporation chamber (EC), high efficiency heat transfer was obtained through relative separation of heat and mass transfer in the wick. Besides that, the visualization of evaporator is designed to observe the evaporation and flow in the evaporator, and start-up and power increasing experiment were conducted

and thermal resistance was also analyzed. Three main experimental stages, pre-boiling, boiling and steady stage were experimentally observed during start-up process.

By changing the flat evaporator structure left between the bottom surface of the evaporator wick gap constitutes a phase transition space (steam chamber), the outlet pressure of the steam chamber is provided with a buffer space (equalization chamber), aspiration there is no liquid-vapor interface of the inner core, the steam chamber because the phase change working fluid to generate steam driving force, reflux condensate through the wick constantly dropped the steam chamber to generate capillary suction force (reflux condensate in capillary suction force under the incessant trickle vapor chamber and the heating surface is heated and evaporated) causing relative separation heat and mass transfer, the steam chamber is formed by a phase change working fluid to generate energy conversion and low-impedance drive the working fluid circulating new physical mechanism. This article from the theoretical innovation of view, the establishment of a flat-loop heat pipe visualization evaporator for a loop heat pipe evaporator experimental system follows a new physical mechanism under the action were to start and variable condition experiment, and the thermal analysis.

3. RESULT AND DISCUSSION

3.1 the start-up specification of LHP

LHP presence during startup with a lot of very complex heat and mass transfer phenomena, including redistribution and cycle working fluid circulating in the various parts of the loop heat pipe, accompanied by complex during nucleate boiling, evaporation and condensation phase transition and other processes, and the above-mentioned phenomenon has been extended and will be accompanied by the entire LHP system have reached a relatively stable operation of state. When

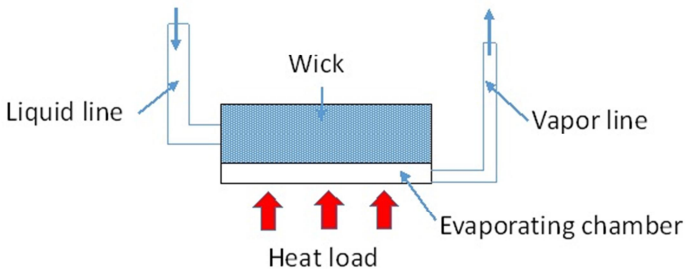


Fig.1 Schematic diagram of the evaporator

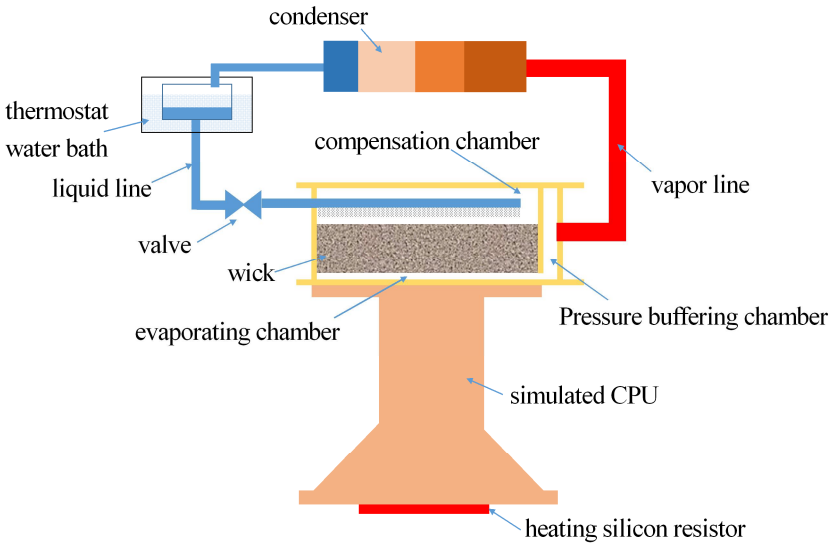


Fig. 2 schematic diagram of the experimental apparatus

the analog CPU heat source heat transfer to the evaporator plate evaporator does not require any other treatment, when required to meet its start condition, the evaporator will achieve spontaneous start. Loop heat pipe evaporator before starting generally require a long lead time to complete the boot process[6] . Throughout the course of the loop heat pipe start, the entire range of the evaporation temperature due to heat accumulation and will be continuing to rise, until the evaporator refrigerant superheat able to achieve the desired start and complete a phase change, absorbs heat and heat well passing out the evaporator, the final operation of the system to achieve steady operating temperature. As long as the steam Evaporating memory space, and the load acting on the heat transfer to the bottom of the evaporator wick internal meniscus evaporated at phase transition will occur immediately. To ensure effective evaporation phase change generated when inside the evaporator filled with liquid refrigerant, the liquid refrigerant must have a certain degree of superheat in order to ensure the above-mentioned phenomenon. Start time for the entire loop heat pipe system, it is from the thermal load applied to the system completes the required start time. Start with less time spent is one of a judgment loop heat pipe system performance advantages and disadvantages of the indicators, in addition to the smaller loop heat pipe also start superheat researchers want.

Complex phenomenon loop heat pipe internally generated during the start making it in the boot process can be disturbed by various factors, to start the process of experimental research can further help understand the mechanism starts, clear the various factors that impact on the startup process and different after starting the start situation affect the stable operation of all essential[5]. LHP system itself is relatively more complicated, the evaporator section generates an input phase change of steam condensing section, condenser section of the liquid refrigerant output and an input evaporator section, in addition, other intermediate LHP occurs during evaporation condensation the working fluid transfer and transport of heat input and output constitute the heat load and the structure of the loop heat pipe outer relevant[5]. Therefore, this paper in order to avoid transmission and refrigerant condensers and other parts bring additional influence, in the case of open-loop heat pipe loop, this section mainly through a series of experimental test results of different height under the loop vaporization chamber heat pipe system startup characteristics under different starting power, as well as inside the evaporator wick and the vapor-liquid two-phase distribution. Flatbed LHP started as a result of the experiment is good or bad is an important basis for judging the merits of its performance, as well as whether the normal start, also decided on a flatbed loop heat pipe can be applied in practical engineering. Traditional LHP startup process can be roughly divided into the following three stages[4]:

(1) a phase change inside the evaporator head sufficient vapor pressure of the liquid working steam channel, the steam line and the front part of the area of the condenser pressure to the evaporator in the compensation chamber;
(2) the wick capillary suction force is increasing, resulting in capillary pressure head sufficient to complete the drive fluid circuit fluid circulation;
(3) LHP complete all the startup process, the entire LHP system will eventually reach steady state operation.

In the course of the experiment the loop heat pipe system can start LHP judgment there are two standards for reference[10]:

(1) steam outlet temperature rose sharply and eventually reaches a stable value, indicating that the steam pipe and the steam is saturated steam occurs;
(2) loop heat pipe fluid capable of forming a positive closed cycle.

In addition, after the successful launch its own flatbed LHP may be in two different operating status [17]:

(1) the system is in steady state operation, LHP each part of the temperature measurement points remained stable throughout the operating process;
(2) the system is in a state of periodic temperature fluctuations, LHP each part of the temperature measuring point temperature temperature fluctuations occur in a certain period of operation of the entire process.

Figure3-1 shows the experimental device measuring point temperature curve during start-up over time. After the start of the experiment to simulate a sharp rise in CPU temperature heat source and the evaporator plate, the slow rise of other measuring point temperature, temperature profile at the beginning of decline is because the experimental process heating power adjustment due to instability. From the experimental data showed: Analog CPU core temperature of the heat source and the evaporator plate the average temperature difference is less than 5.8℃,while the evaporator plate three thermocouple temperature difference of up to 2.4 ℃, a minimum of 1.0 ℃, visible, although the heating

power increases doubled, but the bottom of the evaporator average temperature effect is still good. When heated to 8-9 minutes, evaporation chamber has more bubbles and more bubbles merge to a single bubble or multiple bubbles between the equalizing chamber main propulsion. When heated with 58.5W power as part of the saturated liquid vaporization chamber are pushed to the pressure chamber at a pressure difference, when the temperature fluctuation frequency and amplitude are small. When heated to about 10 minutes, a large amount of bubbles continuously generated in the evaporation chamber, steam outlet temperature experienced a relatively large fluctuations after a relatively short time in a relatively stable state. At the same time the steam pipe outlet temperature reaches the saturation temperature, saturated steam through the steam pipe into the cooling water tank and has been allowed to cool. At the same time, the liquid supply system needs to start to replenish the liquid supply chamber due to evaporation of liquid refrigerant evaporates declining phase change working fluid. You can determine at this time the cycle has started up completely, and the start time of 760s. In addition, Figure 3-2 shows, 205 and 206 due to the constant temperature measurement points to supply fluid, cyclical fluctuations in temperature, which is caused by the mixing of hot and cold, but temperatures are lower than 90 ℃, the wick is no bubble produce. For fluid temperature to maintain a certain degree of supercooling can be effectively suppressed, and back through the thermal equalizing chamber and the compensation chamber separator drain heat to avoid boiling generated in the compensation chamber to block the wick in the normal flow of the working fluid during transport . When Visualization flat evaporator in thermal equilibrium with the environment, and the evaporator reaches a steady state operation, the steam outlet in the form of temperature fluctuations into a high-frequency, low amplitude, the steam temperature is basically in a stable state. Analysis, because this time the various parts of the evaporator and the working fluid also in thermal equilibrium, continuous and stable bubble generation, steam generated in the evaporation chamber to push the liquid pressure equalization chamber, thin film, this time sparkling group constantly formed at the center of heated floor area of Chip loop heat pipe is mainly used in high heat flux cooling device cooling equipment in the field, it is inevitable in the course of operation of these devices will appear in the start and stop of power equipment, power changes, high heat flux devices are generally related to its own usage[9]. This requires a strong cooling equipment

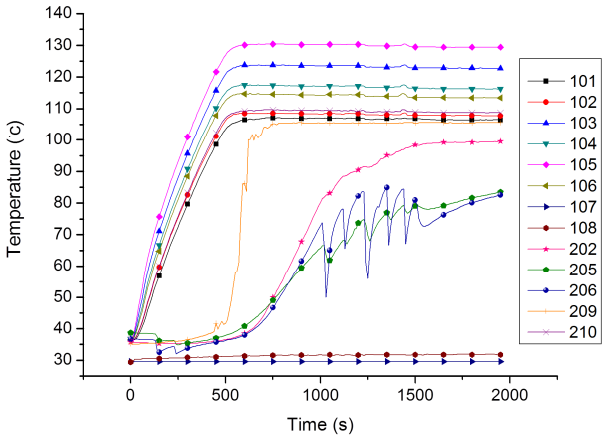


Fig.3-1 Start-up specification under constant hear load

variable parameter operation, when the outside heat changes, cooling equipment can quickly be self-regulation enables a short time and again to reach thermal load matching system. Variable Working Conditions response characteristics of the loop heat pipe long-running process is very important, especially applied to the CPU cooling process loop heat pipes, loop heat pipe, if not timely thermal load applied to the heating surface can cause the system to respond fail, causing CPU due to inability to timely away the heat and makes itself a sharp rise in temperature, which can withstand temperatures of more than burned.

Figure 3-2 evaporation chamber height of 3mm, the figure shows the evaporator process variable parameter operation began in the output power from 20W to 20W and increase incrementally until 220W evaporator during each measuring point temperature curve over time. As it can be seen from Figure 3-2, when the heating power is less than 60W, a sharp rise in the simulation phase CPU temperature heat source and the evaporator plate, the entire evaporator under constant heating simulation CPU heat source and heat build-up in the process, when the liquid working quality is difficult to achieve the desired superheat start, nucleate boiling is difficult to form. When the heating power of about 60W, steam temperature begins to fluctuate due to the heated liquid working gas remaining in the overflow from the working fluid caused. When the heating power at 80W, evaporator with the environment by natural convection and radiation heat sinks heat has reached the limit, with the bottom of the heating power increases the evaporation chamber began to produce sporadic bubbles, resulting in increased steam outlet temperature fluctuations occur until the bubble continuous emergence of the final degree steam outlet temperature fluctuations

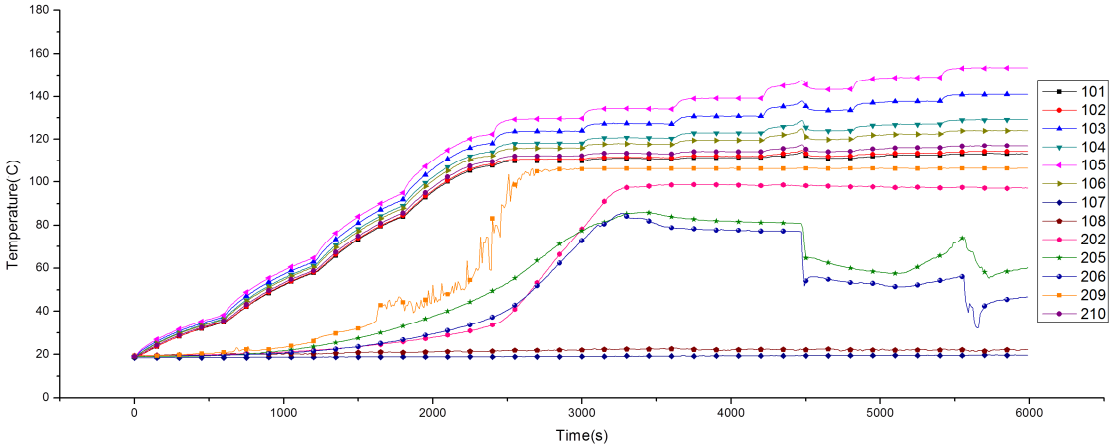


Fig.3-2 Start-up specification under Variable heat load

waning. When the heating power of 100W, the system needs to start for liquid evaporation chamber liquid refrigerant superheat reaches the desired start and stable nucleate boiling steam generation increased more obvious cause, the bottom of the steam chamber to form a film boiling. In this case the steam pipe outlet temperature and steam saturation temperature is closer to the beginning of a large amount of steam into the cooling water tank for cooling. Thereafter heating power continues to increase, with the bottom of the vaporization chamber compensation chamber capable of maintaining a stable thin film nucleate boiling. Figure 3-18, after the heating power reached 140W, evaporator plate temperature with increasing heating power has increased slightly (101, 102 and 210 as shown in Figure 3-2), then gradually increase the amount of liquid supply (205, 206 as shown in Figure 3-18), the steam temperature has remained stable throughout the evaporator loop more stable. When the heating power of 220W, the floor still maintain low temperature growth, the entire evaporator through evaporation chamber stable nucleate boiling heat away continuously to maintain normal operation. The 160W when the base plate and simulation CPU temperature Figure 3-2 brief upward trend, which is due to the supply amount of evaporation does not match, resulting in thin film backplane, some regions even lack of fluid, resulting heat can not be evaporated away result, after increasing the amount of liquid supply, backplane and simulation CPU temperature gradually returned to normal.

3.2 Evaporator thermal resistance

Figure 3-3 through Figure 3-6 From the final heating power of 58.5W evaporator thermal stability at 0.152 ℃ / W, heating power is 113.5W evaporator thermal stable at 0.053 ℃/W, heating power when 174.5W evaporator thermal stability at 0.048 ℃ /W, the heating power is 201.1W evaporator thermal stability at 0.036 ℃ / W.

Figure 4-7 shows the height of 3mm, the loop heat pipe system resistance curve evaporator evaporator chamber changing conditions during operation. As can be seen from Figure 4-7 in the vaporization chamber when the trend is 3mm thermal resistance with approximately 1mm change when similar. When the heating power of about 80W, evaporator, thermal resistance appeared significantly reduced. When the final heating power of 220W, thermal evaporator was maintained at 0.041 ℃/W. Figure 4-7 shows the height of 3mm, the loop heat pipe system curve of the total thermal resistance of the vaporization chamber in the process variable condition. As it can be seen from Figure 4-8, when the total thermal resistance 0-60W also experienced cyclical fluctuations. With increasing heating power, the total thermal resistance changes gradually leveled off, culminating in the heating power of 220W, the total thermal resistance remained at 0.406 ℃ / W or so.

4. CONCLUSIONS

Loop heat pipe system startup and variable parameter operation results were carried collated and analyzed. The results show:

(1) loop heat pipes start to go through a phase accumulator and to achieve a certain power to start, when the thermal load is applied to the base plate of the heat load exceeds the start, reaching sufficient starting superheat temperature between the bottom plate and the liquid refrigerant, circulation can be established. With increasing heating power, the start-up time is gradually

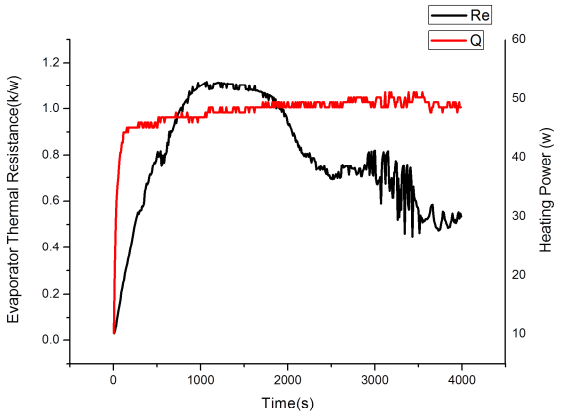


Fig.3-3 Evaporator thermal resistance (58.5W)

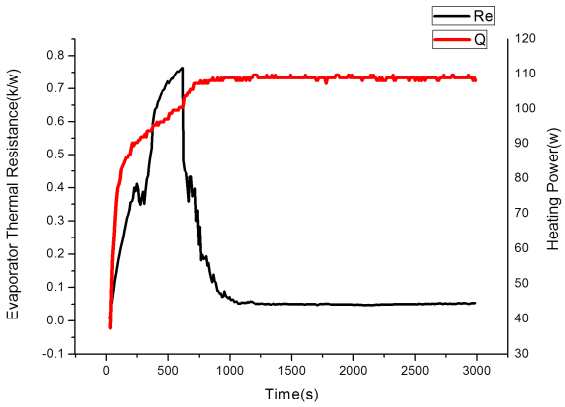


Fig.3-4 Evaporator thermal resistance (113.5W)

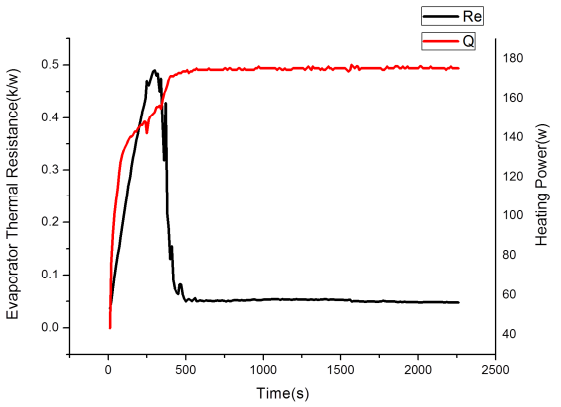


Fig.3-5 Evaporator thermal resistance (174.5W)

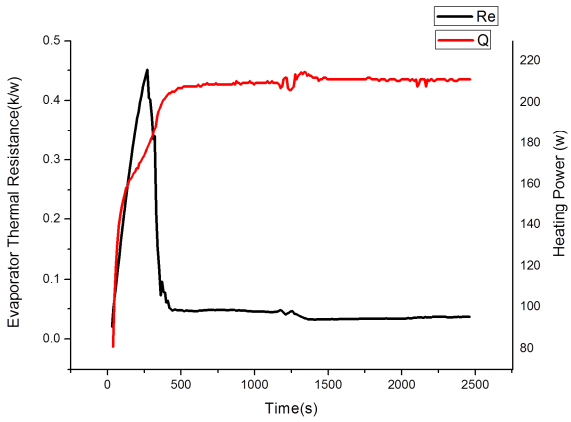


Fig.3-6 Evaporator thermal resistance (201.5W)

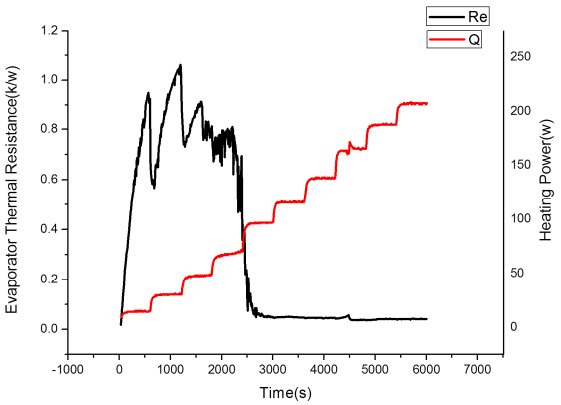


Fig.4-7 Evaporator thermal resistance (Variable)

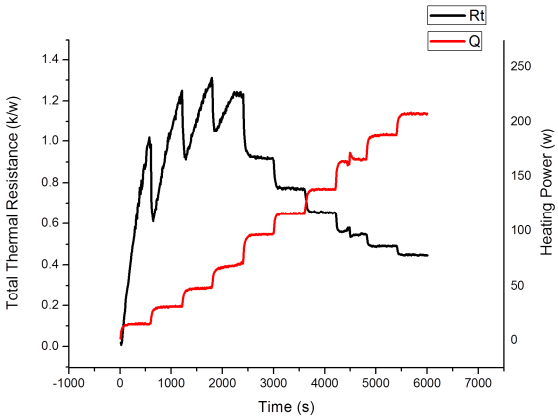


Fig.4-8 Total thermal resistance (Variable)

shortened, regardless of the size of the vaporization chamber height;

(2) the height of the evaporator vaporization chamber floor temperature level will have an impact, higher evaporation chamber highly beneficial to drips and steam discharged from the evaporation chamber, the lower the evaporation chamber highly beneficial to inhibit the loop heat pipe dry-up phenomenon generated by the evaporator. With increasing heating power, the evaporator at the average temperature of the soleplate gradually rises stable, this phenomenon has nothing to do with the height of the evaporation chamber;

(3) through the evaporator visualization experiments we found that with increasing heat flux plate, liquid vaporization chamber exhibits typical boiling heat transfer of three processes: natural convection zone, nucleate boiling over boiling zone and area;

(4) vaporization chamber height greater impact on the total thermal resistance and thermal evaporator. In the experimental heating range, different vaporization chamber height, the total thermal resistance and thermal evaporator can effectively maintained at a low level at a higher heating power. However, with the increase of the height of the vaporization chamber, particularly when the vaporization chamber height 5mm, when the heating power of 200W, the dry out phenomenon occurs vaporization chamber, the vapor pressure of the liquid due to the vaporization chamber a large head can not be dropped on the floor, while the other three vaporization chamber height at the same heating power, wick liquid still valid dripping on the floor, forming a boiling heat transfer.

(5) in the production of this type of loop heat pipe, we should uphold in the loop heat pipe cooling equipment to meet the maximum thermal load of the premise, as far as possible the use of higher vaporization chamber height, so conducive to the discharge of steam from the evaporation chamber , it is possible to reduce the temperature of the evaporator cavity floor and reducing the evaporator loop heat pipe thermal resistance and total thermal resistance purposes.

ACKNOWLEDGEMENT

Financial grants from the National Natural Science Foundation (loop fluid phase change heat transfer mechanism of power-driven, No.51376137) are gratefully acknowledged.

REFERENCES

[1] Xiaojun Quan,Ming Gao, Ping Chenget al. An experimental investigation of pool boiling heat transfer on smooth/rib surfaces under an electric field[J]. International Journal of Heat and Mass Transfer. 2015. 85: 595-608

[2] Shuai Gong,Ping Cheng. Numerical simulation of pool boiling heat transfer on smooth surfaces with mixed wettability by lattice Boltzmann method[J]. International Journal of Heat and Mass Transfer. 2015. 80: 206-216

[3] Charles H. Johnson,Cheng Ping. Possible similarity solutions for free convection boundary layers adjacent to flat plates in porous media[J]. International Journal of Heat and Mass Transfer. 1978. 21(6): 709-718

[4] W. J. Minkowycz,Cheng Ping. Free convection about a vertical cylinder embedded in a porous medium[J]. International Journal of Heat and Mass Transfer. 1976. 19(7): 805-813

[5] Yu. F. Maydanik. Loop heat pipes[J]. Applied Thermal Engineering. 2005. 25(5-6): 635-657

[6] Mishkinis Donatas,Sodtke Christof,Ochterbeck Jayet al. Non-dimensional Analysis and Scaling Issues in Loop Heat Pipes [M] American Institute of Aeronautics and Astronautics, 2003

[7] Randeep Singh,Thang Nguyen,Masataka Mochizuki. Capillary evaporator development and qualification for loop heat pipes[J]. Applied Thermal Engineering. 2014. 63(1): 406-418

[8] Leonard L. Vasiliev. Heat pipes in modern heat exchangers[J]. Applied Thermal Engineering. 2005. 25(1): 1-19

[9] Xianping Chen,Huaiyu Ye,Xuejun Fanet al. A review of small heat pipes for electronics[J]. Applied Thermal Engineering. 2015:

[10] Yu. F. Maydanik, M. A. Chernysheva, V. G. Pastukhov. Review: Loop heat pipes with flat evaporators[J]. Applied Thermal Engineering. 2014. 67(1-2): 294-307

[11] Mariya A. Chernysheva,Yury F. Maydanik. 3D-model for heat and mass transfer simulation in flat evaporator of copper-water loop heat pipe[J]. Applied Thermal Engineering. 2012. 33-34: 124-134

[12] Yu. Maydanik, S. Vershinin, M. Chernyshevaet al. Investigation of a compact copper–water loop heap pipe with a flat evaporator[J]. Applied Thermal Engineering. 2011. 31(16): 3533-3541

[13] Zhu Kai, Yang Yang, Wang Ya Bo, Wei Jie. Experimental Investigation and Visual Observation of A Vapor-liquid Separated Flat Loop Heat Pipe Evaporator [J]. Applied Thermal Engineering.

Development and Mass Production of Loop Heat Pipes

Yury F. Maydanik[1*], Arkadiy V. Ivanov[2] and Mikhail Yu. Maidanik[2]

[1] Head of laboratory, Institute of Thermal Physics, Ural Branch of the Russian Academy of Sciences, 107a Amundsena St., Yekaterinburg, 620016, Russia
[2]Thercon-LHP, Ltd., Russia, lhp@tcontr.com

Abstract

Loop heat pipes (LHPs) are passive highly effective heat transfer devices. Thanks to their outstanding thermal characteristics and the ability to adapt to various application conditions, LHPs have been attracting developers' and researchers' attention during many years. A lot of various modifications of these devices have been developed by now. However, LHP mass production was bounded by their relatively high price compared to conventional heat pipes. Therefore, the development of new manufacturing techniques for inexpensive LHPs, suitable for mass production, is a crucial task. This paper contains the information about miniature LHPs mass production, launched in 2014 in Russia.

Keywords: Electronics cooling; Loop heat pipe; Mass production; Thermal control system

1. INTRODUCTION

Loop heat pipes (LHPs) were first developed for thermal control systems of airspace engineering in 1972 in the Former Soviet Union [1]. As early as 1978-79 a small series of these devices with acetone as a working fluid was produced. In 1989 the world's first flight experiments with LHPs were conducted aboard the Soviet spacecrafts "Gorizont" and "Granat" which demonstrated the operating capacity of the given devices in space conditions [2]. At the present time several hundreds of LHPs are successfully operating in thermal control systems of spacecrafts [3-5]. However, they are quite expensive devices which cannot be considered as an object for mass production and application.

Early in the 2000s new challenges appeared which were connected with the growth of heat loads of components of microelectronics, microwave engineering, LEDs, etc. Miniature LHPs with evaporators 6-10 mm in diameter and vapor lines 2-3 mm in diameter, which had a capacity of up to 200 W and were adapted to mass production, were created in response to this [6, 7]. Compact copper-water LHPs with flat evaporators and a capacity of about 1 kW and above were also created [8].

2. MANUFACTURING OF LHPS

LHPs can be manufactured with different working fluids: water, ethanol, heptane, acetone, ammonia and also with various freons, which cover working temperature range from -50°C to 150°C.

Stainless steel, nickel, titan, copper are used as a constructive material. LHPs assembling can be accomplished by soldering with various solder alloys, argon-arc welding or laser welding. The general view of LHPs assembling area is shown in Fig.1



Fig. 1 General view of LHPs assembling area

Special attention is paid to LHPs hermeticity monitoring. For this purpose helium leak detectors and other methods, guaranteeing 100% hermeticity of the devices during long working life, are used.

The unique equipment is used to manufacture capillary structures of various sizes and shapes with pore size of 1 - 50 micron. To produce miniature LHPs in particular, with ammonia as a working fluid, high working fluid charging accuracy and filling system hermeticity are essential. High performance equipment, providing charging accuracy up to ±0.01 cm^3 and operating on manual, semiautomatic and automatic modes is used to ensure the necessary requirements are met. Fig.2 shows the general view of stations for LHP filling.

*Corresponding author: maidanik@etel.ru,
Phone: +7 (343) 267-87-91



Fig. 2 General view of the equipment for LHP filling

In order to confirm specified performance, LHPs are subjected to thermal testing with various heat sinks in normal conditions or in a special climatic chamber at low and high temperatures. The external view of the test bench is shown in Fig. 3.

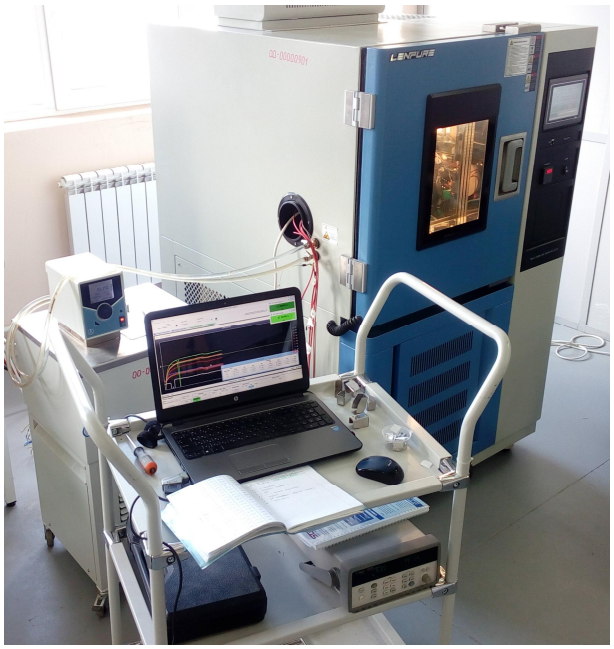


Fig.3 External view of the test bench

Fig. 4 shows miniature LHPs with ammonia as a working fluid, manufactured serially. The length of the devices is 400 mm, mass – 27 g, maximum capacity – 200 W.

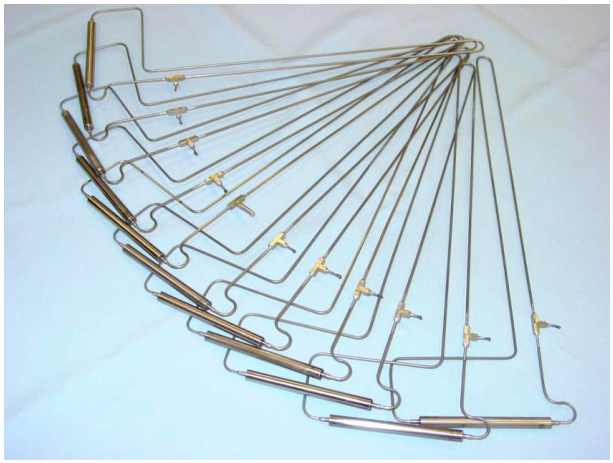


Fig.4 External view of miniature LHPs

REFERENCES

[1] Yu.F. Maydanik, "Loop heat pipes", *Applied Thermal Engineering, Elsevier B.V.* (2005) 635–657.

[2] A.A. Orlov, K.A. Goncharov, E.Yu. Kotliarov, et al., "The loop heat pipe experiment on board the "Granat" spacecraft", *Proceedings of the 6th European Symposium on Space Environmental Control Systems, Noordwijk,* the Netherlands (1997) 341-353.

[3] D. Kozmine, K. Goncharov, M. Nikitkin, et al., "Loop heat pipes for space mission Mars 96", *Proceedings of 26th International Conference on Environmental Systems, Monterey,* the USA, Paper #961602 (1996)

[4] C.L. Baker, E.W. Grob, T.V. McCarthy, et al., "Geoscience Laser Altimetry System (GLAS) on-orbit flight report on the propylene loop heat pipes (LHPs)", *Proceedings of the International Two-Phase Thermal Control Technology Workshop*, Noordwijk, the Netherlands (2003)

[5] K. Goncharov, A. Golikov, "10 years experience of loop heat pipes operation on board "YAMAL-200" satellite", *Pre-prints of the 17th International Heat Pipe Conference*, Kanpur, India, Paper #106 (2013)

[6] V.G. Pastukhov, Yu.F. Maydanik, S.V. Vershinin, and M.A. Korukov, "Miniature loop heat pipes for electronics cooling", *Applied Thermal Engineering, Elsevier B.V.* (2003) 1125-1135.

[7] Yu. Maydanik, S. Vershinin, "Development and results of testing miniature LHPs with cylindrical evaporators", *Proceedings of the 14th International heat Pipe Conference*, Florianópolis, Brazil (2007) 305-310.

[8] Yu. Maydanik, S, Vershinin, M. Chernysheva, and S. Yushakova, "Investigation of a compact copper-water loop heat pipe with a flat evaporator", Applied Thermal Engineering, Elsevier B.V., (2011) 3533–3541.

3. Pulsating Heat Pipes/ Oscillating Heat Pipes

Modeling and Experimental Investigation of a Thermally Driven Self-oscillatingPump

Marijn P. Zwier[1], Wessel W. Wits[1] and Henk Jan van Gerner[2]

[1]*Faculty of Engineering Technology, University of Twente, P.O. Box 217, 7500 AE Enschede, The Netherlands*
[2]*Thermal Control Group, Space Division, Netherlands Aerospace Centre, 8316 PR Marknesse, The Netherlands*

Abstract

This paper explores the pumping characteristics and behavior of a thermally driven self-oscillating pump. The pump consists of a single wickless capillary tube with a circular cross-section. The tube is closed at one end and has a T-section with two check valves at the other end. The check valves provide for a one directional flow. The tube represents the simplest version of a pulsating het pipe. An experimental setup has been built to investigate the influence of various design parameters (e.g. the evaporator input power, condenser temperature and condenser coolant mass flow) on the output mass flow and pressure head of the pump. During the experiments the performance of the check valves had a negative influence on the output mass flow. To determine this influence, a video analysis of the fluid oscillation of the pump without the check valves was conducted. The results of this baseline experiment were compared with the results of the pump with valves. The average output mass flow of the pump with valves was approximately 0.0010 kg/s with a maximum measured pump flow of 0.0013 kg/s. The maximum pressure head delivered by the pump was 0.25 bar. A numerical model of the vapour bubble oscillation was developed to get a better understanding of the pump and its working principles. The model is based on the conservation of mass, momentum and energy, and resulted in a non-linear system of coupled differential equations. Overall, the experiments conducted with the thermally driven self-oscillating pump have shown that the pump has good potential to be used in aerospace applications.

Keywords: Evaporation/condensation; Oscillating meniscus; Pump efficiency; Pumping Characteristics; Pulsating heat pipe; Two-phase oscillating flow.

■ *Published in Applied Thermal Engineering, Volume 126, 5 November 2017, Pages 1126-1133, https://doi.org/10.1016/j.applthermaleng.2017.02.063*

Oscillation of an Isolated Liquid Plug Inside a Dry Capillary

Vyas Srinivasan[1], Siddhartha Kumar[2], Md. Asfer[1] and Sameer Khandekar[1]

[1] *Department of Mechanical Engineering, Indian Institute of Technology Kanpur, Kanpur 208016, India*
[2]*Department of Mechanical Engineering, PDPM Indian Institute of Information Technology, Design and Manufacturing, Jabalpur 482005, India*

Abstract

Pulsating Heat Pipe (PHP) is an interesting device, which functions due to the thermally induced self- sustained oscillation of liquid-vapor interface in micro-channel. Taylor bubble flow is a primary flow pattern in PHPs. Several other devices such as micro-reactors, lab-on-chips, etc. also work by harnessing the unique transport phenomena of Taylor bubbles (vapor/gas bubbles followed by liquid plugs). Apart from these technical applications, such a flow pattern, consisting of gas/liquid two-phase flow inside in confined geometries is rich in flow physics. It is characterized by several interesting features such as three-phase contact line, contact angle hysteresis, thin-film dynamics, micro-scale evaporation/condensation, pinning etc. In this background, understanding the hydrodynamics of isolated liquid plug with air on both sides (unit-cell of Taylor bubble) provides a valuable insight to enrich the understanding and modeling of such flows. This work reports an experimental study performed to discern the flow physics of an oscillating isolated liquid plug inside a square capillary tube (1 mm × 1 mm). Flow oscillations are realized by a cam- follower mechanism and the working fluid (water) is made to oscillate at two different frequencies: 0.25 Hz and 0.35 Hz. The flow is visualized with a micro-PIV apparatus. The results of contact angle variation during the oscillation and variation in velocity during reversal of flow direction is discussed. It is seen that near the interface the flow gets disturbed due to the presence of the meniscus (free-slip boundary condition), leading to flow recirculation. This recirculation leads to significant impact on transport phenomena of flows in mini/ microchannel.

Keywords: PHP; Three-phase contact line; Oscillating liquid plugs; Micro PIV

■*Published in Heat and Mass Transfer (2017) 53: 3353. https://doi.org/10.1007/s00231-017-2064-x*

A Pulsating Heat Pipe Cooler for Integrated High Power LEDs

Lucang Lv[1], Ji Li[2] and Guohui Zhou[1]

[1] *School of Engineering Science, University of Chinese Academy of Sciences, 19A Yu-quan-lu Road, Shijingshan District, Beijing, China*
[2] *Laboratory of Advanced Thermal Management Technologies, School of Engineering Science, University of Chinese Academy of Sciences, 19A Yu-quan-lu Road, Shijingshan District, Beijing, China*

Abstract

This paper presents a closed loop pulsating heat pipe with specific pipe arrangement for high power LED cooling. It has three turns made of copper capillary tube with 2 mm ID and 4 mm OD. The interval between pipes in the evaporator was designed to be 1 mm to achieve a small evaporator area for mounting LED chips. Two CLPHPs were fabricated and charged with DI water and methanol, respectively. Under air natural convection, the effects of gravity force and working fluid on the heat transfer performance were investigated carefully. Results show that the water-CLPHP performed better with a minimum total thermal resistance of 0.49 oC/W at 260 W. In addition, the gravity force can help the CLPHP starting up and enhance the robustness of the temperature vibration at steady state. Finally, the real application to a 100 W LED chip cooling indicates that the proposed CLPHP can meet the thermal control requirement for integrated high power LEDs. Nevertheless, further modification is necessary to improve the working performance of this type of CLPHP.

Keywords: Pulsating heat pipe; Pipe arrangement; Gravity; Working fluid; Heat transfer performance.

■ *Published in Heat and Mass Transfer (2017) 53: 3305. https://doi.org/10.1007/s00231-017-2050-3*

Experimental Study on a Hydrogen Pulsating Heat Pipe with Different Adiabatic Lengths

Haoren Deng[1], Xiao Sun[1], Dongyang Han[1], Shunhao Wang[1], Bo Jiao[3], J.M. Pfotenhauer[4] and Zhihua Gan[1,2]

[1] *Institute of Refrigeration and Cryogenics, Zhejiang University, Hangzhou, 310027, PR China*
[2] *Key Laboratory of Refrigeration and Cryogenic Technology of Zhejiang Province, Hangzhou, 310027,PR China* [3] *Department of Mechanical Engineering, Rongcheng Campus , Harbin University of Science and Technology, Rongcheng 264316, PR China*
[4] *Department of Mechanical Engineering, University of Wisconssin Madison, Madison, 53706, USA*

Abstract

Pulsating heat pipes (PHPs) are promising heat transfer devices due to their high heat transfer rate, simple construction and low manufacturing cost. Most previous investigations focused mainly on their performance at room temperature. In order to better understand their heat transport capacity in cryogenic field, a PHP with liquid hydrogen as working fluid has been developed. The effect of heat load on the heat transfer performance of two units with different lengths of adiabatic section (100 and 500mm respectively) has been studied at a fixed filling ratio. It can be found that PHPs can keep the temperature stable in the pulsation process when the heat load increases. The average effective thermal conductivity of the PHP with 500mm adiabatic section is almost three times as much as that with 100mm. It achieves the highest effective thermal conductivity of 57910W/m·K at10W. This study shows potential advantages of PHPs to effectively transport heat over a long distance.

Keywords: Adiabatic section; Cryogenic pulsating heat pipe; Heat transfer characteristic; Hydrogen.

■ *Published in Heat Transfer Engineering, Vol. 40, Issue 3, 2019.*

In Situ Investigation of Liquid Films in PHP

Laura Fourgeaud[1], Vadim Nikolayev[2], Eric Ercolani[3], Jérôme Duplat[4] and Philippe Gully[3]

[1] *Ph.D. student, PSA, Route de Gisy, 78943 Vélizy-Villacoublay, France and CEA, Université Grenoble Alpes, INAC-SBT, 38000 Grenoble, France*
[2] *Senior researcher, Service de Physique de l'Etat Condensé, CEA, CNRS, Université Paris-Saclay, CEA Saclay, 91191 Gif-sur-Yvette Cedex, France*
[3] *Engineer-researcher, CEA, Université Grenoble Alpes, INAC-SBT, 38000 Grenoble, France*
[4] *Professor, Université Grenoble Alpes, CEA, INAC-SBT, 38000 Grenoble, France*

Abstract

To understand the functioning of the pulsating or oscillating heat pipe (PHP), a liquid film deposited by an oscillating meniscus is studied experimentally inside the simplest, single branch PHP, which is a straight capillary sealed from one end. The PHP capillary is of rectangular section of high aspect ratio. The evaporator is transparent so that the films can be studied by two complementary optical methods: grid deflection method and interferometry. We were able to measure both the dynamic film profile during the self-induced meniscus oscillations. It as been shown that the PHP films have the same origin as those of the Taylor bubbles; their thickness after deposition is well described by the classical formulas. Their shape however is nontrivial due to the presence of the receding triple liquid-vapor-solid contact line. Instead of being wedge-shaped like in capillary heat pipes, the film slope is very weak, with a growing in time ridge adjacent to the contact line. It is shown that this ridge is the capillary dewetting ridge. Such results can be generalized to the conventional multi-branch PHP.

Keywords: Pulsating heat pipe; Oscillation; Liquid films; Interferometry; Optical grid deflection technique.

■ *Published in Applied Thermal Engineering, Volume 126, 5 November 2017, Pages 1023-1028, https://doi.org/10.1016/j.applthermaleng.2017.01.064*

Experimental Studies of Surface Modified Oscillating Heat Pipes

Tzong-Shyng Leu and Cheng-Han Wu

Department of Aeronautics and Astronautics, National Cheng Kung University, Tainan 701, Taiwan

Abstract

Oscillating heat pipe (OHP) is a two-phase heat transfer device which has the characteristics of simple construction, high heat flux capability and no need of wicking structures for liquid transport. There are many studies in finding the ways how to improve the system performance OHP. In this paper, studies of the effects of contact angle (θ_c) on the inner wall of OHP system have been conducted first. In this paper, glass OHP systems with unmodified (θ_c=26.74°), superhydrophobic (□c =156.2o), superhydrophilic (□c <10o) and hybrid (superhydrophilic within evaporator region and superhydrophobic within condensation region) surfaces, are studied. The research results indicated that thermal resistance of these four OHP systems can be significantly affected by different surface modification approaches. Although superhydrophobic OHP system can still work, the thermal resistance (R_{th}) is the highest one of the four OHP systems, R_{th}=0.36 at 200W. Unmodified pure glass and superhydrophilic OHP systems has similar performance. Thermal resistances are 0.28 and 0.27 at 200W respectively. The hybrid OHP (superhydrophilic evaporator region and superhydrophobic condensation region) achieves the lowest thermal resistance, R_{th}=0.23 at 200W in this study. The exact mechanism and effects of contact angle on OHP systems are investigated with the help of flow visualization. By comparing the flow visualization results of OHP systems before and after surface modification, one tries to find the mechanism how the surface modified inner wall surface affects the OHP system performance. In additional to the reason that the superhydrophobic dropwise condensation surface inside the hybrid OHP system, more stable circulation flow is found within hybrid OHP system. The flow patterns are mist and slug flow in every other tube that generates an unbalanced flow resistance for two phase interfacial flow within hybrid OHP system. It is identified as another main mechanism for better performance of the hybrid OHPsystem.

Keywords: Flow visualization; Oscillating heat pipe; Surface modification; Superhydrophilic; Superhydrophobic.

■*Published in Heat Mass Transfer (2017) 53: 3329. https://doi.org/10.1007/s00231-017-2051-2*

Innovative Thermal Design Satellite with Networked Variable Conductance Oscillating Heat Pipes

Naoko Iwata[1], Hiroyuki Ogawa[1], Yoshiro Miyazaki[2], Hiroki Kawai[3] and Seisuke Fukuda[1]

[1]*Japan Aerospace Exploration Agency, 3-1-1 Yoshinodai, Chuo-ku, Sagamihara, Kanagawa 252-5210, Japan*
[2]*Thermal Control Laboratory Inc., 6-13-608 Bunkyo, Fukui 910-0017, Japan*
[3]*Asahi Kinzoku Kogyo CO, LTD., 6-13-608 Bunkyo, Fukui 910-0017, Japan*

Abstract

One useful type of an oscillating heat pipe (OHP) is a variable conductance OHP called VC-OHP in contradistinction to the conventional fixed conductance OHP. The operating temperature of an OHP connected to a temperature-controlled liquid reservoir can be controlled by the temperature of the liquid reservoir such that the operation temperature is almost identical to the liquid reservoir temperature. In this study, a thermal-design-free structure using a VC-OHP network is proposed for use in next-generation small satellites. No thermal design iteration is necessary and instruments can be mounted without consideration of the thermal design: as a result of the temperature controllability of the VC-OHPs, the temperatures of the structure panels mounted with all instruments are kept constant even if the locations of the instruments or their heat dissipation characteristics change. A model structure with a 300 m^3 volume mounting three VC-OHPs was made and tested to demonstrate the thermal-design-free concept. Eighteen heaters are mounted on the two panels to simulate the instruments' heat generation and their heat dissipation to other four panels. Thermal performance tests are conducted under thermal vacuum conditions. The model structure was then mounted on an aircraft and thermal performance under microgravity conditions was examined. The temperatures of the two panels mounting the heaters are maintained at a constant value and are controlled by the reservoir temperature when the amount or the distribution of the heat dissipation is changed. The temperatures of the two panels were maintained when the heat load was input into the radiator. These experiments demonstrate the thermal-design-free concept.

Keywords: Oscillating heat pipe; Variable conductance; Thermal design; Microgravity test.

■ *Published in Heat Pipe Science and Technology, An International Journal, 2018*

Visualizations of the Flow Patterns in a Closed Loop Flat Plate PHP with Channel Diameter Above the Critical One and Tested Under Microgravity

Vincent Ayel[1], Lucio Araneo[2], Pietro Marzorati[2], Cyril Romestant[1], Yves Bertin[1] and Marco Marengo[3]

[1]*Pprime Institut CNRS – ENSMA – Université de Poitiers, UPR 3346, Futuroscope-Chasseneuil, France*
[2]*Politecnico di Milano, Dipartimento di Energia, Milano, Italy*
[3]*University of Brighton, School of Computing, Engineering and Mathematics, Brighton, UK*

Abstract

In this paper the experimental study on a flat plate pulsating heat pipe (FPPHP), tested under microgravity during the ESA 62th parabolic flight campaign, is presented. The PHP is made of a thin copper plate, in which a unique multi-turned channel is machined, and then it is closed on its top face by a transparent borosilicate plate. The equivalent hydraulic diameter of the square channel (2.5 x 2.5 mm^2) is above the critical diameter of the working fluid. This induces a stratification of the liquid/vapor phases under normal gravity, whatever the orientation. During the parabolic flight campaign, the FPPHP is tested under vertical orientation. During normal gravity phases, the fluid stratifies with the liquid in the bottom zones, and vapor at the top zones. Thus the thermo-hydraulic transfer mode in this operation was either purely pool boiling inside completely filled channels (at the edges of the PHP plate), or annular flow pattern inside empty channels (in the center of the PHP plate). During microgravity phases, the fluid distributed naturally into a slug-plug flow pattern, with almost immediate trend to dry-out, followed by fast fluid overall motions leading to heat and mass transfers from evaporator towards the condenser zone, caused by some liquid small plugs moving towards the evaporator. These periods of stop-and-start motion were consecutive during the 20s of microgravity, and led to associated temperature oscillations.

Keywords: Pulsating Heat Pipes; Flow Pattern; Microgravity; Visualizations.

■ *Published in Heat Transfer Engineering, Vol. 40, Issue 3, 2019.*

Motion of liquid plugs between vapor bubbles in capillary tubes: a comparison between fluids

Rémi Bertossi[1], Vincent Ayel[2], Balkrishna Mehta[3], Cyril Romestant[2], Yves Bertin[2] and Sameer Khandekar[4]

[1]*IPSA, Direction de la Recherche et de l'Innovation de l'IPSA, Ivry-sur-Seine, France*
[2]*Pprime Institut CNRS – ENSMA – Université de Poitiers, UPR 3346, Futuroscope-Chasseneuil, France*
[3]*Indian Institute of Technology Guwahati, Guwahati, India*
[4]*Indian Institute of Technology Kanpur, Kanpur, India*

Abstract

Pulsating heat pipes (PHP) are now well-known devices in which liquid/vapor slug flow oscillates in a capillary tube wound between hot and cold sources. In this context, this paper focuses on the motion of the liquid plug, trapped between vapor bubbles, moving in capillary tubes, to try to better understand the thermo-physical phenomena involved in such devices. This study is divided into three parts. In the first part, a previous model [1-2], simulating the evolution of the vapor pressure during the evaporation process near the triple line zone, is briefly presented and numerical results are compared to experimental ones. Four typical results are particularly delineated. In the second part, a transient model allows to compare, in terms of pressure and duration, the motion of a constant-length liquid plug trapped between two bubbles subjected to a constant difference of vapor pressure: the results highlight that the performances of the four fluids are very different. Finally, a third model that can be considered as an improvement of the second one is presented: here, the liquid slug is surrounded by two vapor bubbles, one subjected to evaporation, the pressure in both bubbles is now a result of the calculation. This model still allows to compare the behaviors of the fluid. Even if our models are quite far from a complete model of a real PHP, results do indicate towards the applicability and suitability of different fluids as working fluids for PHPs, particularly in terms of the flow instabilities which they generate.

Keywords: Taylor bubble flow; Pulsating Heat Pipes; Liquid plug motion.

■ *Published in Heat Mass Transfer (2017) 53: 3315. https://doi.org/10.1007/s00231-017-2052-1*

Hybrid Pulsating Heat Pipe for Space Applications with Non Uniform Heating Patterns: Ground and Microgravity Experiments

C. Mangini[1], M. Mameli[2] , D. Fioriti[2], S. Filippeschi[2], L. Araneo[3] and M.Marengo[4]

[1]*Faculty of Engineering, University of Bergamo, Dalmine, Italy*
[2]*DESTEC, University of Pisa, Pisa, Italy.*
[3]*Faculty of Engineering, Polytechnic of Milan, Milan, Italy*
[4]*School of Computing, Engineering and Mathematics, University of Brighton, England*

Abstract

A hybrid Loop Thermosyphon/Pulsating Heat Pipe named Space Pulsating Heat Pipe (SPHP) is tested both on ground and in hyper/micro-gravity conditions during the 63rd ESA Parabolic Flight Campaign. The device, partially filled up with FC-72 (50% Filling Ratio), is made of an aluminum tube (Inner/Outer Diameter 3 mm/5 mm) bent into a planar serpentine with five curves at the evaporator zone. A transparent section closes the loop in the condenser zone, permitting the fluid flow visualization. Each of the five heaters, mounted alternatively on the branches, just above the curves, is controlled independently, in order to test different heating distributions. The device is tested at different total heat inputs (50 W, 70 W and 90 W), both on ground and in hyper/micro gravity conditions. Data are collected by recording the heat power provided to each heater, the tube wall temperatures, the fluid pressure and fast speed images up to 200 fps are also recorded in the transparent section. An image processing software is developed in order to calculate the bubble flow velocity. On ground, where the device acts like a thermosyphon, the non-uniform heating promotes the fluid net circulation in a preferential direction, stabilizing the operation of the device and thus increasing the thermal performance with respect to the homogeneous heating. The parabolic flight tests point out a working mode in microgravity for such SPHP: the sudden absence of buoyancy force, activating an oscillating slug/plug flow regime, allows the device to work also without gravity assistance. It was found that particular heating distributions can shorten the stop-over periods observed when the device is uniformly heated up, stabilizing a pulsating two-phase flow motion when the gravity field is absent.

Keywords: Thermosyphon; Pulsating heat pipe; Microgravity; Flow visualization.

■ *Published in Applied Thermal Engineering, Volume 126, 5 November 2017, Pages 1029-10243, https://doi.org/10.1016/j.applthermaleng.2017.01.035*

An Experimental Investigation of Operating Limit in an Oscillating Heat Pipe

Yulong Ji[1], Qingzhen Zhang[1], Chao Chang[1] and Hongbin Ma[2]

[1] *Marine Engineering College, Dalian Maritime University, Dalian, Liaoning 116026, China*
[2] *Department of Mechanical & Aerospace Engineering, University of Missouri, Columbia, Missouri 65211, U.S.A.*

Abstract

n experimental investigation of a copper oscillating heat pipe (OHP) was conducted to determine the operating limit. The OHP has six turns and three sections: evaporator, condenser and adiabatic sections with lengths of 40 mm, 64 mm, and 51 mm, respectively. Alcohol and alcohol/Al2O3 nanofluid served as the working fluid including the effects of filling ratios ranging from 30% to 50%, operating temperature from20℃to60℃, and tiltangles(orientation) from 0° to 90°. The experimental results show that (1) the alcohol/Al 2O3 nanofluid can increase the operating limit of the OHP, however, it decreases the heat transfer performance at a low power input; (2) the operating limit increased as the filling ratio increased from 30% to 50%; (3) the operating limit decreased as the operating temperature increased from 20℃ to 60℃; and (4) the operating limit increased as the tilt angle increased.

Keywords: Oscillating heat pipe (pulsating heat pipe); Alcohol; Nanofluid; Operating limit.

Double Condenser Pulsating Heat Pipe Cooler

Daniele Torresin, Francesco Agostini, Adrian Mularczyk, Bruno Agostini and Mathieu Habert

ABB Switzerland Ltd., Corporate Research, Segelhofstrasse 1K, 5405, Baden-Dättwil, Switzerland

Abstract

A novel pulsating heat pipe cooler (PHP) based on automotive technology is presented. This technology uses numerous aluminium Multiport Extruded (MPE) tubes disposed in parallel to achieve the desired compactness. The sub-channels of the MPEs are connected in a serpentine manner by means of fluid distribution elements integrated in the two condenser manifolds. This configuration enables the oscillation of liquid slugs and elongated bubbles between the evaporator and the condenser areas. This power electronics cooling system with a double condenser area was experimentally characterized and the thermal performances measured with R245fa are presented in this paper. The influence of different parameters such as the heat load, fluid filling ratio and orientation are investigated. The results show that the device is orientation-free: the performance was identical in all orientations, vertical, horizontal andanti-vertical.

Keywords: Pulsating heat pipe; Double condenser; Heat transfer; Power electronic.

■ *Published in Applied Thermal Engineering, Volume 126, 5 November 2017, Pages 1051-10257, https://doi.org/10.1016/j.applthermaleng.2017.02.066*

Visualization and Thermal Resistance of Magnetic Nanofluid Pulsating Heat Pipe

Ying-Chang Liu, Yao-Chun Wang, Hung Wang and Shung-Wen Kang

Department of Mechanical and Electro-Mechanical Engineering, Tamkang University,
151 Ying-Chuan Road, Tamsui, 25137 Taipei, Taiwan

Abstract

Using a nanofluid as the working fluid in pulsating heat pipes (PHPs) is an attractive technique in heat transfer enhancement nowadays. Applying the magnetic field on the magnetic nanofluid charged PHP enhances the thermal performance. In order to study the mechanism that a magnetic field with magnetic nanofluid can help to reach start-up faster in low heat input. A glass manufactured PHP with 5 turns, andinternal diameter 3mm, outer diameter 6mm was used to conducted experiments in this research. The heat input was applied at 20, 55, 90, 125 and 160 W. DI Water and Fe_3O_4 nanofluid with concentration of 90ppm, 270ppm and 450ppm were used as working fluid. Cooling water temperature was set at 25°C. Experiment was conducted with and without magnetic field. A video camera was set to observe the motion of working fluid in PHP, and temperatures were measured.
The results show that addition of magnetic nanofluid can improve the performance of pulsating heat pipe, and under the magnetic field thermal resistance reduces with an increase heat input for all experimental parameters. When the heat input was increased from 20W to 55W, a significant drop in thermal resistance was observed. In addition, particles of the nanofluid securely deposit on the wall under the influence of magnetic field. Nanofluid enhanced boiling by depositing layer of nanoparticles on the boiling surface.

Keywords: Pulsating heat pipe; Magnetic nanofluid; Magnetic field; Visualization.

■ *Published in Applied Thermal Engineering, Volume 126, 5 November 2017, Pages 1044-10250, https://doi.org/10.1016/j.applthermaleng.2017.02.051*

Ammonia Pulsating Heat Pipe: a New Full Visualization Experiment and the Operating Mechanism Study

Z. H. Xue*, L. Chen, M. H. Xie, W. Qu and W. Li

China Academy of Aerospace Aerodynamics (CAAA), Beijing 100074, China

Abstract

This paper presents a novel study on performance of pulsating heat pipe using ammonia as working fluid. Firstly, a new full visualization experiment with high speed camera is conducted, to study the relationship between the flow patterns and thermo-hydrodynamics of the PHP. The tested PHP, consisting of 6 turns, is fully made of quartz glass tubes with 6 mm outer diameter and 2 mm inner diameter. The filling ratio for ammonia fluid is 70%. Wall temperature fluctuations of several key positions are recorded under a series charge of heat inputs, which are from 25W to 520W. In visualization results, the motion identities, flow pattern variations, breakup and coalescence between the vapor plugs and liquid slugs are illustrated and discussed. In addition, the actual velocity of the vapor is computed from the experimental measurement in this paper, which is never found in other literature but is very important for the mechanism study in theoretical model.

Keywords: Pulsating heat pipe; Ammonia fluid; Heat transfer; Visualization; Flow pattern; Velocity capture; Operating mechanism

Experimental Research on Start-up characteristics and Heat Transfer Performance of Pulsating Heat Pipe with Rectangular Cross-section

Wang Xuehui[1], Hua Chao[1], Gao Xu[2], Zheng Haoce[1], Han Xiaohong[1], Chen Guangming[1]

[1] *Key Laboratory of Refrigeration and Cryogenic Technology of Zhejiang Province, Institute of Refrigeration and Cryogenics, Zhejiang University, Hangzhou 310027, PR China*

[2] *The State Key Laboratory of Technologies in Space Cryogenic Propellants, Beijing 100028, PR China*

Abstract

As a simple and high efficiency heat transfer device, pulsating heat pipe (PHP) has a bright application prospect in dissipating the heat, especially when the heat flux is very high. As so far, most studies concentrated on the heat transfer performances of small diameter PHPs (d≤3mm). However, the large diameter PHPs may have better performance due to the larger heat capacity of the working fluid at the same filling ratio and less possibilities to occur the dry-out phenomenon under high heat flux conditions. Compared with PHP with circular channel, the PHP with rectangular channel has some special advantages due to the unique structure. On the basis of this, an experimental setup of PHP with rectangular cross-section and 4 mm equivalent inner diameter was built and the influences of cross-section shape on the start-up and heat transfer performance of the PHP were investigated. The experimental results indicated that the start-up process shift from "smooth start-up mode" to "sudden start-up mode" with the increase of heat flux. The minimum start-up power of the PHP with rectangular channel was 1.5-2 times greater than that of the PHP with circular channel. Furthermore, the thermal resistance of the PHP with rectangular channel was only 30 % - 40 % of the PHP with circular channel under the same operating conditions. The results also showed that there existed an optimum filling ratio which was about 0.3 for the tested PHP. This paper can be a solid foundation for further studies on the PHP.

Keywords: Heat transfer; Large diameter; Pulsating heat pipe; Rectangular channel; Thermal resistance.

■ *Published in Applied Thermal Engineering, Volume 126, 5 November 2017, Pages 1058-10262, https://doi.org/10.1016/j.applthermaleng.2017.02.106*

Thermal Performance Comparison of Closed-Loop Oscillating Heat Pipes with and without Internal Microgrooves

Jian Qu[1], Xiao Jun Li[1], Qian Wang[1] and Qin Sun[2]

[1] *School of Energy and Power Engineering, Jiangsu University, Zhenjiang, Jiangsu, 212013 China*

[2] *Research center of fluid machinery engineering and Technology, Jiangsu University*

Abstract

The thermal performance of four closed-loop oscillating heat pipes (OHPs) with and without internal microgrooves was experimentally investigated and compared at vertical and horizontal orientations. These OHPs are all made from copper capillary tubes and have three turns with lengths of 70, 230 and 110 mm at the evaporator, adiabatic and condenser sections, respectively. Deionized water was used as the working fluid at a volumetric filling ratio of 50%. The internal diameters (IDs) of three smooth-tube OHPs are 3.4, 4.0 and 4.8 mm, respectively, and the internal hydraulic diameter of the micro-grooved OHP is about 2.82 mm. Experimental results show that the introduction of microgroove structure enable a profound improvement of OHP performance and reduce its startup power input as well. Within the experimental range, compared to the 3.4, 4.0 and 4.8 mm ID OHPs, the reductions in the thermal resistance of micro-grooved OHP were about 41.7%, 35.6% and 30.9%, respectively, at the maximum heating power input of about 305 W. The corresponding reductions in the evaporator temperature were about 12.1oC, 11.8oC and 7.6oC, respectively. It is found that the phase-change intensification both at the heating and cooling sections, the helical microgroove induced rotary motion of working fluid, and enhanced liquid backflow to the evaporator due to capillary action account for the heat transfer enhancement of the micro-grooved OHP.

Keywords: Oscillating heat pipe; Microgroove; Thermal performance; Start-up; Capillary action.

■ *Published in Heat and Mass Transfer, Vol. 53, issue 11, (https://doi.org/10.1007/s00231-017-2082-8)*

Experimental Investigation on Silicon-Based Pulsating Heat Pipes with Different Channel Geometries

Jungseok Lee and Sung Jin Kim

Department of Mechanical Engineering, Korea Advanced Institute of Science and Technology, Daejeon 305-701, Korea

Abstract

Experimental investigations on the effect of the channel geometry on thermal performance of the micro pulsating heat pipe (MPHP) were performed. The fabricated MPHPs have the circular and square channels with 390, 480, and 570 μm hydraulic diameters. A transparent glass wafer was used as a cover to allow flow visualization. The thermal performance of the MPHPs charged with FC-72 was evaluated in a vertical position. The overall thermal performance of the square channel MPHP is better than that of the circular channel MPHP with respect to not only the thermal resistance but also the operating range. In both cases of the cross- sectional shapes, as the hydraulic diameter increases, the minimum thermal resistance decreases and the maximum heat throughput increases. The square channel MPHP has not only a lower thermal resistance but also a larger maximum heat throughput than the circular channel MPHP. When the MPHPs reach the operating limit at excessive input power, the thermal resistance increases significantly with a stopover phenomenon: the amplitude of an oscillation frequent decreases. A model for the operating limit was proposed based on flow visualization. The MPHPs reach the operating limit when the film flow rate is smaller than the evaporation rate through the liquid film according to the proposed model.

Keywords: Micro pulsating heat pipe (MPHP); Channel geometry; Operating limit; Maximum heat throughput.

A Study on Thermal Performance of Parallel Connected Oscillating Heat Pipe

Byeong Chan Kim, Longnan Li, Ji Hoon Kim and Daejoong Kim

Department of Mechanical Engineering, Sogang University, Seoul 151-700, Republic of Korea

Abstract

A series of experiments was performed to investigate thermal performance of single, parallel connected and 2 turns oscillating heat pipe (OHP) using different working fluid. The copper capillary tube was used which has internal and external diameter 2.2mm and 3.2mm respectively. Working fluids were selected as ethanol, deionized water and filling ratio was 50% for all experiment. All OHPs were tested in vertical orientation and under the same adiabatic, condensation, evaporation condition except geometry. Theoretical thermal resistance of parallel connected OHP was calculated based on thermal resistance of single OHP. Least input power for single OHP that working fluid oscillating inside system could be known by comparing theoretical and experimental thermal resistance of parallel connected OHP. Also, Thermal resistance of 2 turns OHP is larger than parallel connected OHP at low input power. But for high input power, parallel connected OHP is better than 2turns.

Keywords: Oscillating heat pipe; Pulsating heat pipe; Parallel connect; Thermal performance.

■ *Published in Applied Thermal Engineering, Volume 126, 5 November 2017, Pages 1063-1068, https://doi.org/10.1016/j.applthermaleng.2017.05.191*

Volume and Saturation Temperature Variation of an Expanding Taylor Bubble in a Heated Capillary

Antoine Voirand, Adel M. Benselama and Yves Bertin

Institut PPrime, ISAE-ENSMA, 1 Av. Clément Ader, 86360 Poitiers, France

Abstract

Modelization of expanding non-isothermal bubbles in a capillary, as a contribution to the understanding of the physical phenomena taking place in Pulsating Heat Pipes, is the scope of this paper. The liquid film problem is simplified and solved in the manner of Wilson *et al*. [14], with a different thermal problem treatment, while the liquid slug dynamics is solved using Lucas [17] and Washburn [18] model. Mass and energy balance on the vapor phase allows a complete description of the expanding bubble to be written. The liquid and vapor phases are coupled only by the saturation temperature associated with the vapor pressure, assumed uniform throughout the bubble. Results show no dependence of the bubble dynamics on the initial vapor temperature after a transient stage, and give evidence of a minimal onset heat flux density to be applied in order the bubble to effectively expandendlessly.

Keywords: Pulsating heat pipe; Bubble dynamics; Slug flow.

Experimental Study on the Effect of the Ratio of Adiabatic Section Length to Condenser Length on the Thermal Performance of Pulsating Heat Pipes

Juno Kim and Sung Jin Kim

Department of Mechanical Engineering, KAIST, 291 Daehak-ro, Yuseong-gu, Daejeon, Korea

Abstract

The effect of the ratio of adiabatic section length to condenser section length on the thermal performance of micro pulsating heat pipes (MPHPs) was investigated experimentally. Silicon-based PHPs with hydraulic diameter of 667μm and thickness of 1.5mm were fabricated using MEMS techniques. The condenser section and adiabatic section lengths were varied while the evaporator section and the total length were fixed at 20 mm and 100 mm, respectively. The thermal resistance was evaluated from temperature measurement and flow visualization was conducted using high speed camera simultaneously. The optimum condenser section length, for which the thermal resistance of PHPs was the lowest, was found to be 10mm experimentally. When the condenser section length became larger than the optimum length, the stopover phenomenon was observed through flow visualization. The formation of the liquid film in evaporator section and adiabatic section of PHPs was affected by the stopover behaviors. The variations in temperature of the evaporator section with time was less significant as the condenser section length decreased due to continuous liquid film supply.

Keywords: Condenser length; Dryout; Flow visualization; Liquid film; Silicon-based PHPs; Stopover; Thermal resistance.

Experimental Investigation of a Novel Solar Collector with Pulsating Heat Pipe

H. Kavoosi Balotaki[1] and M.H. Saidi[2]

[1]*Ph.D Student, Center of Excellence in Energy Conversion, School of Mechanical Engineering, Sharif University of Technology, Tehran, Iran*

[2]*Professor, Center of Excellence in Energy Conversion, School of Mechanical Engineering, Sharif University of Technology, P.O. Box: 11155-9567, Tehran, Iran*

Abstract

In this study, reports the results obtained from design, construction and performance of a novel solar collector with pulsating heat pipe (SCPHP), which is benefited from the undeniable advantages of pulsating heat pipe (PHP) as a fast responding, flexible and high performance thermal conducting device. SCPHP consists of two major sections: the evaporator and condenser. The effects of different parameters such as filling ratio of PHP, water flow rate, condenser inlet temperature, intensity of solar radiation and inclination angle of SCPHP on the efficiency of this collector were examined.

Keywords: Solar collector; Pulsating heat pipe; Efficiency; Filling ratio; Inclination angle.

Effect of Tube Heat Conduction on the PHPStart-Up

Iaroslav Nekrashevych and Vadim Nikolayev

Service de Physique de l'Etat Condensé, CEA, CNRS, Université Paris-Saclay, CEA Saclay, 91191 Gif-sur-Yvette Cedex, France

Abstract

The pulsating heat pipe (PHP) functioning is not completely understood, the absence of calculation tools that would allow their dimensioning is a substantial obstacle to their development. The crucial question about the PHPs concerns their start-up, i.e. the oscillation inception. In this work, we simulate numerically the start-up of multi-branch PHP accounting for the fluid-tube thermal interaction and bubble generation (boiling). The theoretical model that generalizes an earlier proposed approach is described. It is shown that the account of tube heat conduction changes completely the start-up conditions. In particular, in the presence of tube heat conduction the PHP cannot provide stable oscillations without bubble generation. While the bubble generation may not be directly involved into the development of first oscillations, its role is crucial in preventing the oscillations halt. The mechanism of the oscillation sustainment by bubble generation is discussed in detail. The PHP dry-out is simulated. The PHP simulation shows basic phenomena of bubble interaction observed experimentally by other groups.

Keywords: Pulsating heat pipe; Oscillation; Liquid films; Phase change; Simulation.

■ *Published in Applied Thermal Engineering, Volume 126, 5 November 2017, Pages 1077-1082, https://doi.org/10.1016/j.applthermaleng.2017.08.117*

Condenser Temperature Effect on the Transient Behavior of a Pulsating Heat Pipe

L. A. Betancur[1], D. Mangini[2], M. Mameli[3], S. Filippeschi[4], L. K. Slongo[5], K. Paiva[5], M. Mantelli[5] and M. Marengo

[1]*Dr., Mechanical Engineer Department, Federal University of Santa Catarina,*
[2]*Dr., University of Bergamo, Italy, daniele.mangini@unibg.it*
[3]*Dr., DESTEC, University of Pisa, Italy*[3]
[4]Prof., DESTEC, University of Pisa, Italy
[5]Professor, Mechanical Engineering Department, Federal University of Santa Catarina UFSC, Brazil
[6]*Professor, School of Computing, Engineering and Mathematics, University of Brighton, England*

Abstract

A Pulsating Heat Pipe filled up with distilled water has been designed and tested at different condenser wall temperatures and heat power inputs. The device consists in a copper tube (internal and external diameters of 3.18 and 4.76 mm), bended into a planar serpentine with five U-turns in the heated zone. The tube is closed in a loop, evacuated and partially filled with pure water, with a filling ratio of 50%. The heating section is equipped by means of two heating elements able to dissipate up to 350W as total. A cold plate, directly connected to a thermal bath, keeping the condenser at a constant temperature in the range of 10 °C up to 60 °C, permits to perform tests at different condenser temperature levels. The temperature evolutions recorded both at the condenser and at the evaporator zone allow to evaluate the overall PHP thermal performance for all the configurations tested. The experimental results show different temperature superheats at different heat fluxes as the condenser temperatures and the input powers are changed. Based on experimental data, a theoretical analysis of the heat transfer mechanisms for the dynamic behavior of the PHP has been made. The most relevant equations of boiling and evaporation have been compared with the experimental results. Based on Roshenow equation, a simplified conductive model is proposed, which is compared with experimental data. It is found that the model is in good agreement with the experimental results, especially after the full activation.

Keywords: Condenser temperature; Pulsating heat pipe; Roshenow correlation; Start-up.

■ *Published in Heat Pipe Science and Technology, An International Journal, 2019*

Experimental Investigation of Oscillating Heat Pipes under Direct Current and Pulse Width Modulation Heating Input Conditions

Brent S. Taft[1] and Matthew Rhodes[2]

[1]*Mechanical Engineer, United States Air Force Research Laboratory, Kirtland AFB, New Mexico 87117, U.S.A.*
[2]*Graduate Student, Mississippi State University, Mississippi 39762, U.S.A.*

Abstract

An experiment was designed to quantify any change in thermal performance of an oscillating heat pipe (OHP) subjected to Pulse Width Modulation (PWM) power input as opposed to the more traditional Direct Current (DC) power input/heating. Two identical ThermAvant Technologies aluminum 152.4 x 50.8 x 2.0 mm3, 34 loop closed-loop OHPs with 1 x 1mm square channels were procured. One OHP was filled with acetone (54% by volume at room temperature) and another filled with R-134a (55% by volume at room temperature). The OHPs were tested horizontally with DC and PWM (at 2.88 Hz) heat inputs of 0 to 40 W. Three trials of each OHP and power type were performed. It was found that nearly all trials of each OHP were within one standard deviation of one another. Based on these results and prior findings in OHP performance repeatability it is reasonable to conclude that the use of PWM power input does not influence the thermal performance of a flat-plate OHP of this design.

Keywords: Direct current (DC); Oscillating heat pipe (OHP); Pulsating heat pipe (PHP); Pulse width modulation (PWM).

■ *Published in Applied Thermal Engineering, Volume 126, 5 November 2017, Pages 1018-1022, https://doi.org/10.1016/j.applthermaleng.2017.02.064*

Experimental Investigation on the Thermal Performance of Pulsating Heat Pipes with Asymmetric Channels

Dong Soo Jang[1], Dongwoo Kim[1], Dowon Cha[1], Hanseok Mun[1] and Yongchan Kim[2]

[1]*Graduate School of Mechanical Engineering, Korea University, Seoul 136-713, Korea*
[2]*Department of Mechanical Engineering, Korea University, Seoul 136-713, Korea*

Abstract

In this study, the thermal performance of pulsating heat pipes was investigated with various asymmetric channel designs. The pulsating heat pipes were fabricated in the form of flat plate heat spreader, which had closed loop channels of square cross section. The asymmetric ratios of channel cross sectional areas were 1.0, 1.5, and 2.3. The depths of channels were 0.4, 0.6, and 0.8 mm. FC-72 was used as a working fluid and the filling ratio of the working fluid was 50%. The oscillating and circulating motion of the working fluid was observed and its flow patterns were investigated. The effect of the channel asymmetric ratio and channel depth on the heat transfer characteristics was investigated under various heat inputs.

Keywords: Asymmetric channel; Pulsating heat pipe; Thermal performance

Study on Thermal Cycle in Oscillating Heat Pipes by Numerical Analysis

Takurou Daimaru[1*], Shuhei Yoshida[1] and Hiroki Nagai[1]

[1]*Department of Aerospace Engineering, Tohoku University, Sendai 980-8579, Japan*

Abstract

This paper discusses a thermal cycle in an Oscillating Heat Pipe (OHP). An OHP is a two-phase heat transfer device using self-exited oscillation. Over the past few decades, a considerable number of studies has been conducted to understand physics in OHPs. However, little is known about the thermal cycle in the OHPs. In this study, we develop a one-dimensional slug flow model to reproduce thermal and hydrodynamic phenomena in OHPs. Fast Fourier Transform (FFT) and a cross-correlation analysis are used as data processing methods for oscillation waveform. A multi-branch OHP that consists of a stainless steel pipe wall and the working fluid of R134a is simulated. Numerical results showed the pressure propagation in the OHP. The vapor volume oscillates with the same frequency as pressure. Moreover, the vapor plug obtains energy and does work according to the direction of pressure propagation. As a result, it was found that propagation of energy is a reason for the pressure propagation in the OHP.

Keywords: Numerical analysis; Oscillating Heat Pipes; Propagation phenomena; Thermal cycle

1. INTRODUCTION

Oscillating Heat Pipes (OHP) or Pulsating Heat Pipes (PHP) were invented in 1990 by H. Akachi in Japan [1]. An OHP consists of bent metal mini channels and saturated working fluid [2]. An OHP has heating, adiabatic, and cooling sections along a direction of heat transport. In a nominal operating condition, the working fluid separates into liquid slugs and vapor plugs, and they form a slug flow state because of the strong capillary force in the mini channel [3]. On application of heat to the heating section, liquid slugs start the self-excited oscillation by the pressure difference along a flow path [4]. OHPs transport heat by forced convection of liquid slugs and the phase change phenomena in liquid films surrounding vapor plugs [5, 6]. The self-exited oscillation starts by triggers of initial disturbances including vapor-liquid distribution, boiling, merging of liquid slugs, etc. [7, 8]. OHPs are much thinner and lighter than conventional heat pipes because they do not have internal wick structures. However, basic operational principles of OHPs are not understood clearly because internal thermal and hydrodynamic phenomena are complex [9]. A self-excited oscillation as a primary operational principle of OHPs is a phenomenon that oscillation is generated by a characteristic of a system even if inputs to the system are linear. A reason that a self-exited oscillation in an OHP becomes more complex than a general case is because number of turns existing in the heating section is not single but multiple. Thus, problem is not simple expansion

*Corresponding author:
daimaru.takurou@aero.mech.tohoku.ac.jp,
Phone & Fax: +81-22-795-4075

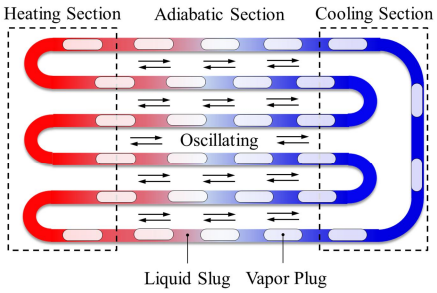


Fig. 1. An oscillating Heat Pipe.

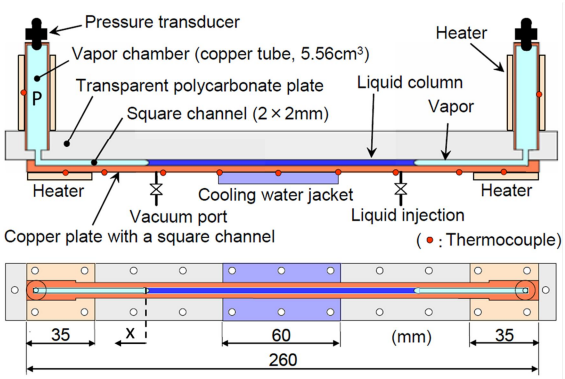


Fig. 2. Nagasaki's experimental apparatus [14].

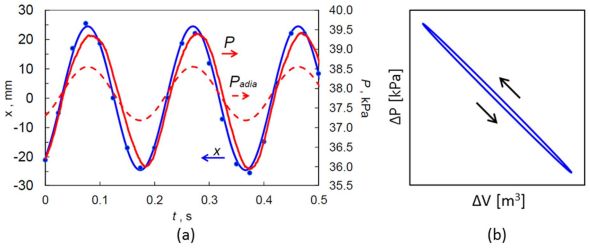


Fig. 3. (a) Displacement of liquid column and pressure oscillation [14], (b) An expected thermal cycle in a single-branch OHP.

or compression of a single vapor plug. Oscillations in each channel should affect each other and these oscillations may be connected.

In previous studies, visualization experiments and numerical analysis were conducted by using a straight tube [10, 11, 12, 13]. Nagasaki et al. studied oscillation mechanism of the liquid column in the closed ends single-branch OHP [14]. Fig. 2 shows Nagasaki's experimental apparatus. They investigated relation between the position of liquid column x and the pressure of vapor P. As shown in Fig. 3(a), the vapor pressure showed the periodic oscillation waveform and its amplitude was larger than the case assuming the adiabatic condition P_{adia}. In addition, the position of liquid column oscillated in the coordinate phase with the vapor pressure. The thermal cycle, which we will pay attention, was not mentioned in their study. However, the cycle should be a straight shape as shown in Fig. 3(b) because volume of the vapor was anti-phase of the vapor pressure. The straight shape of cycle means energy, which the vapor obtained by compression, is equal to the work, which the vapor does by expansion. Previous studies helped to advance understanding of the operational principle. However, this theory has not been developed to multi-branch OHPs so far.

This paper presents a numerical slug flow model of a multi-branch OHP and describes data processing methods for oscillation waveform of physical parameters. Pressure propagation and thermal cycles in the OHP will be discussed.

2. NUMERICAL MODELING

A schematic diagram of the numerical model is shown in Fig. 4. It is a one-dimensional model along the flow path and has domains of the pipe wall and working fluid. As shown in Fig. 5, the working fluid domain consists of liquid slugs, vapor plugs, and liquid films. The pipe wall and each liquid slug have meshes for temperature calculation. The mesh of the pipe wall is fixed spatially, whereas the meshes of the liquids can move in the working fluid domain [15]. Primary assumptions are as below:

a) The inner flow regime is slug flow, which is uniform along radial direction. The liquid phase is treated as incompressible flow.
b) Vapor plugs are treated as ideal gases. Temperature and pressure are uniform within each vapor plug.
c) Liquid films maintain constant thickness. Friction between vapor plugs and films, between pipe wall and liquid film is not considered.

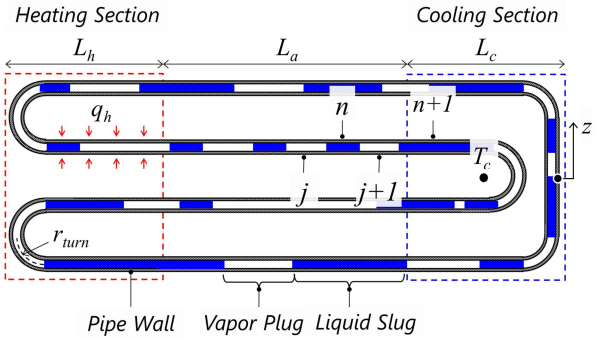


Fig. 4. Schematic diagram of the numerical model.

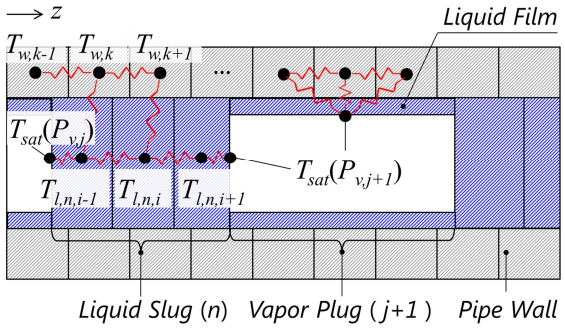


Fig. 5. Thermal network.

d) Mass and volume changes in the liquid slugs as a result of the generation and absorption of liquid films and via phase change in interfaces with vapors are not considered.
e) The front and rear meniscus of liquid slugs are treated as flat cross section in terms of heat transfer.
f) Heat flux in the heating section is spatially uniform and temporally constant.

2.1 Pipe Wall Temperature

The energy equation for the wall is a one-dimensional heat equation including heat transfer with the external heat, and working fluid. The entire tube wall is subdivided into N_w sub-volumes, and the temperature of each sub-volume, numbered k, is calculated using Eq. (1) and (2):

$$\left[c_{p,w}\rho_w A_w \frac{\partial T_w}{\partial t} = q_{ex} p_{out} - q_{w-f} p_{in} + k_w A_w \frac{\partial^2 T_w}{\partial z^2} \right]_k \quad (1)$$

where

$$q_{ex,k} = \begin{cases} q_h & : heating\ \ section \\ 0 & : adiabatic\ \ section \\ h_c\left(T_c - T_{w,k}\right) & : cooling\ \ section \end{cases} \quad (2)$$

2.2 Liquid Slug Temperature and Pressure

The energy equations for liquid slugs are also one-dimensional heat equations, which include heat transfer with the pipe wall. The equations for both ends of a mesh are solved by using the saturation temperature of adjacent vapor plugs as boundary conditions. The number of sub-volumes in a mesh is determined according to the length of the liquid slugs at the first-time step and is maintained during calculation. The temperature change of each sub-volume numbered *i* is calculated using Eq. (3):

$$\left[c_{p,l}\rho_l A_{cr}\frac{\partial T_l}{\partial t} = q_{w-f}\,p + k_l A_{cr}\frac{\partial^2 T_l}{\partial z^2} \right]_{n,i} \tag{3}$$

$$q_{w-f,k} = h_{l,n}\left(T_{w,k} - T_{l,n,i}\right) \tag{4}$$

The value of the heat flux between the pipe wall and the liquid slug, which is expressed in Eq. (4), is calculated based on the forced convection heat transfer in the circular pipe. The heat transfer coefficient calculated in different equations depends on the flow regime of the laminar, transient, and turbulent. A thermally developing flow is assumed for the laminar flow, but developed steady flow correlations are employed for transient and turbulent flows. The inner flow regime is determined by the Reynolds number. The averaged thermal properties along the length of the liquid slug are used to calculate these dimensionless numbers and heat transfer coefficient.

$$\left[\mathrm{Re}_l = \frac{\rho_l u_l D_{in}}{\mu_l} \right]_n \tag{5}$$

$$\left[\mathrm{Pr}_l = \frac{\mu_l\, c_{p,l}}{k_l} \right]_n \tag{6}$$

(a) Laminar flow ($\mathrm{Re}_{l,n} < 2000$) [16]

$$\left[h_l = \left(\frac{k_l}{D_{in}}\right)\cdot 1.953 \cdot \left(\mathrm{Re}_l\,\mathrm{Pr}_l\frac{D_{in}}{L_l}\right)^{1/3} \right]_n$$

$$when \quad \left[\mathrm{Re}_l\,\mathrm{Pr}_l\frac{D_{in}}{L_l} \right]_n \geq 33.3 \tag{7}$$

$$\left[h_l = \left(\frac{k_l}{D_{in}}\right)\cdot \left(4.364 + 0.0722\mathrm{Re}_l\,\mathrm{Pr}_l\frac{D_{in}}{L_l}\right) \right]_n$$

$$when \quad \left[\mathrm{Re}_l\,\mathrm{Pr}_l\frac{D_{in}}{L_l} \right]_n < 33.3 \tag{8}$$

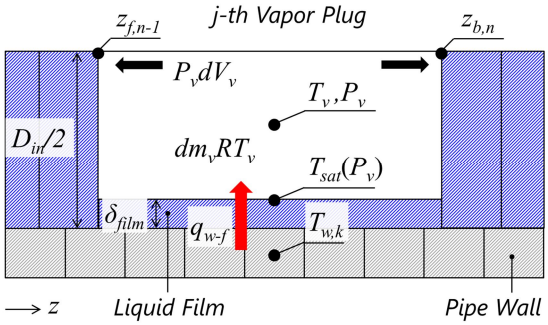


Fig. 6. Schematic of the vapor plug sub-section.

(b) Transient flow ($2000 \leqq \mathrm{Re}_{l,n} \leqq 10000$)
Gnielinski correlation

$$\left[h_l = \left(\frac{k_l}{D_{in}}\right)\cdot\left(\frac{(f_\tau/8)\left(\mathrm{Re}_l - 10^3\right)\mathrm{Pr}_l}{1+12.7\left(f_\tau/8\right)^{1/2}\left(\mathrm{Pr}_l^{2/3}-1\right)}\right) \right]_n \tag{9}$$

where, f_τ is the friction factor of the liquid slug.

(c) Turbulent flow ($\mathrm{Re}_l > 10000$)
Dittus-Boelter correlation

$$\left[h_l = \left(\frac{k_l}{D_{in}}\right)\cdot 0.023\,\mathrm{Re}_l^{0.8}\,\mathrm{Pr}_l^{0.4} \right]_n \tag{10}$$

Assuming the pressure of liquid slugs to be linear along its length, the pressure of adjacent vapor plugs is used as boundary conditions.

2.3 Vapor Plug Temperature and Pressure

In this model, the temperature is uniform within each vapor plug because speed of the heat transfer is very fast in the vapor phase. Therefore, the energy equation takes a combined approach. Fig. 6. shows the heat transfer path for the *j*-th vapor plug. Eq. (11) considers heat transfer between tube wall and vapor through the liquid film. The saturation temperature in vapor pressure is used to calculate the heat flux, because vapor-liquid film interface should be saturation condition. Simultaneously, this means that a steep temperature gradient exists around vapor and liquid film [11]. The total mass change within a vapor plug is calculated by Eq. (11). Temperature of *j*-th vapor plug is calculated by Eq. (12), where the "work" of the vapor plug is considered too. Finally, the ideal gas law, Eq. (13), calculates the pressure of vapor. It is important to note that the pressure cannot exceed the saturation pressure of the vapor temperature, calculated from Eq. (12). If the pressure is higher than saturation pressure, ideal gas law is no longer valid and pressure set to the saturation pressure, calculated by Eq. (14) [5].

$$q_{w-f,k} = {k_l}/{\delta_{film}} \left(T_{w,k} - T_{sat}\left(P_{v,j}\right)\right) \tag{10}$$

$$\left[dm_v = \int_{z_{b,n}}^{z_{f,n-1}} \left\{ {q_{w-f,k} p_{in}}/{H_{LG}} \right\} dz \right]_j \tag{11}$$

$$\left[dT_v = \frac{-P_v dV_v + dm_v R T_v}{c_{v,v} m_v} \right]_j$$

$$where \ \left[dV_v = A_{cr}\left(u_{l,n} - u_{l,n-1}\right) \right]_j \tag{12}$$

$$\left[P_v = \left(m_v R T_v\right)/V_v \right]_j \tag{13}$$

$$\left[P_v = P_{sat}\left(T_v\right) \right]_j \ when \ \left[P_v > P_{sat}\left(T_v\right) \right]_j \tag{14}$$

2.4 Liquid Slug Momentum and Velocity

The momentum equation for *n*-th liquid slug is written by following an ordinary differential equation. The liquid slug is treated with a combined parameter approach, as shown Fig. 7. The left hand side of Eq. (15) is the change in the momentum at each time step.

$$\left[\frac{d\dot{m}_l}{dt} = A_{cr}\left(dP_v - \left(1-\eta_{turn}\right)dP_\tau - \eta_{turn} dP_{turn}\right) \right]_n \tag{15}$$

The first term on the right hand side is the pressure difference between adjacent vapor plugs. This term is caused by the pressure change as a result of the work and phase change of vapor plugs.

$$dP_{v,n} = \left\{P_v\left(T_v\right)\right\}_j - \left\{P_v\left(T_v\right)\right\}_{j+1} \tag{16}$$

The pressure loss in circular pipes is given by Eq. (17), and the friction factor, *f*, is calculated for the cases of laminar flow and turbulent flow regimes. Correlation for a steady developed flow is used.

$$\left[dP_\tau = \frac{f_\tau}{2D_{in}} L_l \rho_l u_l^2 \right]_n \tag{17}$$

(a) Laminar flow ($\mathrm{Re}_l < 2000$)

$$\left[f_\tau = 64/\mathrm{Re}_l \right]_n \tag{18}$$

(b) Turbulent flow ($\mathrm{Re}_l \geqq 2000$)

$$\left[f_\tau = 0.3164\,\mathrm{Re}_l^{-0.25} \right]_n \tag{19}$$

The third term on the right hand side is the pressure loss in turn sections. The pressure loss in the turn sections is defined by Eq. (20). The friction factor, f_K, is calculated as the ratio to friction factor in the straight sections [17,18]. The transient Reynolds number (Re_{turn}) is determined by Eq. (24).

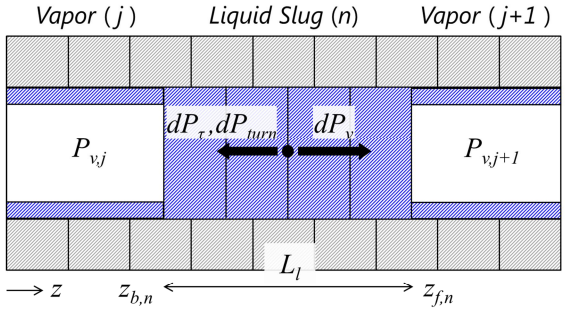


Fig. 7. Schematic of the force balance in the liquid slug

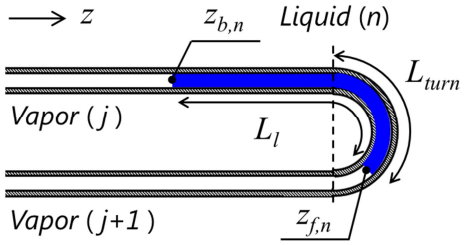


Fig. 8. Schematic of the turn section.

$$\left[dP_{turn} = \frac{f_K}{2D_{in}} L_l \rho_l u_l^2 \right]_n \tag{20}$$

(a) Laminar flow ($\mathrm{Re}_l < \mathrm{Re}_{turn}$) [17]

$$f_{turn}/f_\tau = 0.1008 De^{1/2}\left(1 + 3.945 De^{-1/2} + 7.782 De^{-1} + 9.097 De^{-3/2} + 5.608 De^{-2}\right) \tag{21}$$

(b) Turbulent flow ($\mathrm{Re}_l \geqq \mathrm{Re}_{turn}$) [17]

$$f_K/f_\tau = \left\{ \mathrm{Re}_l \left(\frac{D_{in}}{2r_{trun}} \right)^2 \right\}^{0.05} \tag{22}$$

Here, Dean number (*De*) is calculated in Eq. (23).

$$De = \mathrm{Re}_l \sqrt{\frac{D_{in}}{2r_{turn}}} \tag{23}$$

$$\mathrm{Re}_{turn} = 2\times 10^4 \left(\frac{D_{in}}{2r_{turn}} \right)^{0.32} \tag{24}$$

When the liquid slug exists in turn sections, the spatial ratio is taken into account, as shown Fig. 8. The spatial ratio for turn sections are described as:

$$\left[\eta_{turn} = L_{turn}/L_l\right]_n \tag{25}$$

Finally, the velocity of the liquid slug is estimated from the momentum of the liquid slug:

$$\left[u_l = \frac{\dot{m}_l}{A_{cr} L_l \rho_l}\right]_n \tag{26}$$

Displacements of liquid slugs are described as:

$$\left[dz = u_l dt\right]_n \tag{27}$$

2.5 Numerical Procedure

As a result of volume and mass changes in the vapor plugs, the vapor plugs may collapse and the liquid slugs merge into each other. In such a case, the meshes of the liquid slugs are combined for temperature calculation. Further, the momentum and length of the new liquid slug are set to the sum of the values of the old merged liquid slugs:

$$\dot{m}_{l,n,new} = \dot{m}_{l,n,old} + \dot{m}_{l,n-1,old}\ ,\ L_{l,n,new} = L_{l,n,old} + L_{l,n-1,old}$$
$$when\ \ V_{v,j} < 0\ \ or\ \ m_{v,j} < 0 \tag{27}$$

A flowchart of the calculation procedure is shown in Figure 9. Calculation is implemented in each sub-section. The fourth order Runge-Kutta method was used for numerical stability of calculation. When merging occurs during the loop, modification of temperature meshes and momentums of liquid slugs is dealt outside of the loop [6].

3. CALCULATION CONDITIONS

Table 1. shows design parameters of the calculated OHP, and Table 2. shows calculation conditions. The thickness of liquid films is fitting parameter, but correlation [18] for an isothermal case may be useful for rough estimation. Mean velocity of 0.25 m/s and temperature of 10 °C is assumed in this calculation case.

$$\delta_{film} = D_{in} \frac{0.67 Ca_l^{2/3}}{1 + 3.35 Ca_l^{2/3}} \tag{28}$$

$$where\ \ Ca_l = \frac{\mu_l u_l}{\sigma_l} \tag{29}$$

Fig. 10 shows computational domain and initial vapor-liquid distribution. Liquid slugs are equally distributed in the flow path in the initial distribution. Length of each liquid is 92 [mm].

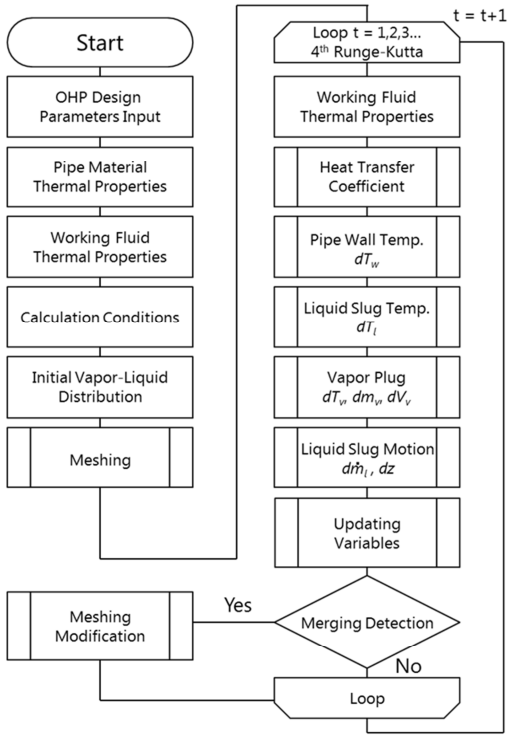


Fig. 9. Flowchart of the calculations.

Table 1. Design parameters.

Pipe wall material		stainless steel	[-]
Working fluid		R134a	[-]
Charging ratio of W.F.		50	[%]
Heating section length	L_h	100	[mm]
Adiabatic section length	L_a	80	[mm]
Cooling section length	L_c	100	[mm]
Pipe diameter (In/Out)	D_{in}/D_{out}	0.8 / 1.6	[mm]
Number of turns		16	[-]
Radius of turns	r_{turn}	3	[mm]

Table 2. Calculation conditions.

Heat input	Q_h	20	[W]
Heat flux	q_h		[W/m^2]
Initial temperature	T_{int}	10	[°C]
Cooling temperature	T_c	10	[°C]
H.T. coeff. in cooling plate	h_c	1000	[W/m^2/K]
Liquid film thickness	δ_{film}	30	[μm]
Time step	dt	0.0010	[s]
Number of time steps		100000	[-]
Mesh size for temperature	dz	1	[mm]

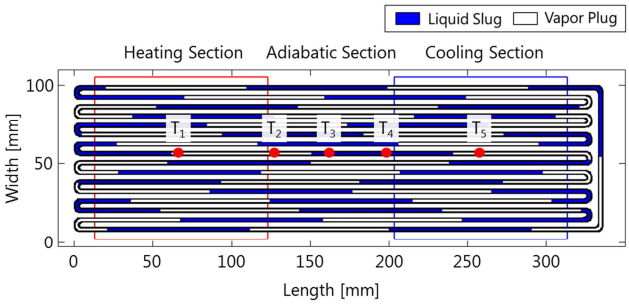


Fig. 10. Computational domain and initial distribution

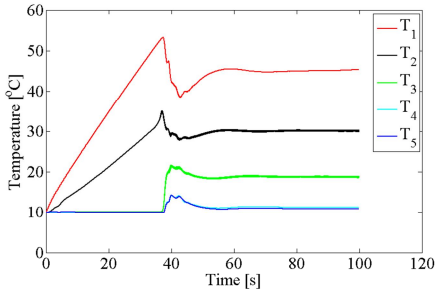


Fig. 11. Temperature history of the pipe wall.

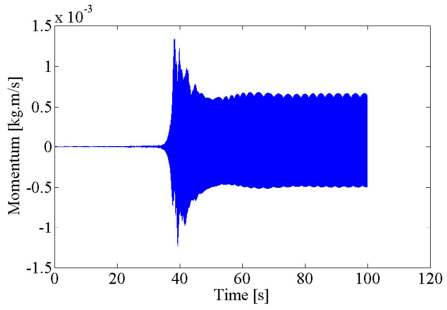


Fig. 12. Momentum history of the liquid slug No.5.

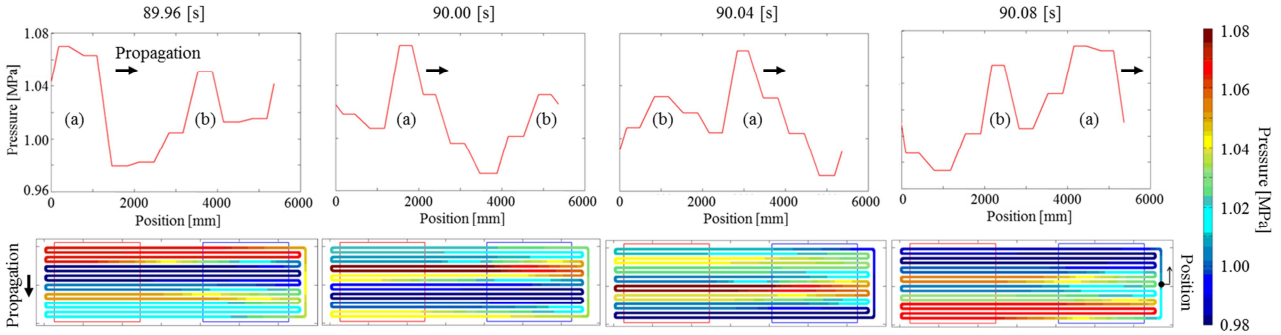


Fig. 13. Pressure distribution and pressure field.

4. RESULTS AND DISUCUSSION

Fig. 11 and Fig. 12 show the temperature history of the pipe wall and the momentum history of the liquid slug respectively. The temperature in the heating section increased linearly in the beginning, then decreased at around 40 s and converged after that. Here, the momentum of one liquid slug (No.5) is shown in Fig. 12. The momentum also started oscillation at the almost same time as the decrease of temperature. This change means that the liquid slug starts oscillation. Thus, it is clear that oscillation of the working fluid transports heat from the heating to cooling section. This result agrees with basic operational characteristics of OHPs.

4.1 Propagation Phenomenon

Pressure propagation occurred, when liquid slugs oscillated. Fig. 13 shows the pressure distribution in the working fluid along the flow path and the pressure field in the OHP during one period of the oscillation. In the pressure distribution, one large (a) and one small (b) pressure peaks exist. Then, they traveled along the direction of position axis as time gained. The larger peak (a) maintained almost same value, but the smaller peak (b) slightly transformed during the propagation. Pressure difference between higher and lower pressure region was close to 100 [kPa]. The pressure distribution and propagation can be seen more clearly in the pressure filed. The pressure gradient is smaller in the same channel, but it is larger in different channels. This propagation phenomenon is a remarkable result, which cannot be obtained by experiment with the point measurement of a pressure sensor. Furthermore, this is an evidence that oscillations of liquids are connected in a multi-branch OHP because motions of liquid slugs are eventually driven by the pressure difference. Let us pursue the reason for the pressure propagation in following sections.

4.2 Thermal Cycles

First, we discuss single vapor same as the case of single-branch OHP. Fig. 14 shows pressure and volume history of the vapor plug No.5. Pressure and volume are completely anti-phase. Results of Fast Fourier Transform (FFT) are shown Fig. 15. Power spectrums of both pressure and volume have two peaks in frequency. The frequency of 6.2 Hz corresponds to a larger peak in the pressure distribution shown in Fig. 13, and 12.4 Hz includes the smaller peak too. Thermal cycle is made from pressure and vapor volume by normalization, as shown in Fig. 18(a). The thermal cycle is straight shape same as the case of single-branch OHP. However, this is not a direct reason of pressure propagation because this type of cycle represents neither obtaining energy from outside nor doing work to outside.

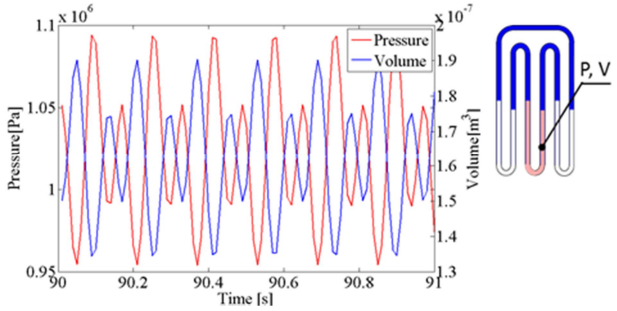


Fig. 14. Pressure and volume histories in the vapor No.5.

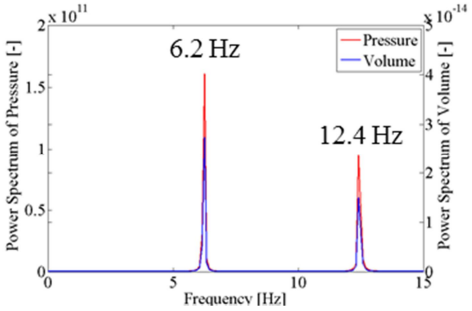


Fig. 15. Oscillation frequencies.

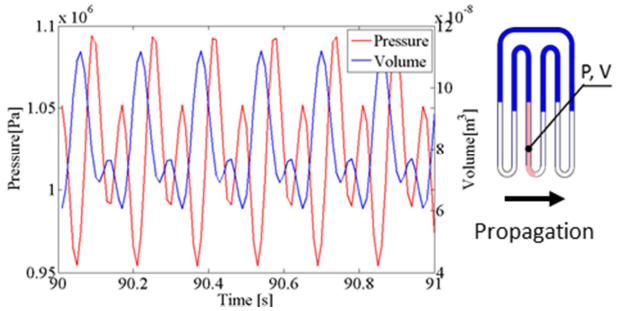


Fig. 16. Pressure and volume histories in upper channel.

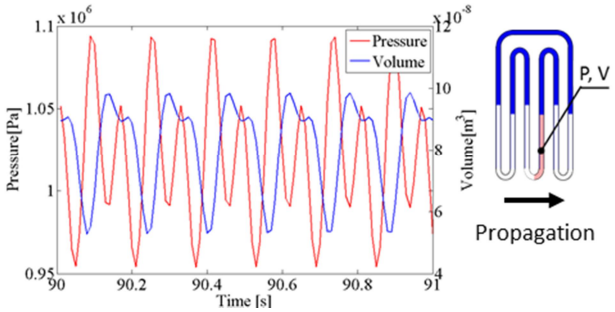


Fig. 17. Pressure and volume histories in down channel.

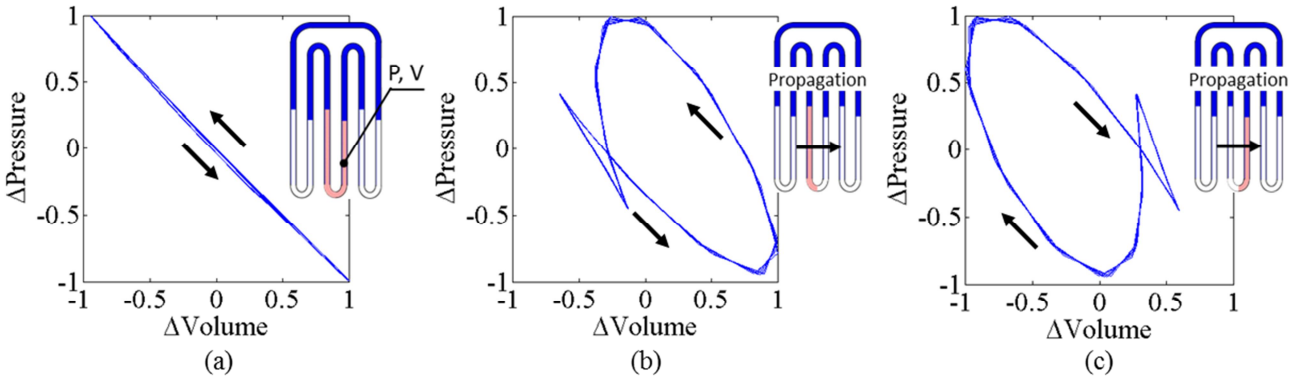


Fig. 18. Thermal cycles, (a) single vapor plug, (b) upper channel, (c) down channel.

Next, thermal cycles in each channel are discussed. The volume of single vapor was divided into two parts. According to the direction of pressure propagation, these are called “upper channel” and “down channel”. Pressure and volume histories are shown in Fig. 16 and 17. In these cases, pressure and vapor histories are not completely anti-phase. Same as the case of Fig.18(a), thermal cycles are shown in Fig. 18(b) and 18(c). These cycles are elliptical shapes, which are different from the case of single vapor plug. The cycle was left direction in the upper channel and right direction in the down channel. Vapor can obtain energy by compression in the right direction of a thermal cycle. Contrarily, vapor does work to outside in the left direction. Thus, it can be considered that the vapor plug obtains energy in the upper channel, and then transmits that energy to the next channel in the down channel. This phenomenon is the propagation of energy, and it can be the reason of pressure propagation in the OHP.

As validation of this hypothesis, phase difference in energy waveforms was calculated by using vapor plug No.1 as a reference. The period of energy propagation should be same as that of pressure oscillation if energy propagation is a reason of pressure propagation. Fig. 19 shows examples of waveforms. Firstly, a time delay between two waveforms was calculated by the cross-correlation analysis as shown in Fig. 20. Next, phase difference was calculated by using strongest frequency of pressure oscillation, 6.2 Hz, as shown Fig.21. The phase difference between each vapor was almost 45 degrees, which is equal to value dividing one period (360 degrees) by the number of vapor plugs. In addition, the total amount of difference was 360 degrees. These suggest that energy propagates through vapors, and propagation period is same as pressure propagation. From the above discussion, we can conclude that pressure propagation occurred by that of vapor energy as work.

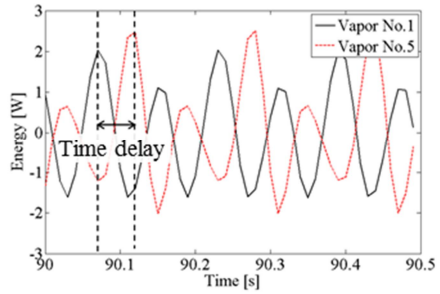


Fig. 19. Energy waveforms of vapors No.1 and 5.

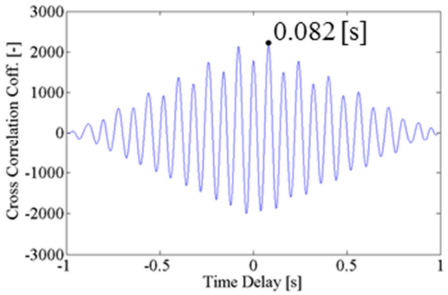


Fig. 20. Time delay of energy bet. vapors No. 1 and 5

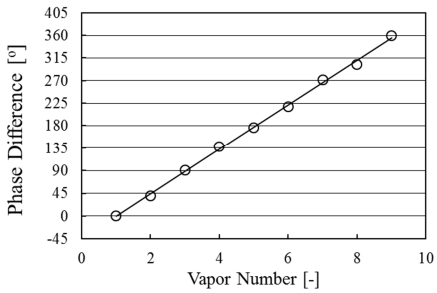


Fig. 21. Phase Difference

5. CONCLUSIONS

This paper presented numerical modeling method of a multi-branch OHP. Propagation phenomenon of pressure occurred in the simulation. The vapor plug obtained energy and did work according to the direction of propagation. Basing on these results, we found pressure propagation occurred due to vapor energy as work. Finally, the consideration was validated by the waveform analysis.

ACKNOWLEDGEMENT

This work was partially supported by a Japan Society for the Promotion of Science (JSPS) Grant-in-Aid for JSPS Fellows (Grant No. 26-3928).

NOMENCLATURE

A : Area [m^2]
h : Heat transfer coefficient ($W/m^2/K$)
k : Thermal Conductivity (W/m/K)
l : Liquid slug
L : Length (m)
m : Mass (kg)
P : Pressure (Pa)
T : Temperature (K)
u : Velocity (m/s)
v : Vapor plug
V : Volume (m^3)
z : Position (m)
w : Pipe wall

REFERENCES

[1] Akachi, H., U.S. Patent, Patent No. 4921041, May 1, 1990.
[2] Akachi, H. et al., Pulsating Heat Pipes, *Proc. of the 5th Int. Heat Pipe Symp.*, Melbourne, Australia (1996) 208-217.
[3] Khandekar S. et al., An Insight into Thermos-Hydrodynamic Coupling in Closed Loop PHPs, *Int. J. of Thermal Sciences*, 43 (2004) 13-20.
[4] Miyazaki, Y. et al., Oscillatory Flow in the OHP, *Proc. of 11th IHPC,* Tokyo, Japan (1999) 367-372.
[5] Shafii, B. et al., Thermal Modeling of Unlooped and Looped PHPs, *J. of H. T.*, 123 (2001) 1159-1172.
[6] Nikolayev, V., A Dynamic Film Model of the PHP, *J. of Heat Transfer*, 113 (2011) 081504-1-9.
[7] Nikolayev, V., Oscillatory Instability of the Gas-Liquid Meniscus in a Capillary under the Imposed Temperature Difference, *Int. J. of Heat and Mass Transfer*, 64 (2013) 313-321.
[8] Daimaru, T. et al., Mathematical Modeling and Experimental Validation of OHPs," *Proc. of 44th Int. Conf. on Environmental Systems*, Tucson, Arizona (2014) ICES-2014-121.
[9] Zhang, Y. et al., Advanced and Unsolved Issues in PHPs, *Heat Transfer Eng.* 29 (1) (2008) 20-44.
[10] Kato, S. et al., A Single, Straight-tube PHP, *Int. J. of Heat and Mass Transfer*, 64 (2013) 254-262.
[11] Gully, P. et al., Evaluation of the Vapor Thermodynamic State in PHP, *Proc. of the 17th International Heat Pipe Conf.*, Kanpur, India, (2013).
[12] Dobson, R., Theoretical and Experimental Modeling of an Open OHP Including Gravity, *Int. J. of Thermal Science*, 43 (2004) 113-119.
[13] Das, P. et al., Thermally Induced Two-Phase Oscillating Flow Inside a Capillary Tube, *Int. J. of Heat and Mass Transfer*, 53 (2010) 3905-3913.
[14] Nagasaki T. et al., Study on the Mechanism of Liquid Column Oscillation in PHP, *Proc. of 48th Japanese Symp. on H. T.*, Okayama, Japan (2011).
[15] Mameli, M. et al., Thermal Simulation of a PHP: Effects of Different Liquid Properties on a Simple Geometry, *H. T. Eng.* 33 (14) (2012) 1177-1187.
[16] Shah,.K., Thermal Entry Length Solutions for the Circular Tube and Parallel Plates, *Proc. of the 3rd National H. Mass T. Conf.*, India (1975) HMT-11–75.
[17] Ito, H., Laminar Flow in Curved Pipes, *J. of Applied Mathematics and Mechanics*, 40 (1969) 653-663.
[18] Aussillous, P. et al., Quick Deposition of a Fluid on the Wall of a Tube," *Physics of Fluid*, 12 (10) (2000) 2367-2371.

Performances and Limits of a Multi-source Pulsating Heat Pipe Tested Under High Heat Flux Density

David Dufraisse[1*], Vincent Ayel[1], Yves Bertin[1] and Cyril Romestant[1]
[1]*Institut P', département Fluide, Thermique et Combustion, UPR 3346,*
Téléport 2 - 1 avenue Clément Ader - BP 40109, 86961 Futuroscope Chasseneuil-du-Poitou

Abstract

During the past few years, pulsating heat pipes (PHP) have been the subject of many experimental studies, but its working mechanisms and limits are still not fully established. Recently, lots of studies have focused on the improvement of its performances through geometric or fluidic parameters [1-4]. Nevertheless, most of them have been done on rather small pulsating heat pipes (except [2]) and therefore small heat power inputs. In this paper, the behavior of a copper pulsating heat pipe subject to high heat flux density and multiple heat sources will be presented. This study will compare the behavior of this device with bibliography and highlight its limits. Parameters such as heat power input and cold source temperature will be tested in order to extend the characterization of the pulsating heat pipe behavior for high input power. This paper will also present the impact of the heating pattern on the behavior of the PHP, particularly on the performances and stop of oscillations.

Keywords: Oscillating/pulsating heat pipe; Multiple sources; Heating pattern; High heat flux;

1. INTRODUCTION

Pulsating heat pipes (PHP), although studied since the 90's, by the way of experimental studies or attempt of modelling in order to characterize precisely its working behavior, have only been little studied concerning high heat power input/high heat flux density or non-uniform heating patterns.

As far as we know, the highest heat power input found in the literature reached values exceeding 4 kW [2]. The PHP tested was made of a 20 U-turns copper tube having an inner diameter of 2.5 mm, and an overall length of around 60 cm. This study resulted in a thermal conductance close to 100 $W.K^{-1}$ and observations such as an improvement of performances with heat power input and cold source temperature, regardless of the tested fluid (water, methanol, acetone and N-pentane).

Earlier, for Lin et al. [3], a dry-out limit of their PHP up to 2 kW was observed for a filling ratio of 50% of FC72 (compared to values of 38% and 32% for which PHP was even not operating). Their PHP was made of a copper tube with 40 U-turns of 446 mm long and 1.75 mm in inner diameter.

In another study of Yang et al. [4], a heat flux density of 32 $W.cm^{-2}$ caused a dry-out of the PHP at 390 W for a 50% filling ratio R-123 in a 1 mm inner diameter copper tube with 2 U-turns. It was observed that a lower tube diameter of the oscillating heat pipe fosters a higher dry-out limit and better performances, contrary to what was observed in [2]. The authors also concluded that using R123, a 50% filling ratio seemed to lead to optimum performances and higher dry-out limits compared to 30% and 70%.

Concerning non-uniform heating patterns, very few studies can be found in the literature. According to Kammuang-Lue et al. [5], using different heating patterns has shown best performances for an increasing local heat flux carried from adiabatic to end of evaporator.

In a model of Jianseng et al. [6], comparing uniform and non-uniform heating patterns, like alternating the heating of one tube and the not-heating of the next tube of each U-turn, showed that non-uniform heating pattern can reduce start-up periods but increase the thermal resistance of PHPs.

More recently, experiments made by Mangini et al. [7] showed that the previous asymmetrical position of the heaters has a direct effect on the fluid motion during interconnected thermosyphons behavior when operating in vertical bottom heated mode. Alternating heating on either side of each U-turn generates an alternation of up-headers and down-comers leading to a preferential direction for fluid motion and therefore a net circulation. This was observed with an aluminum PHP based on a 5 U-turns tube of 3 mm inner diameter filled with 50% of FC72.

Starting with so few papers in the literature on such subject, the primary focus of this paper is to present some experimental results of a parametric study made on a new kind of pulsating heat pipe, leading to interesting conclusions concerning the

*Corresponding author: david.dufraisse@ensma.fr,
Phone: +33-54-949-8136

performances and dry-out limits under high heat power supply and heat flux density. The impact of cold source temperature and heat power on uniform and non-uniform heating pattern will also be presented.

2. EXPERIMENTAL SET-UP

The pulsating heat pipe is based on a copper tube of inner diameter D_{in} = 2 mm and outer diameter D_{out} = 3.2 mm. This tube is silver-brazed within grooves of three different evaporator blocks and also within grooves of a central triangular condenser, the whole forming a 3-pointed star (see figures 1 & 2). The tube successively connects one evaporator to one of the condenser face and then to the next evaporator. This results in the cooling of each source by two of the condenser faces (source 1 with faces 1 and 3, source 2 with faces 1 and 2 and source 3 with faces 2 and 3 of the condenser). When all three evaporators are covered this makes a layer and the tube then covers the next layer. This creates an alternate source to cool. A so-called "adiabatic zone" exists between each evaporator block and condenser area.

Unfortunately, for confidentiality reasons, the overall dimensions of the PHP cannot be disclosed in this paper, as well as the heat powers applied regarding the operating conditions, and the resulting thermal conductances. However, the authors will try to highlight the major part of interesting data emerging from this experimental study.

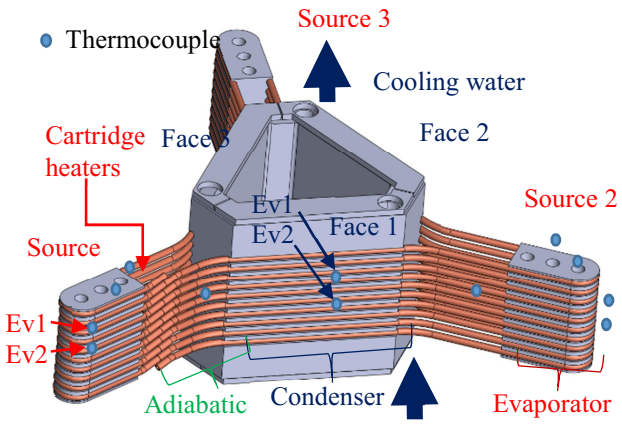


Fig. 1. Schematic 3D view of the experimental device.

The device made of ten layers of alternating tubes is looped on both extremities near source 1 and connected to two valves (see Fig. 2), one for filling and closed during an experimental test campaign with a fluid, and the other opened and connected to a pressure sensor (GE PTX5076-TA-A3-CA-HO-PS, 10 bars absolute, ±200 Pa). The inner surface of the tube was preliminary cleaned and oxidized to reach its final surface condition (figure 2). Overall external geometrical dimensions of the PHP are as contact between tube and copper blocks in evaporator and condenser section have almost the same length. This length will be the reference for nondimensionalization. Adiabatic section length is only 5/8 of this contact length. Evaporator and condenser copper block height are respectively about 7/10 and 11/10 relative to the reference length.

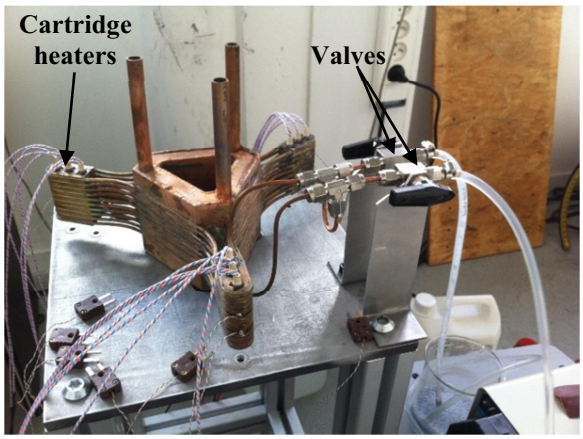


Fig. 2. Photograph of the experimental apparatus (during the tube cleaning/oxidation phase).

The evaporator, adiabatic and condenser areas of the PHP have been instrumented by means of 24 T-type thermocouples of 0.2 mm outer diameter. Eighteen thermocouples are soldered on two of the ten tubes (respectively tubes 4 and 7, Fig. 1), and six thermocouples are soldered on top of the evaporator copper blocks. Ten thermal sensors instrument each part of the system, two on the tubes in evaporator zone ($T_{ev1,1}$ to $T_{ev1,2}$), two on top of the evaporator copper blocks close to the cartridge heaters, two on the tubes in adiabatic zones ($T_{ad1,1}$ to $T_{ad1,2}$) and two on the tubes in the condenser zone ($T_{co1,1}$ to $T_{co1,2}$). It is worth emphasizing that the measured temperatures are on the copper tubes and on the copper blocks, and not in the cartridge heaters, neither in the cooling fluid nor in the working fluid inside the tubes of the PHP. All measurements are extrusive, except for the pressure sensor. The software interface between all components (thermal sensors, electrical power supply and cryostat) have been developed using Labview®.

The PHP has been instrumented with nine cartridge heaters (VULCANIC VULSTAR 10163-36, Fig. 1 and 2) linearly inserted in the three evaporator blocks and powered by an electric power supplier (Regatron TopCon Quadro); on the opposite side, the condenser is cooled by a 50% ethylene-glycol/water mixture flow crossing the

copper block and whose temperature is controlled by means of a cryostat (Huber UC080T) allowing maintaining its temperature close to a fixed setpoint (stabilized between ±0.1°C). The evaporator and the adiabatic zone have been insulated (with glass wool $\lambda \approx 0.035$ W.m^{-1}.K^{-1} and Rockwool $\lambda \approx 0.04$ W.m^{-1}.K^{-1}).

During the experiments, the heat power input was stepwise increased, temperatures were recorded, but performances are only based on temperatures measured during a so-called steady-state (*i.e.* with fluctuating temperatures but whose behavior no longer varies with time), implying enough measurements, after which heat power is increased again. The procedure was repeated until the evaporator temperature reached a maximum temperature limit, T_{max}, fixed at 183°C for security reasons, or maximum power input fixed by the limitation of the electric power supply.

As it is usual to do with pulsating heat pipes, the thermal conductance G is determined as:

$$G = \frac{Q - Q_{loss}}{T_{evap} - T_{cond}} \quad (1)$$

where Q is the total heat power input delivered by the electric power supply, and Q_{loss} the heat losses to the ambient. The heat loss coefficient G_{loss} has been calculated through preliminary measurements made on the empty PHP:

$$Q_{loss} = G_{loss}(T_{evap} - T_{air}) \quad (2)$$

T_{evap} is the average temperature of the tubes in the three evaporator zones, calculated as:

$$T_{evap} = \frac{1}{6}\sum_{i=1,j=1}^{i=3,j=2} T_{ev\ i,j} \quad (3)$$

In the same way, T_{cond} is the average temperature of the tubes in the condenser zone:

$$T_{cond} = \frac{1}{6}\sum_{i=1,j=1}^{i=3,j=2} T_{co\ i,j} \quad (4)$$

Finally, the filling ratio (FR) of the working fluid in the PHP is defined as:

$$FR = \frac{V_l}{V_{tot}} \quad (5)$$

In the above equation, V_l is the volume of liquid of the working fluid inserted in the PHP, V_{tot} the inner total volume of the tube (the dead volumes including connections, valves and pressure sensor have been taken into account and are supposed to be filled by only liquid phase during operation).

Finally, the pulsating heat pipe was tested under the following operating conditions:

- Working fluid: N-pentane;
- Filling ratio: FR ≈ 50% or 70% at 20°C;
- Orientation: horizontal orientation, according to the photograph of Fig. 2;
- Heat power input: increased stepwise from 0 W into maximum value.

3. EXPERIMENTAL RESULTS

3.1 PHP response to equally distributed power among sources

In the following sections, as mentioned above, the results in terms of heat power applied and thermal conductance will be presented in their dimensionless form. However, in order to show the very high cooling potential of such system, it should be noted here that *the maximal heat power tested during the experimental test campaign, for equally distributed heat power among sources,* ***exceeded 8 kW*** *for the best operating conditions*! In such cases this limit was fixed by the electric power supply rather than by a dry-out of the device. This already shows a cooling potential for this device never reached in the literature as far as the authors know. Thereafter, the behavior of the heat pipe will be presented in dimensionless form.

3.1.1 Influence of heat power input and cold source temperature

Heat power input and cold source temperature are well-known parameters impacting pulsating heat pipes performances. It is well-established that increasing heat power input and cold source temperature improves thermal performances until dry-out. But, as cold source temperature increases, the operating limit is reached with less and less heat power applied [4]. In this current study, we aim to compare the behavior of this genuine experimental device with well-known behavior of classical pulsating heat pipes regarding heat power input and cold source temperature as primary parameters. One of the first key point to identify is whether or not performances increase with heat power input until the dry-out limit is reached.

In our experimental campaign, each test is set with a constant cold source temperature and a stepwise increasing heat power input. The experiment stops when maximum power input is reached or if temperature limit T_{max} is exceeded. A typical experimental test is presented on Fig. 3, for N-pentane as working fluid (FR = 70%) and a cold source temperature (T_{cryo}) of 10°C. The heat power input has been nondimensionalized from its maximum heat power value reached. One can

observe on the curves of Fig. 3 the fluctuating behavior of one representative thermocouple in the evaporator $T_{ev1,1}$ as a function of time and heat power. Note that the five other thermocouples in the evaporator zones present very similar values and behavior during operation.

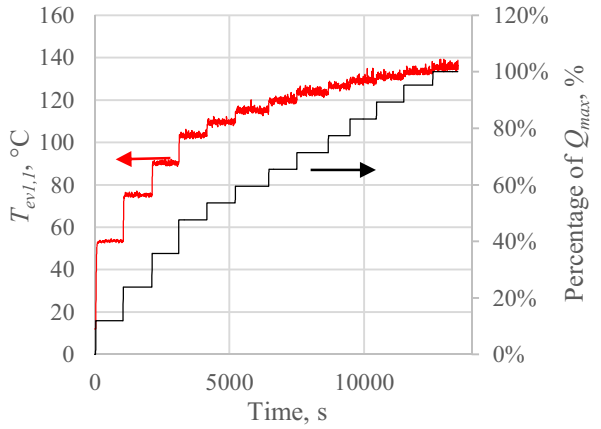


Fig. 3. Temporal evolution of evaporator temperature (N-pentane, FR = 70%, T_{cryo} = 10 °C).

The higher conductance and heat flux density have been obtained from maximum heat power inputs resulting in an average evaporator temperature of around 151°C with cold source fixed at 40°C. Fig. 4 presents some dimensionless thermal conductances G^* as functions of dimensionless heat power applied, Q^*, for three cold source temperatures:

$$G^* = \frac{G}{G_{max}} \qquad (6)$$

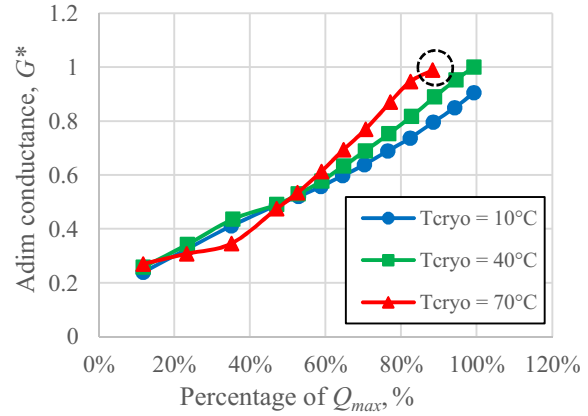


Fig. 4. Performances of the PHP for heat power input equally distributed between sources (N-pentane, FR = 70%).

It can be observed that heat power input improves performances as in classic pulsating heat pipes (up to five times from 10% to 100% of Q_{max}). Moreover one can see that with power input higher than 50% of its maximal value the thermal performances also increase with cold source temperature. Below this value, the behavior remains very similar whatever the temperature.

However, it can also be observed that, for a cold source temperature of 70°C, maximum heat power input wasn't reached (experiment was stopped at 90 % of the maximum power input reached for the two other temperatures, see dotted black circle); this is due to sudden evaporator temperature rise until exceeding the temperature limit (T_{max} = 183°C), as will be seen hereafter. This brutal temperature increase is the result of a dry-out stopping the oscillatory behavior of the system in the evaporator zones.

3.1.2 Dry-out occurrence detection

The dry-out criteria is not well-known in the literature. In this part, an attempt to identify some parameters in current operating conditions will be developed.

Fig. 5 presents the steady-state evaporator average temperature during tests as function of heat power input, corresponding to operating conditions of Fig. 4. It can be seen that only one dry-out is noticeable (mentioned above and shown by the dotted black circles of Fig. 4 and 5)), for an evaporator temperature of 164°C, for the cold source temperature of 70°C. One can also notice that experiments with lower cold source temperatures present lower temperature recordings. Hence a temperature of 164°C wasn't reached in the latter conditions, even for the maximum heat power input. It is obvious that increasing cold source temperature increases the overall temperature of the system. One can therefore assert that the heat power input triggering dry-out of the system decreases with increasing cold source temperature, because less power input is needed to reach the same temperature level.

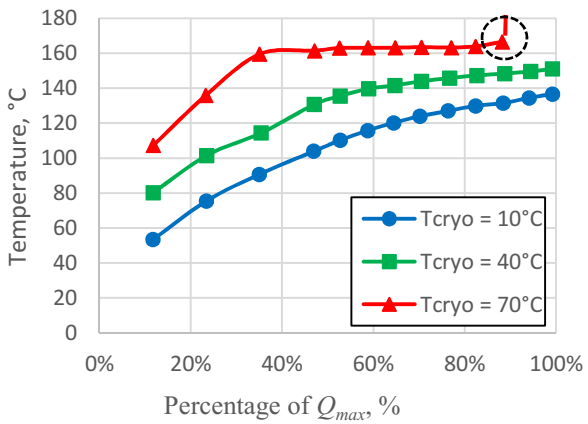


Fig. 5. Steady-state temperatures of the PHP for heat power input equally distributed between sources (N-pentane, FR = 70%).

Starting from the observation of this phenomenon for a cold source temperature of 70°C, the heat power input triggering dry-out has then been studied more precisely for cold source temperature values ranging from 55°C and 70°C. One can see on Fig. 6 the evolution of T_{evap} recorded just before dry-out, and the corresponding dimensionless heat power input triggering dry-out as functions of cold source temperature. It can first be noted that the evaporator temperature before dry-out increases slowly but remains quite constant (around 162°C), whatever T_{cryo}. On the contrary, the heat power input necessary to trigger dry-out decreases with cold source temperature and therefore appears to be a criterion less sensitive than the temperature, in such conditions. Indeed, if the temperature limit remains quite constant, a lower power input is needed to reach the same temperature level with a higher cold source temperature. Hence cold source temperature seems to be an important parameter for dry-out limitation detection. It is nonetheless not established that evaporator temperature is the only limiting parameter.

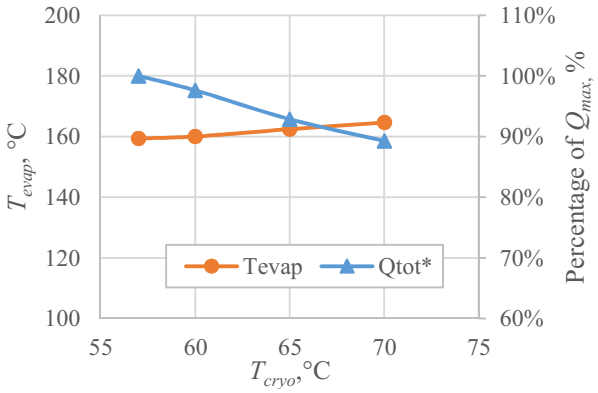


Fig. 6. Evaporator temperature and heat power input triggering dry-out, as functions of T_{cryo}
(N-pentane, FR = 70%).

3.2 PHP response to unequally distributed power among sources

3.2.1 Dry-out limit vs. number of operating sources

In the following, results showing the behavior of the PHP tested with non-uniform heat power supply among sources will be presented. This non uniformity will be defined as "heating pattern" to characterize the heat powers mapping between the three sources. First of all, Fig. 7 presents the maximum heat power applied per source, $Q^*_{i,max}$, relative to maximum value reached for equally distributed power (Section 3.1), before dry-out occurs in the most loaded source. One can observe that the dry-out occurs at much lower heat powers input, depending on the number of operating supplied sources compared to uniform heating pattern equally distributed among them.

One can assume that a dry-out limit, depending on the heating pattern, exists and it can here been observed that this limit increases with number of operating sources. Starting from this, focus will be made on one source having an increasing heat power input compared to the two others maintained at constant and equal heat powers applied.

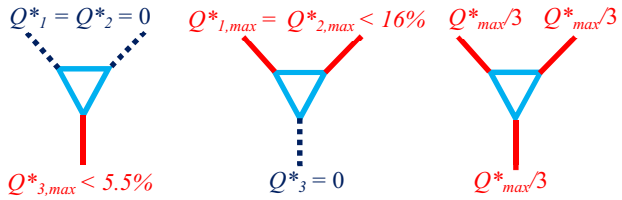


Fig. 7. Percentage of maximum heat power triggering dry-out *vs.* number of operating sources
(N-pentane, FR = 50%, T_{cryo} = 10°C).

3.2.2 Dry-out limit for increasing heat power applied Q_3 (with $Q_1 = Q_2 = Cte$)

During heat power input increase of Q_3 compared to the fixed two others, one can observe on figure 8 a corresponding temperature rise of this evaporator zone 3, much more important than when all three sources are uniformly heated, and for much lower heat power values. It can be seen that, for a heat power difference increase of Q_3, relative to Q_1 and Q_2 (fixed here at 500 W), from 0 to +100 W, the temperature difference between sources reaches around 5°C, whereas for equally distributed heat power among sources, the maximum temperature difference is of 2.6°C for a global power difference increase from 0 to +300 W, hence from 0 to +100 W per source (corresponding to the same local heat power difference).

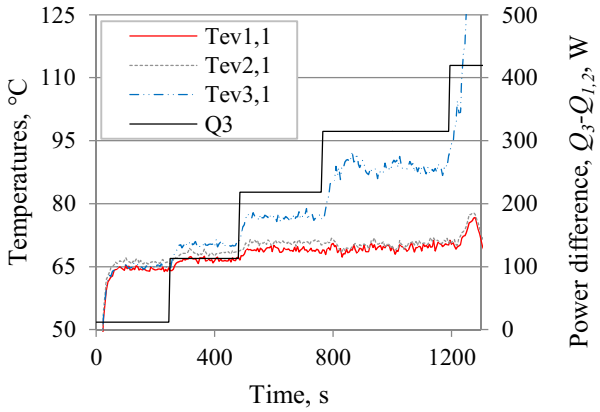


Fig. 8. Influence of increasing Q_3 on evaporator temperatures (N-pentane, FR = 70%, T_{cryo} = 10°C, Q_1 = Q_2 = 500 W)

The temperature increase is even higher with much more heat power difference and will lead to a dry-out of the most heated source compared to the two others, remaining quite stable, as can be seen after 1200 s on figure 8. One can also notice on this figure that the source 3 temperature before dry-out (around 90°C) is much lower than its value reached for equally distributed heat power (around 162°C at Q_{max}).

Figure 9 plots the corresponding condenser temperatures during the test of figure 8. One can notice that, temperatures are increasing in faces 2 and 3 of the condenser which are related to source 3 of the evaporator while face 1 of the condenser related to source 1 and 2 of the evaporator is quite stable and not contributing to source 3 cooling. Nevertheless, one can see that, when dry-out occurs after 1200 s, condenser temperatures decrease with less fluctuations. This is representative of the stop of oscillation.

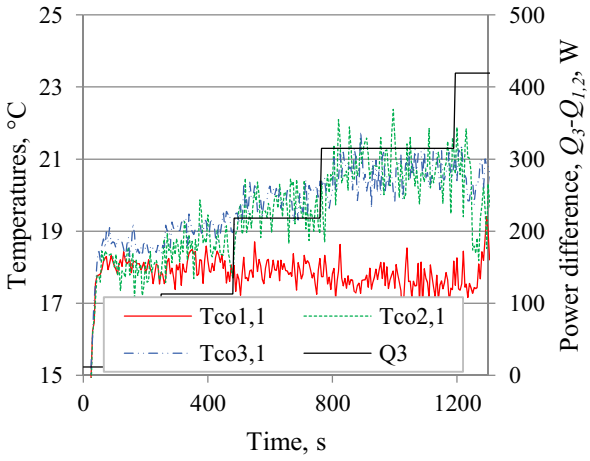


Fig. 9. Influence of increasing Q_3 on condenser temperatures (N-pentane, FR = 70%, T_{cryo} = 10°C, $Q_1 = Q_2$ = 500 W)

3.2.3 Dry-out limit for decreasing heat power applied Q_3 (with $Q_1 = Q_2 = Cte$)

Let us now take an interest to the PHP behavior when the latter is subjected to a decrease of one of its hot sources (Q_3), compared to the two others ($Q_1 = Q_2$). It can be seen on figure 10 that, during a heat power decrease of Q_3 compared to the two others, and starting from an initial uniform heat power input of 1 kW per source, a very important decrease of the temperature of source 3 ($T_{ev,3}$) occurs, but also a smooth decrease of that of the other sources. For these operating conditions and a filling ratio of 70%, no dry-out has been detected with decreasing heat power applied to source 3.

Nonetheless, it can be seen on figure 11 that, for a filling ratio of 50% of N-pentane, if a heat power decrease of Q_3 causes a slight temperature decrease of the corresponding temperature of source 3, and a small temperature decrease of source 2, unexpectedly, it also causes a slight temperature increase of source 1, followed by source 2. This heat power decrease will lead to a dry-out of source 1 for a heat power difference between sources of -140 W.

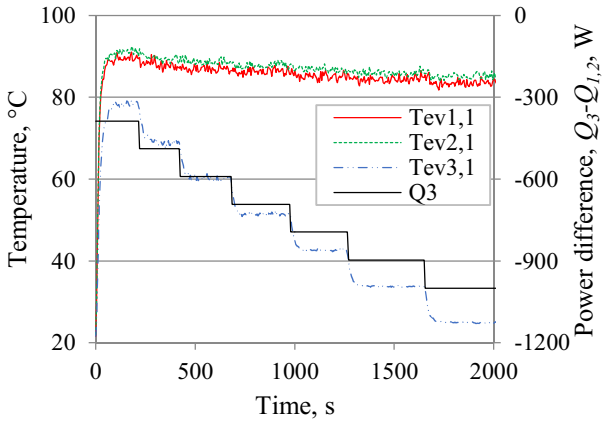


Fig. 10. Influence of decreasing Q_3 on evaporator temperatures (N-pentane, FR = 70%, T_{cryo} = 10°C, $Q_1 = Q_2$ = 1 kW)

A runaway effect of the dry-out sources might be attributed to the evolution of local filling ratio due to heat power difference. Indeed, the hotter the source compared to the others, the less liquid it will contain due to pressure and local vapor volume increase but also due to more condensation in colder zones. Therefore the local filling ratio of hotter sources will decrease such as the performances if filling ratio gets lower than the optimum one (around 50%), increasing even more the temperature increase in a self-aggravating effect.

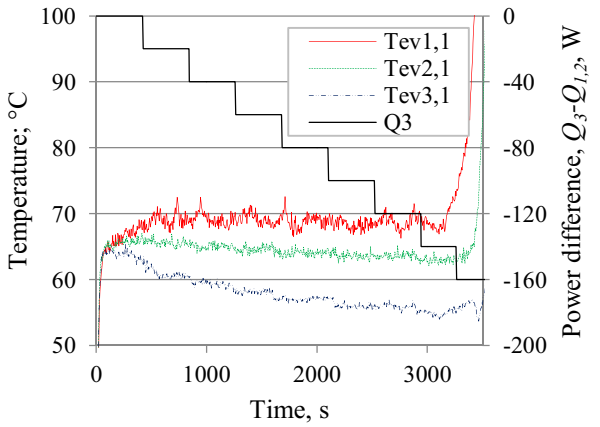


Fig. 11. Influence of decreasing Q_3 on evaporator temperatures (N-pentane, FR = 50%, T_{cryo} = 10°C, $Q_1 = Q_2$ = 500 W)

On the opposite side, a self-stabilizing effect can be assumed if the filling ratio is higher than the optimal one reported in the literature (for example 70% instead of 50%). Indeed the dry-out would decrease local filling ratio and therefore get the filling ratio closer to its optimum while increasing performances, permitting a higher power difference before dry-out.

3.2.4 Dry-out parameters

It has been observed below that, in equally distributed heat power between sources, there seems to be a rather constant temperature limit before dry-out occurs despite cold source temperature variations; but, in figure 12, one can observe that, for a fixed value of the filling ratio in non-uniform heat power distribution, the temperature before dry-out seems to increase with cold source temperature, and also with heat power initially applied to the three hot sources: the more the sources are heated, the more likely they are to support a heat power difference.

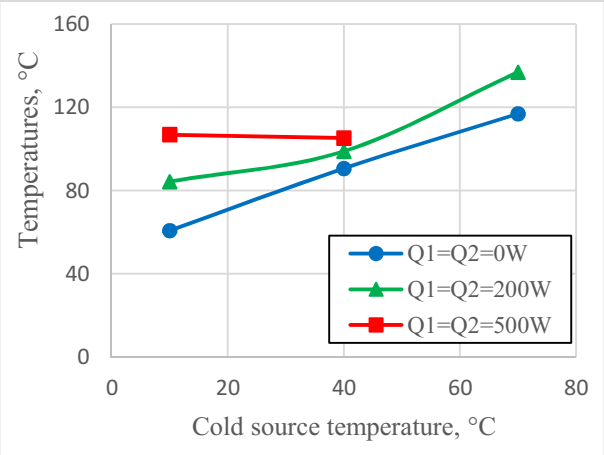


Fig. 12. Evaporator temperatures before dry-out for increasing Q_3 as functions of T_{cryo} (N-pentane, FR = 70%)

Note that the temperature before dry-out is not reported on figure 12 for T_{cryo} = 70°C and $Q_1 = Q_2$ = 500W because the temperature security limit was reached before dry-out occurs. It can then be asserted that this limit will be higher than 182°C.

4. CONCLUSIONS

In this paper, a specific pulsating heat pipe is presented, showing its cooling capabilities, both in terms of equally distributed heat powers applied among sources, and of non-uniform heating patterns leading to premature dry-out of the more heated sources. The maximal heat power applied reached values exceeding 8 kW. This pulsating heat pipe showed its higher performances (thermal conductance) for the maximal heat power input or just before dry-out. Indeed, the performances improvement with heat power input and cold source temperature observed in bibliography (up to 4 kW, [2]) can be extended to power input exceeding 8kW until dry-out occurs. At equally distributed power input, evaporator temperature before dry-out seems to be quite constant whatever the cold source temperature. Reaching this temperature level requires less power input with a higher condenser temperature reducing the dry-out limit.

PHP operation is also possible with heat power input unequally distributed among different evaporator zones. Such a heating pattern with power difference among different areas will have unfortunately lower dry-out limits, depending mainly on the number of sources supplied and the filling ratio.

A runaway or self-stabilizing effect can be observed with heat power difference between one and the other sources depending on the filling ratio.

Finally, the maximum temperature reached in an increasing heat power source, compared to the two other ones with fixed heat power, seems to increase with increasing cold source temperature T_{cryo} and increasing heat power applied to the constant sources ($Q_1 = Q_2$).

ACKNOWLEDGEMENT

The authors wish to thank the French National Research Agency ANR in the frame of the TDM-AAP project ‘AARDECO’, who supported this work.

NOMENCLATURE

D	:	Diameter (m)
FR	:	Filling Ratio (%)
G	:	Conductance ($W.K^{-1}$)
Q	:	Power (W)
T	:	Temperature (°C)
V	:	Volume (m^3)
λ	:	Thermal conductivity ($W.m^{-1}K^{-1}$)

Subscripts

adia/ad	:	adiabatic
air	:	air
cond/co	:	condenser
cryo	:	cryostat
evap/ev	:	evaporator
in	:	inner
l	:	liquid
loss	:	losses
max	:	maximum
out	:	outer
tot	:	total
*	:	dimensionless

REFERENCES

[1] Charoensawan, P., Khandekar, S., Groll, M., Terdtoon, P., Closed loop pulsating heat pipes: Part a: parametric experimental investigation, *Applied Thermal Engineering,* 23 (2003) 2009-2020.

[2] Ayel, V., Bertin, Y., Romestant, C., Burban, G., Experimental study of pulsating heat pipes tested in horizontal and vertical positions, *Proc. of 15th International Heat Pipe Conference*, Clemson SC, USA (2010) 6 p.

[3] Lin, L., Ponnappan, R., and Leland, J., Experimental investigation of oscillating heat pipes, *Journal of Thermophysics and Heat Transfer*, 15 (4) (2001) 395-400.

[4] Yang, H., Khandekar, S. and Groll, M., Operational limit of closed loop pulsating heat pipes, *Applied Thermal Engineering,* 28 (2008) 49–59.

[5] Kammuang-lue, N., Sakulchangsatjatai, P. and Terdtoon, P., Multiple Heat Source Arrangements of a Vertical Closed-Loop Pulsating Heat Pipe, *Proc. of 10th International Heat Pipe Symposium*, Taipei, Taiwan (2011) 184–189.

[6] Jiansheng, W., Zhenchuan, W. and Meijun, L., Thermal performance of pulsating heat pipes with different heating patterns, *Applied Thermal Engineering*, 64 (2014) 209-212.

[7] Mangini, D., Mameli, M., Georgoulas, A., Araneo, L., Filippeschi, S. and Marango, M., A pulsating heat pipe for space applications: Ground and microgravity experiments, *International Journal or Thermal Sciences,* 95 (2015) 53-63.

Thermo-hydrodynamics of Phase-change Induced Oscillating Taylor Bubble Flows

Vyas Srinivasan[1], Manoj Rao[2], Sameer Khandekar[1], Frédéric Lefèvre[2], Jocelyn Bonjour[2]

[1] *Department of Mechanical Engineering, Indian Institute of Technology Kanpur, Kanpur 208016, India*
[2] *CETHIL UMR5008, Université de Lyon, CNRS, INSA-Lyon, Univ. Lyon 1, F-69621, Villeurbanne, France*

Abstract

This paper presents a synthesis of experimental results and theoretical analyses obtained in the frame of a joint collaborative research program between France in India, devoted to understanding of Taylor bubble/slug flows in mini channel geometries, under diabatic/adiabatic, oscillating/non oscillating flow conditions. This type of flow is especially encountered inside Pulsating Heat Pipes (PHP), in which the self-sustained thermally driven oscillating flow is generated by evaporation/condensation mass exchange process. Specialized and dedicated range of experiments was conducted using High Speed Videography (HSV), Particle Image Velocimetry (PIV) and Infra-Red Thermography (IRT). New understanding of the local thermo-hydrodynamics of Taylor bubbles and slugs was obtained owing to a specific experimental test bench in which the working fluid and the operating temperatures could be chosen by the user. The experimental results clearly showed that evaporation of the thin film is responsible for the oscillation patterns that are observed. In addition, experimental results obtained using a mechanical oscillation system in isothermal conditions show that classical correlations used to calculate pressure drops inside the liquid slug are quite satisfactory, in the case of this particular oscillating flow. PIV and IRT for non-boiling two-phase systems, both in adiabatic/diabatic conditions and oscillating/non-oscillating flows were also undertaken. Evaporation of the laid down liquid thin-film during motion of an isolated partially wetting liquid plug revealed that the hydrodynamic considerations of Taylor's law for predicting thin-film thickness is well able to predict the evaporative mass flux under diabatic conditions. Various flow aspects of liquid plugs were delineated. It is believed that such fundamental studies will provide the necessary framework for 'unit-cell' modelling approach of pulsating heat pipes.

Keywords: oscillating flow, Taylor bubble, pressure drop, pulsating heat pipe, liquid film, numerical modelling

1. INTRODUCTION

A detailed review on advanced and unsolved issues in pulsating heat pipes (PHP) was written by Zhang and Faghri [1]. It has been shown that the number of relevant parameters to characterize a PHP is so large that it is difficult to explicitly discriminate the effect of one parameter among the others. At least, researchers agree that the oscillations in a pulsating heat pipe are driven by instabilities that appear due to coupling of the adiabatic vapor compression and phase-change mass exchange process [2]. Nevertheless, changing the nature of the fluid, the tube material, the temperature of the evaporator or the condenser, the diameter of the tube, etc. bring into focus a very wide range of behaviors that are generally still not well understood. Detailed quantitative information of flow and heat transfer processes inside PHPs is still lacking.

To decipher the complete PHP dynamics, one has to begin with a simple system of a minimal complexity, which is a straight capillary containing a single couple or unit-cell, with one liquid plug and one vapour bubble. Although such a system seems to be apparently simple, it contains the main phenomena involved in the multi-bubble PHP. One can notice the evaporation/condensation of liquid, formation of continuous menisci and wetting films, motion of menisci and contact lines (film edges), and viscous friction during the bubble motion, among other phenomena that govern the PHP dynamics. The motion of constrained bubbles in capillaries (Taylor bubbles) is well studied under isothermal conditions [3], [4]. The evaporation at the contact lines and in the thin films has also been actively studied as a separate system [5][6]. The evaporation in the constrained bubble geometry is studied in the domain of convective boiling [7]. The dewetting in capillaries has also been considered [8]. The oscillation of bubbles at isothermal conditions has been studied by Lips and Bonjour [9]. However, the conjunction of phase-change and oscillating dynamics introduces new challenges.

Since 2010, the number of experimental works dealing with the physical phenomena occurring in

a straight capillary containing a unit-cell, i.e. a single-couple, with one liquid plug and one vapour bubble has increased remarkably. This shows an acknowledgement by scientific community of the necessity of fundamental studies related to PHPs.

From a modeling perspective, this approach was initiated by Zhang and Faghri [10] and Dobson [11], who theoretically studied the governing mechanisms of a single branch of the PHP, consisting of one vapour bubble and one liquid slug. Das et al. [12] developed a similar approach, including the two-phase equilibrium that occurs locally at the liquid vapour-interface, especially along the time-varying wetting thin film which gets laid down by the liquid plug during its journey from the evaporator towards the condenser and through which the major part of the heat and mass transfer occurs.

This paper presents a synthesis of experimental results and theoretical analyses obtained in the frame of a joint collaboration program between France in India. More precisely, the objectives of the project were to study thermo-hydrodynamics of phase-change induced oscillating Taylor bubble flows in mini channels under various boundary conditions.

2. EXPERIMENTAL BENCHES

Two specific experimental test benches were developed to:

- Analyze self-sustained thermally driven two-phase oscillations between two sources, wherein the operating temperatures could be chosen by the user.
- Estimate the pressure drops within an oscillating two-phase flow.
- Discern the local liquid thin-film evaporation mechanism under diabatic conditions.

2.1 Oscillating two-phase capillary flow

This section presents the experimental bench developed to observe the system consisting of a liquid slug and a vapour plug oscillating in a tube closed at one end and connected to a reservoir at a constant pressure P_r at the other end [15]. The vertical transparent capillary tube (Fig. 1), made of glass, has a diameter equal to 2 mm. The liquid slug oscillates between a heat source (length = 200 mm) at temperature T_e located near the closed side and a heat sink (length = 200 mm) at temperature T_c located near the reservoir. In between, an adiabatic section separates the condenser and the evaporator (length = 10 mm).

The evaporator and the condenser are transparent heat exchangers, whose temperatures are controlled by two thermostatic baths. A third thermostatic bath is used to control the temperature of the reservoir, and thus its saturation pressure. The two-phase oscillatory flow is characterized by simultaneous vapour pressure and temperature measurements and meniscus displacement tracking in synchronization with each other. Two high speed cameras are simultaneously used to track the meniscus displacement and movement of the triple-line inside the evaporator.

Also a new experimental bench (Fig. 2) was built to measure the frictional pressure drop of oscillating single-phase flow, taking the same dimensions as discussed above. The size of the capillary tubes is kept 2 mm internal diameter and 6 mm outer diameter. Length of the capillary tube is taken as 700 mm. This tube is dipped inside the reservoir. Keller® make differential pressure transducer is connected at one end of the capillary tube, and other end to the reservoir, so as to measure the pressure difference during the oscillations of the meniscus. The liquid inside the reservoir-capillary tube system is externally excited using a pressure function generator connected at the reservoir to move the meniscus in the desired oscillating pattern. A high speed camera is simultaneously used to track meniscus displacement. The pressure measurements are synchronized with the video camera with external trigger in the data acquisition system.

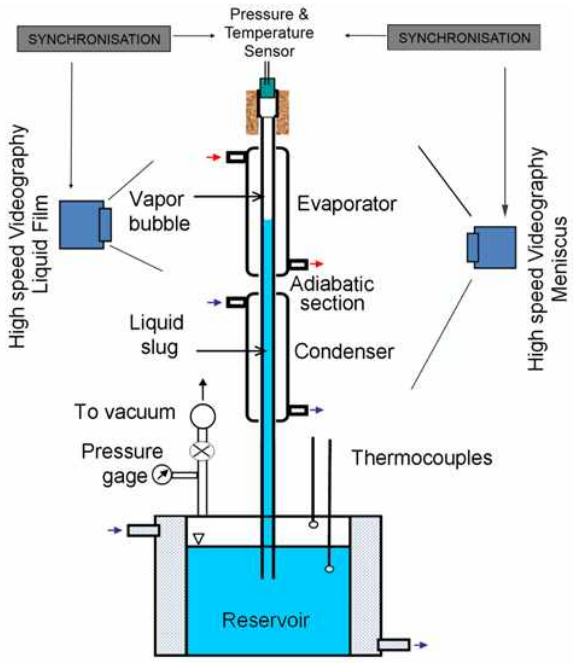


Fig. 1. Experimental bench for self-sustained thermally driven two-phase oscillations [14][15].

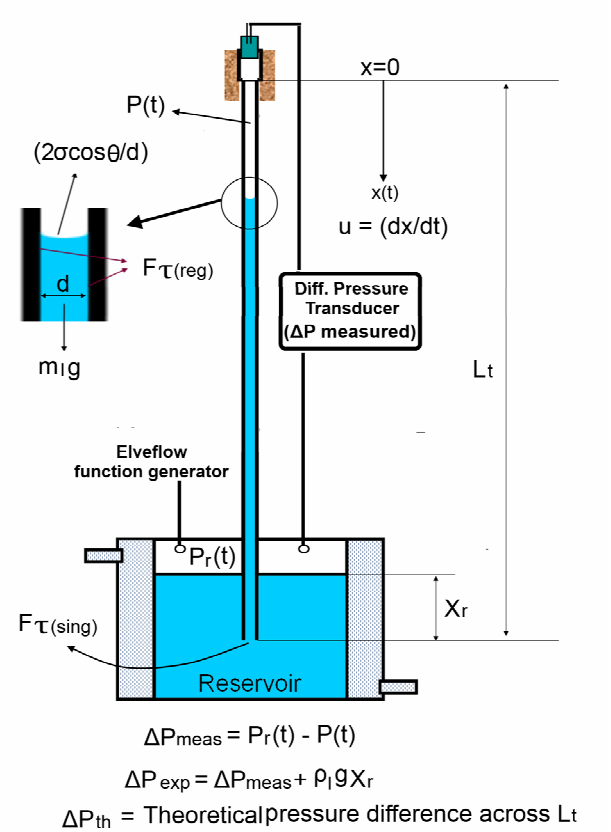


Fig. 2. Experimental bench for pressure drop measurements within self-sustained thermally driven two-phase oscillations.

2.2 Non-oscillating two-phase capillary flow

This section deals with the experimental setup to discern the evaporation mechanism of an isolated liquid plug (methanol) moving inside a capillary tube maintained at constant temperature. The schematic of the experimental setup is shown in Fig. 3. It is well known that a moving liquid plug lays down a thin-film behind the rear meniscus, whose thickness is predicted based on hydrodynamic consideration as (Aussillous and Quere [12]):

$$\frac{\delta}{r} = \frac{1.34Ca^{2/3}}{1+1.34*2.5Ca^{2/3}} \quad (1)$$

The experiment was developed to understand the evaporation of such laid down thin-film. Liquid plug (methanol) of known *L/D* ratio was placed inside a glass capillary tube of I. D. 1.5 mm. The liquid plug at rest is made to move by pushing air at constant flow rate (~25 mlph) through the section of capillary tube (length of 20 cm) that remains un-heated. In this section, the liquid plug reaches a steady motion with uniform velocity (Ca ~ 2×10^{-05}). It then passes through the heated section of the capillary tube (length 20 cm). The heated section is maintained at constant temperature by means of transparent tube-in-tube heat exchanger, the outer side of which is maintained at required temperature by circulating hot water (from a constant temperature bath, Julabo® - F25, ±0.1ºC). The choice of methanol (saturation temperature = 65 ^{o}C at 1 atm) allows the use of water as fluid for heat exchanger. The entire set up is transparent to facilitate high speed recording (250 fps, Photoron® SA-3) of the liquid plug in this heated section.

The recorded images were then processed to find the evaporation rate at each temperature. Digital image processing was carried out in MATLAB® to get the instantaneous liquid plug velocity. Equation (1) was then used to get the liquid thin-film thickness based on the obtained instantaneous velocity. Having known the theoretical value of thin-film thickness, the reduction in bulk length of the liquid plug is theoretically calculated. This theoretical reduction in liquid plug length is then compared with the experimentally observed length of the liquid plug. This allows the verification of Taylor's law of predicting thin-film thickness at diabatic conditions. The results of this experiment are elaborated in Section 3.3. In addition, the thin-film formation during motion of the liquid plug at adiabatic condition was captured using confocal microscopy (Leica®-Model-TCS-SP5-II), where dewetting of the thin-film was observed. Fig. 4 shows the schematic of evaporation from the thin-film along with the thin-film formation captured using confocal microscope.

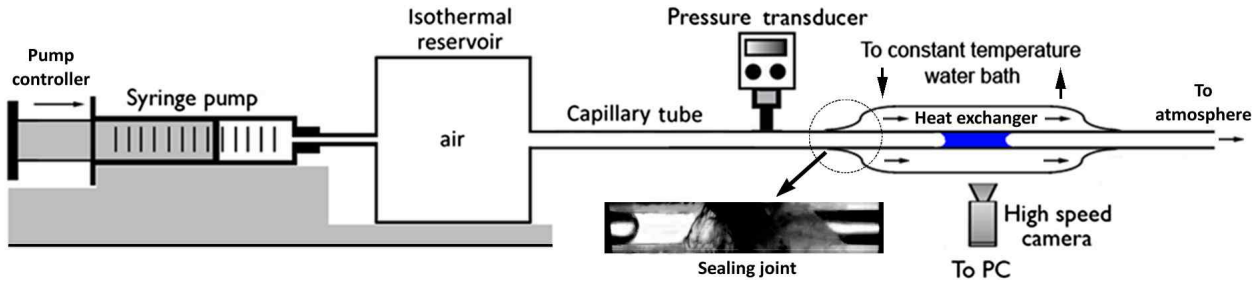


Fig. 3: Schematic of experiment to study evaporation of a moving isolated liquid plug [26].

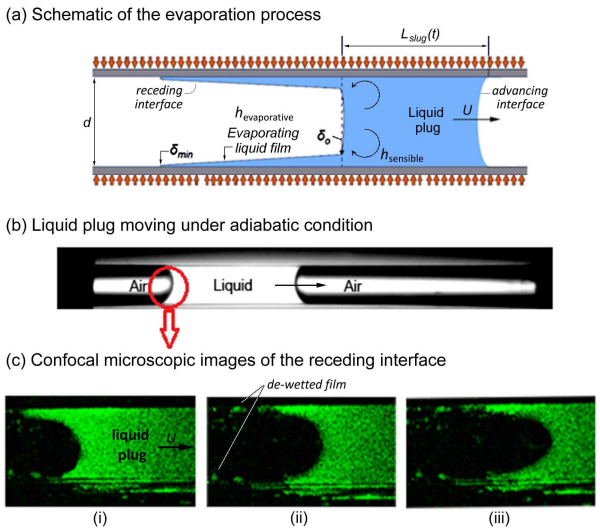


Fig. 4: (a) Schematic of the evaporation process at the thin-film (b) Image of liquid plug (L/D = 6.7), under adiabatic flow condition, and, (c) Since the liquid thin-film is in order of micro-meter, visualizing it with high speed camera is not possible. Hence the same flow condition is replicated under confocal microscopy to clearly show the existence of liquid thin-film during motion[26].

3. EXPERIMENTAL RESULTS AND THEORETICAL ANALYSES

Experimental results obtained with the above described experimental benches has brought new information about the dynamics of the liquid film laid down by the meniscus leaving the evaporator, pressure drops in oscillating flows, and the evaporation mechanism of the drained thin-films.

3.1 Dynamics of the liquid film

Fig. 5 shows experimental results obtained with FC72 as the working fluid: the temporal variation of vapor pressure, along with the location of the meniscus and the triple-line are plotted for the case of P_r = 0.5 bar, T_e = 46ºC and T_c =20ºC (similar results were obtained for other fluids and conditions [16]). It is observed that meniscus movement and pressure variation are quasi-periodic and nicely repeatable. When the meniscus moves towards the condenser (downward motion), a thin liquid film gets drained or laid on the tube wall. Evaporation of this film adds mass to the vapor space and helps in increasing the vapor pressure. Until the time the liquid film laid down by the downward moving meniscus is completely evaporated, the meniscus is not able to re-enter the evaporator, and thus moves back again twice into the condenser. Thus, two strokes are seen to occur in the condenser section. The meniscus re-enters the evaporator section, after the second stroke in the condenser is over, and then the quasi-periodic cycle continues. The maximum high level reached by the meniscus inside the evaporator is rather constant and close to x = 80 mm for the different condenser temperatures. This tends to suggest that the amount of vapour generated during one cycle at the evaporator is rather constant, since it is proportional to the length of the liquid film drained by the meniscus in the evaporator.

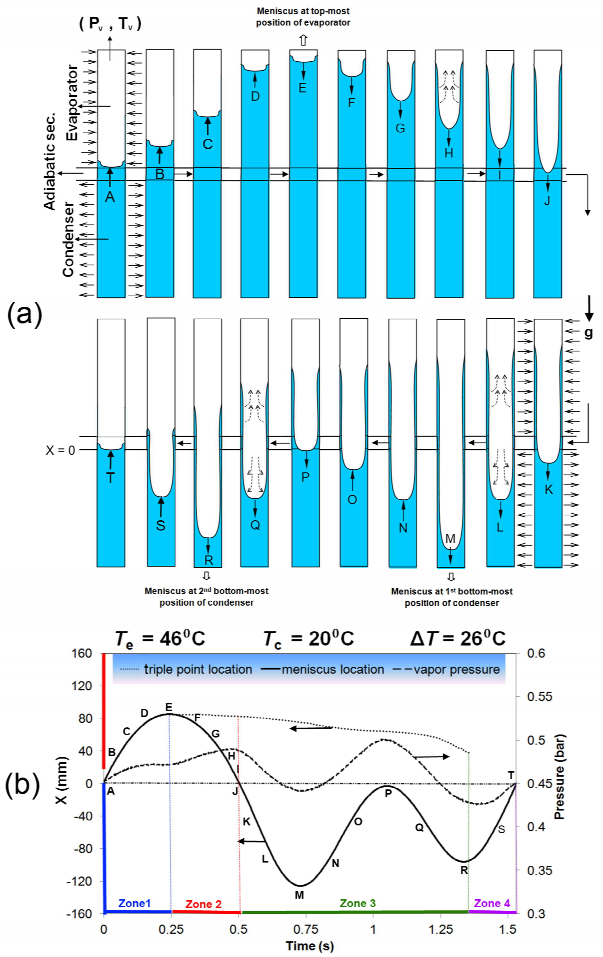


Fig. 5. (a) Schematic explaining the events during one cycle of the meniscus motion. (b) Time evolution of the meniscus location, triple line location and vapor pressure during one complete cycle [15].

The experiment provides the instantaneous location of the meniscus inside the capillary tube during its oscillatory motion. Therefore, the instantaneous volume of vapour is also known. The instantaneous pressure and temperature of the vapour plug is also known from the measurements. Furthermore, it was shown that the vapour temperature is always above the saturation temperature [16][17]. Therefore, ideal gas equation can be invoked to obtain the instantaneous mass of vapour inside the system. From mass and energy balance consideration, the liquid film thickness

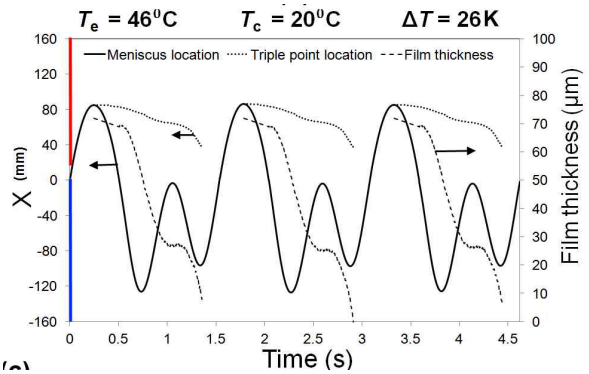


Fig. 6. Temporal variations of film thickness, and location of meniscus and triple line [16].

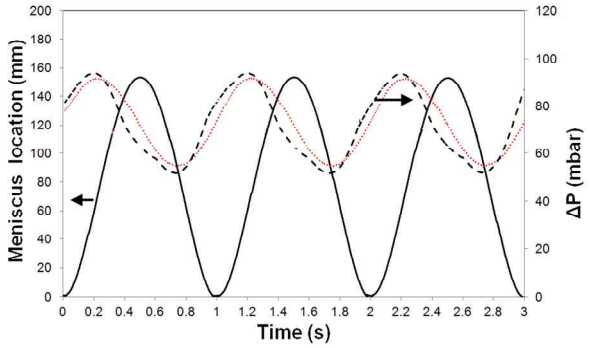


Fig. 7. Experimental bench for pressure drop measurements within self-sustained thermally driven two-phase oscillations.

variation can also be calculated from this experiment [16]. Two different modes of evaporation are observed inside the system: one at the triple-line and one at the liquid-vapour interface.

Fig. 6 shows temporal variation of the location of meniscus/triple-line and the film thickness calculated using this approach for the same experimental data. The mean estimated initial liquid film thickness is estimated to be in the order of 70 μm, which is in line with classical correlations.

When the temperature difference increases between the heat source and the heat sink, different meniscus dynamics, with excellent repeatability, were observed. The experimental results clearly demonstrate that evaporation of the liquid film, both at the triple line and on the liquid-vapour interface is responsible for these patterns. Considering that no comprehensive model of PHP system is available, the conclusions and directions provided in this study are important for building a broad understanding.

3.2 Pressure drops in oscillating flows

This section presents new experimental results obtained with FC72 in vertical orientation of the tube to measure the frictional pressure drop (Fig. 2). The liquid inside the reservoir-capillary tube system is externally excited using a pressure function generator connected at the reservoir to move the meniscus in desired oscillating pattern. This external excitation of the liquid generated similar conditions of meniscus oscillations as the thermally induced oscillations inside the capillary tube.

The experiments were performed for a frequency of oscillation of 1 Hz so as to compare to the typical frequency range of the experiments in diabatic conditions. The meniscus oscillations recorded during the experiment enabled to calculate the temporal variations of liquid slug velocity and its instantaneous mass.

The meniscus location (black line) and the experimental instantaneous differential pressure drop (red dotted line) are plotted in Fig. 7. The results are compared to classical correlations for pressure drops in fully developed flow inside a tube (black dotted line). A good agreement is observed between the theoretical and experimental data, which shows that classical correlations used to calculate pressure drops inside the liquid slug are relevant in the case of an oscillating flow.

3.3 Thin film evaporation

Fig. 8 shows the result of the same experimental and theoretical procedures (as per section 2.2), when it was carried out for different lengths of liquid plug moving through the heater section with different constant wall temperatures ($T_{wall} < T_{sat}$, in all cases). Note that the time elapsed (~ 55 s) for the liquid-plug motion in the adiabatic section of capillary is not shown here; In Figure 8a-d, a shift in real-time for recording different L/D is observed; for instance, the data for L/D = 13.3 begins at ~ 63 s, whereas the data for L/D = 6.7 starts from ~ 56 s. This is because, longer liquid plug takes more time to completely appear in the field of view of high-speed camera, after which the digital image processing commences. To supplement the graph, Fig. 9 shows the images obtained at different sections of the heater region for L/D = 6.7, at different temperatures. The images clearly show the change of length of bulk liquid plug, due to the rate of evaporation being higher, as the applied wall temperature increases. Note also the change in slope of the curve representing the reduction of plug length with time, as wall temperature is increased, due to the enhanced rate of evaporation with increasing

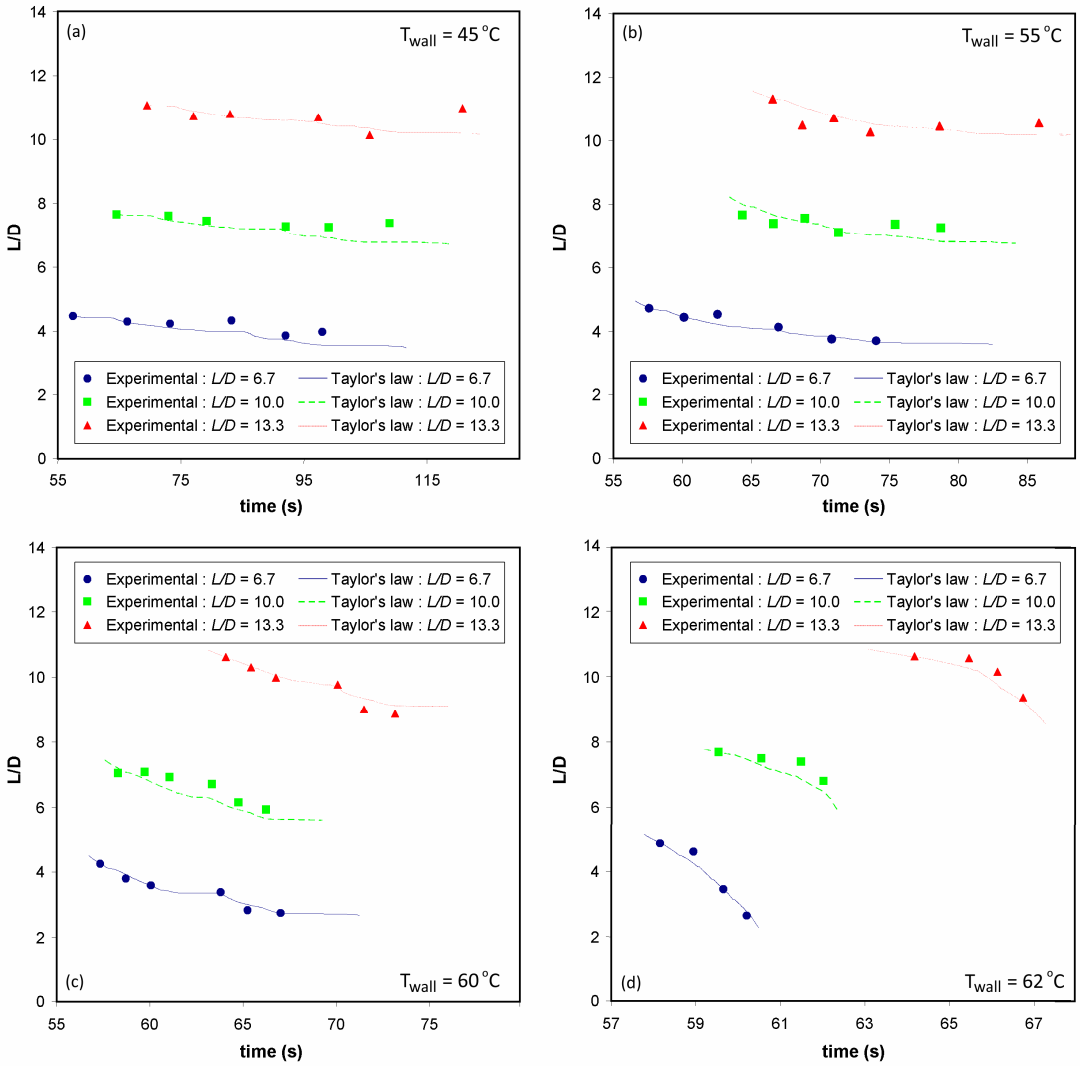


Fig. 8: Change of length with time due the effect of thin-film drainage and thin-film evaporation, for different initial *L/D* ratios at a constant wall temperature of (a) 45ºC (b) 55°C (c) 60°C, and (d) 62°C [26].

temperature. These results indicate that, independent of the initial length of liquid plug, Taylor's law can still be used to predict thin-film thickness under diabatic conditions. This means that the reductions of length of bulk liquid due to evaporation at different wall temperatures (lesser than saturation temperature) continue to obey the drainage theory of thin-film. As a consequence of this, the evaporative mass flux from thin-film during the flow can be predicted based on Taylor's law itself. The physical understanding of the observed trend is explained in terms of the competing mechanisms at play during the flow process, namely: (a) Drainage of thin-film due to motion and, (b) Evaporation of thin-film. This indicates the fact that the major source of heat/mass transport is from the thin-film region, which can indeed be predicted based on Taylor's law, once the instantaneous Capillary number is known.

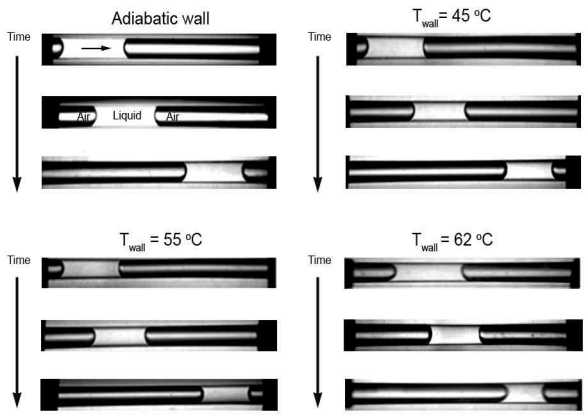


Fig. 9: Images obtained to capture the change the liquid plug length (*L/D* = 6.7) with time as it flows through the length of heater section, maintained at different wall temperature. For the same liquid plug length, it can be clearly seen that, higher wall temperature causes more evaporation from the thin-film, thereby leading to greater reduction of length of bulk liquid [26].

4. SUMMARY AND CONCLUSIONS

Mathematical modeling of PHPs through 'first' principles is an unsolved contemporary problem. Simplifications and assumptions made in all the modeling approaches developed so far render them unsuitable for engineering design because the abstractions contained therein are not in sync with the real time transport processes taking place in the device. At present, there are no theoretical models or correlations available that can predict the complex thermo-hydrodynamic transport behavior of PHPs. This prevents their widespread use in industrial applications.

The experiments reported in this paper have been specifically conducted to help mathematical modelling of the system dynamics using the unit-cell approach. Several important conclusions can be made based on these experiments, some of which are elaborated below:

Thin film evaporation and condensation plays a very crucial role in the overall dynamics. Unless this is included in the global model, realistic predictions cannot be made. Corollary to this is the fact that unless mass addition/removal from the vapor space is considered, the amplitude of oscillations observed in actual experiments cannot be predicted. Treating the vapor as an ideal gas with only sensible heating/ cooling is not sufficient (Rao et al., [15]; Mameli et al. [21]).

The frictional pressure drop required to sustain the flow, especially in the liquid plugs with small *L/D* ratios, may be substantially higher than what is predicted by assuming a simple Poiseuille flow inside them. The fluid flow pattern in the oscillating two-phase 'unit-cell' system (that is, one Taylor bubble with adjoining liquid plug, as has been depicted in Fig. 2) is rather complex leading to high viscous dissipation. Moreover, three-phase contact lines tend to form inside the system, especially in the evaporator subsection, which lead to very high local dissipation (Srinivasan et al, [26][27]; Janeček and Nikolayev [18]). As L/D ratio increases, classical Poiseuille friction is sufficient to describe the flow.

Inertia forces play a significant role in the manifestation of flow physics of the device. Sudden acceleration and deceleration of the 'unit-cell' and its interaction with surface and capillary forces lead to complex flow phenomena, including breakage of liquid plugs into smaller fragments. While most hydrodynamic theories of visco-capillary flows are valid for low Capillary number (less than 10^{-3}) situations and high wettability conditions, engineering scale PHP devices do not pose such ideal situations. Partial wetting and relatively large Capillary numbers are routinely prevalent (Khandekar et al., [2]; Rana et al., [25]; Mehta and Khandekar, [22]).

The radial heat transfer to/from the liquid-vapor system must happen via the capillary tube material. Unlike a conventional heat pipe which attains a quasi-steady state, the transient oscillatory flow patterns inside a PHP manifests itself as a conjugate (conduction–convection) problem. Hence, the interplay of diffusional and convective time-scales of the system strongly affects the ensuing thermal-hydraulic response. In effect, thermal properties of the tube material are vital in predicting the overall system dynamical response (Nikolayev [23]; Rao et al. [14]; Rao et al. [15]).

It has been conjectured that non-equilibrium states of liquid and vapor are quite likely to coexist during the normal operation of PHPs. Conclusive experimental evidence is yet to come, however initial results do point towards this fact. It requires very precise and repeatable dynamic temperature measurements of local vapor and fluid film temperature so as to ascertain non-equilibrium condition and/or metastability. On one asymptote is the assumption that vapor and liquid in the Taylor bubbles are always under thermodynamic equilibrium. This essentially means that the relaxation time-scales of the phase-change by heat addition/subtraction are much faster than the typical characteristics time-scales of internal fluid flow and heat transfer through the walls in the PHP system. However, the essence of the entire PHP thermal phenomena lies in its transient thermo-fluidic characteristics. While one can talk about a 'quasi-steady' state in a global or lumped sense, nothing is, in fact, steady on the local level inside an operating PHP. Hence, the assumption of thermodynamic equilibrium between adjacent vapor bubbles and liquid plugs may not be the most appropriate postulation. The rapid inertial transient flow, vis-à-vis evaporation/condensation time scales, may lead to situations wherein superheated vapor and/or sub-cooled liquid co-exists for finite metastable timescales (Khandekar [19]; Nikolayev [24]; Rao et al., [15]).

ACKNOWLEDGEMENTS

Financial support from the Indo-French Centre for the Promotion of Advanced Research, New Delhi (Project #: IFCPAR: 4408-1/2010), is gratefully acknowledged. This work was also supported by the ANR in the frame of the TDM-AAP project ''AARDECO".

NOMENCLATURE

P_r : Pressure of the reservoir (Pa)
T_c : Temperature of the condenser (K)
T_e : Temperature of the evaporator (K)
δ : Liquid thin-film thickness (m)
r : Radius of tube (m)
Ca : Capillary number ($\mu v/ \sigma$)

REFERENCES

[1] Zhang, Y., Faghri, A., Advances and unsolved issues in pulsating heat pipes, *Heat Trans. Engg.,* 29 (2008) 20-44.

[2] Khandekar, S., Panigrahi, P. K., Lefèvre, F., Bonjour, J., Local hydrodynamics of flow in a pulsating heat pipe: a review, *Front. Heat Pipes*, 1 (2010) 1-20.

[3] Reinelt, D.A., The rate at which a long bubble rises in a vertical tube, *J. Fluid Mech.*, 175 (1987) 557-565.

[4] Bico, J., Quere, D., Falling slugs, *J. Coll. Interface Sc.*, 243 (2001) 262–264.

[5] Stephan, P.C., Busse, C.A. Analysis of the heat transfer coefficient of grooved heat pipe evaporator walls, *Int. J. Heat Mass Trans.*, 35 (1992) 383–391.

[6] Nikolayev, V.S., Dynamics of the triple contact line on a nonisothermal heater at partial wetting, *Phy. Fluids*, 22 (2010) 082105.

[7] Thome, J.R., Dupont, V., Jacobi, A., Heat transfer model for evaporation in microchannels, Part I: Presentation of the model, *Int. J. Heat Mass Trans.*, 47 (2004) 3375-3385.

[8] Callegari, G., Calvo, A., Hulin, J.P., Dewetting processes in a cylindrical geometry, *Euro. Phy. J.*, 16 (2005) 283-290.

[9] Lips S., Bonjour J., Oscillating two-phase flow in a capillary tube: experiments and modeling, Proc. 14th Int. Heat Pipe Conf., Florianopolis, Brazil, (2007).

[10] Zhang, Y., Faghri, A., Heat transfer in a pulsating heat pipe with open end, *Int. J. Heat and Mass Transfer*, 45 (2002) 755-764.

[11] Dobson, R.T., Theoretical and experimental modeling of an open oscillatory heat pipe including gravity, *Int. J. Therm. Sc.*, 43 (2004) 113-119.

[12] Das, S., Nikolayev, V.S., Lefèvre, F., Pottier, B. Khandekar, S., Bonjour, J., Thermally induced two-phase oscillating flow inside a capillary tube *Int. J. Heat Mass Trans.*, 53 (2010) 3905-3913.

[13] Aussillous P and Quere D, Quick deposition of a fluid on the wall of a tube. *Phy. Fluids* 12 (2000) 2367–2371.

[14] Rao, M., Lefèvre, F., Khandekar, S., Bonjour J., Understanding transport mechanism of a self-sustained thermally driven oscillating two-phase system in a capillary tube, *Int. J. Heat Mass Trans.*, 65 (2013) 451–459.

[15] Rao, M., Lefèvre, F., Khandekar, S., Bonjour, J., Heat and mass transfer mechanisms of a self-sustained thermally driven oscillating Liquid-Vapour meniscus, *Int. J. Heat Mass Trans.*, 86 (2015) 519-530.

[16] Rao, M., Lefèvre, F., Khandekar, S., Bonjour, J., Thermally induced two-phase oscillating flow in a capillary tube: theoretical and experimental investigations, *16th Int. Heat Pipe Conf.*, Lyon, France, (2012).

[17] Gully, P., Bonnet, F., Nikolayev, V., Luchier, N., Tran, T.Q., Evaluation of the vapour thermodynamic state in PHP, *17th Int. Heat Pipe Conf.,* Kanpur, India, (2013).

[18] Janeček, V., Nikolayev, V.S., Apparent-contact-angle model at partial wetting and evaporation: Impact of surface forces, *Phy. Rev.-E*, 87 (1), #012404, (2013).

[19] Khandekar S., Thermo-hydrodynamics of closed loop pulsating heat pipes, Doctoral dissertation, University of Stuttgart, Stuttgart-Vaihingen, Germany, (2004) (available at: http://elib.uni-stuttgart.de/opus/volltexte/2004/1939/

[20] Mameli M., Pulsating Heat Pipes: Numerical Modeling and Experimental Assessment, Doctoral dissertation, University Bergamo, Italy, (2012).

[21] Mameli M., Marengo M. and Khandekar S., Local heat transfer measurement and thermo-fluid characterization of a pulsating heat pipe, *Int. J. Therm. Sc*., 75 (2014) 140-152.

[22] Mehta B. and Khandekar S., Taylor Bubble-train Flow and Heat Transfer in the Context of Pulsating Heat Pipes, *Int. J. Heat Mass Trans.*, 79 (2014). 279–290.

[23] Nikolayev, V.S., Effect of tube heat conduction on the single branch pulsating heat pipe start-up, *Int. J. Heat Mass Transf.,* 95 (2016) 477–487.

[24] Nikolayev, V.S., Oscillatory instability of the gas-liquid meniscus in a capillary under the imposed temperature difference, *Int. J. Heat Mass Transf.,* 64 (2013) 313–321.

[25] Rana G. R., Sikarwar B. S., Khandekar S., Panigrahi P. K., Hydrodynamics of a Confined Meniscus in a Square Capillary Tube at Low Capillary Numbers, *Front. Heat Pipes*, 5 (1), (2014).

[26] Srinivasan V., Marty-Jourjon V., Khandekar S., Lefèvre F. and Bonjour J., Evaporation of an Isolated Liquid Plug Moving Inside a Capillary Tube, *Int. J. Heat Mass Trans.*, 89 (2015) 176-185.

[27] Srinivasan V., Khandekar S., Bouamrane N., Lefèvre F. and Bonjour J., Motion of an isolated liquid plug inside a capillary tube: Effect of contact angle hysteresis, *Exp. in Fluids*, 56:14:6 pages, (2015).

An Improved Correlation to Evaluate the Thermal Resistance of Pulsating Heat Pipes

Jean-antoine Gruss[1], Damien Gloriod[2], Nadia Caney[2], Geneviève Geffraye[1], Alain Memponteil[1]

[1] Univ. Grenoble Alpes, CEA LITEN DTBH, F-38000 Grenoble, 17 rue des Martyrs, F-38054 Grenoble Cedex 9, France
[2] Univ. Grenoble Alpes, UJF-Grenoble 1 / Grenoble-INP / CNRS, LEGI UMR 5519, F-38041 Grenoble, France

Abstract

The pulsating heat pipes (also named oscillating heat pipes) invented by Akachi have some advantages compared to other types of heat pipes and diphasic loops, they are a very compact, simple and costless heat transfer device and it may work more or less against gravity. However physical phenomena's involved are multiple and complex, and so far there is a lack of simple design correlations. The development of pulsating heat pipes applications is limited by this fact.

In this study we review thermal resistance correlations from the literature and compare those correlations with existing experimental data from the bibliography including tests performed in our laboratory.

We have modified the Khandekar correlation, introducing a modified Jakob number Ja* in order to take into account the effect of various temperature differences between the liquid and vapor phase, and negative inclinations.

The modified correlation fits reasonably well with the data and permits to extend the validity range to design pulsating heat pipes with various diameters, lengths, inclinations, number of loops, fluids and temperature differences.

Keywords: Design, Correlation, Pulsating heat pipe, Thermal resistance

1. INTRODUCTION

The pulsating heat pipes (PHP) invented by Akachi [1] has some advantages compared to other types of heat pipe and diphasic loops, they are a very compact, simple and costless heat transfer device and it may work more or less against gravity. However physical phenomena involved are multiple and complex, and so far there is a lack of physical models and design correlations. The development of PHP applications is limited by this fact.

One important element in the design phase of a PHP is the prediction of its thermal resistance.

There are a lot of parameters involved in the operation of PHP. Indeed, there are geometrical parameters as the lengths of heating, cooling and adiabatic zones, the number of loops, the internal diameter of tubes, the spatial orientation and the filling ratio (fluid volume/total internal volume).

These parameters are independent or interact each other. Moreover, fluid physical properties as vapor and liquid density, liquid heat capacity, viscosity, surface tension play a role, as the nature of the tube itself: rugosity, wetting, thermal inertia.

The type of heat input (temperature or flux imposed) as the heat flux intensity may give various flow configurations, as slug annular…in the PHP.

*Corresponding author: gruss@cea.fr,
Phone: +33-0438783725, Fax: +33-0438785161

This multitude of parameters, as well as the chaotic behavior of the operation of PHP makes it very difficult to develop a universal physical model able to predict PHP thermal performances.

To develop PHP's industrial applications, there is a need to have simple « engineering correlations », even with limited range of parameters, able to predict maximum heat flux and thermal resistance.

This study aims to review and compare existing thermal resistance correlations, and extend the parameter range using experiments from the literature as well as our own data's.

2. THERMAL RESISTANCE CORRELATIONS

2.1 Introduction

We tried to develop two kinds of approaches to evaluate thermal resistance correlations:

- an approach based on non-dimensional groups fitted to experimental data's
- an approach using neuronal networks trained with experimental data's.

The first approach which is more physical and easier to use for engineering will be detailed in this study.

2.2 Khandekar's correlation

The Khandekar [2] correlation permits to predict the heat flux for a 60°C temperature difference ($\Delta T=T_{evap}-T_{cond}$=80-20=60°C). The correlation has

been established with closed loop PHP with various lengths (L_{evap}=L_{adia}=L_{cond}=10cm or 15cm), number of straight branches (N=10, 22, 32, 46), two internal diameters (Di=1mm and 2 mm) and three fluids (R123, water and ethanol). The correlation applied to these experiments is able to calculate the transferred heat flux with a maximum error of ±30%.

$$\dot{q} = \frac{\dot{Q}}{\pi.D_i.N.L_{evap}} \quad (1)$$

$$\dot{q} = 0.54.\exp(\beta)^{0.48}.Ka^{0.47}.Pr_l^{0.27}.Ja^{-1.43}.N^{-0.27} \quad (2)$$

The correlation uses several non-dimensional numbers:
The Karman number *Ka*:

$$Ka = f.Re^2 = \frac{\rho_l.\Delta P_l.D_i^2}{\mu_l.L_{eff}} \quad (3)$$

With: $L_{eff} = \frac{L_{evap}+L_{cond}}{2} + L_{adia}$ (4)

It gives an appropriate velocity scale.
The Prandtl number *Pr*:

$$Pr = \frac{c_p*\mu}{\lambda} \quad (5)$$

It is the ratio between viscous and thermal diffusion rate.
The Jakob number *Ja*:

$$Ja = \frac{Cp*\Delta T}{h_{fg}} \quad (6)$$

This number represents the ratio between sensible and latent heat.

2.3 Charoensawan's correlation

This correlation uses the Kutateladze number [7] to predict the heat flux. This number was developed in pool boiling field. It is the ratio between inertia and hydrostatic forces on a bubble.

$$q = Ku \times \left[h_{fg}.\rho_v^{0,5}.\left(\sigma.g(\rho_l - \rho_v)\right)^{0,25}\right] \quad (7)$$

The Charoensawan [4] correlation predicts the heat flux only in horizontal position of the PHP. This correlation uses the same non-dimensional groups as the Khandekar correlation (2).

$$Ku = 2.13.10^{-9}\, Pr_l^{0.75}\left(Ja'\right)^{-0.38}\, Bo^{-0.84}\, Ka^{0.58}\left(\frac{k_c}{k_a}\right) \quad (8)$$

The Jakob number *Ja'* has been modified to take into account the liquid and vapor fractions using the filling ration *FR* (liquid/total volume in PHP)

$$Ja' = \frac{FR.Cp_l.\Delta T}{(1-FR)h_{fg}} \quad (9)$$

The *Bo* (Bond number is the ratio between the gravitational term and surface tension forces.

$$Bo = \frac{g.(\rho_l-\rho_v).Di^2}{\sigma} \quad (10)$$

kc/ka is the ratio of thermal conductivities of the liquid coolant to the cooling air used for the experiments.

The correlation has been developed on closed loop PHP with lengths L_{evap}=L_{adia}=L_{cond}=5 and 10cm, various branch numbers *N*, three different diameters (Di=1, 1.5 and 2mm) and two different fluids (water and ethanol). Contrary to the Khandekar correlation, the temperature difference between evaporator and condenser is not fixed. The accuracy at horizontal position is ±30%.

2.4 Rittidech's correlation

The Rittidech correlation [6], using the Kutateladze number, predicts the heat flux of the PHP in horizontal position:

$$Ku_0 = 0.0052\left[\left(\frac{D_i^{4.3}L_t^{0.1}}{L_{evap}^{4.4}}\right)n^{0.5}\left(\frac{\rho_v}{\rho_l}\right)^{-0.2}Pr_v^{-25}\right]^{0.116} \quad (11)$$

The correlation gives the information of the correct operation of the PHP in horizontal inclination. The Kutateladze number must be higher than Ku_{L0} defined as:

$$Ku_{L0} = 0.0003\left[\left(\frac{D_i^{6}.L_t^{4.2}}{L_{evap}^{10.2}}\right)n^{-0.2}\left(\frac{\rho_v}{\rho_l}\right)^{2}Pr_v^{-0.2}\right]^{-0.111} \quad (12)$$

The correlation has been developed with open loop PHP with various lengths L_{evap}=L_{adia}=L_{cond}=5, 10cm or 15cm), various branch numbers, three diameters (Di=0.66, 1.06 and 2.03 mm) and three fluids (R123, water and ethanol).

Lt is the total length of the PHP (5, 10 and 15 m)

The correlation accuracy applied to these experiments with a 60°C temperature difference is ±30%.

2.5 Katpradit's correlation

The Katpradit correlations [6] predict the maximum heat flux at evaporator before dry-out.

The maximum heat flux in horizontal position is:

$$Ku_0 = 53680\left(\frac{D_i}{L_{evap}}\right)^{1.127}.\left(\frac{C_p.\Delta T}{h_{fg}}\right)^{1.417}.\left[D_i\left(\frac{g.(\rho_l-\rho_v}{\sigma}\right)^{0.5}\right]^{-1.32} \quad (13)$$

The maximum heat flux in vertical position, PHP being heating down is:

$$Ku_{90} = 0.0002.\left(\frac{D_i}{L_{evap}}\right)^{0.92}\left(\frac{C_p.\Delta T}{h_{fg}}\right)^{-0.212}.\left[D_i.\left(\frac{g.(\rho_l-\rho_v)}{\sigma}\right)^{0.5}\right]^{-0.59}.\left[1+\left(\frac{\rho_v}{\rho_l}\right)^{0.25}\right]^{13.06} \quad (14)$$

The correlation has been tested on open loop PHP with various lengths (L_{evap}=L_{adia}=L_{cond}=5, 10cm or 15cm), various branch numbers, three diameters (Di=0.66, 1.06 and 2.03 mm) and three fluids (R123, water and ethanol). The accuracy obtained on these experiments with T_{adia}=60°C is ±18% in horizontal position and ±29% in vertical heating down position.

2.6 Synthesis

We give in Table 1 the list of correlations, and the parameters range on experiments from which they were established.

Table 1 : Parameters range for correlations

Correlation	Loop	Fluid	Inclinationβ	ΔT (°C)	Di (mm)	Le=La=Lc (mm
Khandekar [2]	Closed	R123, water, ethanol	0-90	60	1-2	150
Charoensawan[4]	Closed	Water, ethanol	0	var.	1-2	50-150
Rittidech [5]	Open	R123, water, ethanol	0	60	0.66-2.03	50-150
Katpradit [6]	Open	R123, water, ethanol	0-90	NA	0.66-2.03	50-150

3. COMPARISON OF EXPERIMENTS WITH EXISTING CORRELATIONS

3.1 Experiments used

We give in Table 2 the experiments used for this study.

Table2 : List of experiments

Reference	Loop	Fluid	N	Di (mm)	Levap (mm)	Ladia (mm)	Lcond (mm)	Lot (mm)	Inclination
Gruss [7]	Closed	Acetone	16	1.3	35	0	140	2.28	-90<β<90°
Khandekar [8]	Closed	Water	46	2	100	100	100	14.4	0<β<90°
Khandekar [8]	Closed	Water	32	2	100	100	100	9.6	0<β<90°
Khandekar [8]	Closed	Water	32	2	150	150	150	13.8	0<β<90°
Bensalem [9]	Open	Acetone	40	2.5	180	190	200	22.8	-90<β<90°
Bricard [10]	Open	Water	80	1.2	180	190	200	45.6	-45<β<45°

3.2 Comparison of correlations

We first used our own experiments [7] to see if our experimental results fits with the various correlations from the literature.

We give in Figures 1 and 2 the relative error (experiment/correlation) in horizontal and vertical heat down position for these correlations.

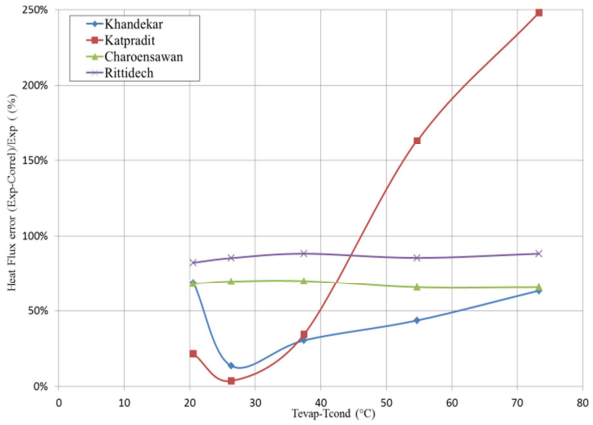


Fig. 1. Error between experimental study of Gruss et al. [7] and literature correlations for horizontal position

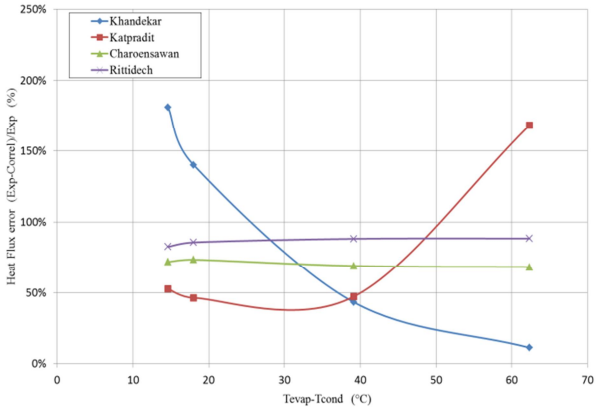


Fig. 2. Error between experimental study of Gruss et al. [7] and literature correlations for vertical heat down position

We can see that the Khandekar's correlation (2) has the best fit with our experiments; however the error is much higher for small ΔT, as the correlation was established with high ΔT (60°C). We then choose to use and modify this correlation later on in this study.

3.3 Comparison of experiments with the Khandekar correlation

We give in Figure 3 the comparison of the heat flux measured and predicted by the Khandekar correlation (2) for all experiments listed in Table 1.

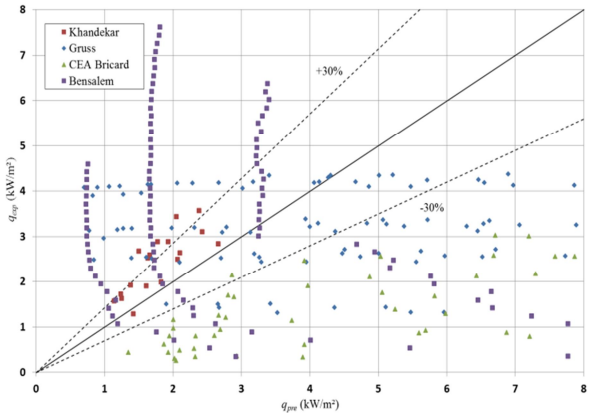


Fig. 3. Comparison of experiments with Khandekar correlation

We can see on that figure that the correlation doesn't well predict the experiments, except for those that were used to establish the correlation.

The experiments with negative inclinations and at low temperature difference are especially not well predicted, which is understandable because Khandekar did not use experiments with those conditions.

4. DEVELOPMENT OF A MODIFIED CORRELATION

4.1 Fit of the Khandekar correlation

Using all the experiments from Table 1, using the Microsoft Excel solver, we have fitted all the coefficients A to F in the correlation (15) which uses the same non dimensional groups as the Khandekar correlation (2).

$$q = A.\exp(\beta)^B.Ka^C.Pr_l^D.Ja^E.N^F \qquad (15)$$

The Table 3 gives the coefficients for Khandekar correlation and the present fitted correlation.

Table 3: Correlation coefficients

Coefficient	Khandekar	New fit
A	0.54	21701
B	0.48	0.16
C	0.47	0.2
D	0.27	-2.17
E	-1.43	0.32
F	-0.27	-0.22

We give in Figure 4 the comparison of the heat flux measured and predicted by the new correlation.

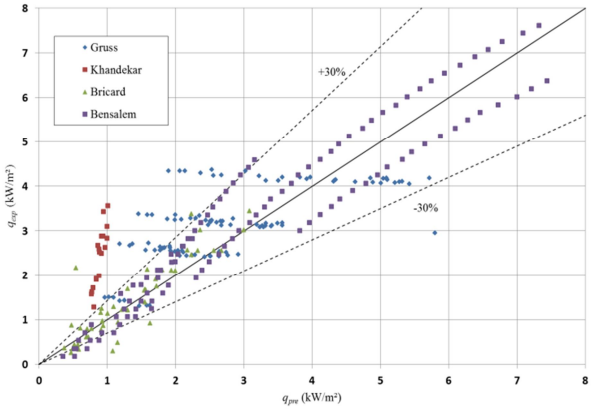


Fig. 4. Comparison of experiments with refitted Khandekar correlation

As we can see, the present correlation predicts better the experiments (mean deviation of 26%), but the Khandekar experiments are not well predicted: mean deviation is 61%, it was 26% for the original one.

4.2 Modification of the Jakob number in the Khandekar correlation (2)

In the Jakob number, the ΔT represents the temperature difference between evaporator and condenser walls.

In the Khandekar experiments, the ΔT value is always the same (60°C), as the other parameters in the Jakob number Cp_l and h_{fg} are more or less constant, the Jakob number is fixed.

For a better physical meaning, as the PHP is a diphasic system, we take for ΔT the temperature difference between the liquid and the vapor phases of the fluid in the evaporator and the condenser supposed to be at saturation.

$$\Delta T = Tsat(P_l) - Tsat(P_v) \qquad (16)$$

We may then apply the Clapeyron formula

$$\frac{\Delta P}{\Delta T} = \frac{h_{fg}}{T(\Delta V)} \qquad (17)$$

$$\text{With } \Delta V = \left({}^1/_{\rho_v} - {}^1/_{\rho_l}\right) \qquad (18)$$

ΔV being the volumetric expansion

As there are meniscus in the plug flow, we can express the pressure loss according to the capillary forces in the tube:

$$\Delta P \approx \frac{\sigma}{D_i} \qquad (19)$$

From these equations, we can deduce a modified Jakob number Ja^*

$$Ja^* = \frac{Cp_l \times T_{evap}\left({}^1/_{\rho_v} - {}^1/_{\rho_l}\right)}{{h_{fg}}^2} \times \frac{\sigma}{D_i} \qquad (20)$$

Using this new Jakob number, we refit a new correlation as in paragraph 4.1

$$q = A.\exp(\beta)^B Ka^C Pr_l^D Ja^{*E} N^F \quad (21)$$

The Table 4 gives the coefficients for the original Khandekar correlation (2), the refitted Khandekar one, and the new correlation with the modified Jakob Ja^*

Table 4 : Correlation coefficients

Coefficient	Khandekar	Khandekar refitted	Khandekar with Ja*
A	0.54	21701	25360
B	0.48	0.16	0.12
C	0.47	0.2	0.49
D	0.27	-2.17	-1.5
E	-1.43	0.32	0.53
F	-0.27	-0.22	-0.18

We give in Figure 5 the comparison of the heat flux measured and predicted by the new correlation with the modified Jakob number, Ja^*.

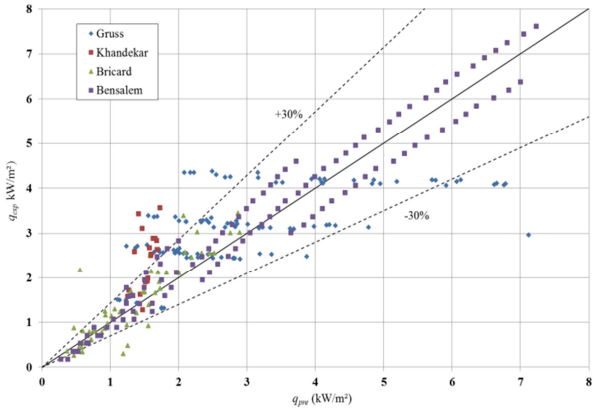


Fig. 5. Comparison of experiments with Khandekar correlation with modified Jakob number Ja^*

5. CONCLUSIONS

The new correlation extends the validity range of the previous correlations commonly used in the literature. Indeed, the new correlation permits to predict the heat flux in any inclination, for a large range of temperature difference (some °C to several tens of °C) and for various lengths.

We give in Table 5 the parameters range and the error results for the original and the new correlation.

The mean error for the prediction of heat flux is 23%, even the error for Khandekar experiments is slightly improved (26%).

Table 5 : Correlation coefficients

	Khandekar correlation	New correlation
PHP loop	Closed	Closed and Open
Fluid	Water, ethanol, R123	Water, acetone
Inclination β (°)	0°<β<+90°	-90°<β<+90°
ΔT evap/cond (°C)	60	4 to 91
Total length Lt (m)	9.6 to 14.4	2.3 to 45.6
Number of branches N	32 et 46	16 to 80
Internal diameter Di (mm)	2	1.2-1.25-2-2.5
Mean error all exp.	256%	23%
Mean error on Khandekar exp.	26%	27%

This study is under way to extend further on the validity range for other geometrical parameters and fluids.

NOMENCLATURE

Bo : Bond number
C_p : Heat capacity (J/Kg.K)
Di : Internal diameter of tubes (m)
FR : Filling Ratio
h_{fg} : Latent heat of fluid
Ja : Jakob number
Ja' : Charoensawan modified Jakob number
Ja^* : This study modified Jakob number
k : Thermal conductivity (W/m.K)
Ka : Karman number
L : Length (m)
P : Pressure (Pa)
Pr : Prandtl number
$\dot{q}$: Heat flux (W/m^2)
N : Number of PHP straight branches
T : Temperature (°C)

Greeks:

ΔP : Pressure loss (Pa)
ΔV : Volumetric expansion
β : Inclination of the PHP from horizontal (°) >0 heat down (favourable) <0 heat above
μ : Viscosity (Pa.s)
σ : Surface tension (N/m)

Subscripts:

a : Air
c : Coolant
$adia$: Adiabatic
$cond$: Condenser
eff : Effective
$evap$: Evaporator
l : Liquid
t : Total
v : Vapor

REFERENCES

[1] Akachi H, Structure of a heat pipe, *Patent US4921041*, 1990
[2] Khandekar S, Thermo-hydrodynamics of Closed

Loop Pulsating Heat Pipes, *PhD Thesis*, Stuttgart University, 2004

[3] Kutateladze SS, Valukina VV, Gogonin II, Relationship between critical heat flux and heater diameter in the boiling of a saturated liquid in free convection conditions, *Journal of Engineering Physics,* 301, 1967

[4] Charoensawan P, Terdtoon P, Thermal Performance Correlation of Horizontal Closed-Loop Oscillating Heat Pipes, *9th Electronics Packaging Technology Conference*, 2007

[5] Rittidech S, Terdtoon P, Murakami M, Kamonpet P, Jompakdee W, Correlation to predict heat transfer characteristics of a closed-end oscillating heat pipe at normal operating condition, *Appl. Th. Eng*., pp 497-510, 2003

[6] Katpradit T, Wongratanaphisan T, Terdtoon P, Kamonpet P, Polchai A, Akbarzadeh A, Correlation to predict heat transfer characteristics of a closed end oscillating heat pipe at critical state, *Appl. Th. Eng.*, 25, pp 2138-2151, 2005

[7] Gruss JA, Frére A, Maisse A, Soriano O, Development of pulsating heat pipe with a central heating zone, *Proc. of IX Minsk International Seminar "Heat Pipes, Heat Pumps, Refrigerators, Power Sources*", Minsk, Belarus, 07-10 September, 2015

[8] Khandekar S, Charoensawan P, Groll M, Terdtoon P, Closed Loop Pulsating Heat Pipe Part A: parametric experimental investigation, *Appl. Th. Eng.*, 23 (2003) 2009-2020

[9] Bensalem A, Contribution à l'analyse du comportement de caloducs oscillants à finalité spatiale par voies expérimentale et numérique, *Ph D Thesis*, Université de Poitiers, 2008

[10] Bricard A, Etude et modélisation de caloducs oscillants, *Personal communication* , 2002

A study on Circulation Flow of Oscillating Heat Pipe with Check Valves by Visualization

Shuhei Yoshida[1], Takurou Daimaru[1], Hiroki Nagai[1*]

[1]*Department of Aerospace Engineering, Tohoku University, Sendai, Miyagi 9800845, Japan*

Abstract

Visualization experiments on an Oscillating Heat Pipe with check valves (CVOHP) were conducted. To observe an internal flow, the CVOHP was made of a Teflon tube. Moreover, a luminescent paint, Rhodamine-B, which is excited by a UV-LED light, was dissolved in a working fluid, HFC-134a. During experiments, the internal phenomena were captured by a high-speed camera and an area scan camera. For the pressure and temperature measurements, we used pressure sensors and thermocouples respectively. The results show that an oscillating flow occurs at lower heat inputs, and then, it moves to a circulation flow. On the other hand, at higher heat inputs, a circulation flow can be regularly observed. To understand the properties of these two internal flows, we applied mutual-correlation analysis to two pressure values obtained from the pressure sensors located at two different positions. As a result, it was revealed that those pressures oscillated almost the opposite phase during an oscillating flow and almost the same phase during a circulation flow respectively. Based on the above results, internal phenomena of a CVOHP can be known by using the relationship between two pressure values. Furthermore, it means that there is a high possibility that a travelling wave of pressure exists during an oscillating flow and does not during a circulation flow.

Keywords: Oscillating heat pipe; Check valve; Visualization; Pressure; Internal flow

1. INTRODUCTION

In recent years, as a heating density of electrical devices installed in space vehicles has been increasing, a limit of heat rejection has emerged as a critical problem. For solving the problem, an Oscillating Heat Pipe (OHP) invented by Akachi, a Japanese researcher, has attracted attention, which has a very simple structure and high heat-transfer capability [1], [2], [3]. It consists of a metal capillary tube bent into several U-shapes and a working fluid as shown in Fig. 1 [4]. After being filled into an OHP, it randomly distributes as vapor plugs and liquid slugs. The heat applied to a heating section is mainly transferred by an oscillating flow with high effective thermal conductivity using sensible and latent heat. The oscillating flow is driven, without power supply, by pressure differences between adjacent turns due to evaporation and condensation of a working fluid.

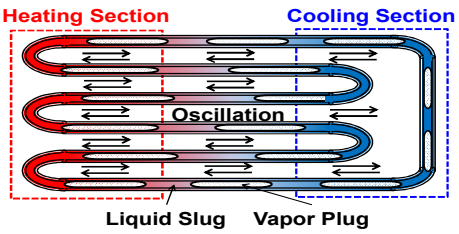


Fig. 1. Schematic of OHP [4]

*Corresponding author: nagai.hiroki@aero.mech.tohoku.ac.jp, Phone: +81-22-795-7897, Fax: +81-22-795-7897

Various studies have been conducted by many researchers to understand complex internal phenomena of an OHP [5]. An oscillating flow is a significant phenomenon in the OHP as mentioned above [6]. On the one hand, Maezawa et al. (1999) clarified that a circulation flow which means a working fluid flows in a one-way direction can be observed by using the influence of gravity, inclining the heating section of the device toward the downside [7]. Moreover, it has been shown that the heat-transfer capability of a circulation flow is superior to that of an oscillating flow [7]. Regarding the oscillating flow, the pressure characteristics have also been researched. In particular, Miyazaki et al. (1999) constructed the wave equation for the pressure and proposed that a travelling wave of pressure exists during an oscillating flow [8]. Though the hypothesis has been already demonstrated by Daimaru et al. using the internal flow modelling of an OHP [9], [10], [11], there is no case where the phenomenon was experimentally observed. From these previous researches, it became clear that the pressure property is strongly linked to the internal flow which is closely related to the thermal transport characteristics. However, while our understanding of an OHP's phenomenon is becoming deeper, it has found that there are some cases in which it cannot work properly due to the insufficient supply of working fluids to heat transfer areas [12]. Therefore, in place of an OHP, an Oscillating Heat

Pipe with Check Valves (CVOHP) which can improve the above situation is attracting a great deal of attention.

A CVOHP is made by installing several check valves shown in Fig. 2 to the middle part of an OHP [4]. A check valve can control a working fluid to flow in a one-way direction and help working fluids to return to heat transfer areas [12]. As a result, a circulation flow mainly occurs in a CVOHP [13]. However, for the pressure characteristics of the flow, there are a lot of parts remain unexplained as mentioned above. To this end, in this research, to understand pressure characteristics of a CVOHP due to differences of internal flows, we conducted visualization experiments on them with pressure and temperature measurements.

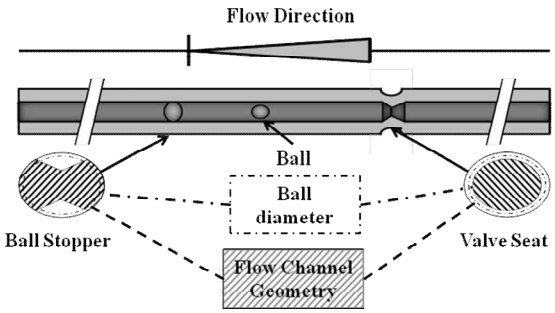


Fig. 2. Schematic of check valve [4]

2. EXPERIMENTAL SETUP

Fig. 3 and Table. 1 show the CVOHP we manufactured and its specifications respectively. The CVOHP are made of a Teflon tube, and 15 check valves are installed to alternate tubes of the middle part. For more efficiently heat exchange, it is fitted into the groove on an aluminum plate. The plate is painted in black for suppressing the undesired excessive reflection of light.

The CVOHP is heated and cooled through the aluminum plates by a silicon rubber heater (heating surface area: 0.0336 m^2) and a water-cooled chiller respectively as shown in Fig. 4. HFC-134a is employed as a working fluid. A luminescent dye, Rhodamine B dissolved in the working fluid was excited by four UV-LED lights (emission peak wavelength: 400 nm). During experiments, internal phenomena were recorded by a high high-speed camera (frame rate: 250 fps, exposure time: 4000 μs) and an area scan camera (frame rate: 25 fps, exposure time: 30000 μs) using a 440nm high path filter. Furthermore, the entire setup is shaded by a blackout curtain. For pressure and temperature measurements, we used 2 pressure sensors and 32 thermocouples referring to Fig. 5, and its sampling rate is 500 Hz and 2 Hz respectively.

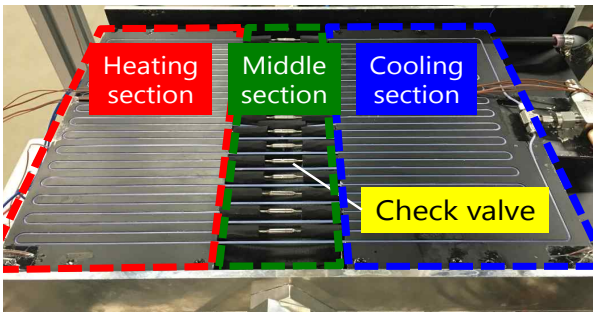


Fig. 3. CVOHP for visualization

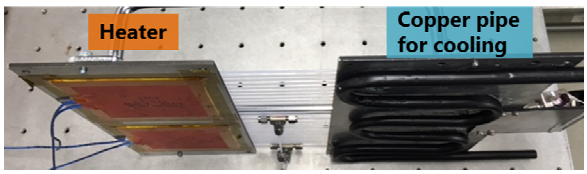


Fig. 4. Installation of a heater and a copper pipe for a water cooled chiller

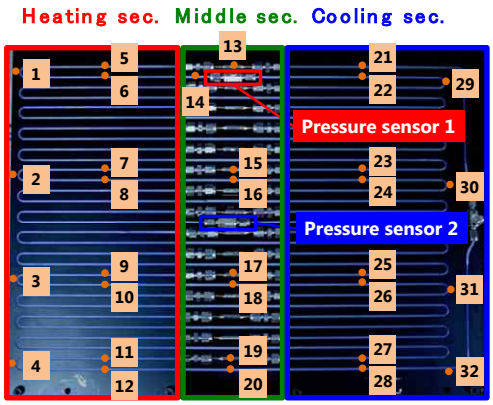


Fig. 5. Positions of pressure sensors and thermocouples

Table 1. Specifications of CVOHP

Pipe material	Teflon
Check valve material	Stainless
Plate material	Aluminum
Luminescent dye	Rhodamine B
Working fluid	HFC-134a
Number of turns	15
Number of check valves	15
Inner diameter	0.8 mm
Outer diameter	1.6 mm
Length of heating sec.	120 mm
Length of cooling sec.	120 mm
Length of middle sec.	80 mm

3. EXPERIMENTAL CONDITIONS

Table 2 shows the experimental conditions of this research. The filling ratio of the working fluid is set to 50 wt. %. The experiments are conducted by changing heat input (Q) within 10 – 60 W. During experiments the temperature of the cooling section and the inclination angle of the device are held at 10 °C and 0 ° respectively. The heat is applied for 1800 seconds at each heat input.

Table 2. Experimental conditions

Filling ratio	50 wt.% (25 °C)
Heat input (Q)	10 – 60 W
Temp. of cooling sec.	10 °C
Inclination angle	0 °
Testing time	1800 s

4. RESULTS AND DISCUTTION

4.1 Thermal Characteristics

Firstly, we clarify basic performance of the CVOHP. Fig. 6 shows the temperature history in the case of heat input power Q from 10 W to 60 W. After the heating starts, the temperature of the cooling section rises following the temperature rise in the heating section. It shows the CVOHP starts up and transports the heat from the heating section to the cooling section. From the temperature history (Q = 20 W) shown in Fig. 7, it is observed that the temperature of the cooling section drops at the same time that that of the heating section rises at lower heat inputs. That is, the CVOHP occasionally stops transporting the heat at lower heat inputs. On the other hand, the temperature history (Q = 50 W) shown in Fig. 8 indicates that the phenomenon that the heat transportation stops seen at Q = 20 W are not observed. That is, the CVOHP continuously works at higher heat inputs.

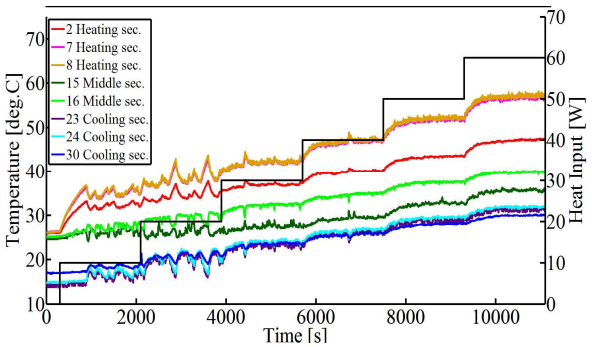


Fig. 6. Temperature history (Q = 10 – 60 W)

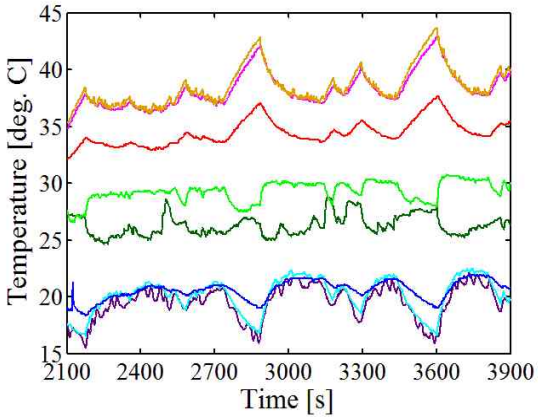


Fig. 7. Temperature history (Q = 20 W)

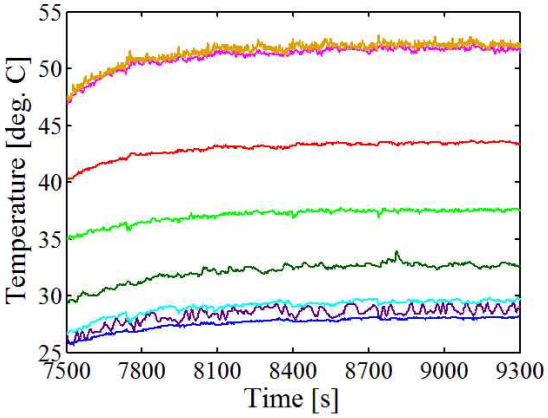


Fig. 8. Temperature history (Q = 50 W)

Fig. 9 shows that the thermal resistance calculated by Eq. (1). We used the average temperature during last 300 seconds at each heat input. In this case, the error bars mean standard deviation. As a result, the thermal resistance and its variation decrease with increase of heat input. That is, the heat transport capability of the CVOHP improves as heat input increases.

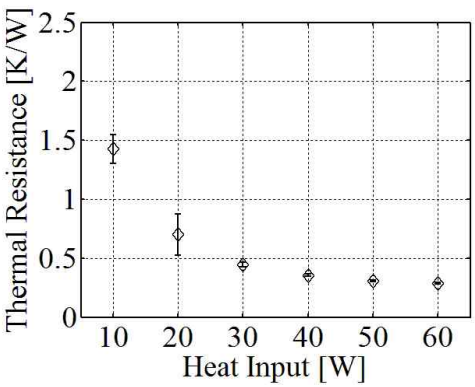


Fig. 9 Thermal resistance (Q = 10 – 60 W)

$$R = (T_2 - T_{30})/Q \quad (1)$$

4.2 Pressure Characteristics and Internal Flows

Fig. 10 shows the pressure history in the case of heat input power Q from 10 W to 60 W. It can be seen that the pressure at lower heat inputs intermittently stops and fluctuates according to the temperature history shown in Fig. 6. On the other hand, the pressure at higher heat inputs continuously fluctuates.

Fig. 11 and 12 show the typical pressure fluctuation in detail at lower and higher heat inputs respectively. In addition, Fig. 13 and 14 show the visualized image obtained by the area scan camera. Concerning each image, it is distinctly divided into two parts. A white one means a liquid slug, and a black one means a vapor plug. To better understand an internal flow, gas-liquid boundaries in alternate pipes are connected with a red line. From Fig. 11 and photo images, it was revealed that an oscillation flow occurs while the pressure is fluctuating with an amplitude of several kilopascals and a circulation flow occurs while the pressure is varying with an amplitude of several tens of kilopascals at lower heat inputs. According to the above results, it was found that an oscillating flow occurs even inside a CVOHP, which has not been clarified before. Looking at the images in detail, it can be seen that the waveform of the red line momentarily changes, that is, the oscillating flow occurs as shown in Fig. 13. Additionally, from Fig. 14 which shows the internal flow approximately 9 seconds after the flow occurs, the following result can be obtained: All gas-liquid boundaries exist near the middle section (t = 9.80 s). Some of them start moving toward the direction of the cooling section (t = 10.12 – 10.44 s). After one boundary reaches the neighbored pipe, the flow starts circulating (t = 10.76 s). Most of the boundaries reach the neighbored pipe, and the circulation flow occurs over the whole CVOHP inside (t = 11.40 s). In contrast, Fig. 12 shows that at higher heat inputs the pressure constantly fluctuates with an amplitude of several tens kilopascals.

It means that a circulation flow continuously occurs at higher inputs. During the period, it is confirmed that a circulation flow as shown in the latter part of Fig. 14 continuously occurs.

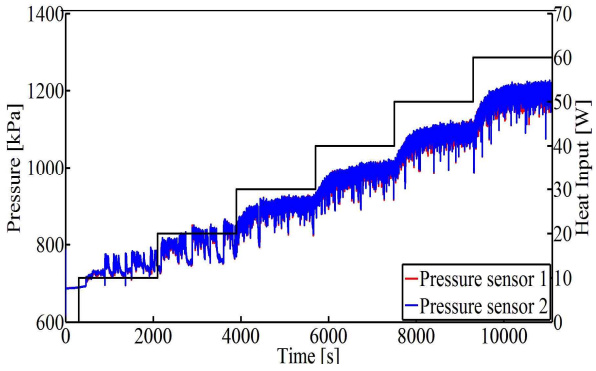


Fig. 10. Pressure history (Q = 10 – 60 W)

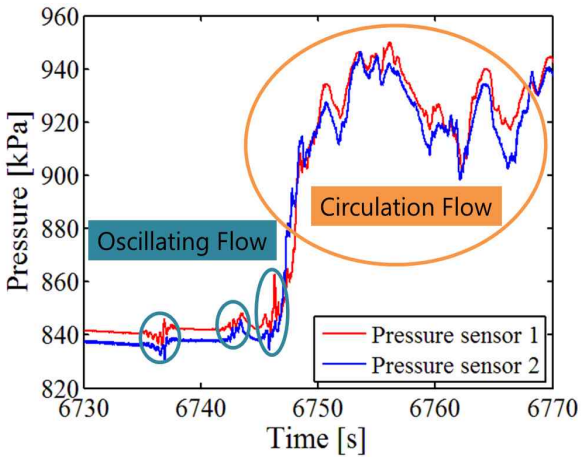


Fig. 11. Pressure history (Q = 20 W)

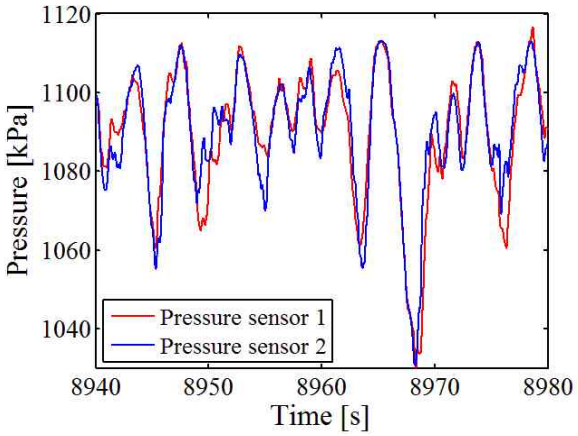


Fig. 12. Pressure history (Q = 50 W)

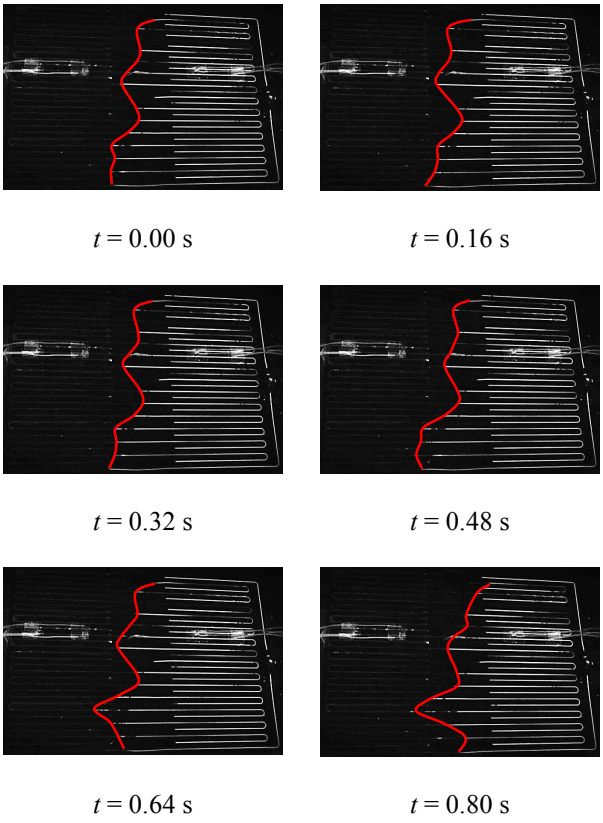


Fig. 13. Photo images when an oscillating flow occurs (Q = 20 W)

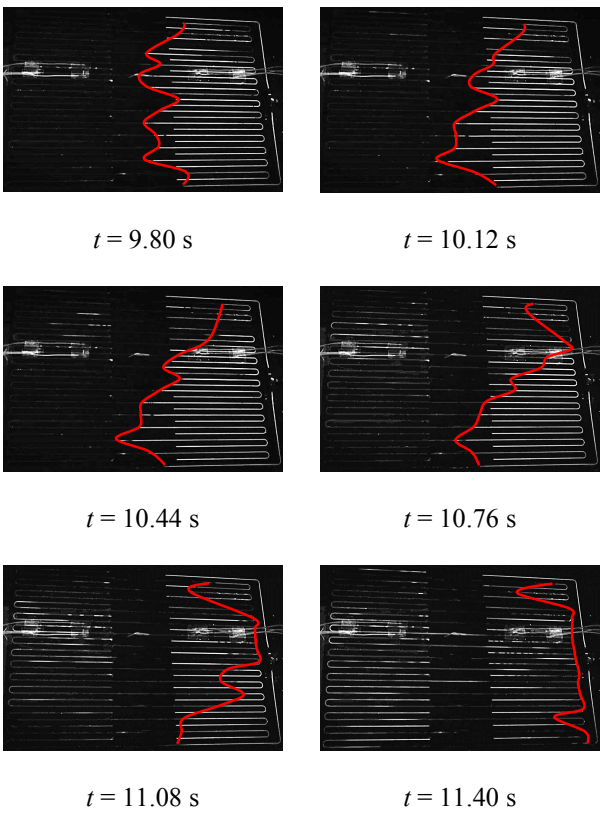


Fig. 14. Photo images when a circulation flow occurs (Q = 20 W)

4.3 Mutual-Correlation Analysis between Two Pressure Values

We performed a mutual correlation analysis between two pressure values during an oscillating flow and a circulation flow for understanding the relationship between pressure characteristics and internal flows. Fig. 15 shows the typical pressure history while an oscillating occurs in detail. It is known that the oscillation frequency of the pressure at that time is 1.94 Hz shown in Fig. 16. Moreover, according to Fig. 17, when an oscillating flow occurs, the time difference between two pressure values is 0.216 seconds. Based on these results, the phase difference between two pressure values is calculated as 149°. On collating the calculated result with the theory of propagation of the pressure wave as mentioned above, the position of two pressure measurements in this experiment is illustrated in Fig. 18. Assuming that during an oscillating flow, the pressure wave propagates in the direction as shown in Fig. 18, the propagation distance from pressure 1 to 2 and from 2 to 1 is approximately 4480 and 5250 mm respectively. By using these values, the phase difference between two pressure values is estimated as below.

$$360° \times \frac{4480\,mm}{5250\,mm + 4480\,mm} \approx 166° \qquad (2)$$

The estimation value approximately agrees with the experimental value. Thus, it was confirmed that the consistency of the theory about the propagation of the pressure wave and the validity of the experiment. The slight difference between estimated and experimental value is attributed to the difference in the number of check valves in the propagation way. That is, it takes longer time for pressure to pass through the way with more check valves because of its flow resistance.

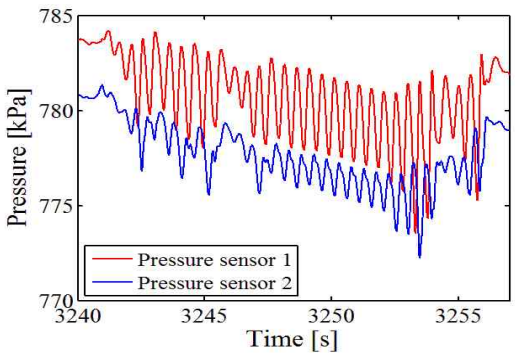


Fig. 15. Detailed pressure history when an oscillating flow occurs

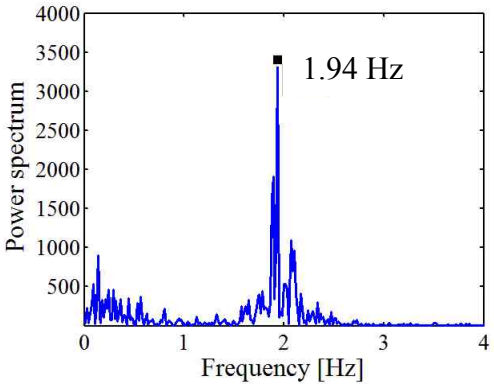


Fig. 16. FFT analysis result of the pressure value when the oscillating flow occurs

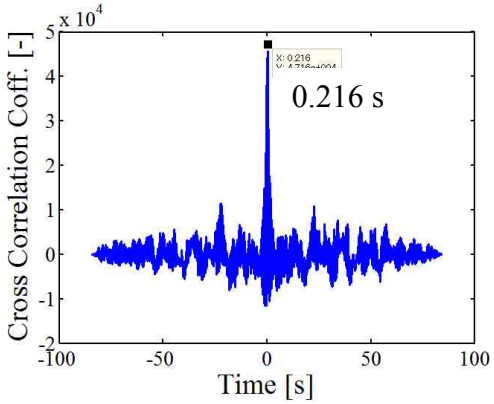


Fig. 17. Mutual-correlation analysis result of the pressure value when the oscillating flow occurs

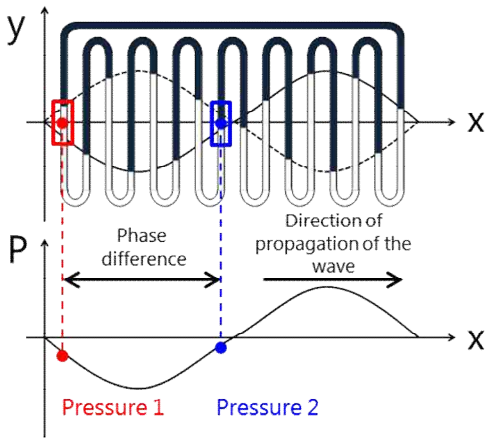


Fig. 18. Propagation of the pressure wave when an oscillating flow occurs

Fig. 19 shows the typical pressure history while a circulation flow occurs in detail. The oscillation frequency of the pressure at that time is 0.092 Hz, referring to Fig. 20. In addition, from Fig. 21, when a circulation flow occurs, the time difference between two pressure values is 0.058 seconds. Based on the above results, the phase difference between two pressure values is calculated as 1.85 °. The result suggests that it is not observed that a pressure wave propagates when a circulation flow occurs.

From these findings, it is revealed that those two pressures are almost the opposite phase during an oscillating flow, and almost the same phase during a circulation flow respectively. Therefore, we could understand an internal flow without visualization using the relationship between the phase difference of pressure and the internal flow. Additionally, the relationship could be applied to other experiments considering its position of pressure measurement.

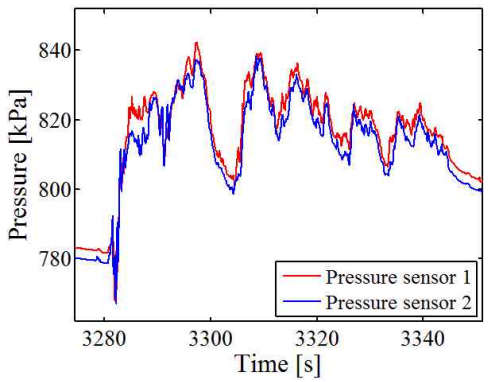


Fig. 19. Detailed pressure history when a circulation flow occurs

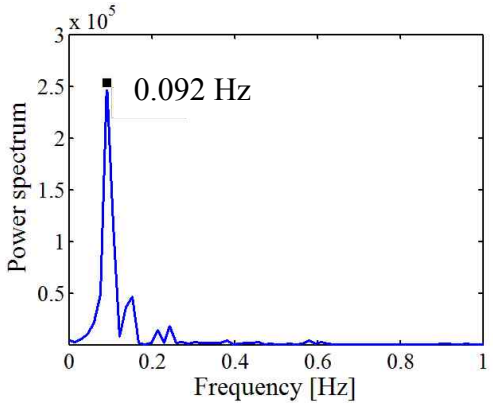


Fig. 20. FFT analysis result of the pressure value when the circulation flow occurs

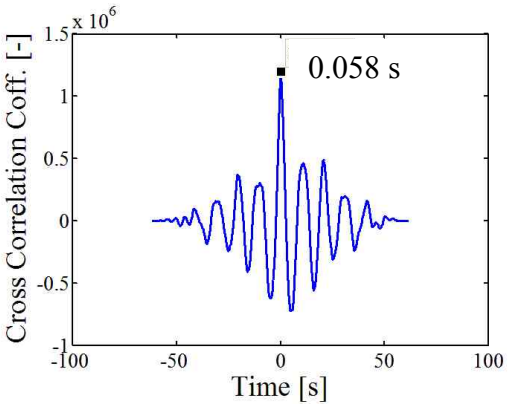


Fig. 21. Mutual-correlation analysis result of the pressure value when the circulation flow occurs

5. CONCLUSIONS

Flow visualization experiments with pressure measurements on a CVOHP have been successfully performed. As a result, it has become clear that both an oscillating flow and a circulation flow occur at lower heat inputs. During that period, the CVOHP occasionally stops transporting the heat according to the internal flow. Meanwhile, a circulation flow continuously occurs at higher heat inputs. From the mutual-correlation analysis, it was shown that the phase difference between two pressures is approximately opposite and same during an oscillating flow and a circulation flow respectively. This result suggests that there is no propagation of a pressure wave when a circulation flow occurs. Additionally, the relationship between pressure and an internal flow obtained by this study could be applied to other experiments for understanding an internal flow without visualization.

NOMENCLATURE

R : Thermal resistance (K/W)
T_n : Temperature of No. n thermocouple (°C)
Q : Heat load (W)

REFERENCES

[1] Akachi, H., U.S. Patent 4921041, (1990)
[2] Akachi, H., U.S. Patent 5219020, (1993)
[3] *P* Akachi, H., Polasek, F. and Stulc, P., Pulsating heat pipe, *proceedings of the 5th International Heat Pipe Symposium*, Melbourne, Australia, (1996) 208-217
[4] Okamoto, A., Ando, M., Maeda, M. and Sugita, H., Initial evaluation of on-orbit experiment of flat-plate heat pipe onboard SDS-4, *56th Space Science and Technology Conference*, Oita, Japan, (2012) JSASS-2012-4266
[5] Nagasaki, T., Review of Pulsating Heat Pipes, *Journal of the Heat Transfer Society of Japan*, vol.44, No.186, (2005) 13-17
[6] Miyazaki, Y. and Arikawa, M., Oscillatory flow in the oscillating heat pipe, *11th International Heat Pipe Conference*, vol.2, (1999) 143-148
[7] Gi, K., Sato, F. and Maezawa, S., Flow visualization experiment on oscillating heat pipe, *11th International Heat Pipe Conference*, Tokyo, Japan, vol. 2, (1999) 149-153
[8] Miyazaki, Y., Pressure Oscillation of Oscillating Heat Pipes, *Memoirs of the Fukui Institute of Technology*, vol. 29, (1999) 145-150
[9] Daimaru, T., Yoshida, S., Nagai, H., Okamoto, A., Ando, M. and Sugita, H., Mathematical Modeling and Experimental Validation of Oscillating Heat Pipes, *Proceedings of 44th International Conference on Environmental Systems*, Arizona, USA, (2014) ICES-2014-121
[10] Daimaru, T., Yoshida, S. and Nagai, H., A Consideration of Startup Behavior of Oscillating Heat Pipes, *58th Space Science and Technology Conference*, Kagoshima, Japan, (2014) 5
[11] Daimaru, T., Yoshida, S. and Nagai, H., Study on Thermo Dynamic Cycle in Oscillating Heat Pipes by Numerical Analysis, *36th Japan Symposium on Thermophysical Properties*, Miyagi, Japan (2015) 69-71
[12] Miyazaki, Y., Oscillating Heat Pipe with Check Valves, *Memoirs of the Fukui Institute of Technology*, vol. 32, (2002) 389-392
[13] Miyazaki, Y., Polasek, F. and Akachi, H., Oscillating Heat Pipe with Check Valves, *Proceedings of the 6th International Heat Pipe Symposium*, Chiangmai, Thailand, (2000) 389-393

Heat Transfer Characteristics of Flat Plate Pulsating Heat Pipe using Self-rewetting Fluids

Koki Yamagami[1], Koji Fumoto[1*], Raffaele Savino[2], Tsuyoshi Kawanami[3] and Takao Inamura[1]

[1]*Department of Intelligent Machines and Engineering, Hirosaki University, 3 Bunkyo-cho, Hirosaki 036-8561, Japan*
[2]*Department of Industrial Engineering, University of Naples Federico II, Naples, Italy*
[3]*Department of Mechanical Engineering, Kobe University, 1-1 Rokkodai-cho, Nada-ku, Kobe 657-8501, Japan*

Abstract

The heat-transfer performance of a pulsating heat pipe (PHP) was evaluated. The aluminum-plate PHP consists of 24 parallel 2×2 mm^2 square channels. Water and self-rewetting fluids were used as the working fluids. The self-rewetting fluid is a dilute aqueous solution of alcohols (such as butanol and pentanol) that consist of a large number of carbon atoms. These solutions can be considered self-rewetting fluids, owing to the non-linear temperature dependence of the corresponding surface tension and the ability to spontaneously wet a hotter region. The experimental results indicated that, compared with the water, the self-rewetting fluid resulted in a significantly better heat-transfer performance; this resulted from a decrease in the temperature difference between the heating and cooling sections and the thermal resistance. Moreover, flow visualization of the heating section revealed that the boiling phenomena of the self-rewetting fluid are more pronounced than those associated with the water. In the case of the self-rewetting fluid, the temperature and pressure fluctuations were both stable and continuous, owing to the occurrence of these phenomena.

Keywords: Flow visualization, Heat transfer performance evaluation, Pulsating heat pipe, Self-rewetting fluids

1. INTRODUCTION

In recent years, the demand for satellites and various types of spacecraft has increased and hence, development of the required high-performance and high-density internal components is ongoing. The heat flux of electronics is also increasing rapidly and therefore, the demand for more efficient heat-control devices, than those currently available, has also increased. Moreover, a low-weight and small (owing to size limitations stemming from the miniaturization of electronics) thermal-control device that uses minimal power, is highly desirable. Pulsating heat pipes have therefore attracted attention as the next generation of thermal-control devices that meet these requirements.

The pulsating heat pipe (PHP) is a new type of efficient heat-transfer device, which was introduced in the mid-1990s by Akachi [1]. The basic structure of a typical PHP consists of a meandering capillary tube that is partially filled with a working fluid, as shown in Figure 1. The PHP transports heat via pulsation of the working fluids in the flow channel; these pulsations result from pressure fluctuations associated with evaporation and condensation. In addition, the high heat-transfer performance, owing to sensible and latent heat, constitutes a unique feature that renders PHP superior to convectional heat pipes. The PHP is also well-suited for miniaturization, owing to its simple no-pump structure, and can be operated under low gravity. Owing to these attributes, the PHP constitutes a promising means of solving the internal heat-generation problems associated with spacecraft.

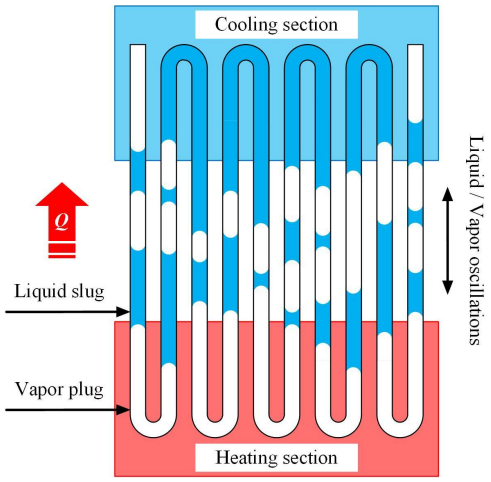


Figure 1 Structure of a PHP.

Several studies, via experiments, of the heat-transfer characteristics of PHP have revealed the parameters (geometry, filling ratio, inclination angle, working fluid, etc.) that affect the performance of PHP. For example, Fumoto et al. [2] have evaluated the performance of the PHP, when self-rewetting fluids were used as the working fluid sealed inside the PHP. The self-rewetting fluids are alcohol dilute aqueous solutions (such as butanol and pentanol)

*Corresponding author: kfumoto@hirosaki-u.ac.jp, Phone: +81-172-39-3676, Fax: +81-172-39-3676

that consist of four or more carbon atoms. According to these authors, use of the self-rewetting fluids yields a higher heat-transport capability of the PHP compared to that resulting from the use of water. Yanxin et al. [3] determined, via experiments, the strengthening effect of self-rewetting fluids on this heat-transport capability. They found that the self-rewetting fluid, as the working fluid of the PHP, leads to a decrease in the thermal resistance and extends the effective operating range of the PHP. The aforementioned results confirm the heat transfer performance-enhancement effect of self-rewetting fluids. However, the mechanism governing this mechanism remains unclear.

Therefore, the main purpose of this study is to clarify the performance-enhancement mechanism by using self-rewetting fluids in a flat-plate aluminum PHP.

2. EXPERIMENTS

2.1 Experimental apparatus

Figure 2 shows the experimental apparatus, which consists of a PHP, an electrical power input source, as well as a water-cooling system, vacuum device, working fluid supply unit, temperature and pressure data logger, high-speed camera system, and a PC. As Figure 3 shows, the 236×119×3 mm^3 aluminum-plate PHP test sections consist of 24 parallel square channels that form a meandering open loop (cross-section: 2×2 mm^2, length per tube: 180 mm). A polycarbonate plate with a thin transparent silicon sheet was used to cover the top of the PHP, to allow visualization of the internal flow phenomena, from above. The heating section consisted of two cartridge heaters (ϕ10×60 mm) embedded in an aluminum heating block (75×40×20 mm^3), and the power supplied to the heaters was varied from 0–320 W. The aluminum cooling block (75×40×20 mm^3) was cooled by a water jacket connected to a water-circulation system. The cooling and heating blocks were attached, in separate locations, to the back face of the PHP. The temperature of the PHP was measured by nine K-type thermocouples (with a wire diameter of 127 μm) that were attached to the back face of the PHP. Three thermocouples, each, were attached to the cooling section (T_1−T_3), symmetrically placed in the heating section (T_7−T_9), and placed in the adiabatic section along the center line (T_4−T_6), respectively. In addition, in order to measure the pressure inside the PHP, pressure sensors were integrated into the polycarbonate plate in both the heating and cooling sections (see Figure 4). Two types of working fluids, namely, deionized water, and a self-rewetting fluid, were used in the present study. The self-rewetting fluid was prepared by adding 1-butanol to deionized water, thereby yielding an aqueous solution of specified mass concentration.

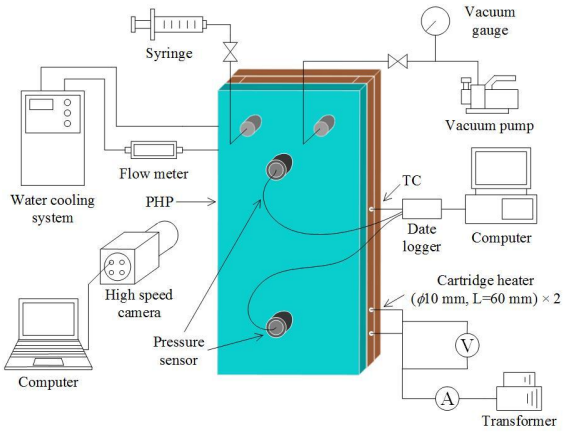


Figure 2 Schematic of the experimental apparatus.

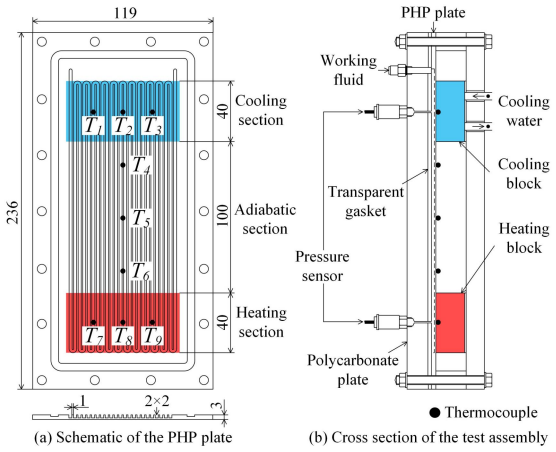


Figure 3 Components of the PHP.

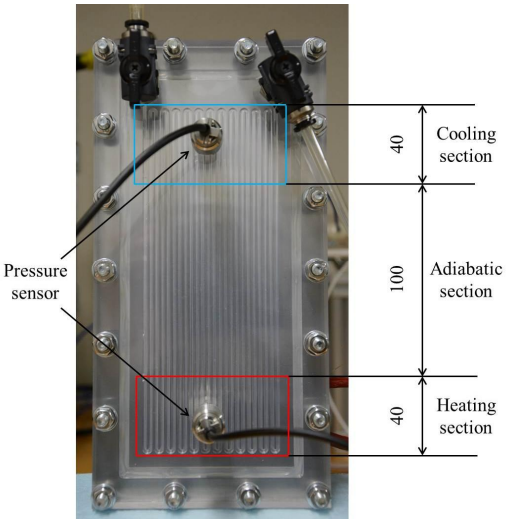


Figure 4 Photo of the PHP.

2.2 Experimental procedure

To charge the PHP to a specified filling ratio (FR), the heat pipe was vacuumed to a pressure of 3 kPa, by using a gauge. A specified amount of the working fluid was then injected into the PHP, by using a syringe. The filling ratio was confirmed by using an electronic balance to measure the mass of the syringe before and after the filling operation. The power supplied to the cartridge heater block was adjusted after the back face of the PHP reached a steady-state temperature condition. When a heating-section temperature of 120 ºC was reached, the experiment was terminated by switching off the heater. The experiment was performed under the following conditions: constant temperature of 20 °C, cooling water circulation, FR of 50 vol.%, working fluids with concentrations of 1, 3, and 7.15 wt.% of a butanol aqueous solution, and a vertical bottom heat mode.

2.3 Data reduction

The thermal resistance (R) and the temperature difference between the heating and cooling sections (ΔT) constitute important parameters that describe the heat-transfer performance of the PHP. R and ΔT are given as:

$$R = \Delta T / Q \quad (1)$$

$$\Delta T = T_{h,ave} - T_{c,ave} \quad (2)$$

Where Q, $T_{h,ave}$, and $T_{c,ave}$ are the heat input power to the PHP, and the average temperature of the heating and cooling sections in the steady state, respectively

3. RESULTS AND DISCUSSION

3.1 Self-rewetting fluid

In this study, a butanol aqueous solution is used as the self-rewetting fluid; the thermo-physical properties of the working fluids used in the experiments are listed in Table 1. Previous studies have shown that, with increasing temperature, the surface tension behavior of self-rewetting fluids differs from that of ordinary pure fluids. Figure 5 shows the surface tension of an ordinary pure material and a self-rewetting fluid [4, 5], as a function of the temperature. The surface tension of the ordinary pure fluid (e.g., water and butanol) decreases linearly with increasing temperature. In contrast, the surface tension of the self-rewetting fluid (e.g., butanol aqueous solution) decreases gradually with increasing temperature, reaching a minimum at ~60 °C, and gradually increases thereafter. Therefore, in the case of a self-rewetting fluid on a heated surface, liquid-vapor interfaces and temperature gradients lead to surface tension-driven convection, as shown in Figure 6. An enhanced heat-transfer performance, owing to this convection, is therefore expected; this convection should also prevent dry-out of the heated surface [6, 7].

Table 1 Properties of working fluids.

	Working fluid (at 20 ºC, 1 atm)	
	Water	Butanol
Molar mass [g/mol]	18.02	74.1
Density [g/cm^3]	0.998	0.81
Boiling point [ºC]	100	117.65
Latent heat [MJ/kg]	2.26	0.58
Surface tension [mN/m]	71.7	24.57
Solubility in water [g/mL]	—	7.15

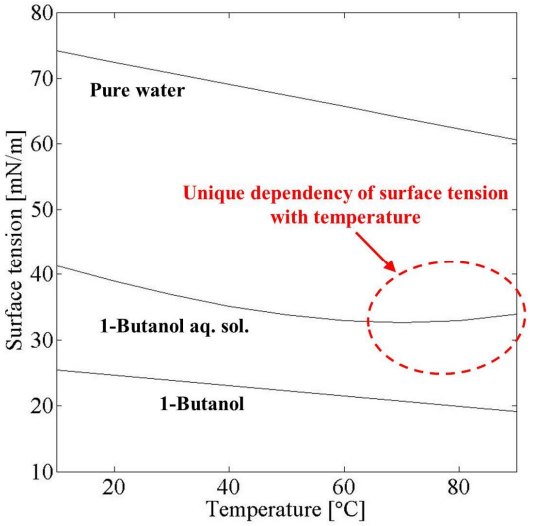


Figure 5 Temperature-dependence of the surface tension.

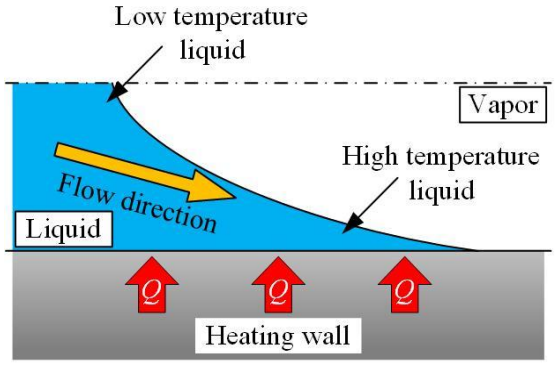


Figure 6 Surface tension-driven convection.

3.2 Heat transfer performance

Figure 7 shows the dependence of the thermal resistance on the heating power, in the case of the bottom heat mode and FR=50 vol.%. As the figure shows, the resistance decreases with increasing heat input power, irrespective of the type of working fluid. Moreover, at high input power (i.e., Q>160 W), the resistance of the PHP that uses butanol aqueous solution is lower than that of the PHP, which uses water. This results from the unique surface tension effect, associated with the solution, which leads to a lower input-power-induced temperature increase of the heating section, than that resulting from the use of water. The figure also shows that the heat-transfer performance of the solutions is relatively independent of the concentration of butanol. This results from an increase in the positive gradient of surface tension, and hence surface tension-driven convection toward the heating surface, with increasing concentration of butanol. However, sensible heat transfer of the solution decreases with increasing butanol concentration. The overall heat transfer in a PHP arises mainly from the exchange of sensible heat and therefore, the performance enhancement changes only slightly (or modestly) when a certain concentration of butanol is exceeded.

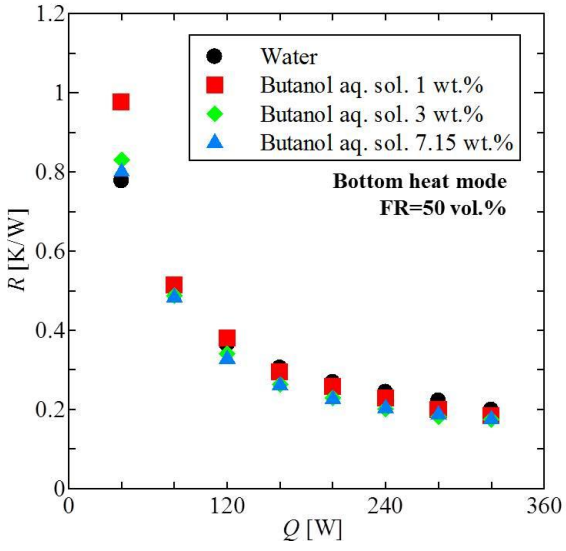
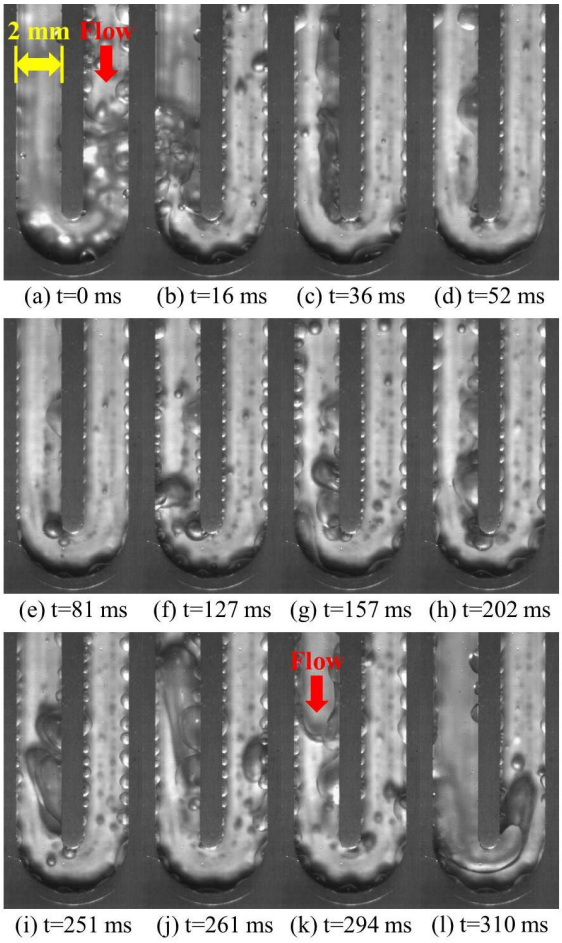


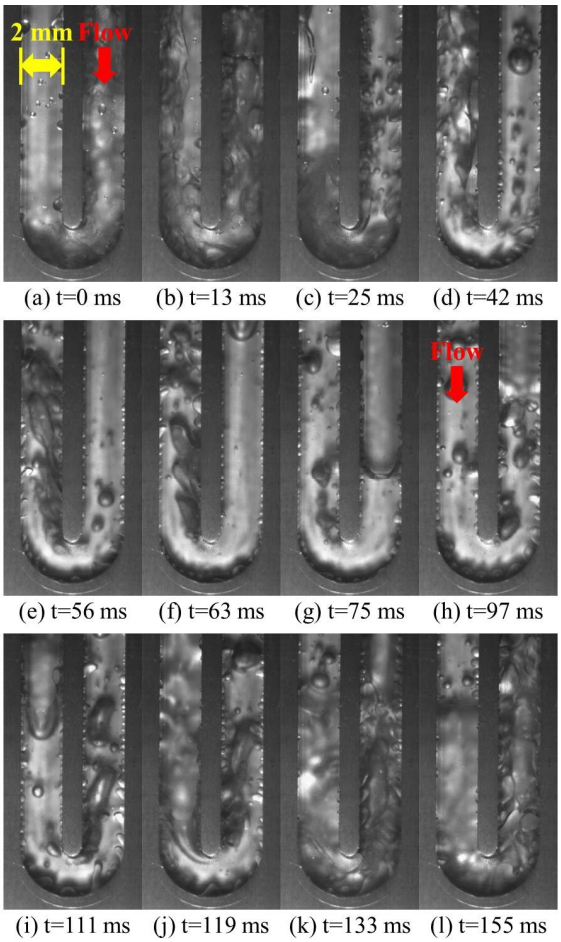
Figure 7 Thermal resistance.

3.3 Flow visualization of the heating section

Figure 8 shows a series of images that comprise a high-speed movie of the heating section. Water (a) and butanol aq. sol. 3 wt.% (b) constitute the working fluids and the filling ratio, heat input power, and orientation of the PHP are FR=50 vol.%, Q=320 W, and bottom heat mode, respectively. Flow visualization of the section revealed that the flow boiling phenomena (of the section) consist of four sequential steps (i–iv), namely, the: (i) occurrence of boiling bubbles, (ii) growth of the bubbles on the heated surface, (iii) coalescence of the grown bubbles, and (iv) separation of the coalesced bubbles from the heated surface, by the movement of liquid slugs or vapor plugs. In the case of the PHP that used water, growth of the bubbles on the heated surface was extremely slow, and the inflow frequency of liquid slug or vapor plug was low (see Figure 8(a)). Use of the butanol aq. sol. 3 wt.% resulted, however, in many boiling bubbles on the heated surface, and the boiling cycle was shorter than that of the water (see Figure 8(b)). These results suggest that the occurrence of boiling phenomena, on the heated surface, influences the heat transfer performance-enhancement mechanism of the PHP.



(a) Water, Q=320 W



(a) t=0 ms (b) t=13 ms (c) t=25 ms (d) t=42 ms

(e) t=56 ms (f) t=63 ms (g) t=75 ms (h) t=97 ms

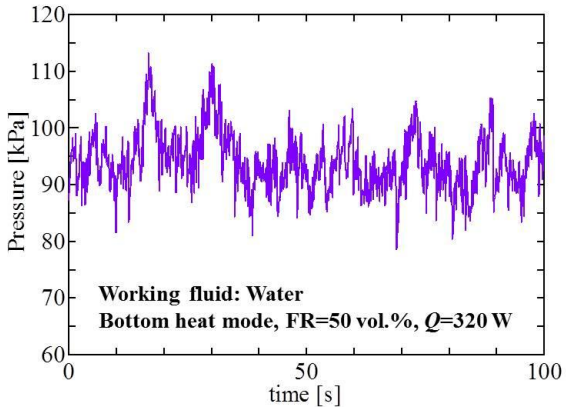
(i) t=111 ms (j) t=119 ms (k) t=133 ms (l) t=155 ms

(b) Butanol aq. sol. 3 wt.%, Q=320 W

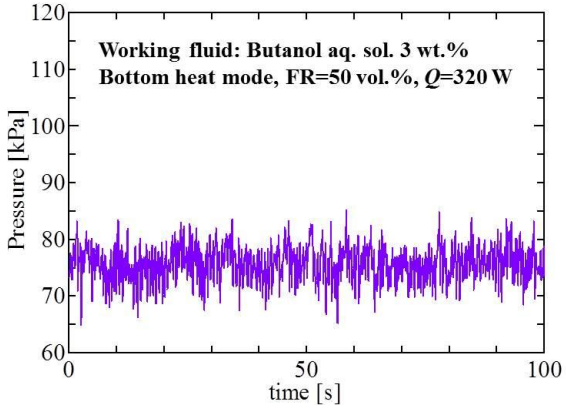
Figure 8 Flow visualization of the heating section.

3.4 Pressure history of the heating section

Figure 9 shows the pressure history of the heating section when the filling ratio, heat input power, and orientation of the PHP are FR=50 vol.%, Q=320 W, and bottom heat mode, respectively. In a PHP, the pulsating phenomenon of the working fluid is excited by the pressure fluctuation. Furthermore, the heat transfer in a PHP is dominated by the sensible heat of the liquid slug that moves between the heating and cooling sections. The behavior of pressure fluctuation is therefore directly related to the heat-transfer performance of the PHP. Large pressure fluctuations, over almost the entire timespan, occur when water is used as the working fluid; these fluctuations are accompanied by a non-periodic unstable oscillation (see Figure 9(a)). In addition, the pressure history of the water confirms the rapid pressure increase, indicating that a local dry-out occurs in the heating section. In contrast to those observed for water, the pressure oscillations are continuous in the case of butanol aq. sol. 3 wt.%, and the amplitude is constant (see Figure 9(b)). The aforementioned results indicate that the enhanced performance of self-rewetting fluids arises from the high frequency and stabilization of pressure oscillation, owing to the occurrence of the boiling phenomenon.



(a) Water, Q=320 W



(b) Butanol aq. sol. 3 wt.%, Q=320 W

Figure 9 Pressure history of the heating section.

4. CONCLUSIONS

The heat-transfer performance, flow boiling behavior, and pressure fluctuation of a PHP were investigated by performing a series of experiments. The main conclusions of this study are summarized as follows:

1. Owing to a lower thermal resistance, the PHP using butanol aqueous solutions exhibited superior heat-transfer performance, compared to its counterpart that used water as a working fluid.
2. The boiling phenomenon results from the unique surface tension effect associated with butanol aqueous solutions.

3. The enhanced heat-transfer performance, owing to the self-rewetting fluids, results mainly from an increase in the pressure frequency; this increase is induced by the boiling phenomenon that occurs in the heating section.

ACKNOWLEDGEMENT

The authors would like to acknowledge the financial support given by a research grant from The Mazda Foundation, Japan.

NOMENCLATURE

Q : Heater input power, W
T : Temperature, °C
DT : Temperature difference, °C
$T_{h,\,ave}$: Average heating section temperature, °C
$T_{c,\,ave}$: Average cooling section temperature, °C
R : Thermal resistance, K/W

Subscripts
1~9 : Thermocouple location
h : Heating section
c : Cooling section
ave : Average

REFERENCES

[1] Akachi, H., Motoya, S., and Maezawa, S., Thermal Performance of Capillary Tunnel Type Flat Plate Heat Pipe, *Proc. of 7th Int. Heat Pipe Conference*, Albuquerque, New Mexico, (1995).
[2] Fumoto, K. and Kawaji, M., Improvement in Pulsating Heat Pipes Using a Self-rewetting Fluid: Cases of 1-Butanol and 1-Pentanol, *Thermal science and engineering*, Vol.19, No.1 (2011), pp.1-7.
[3] Yanxin, H., Tengqing, L., Xuanyou, L., Shuangfeng, W., (2014) Heat transfer enhancement of micro oscillating heat pipes with self-rewetting fluid, *Int. J. Heat Mass Transfer*, 70, pp. 496-503.
[4] JSME Date Book, *Thermophysical Properties of Fluids 4th Edition*, (1991).
[5] Vochten, R., Peter, G., Study of the Heat of Reversible Adsorption at the Air-Solution Interface, *J. Colloid and Interface Sci.*, 42, (1973), pp. 320-327.
[6] Nishiguchi, S., Shoji, M., A Study of Critical Heat Flux of Butanol Aqueous Solution, *Proc. of the ASME 2009 7th International Conf. on Nanochannels, Microchannels, and Minichannels*, (2009), pp. 43-48.
[7] Wijk, W. R., Vos, A. S., Stralen, S. J. D., Heat Transfer to Boiling Binary Liquid Mixture, *Chemical Engineering Science*, 5, (1956), pp. 68-80.

4. Two-phase Thermosyphons/ Loop Thermosyphons/ Separate-type Heat Pipes/ Wickless Heat pipes

Experimental Study on Different Control Modes of CSHP

Jingyu Cao[1], Gang Pei[1], Jiao Dongsheng[1], Zhao Pinghui[2], Li Jing[1] and Wang Yunyun[3]

[1]*Department of Thermal Science and Energy Engineering, University of Science and Technology of China, Hefei 230027, China*
[2]*School of Nuclear Science and Technology, University of Science and Technology of China, Hefei 230027, China*
[3]*Key Laboratory of Optoelectronic Devices and Systems of Ministry of Education and Guangdong Province, College of Optoelectronic Engineering, Shenzhen University, Shenzhen 518060, China*

Abstract

Controllable separate heat pipes (CSHPs) can be widely applied in cool-storage refrigerators powered by solar energy or electricity with time-of-use price policy and other temperature control applications. However, thecontrolmode of CSHP has yet to be further optimized. In this study, a CSHP was designed and tested. The heat transfer process of CSHP can be intermittently stopped and started to control the heat transfer and the loading temperature. Valves are added on the vapor line and the liquid line; hence, three control modes were available to start and stop the heat transfer process of the CSHP. For each control mode, the valve location was varied and the start–stop performances of CSHP were analyzed under various test conditions. Control mode A performs well and is affected weakly by the valve location. The control ability of control mode B is acceptable only when the valve is located on the lower liquid line. The start-stop performance of control mode C is better than that of control mode A and B; and with its best valve location, CSHP starts up quickly in approximately 25 seconds and stops in about 75 seconds under various test conditions. Analysis of the three different control modes revealed that control mode C is the optimal one and that control mode A is also acceptable for cost saving.

Keywords: Heat pipe; Thermosyphon loop; Start-stop; Control mode.

Long Horizontal Vapordynamic Thermosyphons for Renewable Energy Sources

Leonard L.Vasiliev[1], A.S. Zhuravlyov[1], M.I. Rabetsky[1], L.P. Grakovich[1] Leonid L.Vassiliev Jr.[1] Alexander Shapovalov[2] and Alexei Rodin[2]

[1]*Luikov Heat and Mass Transfer Institute, National Academy of Sciences, Minsk, Belarus*
[2]*P.O. Sukhoi State Technical University of Gomel, Belarus*

Abstract

Thermosyphons of the large length are of great interest for being used as heat exchangers for recuperation of alternative energy sources and upgrading their potential with the aid of heat pumps. Some examples of vapordynamic themosyphons (VDT) application as the system of thermal control for solar collectors, in the air conditioning systems, devices combating snow drifts and icing on the active parts of the railway transport track structure, foodstuff baking ovens and roasters, driers, etc. are considered. It is concluded that VDT used for air conditioning, ground heat exchangers and seasonal thermal storage systems connecting with solar thermal collectors have a good opportunities.

Keywords: Heat transfer intensification; Renewable energy sources; Heat pipe; Thermosyphon.

■ *Published in Heat Transfer Engineering, Vol. 40, Issue 3, 2019.*

Effect of Heat Source Size on Cooling Performance of a JEST-type Loop Thermosyphon

Ayaka Suzuki[1], Kaoru Sato[2], Yasushi Koito[1] and Toshio Tomimura[1]

[1]*Department of Advanced Mechanical Systems, Kumamoto University, Kumamoto 860-8555, Japan*
[2]*R&D Division, Panasonic Ecology Systems Co., Ltd., Aichi 486-8522, Japan*

Abstract

A JEST (Jet Explosion Stream Technology) - type loop thermosyphon consists of an evaporator section and a condenser section. These sections are connected by a vapor line and a liquid line. Also, the present loop thermosyphon has new mechanisms: a check valve is located between the liquid line and the evaporator, and a jet induction tube is located in the evaporator. These mechanisms aim at inducing the jet stream in the evaporator for exceeding the cooling performance of the conventional thermosyphons. Fundamental experiments were conducted on the operational characteristics and the cooling performance of the loop thermosyphon.. In this study, the experiments were carried out by changing the heat source size as 1.77 cm2, 4.15 cm2 and 7.07 cm2. From the experimental results, it is confirmed that, irrespective of the heat source sizes, theloop thermosyphon promptly responds to the change in the heated generation rate. As expected, the heated surface temperature is affected by the heat source sizes; however, the other temperatures and the circulating mass flow rate of the working fluid are hardly affected by the heat source size. In addition, it is also revealed that the heat transfer coefficient at the evaporator is greatly higher than that of the conventional thermosyphons.

Keywords: Heat source size; Heat transfer coefficient; JEST; Loop thermosyphon.

■ *Published in "Heat Pipe Science and Technology, An International Journal"*

Simulation and Experimental Validation of a 400 m Vertical CO_2 Heat Pipe for Geothermal Application

Johann-Chr. Ebeling[1], Stephan Kabelac[1], Sebastian Luckmann[2] and Horst Kruse[2]

[1]*Institute for Thermodynamics, Leibniz University of Hannover, Callinstr. 36, 30167 Hannover, Germany*
[2]*FKW-Research Center for Refrigeration Technology and Heat Pumps GmbH, Weidendamm 14, 30167 Hannover*

Abstract

Geothermal heat pipes are an effective heat source for heat pumps used for space heating. Because the area for the installation of borehole heat exchangers is limited in urban areas (one site per borehole), the maximum heat extractable from one borehole shall rise. In cooperation with the FKW Hannover, the Institute for Thermodynamics of the Leibniz University of Hannover is investigating the thermodynamic behavior of CO_2 driven geothermal heat pipes of higher thermal power. Therefore,twodifferenttypesof geothermal heat pipes with a length of 400 m each have been installed. Furthermore,a numerical simulation of the heat and mass transfer within the pipes is under development. The experimental setup and first results of the experiments are presented as well as the current status of the numerical simulation. A comparison of the two different types of heat pipes and a comparison of the experimental data with the numerical simulation isgiven.

Keywords: CO_2; Geothermal heat pipe; Helically corrugated pipe; Numerical simulation; Thermosyphon; TPCT.

■ *Published in Heat and Mass Transfer, Vol. 53, issue 11 (DOI: https://doi.org/10.1007/s00231-017-2014-7)*

An Exhaust Heat Recovery System Utilizing Thermoelectric Generators and Heat Pipes

Bradley G. Orr, Aliakbar Akbarzadeh and Petros Lappas

School of Aerospace, Mechanical and Manufacturing Engineering, RMIT University, Plenty Road, Bundoora, Victoria, 3083 Austra

Abstract

Exhaust heat recovery systems are used to make use of otherwise wasted heat from a car engine. The purpose of exhaust heat recovery systems is to potentially reduce the fuel consumption of the car and consequently reduce CO_2 emissions and running costs. The unique system design described herein utilizesthermoelectric generators (TEGs) and heat pipes with its key advantage being it is a passive solid state design. The use of heat pipes allows for more flexible designs as the TEG location is not limited to the exhaust pipe surface. Testing was undertaken on a car with a 3.0L V6 engine. In all test conditions the power loss due to pressure drop in the exhaust duct was always lower than the electrical power output. Repeat tests were conducted and the results were found to be consistent. When testing the system at different orientations, the bottom heat mode was found to be the best option. After all testing, the maximum power output of the system was 38W from the 8 62mmX62mm TEGs used. The rate of heat transfer in this case was 1541W with the resultant TEG efficiency being 2.46%. The calculated potential reduction in CO_2 emissions, fuel consumption andfuel costs was1.57%.

Keywords: Automotive; Power generation; Thermoelectric generator; Heat pipes; Exhaust heat recovery.

■ *Published in Applied Thermal Engineering, Volume 126, 5 November 2017, Pages 1185-1190, https://doi.org/10.1016/j.applthermaleng.2016.11.019*

Study of Thermal Characteristics in a Reverse Thermosyphon Loop

Meng-Chang Tsai[1], Hung Wang[2], Fong-Hao Wu[1], How-Ming Lee[1], Heng-Yi Li[1] and Shung-Wen Kang[2]

[1]*Physics Division, Institute of Nuclear Energy Research*
1000, Wenhua Rd., Jiaan Village, Longtan, Taoyuan, 32546 Taiwan, ROC [2]*Department of Mechanical and Electro-Mechanical Engineering, Tamkang University 151, Ying-Chuan Rd., Tamsui, Taipei, 25137 Taiwan, ROC*

Abstract

The development of two-phase reverse thermosyphon loop (RTL) was used to solve the defect of convectional thermosyphon that only natural upward movement of vapor steam and downward movement of cold liquids. The two phase reverse RTL is a passive, spontaneous device, such like a heat pipe without wick structure and valves, driven by thermal energy and downward transfer extremely high heat flux. A prototype of two-phase reverse thermosyphon loop (RTL), had been building, testing, and observing its characteristic and performance. This experimental study simultaneous investigated of the effect of various filling ratio and cooling temperature at different input power. 95 % ethyl alcohol (ethanol) was used to be the working fluid. The different steady cooling temperature of 15, 20, 25, 30 °C was controlled by a thermostatic water bath apparatus. Temperature distribution and thermal resistance were measured while increasing the input power in a series of steps (80, 100, 120, 140, 160, 180, 200, 220, 240, 260, and 270 W) until to the heater limited density. The preliminary results show that the best thermal resistance 0.35 $°C \cdot W^{-1}$ at 60 % fill ratio with 65 $kW \cdot m^{-2}$ input power. The test absorbed clear temperature waveform between T_6 and T_7 which with a constant frequency around 40 to 45 second a period. A new RTL equation has been built to predict maximum heat flux by pressure and exceed temperature. In sensitivity analysis found that pressure is the most important factor affects the maximum heat flux.

Keywords: Heat Pipe; Reverse Thermosyphon Loop; Sensitivity analysis.

Thermal Behavior of Heat Pipe Assisted Alkali-Metal Thermoelectric Converter

Ji-Su Lee[1], Wook-Hyun Lee[3,], Ri-Guang Chi[1], Won-Sik Chung[1], Seok-Ho Rhi[1,*], Kye-Bock Lee[2], Seon-Yong Jeong[2], Jong-Chan Park[1] and Young-SooLee[3]

[1]*Thermal Engineering Lab., Graduate school of Mechanical Engineering, Chungbuk National University, 1 Chungbuk -ro, SeoWon-gu, Cheongju, Chungbuk, Korea*
[2]Fluid Engineering Lab.,Graduate School of Mechanical Engineering, Chungbuk National University, 1 Chungbuk -ro, SeoWon-gu, Cheongju, Chungbuk, Korea
[3]*Energy Efficiency Research Division, Korea Institute of Energy Research, 102 Gajeong-ro, Yuseong, Daejeon, Korea*

Abstract

Alkali Metal Thermal to Electric Converter (AMTEC) is a device for changing thermal energy directly to electrical energy by using the alkali metal such as sodium and potassium as the working fluid. It consists of Beta-Alumina Solid Electrolyte (BASE) tubes, low pressure Chamber, high pressure chamber, evaporator and condenser. When the ionized sodium passes through BASE having ion conductivity, then the electricity is generated. The efficiency of the device directly depends on the temperature difference between top and bottom of AMTEC. The efficiency of AMTEC can be improved with the optimum design of components of AMTEC such as a condenser, an evaporator, BASE tubes and artery wick. In addition, radiation shield installed in the low pressure chamber of AMTEC was investigated experimentally and numerically to find the optimum design which it can protect the radiation heat loss to the condenser and wall. Therefore, simulation and experimental studies were carried out to analyze the effect of thermal radiation on AMTEC with various parameters, such as the size of a low pressure chamber and the shape of radiation shield. As a result of CFD simulation to decide the optimum size of a low pressure chamber, the most suitable height and diameter of low pressure chamber is respectively 270 mm and 180 mm with 8 BASE tubes. BASE is 150 mm high, 25 mm in diameter, 105 mm in concentric diameter of BASEs. In the experimental study, power generation is decreased with increasing temperature ratio (T_{Cond}/T_B). The minimum dimensionless value for temperature is appeared when a radiation shield made of 500 mesh Nickel wire is installed and it is 0.4611. As a result of CFD simulation to find out the best position and shape of radiation shield, the maximum power is generated when a stainless steel shield is installed in the middle between BASE and Condenser and it is 61.1 W.

Keywords: Heat Pipe; AMTEC; Alkali Metal; Heat Transfer; Thermoelectric; Energy Conversion.

■ *Published in Heat and Mass Transfer (2017) 53: 3373. https://doi.org/10.1007/s00231-017-2077-5*

Heat Transfer Capacity of a Closed Loop Two-Phase Ammonia-Stainless Steel Thermosyphon in Lunar Gravity

Ke Wu [1], Jian-Fu Zhao [1], Zhen-Dong Li [1], Hong-Xing Zhang [2], Jiang He [2] and Jian-Yin Miao [2]

[1] *Key Laboratory of Microgravity/CAS, Institute of Mechanics, Chinese Academy of Science, Beijing 100190, China*
[2] *Beijing Key Laboratory of Space Thermal Control Technology, Institute of Spacecraft System Engineering, China Academy of Space Technology, Beijing 100094, China*

Abstract

The performance of the closed loop two-phase thermosyphon designed for the Chinese lunar rover in lunar gravity (g/6) is simulated numerically based on a verified numerical model. The predicted results are compared with the experimental data obtained from a ground simulation test, showing a satisfied agreement. It is also shown that the prediction by using Duschatko model for interfacial friction factor in two-phase annular flow region is more consistent with the experimental data, indicating that Duschatko model can be used as the optimal model for the design and system simulation of closed loop two-phase thermosyphons under low gravity, small diameter and low flow rate condition. The difference of the predicted heat transfer capacity of closed loop two-phase thermosyphons by different empirical models may reflect the influence of gravity on the two-phase flow structures, which can be used to analyze the reliability and credibility of ground experiments. The analysis shows that the ground simulation experiment may provide a higher flow resistance and thus a lower heat transfer capability, which is on the conservative side for engineering applications.

Keywords: Chang'E-3; Closed loop two-phase thermosyphon; Heat transfer capacity; Lunar gravity; Numerical simulation.

Study on Heat Pipe Assisted Thermoelectric Power Generation System from Exhaust Gas

Ri-Guang Chi, Jong-Chan Park, Won-Sik Chung, Seok-Ho Rhi and Kye-Bock Lee

School of Mechanical Engineering, Chungbuk National University, 52 Naesudong -ro, Heungduk-gu, Cheongju, Chungbuk, Korea

Abstract

Currently, most fuel consumed by vehicles is extracted to the environment as thermal energy through the exhaust pipe. Recently, eco-friendly vehicle technology needs new ways to increase the recycling efficiency of waste thermal energy. The present study investigated how to improve the maximum power output of a TEG (Thermoelectric generator) system assisted with heat pipe. Conventionally, driving energy efficiency of internal combustion engines is less than 35%. Thermoelectric power generation (TEG) with seebeck elements is a new way of green recycling technology. The TEG system can utilize low temperature waste heat efficiently such as industrial waste heat and solar energy etc. Also, heat pipe can transfer heat from automobile exhaust gas to TEG. To improve the efficiency of thermal power generation system with heat pipe, effects of various parameters such as inclination angle, charged amount of the heat pipe, condenser temperature and size of thermoelectric element were investigated. Experimental studies, CFD simulation, and theoretical approach on thermoelectric modules were carried out and the TEG system with heat pipe (15-20% charged, 20-30^{o} inclined configuration) showed the best performance.

Keywords: Heat pipe; Thermoelectric Power; Seebeck effect; Power generation.

■ *Published in Heat and Mass Transfer (2017) 53: 3373. https://doi.org/10.1007/s00231-017-2077-5*

Length Effect on Entrainment Limitation of a Wickless Heat Pipe

Joseph Seo and Jae-Young Lee

Handong Global University, 588 Handong-ro, Pohang 791-780, Republic of Korea

Abstract

Heat pipes, which are heat-transfer devices of high thermal conductance, have been studied intensively because of their applicability and efficiency. However, only a small number of studies have been conducted on relatively long heat pipes. Here, the thermal hydraulic characteristics of a long heat pipe are studied. In particular, the entrainment limit, one of the important design parameter, is examined, so as to determine their sensitivities to the length-to-inner-diameter (L/D) ratio. Experiments are conducted to measure limitations of the heat pipe for various length scales. It is found that, entrainment limitation points are affected by L/D value of heat pipe that is not considered in former correlations. Thus, a new modifying factor including effect of L/D is formulated from experimental results. The correlation with modifying factor showed good agreement with both experimental results of formal researches and present study.

Keywords: Heat pipe; L/D ratio; Entrainment limit; Thermosyphon; Heat removal; Thermalperformance.

Numerical Investigation of a CO_2 Loop Thermosyphon for Free Cooling of Data Centers

Hainan Zhang[1,2], Shuangquan Shao[1] and Changqing Tian[1]

[1] *Technical Institute of Physics and Chemistry, Chinese Academy of Sciences, Beijing 100190, China*
[2] *University of Chinese Academy of Sciences, Beijing 100049, China*

Abstract

The energy consumption of data centers is increasing rapidly, and30%~50% of the total is consumed by the cooling equipment. Free cooling, which means using natural cooling source to cool data centers in cold seasons, is an effective way for saving cooling energy. Loop thermosyphon is an ideal free cooling equipment for its superior heat transfer ability. Most working fluids used presently in loop thermosyphon destroy the ozone layer and it is necessary to investigate the performance of environment friendly fluids, so CO_2 is investigated as a substitute. In this paper, it is built and validated that a distributed-parameter model of a CO_2 loop thermosyphon for free cooling. The performance is compared with traditional working fluids and the effects of some key geometric parameters are evaluated. The results show that the optimal filling ratios for CO_2, R22 and R134a are 120%, 100% and 90% and the heat transfer rate at the optimal filling ratios of the three fluids have no obvious difference. The circulation flow rate of CO_2 is much smaller than that of R22 and R134a. For CO_2 loop thermosyphon, the heat transfer rate decreases with the increase of pipe length and increases with the increase of riser diameter. The heat transfer rate increases with the increase of height difference and the effect is greater when the temperature difference is large. The heat transfer rate increases with increasing tube number of evaporator while the increment is little when tube number is more than80.

Keywords: Loop thermosyphon; CO_2; Free cooling; Data center; Simulation.

■ *Published in Applied Thermal Engineering, Volume 126, 5 November 2017, Pages 1134-1140, https://doi.org/10.1016/j.applthermaleng.2016.12.135*

Energy Saving Potentials from the Application of Heat Pipes on Geothermal Heat Pump Systems

Hyunjeong Lim and Minsung Kim

[1]*School of Energy Systems Engineering, Chung-Ang University, Seoul 06974, Korea*

Abstract

A ground-loop heat exchanger is one of the key components to collect low grade heat out of the heat source for a ground source heat pump system. Typical ground source heat pumps consist of a refrigerant loop operated by a compressor and a geothermal brine loop operated by a circulation pump. Although ground source heat pumps are known as one of the most efficient HVAC devices, their performance still need to be upgraded since the energy consumption by the peripherals like the circulation pump are considerable and estimated around 13% of the total electricity input. By this additional energy input, the ground source heat pump costs the coefficient of performance (COP) by 15%. In order to reduce the ground circulation energy, a variety of researches such as direct expansion geothermal heat pumps are studied, but no apparent performance improvement was found due to other negative effects like the increase of pressure drop in the ground loop. In this study, the energy saving potential using heat pipe as ground heat exchanger was investigated.

Keywords: Ground source heat pump; Heat pipe; Thermosyphon; Heating seasonal performance factor (HSPF); Direct expansion; Ground-loop heat exchanger.

■ *Published in Applied Thermal Engineering, Volume 126, 5 November 2017, Pages 1191-1198, https://doi.org/10.1016/j.applthermaleng.2017.04.086*

The Design of a Split Loop Thermosyphon Heat Exchanger for Use in HVAC Applications

Daniel Reist[1], Michael Ellis[1], Mark C. Stevens[1], and Pete M. Dussinger[1]

[1]Advanced Cooling Technologies, Inc., 1046 New Holland Avenue, Lancaster, PA 17601

Abstract

While the heat pipe is traditionally considered for thermal management of electronics and relatively small scale systems, heat pipes should also be considered in larger commercial/industrial applications. One area in particular is in Heating, Ventilation, and Air Conditioning (HVAC) systems. Heat pipe heat exchangers can be used to realize significant energy savings where large volumes of ventilation air are required to achieve indoor air quality standards. In this paper, the authors describe an innovative, passive, split loop thermosyphon air-to-air heat exchanger. Design methodology and trade-offs will be explored and the final design performance will be compared to alternative solutions. Also included in the paper is a case study demonstrating the practical use of the technology at a hospital in Seoul, South Korea.

Keywords: Energy recovery; HVAC; Split loop thermosyphon; Air-to-air heat exchanger

1. INTRODUCTION

Maintaining a high level of indoor air quality requires a significant amount of ventilation air. Stale indoor air must be frequently exchanged with fresh outside air. This outside air that is brought into the building must be heated in the winter and cooled in the summer by the active HVAC system to maintain the indoor air temperature at about 22°C. The heating and cooling of the outside air requires a tremendous amount of energy for a large building like a hospital. The American Society of Heating, Refrigerating, and Air-Conditioning Engineers (ASHRAE) Standard 62.1 defines the required levels of ventilation (number of room air volume exchanges per hour) for acceptable indoor air quality. ASHRAE standards also drive local building codes.

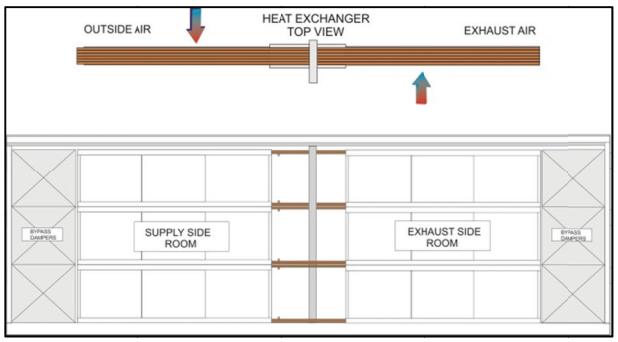


Fig. 1. Top/Front View of a large (1.2m tall x 2.9m wide) Split Loop Thermosyphon Heat Exchanger

At the same time as outdoor air is being drawn into the building, an equal amount of indoor air that has been previously conditioned to 22°C is being discharged from the building. These two air streams pass through ACT's split loop thermosyphon air-to-air heat exchanger, shown in Figure 1. In the winter, the heat from the warm discharge air is transferred passively by the heat pipe heat exchanger to the incoming outside air. Therefore, the demand on the active heating system is significantly less.

The difference between a standard air to air heat pipe heat exchanger and a split loop thermosyphon is found in the circuiting between the warm and cool side heat exchanger coils. A standard air-to-air heat pipe heat exchanger has many individual heat pipes that run the entire length of the heat exchanger, with the evaporator portion of the heat pipe extending into the warm air duct and the condenser end of the heat pipe terminating in the cool air duct. Each heat pipe functions similarly to traditional heat pipe theory with the vapor flowing down the center of the pipe while the liquid returns along the wall.

Alternatively, a split loop thermosyphon is divided into a fewer number of circuits, typically one circuit per row of tubes in the heat exchanger coil. Each row is a dedicated circuit which shares a common liquid and vapor header which allows the liquid and vapor to flow in the same direction. This type of design does not reach the limits (entrainment, flooding) of the traditional counter-flow heat pipe; and therefore, the split loop thermosyphon is able to transfer more heat per unit volume than the standard, heat pipe air-to-air heat exchanger. Another benefit is that because the system contains only two connecting tubes per circuit, retrofit into many applications with minimal changes to existing ductwork or separation walls is possible.

2. DESIGN

The type of air-to-air heat exchanger discussed here consists primarily of linked finned-tube heat exchangers, as shown in Fig. 2. Each finned-tube may be connected individually or through a manifold. The tubes are then filled in a way to ensure the working fluid is at saturation with vapor and liquid existing at equilibrium. During operation, one finned-tube heat exchanger is exposed to a relatively colder air stream while the other experiences a relatively warmer air stream. This causes the working fluid to maintain equilibrium by transferring thermal energy from the warmer portion to the colder portion by latent heat. This results in extremely efficient and isothermal heat transport.



Fig. 2. Air-to-Air Heat Exchanger Designed to Enhance Dehumidification Performance and Conserve Energy in a Conventional HVAC System.

An air-to-air heat exchanger can be arranged as counter- or parallel-flow. In general, counter-flow heat exchangers can obtain higher heat exchanger effectiveness values than parallel-flow heat exchangers. In other words, they are able to use more of the working fluid heat capacity than their counterpart. However, sometimes installation geometry prevents a counter-flow arrangement.

In addition, the isothermal nature of a heat pipe or thermosyphon based heat exchanger must be considered. These types of air-to-air heat exchangers consist of rows of tubes that contain a fluid at saturation. As a result, each row acts like an evaporative or condensing heat exchanger at a temperature that depends on a balance between the exhaust and supply air temperatures. As air moves through a heat pipe based air-to-air heat exchanger, the saturation temperature of each bank differs based on this balance. Unlike a typical finned-tube heat exchanger, the result is that each bank of tubes exists at a different, although isothermal, temperature.

So the type of heat exchanger described here acts like a condensing or evaporative heat exchanger relative to each row but a counter- or parallel-flow heat exchanger overall. Furthermore, in a split loop thermosyphon heat exchanger, some of the rows may be tied together. In fact, all of the rows could be tied together. However, this would result in a single temperature among all of the finned-tubes and decrease the overall effectiveness of the air-to-air heat exchanger as this arrangement reduces the available temperature potential and therefore heat capacity of the working fluid.

For this reason, the orientation of each circuit on one side of the heat exchanger relative to the matching circuit on the opposite side of the heat exchanger must be considered. The impact of temperature difference between each of the rows in the heat pipe heat exchanger is important to maximizing heat exchanger effectiveness. While there is a manufacturing benefit to combining rows of finned-tubes so that they are fed by a single manifold, this benefit must be balanced against heat exchanger performance.

ACT has developed an air-to-air heat exchanger model that optimizes the design based on parameters such as fins per inch, allowable pressure drop, thermosyphon working fluid, and temperature, flow rate, and humidity for each air stream. Based on user inputs, this model optimizes the heat exchanger design either to meet specific energy savings requirements or specific design criteria. The latter is typically used for retrofit applications.

Heat exchanger optimization is based around maximizing energy savings while minimizing the overall heat exchanger dimensions and cost. For a cooling application as shown in Fig. 3, energy savings are calculated by comparing the sensible heat lost by the supply air or gained by the exhaust air. If condensation were to occur in the supply air, the latent heat lost is also included. These savings reduce the load on the primary HVAC system thus reducing the energy consumption required to cool or heat the conditioned space. And these energy savings are provided passively.

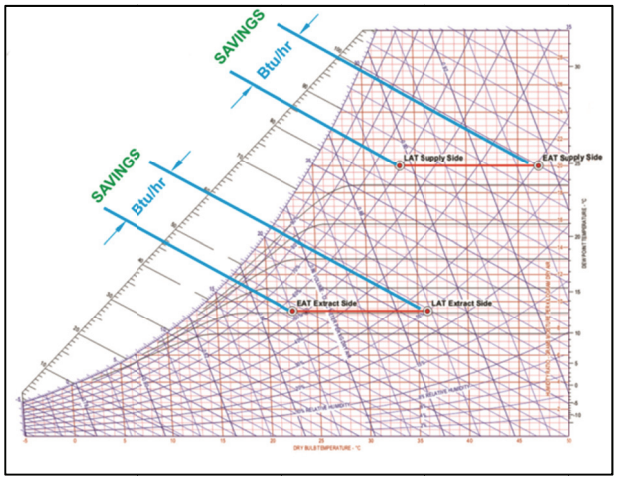


Fig. 3. Energy Savings Example for an Air-to-Air Heat Exchanger.

3. CONTROL

In some applications, control over the amount of heat transfer is desired. For example, there are some periods of time during the cooling season, when the outside air temperature dips below the temperature of the air being ventilated out of the building. The temperature difference is not too large and the air handler remains in the active cooling mode. In this scenario, the air-to-air heat exchanger would be preheating instead of precooling the incoming air, which is counterproductive. In this type of application, control valves can be added to the vapor lines of the split loop thermosyphon. The valves open and close based on the temperature difference between the exhaust air and the outside air. The building management system can also be programmed to open and close the valves for other situations where precooling or preheating of the incoming air stream is not desired. In the latter case, the valves are active and actuated by electric current.

Fig. 4 shows a split-loop thermosyphon unit with active valves. These valves shut off the air-to-air heat exchanger when energy recovery is not necessary due to outdoor conditions. ACT has also developed passive valves that rely on a phase change material to open and shut each thermosyphon circuit based on working fluid temperature. A demonstration unit using these passive valves is shown in Fig. 5.

The passive valves actuate based on the melt temperature of a phase change material. This material can be selected to provide specific set temperatures. As a result, the passive valves can be customized to their operating environment. In addition, the valves can use different melting point materials to provide a cascaded shutoff.



Fig. 4. Split Loop Thermosyphon with Active Control Valves



Fig. 5. Air-to-Air Heat Exchanger with Passive Valves that are Actuated by Phase Change Material.

4. APPLICATION

A split-loop thermosyphon heat exchanger was recently installed by ACT at a hospital facility located in Seoul, South Korea. These heat exchangers have ten rows of finned tubes, process 33 m^3/s of air, and transfer over 175kW. They are capable of offsetting approximately 60% of the heating required for the building, resulting in tremendous energy savings.

Fig 6, the manufacturing benefit of the split-loop thermosyphon is clear: linking several thermosyphon circuits using a single manifold greatly reduces the piping required to assemble the system. Furthermore, charging this system with refrigerant was simplified as, rather than charging hundreds of individually linked tubes, only approximately thirty manifolds were charged. In addition, if this system had

required control, much fewer active or passive control valves would be necessary. This system has been in operation for over half a year.



Fig 6. Split Loop Thermosyphon Air-to-Air Heat Exchanger Installed in a Hospital in South Korea.

5. CONCLUSIONS

ACT has demonstrated the capability of a split-loop thermosyphon to provide significant energy savings and controllability through installation in several large scale HVAC systems. In addition, the manifold design of the split-loop thermosyphon has been shown to increase performance and simplify installation of air-to-air heat exchangers. These benefits together show a promising new application for heat pipe technology.

ACKNOWLEDGEMENT

ACT would like to thank our industrial partners that have provided us with the opportunity to demonstrate the energy efficiency gains possible using split loop thermosyphon systems. We also appreciate the technical expertise of James Bean, who was instrumental in the fabrication and installation of our first systems.

REFERENCES

[1] ANSI/ASHRAE Standard 62.1-2013 - Ventilation for Acceptable Indoor Air Quality

Transient Detailed and Reduced Models of a Two-phase Loop Thermosyphon

Serge H. Bodjona*, Etienne Videcoq, Manuel Girault and Yves Bertin

Institut Pprime CNRS-ENSMA - University of Poitiers - Departement Fluid, Thermal, Combustion, ENSMA Téléport 2, 1, avenue Clément Ader, BP 40109, 86961 FUTUROSCOPE CHASSENEUIL Cedex, France

Abstract

This study investigates numerically a two-phase loop thermosyphon in steady and transient states. In a first step, a 1D two-phase flow model in both mechanical and thermal equilibrium is used. This detailed model considers pure liquid phase or pure vapor phase (liquid line or vapor line) and phase transition (evaporation and condensation). A finite volume hyperbolic solver with the HLLC Riemann solver is used. The system under study being a complex nonlinear system, the detailed model requires extensive computational resources, not suitable for design purposes or real time applications. Hence, in a second step, a reduced model for the overall energetic behavior of the loop thermosyphon is proposed. This reduced model is built using new developments of the Modal Identification Method, traditionally employed in heat transfer. Parameters of a low order dynamical system of equations and spatial modes for each variable are identified through optimization algorithms. The objective of this work is to analyze the accuracy and the computational time gain factor of the reduced model. In order to do this, density, mass flow rate, internal energy, velocity, pressure and temperature fields are computed by both models for a varying heat power at evaporator and compared at different time instants. The results show that the reduced model correctly predicts the loop behavior for a wide variation of the thermal load at evaporator.

Keywords: Loop thermosyphon; Two-phase flow; Heat transfer; Detailed model; Low-order model

1. INTRODUCTION

A two-phase loop thermosyphon (2PLT), which is a passive thermal system, is considered in this study. 2PLT can be found in several applications such as thermal stabilization [1], passive cooling system of the seat electronic box on board commercial aircrafts [2], telecommunication equipment in the outdoor cabinet [3], solar water heater [4], prevention of icing on a buoy [5], geothermal energy [6].

Our interest in this work concerns the modeling of such a system in steady and transient states. Let us first outline some works dealing with this topic. Vincent et al. [7] present a numerical model developed for a two-phase co-current thermosyphon. They use control volume approach and their investigation focuses on transient behavior of the system when the steady-state is disturbed. They conclude that the control volume approach limits the number of variables and describes satisfactorily the behavior of thermosyphon. Bieliński et al. [8] propose a detailed analysis of heat transfer and fluid flow in a new generalized model of thermosyphon loop and its different variants. Their results show that the one-dimensional two-phase separate flow model can accurately describe heat transfer and fluid flow in a 2PLT. Two different models for evaporator and condenser are used by Qu [9]. An integral balance of bubble flow model is used at the evaporator and the liquid film condensation of vapor-liquid concurrent flow model at condenser. After his investigation, one of his conclusions is the density of the vapor-liquid mixture at outlet of evaporator is not that of the vapor. He also remarks that vapor velocity is three orders of magnitude higher than that of the liquid, and so the liquid velocity can be neglected.

In the works cited above in connection with the 2PLT, heat transfer, fluid flow or the behavior of the loop in transient or steady state have been studied in different ways. Most of the time, these 1D models include mass, momentum and energy balances but each with their own specificities. Some authors such as Bieliński et al. [8] use incompressible flow model with Boussinesq approximation and empirical correlation in different parts of the loop. This model considers thermal equilibrium at any point of loop. Other authors such as Vincent et al. [7] or Qu [9] use different models for evaporator, condenser, liquid line and vapor line. This means that for computation, each part of loop has its own model. They are based either on hydraulic flow model or compressible flow model.

In this study we develop a 1D model (Euler equations), which is in mechanical and thermal equilibrium, that includes mass, momentum, internal energy and vapor mass fraction balances. In each part of the loop, the same model is used in the computation. In other words, our model describes thermodynamic equilibrium (saturation or mixture), but also thermodynamic non-equilibrium (pure liquid or pure vapor) phase and so can compute phase transitions (liquid-mixture-vapor). The use of unsteady model allows the equilibrium state of system, whether it exists, to be reached naturally by a resolution of system of equations with respect to time.

*Corresponding author: serge-heziewe.bodjona@ensma.fr

A reduced model of the 2PLT behavior is obtained through the Modal Identification Method (MIM) from the detailed model. Reduced models built with MIM were used for solving efficiently inverse heat transfer problems such as in [10, 11] and were used successfully for real-time state feedback control of MIMO thermal systems [12, 13].

The paper is structured as follows: the 2PLT and its operating cycle are briefly described in section 2. The detailed model of this system and the methodology are presented in section 3. Section 4 is devoted to the reduced model structure and identification. Finally, a validation case will be presented and a comparison between the detailed model and the reduced one will be discussed.

2. TWO-PHASE LOOP THERMOSYPHON (2PLT)

As shown in Fig. 1, the 2PLT is a passive thermal system, mainly composed of an evaporator, a vapor line, a condenser and a liquid line. Its operation lies on the phase change of a working fluid (methanol in our case) and on gravity, which is the driving force of the fluid flow.

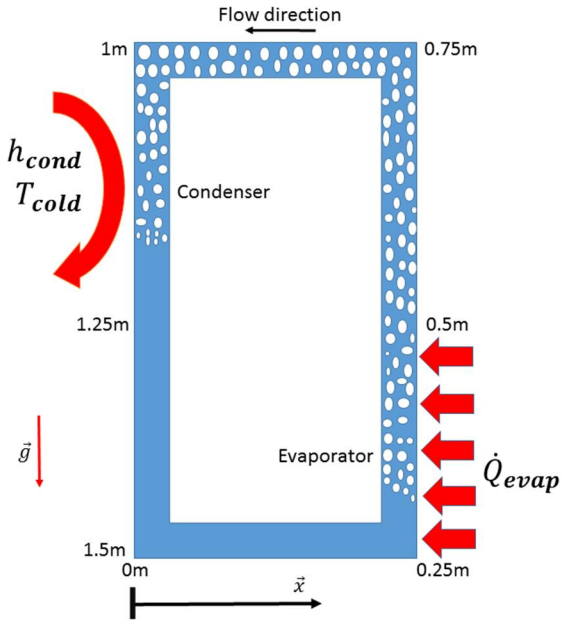


Fig. 1. Schematic representation of a 2PLT.

At the evaporator (0.25m-0.5m), the methanol liquid phase is heated and vaporized. The vapor flows through the vapor line (0.5m-1m) toward the condenser which consists in a low temperature controlled heat exchanger (1m-1.25m). The vapor is cooled and turns into liquid in the condenser. The liquid falls under gravity effect in the vertical liquid line (1.25m-1.5m) and is driven toward the evaporator by the horizontal liquid line (0m-0.25m) where it is heated again. The density of the working fluid in the descending vertical tube (0.25m-0.5m) being greater than the density of the vapor in the ascending vertical tube (0.5m-0.75m), a buoyancy effect appears between both volumes of fluid. This effect is responsible of maintaining the fluid flow in the loop thermosyphon.

3. DETAILED MODEL

3.1 Model description and hypotheses

The model developed here is based on a finite volume approach. A one-dimensional space discretization of the whole loop is performed. Mass, momentum, internal energy and vapor mass fraction conservation equations are then solved on each volume. This approach is coupled with the HLLC Riemann Solver [14] in order to compute the numerical fluxes.

The assumptions are summarized here below:

- The tube cross-section area is constant along the loop.
- Two-phase flow is considered as a homogeneous mixture at both mechanical and thermal equilibrium.
- The mixture flow is compressible.
- Friction effects are approximated by Darcy-Weisbach law.
- Heat conduction into the fluid is neglected.
- Viscous dissipation is neglected in the energy equation.
- The dynamic viscosity of the fluid and of the mixture is constant.
- The heat convection coefficient h_{cond} at condenser is constant.
- Except at evaporator and condenser, heat exchanges with the environment are neglected.

3.2 Flow model

A homogeneous compressible flow mixture is considered [15]. This model is derived from a multiphase model of phase transition [16]. The set of assumptions listed in previous section yields the following set of equations.

$$\begin{cases} \frac{\partial \rho}{\partial t} + \frac{\partial (\rho u)}{\partial x} = 0 \\ \frac{\partial (\rho u)}{\partial t} + \frac{\partial (\rho u^2 + p)}{\partial x} = -\frac{64\mu}{2D_h^2} u + \varepsilon \rho g \\ \frac{\partial (\rho e)}{\partial t} + \frac{\partial (\rho e.u)}{\partial x} = -p \frac{\partial u}{\partial x} + \frac{\dot{Q}}{\Omega} \\ \frac{\partial y}{\partial t} + u \frac{\partial y}{\partial x} = 0 \end{cases} \quad (1)$$

where ε depends on gravity direction:

$$\varepsilon = \begin{cases} -1 & \forall\, x \in [1\text{m}, 1.5\text{m}] \\ 0 & \forall\, x \in]0\text{m}, 0.25\text{m}[\cup]0.75\text{m}, 1\text{m}[\\ 1 & \forall\, x \in [0.25\text{m}, 0.75\text{m}] \end{cases} \quad (2)$$

and

$$\dot{Q} = \begin{cases} \dot{Q}_{evap} & \forall\, x \in [0.25\text{m}, 0.5\text{m}] \\ 0 & \forall\, x \in]0.5\text{m}, 1\text{m}[\cup]1.25\text{m}, 0.25\text{m}[\\ h_{cond} S_{ext} (T_{cold} - T) & \forall\, x \in [1\text{m}, 1.25\text{m}] \end{cases} \quad (3)$$

Closure of system requires equation of state specification.

3.3 Equation of state for pure phases

Each phase is assumed to obey the Stiffened Gas (SG) equations of state (EOS) [17].Then, the SG EOS for each phase k (liquid or gas), is written as follows:

$$v_k = \frac{(\gamma_k - 1) C_{v,k} T}{p + p_{\infty,k}} = \frac{1}{\rho_k} \quad (4)$$

$$e_k = \frac{p + \gamma_k p_{\infty,k}}{(\gamma_k - 1)} v_k + q_k \quad (5)$$

$$h_k = \gamma_k C_{v,k} T + q_k \quad (6)$$

$$G_k = \left(\gamma_k C_{v,k} - q'_k\right) T - C_{v,k} T \ln\left(\frac{T^{\gamma_k}}{(p + p_{\infty,k})^{\gamma_k - 1}}\right) + q_k \quad (7)$$

3.4 Mixture EOS

The following definitions and assumptions are used to build the EOS of the homogeneous mixture [15]:

$$v = y_g v_g + y_l v_l \quad (8)$$

$$e = y_g e_g + y_l e_l \quad (9)$$

$$h = y_g h_g + y_l h_l \quad (10)$$

3.5 Thermodynamic closure of the model

Closure of Eq. (1) requires two equations for the computation of pressure and temperature, both in the zone of the mixture and in the single-phase regions.

For the single-phase regions, the equations that we use to compute respectively pressure and temperature can be written as follows [17]:

$$p = \frac{1}{2}\left[A_g + A_l - \left(p_{\infty,g} + p_{\infty,l}\right)\right] + \left[\frac{1}{4}\left[A_l - A_g - \left(p_{\infty,l} - p_{\infty,g}\right)\right]^2 + A_g A_l\right]^{0.5} \quad (11)$$

where:

$$A_k = \left[\frac{y_k (\gamma_k - 1) C_{v,k}}{y_g C_{v,g} + y_l C_{v,l}}\right]\left[\rho(e - q) - p_{\infty,k}\right] \quad (12)$$

$$q = y_g q_g + y_l q_l \quad (13)$$

and:

$$T = \frac{1}{\rho\left[\frac{y_g (\gamma_g - 1) C_{v,g}}{p + p_{\infty,g}} + \frac{y_l (\gamma_l - 1) C_{v,l}}{p + p_{\infty,l}}\right]} \quad (14)$$

For each phase k, the constants $p_{\infty,k}$, q_k, q'_k, $C_{v,k}$, y_k are determined using four reference points [17].

For the mixture zone, equations must take into account fluid saturation state. Thus, for computation of pressure and temperature, following equations are considered:

$$\frac{h_l - (e + \frac{p}{\rho})}{h_l - h_g} - \frac{v_l - \frac{1}{\rho}}{v_l - v_g} = 0 \quad (15)$$

and:

$$T = T_{sat}(p) \quad (16)$$

4. REDUCED MODEL (RM)

4.1 Overview

The technique used here to build the reduced model is based on the Modal Identification Method (MIM). This latter has been continuously developed for many years. Its use to build RMs designed to solve inverse problems has been tested for several types of problems, for instance linear heat transfer [10], nonlinear heat transfer [11], transport-diffusion of species [18], fluid mechanics [19], showing the benefits obtained.

The general approach consists in three main steps:

- Defining the structure of the RM equations able to adequately describe the involved

physics, usually obtained from the local partial differential equations which govern the physics.

- Generating some input-output data representative of the system dynamics. Those data come from in-situ measurements, or from numerical simulations as in the present work.
- Identifying the parameters of the RM equations through the minimization of a functional based on the quadratic residuals between the previously generated output data of the system on the one hand and the outputs of the RM on the other hand, for the same input data.

The MIM therefore aims to adjust the RM constitutive parameters using optimization techniques, in order for the RM to mimic the data characterizing the input-output dynamics of the system.

4.2 RM equations

It is assumed that each variable may be written as a linear combination of space functions with time-varying coefficients:

$$\rho(x,t) \simeq \sum_{i=1}^{i=n_a} a_i(t)\Phi_{ai}(x) \quad (17)$$

where $\Phi_a(x)$ is a spatial basis for ρ, and $a(t)$ is the reduced state vector.

In the same way, following relations are written for the other variables of the problem: ρu, ρe, u, p and T.

$$\rho u(x,t) \simeq \sum_{i=1}^{i=n_b} b_i(t)\Phi_{bi}(x) \quad (18)$$

$$\rho e(x,t) \simeq \sum_{i=1}^{i=n_c} c_i(t)\Phi_{ci}(x) \quad (19)$$

$$u(x,t) \simeq \sum_{i=1}^{i=n_d} d_i(t)\Phi_{di}(x) \quad (20)$$

$$p(x,t) \simeq \sum_{i=1}^{i=n_c} c_i(t)\Phi_{ei}(x) \quad (21)$$

$$T(x,t) \simeq \sum_{i=1}^{i=n_c} c_i(t)\Phi_{fi}(x) \quad (22)$$

Note that in the present work, the same state vector $c_i(t)$ is chosen for the variables ρe, p and T in order to simplify the structure of RM equations.

It means it is assumed that those 3 variables share the same dynamics.

Let us now define $R_\rho(x,t)$ as the residual of the mass conservation equation:

$$R_\rho(x,t) = \frac{\partial \rho}{\partial t} + \frac{\partial(\rho u)}{\partial x} \quad (23)$$

After inserting Eq. (17) and Eq. (18) into Eq. (23), the residual R_ρ is forced to be orthogonal to the subspace spanned by the spatial functions Φ_a. The Galerkin projection onto Φ_a hence writes:

$$\left(R_\rho(x,t), \Phi_{ak}(x)\right)_L = \int_0^L R_\rho(x,t).\Phi_{ak}(x)dx = 0 \quad \forall\, k \in [1; n_a] \quad (24)$$

It has been demonstrated that this equation becomes:

$$\underline{\underline{L_1}}' \,\overline{\otimes}\, \dot{a} + \underline{\underline{L_2}}' \,\overline{\otimes}\, b = 0 \quad (25)$$

where $\overline{\otimes}$ is the tensor contraction, $\underline{\underline{L_1}}'$ and $\underline{\underline{L_2}}'$ are matrices defined by:

$$\left(\underline{\underline{L_1}}'\right)_{ki} = \int_0^L \Phi_{ai}(x)\Phi_{ak}(x)dx \quad \forall\, k \in [1; n_a] \quad \forall\, i \in [1; n_a] \quad (26)$$

$$\left(\underline{\underline{L_2}}'\right)_{ki} = \int_0^L \frac{\partial \Phi_{bi}(x)}{\partial x}\Phi_{ak}(x)dx \quad \forall\, k \in [1; n_a] \quad \forall\, i \in [1; n_b] \quad (27)$$

After demonstrating that matrix $\underline{\underline{L_1}}'$ is invertible and writing that $\underline{\underline{L_1}} = \left(\underline{\underline{L_1}}'\right)^{-1} \underline{\underline{L_2}}$, Eq. (25) becomes:

$$\dot{a} + \underline{\underline{L_1}} \,\overline{\otimes}\, b = 0 \quad (28)$$

Galerkin projections of the momentum, internal energy and velocity equations are also performed, yielding the following global set of equations:

$$\begin{cases} \dot{a} + \underline{\underline{L_1}} \,\overline{\otimes}\, b = 0 \\ \dot{b} + \underline{\underline{Q_1}} \,\overline{\overline{\otimes}}\, \underline{\underline{b \otimes d}} + \underline{\underline{L_2}} \,\overline{\otimes}\, d \\ + \underline{\underline{L_3}} \,\overline{\otimes}\, c + \underline{\underline{L_4}} \,\overline{\otimes}\, a = 0 \\ \dot{c} + \underline{\underline{Q_2}} \,\overline{\overline{\otimes}}\, \underline{\underline{c \otimes d}} + \underline{\underline{L_5}} \,\overline{\otimes}\, c + V_1\dot{Q} + V_2 = 0 \\ b(t) + \underline{\underline{Q_3}} \,\overline{\overline{\otimes}}\, \underline{\underline{a \otimes d}} = 0 \end{cases} \quad (29)$$

The Modal Identification Method consists in building a reduced model whose form is given by Eq. (29) through an optimization procedure [11] from input-output data. The components of vectors V_1 and V_2, matrices $\underline{L_1}$, $\underline{L_2}$, $\underline{L_3}$, $\underline{L_4}$, $\underline{L_5}$ and tensors $\underline{\underline{Q_1}}$, $\underline{\underline{Q_2}}$, $\underline{\underline{Q_3}}$ are estimated through the minimization of a quadratic functional built on an output error between DM and RM responses. Both Ordinary Least Squares and Particle Swarm Optimization methods are used in the optimization algorithm. In order to simplify the identification procedure, we chose in this study the same basis size for all variables: $n_a = n_b = n_c = n_d = n$.

4.3 RM Identification

The second step consists in generating some input–output data characteristic of the system dynamics. Those data come from numerical simulations as in the present work, or from in-situ measurements. Here the detailed model is used to obtain simulated data $Y^{DM} = [\rho\ \rho u\ \rho e\ u\ p\ T]^T$ in response to the input signal $\dot{Q}_{evap}(t)$ composed of 5 successive steps given in Fig. 2, each one allowing to reach the steady state.

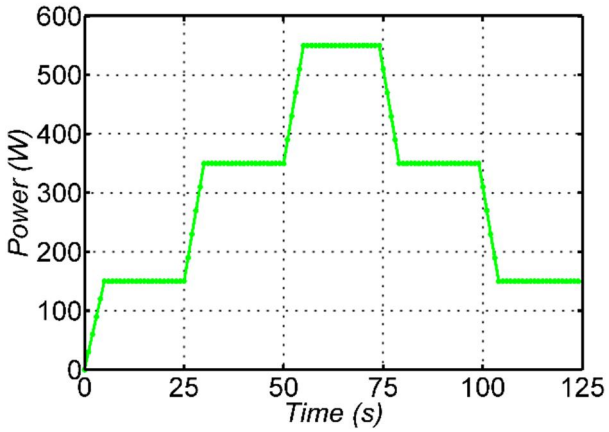


Fig. 2. Time varying thermal load at evaporator.

The density field is for instance given in Fig. 3 at t=63 s in red lines (detailed model). Note that in our study, the number of finite volumes is equal to 150 and corresponds to $\Delta x = 0.01$ m. The initial fields of the computation are drawn in rose lines.

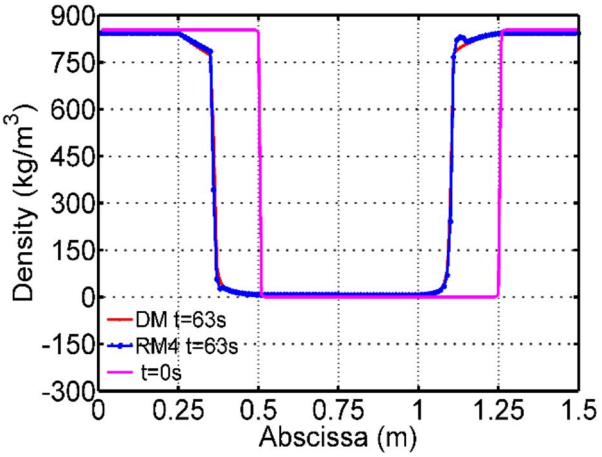


Fig. 3. Density field for RM identification.

The velocity, the internal energy, the pressure and the temperature fields are respectively represented in Fig. 4, Fig. 5, Fig. 6 and Fig. 7.

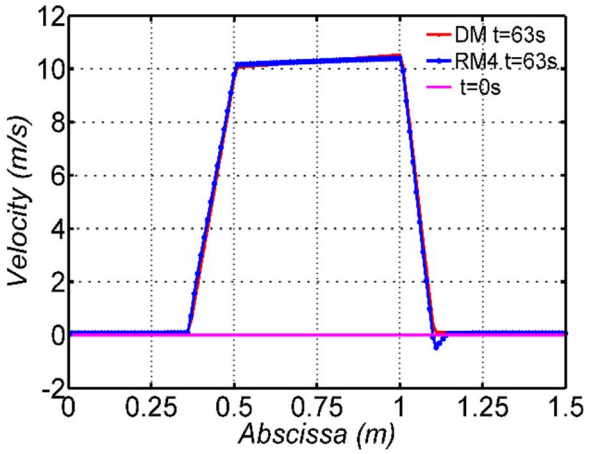


Fig. 4. Velocity field for RM identification.

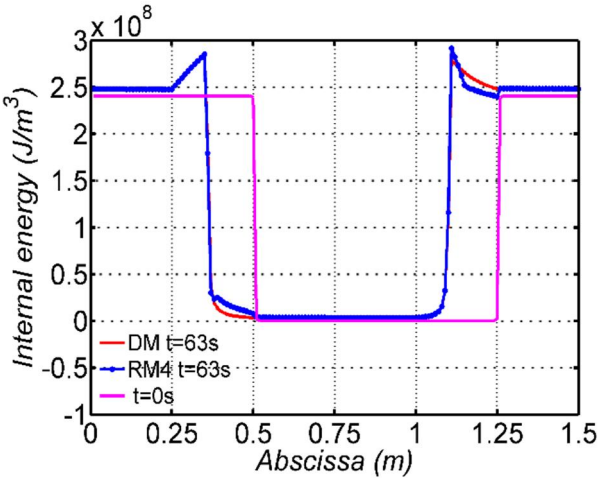


Fig. 5. Internal energy field for RM identification.

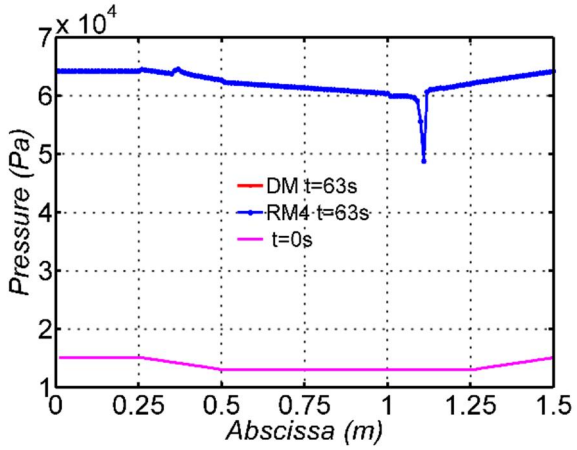


Fig. 6. Pressure field for RM identification.

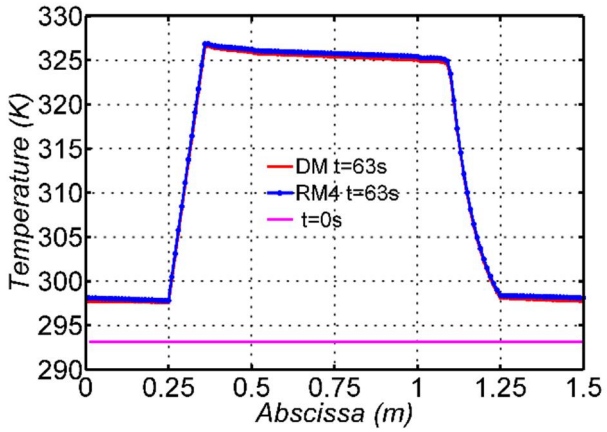


Fig. 7. Temperature field for RM identification.

The last step consists in identifying the RM parameters, which are the components of V_1, V_2, $\underline{\underline{L_1}}$, $\underline{\underline{L_2}}$, $\underline{\underline{L_3}}$, $\underline{\underline{L_4}}$, $\underline{\underline{L_5}}$, $\underline{\underline{Q_1}}$, $\underline{\underline{Q_2}}$, $\underline{\underline{Q_3}}$ in Eq. (29). For a given order n, the parameters are identified through the minimization of a functional based on the quadratic residuals between $Y^{RM}(t)$ and $Y^{DM}(t)$ for the same known input vector $\dot{Q}_{evap}(t)$ given in Fig. 2.

In order to assess the quality of RM, the mean quadratic relative error between fields obtained with DM and RM are computed. For instance, for the density, this error is defined as:

$$\varepsilon_\rho = \left[\frac{\sum_{i=1}^{Nt} \sum_{j=1}^{N} \left(\rho^{RM}(x_j,t_i) - \rho^{DM}(x_j,t_i) \right)^2}{\sum_{i=1}^{Nt} \sum_{j=1}^{N} \left(\rho^{DM}(x_j,t_i) \right)^2} \right]^{0.5} \qquad (30)$$

Relative errors for some variables are summarized in Table 1 for the reduced model of order $n = 4$ (RM4).

Table 1. Errors between DM and RM4.

	ρ	u	ρe	p	T
ε(%)	7.00	3.95	6.19	10.61	7.61

5. RM VALIDATION

Once identified, RM4 is used with another input signal shown in Fig. 8.

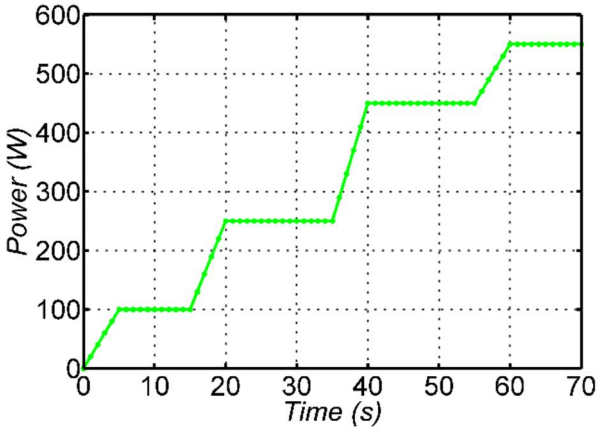


Fig. 8. Time varying thermal load at evaporator. Test function for identified RM of order 4.

The resulting computed variables are compared to the ones computed by DM for the same input signal at t=37 s.

Fig. 9 shows for instance the good agreement between density field computed by DM (red lines) and RM4 (blue lines).

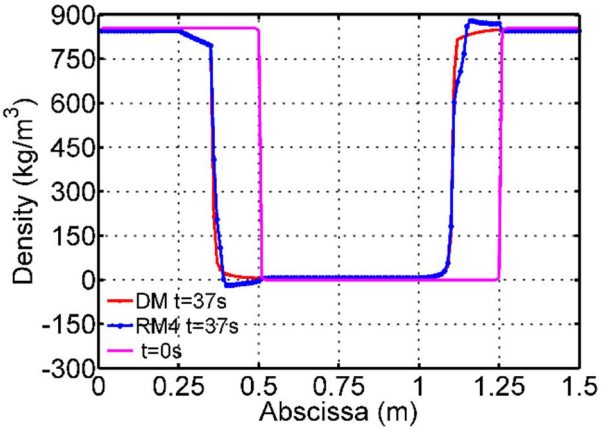


Fig. 9. Comparison of density fields by DM and RM4.

The velocity, the internal energy, the pressure and the temperature fields are respectively represented in Fig. 10, Fig. 11, Fig. 12 and Fig. 13.

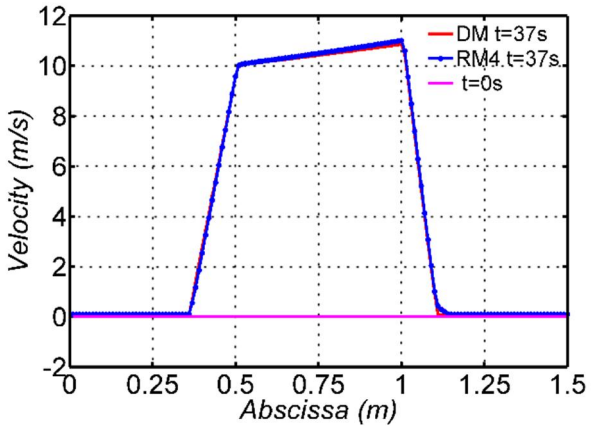


Fig. 10. Comparison of velocity fields by DM and RM4.

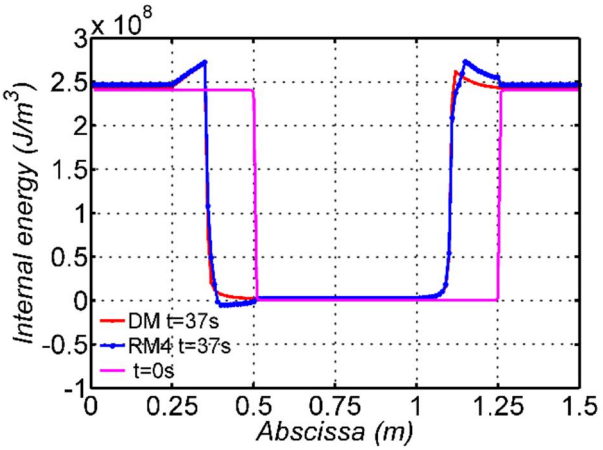


Fig. 11. Comparison of internal energy fields by DM and RM4.

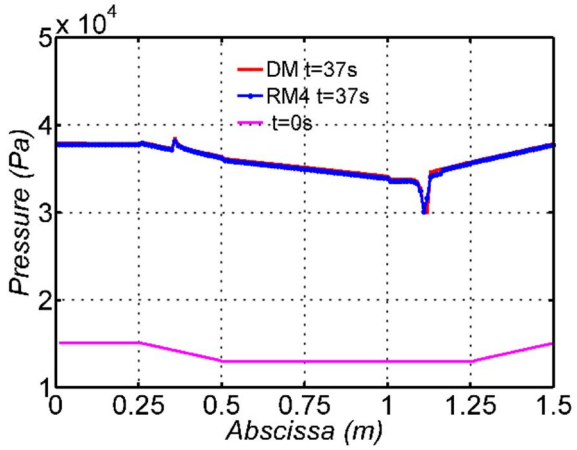


Fig. 12. Comparison of pressure fields by DM and RM4.

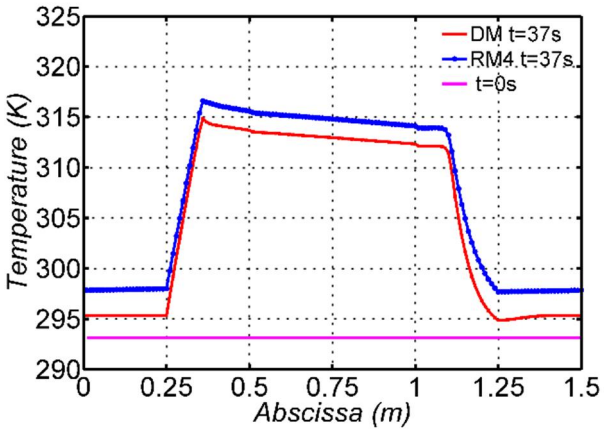


Fig. 13. Comparison of temperature fields by DM and RM4.

The results in terms of relative errors are presented in Table 2.

Table 2. Errors between DM and RM4.

	ρ	u	ρe	p	T
ε(%)	10.27	10.55	10.13	9.09	6.20

The overall behavior of the loop thermosyphon is well reproduced by RM4 in transient and steady states.

6. CONCLUSIONS

In this paper, a 2PLT model is built. The thermodynamic state laws of methanol have been approximated by the Stiffened Gas state laws. The numerical resolution is carried out using a finite volume approach with a one-dimensional space discretization of the loop and a HLLC solver. The test cases show that the overall levels of density, pressure, velocity, temperature, internal energy and vapor volume fraction change considerably when the thermal power at evaporator varies. The numerical results show that the model reproduces satisfactorily the behavior of a two-phase loop thermosyphon. Then, a reduced model of such a two-phase loop is built by the modal identification method. The validation test case shows that the reduced model is able to reproduce the detailed model behavior with a mean relative error about 10% and a computational time gain factor about 1800.

NOMENCLATURE

a : Reduced state vector for density
C_v : Specific heat capacity (J/(kg K))
D_h : Hydraulic diameter (m)
e : Mass internal energy (J/kg)
g : Standard gravity (m/s^2)
h : Heat convection coefficient (W/(m^2 K))
L : MIM parameter matrix
$\dot{m}$: Mass flow rate (kg/s)
N : Number of control volumes
Nt : Number of time steps
n : Number of basis functions
p : Pressure (Pa)
Q : MIM parameter 3rd order tensor
$\dot{Q}$: Power (W)
R : Residual
S : Surface (m^2)
t : Time (s)
T : Temperature (K)
u : Velocity (m/s)
V : MIM parameter vector
v : Specific volume (m^3/kg)
x : Abscissa (m)
y : Vapor mass fraction

Greek symbols
ε : Mean quadratic relative error
γ : Heat capacity ratio
Φ : Basis vector
μ : Dynamic viscosity (kg/(m s))
ρ : Density (kg/m^3)
Ω : Volume (m^3)

REFERENCES

[1] Long, E. L., The long thermopile, *Proc. Permafrost Int. Conf.* (1963) 487-491.
[2] Sarno, C., Tantolin, C., Hodot, R., Maydanik, Y. and Vershinin, S., Loop thermosyphon thermal management of the avionics of an in-flight entertainment system, *Applied Thermal Engineering* 51 (2013) 764-769.
[3] Samba, A., Louahlia-Gualous, H., Masson, S. L. and Nörterhaüser, D., Two-phase thermosyphon loop for cooling outdoor telecommunication equipments, *Applied Thermal Engineering* 50 (2013) 1351-1360.
[4] Li, F. L. J. and Niu, G., An insert-type two-phase closed loop thermosyphon for split-type solar water heaters, *Applied Thermal Engineering* 70 (2014) 441-450.
[5] Larkin, B. S., An experimental study of the two-phase thermosyphon tube, *CSME Trans.* 14 (1971) 1-8.
[6] Kreitlow, D. B., Reistad, G. M., Miles, C. R. and Culver, G. G., Thermosyphon models for downhole heat exchanger applications in shallow geothermal systems, *Int. J. Heat Mass Transfer* 100 (1978) 713-719.
[7] Vincent, C. J. C. and Kok, J. B. W., Investigation of the overall transient performance of the industrial two-phase closed loop thermosyphon, *Int. J. Heat Mass Transfer* 35 (1992) 1419-1426.
[8] Bieliński, H. and Mikielewicz J., Natural circulation in two phase thermosyphon loop with conventional tubes and minichannels, *Heat Transfer - Mathematical Modelling, Numerical Methods and Information Technology,* 19, 475-496.
[9] Qu, W., Hydrodynamics of two-phase loop thermosyphon, *Frontiers in Heat Pipes* 1 (2010) 1-7.
[10] Videcoq, E., Petit, D. and Piteau, A., Experimental modelling and estimation of time varying thermal sources. *International Journal of Thermal Sciences,* 42 (2003), 255-265.
[11] Girault, M., Videcoq, E. and Petit, D., Estimation of time-varying heat sources through inversion of a low order model built with the modal identification method from in-situ temperature measurements. *International Journal of Heat and Mass Transfer,* 53 (2010) 206-219.
[12] Girault, M. and Videcoq, E., Temperature regulation and tracking in a MIMO system with a mobile heat source by LQG control with a low order model, *Control Eng. Practice*, 21 (2013) 333-349.
[13] Videcoq, E., Girault, M., Bouderbala, K., Nouira, H., Salgado, J. and Petit, D., Parametric investigation of Linear Quadratic Gaussian and Model Predictive Control approaches for thermal regulation of a high precision geometric measurement machine, *Applied Thermal Engineering,* 48 (2015) 720-730.
[14] Toro, E., *Riemann solvers and numerical methods for fluid dynamics*, Springer (2009).
[15] Le Martelot, S., Saurel, R. and Le Métayer, O., Steady one-dimensional nozzle flow solutions of liquid-gas mixtures, *J. Fluid Mech.* 737 (2013) 146-175.
[16] Saurel, R., Petitpas, F. and Abgrall, R., Modelling phase transition in metastable liquids: application to cavitating and flashing flows, *J. Fluid Mech.* 607 (2008) 313-350.
[17] Le Métayer, O., Massoni, J. and Saurel, R., Elaborating equations of state of a liquid and its vapor for two-phase flow models, *International Journal of Thermal Sciences,* 43 (2004), 265-276.
[18] Girault, M., Maillet, D., Bonthoux, F., Galland, B., Martin, P., Braconnier, R. et al, Estimation of time-varying pollutant emission rates in a ventilated enclosure: inversion of a reduced model obtained by experimental application of the modal identification method. *Inverse Problems* 24 (2008).
[19] Rouizi, Y., Girault, M., Favennec, Y. and Petit, D, Model reduction by the Modal Identification Method in forced convection: application to a heated flow over a backward-facing step. *International Journal of Thermal Sciences,* 49 (2010), 1354-1368.

Loop Thermosyphon Model for Condensers with Non-condensable Gas Applied to Distillation Units

Luis H.R. Cisterna[1*], Estevan G. Tavares[1], Kênia W. Milanez[1], Tiago W. Uhlmann[1], Fernando H. Milanez[1], and Marcia B.H. Mantelli[1]

[1]*Heat Pipe Laboratory – LABTUCAL, Federal University of Santa Catarina, 88040-900, Florianopolis-SC, Brazil*

Abstract

The falling film distillation has been successfully used in different distillation processes in which binary separation of liquid mixtures is needed. A longitudinal temperature variation of the distillation tube helps to reduce the height of the plants and to improve the energy efficiency of the distillation device as well. To provide the temperature profile over the distillation tube, two-phase loop thermosyphons technology with non-condensable gases is applied. The present work has the objective of presenting a simple mathematical model to describe the condenser temperature profile of a thermosyphon with NCG. The model is identical to the constant cross section fin equation and is employed to determine the condenser temperature profile considering the thermosyphon as a solid rod. The results are compared with experimental data and with two others models. It can be concluded that the analytical proposed model is able to predict the temperature profile along the condenser wall and the thermosyphon operation characteristics.

Keywords: Analytical model; Distillation; Non-Condensable Gas; Loop Thermosyphon.

1. INTRODUCTION

In the last years, a new technology for falling film distillation at atmospheric pressure have been developed, aiming the energetic optimization inside a column and so the reduction of the equipment dimensions [1]. In this new equipment, the energy supply for the distillation is done by means of a two-phase loop thermosyphon. Actually, the falling film distillation occurs essentially in a vertical tube, where the liquid flows counter currently with the vapor generated. The thermal efficiency of the falling film distillation is essential for separation of hydrocarbons. Preliminary studies showed that a suitable and controllable temperature profile along the distillation tube wall can reduce energy waste o and column height [2, 3]. In conventional configuration of the falling film apparatus, to control the surface temperature of evaporation in a pre-determined level is a limiting factor of the process. In many cases, it was impossible to work with higher flow rates because the heating system did not keep the desired temperature.

Two-phase loop thermosyphon technology applied to the distillation column improves heat exchanges between the liquid and vapor phases, necessary in oil distillation towers. Such improvement allows energy savings, increasing separation efficiency, and more importantly, reduces distillation towers size. In order to obtain the desired temperature profile, can be obtained using Non Condensable Gases (NCG) in a two-phase loop thermosyphon where the condenser region is an annular chamber enclosing the distillation tube (Figure 1). The distillation tube is surrounded by the condenser of the thermosyphon, which supplies energy for the distillation process. In the distillation tube, the mixture to be distillated falls in a thin film over the internal surface and, therefore, absorbs part of the heat transported by the vapor. The vapor, in contact with the wall, condensates and, due to the gravity, the resulting fluid falls in the vapor chamber bottom region, returning to the evaporator. The temperature profile control throughout the length of the condenser depends on the power supplied to the evaporator, the amount of NCGs present in the thermosyphon vapor, the vapor condensation and on the mixture to be distilled. The results of this research [2] show the potential technology.

The Heat Pipe Laboratory (LABTUCAL) of the Federal University of Santa Catarina Brazil (UFSC) recently registered a patent [4] of a compact petroleum film distillation device to be used in offshore platforms, in which heat is delivered to the oil film by means of a condenser of a loop thermosyphon. To control the distilling surface

*Corresponding author: lrodriguez@labtucal.ufsc.br
Phone: +55-48-3232-2161

temperature profile, NCG (air) is inserted in the condenser of the device. Therefore, to optimize this distillation equipment, the thermal behavior of vapor and air mixtures inside this condenser must be studied and modeled.

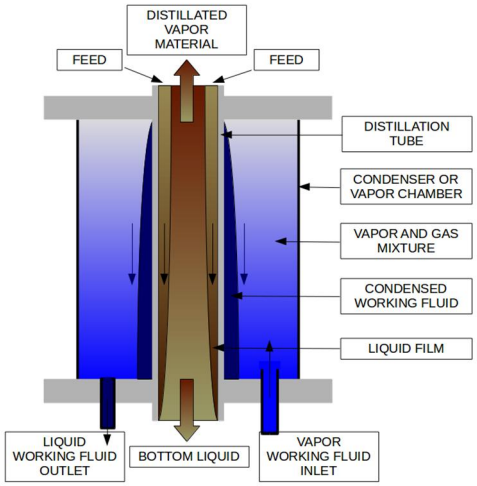


Figure 1. Falling film distillation column scheme.

Different mathematical models have been developed to describe the behavior of the heat pipes and thermosyphons with the presence of NCG, focused to design the gas-loaded variable conductance heat pipes (VCHP) project. These mathematical models are different for heat pipes or thermosyphons, although the effect generated by the presence of NCG at the condenser region in heat pipes and thermosyphons are similar, the heat transfer phenomenon by condensation is very different due to the presence of the porous medium in the heat pipes. For this reason, the models developed for heat pipes cannot be applied directly to thermosyphons [5].

The level of complexity of these models varies from simple one-dimensional models to sophisticated two-dimensional models. The simple one-dimensional flat interface model between vapor and NCG was considered for Marcus e Fleischman (apud [6]). Mass diffusion and heat in the axial direction of the tube has been considered in other more elaborated one-dimensional models [7-10]. The effects of mass and heat diffusion in the axial and radial direction of the tube has been considered in the sophisticated two-dimensional models [12-17].

Evidently, the complex models describe physics with greater precision, but increase the implementation complexity and are computational time required.

In the present work, a mathematical model for two-phase thermosyphon, in steady state conditions, with the presence of NCG was developed. Mass and heat diffusion effects in the axial direction of the thermosyphon were considered in the one-dimension model. The effect of cold tips (decrease of the heat transfer rate at the condenser tip) is also discussed.

The main works from the literature, that served as the basis for the development of the present work model are presented below.

Marcus e Fleischman, 1970 (apud [6]), developed one of the first papers on this topic, known as the flat front model. The model describes the behavior of a heat pipe, in steady state conditions, with a certain amount of NCG. Although the species diffusion in the interphase was not considered in this model, this work was taken as the foundation for the vast majority of models on heat pipes and thermosyphon with the presence of NCG.

Edwards and Marcus [7] presented a one-dimensional mathematical model to describe heat and mass transfer in condenser of heat pipes with NCG. Mass and energy balances were the basis of the present model. The governing equations have been solved by a numerical code. Experimental data shows that the proposed mathematical model predicted correctly the temperature profiles along the heat pipe wall, as well as its operating characteristics (heat rejection versus evaporator temperature). The experimental findings suggest that this model can be used as a design tool for heat pipes with NCG.

Sun and Tien [9] and Bobco [10] developed mathematical models to describe the steady state behavior of a complete heat pipe (evaporator and condenser) with NCG. In both works, some input parameters were obtained from experimental data.

In the present paper, the condenser of thermosyphons operating with NCGs is modeled considering hyperbolic function temperature profiles, inspired in fin temperature profiles, as the condenser tips of gas loaded heat pipes present thermal behaviors similar to those of common fins.

Actually, the cold tip phenomena was observed in experimental tests of sodium thermosyphons run in the Heat Pipe Laboratory. A fin thermal model was proposed to describe the condenser temperature profile, introducing the concept of effective thermal conductivity, which includes the effects of high thermal conductance due to the working fluid condensation, conduction through the tube, and external coefficients of heat transfer (convective and radiative). Similarly to [9, 10], this model requires experimental data to determine the effective thermal conductivity, and consequently, the active (not blocked with NCGs) section length.

This paper presents a simple mathematical model to describe the condenser temperature profile of a thermosyphon with NCG. The model employs an analogy with the thermal fin model to determine the temperature profile considering a thermosyphon as a solid rod. The main difference between the proposed model and the other presented in the literature is that from the design data including: mass of NCG, desired vapor temperature at the evaporator and required total heat transfer rate, it is possible to determine the temperature profile and the condenser active section length, without the need of any empirical parameter

2. ANALYTICAL MODEL

The physical model for the present work mathematical model is a thermosyphon with height L, internal diameter d_{in} and external d_{ex}, as shown in Figure 2. The thermosyphon is divided in four regions: evaporator, adiabatic section, condenser active section and condenser diffusion section. The active section has pure saturated vapor while the diffusion section contains NCG. All these regions interacts among each other. An interactive method to the couple of these regions is needed.

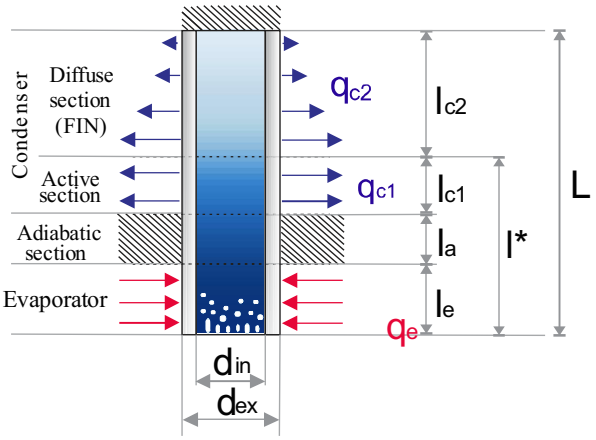


Figure 2. Physical model of a two-phase thermosyphon with NCG of the present work.

At the evaporator, the equivalent resistance circuit analogy is commonly applied to determine the total heat flux in conventional two-phase thermosyphons [18]. Figure 3 shows the scheme of the equivalent thermal resistance circuit modelling.

The heat transfer into the evaporator is given by:

$$q_e = \frac{T_{\infty e} - T_v}{R_1 + R_2 + R_3}, \qquad (1)$$

where the thermal resistances R_1 and R_2 are associated to the external convection and the wall conduction at the evaporator, respectively.

The evaporation thermal resistance (R3) can be determined by:

$$R_3 = \frac{1}{\pi d_{ex} l_e h_e} \qquad (2)$$

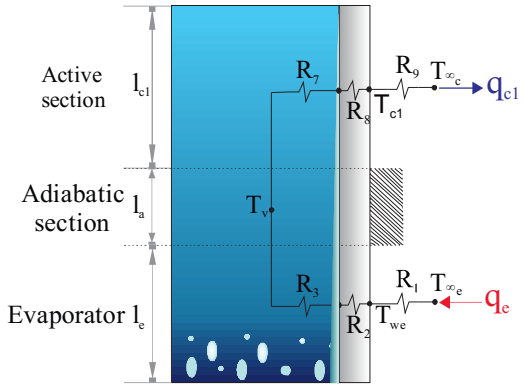


Figure 3. Thermal resistances for the evaporator and for the active condenser section.

Many literature works show different correlations to determine the internal heat transfer coefficient for the evaporator [19-24]. These studies are mainly based on experimental data because the phenomena is too complex and hard to model analytically.

At the adiabatic section, the thermosyphon wall temperature is considered equal to the working fluid vapor temperature. This consideration is valid when the thermal insulation in this section is enough to minimize the radial heat loss.

The presence of NCG is neglected at the active section of the condenser and, therefore, it is possible to predict the heat transfer using the equivalent circuit analogy. The heat transfer at the active section of the condenser is given by:

$$q_{c1} = \frac{T_v - T_{\infty c}}{R_7 + R_8 + R_9} \qquad (3)$$

where R_8 and R_9 are the thermal resistances associated to tube wall conduction and condenser external convection, respectively.

The thermal resistance of the active section of the condenser (R_7) is defined as:

$$R_7 = \frac{1}{\pi d_{ex} l_{c1} h_c} \qquad (4)$$

Mantelli et al [26] showed a comparison of several correlations presented in the literature to determine the convection heat transfer coefficients

h_c. They stated that Kaminaga et al (1997) correlation presented the best agreement with their experimental results.

The main contribution of the present work rests in the condenser heat diffusion section, where the NCG concentration gradients create a temperature gradient. This temperature field is modeled using an analogy with the heat conduction in fins. This hypothesis is not far from the real heat transfer phenomena, as evidenced by [8-10], that modelled where the temperature profile at the condenser using hyperbolic functions, the same that results from fin models.

To develop the present model, the following assumptions are made: steady state, the temperature at the bottom of the diffusion section is constant and equal to the active section wall temperature, the physical properties are constant, external wall radiation is negligible and the NCG is stationary (no natural convection). The diffusion section (condenser region occupied by the NCGs) is considered as a solid with an equivalent thermal conductivity K_{eff}, which takes into consideration the combination of working fluid condensation (of the vapor mixed with the NCGs) and the wall thermal conduction.

Figure 4 shows the scheme of the fin physical model adopted for the NCGs thermosyphon condenser section region, where q_{cond} corresponds to the heat transfer rate by the conduction through this hypothetical solid fin, which thermal conductivity is k_{eff}. Therefore, the heat conduction rate can be expressed by the Fourier's law:

$$q_{cond} = -k_{eff} S \frac{dT_{c2}}{dy}. \tag{5}$$

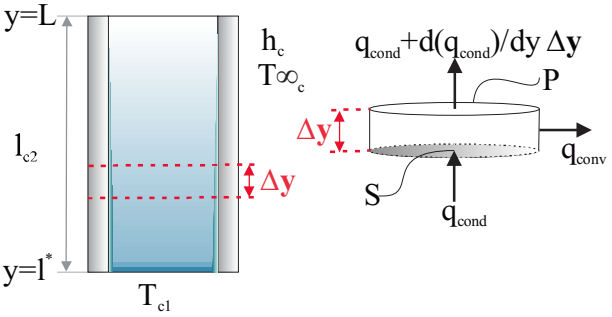


Figure 4. Fin model used to describe the diffusion model of the thermosyphon.

In this control volume, the rejected heat (q_{conv}) is given by:

$$q_{conv} = h_{\infty c}\left(T_{c2} - T_{\infty c}\right) P \Delta y, \tag{6}$$

where h_c is the external convection heat transfer coefficient.

Substituting equations (5) and (6) in the energy balance over the control volume shown in figure 4, one has the following differential equation, for the NCG region, which produces a cold tip:

$$\frac{d^2 T_{c2}}{dy^2} = \frac{h_c\left(T_{c2} - T_{\infty}\right) P}{k_{eff} S}, \tag{7}$$

which is subjected to the boundary conditions:

$$T_{c2}(y = l^*) = T_v, \tag{8a}$$

$$\left.\frac{dT_{c2}}{dy}\right|_{y=L} = 0, \tag{8b}$$

where l^* corresponds the height of the diffusion region, above which the effects of the presence of CNG starts to be observed.

Hence, the temperature profile at the wall at the diffusion region due the presence of NCG can be described by the solution of equation 7:

$$T_{c2}(y) = T_{\infty} + \left(T_v - T_{\infty}\right)\left\{\frac{\cosh\left[m\left(L - y\right)\right]}{\cosh\left[m\left(L - l^*\right)\right]}\right\}, \tag{9}$$

where the m parameter is:

$$m = \left[\frac{4h_{eq}}{k_{eff} d_{ex}}\right]^{1/2}. \tag{10}$$

If the temperature profile is known, it is possible to determine the heat transfer rate at the diffusion section, by the Fourier's law:

$$q_{c2} = -k_{eff} \left.\frac{dT}{dy}\right|_{y=l^*}. \tag{11}$$

In this way, the heat lost in the diffusion section is:

$$q_{c2} = -\pi d_{ex}^2 k_{eff} m\left(T_v - T_{\infty c}\right) \tan h\left[m\left(L - l^*\right)\right]. \tag{12}$$

By the first law of thermodynamics, the heat input at the evaporator section (equation 1) must be equal to the sum of the heat loss from the active section (equation 3) and the diffusion section

(equation 12) of the condenser, considering that the adiabatic section does not exchange heat:

$$q_e = q_{c1} + q_{c2}. \tag{13}$$

Using the thermal resistance circuit model, the temperature of the vapor inside the onset of the diffusion section (NCG region) can be given by:

$$T_{vc2}(y) = q_{conv}(y) R_8^* + T_{c2}, \tag{14}$$

where R_8^* and $q_{conv}(y)$ are the tube wall conduction resistance and the heat rejected by convection in the control volume of thickness Δy (Figure 4), respectively, with:

$$q_{conv} = -\frac{h_{\infty c} P}{m}\left(T_{c1} - T_{\infty c}\right) \frac{\sinh\left[m\left(L - y + \Delta y\right)\right] - \sinh\left[m\left(L - y\right)\right]}{\cosh\left[m\left(L - l^*\right)\right]}, \tag{15}$$

The mass of NCG inside of the thermosyphon at the diffusion section, responsible for the diffusion effect can be determined considering that the NCG behaves as an ideal gas. Considering that there is a temperature equilibrium in each cross-section of the diffusion section, namely, $T_{vc2}(y)=T_{NCG}(y)$. The NCG pressure is given by:

$$P_{NCG}(y) = P_{sat}(T_v) - P_{c2}(y), \tag{16}$$

where $P_{sat}(T)$ is the saturated working fluid vapor pressure at the operation temperature and $P_{c2}(y)$ correspond the saturation pressure of the working fluid at the diffusion section, at the temperature $T_{vc2}(y)$. Therefore, the total mass of NCG can be determined by:

$$m_{NCG} = \frac{S}{R_g}\int_{l^*}^{L}\left[\frac{P_{NCG}(y)}{T_{vc2}(y)}\right]dy. \tag{17}$$

Figure 5 shows the flowchart scheme of the iterative method used in this work. It is important to highlight that the model proposed does not need the experimental temperature profile as input parameter, but, instead, use the NCG mass, the temperature at the evaporator and the desired total heat flux as the input parameters.

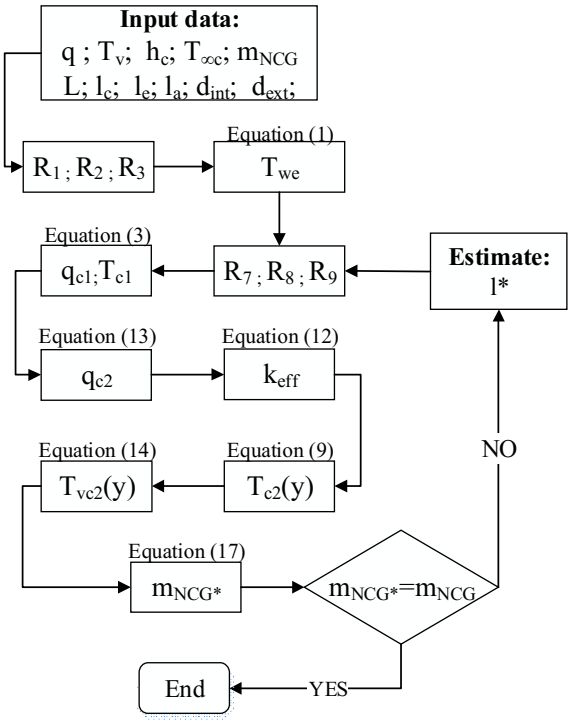


Figure 5. Model flowchart.

3. RESULTS AND DISCUSSION

3.1 Experimental data

Experimental results presented by Tavares [25] were used to validate the model proposed here. The objective of his work was to evaluate the thermal performance and the axial temperature profile of the condenser region of a NCG loaded loop thermosyphon. In those tests, a thin water film flows down by gravity through a distillation vertical tube. Dry air was used as NCG and four power input levels were tested: 150, 250, 350, and 450 W.

3.2 Comparisons between models, and experimental data

Table 1 presents the input and output data for all the cases studied. The input data are: evaporator input heat transfer rate (q_e), vapor temperature (T_v), condenser heat sink temperature ($T_{\infty c}$), condenser external heat transfer coefficient ($h_{\infty c}$) and mass of NCG (m_{NCG}). The output data are: thermosyphon maximum heat transfer rate, that is, with no NCG (q_{max}), heat transfer rate of the active (q_{c1}) and diffuse (q_{c2}) sections, effective thermal conductivity of the diffuse section, that is, considering an equivalent solid rod (k_{eff}), and total length of the active section (l^*).

From Table 1 one can observe that the effective thermal conductivity increases with the heat transfer rate.

Table 1. Analytical model input and output data.

		Case 1	Case 2	Case 3	Case 4
Input data	q_e [W]	450	350	250	150
	T_v [°C]	99.9	96.1	92.8	87.1
	$T_{\infty c}$ [°C]	64	62	62	57
	$h_{\infty c}$ [W/m^{2}K]	580.1	578.5	578.5	574.6
	m_{NCG} [g]	1.1	1.1	1.1	1.1
Output data	q_{max} [W]	693.5	653.1	589.8	572.5
	q_{c1} [W]	149.8	121.7	63.9	24.5
	q_{c2} [W]	300.2	228.2	185.9	125.6
	k_{eff} [W/mK]	1837	1155	924	444
	l^* [m]	0.23	0.20	0.12	0.05

Another important parameter under analysis is the length of the active section *l**. This parameter also increases with the heat transfer rate because of the higher vapor operation temperature, which causes an increase in the vapor saturation pressure and compresses the NCG against the top of the condenser, increasing the length of active section. Figure 6 shows this behavior. For all cases studied here, the proposed model predicts the length of the active section fairly well. Moreover, the model predicts well the temperature profile along the diffuse section of the condenser.

In order to better evaluate the performance of the proposed model, the results were compared with two other models presented in the literature. The first is the flat front model adapted to the thermosyphon studied in this paper. This model is simple and does not consider the mass diffusion effects (Marcus e Fleischmann apud [6]). The second is the wall condensation model available in a commercial software, the ANSYS-CFX [27]. This model takes the advective and diffusive effects in the axial and radial directions into account. These models were chosen because they are the most simple (flat front) and the most complex (CFD) models available in the literature.

Figure 7 shows the thermosyphon operation characteristics, i.e., the heat transfer rate through the condenser versus evaporator temperature. One can observe that, as expected, not only the rejected heat transfer rates obtained by the proposed model are always closer to the experimental data than the flat front model results, but also the condenser temperature profile of the proposed model represents the physical phenomena better than the flat front model (Fig. 8). One can see that the results from the model proposed here and the numerical simulations are practically the same. However, the complexity of the numerical model makes the necessary computational time to reach the solution to be much larger than the present model.

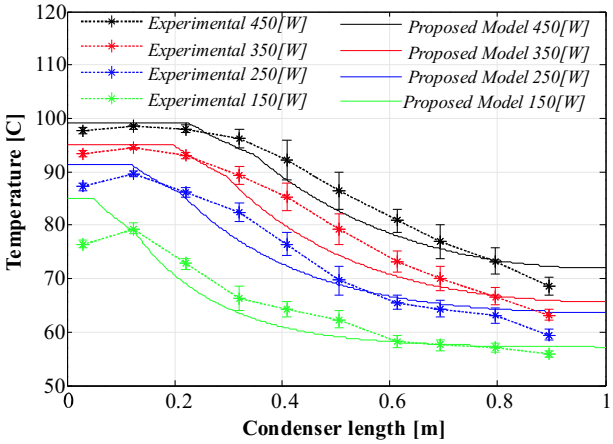


Figure 6. Comparison between experimental data and condenser temperature profiles calculated by the proposed model for all studied cases.

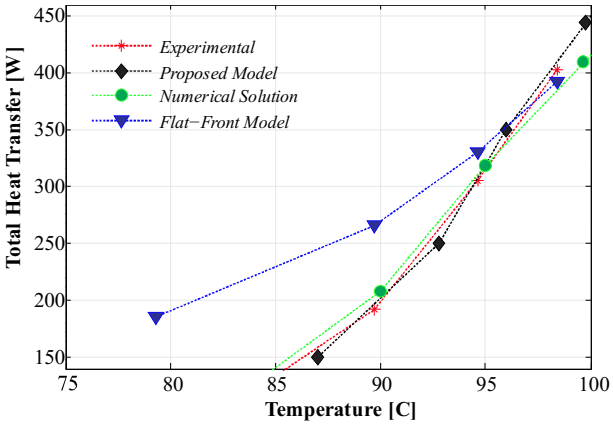


Figure 7. Comparison between the different models results and the thermosyphon characteristics of operation.

Table 2 presents the average deviation of the models (present, numerical and flat-front) from the experimental data shown in Figure 7. The proposed model presented the lowest average deviation, of 0.37%.

Table 2. Average deviation of studied models from experimental data.

	Proposed Model	Numerical Simulation	Flat-Front Model
Average	0.37%	0.75%	4.08%

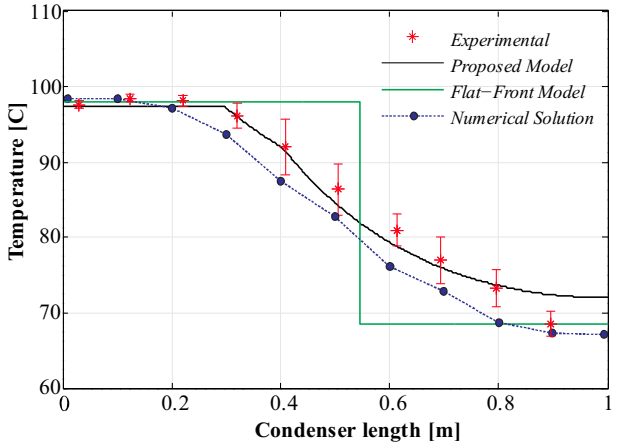


Figure 8. Comparison between the condenser temperature profiles of the distillation unit for an input heat transfer rate of 450 W.

Figure 9 presents the condenser temperature profile obtained from the numerical simulation of the distillation unit for an input heat transfer rate of 450 W.

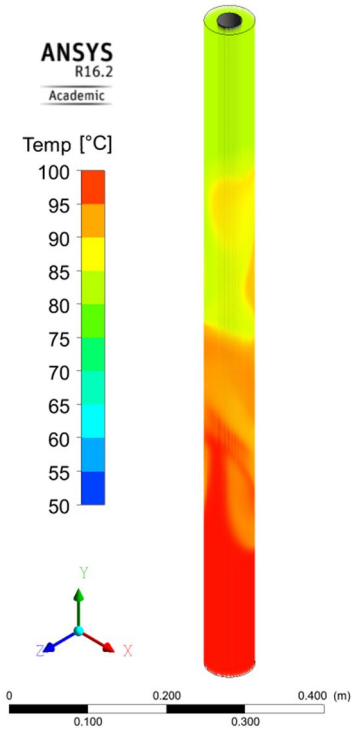


Figure 9. Distillation unit condenser temperature profile obtained from numerical simulation.

From Figure 9, one can observe that there is a portion of the condenser with temperature close to the adiabatic section, which is not affected by the presence of NCG. Therefore, this active section exists and can be modeled using conventional thermosyphon condenser models. Also, it is observed that the heat transfer phenomena is not purely diffusive and one-dimensional. The temperature distribution along the condenser presents three-dimensional vortexes that are common in advective heat transfer processes. However, the proposed one-dimensional, purely diffusive analytical model represents well the physical phenomena that is observed in the experimental results and in the numerical simulation, which considers three-dimensional advective and diffusive models.

6. CONCLUSIONS

In the present paper, a model was proposed to describe the thermal behavior of the condenser section of thermosyphons with NCGs. The condenser is divided into two regions: the active, under the influence of the working fluid in its vapor phase (which can be modelled using usual actual literature models) and the region under the influence of NCGs, which is modelled as a solid fin with an effective thermal conductivity keff. Through comparisons of the proposed model with experimental data and two other models presented in the literature, it was concluded that the proposed analytical model predicted the temperature profile along the condenser wall and the thermosyphon operation characteristics (rejected heat transfer rate through the condenser versus evaporator temperature) correctly. Thus, the utilization of the proposed model is suggested as a design tool for thermosyphons with NCG and specifically in the application of thermosyphons in distillation units.

ACKNOWLEDGEMENT

The authors would like to acknowledge the financial support from CENPES/PETROBRAS and CNPq in the development of this work.

NOMENCLATURE

d	Tube diameter (m)
l	Length (m)
l^*	Total length of active section (m) $l^*=L-l_{c2}$
L	Total thermosyphon length (m)
R	Equivalent thermal resistance (K/W)
q	Heat transfer rate (W)
T	Temperature (°C)
h	Coefficient of heat transfer (W/m^2K)
S	Transversal section tube area (m^2)
P	Perimeter of external tube (m)
k_{eff}	Effective thermal conductivity (W/mK)
P_{NCG}	NCG partial pressure (Pa)
P_{sat}	Vapor saturation pressure in the adiabatic section (Pa)
P_{c2}	Vapor partial pressure in the diffusive section (Pa)
m_{NCG}	Mass of NCG (g)

Subscripts

in	Inner
ex	Outer
e	Evaporator
a	Adiabatic
c1	Active section
c2	Diffuse section
∞e	External to evaporator
∞c	External to condenser
v	Vapor
vc1	Vapor in the active section
vc2	Vapor in the diffuse section
max	Maximum – if there were no NCG

REFERENCES

[1] Jana, A. K., Heat integrated distillation operation, *Applied Energy*, 87 (2010) 1477-1494.

[2] Tavares, E. G., Milanez, K. W., Mantelli, M. B. H., Santos, M. C., Gomes, A. O. and Medina, L.C., Vapor chamber with non-condensable gas applied to film distillation, *Proc. of 15th International Heat Pipe Conference*, Clemson, USA (2010).

[3] Tavares, E. G., Milanez, K. W., Milanez, F.H. and Mantelli, M.B.H., Thermal analisys of a diffusion model applied for a gas-loaded vapor chamber condenser. *Proc. of 16th International Heat Pipe Conference*, Lyon, France (2012).

[4] Oliveira, L. C. M., Santos, M. C., Machado, R. A. F., Mantelli, M. B. H., Marangoni, C., Milanez, K. W., Meneguelo, A. P., Equipamento e processo de destilação com controle de energia pela demanda, Brazil. Patent: BR1020140297, INPI (2014).

[5] Mantelli, M. B. H., Ângelo, W. B. and Borges T., Performance of naphthalene thermosyphons with non-condensable gases – Theoretical study and comparison with data, *International Journal if Heat and Mass Transfer*, 53 (2010) 3414–3428.

[6] Faghri, A., Heat pipe science and technology, Taylor & Francis, (1995).

[7] Edwards, D. and Marcus, B., Heat and mass transfer in the vicinity of the vapor-gas front in a gas-loaded heat pipe, *Journal of Heat Transfer*, 92 (2) (1972) 155-162.

[8] Shukla, K. N., Transient response of a gas-controlled heat Pipe, *AIAII Journal*, 19 (8) (1981) 1063-1070.

[9] K. H. Sun and C. L. Tien, Thermal Performance Characteristics of Heat Pipe, *Int. Heat Mass Transfer*, 18 (1974) 363-380.

[10] Bobco R. P., Variable conductance heat pipe: a first-order model, *Proc. Of AIAA 20th Thermophysics Conference*, Williamsburg, VA, USA (1985).

[11] Cunha, A. F. V., Análise de termossifões que operam a alta temperatura, D.Sc. Thesis, Federal University of Santa Catarina, Florianópolis, SC, Brazil (2008).

[12] Harley, C. and Faghri, A., Transient two-dimensional gas-loaded heat pipe analysis, *ASME J. Heat Transfer,* 116 (3) (1994) 716-723.

[13] Hijikata, K., Chen, S .J. and Tien, C. L., Non-condensable gas effect on condensation in a two-phase closed thermosyphon, *Int. J. Heat Mass Transfer*, 27 (8) (1984) 1319-1325.

[14] Peterson, P. F. and Tien, C. L., Numerical and analytical solutions for two-dimensional gas distribution in gas-loaded heat pipe, *ASME J. Heat Transfer*, 111 (3) (1989) 598-604.

[15] Peterson, P. F. and Tien, C. L., Mixed double-diffusive convection in gas-loaded heat pipe, *ASME J. Heat Transfer,* 111 (1990) 78-83.

[16] Rohani, A. R. and Tien, C. L., Steady two-dimensional heat and mass transfer in the vapor-gas region of a gas-loaded heat pipe, *ASME J. Heat Transfer*, 95 (1973) 377-382.

[17] Zhou, X. and Collins, R. R., Condensation in a gas-loaded thermosiphon, *Int. J. Heat Mass Transfer*, 38 (9) (1995) 1605-1617.

[18] Mantelli, M. B. H., Thermosyphon technology for industrial applications: Heat Pipes and Solid Sorption Transformations. Vasiliev L.L., Kakaç S., CRC Press, Boca Raton, (2013) 411-464.

[19] Imura, H., Yoshida, M. and Ippohshi, S., The visual observation of the flow patterns in two-phase single- and – double- tube thermosyphon, *Proc. of 8th International Heat Pipe Conference*, Beijing, China (1992).

[20] Shiraishi, M., Kikuchi, K. and Yamonishi, T., Investigation of heat transfer characteristics of a two-phase closed thermosyphon, *Proc. of 4th International Heat Pipe Conference*, London, UK (1981).

[21] Chowdhury, F. M., Kaminaga, F., Goto, K. and Matsumura, K., Boiling heat transfer in a small diameter tube below atmospheric pressure on a natural circulation condition, *Journal of Japan Association for Heat Pipe*, 16 (1997) 14–16.

[22] Labuntsov, D. A., Heat transfer problems with nucleate boiling of liquids, *Thermal Engineering*, 19 (1972) 21-28.

[23] Kruzhilin, G. N., Free-convection transfer of heat from a horizontal plate and boiling liquid, *Doklady Akademii Nauk SSSR*, 58 (1947) 1657-1660.

[24] Kutateladse, S. S., Heat Transfer in Condensation and Boiling, *AEC-tr-3770*, 129 (1959).

[25] Tavares, E.G. Análise térmica de uma câmara de vapor com vistas a aplicação em unidades de destilação. *MSc. Dissertation*, Federal University of Santa Catarina, Florianópolis, SC, Brazil (2010).

[26] Mantelli, M. B. H., Carvalho, R. D. M., Colle, S. and Moraes, D. U. C., Study of closed two-phase thermosyphons for bakery oven applications, *Proc. Of 33rd National Heat Transfer Conference,* Albuquerque, New Mexico, USA (1999).

[27] CFX-Solver Theory Guide Release 14.0. *ANSYS Inc.*, 2011.

Theoretical and Experimental Analysis of an Herbs Dryer Assisted by Two-phase Thermosyphons

Luis H.R. Cisterna[1*], Diogo M.M. Caldas[1], , Fernando H. Milanez[1] and , Marcia B.H. Mantelli[1]

[1]*Heat Pipe Laboratory – LABTUCAL, Mechanical Engineering Department, Federal University of Santa Catarina, Campus Universitário Trindade, 88040-900, Florianopolis-SC, Brazil*

Abstract

The main goal of this work is to evaluate the thermal performance of a medicinal herb dryer assisted by two-phase thermosyphon technology. A medicinal herb dryer, assisted by thermosyphons in tree configuration, was developed at the LABTUCAL (Heat Pipe Laboratory) at UFSC (Federal University of Santa Catarina, Brazil). In this new dryer concept, the air heating occurs directly inside of the drying chamber, resulting in a highly homogeneous temperature distribution inside the drying chamber. A simplified mathematical model employing the analogy between thermal and electrical circuits was applied to represent the physical behavior of the tree thermosyphons. The influence of the mixer speed on the total energy consumption per unit of water mass evaporated was analyzed, as well as the drying air temperature and humidity distributions. The results show that the developed dryer is able to guarantee a high homogeneity of temperature and relative humidity of the drying air inside the chamber. As a result, the dried herb has superior quality when compared with other commercially available dryers.

Keywords: Thermosyphon, heat and mass transfer, dryer, medicinal herbs

1. INTRODUCTION

In herb drying process, the consumption of energy is directly related to the time that the herb remains in the drying chamber. As the major part of this energy is used to convert water contained in the leaves to vapor, better dryers can be designed if the main parameters influencing the drying process are identified. Long times and low temperatures levels are associated with medicinal herb drying processes. In Brazil, the applied medicinal herb drying procedures are still very precarious showing lack of technology. Usually, firewood is used as fuel in most of drying process due to its availability and low cost. However, firewood drying processes presents many problems, such as: poor energetic efficiency, contamination of the herb with the combustion gases (which are in direct contact with the herb), non uniform drying, lack of temperature control, lack of hot gases flow control. On the other hand, the use of a thermosyphon technology heat exchanger associated with gas burner, allows for the rational and efficient use of fuel. It provides a clean herb drying process, when the main heat source is burning wood or gas, as thermosyphons are able to transport only heat to the drying chamber leaving the burning gases in the combustion chamber. Also, this technology allows for a much better control of: the applied thermal power, heated air flow distribution and drying temperature level.

Actually, drying is the main method used to preserve the active principles (essential oils) of medicinal herbs. However, fast drying process may cause degradation of the active ingredients, while slow drying process may cause the emergence of undesirable microorganisms. Many authors have already studied the importance of temperature and relative humidity in medicinal herbs drying [1, 2, 3, 4, and 5].

The energy necessary for drying solids can be provided by means of convection heat transfer, where sensible heat is transferred to the material through a drying agent (preheated air), which flows over the solid to be dried, evaporating moisture and carrying out the formed vapor. Recirculation of the drying air can be employed in order to increase the thermal efficiency and provide energy savings. The drying conditions can be controlled by temperature and humidity of the heated air [6]. Several studies involving convective drying are found in the literature. Kiranouidis [7] proposed a mathematical model to predict a conveyor dryer operating parameters, where each drying chamber has an individual heating unit and a fan for circulating the air through the product. This scheme also presents a chamber for mixing

*Corresponding author: lrodriguez@labtucal.ufsc.br
Phone: +55-48-3232-2161

ambient air and process air, in order to control the conditions of relative humidity of the air and save energy. Holowaty (2012)[8] proposed a mathematical model that simulates the behavior of a convective dryer, where the drying air flows through the product with known values of relative humidity and temperature, evaporating moisture and carrying it out of the dryer. Due to the mass and heat exchange processes, the drying air loses its quality by increasing its humidity. That is why the use of several layers of conveyors, one above the other, is avoided.

Regarding the utilization of thermosyphon technology applied to stoves and dryers, Silva and Mantelli [9] evaluated the use of thermosyphons to transport efficiently heat from the combustion chamber to a cooking chamber of a stove, during the process of bread baking. These authors developed a theoretical model to predict the transient temperature distribution inside the cooking chamber of a thermosyphon assisted stove prototype. The results showed a high uniformity of temperature inside the cooking chamber. Later, Mantelli et al. [10,11] continued this study, applying tree configuration thermosyphon technology in bread baking ovens. Highly uniform temperature distribution cooking chamber were obtained and the bread produced showed very good quality. Energy savings of approximately 50%, when compared to commercial gas stoves, were observed. Parametthanuwat et al. [12] studied thermosyphon applications on the smoking process of fish sausage. These authors observed that the thermosyphon technology improves the temperature distribution inside the chamber, decreasing total process time.

This work presents a concept of a new dryer, assisted by thermosyphon technology. The thermosyphons are designed to conduct efficiently heat from a combustion chamber directly to the process air inside the drying chamber, which presents a highly homogeneous temperature distribution. The thermal behavior of the resulting equipment is fully investigated.

2. DRYER PROTOTYPE

A medicinal herb dryer assisted by two-phase thermosyphons, was developed in LABTUCAL (Heat Pipes Laboratory) at UFSC (Federal University of Santa Catarina, Brazil) and it is presented in Figure 1. In this new dryer concept, the heating of the process air happens directly inside the drying chamber, resulting in a highly homogeneous chamber temperature distribution, as mentioned before. A simplified diagram of the dryer can be seen on the Figure 2. In this configuration, the drying air that circulates around the chamber is entirely turbulent and flows in different directions due to the mixer (flat blade disk turbine, located on the vertical wall, opposite to the oven door). The temperature distribution inside the drying chamber is highly homogenous as shown by Mantelli et al.[10].



Figure 1. Herbs dryer assisted by thermosyphon

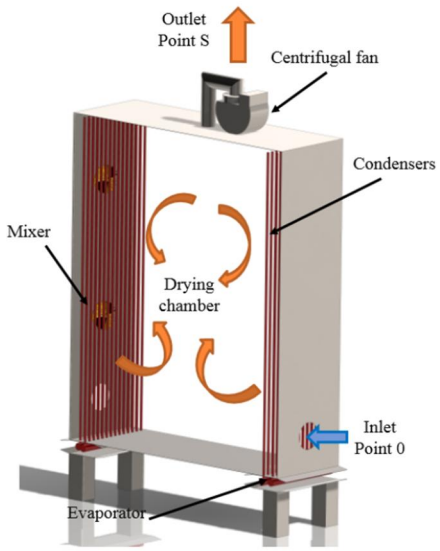


Figure 2. Schematic diagram to the dryer assisted by thermosyphons.

Part of the energy of the hot drying air surrounding the medicinal herbs is used to start the water diffusive process inside the herb leaves. As the water arrives at the leaf surface, it evaporates. As a result, the drying air temperature decreases and the drying chamber relative humidity increases. Heat is delivered to the drying chamber by means of the tree configuration thermosyphon condensers, which consists of vertical tubes located near the

oven vertical lateral walls. Therefore, by keeping the combustive burning conditions stable, the air temperature remains constant during all the process.

In order to keep optimum relative humidity air conditions, it is necessary renew a fraction of the drying air. Thus, air in atmospheric conditions is ventilated to the chamber through a centrifugal fan. The air jet entering the chamber is directed to the center of the mixer, allowing a rapid mixture with the inside drying chamber air, resulting in an air which relative humidity distribution is uniform along the drying chamber.

Figure 3 shows the two two-phase thermosyphons in tree configuration used in the prototype studied. They are composed by one horizontal evaporator tube, with 45 mm of diameter, 800 mm of length and 9 vertical condensers with 27 mm diameter and 755 mm of height. The power input is provided by burners (of natural gas or liquefied petroleum gas - LPG) which are located underneath each evaporator. A metal plate separates the combustion and the drying chambers, avoiding the contact between the combustion gases and the drying air.

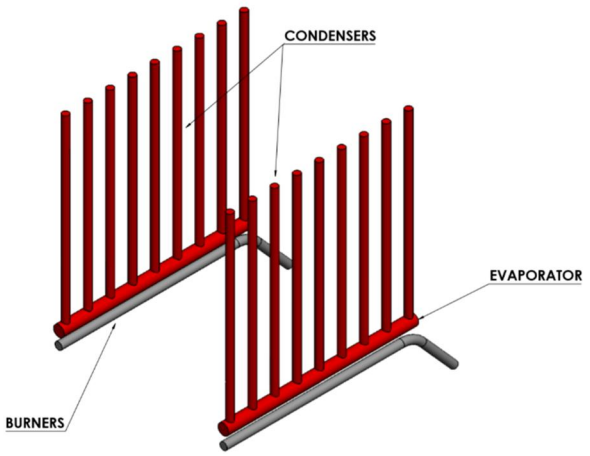


Figure 3. Schematic of the tree thermosyphon

In order to get an efficient hot air mixture, the mixer velocity must be high enough to blow the air, which occupies quickly all the chamber. In other words, the velocity of the air leaving the mixer should be large enough to reach all over the chamber volume, including the thermosyphon condensers. It is well known that the turbulence is an efficient heat transfer process. According to McCabe et al. [13] Reynold numbers larger than 10^4, indicate fluid flow turbulence.

In this work, the Reynold number was defined as:

$$\mathrm{Re}_{D_a} = \frac{nD_a^2\rho}{\mu}, \qquad (1)$$

where n is the rotational speed, D_a corresponds to the total diameter of the mixer (380mm), ρ is the fluid density and μ the dynamic viscosity.

Figure 4 shows the Reynolds number as a function to the mixer frequency. For all the analyzed cases, the Reynolds number is larger than 10^4, which indicates that the dried air is completely turbulent all over the chamber. In other words, the process of air mixture is efficient.

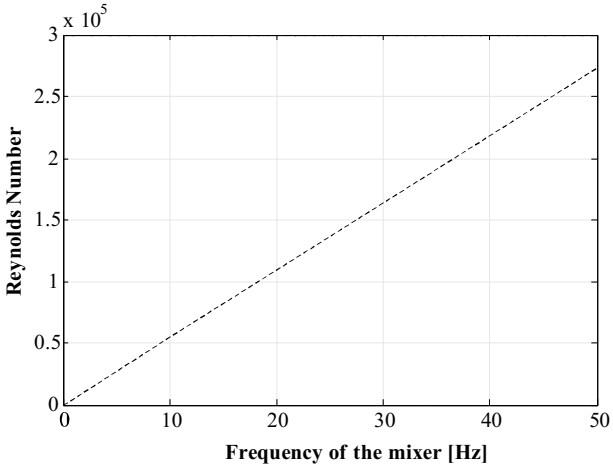


Figure 4. Reynolds number for different frequency of the mixer.

3. THEORETICAL ANALYSIS

Mass and energy balances were performed for the control volume encompassing all the drying chamber. It was considered that the total mass inside the chamber does not change with time and that the vapor mass fraction of water in the air is uniformly spread along the drying chamber. These hypotheses were verified by experiments, as it will be presented later.

From the mass balance, it is possible to obtain the vapor mass fraction time variation in the drying chamber:

$$X_c(t) = X_v + \left(X_c^0 - X_v\right)e^{-X_{air}(t)}, \qquad (2)$$

Where X_c^0 is the initial mass fraction of vapor in the drying chamber and X_v e $X_{air}(t)$ are defined as:

$$X_v = \left(\frac{\dot{m}_0 X_0 + \dot{m}_v}{\dot{m}_0 + \dot{m}_v}\right), \quad X_{air}(t) = \left(\frac{\dot{m}_0 + \dot{m}_v}{M_{air}}t\right), \qquad (3)$$

where, $\dot{m}_0$, $\dot{m}_v$ e $\dot{m}_s$ are respectively the mass flow rate of renovation air, the vapor release rate in the chamber due to drying, and the air mass flow

leaving the system. M_{air} is the air total mass in the drying chamber, and X_0 is the ambient air water mass fraction, defined as:

$$X = \frac{M_v}{M_{air}} = \frac{\omega}{1+\omega}, \quad (4)$$

where M_v is the vapor mass, and ω is the air absolute humidity .

The thermal power consumption during the drying process is obtained by:

$$q_t(t) = \frac{1}{2}\left\{\begin{matrix}\dot{m}_v\left[\left(1-X_c(t)\right)h_c + h_{lv}\right] + \\ \dot{m}_0\left[\left(1-X_c(t)\right)h_c - \left(1-X_0\right)h_0\right]\end{matrix}\right\}, \quad (5)$$

where, h_c e h_0 are respectively the specific enthalpies of the air inside the chamber and ambient air and h_{lv} is the water phase change enthalpy .

The analogy between electrical and thermal circuits [14, 15] was applied to model the steady state operation of the tree termosyphon. Figure 5 shows a schematic of the equivalent thermal circuit adopted in this work, which corresponds to a simplification model of the scheme presented by [14].

The thermal resistances showed in Figure 5 are defined as following: R9 is related to external heat transfer (in this work, the correlation of Churchill e Bernstein, apud [16], was used for the heat transfer coefficient around a circular cylinder); R2 and R8 are related to the heat conduction through the tube wall in the axial direction (evaporator and condenser regions); R3 is related to liquid evaporation and R7 is related to vapor condensation inside tube walls. In this work, the thermal resistances R3 and R7 were determined using the correlations presented by Groll and Rosler [14].

The temperatures of the: evaporator wall (T_{we}), condenser (T_{wc}), vapor (T_v) and the total heat transfer rate (q_t) can be determined by the following equations, obtained through the Figure 4 equivalent thermal circuit.

$$T_{we}(t) = T_v + q_t(t)\left(R_2 + R_3\right) \quad (6)$$

$$T_{wc}(t) = T_v - \frac{q_t(t)}{n_c}\left(R_7 + R_8\right) \quad (7)$$

$$q_c(t) = \frac{n_c\left(T_v - T_{wc}(t)\right)}{R_7 + R_8 + n_c R_9} \quad (8)$$

$$T_v(t) = \frac{\left(R_7 + R_8 + n_c R_9\right)T_{wc}(t) + n_c\left(R_2 + R_3\right)T_c}{n_c\left(R_2 + R_3 + R_9\right) + R_7 + R_8} \quad (9)$$

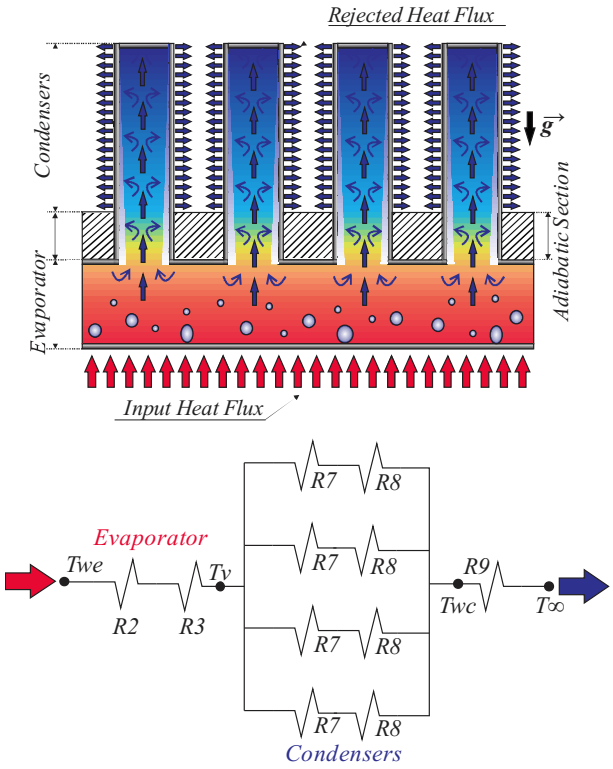


Figure 5. Equivalent thermal circuit adopted in this work

A computational algorithm was developed, using the commercial software Matlab®, to solve by means of an iterative process, the equivalent resistance model, which predicts the thermal behavior of the tree configuration thermosyphons.

4. METHODOLOGY AND RESULTS

Experiments with three different objectives were performed: to validate the analytical models, to study the mixer effect over the temperature distribution and over the relative humidity of the air, and to evaluate the dryer performance by drying the common medicinal mint Mentha x Villosa Huds.

4.1 Analytical model validation

Experiments were performed for the validation of the mathematical models proposed. The drying chamber temperature was maintained at approximately 80°C and the mass flow rate of the renewal air was kept constant at 0.00218±0.0004

kg/s. The Reynolds number inside the drying chamber is kept $1.6x10^5$. To measure the mass flow rate, it was used two trays with approximately 1 liter of water each were used. The water mass of each tray was measured every 10 minutes since the beginning of the experiment. The vapor mass flow rate in each measurement was determined through the following equation:

$$\dot{m}_v = \frac{M^0_{water} - M^f_{water}}{\Delta t}, \quad (10)$$

where M^0_{water} and M^f_{water} are the initial and final mass of the water trays at each time interval of Δt.

Figure 6 shows water mass fraction variation as a function of time inside drying chamber. The water mass fraction was obtained by the equation (4), in which the air absolute humidity value "ω" was obtained experimentally through a humidity sensor. Experimental results present periodic oscillations around the analytical result. It can be observed that the oscillatory behavior happens at every 10 minutes, which corresponds to the moment the dryer door was opened to measure the water mass in the trays.

During the period the door stayed opened, ambient air was introduced in drying chamber and the mixer acted as an air renewal system making the vapor mass in the chamber to decrease. Once the door was closed, as the water tray keeps releasing vapor, the mass fraction of vapor inside the chamber increases until the equilibrium with the renewed air is reached again.

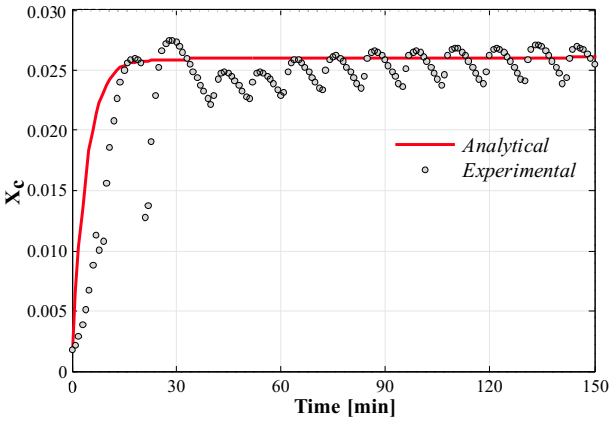


Figure 6. Behavior of evaporation mass inside the dryer chamber

This oscillation effect can also be observed with the thermosyphon temperature. The dryer chamber has a sensor connected to the gas burner responsible to keep the temperature constant during the process (in this case 80°C). Every time the dryer door was opened, the environment air (with lower temperature than the drying air) entered the chamber and mixed with the drying air. To return to the temperature level set, more fuel is released, raising the temperature of the thermosyphon, as showed on Figures 7 and 8. It can observed in these figures that the simplified mathematical model used to predict the wall temperatures of the evaporators and condensers was able to represent the physical behavior of the thermosyphons.

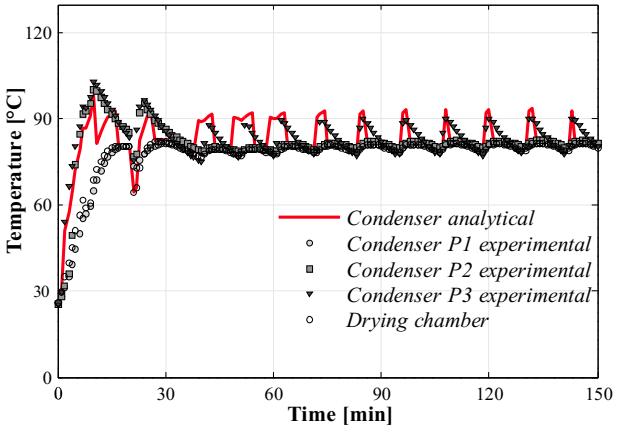


Figure 7. Behavior of the condenser temperature during the drying process (P1, P1, and P3 corresponds respectively to the to the top, middle, and base of the condenser)

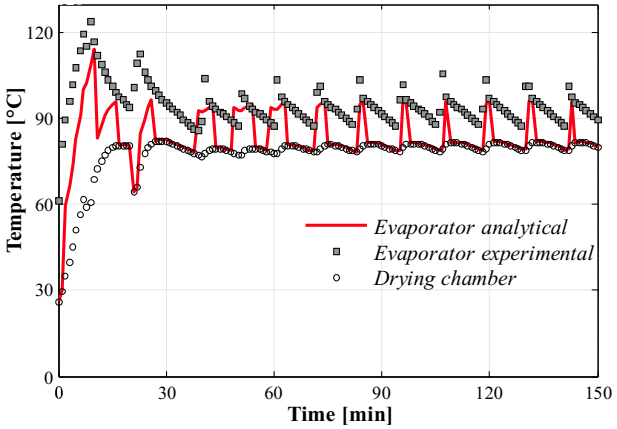


Figure 8. Behavior of the evaporator temperature during the drying process

4.2 Study of the effect of mixer

The objective of this experiment was to study the effect of the mixer on the temperature distribution and on the relative humidity of the dryer air, as well as to determine the influence of the Reynold number in the vapor generation released by the drying product.

Small square sponges of 45 mm with thickness

of 3mm, shown in Figure 9, were used. The sponges were soaked with water to simulate the herb behavior. For each test, it was used the same mass of sponges, and mass of water.

The dryer chamber temperature was kept at approximately 55°C and the mass flow rate of the renewal air was kept constant at 0.00218±0.0004 kg/s. Reynold numbers between $0< Re<2.7x10^5$ were observed inside the drying chamber. The temperatures and the relative humidities of the air at 27 points in the interior of the dryer chamber were monitored (see Figure 10). The measurement points were distributed in 3 wire frame installed on the base, middle, and top of the camera. Each tray has 9 temperature and 9 relative humidity sensors.



Figure 9. Sponges used during the dryer tests.

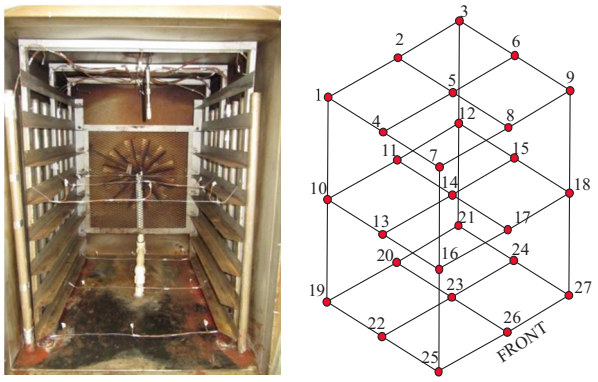


Figure 10. Distribution of the 27 points in the interior of the dryer chamber.

Figure 11 shows the mass flow rate of the total vapor released by the sponges for each Reynold numbers analyzed. It can be observed that the vapor mass flow rate has a close to linear behavior, proportional to the increase of the Reynold number.

The increase of the vapor mass flow rate can also be observed in the Figure 12. This figure shows the 27 measurement points inside of the dryer chamber. For larger Reynolds numbers, the registered values of relative humidity were larger, as, in all the cases, the renewal air mass flow rate was kept constant. Also, it is observed that, regardless the Reynolds number, the dryer always kept the relative humidity very homogeneous inside the dryer chamber.

Figure 13 shows the dryer air temperatures. It can be observed that when the mixer is not working (Re=0), temperature differences up to 12°C within the drying chamber are observed. After the mixer is turned on, regardless of the Reynolds number, the dryer always presents homogeneous temperature distribution.

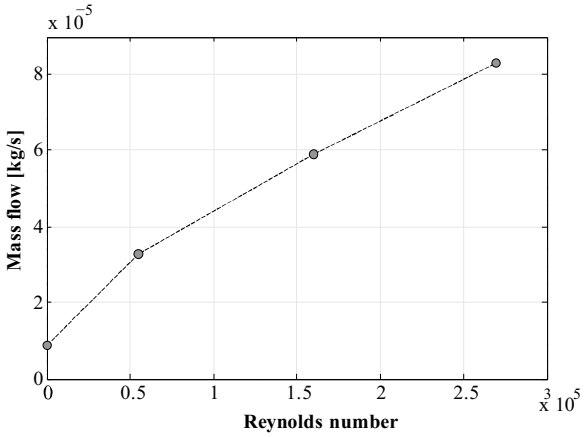


Figure 11. Total vapor mass flow rate released by the sponges for different motor frequencies

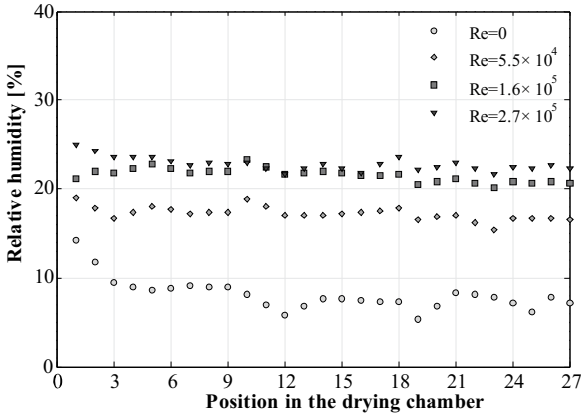


Figure 12. Air relative humidity at the 27 measurement points in the interior of the dryer chamber

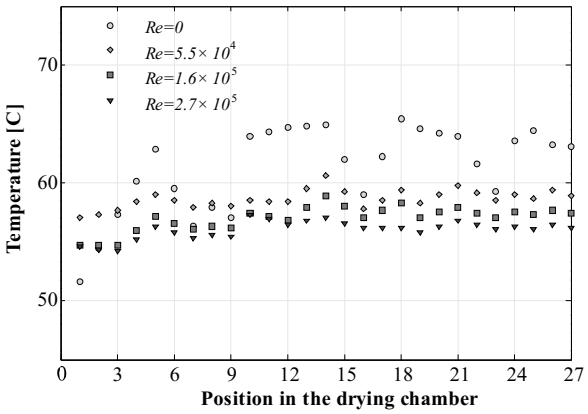


Figure 13. Air temperature at the 27 measurement points in the interior of the dryer chamber

In order to study the energy consumption of the dryer, a plot of the heat power (thermal energy), of the electrical and of the total energy per kg of vapor released in the drying chamber, as a function of the Reynolds number, is shown in Figure 14. One can observe that the largest energy consumption of the dryer occurs when the Reynold number is $2.7x10^5$. The energy consumption does not varies significantly between $5.5x10^4 < Re < 1.6x10^5$.

From this study, it can be concluded that the best dryer performance is found between $5.5x10^4 < Re < 1.6x10^5$. Therefore, the final decision of the best mixer velocity depends on the costs associated with electrical and thermal energies. The option Re=0 (the mixer is not working) is not good because the non-homogenous conditions deteriorate the medicinal herb quality.

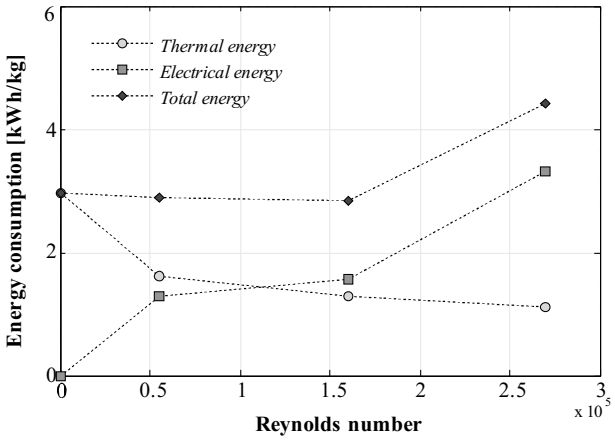


Figure 14. Thermal, electrical and total energy consumption

4.3 Medicinal herb drying

Finally the performance of the dryer was tested while drying a medicinal mint herb (*Mentha x Villosa Huds*). The temperature of the drying chamber was kept approximately constant at 55°C, and the renewal air mass flow rate was maintained constant at 0.00218±0.0004 kg/s. The Reynold number inside the drying chamber was kept at $1.6x10^5$. The mass to surface area ratio of the herb "*in natura*" over the tray was 2.5 kg/m^2. Figure 15, shows the temperature (15a), and the relative humidity (15.b) distributions of the air inside the drying chamber during the process. It can be observed that both the distributions are very homogeneous. These two characteristics lead to a uniform drying process, i.e., the herb dryed has practically the same characteristics everywhere inside the chamber. This feature is the biggest advantage of this dryer in comparison to other equipment available commercially. Figure 16 shows medicinal mint herb (*Mentha x Villosa Huds*) samples before and after drying using the developed dryer. It was observed that independently of the tray position of the herb in the dryer, the final product have the same characteristics of humidity, color and smell.

a)

b)

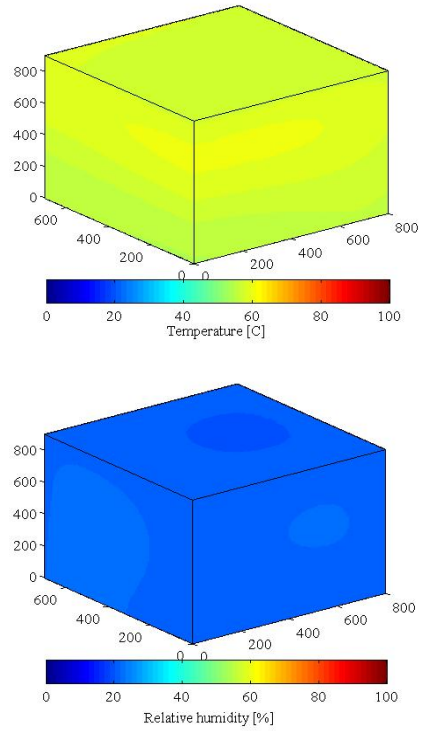


Figure 15. Temperature (a) and relative humidity (b) distributions durying drying



Fig. 16. Medicinal mint herb of (*Mentha x Villosa Huds*) before and after drying

6. CONCLUSIONS

From the results obtained from the analytical and experimental methods, several conclusions can be achieved, as follows.

The vapor mass flow rate model and the simplified mathematical model (used to predict the thermosyphon wall temperature) can represent well the physical behavior of vapor mass fraction and of

the thermosyphon temperatures.

The energy consumption per vapor mass released is minimum between $5.5x10^4 < Re < 1.6x10^5$. The decision of the best Reynolds number in the drying chamber depends on the costs associated with electrical and thermal energies.

When the mixer is turned off (Re=0) peaks of temperatures at discrete points inside the chamber can be large and these non-uniform temperatures may deteriorate the medicinal herb.

The developed dryer is able to guarantee a high homogeneity of temperature and relative humidity of the drying air inside the chamber. As a result, the dried herb has superior quality when compared with other commercially available dryers.

NOMENCLATURE

$X_c(t)$: Vapor mass fraction variation
X_c^0 : Initial mass fraction of vapor water
$\dot{m}_0$: Mass flow rate of air renovation,
$\dot{m}_v$: Mass flow rate of vapor released in the chamber due to drying process
$\dot{m}_s$: Mass flow rate of air leaving the system,
M_{air} : Total mass of air in the drying chamber
X_0 : Mass fraction of vapor water on the environment
M_v : Vapor mass
ω : Absolute humidity on the air
$q_t(t)$: Total heat transfer
h_c : Specific enthalpy of the air in the chamber
h_0 : Specific enthalpy of the air in the environment
h_{lv} : Phase transition enthalpy of the water
T_{we} : Wall temperature of the evaporator
T_{wc} : Wall temperature of the condenser
T_v : Temperature of the vapor
q_t : Thermal total power transferred
n_c : Numbers of condensers
n : rotational speed
M^0_{water} : Initial mass of the trays
M^f_{water} : Final mass of the trays
Δt : Interval of time

REFERENCES

[1] Park, K. J., Vohnikova, Z., Brod, F. P. R., Evaluation of drying parameters and desorption isotherms of garden mint leaves (Mentha crispa L.), *Journal of Food Enginnering*, Campinas, Sao Paulo, Brazil, 1 (51) (2002) 193-199.

[2] Park, K. J. B. et al., Considerações Termodinâmicas das Isotermas: Review, *Revista Brasileira de Produtos Agroindustriais*, Campina Grande, Paraiba, Brazil, 10 (1) (2008) 83-94.

[3] Müller, J., Heindl, A., Drying of medicinal plants, *Medicinal and aromatic plants*, Springer, (2006) 237-252.

[4] Argyropoulos, D. et al., Moisture sorption isotherms and isosteric heat of sorption of leaves and stems of lemon balm (Melissa officinalis L.) established by dynamic vapor sorption, *Lwt - Food Science And Technology*, Stuttgart, Germany, 47 (2012) 324-331.

[5] Argyropoulos, D., Müller, J., Effect of convective drying on quality of lemon balm (Melissa officinalis), *Procedia Food Science: 11th International Congress on Engineering and Food*, Stuttgart Germany, (1) (2011) 1932-1939.

[6] Mujumdar, A.S., *Handbook of Industrial Drying,* New York, Dekker, M, 3. Ed., Inc. 2006.

[7] Kiranoudis, C.T. et al., Design and operational performance of conveyor belt drying structures, *Chemical Engineering Journal*, Athens, Greece, (69) (1998) 27-38.

[8] Holowaty, S., Ramallo, L., Schmalko, M., Intermittent drying simulation in deep bed dryer of yerba mate, *Journal of Food Enginnering,* Posadas, Argentina, (111) (2012) 110-114.

[9] Silva, A.K., Mantelli, M.B.H., Thermal applicability of twophase thermosyphons in cooking chambers-experimental and theoretical analysis, *Applied Thermal Engineering*, Florianopolis, Brazil, (24) (2004) 717-733.

[10] Mantelli, M. et al, Termossifões em árvore aplicados a fornos e cocção de pães: Maior eficiência energética. *1° Seminário da Rede gás e energia*, Rio de Janeiro, Brazil, (2006).

[11] Mantelli, M.B.H., Milanez F.H, Nielitz, G., Tree Configuration Thermosyphon Study, *AIAA Thermophysics Conference,* Toronto, Ontario, Canada (2005).

[12] Parametthanuwat, T., Rittidech, S., Booddachan, K., Thermosyphon installation for energy thrift in a smoked fish sausage oven (TISO), Energy, Thailand, (35) (2010) 2836-2842.

[13] McCabe, W. L., Smith, J. C., Harriott, P., Unit Operations of Chemical Engineering (McGraw Hill Chemical Engineering Series), 7. Ed., United States (2007)

[14] Mantelli, M.B.H., Thermosyphon technology for industrial applications: Heat Pipes and Solid Sorption Transformations. / Vasiliev L.L., Kakaç S., CRC Press, Boca Raton (2013) 411-464.

[15] Faghri, A., Heat pipe science and technology, *Taylor & Francis*, New York (1995).

[16] Bejan, A., Convection Heat Transfer, *Canada: John Wiley and Sons*, 3. Ed., Inc. 2004.

How a Wall Thermosyphon Can Enhance the Energy Savings in a Prefabricated House in Italy

F.Fantozzi[1], S. Filippeschi[1], M. Mameli[1], Marcia B. H. Mantelli[2], Fernando H. Milanez[2]

[1]*Dr. Energy, Systems, Land and Construction Engineering - University of Pisa 56122 - Pisa, Italy*
[2]*Dr. Mechanical Engineering Department, Federal University of Santa Catarina UFSC, Brazil*

Abstract

Energy saving in buildings is one of most important issue for European countries. The energy consumption rate devoted to building is about the 40% with respect the total European energy consumption. Although in the last years many studies have been carried out in order to reach the zero-consumption house by means of passive solar heating, ventilation or thermal insulation, the energy rate due to passive solar heating could be further enhanced.
This paper proposes a method to increase the energy rate coming from the solar opaque elements by using a two phase loop thermosyphon to connect the internal and the outside façade of prefabricated house wall. The evaporator zone is located on the outside side of the wall and it is irradiated by the sunlight while the condenser zone is placed on the internal side of the wall and releases heat to the domestic environment. The temperature differences between the internal and outside wall facades are lower than 30 K) and the heat fluxes at the evaporator changes during the time range from 2 to 7 x 10^4 W/m^2 K. The thermosyphon has been preliminary designed and implanted into a wall for a prefabricated house in Italy. A thermal model of building with the wall enhanced by the wall thermosyphon has been used to evaluate the impact of this solution in terms of energy saving and thermal comfort in a real prefabricated low consumption house. The transient behavior of the building has been simulated day by day during the winter period by using the EnergyPlus™ software.
This solution enhances the thermal comfort of the building by keeping the indoor temperature close to the thermal comfort standard for the most of the day. The annual heating energy demand saving rate is higher than 23% in the case of a low consumption building. These rates reach the maximum of 38.8% in the case of a house ..

Keywords: Wall loop-thermosyphon, energy saving, low-consumption buildings, passive heating

1. INTRODUCTION

Energy saving in buildings is one of most important issues in European countries. There are several strategies to reduce the energy demand in buildings, such as ventilation, thermal insulation, heating and cooling efficiency plants. One of the most effective methods is the use of passive solar energy, which is directly supplied to the building through the windows and through the opaque walls.

This paper proposes a method to increase the energy rate coming from the solar opaque elements by using a loop two phase thermosyphon which directly connects the internal and the external house wall surfaces.

An interesting research trend in this topic at the moment is the use of "smart envelopes" that are able to intelligently use solar energy for the production of both active and passive energy.

Among the active solutions, Giovanardi et al. (2015) [1] present a new unglazed solar thermal collector concept for facade integration in building energy retrofit actions. Roll-bond and metal cladding systems were embedded into the facade and connected to a solar heating and domestic water warming plant.

Zhang et al. (2015) [2] presented a paper on a loop-heat-pipe based solar thermal facade (LHP-STF) installed in a reference residential building. They studied the technical evaluation and the economic advantages of applying this solution in three typical European climates, including North Europe (Stockholm), West Europe (London) and South Europe (Madrid). The research results indicated that the LHP-STF could contribute to the hot water heat load throughout the year, with substantially reduced heating load in the winter, and yet a slight increased cooling load in the summer.

On the other hand, different passive solutions have been alternatively studied and implemented into the building envelopes to reduce the heating load. The most famous solution was proposed by Trombe in France in 1964 and named the “Trombe wall”. This solution is still applied and studied for both unglazed vertical elements [3] and roofs [4]. Another passive solution for the “smart envelopes” use phase change material to reduce the cooling energy demand [5].
Most of buildings envelopes are made of unglazed elements and the passive solutions that uses the solar energy incident on these elements appears full of perspective for energy savings in buildings.

As a first attempt to intelligently recover energy

*Corresponding author: s.filippeschi@ing.unipi.it,
Phone: +39-050-2217153, Fax: +39-050-2217156

from unglazed wall, a new concept with heat pipes or thermosyphons integrated into the facade of a building has been presented by Sun et al. in 2014 [6] and tested by Zhang et al. in 2015 [7] for Chinese climates.

The basic idea consists of a two phase device, named microgravity heat pipe, which presents the evaporator implanted in the outdoor plastering mortar and the condensing section implanted in the cement mortar of the inner surface. The main advantage of this solution is the two-phase device efficient unidirectional heat transfer characteristics given by the gravity driven natural convection inside. The device, indeed, works like a thermal diode that transfers heat directly into the building during winter if the temperature difference between indoor and outdoor is positive and, at the meantime, prevents the heat losses in the opposite case. Sun et al in 2014 [6] propose to insert an intelligent manual valve to stop the natural circulation inside the two-phase device. This allows for preventing building heating in summer and consequently increasing the demand on cooling energy.

In 2015, Zhang et al. [7] tested a Wall Implanted Heat Pipe WIHP made of an evaporator section built with 24 capillary pipes (ID=2.7 mm, 600 mm long) implanted into a mortar plaster and a similar sized condenser implanted into the internal plastering layer. This device has been filled with R600a. They have tested a 1720x1720 mm^2 surface facing south at different outside temperature, with an internal air temperature of 18°C. They found that heat transfer transmittance value of the wall with WIHP ranges from 0.76 to 0.987 W/m^2 K as the outside surface temperature increases from 24 °C to 42 °C. They affirm that this solution decreases the annual energy heating demand by approximatelly 15% in Jinan climate. Starting from the basic idea proposed by Sun et al. [6], this paper presents a completely new concept device to enhance the heat transfer performance in prefabricated house. In particular, this paper presents the design of a new loop-thermosyphon applied to a module of the prefabricated house with metallic case.

The new device has been modeled and applied to a real house sited in Pisa. The energy saving rate and the enhancement in thermal control of this solution have been highlighted.

2. THE WALL THERMOSYPHON

2.1 The Working principle

The device proposed by Sun et al. [6] presents different critical aspects that could be solved and improved. Firstly the heat transfer in the evaporation section is not optimal. The evaporator is made of capillary pipes immersed into a plaster layer. In this configuration, the 2-D temperature distribution shows that most of the solar heat flux incident on the outside facade is conducted through the plaster and it is not absorbed by the metallic pipes of the device.

Secondly, it is also known that in a two-phase devices the main thermal resistances are between the hot source to the evaporator and between the condenser to the cold source, respectively. In the heat pipe proposed by Sun et al. [6] the main thermal resistance is given by the natural convection on the vertical internal wall that is higher than 0.5 m^2 K/W.

There are main critical aspect of the device proposed in [6] are therefore:

1. Low heat transfer efficiency, defined as the ratio between the heat flux transferred by the device and the solar heat flux incident on a large surface. transfer rate of the evaporator;
2. The high thermal resistances for heat transfer between condenser section and cold source (indoor air).

The device that has been proposed in this paper, named Wall Thermosyphon (WT), aims to enhance the performances of the wall Thermosyphon proposed by Sun et al. [6].All the loop thermosyphon is made of anodized aluminum. In particular, the evaporator is a aluminum plate dark painted, where the aluminum tubes are welded or brazed. This solution cannot be applied to all buildings, but it is convenient for several prefabricated houses because the use of metallic walls on the outside facade has found a large diffusion in modern architecture.

This configuration of the evaporator section joined with the external facade is able to solve the critical aspect above listed at point 1.

The condenser is also completely reviewed. We propose to build a hollow space inside the wall, where a finned condenser tube is placed. This cavity is connected both to indoors and outdoors through four opening and closing air vents. The working principle scheme is shown in Fig. 1.

During the winter period, the indoor air vents are opened and the outdoor air vents are closed. During the summer period the opposite scenario is set. The air inside the cavity can be either naturally circulated for a totally passive solution or moved by a fan in case of active device in order to have a better venting control. In this paper, only the natural convection solution has been considered.

Usually, the air is extracted from the room, heated by the condenser and pushed again into the room if the air room temperature is lower than the comfort temperature. If the room air temperature is higher than the comfort inside temperature the warm air is

pushed out from the hollow space. The temperature control is thus made by the vent ports and not by the Thermosyphon itself. This solution is simpler and consequently cheaper and more reliable.

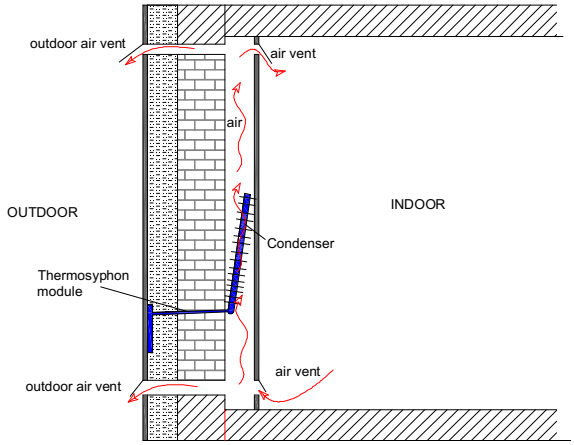


Fig 1. Wall Thermosyphon working principle scheme.

This condenser configuration solves the critical aspect above listed at point 2. Moreover, the advantages of a Loop Thermosyphon with respect to the capillary heat pipe applied in the previous solution is also related to the quicker device start-up, lower minimum heat input necessary to activate the circulation, and higher maximum heat flux and no entertainment limit ([8],[9]).

The wall loop thermosyphon designed for is similar to the thermosyphon described by Milanez & Mantelli in 2010 [10].

The evaporator consists of two vertical aluminum pipes (ID=12 mm) connected with two manifolds (ID=32 mm). The condenser presents a similar disposition, with 5 vertical pipes and two horizontal manifolds. All the dimensions of the loop thermosyphon are shown in Fig. 2.

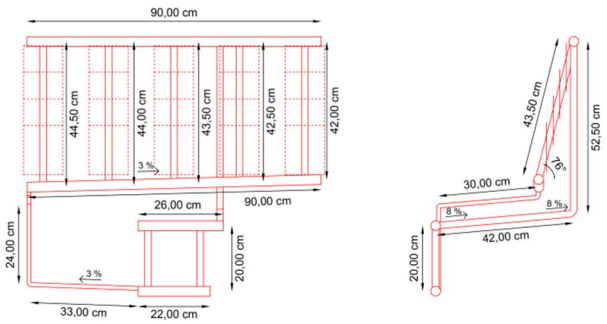


Fig 2. Loop Thermosyphon dimensions.

The evaporator is welded to a dark aluminum plate and the condenser vertical pipes have 15 rectangular fins 10 mm interspaced. The working fluid is the refrigerant R141.

2.2 The reference building

This paper proposes to apply this innovative device in a prefabricated wall of the reference prefabricated house shown in Fig. 3.

The reference building is built with high efficiency solutions and could be labeled as “low consumption house” (in the Italian standard certification labeling procedure with an energy demand lower than 2000 kWh per year). The multilayered outside wall with the embedded WT is shown in Fig. 4.



Fig 3. Reference House Map.

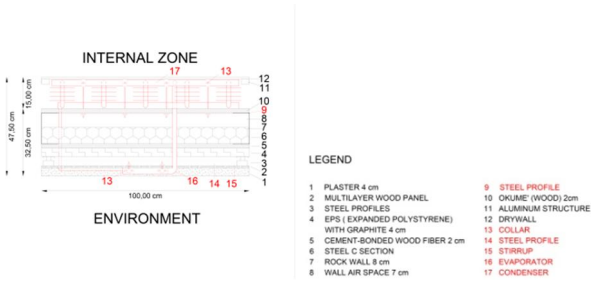


Fig 4. Vertical wall with the embedded wall thermosyphon.

The roof wall is 0.388 m thick and is made of a roofing membrane (3 mm), several plywood layers, a ceiling stagnant air cavity and an expanded polystyrene layer (70 mm).

The windows are made of a composite glass with two layers (4 mm) interspaced with 16 mm of stagnant argon gas. The main building sizes are reported in Table 1 and Table 2.

The walls are previously made in a factory and assembled together to form the building. The wall is therefore made of several modules 1 m wide and 3 m high. Each module is equipped with 3 wall thermosyphons as shown in the wall section and front view presented in Fig. 5.

Table 1. Surfaces of envelope elements

Envelopes elements	Surface [m2]	Window surface [m2]	Door Surface [m2]
Floor	84	-	-
Roof	84	-	-
South Wall	21	1,08	2,4
North Wall	21	-	-
East Wall	36	2,16	-
West Wall	36	4,32	-

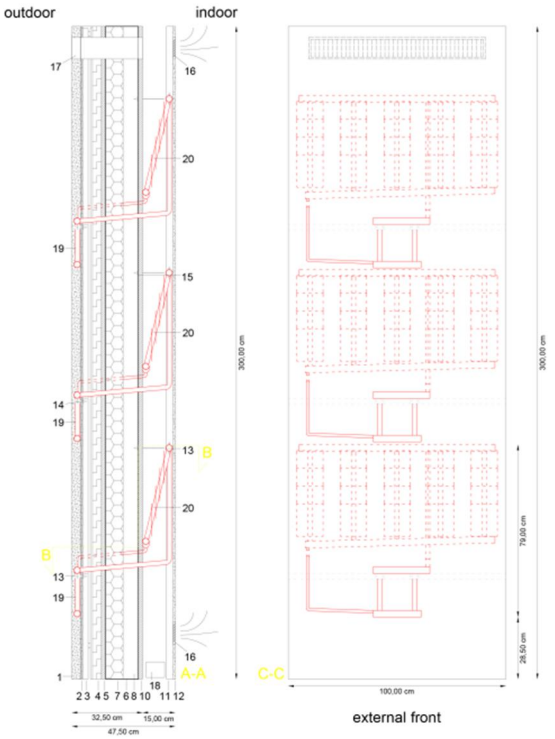


Fig 5. Vertical wall with the embedded wall thermosyphon: section and front view

2.4 Simulation criteria and procedure

2.4.1 Wall Thermosyphon model

The WT heat transfer model is very complex because involves several mechanisms: radiation, convection, two-phase and thermal inertia. The WT is a structure where a wall and a two-phase device are coupled together. The heat transfer process changes in 3D direction and over time. The model of the wall has been simply considered as a lumped capacitance method, where the thermal inertia of the two-phase device has been neglected. The thermosyphon welded to the metallic external façade has been treated as a thermal resistance constant with time.

The behavior of the WT however is highly dependent on the direction of heat transfer through the wall, that is, the temperature difference between the indoor air T_{IA} and the outside façade temperature T_{SW}, according to the following criterion: if $T_{IA} > T_{SW}$ the heat is transferred in a pure conductive regime and the total heat transfer transmittance is equal to that of the outside wall (Table 2). In the case $T_{SW} > T_{IA}$, heat is transferred into the building according to the following relation:

$$q = \frac{T_{SW} - T_{IA}}{R_{wth}} \quad (1)$$

where R_{wth} is the WT thermal resistance given by the sum of R_{th}, thermal resistance of the two-phase devices and R_{air}, thermal resistance of the free convection heat transfer at the condensing section. The thermal inertia of the thermosyphon is negligible in comparison to the wall inertia.

The thermal resistance of the thermosyphons (R_{th}) has been estimated with the model described by Milanez & Mantelli in (2010) [10]. It is equal to 0.03 m^2KW^{-1} and the thermal resistance of the finned condenser section is equal to 0.05 m^2KW^{-1}. The total thermal resistance of the device is therefore 0.08 m^2KW^{-1}.

2.4.2 Building simulation tools

The whole prefabricated house has been simulated during its transient behavior by using commercial software EnergyPlus™ .

EnergyPlus™ uses a finite difference approach based on the Crank-Nicholson scheme which is semi-implicit and based on an Adams-Moulton solution approach. The implemented algorithm uses an implicit finite difference scheme which is also coupled with an enthalpy-temperature function able to account for the phase change energy phenomena. The total heat transfer transmittances of the different elements of this building are shown in Table 2.

The solar heat flux and the temperature changes hourly during a day. To calculate the WT effect in the building transient behavior, the heat flux of a typical day for every month has been hourly calculated and applied to the building as an additional heating load according the scheme shown in figure 6.

Starting form the first hour of the heating period, the temperatures T_{IA} and T_{SW} coming from the simulation have been used to hourly calculate the new heat flux transferred by the WT. This contribution has been considered as a heat load directly input inside the zone in contact with south wall.

Table 2. Heat Transfer Transmittances

Envelopes elements	Total Heat Transfer Transmittance H [W/m^2 K]
Outside Wall	0,21
Inside Wall	0,39
Roof	0,27
Window	1,59
Floor	0,5
Door	1,18

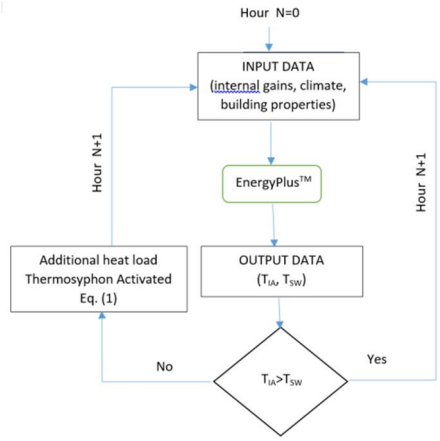


Fig 6. Flow chart of the simulation procedure

2.4.1 Input data

The building simulation is referred to a real house case in Italy with the climate of the central region (Pisa City). The climate data used in this calculation are available in the EnergyPlus™ platform.

Figure 7 shows the irradiating heat flux hourly incident on a south faced vertical surface at different months in a specific day (21st). The months listed in Fig. 7 are included into the standard heating period for Pisa region (1st November-15th April). Figure 8 shows the hourly outdoor dry bulb air temperature at different months during the heating period.

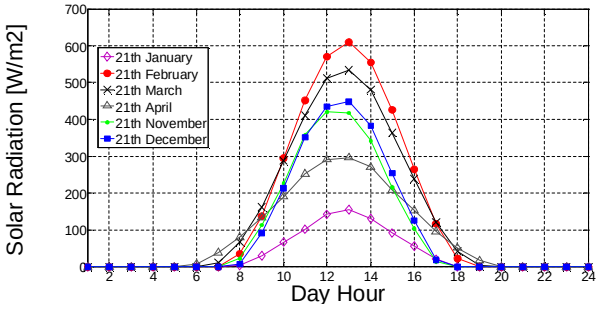


Fig 7. Hourly outside solar radiation incident on vertical south faced surface on the 21st day for several months

The gain due to the people is relative to 2 people with an activity tabled as "Sedentary work" according to the ASRHAE fundamental handbook (2013). The gain due to the lights is equal to 250 W all day long (0.37 radiant fraction, 0.18 sensible fraction). For the ventilation gain, natural convection has been considered a with a constant flow rate of 0.035 m^3/s all day long. The simulations made in this paper are therefore:

CASE A: building with the internal gains and without the WT contribution (reference case).

CASE B: building without internal gains and without the WT contribution.

CASE C: building with the internal gains and with the WT contribution.

CASE D: building without the internal gains and with the WT contribution.

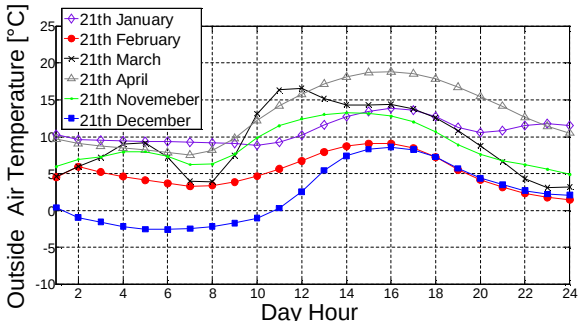


Fig 8. Hourly outside dry bulb air temperature on the 21st day for several months in the heating period

3. RESULTS AND DISCUSSIONS

3.1 The building without thermosyphon (Case A)

In this case, the regime indoor temperature is given by the heat and mass balance with the environment.

The results of each simulation have been discussed by taking into account two main aspects: thermal comfort, given by the indoor temperatures, and energy savings.

The indoor temperatures are presented for the two different inside zones shown in Fig. 3: Living Zone and Sleeping Zone. They are distinguished by the standard temperatures for a optimal thermal comfort, which are 20 °C for the living zone and 18°C for the sleeping zone, respectively.

Figure 9 shows the typical trend of the temperatures during the day for December 15th. The temperatures shown in Fig. 9 are two zones indoor temperatures (living and sleeping or night) and the temperature of the outside wall south faced. The qualitative trend of December is similar to January, February and March.

Fig. 9 shows that the indoor temperatures are almost constant during the day even if they are always lower than the standard temperatures required for a good thermal comfort.

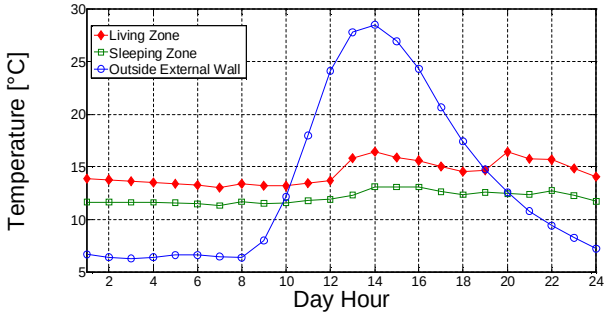


Fig 9. Hourly temperature trend for December 15th

This behavior is typical for low consumption houses that are highly thermally insulated. The blue line of Fig. 9 indicates the evolution of T_{SW} over a day: from 11 a.m. to 6 p.m the outside wall temperature T_{SW} is constantly higher than the indoor air temperature. In these conditions the wall thermosyphon can enhance the heat transfer into the zone.

Different behaviors can be observed for the months of November and April. Fig. 10 shows the typical trend of the characteristic temperatures during November 15th as an example.

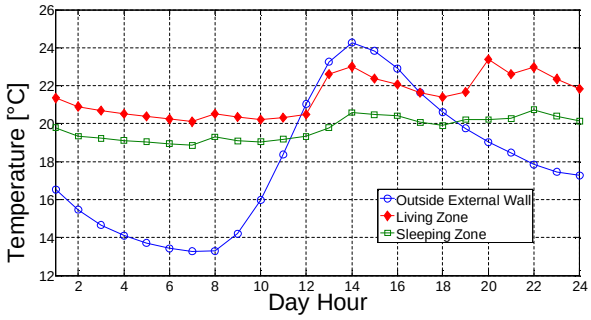


Fig 10. Hourly temperature trend for November 15th

For both November and April the internal gain and the sun are sufficient to keep the indoor air temperature higher than the standard requirement for a good thermal comfort. In these two months, the heating plant will always be switched off. In November the outside wall temperature (blue–line) is never higher than the indoor air. Under this condition the thermosyphon does not work. Figure 11 shows the temperature differences between the outside temperature of the vertical south faced wall T_{SW} and the indoor air T_{IA} at different months. Except for November, this difference reaches a positive value from 11 a.m to 6 p.m during all the heating period.

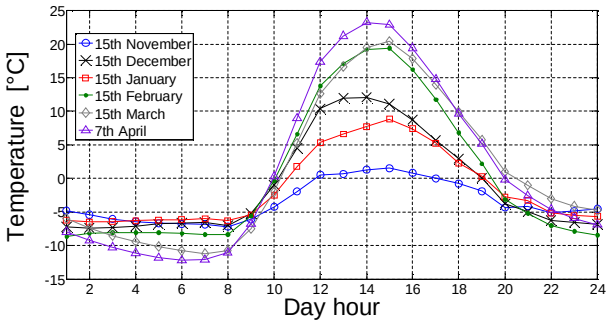


Fig 11. Temperature differences between the outside south faced wall and the indoor air for different months.

For a large period of the heating time, the wall thermosyphon can therefore operate and reduce the energy demand. In April, the warm air is vented outside the building because the indoor temperature is higher than the standard reference.

3.2 Wall Thermosyphon Effect

The reference house is now simulated with the wall thermosiphon devices implanted into the south faced wall. As shown in Fig. 3, the south wall divides the living zone from outdoor and no portion is in the sleeping zone.

As mentioned before, the heating period for Pisa is from November to 15th April, even if in this highly insulated prefabricated house, in November and April the indoor temperatures are high enough to guarantee an optimum thermal comfort without any heating plant. In this case the energy recovered by the wall thermosiphon must be rejected outside.

Figures 12 and 13 show the hourly indoor temperature in the living and in the sleeping zones, as the south wall is with and without the WT. The plain markers are relative to the case with the wall thermosyphon. Figure 12 shows the temperatures calculated for February 15th and Fig. 13 for March 15th.

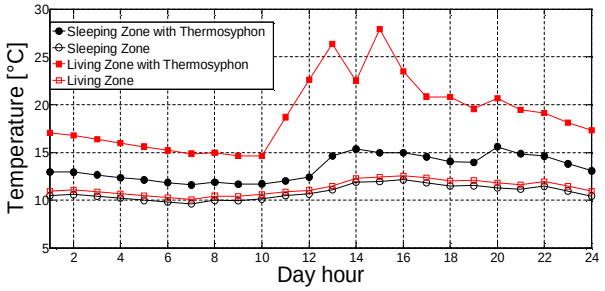


Fig 12. Hourly indoor air temperature trend for February 15th in the living and in the sleeping zones for a south faced wall with and without the thermosyphon.

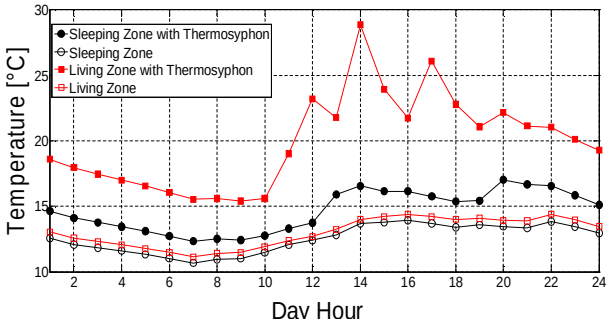


Fig 13. Hourly indoor air temperature trend for March 15th in the living and in the sleeping zones for a south faced wall with and without the thermosyphon

These graphs help us to understand the thermal comfort inside the building. Both the figures show similar trends. The positive effect of the thermosyphon is evident in both the months, even when the outside wall temperature is lower than the indoor air temperature (Fig. 11, periods 1-10 a.m and 8-12 p.m). Since the south faced wall is totally inserted in the living room, the major effect on the indoor temperature is relative to this zone. As the thermosyphon is activated (from 11 a.m.) the indoor air temperature is always higher than the standard reference for the thermal comfort and no additional heating contribute is required. From 13 a.m to 11 p.m a portion of air heated by the thermosyphon must be rejected to the outdoor in order to prevent the discomfort due to the too high temperatures (March case).

Note that both plots (Figs 12 and 13) show temperature oscillations as the indoor temperature approaches to a maximum (2 p.m.). That is because it depends on the iteration time step that was set too high (1 hour). However, it is important to note that even if the iterative procedure could be inaccurate in the indoor temperature evaluation in the hottest hours of the day, it does not affect the energy saving demand evaluation, because these indoor temperatures are higher than 20°C. In these hours the hot air given by the WT device must be therefore rejected to the outdoor.

3.2 Energy saving rate

The effect of the enhanced wall in terms of energy saving rate is high. The annual energy requirement for heating has been calculated zone by zone. The energy amounts necessary to keep the indoor air at 20 °C (Living Zone) or 18°C (Sleeping Zone) were calculates. The annual energy requirement were therefore hourly calculated for every day during the heating period for Pisa.

The simulation was made by considering the building with the input data described in section 2.4.1. It is important to remember that the heating plant can be switch on only for 12 hour per day in Italy. The switching schedule is usually chosen to cover the period where the heat demand is high.

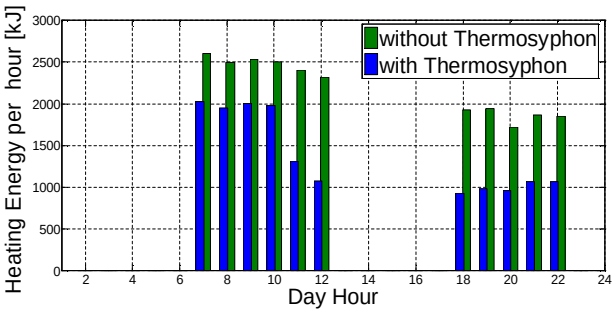


Fig 14. Comparison between the hourly energy heating demand for a building with and without the wall enhanced by thermosyphon in case C(February 21st).

Figures 14 show the comparison between the hourly heating energy requirement evaluated for a building with and without the thermosyphon for a generic day (21st February). It is possible to note that the energy requirement in case of WT is lower even when the thermosyphon is not working (before 11 a.m.).

Table 3 shows the heating energy requirement for several months and the energy saving rate due to the wall enhanced by thermosyphon. It is possible to note that the annual energy requirement per indoor surface is 9.2 kWh/m^2.

Table 3. Energy savings for case C.

Month	Energy demand for heating [kWh]	Energy saving rate due to the wall therm. [kWh]	Energy saving [%]
November	0	0	0
December	186	45	24.08
January	204	43	23.31
February	202	55	27.29
March	177	48	27.08
April (15 days)	0	0	0

The energy saving percentage with respect to the case without TS is higher than 20% for all months. This percentage is really high if one consider that it is related to a low consumption house. It is reasonable to suppose that the energy saving percentages may increase considerably if this

solution would be applied to high consumption houses.

A second simulation was performed on the same building without internal gains (Case D). The annual heating energy requirement per indoor surface grows up to 13.7 kWh/m^2 (47% higher than the previous one). The comparison between the hourly heating energy requirement evaluated for this building with and without the wall enhanced by the thermosyphon is shown in Fig. 15 for a generic day (February 21st).

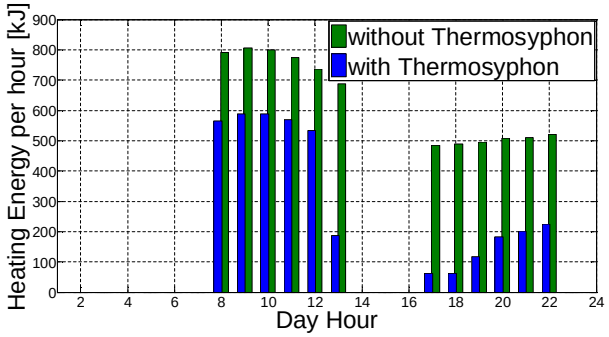


Fig 14. Comparison between the hourly energy heating demand for a building with and without the wall enhanced by thermosyphon in case D (February 21st)

Table 4 reports the heating energy demand without thermosyphon and the energy saving rate evaluated for several months.

Table 4. Energy savings for case D.

Month	Energy demand for heating [kWh]	Energy saving rate due to the wall therm. [kWh]	Energy saving [%]
November	63.4	23.9	37.6
December	299.9	81.1	27.0
January	177.0	56.9	32.1
February	302.3	90.5	29.9
March	289.1	58.1	20.1
April (15 days)	6.1	2.4	38.8

In this scenario, the indoor temperature is never higher than the thermal comfort standard (20 °C) and a heating rate is required even in November (Fig. 15) and April.

As shown in Table 4, the energy saving percentages in this house are really high with respect to the standard retrofit actions to enhance the low consumption house thermal performances. An action on the heating plant that shows energy savings of 10-15% are considered highly performing. Note that in Case D this solution reach a maximum energy saving of 38.8% in April.

4. CONCLUSIONS

This paper presents a preliminary study on a new concept wall with embedded thermosyphons for energy savings in buildings. The thermosyphon has been preliminary designed and implanted into a wall of a real prefabricated house in Italy. A basic thermal thermosyphon model is used to evaluate the impact of this solution in terms of energy saving and thermal comfort.

The building transient behavior has been simulated for each day during the winter period with the EnergyPlus^{TM} software.

Results show that the present solution enhances the building thermal comfort by keeping the indoor temperature close to the thermal comfort standard for the most of the day. The energy saving rates are very high and overcomes rates of 23% of the heating demand in the case of a low consumption building. This rate can reach the maximum of 38.8% in the simulated cases. These rates are relative to a really low-consumption house in a mild Mediterranean climate and could be higher in more rigid climate and in house with high heating demand.

ACKNOWLEDGEMENT

Giacomo Cillari and Sarah Nesi are gratefully acknowledged for their support in the use of the EnergyPlus^{TM} software.

NOMENCLATURE

q : heat flux (W/m^2)
R_{air} : Thermal res.of cond.section (m^2 K/W)
R_{th} : Thermal res.of thermosyphon (m^2 K/W)
R_{wth} : Thermal res.of wall device (m^2 K/W)
T_{IA} : Indoor air temperature (K)
T_{sw} : South faced wall temperature (K)

REFERENCES

[1] Giovanardi A., Passera A., Zottele F., Lollini R., Integrated solar thermal facade system for building retrofit, *Solar Energy* 122 (2015) 1100-1116

[2] Zhang X., Shen J., Adkins D., Yang T., Tang L., Zhao X, He W., Xu P., Liu C., Luo H., The early design stage for building renovation with a novel loop-heat-pipe based solar thermal facade (LHP-STF) heat pump water heating system: Techno-economic analysis in three European climates, *Energy Conversion and Management*, 106 (2015) 964-986

[3] Dehra H., A mathematical model of a solar air

thermosyphon integrated with building envelope, *International Journal of Thermal Sciences*, 102 (2016) 210-227.

[4] Chami N., Zoughaib A., Modeling natural convection in a pitched thermosyphon system in building roofs and experimental validation using particle image velocimetry, *Energy and Buildings* 42 (2010) 1267-1274

[5] Kenisarin M., Mahkamov K., Passive thermal control in residential building susing phase change materials, *Renewable and Sustainable Energy Reviews*, 55 (2016) 371-398

[6] Sun Z., Zhang Z., Duan C. The applicability of the wall implanted with heat pipes in winter of China, *Energy and Buildings* 104 (2015) 36-46

[7] Zhang Z., Sun Z., Duan C., A new type of passive solar energy utilization technology — The wall implanted with heat pipes, *Energy and Buildings* 84 (2014) 111-116.

[8] Vasiliev L.L. Kakaç S., *Heat Pipes and solid sorption transformations Fundamentals and Practical Applications*, Ed. CRC Press- Taylor & Francis Group, (2013)

[9] Franco A., Filippeschi S., Experimental analysis of Closed Loop Two Phase Thermosyphon (CLTPT) for energy systems, *Experimental Thermal and Fluid Science*, (51), (2013), 302-311.

[10] Milanez F H. & Mantelli M B. H., Heat transfer limit due to Pressure drop of a two-phase loop Thermo-syphon, *Heat Pipe Science and Technology, An International Journal* 1(3), (2010), 237-250

[11] *ASHRAE Handbook — Fundamentals,* Handbook Editor, ASHRAE, 1791, Tullie Circle, Atlanta, US (2013)

Mechanism and Technology of High and Super High Temperature Heat Pipes

Wei Qu, Zhihu Xue and Jijun Yu

China Academy of Aerospace Aerodynamics(CAAA), Beijing 100074, China

Abstract

The mechanism and technology of high and super high temperature heat pipes are investigated, discussed and concluded. For the mechanism, atom dimer will differ, depend on temperature of sodium or lithium, and influence the physical properties of vapor essentially. The continuous flow limit will produce and affect the temperature from very low vapor pressure during startup. The possible non-compatibility products include both the oxide of outphase jelly and the non-condensable gases due to the micro cell erosion mechanism. The former may dominate compared with the latter, the Arrhenius model only applies for the latter. For the technology aspects, the distillation method of charging of the alkali metal is compared with the innovated thawed charging. The time and the energy expenditure are decreased more than one order of magnitude. The antioxidation coating of the outer heat pipe is realized, it is essential for the operation in oxygen ambience. Three typical experimental heating methods are illustrated. The overloading experimental technique is discussed and the effects of bond number are given. The high and super high temperature heat pipes are considered to be irreplaceable for many situations.

Keywords: Atom dimer influence; Continuous flow limit; Oxide of outphase jelly; Micro cell erosion; Antioxidation coating

1. INTRODUCTION

The high and super high temperature heat pipes can work from 500℃ up to 1500℃, they have wide applications in space thermal control, solar storage power plant, nuclear thermal control, the constant temperature stoves etc..

The heat pipe between 500℃ and 1200℃ is called as high temperature heat pipe, while if the temperature is over 1200℃, it belongs to super or extreme high temperature heat pipe.

The first heat pipe in China was made in 1972, those stainless steel and sodium heat pipes realized the high temperature stove to make the semiconductor technology reliable. The super high temperature heat pipe of W-Li by USA was tested in 1966. For the nuclear reactor cooled by the high temperature heat pipes, the fuel bars and the high temperature heat pipes are designed to be coupled together. By the high temperature heat pipes, the heat from the pile core is transferred to the heat exchanger, the technology of high temperature thermal radiation is realized. The high temperature heat pipes connect the nuclear power suppliers to the outside and transfer the large amount of heat. When the space nuclear power suppliers work at full, the temperature of heat core can reach 3000~3300K, however, the maximum temperature to be controlled is 800K. So, the high temperature heat pipe is the key problem to be solved for the whole system. Such aspect relates also the miniaturization, and performance optimum of the high temperature heat pipe, and the shape adaptability and coupling with the high temperature radiator etc..

For the past few decades, the sodium and lithium heat pipes were developed a lot. There were different application in many fields as, the thermal control of super high Mach spacecraft, the heat storage and heat transfer of solar power plant, the heat recycling and application of high temperature gas discharge, the thermal control in nuclear energy, the constant temperature of industry stove, etc., in some situations, they are necessary and cannot be realized by other ways.

2. MECHANISM OF HIGH AND SUPER HIGH TEMPERATURE HEAT PIPES

2.1 Dimer Influence of Alkali Metal Vapor

From the angle of equilibrium constant, there are two processes, they are the initial stage from liquid to single atom vapor, and the dimer stage, in which some single atoms change to diatomic molecules. The relative ratio of the dimer to the total depends on the temperature. If sodium or lithium is selected as the working fluid, the physical properties should be calculated according to the ratio of diatomic molecules.

Below the temperature of 300℃, the saturation vapor of sodium will be all as the single atom state. The diatomic molecules Na_2 will be formed with temperature, they exist together with the single atoms in dynamic equilibrium constant.

$$Na_2 \Leftrightarrow 2Na \quad (1)$$

Under the condition of one barometric pressure,

*Corresponding author: weiqucaaa@hotmail.com, Phone: +86-10-6837-6749, Fax: +86-10-6837-4758

the boiling temperature of liquid sodium is 881.4±0.6℃, the ratio of diatomic molecules in its saturation vapor is about 16%.

Similar to sodium, the dimer stage will also exist for the working fluid lithium, the vapor is a mixture, it is composed with single atoms and diatomic molecules.

$$Li_2 \Leftrightarrow 2Li \tag{2}$$

The saturation pressures of sodium and lithium include two parts correspondingly, they are both vapor partial pressures of single atoms and diatomic molecules. The dimer reaction extent is dependent on the temperature by equilibrium constant, the vapor pressure will decrease compared with that of non-dimer.

2.2 Continuum Flow Limit During Startup

Before startup, sodium or lithium in heat pipe is solid under the ambient temperature. Inside the heat pipe is a vacuum state with little air and working fluid vapor, that is rarefied, or it is in free molecule flow state. The vapor density is very low. If the startup conditions cannot make the vapor flow be higher density, or continuous flow, the heat pipe cannot start up normally, this is continuum flow limit.

If the sodium or lithium heat pipe is near the melting point of working fluid, the continuum flow limit becomes possible during heat pipe startup. The vapor can be judged by Knudsen number (*Kn*), if the critical condition is to be the boundary of continuous flow.

$$Kn = \lambda / \mathrm{D} \tag{3}$$

Where, λ is the free path length of the vapor atom or molecule; *D* is the smallest size of the vapor passage. The dynamic theory of molecules tell that, if it is the condition, *Kn*>0.01, then the vapor belongs to the rarefied flow, or free molecule flow; while if, *Kn*≤ 0.01, then it is the continuous flow.

For the low temperature startup of a high or super high temperature heat pipe, the vapor flow inside is rarefied, the free path length of the vapor is following.

$$\lambda = 0.23656\kappa T / (d^2 P) \tag{4}$$

Where, κ is Boltzmann constant, *d* is the collision diameter, *T* and *P* are the corresponding temperature and pressure.

The state equation of ideal gas is expressed as.

$$P = \rho R_g T \tag{5}$$

From Equations (3, 4 and 5), the transition density from the continuous flow to the rarefied flow is as follows.

$$\rho_{tr} = 0.23656\kappa / (d^2 DKnR_g) \tag{6}$$

It is supposed that the heat pipe vapor is saturation, substitute Equation *Kn*=0.01 to Equations (4 and 6), and consider Clausius-Clapeyron Equation, the transition pressure and temperature are obtained as.

$$P_{tr} = P_0 \exp\left[-\frac{h_{fg}}{R_g}\left(\frac{1}{T_{tr}} - \frac{1}{T_0}\right)\right] \tag{7}$$

$$T_{tr} = \frac{P_0}{\rho_{tr} R_g} \exp\left[-\frac{h_{fg}}{R_g}\left(\frac{1}{T_{tr}} - \frac{1}{T_0}\right)\right] = \frac{P_{tr}}{\rho_{tr} R_g} \tag{8}$$

As shown in Fig.1, for sodium high temperature heat pipe and lithium super high temperature heat pipe, the transition temperature versus the passage dynamic diameter are given at the continuous flow limit. The vapor temperature will deviate from the design.

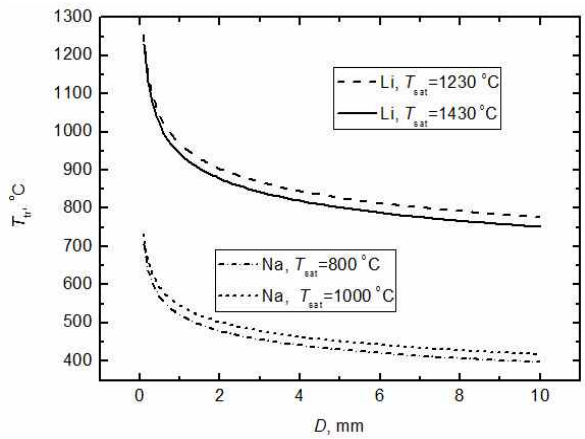


Fig.1. Transition Temperatures of Sodium and Lithum versus passage hydraulic diameters

2.3 Non-compatible Operational Products

For manufacture, firstly the compatibility should be no problem, then the oxygen should be degassed as far as possible. Even so, due to some not careful impurity processes, some jelly materials may collect during long time operation.

2.3.1 Oxide of Outphase Jelly

During high temperature operation, the alkali metal is easy to react with the small amount of oxygen and remnant impurity, to form the oxide of outphase jelly, they can be expressed as $A_xM_yO_z$, the reaction is possible to be as.

$$xA + yM + \frac{z}{2}O_2 = A_xM_yO_z \quad (9)$$

Where, "*A*" stands for Li, Na, K, Cs etc.; "*M*" represents Fe, Cr, Si, Mn, Nb, Mo, W etc.. Such oxides $A_xM_yO_z$ will corrode the heat pipe wick and case, and will make form the micro solid foreign particles in the solvent. Their sizes are usually 10~15nm. Although these oxides are a small amount, they will block up the capillary holes. What is more, they becomes the catalyst to accelerate the reaction.

For manufacture, the capillary wick, the case should be processed carefully, degassed; the alkali metal should be kept pure to be charged in heat pipe. The melting temperature and viscosity of oxides of alkali metal are generally much higher than their elementary substance.

2.3.2 Non-condensable Gas

The more rough, the bigger area and pressure are the solid surface, the more gas amount will be adsorbed. If the surface is cleaned excessively to have small pits, the gas amount can be increased to be 1015 individual/cm^2, the corresponding air mass is 4.8×10^{-8}g. This amount may be larger than that left in heat pipe chamber. If the adsorbed molecule number is *N* per surface unit, the gas molecule mass adsorbed on area *A* is following.

$$M = A\frac{N}{N_0}\mu \quad (10)$$

Where, N_0=6.203×10^{23}/mol, is AFGageiro constant; μ is the average molecular weight of the gas. For air, μ=29.

The heat pipe pressure can be 3Pa by a mechanical pump. The vacuum pressure can be less 10^{-3}Pa by diffusion pump or molecular pump. By theory and performance experiment of high and super high temperature heat pipe, the pressure before charging a high temperature heat pipe is recommended as less than 10^{-4} Pa. At high vacuum degree level, by ideal state equation, the left gas mass in heat pipe chamber can be following.

$$m = \frac{1}{4}\pi d^2 L\frac{\mu_g P}{RT} \quad (11)$$

Where, *d* is the equivalent diameter of the heat pipe; *L* is the length of the heat pipe; μ_g is the average molecular weight of the gas; *P* is the pressure; *T* stands for temperature; *R* is the universal gas constant.

If the heat pipe is 1m long, the dynamic diameter is 10mm, it is vacuumed at 20℃, the relations between the vacuum and gas mass left in sealed system are listed in Table 1.

Table 1. Relations between the vacuum and gas mass left in sealed system.

Pressure, Pa	Mass, g
10	1.24×10^{-7}
1	1.24×10^{-8}
0.1	1.24×10^{-9}
0.01	1.24×10^{-10}
0.0001	1.24×10^{-11}

If a heat pipe is not degassed fully, among the crystal lattices, the remnant gas will be released gradually during operation. Arrhenius studied this process, the response parameter $F(T)$ can be expressed as following.

$$F(T) = C\exp(-\frac{A}{kT}) \quad (12)$$

Where, *C* is a constant; *A* is the activation energy of reaction; *k* is Boltzmann constant, k=1.38^{-23}J/K; *T* is Kelvin temperature. The gas mass produced inside heat pipe is indicated as follows.

$$\dot{m}(t,T) = f(t)F(T) \quad (13)$$

Where, $\dot{m}$ is the mass rate of produced gas during heat pipe operation; *t* is time.

3. TECHNIQUES OF ALKALI METAL CHARGING AND EXPERIMENT

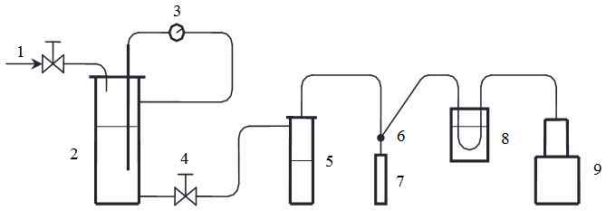
3.1 Charging of Alkali Metal

The alkali metal will be oxidized in the air. For the heat pipe charging, the alkali metal should be protected by inert gas to avoid this reaction.

3.1.1 Distillation Charging Method

For the sodium and lithium working fluid, the distillation charging method to high and super high temperature heat pipes will be processed as: solid→liquid→vapor→liquid→solid.

As illustrated in Fig.2, the distillation system consists of alkali metal tank, valves, distillation tank, cooling sink and vacuum pump assembly etc.. The distillation is accompanied as dynamic vacuum to avoid air leak into the system. In the alkali metal tank, the inert gas is imported to protect the alkali metal. The level meter can display the scale and amount. By distillation of a certain temperature, the alkali metal is cooled to flow into the heat pipe. The cooling sink can stop the alkali metal into the pump.



1.Inert gas; 2.Alkali metal tank; 3.Liquid level meter; 4.Valve; 5.Distillation tank; 6.Tri-connection; 7.Heat pipe; 8.Cooling sink; 9.Molucular pump.

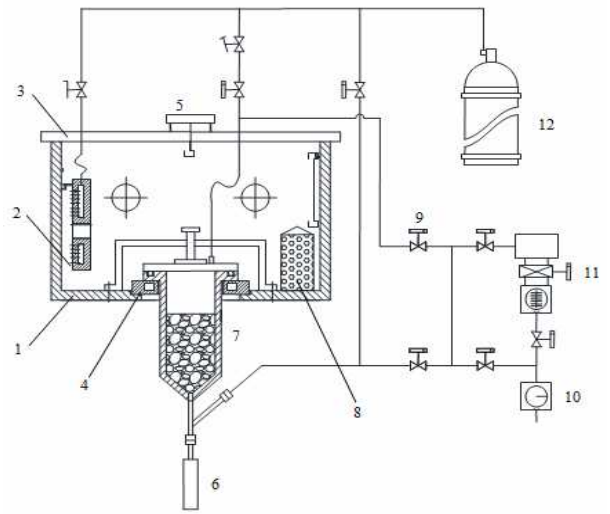
Fig. 2. Distillation charging system of working fluids of alkali metal

3.1.2 Melting Method

The melting method of alkali metal charging was invented. By this way, the alkali metal would be processed as solid→liquid→solid.

Compared with that of distillation, the energy and time consumptions can be reduced a lot, even to more than one order of magnitude. Take sodium for example. The melting temperature is 98℃; the boiling temperature is 882℃ for one atmosphere pressure. For a certain amount of sodium, compared with the non-evaporation, the energy of the heating from 98℃ to 882℃ and then cooling from 882℃ to 98℃, can be saved, one order of magnitude of energy and time are decreased absolutely.

As shown in Fig. 3, the melting charging process is described as following. Under protection of inert gas by valves controlling, the alkali metal can be cut apart into the cylindrical sieve, which is placed in the alkali metal tank beforehand. The scale with hook can display the amount increase. By its bottom triggering, the alkali metal inside the cylindrical sieve is placed in the tank. Through heating outside the tank to a demanded temperature and time, the alkali metal inside tank will be fully melted. Then by valve control, the inert gas will drive the alkali metal into the heat pipe. After degassing the heat pipe, the heat pipe is separated with the system and sealed.



1.Glove box; 2.Cutting board with Inert gas; 3.Transparent cover; 4.Double half cooling support; 5. Scale with hook; 6.Heat pipe; 7.Alkali metal tank; 8.Cylindrical sieve; 9.Valve; 10.Mechanical pump; 11. Molecular pump.

Fig. 3. Melting charging system of working fluids of alkali metal

3.2 Coating of antioxidation outside heat pipe

Generally, the refractory materials can endure high temperature, however their anti-oxidation ability is worse. If the heat pipe works in the oxygen environment, measures much be taken to avoid oxidation. There are three ways to realize anti-oxidation. (1)Protection by inert gas; (2) Alloying of heat pipe case; (3) Coating outside heat pipe case.

Alloying is an effective method to enhance the anti-oxidation of refractory material. However, the mechanical properties of the material will be decreased with the anti-erosion ability. Such as, to increase the anti-erosion ability of Ni base, and Co base metal materials, the contents of Cr and Al should be increased. After a critical ratio, the surface can be oxidized selectively, the thin coating of Cr_2O_3 or Al_2O_3 then can be formed. The following problem is, adding too much Cr content into the Ni base material will lead to brittle phase. Further, too much Al content will also decrease the plasticity of the material, this will worsen the machinability.

The coating outside heat pipe case is commonly Al_2O_3, Cr_2O_3 and SiO_2. The elements of Al, Cr and Si are necessary. The function of Al is to form the thin coating of Al_2O_3. For Cr, it can decrease the critical concentration of Al. The coating is too thin to influence the mechanical property. The coating and the base material can be designed separately to obtain the target heat pipe case.

Base materials of niobium and tungsten are important candidates of super high temperature heat pipe.

Niobium will be oxidized quickly if the temperature is more than 600℃. The better coating of such case heat pipe is Si-Cr-Fe, Cr-Ti-Si or Al-



(a) (b)

Fig. 4. Before (a) and after (b) coating of niobium

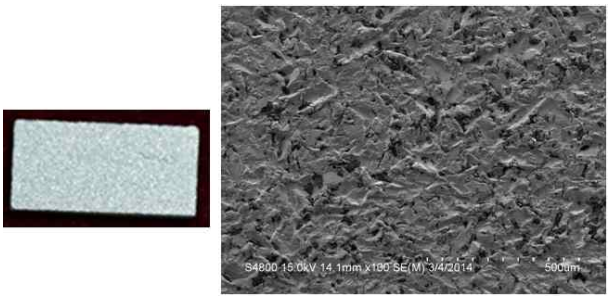
Cr-Si layers. Before (a) and after (b) coating of niobium are shown in figure 7, the coating was realized by the techniques of diffusion and permeation.

The melting temperature of tungsten can reach 3410℃, like niobium, it will also be oxidized in oxygen environment. For the oxygen operation of above 1200℃, one Pt film can be realized by electroplating or chemical plating. The tungsten in the electrolyte solution can also be oxidized easily, the Pt film is hard to be uniform. For this situation, the transition layer can be considered to be formed firstly, then one 2~5μm thickness, uniform and dense Pt film can be coated by electroplating.

As shown in Fig. 5, tungsten plate was coated with Pt film of 5μm thickness.

3.3 Heating mode of heat pipe experiment

There are usually three ways to heat a high or super high temperature heat pipe. (1)Heating by an electric resistance; (2)Heating by a high frequency circuit; (3) Heating by radiation through a graphite or quartz lamp.

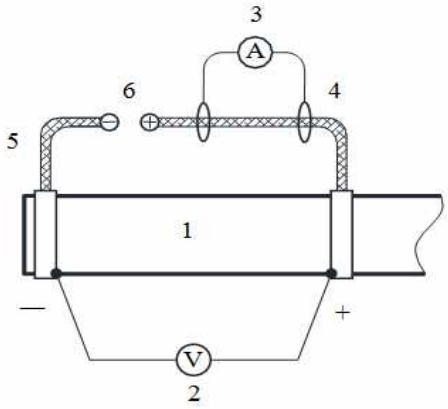


(*a*) overview (*b*) local enlarged

Fig.5. Tungsten plate coated with Pt of 5μm thickness

3.3.1 Heating by Electric Resistance of Evaporator Case of Heat Pipe

If the heating flux to heat evaporator is not big, an electric resistance is commonly used, the evaporator can be twined by the resistance wire. While for the higher temperature heating, the heat pipe case can be treated as an electric resistance. As shown in Fig. 6, sine the heat pipe case has lower electric resistance, low voltage and large current can provide higher heat flux. The positive and negative electrodes of large area can reduce the influence of contact resistance. Due to the smaller measurement range of the ampere meter, current transformer is coupled. The refractory metal case of heat pipe has larger specific resistance compared with good conductors, the heating current can be several hundreds to several thousands amperes, while the voltage is only several voltages. In this case, the special power supply equipment is needed.



1.Heating section of heat pipe; 2.Voltmeter; 3.Ammeter; 4.Current transformer; 5.Cable; 6.DC input.

Fig. 6. Evaporator as an electric resistance, heated and measured by low voltage and high current.

By Ohm law, the heating power is following.

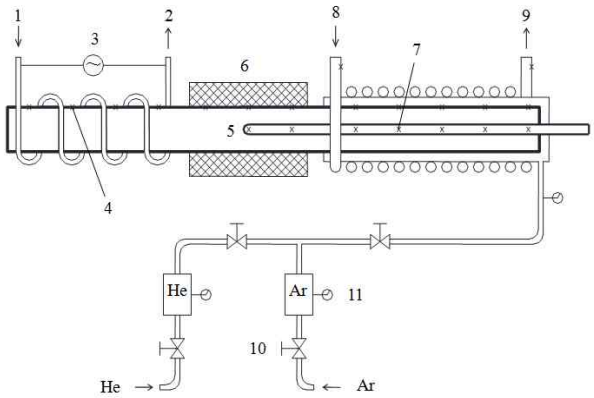
$$Q = I^2 R = \frac{U^2}{R} = UI \tag{14}$$

Where, I is the electric current; R is the electric resistance; U is the voltage.

3.3.2 Heating by High Frequency Circuit

High frequency circuit can transfer power to heat input to heat pipe quickly. If the heat pipe evaporator is put into the circuit spiral, the frequency is about 1MHz, the heat flux can be 300-500W/cm^2. However, the heating flux is not accurate, there are two reasons. One is that the power leakage is serious. The other is that the circuit is made of copper, the cooling water is necessary, it will carry off a large amount of heat. For the temperature measurement, the high frequency will also interfere the thermocouple signal. So, the transferred power should be by the condenser.

One experimental system of high temperature heat pipe by high frequency heating circuit is shown in Fig. 7. To measure the transferred power, there designed one gas layer between the condenser wall and the cooling jacket. Its gap size is only 0.5mm. By the radial conduction and radiation of this gas gap, the cooling water flow rate and temperature difference can define the power from the evaporator. By the gas regulation, the conduction can be also adjusted.



1. 8.Cooling water input; 2. 9.Cooling water output; 3.High frequency power; 4. 7. Thermocouple; 5.Temperature measurement well; 6.Thermal insulation; 10.Valve; 11.Pressure meter.

Fig. 7. Performance testing system of high temperature heat pipe

3.4 Overload Experiment of Heat Pipe

If a heat pipe operates in an environment of vibration or acceleration, the performance will change due to that the capillary flow may be accelerated or choked. The overload experiment setup can realize the performance test of a heat pipe.

The heat pipe has several positions and angles on the rotating setup. The accelerometer can measure the radial, the tangent and the vertical accelerations. The power and the thermocouple connections are by the slip rings.

For less 10g load, 100rpm and 1m radius can realize the experiment on the rotating setup. Under the steady revolution, the acceleration on the capillary flow in the operating heat pipe is uniform. The normal operation demands that the radial overload force should be smaller than the capillary force.

For the capillary wick, if the length is L, the diameter is d, the porsity is ε, the capillary radius is r_c, if the porosity is uniform, then there is.

$$\frac{\pi d^2}{4}\frac{L\varepsilon(\rho_l-\rho_v)}{Ld}a_r \le \frac{2\sigma\cos\theta}{r_c} \tag{15}$$

The ratio of gravity to the capillary force can beexpressed as Bond number as.

$$Bo=\frac{a_r(\rho_l-\rho_v)dr_c}{\sigma} \tag{16}$$

Considering Equations(15,16), there is.

$$\mathrm{B}o \le \frac{8\cos\theta}{\pi\varepsilon} \tag{17}$$

If the acceleration will block the liquid return up, when the overload is added to a heat pipe, the equality sign of Equation (17) gives the boundary of critical normal flow return. If the working fluid wets the capillary wick fully, the wetting angle θ=0. If the porosity value, ε=0.4, then there is, Bo≤6.37.

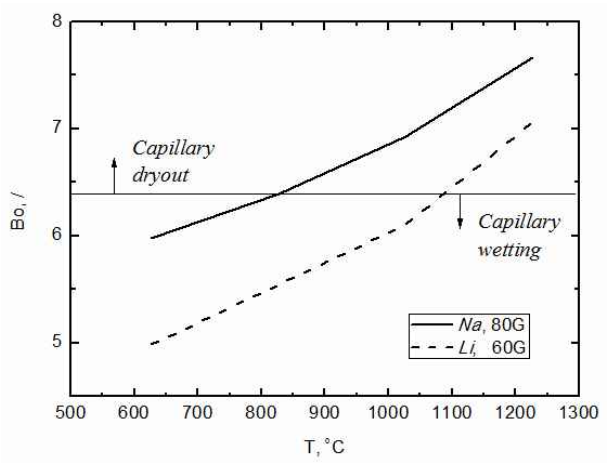


Fig.8. Bond number versus temperature of sodium and lithium heat pipes with artery capillary wick

For the liquid artery heat pipe of sodium and lithium respectively, Bond number versus acceleration g, is illustrated in Fig.8.

For sodium heat pipe, when the acceleration is 80g and lithium heat pipe, when the acceleration is 60g, the temperature has one definite boundaries to operate normally, they are 820 ℃ and 1080℃ respectively.

4. CONCLUSIONS

There are seven results for mechanism and techniques on high and super high temperature heat pipes as follows.

(1) For the working fluid of sodium and lithium, atom dimer will differ depend on temperature, and affect the physical properties of vapor essentially.

(2) The solid state and low vapor pressure of alkali metal will lead to continuous flow limit during startup, and the temperature distribution of heat pipe will be affected.

(3) The possible non-compatibility products include both the oxide of outphase jelly and the non-condensable gases, they are due to the micro cell erosion mechanism.

(4) The heat pipe charging method of distillation was compared with that of the innovated melting technique, the energy consumption and time will decrease less one order of magnitude.

(5) The technique of high temperature endurance and antioxidation coating outside heat pipe is

discussed and realized.

(6) The three experimental methods of heating evaporator are summed up.

(7) For overload experiment of heat pipe, the Bond number will define the boundary of capillary dryout and wetting, its effects are given.

REFERENCES

[1] Liang J. and Cao Y., Closed-form analytical solutions for the radially rotating miniature high-temperature heat pipes including non-condensable gas effects, *Int. J. of Heat & Mass Transfer*, 43 (2000), 3661-3671.

[2] Jang J., Faghri A. and Chang W. et al., Mathematical modeling and analysis of heat pipe startup from the frozen state, *J. of Heat Transfer* (1990), 112, 586-594.

[3] Qu W., Progress Works of High and Super High Temperature Heat Pipes, *Chapter 25, Heat Transfer, InTech* (2011), *525*-549.

[4] Qu W., Ai B. and Yu J., Precise differential mechanism, sodium charging equipment and heat pipe performance, *Proceedings of the 17th Int. Heat Pipe Conference* (2013), India, 20-25.

[5] Jacobson D. L. and Soundararajan P., Failure analysis of a sodium heat pipe with integral lithium fluoride thermal energy storage, *Preprints of Proceedings of the 5th Heat Pipe Conference* (1984), Tsukuba Japan, 115-120.

[6] Faghri A. and Cao Y., Numerical Analysis of Leading Edge and Nosecap Heat Pipes, Advances in Heat Pipe Science and Technology, *Proceedings of 8th Int. Heat Pipe Conference*, Beijing, Int. Academic Publishers (1992), 303-308.

Experimental Investigate on Heat Transfer Performance of Flat Heat Pipe Receiver in Solar Power Tower Plant

Lin Yang [1], Rui W. Zhou[1], Xiang Ling[1*], Hao Peng

[1] *School of Mechanical and Power Engineering, Nanjing Tech University, Nanjing 5 Xin Mo Fan, China*

Abstract

In this study, a novel high temperature two-phase closed flat heat pipe was proposed and investigated experimentally. Compare to other traditional flat heat pipe, this heat pipe Serrated fins inside the closed container, which composes a flat vapor chamber formed evaporator, adiabatic and condenser, and small amount of liquid sodium filled in it. This new structure could increase the heat transfer surface area and accelerate the rate of evaporation and condensation. Experiments were carried out to investigate the temperature uniformity of FHPR under the normal conditions. It is found that the FHPR has well feature of uniformity and stability through startup process experiments with constant heat flux. This research provides guidance for the research and development of flat heat pipe solar receiver, and has important significance for broadening its application in the field of heat utilization of solar energy at high temperature.

Keywords: heat pipe; solar energy; sodium; temperature uniformity

1. INTRODUCTION

Heat receiver is an important component of solar tower power system which plays a decisive role in stable operation. The receiver can deliver thermal power to the working fluid at high flux from 0.3 MW/m^2 to 1MW/m^2 and its working temperature can be higher than 1000℃ [1,2]. The solar incidence flux reflected by heliostat field is inconstant and has a serious effect on stable running and service life of the heat receiver. The flat heat pipe technology is introduced to heat receiver aiming at these problems, which can provide power uniformly and nearly isothermally to the working fluid resulting improved heat receiver performance.

Kun [3] proposed an integrated simulation approach, which couples Monte Carlo ray tracing and Gebhart methods to simulate solar radiation transfer in a solar power tower system with a cavity receiver. Xu et al. [4] puts forward an innovative receiver design for high-temperature solar dish system. The novel design has both the advantages of a honeycomb configuration in enhancing heat transfer performance and uniform flux distribution. At the same time, the design is bundled using tapered tube. The structure of the receiver is simple and the cost is cheap. Luo [5] proposed a novel central receiver design to improve solar tower power efficiency. It combined an external and cavity receiver for boiling and superheating sections. Most established solar tower power plants use water as the heat transfer fluids (HTF), which are mature and cost-effective configurations without extra energy storage requirements. Recently, some researchers have investigated the possibility of separating the boiling and superheating sections. A patentwas filed in 2011 that comprised two external cylinder receivers in series, one for the boiling section and the other for the superheating section [6].

Heat pipe is an excellent heat transfer component, and it has been applied to solar receiver. Because of its importance and technique complexity, heat pipe receiver is the component of advanced solar energy system which has been devoted the most since 1980s. Since then, numerous studies have been carried out. Lu et al. [7] investigated the heat absorption performances of heat receiver with spirally grooved pipe. The basic physical model of heat absorption process was proposed using the general heat transfer correlation of molten salt in spirally grooved pipe. As a conclusion spirally grooved pipe can be a very effective way for heat absorption enhancement of solar receiver, and it can also increase the operating temperature of molten salt. Zhu [8] designed a new type of compound parabolic concentrator solar air collector with flat micro-heat pipe arrays. The instantaneous efficiency could reached 62%. Buttinger et al. [9] developed and investigated a new flat stationary evacuated CPC collector. They reported that heat loss reduction by using thin inert gases is as important as radiation concentration.

*Corresponding author: xling@njtech.com,
Phone: +86-13305196705, Fax: +86-25-83587570

Thermal test confirmed the theoretical results that collector efficiencies greater than 50% are possible at working temperature of 150°C at standard conditions

Based on literature observations, very little attention has been paid to study flat heat pipes receiver applied on solar power tower plant.

2. THE NOVEL FHPR

A novel high temperature two-phase FHPR, illustrated in Fig. 1 was developed and a prototype is fabricated. Fig.2 show the working principal of the novel two-phase FHPR, which is a passive high performance heat transfer device. Serrated fins inside the closed container, which composes a flat vapor chamber formed evaporator, adiabatic and condenser, and small amount of liquid sodium filled in it.

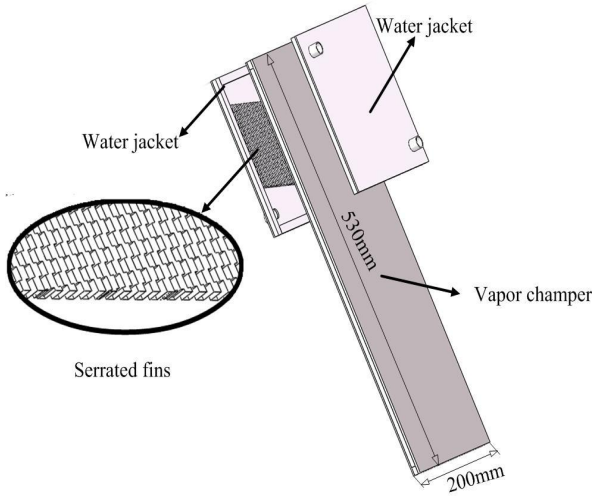


Fig.1 The structure of solar receiver

In such a device, heat is supplied to the evaporator wall, which causes the liquid contained in the pool to evaporate. The generated vapor then moves upwards to the condenser. The heat transported is then rejected into the heat sink by a condensation process. The condensate forms a liquid film which flows downwards due to gravity. The vapor chamber is made of Stainless steel 310s and is constructed of two flat plates with 3 mm in thickness and a frame. Its size is 530mm*200 mm*12 mm with the evaporator, adiabatic and condenser section lengths are 200, 130, 200 mm respectively. The condenser section is composed of water jackets. One side water jacket is 200 mm in height, 200 mm in width, and 9 mm in thickness. Serrated fins brazed inside the vapor chamber and water jackets act to enhance the heat transfer performance, are 6 mm in height, 2 mm in pitch, and 0.2 mm in thickness. Fig. 3 shows the structures of these serrated fins. The prototype was evaluated experimentally to determine the operational and performance characteristics.

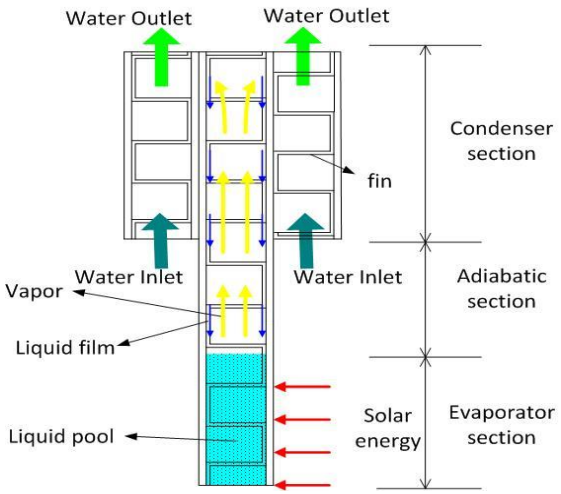


Fig.2 The working principal of solar receiver

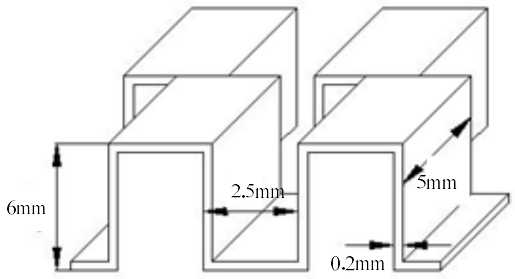


Fig.3 The structure and parameters of fins

3. EXPERIMENTAL SETUP

The experimental test facility shown in Fig.4 was developed and experiments were conducted to evaluate the heat transfer performance of the test sample described above, over a wide range of test conditions. The exprimental system was composed of a vacuum-pumping system, liquid sodium filled system, a test section, a forced-feed water circulation system, a heating unit and mesurement system, and a data acquisition system. A PC was used to monitor, log, and process the experimental data. While liquid sodium shows potential for solar thermal power systems due to its wide range of operation temperatures, it has been carried out to determine their suitability for use in high temperature concentrated solar thermal central-receiver systems for power generation. Before charging the working fluid-Na, the FHPR enclosure was evacuated and maintained at a vacuum pressure of 10^{-3} mbar by using vacuum pump and molecular pump. During the vacuum pumping process, temperature of the

FHPR was heated over 200℃ in order to remove the non-condensable gases. Then the required amount of working fluid-Na is charged while the vacuum line is closed. After the charging process, the two-phase FHPR is vacuumized again in order to extract as much residual air as possible. The filling rate of the working fluid is 40%.

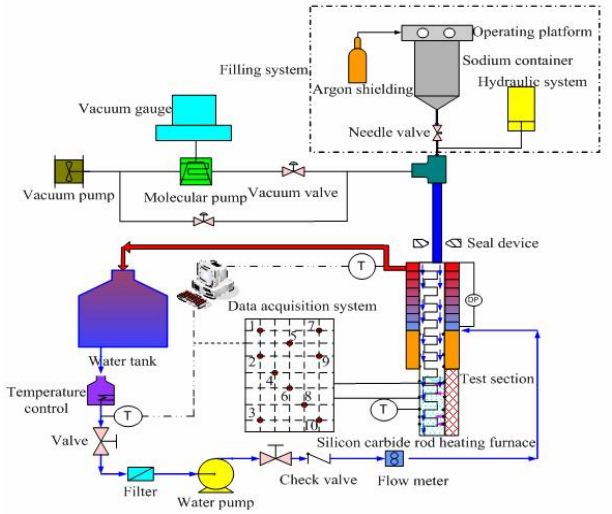


Fig. 4 Schematic of the experimental setup

After the charging working fluid process, instrumentation is made for the FHPR performance analysis. The heating heat flux is supplied by the silicon carbide rod heating furnace connected with wattmeter and variable transformer. Adjusting the output voltage of the transformer can control heat input at one side of the evaporator section of FHPR.

A forced-feed water circulation system included a constant temperature water bath and a water pump. The water circulated through the condenser section of FHPR with a constant flow rate of 0.5 m^3/h is supplied with a constant temperature, where heat was removed from the condenser section by forced convection, and then to a constant-temperature water bath. The constant-temperature water bath was set to the required temperature and held at a constant temperature through the tests.

The entire evaporator and adiabatic section of FHPR was thermally insulated with fiber glass material to minimize the convective losses from the outer surface to surroundings. The measure equipment in experiment includes a flow meter, a differential pressure transmitter and thermocouples. The uncertainties of the experimental results mainly depend on the precisions of these equipment. The precision of flow meter is 0.5% and the precision of differential pressure transmitter is 0.25% which has been determined by producers. In order to monitor the temperature variations along non heating evaporator surface of the FHPR, ten thermocouples were attached to the outer surface of the FHPR as the thermocouples position illustrated in Fig.4. In addition, the inlet and outlet temperature of cooling water are also recorded. Before experiment, all of thermocouples have been verified by standard thermocouple. Those thermocouples were directly connected to a data acquisition/switching system NI-PXI 8102 controlled and processed by a PC. The accuracy of thermocouple including the uncertainty in the data logger is ±0.2 ℃.

4. RESULT AND DISCUSSIONS

The main goal of this study was to investigate the effects of important parameters on the surface temperatures of the evaporator and the condenser section of the FHPR. In the experiment process, The FHPR was heated by silicon carbide rod heating furnace from room temperature to a state of equilibrium. In fact, the input power of 1.5kW includes heat absorption of FHPR and heat absorption in furnace chamber, due to both of FHPR and heating furnace heated from room temperature.

Fig. 5 shows its transient temperature response in the startup process. Fig. 6 also illustrates the wall temperature distribution of the FHPR surface of the experimental results during startup. The filling amount of liquid sodium is 93.12g. The room air temperature is 27.5 ℃ and the water that flows on the condenser section of FHPR is 0.517 m^3/h. From Fig. 5 and Fig. 6 we can see that FHPR could startup normally while heated one side of evaporator. The measured temperature in the other no heated surface had similar startup temperature curves and the transformation temperatures of evaporation section and condenser section is identical respectively. So the FHPR has favorable feature of temperature uniformity. Worth mentioning at this time is the

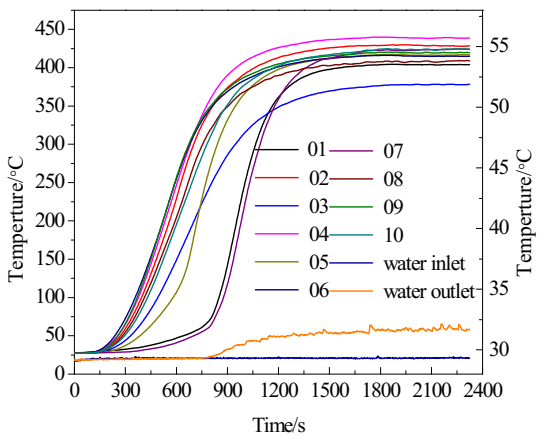


Fig.5 Temperature curve of FHPR during startup process with input power of 1.5Kw

measured temperature is a little bit lower than the actual temperature, which is because the heat dissipation to environmental and the outer surface temperature is lower than the inner surface measured by thermocouples.

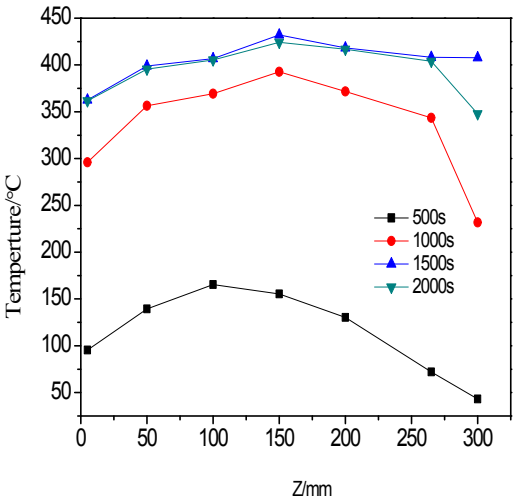


Fig. 6 Wall temperature distribution of FHPR during startup

The analysis will be presented in the following two aspects during startup process, the working substance physical property and the regimes of vapor flow in the FHPR. Working medium (liquid sodium) was frozen before heated. Heat transfer was mainly by conduction. Then liquid sodium was in solid-liquid phase transition state in evaporator section after heat one side of evaporator about 6~8 minutes. Vapor generated at the surface of liquid sodium pool when continuously heat. However, the vapor is free molecular flow in the vapor chamber region bring on the pressure is low. Simultaneously, temperature of adiabatic and condenser section is lower, the sodium in the FHPR which no contact to the parts of the furnace chamber is still in a state of solidification. At this time, working medium coexists in three states: solid, liquid and vapor in the FHPR. As expected, the surface temperature of FHPR is increasing as the heating time is increasing, after about 14 minutes, rising rate of temperature decrease gradually. As the vapor contents increases, free-molecule flow transformers to continuum flow. Corresponding to the second inflection points of curve 5 in figure 5, the sodium in the adiabatic section has been completely melted, and the vapor is in a state of transition flow. The vapor continued to flow to the condenser section lead to temperature of condenser section increase. Corresponding to the first inflection points of curve 1 and 7 in figure 5, the physical state of sodium was from vapor-liquid-solid coexistence to vapor-liquid coexistence. Moreover, the temperature difference between the inlet and outlet of water suddenly increased indicated that FHPR startup. With the heating time increased to 25 minutes later, all the curves in figure 5 tend to get horizontal meant that the vapor in the vapor chamber of FHPR converted to continuum flow regimes. From figure 6, we also can see the temperature of each point varies slightly and achieved a certain temperature after 25 minutes. Meanwhile, the temperature of condensation section is 450℃ which is the actual transition temperature of vapor in the transition from free-molecule flow to continuum flow.

5. CONCLUSION

The heat transfer performance of FHPR applied on solar power tower plants was analyzed experimentally in the present work. In the FHPR, sodium serves as working medium and absorbs heat from evaporator. The generated vapor sodium then moves upwards to heat dissipation process at the condenser. The FHPR has well heat transfer performance and improved feature of temperature uniformity.

ACKNOWLEDGEMENT

The authors acknowledge the financial support provided by funds of the program of National Natural Science Foundation of China (Grant no. 51176071).

REFERENCES

[1] Manuel R, Reiner B, James E.P, An update on solar central receiver systems, projects and technologies, *ASME J Sol Energy Eng*. 124(2) pp:98~108.
[2] Chavez J M. Development and testing of advanced central receiver. *IECEC,*(1991)
[3] Wang K, He Y.L, Qiu Y, Zhang Y.W., A novel integrated simulation approach couples MCRT and Gebhart methods to simulate solar radiation transstem[J]. *Applied Thermal Engineering*. 91
[4] Xu G. Q., Wang Y., Li H. W., Li S., Design and characteristics of a novel tapered tube bundle receiver for high-temperature solar dish system.[J] *Applied Thermal Engineering*. 2015(91):791-799.
[5] Lou. Y., Du X., Wen D.S. Novel design of central dual-receiver for solar power tower[J] *Applied Thermal Engineering*. 2015(91):1071-1081
[6] Gonzalez, M.S., Gonzalez-Aguilar R.O., Quero V.F., Gilaberte R. N., Solar concentration plant for the production of superheated steam, in, Google Patents.2013
[7] Lu J.F., Ding J. Yu T., Shen X.Y. Enhanced heat transfer performances of molten salt receiver with

spirally grooved pipe, *Applied Thermal Engineerin*g. 88(2015):491-498

[8] Zhu. T.T., Diao Y.H, Zhao Y.H., Li F.F., Thermal performance of a new CPC solar air collector with flat micro heat pipe arrays. *Applied Thermal Engineering* 98(2016) 1201-1213.

[9] Buttinger F., Beikircher T., Pröll M., Schölkopf W.. Development of a new flat stationary evacuated CPC-collector for process heat applications. *Sol. Energy*, 84 (2010), pp. 1166–1174

Influence of Charging Ratio, Annular Clearance and Enhanced Boiling Surface on the Thermal Performance of Bubble Jet Loop Thermosyphon

Jongsoo Kim[1*], Sungbok Kim[2] , Sangjin Park[2] , Junha Kim[2] , Jaeyoung Bae[2],
Eonhwa Hwang[2] , Dobin Kim[2] ,and Intaek Oh[2]

[1]*School of Engineering, Pukyoung National University, 365 Sinseonro, Namgu, Busan, 608-739 Korea*
[2] *Graduate School of Pukyoung National University 365 Sinseonro, Namgu, Busan, 608-739 Korea*

Abstract

This paper discusses the basic principles of operation of the Bubble Jet Loop Thermosyphon (BJLT), flow visualization, optimum charging ratio, and the effect of evaporator surface on the thermal performance of BJLT. Commonly, general thermosyphon is affected by inclination angles and it does not operate well at the horizontal condition. So, we invented and designed a BJLT which can operate well in the horizontal condition by using a jetting bubble which is generated at an annular narrow crevice of the evaporator section. Also, the BJLT can work well even though it has a long condenser section. Therefore, the BJLT can be applied to various fields. We conducted a variety of studies on principle of operation of the BJLT and improving the thermal performance of BJLT. We used R-134a as the working fluid and measured each part, then calculated effective thermal conductivity as an indicator of thermal performance.

Keywords: Annular clearance; Bubble jet loop thermosyphon(BJLT); Charging ratio; Enhanced boiling surface

1. INTRODUCTION

The two-phase closed thermosyphon is a simple but effective heat transfer device. It's a vertically oriented wickless heat pipe with a liquid pool at the bottom. It is similar to the wicked heat pipe but relies on gravity to ensure liquid returns from the condenser to the evaporator. Due to their high efficiency, reliability, and cost effectiveness, thermosyphon have been used in many different applications.[1]

The thermal performance of thermosyphon is greatly affected by the inclination angle. Commonly, thermosyphon has the highest thermal performance when the inclination angle is around 50˚, but it doesn't operate well in horizontal condition.[2]

So the development of thermosyphon which can operate well in the horizontal condition is needed for further utilization. Therefore, we designed and developed the Bubble Jet Loop Thermosyphon (BJLT) which can operate well in a horizontal orientation by using a jetting bubble which is generated at a narrow annular crevice (clearance) of the evaporator section. The BJLT possesses all the advantages of the conventional thermosyphon and it can also be reliably operated even though it has long a condenser section at horizontal orientation.

As a result of this, the BJLT is able to be applied to various fields such as floor heating systems (Ondol), controlled horticulture systems, and snow melting systems.

This paper discusses the basic principles of operation of BJLT, flow visualization, optimum charging ratio and annular clearance, and effect of evaporator surface on thermal performance of BJLT.

2. BUBBLE JET LOOP THERMOSYPHON

2.1 Structure of BJLT

In Fig. 1, you can see the shape and structure of the BJLT. The BJLT is composed of two sections. One is the evaporator section where working fluid is boiled and makes bubbles. The other is condenser section which radiates heat transferred from the evaporator section. The end of the condenser section is connected by a U- tube and it becomes a loop type. Most notably, the length of the condenser section is very long compared with the evaporator section.

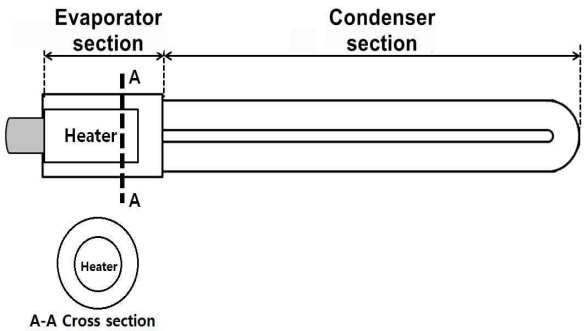


Fig. 1 Schematic of BJLT.

**Corresponding author: jskim@pknu.ac.kr,
Phone: +82-51-629-6368, Fax: +82-51-611-6368

2.2 Principles of Operation

When heat is applied to the evaporator section by a heater, nucleate boiling of working fluid in the evaporator section occurs at the annular clearance between the heater and evaporator section tube, then it vaporizes the working fluid into a number of bubbles and the pressure of the evaporator section rises. Due to pressure differences, the bubbles move to the condenser section where the bubbles are then condensed, releasing its latent heat. Then, condensed fluid returns to the evaporator section.

Because of the nucleate boiling at a narrow and annular clearance, it can create a lot of bubbles and pressure difference. Therefore, the circulating bubbles can move heat from the evaporator section to the condenser sector in the horizontal orientation.

3. EXPERIMENTAL SET UP AND METHOD

A schematic of experimental setup is shown in Fig. 2. We used an electric cartridge heater, and the power of the heater was supplied by using power meter sand slidacs. Temperature was measured at one point of the evaporator section and at three points of condenser section through T-type thermocouples. Then, we calculated the effective thermal conductivity with experimental results by equation (1), and compared them.[3]

$$k_e = \frac{Q \cdot L_{eff}}{A_{cs}(T_{es} - T_{cs})} [kW/mK] \quad (1)$$

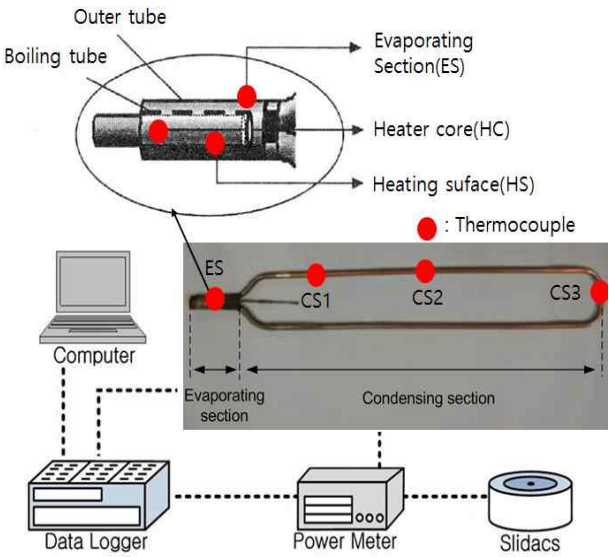


Fig. 2. Schematic of experimental setup of BJLT.

Table 1. Specification of BJLT.

Container material	Copper
Working fluid	R-134a
Length of evaporator section	90mm
O.D. of evaporator section	25.4mm
Length of condenser section	1,700mm(loop)
O.D. of condenser section	12.7mm
Charging ratio	50%

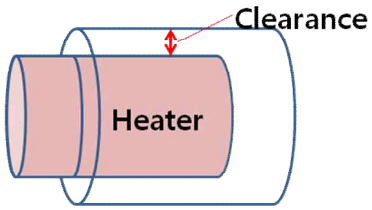


Fig. 3. Clearance of the evaporator section of BJLT.

3.1 Flow visualization

We used a specifically formulated pyrex tube to conduct the visualization experiment of the BJLT. The working fluid was water, and the experiment is conducted at atmospheric pressure. We took a high speed video with a digital camera.

3.2 Optimum charging ratio

We changed the working fluid charging ratio from 30% to 70% of inner volume of the BJLT, measuring every 10%.

3.3 Effect of evaporator clearance on thermal performance

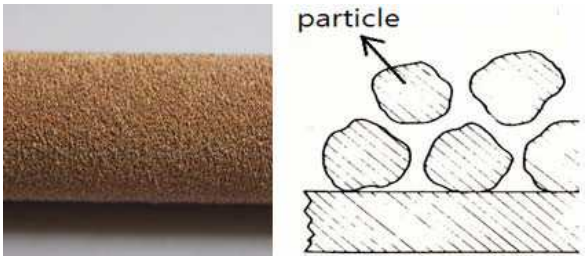
The clearance is an annular narrow gap between the heater and evaporator section tube(Fig.3). We changed the clearance by changing the outer diameter of the evaporator section and fixing the diameter of the heater. Specification is shown in table 2.

Table 2. Specification of clearance.

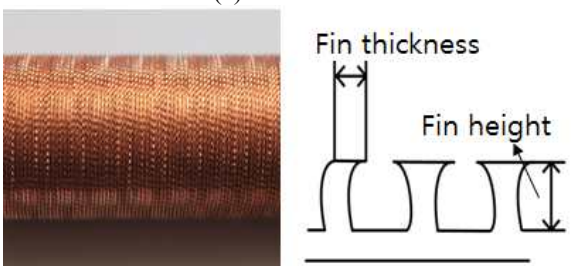
	O.D. of evaporator section	Clearance
Case 1	17.40mm	0.79mm
Case 2	20.22mm	2.17mm
Case 3	23.40mm	3.76mm

3.4 Effect of evaporator surface on thermal performance

We used smooth tube, sintered tube and GEWA-T tube as heater surfaces to investigate the effect of



(a) Sintered tube



(b) GEWA-T tube

Fig. 4 Enhanced boiling surface

the evaporator surface on thermal performance. Fig.4 is a picture of the surface of the sintered tube and GEWA-T tube(facilitate boiling tube). The sintered tube is sintered with copper particles (0.18mm~ 0.25mm) in the copper tube, and the GEWA-T tube is the commercial GEWA-T high flux tube which has a re-entrance cavity.

4. RESULT OF EXPERIMENT

4.1 Flow visualization

The nucleate boiling occurs at the evaporator section. The small bubbles which are caused by nucleate boiling go up due to a gas-liquid density difference of working fluid, and joining other bubbles, they become big bubbles. Then, they move to the condenser section by pressure difference (Fig.5). The flow of the condenser section is shown as the form of a two-phase flow such as wavy flow,

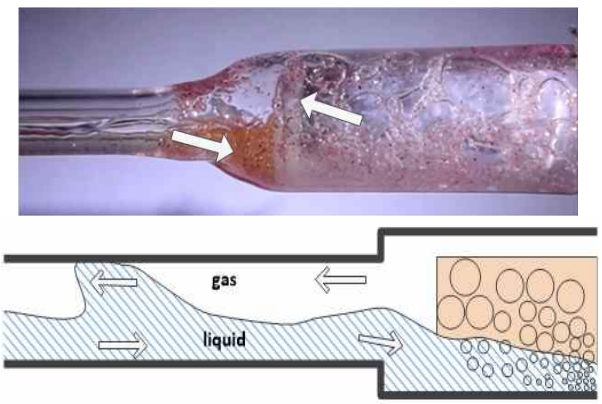


Fig. 5. Nucleate boiling at evaporating section and schematic diagram of evaporating part.

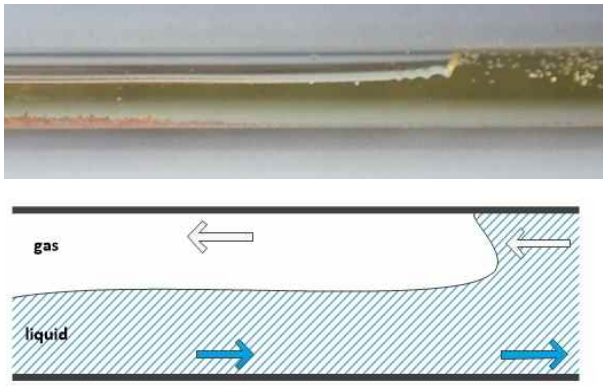


Fig. 6. Flow visualization and schematic diagram at condenser section.

slug flow, and stratified flow(Fig.6). The wave at end of the condenser section doesn't dissipate after they crash, and it returns to the evaporator part circulating through the loop tube (U-tube).

4.2 Optimum charging ratio

Fig.7 is the graph showing variations of effective thermal conductivity with charging ratio. When the charging ratio is 30~50%, the more the charging ratio increases, the more effective thermal conductivity increases. This is because the surface of the heater is more re-wetted with an increase of the charging ratio. However, effective thermal conductivity sharply falls over 50%. This is due to the excessive height of liquefied working fluid and the decreasing of an area of condensation heat transfer at the condenser section.

4.3 Effect of evaporator clearance on thermal performance

The result of the experiment is shown in Table 3.

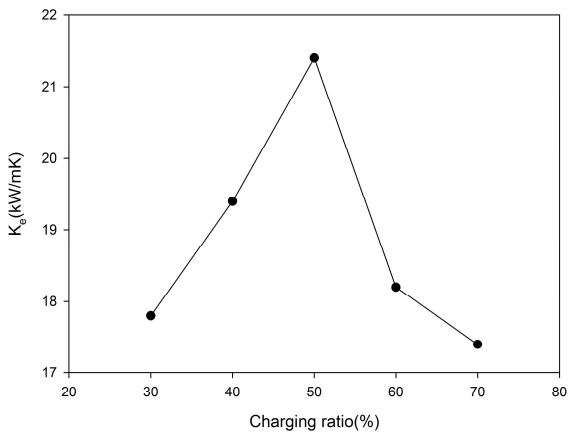


Fig. 7. Effect of charging ratio on effective thermal conductivity.

When clearance is 2.17mm, the effective thermal conductivity is highest under the same heat input condition. This result of experiment suggests that there is optimal clearance of BJLT according to the specification of each BJLT.

Table 3. Effective thermal conductivity according to clearance.

	Clearance	25W	50W	75W
K_e (kW/m·K)	0.79mm	5.09	2.53	0.33
	2.17mm	9.29	5.69	0.52
	3.76mm	4.81	3.53	0.27

4.4 Effect of evaporator surface on thermal performance

Table 4 shows the effective thermal conductivity according to the type of heater surface. The effective thermal conductivity of BJLT using an enhanced boiling surface such as GEWA-T tube and sintered tube is higher than BJLT using a general smooth tube. In particular, when we used sintered tube as the heater surface, the effective thermal conductivity is over 300% higher than using a smooth tube.

Table 4. Effective thermal conductivity according to evaporator surface.

		25W	75W
K_e (kW/m·K)	Smooth tube	10.1	10.7
	GEWA-T tube	27.4	19.2
	Sintered tube	36.1	32.1

5. CONCLUSIONS

We developed and designed the Bubble Jet Loop Thermosyphon(BJLT) which can work normally at horizontal orientation. Conclusion of each experiment to improve thermal performance of BJLT is as follows.

(1) Nucleate boiling at the clearance of evaporator section makes enough bubbles to circulate the working fluid as a two phase flow. Due to this, the BJLT can operate well in a horizontal condition.

(2) Optimum charging ratio of working fluid of the BJLT is 50% of inner volume.

(3) Clearance has influence on the thermal performance of the BJLHP. There is an optimal clearance according to the specification of each BJLT. In our experimental conditions, the effective thermal conductivity is highest when clearance is 2.17mm.

(4) Evaporator surface affects the thermal performance because nucleate boiling occurs on the surface of the heater of the evaporator section. When using an enhanced boiling surface, effective thermal conductivity is higher than when using a general smooth tube. In particular, when using sintered tube as heater surface, the effective conductivity is highest.

NOMENCLATURE

K_e : Effective thermal conductivity (kW/mK)
Q : Quantity of heat (W)
L_{eff} : Effective length (m)
A_{cs} : Cross section area of condenser section (m^2)
T_{es} : Temperature of evaporator section (K)
T_{cs} : Temperature of condenser section (K)

REFERENCES

[1] Amir Faghri., *Heat pipe science and technology*, Taylor and Francis, 1995

[2] The Japan Association for Heat Pipe., *Practical heat pipe*, Nikkan Kogyo Shimbun, 2001

[3] Ready, D. A. and P. A. Kew., *Heat pipes*, 5th ed., Butterworth Heinemann, 2005

[4] Kim, J. S. and Shin, J. S., Development of a High Performance Bubble Jet Loop Heat Pipe Using the Enhanced Nucleate Boiling Surface in Evaporating Section, *Korea Society of Mechanical Engineers*, Vol. 39, No. 4 (2015) 363-367.

[5] Jung, D. G., Woo, J. H., and Kim, J. S., 2011, A study on heat transfer and flow characteristics of bubble jet loop heat pipe, *Proceeding of the KSME conference*, (2011) 775-780.

[6] Hwang, J. H., An experimental study to bubble jet pulsating loop heat pipe, *Proceedings of the KSME 2009 spring annual meeting*, (2009) 263-267.

[7] Hwang, E. H., Park, S. J., Kim, J. H., Kim, D. B., and Kim, J. S., Nucleate Boiling Flow Visualization of Enhanced Heat Transfer Surface in Narrow Annular Spaces, *Proceedings of the SAREK conference*, (2015)326-330.

[8] Jung, H. S., Bui, N. H., Kim, J. H., and Kim, J. S., Basic study on looped oscillating heat pipe, *Proceedings of the KSME conference*, (2001)169-173.

[9] Shin, J. S., Kwon, Y. H., and Kim, J. S., The study of BJLHP performance according to the shape of evaporating section, *Proceedings of the SAREK conference*, (2013)21-25.

[10] Kim, J. S. and Kim, S. B., Thermal Performance of the Bubble Jet Loop Heat Pipe Using Eccentric Heater in Evaporating Section, *The Society of Air-conditioning and Refrigerating Engineers of Korea*, Vol. 27, No. 12 (2015)652-658

A New Modified Model for Simulation of a Two-phase Closed Thermosyphon

Houfa Shen[1],Yucan Fu[2], Jiajia Chen[3*]

1 Graduate Student, Nanjing University of Aeronautics and Astronautics, Nanjing, CHINA
2 Professor, Nanjing University of Aeronautics and Astronautics, Nanjing, CHINA,
Phone: +86 25 84895857, e-mail: yucanfu@nuaa.edu.cn
3 Graduate Student, Nanjing University of Aeronautics and Astronautics, Nanjing, CHINA

Abstract

As a two-phase heat removal divice, heat pipes are playing an more important role in industrial applications. Two phase closed thermosyphons are special type of heat pipes having no wicking material. In this paper, numerical simulation of a vertical two phase closed thermosyphon is performed using the Mixture model and UDF(user defined fuction) in FLUENT 6.3. In order to simulate the condensation more accurately, a new method to caculate the mass transfer rate with real-time updated coefficient of condensation is proposed basic on the previous simulations. The effects of phase change, two phase flow and interfical force are taken into account within the whole domain. The simulation results displayed the evaporation and condensation process clearly and revealed the temperature distributions of thermosyphon have a close relationship with two phase flow.

Keywords: Thermosyphon, Mixture, Evaporation, Condensation, UDF

1. INTRODUCTION

The two-phase closed thermosyphon is an important industrial device with highly effective heat transfer rate through evaporating and condensing its working fluid. In a thermosyphon, heat is added to the evaporation section where a liquid pool exists and then the vapour will be produced in the liquid pool. The produced vapour flows through the adiabatic section towards the condenser due to the pressure defference and exchanges heat with the cold environment in the condenser. The condensates then flow back to the evaporator due to gravity[1]. Thus, a comprehensive CFD modelling was implemented to simulate the details of two-phase flow and temperature distributions inside.

In recent years, numerous studies on CFD numerical simulation of two-phase closed thermosyphons have been published. De. Schepper[2] simulate the process of flow boiling in heat exchanger by integrating the Lee model with ANSYS/FLUENT 13.0. They proposed correlations to caculate the mass and heat transfer between the phases. Although it's feasible to simulate the process of boiling by integrate the Lee model to the solver of FLUENT, it is uncertaim using this way to simulate evaporation and condensation at the same time.

Alizadehdakhel[3] simulate the two-phase flow that include mass and heat trasfer in thermosyphon by using the VOF and UDF techniques. They considered the influence of non-condensable gases to the condensation of saturated vapour. Therefore, they add a coefficient to the correlations when caculating mass and heat transfer.

Fadhl[4,5] studied the temperature distribution and the mechanism of the two-phase flow in thermoyphon by applying the same way with Alizadehdakhel. They discussed the effect of different working liquid of R134a, R404a and water on the operating performance of theromsyphon. The temperature distributions showed good agreement with the experimental data.

Kafee[6] developed a model to simulate the two-phase flow and temperature distribution by using the Euler model and UDF techniques. They improved the correlations to caculate the mass and heat transfer between the phases that were able to simulate the evaporation and condension more accuratly. The axi-symmetric simulation condition was used to reduce cacilation amount in his research.

Lin[7] carried out an experimental investigation and CFD analysis of a oscillating heat pipe using the Mixture or VOF model and UDF methods. The simulation shown vapour bubbles occurred in evaporation section and the vapour plug oscillated owen to the pressure difference. The results showded that the mixture model was more suitable for the two- phase flow simulation

In this paper, a new modified model for simulation of a two-phase closed thermosyphon is proposed by combining the Mixture model with variable correlations to caculate the mass and heat transfer. The real-time corrected correlation is more suitable to analysis the details of two-phase flow and heat transfer phenomena in thermosyphon.

*Corresponding author: *yucanfu@nuaa.edu.cn*,
Phone: *+86 25 84895857*,Fax: +82-84895857

2.THEORY

Currently there are two approaches for the numercial caculation of multiphase flows: the Euler-Lagrange approach and the Euler-Euler approach. In ANSYS FLUENT, there are three different Euler-Euler approach avaliable: the volume of fluid model, the mixture model and the euler model. In the Euler-Euler approach, different phases are treated mathmatically as interpenetrating continua that means the control volume can be occupied by all phases. Since it is necessary to introduce a concept of phasic volume fraction that used to averaging each phasic property within a control volume. The VOF model, the Mixture model and the Euler model is integrated in Ansys/FLUENT, and can be used to simulate the two phase flow along with heat and mass trasfer[8].

2.1 Volume Fraction Equation

The simulation of two phase flow is accomplished by the solution of continuity equation for the volume fraction of one of the phases. The VOF equation relies on the fact that each cells in computation domain is occupied by one phase or combination of the two phases. In other word, in each control volume, the volume of two phases sum to unity.

If α_v is the volume fraction of vapor (primary phase) and α_l is the volume fraction of liquid (second phase), the following condition is necessary to each volume:

$$\alpha_l + \alpha_v = 1 \tag{1}$$

The volume fraction equation is only solved for second phase and the primary phase volume fraction will be computed based on the equation above. Thus, the volume fraction equation of second phase (vapour) are provided as below:

$$\frac{1}{\rho_v}\left[\frac{\partial}{\partial t}\left(\alpha_v\rho_v\right)+\nabla\cdot\left(\alpha_v\rho_v\vec{v_v}\right)=S_m\right] \tag{2}$$

ρ_v and v_v is the density and velocity of vapour . S_m is the mass source term that is used to compute the mass trasfer rate of phase change. The mixture properties of a control volume, such as velocity and density, is given as the volume-fraction-averged and similar as below:

$$\rho_m = \alpha_l\rho_l + \alpha_v\rho_v \tag{3}$$

$$\vec{v_m} = \frac{\alpha_l\rho_l\vec{v_l} + \alpha_v\rho_v\vec{v_v}}{\alpha_l\rho_l + \alpha_v\rho_v} \tag{4}$$

2.2 Momentum Equation

The momentum equation for the mixture can be obtained by adding the individual momentum equations for all phases. It can be expressed as:

$$\frac{\partial}{\partial t}(\rho_m\vec{v}_m)+\nabla\cdot(\rho_m\vec{v}_m\vec{v}_m)=-\nabla p+\nabla\cdot\left[\mu_m(\nabla\vec{v}_m+\nabla\vec{v}_m^{\,T})\right]$$
$$+\rho_m\vec{g}+\vec{F}+\nabla\cdot\left(\sum_{k=1}^{n}\alpha_k\rho_k\vec{v}_{dr,k}\vec{v}_{dr,k}\right) \tag{5}$$

n is the number of phase, $\vec{F}$ is body force, μ_m is viscosity of mixture. $\vec{v}_{dr,k}$ is the drift velocity for secondary phase k: $\vec{v}_{dr,k}=\vec{v}_k-\vec{v}_m$. In compare to the VOF model, the drift force is considered in the momentum equation of mixture model. Thus the mixture model is more precision.

2.3 Energy Equation

The energy equation for the mixture takes the following form:

$$\frac{\partial}{\partial t}\sum_{k=1}^{n}\left(\alpha_k\rho_kE_k\right)+\nabla\cdot\sum_{k=1}^{n}\left(\alpha_k\vec{v}_k\left(\rho_kE_k+p\right)\right)=\nabla\cdot(k_{eff}\nabla T)+S_E \tag{6}$$

k_{eff} is effective conductivity . S_E is energy source term used to compute the heat trasfer rate of phase change.

2.4 Mass and heat trasfer

The mass and energy source term is added to calculate the mass and heat transfer during the phase change process by linking the user-defined function (UDF) to the coservation equation of FLUENT. UDF is a routine that enables users to define their own source terms that can be linked to the solver of FLUENT. Some popular source terms have been proposed by De Schepper et al.[2], which is shown in Table 1. The value of the relaxation time c_c and c_e used in the model is controversial. Bandar Fadhl et al.[4,5] used the VOF model to simulate the temperature profile of a closed thermosyphon with both c_e and c_c equal to 0.1. However, for a simulation of film condensation, if the value of c_c is too small, a significant difference between the interfacial and saturation temperatures will occur. The solution result will also be unreasonable. Therefore, Zhan Yin et al.[9] simulate the three-dimensional film condensation process with the c_c equals to 5×10^4. An agreement on the evaluation of the c_c and c_e has not been reached yet.

Therefore, in this paper, a method of calculating c_e and c_c is proposed. Due to the value of c_e and c_c has a close relationship with the rate of heat and mass transfer, c_e is decided by the experimental results and c_c is real-time updated according to the value of c_e.

Table 1. Construction of mass and energy sources

	Evaporation ($T_{mix} > T_{sat}$)	Condensation($T_{mix} < T_{sat}$)
Liquid phase :	$S_m = -c_e \alpha_l \rho_l \left\| \frac{T_{mix}-T_{sat}}{T_{sat}} \right\|$	$S_m = c_c \alpha_v \rho_v \left\| \frac{T_{mix}-T_{sat}}{T_{sat}} \right\|$
vapor phase:	$S_m = c_e \alpha_l \rho_l / \frac{T_{mix}-T_{sat}}{T_{sat}} /$	$S_m = -c_c \alpha_v \rho_v / \frac{T_{mix}-T_{sat}}{T_{sat}} /$
Energy:	$S_E = -Lc_e \alpha_l \rho_l / \frac{T_{mix}-T_{sat}}{T_{sat}} /$	$S_E = Lc_c \alpha_v \rho_v / \frac{T_{mix}-T_{sat}}{T_{sat}} /$

When thermosyphon works in a steady state, a balance between the evaporation rate and the condensation rate should be reached. Therefore, the relaxation time for condensation c_c can be decided according to the same phase change rate and the steady state can also be judged by the stste of c_c . The corresponding relaxation time for condensation have been caculated using the formula:

$$c_c = c_e \alpha_l \rho_l \left| \frac{T_{eva} - T_{sat}}{T_{sat}} \right| \Big/ \left(\alpha_v \rho_v \left| \frac{T_{con} - T_{sat}}{T_{sat}} \right| \right) \qquad (7)$$

The solving process of c_c is to caculate the total mass of evaporation and condensation within the time step, store these values to the UDM(user define memory) and then solve the equation at the end of the time step. Besides, the latent heat and saturated temperature in this table is decided by the experimental results.

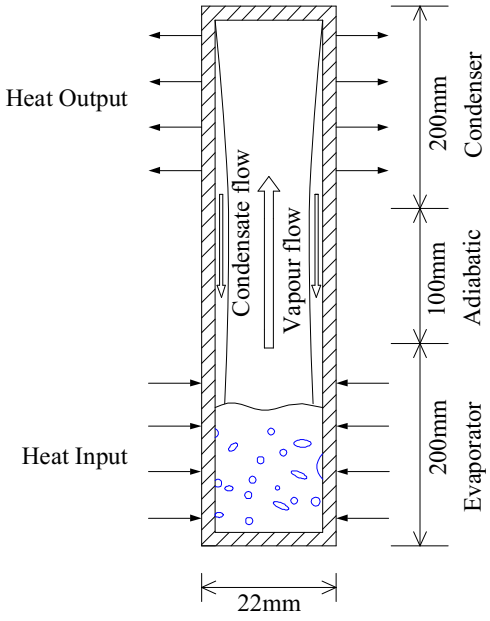


Fig.1. Geometry of thermosyphon

3. CFD MODELING

The 2-D CFD analysis presented in this study was performed by FLUENT 6.3.

3.1 Mesh geometry

The thermosyphon model used in this study is taken from the expremental study of Bandar and Luiz[3], as can be seen in Fig.1, with 500mm and 22mm for the total length and diameters. The thermosyphon can be divided into three sections: the evaporator, adiabatic and condenser. The length of the evaporator and condenser is 200mm and the length of adiabatic is 100mm. The thermosyphon model is meshed by the quadrilateral cell and refined mesh used in the zone where the two-phase flow and heat and mass trasfer will happen. The 2D mesh with 69,092 cells for the total cells is shown in Fig.2, five refined layers of cells are used to capture the thin liquid film.

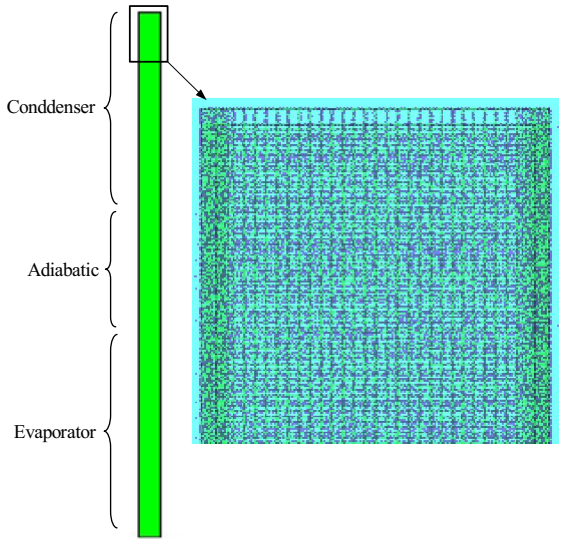


Fig.2. Computational mesh

3.2 Boundary conditions and Solution strategy

In order to minimize the difference between simulation and experment, the accurate boundary conditions is needed. Because the thermosyphon is a enclosed container filled with certain proportion of working liquid, all boundary types of the thermosyphon are defined as non-slip wall. Heat flux of 25025 W m^{-2} and zero is applied on the evaporator and adiabatic walls respectively. The consender section is cooled by the convection heat transfer of cold water. Therefore, a constant convection heat transfer cofficient and free stream tempresture is defined as the boundary conditions on the condenser wall. In order to reduce the total computing time, the properties of water liquid and vapour are defined as constants. Gravitational acceleration of 9.81 m/s^2 which drives the condensed liquid to flowing back towards the evaporator section is applied along the negative axial direction.

Pressure velocity coupling is performed through phase coupled SIMPLE algorithm. A first-order upwind scheme for the determination of momentum and energy is included in the model. Time step of 0.005 s is used for the transient solver. Vapour is defined as the primary phase and liquid is defined as the secondary phase.

4 .SIMULATION RESULTS

When the heat input equals to the heat output , the process of mass and heat transfer in the thermoyphon reached a quasi-steady state. The liquid phase volume fraction contours are presented in Fig.3. A thin liquid film generated all along the inner wall of thermosyphon, which proved the existemce of evaporation and condensation. This process can be shown more clearly in Fig.4., which presents the changes of the average vapour phase volume fraction on the inner wall of evaporator and condenser section with time.

At the beginning of the simulation, the average vapour phase volume fraction at inner wall of evaporator section and condenser section is 0 and 1. With the increasing of temperature, the average vapour phase volume fraction at evaporator section begins to increase, which means the vapour bubbles are produced in the liquid pool. However, after 9 s, vapour volume fraction decreased at evaporator which can be attributed to the back flow of condensate.

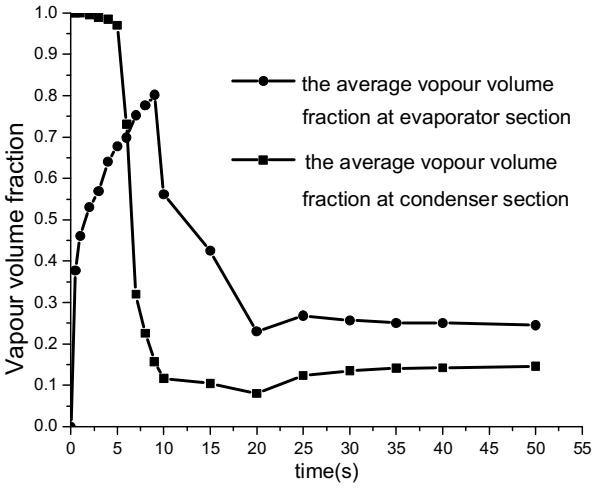


Fig.4. Variation of vapour volume fraction with time

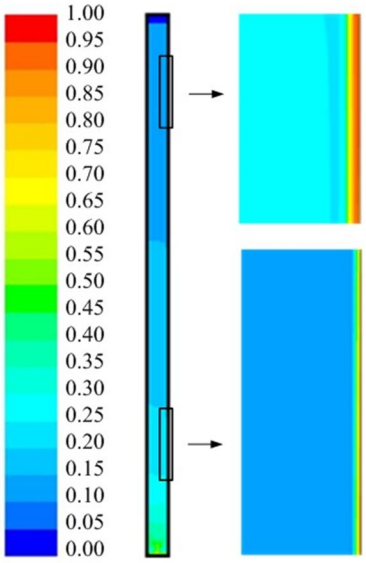


Fig.3. Contours of liquid volume fraction at steady state

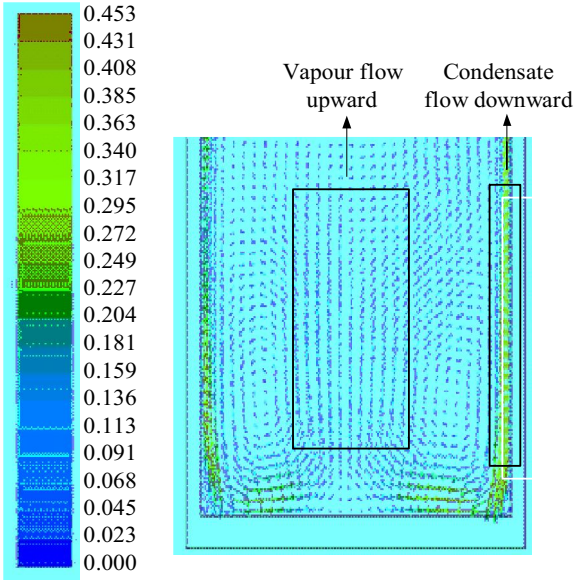


Fig.5. Velocity vectors at steady state

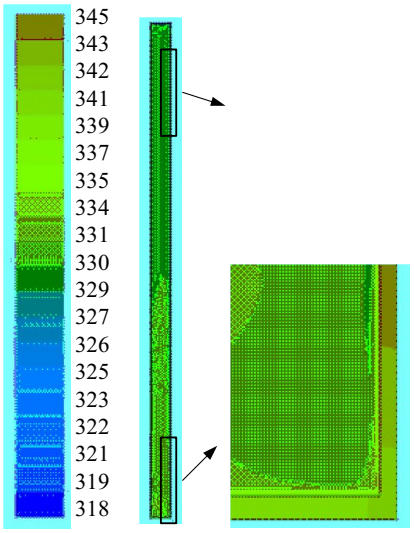


Fig.6. Contours of temperature at steady state

From 0 to 5s, the average vapour volume fraction decreases slowly at condenser section which is because the saturated vapour hasn't reached the condenser's wall. When the saturated vapour reaches the condenser wall and begins to condensation, the average vapour volume fraction decreases sharply. With the liquid film forming in the condenser section, the condensation rate slows down and the vapour volume fraction decreases to a steady state. The movement of vapour and condensates are shown in the Fig.5, which presents the contours of velocity vectors at the bottom of evaporator section. It is obvious that the center zone in thermosyohon is occupied by the rising vapour and the condensates flow down along the inner wall to the bottom of evaporator. It is clear from Fig.5 that condensate flowing down will block the flow of vapour due to the drag force which is taken into account in Mixture model.

The temperature contours are presented in Fig. 6, showing the temperature ditributions of thermos-yphon. As is shown in the Fig. 6, the temperature difference in the center of thermosyphon is much samller than the other position due to the saturated vapour there. The low thermal conductivity of condensate film causes an obvious temperature drop near the inner wall in condensation section. The variation of average temperature on inner wall of evaporator and condenser section with time is shown in Fig. 7. From 0 to 9s, the average temperature at inner wall of evaporator section increases continuously due to the constant heat flux input. The increasing temperature will result in the evaporation of water, so the vapour volume fraction at evaporation section will continue to

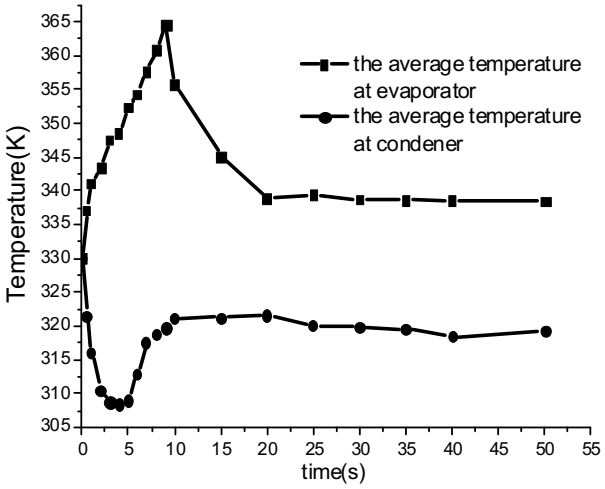


Fig.7. Variation of temperature with time

decrease. It can be verified through Fig.4. After 9 seconds, the temperature of evaporator begins to decrease due to the lower temperature of the condensates that flows down from the condenser section.

From 0 to 5 s, the average temperature at condenser continues to decrease which can be attributed to the effect of cooling water. But after 5 seconds, the temperature of condenser begins to increase slowly to steady state. This change can be explained by the flow of saturated vapour. When the saturated vapour that from evaporation reaches the condenser wall, it releases the latent heat and condenses to liquid, causing a continues increase in the condenser.

5. CONLUSIONS

In this paper, a new method that combines the Mixture model and new algorithm which is used to calculate the mass transfer rate is proposed to simulate the details of two-phase flow and temperature distribution in thermosyphon. The phase change process is shown clearly by the CFD simulation. Therefore, the method of using Mixture model and UDF is capable of simulating the heat and mass transfer process in the thermosyphon.

Furthermore, the model built in the present study can be utilized for the simulation of more complicated two phase systems like axially and radially rotating heat pipe.

ACKNOWLEDGEMENT

Financial grants from the Natural Science Foundation of China (No. 51175254) are gratefully acknowledged.

NOMENCLATURE

P : Local pressure (Pa)
ΔT : Temperature difference between bottom and the surface of liquid layer (K)
T : Temperature (K)
T_{sat} : Saturate temperature (K)
T_{mix} : Temperature of mixture (K)
S_M : Mass source term
S_E : Heat source term
ρ_L : Density of liquid (Kg/m^3)
α : Volume fraction of liquid phase
μ : Viscosity ($N \cdot s/m^2$)
L : Latent heat of working fluid (KJ/kg)
v : Velocity (m/s)
F : Body Force (N)
c_c : Relaxation time of condensation
c_e : Relaxation time of evaporation

REFERENCES

[1] A. Fagri, Heat Pipe Science and Technology, Taylor & Francis, Washington, D.C, 1995.
[2] S.C.K De Schepper, G.J Heynderickx, and G.B. Marin, Modeling the evaporation of a hydrocarbon feedstock in the convection section of a steam cracker, Computers and Chemical Engineering, 33(2009) 122-132.
[3] A. Alizadehdakhel, M. Rahimi. and A. A. Alsairafi, CFD modeling of flow and heat transfer in a thermosyphon, International Communications in Heat and Mass Transfer, 37(2010) 312-318.
[4] B. Fadhl, L.C. Wrobel and H Jouhara, Numerical modelling of the temperature distribution in a two-phase closed hermosyphon, Applied Thermal Engineering, 60(2013) 122-131.
[5] B. Fadhl, L.C. Wrobel and H. Jouhara, CFD modelling of a two-phase thermosyphon charged with R134a and R404a, Applied Thermal Engineering, 78(2015) 482-490.
[6] .K. Kafeel and A. Turan, Axi-symmetric simulation of a two phase vertical thermosyphon using Eulerian two-fluid methodology, Heat Mass Transfer, 49(2013) 1089-1099.
[7] Z. Lin, S. Wang and R. Shirakashi, Simulation of a miniature oscillating heat pipe in bottom heating mode using CFD with unsteady modeling, International Journal of Heat and Mass Transfer, 57(2013) 642-656.
[8] ANSYS FLUENT, Theory Guide(Release 14.0). Multi-phase Flows, ANSYS, Inc., Nobember 2011, 455-568.
[9] Z.Yin, Y. Guo, and B. Sunden, Numerical simulation of laminar film condensation in a horizontal minitube with and without non-condensable gas by the VOF method, Numercial heat transfer, 68(2015) 958-977 .

A Study on the Boiling Heat Transfer Performance of Evaporators with Metal Foam of Loop Type Two-phase Thermosyphon

Dong-Hyun Cho[1], Chan-Yong Gweon[2], Sang-Hun Yun[3]

[1] Professor, Department of Computer aided Mechanical Design Engineering, Daejin University,
1007, Hogukro, Pocheonsi, Gyeinggodo, 11159, Rep. of Korea, Phone: +82-31-539-1973, e-mail: chodh@daejin.ac.kr
[2] CEO, [4]SUNGSAN Co., Ltd., 183, Gahyeon-ro 105 beon-gil, Tongjon-Eup Gimpo-Si. Gyeinggido, 10030, Rep. of Korea
[3] Assistant manager, SUNGSAN Co., Ltd., 183, Gahyeon-ro 105 beon-gil, Tongjon-Eup Gimpo-Si. Gyeinggido, 10030, Rep. of Korea

Abstract

Loop type two-phase thermosyphons are devices that can transfer large amounts of heat flux with the boiling and condensation of the working fluid resulting from small temperature differences. A two-phase thermosyphons with metal form consist of a evaporator, an insulation unit, and a condenser. The working fluid inside the evaporators with metal foam are evaporated by the heating of the evaporator in the lower part of the flexible two-phase thermosyphon and the evaporated steam rises to the condenser in the upper part to transfer heat in response to the cooling fluid outside the tube. The resultant condensed working fluid flows downward along the inside surface of the tube due to gravity. These processes form a cycle. Using R134a refrigerant as the working fluid of a loop type flexible two-phase thermosyphon heat exchanger, an experiment was conducted to see changes in boiling heat transfer performances according to changes in the temperature of the oil for heating of the evaporator with metal form, the temperature of the refrigerant, and the mass flows. According to the results of the present study, strong tendencies for the prediction of the position of gas generation and gas fractions in the evaporator with metal form appeared according to wall heat flux of the evaporators with metal foam. The oil flows in the vicinity of the evaporating tube with metal foam were considered to be natural convection. As the oil temperature in the evaporator with metal foam increased, the boiling steam generation rate of the loop thermosyphon heat exchanger increased. The heat transfer of high density metal foam was higher than the heat transfer of low density metal foam.

Keywords: Evaporator; Heat exchanger; Loop type flexible two-phase thermosyphon; Mmetal form; Performance

1. INTRODUCTION

Cooling systems using loop type two-phase flexible thermosyphon technology can improve cooling performance because these systems release heat using the latent heat resulting from the boiling and condensation of the working fluid so that high performance systems can be implemented and the prices, sizes, and power consumption of the systems can be reduced[1,2]. As such, cooling systems with high speed rotating shafts using the loop type two-phase flexible thermosyphon technology can be made at much lower prices compared to existing cooling systems because they do not required evices such as cooling fluid circulating pumps and chillers[3]. Chen[4] identified an excursive unstable phenomenon from static instability and found out that the unstable phenomenon appeared because areas where pressure drop increased when flow velocity decreased existed in boiling channels. Knaani[5] constructed an electronic component cooling system using a two-phase loop thermosyphon and conducted experimental and theoretical studies on refrigerant pressure drops and rises at individual points of the cycle. Lee at al.[6] studied the instability caused by nucleation in static instability in a natural circulation loop installed with two parallel vertical tubes. According to the study results, a new geysering phenomenon occurred as slug bubbles were generated in the channel.

In the present study, experimental studies were conducted on the heat transfer performance of the evaporator with metal foam of the loop type two-phase flexible thermosyphon that can discharge the large amounts of heat generated by the high speed rotation of the high speed rotation shafts of high voltage motors, generators, and large lathes, simulations were conducted to evaluate the heat transfer performance, and the results were verified through comparison with experimental results.

2. EXPERIMENTAL FACILITY AND METHOD

Fig. 1 shows the loop type two-phase flexible thermosyphon heat exchanger for high speed rotating shaft heat release. The loop type two-phase flexible thermosyphon heat exchanger is installed with an evaporator which is a heating section and a condenser which is a cooling section that are separated from each other. The evaporator and the condenser are assemblies of pipes composed of many pipes and they are constructed

*Corresponding author: chodh@daejin.ac.kr,
Phone: +82-31--539-1973, Fax: +82-31-539-1970

so that they are connected to each other through pipes gathered on the top and bottom. The evaporator and the condenser have conveying pipes in charge of working fluid flows connected to each other and the condenser is installed with a gas/liquid separator that gathers non-condensable gases and an exhaust gas valve. In loop type thermosyphon heat exchangers, because of the characteristics of thermosyphons, the condenser should be installed at a higher location than the evaporator without fail to obtain the pressure difference for circulation of the working fluid.

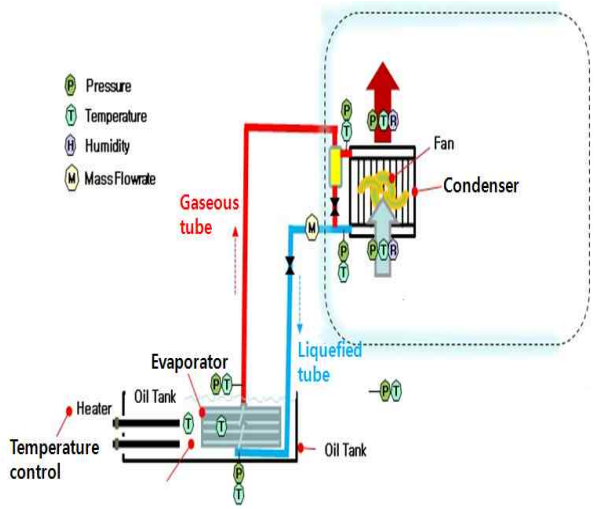


Fig. 1 Loop type two-phase thermosyphon heat exchangers for high speed rotating shaft heat release

Fig. 2 shows Schematic diagram of the experimental facility. The condenser is 480mm wide, 1000mm long and 68mm high. Eighty 12 mm diameter, 1,000mm long copper pipes were installed on the condenser. In addition, exhaust valves were attached to the condenser so that the working fluid can be filled and non-condensable gases can be exhausted. As shown in Fig. 2, for performance experiments of the 6.5kW grade loop type thermosyphon heat exchanger, the height difference between the evaporator and the condenser was set to 1.75m. The outside diameter of the conveying pipe that connects the evaporator with the condenser is 20mm. To prevent leaks from occurring in the conveying zone that connected the evaporator with the condenser, the conveying zone was checked using high pressure nitrogen and the conveying zone was insulated with 25mm thick glass fibers to reduce heat losses to the outside of pipes occurring when the working fluid flows through the steam and fluid flow pipes. To measure individual experimental data in the performance experimental facility, Pressure Transducers (P21AA, 0~2MPa) were installed at the working fluid inlet/outlet of the evaporator so that the saturated vapor pressure of the working fluid can be measured and reviewed in comparison with the saturation temperature. To measure pressure drops in the vapor tube, Pressure Transducers (P21AA, 0~2MPa) were installed at the inlet/outlet of the condenser. One thermocouple (K-type sheath dirt. 1.6mm OD) each was installed at each of the inlet/outlet of the evaporator and the inlet/outlet of the condenser. To measure the oil temperature in the housing of the evaporator and the air temperature in the condenser, three each of thermocouples were installed at the inlet and out let respectively. The experimental data were measured and recorded using a Hybrid Recorder (64 channels). A refrigerant flowmeter was installed at the condenser outlet tube to measure the condensate refrigerant flow rate. In loop type thermosyphon heat exchanger performance experiments, initial temperatures are very important. Therefore, the non-condensable gases remaining in the tube were discharged so that a constant degree of vacuum is maintained in normal states. R-134a was used as a working fluid. The quantity of the injected working fluid was measured on a scale. A slidacs was installed to maintain the oil temperature in the oil housing that supplies heat to the evaporator at 20~80℃ when the experiment was conducted. The temperatures of the working fluid at the inlet and outlet of the evaporator and the condenser at individual layers were compared.

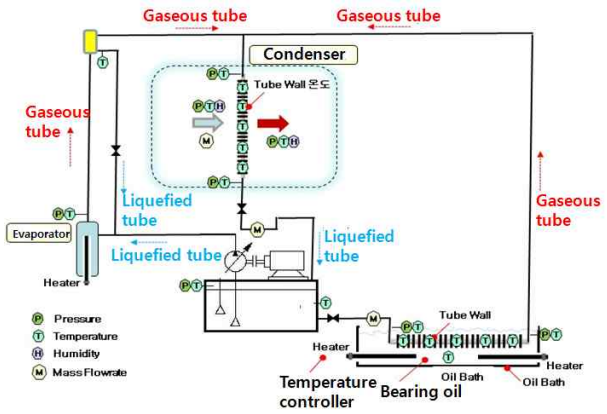
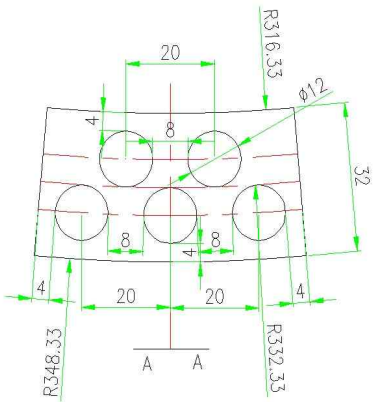


Fig. 2 Schematic diagram of the experimental facility

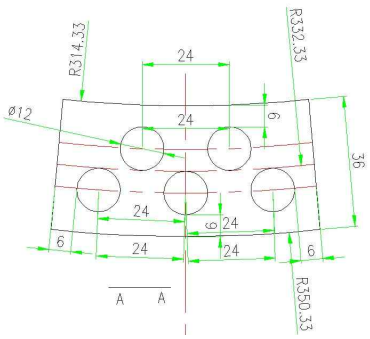
Fig. 3 shows schematic diagram of metal foam. Fig. 4 shows evaporating tube with metal foam. The metal foam thickness are 4, 6, 8mm.

Fig. 5 shows schematic diagram of the evaporator with metal form. Fig. 6 shows evaporator with meatl foam. Fig. 7 shows evaporator with meatl foam of loop type two-phase thermosyphon. The evaporator with metal form of the 6.5kW grade loop type thermosyphon heat exchanger made for the present study is 699mm in the outside diameter,

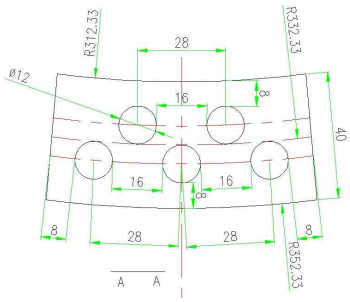
630mm in the inside diameter, and 150mm in the height. In addition, 98 pieces of 12mm diameter copper pipes were installed in the inside of the evaporator with metal form and 100 pieces of 12mm diameter copper pipes were installed on the outside of the evaporator. Furthermore, L type 25mm soft copper pipes were installed on the top and bottom of the evaporator with metal foam



(a) Metal foam thicknenss 4mm



(b) Metal foam thicknenss 6mm



(c) Metal foam thicknenss 8mm

Fig. 3 Schematic diagram of metal foam

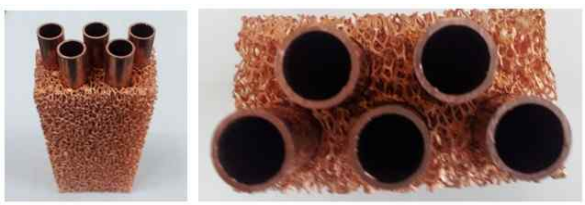


Fig. 4 Evaporating tube with metal foam

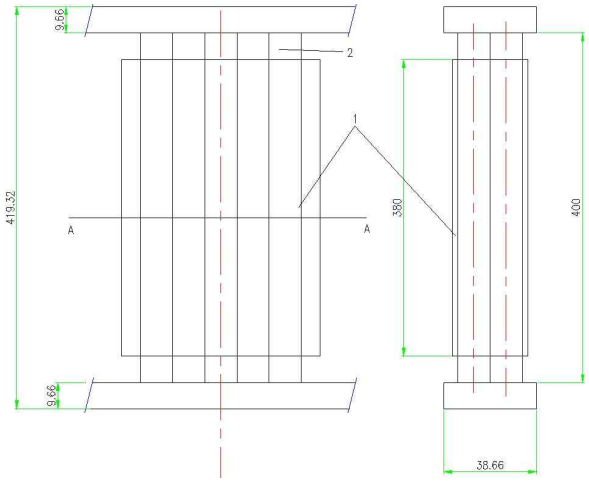


Fig. 5 Schematic diagram of the evaporator with metal foam



Fig. 6 Evaporator with meatl foam

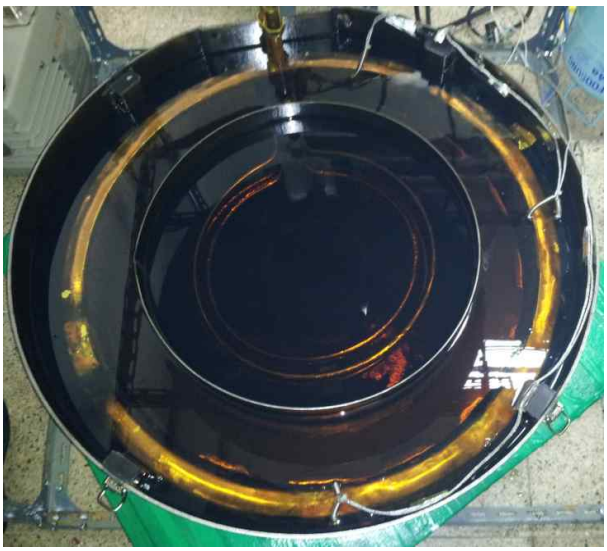


Fig. 7 Evaporator with meatl foam of loop type two-phase thermosyphon

3. RESULTS AND DISCUSSION

3.1 Phase change model simulation of evaporator with metal foam

Fig. 8 shows schematic diagram of evaporating tube with metal foam. Fig. 9 ~Fig. 11 show the shape of a preliminary simulation for evaporator with metal foam of phase change models and related boundary conditions. In the preliminary simulation, the RPI(Rensselaer Polytechnic Institute) model containing relational expressions for nucleation, growth, and breakaway of bubbles on walls provided by ANSYS FLUENT v13 was applied and the boundary conditions provided by ANSYS FLUENT v13 were applied for the simulation shape and boundary conditions.

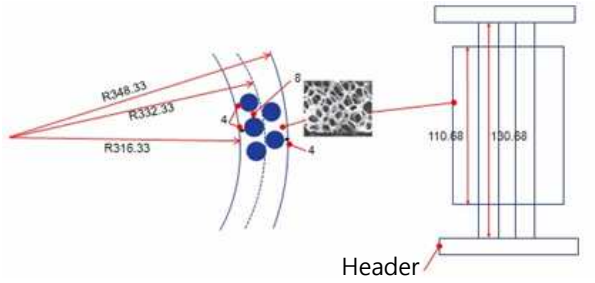


Fig. 8 Schematic diagram of evaporating tube with metal foam

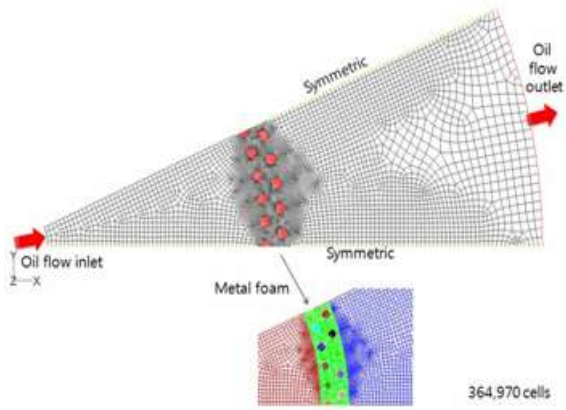


Fig. 9 The modeling of evaporating tube with metal foam

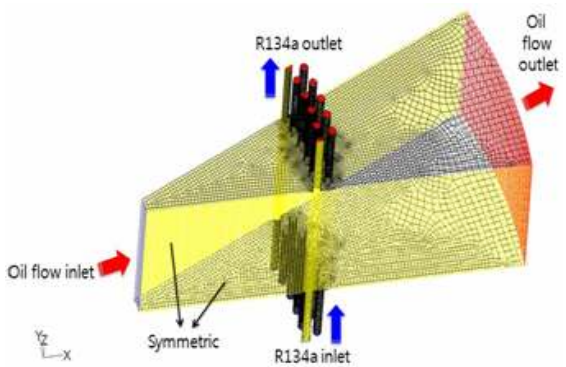


Fig. 10 The grid generation of evaporating tube with metal foam

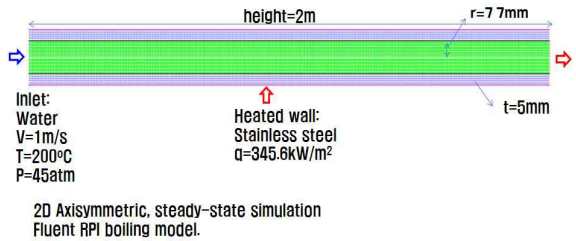


Fig. 11 The shape of the preliminary simulation and related boundary conditions for evaporator phase change models

Fig. 12 shows distributions of gas fraction, gas velocity, liquid velocity, and liquid temperatures in oil housings of evaporator with metal foam. The resultant velocity distribution of the simulation to predict oil flows in the evaporator oil housing of evaporator with metal foam indicated that the effects of oil flows resulting from shaft rotation on the flows of the oil in the vicinity of the heat pipe should not be big. Since the effects of oil flow velocity in the oil housing on the flows of the oil in the vicinity of the evaporating tube with metal foam are predicted to be insignificant based on the results of the simulation to predict oil flows in the evaporator oil housing, the oil flows in the vicinity of the evaporating tube with metal foam are considered to be natural convection.

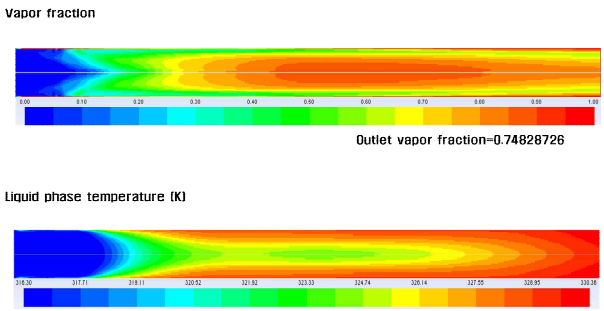


Fig. 12 Distributions of gas fraction, gas velocity, liquid velocity, and liquid temperatures

Fig. 13 and Fig. 14 shows analytical model considering evaporator with the metal foam. The thermal resistance measured in parallel by conduction heat transfer and convective heat transfer. Table 1 shows simulation case. Fig. 13 and Fig. 14 shows the distributions of vapor volume fraction, wall temperatures in the evaporating tube with metal foam. It can be seen that in the evaporating tube with metal foam, the gas begins to be slowly generated from the wall and united on the center and this result was consistent with the gas velocity distribution. In addition, strong tendencies for the prediction of the position of gas generation and gas fractions in

evaporating tube with metal foam appeared according to wall heat flux. As porosity had decreased, vapor fraction increased.

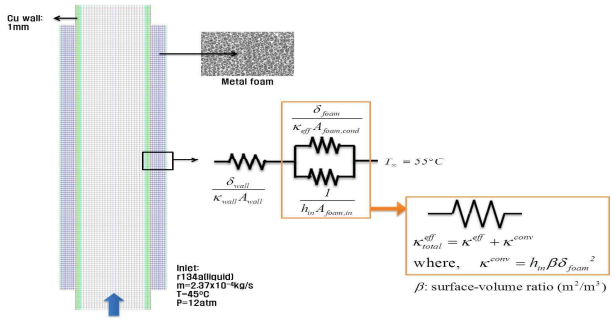


Fig. 13 Analytical model considering the metal Fo am evaporator

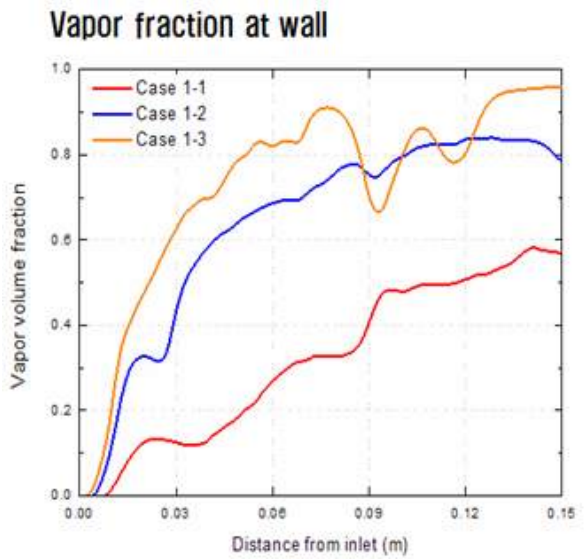


Fig. 13 Vapor volume fraction vs. distance from inlet

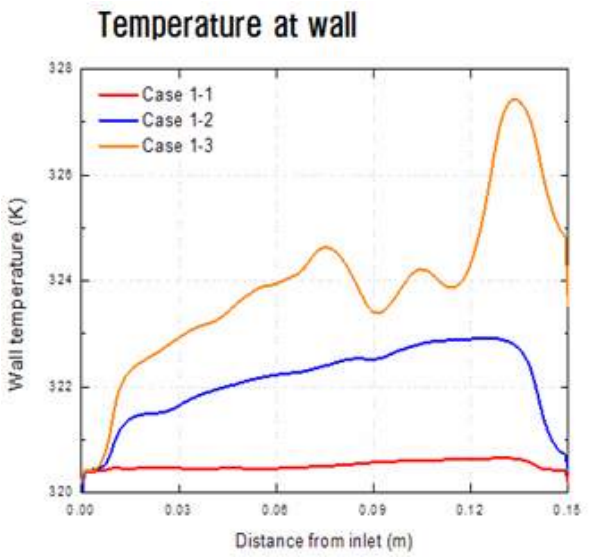


Fig. 14 Wall temperature vs. distance from inlet

Table 1. Simulation case.

case		d_f (m)	d_p (m)	ε	δ_{foam} (m)
1	1	0.5×10^{-3} (assumed)	4×10^{-3}	0.9225	4×10^{-3}
	2		3×10^{-3}	0.8157	
	3		2×10^{-3}	0.5770	

3.2 Results of experiments for evaporator with metal foam

Fig. 15~Fig. 17 show the results of experiments for evaporator with metal foam and Fig. 15 also shows changes in the oil temperature of the evaporator according to heat input of oil. The refrigerant used in the experiments is 134a. The experiments were conducted at refrigerant charge rates of 6~9kg. As the oil temperature in the evaporator with metal foam increased, heat flux of evaporator increased. Therefore As the oil temperature in the evaporator with metal foam increased, the boiling steam generation rate of the loop thermosyphon heat exchanger increased.

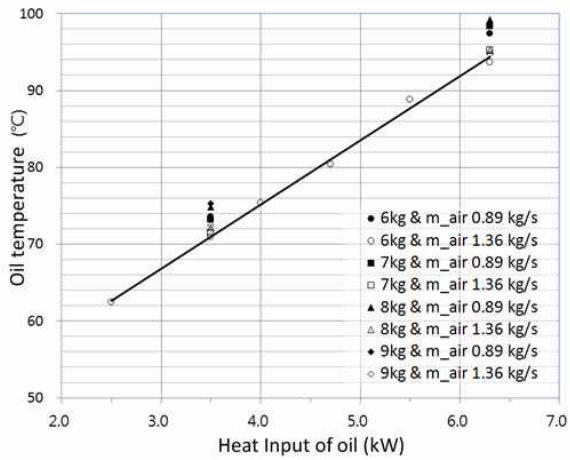


Fig. 15 Oil temperature of evaporator with metal fo am according to heat input of oil

Fig. 16 shows oil temperature of evaporator with low density and high density metal foam. The refrigerant used in the experiments is 134a. The experiments were conducted at refrigerant charge rates of 6~9kg and the air flow rates in the condenser in a range of 0.58~1.36kg/s. As the oil temperature in the evaporator with metal foam increased, heat flux of evaporator increased. The heat transfer of high density metal foam was higher than that of low density metal foam. Fig. 17 shows temperature difference of ambient temperature and oil temperature according to ambient temperature changes. The refrigerant used in the experiments is 134a. Heat transfer performance in accordance with the increased oil temperature increases.

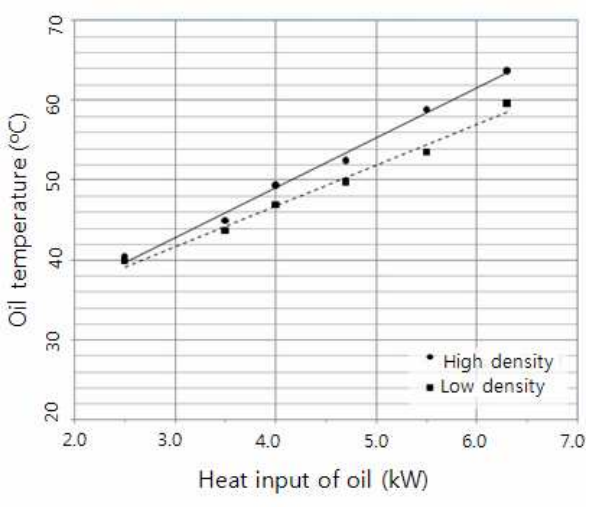


Fig. 16 Oil temperature of evaporator with low density and high density metal foam according to heat input of oil

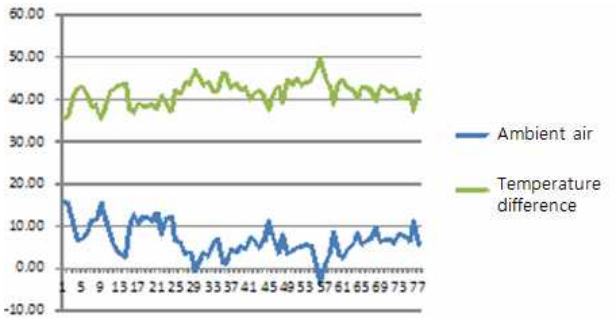


Fig. 17 Temperature difference of ambient temperature and oil temperature according to ambient temperature changes

4. CONCLUSIONS

Experiments of the evaporators with metal foam of loop type two-phase thermosyphon for heat discharge from high speed rotating shafts were conducted using R-134a as a working fluid, experimental studies were conducted on changes in evaporator differences between oil temperatures and evaporator temperatures according to condenser cooling air flow rates, and the experimental results were compared with simulation results. The results are summarized as follows.

(1) Strong tendencies for the prediction of the position of gas generation and gas fractions in the evaporating tube appeared according to wall heat flux of the evaporators with metal foam.
(2) The oil flows in the vicinity of the evaporating tube with metal foam were considered to be natural convection
(3) As the oil temperature in the evaporator with metal foam increased, the boiling steam generation rate of the loop thermosyphon heat exchanger increased.
(4) The heat transfer of high density metal foam was higher than that of low density metal foam
(5) Heat transfer performance in accordance with the increased oil temperature increases.

ACKNOWLEDGEMENT

Financial grants from the Small Medium Business Administration are gratefully acknowledged.

NOMENCLATURE

dp : Pore diameter(m)
d_f : Fiber diameter(m)
δ_{foam} : Thickness of foam
ε : Porosity

REFERENCES

[1] Ali, A.F.M. and McDonald, T.W., 1977, A Thermosyphon Loop Performance Characteristi-cs:Part 2. Simulation Program, ASHRAE Trans, Vol. 83, Part 2, pp260~278
[2] Kyuil Han, Dong-Hyun Cho and Tae-Woo Lim. 2005, Characteristics of Boiling Heat Transfer of Thermosyphon Heat Exchangers with Helical Grooves
[3] Mou K. and Chang H., 1988, Study on Percentage of liquid Filling of separate type Heat Pipe, 3IHPS
[4] Chen, K.S. and Chang, Y. R., 1988, Steady-State Analysis of Two-Phase Natural Circulation Loop, Int. J. Heat Mass Transfer, Vol. 31, No. 5, pp. 931~940
[5] Knaani, A. and Zvirin, Y., 1994, Bifurcation Phenomena in Two-Phase Natural Circulation, Int. J. Multiphase Flow, Vol. 19, No. 6, pp. 1129~1151
[6] Lee, K.W., Chang, K.C., Lee, K.J., Lee, Y.S.and Hong, S.H., 1995, Heat Transportation Technology Separate Heat Pipe Heat Exchanger, Energy R&D Technical Analysis Report, Vol. 17, No. 1&2, pp. 154~166

Experimental and Numerical Study on the Heat Transfer Performance of a Single Thermosyphon

S.H. Oh[1], S.I. Kim[2*], J.W. Choi[2], K.J. Lee[3], W.P. Chun[4]

[1] Energy efficiency research division, Korea Institute of Energy Research, 152, Gajeong-ro, Yuseing-gu, Daejon, 305-343, Korea
[2] Senior Researcher, Energy Efficiency Research Division, Korea Institute of Energy Research
[3] Senior Technologist, Energy Efficiency Research Division, Korea Institute of Energy Research
[4] Principal Researcher, Energy Efficiency Research Division, Korea Institute of Energy Research

Abstract

The heat pipe and the thermosyphon are particularly effective tools in the heat transfer process. Especially, the thermosyphon is a vertically oriented wickless heat pipe, with a liquid pool at the bottom. Due to its relatively simple construction and effective heat transfer ability the thermosyphon has been used a various heat exchangers.

In this study, we performed an experimental and a numerical study about a single thermosyphon. The main parameter is a working fluid filling ratio. The working fluid is HFE-7100 and a filling ratio is set to 80, 100% based on the evaporator section. The air velocity of heat exchange region is about 0.72m/s (Inlet velocity is about 2.92m/s). The heat transfer performance of a single thermosyphone was presented the effective thermal conductivity and the haet transfer rate of the air through heat exchanging zone. Using an experimental result, we validated a result between experimental and numerical studies. The characteristic of the numerical studies is a modeling of single thermosiphon round fin using a porous media. This approach is made it simple for numerical simulation of a heat exchanger using multi array themosyphon. The validation was in progress about a fluid and an energy region and we have confirmed that a numerical simulation using a porous media approach has a proper result.

Keywords: Thermosyphon; Heat transfer; Experimental study and numerical simulation; Porous meida;

1. INTRODUCTION

The two phase thermosyphon are particularly effective tools in the heat transfer and heat exchange process. Especially, the thermosyphon is a vertically oriented wickless heat pipe, with a liquid pool at the bottom. Due to its relatively simple construction, effective heat transfer ability and lower fabrication cost, the thermosyphon has been used a various heat exchangers.

Many studies have been performed on the single thermosyphon's geometry, temperature, working fluid and filling ratio [1], [2], [3]. Previous studies have been reported that a filling ratio of a single thermosyphon had an optimal value according to working fluid and geometry etc.

To improve condensation sector's heat transfer performance, a round or a plate fin is manufactured by thermosyphon. Kim et al. [4], [5] was studied an experimental studies and numerical simulations of straight fin heat sink. Especially, the straight fin heat sink was modeled as a porous medium.

Generally, thermosyphon's application, such as heat exchanger, is used multi-array thermosyphon. To achieve high heat transfer performance of themosyphon's application, the optimization of thermosyphon's array is important as well as the single thermosyphon performance. However to perform optimization by experimental study and numerical study have a limitation by the cost, time etc.

Therefore this study was performed experimental test using a single thermosyphon. And we performed the simple numerical simulation using a porous media method. This method makes it simpler to enable optimization of the multi-array thermosyphon system. The numerical result validation was in progress about a fluid and an energy region using experimental result.

2. EXPERIMENTAL TEST

This study was performed an experimental test about a two phase single thermosyphon. Test facility and a single thermosyphon's geometry is Fig. 1. The working fluid is a HFE 7100. The main parameter of an experimental test is a working fluid filling ratio. In this study, 80, 100% filling ratio is used. The air velocity of condensation region is about 0.72m/s and a vaporization region is heated by hot water. Hot water temperature is about 363.15K. The experimental test is carried out in a steady state condition. The temperature is measured each 3 points at condensation region and vaporization region. The heat transfer performance

*Corresponding author: praygod@kier.re.kr,
Phone: +82-42-860-3168, Fax: +82-42-860-3133

of single thermosyphon was presented an effective thermal conductivity and the result is shown by Fig. 2. The effective thermal conductivity was defined by [6]. The case of 80% filling ratio had a higher effective thermal conductivity than 100% filling ratio. It means that the optimal value of filling ratio is below 80%. The objective of this study is a validation between experimental result and numerical result. Therefore, we do not comment about additional experimental result data.

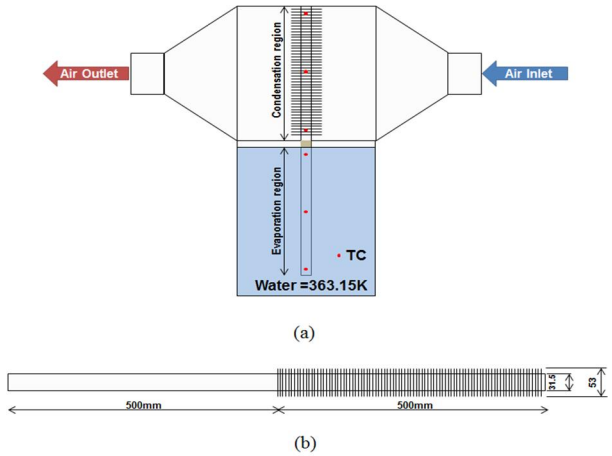


Fig. 1. Experimental apparatus: (a) schematic of test facility; (b) thermosyphon geometry

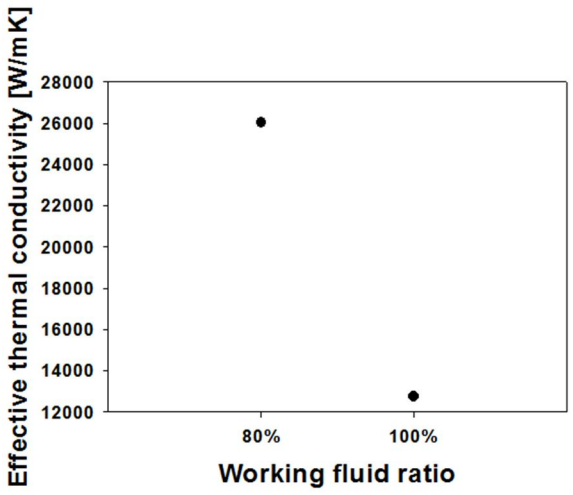


Fig. 2. Graph of effective thermal conductivity vs working fluid filling ratio

3. NUMERICAL SIMULATION

As shown Fig.1, thermosyphon has a round fin. In this study, a round fin is modeled as a porous medium. The porous media governing equation is equation (1).

$$\Delta p/L = -(P_i |v_D| + P_v)v_D \quad (1)$$

In this study, a porous inertial and viscous resistance was determined by a pressure drop value of an experimental test result. The validation of pressure drop value is Fig. 3.

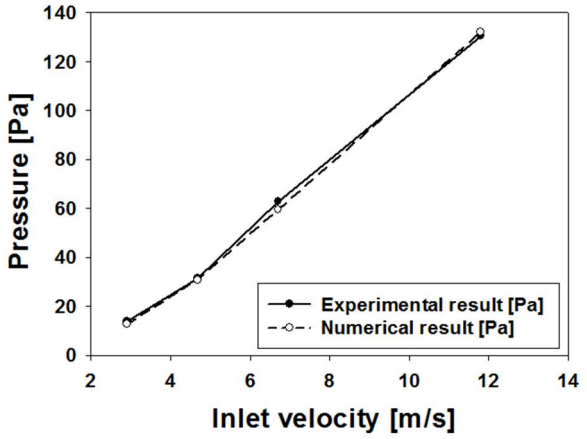


Fig. 3. Graph of pressure drop distribution

In this study, we calculated an effective thermal conductivity using an experimental test result. Therefore, a thermosyphon is modeled as a solid heating core. And we assumed the heating core conductivity is an effective thermal conductivity. The numerical simulation domain and temperature contour plot of domain is Fig. 4. And geometry characteristics and boundary condition is shown Table 1. Case 1 is a filling ratio 80% and case 2 is a filling ratio 100%. All initial condition is originated by experimental experience. Turbulence model was used k-omega turbulence model. And all calculation was performed at steady state condition.

To validate an energy region, we compared outlet air temperature between experimental result and numerical result. The result is presented Fig. 5. The air outlet temperature is in good agreement with the numerical simulation result, respectively.

Table 1. Geometry characteristics and boundary condition

Geometry	
Porosity	0.9
Material	Aluminum
L [m]	0.053
Boundary condition	
Inlet velocity [m/s]	2.92
Heating core bottom temperature [K]	354.65
Case 1 inlet temperature [K]	289.85
Case 2 inlet temperature [K]	290.26

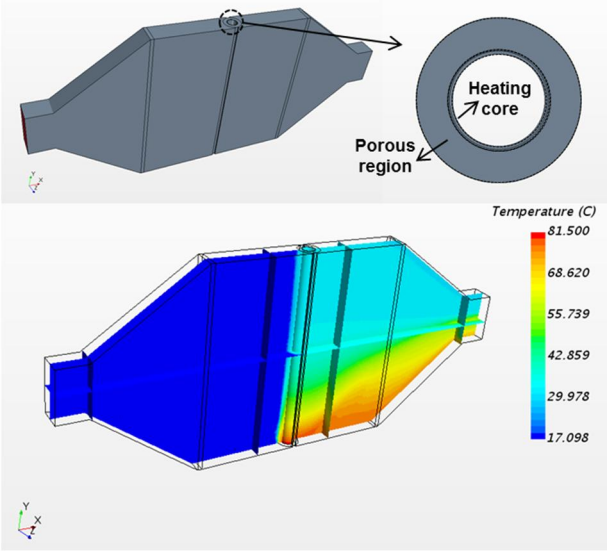


Fig. 4. Image of the numerical simulation domain and temperature contour plot of domain

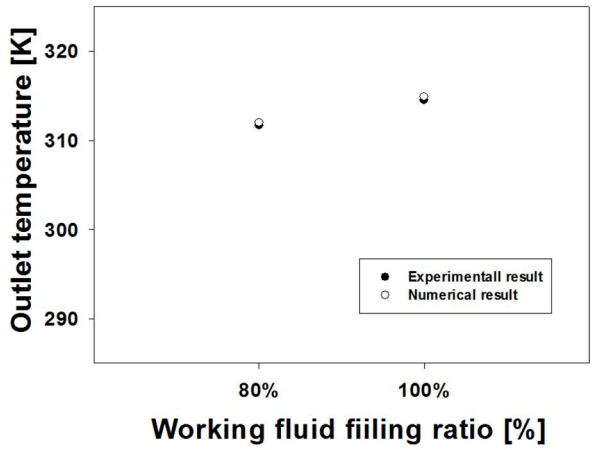


Fig. 5. Graph of outlet air temperature vs working fluid filling ratio

4. CONCLUSIONS

This study dealt with a heat transfer performances of two phase single thermosyphon. Experimental investigations were performed for two case working fluid filling ratio. From experimental result, we also performed a numerical simulation. Especially, we suggested a simple model based on the porous media method in numerical modeling. Finally we compared and validated between experimental and numerical results. However, the test case was too small and a numerical simple model was needed a complement. We will conduct additional research.

ACKNOWLEDGEMENT

This work was supported by the Korea Institute of Energy Technology Evaluation and Planning (KETEP) and the Ministry of Trade, Industry & Energy(MOTIE) of the Republic of Korea (No. 20142020104470).

NOMENCLATURE

p : Pressure drop (Pa)
L : Characteristic length (m)
P_i : Inertia tensor of porous media (kg/m^4)
P_v : Viscous tensor of porous media (kg/m^{3}s)
v_D : Darcy velocity (m/s)

REFERENCES

[1] Noie, S. H., Heat transfer characteristics of a two-phase closed thermosyphon, *Applied Thermal Engineering*, 25 (4) (2005) 495-506.
[2] Hussein, H. M. S., El-Ghetany, H. H., Nada, S. A., Performance of wickless heat pipe flat plate solar collectors having different pipes cross sections geometries and filling ratios, *Energy Conversion and Management*, 47 (2006) 1539-1549.
[3] Jioa, B., Qiu, L. M., Zhang, X. B., Zhang, Y., Investigation on the effect of filling ratio on the steady-state heat transfer performance of a vertical two-phase closed thermosyphon, *Applied Thermal Engineering,* 28 (2008), 1417-1426.
[4] Kim, D., Kim, S. J., Ortega, A., Compact modeling of fluid flow and heat transfer in pin fin heat sinks, *Journal of Electronic Packaging*, 126 (3) (2004) 432-350.
[5] Kim, D., Kim, S. J., Compact modeling of fluid flow and heat transfer in straight fin heat sinks, *Journal of Electronic Packaging*, 126 (2) (2004) 247-255.
[6] Loula, A.S., M. Abd, E., Adel, A. F., Transient analysis of two-phase closed thermosyphon (TPCT) using AL_2O_3 nanofluid , *International Journal of Scientific & Engineering Research*, 12 (4) (2013) 2054-2062

Boiling Heat Transfer Mechanism Inside the Narrow Space of Double-tube Heat Pipe

Risa Suenaga[1*], Masafumi Katsuta[2], Taro Kato[1]

[1]*Department of Modern Mechanical Engineering, Graduate School of Creative Science and Engineering, Waseda University, 3-4-1 Okubo, Shinjuku-ku, Tokyo, 169-8555 Japan*
[2]*Faculty of Science and Engineering, Waseda University*

Abstract

In the recent years, trains have been attracting attention from the viewpoint of environmental issues. By using a double-tube heat pipe to cool inverter control devices, narrow space of the currently applied boiling cooling method also contributes to a lightweight device and will be maintenance-free. With the technological innovation, it is required to develop heat pipe improving cooling performance. In this paper, we analyzed image data from an IR camera and a high speed camera to clarify the boiling heat transfer mechanism inside the narrow space of double-tube heat evaporator and constructed the guideline of the inner tube of the double-tube heat pipe. To evaluate the performance and analyze images, we made two experimental apparatus and have conducted experiments by selecting heat flux in a proper range from 5 to 40 kW/m^2. In terms of the inner tubes' structure, to prevent a decline of the heat transfer coefficient associated with an increase of the heat flux, we placed artificial cavities and holes for water to flow into the narrow space. By use of inner tubes with cavities and holes, the larger heat transfer coefficient was obtained than that without them. As for the heat transfer mechanism in the double-tube heat pipe, we classified the effects into three items and discussed these effects by using the image data from the IR camera and the high speed camera. In addition, we also classified the shapes of bubbles and found that it is significant to generate isolated bubbles artificially to improve the performance.

Keywords: Boiling and evaporation, Boiling heat transfer enhancement, Boiling in narrow space, Double-tube heat pipe

1. INTRODUCTION

Recently, owing to increasing awareness of environmental issues, trains have been attracting attention because of low CO_2 emission and mass transportation. In cooling inverter devices such as VVVF inverter control devices used in trains, forced coolant-feed cooling systems or separate fin cooling systems have been used thus far. However, because of the phase-out of the fluorocarbon refrigerant, heat pipe cooling systems are now mainly used especially for inverters with low heat values. They also contribute to a lightweight device and will be maintenance-free. Accompanied with the technological innovation, increase of power density with the downsizing of the devices deteriorates not only device performance but also inverter efficiency. Therefore, it is required to develop heat pipe improving cooling performance. Heat pipes used for trains are large diameter (larger than 15.88mm) heat pipes and they have shapes of straight tube or U tube. Inside the evaporator of the heat pipe, phase change of the working fluid makes it possible to transport heat. To improve cooling performance, it is important to enhance boiling heat transfer and effectively generate bubbles in evaporator.

In consideration of the efficient structure, we focused on the previous study which found using narrow space in the double-tube evaporator promoted nucleate boiling [1]. Boiling in narrow space enhanced heat transfer further than pool boiling at low superheat. There are many studies focusing on narrow space boiling on horizontal and vertical heating surface. For example, Katto Y., et al. studied about nuclear and transition boiling on a horizontal, parallel disk-surface [2] and Fujita Y., et al. focused on the nucleate boiling heat transfer in narrow space between rectangular vertical surfaces [3][4]. Also in our laboratory, many studies above mentioned subjects have been conducted and they have found that heat transfer performance would be improved by using double-tube evaporator whose inner tube was fixed off-axial.

Therefore, the purpose of this research is to accumulate fundamental data to understand the boiling heat transfer mechanism inside the narrow space and discuss the optimization of the internal structure for putting double-tube heat pipe to commercial application.

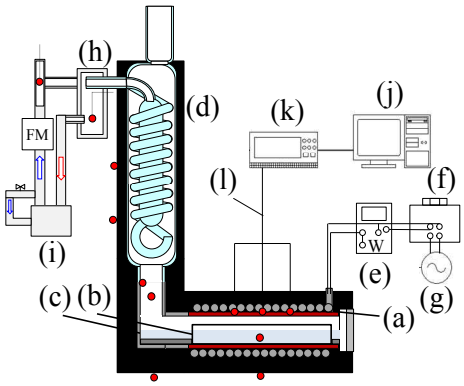
2. EXPERIMENTS

2.1 Experimental test facility

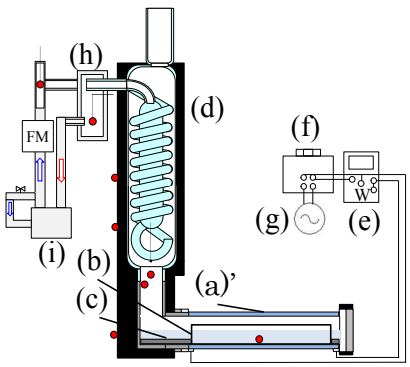
In this study, we used two experimental apparatus to evaluate performance (#1) and analyzed visualized images of the boiling behavior

*Corresponding author: risa.suenaga@akane.waseda.jp,
Phone: +81-03-5286-3251 Fax: +81-03-5286-3251

(#2). The schematics of the experimental apparatus are shown in Fig. 1. Both apparatus had similar geometrical form except the way of heating. Both of them consist of evaporator, adiabatic section and condenser. One wrapped a coil heater around copper pipe wall and the other had a glass heater made by using vapor deposition technique at the test section. Each test was conducted under the atmospheric pressure and working fluid was pure water. The water level could be checked from the polycarbonate window at the edge of the evaporator and the inner tube was set at the bottom by using a SUS bar. Experiments were conducted by selecting heat flux in a proper range from 5 to 40 kW/m^2. For #1, nine T-type thermocouples were placed in the cross sectional direction as shown in Fig. 2 in order to measure the temperature of the heating surface. For #2, we used an IR camera and a high speed camera to observe the boiling behavior and analyzed these data to clarify the heat transfer mechanism.



(i) #1



(ii) #2

(a)	Coil heater
(a')	Glass heater
(b)	Inner tube
(c)	SUS bar
(d)	Condenser
(e)	Watt meter
(f)	Slide regulator
(g)	200V DC power supply
(h)	Mixing chamber
(i)	Thermostat chiller
(j)	Computer
(k)	Data acquisition
(l)	Thermocouples

Fig. 1 Experimental apparatus

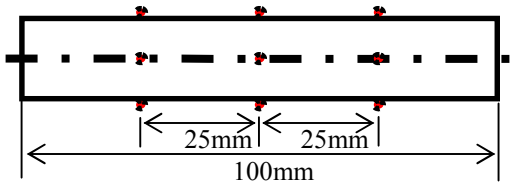


Fig. 2 Temperature measurement points



(i) Coil heater



(ii) Glass heater

Fig. 3 Pictures of test sections

Fig. 3 shows the pictures of the detailed experimental test sections. The test sections are off-axial double-tube evaporator, with water flowing inside the tubes. The outer tubes are 100mm long with inner diameter of 16mm and outer diameter of 20mm. The inner tubes are also 100mm long with inner diameter of 12mm, outer diameter of 14mm, and slit angle of 60degree that are the optimum value the performance improved in the previous study. In addition, to prevent a decline of the heat transfer coefficient associated with an increase of the heat flux, we placed artificial cavities and holes for inner tubes. Parameters of inner tubes are shown in Fig. 4 and Table 1 and we considered the effect of these on the boiling behavior.

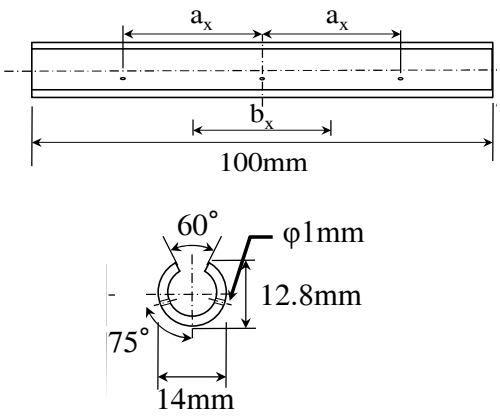


Fig. 4 Parameters of inner tubes

Table 1 Parameters of inner tubes

	Holes			Cavities	
	Number	Angle	Distance	Number	Distance
	a	a_y[deg.]	a_x[mm]	b	b_x[mm]
(a)	none			none	
(b)				2	30
(c)				3	25
(d)	1	75	—	2	30
(e)	2		30	1	—
(f)				2	30
(g)			60		
(h)			75	3	25
(i)	3		30	2	30
(j)			25	3	25
(k)	4				
(-)	Without inner tube				

2.2 Data reduction

2.2.1 Experimental apparatus #1

Heat input Q_{in} was calculated by using following Eqs. (1)-(6).

$$Q_{in} = Q_{el} - (Q_{lah} + Q_{ra}) \quad (1)$$

$$Nu_{air} = 0.53 Ra^{1/4} \qquad (Ra: 10^3 \sim 10^9) \quad (2)$$

$$Ra = \frac{g\beta(T_w - T_{air})D'^3}{va} \quad (3)$$

$$\beta = \frac{1}{T_{film}} \qquad (T_{film} = \frac{T_{air} + T_w}{2}) \quad (4)$$

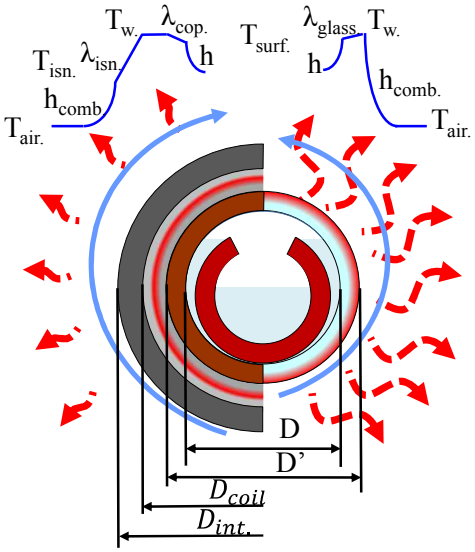


Fig. 5 Heat loss of the evaporator

$$Q_{lah} = \frac{Nu_{air}\lambda}{D'} \times A(T_w - T_{air}) \quad (5)$$

$$Q_{ra} = \left\{ (T_w)^4 - (T_{air})^4 \right\} \times \varepsilon \times \sigma \times A \quad (6)$$

Then we calculated the heat transfer coefficient by using Eqs. (7)-(10).

$$q = \frac{Q_{in}}{A} \quad (7)$$

$$T_{surf.} = T_w - \frac{Q_{in}}{2\pi L\lambda}(\ln\frac{D'}{D'-t}) \quad (8)$$

$$\Delta T_{sat.} = T_{surf.} - T_{sat.} \quad (9)$$

$$h = \frac{q}{\Delta T_{sat.}} \quad (10)$$

2.2.2 Experimental apparatus #2

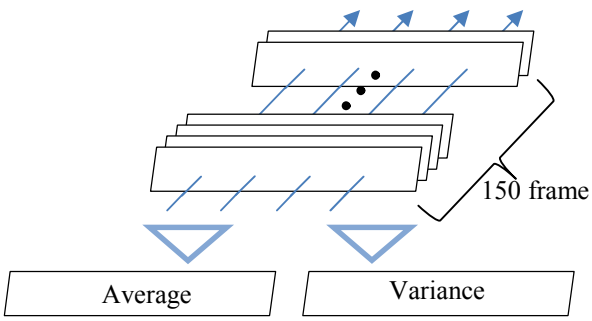


Fig. 6 Method of processing of the IR image data

For the IR camera data, we took the 150 frames in 5 seconds and colored each point depending on the magnitude of values for the distribution of

temperature, histogram, and the dispersion. And for the high speed camera data, binary images were generated by using image processing software and we used these for the performance evaluation.

3. EXPERIMENTAL RESULTS AND DISCUSSION

3.1 Experimental results of #1

Fig. 7 shows the heat transfer coefficient as function of heat flux of apparatus #1.

In this figure, the red dotted lines are results when using tubes having two cavities placed 30mm apart (b, d, f, g, i). And it was recognized that the heat transfer coefficient becomes saturated from nearly 20kW/m^2. This result indicates the boiling behavior change has the significant effect on the heat transfer coefficient.

3.2 Experimental results of #2

As for heat transfer mechanism in the double-tube heat pipe, it is controlled by the flow in the narrow space and the boiling propagation phenomenon. In this research, we classified these effects into three items; namely, inserting the inner tube, by cavities, and by holes.

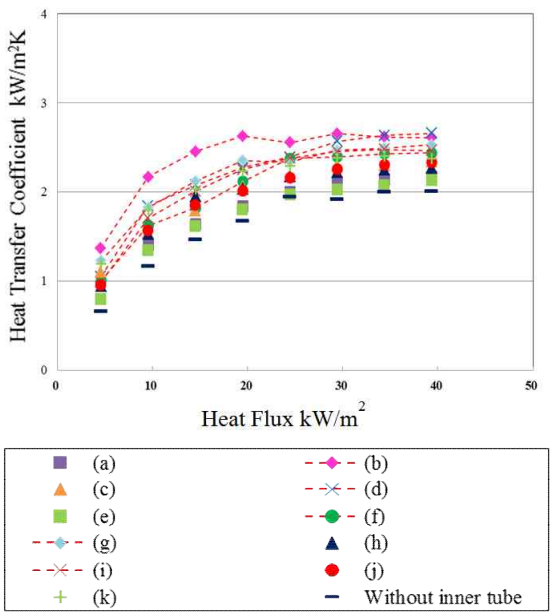
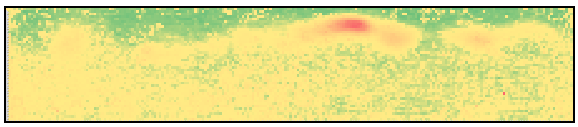


Fig. 7 Heat transfer coefficient vs. Heat flux

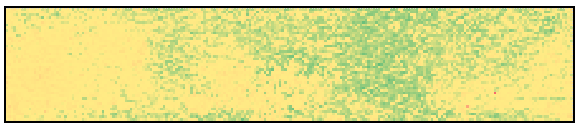
3.2.1 The effect by inserting the inner tube

To consider the effect by inserting the inner tube, the image comparisons from IR camera shown in Fig. 8 and Fig. 9 were used.

Fig. 8 shows the levels of temperature change of each point in five seconds. Red means that the temperature changes largely, and yellow means that the temperature changes small. Fig. 9 shows the temperature distribution: red means the high temperature and blue means the low temperature.

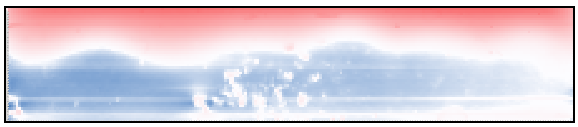


(i) Without inner tube (-)

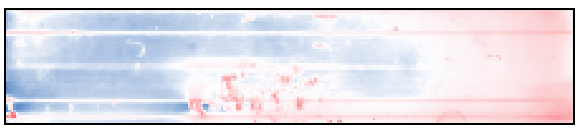


(ii) Without cavities and holes (a)

Fig. 8 The comparison of dispersion between (-) and (a)



(i) Without inner tube (-)



(ii) Without cavities and holes (a)

Fig. 9 The comparison of temperature distribution between (-) and (a)

When not inserting the inner tube, there were apparent temperature differences across the water surface. The red point in Fig. 8 means the temperature change by the water scattering with the bubbles' collapse. While inserting the inner tube, the temperature differences reduced. Therefore, when inserting the inner tube, the wetted area increases and the temperature differences reduce because of the water surface rising by the capillary force and the collapse of the bubbles.

3.2.2 The effect by cavities

To discuss the effect of cavities on the boiling behavior, Fig. 10 was adopted.



(i) Without holes, 2 cavities 30mm apart (b)



(ii) Without holes, 3 cavities 25mm apart (c)



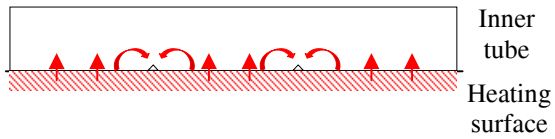
(iii) Without cavities and holes (a)

Fig. 10 Boiling behavior of q=20[kW/m^{2}K]

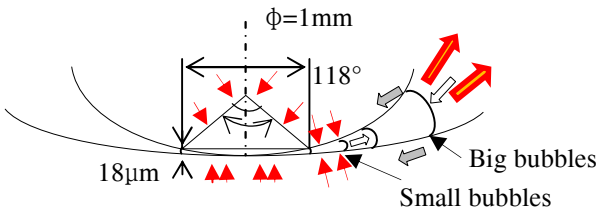
These images show that the bubbles were generated from cavities which were made artificially on the inner tube wall. However, when they were placed 25mm apart, bubbles interfered mutually and coalesced to cause the decline of water surface. It can also be confirmed by the images taken from the bottom of the tubes that the sudden bubbles' generation from the places not having cavities brought about the bubbles' coalescence. While when they were placed 30mm apart, they did not interfere or coalesce. This means bubbles' mutual interfere and coalescence can be controlled if cavities are placed 30mm and more apart. Moreover, cavities have the effect of prompting the premature nucleation in low temperature and controlling the shapes of the bubbles.

Fig. 11 shows the detailed mechanism of the bubbles' generation from the cavities.

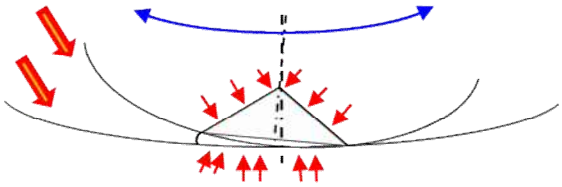
As to the size of the cavities, the angle is 118deg. and the diameter is 1mm. Large bubbles' growth can be explained by the following two stages. First, vapor is trapped in the cavities by the heat input from the heating surface to the inner tube. And then it grows to embed in the cavities. In the second stage, vapor starts out of the 18 μ m space between a cavity and the outer tube. That bubble grows by the evaporative heat transfer between the heating surface and inner tube. It can be seen that the nucleation after the former nucleation occurred the opposite side of the inner tube. Bubbles' growth and the water flowing lead to the axis deviation and it cause the next nucleation. By iterating the above process, bubbles' generation continues one after the other.



(i) Heat input from the heating surface



(ii) Vapor growth in cavities



(iii) Swing of the inner tube

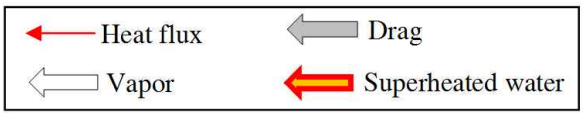


Fig. 11 Mechanism of the bubbles' generation from the cavities

3.2.3 The effect by holes

Then we use the comparison of the boiling behavior shown in Fig. 12 to consider the effect by holes.

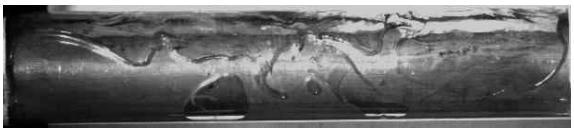
We placed holes to prevent the decline of water surface after intermittent boiling. When holes were placed, water flowed in the narrow gap from the inside of the inner tube and this has the effect of preventing the water level lowering. On the other hand, flows into the narrow space lowered the temperature of the heating surface so that overheating boundary layer's formation which will be the foundation of bubbles' growth inside the narrow space was disturbed. It can be verified in particullar when the holes were placed just above the cavities. At this time, the water flowing from the holes lower the temperature of the water in the narrow space so the bubbles from cavities will be hindered from growing. Because of that, it would be less likely to cause the mixing of the water which the most effective way to keep the high heat transfer coefficient.



(i) Without holes, 2 cavities 30mm apart (b)



(ii) 2 holes 60mm apart, 2 cavities 30mm apart (g)



(iii) 2 holes 30mm apart, 2 cavities 30mm apart (f)



(iv) Without holes and cavities (a)

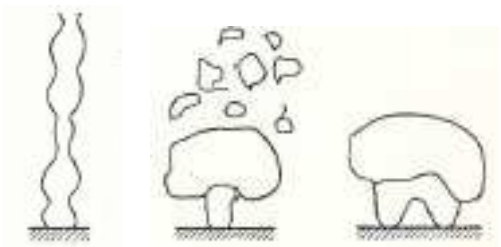
Fig. 12 Boiling behavior of q=20[kW/m^{2}K]

3.3 Relationship between shapes of bubbles and heat flux

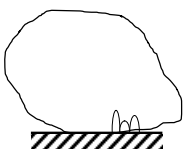
As heat flux increases, shapes of bubbles changes from isolated bubbles to coalesced ones and then going to a dry spot as shown in Fig. 13.



(i) Isolated bubbles



(ii) Coalesced bubbles



(iii) A dry spot

Fig.13 Shapes of bubbles

In a narrow space, it is obvious that water started boiling at low temperature but the burnout heat flux also declined. Therefore, it is significant to generate isolated bubbles artificially so that the performance would improve effectively and stably.

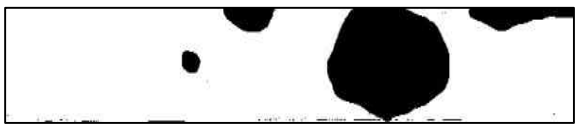
Focusing on the bubbles' generation from the cavities, Fig.14 and Fig.15 show the images to calculate void fraction. We processed image data from the high speed camera and generated binary images of Fig.14 and Fig.15. In these images, the white spaces represent liquid and black spaces represent vapor.



(i) Without holes, 2 cavities 30mm apart (b)



(ii) 2 holes 30mm apart, 2 cavities 30mm apart (f)



(iii) Without holes and cavities (a)

Fig.14 Vapor distribution of q=10[kW/m^{2}K]



(i) Without holes, 2 cavities 30mm apart (b)



(ii) 2 holes 30mm apart, 2 cavities 30mm apart (f)



(iii) Without holes and cavities (a)

Fig.15 Vapor distribution of q=20[kW/m^{2}K]

From the above images, we found that the size of the bubbles increased as the heat flux increased. When calculating the void fraction in the narrow space, it becomes about 60% for the inner tube (b) that achieved the best performance improvement.

4. CONCLUSIONS

- When inserting the inner tube having 2 cavities placed 30mm apart, heat transfer coefficient improved 1.67 times than that of not inserting the inner tube, and 1.51 times than that of inserting the inner tube without cavities and holes.
- The cavities placed 30mm apart have the effect of controlling bubbles' mutual interfere and promoting boiling.
- The water flowing from the holes lower the temperature of the heating surface and the effect of preventing the bubbles' growth.
- In the off-axial double-tube heat pipe, the water flowing leads to the bubbles' generation from the opposite side of the inner tube. Bubbles' generation, the increase of the wetted area, and the induction of the next nucleation are the major boiling heat transfer mechanism.

NOMENCLATURE

Q_{in} : Heat input
Q_{el} : Indication by the watt meter
Q_{lah} : Heat loss by the natural convection
Q_{ra} : Heat loss by the radiation
Nu_{air} : Nusselt number
Ra : Rayleigh number
g : Gravitational acceleration (m/s^2)
β : Thermal expansion coefficient (/K)
T_w : Water temperature (K)
T_{air} : Air temperature (K)
D' : Inside diameter of the outer tube (m)
v : Kinematic viscosity (m^2/s)
a : Thermal diffusivity (m^2/s)
T_{film} : Film temperature (K)
λ : Thermal conductivity (W/(m·K))
A : Heating surface area (m^2)
ε : Emissivity
σ : Stefan-Boltzmann constant (W/ ($m^2 \cdot K^4$))
q : Heat flux (W/m2)
$T_{surf.}$: Heating surface temperature (K)
L : Tube length (m)
t : Tube thickness (m)
$T_{sat.}$: Saturation temperature (K)
h : Heat transfer coefficient (W/($m^2 \cdot K$))

REFERENCES

[1] Katsuta M., and Nagata K., "Boiling induced heat-transfer enhancement using a narrow space", ASME 1992, *The engineering foundation Conf, on Pool and External Flow Boiling*, Vol.1, (1992) 381-386.

[2] Katto Y., Yokoya S. and Teraoka K., "Nucleate and transition boiling in a narrow space between two horizontal, parallel disk-surfaces", *Bull. JSME*, vol. 20, No. 143, (1997) 841-848

[3] Nishikawa K., Fujita Y., Nagashima A. and Kunitomo T., *Progress of Heat transfer engineering*, Youkendou, (1974) 90-98.

[4] Fujita Y., Uchida S. and Nishikawa K., " Nucleate boiling heat transfer in narrow spaces", *Int. Heat & Mass Transfer*., vol. 12, (1969) 863-894

[5] Ishibashi E. and Nishikawa K., "Boiling heat transfer in narrow space, part 1: in case of distilled water in the atmospheric pressure (in Japanese)", *Trans JSME*, vol.33, No.245, (1967) 8121-8129.

[6] Yao S. C. and Chang Y., "Pool boiling heat transfer in a confined space", Int. Heat & Mass Transfer., vol. 26, No. 6, (1983) 638-643.

[7] Bejan A., *Heat transfer*, John Wily & Sons, Inc, (1993) 419-427.

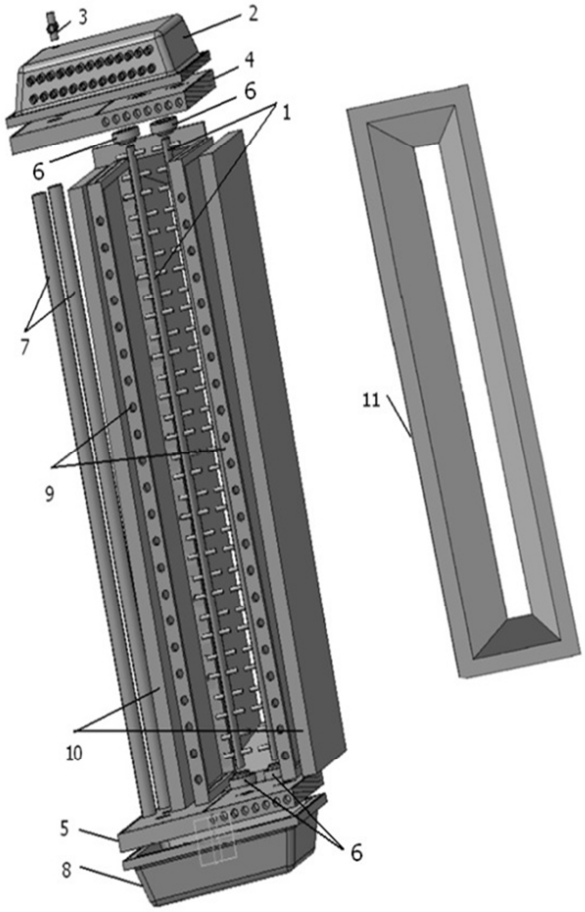
Modeling of Processes in the Waste Heat Boiler with Thermosyphon

Savchenkova Natalia[1], Kravtsov Dmitry[2]

[1] *Ph.D., Ass. Professor, Department of the Heat and Mass Transfer Process and Devices, National Research University "The Moscow Power Engineering Institute",*
[2]*Master's student, Department of the Heat and Mass Transfer Process and Devices, National Research University "The Moscow Power Engineering Institute"*
111250, Moscow, Krasnokazarmennaya str., 14. Tel/fax.: +7 (495) 362-70-40,
e-mail: savchenkovanm@mpei.ru, kdzhurml@mail.ru

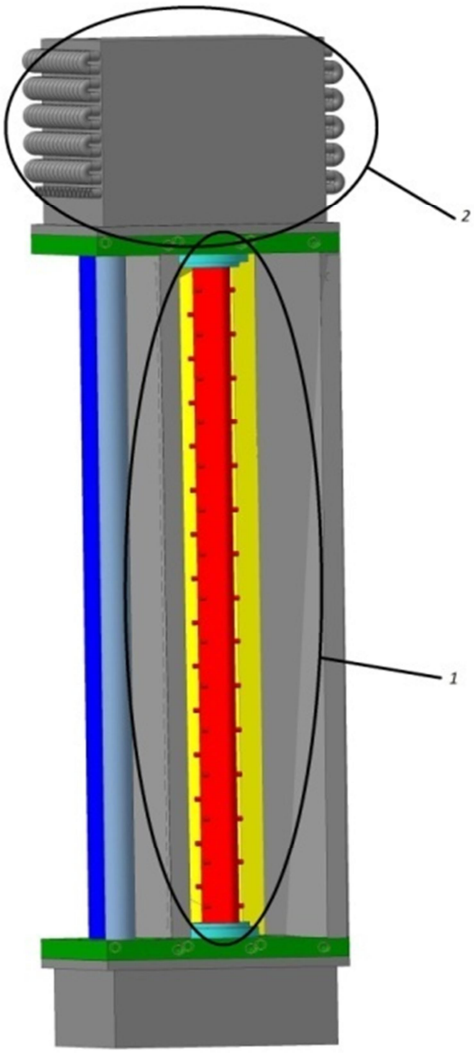
Keywords: heat pipe, thermosyphon, heat transfer, waste boiler, energy saving

Therecovery boiler unit, which uses the heat of exhaust gases. Closed thermosyphonis the heat transfer device that provides heat transfer from the flue gases to the cold water in the evaporation-condensation cycle (picture 1).



Picture 1. The waste heat boiler with thermosyphon: 1 –tubes with ribbed pins, 2 – the cover, 3–branch pipe, 4, 5 – steelplates, 6 – flanges, 7 – tubes for return condensate, 8 – support elements,9 –heating chamber walls, 10 –insulation material, 11 – air duct

The apparatus can consist of onethermosyphon tube or tube bundleof several thermosyphons(1). This part is the main element in which heat transfertakes placefrom flue gas to the liquid through the wall therefore there is a boiling processin tubes.



Picture 2. Total recovery boiler design. 1 – thermosyphon, 2 - regenerative heat exchanger device

Vaporsupplies into the cover (2), which contains of the water tube bundle. Cold water is heated up to the programmed temperature in these tubes by vapor coming from the thermosyphon. The number of tubes depends on the power of the heat boiler.

The tubes are made with ribbed pins onthe walls of the thermosyphonto intensify the process of heat exchange. These pins have staggered arrangement. Their length is 10 mm/per each unit, and the diameter is 5 mm/per each unit. Thermosyphon tube is fixed in the upper and lower flue sheets with the help of flanges.

Tube sheets have the steel platesform of 20 mm thickness because of the pressure increase in the thermosyphon. These tube sheets also contain two condensate return tubes, which serve as support elementsat the same time. The condensate inflows into the lower reservoir and returns into the tube thermosyphondue to the pressure difference.

There is a heating chamber in which the heat transfers from the flue gas to liquid, bounded on both sides of the wall. Heating chamber wallsare made with thermal (heat-) insulation material to avoid heat leakage. Admission and removal gases in the chamber carry outthru the air ducts.

Thermosyphonwas calculated as an evaporator, where the boiling water and flue gases are heat-carrying agents (picture 2). The second part was designed as a regenerative heat exchanger device, there water saturated vapor and cold water flow (e.g. 13 tube corridor with internal diameter 8 mm) are heat-carrying agent. Water saturated vapor heats the water in the tube bundle, then condenses and returns to the thermosyphon.

Result of the calculation obtained that the water consumption is 0.18 kg/s, vapor consumption is 8,552 · 10-3 kg/s. At the same time, the heat convection coefficient of vapor at boiling water is 11220 (at the condensation it is 32870); the heat convection coefficient of water is 2910; the heat convection coefficient of flue gas is 180. Heat capacity of the thermosyphonis 20 kW and 19 kW of the water-heating part. In the calculation of the following formulas were used:

Heat flow the flue gas:

$$Q = G_{fg} \cdot c_{pfg} \cdot \left(t'_{fg} - t''_{fg}\right) = 0{,}35 \cdot 1144 \cdot (400 - 350) = 20{,}02 \cdot 10^3\ W$$

Heat flow the water:

$$Q_w = G \cdot c_{pw} \cdot (t_{steam} - t_w) = 8{,}552 \cdot 10^{-3} \cdot 4208 \cdot (100 - 80) == 719{,}736\ \text{W}$$

The heat transfer coefficient of vapor:

$$\alpha_{vapor} = 3{,}1 \cdot {p_{vapor}}^{0{,}25} \cdot q^{0{,}67} = 3{,}1 \cdot 1{,}031^{0{,}25} \times (203{,}8 \cdot 10^3)^{0{,}67} = 1{,}122 \cdot 10^4 \frac{W}{m^2 \cdot K}$$

The heat transfer coefficient of fluent gas:

$$\alpha_{fg} = 0{,}41 \cdot \left(\frac{\lambda_{fg}}{d_p}\right) \cdot \left(\frac{\omega_{fg} \cdot d_p}{\nu_{fg}}\right)^{0{,}6} \times {Pr_{gf}}^{0{,}3} == 0{,}41 \cdot \left(\frac{0{,}055}{0{,}005}\right) \times \left(\frac{6{,}621 \cdot 0{,}005}{5{,}674 \cdot 10^{-5}}\right)^{0{,}6} \cdot 0{,}647^{0{,}3} = 180{,}287 \frac{W}{m^2 \cdot K} = 180{,}287 \frac{W}{m^2 \cdot K}$$

Efficiencyof the one rib:

$$\eta = \frac{th(m \cdot l_p)}{m \cdot l_p} = \frac{th(19{,}767 \cdot 0{,}01)}{19{,}767 \cdot 0{,}01} = 0{,}987$$

Efficiency of the ribbed surface:

$$\eta_0 = 1 - \frac{\psi - 1}{\psi} \cdot (1 - \eta) = 1 - \frac{1{,}925 - 1}{1{,}925} \times (1 - 0{,}987) = 0{,}994$$

The heat transfer coefficient of the vapor of the hotwater:

$$\alpha_{\text{vapor}} = 0{,}845 \cdot \sqrt[4]{\frac{\lambda_s^3 \cdot g \cdot r_{steam} \cdot \rho_s}{d_i \cdot \nu_s \cdot (t_s - t_m)}} = 0{,}845 \times \times \sqrt[4]{\frac{(683 \cdot 10^{-2})^3 \cdot 9{,}81 \cdot 2256{,}8 \cdot 10^3 \cdot 958{,}4}{0{,}01 \cdot 0{,}295 \cdot 10^{-6} \cdot (100 - 99)}} = 32{,}87 \cdot 10^3 \frac{\text{W}}{\text{m}^2 \cdot \text{K}}$$

Calculation of the recovery boiler thermosyphon carried by the plots with the different heat transfer means.

Plot 1-2

$$dQ^{\circ}_{1-2} = \alpha_{fg} \cdot \eta_{0fg} \cdot F_a \cdot (T_h - T_2),$$

The coefficient of heat transfer of fluent gas:

$$\alpha_{fg} = 0{,}41 \cdot \left(\frac{\lambda_{fg}}{d_p}\right) \cdot \left(\frac{\omega_{fg} \cdot d_p}{\nu_{fg}}\right)^{0{,}6} \times Pr_{gf}{}^{0{,}3}, \frac{W}{m^2 \cdot K}$$

λ_{fg} - flue gas thermal conductivity;
d_p - diameter pins;
ν_{fg} - kinematical viscosity
Pr_{gf} - Prandtl number

The flue gas velocity

$$\omega_{fg} = \frac{G_{fg}}{\rho_{fg} \cdot f_{fg}}, \frac{m}{s}$$

The flue gas section:

$$f_{fg} = b_{hc} \cdot h_{hc} - b \cdot l_{ht} - d_p \cdot l_p \cdot n_p, m^2$$

b_{hc} - the length of the working chamber
h_{hc} - the height of the working chamber
b - ellipse diameter
l_{ht} - heat pipe height
l_p - height pins

The efficiency finned surface:

$$\eta_{0h} = 1 - \frac{\psi - 1}{\psi} \cdot (1 - \eta)$$

The effectiveness of the ribs:

$$\eta = \frac{th(m \cdot l_p)}{m \cdot l_p}$$

$$m = \sqrt{\frac{\alpha_{fg} \cdot P_o}{\lambda_m \cdot S_o}}$$

$$S_o = \pi \cdot \left(\frac{d_p}{2}\right)^2, m^2$$

$$P_o = \pi \cdot d_p, m$$

The thermal conductivity of copper:

$$\lambda_m = 392 - 0{,}0685 \cdot t_m, \frac{W}{m \cdot K}$$

The wall temperature:

$$t_m = \frac{t_{cw} + t_{cfg}}{2}, °C$$

The average water temperature in the thermosyphon tube:

$$t_{cfg} = \frac{t_w + t_s}{2}, °C$$

The average flue gas temperature:

$$t_{cfg} = \frac{t'_{fg} + t''_{fg}}{2}, °C$$

The finning ratio:

$$\psi = \frac{F_p}{F_g}$$

Square tube with fins:

$$F_p = \pi \cdot d_p \cdot l_p \cdot n_p + l_{ht} \cdot P, m^2$$

The pipe finning area excluding:

$$F_g = l_{ht} \cdot P, m^2$$

The perimeter tube:

$$P = 2 \cdot \pi \cdot \left(0{,}5 \cdot \left(\left(\frac{a}{2}\right)^2 + \left(\frac{b}{2}\right)^2\right)\right)^{0{,}5}, m$$

Plot 2-3

$$dQ^э_{2-3} = \lambda_m \cdot \frac{a}{2} \cdot \frac{b}{2} \cdot \frac{T_2 - T_3}{\delta}$$

The thermal conductivity of steel:

$$\lambda_m = 54{,}6 - 0{,}0442 \cdot t_m, \frac{W}{m \cdot K}$$

The wall temperature:

$$t_m = \frac{t_{cm} + t_{cfg}}{2}, °C$$

The average water temperature in the thermosyphon tube:

$$t_{cw} = \frac{t_w + t_s}{2}, °C$$

The average flue gas temperature:

$$t_{cfg} = \frac{t'_{fg} + t''_{fg}}{2}, °C$$

Plot 3-4:

$$dQ^э_{3-4} = \alpha_{steam} \cdot F_g \cdot (T_3 - T_c),$$

The coefficient of heat transfer of fluent gas:

$$\alpha_{fg} = 0{,}41 \cdot \left(\frac{\lambda_{fg}}{d_p}\right) \cdot \left(\frac{\omega_{fg} \cdot d_p}{\nu_{fg}}\right)^{0{,}6} \cdot Pr_{gf}{}^{0{,}3} \frac{W}{m^2 \cdot K}$$

The specific heat of steam flow:

$$q = \alpha_{steam} \cdot (T_3 - T_c), \frac{W}{m^2 \cdot K}$$

Plot 4-5:

$$dQ^{э}_{4-5} = \alpha_{cond} \cdot F_h \cdot (T_h - T_5),$$

The coefficient of heat transfer of steam:

$$\alpha_{steam} = 0{,}845 \cdot \sqrt[4]{\frac{\lambda_s^3 \cdot g \cdot r_{steam} \cdot \rho_s}{d_i \cdot \nu_s \cdot (t_s - t_m)}} \frac{W}{m^2 \cdot K}$$

The area:

$$F_h = \pi \cdot d_i \cdot l_k \, , m^2$$

d_i - inner diameter

Plot 5-6:

$$dQ^{э}_{5-6} = \lambda_m \cdot (\frac{d_c}{2})^2 \cdot \frac{T_5 - T_6}{\delta},$$

The average diameter of the pipe:

$$d_c = \frac{d_i + d_o}{2}, m$$

The thermal conductivity of steel:

$$\lambda_m = 54{,}6 - 0{,}0442 \cdot t_m \, , \frac{W}{m \cdot K}$$

Plot 6-7:

$$dQ^{э}_{6-7} = \alpha_w \cdot F_t \cdot (T_6 - T_c),$$

The coefficient of heat transfer of water:

$$\alpha_w = \frac{Nu_w \cdot \lambda_w}{d_w}, \frac{W}{m^2 \cdot K}$$

Nusselt number of water:

$$Nu_w = 0{,}021 \cdot Re_w^{0,8} \cdot Pr_w^{0,43} \cdot (\frac{Pr_w}{Pr_c})^{0,25}$$

Reynolds number of water:

$$Re_w = \frac{\omega_w \cdot d_o}{\nu_w}$$

The water speed:

$$\omega_w = \frac{G_w}{f \cdot \rho_w}, \frac{m}{s}$$

The water through the orifice tube:

$$f = \frac{\pi \cdot d_w^2}{4}, m^2$$

Water consumption:

$$G_w = \frac{Q}{c_{pw} \cdot (t_w^{"} - t_w')}, \frac{kg}{s}$$

The heat flux:

$$Q = \eta \cdot G \cdot r_s \, , W$$

This device can be used in various heating systems. For example, water (from an external source) is supplied to the first level preheater, then passes demineralizer. Later water flows to the second level preheater and the deaerator. The part of the water flows from the deaerator to the recovery boiler and consumer.

Conclusions

Presented heat exchanger has a number of advantages:

- Simplicity of design;
- Low price: the possibility of manufacturing of some elements with wastes of production;
- Efficiency increase of secondary energy resources;
- Reduced metal consumption;
- Compactness;
- Reduced hydraulic resistance through the use of ribbed pins;
- High heat conductivity of the thermosyphon;
- The use of natural circulation of water;
- Reduction of electricity consumption.

Bibliography

[1] L.N. Sidelkovsky, V.N. Yurenev, Boilers industrial enterprises, Energoatomizdat, 1988.

[2] A.A. Borodkin, V.D. Portnov, V.Y. Shashin, V.N. Fedorov. Calculation heat-and-mass transfer devices, Publishing House MPEI, 1997.

[3] A.M. Baklastov, V.A. Gorbenko, O.L. Danilov, Heat-and-mass transfer industrial processes and plants, Energoatomizdat, 1986.

[4] F.F Tsvetkov, R.V. Kerimov, V.I. Velichko, Book of problems in heat-and-mass transfer, Publishing House MPEI, 2008.

[5] A.L. Efimov, A.V. Danilina, Calculation and intensification of heat transfer in industrial heat exchangers, Publishing House MPEI, 2009.

Experimental Tests on Sodium Thermosyphons

Tiago W. Uhlmann[1], Marcia B. H. Mantelli[1*], Miriam Manzoni[2], Marco Marengo[2], Per Eskilson[3]

[1] Heat Pipe Laboratory (Labtucal), Mechanical Engineering Department, Federal University of Santa Catarina, Florianópolis, Brazil
[2] Università degli Studi di Bergamo, Dept. of Eng. and App. Science, Italy; University of Brighton, School of Computing, Engineering and Mathematics, UK
[3] Cleanergy, Theres Svenssons gata 15, 417 55 Göteborg, Sweden

Abstract

Thermosyphon is a heat transfer device built from an evacuated tube filled with an appropriate volume of working fluid. It operates on a closed two-phase cycle and utilizes latent heat of vaporization and condensation to transfer heat. To understand and evaluate the behavior of sodium thermosyphons and their capacity to transfer heat under temperatures around 1000 °C, four thermosyphons were fabricated, charged, and tested on the Heat Pipe Laboratory, Brazil. Five tests were performed, using an induction heater as heat source. Four of those tests used a copper coil with flowing water as heat sink, while the other used just the environment, allowing heat to be transferred by natural convection and radiation. The temperature difference between inlet and outlet flowing water, the temperature of the external wall in several regions of the thermosyphons, and the mass flow rate of the cooling water were recorded. Two calculation methods to determine the heat transfer rate were applied to the collected data. For cooling by the copper coil heat sink, the forced convection heat absorbed by the flowing water through the coil, was calculated and assumed to be the heat transfer rate through the condenser wall. When the environment was used as the heat sink, the heat transfer rate of the thermosyphon to the ambient was calculated using a literature natural convection correlation and a radiation analytical model. The applications of such analytical methods allowed computing the maximum heat transfer rate of a thermosyphon with a difference of 2.3%, proving that both methods can be used to determine the heat transfer rate of the thermosyphon. Another important observation is that the thermosyphons with ratio between working fluid and evaporator volumes of 80% transferred more heat than ones with filling ratio of 100%.

Keywords: Filling ratio; High temperature; Sodium; Thermosyphon

1. INTRODUCTION

Thermosyphon is a heat transfer device built from an evacuated tube filled with an appropriate volume of working fluid. It operates on a closed two-phase cycle and utilizes the latent heat of vaporization and condensation to transfer heat, creating very small temperature gradients along the thermosyphon length [1, 2]. Different working fluids can be employed, depending on the working temperature level of the system. Water is an excellent fluid for operating on temperatures between 30 and 200 °C; whereas, for temperatures between 500 and 1200 °C, potassium and sodium are among the most suitable working fluids [3].

Most correlations developed to predict the thermosyphon coefficients of heat transfer in the evaporator and condenser were developed for water, refrigeration gases, or alcohols [4, 5] and might not be applicable to other fluids, especially those which start up is in solid state at room temperature, such as sodium. However, even when the appropriate heat transfer correlation is available [6], it is recommended to run experimental tests before using the correlation for designing equipments [7].

*Corresponding author: marcia.mantelli@ufsc.br,
Phone: +55 48 3721-9937

To understand and evaluate the behavior of sodium thermosyphons and their capacity to transfer heat under temperatures around 1000 °C, four thermosyphons were fabricated, charged, and tested on the Heat Pipe Laboratory (LABTUCAL) of the Federal University of Santa Catarina.

Charging procedures of sodium heat pipes and thermosyphons are available in the literature [3, 8, 9] and they have three characteristics in common; first, they require a controlled inert atmosphere to avoid sodium reaction with air and humidity; second, the construction of a specific filling rig is necessary; third, liquid sodium is introduced in the tube. In order to simplify the charging procedure, the fabrication process presented here does not require a specific filling rig and solid sodium is introduced in the tube [10].

2. THERMOSYPHON FABRICATION

The fabrication process can be divided in five steps as follows:

1. Material selection and tube cutting;
2. Tube cleaning;
3. One end smashing, welding and leakage test;
4. Solid sodium tube charging;
5. Vacuum, smashing and weld cutting.

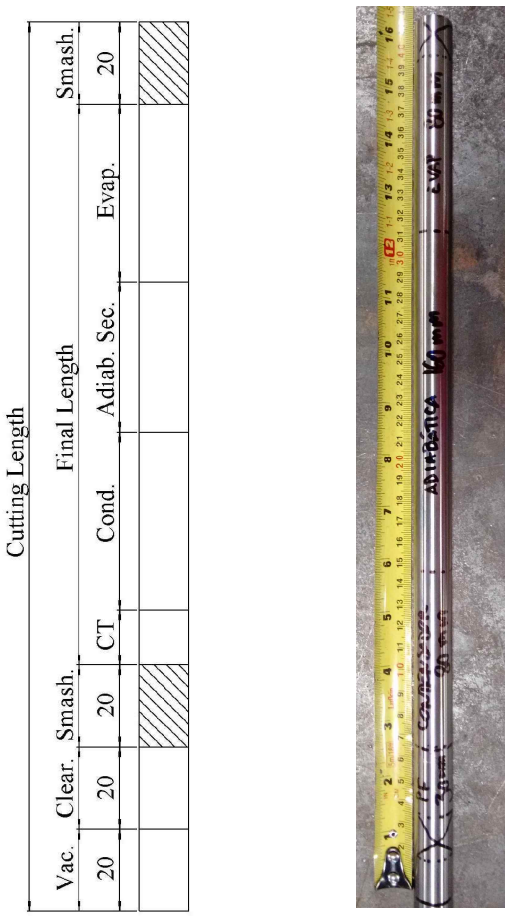


Fig. 1. Thermosyphon cutting length.

These steps will be explained in details in the following text. Table 1 lists the characteristics of the four thermosyphons fabricated through this process.

2.1 Material Selection and Tube Cutting

The tube material must be chosen according to the compatibility with the working fluid. Stainless steel and Inconel alloys are recommended for sodium [3]. In this work, Inconel 600 was used to fabricate the thermosyphons.

The thermosyphon tube cutting and final lengths are different due to the vacuum and smashing procedures. Evaporator, adiabatic section, condenser, and cold tip (CT) lengths compose the final length. Added to this, 40 mm are for smashing procedure, 20 mm for vacuum procedure, and 20 mm of clearance (Fig. 1).

2.2 Tube Cleaning

The tubes were washed with a solution of one part of an industrial degreasing (Quimatic ED Bio) to five parts of distilled water, thus rinsed with abundant distilled water. This process was repeated three times.



Fig. 2. Smashed tube end.

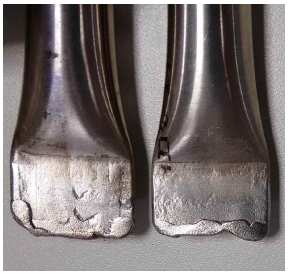


Fig. 3. Welded end.

2.3 One End Smashing, Welding, and Leakage Test

In order to close one side of the tube, the last 20 mm were smashed in a press with a load of 12 ton (Fig. 2). The smashed region was then TIG welded with a current of 70 A (Fig. 3) and a leakage test was performed in the tube using the equipment EDWARDS SPECTRON 5000 that detects traces of helium through its vacuum pumps and a helium detector. If no leakage was found, the tube was taken to the charging procedure.

2.4 Solid Sodium Tube Charging

The Sigma-Aldrich sodium used to charge the thermosyphons was 99.8% pure and was transported immerse in glass bottles with kerosene. In order to avoid the contamination of the glove box inert atmosphere with vapor of kerosene and air, the necessary amount of sodium was placed in a Kitasato flask and vacuum pumped (Fig. 4). Flask with sodium, Inconel tube (already subjected to the 2.1 to 2.3 steps), knife, silicon hoses, pressure scissors, scale, and tube diameter adapter were taken into a glove box filled with inert gas (Argon). Inside the glove box, the flask was opened and the external opaque sodium layer was removed (Fig. 5).

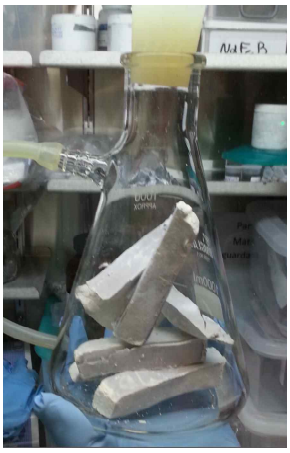


Fig. 4. Sodium in the Kitasato flask.



Fig. 5. Sodium with external layer partially removed.

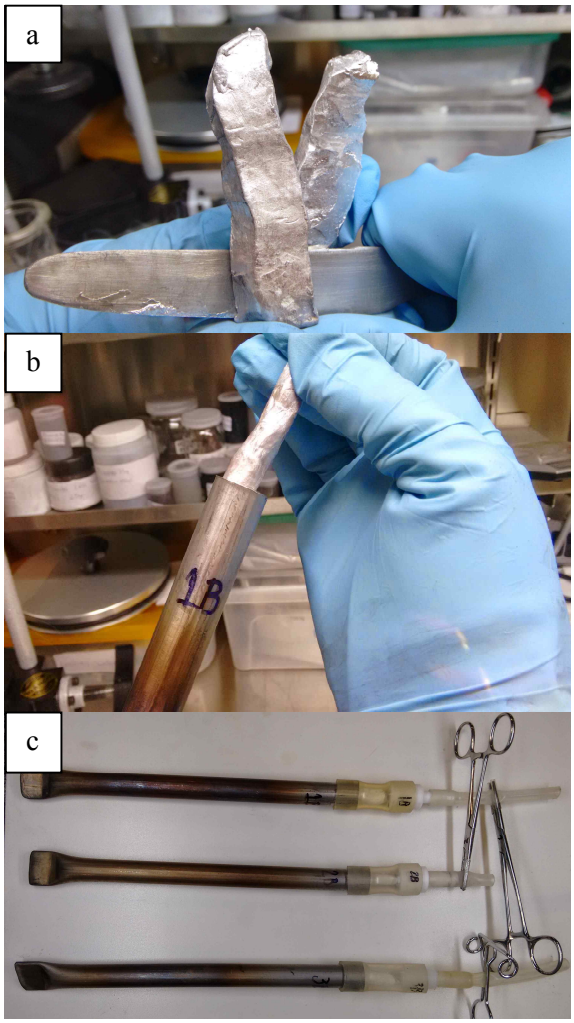


Fig. 6. Charging procedure. a) Cutting sodium in small pieces, b) inserting sodium in the tube, c) tube closed with silicon hoses, tube diameter adapter and pressure scissors.

Sodium was cut in small pieces, weighted, and introduced in the tube. The charged tube was closed with silicon hoses, tube diameter adapter and pressure scissors before has being removed from the glove box (Fig. 6.).

When the volume of sodium at room temperature was above around 22% of the total volume of the thermosyphon, it was necessary to heat up the tube above 98°C while charging with sodium to avoid sodium stacking.

2.5 Vacuum, Smashing and Weld Cutting

Outside the glove box, the tube was vacuum pumped up to 10^{-6} mbar to remove all gases. The silicon hose was closed again with the pressure scissor and the tube was smashed in a press in two steps; first, with a load of 16 ton with a plane mold; second, with a load of 10 ton with a wedge format mold (Fig. 7). In order to close the thermosyphon a

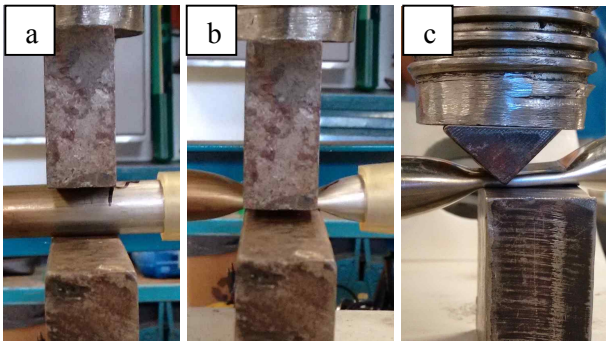


Fig. 7. Smashing. a) tube positioned between two plane molds, b) tube after 16 ton load, c) smashing with a load of 10 ton and a wedge form mold.

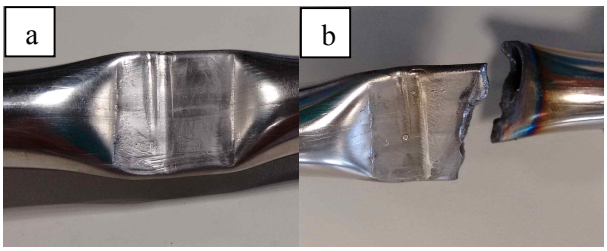


Fig. 8. Weld cutting. a) Before, b) after.

TIG weld cutting with a current of 100 A was performed (Fig. 8).

3. EXPERIMENTAL PROCEDURE AND DATA PROCESSING

Five tests were performed using the experimental procedure adopted in [10]. The induction coil used on tests (see Table 1) 1.1, 1.2, and 2 was of 100 mm of length and on tests 3 and 4 the induction coil was of 320 mm of length. All tests were in the vertical position.

In tests 1.2, 2, 3, and 4 the heat transfer rate was calculated through the copper coil calorimeter measurements using the known equation

$$Q = \dot{m} c_p \left(T_{out} - T_{in} \right). \quad (1)$$

In test 1.1 the heat transfer rate was calculated considering natural convection and radiation to the environment. A correlation for natural convection in vertical cylinders presented by [11] was used to calculate the average coefficient of heat transfer considering the average condenser temperature as the cylinder wall temperature and the temperature of the environment as 30 °C. To calculate the total heat transfer rate through convection and radiation the condenser was divided in 6 parts, where each part was monitored by a thermocouple in the upper and lower regions. The average temperature between

Table 1. Thermosyphons and tests characteristics.

Test		1.1	1.2	2	3	4
Description		TS1	TS1	TS2	TS3	TS4
Tube Material		Inconel 600	Inconel 600	Inconel 600	Inconel 600	Inconel 600
Length [mm]	Evaporator	100	100	100	320	320
	Adiabatic Zone	0	85	85	0	0
	Condenser	145	35	35	124	124
	Cold Tip	0	25	25	25	25
	Total	245	245	245	469	469
Diameter [mm]	Inner	16	16	16	18	18
	Outer	18	18	18	21.34	21.34
Type of Condenser		Environment	Copper Coil	Copper Coil	Copper Coil	Copper Coil
Mass of Sodium (g)		20	20	15.6	78.8	62.1
Filling Ratio at Ambient Temperature		100%	100%	80%	100%	~80%
Maximum Calculated Heat Transfer Rate (W)		487	476	611	730	988
Induction coil current at Max. Calc. Heat Transfer Rate (A)		360	360	360	1660	1660

those two thermocouples was used to calculate the convection and radiation portion of each part. The thermosyphon was considered as a gray body with total hemispherical emissivity according to the linearization of the data presented in [12]:

$$\varepsilon_i = 0.0002 \cdot \overline{T}_i + 0.5734 \qquad (2)$$

and the total heat transfer rate of test 1.1 is given by:

$$Q = \sum_{i=1}^{6} hA_i \left(\overline{T}_i - T_\infty\right) + \sigma\varepsilon_i \left(\overline{T}_i^4 - T_\infty^4\right). \qquad (3)$$

The induction current used in tests 1.1, 1.2 and 2 did not reach the maximum possible induction coil current, but it was limited to 360 A, due to the high temperatures on the evaporator which would cause melting of the thermosyphon wall. In tests 3 and 4 the current of 1660 A was the maximum induction coil current used, which already caused overheating of the induction system. In average, each test last 50 minutes. In all tests, temperature gradients were observed along the thermosyphon, more evident in test 1.1, where heat was transferred to the ambient air.

4. TESTS RESULTS AND ANALYSIS

Fig. 9 shows the tested thermosyphon heat transfer rate as a function of its evaporator temperature for all tests performed. One can see that, for all tests, the thermosyphons only start to transfer more than 200 W after reaching 660 °C. Also, as the temperature of the evaporator increases, the heat transfer rates increases.

Tests with filling ratio (ratio between working fluid and evaporator volumes) of 80% (Test 2 and 4) transferred more heat than those with filling ratio of 100% (Tests 1.1, 1.2, 3), for a same evaporator temperature. It suggests that lower filling ratios are preferable. One reason for this best thermal behavior at lower filling ratio is that, in operation, the sodium expands, overpassing (flooding) the evaporator height. Note that the filling ratio was measured at room temperature. In tests 1.1 and 3, the height of the sodium pool reached the condenser, while in test 2 it reached the adiabatic section.

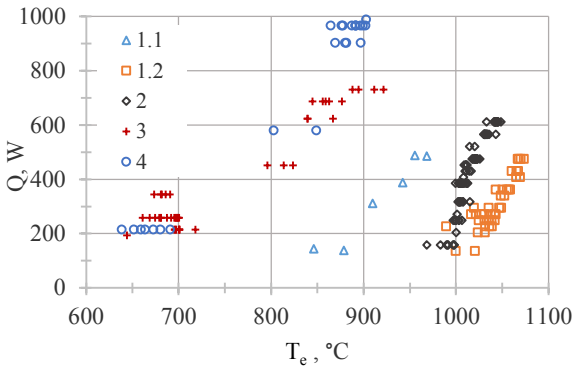


Fig. 9. Heat transfer rate versus temperature of the evaporator.

Table 2. Comparison between two calculation methods of heat transfer rate.

I (A)	Q (W)		Error
	Test 1.1	Test 1.2	
270	141	199	-29.0%
300	311	272	14.4%
330	387	351	10.4%
360	486	475	2.3%

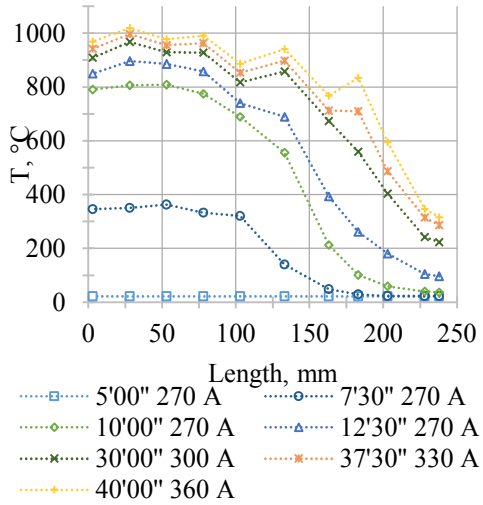
In tests 1.1 and 1.2 (Thermosyphon 1), the same trend for the heat transfer rate increase is verified, but for different temperature levels. The lower temperature level on test 1.1 is attributed to the larger condenser area when compared with 1.2.

Table 2 brings a comparison between the two calculation methods for the heat transfer rate. The calorimeter results of test 1.2 are taken as the standard value for comparison. As the heat transfer rate increases, the error between methods decreases up to 2.3%, showing that both methods are consistent to calculate the maximum heat transfer rate. Also, for the tests when a calorimeter cannot be used, the heat transfer rate can be obtained applying the calculation method proposed for test 1.1, which shows a maximum error of 29.0%.

Test 1.1 presents a clear temperature gradient along the thermosyphon condenser (Fig. 10), with colder temperatures at the thermosyphon tip region. Two hypotheses can be proposed. First, the presence of non-condensable gases (NCG - air) that entered inside the thermosyphon during the last stage of the fabrication process. The NCG concentrates in the tube tip region, avoiding the thermosyphon working fluid to phase change, resulting, therefore, in a colder tip. Second, the heat removal rate is high enough to condense and decrease the sodium temperature on the condenser. As the temperature decreases, the pressure also decreases and the sodium cannot reach the thermosyphon condenser end. In both hypothesis only the heat transferred by conduction through the metallic tube wall is able to reach the condenser end. Further investigations of these hypotheses are recommended. The other tests presented a practically constant temperature before the condenser and a cold tip after.

5. CONCLUSIONS

Four sodium thermosyphons were fabricated, charged, and tested with success in the Heat Pipe Laboratory (Brazil). Five tests were performed with two different heat sinks. One test used the environment and the other four used a water calorimeter, made of a copper coil, as the heat sink. Two heat transfer rate calculation methods were compared and considered valid to calculate the maximum heat transfer rate, with an error of 2.3%.



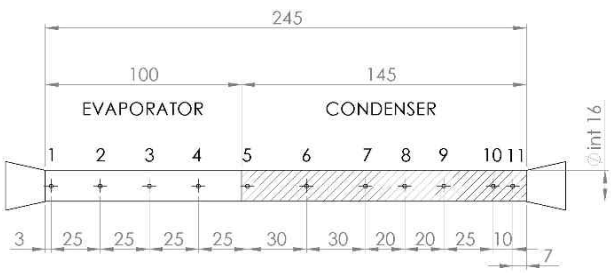


Fig. 10. External wall temperatures along the length for test 1.1.

To the same evaporator temperature, thermosyphons with filling ratio of 80% presented a higher heat transfer rate than ones with filling ratio of 100%, suggesting that lower filling ratios are preferable. A temperature gradient was observed and non-condensable gases or high heat removal were proposed as hypotheses that caused such gradient.

ACKNOWLEDGEMENT

The authors recognize the significant financial support given by Cleanergy AB (Sweden).

NOMENCLATURE

Q : Heat transfer rate (W)
$\dot{m}$: Mass flow rate of water (kg/s)
c_p : Specific heat of water (J/(kg.K))
T_{out} : Output temperature of water (K)

T_{in} : Input temperature of water (K)
ε_i : Total hemispherical emissivity of Inconel 600 (-)
$\overline{T}_i$: Average temperature of part *i* of the condenser (K)
h : Coefficient of heat transfer (W/(m^2.K))
A_i : External area of part *i* of the condenser (m^2)
T_∞ : Temperature of the environment (K)
T_e : Average temperature of the evaporator (°C)

REFERENCES

[1] Peterson, G.P., *An introduction to heat pipes: modeling, testing, and applications,* New York, Wiley-Interscience Publication, (1994).
[2] Mantelli, M.B.H., *Thermosyphon Technology for Industrial Applications, in Heat Pipes and Solid Sorption Transformations - Fundamentals and Practical Applications* by Vasiliev and Kakaç. 1st ed.: CRC Press, (2013), pp. 411.
[3] Reay, D. and Kew, P., *Heat Pipes: Theory, Design and Applications,* Burlington, Butterworth-Heinemann, 5th ed., (2006)
[4] Kaminaga, F., Okamoto, Y., Heat-transfer characteristics of two-phase thermosiphon heat pipe. Part 1. Boiling heat-transfer correlation in heating section, *Heat Transfer – Japanese Research*, vol. 23, pp. 52-65, (1994)
[5] Gross, U., Reflux condensation heat transfer inside a closed thermosyphon, *International Journal of Heat and Mass Transfer*, vol. 35, pp. 279-294, (1992)
[6] Shah, M. M. and A Survey of Experimental Heat Transfer Data for Nucleate Pool Boiling of Liquid Metals and a New Correlation, *International Journal of Heat and Fluid Flow*, vol. 13, pp. 370-379, (1992). http://dx.doi.org/10.1016/0142-727X(92)90007-V.
[7] Dobson, R. T. and Laubscher, R., Heat pipe heat exchanger for high temperature nuclear reactor technology, *Frontiers of Heat Pipes*, vol. 4, p. 1–7, (2013) http://dx.doi.org/10.5098/fhp.v4.2.3002.
[8] Faghri, A., *Heat pipe science and technology*, Taylor & Francis, USA, (1995).
[9] Dillig, M., Leimert, J. and Karl, J., Planar high temperature heat pipes for SOFC/SOEC stack applications, *Fundamentals & Developments of Fuel Cells Conference,* (2013).
[10] Manzoni, M., Uhlmann, T. W., Mantelli, M. B. H., Eskilson, P. and Marengo, M., Numerical Simulation of a Sodium Thermosyphon, *14th UK Heat Transfer Conference*, (2015).
[11] Nellis, G. and Klein, S., *Heat Transfer*, Cambridge University Press, (2006).,
[12] Inconel Alloy 600 Data Sheet. Available in http://www.specialmetals.com/assets/documents/alloys/inconel/inconel-alloy-600.pdf. Accessed in March, 11th 2016.

Numerical Modeling of Heat Transfer Performance of Two-phase Closed Thermosyphon with R245fa based on Sinda/Fluint

Limin Ma, Xiaoying Yin, Linlin Shang, Zhongli Ji

College of Mechanical and Transportation Engineering, China University of Petroleum-Beijing, 102249 China

Abstract

A transient simulation model of two-phase closed thermosyphon has been established by Sinda/Fluint software with R245fa as working fluid. The copper thermosyphon was 3 m long with an inner diameter of 40 mm. The length of evaporator, adiabatic and condenser was 1 m respectively. The evaporator section was immersed in the constant temperature water-bath and the condenser section was cooled by recycled water. The simulation results have been compared with the experiment, and the good agreement confirms that the model is accurate and reliable. Base on this model, the effects of relevant factors, including heat source temperature, inlet temperature of coolant water, filling ratio, condenser section length and inner diameter, have been investigated on heat transfer performances of thermosyphon in the range of 35-95 ℃ of working condition for R245fa. The average relative error of outer wall temperature of the thermosyphon and heat load between simulation and experiment results is 3.9 % and 6.2 % respectively. With the increase of heat source temperature and flow rate of coolant water, heat transfer rate are improved, while the increase of inlet temperature of coolant water results in the decrease of them. The optimum of condenser section length is in the range of 1.0-1.5 m in given working conditions. The optimal filling ratio is 25 % for 0.05 m inner diameter and 15 % for both of 0.03 m and 0.04 m.

Keywords: Two phase closed thermosyphon; Heat transfer experiment; Computer simulation; R245fa; Sinda/Fluint model

1. INTRODUCTION

The two-phase closed thermosyphons (TPCT) with operating temperature in the range of -30-100℃ have been extensively used and explored in a wide range of engineering applications, such as cooling of electronic components[1,2], geothermal utilization[3-5], solar heater systems [6,7], air conditioning (HVAC) systems[8,9,10]. However, compared with the experimental studies, more simulation studies on thermosyphons need to be carried out. Fadhl et al.[11] built a CFD two-dimensional model to predict temperature profiles, using VOF model and adding UDF to the Fluent code, and selecting water as the working fluid. The predicted results have good agreement with the experiment. Fadhl et al [12] built a CFD model to simulate the details of the two-phase flow and heat transfer phenomena during the start-up and steady-state operation, and using R134a and R404a as the working fluids. Jiao et al [13] developed a comprehensive model to investigated the effect of filling ratio on a vertical TPCT. And three types of flow pattern and two types of transition according to the distribution of liquid film and liquid pool are considered. The effects of heat input, operating pressure and geometries of the TPCT are also discussed. Alizadehdakhel et al [14] used VOF and UDF of CFD to model the gas/liquid two phase flow and heat transfer. The CFD predicted temperature profile and compared with experimental results. Huang et al[15] investigated the steady-state characteristics of natural circulation loop (NCL) by a homogenous model with SINDA/FLUINT. Two non-dimensional parameters η_p and η_l are proposed to characterize the operation modes of the NCL.

For low temperature applications, refrigerant R134a is widely used [16]. However, it has a large Global Warming Potential (GWP) and high vapor pressure (>3.0 MPa) when the operating temperature is over 87℃. In this paper, refrigerant R245fa with lower GWP and vapor pressure [17], which is proposed as replacement for R11 and extensively used in high temperature heat pumps[18], was selected as working fluid in the thermosyphon.

In this paper, 1D transient simulation model of the two-phase closed thermosyphon was established by using Sinda/Fluint. Based on this model, the effects of relevant factors, including heat source temperature, inlet temperature of coolant water, filling ratio, condenser section length and inner diameter, have been investigated on heat transfer performances of thermosyphon. And the simulation results have a good agreement with the experimental measurements.

*Corresponding author: malimin@cup.edu.cn, Phone: +86-10-8973-3658, Fax: +86-10-8973-3203

2. EXPERIMENTAL APPARATUS AND PROCEDURE

2.1 Experimental apparatus

To validate the simulation model and results, an experimental apparatus was set up to carry out the heat transfer performances investigation. The experiment system is shown in Fig.1. The system consists of a TPTC, a water bath, the coolant water circuit, vacuum extraction system and measuring instrumentation. The TPCT was manufactured from a 40 mm inner diameter, 3 m long smooth copper tube with a wall thickness of 2 mm. The TPCT was divided into evaporator section, adiabatic section and condenser section evenly, so the length of each section was 1 m. The length of coolant water jacket is 1 m, with 100 mm and 104 mm for the inner and outer diameters respectively.

The evaporator section was immersed in the thermostatic water bath. The maximum heating power was 20kW and the precision of temperature control was 0.3℃. The condenser section was cooled using a water jacket surrounding the TPCT. There was another thermostatic water bath with cooling function to remove the heat that the coolant water absorbed from the condenser section. The precision of temperature control of this water bath was in the range of 0.2 ℃. The adiabatic section was well insulated to decrease heat loss. The TPCT was charged with R245fa as working fluid.

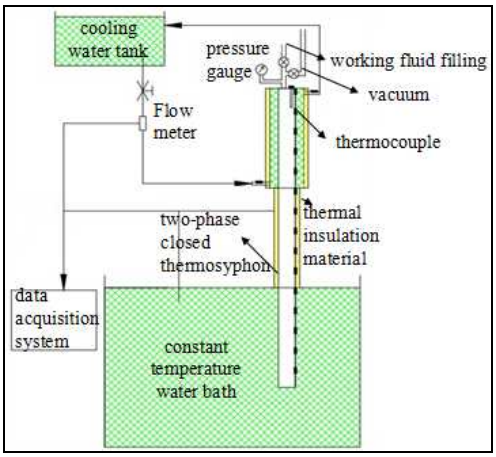


Fig.1 The experimental apparatus of TPCT

Thirty Cu/Con thermocouples have been uniformly distributed to measure the temperature along the outer wall of the thermosyphon. All these thermocouples were calibrated before being mounted and the average precision was ℃0.2 And the flow rate of coolant water was measured by a electromagnetic flowmeter, and its maximum flow rate is 10L/min with the precision of ±0.2%.

Experimental investigation was carried out in different water bath temperature, filling ratio of the working fluid, and inlet temperature and flow rate of coolant water.

2.2 Data reduction

In the absence of the heat amount that the working fluid absorbed from water bath and heat loss from TPCP to the surroundings, the heat transmitted through the TPCP is considered as the heat that the coolant water absorbed in the condenser section.

$$Q = \dot{m}c(t_{\mathrm{cw,o}} - t_{\mathrm{cw,i}}) \tag{1}$$

Thus the performance of a TPCP can be expressed by the general heat transfer equation.

$$Q = kA\left(t_{\mathrm{b}} - \overline{t}_{\mathrm{cw}}\right) \tag{2}$$

The temperature of heat sink ($\overline{t}_{\mathrm{cw}}$) is regarded as the arithmetic mean of the inlet ($t_{\mathrm{cw,i}}$) and outlet ($t_{\mathrm{cw,o}}$) temperature of coolant water.

$$\overline{t}_{\mathrm{cw}} = \left(t_{\mathrm{cw,i}} + t_{\mathrm{cw,o}}\right)/2 \tag{3}$$

So the total heat transfer coefficient can be calculated by equation (2) above.

$$k = Q/A\left(t_{\mathrm{b}} - \overline{t}_{\mathrm{cw}}\right) \tag{4}$$

3. MODEL DESCRIPTION

The commercial software Sinda/Fluint 5.6 has been applied for the modeling of a closed two-phase thermosyphon in this paper. Sinda/fluint is a comprehensive finite difference, lumped parameter solver for analyzing or designing the complex thermal/fluid system. It consists of thermal submodel (Sinda) and fluid submodel (fluint).

3.1 Modeling description

The modeling process is described by the example of condenser section. Fig. 2 shows the modeling diagram of condenser section. In the model, the "node" represents solid, at which energy is conserved. The wall of thermosyphon and coolant water jacket were set up as the nodes, which were the row of Node(n) and Node(m) respectively in Fig. 2. The "lump" represents fluid,

at which energy and mass are conserved, and the working fluid R245fa in thermosyphon and the coolant water in jacket were set up as the lumps, which were the row of Lump(*i*) and Lump(*j*) respectively in Fig.2. The "path" establishes the connection between the lumps, which describes the momentum conservation when there exists mass transfer between the lumps. When the velocity of vapor and liquid can be assumed as same one, with no phase drift or slip flow, the "single" path is used. When the velocity of vapor and liquid can not be assumed as same one, more than one parallel path, twinned paths are assigned. So, in this paper, the path was set up for the coolant water while the twinned paths were set up for the working fluid R245fa. The "tie" establishes the coupling connection between the corresponding solid (nodes) and fluid (lumps).So three series of 'Ties', which were Tie(*k*), Tie(*j*) and Tie(*i*) in Fig.2 respectively, were established.

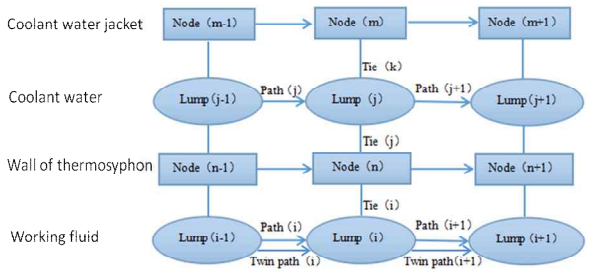


Fig.2 The condenser section of thermosyphon

3.2 Governing equations

(1) Node equation

By applying the principle of conservation of energy to the *n*th node of the wall of thermosyphon in Fig.2, the energy equation has the following form:

$$\left(mc_p\right)_{node(n)}\frac{\partial T_{node(n)}}{\partial t}=G_{n\pm1,n}\left(T_{\mathrm{node}(n\pm1)}-T_{\mathrm{node}(n)}\right)+\left(\dot{Q}_{tie(i)}-\dot{Q}_{tie(j)}\right) \tag{5}$$

where $T_{\mathrm{node}(n)}$ is temperature of the *n*th node; $G_{n\pm1,n}$ the linear heat conductors(W/K) between the ($n\pm1$)th node and the *n*th node with the unit W/K, which is connect to the *n*th; $\left(\dot{Q}_{tie(i)}-\dot{Q}_{tie(j)}\right)$ is the net tie heat rate of the *n*th node, which connect the lumps to thermal nodes. The nodes of the coolant water jacket have the similar energy equation.

(2) Lump equations

The continuity and energy equations of the *i*th lump of the working fluid in Fig.2 are as follows:

$$V_{lump(i)}\frac{d\rho_{lump(i)}}{dt}=\dot{m}_{path(i)}-\dot{m}_{path(i+1)} \tag{6}$$

where $\dot{m}_{path(i)}$ and $\dot{m}_{path(i+1)}$ are the mass flow rate (kg/s) flow into and out of the *i*th lump respectively.

$$\left[V\left(\rho\frac{du}{dt}+u\frac{d\rho}{dt}\right)\right]_{lump(i)}=\left(\dot{m}_{path(i)}h_{path(i)}-\dot{m}_{path(i+1)}h_{path(i+1)}\right)-\dot{Q}_{tie(i)} \tag{7}$$

The lumps of the coolant water have the similar continuity and energy equations.

(3) Path equation

The momentum equation of the *j*th path of the coolant water in Fig.2 is as follows:

$$\frac{L}{A}\frac{d\dot{m}_{path(j)}}{dt}=P_{lump(j-1)}-P_{lump(j)}-\rho g\Delta z-\frac{f}{2\rho}\left(\frac{\dot{m}_{path(j)}}{A}\right)^2 \tag{8}$$

where $\dot{m}_{path(j)}$ is mass flow rate (kg/s) flow from the (*j*-1)th lump into the *j*th lump; $P_{lump(j-1)}$ and $P_{lump(j)}$ are the pressure of the (*j*-1)th lump and *j*th lump respectively; $\rho g\Delta z$ is gravity force and *f* is friction coefficient.

The momentum equation of the *i*th path of the working fluid is as follows:

$$\begin{aligned}\frac{d\dot{m}_{path(i)}}{dt}=&\frac{A}{L}\left(\begin{array}{l}\alpha_{path(i)}\left(P_{lump(i-1)}-P_{lump(i)}-\rho g\Delta z\right)+\\ \frac{1}{\alpha_{path(i)}}\left(FC_{path(i)}\dot{m}_{path(i)}{}^2-\frac{f\cdot\dot{m}_{path(i)}\left|\dot{m}_{path(i)}\right|}{2A^2\rho_{path(i)}}\right)\end{array}\right)\\&+\left(\frac{1}{\alpha_{path(i)}}FD_{path(i)}\cdot\dot{m}_{path(i)}-\frac{1}{\alpha_{tpath(i)}}FD_{tpath(i)}\cdot\dot{m}_{tpath(i)}\right)\\&+\varepsilon_{path(i)}\left(\frac{1}{\alpha_{path(i)}}FG_{path(i)}\cdot\dot{m}_{path(i)}+\frac{1}{\alpha_{tpath(i)}}FG_{tpath(i)}\cdot\dot{m}_{tpath(i)}\right)\\&+\left(\alpha_{tpath(i)}\cdot AM_{tpath(i)}\frac{d\dot{m}_{tpath(i)}}{dt}-\alpha_{path(i)}\cdot AM_{path(i)}\frac{d\dot{m}_{path(i)}}{dt}\right)\end{aligned} \tag{9}$$

where α is void fraction; the subscript *tpath*(*i*) represents the second twin path; *A* is the cross-sectional area of thermosyphon; *FC* is recoverable loss, which is essentially a pressure drop that becomes a pressure gain if the flow is reversed; *FD* is phase interface drag coefficient, which describes the retarding force exhibited by each phase on the other, in proportion to the difference of the velocities of two phases; ε is phase donor rectifier (1 for recipient phase, 0 for donor phase); *FG* is phase momentum transfer coefficient; *AM* is the added mass coefficient which is a correction term that allows each phase to "share" the inertia of the liquid phase. Reversing the subscripts *path*

and *tpath* results in the equation for the second twin. Details of above equations can refer to literature [19].

(4) Tie equation

The heat rate of the *i*th tie is calculated by equation (10):

$$\dot{Q}_{tie(i)} = h \times F \times \left(T_{node(n)} - T_{lump(i)}\right) \tag{10}$$

where h is the heat transfer coefficient (W/m^2), F is the heat transfer area, $T_{node(n)}$ and $T_{lump(i)}$ are the temperature of the *n*th node and *i*th lump respectively.

3.3 Heat transfer coefficient correlation

Based on Sinda/fluint software and heat pipe operating mechanism, appropriate convective heat transfer coefficient correlations for the working fluid R245fa in the evaporator section, adiabatic section and condenser section should be selected.

Rhosenow correlation [20] of pool nucleate boiling was selected to predict the heat transfer coefficient of evaporation process.

$$h = \eta_l \left(\frac{\Delta t}{r}\right)^2 \left(\frac{g(\rho_l - \rho_v)}{\sigma}\right)^{\frac{1}{2}} \left[\frac{C_{pl}}{\mathrm{Pr}_l^s \cdot C_{wl}}\right]^3 \tag{11}$$

In the adiabatic and condenser section, different heat transfer correlations were chosen according to the Reynolds number and considering the influence of free interface to falling liquid film.

When the Reynolds number is less than 7.5 and liquid film flow is smooth laminar, the heat transfer process is considered as pure heat conduction. The Nusselt number correlation[21] is as follows:

$$Nu^* = 0.925\,\mathrm{Re}_l^{-1/3} \tag{12}$$

When the Reynolds number exceeds 7.5, viscous force and surface tension are not enough to suppress interfacial fluctuations. Although it still is laminar liquid film flow, the heat transfer is increased for the interfacial fluctuation increasing the heat transfer surface area and enhancing the disturbance. Therefore, this process is considered as fluctuation laminar flow, and the correlation [22] is as follows:

$$Nu^* = 0.884\,\mathrm{Re}_l^{-1/4} \tag{13}$$

With the further increase of liquid film thickness and flow rate, liquid film flow will be gradually transformed into turbulence, the corresponding correlation [22]is as follows:

$$Nu^* = 0.044\,\mathrm{Pr}_l^{2/5}\,\mathrm{Re}_l^{1/6} \tag{14}$$

Sinda/Fluint does not have the above condensation heat transfer coefficient correlations. So the fluid-solid coupling connection (the "tie") in the adiabatic and condenser section were programmed in FORTRAN by ourselves.

3.4 Model geometry

The model is one-dimensional and geometry of the thermosyphon is exactly the same as the one in the experimental investigation. 30 fluid lumps were set up and uniformly distributed along the axial direction representing the working fluid (R245fa) inside the thermosyphon. Therefore, 29 paths were established to connect the adjacent lumps of working fluid. Using the same method, 30 nodes corresponding to the wall of thermosyphon along the axial direction were set up and uniformly distributed. Three series of ties were established to connect the lumps and nodes in evaporator, adiabatic and condenser section respectively. In the section of coolant water jacket, 10 lumps, 9 paths, 10 nodes and a series of ties were set up and uniformly distributed along the axial direction. The diagram of model is shown in Fig.3.

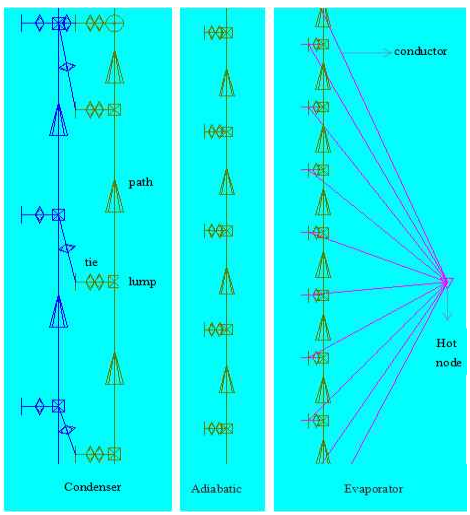


Fig.3 The partial enlargement diagram of condenser, adiabatic and evaporator section

4. SIMULATION RESULTS

4.1 For different water bath temperature t_b

The range of water bath temperature is from 35 ℃ to 95 ℃, and the interval is 5 ℃. The filling ratio of working fluid R245fa is 25%, and the inlet temperature and flow rate of coolant water were 22 ℃ and 1 L·min^{-1} respectively。

The experiment and simulation results of the temperature distribution at different water bath temperature are shown in Fig. 4. The distances between 0 and 1.0 m, 1.0 and 2.0 m, 2.0 and 3.0 m indicate the evaporator, the adiabatic, and condenser section respectively. It can be seen that these simulation results have good agreement with the experiment results. The temperature of outer wall of the TPCT increases with the increase of water bath temperature. Since the inlet temperature of coolant water is controlled to keep 22℃, the temperature difference between condenser section and evaporator section and adiabatic section is increased with the increase of water bath temperature. The average relative error (RE) between simulation and experiment results is 3.9%.

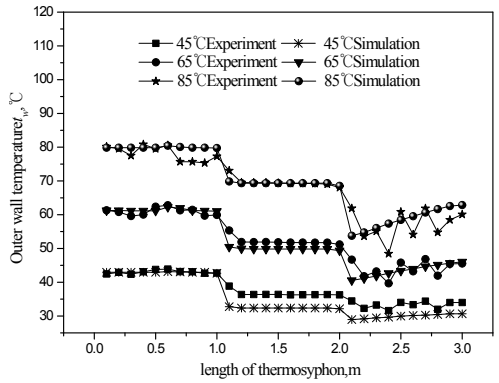


Fig.4 (a)

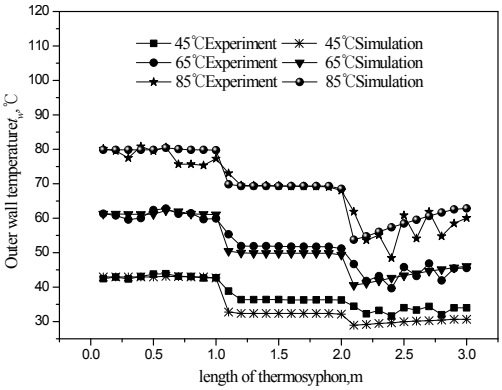


Fig.4 (b)

Fig. 4 Comparison of outer wall temperature at different t_b

Fig. 5 shows that the experimental and simulation results of heat transfer rate Q under different t_b. The heat load rises as t_b increases almost linearly as expected. The simulation results also have good agreement with the experimental results and the RE is 6.2%. The temperature of working fluid R245fa was not measured in the experiment, so it was calculated by simulation.

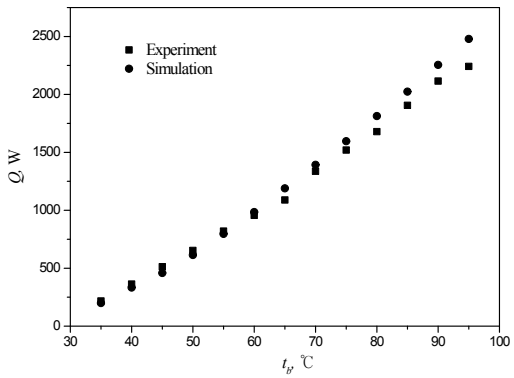


Fig.5 Comparison of Q at different t_b

The varieties of $\overline{t}_{cw,exp}$ and $\overline{t}_{v,cal}$ at different t_b are shown in Fig.6. For the inlet temperature of coolant water was set as℃22, the difference between t_b and $\overline{t}_{cw,exp}$ became larger, while the difference between t_b and $\overline{t}_{v,cal}$ just varied in a small amount with the increasing of t_b. That means the temperature difference in the condenser section becomes gradually large.

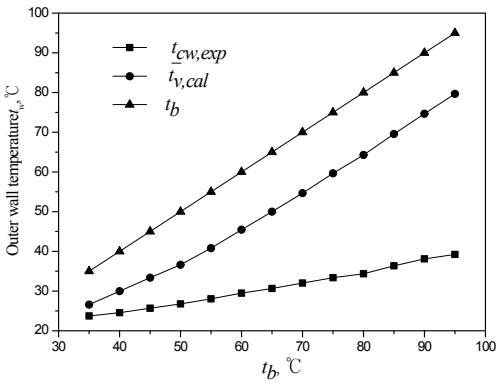


Fig. 6 $\overline{t}_{cw,exp}$ and $\overline{t}_{v,cal}$ at different t_b

Table 1 shows the comparison between experimental and simulation results for the average temperature of coolant water and overall heat transfer coefficient k. In addition, the average temperature and pressure of working fluid R245fa were shown in Table 1. The variety trends of these parameters are consistent with theoretical analysis. It can be concluded from results that the simulation is in a good agreement with the experiment.

4.2 For different inlet temperature of coolant water $t_{wc,in}$

The range of the inlet temperature of coolant water $t_{cw,i}$ is from 30 ℃-60 ℃, flow rate of coolant water is 1 L·min^{-1}, filling ratio is 45%, and water bath temperature t_b is 80 ℃.

Fig. 7 shows comparison of experimental and

Table1 Comparison of experiment results for different t_b

t_b ℃	$\bar{t}_{cw,exp}$ ℃	$\bar{t}_{cw,cal}$ ℃	$R_{E,\bar{t}_{c,cw}}$ %	k_{exp} W·m^{-2}·K^{-1}	k_{cal} W·m^{-2}·K^{-1}	$R_{E,k}$ %	$\bar{t}_{v,cal}$ ℃	$\bar{p}_{v,cal}$ MPa
35	23.7	23.1	1.3	73	62	15.0	26.8	0.15
40	24.6	24.0	0.7	121	98	19.1	30.1	0.17
45	25.7	24.6	1.6	140	121	13.6	33.5	0.19
50	26.8	26.4	1.5	151	130	13.8	36.7	0.22
55	28.0	27.7	1.3	165	144	13.0	41.9	0.26
60	29.5	29.0	1.5	173	158	9.1	45.6	0.30
65	30.7	30.5	0.58	170	176	3.4	50.1	0.34
70	32.0	31.9	0.34	192	194	1.1	54.7	0.40
75	33.4	33.4	0.01	202	218	7.7	59.7	0.46
80	34.4	34.9	1.7	214	240	12.0	64.3	0.52
85	36.4	36.4	0.21	237	253	6.8	69.6	0.60
90	38.1	38.1	0.06	250	271	8.1	74.7	0.69
95	39.2	39.7	1.10	259	286	10.5	79.7	0.78

Table 2 Comparison of experiment results for different $t_{cw,i}$

t_i ℃	$\bar{t}_{cw,exp}$ ℃	$\bar{t}_{cw,cal}$ ℃	$R_{E,\bar{t}_c}$ %	k_{exp} W·m^{-2}·K^{-1}	k_{cal} W·m^{-2}·K^{-1}	$R_{E,k}$ %	$\bar{t}_{v,cal}$ ℃	$\bar{p}_{v,cal}$ MPa
30	42.1	40.8	3.0	207	218	5.2	66.0	0.55
35	44.4	44.6	0.52	178	210	18.3	66.8	0.56
40	48.2	48.4	0.48	178	203	13.7	67.7	0.57
45	51.6	52.2	1.1	177	193	9.3	68.7	0.59
50	55.0	56.0	1.8	170	181	6.6	69.6	0.60
55	58.9	59.8	1.6	178	167	6.6	70.7	0.62
60	62.9	63.6	1.2	138	147	6.4	71.8	0.64

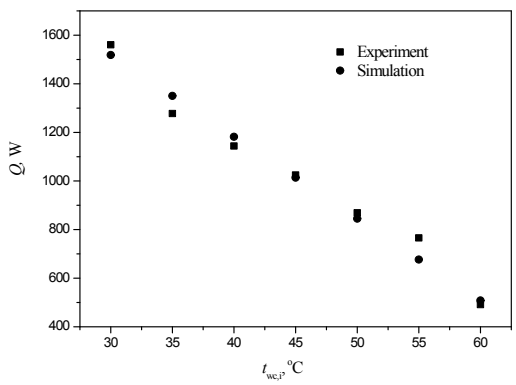


Fig. 7 Comparison of Q at different $t_{cw,\,i}$

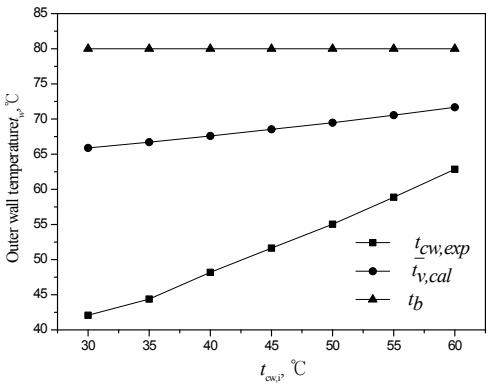


Fig. 8 $\bar{t}_{cw,exp}$ and $\bar{t}_{v,cal}$ at different $t_{cw,\,i}$

simulation Q under different $t_{cw,i}$. Q decreases almost linearly with the increasing of $t_{cw,i}$ as expected. The simulation results also have good agreement with the experimental results and the R_E is 4.3%. The varieties of $\bar{t}_{cw,exp}$ and $\bar{t}_{v,cal}$ at different $t_{cw,i}$ are shown in Fig. 8. For the bath temperature was set as 80 ℃, the difference between t_b and $t_{cw,i}$ became smaller. The working temperature of R245fa increased with the variety of $t_{cw,i.}$ That means the temperature difference in the condenser section becomes gradually small.

Table 2 shows the comparison between experimental and simulation results for the average temperature of coolant water ($\bar{t}_{cw}$) and overall heat transfer coefficient k. In addition, the average working temperature ($\bar{t}_{v,cal}$) and pressure ($\bar{p}_{v,cal}$) of R245fa were shown in Table 1. The variety trends of these parameters are consistent with theoretical analysis. It can be concluded from results that the simulation is in a good agreement with the experiment.

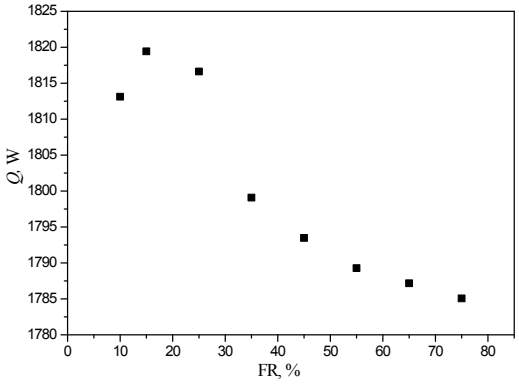


Fig. 9 The simulation results of Q for different FR

5.3 For different filling ratio FR

The range of FR of R245fa was from 10%-75%, and the water bath temperature, coolant water temperature and flow rate, were 80℃, 22℃ and 1 L·min^{-1} respectively. The heat transfer rates Q under different FR are shown in Fig. 9. It can be concluded that the variety of Q is not large for Q just varied from 1785 W to 1820 W. Q under 15% FR is slightly higher than the others. In fact, the dryout phenomenon in evaporator section appeared when 5% FR was calculated.

5.4 For different length of condenser section L_c

The variety of length of condenser section was from 0.5 m to 2.0 m, while the length of evaporator and adiabatic section was kept as 1m. The FR, water bath temperature, coolant water temperature and flow rate were 25%, 80℃, 22 ℃ and 1 L·min^{-1} respectively.

Fig. 10 shows that Q increases with the increasing of L_c, meanwhile its increasing rate gradually becomes smaller. It can be concluded that from Fig.10 that the heat flux q increases first and then decreases with the increasing of L_c. The maximum of q is 4930 W/m^2 when L_c is 1.3 m.

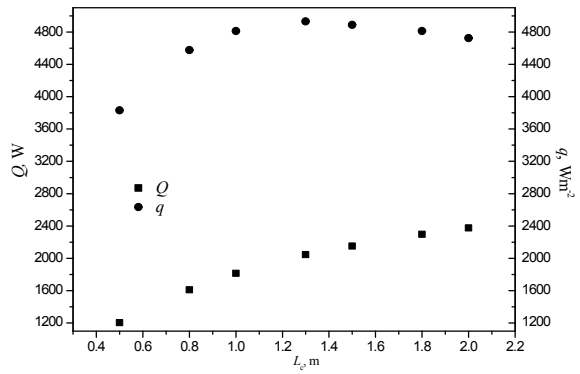


Fig. 10 The simulation results of Q and q for different L_c

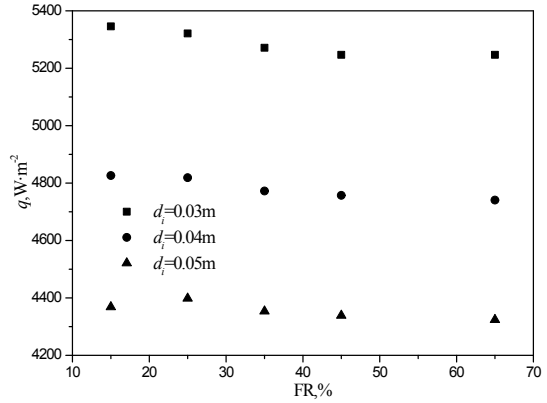


Fig.11 Heat flux q at different FR

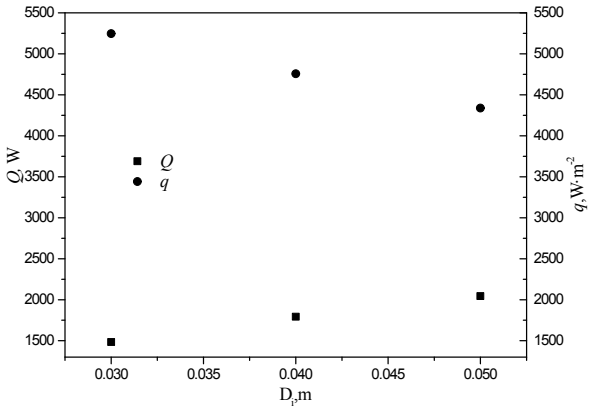


Fig.12 Q and q at different D_i

5.5 For different inner diameter D_i

The D_i was set as 30mm, 40mm and 50mm respectively, and the inner diameter of coolant water jacket was set as 96mm, 100mm and 105mm correspondingly to keep the coolant water with the same flow velocity when the flow rate was still set as 1 L·min-1. The water bath temperature and coolant water temperature were 80℃and 22℃ respectively.

Fig.11 shows that the heat flux q varied with respect to the FR for the D_i of 30mm, 40mm and 50mm.When the D_i is 30mm, the q is highest. The optimum FR for D_i of 30mm, 40mm and 50mm is 15%, 15% and 25% respectively. It can be concluded that the Q increases with the increasing of D_i while the trend of q is just the opposite from Fig. 12.

6. CONCLUSIONS

A transient simulation model of two-phase closed thermosyphon was established by Sinda/ Fluint software with R245fa as working fluid. The copper thermosyphon was 3 m long with an inner diameter of 40mm. The simulation results compared

with the experiment. The average relative error of outer wall temperature of the thermosyphon and heat transfer rate between simulation and experiment results was 3.9 % and 6.2 % respectively when the water bath temperature varied from 35℃-95℃. The good agreement confirms that the model is accurate and reliable. Base on this model, the effects of relevant factors, including heat source temperature, inlet temperature of coolant water, filling ratio, condenser section length and inner diameter, have been investigated on heat transfer performances of thermosyphon. With the increase of heat source temperature and flow rate of coolant water, heat transfer rate are improved, while the increase of inlet temperature of coolant water results in the decrease of them. The optimum of condenser section length is in the range of 1.0-1.5 m in given working conditions. The optimal filling ratio is 25 % for 50 mm inner diameter and 15 % for both of 30 mm and 40 mm.

ACKNOWLEDGEMENT

Financial grants from Beijing Key Laboratory of Process Fluid Filtration and Separation are gratefully acknowledged.

NOMENCLATURE

c	heat specific capacity of coolant water, $J \cdot kg^{-1} \cdot K^{-1}$
c_{pl}	liquid heat specific capacity of working fluid, $J \cdot kg^{-1} \cdot K^{-1}$
c_{wl}	empirical constants
D_i, D_o	inner and outer diameter, m
H	heat transfer coefficient of working fluid, $W \cdot m^{-2} \cdot K^{-1}$
K	overall heat transfer coefficient, $W \cdot m^{-2} \cdot K^{-1}$
$N_u = \frac{\alpha \times d}{k_f}$	coolant water mass flow rate, $kg \cdot s^{-1}$
P	pressure of working fluid, MPa
Pr	Prandtl number
Q_c	heat transfer rate of condenser section, kW
Q_e	heat transfer rate of evaporator section, kW
Q_l	heat loss between Q_e and Q_c, kW
R_E	relative error , %
Re	Reynolds number
r	latent heat, $J \cdot kg^{-1}$
s	empirical constants, for water, s=1, for other fluids, s=1.7
t_b	water bath temperature, ℃
t_c	condenser temperature, ℃
t_v	temperature of working fluid, ℃

Greeks

η_l	liquid dynamic viscosity
σ	surface tension

Subscript

cal	simulation results
exp	experiment results

REFERENCES

[1] Weng, Y., Cho, H., Chang, C. and Chen, S., Heat pipe with PCM for electronic cooling, *Applied Energy*, 88(2011) 1825-1833.

[2] Jouhara, H., Robinson, A. J., Experimental investigation of small diameter two-phase closed thermosyphons charged with water, FC-84, FC-77 and FC-3283, *Applied Thermal Engineering*, 30 (2010) 201–211

[3] Kerrigan, K., Jouhara, H., O'Donnell, G. E. and Robinson, A. J., Heat pipe-based radiator for low grade geothermal energy conversion in domestic space heating, Simul. *Model. Pract. Theory*, 19(2011)1154-1163

[4] Carotenuto, A., Casarosa, C., Martorano, L., The geothermal convector: experimental and numerical results, *Applied Thermal Engineering*, 19(1999) 349-374

[5] Mochizuki, M., Mashiko, K., Shihyakugari, S., Watanabe, Y., Eguchi, K., Namiki, T., Shiraishi, M.. A Demonstration Test of a Large Scale Loop Type Heat Pipe With Showering Nozzles, *Proceedings of the 9th international heat pipe conference*, 1-5 May, 1995, Alubuquerque, USA

[6] Mathioulakis, E., Belessiotis, V. A new heat-pipe type solar domestic hot water system, *Solar Energy*, 72(2002) 13-20.

[7] Ordaz-Flores A, García-Valladares O, Gómez VH. Experimental characterisation and technical feasibility of a closed two-phase vs a conventional solar water heating thermosyphon. *Applied Thermal Engineering* 31(2011)1313–22.

[8] Jouhara, H., Meskimmon, R. Experimental investigation of wraparound loop heat pipe heat exchanger used in energy efficient air handling units, *Energy*, 35(2010)4592-4599.

[9] Noie, S. H., Heat transfer characteristics of a two-phase closed thermosyphon, *Applied Thermal Engineering*, 25(2005) 495-506

[10] Ong, K.S., Haider-E-Alahi, Md., Performance of a R-134a-filled thermosyphon, *Applied Thermal Engineering*, 23(2003) 2373-2381

[11] Fadhl, B., Wrobel, L. C., Jouhara, H., CFD modelling of a two-phase closed thermosyphon charged with R134a and R404a, *Applied Thermal Engineering*, 78(2015)482-490

[12] Fadhl, B., Wrobel, L. C., Jouhara, H., Numerical modelling of the temperature distribution in a two-phase closed thermosyphon, *Applied Thermal Engineering*, 60(2013) 122-131

[13] Jiao, B., Qiu, L. M., Zhang, X. B., Zhang, Y., Investigation on the effect of filling ratio on the steady-state heat transfer performance of a vertical two-phase closed thermosyphon, *Applied Thermal Engineering*, 28(2008) 1417-1426

[14] Alizadehdakhel, A., Rahimi, M., Alsairafi, A. A., CFD modeling of flow and heat transfer in a thermosyphon, *International Communications in Heat and Mass Transfer*, 37(2010) 312-318

[15] Huang, Z.C., Zhang, M.M., Wen, S.Z., He, Z.H.,

Scaling of natural circulation loop operation modes, International *Journal of Heat and Mass Transfer*, 90 (2015) 131-139

[16] Robert W. M., Peter A. K., David A. R., Investigation of low Global Warming Potential working fluids for a closed two-phase thermosyphon, *Applied Thermal Engineering*, 51(2013) 917-925

[17] Lemmon, E. W., Huber, M. L., McLinden, M. D., NIST Standard Reference Database 23: Reference Fluid Thermodynamics and Transport Properites-REFPROP, *National Institute of Standards and Technology, Standard Reference Data Program*, Gaithersburg, 2013, Version 9.1.

[18] Ma, L. M., Wang, H. X., Wang, J. X., Cycle performance evaluation of HFC245fa for high temperature heat pump system, *Acta Energiae Solaris Sinica*, 31(6)(2010)749-754

[19] Cullimore, B.A., Ring, S.G., Johnson, D.A. , SINDA/FLUINT Version 5.6 User's Manual, C&R Technologies Inc, Colorado, USA, 2013

[20] W M Rohsenow. A method of correlating heat transfer data for surface boiling of liquids, *Transactions of the ASME* 74 (1952) 969-976

[21] Gross, U., Reflux condensation heat transfer inside a closed thermosyphon. *International Journal of Heat and Mass Transfer*, 35(2) 1992279-294

[22] Uehara, H., Kusuda, H., Nakaoka T., and Yamada, M., Filmwise condensation for turbulent flow on a vertial plate. *Heat Transfer- Japanese Research*, 12(2) (1983)85-89.

Reverse Thermosyphon in Conjunction with a Ground Source Heat Pump

Heng-Yi Li[1*], Meng-Chang Tsai[1], Wei-Chi Su[1], Fong-Hao Wu[1] and Wei-Chun Liao[1]

[1]*Physics Division, Institute of Nuclear Energy Research, Longtan Township, Taoyuan County, 32546, Taiwan (R.O.C.)*

Abstract

The ground source heat pump (GSHP) is one of the most efficient and reliable heating systems by extracting thermal energy from the ground in cold climate available today. However, the GSHP in Taiwan is requested to provide not only heating but also cooling by rejecting thermal energy to the ground in warm seasons. This problem can be resolved by the proposed scheme, which is a novel reverse thermosyphon in conjunction with a GSHP. The scheme consists of a multifunctional heat pump, a proposed novel reverse thermosyphon as ground heat exchanger (GHE) loop and a ground latent heat storage tank. The multifunctional heat pump is evolved from the integration of the heat pump air conditioner refrigerant loop with domestic water heat exchanger. The latent heat storage tank can provide a high energy storage density and has the ability to store energy at a constant temperature or over a limited range of temperature variation. Not like traditional brine GHE loop, the novel reverse thermosyphom is a self-acting circulation loop for heat transfer. It has a top vessel with porous adsorptive material filled inside, so it is able to transfer heat downward and upward depending on the heat source position. Its operation modes are verified by experiment. Hence, it could not only extract heat from the ground in cold season for space heating and hot water, but also reject heat to the ground in warm seasons for space cooling and hot water. Finally, the proposed scheme is proved to have more energy savings performance than traditional heat pump by theoretical analyzing.

Keywords: Ground source heat pump; Reverse thermosyphon; Hot water supply; Space cooling

1. INTRODUCTION

One international report [1] showed that global energy demand will grow to 2035. Although government policies can influence the pace, in the New Policies Scenario, global energy demand still increases by one-third from 2011 to 2035. Such an increasing energy requirement will aggravate energy shortage and environment pollution. In the U.S. residential buildings, the largest energy consumption is space heating, followed by the water heating and the space cooling [2]. The space heating accounts for about 45%, which is almost half of the total energy consumption in residential buildings. Water heating consumes 18% of the total energy consumption and the percentage of energy consumption for space cooling is half of that for water heating in residential building. Obviously, space heating, water heating and space cooling play essential roles on energy savings. Therefore, improvement in energy efficiency of air-conditioning system can significantly reduce the global energy consumptions.

In recent decades, the ground-source heat pump (GSHP) system becomes an attractive choice for both residential and commercial buildings due to its higher energy efficiency compared with the conventional air-source heat pump (ASHP) system. Generally, when installed in moderate-climate regions, the coefficients of performance (COP) of the GSHP system lies between 3 and 4, which is 20-30% higher than the conventional ASHP system [3].

GSHP systems are clean technologies by using the renewable energy resources. Due to their higher energy utilization efficiencies, they have been used for years in developed and developing countries replacing or supplementary to the conventional air conditioning systems. Because of the unbalance of cooling and heating demands in the residential and commercial buildings during a year, the GSHP systems must be integrated with other supplementary energy storage systems in cooling-dominated or heating-dominated areas. It is well known that thermal energy storage (TES) systems are strategic and necessary technologies for the efficient utilization of renewable energy and energy conservation. Therefore, the combination of GSHP and TES system is an effective mean to address problems resulted from cooling and heating imbalance in different areas. TES systems enable greater and more efficient usage of these fluctuating energy resources by matching the energy supply with the demand. The TES technologies integrated with GSHP systems include ice storage tank, solar collectors, soil, water

*Corresponding author: hyli@iner.gov.tw,
Phone: +886-2-82317717 Ext.7428, Fax: +886-3-4711408

and phase change materials (PCM). The ice storage tanks are used for cooling purpose while solar collectors are used for heating. The soil, water and PCM can be used either for cooling or heating purpose [4]. Latent heat storage (LHS) with PCM can achieve higher energy storage density than any other heat storage techniques. Compared with other heat storage methods, advantages of LHS materials are that heat storage and delivery occur in a narrow temperature interval corresponding to their phase transition temperature and significantly smaller volume change before and after phase transition process. Furthermore, GSHP has ground heat exchanger (GHE) loop with brine inside as the heat carrier. The GHE loop demands an electrically driven pump to circulate the heat carrier, and thus this reduces the GSHP efficiency.

For residential buildings in the subtropical region, like Taiwan [5], there is much cooling load and little heating load in hot climate for most of the year. And the buildings have only heating load in winter. Besides, land area in urban is usually not enough for installing the ground heat exchangers (GHE) of large capacity. Thus GSHP is hard to be marketed in Taiwan. Hence, to solve the problem a novel reverse thermosyphon in conjunction with a GSHP for residential building is proposed. The proposed system consists of a multifunctional heat pump, a novel reverse thermosyphon as GHE loop, and a ground LHS tank. The multifunctional heat pump is evolved from the integration of the air conditioner refrigerant loop with domestic water heat exchanger [6]. The proposed novel reverse thermosyphom is a self-acting circulation loop for heat transfer, which could not only transfer heat from the ground to heat pump in cold season, but also from heat pump to the ground in warm seasons. Hence, driven pump is unnecessary, so space is reduced and reliability is improved. The LHS can provide a high energy storage density and has the ability to store energy at a constant temperature or over a limited range of temperature variation, which is the temperature that corresponds to the phase transition temperature of the PCM. The operating principles of the novel reverse thermosyphon are described and verified. Furthermore, the energy savings performance of proposed scheme is theoretical analyzed.

2. NOVEL REVERSE THERMOSYPHON

The proposed novel reverse thermosyphon has two operation modes, which are top heating mode and bottom heating mode. These modes are verified by experiment.

2.1 Operating principle

The proposed novel reverse thermosyphom is a self-acting circulation loop for heat transfer. Its structure as shown in Fig. 1 contains top vessel, bottom vessel, vapor line and liquid line. Its top vessel has porous adsorptive material filled inside and is filled with working fluid when it is vacuumed. Before start up, liquid working fluid stays in the top vessel, U-shaped compensation pipe and bottom vessel. When the heat source is applied at top vessel, the novel reverse thermosyphon operates in the top heating mode, the top vessel acts as evaporator and bottom vessel acts as condenser, heat is transferred downward like previous reverse thermosyphom [7] does as shown in Fig. 2. The reverse thermosyphom has also several other names, down-pumping heat pipes, passive vapor transport systems, spontaneous downward heat transport systems, periodic two phase thermosyphon and so on [8]. Furthermore, when the heat source is applied at bottom vessel, the novel reverse thermosyphon operates in the bottom heating mode, the bottom vessel acts as evaporator and top vessel acts as condenser, heat is transferred upward like traditional thermosyphom does as shown in Fig. 3.

In the novel reverse thermosyphon, porous adsorptive material inside the top vessel is critical. Before start up, porous adsorptive material keeps liquid working fluid in the top vessel. In the top heating mode, it provides capillary force and blocks the vapor to the liquid line. While in the bottom heating mode, it gives large cooling area.

Under top heating mode, the capillary pressure P_{cap} is provided by the adsorptive material and calculated using the Young-Laplace equation.

$$P_{cap} = 2\sigma \cos\theta / r \tag{1}$$

At this time, the sum of the capillary pressure P_{cap} and the vapor pressure P_{vap} must be greater than the total pressure drop in the loop and due to the gravity. The pressure drop is in vapor line, bottom vessel, liquid line and wick. This can be represented by the following relation.

$$P_{cap} + P_{vap} \geq P_{vl} + P_{bv} + P_{ll} + P_{wk} + P_g \tag{2}$$

While under bottom heating mode, the gravitational pressure head P_g generated in the liquid line must be equal to the total pressure drop and the vapor pressure P_{vap}. Hence, to drive the circulation of the working fluid in the loop, the following requirement has to be satisfied.

$$P_g = P_{vl} + P_{bv} + P_{ll} + P_{wk} + P_{vap} \tag{3}$$

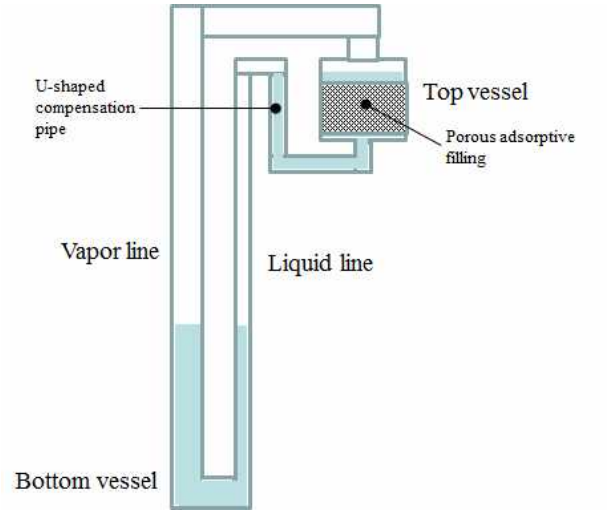


Fig. 1. The novel reverse thermosyphon before start up.

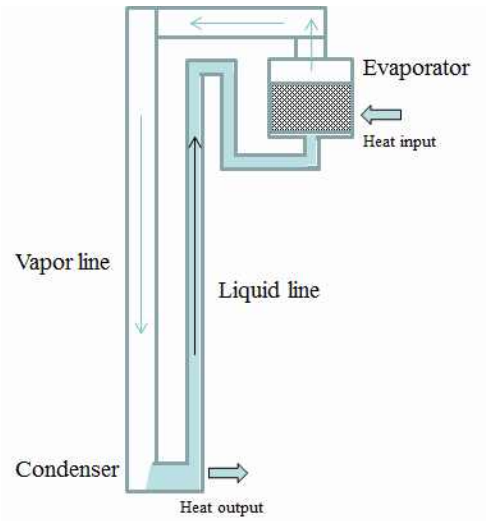


Fig. 2. The novel reverse thermosyphon in top heating mode.

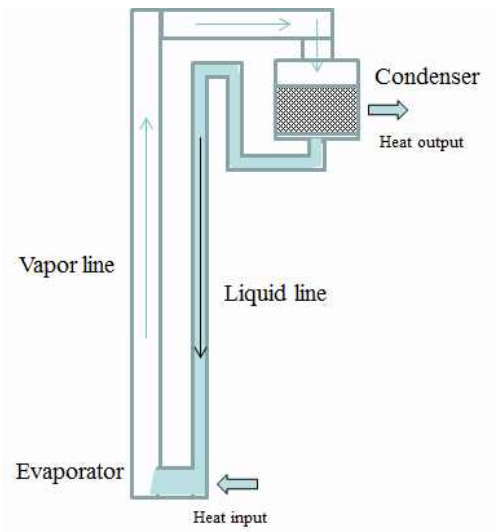


Fig. 3. The novel reverse thermosyphon in bottom heating mode.

2.2 Experimental setup

The experimental setup photograph of the novel reverse thermosyphon is shown in Fig. 4 and 5. Under top heating mode, heating tape is winded around the top vessel as shown in Fig. 4. While under bottom heating mode, heating tape is winded around the bottom vessel as shown in Fig. 5. Besides, the loop is filled with 160 mL ethanol. Dimensions and materials of the experimental setup are listed in Table 1. The adsorptive filling inside the top vessel is sponge-like and made of stainless steel.

Seven pieces of thermocouples, whose mounting locations are shown in Fig. 4 and 5, were firmly attached to measure the following temperatures: room temperature (T0), temperature inside the top vessel (T1), temperature at the top of vapor line (T2), temperature at the top of bottom vessel (T3), temperature at the bottom of bottom vessel (T4), temperature at the middle of the liquid line (T5) and temperature at the bottom of top vessel (T6). And temperature messages are recorded in personal computer automatically through Omega data acquisition module at 1 second interval. Hence, the real-time temperature variation graphs at each point are made.

The experimental tests were performed to investigate the transient responses of the novel reverse thermosyphon in the start-up process and the heat transfer performance. Consequently, the feasibilities under two modes are to be verified.

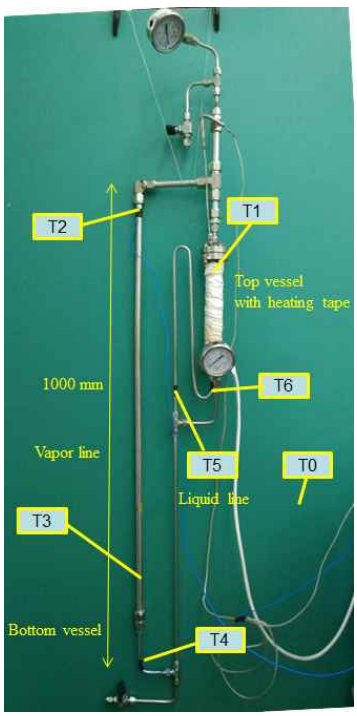


Fig. 4. Photograph of the novel reverse thermosyphon under top heating mode.

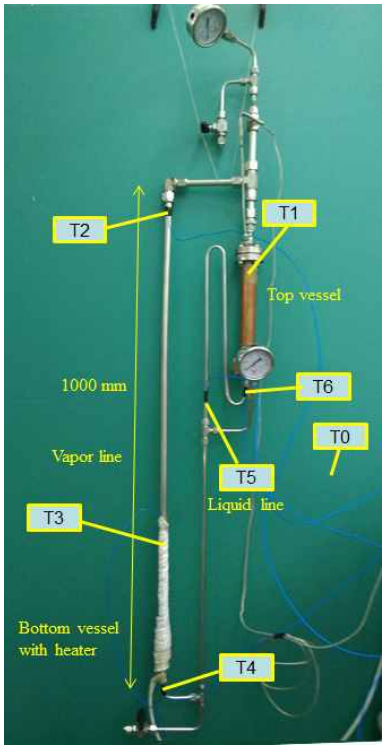


Fig. 5. Photograph of the novel reverse thermosyphon under bottom heating mode.

Table 1 Characteristics of the experimental setup

Component	Dimension	Material
Top vessel	Φ1"·3 mm·200 mm	Copper
Vapor line	Φ½"·1.25 mm·1300 mm	SUS316
Liquid line with bottom vessel	Φ¼"·1.25 mm·1350 mm	SUS316

3. RESULTS AND DISCUSSION

Before the analysis of the experiment result, it is necessary to define the thermal resistance of the two modes as follows:

$$R_{tm}=(T2-T3)/Q \quad (4)$$
$$R_{bm}=(T3-T2)/Q \quad (5)$$

The start-up process is very important in evaluating the performance of the novel reverse thermosyphon. Fig. 6 shows the start-up of the novel reverse thermosyphon at 80 W of thermal power under top heating mode. According to the temperature curves, the start-up process under top heating mode can be divided into three stages: (1) the start-up of the evaporator, (2) the start-up of the condenser and (3) the steady-state stage. At the first stage, heat is put into the evaporator, and the liquid working fluid begins to vaporize and T1 rises rapidly. Then the vapor pours into the vapor line and sweeps the non-condensable gases in the vapor line toward the condenser. The slope of T3 curve is very small. When the hot vapor reaches the condenser inlet, the condenser begins to start up. Then the increase rate of T1 slows down and the increase rate of T3 gets higher. With the increase of the vapor pressure, the volume of the non-condensable gases is getting smaller and the effective condensing area of condenser is getting larger. When the heat removed from the condenser equals the amount put into the evaporator, the novel reverse thermosyphon moves to steady state stage. Under this mode, it starts up when T1 is 58 °C, the rising time is 1717 seconds and the steady state thermal resistance is 0.192 °C/W. At that time, the room temperature is 16.9 °C.

Fig. 7 shows the start-up of the novel reverse thermosyphon at 80 W under bottom heating mode. According to the temperature curves, the first and the second stage of the start-up process under bottom heating mode is shorter than top heating mode. This is because the buoyancy direction is the same as circulation flow. Under this mode, it starts up when T3 is 22 °C, the rising time is 605 seconds and the steady state thermal resistance is 0.112 °C/W. At that time, the room temperature is 14.9 °C. Thus, the feasibilities under two modes are verified.

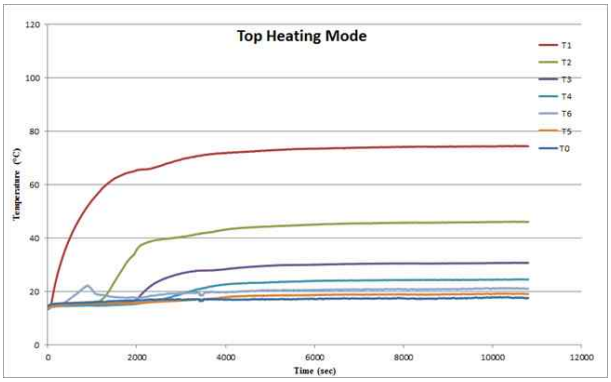


Fig. 6. Start-up of the novel reverse thermosyphon in top heating mode.

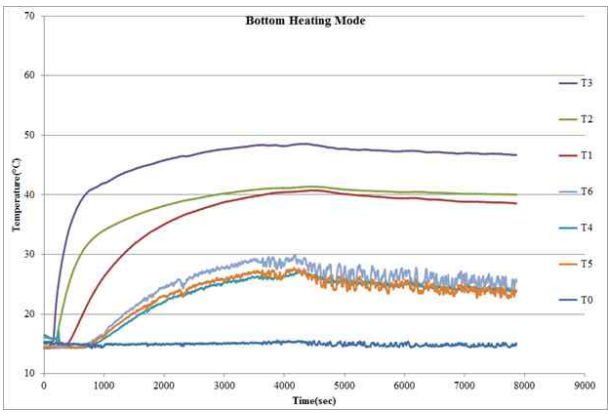


Fig. 7. Start-up of the novel reverse thermosyphon in bottom heating mode.

4. NOVEL GSHP SCHEME

Due to the novel reverse thermosyphon could not only transfer heat downward but also transfer heat upward. The scheme of the reverse thermosyphon in conjunction with a GSHP is proposed to solve the GSHP problem in Taiwan for residential building. Hence, with the novel reverse thermosyphon, the proposed scheme can not only offer heating by extracting thermal energy from the ground in cold seasons, but also cooling by rejecting thermal energy to the ground in warm seasons. It shows better energy efficiency performance by theoretical analyzing.

4.1 System Description

Similar to the previous publication [9-10], the proposed novel GSHP scheme is shown in Fig. 8. The proposed system consists of a multifunctional heat pump, a reverse thermosyphon GHE, and a ground LHS tank. This heat pump is a split type air conditioner that possesses multi-functions: space cooling only, domestic hot water heating only, space heating only, space-cooling-plus-hot-water-heating, and space-heating-plus-hot-water-heating. Each function is determined by operating mode. The operating modes including cooling and heating are switched by the four-way valve at the outlet of the hot water heat exchanger. The circulation refrigerant is R410.

In the warm seasons, the multifunctional heat pump switches to cooling mode by the four-way valve for providing space cooling as its primary task, and produce domestic hot water through the water-bath heat-recovery condenser as its secondary task. In the process, the indoor unit acts as an evaporator and the outdoor unit acts as a condenser, so the water temperature will rise. The performance will drop because of the elevated condenser working temperature and pressure. To overcome this limitation, an air-cooled condenser in the outdoor unit is connected in series with the immersed condenser. This is to overtake the duty of the immersed condenser when the water temperature reaches a high limit.

In the cold season, space heating is needed, so the multifunctional heat pump switches to heating mode by the four-way valve. The air-cooler at the outdoor unit becomes an evaporator. The indoor unit becomes a condenser and then provides space heating.

The air-to-refrigerant heat exchanger in outdoor unit and the novel reverse thermosyphom GHE are coupled and arranged in parallel. Hence, the thermal source can be switched between air and ground by four solenoid valves. For ground source case, the novel reverse operates in top heating mode to reject heat to ground LHS tank during warm seasons, and bottom mode to extract heat during cold seasons. To get the optimum energy saving, three PCMs for LHS tank shown in Table 2 are suggested.

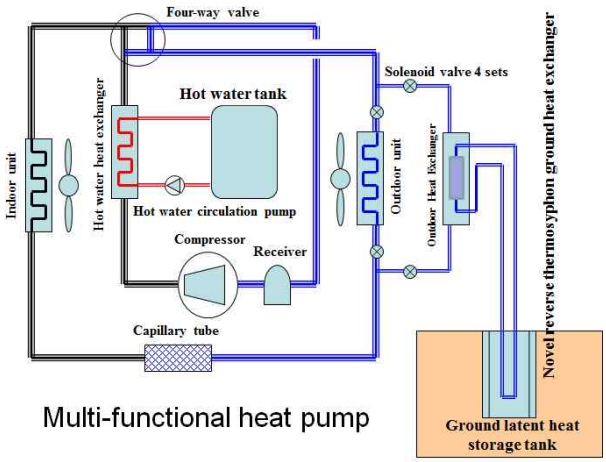


Fig. 8. Schematic of the novel reverse thermosyphon in conjunction with ground source heat pump.

Table 2 Properties of phase change material

Material	Melting point (ºC)	Heat of fusion (kJ/kg)	Thermal Conductivity (W m^{-1} $ºC^{-1}$)
n-Heptadecane	22	215	0.21^{S}
n-Octadecane	28.2	245	0.35^{S}, 0.419^{L}
Paraffin-Wax	32	251	0.514^{S}, 0.224^{L}

Note: ^{S}: solid, ^{L}: liquid

4.2 System Performance

To evaluate the energy savings performance, coefficient of performance (COP) is usually used. Besides, three PCMs as shown in Table 2 are selected in the ground LHS tank for ground source, and their effects are compared with air source.

In cooling mode, the system can be realize two functions, which are space cooling only and space cooling plus hot-water supply.

For space cooling function, there is no hot-water supply and the system COP can be determined by:

$$COP_{c-cm} = \frac{Q_c}{W} \tag{6}$$

For space cooling plus hot-water supply function, the system COP is given as:

$$COP_{cm} = \frac{Q_c + Q_{hw}}{W} \tag{7}$$

In heating mode, the system can be realize two functions, which are space heating only and space heating plus hot-water supply.

For space heating function, there is no hot-water supply and the system COP can be determined by:

$$COP_{h-hm} = \frac{Q_h}{W} \tag{8}$$

For space heating plus hot-water supply function, the system COP is given as:

$$COP_{hm} = \frac{Q_h + Q_{hw}}{W} \tag{9}$$

The multifunctional heat pump model has been established in previous publishing [10] and ASHRAE [11]. With the model, the calculation is performed with software CoolPack [12]. For the comparison of cooling mode in warm seasons, the outdoor air temperature is assumed to be 36 ºC and the indoor air temperature is varied from 25 ºC to 27 ºC. Furthermore, for the comparison of heating mode in cold season, the outdoor air temperature is assumed to be 10 ºC and the indoor air temperature is varied from 21 ºC to 23 ºC.

For the COPs of cooling mode shown from Fig. 9 to Fig. 10, it can be seen that each of the selected PCMs has positive contribution to enhance COP of GSHP. Besides, the COP of the novel GSHP with n-heptadecane in cooling mode is higher than the other two PCMs. This is because its melting point is the lowest. Whereas, the COPs of heating mode shown from Fig. 11 to Fig. 12, it can be seen that each of the selected PCMs also has positive contribution to enhance COP of GSHP, and the novel GSHP with paraffin-wax gets the highest COP of heating mode. This is for the reason that its melting point is the highest. It also can be found that when indoor temperature is increased the COPs in cooling mode rise and the COPs in heating mode fall. However, multifunctional heat pump with different ground LHS source is always better than the traditional air source. Hence, the energy savings performance is demonstrated.

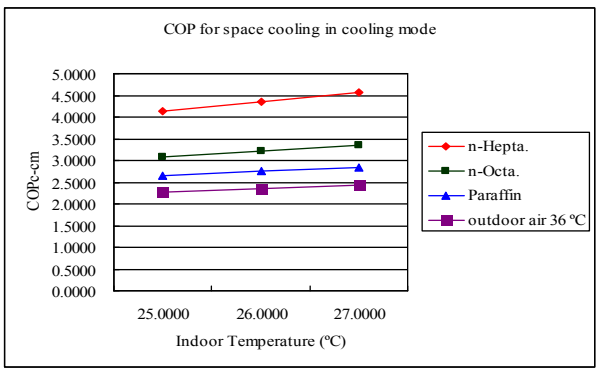


Fig. 9. COP for space cooling in cooling mode.

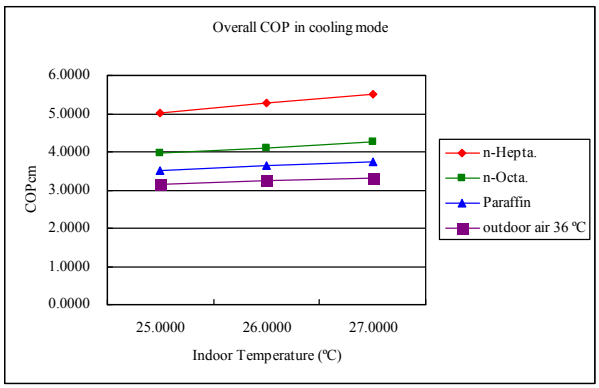


Fig. 10. Overall COP in cooling mode.

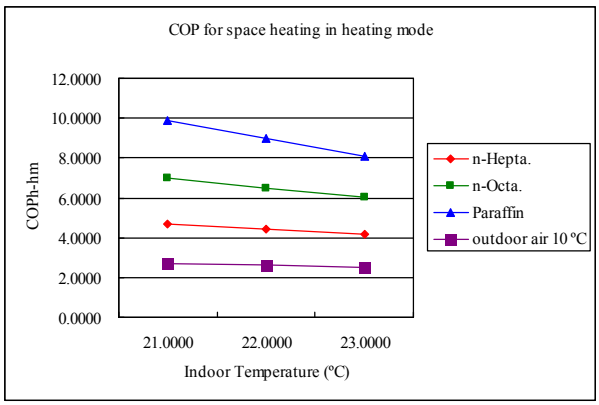


Fig. 11. COP for space heating in heating mode.

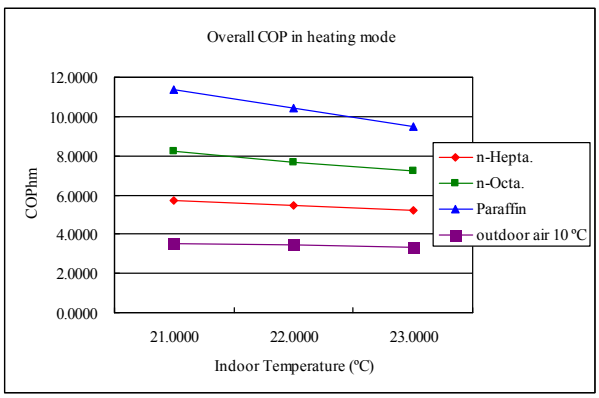


Fig. 12. Overall COP in heating mode.

5. CONCLUSIONS

A novel reverse thermosyphon is proposed and has two operation modes: top heating mode and bottom heating mode. For proper operation, the adsorptive filling inside the top vessel is very critical. Besides, the feasibility is verified by experiment. Under top heating mode, the start-up temperature is 58°C, the rising time is 1717 seconds and the steady state thermal resistance is 0.192°C/W. While under bottom heating mode, the start-up temperature is 22 °C, the rising time is 605 seconds and the steady state thermal resistance is 0.112 °C/W.

The proposed novel reverse thermosyphom is a self-acting circulation loop for heat transfer without circulation pump. It could not only transfer heat downward but also transfer heat upward. Thus, when it in conjunction with a GSHP for residential building, it can not only extract thermal energy from the ground in cold seasons, but also reject thermal energy to the ground in warm seasons.

The GSHP with three selected PCMs inside the ground LHS tank are compared with conventional air source heat pump in heating and cooling modes. Simulation results show that each of the selected PCMs has positive contribution to enhance COP of GSHP for both modes. This demonstrates that the scheme has energy savings performance in cold and warm seasons.

ACKNOWLEDGEMENT

Financial grants from the Institute of Nuclear Energy Research, Atomic Energy Council are gratefully acknowledged.

NOMENCLATURE

COP: Coefficient of performance
P : Pressure (N/m^2)
Q : Heat load (W)
R : Thermal resistance (°C/W)
T : Temperature (°C)
W : The power of compressor and fans (W)
r : Radius of curvature of the meniscus in the wick (m)
σ : Surface tension (N/m)
θ : Contact angle between the liquid and the wick (rad)

Subscripts
bm : Bottom heating mode
bv : Bottom vessel
c : Space cooling
cap : Capillary
cm : Cooling mode
g : Gravity
h : Space heating
hm : Heating mode
hw : Hot water
ll : Liquid line
tm : Top heating mode
vap : Vapor
vl : Vapor line
wk : Wick

REFERENCES

[1] International energy agency, *WORLD ENERGY OUTLOOK* 2013 FACTSHEET.
[2] Doe/Eere, 2010 *Buildings Energy Data book*, 2011.
[3] Yi Man, Hongxing Yang, Jinggang Wang, Study on hybrid ground-coupled heat pump system for air-conditioning in hot-weather areas like Hong Kong, *Applied Energy*, 2010, 87:2826-2833.
[4] Na Zhu, Pingfang Hu, Linghong Xu, Zhangning Jiang, Fei Lei, Recent research and applications of ground source heat pump integrated with thermal energy storage systems: A review, *Applied Thermal Engineering*, 2014, 71:142-151.
[5] Taiwan's Geography and Climate, AsianInfo.org, www.asianinfo.org.
[6] Jie Ji, Tin-tai Chow, Gang Pei, Jun Dong, Wei He, Domestic air-conditioner and integrated water heater for subtropical climate, *Applied Thermal Engineering*, 2003, 23:581-592.
[7] Y. Dobriansky, Concepts of self-acting circulation loops for downward heat transfer (reverse thermosiphons), *Energy Conversion and Management*, 2011, 52:414-425.
[8] S. Filippeschi, On periodic two phase thermosyphons operating against gravity, *International Journal of Thermal Sciences*, 2006, 45:124-137.
[9] Heng-Yi Li, Meng-Chang Tsai, Chi-Fong Ai, A novel thermosyphon for ground heat exchanger, *grand renewable energy 2014 international conference and exhibition*, Tokyo Big Sight, Tokyo, Japan.
[10] Heng-Yi Li, Meng-Chang Tsai, Wei-Chi Su, Wei-Chun Liao, Novel design of ground source heat pump with latent heat storage for residential building, *3nd International Workshop on Heat Transfer Advances for Energy Conservation and Pollution Control*, 2015, Taipei, Taiwan.
[11] ASHRAE Handbook, Fundamental, CD-Rom 1997.
[12] CoolPack version 1.50, http://en.ipu.dk .

Transient Numerical Model for Thermal Performance Analysis of a Two-phase Closed Thermosyphon

Zhongchao Zhao[1*], Hao Hu[1], Xiao Zhang[1], Pengpeng Jiang[1]

[1] School of Energy and Power Engineering, Jiangsu University of Science and Technology, Zhenjiang Jiangsu 212003,China.

Abstract

This paper performs a computational fluid dynamics (CFD) investigation of two-phase flow in a thermosyphon considering phase change heat and mass transfer. A CFD model based on the volume of fluid (VOF) technique was built. The deionozed water was specified as the working fluid of this thermosyphon. The investigation results confirmed that the CFD model is able to reproduce the phenomenon of evaporation and condensation in the thermosyphon. The average wall temperatures and effective thermal conductivity, versus the time, were also analyzed. The variation trend of average temperatures indicated that this investigated thermosyphon starts to work at 4s and reaches a steady-state after 15s. Moreover, the effective thermal conductivity was proved to reach the highest value of 2.27×10^6 W/m · K at initial time during the operation of this investigated thermosyphon.

Key Words: thermosyphon; volume of fluid; multiphase flow; evaporation and condensation

1. INTRODUCTION

A two-phase closed thermosyphon, or a wickless heat pipe, like a wicked heat pipe, transmits heat by using evaporation and condensation of a working fluid that is circulating in a sealed container. However, the two-phase closed thermosyphon relies on gravitational forces to return the working fluid from condenser to evaporator rather than capillary forces produced by wick, compared to the wicked heat pipe [1]. Regarding to the advantages of light weight, wide operating temperature range, compact structure, flexibility, high capacity of heat transfer and great performance of isothermal, the thermosyphon is widely used in many cooling fields that contain electronic components and products [2-4].

A thermosyphon is consisted of three sections, which are evaporator, adiabatic and condenser sections respectively. The evaporator section is heated by a hot source and the condenser section is cooled by a cold source. The adiabatic section placed between evaporator and condenser sections is surrounded with thermal insulation layers. The heat is added to the evaporator section with a liquid pool, which located at bottom of the thermosyphon, and then liquid absorbed the latent heat of evaporation is turned into vapor. The vapor rises up to the condenser section at top of the thermosyphon, where it is condensed and gives up its latent heat. The condensed working fluid, which forms a liquid film along the walls, is back to the evaporator with the gravity.

A great variety of experimental studies have been done by many scholars for understanding thermal characteristics of a thermosyphon [5-11], while limited numerical investigations were performed to figure out internal heat and mass transfer mechanism of a thermosyphon. Annamalai and Ramalingam [12] built a model for a wicked heat pipe by using ANSYS CFX and performed an experimental study. the authors assumed that the section inside the heat pipe was filled with the vapor phase, and the liquid phase only existed in the wick section. The wall temperature of evaporator and condenser and the vapor temperature were compared with the experimental results by the authors. Jaroslaw Legierski et al. [13] provided a model for simulating the temperature along the heat pipe walls at different moments and the vapor velocity inside the heat pipe. They considered the heat pipe as a open system that the evaporator was treated as the inlet of the mass flow rate and the condenser was treated as the outlet of the mass flow rate. The results of the study showed that the value of start-up time of the heat pipe was 20~30s and the evaporation coefficient of water was with value of 1.58×10^{-3}. The range of

*Corresponding author: zhongchaozhao@just.edu.cn,
Phone: +86-0511-84493050.

the effective thermal conductivity also was provided by the authors.

De Schepper et al. [14] employed the UDF and VOF technique to calculate the phase change process of a hydrocarbon feedstock. The authors proposed that UDFs were specified as source terms, which were used to simulate the heating and boiling phenomena in the convection section of a steam cracker. Lin et al. [15] carried out a CFD analysis of miniature oscillating heat pipes (MOHPs) using VOF and Mixture methods. Alizadehdakhel et al. [16] performed an experimental study at different operating conditions in a thermosyphon. They also built a CFD model to compare the CFD predicted temperature profile with experimental results, in which the VOF model was employed.

Fadhl et al. [17] carried out an experimental study and CFD analysis of a two-phase closed thermosyphon using VOF technique. The experimental investigation was performed with the input heat powers of 100.41, 172.87, 225.25, 275.6, 299.52 and 376.14 W. The CFD predicted temperature profile had good agreement with the experimental data under the same input heat powers. In another research reported by Fadhl et al. [18], a two-dimensional model was developed with three working fluids, which were distilled water, R134a and R404a. The different boiling phenomenon was observed between the refrigerants (R134a and R404a) and distilled water in the thermosyphon.

As the above published work showed, most of them put emphasis on the study of the steady state thermal performance of the thermosyphon, while limited numerical investigation focused on the thermal performance during start-up of the thermosyphon. Therefore, the purposed of present work is to simulate vapor-liquid two-phase flow, evaporation and condensation, and other complex physical processes during the operation of a closed thermosyphon. The VOF technique is employed to developed the CFD model, which can track the liquid-vapor interface. In order to calculate the process of phase change, the mass and energy sources compiled by UDFs are used to complete the FLUENT code.

2. CFD MODELING

The objective of this study is to analyze mechanism of phase change and thermal performance of working fluids in a two-phase closed thermosyphon. There are three main methods to the numerical calculations for Euler-Euler multiphase flows, which are the VOF method, the Mixture method and the Eulerian method. The Mixture method and the Eulerian method are fit for the situation that the volume fractions of dispersed-phase exceed 10%, in which the phase is mixed or separated in the flows. As the phase is considered to be immiscible for multiphase flows in the thermosyphon, the VOF method has been adopted as it is applied to simulate the stratified flow or free surface flow.

2.1 VOF model

In VOF model, a single set of Navier-Stokes equations are applied to immiscible phases and the volume fraction of each of the phases are recorded into each cell throughout the computation domain. Thus, the summation of volume fraction of all phases is unity:

$$\alpha_l + \alpha_v = 1 \tag{1}$$

The cell is occupied by liquid phase if a_l=1 and vapor phase if $a_l = 0$. The relation $0 < a_l < 1$ represents that the cell is at the interface between the liquid and vapor phases.The continuity equations for the VOF model have the following form:

$$\nabla \cdot (\alpha_l \rho_l \vec{u}) = -\frac{\partial}{\partial t}(\alpha_l \rho_l) + M_l \tag{2-1}$$

$$\nabla \cdot (\alpha_v \rho_v \vec{u}) = -\frac{\partial}{\partial t}(\alpha_v \rho_v) + M_v \tag{2-2}$$

In which ρ_l is the density of liquid phase and ρ_v is the density of vapor phase.

The continuity equations treat velocity u as the mass-averaged velocity. Meanwhile, the mass transfer rates passing the two-phase interface are represented by M_l and M_v.

The momentum equation for VOF model which considers the effect of gravity and volumetric surface tension can be described as below:

$$\frac{\partial}{\partial t}(\rho\vec{u}) + \nabla \cdot (\rho\vec{u}\vec{u}) = \rho\vec{g} - \nabla p + \nabla \cdot \left[\mu\left(\nabla\vec{u} + \nabla\vec{u}^{T}\right) - \frac{2}{3}\mu\nabla \cdot uI\right] + F_{CSF} \tag{3}$$

Where g represents the acceleration of gravity, p represents the pressure, and I represents the unit tensor.

In Eq.(3) the volumetric surface tension force is calculated by the continuum surface force (CSF) model proposed by Brackbill et al.[19]. Therefore, the surface tension acting as a source term has the following form:

$$F_{CSF} = 2\sigma_{vl}\frac{a_l\rho_l k_v \nabla a_v + a_v\rho_v k_l \nabla a_l}{(\rho_l+\rho_v)} \quad (4)$$

where σ_{vl} is the surface tension coefficient and k is the surface curvature.

In the momentum equation, the physical properties of density and viscosity are depended on the volume fraction of the phases. Therefore, the density ρ and the dynamic viscosity μ are expressed as follows:

$$\rho = a_l\rho_l + a_v\rho_v \quad (5\text{-}1)$$

$$\mu = a_l\mu_l + a_v\mu_v \quad (5\text{-}2)$$

where μ_l and μ_v are the dynamic viscosity of liquid and vapor, respectively.

The energy equation for the VOF model takes the following form:

$$\frac{\partial}{\partial t}(\rho e) + \nabla\cdot\left(\vec{v}(\rho e + p)\right) = \nabla\cdot(k\nabla T) + E \quad (6)$$

Where $k = \alpha_l k_l + \alpha_v k_v$. The energy source term used to compute the heat transfer rates through the interface is represented by E.

In VOF model, the temperature T is the mixture temperature rather than temperature of a specific phase for the energy equation. Meanwhile, the internal energy e treated as a mass-averaged variable is given by:

$$e = \frac{\alpha_l\rho_l e_l + \alpha_v\rho_v e_v}{\alpha_l\rho_l + \alpha_v\rho_v} \quad (7)$$

Where e_l and e_v are calculated based on the specific heat c_p of the phase and the mixture temperature:

$$e_l = c_{p,l}(T - T_{sat}) \quad (8\text{-}1)$$

$$e_v = c_{p,v}(T - T_{sat}) \quad (8\text{-}2)$$

2.2 Mass and heat transfer model

FLUENT™ version 6.3 is used to solve the governing equations of VOF model. A User Define Function (UDF) is linked to the governing equations, which assists to simulate the evaporation and condensation process in the thermosyphon. In the UDF, the mass and heat transfer rates are defined by source terms proposed by De Schepper et al.[14]. Therefore, all source terms are required for the calculation of the mass and heat transfer rates in the following form:

For mass source terms in the evaporation process

$$M_l = -C\rho_l\alpha_l\frac{T_{mix}-T_{sat}}{T_{sat}} \quad (9\text{-}1)$$

$$M_v = -(S_{Ml}) \quad (9\text{-}2)$$

For mass source terms in the condensation process:

$$M_l = C\rho_v\alpha_v\frac{T_{sat}-T_{mix}}{T_{sat}} \quad (10\text{-}1)$$

$$M_v = -(S_{Ml}) \quad (10\text{-}2)$$

For energy source terms in the evaporation and condensation process, respectively:

$$E_e = \left(-C\rho_l\alpha_l\frac{T_{mix}-T_{sat}}{T_{sat}}\right)\cdot LH \quad (11\text{-}1)$$

$$E_c = \left(C\rho_v\alpha_v\frac{T_{sat}-T_{mix}}{T_{sat}}\right)\cdot LH \quad (11\text{-}2)$$

Where T_{mix} is the mixture temperature, T_{sat} is the saturation temperature, and LH is latent heat. The value of coefficients C used to compute the condensation/evaporation rate is normally specified as 0.1.

3. GEOMETRY AND BOUNDARY CONDITIONS

A two-dimensional numerical model was developed for simulating the two-phase flow, when took the axisymmetric structure into consideration for a thermosyphon. The geometry of computational domain is illustrated in Fig. 1, and it is divided into three sections that indicate evaporator, adiabatic and condenser, respectively. Furthermore, the evaporator and condenser sections are with the length of 100mm, while the length of adiabatic is fixed at 50mm. The inner diameter and wall thickness are 8.32 and 0.6mm, respectively. The grids created on geometry were performed with GAMBIT 2.4.6. A total number of 80,000 grids were adopted in order to ensure the grid-independence. It was found that a

very thin liquid film was developed near the inner walls of the thermosyphon, thus the boundary layer technique was applied at the left and right inner walls. Eight layers of cells were meshed, making the initial size and grow factor to be 0.035 and 1.2 respectively.

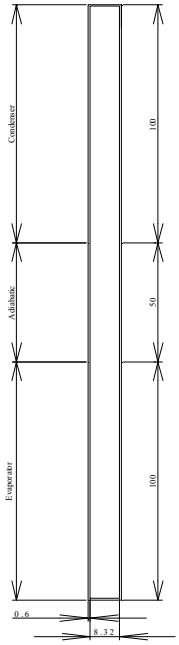


Fig. 1. Geometry and dimensions

In fluid dynamics, there is zero velocity between the fluid and the solid boundary relatively. Therefore, a non-slip boundary condition was applied at the inner walls. A constant heat flux was specified as boundary condition on the evaporator and condenser sections. The value of heat flux acting as boundary condition on the adiabatic section was zero, considering this section was insulated. Furthermore, the water was adopted as the working fluid fixed at 60% of the evaporator volume, and the density that was considered to be depended on the temperature in this model is defined by the steam table in the following form:

$$\rho_l = 249.46 + 6.625 \times T - 0.0184 \times T^2 + 1.532 \times 10^{-5} \times T^3 \quad (12)$$

where T represents the mixture temperature.

4. CFD SOLUTION METHOD

The whole simulation process is transient with a time step of 0.0001s, when start-up and steady-state operation of the thermosyphon was took into consideration. In order to solve the pressure-velocity coupling, the SIMPLE algorithm was selected from the segregated algorithms provided by FLUENT. The first order upwind was adopted for the discretization of momentum and energy equations, which reduced the difficulty of convergence. Meanwhile, the Geo-Reconstruct for the volume fraction combined with the PRESTO for the pressure were included in this model. In the present simulation, the value of the scaled residual of mass and velocity components should be 10^{-4} for the convergence of numerical computation. Water vapor was took as the primary (vapor) phase, and the saturation temperature was with the value of 308.55 K.

5. RESULTS AND DISCUSSION

The numerical simulation was performed to observe the evaporation and condensation phenomenon in a thermosyphon. Furthermore, the wall temperature profile and the effective thermal conductivity of the thermosyphon were obtained during the start-up of a thermosyphon.

5.1 Evaporation and condensation process of numerical simulation of thermosyphon

The pool boiling phenomenon in the evaporator section and liquid film in the condenser section can be visualized in Figs. 2 and 3, respectively. A blue colour represents that the value of the liquid volume fraction is 1, which indicates the presence of only liquid. The liquid volume fraction with value of 0 is

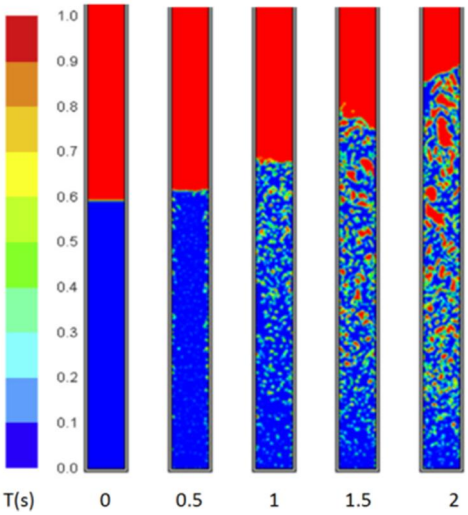


Fig. 2. process of boiling in the evaporator section at different times

represented by a red colour, which indicates the presence of only vapor. The 60 percent of evaporator section is occupied by the liquid pool, displaying in Fig. 2 at 0.0 s.

The heating power of 40W transfers the heat into the liquid pool through the walls of the evaporator section. The evaporation occurs at the positions called nucleation site, where the liquid reached the saturation temperature, as shown in Fig. 2 at 0.5s. The phenomenon is observed that the vapor bubbles form and departure from the inner walls of the evaporator section in Fig. 2 at 1s. As continuous heat input, more and more vapor bubbles form, and then vapor bubbles starts to grow up and coalesce, as shown in Fig. 2 at 1.5s and 2s. Finally, the vapor bubbles rise up to the interface between liquid phase and vapor phase, where the vapor bubbles break up and pass into the region of the vapor phase.

On the contrary, the saturated vapor is condensed in the condenser section when it rises up to the condenser section through the adiabatic section. The process of formation of condensed liquid film can be observed at the inner walls of the condenser section in Fig. 3, where the heat is transferred to external environment. At the beginning, the condensed liquid film is discontinuously along the inner walls of the condenser section, as shown in Fig. 3 at 8s, 9s and 10s. As the continuous transportation of vapor from the evaporator section, more and more condensed liquid occurs at the inner walls of the condenser section. Eventually, the continuous liquid film is visualized in Fig. 3 at 11s, and tacks back to liquid pool of the evaporator section under gravity

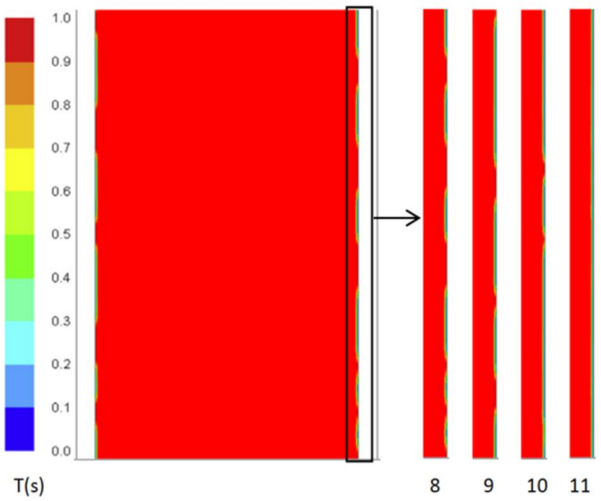
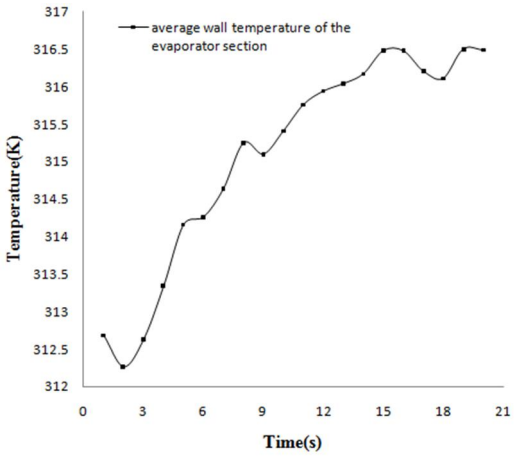


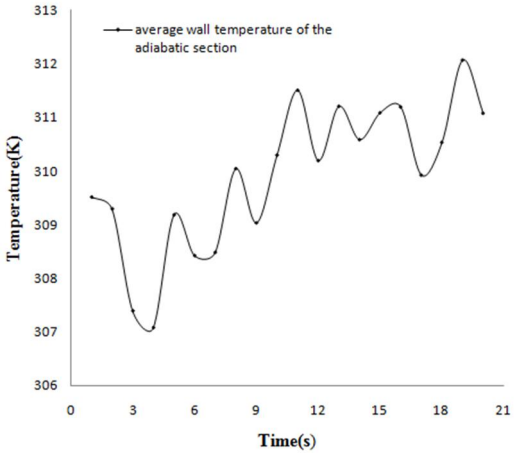
Fig. 3. liquid film in the lower region of condenser section at different times

5.2 Wall temperature profile of numerical simulation of thermosyphon

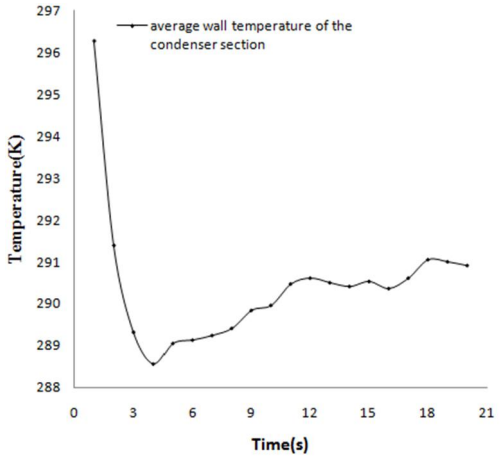
The average wall temperatures, versus the time, for evaporator section, adiabatic section and condenser section are specified by Fig. 4. As a continuous power input, the increasing trend of the



(a)



(b)



(c)

Fig. 4. Average wall temperature profiles for evaporator, adiabatic, and condenser sections at different times

average wall temperature of the evaporator section can be observed in Fig. 4(a) between 0s and 15s. By the heat dissipation of the condenser section, the average wall temperature of the evaporator section are relatively constant after 15s in Fig. 4(a). Compared to the average wall temperature of the evaporator section, the average wall temperature of the adiabatic has limited variation, as shown in Fig. 4(b). Therefore, the centre temperature of the adiabatic can be specified as the saturation temperature of the thermosyphon.

5.3 Effective thermal conductivity of numerical simulation of thermosyphon

In order to evaluate the thermal performance of the thermosyphon, the heat transfer capability of a thermosyphon charged with working fluids is treated as the heat transfer capability of a solid cylinder with equal size. The thermal conductivity of this solid cylinder is specified as the effective thermal conductivity of the thermosyphon with the following correlation：

$$\lambda_{eff} = \frac{4L^2}{d_o^2}\left[1/\left(\frac{\ln(d_o/d_i)}{2(L_e/L)} + \frac{\lambda_w}{h_e d_o (L_e/L)} + \frac{\lambda_w}{h_c d_o (L_c/L)} + \frac{\ln(d_o/d_i)}{2(L_c/L)}\right)\right]\lambda_w \quad (13)$$

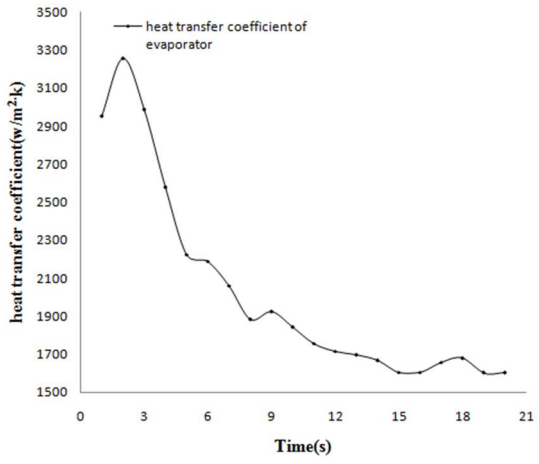
where L, L_e and L_c are the length of total thermosyphon, evaporator and condenser, d_o and d_i are the outer diameter and inner diameter, and λ_w is the thermal conductivity of the wall. The h_e and h_c represent the heat transfer coefficient of the evaporator and condenser with the following form:

$$h_e = \frac{Q}{\pi d_o L_e (T_e - T_s)} \quad (14\text{-}1)$$

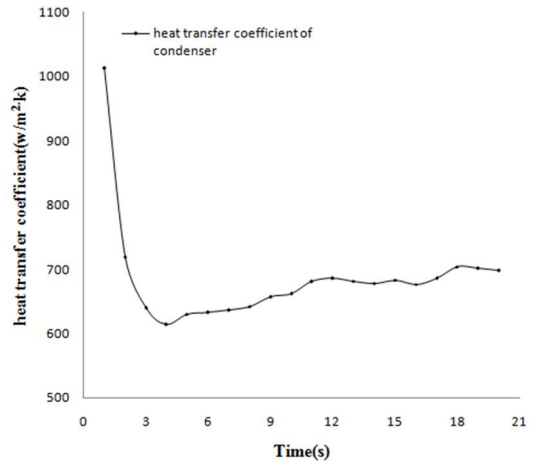
$$h_c = \frac{Q}{\pi d_o L_c (T_s - T_c)} \quad (14\text{-}2)$$

where T_e and T_c are the average wall temperature of evaporator and condenser, and Q represents the power input.

Fig. 5 illustrates the variation of the heat transfer coefficient of evaporator and condenser at different times. By comparison of Fig. 4 and Fig. 5, it can be found that the transfer coefficient of evaporator shows the opposite variation trend with the average



(a)



(b)

Fig. 5. Heat transfer coefficient of evaporator and condenser sections at different times

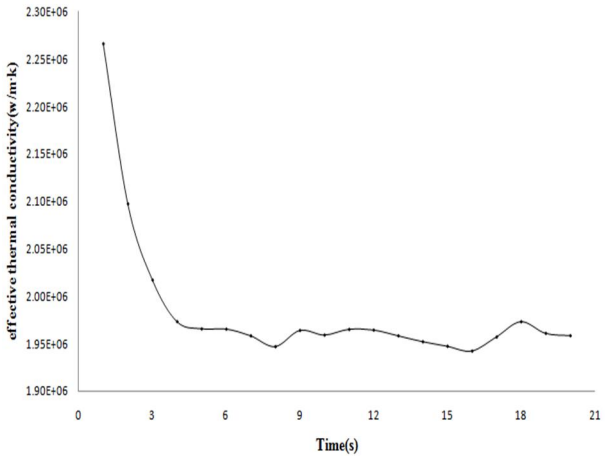


Fig.6. effective thermal conductivity of the thermosyphon at different times

temperature of evaporator, while the transfer coefficient of condenser and the average temperature of condenser have the same variation trend. The effective thermal conductivity, versus the time, is

displayed in Fig. 6. It is apparent that the effective thermal conductivity is with maximum value of 2.27×10^6 W/m · K at initial time, and then shows the decreasing trend by increasing of the time. Eventually, the effective thermal conductivity has limited variation in Fig. 6 after 4s.

6. CONCLUSIONS

In the present paper, a transient two-dimensional model is built with VOF technique for simulation of the complex phenomenon in a thermosyphon. In order to calculate the heat and mass transfer, UDFs is linked to the governing equations of FLUENT by the form of source terms. The CFD results confirmed that this model has the ability to reproduce the process of the pool boiling in the evaporator section and the formation of liquid film in the condenser section during the start-up of thermosyphon.

The average wall temperatures for evaporator, adiabatic and condenser have been investigated at different times. The variation trend of average wall temperatures for evaporator, adiabatic and condenser are obtained during the operation of the thermosyphon. The predicted results show that the thermosyphon with power input of 40W starts to work at 4s and reaches a steady-state after 15s.

The effective thermal conductivity is proposed to evaluate the thermal performance of the thermosyphon. For a constant power input of 40W, it is found that the maximum value of effective thermal conductivity occurs at the initial time. Moreover, the effective thermal conductivity reaches a relative constant value after 4s.

NOMENCLATURE

C : Constant of the evaporation/condensation
d : diameter(m)
E : Energy source term (W/m^3)
e : Internal energy (J/kg)
F_{CSF} : Volumetric surface tension force(N)
g : Acceleration of gravity (m/s^2)
I : unit tensor
k : Surface curvature(1/m)
LH : latent heat(J/kg)
L : Length(m)
M : Mass transfer rate (kg/s)
p : Pressure (Pa)
T : Temperature (K)

Greek symbols

α : Volume fraction
λ : Thermal conductivity (W/m K)
μ : Dynamic viscosity (Pa s)
ρ : Density (kg/m^3)
σ_{vl} : Surface tension coefficient(N/m)

Subscript

CSF : Continuum surface force
c : Condenser
e : Evaporator
eff : Effective
i : Inner
l : Liquid phase
mix : Mixture
o : Out
sat : Saturation
v : Vapor phase
W : Wall

REFERENCES

[1] A. Faghri, *Heat Pipe Science and Technology*, Taylor & Francis, Washington,D.C, (1995).
[2] Y. Weng, H.Cho, C.Chang, S.Chen, Heat pipe with PCM for electronic cooling, *Appl. Energy*, 88(2011) 1825-1833.
[3] Vasiliev L, Lossouarn D, Romestant C, Alexandre A, Bertin Y, Piatsiushyk Y, Romanenkov V, Loop heat pipe for cooling of high-power electronic components, *International Journal of Heat and Mass Transfer*, 52(2008)301-308.
[4] M. Zhang, Z. Liu, G. Ma, S. Cheng, Numerical simulation and experimental verification of a flat two-phase thermosyphon, *Energy Convers, Manag*, 50(2009) 1095-1100.
[5] Hichem Farsi, Jean-Louis Joly, Marc Miscevic, Vincent Platel, Nathalie Mazet, An experimental and theoretical investigation of the transient behavior of a two-phase closed thermosyphon, *Applied Thermal Engineering*, 23(2003)1895-1912.
[6] Vadim Tsoi, Shyy Woei Chang, Kuei Feng Chiang, Chuan Chin Huang, Thermal performance of plate-type loop thermsyphon at sub-atmospheric pressures, *Applied Thermal Engineering*, 31(2011) 2556-2567.
[7] Wei Guo, Darin W.Nutter, An experimental study of axial conduction through a thermosyphon pipe wall, *Applied Thermal Engineering*, 29(2009)3536-3541.
[8] Qi Baojin, Zhang Li, Xu Hong, Sun Yan, Heat transfer characteristics of titanium/water two-phase closed thermosyphon, *Energy Conversion and Management*, 50(2009)2174-2179.

[9] P. Amatachaya, W. Srimuang, Comparative heat transfer characteristics of a flat two-phase closed thermosyphon (FTPCT) and a conventional two-phase closed thermosyphon (CTPCT), *International Communications in Heat and Mass Transfer*, 37 (2010)293-298.

[10] Shi Liu, Jingtao Li, Qi Chen, Visualization of flow pattern in thermosyphon by ECT, *Flow Measurement and Instrumentation*, 18(2007) 216- 222.

[11] S.H. Noie, Heat transfer characteristics of a two-phase closed thermosyphon, *Applied Thermal Engineering*, 25(2005)495-506.

[12] A.S. Annamalai, V. Ramalingam, Experimental investigation and computational fluid dynamics analysis of a air cooled condenser heat pipe, *Thermal Science*, 15(2011) 759-772.

[13] J. Legierski, B. Wiecek, G. de Mey, Measurements and simulations of transient characteristics of heat pipes, *Microelectronics Reliability*, 46(2006) 109-115.

[14] S. CK. De Schepper, G.J. Heynderickx, G.B. Marin, Modeling the evaporation of a hydrocarbon feedstock in the convection section of a steam cracker, *Computers & Chemical Engineering*, 33(2009)122-132.

[15] Z. Lin, S. Wang, R. Shirakashi, L. Winston Zhang, Simulation of a miniature oscillating heat pipe in bottom heating mode using CFD with unsteady modeling, *International Journal of Heat and Mass Transfer*, 57(2013)642-656.

[16] A. Alizadehdakhel, M. Rahimi, A.A. Alsairafi, CFD modeling of flow and heat transfer in a thermosyphon, *International Communications in Heat and Mass Transfer*, 37(2010)312-318.

[17] B. Fadhl, Luiz C. Wrobel, HussamJouhara, Numerical modeling of the temperature distribution in a two-phase closed thermosyphon, *Applied Thermal Engineering*, 60(2013)122-131.

[18] B. Fadhl, Luiz C. Wrobel, HussamJouhara, CFD modeling of a two-phase closed thermosyphon charged with R134a and R404a, *Applied Thermal Engineering*, 78(2015)482-490.

[19] J.U. Brackbill, A continuum method for modeling surface tension, *Journal of Computational Physics*, 100(1995)335-354.

Turbulent Film Condensation in Thermosyphons

A. Nouri-Borujerdi

School of Mechanical Engineering, Sharif University of Technology, Tehran, Iran

Abstract

In this study a new mathematical model is developed for investigation of shear stress at liquid-vapor interface as well as heat transfer of turbulent condensation film in a thermosyphon by solving numerically the governing equations of mass, momentum and energy. Momentum flux of the vapor in the core region of the thermosyphon pipe to the outer surface of the liquid film is taken into account. The saturation temperature of the working fluid varies in the range of $315K < T_{sat} < 373K$. It is found that for large film condensation on condenser surface, estimation of the velocity and temperature by applying momentum and energy equations of inner layer in turbulent flow proved to be successful. Extension of these results in the estimation of average condensation heat transfer coefficients is found to be successful. The present theoretical results are further compared with the recent experimental data and the agreement between the two is found to be very satisfactory.

Keywords: Counter current two-phase flow; Turbulent condensation film; Annular flow; Heat transfer, condenser

1. INTRODUCTION

Thermosyphon is a vertical tube closed at both ends in which a working fluid circulates naturally between the heating zone or evaporator at the bottom and the cooling zone or condenser at the top section. In other words, the thermosyphon transmits heat upwards and downwards by self-acting flow loops. Vapor is produced in the heating zone and moves upward spontaneously. The vapor is subsequently condensed in the cooling zone and moves downward on the wall surface by the gravitational force. Heat can be transferred in circulation loops in two ways: one with vapor as the latent heat of evaporation and the other one with liquid as the sensible heat of the liquid.

Yandri et al. [1] built and tested a laboratory installation in which water vapor as the working agent is condensed by yielding heat to the condenser and returns to the heating zone again. The vertical distance of heat transfer for the installation was about 1 m. A vacuum pump was used to produce and support the negative pressure, which considerably reduces the loop reliability.

Pan [2] and Faghri [3] considered the liquid film condensation by taking into account the interfacial shear due to the mass transfer and interfacial velocity. They showed that the effect of interfacial shear on the film flow is small.

Nouri-Borujerdi and Layeghi [4] simulated the vapor flow and pressure drop along a concentric annular heat pipe for various asymmetric and symmetric heat addition and rejection circumstances. They showed that under asymmetric heat addition and rejection circumstances, a number of recirculation zones may be created at both of the evaporator and condenser sections. They discussed qualitatively that these recirculation zones can be very effective zones for increasing heat transfer between objects of different diameters even at high radial Reynolds numbers.

Many workers have analyzed the conventional heat pipes using a variety of numerical and experimental techniques. Terpstra and Van Veen [5], and Peterson [6] have published several of these techniques, theories, and applications of different heat pipe structures. Gaugler [7] utilized a wicking material as part of a passive two-phase heat transfer device capable of transferring large quantities of heat with a minimal temperature drop.

In this paper, a new mathematical model is presented for calculation of liquid film thickness as well as Nusselt number in a turbulent regime. Also, to better design and manufacture of various types of two-phase thermosyphon, the effects of liquid Prandtl number have been analyzed.

2. PHYSICAL MODEL

Fig. 1 shows the condenser surface of a thermosyphon as a vertical tube closed at both ends in which the working fluid circulates naturally between the heating and the cooling zone. The wall temperature of the condenser is assumed to be at constant temperature T_w and the fluid saturation

*Corresponding author: anouri@sharif.edu,
Phone: +98-21-6616-5547, Fax: +98-21-6600-0021

temperature corresponding to the system pressure is $T_{sat} > T_w$.

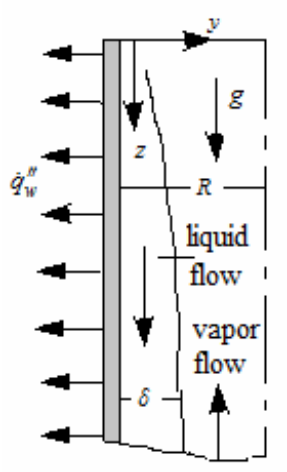


Fig. 1 Liquid film on the vertical surface of condenser

There are three possible distinct flow regimes. Near the top of the surface, the mass flow rate is low and the flow is laminar. In this regime, corresponding to approximately Reynolds number by $\mathrm{Re} = \bar{u}_f D_h / \nu_f < 30$, the surface of the film is smooth. This region has a negligible effect in comparison with the other regions and can be neglected. Further down the surface, as the mass flow rate of condensate increases, a series of regular ripples appear on the surface of the film. The wavy region has been found to correspond approximately to $30 < \mathrm{Re} < 1800$. Eventually for $\mathrm{Re} > 1800$, the flow in the liquid film becomes fully turbulent.

It is assumed that the flow regime of the liquid film is turbulent. In this regard, we can imagine the inner region of the turbulent boundary layer velocity profile is situated close enough to the wall such that the convective terms of the momentum equation are sufficiently small. Then the apparent shear stress does not vary with y and is identical to the wall shear stress.

$$1 = \left[1 + \frac{\varepsilon_M}{\nu_f}\right] \frac{du_f^+}{dy^+} \tag{1}$$

$u_f^+ = u_f / u_t$, $y^+ = y u_t / \nu_f$, $u_t = \sqrt{\tau_w / \rho_f}$ and y is measured inwards and normal to the wall.

ε_M / ν_f denotes the ratio of eddy diffusivity to kinetic viscosity. Driest [8] showed that a good approximation to ε_M / ν_f could be obtained by:

$$\frac{\varepsilon_M}{\nu_f} = b \frac{du_f^+}{dy^+} \tag{2}$$

where $b = k^2 y^{+2} \left[1 - \exp(-y^+ / 26)\right]^2$ and $k = 0.4$.

In a similar manner, the convective terms of the energy equation are sufficiently small. Then the apparent heat flux does not vary with y and is identical to wall heat flux,

$$\dot{q}_w'' = k_f \left[1 + \frac{\varepsilon_H}{\alpha_f}\right] \frac{dT}{dy} \tag{3}$$

The second term in the bracket is calculated as $\varepsilon_H / \nu_f = (\mathrm{Pr} / \mathrm{Pr}_t)(\varepsilon_M / \nu_f)$ in which Pr and Pr_t are Prandtl and turbulent Prandtl numbers respectively.

It is noteworthy assume that the turbulent conduction across the liquid film is more significant than the convective component, or

$$\frac{d(\delta \bar{u}_f)}{dz} = \frac{\dot{q}_w''}{\rho_f h_{fg}} \tag{4}$$

$\delta = \delta(z)$ is the liquid film thickness and $\bar{u}_f$ is the mean liquid film velocity and is obtained from the following expression by introducing Eqs. (2) and (1).

$$\delta \bar{u}_f = \nu_f \int_0^{\delta^+} u_f^+ dy^+ = \nu_f \int_0^{\delta^+} dy^+ \int_0^{y^+} \frac{2dy^+}{1 + \sqrt{1 + 4b}} \tag{5}$$

Inserting Eq. (5) into Eq. (4), the final result reads

$$\frac{d\delta^+}{dz^+} = \frac{\dot{q}_w''}{\rho_f u_t h_{fg} \int_0^{\delta^+} \frac{2dy^+}{1 + \sqrt{1 + 4b}}} \tag{6}$$

where, $z^+ = z u_t / \nu_f$

Eq. (3) can be integrated formally to obtain

$$\frac{T - T_w}{\frac{\dot{q}_w''}{\rho_f C_p u_t}} = \int_0^{y^+} \frac{2dy^+}{\frac{2}{\mathrm{Pr}} + \frac{1}{\mathrm{Pr}_t}(-1 + \sqrt{1 + 4b})} \tag{7}$$

Removing $\dot{q}_w''$ between Eqs. (6) and (7), the final result will be as:

$$\frac{d\delta^+}{dz^+} = \frac{0.25 Ja}{\int_0^{\delta^+} \frac{dy^+}{1 + \sqrt{1 + 4b}} \int_0^{\delta^+} \frac{dy^+}{\frac{2}{\mathrm{Pr}} + \frac{1}{\mathrm{Pr}_t}(-1 + \sqrt{1 + 4b})}} \tag{8}$$

where $Ja = C_p(T_{sat} - T_w)/h_{fg}$.

With the help of Eq. (7), the local Nusselt number of the liquid film on the surface of the condenser surface is

$$Nu = \frac{\dot{q}''_w D_h}{(T_{sat} - T_w)k_f} = \frac{2\,\mathrm{Pr}\,\delta^+}{\int_0^{\delta^+} \frac{dy^+}{\frac{2}{\mathrm{Pr}} + \frac{1}{\mathrm{Pr}_t}(-1+\sqrt{1+4b})}} \quad (9)$$

$D_h = 4\delta$ and δ denote the liquid film thickness.

The force balance on the condensate liquid film is

$$\tau_w + \rho_f \delta g + \frac{(R-\delta)^2}{2R}\rho_g g - \frac{\partial P}{\partial z} = 0 \quad (10)$$

and wall shear stress will be

$$\tau_w = \frac{f_{TP}}{2}\rho_f \bar{u}_f^2 \quad (11)$$

Also, from forces balance on liquid and vapor phase and removal the gradient pressure between them, we have

$$\tau_w + \frac{R^2+\delta^2}{R(R+\delta)}\tau_i = (\rho_f - \rho_g)\delta g \quad (12)$$

There is momentum flux from the vapor in the core region of the thermosyphon pipe to the outer surface of the liquid film that is equal to a shear stress acting on the liquid-vapor interface as

$$\tau_i = \dot{m}_v(\bar{u}_g - 2\bar{u}_f) = \frac{\dot{q}''_w}{h_{fg}}(\bar{u}_g - 2\bar{u}_f) \quad (13)$$

Substituting Eqs. (11) and (13) into Eq. (12) and (10) then gives two equations for calculation of heat flux and the pressure gradient respectively.

3. SOLUTION METHOD

To determine the heat transfer coefficient between the liquid film and the condenser surface, it is first required Eq. (8) to be solved numerically. Solution of this integral differential equation is a cumbersome task. To do that, we integrated Eq. (8) numerically and the data of the result was fitted as $\delta^+ = \delta(z^+)$, then this expression inserted into Eq. (9) to obtain the Nusselt number.

4. RESULTS AND DISCUSSION

A closed two-phase water-vapor thermosyphon made of a thin copper tube with length $L_c = L_e = 0.3\,m$ and $L_a = 0.4\,m$ has been considered. The saturation temperature varies in the range of $315\,K < T_{sat} < 373\,K$.

Fig. 2 shows the dimensionless turbulent velocity distribution in the liquid film. The ordinate axis is normalized by the shear velocity. As we can see, the velocity in the vicious sublayer is proportional to the distance from the surface and after that increase the logarithmic. Fig. 3 illustrates the mean temperature distribution across the liquid film as a function of molecular Prandtl number. The ordinate axis is normalized by the wall heat flux as well as the shear velocity. T and T_w are the local film and the wall surface temperatures respectively. The different curves represent lines of constant Prandtl numbers. The results indicate that the local temperature difference between the liquid film and the wall in near region is more significant than that of the far region and this difference is more for higher Prandtl number. This indicates that the resistance to flow of heat in liquid with high Prandtl number is found in the laminar sublayer or in the buffer layers.

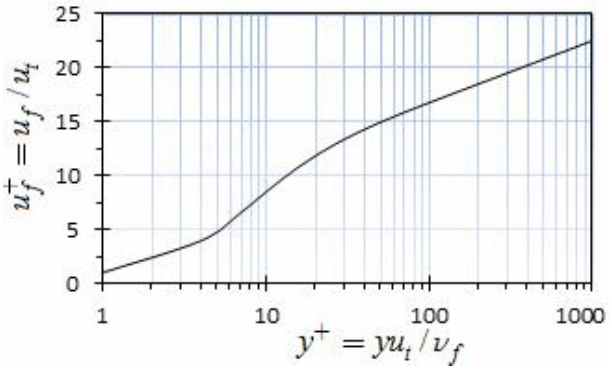


Fig. 2 Dimensionless turbulent velocity distribution in the liquid film

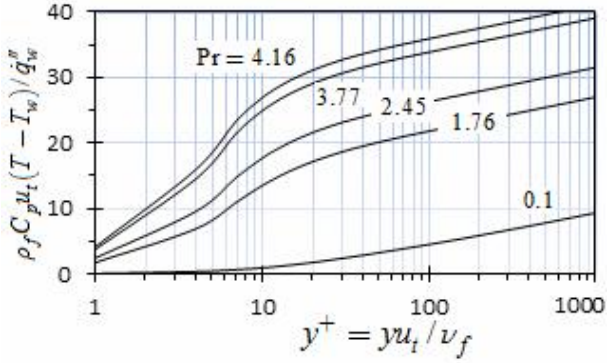


Fig. 3 Mean temperature distribution across the liquid film as a function of molecular Prandtl number

Fig. 4 depicts the dimensionless film thickness distribution along the surface of the condenser as a function of molecular Prandtl number. The abscissa is the ratio of $z^+ = z u_t / \nu_f$ and Ja is called Jakob number and is defined as $Ja = C_{pf}(T_{sat} - T_w)h_{fg}$ where T_{sat} is the liquid saturation temperature. The ordinate is $\delta u_t / \nu_f$. The liquid film thickness at any cross section of the thermosyphon can be evaluated from the curves of Fig. 4. Fig. 5 states Nusselt number distribution along the surface as a function of molecular Prandtl number. The ordinate reports the Nusselt number $Nu = \dot{q}''_w D_h / k_f (T_{sat} - T_w)$ where D_h and k_f denote the hydraulic diameter and the liquid thermal conductivity respectively. The result of this figure shows that the Nusselt number at any cross section is more inclined after a distance, $Ja\, z^+ > 10^4$ for a higher Prandtl number.

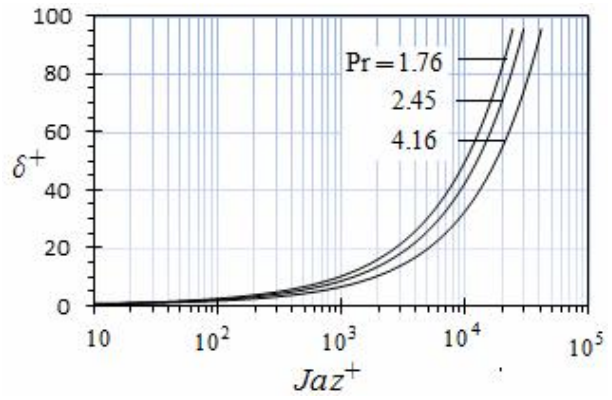


Fig. 4 Dimensionless film thickness distribution along surface as a function of molecular Prandtl number

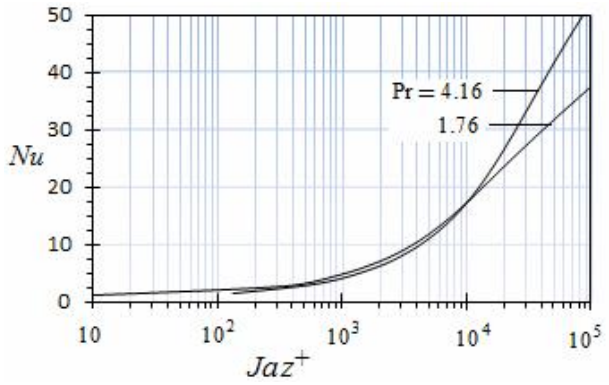


Fig. 5 Nusselt number distribution along surface as a function of molecular Prandtl number

5. CONCLUSIONS

In this study a new mathematical model for investigation of heat transfer of turbulent condensation film is developed in a thermosyphon. The governing equations of mass, momentum and energy equations were solved numerically. The interface shear stress at the vapor condensate film is taken into account. The results show that for large film condensation on condenser surface, estimation of the velocity and temperature by applying momentum and energy equations of inner layer in turbulent flow proved to be successful. Extension of these results in the estimation of average condensation heat transfer coefficients is found to be successful.

NOMENCLATURE

C_P : Constant pressure specific heat (kJ/kg.K)
D : Diameter (m)
f : Friction factor
g : Gravity acceleration (m/s^2)
h_{fg} : Latent heat (kJ/kg)
Ja : Jakob number, $C_P(T_{sat} - T_w)/h_{fg}$
k : Constant or thermal conductivity (W/m.K)
$\dot{m}$: Mass flow rate (kg/m^2.s)
Nu : Nusselt number, $\dot{q}''_w D_h /(T_{sat} - T_w)k_f$
Pr : Prandtl number, ν / α
$\dot{q}''_w$: Heat flux (W/ m^2)
R : Pipe radius (m)
Re : Reynolds number, $\overline{u}\, D_h / \nu$
T : Absolute temperature (K)
u : Velocity (m/s)
y : Distance from wall (m)

Greek Letters

α : Molecular thermal diffusivity (m^2/s)
δ : Fil thickness (m)
ε : Diffusivity (m^2/s)
ν : Kinetic viscosity (m^2/s)
ρ : Density (kg/m^3)
τ : Shear stress (N/ m^2)

Subscripts

f : Liquid
g : Gas or vapor
h : Hydraulic or heat
i : Interface
M : Momentum
sat : Saturation
t : Turbulent
TP : Two-phase
w : Wall

Superscripts

$\overline{\ }$: Mean

5. Special Heat Pipes/ Novel Design of Heat Pipes

Hybrid Variable and Constant Conductance Heat Pipes for Lunar and Martian Environments and High Heat Flux Space Applications

Mohammed T. Ababneh, Calin Tarau and William G. Anderson

[1]*Advanced Cooling Technologies, Inc., 1046 New Holland Ave. Lancaster, PA 17601, USA*

Abstract

A hybrid wick heat pipe has a porous wick in the evaporator, and a grooved wick in the adiabatic and condenser sections. This paper will discuss four different applications for hybrid wick heat pipes: 1. Adverse evaporator elevations for landers and rovers, 2. High heat flux applications, 3. Vertical startup with a liquid column during ground testing, and 4. Freeze/thaw tolerant water heat pipes. The next generation of Lunar polar rovers and equatorial landers is among the immediate NASA applications. A Variable Conductance Heat Pipe (VCHP) is required that can operate during large adverse tilts in the evaporator, shut down during the long Lunar night and operate over a wide range of sink temperatures on the planetary surface. Also, future spacecraft and instruments developed for NASA's Science Mission Directorate will include highly integrated electronics, suchas for CubeSat/SmallSat. Thermal transport requirements for future missions continue to increase, approaching several kilowatts. At the same time the heat acquisition areas have trended downward, thereby increasing the incident heat flux. A hybrid wick heat pipe will allow such devices to operate at higher heat fluxes as compared to axial groove design. Vertical start-up with a liquid column is mitigated experimentally with a hybrid wick. The experimental results proved that the large number of nucleation sites in sintered wicks facilitates boiling initiation in pool boiling systems and, consequently, the temperature spikes are minimized. Finally, a hybrid titanium/water heat pipe radiator assembly suitable for waste heat rejection from a Spacecraft Fission Power system such as the Kilopower system is also required. A prototype titanium heat pipe and several aluminum face sheets were joined with S-bond and tested for bond quality and overall thermal performance. Tests were performed successfully both in ambient and in vacuum validating the direct bond. The full length versions of the final deliverable hybrid grooved/screened titanium-water heat pipes for Kilopower system with radiators and the hybrid grooved/sintered CCHPs and VCHPs for high heat flux space applications and planetary surface are under development.

Keywords: Constant Conductance Heat Pipes (CCHPs); Hybrid wick; Lunar and Martian environments; Variable Conductance Heat Pipes (VCHPs); High heat flux heat pipe wicks; Vertical start-up.

Thermo-Mechanical Characterization of Flexible HeatPipes

Tanmay Jaipurkar[1], Sameer Khandekar[1],
Pushpit Kant[1], Bishakh Bhattacharya[1] and Siddharth Paralikar[2]

[1] *Department of Mechanical Engineering, Indian Institute of Technology Kanpur, Kanpur, 208016, India*
[2] *Golden Star Technical Services Pvt. Ltd., Pavana Complex, A39/T204, M.I.D.C., Bhosari, Pune - 411 026, India*

Abstract

The paper describes the ongoing development, testing and characterization of thermal and vibrational performance of a flexible heat pipe. The heat pipe is to be designed for passive thermal management wherein passive heat transfer is required to be coupled with vibration isolation. The evaporator section, to which the heat-load is attached, is to be vibration-isolated from the radiator or the condenser section. The inherent flexibility of the heat pipe prevents it and the thermal load from getting damaged or deformed under mounting and launch related stress. The flexibility also helps in maintaining the precision in positioning if in case the heat source is a camera or other scanning device. The flexibility is provided in the adiabatic section of the heat pipe using a flexible bellow. The major technical challenge faced during manufacturing of the heat pipe is integrating the capillary wick in the flexible bellow maintaining continuity and proper thermal contact under deformations. The heat pipe is developed for the maximum heat carrying capacity of 50W-70W and to sustain mounting and transporting loads. The operating temperature range of temperature is 10°C to 100°C. The heat pipes use water as the working fluid. The heat pipes which are tested have internal diameters of 10 mm and 6 mm respectively, and are 270 mm long with different wick structures. The bellow used in the heat pipe is tested for deformations under hydrostatic pressure. Natural frequency of bellow is also measured experimentally by using Laser Doppler Vibrometer (LDV). A finite element model for the bellow is developed and it is benchmarked against experiments.

Keywords: Heat pipes; Metallic bellows; Natural frequency; Thermal performance testing.

■ *Published in Applied Thermal Engineering, Volume 126, 5 November 2017, Pages 1199-1208, https://doi.org/10.1016/j.applthermaleng.2017.01.036*

Heat Pipes with Variable Thermal Conductance Property Developed for Space Applications

V. Kravets[1], Ye. Alekseik[1], O. Alekseik[1], S. Khairnasov[1], V. Baturkin[2], T. Ho[2] and L. Celotti[3]

[1] *Heat Pipes Laboratory of Heat-and-power engineering faculty, National Technical University of Ukraine "Kyiv polytecnic institute", Kyiv, 03056 Ukraine*

[2] *DLR Institut für Raumfahr systeme, Explorations systeme RY-ES, Bremen, 28359 Germany*

[3] *Active Space Technologies GmbH, Berlin, 12489 Germany*

Abstract

The activities presented in this paper focus on a new approach to provide passive regulation of the electronic unit thermal regime of the MASCOT lander (DLR) onboard the NEA sample return mission Hayabusa 2 (JAXA), by using heat pipes. It provides information on the development and testing of heat pipes with variable thermal conductance in a predetermined temperature range. Such heat pipes act as thermal switches, but their construction does not include additional elements inherent to gas loaded heat pipes (GLHP) and thermal diode heat pipes (TDHP). Copper heat pipes with metal fibrous wick were chosen as baseline design. We have obtained positive results by choosing heat carrier and structural parameters of wick (i.e. pore diameter, porosity and permeability). A rising of heat pipes thermal conductivity from 0.04 to 2.1 W/K was observed in the temperature range between -20°C…+55°C. The heat pipes transferred predetermined power not less than 10 W within the temperature range of +20°C… +55°C. These heat pipes are in flight since December 2014 and the telemetric data obtained in September 2015 showed normal operation of the thermal control system.

Keywords: Heat pipe; Metal fiber; Space applications; Thermal conductance; Wick.

■ *Published in J Mech Sci Technol (2017) 31: 2613. https://doi.org/10.1007/s12206-017-0503-8*

Modeling of a Revolving Heat Pipe for Cooling of Grinding Wheels

Jiajia Chen[1], Yucan Fu[2], Houfa Shen[3], Dan Ewing[4] and Chan Y. Ching[5]

[1] *Graduate Student, College of Mechanical and Electrical Engineering, Nanjing University of Aeronautics and Astronautics, Nanjing, CHINA*

[2] *Professor, College of Mechanical and Electrical Engineering, Nanjing University of Aeronautics and Astronautics, Nanjing, CHINA* [3] *Graduate Student, College of Mechanical and Electrical Engineering, Nanjing University of Aeronautics and Astronautics, Nanjing, CHINA*

[4] *Research Associate, Dept. of Mechanical Engineering, McMaster University, Hamilton, ON, CANADA*

[5] *Professor, Dept. of Mechanical Engineering, McMaster University, Hamilton, ON, CANADA*

Abstract

A novel two phase heat transport system within the annular disk of grinding wheels has been proposed for cooling grinding wheels. The cylindrical grinding surface is the evaporator and the cooled rotating sides are the condenser. A simplified two-dimensional geometry, modeled as a revolving heat pipe, is used to investigate the heat transfer in the evaporator section of this system. The rotation of the wheel is incorporated in the model as an artificial gravity, which in this instance is as high as 11250g. Simulations are performed using the volume of the fluid (VOF) model in ANSYS/FLUENT. Nucleate boiling is suppressed in the liquid layer at the evaporator due to the high acceleration. Instead, the natural convection heat transfer is enhanced with evaporation at the liquid-vapor interface. The heat transfer coefficient for the evaporator increases with time after natural convection develops, and approaches a uniform value. The corresponding Nusselt number is about 7.5% lower than that from the correlation of Holzbecher and Steiff (1995) for laminar natural convection of water.

Keywords: Revolving heat pipe; Modeling; Grinding wheel; Cooling.

Design of a Thermosyphon-Based Thermal Valve for Controlled High-Temperature Heat Extraction

Christopher Oshman[1], Corey Hardin[1], Jonathan Rea[1], Michele L. Olsen[2], Nathan Siegel[3], Phil Parilla[2], David Ginley[2] and Eric S. Toberer[1,2]

[1]*Physics Department, Colorado School of Mines, Golden, CO 80401, U.S.A*
[2]*National Renewable Energy Laboratory, Golden, Colorado 80401, U.S.A.*
[3]*Mechanical Engineering Department, Bucknell University, Lewisburg, 17837, U.S.A.*

Abstract

Conventional concentrated solar power (CSP) is a reliable alternative energy source that uses the sun's heat to drivea heat engine to produce electrical power. An advantage of CSP is its ability to store thermal energy for use during off-sun hours which is typically done by storing sensible heat in molten salts. Alternatively, thermal energy may be stored as latent heat in a phase-change material (PCM), which stores large quantities of thermal energy in an isothermal process. On-sun, the PCM melts, storing energy. Off-sun, the latent heat is extracted to produce dispatchable electrical power. This paper presents the design of a thermosyphon-based device with sodium working fluid that is able to extract heat from a source as demand requires. A prototype has been designed to transfer 37 kW of thermal energyfroma 600°C molten PCM tank to an array of 9% efficient thermoelectric generators (TEGs) to produce 3 kW of usable electrical energy for 5 hrs. This "thermal valve" design incorporates a funnel to collect condensate and a central shut-off valve to control condensate gravity return to the evaporator. Three circumferential tubes allow vapor transport up to the condenser. Pressure and a thermal resistance models were developed to predict the performance of the thermal valve. The pressure model predicts that the thermal valve will function as designed. The thermal resistance model predicts a 5500x difference in total thermal resistance between "on" and "off" states. The evaporator and condenser walls comprise 96% of the "on" thermal resistance, while the small parasitic heat transfer in the "off" state is primarily (77%) due to radiation losses. This simple and effective technology can have a strong impact on the feasibility, scalability, and dispatchability of CSP latent storage. In addition, other industrial and commercial applications can benefit from this thermal valve concept.

Keywords: PCM; Sodium; Thermal Valve; Thermosyphon.

■ *Published in Applied Thermal Engineering, Volume 126, 5 November 2017, Pages 1141-1147, https://doi.org/10.1016/j.applthermaleng.2017.01.038*

Preliminary Investigation on Operation Characteristics of a High Temperature Special-Shaped Heat Pipe Used in a Solar Thermochemical Reactor

Ma Tingting, Wang Xiaoyuan, Zhu Yuezhao and Zeng Jinling

School of Mechanical and Power Engineering, Nanjing Tech University, Nanjing 211816, PR China

Abstract

Solar energy can be transformed and stored as chemical fuels through the high-temperature thermochemical processes driven by concentrated solar irradiation. Solar thermochemical reactors are the crucial equipment to these processes. A solar thermochemical coupling phase change reactor (STPCR) integrated with heat pipe technology is presented. The core part of this reactor is a high temperature special-shaped heat pipe (HTSSHP) which is composed of a flat heat pipe in disk-shape connected to multiple cylindrical heat pipes. A 2kW HTSSHP prototype with sodium as the working fluid was fabricated and tested under various heat inputs and inclination angles. The evaporating behaviors of sodium during startup were investigated. And the temperature pulsation phenomenon on heat absorber surface was observed in startup for a short period at heat flux up to 47.2kW/m^2, implying film boiling occurs. Further, the operation characteristic of HTSSHP was experimentally proven steady under various heat fluxes and inclination angles, and it showed a good ability to spread temperature at the cooling side where the thermo chemical processes take place. This work will facilitate the preliminary understanding of the operation characteristics in HTSSHP.

Keywords: Solar thermo chemical reactor; Sodium heat pipe; Evaporating behavior; Isothermal characteristic.

■ *Published in Heat Transfer Engineering, Vol. 40, Issue 3, 2019.*

Characterization of a High Performance Ultra-Thin Heat Pipe Cooling Module for Mobile Hand Held Electronic Devices

Mohammad Shahed Ahamed, Yuji Saito, Koichi Mashiko and Masataka Mochizuki

Thermal Technology Division, Electronics Company Fujikura Ltd., 1-5-1 Kiba, Koto-Ku, Tokyo 135-8512, JAPAN

Abstract

In recent years the application of heat pipe is widening to the field of mobile hand held electronic devices such as smart phone, tablet PC, digital camera etc. With the development in technology these devices have different user friendly features and applications; which require very high clock speed of the processor. In general, high clock speed generates a lot of heat which need to be spreaded or removed to eliminate the hot spot on the processor surface. However, it is a challenging task to achieve proper cooling of such electronic devices mentioned above because of its confined space and concentrated heat sources. Regarding to this challenge, previously ultra-thin heat pipe is introduced; this heat pipe consists of a special fiber wick structure named as "Center Fiber Wick" which can provide sufficient vapor space on the twos sides of the wick structure. Besides previously by using this kind of ultra-thin heat pipe a cooling module to eliminate the hot spot issue of smart phone was proposed. This cooling module consists of a ultra-thin heat pipe and a metal plate. By changing the width, the flattening thickness and the effective length of the ultra-thin heat pipe; in this paper several studies have been conducted to characterize the thermal properties of the proposed cooling module. As well as, effect on thermal properties when changing the number of heat pipes in a single module has been studied. Characterization and comparison have been conducted both experimentally and theoretically.

Keywords: Heat pipe; Heat spreading; Mobile devices; Fiber wick; Thermal conductivity.

■ *Published in Heat and Mass Transfer, Vol. 53, issue 11 (DOI: https://doi.org/10.1007/s00231-017-2022-7)*

The Two-Phase Spreading of High Heat Fluxes Density Dissipative Components for Space and Non-Space Applications

Mikaël Mohaupt[1], Stéphane Van Oost[1] and Laurent Barremaecker[1]

[1]*Euro Heat Pipes, Rue de l'industrie 24, Nivelles, Belgium*

Abstract

The two-phase spreading is described extensively in this study and represents key issue in many application fields such as space satellites and launchers, aeronautics, railways as well as in computer world. Considering constant increase of surface heat fluxes to dissipate in electronic field, the thermal management is a key challenge to be addressed. Effective spreading of the heat offers an elegant and performant way to reduce electronic equipment temperatures or increase their waste heat power. The conductive technologies are analyzed showing performances and reliability limitations. To solve the problem, Euro Heat Pipes proposes a two-phase spreading technology. Main design guidelines and boundary conditions influences are extensively described to take full advantages of the two-phase technology in the spreading issue. An innovative solution is proposed to enhance the thermal performances of the device over a wide range of temperatures with the implementation of a reservoir inside the device that will enhance hydraulic and thermal performances over a wide operating temperatures range. This EHP patented concept is described and benefits are exposed. The proposed two-phase concept is applied on an aeronautic representative application to perform the full thermal characterization. The thermal performance is notably stable on the entire tested temperatures range and validates thermal resistance gain between 58% and 87%. Such an electronic temperature reduction enables a significant reliability increase or the raise of heat power to transport.

Keywords: Flat heat pipe; Spreading; Two-phase spreader; Electronic modules; Space; Aeronautics

Hot Reservoir Stainless-Methanol Variable Conductance Heat Pipes for Constant Evaporator Temperature in Varying Ambient Conditions

Jens Weyant[1], Darren Campo[2], Calin Tarau[3]

Advanced Cooling Technologies, Inc, 1046 New Holland Ave, Lancaster, PA 17601 USA
1 Manager, Defense/Aerospace Products, 717-295-6093, jens.weyant@1-ACT.com
2 Lead Engineer, Custom Products, 717-295-6821, darren.campo@1-ACT.com
3 Lead Engineer, Defense/Aerospace Products, 717-295-6066, calin.tarau@1-ACT.com

Abstract

Precision electronics require tight temperature control to operate at maximum performance. This becomes challenging with large fluctuations in ambient conditions. For this high altitude (20Km) application, ambient temperatures vary from -85°C to -45°C and the allowable temperature range for the cooled device is from 15°C to 30°C. Traditional approaches to cool a device with these requirements include active means of throttling coolant flow, whether it's from a fan or pumped single phase system. These active systems require additional power and weight, which results in decreased reliability. Variable conductance heat pipes (VCHPs) represent an attractive solution since they can be passive devices. VCHPs are similar to conventional heat pipes but have a reservoir and a controlled amount of non-condensable gas (NCG) inside the reservoir. The NCG expands and contracts depending on operating conditions in the evaporator to occupy condenser surface area which will cause a change in thermal resistance from the evaporator to the condenser. This work showed in two distinct steps how a hot reservoir VCHP was used to provide a passive thermal solution. The first step demonstrated theoretically the feasibility of a full scale VCHP capable to reject the required power of 90W maintaining the device temperature within the allowable range while the heat sink temperature swept the earlier mentioned range. For this VCHP, a finned condenser was designed to reject the heat into the ambient. During the second step a stainless steel/methanol lab hot reservoir VCHP prototype was developed to validate the full scale predictions obtained in the first step. Since the lab prototype used a chiller block attached to the condenser tube to replace the fin structure and the ambient air, the full scale boundary conditions were recalculated to accommodate the lab conditions. The new sink temperature range became -20°C to 15°C while the new target device temperature became 26 to 37°C. The paper also discusses some fabrication and charging details. Overall, the lab VCHP prototype testing validated the full scale modeling predictions through two experimental data points.

Keywords: Variable conductance heat pipe, Heat pipe, Thermal control, Passive thermal solution

1. INTRODUCTION

While continuously increasing in complexity, the payloads of high altitude atmospheric vehicles need thermal management systems to reject their waste heat and to maintain a stable temperature as the air (ultimate heat sink) temperature swings between -85°C and -45°C. It is shown in [1] that constant conductance heat pipes have been utilized on balloon payloads to effectively move the waste heat over significant distances and dissipate the heat into the ambient [1]. The drawback of this thermal solution is that the conductance cannot effectively be reduced under cold operating or cold survival environment conditions, so an active heater requiring significant energy is required to keep the payload warm. As discussed in this paper, a variable conductance heat pipe (VCHP) can be used to increase the thermal resistance as the sink temperature drops, keeping the instrument section warm.

Typical spacecraft VCHPs have the non-condensable gas (NCG) reservoir located at the end of the condenser where its temperature is maintained with electrical heaters. This solution is active.

A VCHP theoretical and experimental study is presented in [1] where the thermal control performance of two VCHP configurations, a cold reservoir VCHP (standard) and a hot reservoir VCHP are compared. For the cold reservoir VCHP configuration, the reservoir is thermally and physically connected to the condenser following its temperature. For the hot reservoir VCHP configuration, the reservoir is thermally and physically connected to the evaporator also following its temperature. Although both solutions are passive, the hot reservoir shows a significantly tighter temperature control, as the ultimate heat sink (ambient air) experiences wide temperature swings.

The proposed solution in this work is similar to the hot reservoir VCHP configuration presented in [1, 2] where the reservoir follows the evaporator temperature, eliminating the need for electrical

energy to regulate the heat flow and, consequently, the payload temperature. Again, this thermal management solution is passive.

2. BACKGROUND – VARIABLE CONDUCTANCE HEAT PIPES

A simple VCHP is shown below in Figure 1. It is similar to a conventional heat pipe but has a reservoir and controlled amount of non-condensable gas (NCG) inside the reservoir. When the heat pipe is operating, the NCG is swept toward the condenser end of the heat pipe by the flow of the working fluid vapor. The NCG then blocks the working fluid from reaching a portion of the condenser. The VCHP works by varying the amount of condenser available to the working fluid. As the evaporator temperature increases, the vapor temperature (and pressure) rises, the NCG compresses (Figure 1 top) and more condenser is exposed to the working fluid. This increases the conductivity of the heat pipe and drives the temperature of the evaporator down. Conversely, if the evaporator cools, the vapor pressure drops and the NCG expands (Figure 1 bottom). This reduces the amount of available condenser, decreases the heat pipe conductivity, and maintains the evaporator temperature up [2].

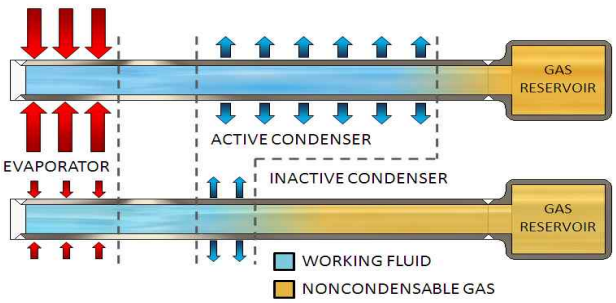


Figure 1. The working of a variable conductance heat pipe (VCHP) is illustrated. At high heat load the temperature dependent saturation pressure of the working fluid is high and compresses the non-condensable gas (NCG) into the reservoir. At lower heat input the working fluid temperature and pressure is lower, and the non-condensable gas expands into the condenser.

For the VCHP shown in Figure 1, the degree of control depends primarily on two factors: the slope of the working fluid vapor pressure curve and the ratio of reservoir and condenser volumes. Working fluids having steeper vapor pressure curves at the particular operating temperature result in tighter temperature control. Small changes in temperature result in large changes in pressure and subsequently large changes in the NCG volume/ condenser length. Similarly, large reservoir volumes improve control because a given pressure change results in a larger change in the position of the gas/vapor interface in the condenser.

Schematics of the two VCHP configurations, hot and cold reservoir, are shown in Figure 2. Configuration 1 (hot reservoir VCHP) has the reservoir attached to the evaporator and the reservoir temperature will mainly follow the evaporator (payload) temperature. Configuration 2 (cold reservoir VCHP) has the reservoir attached to the condenser and the reservoir temperature will follow the condenser (or sink) temperature.

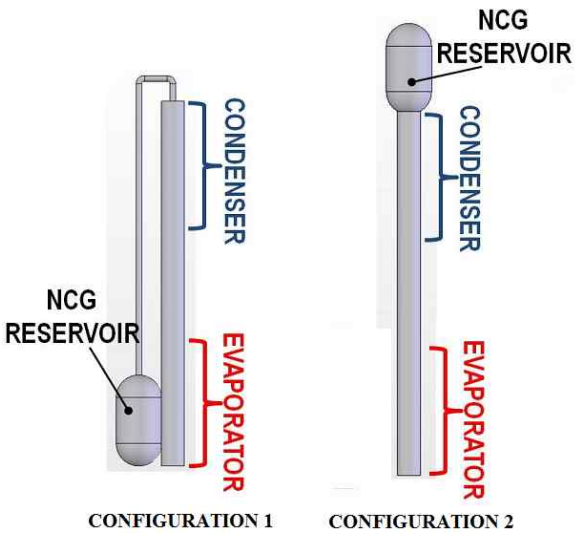


Figure 2. Potential VCHP configurations: Configuration 1 – reservoir attached to the evaporator (hot reservoir); Configuration 2 - reservoir attached to the condenser (cold reservoir).

Configuration 1 was selected as passive thermal control solution for further development that is discussed in this paper.

3. FULL SCALE VCHP MODELING AND DESIGN

Two main parameters are initially set during the process of VCHP modeling and design. First parameter is finding/setting the thermal resistance between the ultimate heat sink and vapor in the condenser such a way that the maximum allowable vapor temperature is reached when the device rejects full power into a heat sink at its highest temperature. This parameter involves the condenser size and its external features. Since, for

the discussed application, heat is removed from the condenser by forced convection, these features are fins. Since the drag induced on the vehicle must be minimized, the intrusiveness of the condenser into the environment must be also minimized. The result will be a short condenser. Then second parameter that needs to be set is the NCG reservoir size. This task will be done based on both the condenser size and the fact that when minimum power is rejected into a heat sink at its lowest temperature, the vapor temperature will still be above the minimum allowable value. If survival is one of the operation modes, then minimizing the survival power by placing the NCG front into the adiabatic region of the VCHP, as far as possible from the condenser, is another consideration in setting the reservoir size.

3.1 Finned Condenser Design

The ultimate heat sink for this application is free-stream air. To aid heat rejection, the condenser end of the VCHP is fitted with aluminum fins as seen in Figure 3.

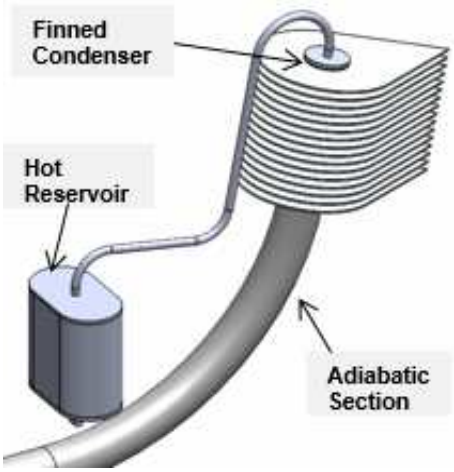


Figure 3. Aerodynamically shaped fins are attached to the condenser

The fin pitch and thickness are optimized to balance fin efficiency and overall weight. This calculation is performed using a parallel resistance network of flow through the heat sink and the bypass air flow. Figure 4. shows the results from this calculation. For this application, the fin stack is made of .81mm (0.032") thick fins with a 3.34mm (0.131") pitch. With this design the resultant ΔT is 59°C which is the temperature difference between the ultimate heat sink, the air, and the outer surface of the condenser tube.

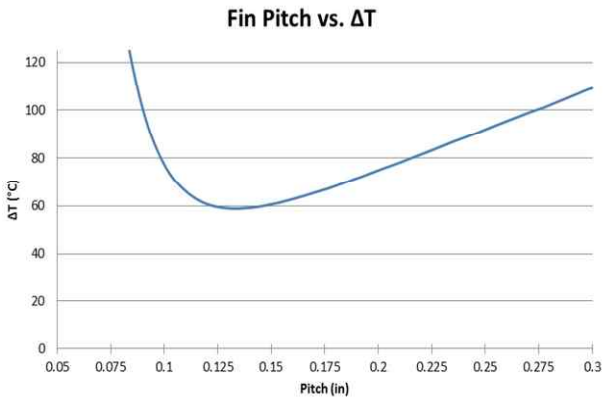


Figure 4. Optimum fin pitch for an annular fin in a free air stream using a .81mm thick fin.

3.2 Thermal Control Modeling Predictions

As mentioned above, once thermal resistance between vapor and ultimate heat sink is set, the reservoir size is the next parameter to be set in defining the thermal control capability of the device.

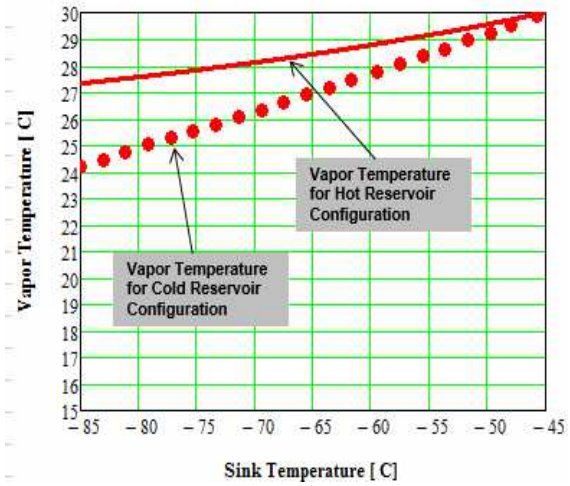


Figure 5. Full scale VCHP evaporator temperature variation as the sink temperature sweeps the entire design range.

A VCHP model based on flat front theory [3] was developed and used to analyze the full scale VCHP solution (hot reservoir) selected for the presented work. The cold reservoir configuration was analyzed as well for reference. The most relevant results are presented above in Figure 5 where VCHP thermal control performance is shown as a function of sink temperature for a 37 cm^3 reservoir volume and a 10cm^3 condenser volume.

As seen in Figure 5 the sink temperature sweeps the entire range between -85 and -45ºC specified by the design requirements. As expected, Configuration 1 (hot reservoir) provides a better (tighter) temperature control than Configuration 2 (cold reservoir). The vapor temperature change while heat sink experiences all the temperatures within the prescribed range is 2.7°C for the hot reservoir configuration and 6°C for the cold reservoir configuration. In conclusion, despite the choice for the hot reservoir configuration, the cold reservoir configuration also shows suitability for the application.

The final design parameters of the full scale hot reservoir VCHP are shown in Table 1.

Table 1. Full scale VCHP dimensions

Envelope Material	304 Stainless Steel
Working Fluid	Methanol
Non-Condensable Gas	Argon
Heat Pipe Diameter	16mm
Heat Pipe Length	0.630m
Evaporator Length	0.445m
Condenser Length	57mm
Condenser Volume	10cm^3
Reservoir Volume	37cm^3
Connecting Tube Diameter	3.2mm
Connecting Tube Length	0.4m
Tube wall thickness	0.5mm
Number of Screen Wraps	4
Total Mass	190g (no fins)

4. PROTOTYPING AND TESTING

To demonstrate the validity of the design, prototype units were designed and fabricated. Stainless steel and methanol were selected as the envelope and working fluid material pairing. The condenser end was vertically oriented with gravity assistance to return the fluid back to the evaporator. The evaporator was horizontal with a single wrap of mesh screen for promoting vaporization around the full circumference of the pipe. The pipe dimensions are listed below in Table 2. For testing, a liquid nitrogen chiller block replaced both the air cooled heat sink and the aluminum fins to obtain better control of testing at various condenser temperatures. Because of these changes on the heat rejection side, the boundary conditions applied to the full scale design were replaced by new values to accommodate the new thermal resistance between the vapor and the ultimate heat sink that in the lab was liquid nitrogen. As lab boundary conditions, the heat sink temperature changed between -25 and 15ºC while the evaporator temperature was allowed to change between 26 and 37ºC.

Table 2. Lab prototype VCHP dimensions

Envelope Material	304 Stainless Steel
Working Fluid	Methanol
Non-Condensable Gas	Argon
Heat Pipe/Reservoir Diameter	17.5mm
Heat Pipe Length	0.627m
Evaporator Length	0.445m
Condenser Length	50.8mm
Reservoir Length	177.8mm
Connecting Tube Diameter	3.2mm
Connecting Tube Length	0.355m

The lab prototype modeling was carried based on the specific boundary conditions that are presented above. The results are presented later in the paper, in Figure 9, where they are compared to the experimental results.

4.1 Fabrication

The heat pipe envelope was constructed from thin-wall 304 stainless steel tubing with the condenser length bent at a 101° angle from the evaporator centerline. A single wrap of mesh screen was attached along the inner diameter of the evaporator and end caps were welded at each end. End caps were welded onto the reservoir section with a fill tube and bellows valve for charging the pipe with methanol and argon. The connecting tube was bent and welded in place to join the reservoir and heat pipe envelope.

After dimensional inspection, the empty assembly underwent a vacuum bake to eliminate contaminates prior to fluid filling. Once a nominal mass of methanol was charging in the pipe, the heat pipe was tested in the processing fixture to vent any remaining non-condensable gas and adjust the fluid charge. The heat pipe was put under load to observe baseline performance at design power.

4.2 Testing Preparations

A fixture was developed for charging the assembly with methanol to make a functional heat pipe, for charging with argon for thermal control,

and for testing the performance in cold and hot ambient conditions. This assembly is shown in Figure 6. The test and charging stand consisted of two aluminum heater blocks: one for the evaporator region to apply fixed power into the pipe, and another for the reservoir that could hold the envelope temperature to match the evaporator temperature to prevent pooling of methanol outside the heat pipe region. A flexible strip heater was wrapped around the connecting tube between the heat pipe envelope and reservoir for the same purpose. Each evaporator block used electrical cartridge heaters for power input.

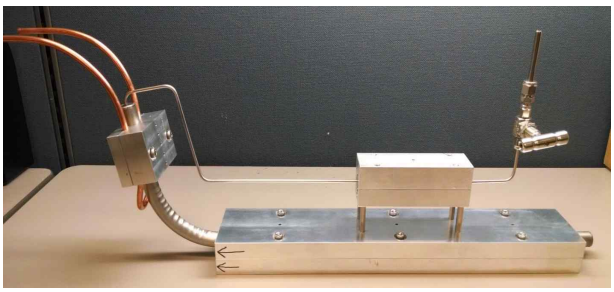


Figure 6. Hot reservoir VCHP in heater block and condenser block assembly

In the real-world application, an array of epoxied aluminum fins on the condenser length would be used for heat rejection to ambient. However due to the need to easily ramp between a range of sink temperatures to demonstrate variable conductance, the fins were replaced with a liquid nitrogen-cooled cold plate. Liquid nitrogen flowed through the copper tubing embedded in an aluminum block at a controlled rate to simulate the cold and hot ambient temperature. The surface temperature of the cold plate was set to match the ambient air temperature plus the temperature drop from the resistance of the fin stack at design power.

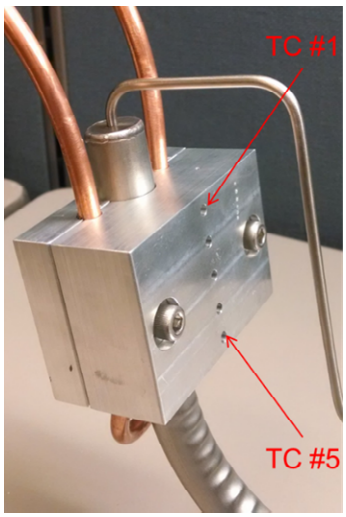


Figure 7. Condenser end thermocouple layout

Type T thermocouples were fixed to the reservoir and evaporator regions. A series of thermocouples was incrementally placed on the condenser for tracking the gas front based on the read-out of adjacent points and identifying a steep temperature gradient, as shown in Figure 7. The valve was left on the fill tube for quickly adjusting the charge of methanol and argon during and between tests for optimal performance.

4.3 VCHP Charging

After the prototype with a methanol-only charge was validated as a functioning heat pipe, ACT made preparations for inputting a discrete amount of argon for controlling the evaporator temperature within the desired range. A large capacity tank with a pressure gauge was placed in between an argon cylinder and the heat pipe fill tube and valve. A vacuum pump evacuated the tank and the plumbing that connected all components. After drawing a vacuum, the tank was filled with argon to the pressure that corresponded to methanol's saturation pressure at the desired operating temperature of 27°C. The heat pipe processing assembly was configured to design power at the minimum ambient condition of -25°C. The system was allowed to start-up before introducing the argon into the heat pipe vapor space.

4.4 VCHP Demonstration Test

After a brief period of operation at the minimum ambient condition, the fill tube valve was opened to allow argon to enter the heat pipe. The plot shown in Figure 8 details the time history of the initial argon charge and cold/hot ambient cycle. At time 2200s when the valve is opened, the condenser region thermocouples sharply decrease to meet the cold block temperature. This is evidence that the argon has swept into the condenser and pushed back the methanol vapor, which has weaker vapor pressure coming from a cold evaporator.

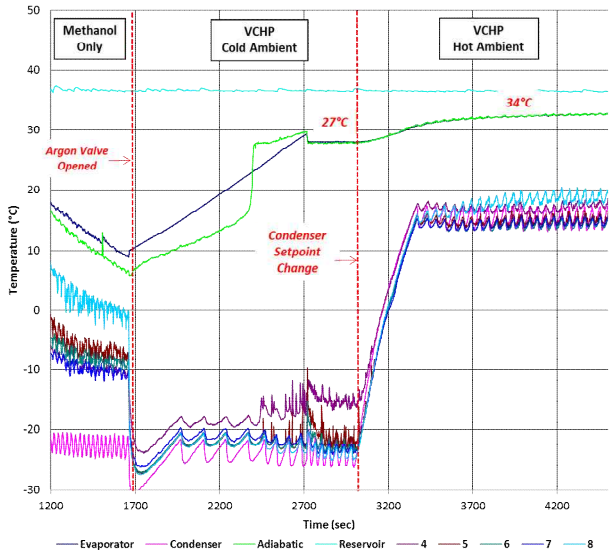


Figure 8. VCHP charging and demonstration from a functioning methanol heat pipe. Vapor temperature is investigated for two condenser set points.

Over the next several minutes, the thermal mass of the evaporator and heater block rose in temperature from -5°C to before reaching an abrupt plateau at 27°C, which was dictated by the pressure of the argon tank. At this stage, the valve leading to the argon tank is closed and the system continues to operate at its new steady state value.

Slightly past 5000s, the condenser setpoint is manually increased to 15°C to simulate the hot ambient condition. Once again, the system undergoes a brief transient to a new steady state value. However, rather than increasing by the same 40°C margin as the condenser, the evaporator increases only 7 degrees before settling at 34°C.

The noticeable difference between the cold and hot ambient tests shown in Figure 8 is the change in temperature difference across the evaporator and condenser. During the cold ambient test, the delta is 52°C compared to 19°C in the hot ambient test with no change in power input. This is another demonstration of the variable conductance characteristic of the heat pipe. When the condenser set point is increased, the hot methanol vapor coming from the evaporator is able to sweep the argon back into the reservoir to open up more condenser surface area to dump heat, thus lowering its resistance relative to the cold ambient demonstration.

4.5 Testing Results Comparison with the Modeling Predictions

A comparison between the experimental data and the corresponding modeling predictions performed for the testing prototype geometry and boundary conditions is shown below in Figure 9. As seen only two experimental data points were obtained that correspond to steady states of the testing VCHP for two sink set points, -24°C and 15°C respectively. For the first sink temperature (-24°C) the vapor temperature was 27°C while for the second sink temperature (15°C) the vapor temperature was 34°C. Theoretical vapor temperature predictions that correspond to the same sink temperatures were 30°C for the cold sink data point and 33.6°C for the hot sink data point as shown in Figure 9.

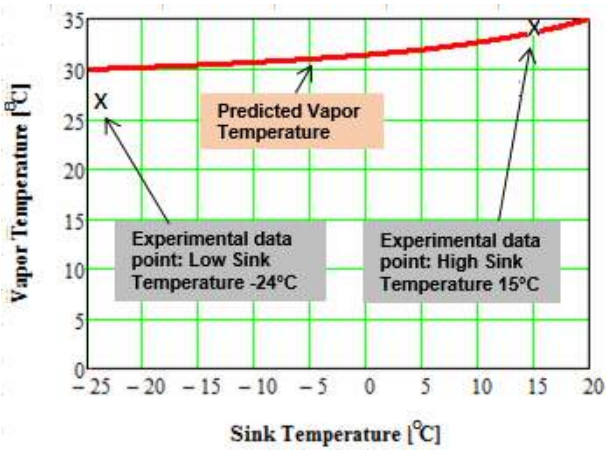


Figure 9. Comparison between the modeling predictions performed for the testing prototype geometry and boundary conditions and actual testing results

5. CONCLUSIONS

A hot reservoir VCHP was selected for an aerospace application where the heat sink is high altitude ambient air. A full scale design was performed that demonstrated full feasibility of the chosen thermal management solution. To validate the model used to design the full scale device, a lab hot reservoir VCHP prototype was designed, fabricated, and tested. During a single continuous test, ACT demonstrated a working methanol heat pipe, initial charging of argon to achieve the VCHP thermal control function, and a narrow window of evaporator temperatures after cycling through a much wider range of heat sink temperatures. The lab prototype testing results validated the VCHP model used to design the full scale hot reservoir VCHP.

ACKNOWLEDGEMENT

The authors address special thanks to ACT technicians Chris Stover, Larry Waltman, and Jordan Tingley for their effort in development,

fabrication, and testing of the Hot Reservoir VCHP prototype.

REFERENCES

[1] Tarau, C., Anderson, W. G.,"Variable Conductance Thermal Management System for Balloon Payload, 20th AIAA Lighter-Than-Air Systems Technology Conference, Daytona Beach, FL, March 2013

[2] Anderson, W.G. "Variable Conductance Heat Pipes for Variable Thermal Links," 16th International Heat Pipe Conference, Lyon, France, May 20-24, 2012

[3] Marcus. B.D., "Theory and Design of Variable Conductance Heat Pipes," NASA Report NASA- CR-2018, April, 1972. Available from the NASA Technical Reports Server, http://ntrs.nasa.gov/.

Gas-controlled Heat Pipes for Thermal Control System of Small Spacecraft

Konstantin A. Goncharov[1], Yuriy V. Panin[1], Kirill N. Korzhov[1], Adik R. Gutkin[2]

[1]*Heat Pipe Center of Lavochkin Association, Khimky 141400, Moscow region, Russia*
[2]*Research Institute of Electromechanics, Istra, Moscow region, Russia*

Abstract

This paper presents development result of variable conductive gas-controlled heat pipes (VCHP) made of aluminum extrusion with axial grooves, designed for small spacecraft.

We have shown two types of ammonia VCHP that differ in design of cold reservoir. Neon is used as control gas. Design features of both VCHP and methods of thermal parameters determination are presented here.

We used two different methods of thermal tests to verify VCHP design parameters. We carried out atmospheric tests, when heat power was rejected by conductive method and vacuum tests, when radiation panel was used for heat rejection. Also, we have studied influence of transferred heat power, condenser temperature and condenser conditions on location of vapor/gas front. Experimental studying of possibility of active VCHP control by means of the heater mounted to the reservoir with NCG was performed.

Criteria for application of VCHP with simple and more complicated design of the cold reservoir are suggested in this paper. Recommendations for VCHP application in thermal control system of spacecraft are given.

Key words: Axial groove heat pipe (AGHP); variable conductive heat pipe (VCHP); non-condensable gas (NCG); ammonia; neon.

1. INTRODUCTION

AGHP have been successfully used in thermal control systems (TCS) for more than forty years. Generally, AGHP are used as heat pipes (HP) of constant conductance and are applied as parts of honeycomb panels. Diode and variable conductive HP are required more frequently. History of controlled and self-controlled HP development started practically from the first HP experiments [1,2,3]. It is well known that one of the first methods, providing passive control of HP conductance was injection of non-condensable gas (NCG) into HP. The NCG blocks a part of the condenser and prevents vapor condensation in the HP zone, occupied with NCG. Such HP are named as gas-controlled variable conductive heat pipes (VCHP) [4].

The key feature of VCHP that gives it possibility to compete with the more improved designs of the controlled HP like the LHP is its simplicity and reliability, because passive VCHP are self-controlled and does not require any special temperature sensors, actuators and additional power sources. All this, makes application of VCHP desirable, especially in TCS of small SC, where evaporation and condensation zones are located at a short distance from each other, and total power values of TCS do not exceed 100 W.

The small SC consists of a service platform and payload. Every module content its autonomous TCS. Separately from the platform, there is a frame with adjusting propulsion unit (APU) and multi-area scanning device (MSD).

1.1 VCHP of APU

The APU is not connected to the platform, so excess heat power (of about 70 W) is transferred by HP to its own radiator. In order to reduce the power consumption, we applied VCHP. The minimum power value, at which the HP evaporator temperature must not fall lower than 5 °C, shall be of 7 W.

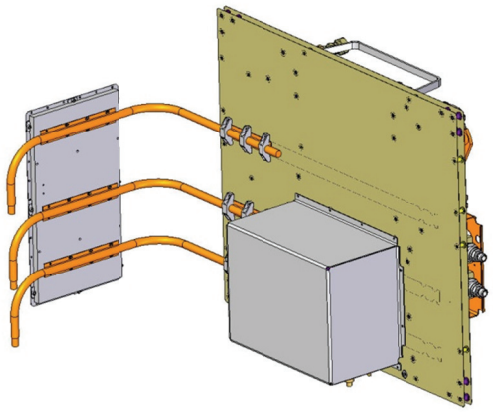


Fig. 1. General view of VCHP for APU.

*Corresponding author: heatpipe@laspace.ru,
Phone/Fax: +7- 495-573-63-74

1.2 VCHP of MSD

The heat power from MSD body transferred through VCHP to the radiator. Like in the previous case, VCHP are required to ensure the object temperature of not lower than 10 °C, when the minimum heat release does not exceed 10 W.

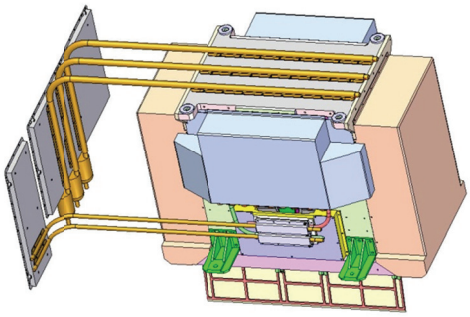


Fig. 2. General view of VCHP for MSD.

VCHP may realized on basis of the available AGHP design which heat-transferred capacity is already known. The distinctive feature of many VCHP, regardless of the capillary structure type, is that they have non-condensable gas (NCG) reservoir. Temperature accuracy limit of the passive controlled VCHP depends on correlation of reservoir/condenser volumes. However, existence of the NCG reservoir as an additional design component, results in difficulties of its placing in the available layout. Therefore, we applied VCHP without the NCG reservoir where it was possible.

The reservoir design based on the accuracy of control and design limitation for small SC.

2. VCHP DEVELOPMENT

2.1 Modelling

At the first stage, we determined parameters of AGHP of constant conductivity when the heat power release was at its maximum. For calculation of AGHP parameters, we used our software «GROOVE 1.0» based on one-dimensional model of hydrodynamics and heat-and-mass transfer without accounting gravity force.

Solution algorithm comes to finding of saturation temperature t_s and maximum heat flow Q_{max}, suitable to boundary conditions. The calculation determines maximum transferred heat power of HP - Q_{max}, necessary for the set operating temperature, as well as thermal resistance in the zones of heat power supply R_{evap} and heat rejection R_{cond} and other parameters of HP.

At the second stage, was determine the volume of NCG reservoir and NCG mass. The mathematical model of VCHP based by the flat front model (vapor-NCG) without accounting diffusion and heat-conductivity of pipe wall.

We supposed that NCG complies with the ideal gas laws, and the state equation is as follows [1]:

$$P_{ncg}V = \left({}^{m_{ncg}}/_{M_{ncg}}\right) RT_{sc} \quad (1)$$

From the equation (1) we can obtain the charging mass of inert gas:

$$m_{NCG} = \frac{P_{NCG}VM_{NCG}}{RT_{sc}} \quad (2)$$

In a balance state, NCG pressure P_{NCG} will be equal to the pressure of vapor in the active part of the condenser P_{va}. The pressure of saturated vapor is a temperature function T_{va}. Accepting the "flat front" model of vapor/gas, and neglecting vapor diffusion in NCG, let's assume that NCG volume is composed of reservoir volume V_r and the part of the condenser filled with NCG:

$$V = V_r + \pi\left({}^{d}/_{2}\right)^2 (L_c - L_{ca}) \quad (3)$$

By putting the equation (3) into the equation (2) we have:

$$m_{NCG} = \frac{P_{va}M_{NCG}\left[V_r + \pi\left({}^{d}/_{2}\right)^2 (L_c - L_{ca})\right]}{RT_{sc}} \quad (4)$$

Calculations permit to determine the VCHP reservoir volumes, necessary for controlling with the set accuracy. The parameters of VCHP are shown in the table 1.

Table 1. Basic design parameters of VCHP.

Name	Q_{min}, W	Q_{max}, W	T_{min}, °C	T_{max}, °C	V_{res}, cm^3
VCHP APU	7	35	5	30	9
VCHP MSD	10	40	10	25	62

2.2 VCHP design

VCHP are developed and based on the design of constant conductive AGHP. The VCHP bodies are made of 14 mm high aluminum extrusion and have similar geometry of the grooves. Fig. 3 presents VCHP cross section.

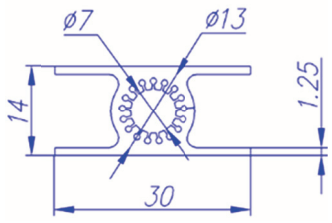


Fig. 3. VCHP cross section

2.2.1 VCHP of APU design

Reservoir for NCG APU VCHP designed as an extension of the HP body with partially cutting grooves. This is a classical type of a simple VCHP. Correlation of reservoir/condenser volumes is only 1,2 to 1, but has the advantages over more complicated structures with separate reservoirs.

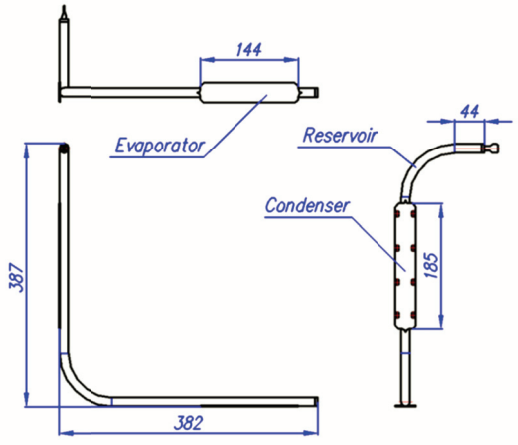


Fig. 4. General view APU VCHP.

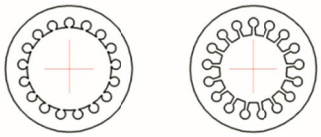


Fig.5.Cross section of reservoirs APU VCHP.

2.2.2 VCHP of MSD design

MSD VCHP has a balloon-shaped reservoir made of stainless steel. Correlation of reservoir/ condenser volumes is 6 to 1, and it is attached to the VCHP condenser by means of bimetallic connector.

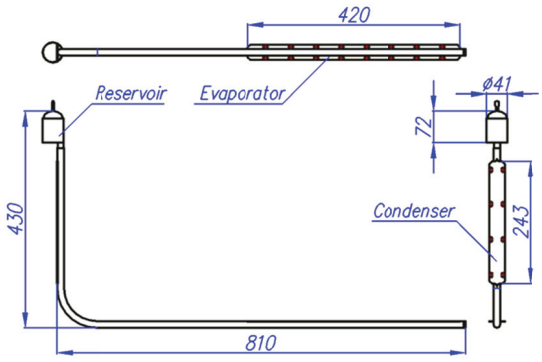


Fig. 6. General view MSD VCHP.

The inner part of the reservoir has a capillary structure made of stainless steel mesh. It connect liquid phase of the working fluid in reservoir to axial grooves [5]. The reservoir body operates under pressure, so in order to provide sufficient strength for the suitable mass. Therefore, we used stainless steel. Low conductivity of SS and bimetallic connector decreases heat flows from condenser to reservoir that has a positive impact on the HP control accuracy [6].

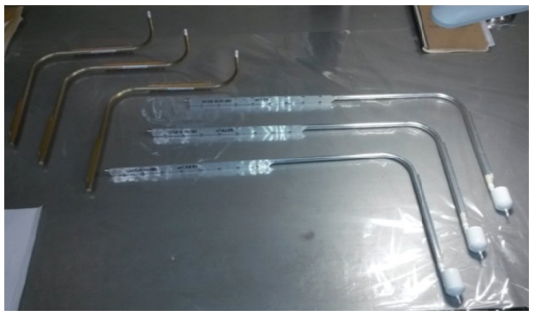


Fig. 7. VCHP view.

2.2.3 Working fluid and NCG

The VCHP shall be charged with the precise amount of working fluid and NCG to obtain the required heat power transfer capacity and to block the condensation zone at the set temperature and minimum heat release.

Ammonia was chosen as the working fluid, as in this temperature range, it has the best parameters in comparison with the other working fluids and suits both to aluminum body and metallic reservoir with its wick.

The operating temperature range of the working fluid must be higher than critical temperature of NCG and must not be in contact with HP working fluid and its surface. Also, it is advisable to have its molar mass close to ammonia in order to decrease diffusion of concentration. Taking into account all these reasons, we have chosen **neon** as NCG.

3. VCHP THERMAL TESTS

During experiments, we were studying influence of the following criteria: heat power change, values of condenser temperature, various conditions of heat rejection (conductive and radiant).

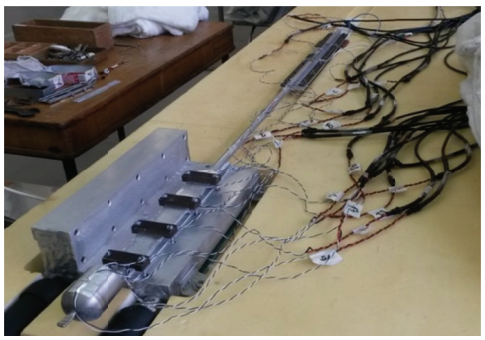


Fig. 8. VCHP atmospheric test.

Experimental test in atmosphere for VCHP provided with the special thermal insulation, like a foam with thermal resistance more than 10 K/W. Condenser cooling performed by liquid heat exchanger (fig. 8). The reservoir covered with thermal insulation separately. For measurement of temperatures were used platinum sensors with resistance of 1000 Ohm.

Tests result for APU VCHP showed that at condenser temperature of minus 40°C, the condenser was completely filled with neon. Ammonia vapor reaches the point at the end of transport zone.

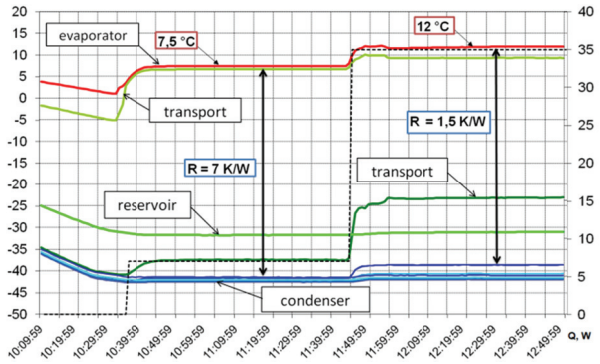


Fig. 9. APU VCHP atmospheric tests result (T_{min}).

For heat power 7W thermal resistance of VCHP is 7 K/W and this allows keeping temperature in evaporation zone at the level of 7,5 °C (see fig. 9 and 10). When heat power supplied to evaporator is of 35 W and condenser temperature is of minus 40 °C, the condenser is filled with NCG, temperature in evaporation zone is at the level of 12 °C. After heat power increasing up to the maximum values, thermal resistance substantially decreases and at the power of 200W, it comes down to the value of 0,3 K/W and evaporator temperature comes up to 32 °C caused by the filling of the most part of the condenser with NCG.

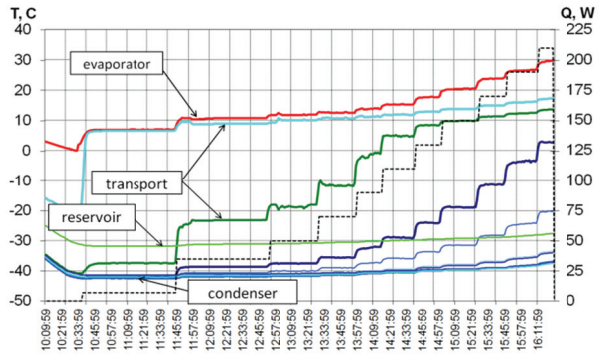


Fig. 10. APU VCHP atmospheric tests result (T_{max}).

Tests result for MSD VCHP showed that at heat power supply to evaporator of 10W and condenser temperature of minus 40°C, the condenser was completely filled with gas. Vapor reaches the point at the end of transport zone. In this case, temperature in evaporation zone at the level of 11°C.

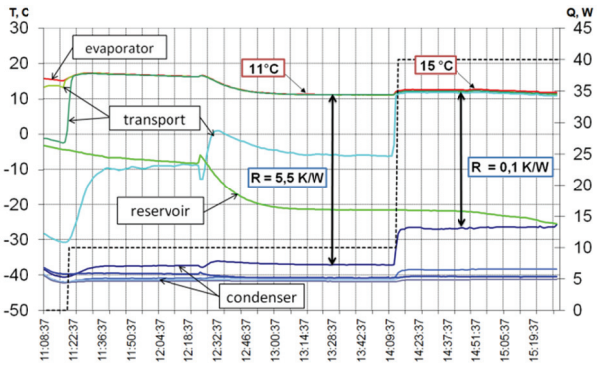


Fig. 11 MSD VCHP atmospheric tests result (T_{min}).

When heat power is of 40 W and condenser temperature is of minus 40 °C, temperature in evaporation zone at the level of 12 °C. After heat power increasing up to the maximum values, thermal resistance substantially decreases and at the power of 200W, it comes down to the value of 0,1 K/W, and evaporator temperature comes up to 15 °C. (see fig. 11, 12, 13).

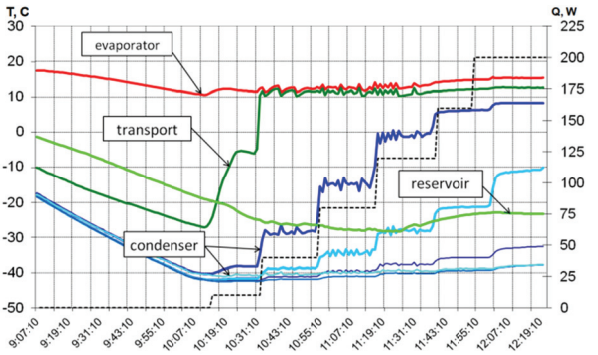


Fig. 12. MSD VCHP atmospheric tests result (T_{max}).

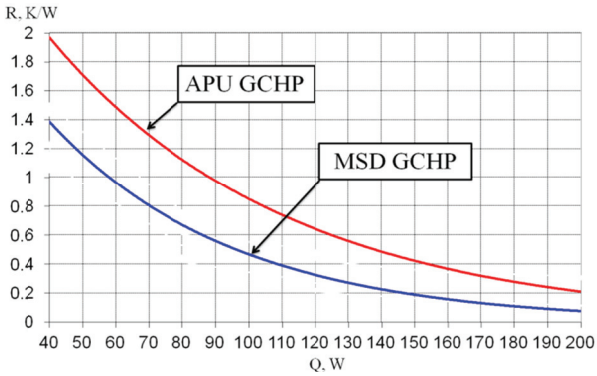


Fig. 13. Dependence of VCHP thermal resistance on heat transfer capability in atmosphere with liquid heat exchanger.

After atmospheric tests we carried out **thermal vacuum tests** with radiant heat rejection. VCHP condenser cooling was performed by the radiator (fig. 14). Multilayer insulation was used for coating all surfaces of VCHP except radiation surface.

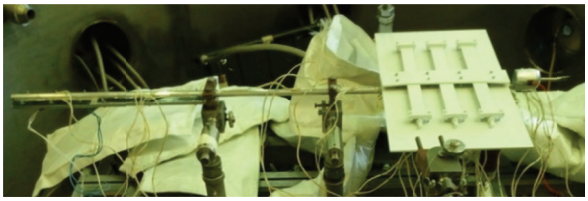


Fig. 14. Mounting of VCHP to the vacuum test bench.

TV test results showed that minimal boundary of control at heat power of 7 W was 8 ºC, that correspond to results at atmospheric tests and calculation prediction. And upper boundary of control at maximum power of 40 W was 40 ºC. Thermal resistance decreases from value of 8 K/W and it comes down to the value of 0,5 K/W, and evaporator temperature comes up to 15 °C. At this condition observed low efficiency of radiator heat dissipation (fig.15).

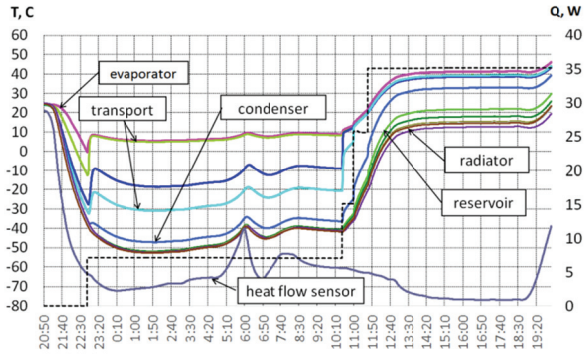


Fig. 15. APU VCHP TV tests result.

Similarly, results of MSD VCHP TV testing were received (fig.16). Test results showed that minimal boundary of control at heat power of 10 W and radiator temperature of minus 40 °C was 7 ºC, that lower than value received at atmospheric tests. This is explained by the fact that during the vacuum test the reservoir temperature was twice lower than atmospheric tests.

Upper boundary of control at maximum power of 40 W temperature comes up to limit and consist 33ºC of evaporator temperature. The thermal resistance comes to the value of 0,45 K/W at maximum opened radiator, that explained low efficiency of radiator heat dissipation.

Additionally, during the experiment we checked the possibility of active control by means of the 5W heater, mounted to the reservoir of VCHP.

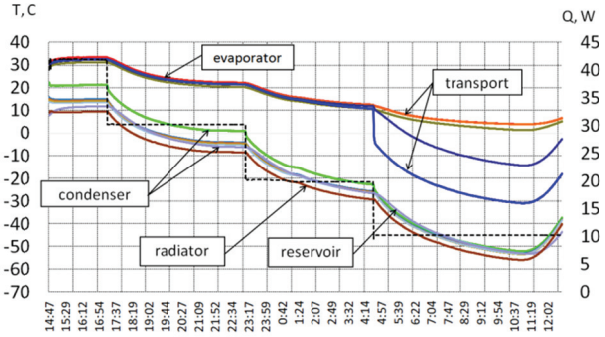


Fig. 16. MSD VCHP TV tests result.

After switching on the heater, the condenser started blocking quickly that allowed to increase HP resistance at the evaporator temperature of 20 °C and heat power of 30W (fig 17).

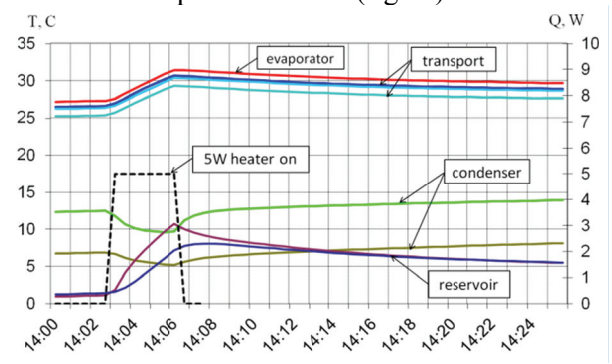


Fig. 17. Vacuum tests for VCHP of MSD.

Next step of TV tests were carried out by simulating dynamic operation conditions. VCHP evaporator was mounted to the heat capacity of 28 kg (payload simulator).

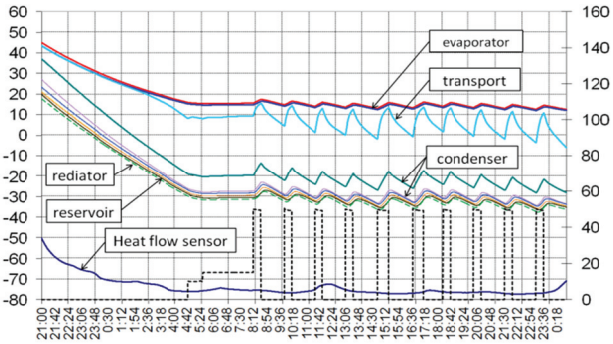


Fig.18. VCHP APU tests in condition of simulating of operation in SC.

During 23 minutes heat power of 50 W was supplied in cycles to the heat capacity. Time-out between heat cycles was of 72 min (one orbital cycle). After 10 cycles of heat power supplying to the heat capacity, VCHP reached inter stationary mode payload temperature at the level of 6 ºC. Results of APU VCHP dynamic TV test shown in fig.18.

Results of MSD VCHP dynamic TV test shown in fig.19.

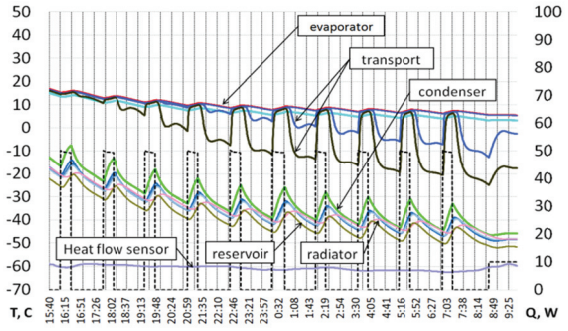


Fig.19. VCHP MSD tests in condition of simulating of operation in SC.

4. TEST REVIEW

We presented two methods of VCHP thermal tests. The two methods differ in a way of condenser cooling. We determined that atmosphere test with heat rejection by means of liquid heat exchanger gives quite better result on the upper boundary of control in comparison with radiation cooling in vacuum condition by means of nitrogen screen.

The possibility of VCHP active control by means of the heater mounted to the reservoir with NCG was experimentally proved. After switching on the heater of 5W, mounted to the reservoir body, temperature in evaporation zone instantly increased and decreased in condensation zone. This fact shows great dependence of gas temperature on the occupied volume. It is important to take into account the reservoir temperature parameter for the system design.

TV dynamic test with thermal capacity showed that the requirements set for the payload can be greatly exceeded. When carrying out the tests in accordance with operating cyclogram and applied heat capacity of 40W, the payload correspond required temperature range.

Test results confirm the possibility of application of aluminum heat pipe body as a reservoir, but due to the fact that accuracy depends on reservoir volume and its actual temperature. It would be more advisable to use reservoir made from stainless steel.

5. CONCLUSIONS

Were developed and tested two most widespread types of VCHP: with reservoir and extended body.

Calculation model admits a completely flat front between vapor and NCG. Calculation of VCHP were carry put using the simplified procedure.

Tests of two types of VCHP were carried out in the atmosphere and in vacuum steady state and dynamics modes. Tests have shown:

- The simplify method calculation is allowed, but it is necessary in the future to take into account the diffusion, thermal conductivity, gravity and make the two-dimensional calculation.
- The task of cooling systems of small autonomous spacecraft completely satisfied.

Application of VCHP with “cold” reservoir is reasonable for the systems which have rather wide temperature range of operation. As an example, for autonomous cooling of Nickel Hydrogen Storage Battery, and different types of payload with temperature range ±10ºC from the nominal. Application of these VCHP is advisable at low heat transfer power from 5 to 50 W.

NOMENCLATURE

t_s	: Saturation temperature (K)
R_{evap}	: Evaporator thermal resistance (K/W)
R_{cond}	: Condenser thermal resistance (K/W)
P_{ncg}	: NCG pressure (Pa)
V	: NCG volume (m^3)
m_{ncg}	: NCG charging mass (kg)
M_{ncg}	: NCG molar mass (mol)
R	: Universal gas constant (J/mol·K)
T_{sc}	: Heat sink temperature (K)
L_c	: Length of the condenser (м)
T_{min}	: Minimum evaporator temperature (K)
T_{max}	: Maximum evaporator temperature (K)
Q_{min}	: Heat power at T_{min} (W)
Q_{max}	: Heat power at T_{max}(W)

REFERENCES

[1] T.A. Wyatt Controllable heat pipe experiment for the SE-4 satellite, *JHU Tech. Memo*. APL-SDO-1134, John Hopkins University, Appl. Phys. Lab., Ad 695433, 1965.

[2] W. Bienert, Heat pipes for temperature control. *Fourth Intersociety Energy Conversion Conference*, Washington DC, Dynatherm Corp., Cockeysville September 1969, pp. 1033-1041.

[3] J. Kirkpatrick, B. Marcus, B. Marcus "Variable Conductance Heat Pipe Flight Experiment", Paper № 71-4144, *AIAA Thermophysics Conf.* Tullahoma, Tenn. April, 1971.

[4] P. Dunn, D.A. Reay "Heat Pipes", Second Edition, Pergamon Press, 1977.

[5] S.W. Chi, “Heat Pipe Theory and Practice,”. McGraw-Hill, New York, 1976.

[6] P.A. Mirzoyan , O.M. Schalya, "Effect of pipe wall conduction and vapor diffusion on longitudinal profile of Gas-Controlled HP," - *Proceedings of the Moscow Energy Institute №198,* p.99-104, 1974 .

[7] Alet I. "VCHP Radiator for the “SIGMA” Space Telescope" Prepr. 6th IHPC, may 25-29, 1987, Grenoble, France. sess. 2nd, pp. 329-332.

Design and Numerical Simulation of a Flexible Heat Pipe for Human Cooling Application

Luis M. Tapia[1] and Gerardo Carbajal[2*]

[1]*Advance Manufacturing Engineer, Stryker Global Supply, Arroyo, PR 00714, USA*
[2]*Mechanical Engineering Department, School of Engineering, University of Turabo, Gurabo 00778, U.S.A.*

Abstract

A two dimensional design, analysis and numerical simulation were performed to a flexible cooling system heat pipe for human application. This study presents an innovative flexible design heat pipe to be incorporated on a piece of cloth with the intent to maintain comfortable human body temperature. One of the main advantages of this design is the vast potential application for the device, especially for people exposed to long periods of high temperatures or extremely warm weather conditions. The propose design is compact and easy to manufacture. A detailed theoretical model was developed and solved numerically. The numerical simulation replicated the overall thermal operation, interaction and boundary conditions of the cooling system with the ambient. The numerical results show that the proposed cooling system is able to achieve its purpose: remove heat from the chest (warmer area) and release it to the shoulder (colder area). Preliminary results using metabolism model suggest that approximately 50W of energy is released from the trunk of the body. The calories burned during the metabolism process depend on the human activity. To simplify the analysis normal to moderate human activity was considered. The numerical results suggest a promising performance of the proposed cooling system design. The temperature difference between the evaporator (chest body surface) and the condenser upper surface were in the range from 2.1°C to 3.6°C. An additional transient analysis revealed that the heat pipe was able to reach steady state conditions after 15 minutes of full operation.

Keywords: At least four keywords; heat pipe, metabolism, cooling system, condenser.

1. INTRODUCTION

One of the most exciting developments in heat transfer over the last 20 years is the heat pipe. The heat pipe is a device with very high thermal conductance, is really an improved version of the earlier thermosiphon [1]. Nowadays heat pipes are used in several applications, where one has limited space and the necessity of a high heat flux. It is also used in heat transfer systems, cooling of computers, cell phones and cooling of solar collectors. By means of a heat pipe it is possible to connect the processor cooling unit to a bigger cooling. It is also used at the Alaska pipe line, where you use the low temperature of the ground to cool the transported fluid down. The basic principle of heat pipes is the internal evaporation and condensation process [2]. During the history of heat pipes different human body application has been develop. NASA completed an investigation to develop a technique to control the body temperature of an astronaut wearing an extravehicular space suit [3]. In addition to this application the US Army did research for the hand warming for extremely cold conditions. The method for maintaining human's temperatures during hot wheatear condition proposed involves applying heat pipe technology directly to a smart coat. According to the literature review, it is not a common application for heat pipes to heat transfer for humans. In the next section it is presented the proposed heat pipe design for human cooling applications.

*Corresponding author: gcarbajal1@suagm.edu,
Phone: +1-787-743-7979, Fax: +1-787-744-5476

2. THEORETICAL MODEL

2.1 Heat Generation by Human Body

The human body is subject to the same laws of physics as other objects, gaining and losing heat by conduction, convection and radiation. Conduction between bodies and/or substances in contact; convection involving the transfer of heat from a warm body to a body of air above it or inside the human body and here the blood, gases and other fluids is the medium, radiant heat transfer is a major mechanism of thermal exchange between human body and the surface surrounding environment. These three effects in most situations operate simultaneously. In human body, metabolic processes generate its own heat as well, similar to an internal combustion engine. The metabolism regulates the human body at almost constant temperature. In other words, a human body can be modeled an isothermal system (constant temperature)In order to maintain a constant

temperature, it absorbs and emits energy to be in equilibrium, stimulation is applied to the body surface, this make the activity of metabolism induced to body surface[4]. Our living bodies generate heat because we are homoeothermic (warm-blooded) creatures. The rate at which heat is produced depends primarily on our metabolic rate. Metabolic rate is our ability to generate heat is mostly a function of our level of muscular activity. Some of the energy generated by muscular activity will be directly translated into work (force per distance) and the excess energy will be dissipated as heat. Met is a units, each human body in a classroom is producing about 1 met (1 unit of metabolic rate) of waste heat [5]. Heat exchange with the environment is primarily via the skin, the met unit is defined in terms of both heat energy and surface area. For the unit MET is equal to 58.2W/m^2.

2.2 The Human Body Temperature Distribution

The skin is the largest organ in the human body. It protects the body from the sun's rays. It also keeps body temperature normal (37 °C). Skin temperature depends on air temperature and time spent in that environment. Such weather factors as wind chill and humidity cause changes in skin temperature. The normal temperature of skin is about 33 °C or 91 °F. The flow of energy to and from the skin determines our sense of hot and cold [8]. Heat flows from higher to lower temperature, so the human skin will not drop below that of surrounding air, regardless of wind. If a person was to be in a warm room and her skin temperature was cooler than the air, her skin temperature would rise. The opposite would happen in a cold room and warm skin temperature. The person's temperature would decrease. Humans fight air temperature by becoming warm or cold. When warm, they sweat. When cold, they get chills. On a trip during a windy and snowy day, a man recorded his skin and body temperature while climbing a mountain. The skin temperature of his toe was about 15 °C. At the same time, the temperature of his chest was 32 °C. Figure 1 shows different skin temperatures [6].

2.3 The Flexible Heat Pipe

The system proposed here intents to use heat pipe technology to transfer heat from the upper body to the surrounding environment and keep the body in comfortable conditions. Patrolling motorbike law enforcement personnel, military personnel, and people that are continuously exposed to direct sun radiation in an environment with high temperature and relative humidity are our main goal. The heat pipe will extract heat from the upper body using the evaporating of the heat pipe, transferring this heat to the condensing side to liberate to the environment via convection heat transfer.

The proposed geometry depicted in Fig. 2 was adapted to fit outside area of the human body; the dimensions shown corresponded to a normal person. These dimensions were taken into account to be able to get the two dimensional representation of the heat pipe. The 2D model was drawn in SolidWorks, and it represents the dimensions of the heat pipe. Figures 2 and 3 illustrate the different views of the geometry used in the simulation.

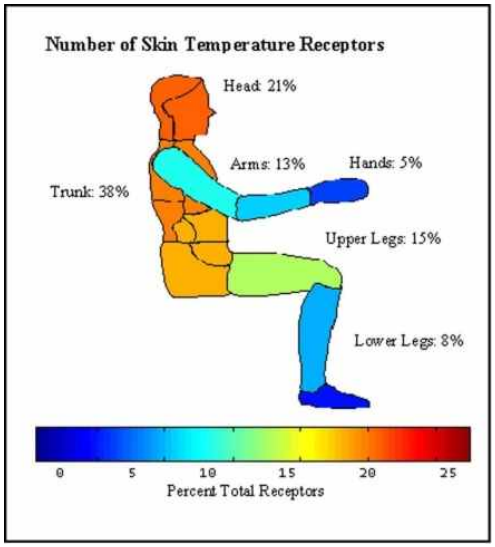


Fig. 1. The skin temperature receptors [6].

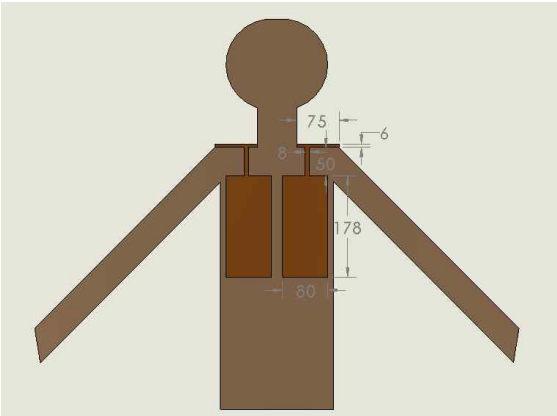
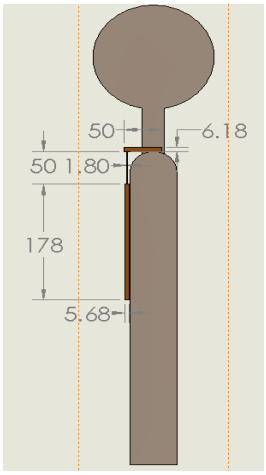
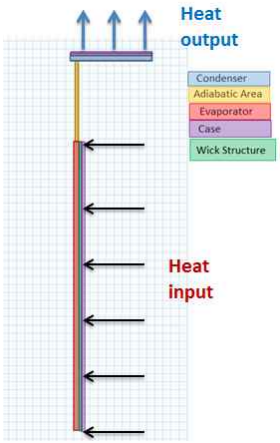


Fig. 2. Front View Human Body with HTP (units in mm).



(a)



(b)

Fig. 3. (a) Side View Human Body with HTP (units in mm), (b) Heat pipe configuration

2.4 The Governing Equations

The governing equations which control the fluid flow, heat transfer and energy interaction in the heat pipes are the differential equations of the continuity, momentum and energy equation, respectively. In the saturated wick structure an extension to the momentum equation is used to include the Darcy's term. Additionally, the energy equation was modified to include the effect of the porosity. Due to the complexity of the problem computational fluid dynamic software (CFD) was used to evaluate the fluid flow and thermal interaction of the system. Comsol Multyphysics was the CFD software used in the present analysis to evaluate the heat pipe performance. To simulate the heat pipe a simplified two dimensional geometry was designed. The major constrains to selected the final geometry was to include the warmer spot areas of the human body and determine the appropriate dimensions of the device; for more information about the geometry refer to the proposed thermal device.

In order to simplify the analysis it was assumed a two dimensional model and steady state conditions. The following equations were used to calculate the velocity field and temperature distribution of the model.

The continuity, momentum and energy equation for the vapor core [7]:

$$\nabla \cdot \mathrm{V} = 0 \tag{1}$$

$$\nabla.(\rho \mathrm{VV}) = \rho g - \nabla p + \mu \nabla^2 \mathrm{V} \tag{2}$$

$$\nabla.(c\mathrm{VT}) = \nabla.(k\nabla \mathrm{T}) \tag{3}$$

The continuity, momentum and energy equation for the wick structure [7]:

$$\nabla \cdot \mathrm{V} = 0 \tag{4}$$

$$\varphi^{-1}\nabla \cdot (\rho \mathrm{VV}) = \rho g - \nabla p + \frac{\mu}{\varphi}\nabla^2 \mathrm{V} - \frac{\mu}{\mathrm{K}}\mathrm{V} - \frac{\rho \mathrm{C_E}}{\mathrm{K}^{1/2}}|\mathrm{V}|\mathrm{V} \tag{5}$$

$$\nabla.(c\mathrm{T}\bar{\mathrm{V}}) = \nabla.(k_{\mathrm{eff}}\nabla \mathrm{T}) \tag{6}$$

The energy equation for the case material [7]:

$$\nabla^2 \cdot \mathrm{T} = 0 \tag{7}$$

For the condenser side two different approaches were developed. The human body was exposed to different activities for the analysis; it was assumed that for light activities the dissipation of heat on the condenser side will be dominated by natural convection. For other activities, it was assumed force convection. The speed of the air flow was assumed to be the relative velocity of the person to the ambient air. The next equations were used to evaluate the natural convective coefficient conditions at the condenser side [8].

$$\overline{Nu}_L = \frac{\bar{h}L}{k} = \frac{4}{3}\left(\frac{Gr_L}{4}\right)^{1/4} g(\mathrm{Pr}) \tag{8}$$

Where:

$$g(\mathrm{Pr}) = \frac{0.75\,\mathrm{Pr}^{1/2}}{\left(0.609 + 1.221\,\mathrm{Pr}^{1/2} + 1.238\,\mathrm{Pr}\right)^{1/4}} \tag{9}$$

$$Gr_L = \frac{g\beta(T_s - T_\infty)L^3}{\upsilon^2} \tag{10}$$

The boundary conditions on the case area which is in contact with the body, a contact heat flux were applied. The input value for the heat flux was obtain depending on the human activity assume for the analysis the values can be found on the

appendix. On the outer case which is exposed to the ambient will also depend on type of activity of the human, for sedentary and low motion low heat fluxes were used and for high motion actives differences heat fluxes were used depending on the activity. For low motion activities was assumed a natural or free convection and high motion activities force convection and will depend on the velocity that the person is moving; therefore force convection was calculated and put as an input for the analysis. For the heat transfer along the heat pipe the porous media feature was used to be able to couple all the heat inputs.

After creating the model the next step was to found if the model is independent from the mesh size. For this study two differences variables were analyze to found the point where they do not fluctuate. The variables used were the temperature along the heat pipe and the velocity of the fluid. Figure 4 is a representation of how these two variables behaves as function of the elements quantities. The mesh used for the model was the setting as extremely fine which results on 26405 elements. In the fluid flow the laminar flow was selected and confirmed to be laminar after execution. The Reynolds number value for the highest velocity was computed, its value was 2.36 (see fig. 5). For the wick structure fluid flow Darcy's law is the one which dominate this area. The fluid used was water, the wick structure material Nickel and the case material Stainless Steel, see Table 1.

Table 1. Materials and working fluid.

Container material	Stainless steel
Wick material	Nickel
Working fluid	Water

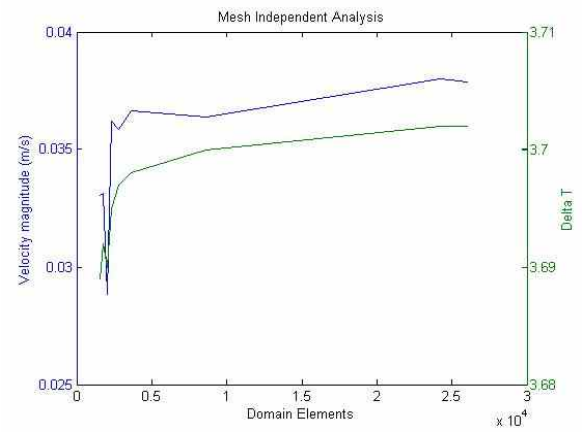


Fig. 4. Mesh independence analysis for the velocity in the vapor core and temperature.

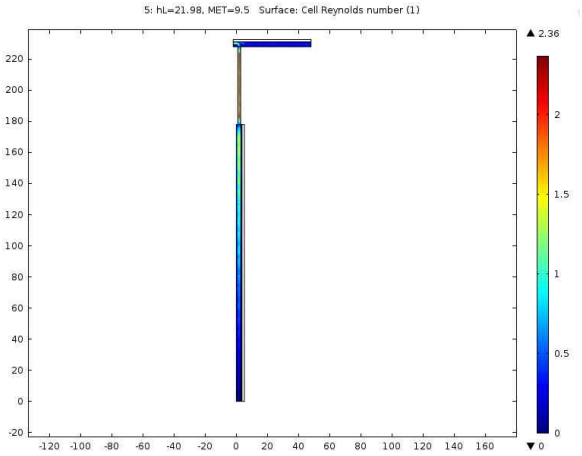


Fig. 5. Side View Human Body with HTP (units in mm).

3. RESULTS

3.1 Low motion activities

The temperatures along the different parts of the heat pipe are illustrated in the next figures. The vertical axis represents the temperature change along different points. As mention in previous section the heat pipe has three major parts the evaporator, adiabatic area and condenser. In Fig. 6, the horizontal axis represents the position in the heat pipe. Points 1 to 8 represents the evaporator, 9 to 15 the adiabatic area and from 16 to 22 the condenser. In this first set the person activity is assumed to be sedentary and low motion activities. The heat flux values were from 0.8 up to 2 MET and in the condenser side the natural convection coefficient was 2.88 ($W/m^2 \cdot K$). The contour plot velocity at the vapor core, heat pipe contour plot temperature and the vapor temperature are shown in Figs. 7-9.

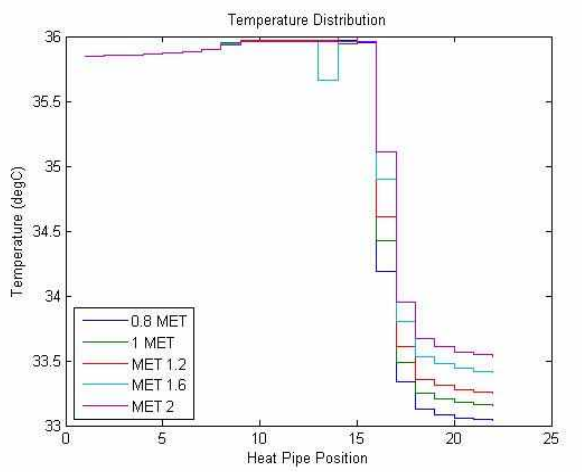


Fig. 6. Temperature response along the Heat Pipe.

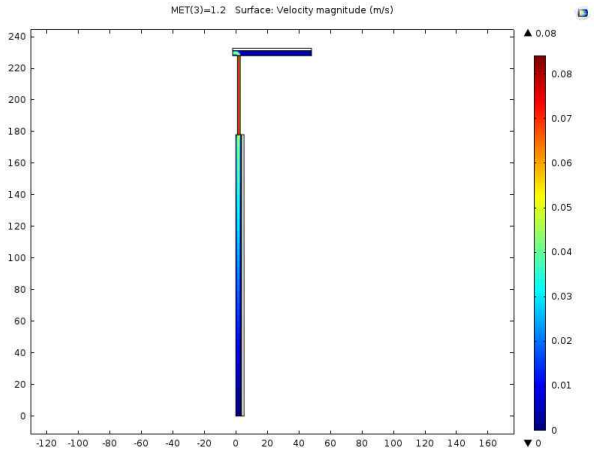


Fig. 7. Contour plot of the vapor velocity along evaporator/adiabatic/condenser sections.

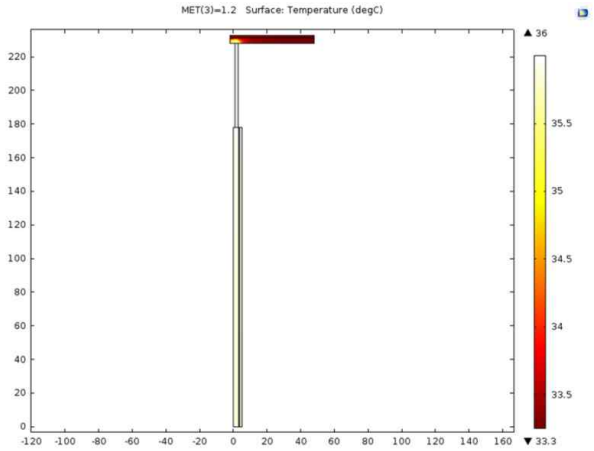
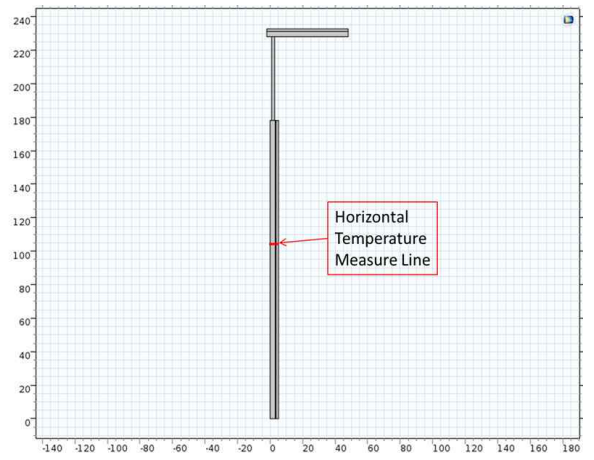
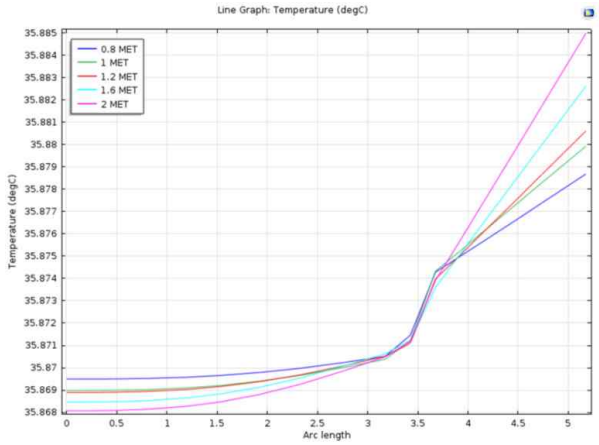


Fig. 8. The heat pipe contour plot temperature distribution.



(a)



(b)

Fig. 9. (a) Reference horizontal line, (b) Temperature distribution along the horizontal line.

Figure 9 depicts the temperature along the evaporator/wick-structure/vapor case. It can be notice that the maximum temperature are on the evaporator section, then it decreases linearly in the case material and wick; a similar behavior is observed in the vapor core. The highest temperature drop is observed for the case due to material physical properties corresponding to stainless steel. Another material option for the case is copper; however it could be toxic for human applications [12].

3.2 High motion activities

For the second set of results the person is assume to be not sedentary and be on motion activities. The heat flux values were from 3.4 up to 9.5 MET and in the condenser side the force convection using different convection coefficient depending on the activity, for example if the person is running at 15 km/h the convection coefficient was 22 ($W/m^2 \cdot K$). Figure 10 represents the temperature change along the vertical axis and the horizontal axis position in the heat pipe. Points 1 to 8 represents the evaporator, 9 to 15 the adiabatic area and from 16 to 22 the condenser. Figure 11 represents the velocity of the liquid water in the wick.

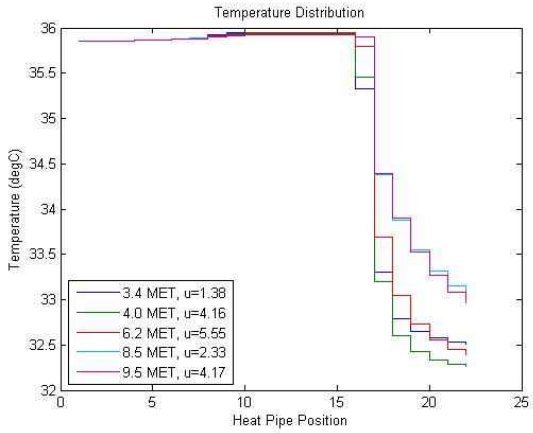


Fig. 10. Temperature response for different METs.

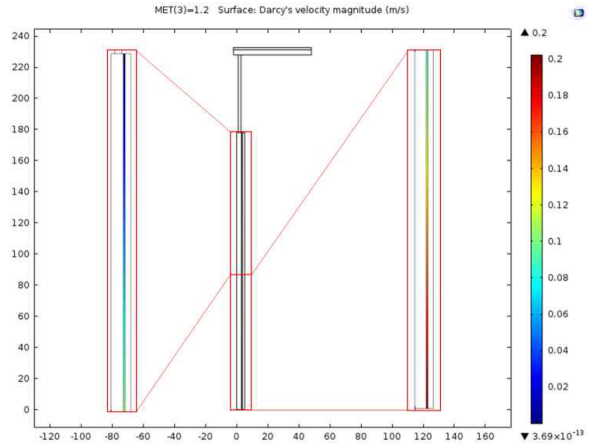


Fig. 11. Contour plot of the liquid velocity in the wick material.

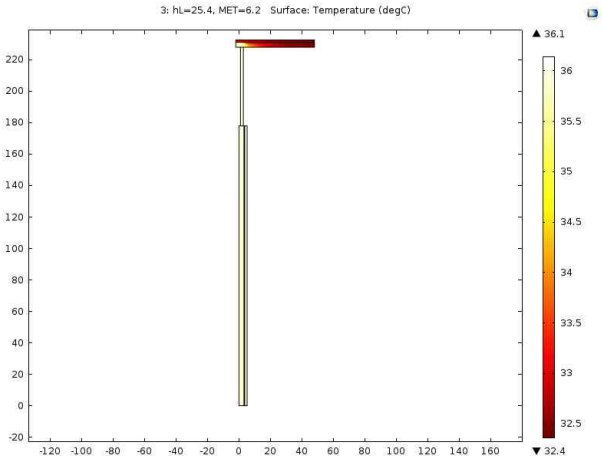


Fig. 12. The heat pipe contour plot temperature distribution.

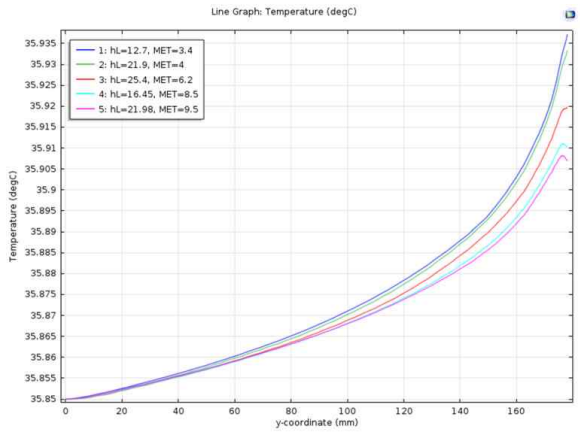


Fig. 13. Contour plot temperature distribution.

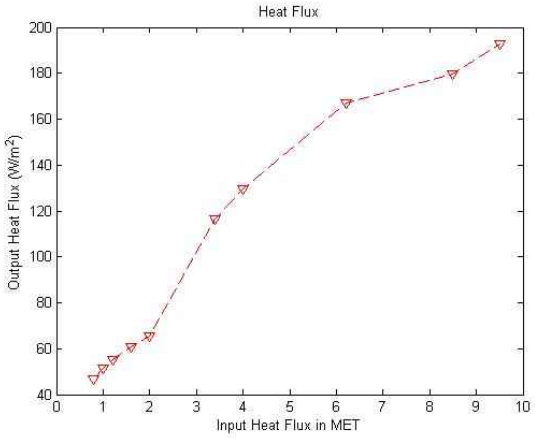


Fig. 14. Cooling rate vs. different heat flux inputs.

From Figs. 12-13 it was found that the highest temperature difference between the condenser and evaporator was 3.6°C, and it corresponded to the heat flux input of 4 MET; this was due to the person activity for this case that was to be bicycling at 15 km/h. For other activities like walking at 5 km/h, the temperature difference was 3.5°C.

4. CONCLUSIONS

A detailed numerical calculation was performed; it replicated the overall thermal operation and interaction of the proposed heat pipe with the ambient conditions. The numerical results show that the proposed cooling system is able to achieve its purpose: remove heat from the chest (warmer area) and release it to the ambient (colder area). The modeling of the system includes different mechanisms of the cooling process: natural and forced convection. Two different scenarios were analyzed assuming person was in low and high motion activities. The temperature difference between the body surface and the condenser upper surface were form 2.1°C up to 3.6°C.

ACKNOWLEDGEMENT

The authors would like to thanks the financial support of the Chair of Department of Mechanical Engineering and the Dean of the School of Engineering at Universidad del Turabo.

NOMENCLATURE

c : Specific heat (J/(kg·K))
C_E : Ergun's coefficient
c : Constant
Gr : Grashof number

h : Fonvective coefficient (W/(m^2·K))
k : Thermal conductivity (W/(m·K))
K : Permeability (m^2)
L : Length (m)
Nu : Nusselt number
P : pressure (Pa)
Pr : Prandtl number
Re : Reynolds number
T : Temperature (C)
t : Time (s)
V : Velocity vector (m/s)
x : x-coordinate system (m)
y : y-coordinate system (m)
μ : Viscosity (Pa·s)
ρ : Density (kg/m^3)
υ : Kinematic viscosity (m^2/s)
φ : porosity

REFERENCES

[1] Faghri A., Reynolds D.B., Bahramian. B, An innovative method for hand protection from extreme cold using heat pipe, *United States Army Natick,* Massachusetts, (1992), Technical Report/TR-93/ 005.
[2] Korn F., Heat pipes and its applications, *2008 MVK160 Heat and Mass Transport*, Lund, Sweden (2008).
[3] Shlosinger A.P., *Heat Pipe Devices for Space Suit Temperature Control*, NASA Contractor Report, NASA CR-1400 (1969).
[4] n.d. Architectural Thermodynamics and Human Comfort in Hot Climates, Retrieved on December 5, 2014. http://archive.unu.edu/unupress/unupbooks/ 80a01e/80A01E04.htm.
[5] Cornell University Ergonomics Web (n. d.), DEA3500: Ambient Environment: Thermal Conditions. Retrieved February 5, 2015 from http://ergo.human.cornell.edu/studentdownloads/D EA3500notes/Thermal/thcondnotes.html.
[6] Elert G., Temperature of a Healthy Human (Skin Temperature)(2001). Retrieved January 20, 2015, from http://hypertextbook.com/facts/2001/AbantyFarzan a.shtml.
[7] Carbajal G., Sobhan C.B, Peterson G.P., Dimensionless governing equations for vapor and liquid flow analysis of heat pipes, *Journal of Thermophysics and Heat Transfer*, 20 (1) (2006)
[8] Bergman, T. L., Lavine A. S., Incropera F. P., Dewitt D. P., *Fundamentals of Heat and Mass Transfer*, Seventh Edition, Jonh Willey, (2011) 599-602
[9] Acros.com, MSDS for Copper, Retrieved May 2, 2015 from http://www.ch.ntu.edu.tw/~genchem99/ msds/exp4/Cu.pdf

A Two-phase loop Cooling System with Capillary Evaporator Employing Bi-layer Copper Wick

Y. An[1], H. Kang[2*], B. Sung[3], K. Yim[3], D.-A. Borca-Tasciuc[4], J. Choi[5*]
[1] *Keumkang heavy industry Co. Ltd., Republic of Korea*
[2] *Dongeun A.T.S, Republic of Korea*
[3] *Dept. of Mechanical Engineering, Shin Ansan University, Republic of Korea*
[4] *Mechanical, Aerospace, and Nuclear Engineering Department, Rensselaer Polytechnic Institute, NY USA*
[5] *LG Electronics Inc., Republic of Korea*

Abstract

A bi-layer wick was proposed to enhance capillary wicking while having minimal impact on flow resistance. A very thin layer consists of copper nanoparticles was textured at the top of porous wick composed of copper micro-particles. The bi-layer wick was lined inside an evaporator designed to fit confined spaces available in server configurations, and then investigated experimentally through an experimental setup. The results will address the two-phase loop cooling devices using the bi-layer wick to significantly increase the heat transfer rate at given design and performance constraints.

Keywords: capillary evaporator, bi-layer wick, two-phase loop cooling, and copper nanoparticle

1. INTRODUCTION

The maintenance cost of high density power servers with active air cooling technologies accounts for approximately 50% of the operating cost of multi-megawatt data centers. Moreover the cost is expected to increase rapidly because an ever increase in power density [1]. Thus, two-phase loop cooling systems are being intensively explored for thermal management in these applications [2].

The two-phase loop cooling system is a closed loop and phase-change cooling device schematically illustrated in Figure 1. It transfers a large amount of heat produced by hot chips to remote locations outside the server enclosure, when the working fluid evaporating at the hot side condenses in the condenser. The fluid is recirculated via capillary pressure in a porous wick lining the evaporator. Their use in server enclosures also allows for a higher air temperature at the inlet of the enclosure, further relaxing constrains associated with cooling, and reducing energy expenditures. However, the two-phase loop cooling is not adopted in large commercial systems due to the complex design constraints associated with requirements (to overcome high pressure drop) for providing high cooling rates over distances of 1m or more.

In this context, there is a strong demand to redesign the evaporator module to increase the cooling rate through enhanced capillary wicking. Thus, this work proposes a new structure for the evaporator chamber employing a bi-layer copper wick to increase the heat transfer performance of the evaporator.

*Corresponding author: hkkang67@hanmail.net, Phone: +82- 32-675-9490 (H. Kang), choijeehoon@gmail.com

2. BI-LAYER WICK FABRICATION

Figure 2 is outlined in terms of fabrication processes. Irregularly shaped pure copper particles of 100~150 μm diameter were sintered to fabricate micro-porous wick samples of 1 mm thickness by using a high temperature isothermal furnace integrated with a sodium heat pipe. All of the sintering processes were performed in vacuum of maximum 10^{-3} torr to minimize the oxidization of copper powders. On the basis of Archimedes' principle, the porosity of the micro-porous wick samples was measured as 0.5 ± 0.02. More details about the sintering are described in in reference of Choi *et al* [3].

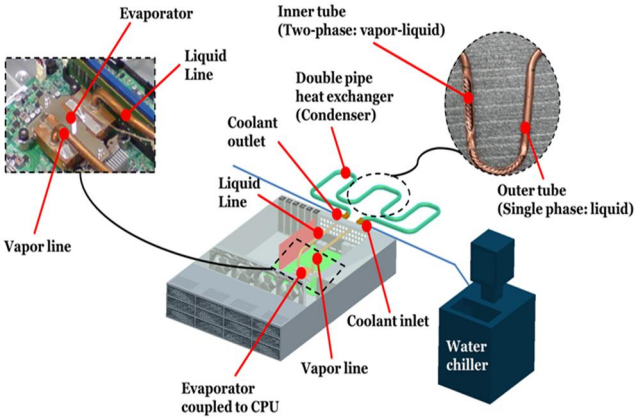


Fig. 1. Schematic of two-phase loop cooling system.

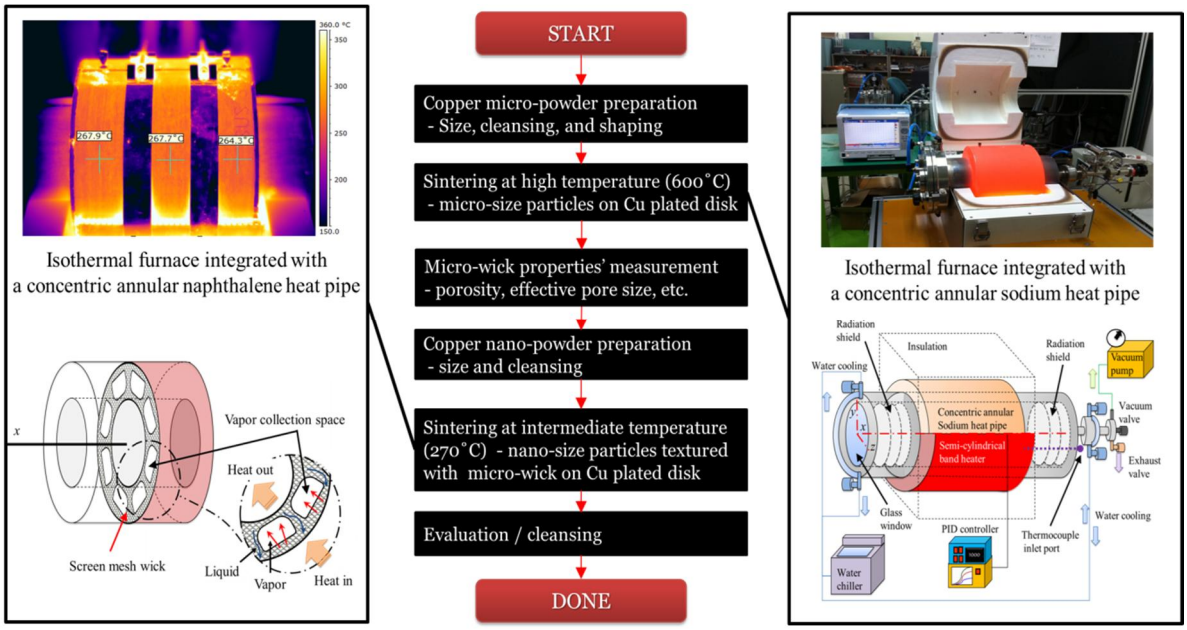


Fig. 2. Fabrication steps of mono- and bi-layer wick.

A new evaporator, as shown in the left inset of Fig.1, incorporates a rectangular chamber, which contains the mono-porous wick as an inner lining as shown in Fig. 3.

Then the micro-porous wick was textured with a nano-porous layer in a subsequent step. The nano-porous layer was uniformly sintered from copper powders with about 300 nm, which formed a thin layer on top of micro-porous wick. The nano-layer is very thin film of 40 ± 0.5 µm in thickness. This step was implemented with carbon graphite molds at the interior center of a naphthalene heat pipe furnace that provides intermediate isothermal temperature of 270 °C and vacuum conditions [4].

The morphology of mono-and bi-layers were characterized by scanning electron microscopy (SEM), JSM-6390A from JEOL, Inc. As depicted in Fig. 4, the bi-layer porous wick has two characteristic pore sizes, with a main layer consisting of large, microscale particles/pores and a second layer on surface of nano particles/pores.

Permeability and maximum capillary pressure of bi-porous wick were measured with an in-house built apparatus described in detail in Reference [3,5]. As listed in Table 1, the capillary pressure of the bi-layer wick is higher than that of the mono-layer wick, while the bi-layer wick has minimal impact on permeability.

3. DESCRIPTION OF SYSTEM

The two-phase loop cooling system was designed to be integrated within a high power density server for data centers employ servers that are specifically devised for the delivery of cloud services, including multicore semiconductor processors.

The evaporator having thickness of 9 mm was designed to fit confined spaces available in server configurations and incorporated to fit the semiconductor, which has a dimension of 30 × 30 mm. The evaporator chamber is made of copper.

Vapor and liquid transport lines of outer diameters of 7.94 mm (inner diameter of 6.54 mm) were made of copper. The condenser composed of a double pipe heat exchanger used to complete the loop.

Table 1. Permeability and maximum capillary pressure of mono-and bi-layer wicks.

	Mono-layer	Bi-layer
Permeability (m^2)	$7\pm1\times10^{-12}$	$3.73\pm0.56\times10^{-13}$
Max. capillary pressure (kPa)	3±1	8.28±1.24

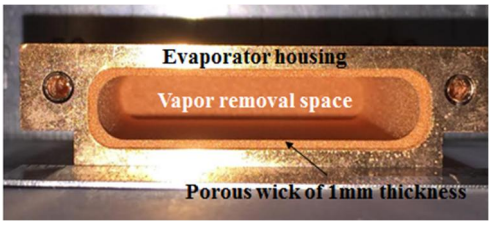
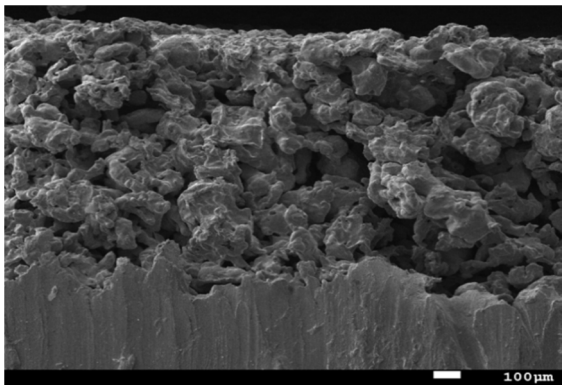
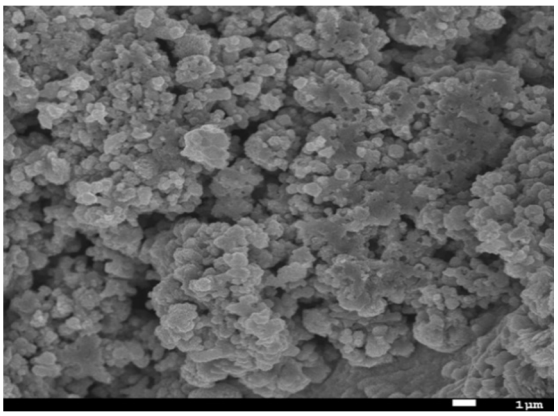


Fig. 3. Mono-porous wick as an inner lining in evaporator housing.



(a)



(b)

Fig.4. Scanning electronic microscopy images of bi-layer porous wick: (a) Micro-porous layer on evaporator chamber (cross-section);(b) Nano-porous layer on the surface of the wick (top view).

The total length of the transport and condenser line of the two-phase loop cooling system is 1.5 m, and then n-Pentane of 39.5 ml was charged as working fluid.

4. PERFORMANCE TESTING

Testing was carried out with systems employing evaporators based mono-layer wick and bi-layer wick; the loop cooling systems were otherwise identical and experiments were performed using same conditions/parameters.

A heat load simulator connected to a DC power supply unit was designed as depicted in Fig.5. The simulator consisted of a pure copper block with four cartridge heaters 6 mm in diameter (each with a power rating of 100 W).

To measure copper block temperatures, four K-type sheath thermocouples of 0.125 mm thickness were (as denoted in Fig.5) embedded horizontally along the center axial line of the copper block and separated by 5 mm gaps. A square surface of 30 × 30 mm, equivalent to that of the top surface of the simulator, was used as the heater surface, while the insulation layers consisting of PEEK - polyether ether ketone (k = 0.25 W/m˚C) and glass fiber (k = 0.046 W/m˚C) were used for restraining the conduction heat losses along the copper block. Bakelite (k = 0.25 W/m˚C) was chosen as the housing material to prevent conduction heat losses. The heat loss through the back side and convection and radiation from the lateral side were estimated to be 1% of the applied power.

Assuming one-dimensional, steady-state heat conduction, the heat flux, $Q^{"}$, at the heater surface can be obtained from:

$$Q^{"} = -k_h \frac{T_1 - T_4}{\Delta x} \quad (1)$$

where k_h is the thermal conductivity of the copper block, Δx is the length over which the temperature change between T_1 and T_4. The heat transferred from the heater surface to the bottom area of the base plate, A_b, is determined from the following expression:

$$Q = Q^{"} A_b \quad (2)$$

The experimental errors of the simulator were also considered from the repeatability of the data in obtaining the overall uncertainties: the temperature difference of ± 0.8 % and k_h of ± 3.01 %. The experimental uncertainties of Q can be estimated using an error propagation method [6] as follows:

$$\frac{U_Q}{Q} = \sqrt{\left(\frac{U_{\Delta k_h}}{k_h}\right)^2 + \left(\frac{U_{\Delta A_b}}{\Delta A_b}\right)^2 + \left(\frac{U_{\Delta T}}{\Delta T}\right)^2 + \left(\frac{U_{\Delta x}}{\Delta x}\right)^2} \quad (3)$$

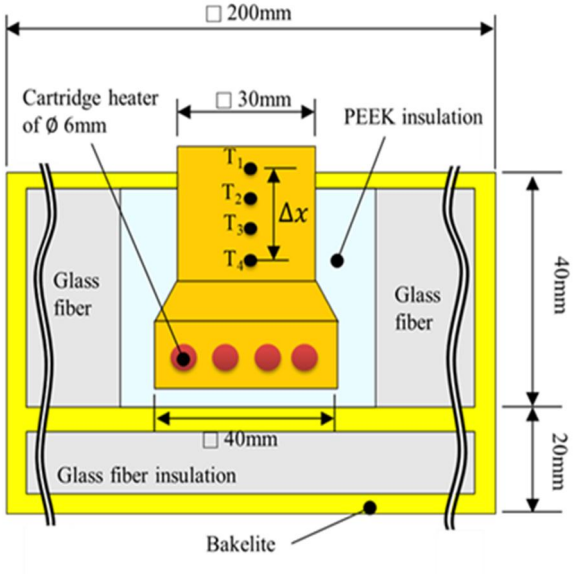


Fig. 5. Schematic of a heat load simulator.

The uncertainty of Q calculated from Eq.(3) is less than 9.94%, although heat losses may also contribute with up to 5% in uncertainty.

A phase-change thermal grease was applied as a thermal interface material to the contact area between the evaporator and the top surface of the copper block to reduce contact thermal resistance. T-type thermocouples (0.125 mm thickness with an uncertainty of ± 0.5 °C) were used to measure the local temperature of the loop system. All of the temperature data were automatically collected by a data acquisition system. Using a water chiller, the heat rejection step was accomplished by the forced convection of constant coolant (water) at a temperature of 20 ± 1°C.

5. RESULTS AND DISCUSSION

During testing, the temperature was recorded at different heat loads, Q, applied to the evaporator base. From this data, the average temperature of the simulator, T_h, for both evaporators is shown in Fig. 6. As can be seen from this figure, both systems were able to cope with heat transfer rates as high as 200W, while the simulator temperature remained well below 60°C. However, the dry-out occurred in the evaporator with mono-layer wick as heat load input increased over 200W.

As opposed to the mono-layer wick, the evaporator with the bi-layer performed well up to 340 W; T_h was 70.2 °C at this high heat transfer rate. As expected, even though permeability decreases about one magnitude as listed in Table 1, the enhanced capillary pressure of the bi-layer wick can overcome higher pressure drop in the flow loop of the cooling system, hence the heat transfer limitation of the loop cooling system could be improved. Moreover, the smaller pores of thin layer exhibit higher capillary pressure would ensure sufficient liquid feedback throughout the wick via the larger pores to avoid dry out. Therefore, the use of the bi-layer wick enables to allow for larger separation distance between the heat source and heat rejection side at high cooling rates.

Further understanding of performance testing can be obtained from Fig. 7 which shows the total thermal resistance (R_t) of the loop cooling system as function of the applied heat load. The total thermal resistance is usually used to characterize the overall performance and it is defined as:

$$R_t = \frac{T_h - T_{wi}}{Q} \qquad (4)$$

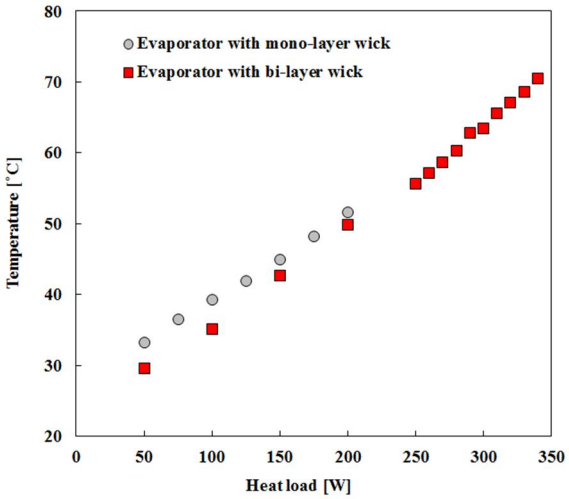


Fig. 6. Average simulator temp. as function of heat load.

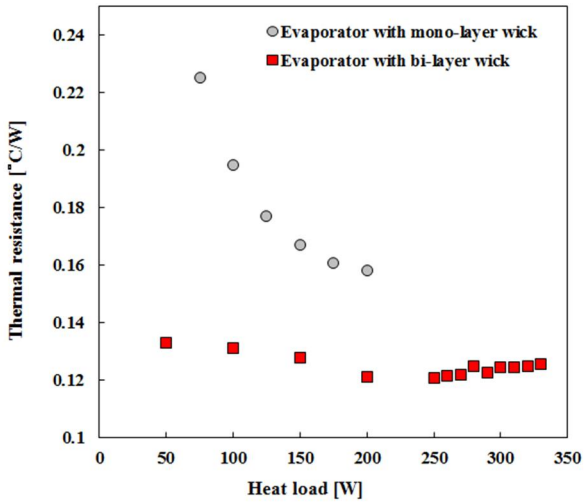


Fig. 7. Total thermal resistance as function of heat load.

where T_{wi} is the inlet temperature of the coolant. At a glance, the thermal resistance associated with the mono-layer is larger than that of the bi-layer.

Since all other apparatus and testing parameters are the same for the two evaporators, the difference in R_t comes from mono-and bi-layer wick impacts overall system performance. The results indicate that the evaporator with bi-layer is able to ensure a lower operating temperature, which is the key in providing adequate cooling of the complex design constraints.

6. CONCLUSIONS

This paper explores an advanced capillary evaporator employing bi-layer copper wick, able to provide high cooling rate at low operational temperature at larger separation distance between the heat source and heat rejection side. The bi-layer wick has two characteristic pore sizes, with a

main layer consisting of micro-scale pores and a second layer on surface of nano-scale pores. The bi-layer wick was integrated with the evaporator as an inner lining by using isothermal heat pipe furnaces. Experimental characterization shows that the evaporator with bi-layer wick can reach a heat load higher than the evaporator with mono-layer wick.

REFERENCES

[1] The Total Cost Ownership of Data Centers, Qpedia Thermal Magazine (2011) 14-16.
[2] M.M. Ohadi, et al., "A comparison analysis of air, liquid, and two-phase cooling of data centers", *Proc. of 28th annual IEEE SEMI-THERM Symp*, CA, USA (2012) 58- 63.
[3] Choi, J., Sano, W., Zhang, W., Yuan, Y., Lee, Y., and Borca-Tasciuc, D.-A., Experimental investigation on sintered porous wicks for miniature loop heat pipe applications, *Experimental Thermal and Fluid Science* 51 (2013) 271–278.
[4] Choi, J., Yuan, Y., Borca-Tasciuc, D.-A. and Kang, H., Design, construction, and performance testing on an isothermal naphthalene heat pipe furnace, *Review of Scientific Instruments* 85(9) (2014) 095105.
[5] Choi, J., Yuan, Y., Sano, W. and Borca-Tasciuc D-A, Low temperature sintering of copper biporous wicks with improved maximum capillary pressure, *Material letters*, 132(1) (2014) 349-352.
[6] Kline, S. J., and McClintock, F. A., Describing Uncertainties in Single-Sample Experiments, *Journal of Mechanical Engineering* 75 (1953) 3-8.

6. Vapor Chambers/ Flat Heat Pipes

Some Important Factors Affect the Q_{max} Measurement of the Vapor Chamber

Wei-Keng Lin[1] and J.K. Chen [2]

[1]*Engineering & System Science Dept., National),Taiwan*

Abstract

This paper presents some of the important parameters while measure the vapor chamber axial thermal resistance. The experiment also included how to improve the accuracy of the axial thermal resistance by using different fixtures in different conditions. Using a water jacket as an example, the laboratory equipment includes a water jacket without flow channel (Type A), water jackets with flow channel (Type B, Type C), a copper block with thermal couples, two Bakelite supports and an aluminum clamp. The research shows that the experiment with an aluminum clamp, Type B water jacket without Bakelite support and copper block will get the best performance.

In addition, a thermal diffusivity of vapor chamber measurement device is also developed in experiment. The results indicate that one-dimension mode is fit when vapor chamber aspect ratio τ less than 0.1, while two-dimension mode is suggested when aspect ratio larger than 0.1. Four pure metals were analyzed in experiment and compare with its standard thermal diffusivity, all the error are within 10%. The repeatability error is less than 5%.

Keywords: Thermal resistance; Thermal diffusivity; Vapor chamber; heat pipe.

■ *Published in Applied Thermal Engineering, Volume 126, 5 November 2017, Pages 1148-1155, https://doi.org/10.1016/j.applthermaleng.2016.12.106*

Development of Vapor Chamber Heat Spreader for Supercomputer Processor Packaging Cooled by Liquid Cold Plate

Yuichi Yokoyama[1], Thanh-Long Phan[2], Yuji Saito[2], Koichi Mashiko[2] and Masataka Mochizuki[2]

[1] *Thermal Technology Division, Electronics Business Company Fujikura Ltd.,*
1-5-1, Kiba, Koto-Ku, Tokyo 135-8512, Japan, Tel: +81-3-5606-1174, Email: yuichi.yokoyama@jp.fujikura.com
[2]*Thermal Technology Division, Electronics Business Company Fujikura Ltd.*

Abstract

Despite newer semiconductor fabrication and multiprocessor system-on-chips architecture can be lowering power consumption of a processor core, but for higher performance processor demanding, the number of cores integrated on a single die processor keep raising which make total power consumption of a processor die is keep raising, while processor die area almost unchanged. As a typical thermal solution for this problem, metals cover with high thermal conductivity on the top of processors die which calls Integrated Heat Spreader (IHS). The function of this metal plate is for spreading the heat from small area of processors die to the larger area of its surface for the better heat dissipation, then transfer the heat to the various cooling components. In the current technology, the IHS mostly is made of solid copper plate. In high performance processors for super computer producing a power of over 300 Watts requires lower spreading thermal resistance of IHS, however this is limited by the thermal conductivity of copper metal. To meet thermal design of near future high power processor, it is necessary to reduce thermal resistance of each component of cooling system. The spreading thermal resistance of heat spreader component of processor packaging is a significant ratio to overall thermal resistance of system. This paper presents a newly solution to reduce spreading thermal resistance of heat spreader using vapor chamber. The vapor chamber has size of 50x50mm with 5mm thickness and tested with heater size of 15x15mm using liquid cooling as a sink. Proposed vapor chamber spreading thermal resistance is 60% smaller than that in solid copper which helped to reduce 27% of total thermal resistance of cooling system of processor.

Keywords: Integrated heat spreader; Vapor chamber; Micro channel; Super computer cooling system; Processor packaging system.

Fundamental Experiments of a Polymer-based Vapor Chamber (Effect of Inclination Angle)

Fumihiko Hideyama[1*], Shuto Nonoshita[2], Yasushi Koito[1], Toshio Tomimura[1]

[1] *Department of Advanced Mechanical Systems, Kumamoto University, 2-39-1 Kurokami, Chuo-ku, Kumamoto Japan*
[2] *Graduate School of Science and Technology, Kumamoto University, 2-39-1 Kurokami, Chuo-ku, Kumamoto Japan*

Abstract

A vapor chamber is essentially a flat-plate heat pipe and it has been used as a high-end heat removal device. The vapor chamber utilizes a latent heat of a phase change of a working fluid, and therefore a large quantity of heat is transported with a small temperature drop. Moreover, since the vapor chamber has a large heat sink in comparison with a heat source, the vapor chamber spreads the heat uniformly. A final goal of this study is to integrate the vapor chamber into a polymer material. If the mechanism of the vapor chamber is integrated into the polymer material, a heat transport performance of the polymer material can be improved. Besides, the production of the heat transport device having the flexibility can be expected because the polymer materials have the flexibility. In this study, the vapor chamber was fabricated on the polycarbonate board and fundamental experiments were performed to evaluate the effect of an inclination angle. A sintered copper powder and water were used as a wick structure and a working fluid, respectively. In the experiments, the transient variations of the temperatures were measured changing an amount of the working fluid and an inclination angle. Moreover, a thermal circuit of the vapor chamber was made to analyze the heat transfer characteristics of the vapor chamber. From the experimental results, the effectiveness of the latent heat transfer in the vapor chamber was confirmed. Furthermore, an effective thermal conductivity was evaluated from the experimental results and the thermal circuit. Effect of the inclination angle on the heat transfer characteristics of the vapor chamber were clarified.

Keywords: Heat transfer; Vapor chamber; Phase change; Inclination angle; Effective thermal conductivity

1. INTRODUCTION

In recent years, a problem of an increase of a heat generating density has been remarkable. Therefore, a heat transport device is required to transport heat from a heat source to a heat sink. A heat transport device such as a vapor chamber and a heat pipe is expected to solve the problem.

As described above, the vapor chamber is the high-end heat removal device, and also called flat-plate heat pipe. The vapor chamber utilizes the latent heat of the phase change of a working fluid, and therefore a large quantity of heat is transported with a small temperature drop. Moreover, since the vapor chamber has a large heat sink in comparison with a heat source, the vapor chamber spreads heat uniformly. Thus, the vapor camber transports a lot of heat in comparison with the general cylindrical heat pipe. Besides, the vapor chamber operates continuously without any additional power because the working fluid is pumped back from a cooled section to a heated section by capillary force of a wick structure placed inside the vapor chamber.

In recent years, the heat transport devise has been used in various electronic devise. Therefore, the operation is required under conditions of various use. Ghanbarpour *et al*. [1] conducted the experiment about a heat pipe having an inclination angle (0 º, 30 º, 60 º, 90 º) from the horizontal state. A silver nanofluids was used as the working fluid. Nazarimanesh *et al*. [2] carried out the study about the U-shaped heat pipe at various inclination angles and broad range of entrance power. The silver nanofluids was used as the working fluid. In addition, Chao *et al*. [3] conducted the study about the heat pipe having the flexible adiabatic section made of the polyurethane polymer between a copper evaporator and a condenser. As mentioned above, a lot of studies about the heat pipe have been conducted and reported. Although many researchers such as Faghri [4] and Mochizuki *et al*. [5] have studied the vapor chamber, the detailed study of the vapor chamber having the inclination angle is limited.

A final goal of this study is to integrate the vapor chamber into a polymer material. If the mechanism of the vapor chamber is integrated into the polymer material, a heat transport performance of the polymer material is improved. Besides, the development of the heat transport device having the flexibility is expected because the polymer materials have the flexibility. In our previous studies, a capillary-wick heat pipe [6], a thermosyphon type heat pipe, a loop heat pipe and a pulsating heat

*Corresponding author: i.hide.1019@gmail.com,
Phone: +81-096-342-3760, Fax: +81-096-342-3760

pipe were fabricated on the polycarbonate board and fundamental experiments were carried out. In the authors' previous study [7], the vapor chamber was fabricated on the polycarbonate board and the fundamental experiment was carried out in the horizontal mode. In the present study, the fundamental experiments are carried out to investigate the effect of an inclination angle. Then the effect of the inclination angle on the heat transfer characteristics of the vapor chamber are evaluated.

2. DETAILS OF VAPOR CHAMBER

The vapor chamber fabricated in this study is shown in Fig. 1. It has three sections; a heated section, an adiabatic section and a cooled section. Moreover, the cooled section of the vapor chamber is larger than the heated section. The heated section and the cooled section are 10 × 10 mm and 100 × 100 mm, respectively. The heat-transport space (length of 90 mm, depth of 5.0 mm) of the vapor chamber was processed on the polycarbonate board (thickness of 8.0 mm) and sealed by using an O-ring and a copper plate (thickness of 2.0 mm). Two copper tubes placed on the polycarbonate board were used to evacuate the air inside the vapor chamber and charge the working fluid into the vapor chamber. Water was used as the working fluid. Furthermore, a wick structure made of a sintered copper powder was placed inside the vapor chamber to return the working fluid from the cooled section to the heated section.

As shown in Fig. 1, the temperature of the vapor chamber was measured at 7 points. A K-type thermocouple was used to measure the temperature. The thermocouples were placed at the heated section (T_H), the adiabatic section (T_1 ~ T_3) and the cooled section (T_{C1} ~ T_{C3}). The distance between T_H and T_{C2} is 80 mm; the intervals of each measurement point between T_H and T_{C2} are 20 mm. The intervals of each measurement point at the cooled section are 15 mm, therefore the distance between T_{C1} and T_{C3} is 30 mm. Small grooves were made on the copper plate to place each thermocouple.

3. EXPERIMENTAL APPARATUS

The experimental apparatus used in this study is shown in Fig. 2. The experimental apparatus consists of the vapor chamber shown in the center and other several peripheral equipment. The points of the experimental apparatus are described below because the experimental apparatus is essentially same as the previous one [7]. A heater, a volt slider and a wattmeter were used to heat the vapor chamber. The pressure inside the vapor chamber was measured by

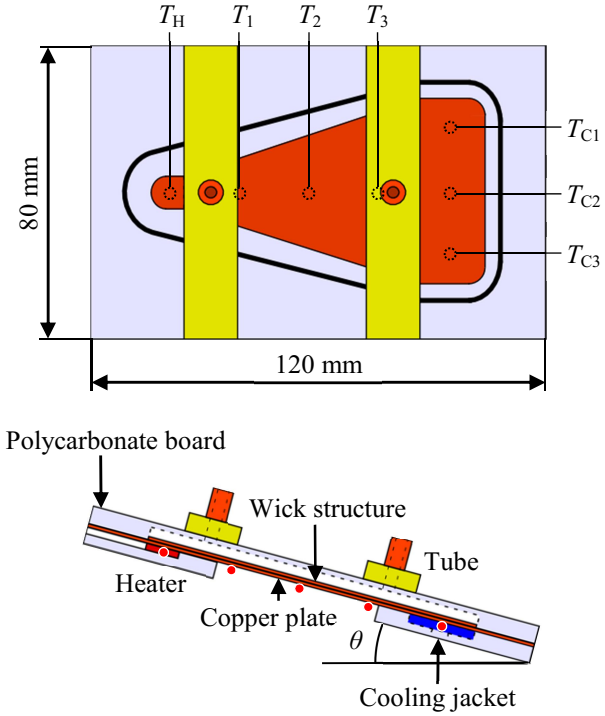


Fig. 1. Schematic diagram of the vapor chamber (upper : front view, lower : cross section).

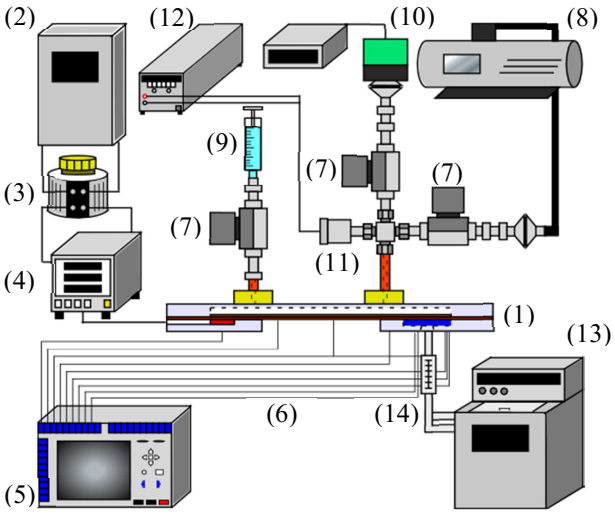


Fig. 2. Experimental apparatus.

using a vacuum gage and a pressure transducer. A thermostatic bath was prepared to maintain a cooling water temperature and circulate the cooling water between itself and a cooling jacket.

4. EXPERIMENTAL PROCEDURE

In experiments, at first, the air was evacuated by using a vacuum pump and the working fluid was charged into the vapor chamber by using a syringe. Secondly, the heat was supplied by the heater attached to the heated section while the cooling water was circulated to cool the vapor chamber. Then the transient change in the temperature of the vapor chamber was measured by using K-type thermocouples. The vapor chamber was covered with a thermal insulator to reduce heat losses.

The experimental condition is shown in Table 1. The experiments were conducted changing an amount of the working fluid and the inclination angle indicated in Fig. 1. The inclination angle was changed as shown in Table 1. The working fluid was water. The cooling water temperature in the thermostatic bath was held at 20 ºC. For comparison, the experiment at V = 0 mL was also conducted. Furthermore, a numerical analysis was conducted about the heat transfer characteristics of the vapor chamber in the case where the working fluid is not charged. Then the heat losses were estimated by comparing the numerical results with the experimental ones.

5. RESULTS AND DISCUSSION

In this study, because the difference in temperature among T_{C1} ~ T_{C3} is small, the following temperature T_C was used to evaluate the temperature at the cooled section.

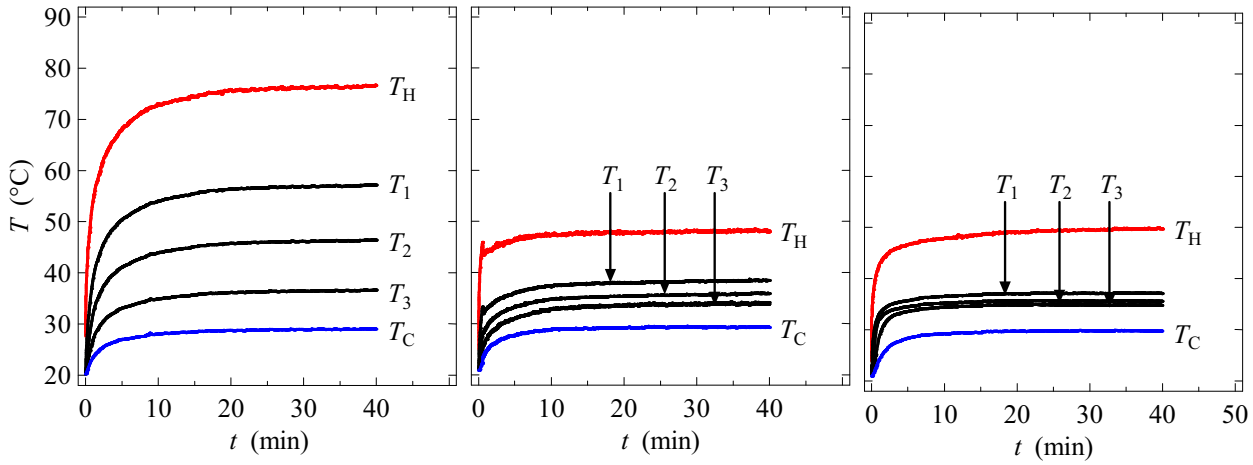
$$T_C = \frac{T_{C1} + T_{C2} + T_{C3}}{3} \quad (1)$$

5.1 Heat transfer characteristics

Fig. 3 shows the transient change in the temperatures (T_H, T_1, T_2, T_3 and T_C) of the vapor chamber. The ordinate and the abscissa are the temperature and the time from the start of heating. These temperatures are obtained in the top heat mode and the bottom heat mode at θ = 45 º, V = 5.0 mL and Q_{in} = 30 W. For comparison, the experimental result at V = 0 mL is also shown in Fig. 3. From Fig. 3, each temperature (T_H, T_1, T_2, T_3 and T_C) increases from the start of heating, and then they come to the steady-state temperature in all cases. However, the temperature difference between T_H and T_C at V = 5.0 mL is smaller than that at V = 0 mL. From this result, when the working fluid is charged, the effect of the latent heat transfer of evaporation and condensation of the working fluid is confirmed. Table 2 shows the operating conditions where the steady-state temperature distribution of the vapor chamber was obtained.

Table 1. Experimental conditions.

Working fluid	Water
Cooling water temperature (ºC)	20
Liquid volume, V (mL)	2.0, 3.0, 4.0, 5.0, 6.0
Heat input, Q_{in} (W)	30
Inclination angle, θ (º)	± 35, ± 45



(a) Without working fluid

(b) With working fluid (V = 5.0 mL, θ = - 45 º) (Bottom heat mode)

(c) With working fluid (V = 5.0 mL, θ = + 45 º) (Top heat mode)

Fig. 3. Transient variations of the temperatures of the vapor chamber (Q_{in} = 30 W).

Table 2. Conditions for the steady-state operation.

		V (mL)				
		2.0	3.0	4.0	5.0	6.0
$\theta = 35$ º	Bottom	×	×	○	○	○
	Top	×	×	○	○	○
$\theta = 45$ º	Bottom	×	×	○	○	○
	Top	×	×	○	○	○

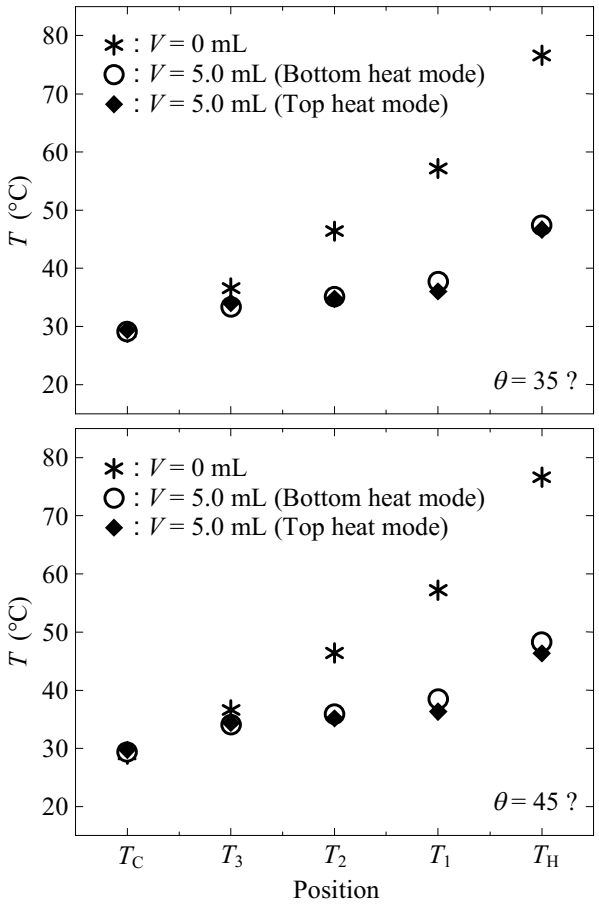


Fig. 4. Temperature distribution of the vapor chamber.

Fig. 4 shows the temperature at each measurement point after 40 minutes from the start of heating. The ordinate is the temperature and the abscissa is the measurement point of the temperature (T_H, T_1, T_2, T_3 and T_C). For comparison, the experimental result at V = 0 mL is also shown in Fig. 4. The temperature of each measurement point at V = 5.0 mL is smaller than that at V = 0 mL except for the temperature at the cooled section. Therefore, the effect of the latent heat transfer of evaporation and condensation of the working fluid is confirmed. Besides, the temperatures at T_H, T_1 and T_2 of the top heat mode are smaller than those of the bottom heat mode. When the vapor chamber operates in the top heat mode, the excess working fluid flows to the cooled section, and then the evaporation of the working fluid is more intense than the bottom heat mode. As a result, the heat transfer performance of the vapor chamber in the top heat mode is high. This phenomena were observed in both inclination angles (θ = 35 º, 45 º).

5.2 Effective thermal conductivity

In this study, the heat transfer characteristics of the vapor chamber was evaluated by an effective thermal conductivity, λ_{eff}. First, a thermal circuit between the heated section and the cooled section of the vapor chamber was made as shown in Fig. 5. In this study, a heat conduction in the polycarbonate board was neglected because it was very small compared to the heat conduction in the copper plate. The effective thermal conductivity of the vapor chamber is calculated by the following equation:

$$\lambda_{eff} = \frac{Q_{VC}}{T_H - T_C} \frac{L}{A_{VC,C} - A_{VC,H}} \ln \frac{A_{VC,C}}{A_{VC,H}} \quad (2)$$

where Q_{VC} is the heat flow rate through the vapor chamber and L the length of the heat-transport space, $A_{VC,H}$ and $A_{VC,C}$ are the cross sectional area of the heat-transport space at the heated section and the cooled section, respectively.

Fig. 6 shows the effective thermal conductivity at θ = 35 º, 45 º in the top heat mode and the bottom heat mode. The ordinate is the effective thermal conductivity, λ_{eff}, and the abscissa is the amount of the working fluid, V. The effective thermal conductivity tends to decrease with the increase in the amount of the working fluid. This tendency is also found in the case where the vapor chamber is placed horizontally. When the vapor chamber operates in the bottom heat mode, the excess working fluid flows to the heated section. Then the phase change of the working fluid is restrained at the heated section. On the other hand, when the vapor chamber operates in the top heat mode, the excess working fluid flows to the cooled section. Then the thermal resistance at the cooled section increases. The more amount of the working fluid increases, the greater those effects are. As the result, the effective thermal conductivity tends to decrease. Moreover, the effective thermal conductivity in the top heat mode is larger than the bottom heat mode in all experimental conditions. As mentioned above, when the vapor chamber operates in the top heat mode, the excess working fluid flows to the cooled section. Therefore, the evaporation of the working fluid in the top heat mode is intense in comparison with the bottom heat mode. As the result, Q_{VC} in the top heat mode is larger than that in the bottom heat mode. As shown in Fig. 5, Q is divided into two. Therefore,

Q_{CU} decreases with the increase in Q_{VC}. For this reason, the temperature difference between T_1 and T_3 in the top heat mode is smaller than the bottom heat mode as shown in Fig. 3. The difference in the effective thermal conductivity between θ = 35 º and θ = 45 º is hardly found. As shown in Fig. 6, some dispersions in the effective thermal conductivity is found. In this study, the effective thermal conductivity is 830 W/(m·K) in maximum at θ = 35 º in the top heat mode and 834 W/(m·K) in maximum at θ = 45 º in the top heat mode.

6. CONCLUSION

The vapor chamber was integrated into the polycarbonate board and fundamental experiments were performed to evaluate the effect of an inclination angle.

From the experimental results, the effect of the latent heat transfer of the vapor chamber in the bottom heat mode and the top heat mode was confirmed. Moreover, the effective thermal conductivity was also evaluated from the experimental results and the thermal circuit. The effective thermal conductivity in the top heat mode was larger than the bottom heat mode. However, the difference in the effective thermal conductivity between θ = 35 º and θ = 45 º is hardly found. In this study, the effective thermal conductivity is 830 W/(m·K) in maximum at θ = 35 º in the top heat mode and 834 W/(m·K) in maximum at θ = 45 º in the top heat mode.

ACKNOWLEDGEMENT

This work was supported by JSPS KAKENHI Grant Number 26420150.

NOMENCLATURE

Q	:	Heat flow rate (W)
T	:	Temperature (ºC)
t	:	Time (min)
V	:	Working fluid volume (mL)
λ	:	Thermal conductivity (W/(m·K))

Subscripts

1 ~ 3	:	Positions
C	:	Cooled
CU	:	Copper
eff	:	Effective
H	:	Heated
in	:	Input
VC	:	Vapor chamber

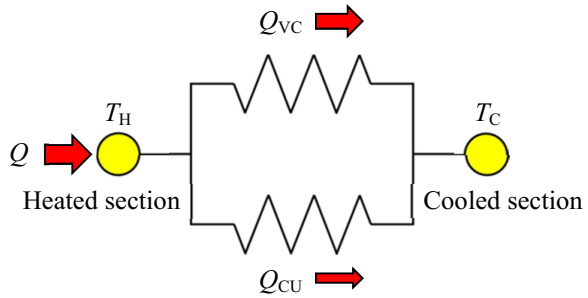


Fig. 5. Thermal circuit of the vapor chamber

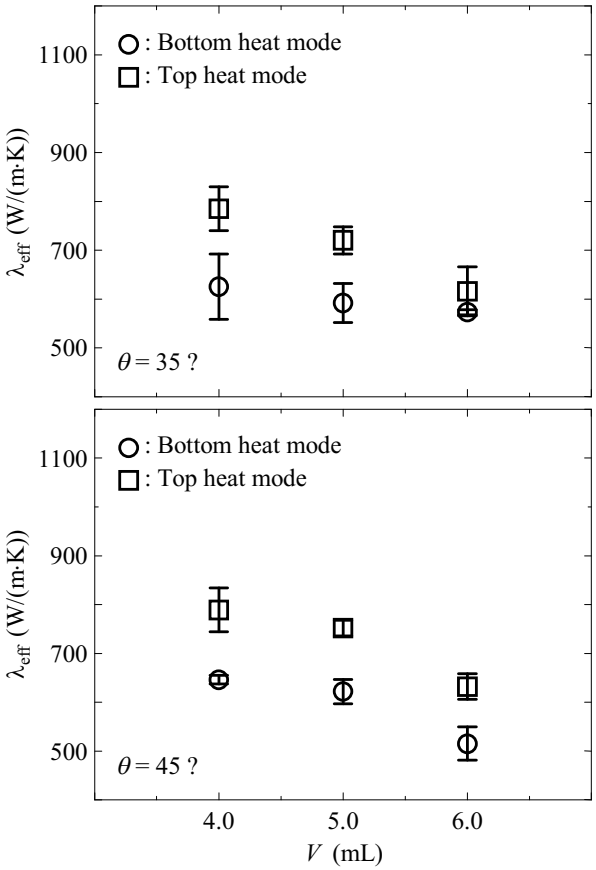


Fig. 6. Effective thermal conductivity of the vapor chamber.

REFERENCES

[1] Ghanbarpour, M., Nikkam, N., Khodabandeh, R., Toprak, M.S., Thermal performance of inclined screen mesh heat pipes using silver nanofluids, *International Communications in Heat and Mass Transfer*, 67 (2015) 14-20.

[2] Nazarimanesh, M., Yousefi, T., Ashjaee, M., Experimental study on the effects of inclination situation of the sintered heat pipe on its thermal performance, *Experimental Thermal and Fluid Science*, 68 (2015) 625-633.

[3] Chao, Y., Chengyi, S., Wen, S., Peng, T., Tao, D., Flexible heat pipes with integrated bioinspired

design, *Progress in National Science: Materials International*, 25 (2015) 51-57.

[4] Faghri, A., Review and advances in heat pipe science and technology, *ASME Journal of Heat Transfer*, 134 (12) (2012) 123001-1.

[5] Mochizuki, M., Nguyen, Th., Mashiko, K., Saito, Y., Nguyen, Ti., Wuttijumnong, V., A review of heat pipe application including new opportunities, *Frontiers in Heat Pipes*, 2 (2011) 013001.

[6] Koito, Y., Maehara, H., Shimada, D., Tomimura, T., A capillary-wick heat pipe fabricated on a plastic board (Fundamental experiments on heat transport characteristics), *Proceedings of the InterPACK2015*, InterPACKICNMM2015-48308 (2015).

[7] Hideyama, F., Nonoshita, S., Koito, Y., Tomimura, T., Fabrication of a vapor chamber on a plastic board, *Proceedings of InterPACK2015*, Inter PACKICNMM2015-48554 (2015).

7. Micro Heat Pipes

An Interfacial Transport Analysis of Micro Heat Pipe

Eui Guk Jung[1] and Joon Hong Boo[2]

[1]Air Solution Laboratory, LG Electronics Inc., Chang Won 641-713, Korea
[1]School of Aerospace and Mechanical Engineering, Korea Aerospace University, Goyang-si 412-791, Korea

Abstract

A numerical modeling work was accomplished to analysis heat and mass transfer in phase change interface of micro heat pipes. The model describes the distribution of liquid, vapor, mass flow rate for the phase change, wall temperature, pressure drop, and heat transfer rate in a micro heat pipe under operation. The reference shape of micro heat pipe is triangular, but the model can be applied to various shapes by considering the hydraulic diameter. Thus far, the phase change interface has been commonly modeled using the Young-Laplace capillary equation for the thermal performance prediction of micro heat pipes. The phase change ratio has been simulated using terms such as the vapor pressure, liquid pressure, and capillary pressure. In this study, a thermal numerical model for micro heat pipes was developed by augmented the Young-Laplace equation, which is widely used in liquid thin-film theory. Terms excepted in previous works, such as the disjoining pressure and Marangoni effects, were considered, and their influences on the heat transfer were analyzed and discussed. The disjoining pressure has an appreciable influence on the heat transfer, and the Marangoni term can influence the heat transfer rate if the curvature of the interface is large or the temperature gradient is high. The validity of the model was verified by experimental results for the wall temperature of a micro heat pipe, wherein the temperature difference was evaluated to be within 5.6°C.

Keywords: Micro heat pipe; Phase change interface; Liquid thin-film theory; Film thickness; Augmented Yong- Laplace equation; Heat transfer rate.

■ *Published in Heat and Mass Transfer (2017) 53: 3363. https://doi.org/10.1007/s00231-017-2074-8*

Discussion on the Solar Concentrating Thermoelectric Generation Using Micro- Channel Heat Pipe Array (STEG-MCHP)

Guiqiang Li[1], Wei Feng[2], Song Lv[1], Yi Jin[2], Xiao Chen[3] and Jie Ji[1]

[1]Department of Thermal Science and Energy Engineering, University of Science and Technology of China, 96 Jinzhai Road, Hefei City, 230026, China
[2]Department of Precision Machinery and Precision Instrumentation, University of Science and Technology of China, Hefei, Anhui, China
[3] State Key Laboratory of Fire Science, University of Science and Technology of China, 96 Jinzhai Road, Hefei City, 230026, China

Heat pipe is a high efficient tool in solar energy application. In this paper, a novel solar concentrating thermoelectric generation using micro-channel heat pipe array (STEG-MCHP) was presented. The flat-plate micro-channel heat pipe array not only has a higher heat transfer performance than the common heat pipe, but also can be close to the TEG, which can further reduce the thermal resistance between the heat pipe and the TEG. The preliminary comparison experiment was also introduced to indicate the advantage of the STEG-MCHP. The optimization based on the model verified by the experiment was demonstrated, and the concentration ratio and selective absorbing coating area were also discussed. In addition, the cost analysis was also made to compare to the common solar concentrating TEGs in series. The outcome shows that the solar concentrating thermoelectric generation using micro-channel heat pipe array owns the higher electrical efficiency and lower cost, which provide a suitable way for solar TEG application.

Keywords: TEG; Micro-channel heat pipe; Electrical efficiency; Cost analysis

■*Published in Heat and Mass Transfer, Vol. 53, issue 11 (DOI: https://doi.org/10.1007/s00231-017-2026-3)*

Electric Motor Thermal Management System Using L-Shaped Flat Heat Pipes

Nandy Putra and Bambang Ariantara

Applied Heat Transfer Research Group, Mechanical Engineering Department,
Universitas Indonesia, Kampus UI, Depok 16424, Jawa Barat, Indonesia

Abstract

Heat generation in an electric motor will increase its temperature. The excessive working temperature will reduce the motor performance and shorten its lifetime, and a thermal management system is needed to reduce the working temperature. The objective of this study is to determine the performance of the electric motor thermal management system using L-shaped flat heat pipes experimentally. Evaporator sections of heat pipes are typically placed inside the motor housing or buried in the motor shaft while the condenser sections are placed outside the motor housing and cooled with circulated liquid or air stream. However, in this study, the heat pipes were placed on the surface of the motor housing thus simplifying installation and maintenance. A prototype was made of a 0.5 HP conventional electric motor where the rotor and the coil were replaced by a cartridge heater to simulate the heat generation and to simplify the heat generation adjustment. Eight pieces of L-shaped flat heat pipes were mounted on this prototype. Each evaporator section was mounted on a heat pipe holder that was inserted between the motor fins. Each condenser section was placed in front of the motor fan. Heat sinks were mounted on each condenser section to increase the rate of heat transfer to the ambient air. The heat pipes were made of flattened copper tubes with sintered copper capillary wick and water as working fluid with a filling ratio of 50%. Experiments were conducted with varied heating power while the fan speed was kept constant. The thermal resistance of the motor fins - heat pipe - heat sink did not change much with the heat load. It reached a minimum value of 0.28 °C/W at the heat load of 150 W. The motor surface temperature is reduced from 102.2 °C to 68.4 °C or a reduction by 33.8°C.

Keywords: Electric motor; L-shaped flat heat pipe; Performance; Thermal management system.

■ *Published in Applied Thermal Engineering, Volume 126, 5 November 2017, Pages 1156-1163, https://doi.org/10.1016/j.applthermaleng.2017.01.090*

Development of an Aluminum Flat Heat Pipe with Carbon Wire Wick

Yoon Woo Park[1], Seok Hwan Moon[1], Seok Ho Rhi[2], Kwang Seong Choi[1] and Jin Ho Lee[1]

[1]*3 Dimensional New Devices Research Section, ETRI, Daejeon 34129, Korea*
[2]*Department of Mechanical Engineering, Chungbuk University, 1 Chungdae ro, Cheongju 28644, Korea*

Abstract

Flat plate heat pipe is required to be thin in order to apply 3D electronic package etc. This leads to a problem for declining the heat transfer rate. There are many studies to overcome performance problem for enhancing capillary force, for example various groove shape, using screen mesh, and mixed structure as a wick. Nevertheless, these studies have not been generating remarkable results. For this study, we try on carbon wire to wick structure to improve heat transfer rate at Aluminum Flat Heat Pipe(AFHP). Fabricated flat heat pipe for this study uses the aluminum container with 2 mm thickness, 12 channels to width direction, and made by extrusion. The cross section of aluminum container is designed as groove wick structure at one sideof the channel for inserting carbon wire at the other side. Carbon wire diameter is 7 ㎛, and the sharp edgesmade by between carbon wires can contribute to create capillary force. 1k carbon wire consists of thousand carbon filament. We developed a process for carbon wire attaching to the aluminum container. One of the main technology we developed is that we bended aluminum container's both ends for attach carbon wire to aluminum container and cut aluminum container, carbon wire at one go for vacuum and seal at aluminum container. We fabricated four kinds of carbon wire heat pipe to evaluate heat pipe's performance. Difference of carbon wire heat pipe is inserted with carbon wire quantity 3 k, 5 k, 7 k, 10 k. We have obtained the result that 5 k carbon wire wick heat pipe showed the highest isothermal performance. 5 k carbon wire wick heat pipe recorded a lower temperature difference between evaporator and condenser of about 8.7 %, 55.6 %, and 3times contrast 3 k, 7 k, 10 k carbon wire wick heat pipe.

Keywords: Carbon wire; Aluminum heat pipe; Capillary force; Extrusion.

■ *Published in Applied Thermal Engineering, Volume 126, 5 November 2017, Pages 1177-1184, https://doi.org/10.1016/j.applthermaleng.2017.02.042*

A New Encapsulation Method Using Low-Melting-Point Alloy to Seal Micro Heat Pipe

Congming Li[1], Xiaodong Wang[1,2], Chuanpeng Zhou[1], Yi Luo[1,2], Zhixin Li[1] and Sidi Li[1]

[1]*Key Laboratory for Micro/Nano Technology and System of Liaoning Province, Dalian University of Technology, Dalian 116023, China*
[2]*Key Laboratory for Precision and Non-traditional Machining of Ministry of Education, Dalian University of Technology, Dalian 116023, China*

Abstract

This paper presents a new method of using low-melting-point alloy (LMPA) to seal micro heat pipe (MHP), and corresponding MHP structures with the charging and sealing channels were designed. Aiming to study the sealing of MHP using LMPA, three different auxiliary structures, which were made of glass and Si substrate, were investigated. They are one rectangular structure and two triangular structures with different corner angles. The auxiliary channels for LMPA has 0.5mm of width and 135μm of depth. A certain amount of LMPA was heated to the temperature near its melting point. The experimental results show that the flow speed of liquid LMPA in channels plays an important role in the sealing of MHP and that well sealing performance of both rectangular structure and triangular structures can be implemented when flow speed is low. Moreover, the sealing performance of triangular structures is better than that of rectangular structures under the condition of high flow speed. Therefore, triangular structures are more suitable for sealing of MHP.

Keywords: Encapsulation; Low-melting-point alloy; Micro heat pipe; Sealing.

■ *Published in J Mech Sci Technol (2017) 31: 2621. https://doi.org/10.1007/s12206-017-0504-7*

Combination of Thermal Storage and Heat Spreading for High Power Portable Electronics Cooling

Zhiwei Li[1], Lvcang Lv[1] and Ji Li[2]

[1]*School of Engineering Science, University of Chinese Academy of Sciences, 19A Yu-quan-lu Road, Shijingshan District, Beijing, China*
[2] *Laboratory of Advanced Thermal Management Technologies, School of Engineering Science, University of Chinese Academy of Sciences, 19A Yu-quan-lu Road, Shijingshan District, Beijing, China*

Abstract

This study proposed a novel cooling method by combining a liquid-metal phase-change material module (LMPCM) and a flat heat pipe thermal spreader (FHP) together to cool electronic devices. In this mechanism, the liquid-metal phase change material module and the flat heat pipe function as thermal storage and heat spreader, respectively. Thermal performance of this novel design was experimentally evaluated at both steady and transient heating conditions with different heating power inputs. Results indicate that the LMPCM+FHP modules could effectively restrain the temperature rise of electronic chips and prolong electronic devices' usage time. Besides, the FHP-LMPCM module outperformed other modules including the LMPCM-FHP module, LMPCM module, FHP module and copper plate. Moreover, it was found that the FHP-LMPCM module could maintain the temperature of electronic device within an allowable temperature range even if the PCM had completely melted under transient-state heating conditions, which demonstrates that the proposed method is very promising solution to the thermal management of high power portable electronics.

Keywords: Combination; Flat heat pipe; Liquid metal phase change material; Portable devices; Thermal management

Development of Thin Heat Pipe for Thin and High Performance Note-book PC

Yoji Kawahara[1], Yuji Saito[1], Mohammad Shahed Ahamed[1], Yuichi Yokoyama[1]

[1]*Thermal Technology Division, Electronics Business Company Fujikura Ltd*
1-5-1, Kiba, Koto-Ku, Tokyo 135-8512, Japan

Abstract

Lower TDP (Thermal Design Power) CPU is developing for mobile note-book PC. TDP of the latest CPU is only 4.5W and it becomes possible to cool by fan-less cooling module. However, in a high-end model of mobile note-book PC, TDP of CPU is large and is increasing to get higher performance. Therefore, a more efficient cooling module is demanded. And because thin and stylish case design is needed, thinner cooling module is demanded. In addition, it is necessary to obtain a steady performance even by various postures in tablet note-book PC of 2in1 type. Therefore, we are developing the thinner heat pipe that has larger Qmax (Maximum Heat Transfer) and better top heat performance. We are using center fiber wick structure which is arranged fine fiber wick in central part of pipe for thin heat pipe. Fine fiber wick which is small capillary radius has high capillary force. And because its liquid pass is along longer direction in the pipe, the pressure loss of the liquid flow is low. And because fine fiber wick can easily adjust the wick space by adjusting the number of fibers, it can keep vapor space with good balance in narrow space of thin heat pipe. Therefore, center fiber wick structure is very suitable for thin heat pipe. We are developing the wick structure to combine the carbon fiber to the center fiber wick in order to improve thermal performance further more. This paper reports that the performance evaluation result of thin heat pipe using combined wick structure.

Keywords: thin heat pipe, note-book PC, wick structure, maximum heat transfer, top heat mode, carbon fiber

1. INTRODUCTION

In the latest CPU for mobile note-book PC, not only the performance is enhanced but also electrical power efficiency is improved for lower power consumption.

TDP (Thermal Design Power) of the CPU used for the usual tablet type PC is only 4.5W, therefore it is possible to cool by fan-less cooling. TDP of the CPU used for the usual thin note-book PC is 15W. In this case, it is necessary to cool by forced convection cooling. The cooling module which combined a fan with thin heat pipe is generally used. Because TDP 15W is not so high, making thin cooling module is relatively easy.

However, in a high-end model of mobile note-book PC, TDP of CPU is about 2 times of the usual thin note-book PC, 28W~35W. Therefore the high-performance cooling module which can correspond to high power CPU is still demanded. And because thin and stylish case design is required, thinner cooling module is demanded. In addition, it is necessary to obtain a steady performance even by various postures in tablet note-book PC of 2in1 type.

Therefore, the thinner heat pipe which has larger Qmax (Maximum Heat Transfer) and better top heat performance is developping.

Ahamed et al. developed the new concept of fiber wick structure which is called "center fiber wick" [1], [2], [3], [4] and [5]. By using "center fiber wick" structure, it can obtain high performance thin heat pipe which has higher Qmax.

New wick structure which is combined the carbon fiber to the center fiber wick is developing in order to improve thermal performance further more. This paper reports that the performance evaluation result of thin heat pipe using combined wick structure.

2. WICK STRUCTURE

Fine axial grooves on the inner wall of the pipe, mesh, fine fiber and sintered powder are generally used for the wick structure of heat pipe.

The center fiber wick structure which is placed fine fiber wick at center position is especially suitable for the thinner heat pipe which internal space is quite narrow. Fine fiber wick which is small capillary radius has high capillary force. And because its liquid pass is along longer direction in the pipe, the pressure loss of the liquid flow is low. And because fine fiber wick can easily adjust the wick space by adjusting the number of fibers, it can keep vapor space with good balance in narrow space of thin heat pipe.

Figure 1 shows a cross-section of the heat pipe with the center fiber wick structure. Fiber bundle which is placed center of the pipe is liquid pass. And space of both sides of fiber bundle is vapor pass.

*Corresponding author: yoji.kawahara@jp.fujikura.com, Phone: +81-3-5606-1174, Fax: +81-3-5606-1514

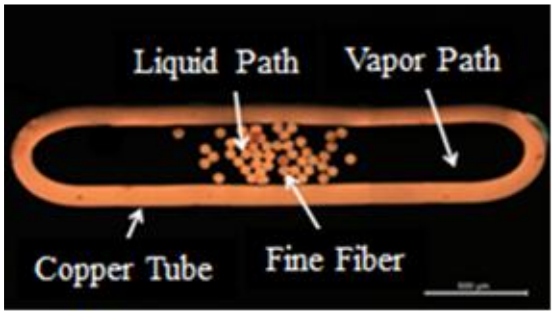


Fig. 1 Cross-section of the heat pipe with the center fiber wick structure

Figure 2 shows the X-ray photograph in bend part of center fiber wick heat pipe. Because the fiber bundle is fixed on the Copper pipe by sintering, it is possible to keep the center position even if the bending process is applied.

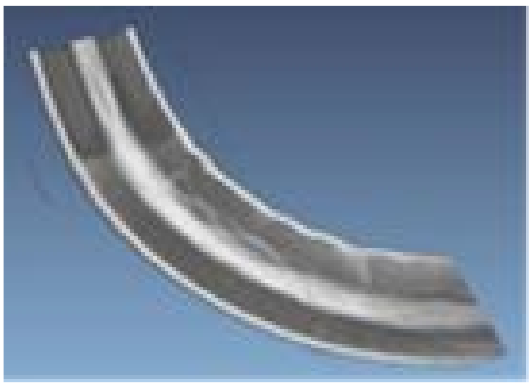


Fig. 2 X-ray photograph in bend part of center fiber wick heat pipe

The capillary limit is the major limitation of heat pipe for CPU cooling. When the total of vapor flow pressure drop, liquid flow pressure drop and gravity force is exceeding the capillary force, local dry-out is occurred. (QL)max (Heat Transport Capability Factor) of heat pipe concerning for capillary limit is given by equation (1) [6].

$$(QL)_{\max} = \frac{\frac{2\sigma\cos\theta}{r_p} - \rho_l g D\cos\beta + \rho_l g L\sin\beta}{\frac{32\mu_v}{\lambda A_v \rho_v D_{h,v}^2} + \frac{\mu_l}{\lambda A_w \rho_l K}} \quad (1)$$

And Qmax is given by equation (2) [7].

$$Q_{\max} = \frac{(QL)_{\max}}{L_{eff}} \quad (2)$$

Effective length of heat pipe Leff is defined as equation (3) [6].

$$L_{eff} = \frac{1}{2}L_e + L_a + \frac{1}{2}L_c \quad (3)$$

Equation (1) can be simplified as equation (4) [6].

$$(QL)_{\max} = \frac{2KA_w(1+\eta)\cos\theta F_l}{r_p} N_l \quad (4)$$

η, Fl and Nl are defined as following equations [6].

$$\eta = \frac{r_p D\cos\beta}{2H\cos\theta} + \frac{r_p L\sin\beta}{2H\cos\theta} \quad (5)$$

$$H = \frac{\sigma}{\rho_l g} \quad (6)$$

$$F_l = \frac{1}{1+\frac{\nu_v}{\nu_l}\frac{32K}{D_{h,v}^2}\frac{A_w}{A_v}} \quad (7)$$

$$N_l = \frac{\rho_l \lambda \sigma}{\mu_l} \quad (8)$$

Using equation (2) and (4), Maximum Heat Transfer Qmax is expressed as equation (9) [6].

$$Q_{\max} = \frac{2KA_w(1+\eta)\cos\theta F_l}{r_p L_{eff}} N_l \quad (9)$$

From the equation (9), larger permeability K and smaller capillary radius r_p make higher Qmax.

Capillary radius rp of fiber wick is given by equation (10) [6].

$$r_p = \frac{d + \sqrt{32K/\varepsilon}}{2} \quad (10)$$

Where d is the fiber diameter.

By using carbon fiber wick which fiber radius d is much smaller than copper fiber wick, capillary radius can make smaller.

Carbon fiber wick cannot be fixed to copper pipe by sintering. By wrapping the carbon fiber wick by the copper fiber wick and sintering the copper fiber to the copper pipe, this combination wick becomes to be able to fix in the center of the copper pipe. Figure 3 shows a cross section view rough sketch of carbon fiber combined wick structure.

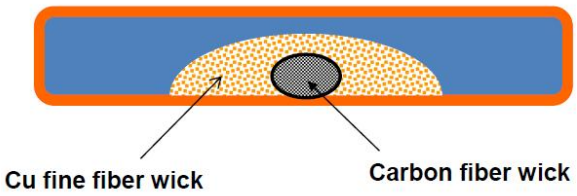


Fig. 3 Carbon fiber combined wick structure

Carbon fiber wick can get high capillary force by small capillary radius. On the other hand, permeability K will be small and liquid flow pressure drop will be large. Therefore when carbon fiber wick is used for the fill length of heat pipe, liquid flow pressure drop becomes too high and it cannot improve Qmax. So carbon fiber wick is installed only the part of evaporation side of heat pipe.

Figure 4 shows the picture of internal heat pipe installed carbon fiber wick in the part of the full length. It can see Carbon fiber is wrapped into the Cu fine fiber wick and fixed to Cu pipe.

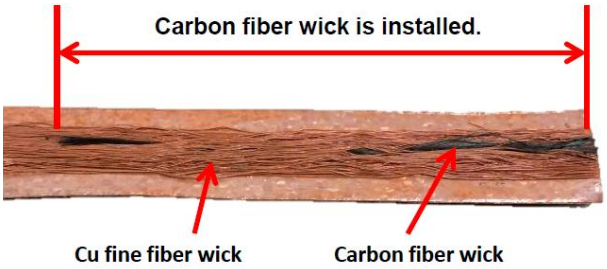


Fig. 4 the picture of internal heat pipe installed carbon fiber wick

3. TEST SAMPLE AND TEST SET-UP

Heat Pipe samples which have combination wick copper fine fiber and carbon fiber were made and thermal performance was compared with single copper fine fiber wick.

Original pipe diameter is 6mm and pressed thickness is 1.4mm. And the length is 2 kinds, 160mm and 270mm for each wick type. As for the carbon fiber combination wick, 1.2mm and 1.0mm thickness sample were made and evaluated.

Figure 5 shows the picture of test sample.



Fig. 5 Picture of test sample

And Table 1 shows the list of test sample.

Table 1 List of test sample

Sample No.	Original Diameter [mm]	Press thickness [mm]	Length [mm]	Wick type
No.1	6	1.4	160	Copper fine fiber
No.2			270	
No.3			160	Combination wick copper fine fiber and carbon fiber
No.4			270	
No.5		1.2	160	
No.6			270	
No.7		1.0	160	
No.8			270	

Figure 5 shows the thermal test set-up.

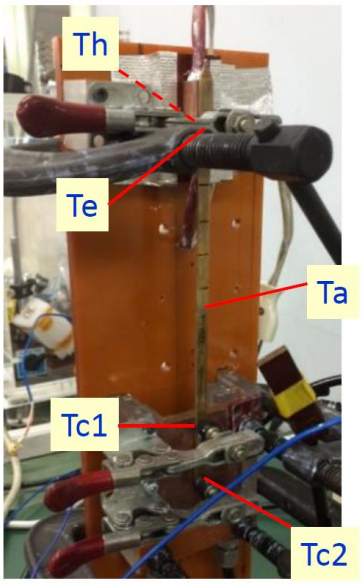


Fig. 5 Thermal test set-up

Cartridge heater embedded in the 40mm x 12mm copper block is used as the heat source. Heating length of heat pipe is 40mm. As the water-cooling condenser, copper block consists of water circulation path is used. Condensation length of heat pipe is adjusted to 60mm.

Temperature measurement points are as follows.

Th : Temperature of the heater surface

Te : Temperature of the evaporation part of heat pipe

Ta : Temperature of the adiabatic part of heat pipe

Tc1, Tc2: Temperature of the condensation part of heat pipe

The posture of the thermal performance test was done by both of horizontal and vertical top heat mode.

And temperatures at all the points are recorded until the temperature at the evaporator becomes steady. All the thermal tests have been done with adjusting adiabatic temperature to 60 Celsius. In

this paper, we mentioned this temperature as the operating temperature of the heat pipe.

4. RESULTS AND DISCUSSION

Evaluation of performance is done based on the heat pipe thermal resistance, Rhp that is calculated by the following equation (11).

$$R_{hp} = R_{ec} = \frac{(T_e - T_{c2})}{Q} \qquad (11)$$

Here, Q is the heat input.

Figure 6 shows the thermal performance comparison data between copper fine fiber wick and carbon fiber combination wick for the sample of 1.4mm thickness and 160mm length at horizontal posture.

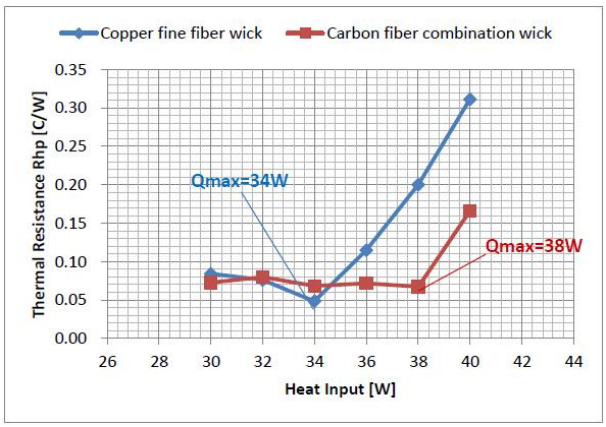


Fig. 6 Thermal performance comparison data between copper fine fiber wick and carbon fiber combination wick for the sample of 1.4mm thickness and 160mm length at horizontal posture

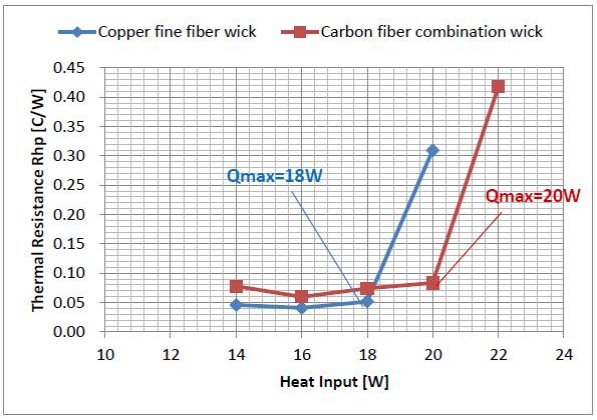


Fig. 7 Thermal performance comparison data between copper fine fiber wick and carbon fiber combination wick for the sample of 1.4mm thickness and 270mm length at horizontal posture

And Figure 7 shows the thermal performance comparison data between copper fine fiber wick and carbon fiber combination wick for the sample of 1.4mm thickness and 270mm length at horizontal posture.

Both results show that the Qmax of carbon fiber combination wick is about 10% higher than copper fine fiber wick. The value of thermal resistance is almost same level and the difference between each wick type was not seen.

Figure 8 shows the thermal performance comparison data between copper fine fiber wick and carbon fiber combination wick for the sample of 1.4mm thickness and 160mm length at vertical top heat mode.

And Figure 9 shows the thermal performance comparison data between copper fine fiber wick and carbon fiber combination wick for the sample of 1.4mm thickness and 270mm length at vertical top heat mode.

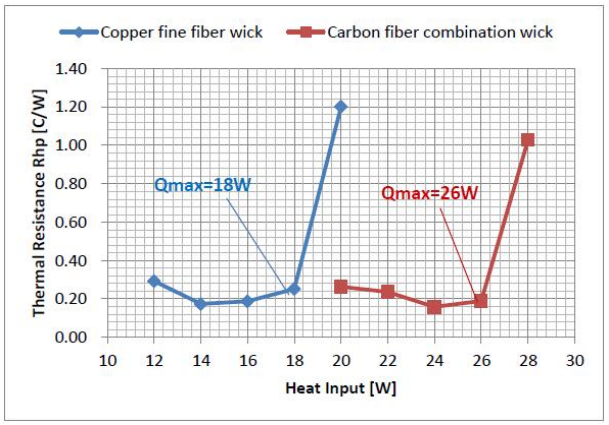


Fig. 8 Thermal performance comparison data between copper fine fiber wick and carbon fiber combination wick for the sample of 1.4mm thickness and 160mm length at vertical top heat mode

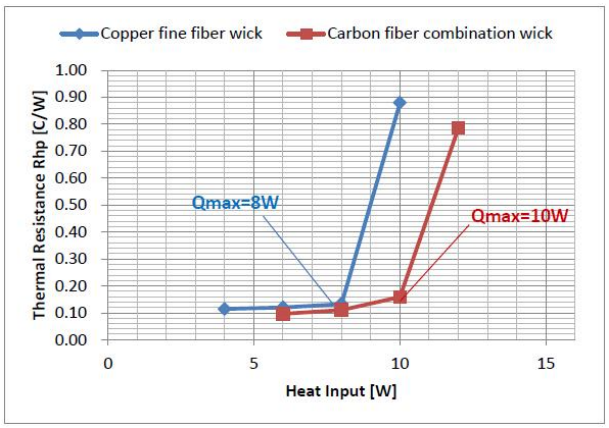


Fig. 9 Thermal performance comparison data between copper fine fiber wick and carbon fiber combination wick for the sample of 1.4mm thickness and 270mm length at vertical top heat mode

The improvement effect for Qmax by carbon fiber combination wick can see more clearly at vertical top heat mode. The result of 160mm length sample shows that it obtained about 45% higher Qmax than copper fine fiber wick. Even in the result of longer length 270mm sample, Qmax of carbon fiber combination wick is about 25% higher than copper fine fiber wick.

Figure 10 shows the thermal performance test result in length 160mm of the various thickness samples of the carbon fiber combination wick.

And Figure 11 shows the thermal performance test result in length 270mm of the various thickness samples of the carbon fiber combination wick.

When the heat pipe thickness becomes thin, Qmax will be small. From these results, even 1mm thickness, Qmax of 160mm length is 20W and Qmax of 270mm is 10W. It will be useful for the thin mobile note-book PC cooling.

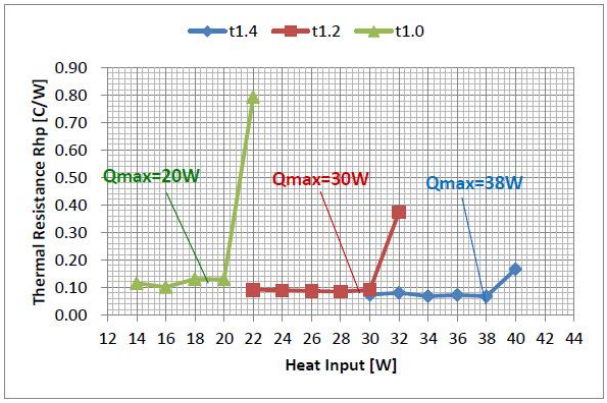


Fig. 10 thermal performance test result in length 160mm of the various thickness samples of the carbon fiber combination wick

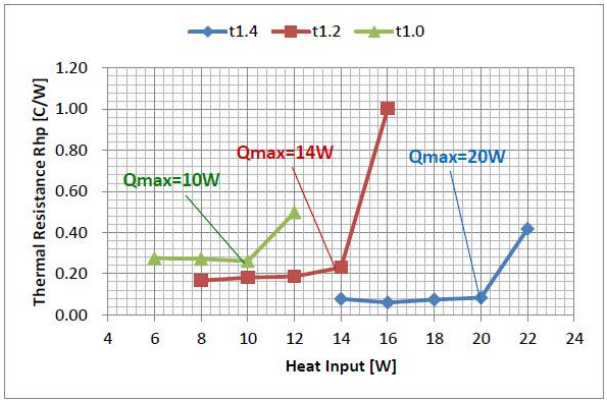


Fig. 11 thermal performance test result in length 270mm of the various thickness samples of the carbon fiber combination wick

Figure 12 shows calculation result of (QL)max. It is calculated by equation (2) and the test results shown in Fig. 10 and Fig.11. It can be seen (QL)max is proportional to the thickness of the heat pipe.

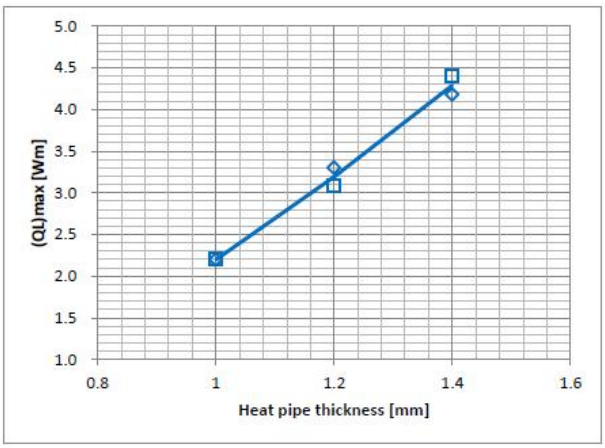


Fig. 12 Calculation result of (QL)max.

2. CONCLUSIONS

To improve thermal performance of heat pipe, new wick structure by using carbon fiber which can make the capillary radius smaller was experimented.

Carbon fiber combination wick was provide about 10% higher Qmax than copper fine fiber wick at horizontal posture. And the improvement effect for Qmax by carbon fiber combination wick can see 25~45% at vertical top heat mode.

The value of thermal resistance is almost same level and the difference between each wick type was not seen.

Even 1mm thickness and 270mm long heat pipe, Qmax of carbon fiber combination wick still can keep 10W.

It will be useful for the thin mobile note-book PC cooling.

NOMENCLATURE

A : Cross-sectional area (m^2)
D : Dimeter (m)
d : Fiber diameter (m)
F : Body force (N)
H : Wicking height factor (m^2)
K : Permeability (m^2)
L : Length (m)
N : Transport factor (Wm^{-2})
P : Pressure (Pa)
Q : Heat input (W)
QL : Heat transport factor (Wm)
R : Thermal resistance (K/W)

r : Radius (m)
T : Temperature (K)
β : Heat pipe orientation with respect to gravity (rad)
ε : Porosity
η : Gravity factor
θ : Contact angle (rad)
λ : Heat of vaporization (Jkg^{-1})
μ : Viscosity (Nsm^{-2})
ν : Kinematic viscosity (m^2s^{-1})
ρ : Density (kgm^{-3})
σ : Surface tension (Nm^{-1})

REFERENCES

[1] Ahamed M. S., Mochizuki M., Saito Y., Mashiko K., Mabuchi T., Horiuchi Y., "Experimental Study of Thin Flat Heat Pipe with a Special Fiber Wick Structure", Proc. of the 9th Int. Heat Pipe Symposium, Kualalumpur, Malaysia, Nov. 80-85, 2008.

[2] Ahamed M. S., Mochizuki M., Saito Y., Mashiko K., Kawahara Y., Tahara Y., "Investigation of Thermal Performance of Thin Heat Pipe with Fiber Wick Structure", 48th National Heat Transfer Symposium, Okayama, Japan, Jun 01-03, 2011.

[3] Ahamed M. S., Mochizuki M., Saito Y., Mashiko M., Kawahara Y. and Tahara Y., "Experimental and Theoretical Study of the Dominating Limiting Factors in Thin Heat Pipe with Fiber Wick Structure", 10th International Heat Pipe Symposium, Taipei, Taiwan, Nov. 6-9, 2011.

[4] Ahamed M. S., Mochizuki M., Saito Y., "Experimental & Theoretical Study of the Dominant Limiting Factors in Thin Heat Pipe with Fiber Wick Structure", Thermal Engineering Conference, Kumamoto, Japan, Nov17-18, 2012.

[5] Ahamed M. S., Mochizuki M., Saito Y., Mashiko K., "Hot Spot Elimination By Thin And Smart Heat Spreader", InterPACK2015 & ICNMM2015, San Francisco, CA, USA, July 6-9, 2015

[6] E. A. Skrabek., W. B. Bienert., "Heat Pipe Design Handbook", Contract No.NAS9-11927, Aug. 1972.

Author Index

***Author index is sorted by the authors' last names.**

Name	Page
A	
Ababneh, Mohammed Taha	*401*
Abdulshaheed, Ahmed	*59*
Agostini, Bruno	*226*
Agostini, Francesco	*226*
Ahamed, Mohammad Shahed	*79, 440, 404*
Ai, Bangcheng	*30*
Akbarzadeh, A.	*85*
Akbarzadeh, Aliakbar	*281*
Albertin, Thomas	*33, 109*
Alekseik, O.	*402*
Alekseik, Yevheniy Serhiyovych	*402*
An, Yongchan	*233*
Anderson, William G.	*96, 401*
Andraka, Charles E.	*37*
Antonov V.	*182*
Araneo, Lucio	*224, 225*
Aranguren, Patricia	*34*
Ariantara, Bambang	*444*
Asfer, Md.	*221*
Astrain, David	*34*
Ayel, Vincent	*224, 225, 242*
B	
Bae, Jaeyoung	*187, 334*
Bai, Lizhan	*30*
Balykin, M.	*182*
Barremaecker, L.	*111*
Baturkin, V.	*402*
Baturkin, Volodymyr	*402*
Beard, Derek	*96*
Benselama, Adel Mustapha	*230*
Bertin, Yves	*224, 225, 230, 242, 289*
Bertossi, Rémi	*225*
Betancur, Luis Alonso	*232*
Bhattacharya, Bishakh	*401*
Billet, Cyrille	*143*
Biswas, Gautam	*108*
Bodjona, Serge Hèzièwè	*289*
Boersma, Bendiks Jan	*72*
Bonjour, Jocelyn	*250*
Boo, Joon Hong	*32, 443*
Borca-Tasciuc, Diana-Andra	*425*
Buz, V.	*182*

Name	Page
C	
Caldas, Diogo M. M.	*305*
Campo, Darren	*405*
Caney, Nadia	*258*
Cao, Jingyu	*279*
Carbajal, Gerardo J.	*418*
Celik, Metin	*72*
Celotti, Luca	*402*
Cha, Dowon	*233*
Chang, Chao	*226*
Chang, Wei	*59*
Chattopadhyay, Himadri	*108*
Chaudhary, S. K.	*31*
Chen, Guangming	*228*
Chen, Jhe-kai	*433*
Chen, Jiajia	*338, 402*
Chen, Siyuan	*30, 35*
Chen, Xiao	*443*
Chen, Yang	*105*
Chi, Ri-Guang	*282, 283*
Chiamulera, Maria Eduarda	*32*
Ching, Chan Y.	*402*
Cho, Dong-Hyun	*344*
Cho, Hyokjin	*178*
Choi, Jeehoon	*425*
Choi, Jong Won	*350*
Choi, K. S.	*444*
Chuan, Y. H.	*109*
Chun, Won Pyo	*350*
Chung, Won Bok	*190*
Chung, Won-Sik	*282, 283*
Cisterna, Luis Hernán Rodríguez	*297, 305*
Coulloux, Jérôme	*33, 109*
D	
Daimaru, Takurou	*234, 264*
Dandaleix, L.	*111*
Date, A.	*85*
De Jong, Wiebren	*72*
Deng, Haoren	*222*
Ding, Lai Chet	*85*
Ding, Ting	*105*
Duan, Bin	*110*
Dufraisse, David	*242*
Duplat, Jérôme	*223*
Dupont, Vincent	*143*
Dussinger, Peter M.	*285*
Dutour, Sebastien	*108*

Name	Page
E	
Ebeling, Johann-Christoph	280
Ercolani, Eric	223
Eskilson, Per	364
Ewing, Dan	402
F	
Fabrègue, Damien	107
Fantozzi, F.	313
Feng, Wei	443
Figus, Christophe	111
Filippeschi, Sauro	225, 232, 313
Fioriti, Davide	225
Fourgeaud, Laura	223
Fu, Yucan	338, 402
Fukuda, Seisuke	224
Fumoto, Koji	271
G	
Gam, Kee Sool	106
Gan, Zhihua	222
Gao, Xu	228
Geffraye, Geneviève	258
Gerner, Henk Jan van	221
Ginley, David	403
Giraudon, Rémi	107
Girault, Manuel	289
Glogiod, Damien	258
Golikov, A.	182
Goncharov, Konstantin	182
Goncharov, K.	182
Gracovich, L. P.	279
Grakovich, Leonid	90
Gremillard, Laurent	107
Gruss, Jean antoine	258
Gully, Philippe	223
Guo, Yuandong	117
Gutkin, Adik R.	412
Gweon, Chan-Yong	344
H	
Habert, Mathieu	226
Han, Dongyang	222
Han, Hantao	30
Han, Xiaohong	228
Hardin, Corey	403
Hatakenaka, Ryuta	138
He, Jiang	105, 117
He, Song	131
Hideyama, Fumihiko	434
Hill, J.	111
Ho, T.	402
Hou, Guanyu	90
Hu, Hao	386
Hu, Longfei	30, 35
Hua, Chao	228
Huang, Bin-Juine	109
Huang, Guanghan	59
Huo, Yuhua	105
Hwang, Eonhwa	187, 334
Hwang, Seon Hong	190
I	
Inamura, Takao	271
Ivanov, Arkadiy	217
Iwata, Naoko	198, 224
J	
Jadhav, Tushar Shivajirao	29
Jaipurkar, Tanmay	401
Jandačka, Jozef	34
Jang, Dong Soo	233
Jeon, Sora	29
Jeong, Sangkwon	178
Jeong, Seon-Yong	282
Ji, Jie	443
Ji, Yulong	226
Ji, Zhongli	370
Jiang, Chi	110
Jiang, Pengpeng	386
Jiao, Bo	222
Jiao Dongsheng	279
Jin, Lingxue	178
Jin, Yi	443
Joo, Hong-Jin	36
Joung, Wukchul	33, 36, 106
Jung, Eui Guk	443
K	
Kabelac, S.	280
Kaled, Ahmed	108
Kandhekar, Sameer	221, 225, 250, 401
Kang, Hwankook	425
Kang, Shung Wen	227, 281
Kant, Puspit	401
Kato, Taro	353
Katsuta, Masafumi	353
Kaviany, M.	3
Kavoosi Balotaki, Hassan	231
Kawahara, Yoji	79, 446
Kawanami, Tsuyoshi	271
Khairnasov, Sergii	37
Khandare, S. S.	31
Khandekar, Sameer	255
Kim, Byeong Chan	229
Kim, Daejoong	229
Kim, Dobin	229
Kim, Dongwoo	233
Kim, Hyun Gon	32

Name	Page
Kim, Ji Hoon	229
Kim, Jong Soo	187
Kim, Junha	187
Kim, Juno	230
Kim, Minsung	284
Kim, Sang Sik	4, 190
Kim, Sung Il	350
Kim, Sung Jin	229, 230
Kim, Sungbok	187, 334
Kim, Yongchan	233
Kim, Yong-Gyoo	106
Kim, Yoon Sung	190
Kirdnaimongkol, Chayatis	79
Koito, Yasushi	67, 280, 434, 435
Korzhov, K.	182
Korzhov, Kirill N.	412
Kravets, V.	402
Kravtsov Dmitry	360
Kruse, H.	280
Kulakov, Andrei	151
Kumar, Siddhartha	221
Kwak, Hee-Youl	36
Kwon, Su Yong	33

L

Ladekar, Chandrakishor Laxman	31
Lapensee, S.	151
Lappas, Petros	281
Laurent, Barremaecker	404
Lee, J. H.	444
Lee, Jae Young	283
Lee, Ji-su	282
Lee, Joohyun	36
Lee, Jungseok	229
Lee, Key-Bock	282, 283
Lee, Kye Jung	350
Lee, Sang Yong	4
Lee, Wook-Hyun	282
Lee, Young-Soo	282
Lefevre, Frederic	250
Lenhard, Richard	34
Leu, Tzong-Shyng	223
Li, Chen	59
Li, Congming	445
Li, Guiqiang	443
Li, Heng Yi	281
Li, Ji	222, 445
Li Jing	279
Li, Longnan	229
Li, Sidi	445
Li, Wei	35
Li, Xiao Jun	228
Li, Xueqiang	443
Li, Zhendong	282
Li, Zhiwei	445
Li, Zhixin	445
Liao, Wei Chun	379
Lim, Hyunjeong	284
Lin, Guiping	30, 105
Lin, Wei-keng	433
Ling, Xiang	329
Lips, Stéphane	107
Liu, Wei	110, 131
Liu, Zhichun	110
Lu, Qin	30
Lu, Ying-Chang	227
Luckmann, S.	280
Luo, Xiaobing	110
Luo, Yi	445
Lv, Lucang	222
Lv, Song	443
Lv. Wei	35

M

Ma, Hongbin	226
Ma, Limin	370
Ma, Tingting	403
Maehara, Hiroyuki	67
Maire, Eric	223
Malcho, Milan	34
Mameli, Mauro	225
Mangini, Daniele	225
Mantelli, Marcia Barbosa Henriques	32, 297, 305, 313, 364
Manzoni, Miriam	364
Marengo, Marco	224, 364
Marzorati, Pietro	224
Mashiko, Koichi	38, 404, 433
Maydanik, Mikhail Yu.	217
Maydanik, Yury F.	217
Mehta, Balkrishna	225
Memponteil, Alain	258
Mera, Juan Pablo Florez	32
Mi, Min	105
Miao, Jian-Yin	16, 30, 105, 117, 282
Mikael, Mohaupt	404
Milanez, Fernando Henrique	297, 305, 313
Milanez, Kênia Warmling	297
Mishkinis, Donatas	151, 167
Miyakita, Takeshi	138
Miyazaki, Yoshiro	224
Mo, Qing	117
Mochizuki, Masataka	38, 46, 79, 124, 404, 433
Moon, Guee-Won	178
Moon, S. H.	37, 444
Mun, Hanseok	233

N

Nagai, Hiroki	234
Nagano, Hosei	106, 107, 159
Nakamura, Kazuya	159
Nekrashevych, Iaroslav	231
Nguyen, Thang	38, 46, 79
Nguyen, Tien	46, 79
Nicolle, Thomas	143
Nikolayev, Vadim S.	231, 223
Ning, Xianwen	105

Name	Page
Nishchyk, Oleksandr	*37*
Nishikawara, Masahito	*106*
Nonoshita, Shuto	*434, 435*
Nouri-Borujerdi, A.	*54, 394*
O	
Odagiri, Kimihide	*107*
Ogawa, Hiroyuki	*198*
Oh, Intaek	*187*
Oh, Sang Hyun	*350*
Okamoto, Atsushi	*138*
Olsen, Michele	*403*
Orr, Bradley Glenn	*85*
Oshman, Christopher	*403*
P	
Panin, Yuriy V.	*412*
Paralikar, Siddharth	*401*
Parilla, Philip	*403*
Park, Cheol Min	*190*
Park, Jong-Chan	*282, 283*
Park, Sangjin	*187, 334*
Park, Yoonwoo	*37, 444*
Paulussen, Geert	*72*
Pei, Gang	*279*
Peng, Hao	*329*
Pfotenhauer, John	*222*
Phan, Thanh-Long	*124, 433*
Pouryoussefi, Sam M	*110*
Prado, Paula	*151*
Prado-Montes, Paula	*167*
Prat, Marc	*106*
Pronk, Pepijn	*72*
Putra, Nandy	*444*
Q	
Qu, Jian	*228*
Qu, Wei	*227*
R	
Raay, Thomas van	*38*
Rabetsky, M. I.	*279*
Rao, Manoj	*250*
Rea, Jonathan	*403*
Reist, Daniel	*285*
Remeli, M. F.	*85*
Rhi, Seok-Ho	*444*
Rhodes, Matthew	*232*
Riele, Gert Jan te	*31*
Rodin, Alexei	*279*
Rodríguez, Antonio	*34*
Romestant, Cyril	*224, 225, 242*

Name	Page
S	
Saidi, Mohammad Hassan	*231*
Saito, Yuji	*38, 46, 79, 124, 404, 433, 446*
Sartre, Valérie	*107*
Sato, Kaoru	*280*
Sato, Yuji	*38, 46, 79, 124, 404, 433, 446*
Savchenkova, Natalia	*360*
Savino, Raffaele	*271*
Seo, Joseph	*283*
Shang, Linlin	*370*
Shao, Shuangquan	*284*
Shapovalov, Alexander	*279*
Sharma, Bharat. B.	*108*
Samanta, Sudip. K.	*108*
Shen, Houfa	*338, 402*
Shibano, Yasuko	*198*
Shimada, Daisuke	*67*
Shu, Shili	*35, 90*
Siegel, Nathan	*403*
Singh, B.	*85*
Singh, Randeep	*38, 46, 124*
Slongo, Leonardo Kessler	*232*
Srinivasan, Vyas	*221, 250*
Stevens, Mark C.	*285*
Sturnack, Laurent	*72*
Su, Wei Chi	*379*
Suenaga, Risa	*353*
Sugita, Hiroyuki	*138*
Sun, Qin	*228*
Sun, Xiao	*222*
Sung, B.	*425*
Suzuki, Ayaka	*280*
T	
Taft, Brent	*232*
Tapia, Luis	*418*
Tarau, Calin	*96, 401, 405*
Tavares, Estevan Grosch	*297*
Tian, Changqing	*284*
Tian, Sicong	*35, 90*
Toberer, Eric	*403*
Tomimura, Toshio	*67, 280, 434, 435*
Tong, Cunzhu	*35, 90*
Torres, Alejandro	*151*
Torresin, Daniele	*226*
Tsai, Meng Chang	*281*
U	
Uhlmann, Tiago Walter	*297, 364*
V	
Van Oost, Stéphane	*404*
Vasiliev, Leonard Leonidovich	*35, 90, 279*

Name	Page
Videcoq, Etienne	*289*
Vielra De Paiva, Kleber	*232*
Voirand, Antoine	*230*
W	
Wang, Hung	*227, 281*
Wang, Lijie	*35, 90*
Wang, Lu	*105, 117*
Wang, Qian	*228*
Wang, Shunhao	*222*
Wang, Xiaodong	*445*
Wang, Xiaoyuan	*403*
Wang, Xuehui	*228*
Wang, Yabo	*209*
Wang, Yunyun	*279*
Wei, Jie	*443*
Weyant, Jens	*405*
Wits, Wessel	*31, 221*
Wu, Cheng-Han	*223*
Wu, Fong Hao	*281, 379*
Wu, Hao	*35, 90*
Wu, Ke	*282*
X	
Xie, Minghui	*227*
Xue, Zhi Hu	*30, 227, 322*
Y	
Yakomaskin, Alexander A	*203*
Yamada, Tadao	*46*
Yamagami, Koki	*271*
Yang, H.M.	*37*
Yang, Jinguo	*131*
Yang, Lin	*329*
Yang, P. E.	*109*
Yang, Rui	*30*
Yau, Y. H.	*85*
Yim, Kwangbin	*425*
Yin, Xiaoying	*370*
Yokoyama, Yuichi	*433, 446*
Yoshida, Shuhei	*234, 264*
Yu, Jijun	*322*
Yun, Sang-Hun	*344*
Z	
Zaripov, Vladlen	*37*
Zeng, Jinling	*403*
Zhang, Hainan	*284*
Zhang, Hongxing	*105, 117*
Zhang, Qingzhen	*226*
Zhang, Xiao	*386*
Zhang, Yuwen	*110*
Zhao, Jianfu	*282*
Zhao, Pinghui	*279*
Zhao, Shuo	*209*
Zhao, Zhongchao	*386*
Zheng, Haoce	*228*
Zheng, Mingzhu	*209*
Zhou, Chuanpeng	*445*
Zhou, Guohui	*222*
Zhou, Rui W.	*329*
Zhu, Kai	*209*
Zhu, Yuezhao	*403*
Zhuravlyov, A. S.	*279*
Zwier, Marijn P.	*221*